K.A. Gschneidner, Jr.,
J.-C.G. Bünzli and V.K. Pecharsky
Editors

HANDBOOK ON THE PHYSICS AND CHEMISTRY OF RARE EARTHS

Volume 40

North Holland

HANDBOOK ON THE PHYSICS AND CHEMISTRY
OF RARE EARTHS
VOLUME 40

HANDBOOK ON THE PHYSICS AND CHEMISTRY OF RARE EARTHS

✠Deceased.

HANDBOOK ON THE PHYSICS AND CHEMISTRY OF

RARE EARTHS

VOLUME 40

EDITORS

Karl A. GSCHNEIDNER, Jr.
Member, National Academy of Engineering
The Ames Laboratory, U.S. Department of Energy, and
Department of Materials Science and Engineering
Iowa State University
Ames, Iowa 50011-3020
USA

Jean-Claude G. BÜNZLI
Swiss Federal Institute of Technology, Lausanne (EPFL)
Laboratory of Lanthanide Supramolecular Chemistry
BCH 1402
CH-1015 Lausanne
Switzerland

Vitalij K. PECHARSKY
The Ames Laboratory, U.S. Department of Energy, and
Department of Materials Science and Engineering
Iowa State University
Ames, Iowa 50011-3020
USA

Amsterdam • Boston • Heidelberg • London • New York • Oxford
Paris • San Diego • San Francisco • Singapore • Sydney • Tokyo
North-Holland is an imprint of Elsevier

North-Holland is an imprint of Elsevier
Radarweg 29, PO Box 211, 1000 AE Amsterdam, The Netherlands
The Boulevard, Langford Lane, Kidlington, Oxford OX5 1GB, UK

First edition 2010

British Library Cataloguing in Publication Data
A catalogue record for this book is available from the British Library

Library of Congress Cataloging-in-Publication Data
A catalog record for this book is available from the Library of Congress

ISBN: 978-0-444-53220-6
ISSN: 0168-1273

Printed and Bound in Great Britain

10 11 12 10 9 8 7 6 5 4 3 2 1

PREFACE

Karl A. Gschneidner Jr., Jean-Claude G. Bünzli, Vitalij K. Pecharsky

These elements perplex us in our reaches [sic], baffle us in our speculations, and haunt us in our very dreams. They stretch like an unknown sea before us – mocking, mystifying, and murmuring strange revelations and possibilities.

Sir William Crookes (February 16, 1887)

This volume of the *Handbook on the Physics and Chemistry of Rare Earths* adds four chapters to the series which focus on stunning compounds and unusual spectroscopic methods, describing a mix of experimental and theoretical data. It opens with a review (Chapter 244) on magnetic circular dichroism (MCD), a very informative spectroscopy, although not yet widespread. The following chapters illustrate the state of the art in subjects as varied as molecular lanthanide clusters, the synthesis of which still relies on random self-organization (Chapter 245), low-valence organometallic compounds which were long thought to be too unstable to be isolated (Chapter 246), and lanthanide and actinide polynuclear helicates in which organic ligand strands wrap helically by self-assembly around metal centers (Chapter 247). Each chapter also discusses present and potential applications of the technique or compounds reviewed.

CHAPTER 244. MAGNETIC CIRCULAR DICHROISM OF LANTHANIDES

By CHRISTIANE GÖRLLER WALRAND AND LYNDA FLUYT
Katholieke Universiteit, Leuven, Belgium

Magnetic circular dichroism (MCD) measures the difference in absorption of left and right circularly polarized light. MCD is complementary to the classical absorption technique but much more powerful since the shape, sign, and magnitude of the experimental signals can be exploited to gain structural and electronic information. The theory of absorption and MCD is discussed in detail for both magnetic and induced electric dipole transitions of lanthanides. Emphasis is put on subtle matters like

conventions for phases, normalization, factors for randomly oriented molecules, the sign properties, and dimension of quantities. The latter point is quite crucial in a field in which the quantities used often have unusual units and the care with which the authors have dealt with this aspect will be very useful to the reader. Furthermore, C. Görller-Walrand and L. Fluyt carefully establish the relationship between theoretical and experimental quantities and illustrate it with examples pertaining to D_{2d}, C_{4v}, and D_{3h} symmetry. In particular, information on the coordination environment of the metal ion can be gained from the shape and sign of the MCD signal when interpreted in terms of group theory and associated selection rules for induced electric dipole transitions. In this context, the magnetic dipole transition $^5D_1 \leftrightarrow {}^7F_0$ of Eu^{III} is proposed by the authors as reference for scaling MCD intensities. Finally, the MCD spectra of aqueous solutions of 10 lanthanide perchlorates are displayed together with the corresponding absorption spectra and transitions that are listed with their full parameters; this constitutes a useful database for experimental spectroscopists.

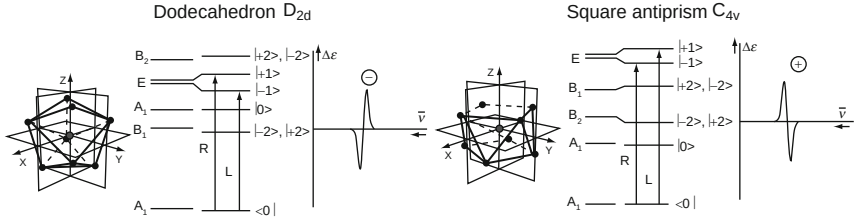

CHAPTER 245. CLUSTER COMPOUNDS OF RARE-EARTH ELEMENTS

By Z. ZHENG
University of Arizona, Tucson, USA

Polynuclear complexes of rare earths (R) featuring cluster-like, polyhedral core structures have quietly emerged in the past two decades. The repetitive appearance of certain prevalent core motifs and the envisioned applications of these otherwise elusive species have stimulated the development of methodologies for their rational and reproducible synthesis. This chemistry has now developed into an exciting area of rare-earth research which is presented in a systematic way by Z. Zheng. Although a number of interesting and potentially useful applications have been demonstrated, this field is still dominated by its synthetic and structural aspects so that rare-earth clusters are described in this chapter according to their synthetic methods and distinct compositional and structural features.

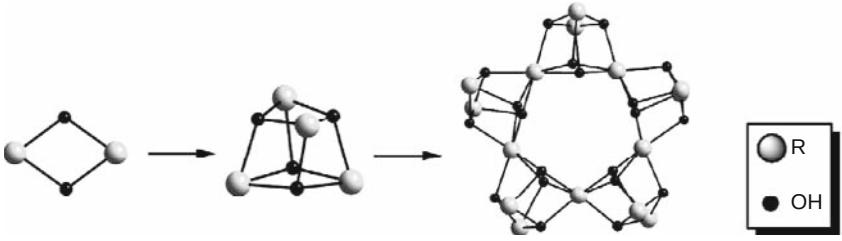

The clusters can be assembled either under conditions typical of organometallic synthesis or by deliberate hydrolysis. The first type of synthesis is achieved through aggregation of recognizable mononuclear units with the help of multidentate organic bridging and/or chelating ligands. The other clusters are obtained by deliberate hydrolysis of the metal ions, generally supported by hydrolysis-limiting organic ligands. Connections between individual metal atoms within the cluster core are provided by bridging oxo and hydroxo ligands. Besides their appealing structures, many of these clusters display interesting properties, and may be envisaged as precursors for oxide-based advanced materials, as synthetic nucleases for the hydrolytic cleavage of nucleic acids, as novel contrast-enhancing agents for biomedical imaging, or as catalysts for promoting novel chemical transformations. Research activities in this particular rare-earth chemistry are thus expected to grow in the future with possible discovery of new species having unusual structures and useful applications, despite the fact that such clusters still cannot be planned and are inevitably characterized by random self-organization. The chapter ends by a table in which proven applications of rare-earth clusters are listed.

CHAPTER 246. MOLECULAR CHEMISTRY OF THE RARE-EARTH ELEMENTS IN UNCOMMON LOW-VALENT STATES

By FRANÇOIS NIEF
École Polytechnique, Palaiseau, France

François Nief's chapter reports on the molecular chemistry of rare earths in uncommon low-valence states: zerovalent, monovalent, and also divalent, but to the exclusion of Sm^{II}, Eu^{II}, and Yb^{II} which have been widely studied and are thus considered as common. The relevance of this subject stems from the discovery in the past 10–15 years of stable molecular

complexes in which the rare-earth element is in an uncommon low-valence state. The chapter describes the molecular reactivity of NdI_2, DyI_2, and NdI_2, including their applications in organic and polymer chemistry, followed by the chemistry of isolable molecular (mostly organometallic) complexes of La^{II}, Ce^{II}, Nd^{II}, Dy^{II}, and Tm^{II}. All complexes are very powerful reducing agents, the most highly reactive being those of La^{II}, Ce^{II}, and Nd^{II}. There are also quite a number of rare-earth-based systems which are able to reduce dinitrogen into a coordinated diazenide dianion: these systems involve not only divalent species but also trivalent rare-earth alkoxides, amides, or cyclopentadienides in combination with a chemical reducing agent (usually an alkali metal). The important question of the presence of uncommon divalent states in this latter case is still unsettled.

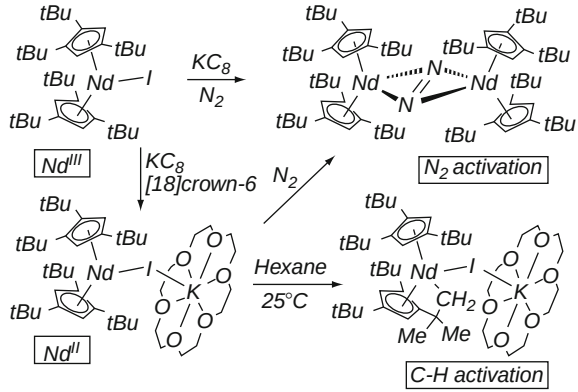

In the specific case of scandium, mono- and mixed-valence species can also be isolated together with divalent complexes; for instance, a Sc^{I} organometallic compound could be obtained under relatively mild conditions. Finally, the author describes the few known zerovalent bis(arene) rare-earth complexes which have been obtained by co-condensation of arenes or heteroarenes with metal vapors. In his conclusion, F. Nief notes that the low-valence molecular chemistry of rare earths, which was once thought to be restricted to divalent samarium, europium, and ytterbium, has been extended to several other rare earths, as well as to lower valence oxidation states. It is the opinion of the author that this research area is likely to find fascinating developments in a near future.

CHAPTER 247. SELF-ASSEMBLED LANTHANIDE HELICATES: FROM BASIC THERMODYNAMICS TO APPLICATIONS

By CLAUDE PIGUET
Université de Genève, Geneva, Switzerland and
JEAN-CLAUDE G. BÜNZLI
École Polytechnique Fédérale de Lausanne (EPFL), Lausanne, Switzerland

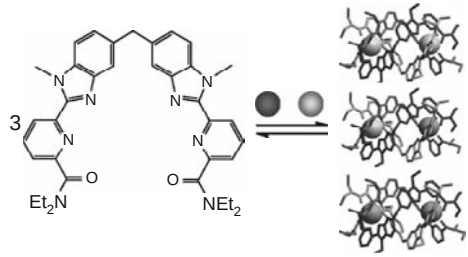

C. Piguet and J.-C. Bünzli draw the attention of the reader on the fascination for helical edifices and objects which appears to be as old as humanity, cf. the single-stranded helical construction of the Babel tower, the helical patterns displayed by the secondary structure of proteins pointed out by L. Pauling in 1951, or double-stranded DNA. In the mid-1980s, J.-M. Lehn relied on coordination bonds for helically wrapping ligand strands around a central axis defined by metal ions: helicate science was born.

This review focuses on the thermodynamically controlled self-assembly of lanthanide helicates of various nuclearity and metallicity. It firstly describes mononuclear precursors in order to set the bases for discussing size-discriminating effects, structural features in which weak π-stacking interactions play a prominent role, and photophysical properties. The next two chapters bring together concepts indispensable to the understanding of the formation of both homo- and heterometallic helicates, namely the principles of ligand design and the thermodynamics of the recognition processes; consequences on structural, magnetic, and optical properties follow suit. The central part of the review is devoted to the description of the site-binding model which relies on microscopic stability constants and parameters to model the thermodynamic stability of 4f helicates; the origin of the stability of several supramolecular edifices is unraveled on the basis of a fit of experimental stability constants with this model. When it comes to applications, 4f homometallic binuclear helicates are ideal luminescent probes for bioanalyses (e.g., DNA assays) and live cell imaging and sensing.

Modification of the ligand denticity (pentadentate instead of hexadentate) allows the assembly of nd–4f helicates which exhibit a rich variety of magnetic and spectroscopic properties combining the intrinsic features of both types of metal ions thanks to intermetallic communication within the helical molecules. The overview ends by describing helical structures found in coordination polymers, as well as some 5f helicates.

CONTENTS

This page intentionally left blank

CONTENTS OF VOLUMES 1–39

VOLUME 4: Non-metallic compounds – II
1979, 1st repr. 1984; ISBN 0-444-85216-6

VOLUME 5
1982, 1st repr. 1984; ISBN 0-444-86375-3

VOLUME 6
1984; ISBN 0-444-86592-6

VOLUME 7
1984; ISBN 0-444-86851-8

VOLUME 8
1986; ISBN 0-444-86971-9

VOLUME 9
1987; ISBN 0-444-87045-8

VOLUME 10: High energy spectroscopy
1987; ISBN 0-444-87063-6

VOLUME 11: Two-hundred-year impact of rare earths on science
1988; ISBN 0-444-87080-6

VOLUME 12
1989; ISBN 0-444-87105-5

VOLUME 13
1990; ISBN 0-444-88547-1

VOLUME 14
1991; ISBN 0-444-88743-1

VOLUME 15
1991; ISBN 0-444-88966-3

VOLUME 16
1993; ISBN 0-444-89782-8

VOLUME 20
1995; ISBN 0-444-82014-0

VOLUME 21
1995; ISBN 0-444-82178-3

VOLUME 22
1996; ISBN 0-444-82288-7

VOLUME 27
1999; ISBN 0-444-50342-0

VOLUME 28
2000; ISBN 0-444-50346-3

VOLUME 29: The role of rare earths in catalysis
2000; ISBN 0-444-50472-9

VOLUME 30: High-Temperature Superconductors – I
2000; ISBN 0-444-50528-8

VOLUME 31: High-Temperature Superconductors – II
2001; ISBN 0-444-50719-1

VOLUME 32
2001; ISBN 0-444-50762-0

VOLUME 37: Optical Spectroscopy
2007; ISBN 978-0-444-52144-6

VOLUME 38
2008; ISBN 978-0-444-52143-9

VOLUME 39
2009; ISBN 978-0-444-53221-3

INDEX OF CONTENTS OF VOLUMES 1–40

This page intentionally left blank

CHAPTER **244**

Magnetic Circular Dichroism of Lanthanides

Christiane Görller-Walrand and **Linda Fluyt**

Contents

Coordination Chemistry Division, Department of Chemistry, K.U. Leuven, Celestijnenlaan 200F, 3001 Heverlee, Belgium

Handbook on the Physics and Chemistry of Rare Earths, Volume 40
ISSN 0168-1273, DOI: 10.1016/S0168-1273(10)40004-5

List of Symbols and Abbreviations

β	Bohr magneton
ε	molar absorptivity
κ	absorption coefficient
λ	wavelength
μ	magnetic permeability in a non-absorbing medium
$\hat{\mu}$	complex magnetic permeability
μ_z	Zeeman operator

v	frequency
$\bar{v}$	wave number
θ	ellipticity
ρ	light polarization
ω	angular frequency
$\boldsymbol{\mathcal{A}}_1$	MCD parameter for the $\boldsymbol{\mathcal{A}}$ term
$\boldsymbol{\mathcal{B}}_0$	MCD parameter for the $\boldsymbol{\mathcal{B}}$ term
c	speed of light
$\boldsymbol{\mathcal{C}}_0$	MCD parameter for the $\boldsymbol{\mathcal{C}}$ term
CD	natural circular dichroism
d_A	degeneracy of level A
Dod	dodecahedron
DOM	damped oscillator model
$\boldsymbol{\mathcal{E}}$	energy
$\vec{\boldsymbol{E}}$	electric field
${}^{\mathrm{ED}}O = \vec{\boldsymbol{m}}$	(induced) electric dipole operator
$\vec{\boldsymbol{E}}_{\mathrm{mac}}$	macroscopic field
$\vec{\boldsymbol{E}}_{\mathrm{mic}}$	electric field including medium effects
f	oscillator strength
h	Planck's constant
$\vec{\boldsymbol{H}}$	magnetic field
$\boldsymbol{\mathcal{H}}_0$	unperturbed Hamiltonian
H_z	magnetic field along z
J	total angular momentum
k	Boltzmann's constant
l.c.p.	left circularly polarized light
M	magnetic quantum number
MCD	magnetic circular dichroism
MCPL	magnetic circular-polarized luminescence
${}^{\mathrm{MD}}O = \vec{\boldsymbol{\mu}}$	magnetic dipole operator
m_{e}	electron mass
MORD	magnetic optical rotation dispersion
n	refractive index in a non-absorbing medium
$\hat{n}$	complex refractive index
$\boldsymbol{\mathcal{N}}$	Avogadro's number
N_a	number of molecules per cm^3 on level a
ODA	oxidiacetate
ORD	natural optical rotation dispersion
r.c.p.	right circularly polarized light
$\vec{\boldsymbol{S}}$	Poynting vector
SAP	square antiprism
TCTP	tricapped trigonal prism

1. INTRODUCTION

In magnetic circular dichroism (MCD), the difference in absorption of left and right circularly polarized light is measured as a function of the energy ($\boldsymbol{\mathcal{E}}$) scale or any quantity related to it: wave number ($\bar{\nu}$), frequency (ν), angular frequency (ω) or wavelength (λ). Note that the use of wavelength in spectroscopy is always dangerous, as λ is inversely proportional to the energy and the relationship between energy and λ is obviously not linear.

The phenomenon of MCD is induced in all matter by applying a uniform longitudinal magnetic field (H_z). This means that the field is applied parallel to the propagation direction of the light (z). Further on, the field strength in this direction will be indicated by H. From an experimental point of view a split coil electromagnet (± 1 tesla) or supermagnet (± 10 tesla) is necessary to allow the light to reach, through several windows, the sample holder. From a theoretical point of view the Zeeman perturbation is therefore applied along the z-axis. This will completely lift the degeneracy of the crystal field electronic state manifold according to the magnetic quantum number (M), or any combination of the quantum numbers that describe the crystal field states. In the theory section, it will be seen that the zero-order crystal field functions are best chosen so that they diagonalize the Zeeman operator.

In that section, it will also become evident that MCD can only be measured along an optical axis, thus on uniaxial or cubic crystals, or solutions (in which the molecules are randomly oriented). This means that the propagation direction of the light (z), the magnetic field (H_z) and the optical axis of the molecule or crystal are parallel to each other and that the light is vibrating in the xy plane. If the molecule and the crystal have not the same principal axis, a transformation must be performed according to the reference axis system with z as propagation direction (see Section 6).

Left and right circularly polarized light is applied alternatively by a piezoelectric device (or in the past a Pockel cell) and the transitions between the Zeeman components lead to signals that are substracted from each other: $\Delta\varepsilon = \varepsilon_{\mathrm{l}} - \varepsilon_{\mathrm{r}}$ (molar absorptivity for left and right circularly polarized light). In this sense, MCD is fully complementary to classical absorption spectrometry. MCD, however, is much more powerful as the experimental signals are characterized by a shape, a sign and a magnitude. They give information on the characterization of the wave functions and thus electronic states that are labelled according to the M quantum numbers or a combination of them. Through their shape properties, the MCD signals point unambiguously to degenerate states. Their sign property is also very important as will be described later. The magnitude of the signal is the Zeeman splitting that is related to the magnetic moment by βH.

The aim of this chapter is to link the MCD theory to the lanthanide theory for crystal field splitting and transition intensity. We have based the theory on the very few papers that are due to pioneers in the field. These are for MCD: (Buckingham and Stephens, 1966; Stephens, 1976), the book (Piepho and Schatz, 1983), for the lanthanide theory: (Judd, 1962), the book (Wybourne, 1965) and for the experimental data: (Carnall, 1979). With humility we will also refer to our previous reviews (Görller-Walrand and Binnemans, 1996, 1998) so that we remain as much as possible consistent with the quantities we use and their symbols.

Our main goal in this chapter is indeed to connect the experimental signals (ε for absorption and $\Delta\varepsilon$ for MCD) with the theoretical intrinsic properties of the molecules, transition moments for absorption and, additionally, magnetic moments for MCD. These contain in fact the matrix elements in the transition operators ${}^{\mathrm{ED}}O = \vec{\boldsymbol{m}}$ (electric dipole) and ${}^{\mathrm{MD}}O = \vec{\boldsymbol{\mu}}$ (magnetic dipole) and the Zeeman operator μ_z. They are described by quantities like the dipole strength (D) or oscillator strength (f) for absorption and in the famous $\boldsymbol{\mathcal{A}}_1$, $\boldsymbol{\mathcal{B}}_0$ and $\boldsymbol{\mathcal{C}}_0$ parameters for MCD.

If the theory can be found in a very concise form in the references previously mentioned, here however we use the ''pedestrian'' way by starting ''all from the beginning'':

- What is light and what is ''circularly polarized light''?
- What is a molar absorption coefficient (ε)?
- What is quantum mechanically a matrix element in $\vec{\boldsymbol{m}}$, $\vec{\boldsymbol{\mu}}$ or μ_z?
- How does one go from the classical wave theory of light as an electromagnetic field, to the quantum mechanical theory of Einstein for absorption (and of course emission) that considers the corpuscular interaction between a photon and an electron.

Intentionally a long section is devoted to the absorption theory. We derive the expressions for both linearly polarized light (x and y) and circularly polarized light ($+$ and $-$ for right and left circularly polarized light). We derive the expressions for the electric dipole mechanism (ED) and the magnetic dipole mechanism (MD).

We apologize for being sometimes exhaustively repetitive, but we think it helps to draw the attention of the reader on difficult and subtle matters like:

- Phase factors and normalization factors
- Properties of real and complex quantities, always keeping in mind that the complex formalism used to describe the electric and magnetic field of light is only ''formal''. Light is a ''real'' electromagnetic progressive wave that vibrates cosinusoidal in the xy plane as a function of time and space.

– Factors that are misleading in the application of Einstein's theory to spectroscopic measurements (Eyring et al., 1944; McGlynn et al., 1972; Pauling and Wilson, 1935) and that are also described in the books by Atkins (1970, 1978, 1984, 1997, 2000). Note that consulting the various editions can be very helpful to unravel the details of dimensions and units.

Indeed, Einstein supposes that light is propagating in all directions so that statistically it can be described by considering 1/3 of the radiation following x, 1/3 following y and 1/3 following z. If this is applied to a medium in which the molecules are randomly oriented (e.g., a solution) Einstein's coefficient B is expressed as follows, with $|m_x|$, $|m_y|$ and $|m_z|$ being the corresponding absolute squared matrix elements:

$$B = \frac{1}{3}\left[|m_x|^2+|m_y|^2+|m_z|^2\right].$$

In spectroscopic measurements, light is oscillating only in the xy plane so that only the operators O_x or O_y (or $O_\pm$) are active. Moreover for circularly polarized light, a matrix element describing O_+ is always ''entangled'' with a matrix element for O_- of same magnitude.

– Corrections for refractive indices that are different at the macroscopic and microscopic level, as well as for the electric and magnetic dipole mechanisms
– Relationships between the different energy scales expressions ($\mathcal{E}$, energy; ν, frequency; $\bar{\nu}$, wave number; ω, angular frequency; λ, wavelength), especially important in related quantities like shape functions or bandwidths.

As in the previous reviews, we put much emphasis on the dimensions of all used quantities. We work with the ''Gauss cgs system'' where electric and magnetic quantities have the same dimensions with respect to the three basic dimensions: T, time; M, mass; and L, space.

The problem of dealing with the units is postponed until further, where the molar absorptivity ε is expressed in l mol^{-1} cm^{-1}, the dipole strength in Debye^2 (D^2), the oscillator strength is dimensionless and the MCD parameters $\mathcal{A}_1$ in D^2, $\mathcal{B}_0$ in D^2 cm and $\mathcal{C}_0$ in D^2. More details can be found for absorption in Section 3.6 (see Eq. (138)) and for MCD in Section 4.2.5 (see Eq. (187)) and in Section 4.3.1 (see Eq. (201)).

From another point of view MCD can be regarded as the absorptive counterpart of magnetic optical rotation dispersion (MORD): the well-known Faraday effect. This is the reason why in the past the spectra were given in the units of natural optical rotation per magnetic field

($^{\circ}\text{gauss}^{-1}\ \text{mol}^{-1}\ \text{dl}\ \text{dm}^{-1}$). We discuss these aspects in Section 4.3 in which natural optical rotation dispersion (ORD), natural circular dichroism (CD) and their equivalents in a magnetic field (MORD and MCD) are described (Eyring et al., 1968; Schellman, 1975).

In this chapter, the application of MCD to lanthanides is discussed, a field for which the literature is scarce, contrary to the MCD of *d* transition metals. This could be due to the fact that the coordination effects on lanthanides are much smaller, thus less observable and that the interpretation needs the use of Racah's irreducible tensor method (Racah, 1960, 1964). On the other hand, the small bandwidth of the peaks allows one to observe the Zeeman effect directly, as sometimes it is of the same order of magnitude as the crystal field. Therefore if the $\mathcal{A}_1$, $\mathcal{B}_0$ and $\mathcal{C}_0$ formalism put forward by Stephens (1976) is still present in all papers devoted to MCD, it is better for simulating the spectra to diagonalize the full perturbation matrix including electron repulsion, spin–orbit coupling, crystal field and the Zeeman perturbation and to look at the transition probabilities of left and right circularly polarized light and substract them from each other. Therefore, we are especially grateful to M. Reid, for having made his programs available to us for MCD calculations (Reid, 1988).

At the end of the 1960s and 1970s, all spectroscopists agreed upon the fact that MCD was very powerful and a beautiful technique as it describes the ultimate intrinsic electronic properties of matter: the characterization of a Zeeman level by a signal that has a sign. This is not the case in EPR or classical Zeeman spectroscopy which measure the energy difference between two states (e.g., $\Delta M = \pm 1$) but which cannot tell which one is lying higher in energy. While the theory of MCD is beautiful, applications became scare because of the technical constraints of this experimental technique:

(i) Light must propagate parallel to the direction of the field through a split coil electromagnet or supermagnet, which is not the case for EPR or NMR.
(ii) Most applications demand high magnetic fields only obtainable with a supermagnet working at He temperature.
(iii) The setup requires the constraints of the He cryogeny on one hand and simultaneously a series of quartz windows to let the circularly polarized light pass through all the compartments for eventually reaching the sample.

One may, however, be optimistic for the future of MCD if high-temperature superconducting magnets develop and if the optical quartz system can be replaced by optical fibres that could lead the circularly polarized light to the sample in an easier way.

2. QUALITATIVE PRESENTATION OF MAGNETIC CIRCULAR DICHROISM ($\mathcal{A}$, $\mathcal{B}$ AND $\mathcal{C}$ TERMS)

2.1 Principle of MCD spectroscopy

In the presence of a magnetic field, each molecule sustains a Zeeman splitting of its electronic states. When irradiated with circularly polarized light, this leads to a difference in absorption between left and right circularly polarized light. This property ($\Delta\varepsilon = \varepsilon_- - \varepsilon_{+)}$ is measured as a function of the energy of the incident light. Originally the MCD signal has been treated as a superposition of the so-called $\mathcal{A}$, $\mathcal{B}$ and $\mathcal{C}$ terms according to Stephens' formalism (Stephens, 1976). A pictorial description of these terms can best be illustrated by the simple example of a ${}^1P \leftarrow {}^1S$ transition.

2.2 The $\mathcal{A}$ term

An $\mathcal{A}$ term arises when degenerate levels are split by the magnetic field. As illustrated in Figure 1, absorption of left circularly polarized light induces a transition to the upper Zeeman component while right absorption terminates onto the lower level.

The sign of the derivative-shaped $\mathcal{A}$ term (which is equal to $\Delta\varepsilon_{\max} - \Delta\varepsilon_{\min}$) is positive when $\Delta\varepsilon$ is positive at high energy.

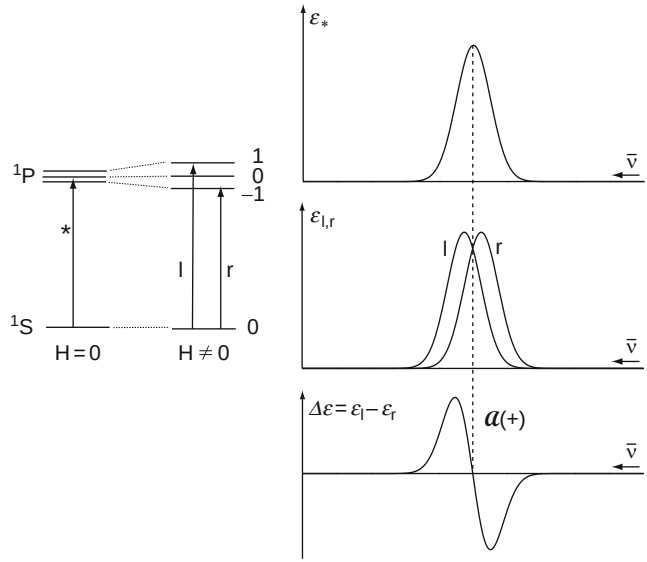

FIGURE 1 Definition and sign of the $\mathcal{A}$ term. *, Non-polarized light; l and r, left and right circularly polarized light.

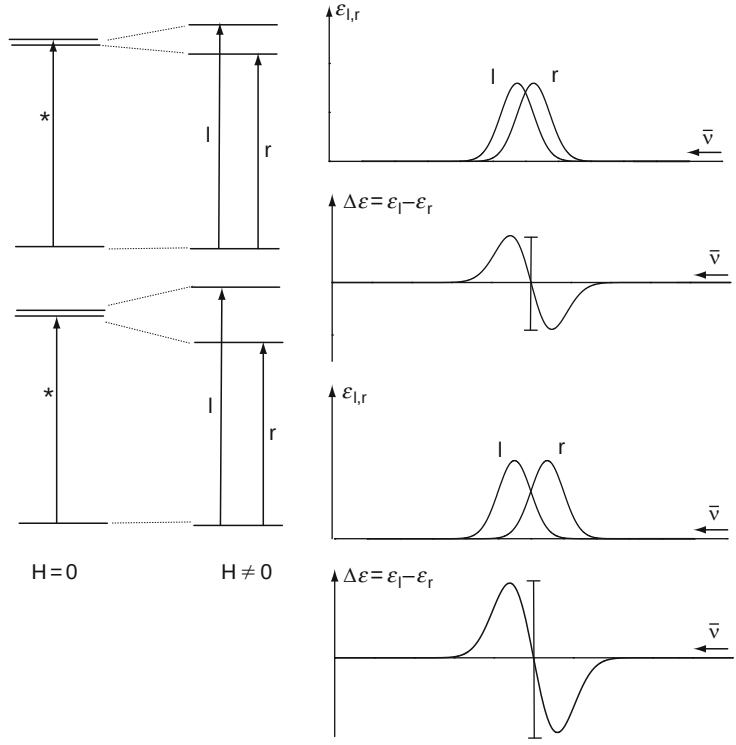

FIGURE 2 Relationship between the magnitudes of the Zeeman splitting and the $\mathcal{A}$ term.

Even without any theoretical derivation of the $\mathcal{A}$ term properties, it is clear that the intensity is not only dependent on the transition probabilities for left and right circularly polarized light but also on the Zeeman splitting and the bandwidth of electronic levels involved in the transition. The narrow peaks, typical for the lanthanides, will influence favourably the MCD signal. Indeed, the MCD signal for the $\mathcal{A}$ term is inversely proportional to the bandwidth (see Sect. 5.3 in Piepho and Schatz (1983)). The relation between the magnitude of the $\mathcal{A}$ term and the Zeeman splitting is shown on Figure 2. The value of $\Delta\varepsilon_{\max} - \Delta\varepsilon_{\min}$ is directly proportional to the Zeeman splitting, so that if the latter doubles for example, the magnitude of the $\mathcal{A}$ term will also double.

2.3 The $\mathcal{B}$ term

The $\mathcal{B}$ term is due to the mixing by the magnetic field of other states in the ground and/or excited states. Since this mixing is described by second-order perturbation theory, the $\mathcal{B}$ term is expected to be small. In Figure 3,

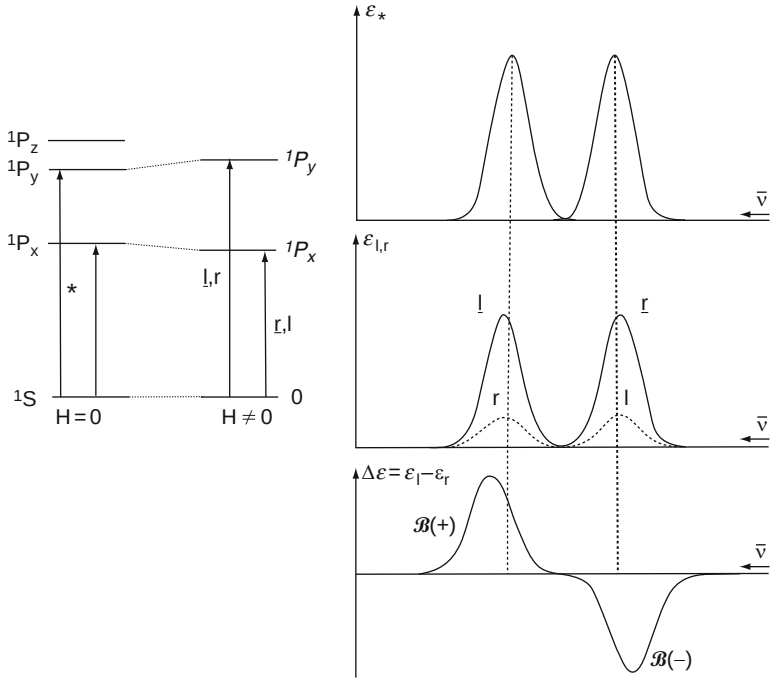

FIGURE 3 Definition and sign of the $\mathcal{B}$ terms. $^1P_y = i/\sqrt{2}(^1P_{-1} + {}^1P_{+1})$, ^1P_y contains more $^1P_{+1}$ than $^1P_{-1}$. $^1P_x = 1/\sqrt{2}(^1P_{-1} + {}^1P_{+1})$, ^1P_y contains more $^1P_{-1}$ than $^1P_{+1}$.

the mixing of the levels ^1P_x and ^1P_y results in states containing unequal amounts of $^1P_{+1}$ and $^1P_{-1}$ character. If $|+1\rangle$ dominates in one, $|-1\rangle$ is dominating in the other one with the same magnitude. Thus if a positive $\mathcal{B}$ term is found somewhere, a negative $\mathcal{B}$ term is always found somewhere else with equal magnitude.

Both left and right absorption occurs to the individual Zeeman components with an intensity depending on the relative amounts of $^1P_{+1}$ and $^1P_{-1}$. It is the absorption-like temperature-independent $\mathcal{B}$ term which makes the MCD a universal phenomenon since no degeneracies are required. It is clear that two nearby-lying $\mathcal{B}$ terms collapse in a single signal which looks like an $\mathcal{A}$ term.

2.4 The $\mathcal{C}$ term

For absorption processes, the $\mathcal{C}$ term exists only when the ground state is degenerate. Its appearance is that of an absorption-like band and it is positive if the absorption for l.c.p. light is larger than for r.c.p. light. The different magnitude of the left and right absorption finds its origin in the

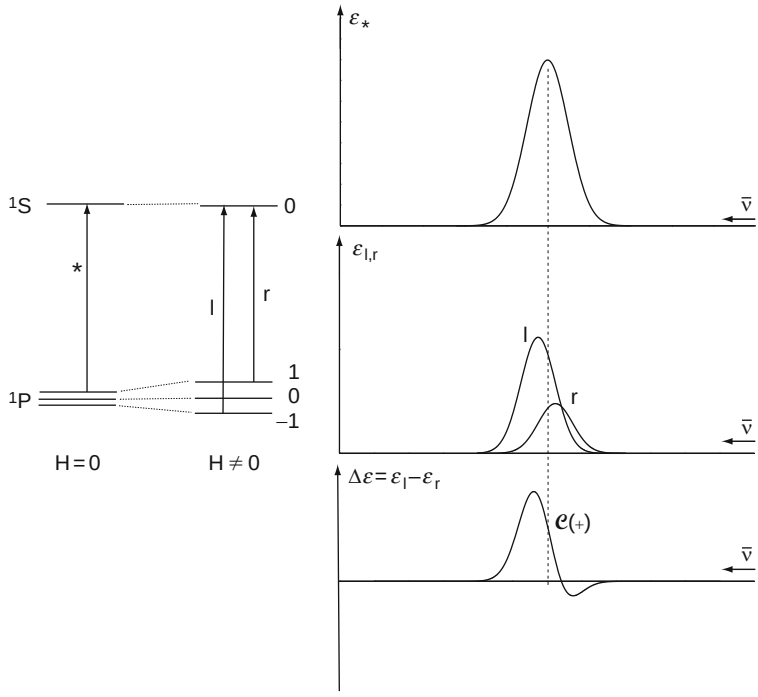

FIGURE 4 Definition and sign of the $\mathcal{C}$ term.

temperature-dependent population difference in both Zeeman levels. At low temperature, the $\mathcal{C}$ term is much more intense than at higher temperature. It should be noted that the splitting of the degeneracy also gives rise to an $\mathcal{A}$ term, giving a derivative-shaped contribution to the final signal as can be seen on Figure 4.

3. QUANTITATIVE THEORETICAL TREATMENT OF THE ABSORPTION THEORY

3.1 Interaction between light and matter in a non-absorbing medium

3.1.1 Electric and magnetic field vector

Light is an electromagnetic cosinusoidal, transversal travelling wave. It is composed of electric and magnetic fields, perpendicular to each other and to the propagating direction, and oscillating in both space and time. In classical physics, light is considered as being an electromagnetic radiation. The electric and the magnetic fields $\vec{E}$ and $\vec{H}$ travelling in the

+z-direction through a *non-absorbing medium* are both described mathematically by cosinusoidal waves of the form:

$$\overrightarrow{\boldsymbol{A}}(z,t) = A_0 \cos(\omega t - k' z + \phi)\overrightarrow{\boldsymbol{e}}, \tag{1}$$

with

$$\begin{aligned} \omega t - k' z &= 2\pi v t - \frac{2\pi}{\lambda'} z = 2\pi \left(\frac{t}{T} - \frac{z}{\lambda'} \right) \\ &= 2\pi v \left(t - \frac{z}{v\lambda'} \right) = \omega \left(t - \frac{z}{c'} \right) \\ &= \omega \left(t - \frac{nz}{c} \right). \end{aligned} \tag{2}$$

Because

$$\begin{aligned} &v\lambda = c, \quad v\lambda' = c', \quad \frac{\lambda}{\lambda'} = \frac{c}{c'} = \frac{k'}{k} = n, \\ &\bar{\nu} = \frac{1}{\lambda}, \quad \nu = \frac{1}{T}, \quad \omega = 2\pi\nu = \frac{2\pi}{T} = 2\pi\bar{\nu}c = \frac{2\pi c}{\lambda} = kc, \end{aligned} \tag{3}$$

where

$\overrightarrow{\boldsymbol{A}} = \overrightarrow{\boldsymbol{E}}(z,t)$ is the electric field vector or $\overrightarrow{\boldsymbol{A}} = \overrightarrow{\boldsymbol{H}}(z,t)$ is the magnetic field vector

A_0: the amplitude — dim: $M^{1/2}L^{-1/2}T^{-1}$ (force/charge)

$\boldsymbol{\omega}$: the angular frequency (in radians s^{-1}) — dim: T^{-1}

t: the time variable — dim: T

k: the angular wave number in vacuum — dim: L^{-1}

k': the angular wave number in a medium — dim: L^{-1}

z: the place variable — dim: L

ϕ: the phase — dim: /

$\overrightarrow{\boldsymbol{e}}$: the normalized unit vector describing the polarization state of the field

ν: the frequency — dim: T^{-1}

T: the period — dim: T

λ: the wavelength in vacuum — dim: L

λ': the wavelength in a medium — dim: L

c: the speed of light in vacuum — dim: LT^{-1}

c': speed of light in a medium — dim: LT^{-1}

n: the refractive index (n = 1 for vacuum) — dim: /

$\bar{\nu}$: the wavenumber in vacuum — dim: L^{-1}

$\bar{\nu}'$: the wavenumber in a medium — dim: L^{-1}

The electromagnetic wave corresponding to a linearly polarized light along x is presented on Figure 5.

3.1.2 Polarization of light

Polarization can be described by considering $\overrightarrow{\boldsymbol{E}}$ as the resultant of two components, one along x and the other one along y. The magnetic field vector is obtained by a counter-clockwise rotation of 90° of the $\overrightarrow{\boldsymbol{E}}$ vector in the right axis system (see Figure 5).

$$\overrightarrow{\boldsymbol{E}}(z,t) = E_x \overrightarrow{\boldsymbol{e}_x} + E_y \overrightarrow{\boldsymbol{e}_y} \tag{4}$$

with

$$\begin{aligned} E_x &= E_{0,x} \cos(\omega t - k' z + \phi_x), \\ E_y &= E_{0,y} \cos(\omega t - k' z + \phi_y), \end{aligned} \tag{5}$$

and

$$\Delta\phi = \phi_y - \phi_x. \tag{6}$$

3.1.2.1 Linearly polarized light along x *and* y

The conditions $E_{0,x} = E_0$ and $E_{0,y} = 0$ result in an $\overrightarrow{\boldsymbol{E}}$ vector along the x-axis (see Figure 6):

$$\overrightarrow{\boldsymbol{E}}_{\substack{x \\ y}}(z,t) = E_{\substack{x \\ y}} \overrightarrow{\boldsymbol{e}_x} = E_0 \cos(\omega t - k' z + \phi) \overrightarrow{\boldsymbol{e}_{\substack{x \\ y}}}. \tag{7}$$

Linearly polarized light along y simply involves an interchange of x into y.

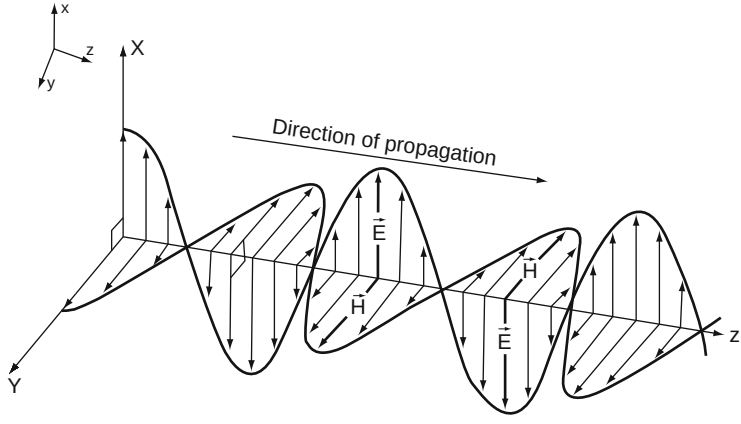

FIGURE 5 Linearly polarized plane wave travelling along the z-direction. A right-handed reference axis system is drawn at the left.

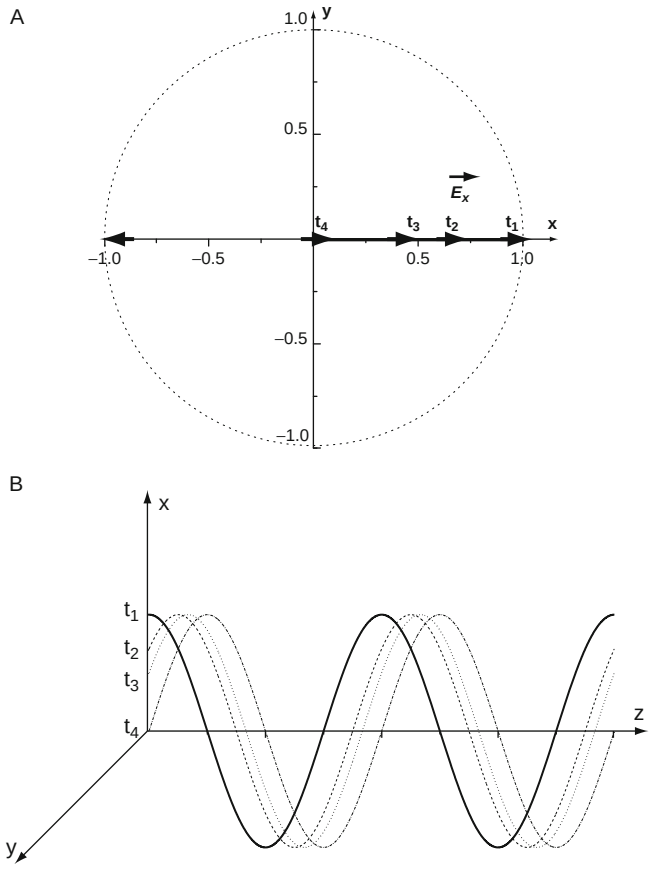

FIGURE 6 Linearly polarized light along the *x*-direction (A) as a function of time in the plane $z = 0$ and (B) as a function of z at $t_1 = 0$ s, $t_2 = T/8$ s, $t_3 = T/6$ s and $t_4 = T/4$ s (T is the period). The phase ϕ is equal to 0.

3.1.2.2 Circularly polarized light

Left circularly polarized light corresponds to $\Delta\phi = -\pi/2 + 2n\pi$ ($n = \pm 1, \pm 2, \ldots$), right circularly polarized light to $\Delta\phi = \pi/2 + 2n\pi$ ($n = \pm 1, \pm 2, \ldots$). The amplitudes are $E_{0,x} = E_{0,y} = E_0$.

$$\overrightarrow{\boldsymbol{E}}_{-}(z,t) = E_0[\cos(\omega t - k'z)\overrightarrow{\boldsymbol{e}_x} + \sin(\omega t - k'z)\overrightarrow{\boldsymbol{e}_y}], \tag{8}$$

$$\overrightarrow{\boldsymbol{E}}_{+}(z,t) = E_0[\cos(\omega t - k'z)\overrightarrow{\boldsymbol{e}_x} - \sin(\omega t - k'z)\overrightarrow{\boldsymbol{e}_y}]. \tag{9}$$

In a time scheme, looking at a wave that is travelling toward the reader, the $\overrightarrow{\boldsymbol{E}}_{-}$ vector rotates counter-clockwise from x to y in a quarter of a period $t = T/4$ (see Figure 7).

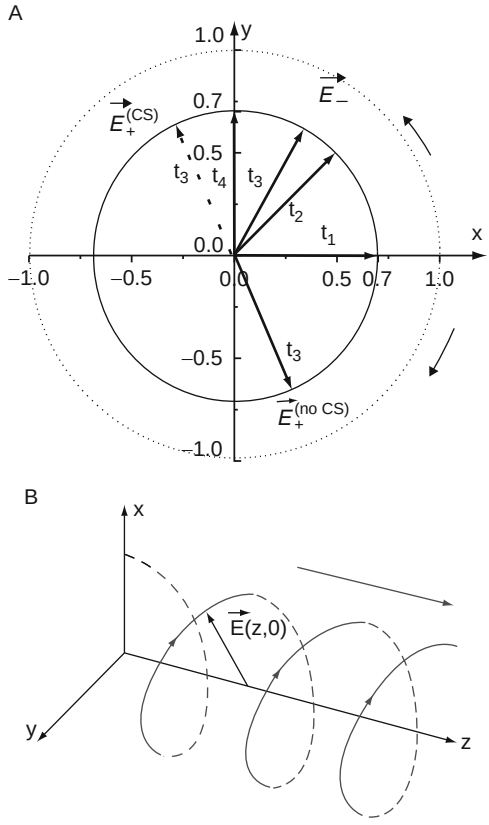

FIGURE 7 Left circularly polarized light (A) as a function of time in the plane $z = 0$; (B) as a function of z at $t_1 = 0$ s, $t_2 = T/8$ s, $t_3 = T/6$ s and $t_4 = T/4$ s (T is the period). Note: $\vec{E}_+$ is drawn with (– – –) and without (—) Condon–Shortley convention (see Section 3.1.2.6).

In a space scheme, $\vec{E}_-$ goes from x to $-y$ in a quarter of the wavelength $z = \lambda/4$.

For $\vec{E}_+$ the opposite is obtained.

3.1.2.3 Elliptically polarized light

For arbitrary values of $\Delta\phi$, $E_{0,x}$ and $E_{0,y}$ light becomes elliptically polarized.

With $\phi_x = 0$ and $\phi_y = \phi$ one obtains

$$\begin{aligned}\vec{E}_{\text{ellipt.}}(z,t) &= E_{0,x}\cos(\omega t - k'z)\vec{e}_x + E_{0,y}\cos(\omega t - k'z + \phi)\vec{e}_y,\\ &= E_{0,x}\cos(\omega t - k'z)\vec{e}_x + E_{0,y}[\cos(\omega t - k'z)\cos\phi\\ &\quad - \sin(\omega t - k'z)\sin\phi]\vec{e}_y,\end{aligned} \tag{10}$$

so that

$$\begin{aligned} E_x &= E_{0,x}\cos(\omega t - k'z), \\ E_y &= E_{0,y}[\cos(\omega t - k'z)\cos\phi - E_{0,y}\sin(\omega t - k'z)\sin\phi] \end{aligned} \tag{11}$$

or

$$\begin{aligned} \cos(\omega t - k'z) &= \frac{E_x}{E_{0,x}}, \\ \sin(\omega t - k'z) &= \left(-\frac{E_y}{E_{0,y}} + \cos(\omega t - k'z)\cos\phi\right)\frac{1}{\sin\phi} \\ &= \left(-\frac{E_y}{E_{0,y}} + \frac{E_x}{E_{0,x}}\cos\phi\right)\frac{1}{\sin\phi} \end{aligned} \tag{12}$$

and

$$\begin{aligned} 1 &= \frac{E_x^2}{E_{0,x}^2} + \left(-\frac{E_y}{E_{0,y}} + \frac{E_x}{E_{0,x}}\cos\phi\right)^2 \frac{1}{\sin^2\phi} \\ &= \frac{E_x^2}{E_{0,x}^2}\left(1 + \frac{\cos^2\phi}{\sin^2\phi}\right) + \frac{E_y^2}{E_{0,y}^2\sin^2\phi} - 2\frac{E_x E_y\cos\phi}{E_{0,x}E_{0,y}\sin^2\phi} \end{aligned} \tag{13}$$

or

$$\frac{E_x^2}{E_{0,x}^2} - 2\frac{E_x E_y\cos\phi}{E_{0,x}E_{0,y}} + \frac{E_y^2}{E_{0,y}^2} = \sin^2\phi, \tag{14}$$

which represents the equation of an ellipse (see Figure 8).

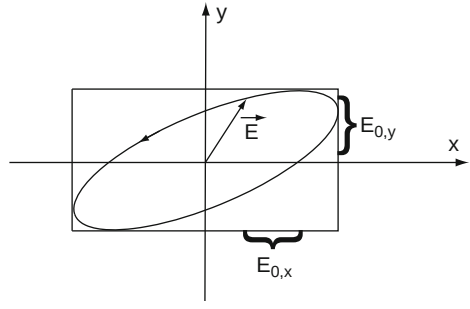

FIGURE 8 Elliptically polarized light.

3.1.2.4 Non-polarized light

A typical monochromatic light source is non-polarized. In the case of a phase change $\Delta\phi$ that is no longer constant, the $\vec{E}$ vector will seem to be tracing out ellipses with different orientations. If the changes in $\Delta\phi$ are so

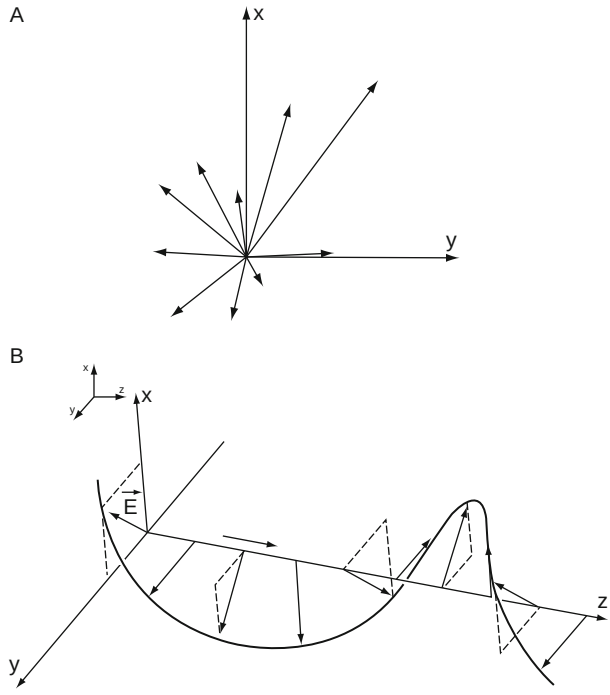

FIGURE 9 Non-polarized light: (A) projection in the *x*, *y* plane and (B) as a function of *z* at $t = 0$.

rapid that the individual forms cannot be registered, the two functions E_x and E_y are said to be completely uncorrelated in phase and the component waves are said to be non-coherent. The different polarizations are then time averaged (see Figure 9).

3.1.2.5 Magnetic field vector $\vec{H}$

The magnetic field vector $\vec{H}$ is obtained by a rotation of 90° of the electric field vector $\vec{E}$. This can be achieved by the following rotation matrix and the introduction of a factor describing the relation between $\vec{E}$ and $\vec{H}$. We recall that $\vec{E}$ and $\vec{H}$ have, following our conventions, the same dimensions:

$$R(90^\circ) = \begin{pmatrix} 0 & -1 \\ 1 & 0 \end{pmatrix}, \tag{15}$$

so that

$$\vec{H}(z,t) = \frac{n}{\mu} R\vec{E}(z,t) \tag{16}$$

or

$$\begin{pmatrix} H_x \\ H_y \end{pmatrix} = \frac{n}{\mu} \begin{pmatrix} 0 & -1 \\ 1 & 0 \end{pmatrix} \begin{pmatrix} E_x \\ E_y \end{pmatrix}, \tag{17}$$

where

n: is the refractive index dim: /
μ: the magnetic permeability dim: /

For non-magnetic materials the approximation can be made that $\mu = 1$.

Thus for linearly polarized light along x and y, the magnetic fields H_y and H_x become, respectively,

$$E_x = E_{0,x} \cos(\omega t - k' z) \tag{18}$$

$$H_y = H_{0,y} \cos(\omega t - k' z) = n_x E_{0,x} \cos(\omega t - k' z) = n_x E_0 \cos(\omega t - k' z) \tag{19}$$

and

$$E_y = E_{0,y} \cos(\omega t - k' z + \Delta\phi) = E_0 \cos(\omega t - k' z + \Delta\phi) \tag{20}$$

$$\begin{aligned} H_x &= -H_{0,x} \cos(\omega t - k' z + \Delta\phi) \\ &= -n_y E_{0,y} \cos(\omega t - k' z + \Delta\phi) \\ &= -n_y E_0 \cos(\omega t - k' z + \Delta\phi). \end{aligned} \tag{21}$$

3.1.2.6 Electric and magnetic dipole vectors for linearly and circularly polarized light (with normalization and Condon–Shortley factors)

Since a quantum mechanical treatment will be used later, we introduce now, in addition to the normalization factor, the Condon–Shortley convention which leads to the following equations.

For linearly polarized light along x and along y:

$$\begin{aligned} \overrightarrow{\boldsymbol{E}}_{\substack{x \\ y}}(z,t) &= E_{\substack{x \\ y}} \overrightarrow{\boldsymbol{e}}_{\substack{x \\ y}} = E_0 \cos(\omega t - k' z) \overrightarrow{\boldsymbol{e}}_{\substack{x \\ y}} \\ &= \Re E_0 [\exp(\mathrm{i}(\omega t - k' z))] \overrightarrow{\boldsymbol{e}}_{\substack{x \\ y}} = \Re E_0 \left[\exp\left(\mathrm{i}\omega \left(t - \frac{n_{\substack{x \\ y}} z}{c} \right) \right) \right] \overrightarrow{\boldsymbol{e}}_{\substack{x \\ y}}, \end{aligned} \tag{22}$$

$$\begin{aligned} \overrightarrow{\boldsymbol{H}}_{\substack{x \\ y}}(z,t) &= \pm H_{\substack{y \\ x}} \overrightarrow{\boldsymbol{h}}_{\substack{y \\ x}} = \pm H_0 \cos(\omega t - k' z) \overrightarrow{\boldsymbol{h}}_{\substack{y \\ x}} \\ &= \pm \Re H_0 [\exp(\mathrm{i}(\omega t - k' z))] \overrightarrow{\boldsymbol{h}}_{\substack{y \\ x}} \\ &= \pm \Re H_0 \left[\exp\left(\mathrm{i}\omega \left(t - \frac{n_{\substack{x \\ y}} z}{c} \right) \right) \right] \overrightarrow{\boldsymbol{h}}_{\substack{y \\ x}} \\ &= \pm n_{\substack{y \\ x}} \Re E_0 \exp\left(\mathrm{i}\omega \left(t - \frac{n_{\substack{x \\ y}} z}{c} \right) \right) \overrightarrow{\boldsymbol{h}}_{\substack{y \\ x}} \end{aligned} \tag{23}$$

For circularly polarized light:

$$\begin{aligned}\overrightarrow{\boldsymbol{E}}_{\pm}^{\mathrm{CS}}(z,t) &= \mp\frac{1}{\sqrt{2}}E_0[\cos(\omega t - k'z)\overrightarrow{\boldsymbol{e}_x} \mp \sin(\omega t - k'z)\overrightarrow{\boldsymbol{e}_y}] \\ &= \mp\frac{1}{\sqrt{2}}\Re E_0[\exp(\mathrm{i}(\omega t - k'z))][\overrightarrow{\boldsymbol{e}_x} \pm \mathrm{i}\overrightarrow{\boldsymbol{e}_y}] \\ &= \mp\frac{1}{\sqrt{2}}\Re E_0\left[\exp\left(\mathrm{i}\omega\left(t - \frac{n_{\pm}z}{c}\right)\right)\right][\overrightarrow{\boldsymbol{e}_x} \pm \mathrm{i}\overrightarrow{\boldsymbol{e}_y}],\end{aligned} \tag{24}$$

$$\begin{aligned}\overrightarrow{\boldsymbol{H}}_{\pm}^{\mathrm{CS}}(z,t) &= \mp\frac{1}{\sqrt{2}}H_0[\cos(\omega t - k'z)\overrightarrow{\boldsymbol{h}_y} \pm \sin(\omega t - k'z)\overrightarrow{\boldsymbol{h}_x}] \\ &= \mp\frac{1}{\sqrt{2}}\Re H_0[\exp(\mathrm{i}(\omega t - k'z))][\overrightarrow{\boldsymbol{h}_y} \mp \mathrm{i}\overrightarrow{\boldsymbol{h}_x}] \\ &= \mp\frac{1}{\sqrt{2}}\Re H_0\left[\exp\left(\mathrm{i}\omega\left(t - \frac{n_{\pm}z}{c}\right)\right)\right][\overrightarrow{\boldsymbol{h}_y} \mp \mathrm{i}\overrightarrow{\boldsymbol{h}_x}] \\ &= \mp\frac{1}{\sqrt{2}}n_{\pm}\Re E_0\left[\exp\left(\mathrm{i}\omega\left(t - \frac{n_{\pm}z}{c}\right)\right)\right][\overrightarrow{\boldsymbol{h}_y} \mp \mathrm{i}\overrightarrow{\boldsymbol{h}_x}].\end{aligned} \tag{25}$$

3.1.2.7 Linearly polarized light as the resultant of left and right circularly polarized light and vice versa

To make all types of polarization conform with the normalization factor, a point of high importance for MCD, we consider the following schemes. The Condon–Shortley convention, which is very inconvenient for the purpose of visualization and does not contribute to a better understanding, is not taken into consideration in the following figures. However, calculations will obviously have to take it into account.

3.1.2.7.1 Linearly polarized light Linearly polarized light can always be regarded as being the resultant of right and left circularly polarized light (see Figure 10). Without Condon-Shortley convention one obtains:

$$\begin{aligned}\overrightarrow{\boldsymbol{E}}_x(z,t) = E_x\overrightarrow{\boldsymbol{e}_x} &= \frac{1}{\sqrt{2}}(\overrightarrow{\boldsymbol{E}}_- + \overrightarrow{\boldsymbol{E}}_+) \\ &= \frac{1}{\sqrt{2}}\left[\frac{1}{\sqrt{2}}\left(E_0[\cos(\omega t - k'z)\overrightarrow{\boldsymbol{e}_x} + \sin(\omega t - k'z)\overrightarrow{\boldsymbol{e}_y}]\right)\right] \\ &+ \frac{1}{\sqrt{2}}\left[\frac{1}{\sqrt{2}}\left(E_0[\cos(\omega t - k'z)\overrightarrow{\boldsymbol{e}_x} - \sin(\omega t - k'z)\overrightarrow{\boldsymbol{e}_y}]\right)\right],\end{aligned} \tag{26}$$

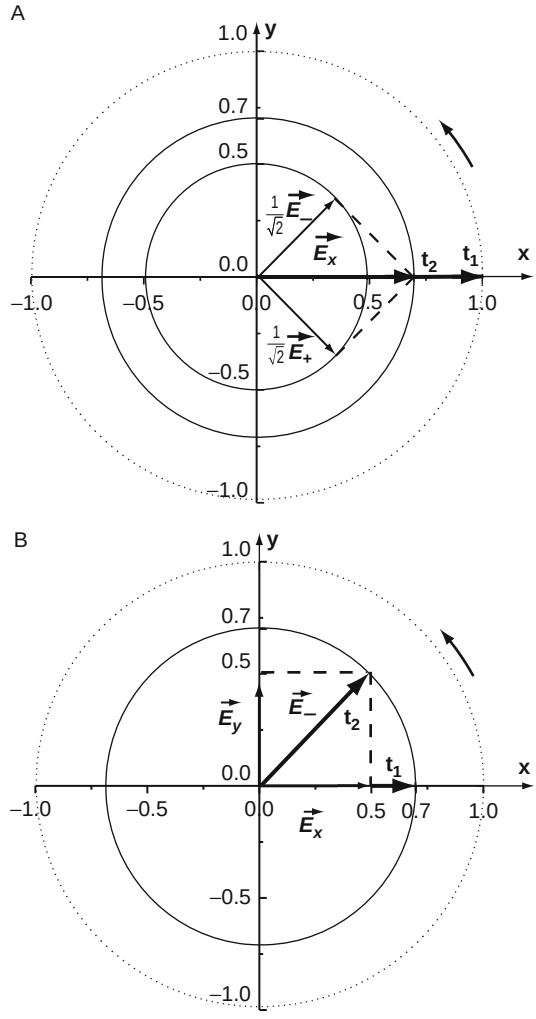

FIGURE 10 (A) Linearly polarized light as a resultant of left and right circularly polarized components ($t_1 = 0$ s, $t_2 = T/8$ s) and (B) Left circularly polarized light as a resultant in linearly polarized light along x and y ($t_1 = 0$ s, $t_2 = T/8$ s). Drawings without Condon–Shortley convention.

$$\vec{\boldsymbol{E}}_y(z,t) = E_y\vec{\boldsymbol{e}_y} = \frac{1}{\sqrt{2}}(\vec{\boldsymbol{E}}_- - \vec{\boldsymbol{E}}_+). \tag{27}$$

If the Condon–Shortley convention is used (see Eq. (24)) one obtains:

$$\overrightarrow{\boldsymbol{E}}_{-}^{\mathrm{CS}} = \overrightarrow{\boldsymbol{E}}_{-} = \frac{1}{\sqrt{2}}\left(E_0[\cos(\omega t - k'z)\overrightarrow{\boldsymbol{e}_x} + \sin(\omega t - k'z)\overrightarrow{\boldsymbol{e}_y}]\right), \tag{28}$$

$$\overrightarrow{\boldsymbol{E}}_{+}^{\mathrm{CS}} = -\frac{1}{\sqrt{2}}\left(E_0[\cos(\omega t - k'z)\overrightarrow{\boldsymbol{e}_x} - \sin(\omega t - k'z)\overrightarrow{\boldsymbol{e}_y}]\right), \tag{29}$$

$$\begin{aligned}\overrightarrow{\boldsymbol{E}}_x(z,t) = E_x\overrightarrow{\boldsymbol{e}_x} &= \frac{1}{\sqrt{2}}(\overrightarrow{\boldsymbol{E}}_{-}^{\mathrm{CS}} - \overrightarrow{\boldsymbol{E}}_{+}^{\mathrm{CS}}) \\ &= \frac{1}{\sqrt{2}}\left[\frac{1}{\sqrt{2}}\left(E_0[\cos(\omega t - k'z)\overrightarrow{\boldsymbol{e}_x} + \sin(\omega t - k'z)\overrightarrow{\boldsymbol{e}_y}]\right)\right] \\ &- \left[-\frac{1}{\sqrt{2}}\left(E_0[\cos(\omega t - k'z)\overrightarrow{\boldsymbol{e}_x} - \sin(\omega t - k'z)\overrightarrow{\boldsymbol{e}_y}]\right)\right],\end{aligned} \tag{30}$$

$$\begin{aligned}\overrightarrow{\boldsymbol{E}}_y(z,t) = E_y\overrightarrow{\boldsymbol{e}_y} &= \frac{1}{\sqrt{2}}(\overrightarrow{\boldsymbol{E}}_{-}^{\mathrm{CS}} + \overrightarrow{\boldsymbol{E}}_{+}^{\mathrm{CS}}) \\ &= \frac{1}{\sqrt{2}}\left[\frac{1}{\sqrt{2}}\left(E_0[\cos(\omega t - k'z)\overrightarrow{\boldsymbol{e}_x} + \sin(\omega t - k'z)\overrightarrow{\boldsymbol{e}_y}]\right)\right] \\ &+ \left[-\frac{1}{\sqrt{2}}\left(E_0[\cos(\omega t - k'z)\overrightarrow{\boldsymbol{e}_x} - \sin(\omega t - k'z)\overrightarrow{\boldsymbol{e}_y}]\right)\right].\end{aligned} \tag{31}$$

3.1.2.7.2 Circularly polarized light Circularly polarized light can be regarded as being the resultant of linearly polarized light along x and along y, see Eq. (24) and Figure 10.

3.1.2.7.3 Non-polarized light Non-polarized light can statistically be seen as the resultant of half of the components following $\overrightarrow{\boldsymbol{E}}_x$ and half of the components following $\overrightarrow{\boldsymbol{E}}_y$ or equivalently of half of left ($\overrightarrow{\boldsymbol{E}}_{-}$) and half of right ($\overrightarrow{\boldsymbol{E}}_{+}$) circularly polarized components.

3.1.2.7.4 Comment on Einstein's isotropic radiation The time-dependent perturbation theory developed by Einstein is somewhat tricky in the sense that Einstein introduces ''an isotropic radiation bath'' which consists of 1/3 of $\overrightarrow{\boldsymbol{E}}_x$, 1/3 of $\overrightarrow{\boldsymbol{E}}_y$ and 1/3 of $\overrightarrow{\boldsymbol{E}}_z$ components.

In fact, this case never occurs in spectroscopy since radiation is defined as a transversal wave in the x, y plane.

3.1.3 Intensity in a non-absorbing medium

The intensity I of the radiation along z is the energy passing per unit of time through a unit area perpendicular to the z-axis and is given by the time-averaged value of the Poynting vector $\vec{S}$.

$$I(z) = |\vec{S}(z)| \qquad \text{dim: } \mathrm{MT}^{-3} = \mathrm{ML}^2\mathrm{T}^{-2}\mathrm{T}^{-1}\mathrm{L}^{-2}\,\text{energy}/(\text{time} \times \text{area}) \tag{32}$$

with

$$\vec{S} = \left(\frac{c}{4\pi}\right)\vec{E} \times \vec{H} = \left(\frac{c}{4\pi}\right)n\vec{E} \times \vec{E}. \tag{33}$$

In determinant notation:

$$\vec{S} = \frac{c}{4\pi}\begin{vmatrix} \vec{e}_x & \vec{e}_y & \vec{e}_z \\ E_x & E_y & E_z \\ H_x & H_y & H_z \end{vmatrix}, \tag{34}$$

$$\vec{S}(z) = \frac{c}{4\pi}(E_x H_y - E_y H_x)\vec{e}_z. \tag{35}$$

So that the time-averaged Poynting vector is equivalent to the time-averaged squared electric field vector $|\vec{E}(z,t)|^2$, as given by

$$|\vec{S}(z)| = \left(\frac{c}{4\pi}\right)n|\vec{E}(z,t)|^2. \tag{36}$$

Only time average values are to be taken into account since for IR, UV and VIS light the wavelength can be considered as constant over the whole molecule (e.g., 5000 Å with respect to 10 Å) so that no space dependency has to be considered.

Time averaging a function $f(\omega t)$ over an interval of one period is done by

$$|f(\omega t)| = \frac{1}{2\pi}\int_{\omega t(t=0)}^{\omega t(t=T)} f(\omega t)\mathrm{d}\omega t = \frac{1}{2\pi}\int_0^{2\pi} f(\omega t)\mathrm{d}\omega t. \tag{37}$$

Therefore, the intensity in a non-absorbing medium is expressed by the following equations.

For *linearly polarized light along x and y*:

$$
\begin{aligned}
I_{\substack{x\\y}}(z) &= \frac{c}{4\pi} n_{\substack{x\\y}} |\overrightarrow{\boldsymbol{E}}_{\substack{x\\y}}(z,t)|^2 \\
&= \frac{c}{4\pi} E_0 H_0 \frac{1}{2\pi} \int_0^{2\pi} \cos^2 \omega t \, \mathrm{d}\omega t \\
&= \frac{c}{8\pi} E_0 H_0 = \frac{c}{8\pi} n_{\substack{x\\y}} E_0^2,
\end{aligned}
\tag{38}
$$

where $|\overrightarrow{\boldsymbol{E}}_{\substack{x\\y}}(z,t)|^2$ is the absolute square of the time-averaged electric field vector over a period T.

For *circularly polarized light*:

$$
\begin{aligned}
I_{\pm}(z) &= \frac{c}{4\pi} n_{\pm} |\overrightarrow{\boldsymbol{E}}_{\pm}(z,t)|^2 \\
&= \frac{c}{4\pi} \frac{1}{2\pi} \int_0^{2\pi} \frac{1}{2} E_0 H_0 \mathrm{d}\omega t \\
&= \frac{c}{8\pi} E_0 H_0 = \frac{c}{8\pi} n_{\pm} E_0^2,
\end{aligned}
\tag{39}
$$

where $|\overrightarrow{\boldsymbol{E}}_{\pm}(z,t)|^2$ is the absolute square of the time-averaged electric field vector over a period T.

Note that the same final result is obtained for linearly and circularly polarized light because of the normalization vector.

3.2 Interaction between light and matter in an absorbing medium

3.2.1 Intensity decrease and relation to κ

In an *absorbing medium*, the refractive index n and the magnetic permeability μ are formally replaced by the complex refractive index $\hat{n}$ and the complex magnetic permeability $\hat{\mu}$, respectively,

$$\hat{n} = n - \mathrm{i}\kappa, \tag{40}$$

$$\hat{\mu} = \mu - \mathrm{i}\kappa, \tag{41}$$

where:
κ: is the absorption coefficient of the medium in the z-direction, dim: /
n: the refractive index in a non-absorbing medium and dim: /
μ: the magnetic permeability in a non-absorbing medium dim: /

In the connection between E_0 and H_0, $\hat{n}/\hat{\mu}$ can be replaced by n since the complex refractive index can be set equal to n and the complex magnetic permeability $\hat{\mu}$ can be set equal to 1.

The previous expressions for the wave vectors for linearly and circularly polarized light have to be modified as follows.

Electric field vector for linearly polarized light along x and y when $\kappa \neq 0$

$$\overrightarrow{\underset{y}{\boldsymbol{E}}}_{x}(z,t) = \Re E_0 \exp\left(\mathrm{i}\omega\left(t - \frac{\hat{n}_{\underset{y}{x}} z}{c}\right)\right)\overrightarrow{\underset{y}{\boldsymbol{e}}}_{x}, \tag{42}$$

$$\begin{aligned}\overrightarrow{\underset{x}{\boldsymbol{H}}}_{y}(z,t) &= \pm\Re H_0 \exp\left(\mathrm{i}\omega\left(t - \frac{\hat{n}_{\underset{y}{x}} z}{c}\right)\right)\overrightarrow{\underset{y}{\boldsymbol{h}}}_{x} \\ &= \pm\Re \underset{y}{n}_{x} E_0 \exp\left(\mathrm{i}\omega\left(t - \frac{\hat{n}_{\underset{y}{x}} z}{c}\right)\right)\overrightarrow{\underset{y}{\boldsymbol{h}}}_{x}\end{aligned} \tag{43}$$

or

$$\overrightarrow{\underset{y}{\boldsymbol{E}}}_{x}(z,t) = \Re E_0 \exp\left(\mathrm{i}\omega\left(t - \frac{\underset{y}{n}_{x} z}{c}\right)\right)\exp\left(-\frac{\omega \underset{y}{\kappa}_{x} z}{c}\right)\overrightarrow{\underset{y}{\boldsymbol{e}}}_{x}, \tag{44}$$

$$\begin{aligned}\overrightarrow{\underset{x}{\boldsymbol{H}}}_{y}(z,t) &= \pm\Re H_0 \exp\left(\mathrm{i}\omega\left(t - \frac{\underset{y}{n}_{x} z}{c}\right)\right)\exp\left(-\frac{\omega \underset{y}{\kappa}_{x} z}{c}\right)\overrightarrow{\underset{y}{\boldsymbol{h}}}_{x} \\ &= \pm\Re \underset{y}{n}_{x} E_0 \exp\left(\mathrm{i}\omega\left(t - \frac{\underset{y}{n}_{x} z}{c}\right)\right)\exp\left(-\frac{\omega \underset{y}{\kappa}_{x} z}{c}\right)\overrightarrow{\underset{y}{\boldsymbol{h}}}_{x}\end{aligned} \tag{45}$$

Electric field vector for circularly polarized light when $\kappa \neq 0$

$$\overrightarrow{\boldsymbol{E}}_{\pm}(z,t) = \mp\frac{1}{\sqrt{2}}\Re E_0\left[\exp\left(\mathrm{i}\omega\left(t - \frac{\hat{n}_{\pm} z}{c}\right)\right)\right][\overrightarrow{\boldsymbol{e}_x} \pm \mathrm{i}\overrightarrow{\boldsymbol{e}_y}], \tag{46}$$

$$\overrightarrow{\boldsymbol{H}}_{\pm}(z,t) = \mp\frac{1}{\sqrt{2}}\Re H_0\left[\exp\left(\mathrm{i}\omega\left(t - \frac{\hat{n}_{\pm} z}{c}\right)\right)\right][\overrightarrow{\boldsymbol{h}_y} \mp \mathrm{i}\overrightarrow{\boldsymbol{h}_x}] \tag{47}$$

or

$$\overrightarrow{\boldsymbol{E}}_{\pm}(z,t) = \mp\frac{1}{\sqrt{2}}\Re E_0 \exp\left(\mathrm{i}\omega\left(t - \frac{n_{\pm} z}{c}\right)\right)\exp\left(-\frac{\omega \kappa_{\pm} z}{c}\right)[\overrightarrow{\boldsymbol{e}_x} \pm \mathrm{i}\overrightarrow{\boldsymbol{e}_y}], \tag{48}$$

$$\begin{aligned}\overrightarrow{\boldsymbol{H}}_{\pm}(z,t) &= \mp\frac{1}{\sqrt{2}}\Re H_0 \exp\left(\mathrm{i}\omega\left(t-\frac{n_{\pm}z}{c}\right)\right)\exp\left(-\frac{\omega\kappa_{\pm}z}{c}\right)[\overrightarrow{\boldsymbol{h}}_y \mp \mathrm{i}\overrightarrow{\boldsymbol{h}}_x] \\ &= \mp\frac{1}{\sqrt{2}}\Re n_{\pm}E_0 \exp\left(\mathrm{i}\omega\left(t-\frac{n_{\pm}z}{c}\right)\right)\exp\left(-\frac{\omega\kappa_{\pm}z}{c}\right)[\overrightarrow{\boldsymbol{h}}_y \mp \mathrm{i}\overrightarrow{\boldsymbol{h}}_x].\end{aligned} \tag{49}$$

Intensity decrease with $\kappa \neq 0$

The intensity is the time-averaged Poynting vector multiplied by $c/4\pi$ (see Eq. (32)):

$$I(z) = \frac{c}{4\pi}|\overrightarrow{S}| = \frac{c}{4\pi}|\overrightarrow{\boldsymbol{E}} \times \overrightarrow{\boldsymbol{H}}|. \tag{50}$$

In the expression now appears the time-depending factor ($\mathrm{e}^{\mathrm{i}\omega t}$) and two space-depending factors ($\mathrm{e}^{-\mathrm{i}\omega nz/c}$) and ($\mathrm{e}^{-\omega\kappa z/c}$). The time average factor is the same as in Eqs. (38) and (39) leading to $(c/4\pi)(E_0^2/2)$.

As the wavelength is much larger than the dimension of the molecule (e.g., 5000 Å with respect to 10 Å) the space-depending factors can be put equal to one, meaning that they are constant over the whole molecule. However, the mathematical treatment becomes more subtle when it comes to introducing the absorption coefficient κ (that will later be related to the molar absorption coefficient ε). A subscript z_κ has to be introduced, meaning that at the absorption frequency ν_{a-j} corresponding to the frequency of the transition from level a to level j or in a close vicinity, the expressions ($\mathrm{e}^{-\mathrm{i}\omega nz/c}$) and ($\mathrm{e}^{-\omega\kappa z/c}$) have a fixed value (see Piepho and Schatz, 1983, pp. 11 and 17). Within the frame of the fixed coordinate system of a molecule, the space-dependent factors may be expressed as a series:

$$\begin{aligned}\mathrm{e}^{-\mathrm{i}\omega nz_\kappa/c} &= \mathrm{e}^{-\mathrm{i}2\pi\nu nz_\kappa/c} = \mathrm{e}^{-\mathrm{i}2\pi nz_\kappa/\lambda} = 1 - \mathrm{i}\omega nz_\kappa/c = 1 \\ \mathrm{e}^{-\omega\kappa z_\kappa/c} &= \mathrm{e}^{-2\pi\nu\kappa z_\kappa/c} = \mathrm{e}^{-2\pi\kappa z_\kappa/\lambda} = 1 - \omega\kappa z_\kappa/c = 1.\end{aligned} \tag{51}$$

Integration along z over the optical pathway yields:

$$\int_{I_0}^{I}\frac{\mathrm{d}I(z)}{I(z)} = -\int_0^d \frac{2\omega\kappa}{c}\mathrm{d}z. \tag{52a}$$

So that intensity becomes

$$\begin{aligned} I(z) &= \frac{c}{4\pi} n |\vec{\boldsymbol{E}}(z)|^2 = \frac{c}{8\pi} n E_0^2 \exp\left(-\frac{2\omega\kappa d}{c}\right) \\ &= I(0) \exp\left(-\frac{2\omega\kappa d}{c}\right) \end{aligned} \tag{52b}$$

or through derivation

$$\begin{aligned} \frac{\mathrm{d}I(z)}{\mathrm{d}z} &= -I(z)\frac{2\omega\kappa}{c} \\ &= \frac{c}{8\pi} E_0^2 \frac{2\omega\kappa}{c}, \end{aligned} \tag{53}$$

leading to

$$\kappa = -\frac{\mathrm{d}I(z)}{\mathrm{d}z}\frac{1}{n v |E(z)|^2}. \tag{54}$$

If electric dipole and magnetic dipole mechanisms are considered (see Section 3.4), we have

$$\begin{aligned} \mathrm{d}I(z)^{\mathrm{ED}} &= -nv|E(z)|^2 \kappa^{\mathrm{ED}} \mathrm{d}z, \\ \mathrm{d}I(z)^{\mathrm{MD}} &= -\frac{1}{n} v |H(z)|^2 \kappa^{\mathrm{MD}} \mathrm{d}z. \end{aligned} \tag{55}$$

3.2.2 Shape function of the light beam

Because light is not strictly monochromatic it is convenient to introduce a shape function and to write the intensity as a function of frequency:

$$I(z, v) = I(z) f(v), \tag{56}$$

where:

$I(z, v)$ is the intensity of the radiation at place z and frequency v, dim: $\mathrm{MT}^{-2} = \mathrm{ML}^2\mathrm{T}^{-2}\ \mathrm{T}^{-1}\ \mathrm{L}^{-2}\ \mathrm{T}$

$I(z)$ the intensity of the radiation at place z, and dim: $\mathrm{MT}^{-3} = \mathrm{ML}^2\mathrm{T}^{-2}\ \mathrm{T}^{-1}\ \mathrm{L}^{-2}$

$f(\mathrm{v})$ a shape function. dim: T

The shape function f(v) has the following properties:

$$\int f(v)\mathrm{d}v = 1, \tag{57}$$

$$\int \frac{\partial f(v)}{\partial v}\mathrm{d}v = 0, \tag{58}$$

$$\int \frac{\partial f(v)}{\partial v} v \, \mathrm{d}v = -1, \tag{59}$$

$$\int f(v) v^n \mathrm{d}v = v_0^n \tag{60}$$

where

$f(v)$	dim: T
$\mathrm{d}v$	dim: T^{-1}
$\frac{\partial f(v)}{\partial v}$	dim: T^2
v_0: the frequency of the absorption maximum	dim: T^{-1}

Relating the frequency v to other units of the energy $\mathcal{E}$ following:

$$\mathcal{E} = hv = hc\bar{v} = \frac{h}{2\pi}\omega = h\frac{c}{\lambda}, \tag{61}$$

it is clear that

$$\int f(v)\mathrm{d}v = \int f(\mathcal{E})\mathrm{d}\mathcal{E} = \int f(\bar{v})\mathrm{d}\bar{v} = \int f(\omega)\mathrm{d}\omega = \int f(\lambda)\mathrm{d}\lambda = 1 \tag{62}$$

with

$$f(v) = hf(\mathcal{E}) = \frac{1}{c} f(\bar{v}) = 2\pi f(\omega) \qquad \text{dim: T}, \tag{63}$$

$$f(\mathcal{E}) = \frac{1}{h} f(v) = \frac{1}{hc} f(\bar{v}) = \frac{2\pi}{h} f(\omega) \qquad \text{dim: } M^{-1}L^{-2}T^2, \tag{64}$$

$$f(\bar{v}) = cf(v) = chf(\mathcal{E}) = 2\pi c f(\omega) \qquad \text{dim: L}, \tag{65}$$

$$f(\omega) = \frac{1}{2\pi} f(v) = \frac{h}{2\pi} f(\mathcal{E}) = \frac{1}{2\pi c} f(\bar{v}) \qquad \text{dim: T}. \tag{66}$$

We then have by integration

$$\int I(z, v)\mathrm{d}v = \int I(z) f(v)\mathrm{d}v = I(z). \tag{67}$$

It is also convenient, in the framework of Einstein's theory for radiation, to introduce the energy density ρ as:

$$\rho(v) = \frac{I(z, v)}{c} = \rho f(v), \tag{68}$$

where:

$\rho(\nu)$: is the energy density at frequency ν — dim: $MT^{-1}L^{-1} = ML^2T^{-2}L^{-3}T$ (energy/volume) x time

ρ: the energy density — dim: $ML^{-1}T^2 = ML^2T^{-2}L^{-3}$ energy/volume

The shape functions most encountered in the analysis of absorption profiles are Gaussian function, Lorentzian function, Voigt function and the damped oscillator model. The mathematical expressions of these functions can be described in function of the variable $\bar{\nu}$ and in function of two parameters, one characterizing the band maximum $\bar{\nu}_0$ and one describing the bandwidth. For the latter, different descriptions can be used:

Γ: is the half-width at half-height dim: same as energy scale ($\mathcal{E}, \nu, \bar{\nu}, \omega, \lambda$)

Δ: is the half-width at height $1/e$ dim: same as energy scale ($\mathcal{E}, \nu, \bar{\nu}, \omega, \lambda$)

$$\Delta = \frac{\Gamma}{\sqrt{\ln 2}}. \tag{69}$$

Gaussian function:

$$f_G(\bar{\nu}, \bar{\nu}_0) = \frac{\sqrt{\ln 2}}{\sqrt{\pi}\Gamma_G} \exp\left[-\frac{(\bar{\nu} - \bar{\nu}_0)^2 \ln 2}{\Gamma_G^2}\right]. \tag{70}$$

The Gaussian function (see Figure 11A) is symmetrical around the band maximum $\bar{\nu}_0$. The maximum value (for $\bar{\nu} = \bar{\nu}_0$) is $\sqrt{\ln 2}/\sqrt{\pi}\Gamma_G$.

Lorentzian function:

$$f_L(\bar{\nu}, \bar{\nu}_0) = \frac{\Gamma_L}{\pi[\Gamma_L^2 + (\bar{\nu} - \bar{\nu}_0)^2]}. \tag{71}$$

The Lorentzian function (see Figure 11B) is also symmetrical around the band maximum $\bar{\nu}_0$. The maximum value (for $\bar{\nu} = \bar{\nu}_0$) is $1/\Gamma_L\pi$.

Comparing the Lorentzian function with the Gaussian function (see Figure 11B) it is clear that the Gaussian maximum value is higher than the Lorentzian one. The latter is also smaller at $\bar{\nu} = \Gamma$, but the principal distinguishing characteristic of the Lorentzian function is its significant wings.

Voigt function:

The Voigt function (see Figure 11B) is the convolution of Lorentzian and Gaussian functions:

$$f_V(\mu, \xi) = \frac{1}{\Gamma_G}\left(\frac{\ln 2}{\pi}\right)^{1/2} \int_{-\infty}^{+\infty} \frac{\exp(-\zeta^2)}{\mu^2 + (\xi - \zeta)^2} d\zeta, \tag{72}$$

where

$$\xi = \frac{\nu - \nu_0}{\Gamma_G}\sqrt{2 \ln 2} \tag{73}$$

and

$$\mu = \frac{\Gamma_L}{\Gamma_G}\sqrt{2\ln 2}. \tag{74}$$

In Figure 11B, a comparison is made between a Lorentzian and a Gaussian peak, each of width 2 and a Voigt peak with both widths equal to 2. The Voigt peak has wings broader than the Gaussian's, but not as broad as the Lorentzian's one.

Damped oscillator model (DOM):

$$f_{DOM}(\bar{\nu}, \bar{\nu}_0) = \frac{4\bar{\nu}^2\Gamma_{DOM}}{\pi[(\bar{\nu}_0^2 - \bar{\nu}^2)^2 - 4\bar{\nu}^2\Gamma_{DOM}^2]}. \tag{75}$$

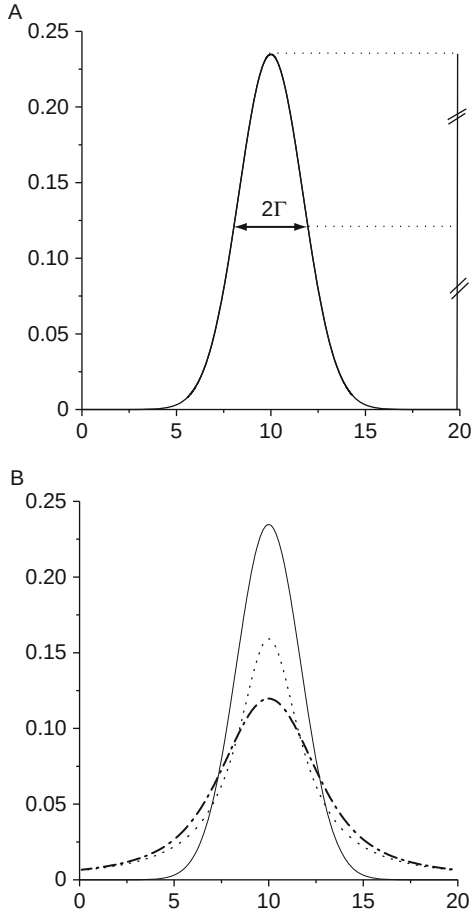

FIGURE 11 (A) Gaussian function ($\Gamma_G = 2$, $\bar{\nu}_0 = 10$) and (B) comparison between Gaussian (—), Lorentzian (. . .) and Voigt (– · –) functions ($\Gamma_G = 2$, $\Gamma_L = 2$, $\bar{\nu}_0 = 10$).

The DOM (see Figure 12) is asymmetrical around the band maximum $\bar{\nu}_0$. The maximal value is $1/\Gamma\pi$.

A comparison between the DOM and the Lorentzian shape function is given in Figure 12.

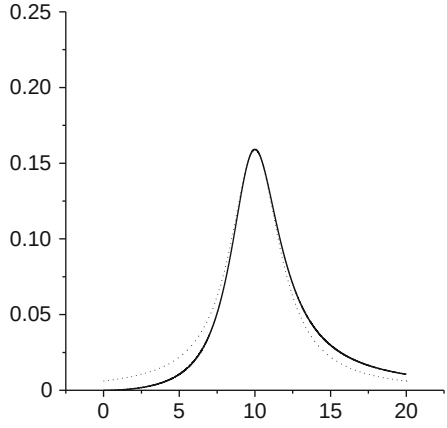

FIGURE 12 Comparison between Damped oscillator model (—) and Lorentzian (. . .) functions ($\Gamma_L = 2$, $\Gamma_{DOM} = 2$, $\bar{\nu}_0 = 10$).

3.3 Quantum mechanical treatment of radiation theory

3.3.1 Introduction

The previous expressions for the intensity decrease per unit time and per unit area will now be treated by quantum mechanics. It is related to the transition probability $\mathrm{d}|a_m|^2/\mathrm{d}t$. This is the probability per unit of time that a photon of energy $h\nu(=\boldsymbol{\mathcal{E}}_{ja})$ is absorbed and induces a transition from a state a to a state j. The decrease in intensity given by Eq. (55) can be written as the product of the energy of the transition with the number of molecules on the absorption area and with the transition probability.

We obtain

$$\mathrm{d}I(z) = -h\nu N_a \frac{\mathrm{d}|a_m|^2}{\mathrm{d}t}\mathrm{d}z, \tag{76}$$

where:

$h\nu = \boldsymbol{\mathcal{E}}$: is the energy of a photon
$= hc\bar{\nu} = \hbar\omega = hc/\lambda = \mathrm{h}\omega/2\pi$ dim: $\mathrm{ML^{-2}T^{-2}}$

N_a: the number of molecules per cm^3 on level a dim: $\mathrm{L^{-3}}$

$\mathrm{d}z$: the infinitesimal optical pathway dim: L

$N_a\mathrm{d}z$: the number of absorbing molecules per cm^2 dim: $\mathrm{L^{-2}}$

$\dfrac{\mathrm{d}|a_m|^2}{\mathrm{d}t}$: the absorption probability per unit time at $\boldsymbol{\mathcal{E}}_{ja}$, energy due to a transition $j \leftarrow a$. dim: $\mathrm{T^{-1}}$

Calculation of $\mathrm{d}|a_m|^2/\mathrm{d}t$ is done by the standard time-dependent perturbation theory with $\mathcal{H}_0$ being the unperturbed Hamiltonian and $\mathcal{H}_1$ the Hamiltonian describing the interaction with light.

3.3.2 Electric dipole transitions

In MCD literature (Piepho and Schatz, 1983; Schellman, 1975; Stephens, 1976) and in the paper written by Judd (Görller-Walrand and Binnemans, 1998; Judd, 1962) the electric dipole perturbation Hamiltonian is given as

$$\mathcal{H}^{\mathrm{ED}} = \mathcal{H}_1 = -\vec{\boldsymbol{m}} \cdot \vec{\boldsymbol{E}}_{\mathrm{mic}} = -\alpha \vec{\boldsymbol{m}} \cdot \vec{\boldsymbol{E}}_{\mathrm{mac}} = -\frac{(n^2+2)}{3} \vec{\boldsymbol{m}} \cdot \vec{\boldsymbol{E}}(z,t), \quad \text{dim: } \mathrm{ML^2T^{-2}} \tag{77}$$

with

$$\vec{\boldsymbol{m}} = -\sum_j |e| \vec{\boldsymbol{r}_j} = -|e| D_\rho^{(1)} = {}^{\mathrm{ED}}O_\rho^{(1)} = \hat{\boldsymbol{r}}_\rho^{(1)}, \quad \text{dim: } \mathrm{M^{1/2}L^{5/2}T^{-1}} \tag{78}$$

where:

$\vec{\boldsymbol{m}}$: is the electric dipole operator or electric moment dim: $\mathrm{M^{1/2}L^{5/2}T^{-1}}$

$|e|$: the absolute charge of the electron dim: $\mathrm{M^{1/2}L^{3/2}T^{-1}}$

$\cdot$: the scalar product

$\vec{\boldsymbol{E}}_{\mathrm{mic}}$: the electric field due to the light wave, including medium effects. $\vec{\boldsymbol{E}}_{\mathrm{mic}}$ is related to the macroscopic field $\vec{\boldsymbol{E}}_{\mathrm{mac}}$ by a dielectric factor (Lorentz effective field correction α) and $\vec{\boldsymbol{E}}(z,t) = \vec{\boldsymbol{E}}_{\mathrm{mac}}$ dim: $\mathrm{M^{1/2}L^{-1/2}T^{-1}}$

$\alpha = \dfrac{n^2+2}{3}$: the Lorentz correction for the electric field dim: /

j runs over the number of electrons of the electric dipole operator

$\vec{\boldsymbol{r}_j}$: the position vector of electron j dim: L

$\hat{\boldsymbol{r}}_\rho^{(1)}(\mathrm{r}_j, \theta_j, \phi_j)$: the position vector of electron j in tensor formalism dim: L

$D_\rho^{(1)}$: transition operator in tensor notation (similar to $\hat{D}_\rho^{(1)}$ in Görller-Walrand and Binnemans (1998)) with polarization numbers ρ dim: L

${}^{\mathrm{ED}}O_\rho^{(1)}$ and ${}^{\mathrm{MD}}O_\rho^{(1)}$: the transition operator in tensor notation for ED and MD respectively

$$\vec{\boldsymbol{m}} = m_x \vec{\boldsymbol{e}_x} + m_y \vec{\boldsymbol{e}_y} + m_z \vec{\boldsymbol{e}_z}, \tag{79}$$

where

$m_{\substack{x \\ y}}$: is the component of the electric dipole operator $\vec{\boldsymbol{m}}$ along x or y:

$$\vec{\boldsymbol{m}} = -m_- \vec{\boldsymbol{e}_+} - m_+ \vec{\boldsymbol{e}_-} + m_z \vec{\boldsymbol{e}_z} \tag{80}$$

and

$$m_{\pm} = \mp\frac{1}{\sqrt{2}}(m_x \pm \mathrm{i}m_y) \tag{81}$$

and vice versa:

$$m_x = \frac{1}{\sqrt{2}}(m_- - \mathrm{i}m_+) \quad \text{and} \quad m_y = \frac{\mathrm{i}}{\sqrt{2}}(m_- + \mathrm{i}m_+), \tag{82}$$

$$\overrightarrow{e}_{\pm} = \mp\frac{1}{\sqrt{2}}(\overrightarrow{e}_x \pm \mathrm{i}\overrightarrow{e}_y), \tag{83}$$

and vice versa:

$$\overrightarrow{e}_x = \frac{1}{\sqrt{2}} \quad (\overrightarrow{e}_- - \overrightarrow{e}_+) \quad \text{and} \quad \overrightarrow{e}_y = \frac{\mathrm{i}}{\sqrt{2}}(\overrightarrow{e}_- + \overrightarrow{e}_+). \tag{84}$$

The time dependence of $\overrightarrow{E}(z,t)$ can be removed by integration so that from now on $\overrightarrow{E}(z,t)$ becomes $\overrightarrow{E}(z)$.

For *linearly polarized light* along x and y the Hamiltonian is written as

$$\mathcal{H}^{\mathrm{ED}}_{\substack{x\\y}}(z) = -\frac{\left(n^2_{\substack{x\\y}}+2\right)}{3} m_{\substack{x\\y}} \overrightarrow{e}_{\substack{x\\y}} \left|\overrightarrow{E}_{\substack{x\\y}}(z)\right| \overrightarrow{e}_{\substack{x\\y}} = m_{\substack{x\\y}} \left|\overrightarrow{E}_{\substack{x\\y}}(z)\right|, \tag{85}$$

$$\mathcal{H}^{\mathrm{ED}}_{\substack{x\\y}}(z) = -\frac{\left(n^2_{\substack{x\\y}}+2\right)}{3} \left|\overrightarrow{E}_{\substack{x\\y}}(z)\right| \Re\left\{m_{\substack{x\\y}} \mathrm{e}^{\mathrm{i}\omega t}\right\}. \tag{86}$$

For a single line corresponding to a transition from a ground state a to an excited state j time-dependent perturbation theory gives

$$\frac{\mathrm{d}|a_m|^2}{\mathrm{d}t} = \frac{1}{t}\left|\frac{2\pi}{h}\int_0^t \mathrm{e}^{\mathrm{i}\omega t}\left\langle a\left|\mathcal{H}^{\mathrm{ED}}_{\substack{x\\y}}\right|j\right\rangle \mathrm{d}t\right|^2, \tag{87}$$

where $|a\rangle$ and $|j\rangle$ are eigenstates of $\mathcal{H}_0$.

Equation (87) leads to the following result for ED transitions:

$$\frac{\mathrm{d}|a_m|^2}{\mathrm{d}t} = \frac{\left(n^2_{\substack{x\\y}}+2\right)^2}{9} \frac{2\pi^2}{h^2} \left|\overrightarrow{E}_{\substack{x\\y}}(z)\right|^2 \left|\left\langle a\left|m_{\substack{x\\y}}\right|j\right\rangle\right|^2 f(v). \tag{88}$$

Introducing $\mathrm{d}|a_m|^2/\mathrm{d}t$ in the expression for the intensity attenuation (see Eqs. (55) and (76) gives

$$\begin{aligned} \mathrm{d}I(z) &= -n_{\substack{x\\y}} v \left|\overrightarrow{E}_{\substack{x\\y}}(z)\right|^2 \kappa^{\mathrm{ED}}_{\substack{x\\y}} \mathrm{d}z \\ &= -hvN_a \frac{\left(n^2_{\substack{x\\y}}+2\right)^2}{9} \frac{2\pi^2}{h^2} \left|\overrightarrow{E}_{\substack{x\\y}}(z)\right|^2 \left|\left\langle a\left|m_{\substack{x\\y}}\right|j\right\rangle\right|^2 f(v)\mathrm{d}z. \end{aligned} \tag{89}$$

For *linearly polarized light along x and y* one obtains

$$\kappa_{\substack{x\\y}}^{\mathrm{ED}} = \frac{\left(n_{\substack{x\\y}}^2+2\right)^2}{9n_{\substack{x\\y}}} \frac{2\pi^2}{h} N_a \left|\left\langle a\left|m_{\substack{x\\y}}\right|j\right\rangle\right|^2 f(\nu). \tag{90}$$

Similar expressions can be derived for *circularly polarized light*, keeping in mind that formally, complex polarization phase vectors are used so that now the equivalent of Eq. (85) is

$$\begin{aligned}\mathcal{H}_{\pm}^{\mathrm{ED}}(z) &= -\frac{(n_{\pm}^2+2)}{3} m_{\pm} \overrightarrow{e}_{\mp} |\overrightarrow{E}_{\pm}(z)| \overrightarrow{e}_{\pm} = m_{\pm} |\overrightarrow{E}_{\pm}(z)| \\ &= -\frac{(n_{\pm}^2+2)}{3} (m_{\pm} \overrightarrow{e}_{\mp} \bullet E_0 \overrightarrow{e}_{\pm}) \\ &= -\frac{(n_{\pm}^2+2)}{3} |\overrightarrow{E}_{\pm}(z)| \Re\{m_{\pm} \mathrm{e}^{\mathrm{i}\omega t}\}\end{aligned} \tag{91}$$

and

$$\frac{\mathrm{d}|a_m|^2}{\mathrm{d}t} = \frac{(n_{\pm}^2+2)^2}{9} \frac{2\pi^2}{h^2} |\overrightarrow{E}_{\pm}(z)|^2 |\langle a|m_{\pm}|j\rangle|^2 f(\nu), \tag{92}$$

$$\begin{aligned}\mathrm{d}I(z) &= -n_{\pm} \nu |\overrightarrow{E}_{\pm}(z)|^2 \kappa_{\pm}^{\mathrm{ED}} \mathrm{d}z \\ &= -h\nu N_a \frac{(n_{\pm}^2+2)^2}{9} \frac{2\pi^2}{h^2} |\overrightarrow{E}_{\pm}(z)|^2 |\langle a|m_{\pm}|j\rangle|^2 f(\nu) \mathrm{d}z,\end{aligned} \tag{93}$$

so that finally for the ED mechanism and circularly polarized light one obtains

$$\kappa_{\pm} = \frac{(n_{\pm}^2+2)^2}{9n_{\pm}} \frac{2\pi^2}{h} N_a |\langle a|m_{\pm}|j\rangle|^2 f(\nu). \tag{94}$$

3.3.3 Magnetic dipole transitions

Keeping in mind that the same phase relationships hold between $\overrightarrow{\boldsymbol{\mu}}$ and $\overrightarrow{\boldsymbol{m}}$ as between $\overrightarrow{\boldsymbol{H}}$ and $\overrightarrow{\boldsymbol{E}}$, exactly the same expressions can be derived for magnetic dipole transitions. The correction α' for the medium can be set equal to 1:

$$\begin{aligned}\mathcal{H}^{\mathrm{MD}} &= \mathcal{H}_1 = -\overrightarrow{\boldsymbol{\mu}} \bullet \overrightarrow{\boldsymbol{H}}_{\mathrm{mic}} = -\alpha' \overrightarrow{\boldsymbol{\mu}} \bullet \overrightarrow{\boldsymbol{H}}_{\mathrm{mac}} \\ &= -\overrightarrow{\boldsymbol{\mu}} \bullet \overrightarrow{\boldsymbol{H}}(z,t) = \beta(L+2S)_{\rho}^{1} H \quad \text{dim: } \mathrm{M L^2 T^{-2}}\end{aligned} \tag{95}$$

with

$$\begin{aligned}\vec{\boldsymbol{\mu}} &= -\frac{|e|\hbar}{2m_e c}(\vec{\boldsymbol{L}} + 2\vec{\boldsymbol{S}}) = -\frac{|e|\hbar}{2m_e c}\sum_j(\vec{\boldsymbol{l}_j} + 2\vec{\boldsymbol{s}_j}) \\ &= -\beta(L+2S)^{(1)}_{\rho} = {}^{\mathrm{MD}}O^{(1)} \quad \text{dim: } \mathrm{M}^{1/2}\mathrm{L}^{5/2}\mathrm{T}^{-1},\end{aligned} \tag{96}$$

where:
$\vec{\boldsymbol{\mu}}$: is the magnetic dipole operator
$|e|$: the absolute charge of the electron dim: $\mathrm{M}^{1/2}\mathrm{L}^{3/2}\mathrm{T}^{-1}$
m_e: the mass of the electron dim: M
$\vec{\boldsymbol{H}}_{\mathrm{mic}}$: the magnetic field due to the light wave, including medium effects. $\vec{\boldsymbol{H}}_{\mathrm{mic}}$ is related to the magnetic field $\vec{\boldsymbol{H}}$ that is only due to the electromagnetic radiation by the magnetic permeability α'.
α': the magnetic permeability which can be approximated to 1 for non-magnetic materials
H: the magnetic field strength dim: $\mathrm{M}^{1/2}\mathrm{L}^{-1/2}\mathrm{T}^{-1}$
$(L+2S)^{(1)}_{\rho}$: the tensor of rank 1 and components ρ dim:/
$\beta = \frac{|e|\hbar}{2m_e c}$: the Bohr magneton dim: $\mathrm{M}^{1/2}\mathrm{L}^{5/2}\mathrm{T}^{-1}$
$\vec{\boldsymbol{L}}$: the total orbital angular momentum operator dim:/
$\vec{\boldsymbol{S}}$: the total spin angular momentum operator dim:/

$$\vec{\boldsymbol{\mu}} = \mu_x\vec{\boldsymbol{h}}_x + \mu_y\vec{\boldsymbol{h}}_y + \mu_z\vec{\boldsymbol{h}}_z, \tag{97}$$

where $\mu_{\substack{y\\x}}$ is the component of the magnetic dipole operator $\vec{\boldsymbol{\mu}}$ along y or x:

$$\vec{\boldsymbol{\mu}} = -\mu_-\vec{\boldsymbol{h}}_+ - \mu_+\vec{\boldsymbol{h}}_- + \mu_z\vec{\boldsymbol{h}}_z \tag{98}$$

and[1]

$$\mu_\pm = \mp\frac{1}{\sqrt{2}}(\mu_y \mp \mathrm{i}\mu_x) \tag{99}$$

and vice versa:

$$\mu_x = \frac{1}{\sqrt{2}}(\mu_- - \mathrm{i}\mu_+) \quad \text{and} \quad \mu_y = \frac{\mathrm{i}}{\sqrt{2}}(\mu_- + \mathrm{i}\mu_+) \tag{100}$$

and with

$$\vec{\boldsymbol{h}}_\pm = \mp\frac{1}{\sqrt{2}}(\vec{\boldsymbol{h}}_y \mp \mathrm{i}\vec{\boldsymbol{h}}_x) \tag{101}$$

[1] Note that a different phase convention has been used in Piepho and Schatz (1983, p. 122).

and vice versa:

$$\vec{h}_x = -\frac{\mathrm{i}}{\sqrt{2}}(\vec{h}_- + \vec{h}_+) \quad \text{and} \quad \vec{h}_y = \frac{1}{\sqrt{2}}(\vec{h}_- - \vec{h}_+) \tag{102}$$

For *linearly polarized light along x and y*, meaning that the electric field vector is parallel to, respectively, the *x*- and *y*-axis ($\vec{E}_{\substack{x\\y}}$ corresponds to $\vec{H}_{\substack{x\\-y}}$), the perturbation Hamiltonian for the MD mechanism can be written as

$$\mathcal{H}^{\mathrm{MD}}_{\substack{x\\y}}(z) = \mp\alpha' \left|\vec{H}_{\substack{y\\x}}(z)\right| \Re\left\{\mu_{\substack{y\\x}} \mathrm{e}^{\mathrm{i}\omega t}\right\} = \mp\left|\vec{H}_{\substack{y\\x}}(z)\right| \Re\left\{\mu_{\substack{y\\x}} \mathrm{e}^{\mathrm{i}\omega t}\right\}. \tag{103}$$

We have

$$\begin{aligned}
\frac{\mathrm{d}|a_m|^2}{\mathrm{d}t} &= \alpha'^2 \frac{2\pi^2}{h^2} \left|\vec{H}_{\substack{y\\x}}(z)\right|^2 \left|\left\langle a \left| \mu_{\substack{y\\x}} \right| j \right\rangle\right|^2 f(\nu) \\
&= \alpha'^2 \frac{2\pi^2}{h^2} \left|\vec{H}_{\substack{y\\x}}(z)\right|^2 \left|\left\langle a \left| \vec{L}_{\substack{y\\x}} + 2\vec{S}_{\substack{y\\x}} \right| j \right\rangle\right|^2 \beta^2 f(\nu) \\
&= \frac{2\pi^2}{h^2} \left|n_{\substack{x\\y}} \vec{E}_{\substack{x\\y}}(z)\right|^2 \left|\left\langle a \left| \mu_{\substack{y\\x}} \right| j \right\rangle\right|^2 f(\nu) \quad \text{as}\, \alpha' = 1.
\end{aligned} \tag{104}$$

Introducing $\mathrm{d}|a_m|^2/\mathrm{d}t$ in the expression for the intensity attenuation gives

$$\begin{aligned}
\mathrm{d}I(z) &= -\frac{1}{n_{\substack{x\\y}}} \nu \left|\vec{H}_{\substack{y\\x}}(z,t)\right|^2 \kappa^{\mathrm{MD}}_{\substack{x\\y}} \mathrm{d}z \\
&= -h\nu N_a \frac{2\pi^2}{h^2} \left|\vec{H}_{\substack{y\\x}}(z,t)\right|^2 \left|\left\langle a \left| \mu_{\substack{y\\x}} \right| j \right\rangle\right|^2 f(\nu) \mathrm{d}z,
\end{aligned} \tag{105}$$

so that finally for the MD mechanism and linearly polarized light along *x* and *y* one obtains

$$\kappa^{\mathrm{MD}}_{\substack{x\\y}} = n_{\substack{x\\y}} \frac{2\pi^2}{h} N_a \left|\left\langle a \left| \mu_{\substack{y\\x}} \right| j \right\rangle\right|^2 f(\nu). \tag{106}$$

For *circularly polarized light* similar derivations result in

$$\mathcal{H}^{\mathrm{MD}}_{\pm}(z) = -\alpha' |\vec{H}_{\pm}(z)| \Re\{\mu_{\pm} \mathrm{e}^{\mathrm{i}\omega t}\}. \tag{107}$$

We have

$$\begin{aligned}
\frac{\mathrm{d}|a_m|^2}{\mathrm{d}t} &= \alpha'^2 \frac{2\pi^2}{h^2} |\vec{H}_{\pm}(z)|^2 |\langle a|\mu_{\pm}|j\rangle|^2 f(\nu) \\
&= \frac{2\pi^2}{h^2} |n_{\pm} \vec{E}_{\pm}(z)|^2 |\langle a|\mu_{\pm}|j\rangle|^2 f(\nu).
\end{aligned} \tag{108}$$

Introducing $\mathrm{d}|a_m|^2/\mathrm{d}t$ in the expression for the intensity attenuation gives

$$\mathrm{d}I(z) = -\frac{1}{n} v |\vec{\boldsymbol{H}}(z,t)|^2 \kappa_{\pm} \mathrm{d}z = -hvN_a \mathrm{d}z \frac{2\pi^2}{h^2} |\vec{\boldsymbol{H}}(z,t)|^2 |\langle a|\mu_{\pm}|j\rangle|^2 f(v)\mathrm{d}z, \tag{109}$$

so that finally

$$\kappa_{\pm}^{\mathrm{MD}} = n_{\pm} \frac{2\pi^2}{h} N_a |\langle a|\mu_{\pm}|j\rangle|^2 f(v) = n_{\pm} \frac{2\pi^2}{h} N_a |\langle a|\vec{\boldsymbol{L}}_{\pm} + 2\vec{\boldsymbol{S}}_{\pm}|j\rangle|^2 \beta^2 f(v). \tag{110}$$

3.4 The dipole strength

The dipole strength is defined as the absolute square of the matrix element for the transition:

$$D_{\rho}^{\mathrm{ED}} = |\langle a|^{\mathrm{ED}} O_{\rho}^{(1)}|j\rangle|^2, D_{\rho}^{\mathrm{MD}} = |\langle a|^{\mathrm{MD}} O_{\rho}^{(1)}|j\rangle|^2, \tag{111}$$

where
$D_{\rho}^{\mathrm{ED\,or\,MD}}$: is the dipole strength dim: M L^5 T^{-2} or e^2 L^2;
$^{\mathrm{ED}}O_{\rho}^{(1)} = m_{\rho}$
$^{\mathrm{MD}}O_{\rho}^{(1)} = \mu_{\rho}$

ρ : polarization of the light
$= +$ or $-$ for right or left circularly polarized light
$= x$ or y for linearly polarized light along x or y.

On macroscopic scale the following approximation is made:

$$n_{\pm} = n_{\substack{x \\ y}} = n. \tag{112}$$

Indeed, only the difference is significant. This difference is drastically increased by applying a magnetic field; this is the basis of magnetic optical rotation and MCD.

3.4.1 Electric dipole transitions

For *linearly polarized light*:

$$D_{\substack{x \\ y}}^{\mathrm{ED}} = \left|\langle a|m_{\substack{x \\ y}}|j\rangle\right|^2, \tag{113}$$

so that

$$\kappa_{\substack{x\\y}}^{\mathrm{ED}} = \frac{(n^2+2)^2}{9n}\frac{2\pi^2}{h}N_a D_{\substack{x\\y}}^{\mathrm{ED}} f(v) \tag{114}$$

or in other dimensions for $f(v)$:

$$\begin{aligned}\kappa_{\substack{x\\y}}^{\mathrm{ED}} &= \frac{(n^2+2)^2}{9n}2\pi^2 N_a D_{\substack{x\\y}}^{\mathrm{ED}} f(\boldsymbol{\mathcal{E}}) \\ &= \frac{(n^2+2)^2}{9n}\frac{4\pi^3}{h}N_a D_{\substack{x\\y}}^{\mathrm{ED}} f(\omega) \\ &= \frac{(n^2+2)^2}{9n}\frac{2\pi^2}{hc}N_a D_{\substack{x\\y}}^{\mathrm{ED}} f(\bar{v}) \\ &= \frac{(n^2+2)^2}{9n}\frac{2\pi^2 c}{h}N_a D_{\substack{x\\y}}^{\mathrm{ED}} f(\lambda)\end{aligned} \tag{115}$$

and vice versa:

$$D_{\substack{x\\y}}^{\mathrm{ED}} = \frac{9n}{(n^2+2)^2}\frac{h}{2\pi^2}\frac{1}{N_a f(v)}\kappa_{\substack{x\\y}}^{\mathrm{ED}}. \tag{116}$$

For *circularly polarized light*:

Circularly polarized light can only propagate along an optical axis, where $|\langle a|m_+|j\rangle|^2 = |\langle a|m_-|j\rangle|^2$, so that

$$D_{\pm}^{\mathrm{ED}} = |\langle a|m_{\pm}|j\rangle|^2 = \frac{1}{2}\left[|\langle a|m_+|j\rangle|^2 + |\langle a|m_-|j\rangle|^2\right], \tag{117}$$

then

$$\kappa_{\pm}^{\mathrm{ED}} = \frac{(n^2+2)^2}{9n}\frac{2\pi^2}{h}N_a D_{\pm}^{\mathrm{ED}} f(v) \tag{118}$$

and vice versa:

$$D_{\pm}^{\mathrm{ED}} = \frac{9n}{(n^2+2)^2}\frac{h}{2\pi^2}\frac{1}{N_a f(v)}\kappa_{\pm}^{\mathrm{ED}}. \tag{119}$$

3.4.2 Magnetic dipole transitions

For *linearly polarized light*:

$$D_{\substack{x\\y}}^{\mathrm{MD}} = \left|\langle a|\mu_{\substack{y\\x}}|j\rangle\right|^2 = \beta^2\left|\left\langle a\left|\overrightarrow{\boldsymbol{L}}_{\substack{y\\x}} + 2\overrightarrow{\boldsymbol{S}}_{\substack{y\\x}}\right|j\right\rangle\right|^2, \tag{120}$$

so that

$$\kappa^{\mathrm{MD}}_{\substack{x\\y}} = n\frac{2\pi^2}{h}N_a D^{\mathrm{MD}}_{\substack{y\\x}} f(v) \tag{121}$$

and vice versa:

$$D^{\mathrm{MD}}_{\substack{y\\x}} = \frac{1}{n}\frac{h}{2\pi^2}\frac{1}{N_a f(v)}\kappa^{\mathrm{MD}}_{\substack{y\\x}}. \tag{122}$$

For *circularly polarized light*:

$$\begin{aligned} D^{\mathrm{MD}}_{\pm} &= |\langle a|\mu_{\pm}|j\rangle|^2 = \beta^2\left|\left\langle a\left|\vec{\boldsymbol{L}}_{\pm}+2\vec{\boldsymbol{S}}_{\pm}\right|j\right\rangle\right|^2 \\ &= \frac{1}{2}\left[|\langle a|\mu_{+}|j\rangle|^2+|\langle a|\mu_{-}|j\rangle|^2\right], \end{aligned} \tag{123}$$

so that

$$\kappa^{\mathrm{MD}}_{\pm} = n\frac{2\pi^2}{h}N_a D^{\mathrm{MD}}_{\pm} f(v) \tag{124}$$

and vice versa:

$$D^{\mathrm{MD}}_{\pm} = \frac{1}{n}\frac{h}{2\pi^2}\frac{1}{N_a f(v)}\kappa^{\mathrm{MD}}_{\pm}. \tag{125}$$

3.4.3 Important remark

In Einstein's theory, the dipole strength is defined for an ''isotropic radiation bath'':

$$\begin{aligned} D_{\mathrm{isotropic}} &= \frac{1}{3}\left[|O_x|^2+|O_y|^2+|O_z|^2\right] \\ &= \frac{1}{3}\left[|O_{+}|^2+|O_{-}|^2+|O_z|^2\right]. \end{aligned} \tag{126}$$

This has implications for the formulation of the oscillator strength, introducing a factor 1/3 that was very misleading in MCD theory. In our pedestrian development we have tried to unravel these difficulties step by step and will always use the dipole strengths D^{ED} and D^{MD} as defined by Eqs. (113), (116), (117), (119), (120), (122), (123), (125) and, when necessary, use $D_{\mathrm{isotropic}}$ (see Eq. (126)).

3.5 Lambert–Beer's law: Relationship between κ and ε

The relationship between the absorption coefficient κ and the molar absorptivity ε is given by Lambert–Beer's law. The attenuation of the intensity over an infinitesimal optical path length dz is given by the derivative d$I(z)$/dz in Eq. (53):

$$\frac{\mathrm{d}I(z)}{I(z)} = -\frac{2\omega\kappa}{c}\mathrm{d}z, \tag{127}$$

Or by integration:

$$\int_{I_0}^{I} \frac{\mathrm{d}I(z)}{I(z)} = -\int_0^d \frac{2\omega\kappa}{c}\mathrm{d}z, \tag{128}$$

$$\ln I(z) - \ln I_0(z) = -\frac{2\omega\kappa}{c}(d-0), \tag{129}$$

$$\ln\frac{I_0(z)}{I(z)} = \frac{2\omega\kappa}{c}d. \tag{130}$$

After conversion to base-10 logarithms, one obtains the well-known Lambert–Beer's law:

$$\log\frac{I_0(z)}{I(z)} = \frac{1}{2.303}\ln\frac{I_0(z)}{I(z)} = \frac{1}{2.303}\frac{2\omega\kappa d}{c} = \varepsilon C_a d = A, \tag{131}$$

where:

ε: is the molar absorptivity (in l mol^{-1} cm^{-1})	dim: L^2
ω: the angular frequency (in radians s^{-1})	dim: T^{-1}
κ: the absorption coefficient	dim: /
C_a: the concentration of particles in energy level a (in mol l^{-1})	dim: L^{-3}
c: the speed of light (in cm s^{-1})	dim: L T^{-1}
d: the optical path length (in cm)	dim: L
A: the absorbance	dim: /

Thus, the molar absorptivity ε is related to the absorption coefficient κ by

$$\varepsilon = \frac{2\omega\kappa}{2.303cC_a} \quad (\text{in l mol}^{-1}\,\text{cm}^{-1}) \qquad \text{dim: L}^2 \tag{132}$$

and, vice versa, the absorption coefficient κ is related to ε by

$$\kappa = \frac{2.303cC_a\varepsilon}{2\omega}. \qquad \text{dim: /} \tag{133}$$

The transmittance T is defined as

$$T = \frac{I(z)}{I_0(z)} = \exp\left(\frac{-2\omega\kappa z}{c}\right) = \exp\left(\frac{-4\pi\nu\kappa z}{c}\right) = \exp\left(\frac{-4\pi\kappa z}{\lambda}\right). \quad \text{dim: /} \tag{134}$$

3.6 Relationship between the molar absorptivity ε and the dipole strength D

3.6.1 Relationship between ε^{ED} and D^{ED}

Introducing κ (Eqs. (90, 94) and (114, 118)) in the expression for ε and from Section 3.2.2 on the shape functions, one obtains

$$\varepsilon_\rho^{ED} = \frac{2\omega\kappa_\rho^D}{2.303cC_a} = \frac{2\omega}{2.303cC_a}\frac{(n^2+2)^2}{9n}\frac{2\pi^2}{h}N_a D_\rho^{ED} f(v). \tag{135}$$

The number of molecules per cm^3, N_a is related to the concentration in mol l^{-1} C_a by

$$N_a = \mathcal{N} \times C_a \times 10^{-3}, \tag{136}$$

where $\mathcal{N}$ is the Avogadro's number dim: /

so that

$$\varepsilon_\rho^{ED} = \frac{(n^2+2)^2}{9n}\frac{\mathcal{N}}{2303c}\frac{8\pi^3}{h}D_\rho^{ED} v f(v) \tag{137}$$

and

$$\begin{aligned}\varepsilon_\rho^{ED} &= \frac{(n^2+2)^2}{9n}\frac{\mathcal{N}}{2303c}\frac{8\pi^3}{h}D_\rho^{ED}\bar{v}f(\bar{v}) \\ &= \frac{(n^2+2)^2}{9n}326.6\times10^{36}D_\rho^{ED}\bar{v}f(\bar{v}) \quad (D_\rho^{ED}\text{ in esu}^2\,\text{cm}^2) \\ &= \frac{(n^2+2)^2}{9n}326.6D_\rho^{ED}\bar{v}f(\bar{v}) \quad (D_\rho^{ED}\text{ in Debye}^2),\end{aligned} \tag{138}$$

where

$$\begin{aligned}\frac{8\pi^3\mathcal{N}}{2303hc} &= \frac{8\times(3.14159)^3\times6.02214\times10^{23}}{2303\times6.62554\times10^{-27}\,\text{erg s}\times2.997925\times10^{10}\,\text{cm s}^{-1}} \\ &= 326.6\times10^{36}\,\text{erg}^{-1}\,\text{cm}^{-1} \\ &= 326.6\times10^{36}\,\text{esu}^{-2} \qquad \text{dim: } T^2M^{-1}L^{-3},\end{aligned}$$

ε: is the molar absorptivity in mol^{-1} lcm^{-1} dim: L^2
$\bar{v}$: the wavenumber in cm^{-1} dim: L^{-1}
d$\bar{v}$: in cm^{-1} dim: L^{-1}
n: the refractive index dim: /
$\mathcal{N}$: the Avogadro number = 6.02214 x 10^{23} dim: /
c:= 2.997925 $\times$ 10^{10} cm s^{-1} dim: LT^{-1}
h:= 6.6261 $\times$ 10^{-27} erg s dim: ML^{2}T^{-1}
D_ρ^{ED}: the dipole strength in Debye^2(D^2)
or in esu^{2}cm^2 dim: ML^{5}T^{-2} or e^{2}L^2
1 Debye = 10^{-18} esu cm

Note that the dimensions of the shape function are no longer important as it appears as $v\mathrm{f}(v)$ that can be replaced by $\bar{\nu}f(\bar{\nu})$ or any other quantity. This was not the case for κ. Because a transition has no infinitively small linewidth, ε is integrated over an infinitesimal wave number region $d\bar{\nu}$. We consider $\varepsilon/\bar{\nu}$ rather than ε

$$\int \frac{\varepsilon_\rho^{\mathrm{ED}}}{\bar{\nu}} \mathrm{d}\bar{\nu} = \int \frac{(n^2+2)^2}{9n} \frac{\mathcal{N}}{2303c} \frac{8\pi^3}{h} D_\rho^{\mathrm{ED}} f(\bar{\nu}) \mathrm{d}\bar{\nu} \tag{139}$$

With:

$$\int f(\bar{\nu}) \mathrm{d}\bar{\nu} = 1,$$

$$\begin{aligned} \int \frac{\varepsilon_\rho^{\mathrm{ED}}}{\bar{\nu}} \mathrm{d}\bar{\nu} &= \frac{(n^2+2)^2}{9n} \frac{\mathcal{N}}{2303c} \frac{8\pi^3}{h} D_\rho^{\mathrm{ED}} \\ &= \frac{(n^2+2)^2}{9n} 326.6 \times 10^{36} D_\rho^{\mathrm{ED}} \quad (D_\rho^{\mathrm{ED}} \text{ in esu}^2\,\text{cm}^2) \\ &= \frac{(n^2+2)^2}{9n} 326.6 D_\rho^{\mathrm{ED}} \quad (D_\rho^{\mathrm{ED}} \text{ in Debye}^2) \end{aligned} \tag{140}$$

and vice versa:

$$D_\rho^{\mathrm{ED}} = 3.062 \times 10^{-3} \frac{9n}{(n^2+2)^2} \int \frac{\varepsilon_\rho^{\mathrm{ED}}}{\bar{\nu}} \mathrm{d}\bar{\nu} \quad (D_\rho^{\mathrm{ED}} \text{ in Debye}^2) \quad (\varepsilon \text{ in mol}^{-1}\text{l cm}^{-1}). \tag{141}$$

The integral $\int \frac{\varepsilon}{\bar{\nu}} \mathrm{d}\bar{\nu}$ is called the zeroth moment of a transition.

$$<\boldsymbol{\varepsilon}>_0 = \int \frac{\boldsymbol{\varepsilon}}{\bar{\boldsymbol{\nu}}} \mathrm{d}\bar{\boldsymbol{\nu}} \tag{142}$$

Using Lambert–Beer's law, $A = \varepsilon C_a d$, one can rewrite this equation as

$$D_\rho^{\mathrm{ED}} = 3.062 \times 10^{-3} \frac{9n}{(n^2+2)^2} \frac{1}{C_a d} \int \frac{A_\rho^{\mathrm{ED}}(\bar{\nu})}{\bar{\nu}} \mathrm{d}\bar{\nu}. \tag{143}$$

3.6.2 Relationship between $\varepsilon^{\mathrm{MD}}$ and D^{MD}

From Eqs. (106), (110), (121) and (124), similar derivations for MD than for ED lead to

$$\varepsilon_\rho^{\mathrm{MD}} = \frac{2\omega\kappa_\rho^{\mathrm{MD}}}{2.303cC_a} = \frac{2\omega}{2.303cC_a} n \frac{2\pi^2}{h} N_a D_\rho^{\mathrm{MD}} f(\nu) \tag{144}$$

or

$$\begin{aligned}\varepsilon_\rho^{\mathrm{MD}} &= n\frac{\mathcal{N}}{2303c}\frac{8\pi^3}{h}D_\rho^{\mathrm{MD}}\nu f(\nu)\\ &= n\frac{\mathcal{N}}{2303c}\frac{8\pi^3}{h}D_\rho^{\mathrm{MD}}\bar{\nu}f(\bar{\nu}),\end{aligned} \tag{145}$$

where
D_ρ^{MD}: is the dipole strength in Debye^2(D^2) dim: $\mathrm{ML^5T^{-2}}$ or $\mathrm{e^2L^2}$
$1D{=}10^{-18}$ esu cm

or in terms of $\frac{\varepsilon}{\bar{\nu}}$:

$$\int\frac{\varepsilon_\rho^{\mathrm{MD}}(\bar{\nu})}{\bar{\nu}}\mathrm{d}\bar{\nu} = \int n\frac{\mathcal{N}}{2303c}\frac{8\pi^3}{h}D_\rho^{\mathrm{MD}}f(\bar{\nu})\mathrm{d}\bar{\nu}, \tag{146}$$

which results in

$$\begin{aligned}\int\frac{\varepsilon_\rho^{\mathrm{MD}}(\bar{\nu})}{\bar{\nu}}\mathrm{d}\bar{\nu} &= n\frac{\mathcal{N}}{2303c}\frac{8\pi^3}{h}D_\rho^{\mathrm{MD}}\\ &= n\ 326.6\times10^{36}D_\rho^{\mathrm{MD}}\quad(D_\rho^{\mathrm{MD}}\,\mathrm{in\,esu^2\,cm^2})\\ &= n\ 326.6D_\rho^{\mathrm{MD}}\quad(D_\rho^{\mathrm{MD}}\,\mathrm{in\,Debye^2})\\ &= n\ (326.6\times10^{36})\times(9.273\times10^{-21})^2\quad D_\rho^{\mathrm{MD}}\ (D_\rho^{\mathrm{MD}}\,\mathrm{in}\,\beta^2)\\ &= n\ 326.6\times(9.273\times10^{-3})^2\quad D_\rho^{\mathrm{MD}}\ (D_\rho^{\mathrm{MD}}\,\mathrm{in}\,\beta^2),\end{aligned} \tag{147}$$

where β is the Bohr's magneton;

$$\begin{aligned}\beta^2 &= (9.273\times10^{-21})^2 \cong 86\times10^{-42}\,\mathrm{esu^2\,cm^2}\\ &= (9.273\times10^{-3})^2\,\mathrm{Debye^2} \cong 86\times10^{-6}\,\mathrm{Debye^2};\end{aligned}$$

and

$$D_\rho^{\mathrm{MD}} = 3.062\times10^{-3}\frac{1}{n}\int\frac{\varepsilon_\rho^{\mathrm{MD}}(\bar{\nu})}{\bar{\nu}}\mathrm{d}\bar{\nu}\quad(D_\rho^{\mathrm{MD}}\,\mathrm{in\,Debye^2}). \tag{148}$$

It is important to realize that the dipole strength for MD transitions are five orders of magnitude smaller than for the *allowed* ED transitions. However, the *induced electric dipole* transitions in lanthanides are of the same magnitude as the magnetic dipole transitions.

Using Lambert–Beer's law, $A = \varepsilon C_a d$, one can rewrite this equation as:

$$D_\rho^{\mathrm{MD}} = 3.062\times10^{-3}\frac{1}{n}\frac{1}{C_a d}\int\frac{A_\rho^{\mathrm{MD}}(\bar{\nu})}{\bar{\nu}}\mathrm{d}\bar{\nu}\quad(D_\rho^{\mathrm{MD}}\,\mathrm{in\,Debye^2}). \tag{149}$$

3.6.3 Relationship between ε and D for mixed ED–MD transitions

In general, transitions have partial magnetic dipole and partial induced electric dipole character. The total experimental dipole strength $D^{\exp}$ then contains contributions of both electric dipole and magnetic dipole transitions:

$$\int \frac{\varepsilon_\rho^{\exp}(\mathrm{d}\bar{\nu})}{\bar{\nu}} = 326.6 D_\rho^{\exp} = 326.6 \left(\frac{(n^2+2)^2}{9n} D_\rho^{\mathrm{ED}} + n D_\rho^{\mathrm{MD}} \right) \qquad (150)$$

$(D_\rho^{\mathrm{ED}}, D_\rho^{\mathrm{MD}}$ expressed in Debye$^2)$.

3.7 Oscillator strength

The quantum theory associates an ''oscillator'' with each possible transition, and it is usual to assign a dimensionless *oscillator strength f* to each transition. The oscillator strength is a measure of the strength of a transition and it is the ratio of the actual intensity to the intensity radiated by an electron oscillating harmonically (=obeying Hooke's law force) in three dimensions. For a three-dimensional harmonic oscillator, $f = 1$. This is essentially the value found for transitions, such as the *D*-lines of sodium, for which only one electron contributes to the transition. For weaker transitions, we might say that less than one electron is participating in the transition, but it is more realistic to say that the transition involves compensating changes in the distributions of the other electrons. It is nevertheless convenient to consider the problem as if it involves a fractional part of an oscillator. For allowed (electric dipole) transitions, *f* lies theoretically in the neighbourhood of unity, but a value of 10^{-1} is more realistic. If the transition is forbidden *f* becomes much smaller than 1, but rarely reaches zero since there is almost always some perturbation mixing states so that the selection rule does not hold any more.

The oscillator strength can be calculated theoretically and determined experimentally, and so its importance lies in the connection it provides between theory and reality, as well as its usefulness for classifying the strength and nature of transitions.

The following equation that is given in most textbooks (Atkins, 1970; Eyring et al., 1944; McGlynn et al., 1972; Pauling and Wilson, 1935) relates the dimensionless oscillator strength *f* to the dipole matrix elements for ''an isotropic radiation bath'' (see Section 3.4.3 and Eq. (126)):

$$\begin{aligned} f_{\mathrm{isotropic}} &= \frac{8\pi^2 m_e \bar{\nu}_0 c}{3he^2} D_{\mathrm{isotropic}} \\ &= 4.7 \times 10^{-7} \bar{\nu}_0 D_{\mathrm{isotropic}} \end{aligned} \qquad \text{dim: /} \quad (151)$$

and vice versa:

$$D_{\text{isotropic}} = \frac{2.1 \times 10^6 \times f_{\text{isotropic}}}{\bar{\nu}_0}. \tag{152}$$

With the definition of D in Eqs. (113), (116), (117), (119), (120), (122), (123) and (125) the factor 1/3 disappears and we find (Görller-Walrand and Binnemans, 1998; Piepho and Schatz, 1983; Stephens, 1976):

$$\begin{aligned} f &= \frac{8\pi^2 m_e \bar{\nu}_0 c}{he^2} D \\ &= 1.41 \times 10^{-6} \bar{\nu}_0 D \end{aligned} \tag{153}$$

and vice versa:

$$D = \frac{7.089 \times 10^5 \times f}{\bar{\nu}_0}, \tag{154}$$

where
$\bar{\nu}_0$: is the wavenumber at the absorption maximum (in cm^{-1})
e: the charge of one electron = 4.803×10^{-10} esu
m_e: the mass of electron = 9.110×10^{-28}g
h: 6.6261 x 10^{-27} erg s
D: the dipole strength in Debye^2 dim: ML^5T^{-2}

It is noteworthy that two transitions which have the same oscillator strength do not have the same dipole strength because the value of f is divided by $\bar{\nu}_0$ in the expression of D. It is even possible that a transition having a larger oscillator strength than a second one has the lowest dipole strength.

The relationship between f and ε is based on Eq. (141) for ED and on Eq. (148) for MD transitions:

$$\begin{aligned} f &= 4.32 \times 10^{-9} \bar{\nu}_0 \frac{1}{\chi} \int \frac{\varepsilon(\bar{\nu})}{\bar{\nu}} \mathrm{d}\bar{\nu} \\ &= 4.32 \times 10^{-9} \frac{1}{\chi} \int \varepsilon(\bar{\nu}) \mathrm{d}\bar{\nu}. \end{aligned} \tag{155}$$

This relationship is independent of the convention used for the dipole strength. It depends only on the integrated spectral intensity.

In some books, for example, Wybourne (1965), the expression of f is given separately for ED and MD transitions as

$$\begin{aligned} f^{\text{ED}}_{\text{isotropic}} &= \frac{(n^2+2)^2}{9} \frac{8\pi^2 m_e c}{3he^2} \bar{\nu}_0 D^{\text{ED}}_{\text{isotropic}} \\ &= \frac{(n^2+2)^2}{9} 4.7 \times 10^{-7} \bar{\nu}_0 D^{\text{ED}}_{\text{isotropic}} \quad (D \text{ in Debye}^2), \end{aligned} \tag{156}$$

$$f^{\mathrm{MD}}_{\mathrm{isotropic}} = n\frac{8\pi^2 m_e c}{3he^2}\bar{\nu}_0\left(\frac{e\hbar}{2m_e c}\right)^2 D^{\mathrm{MD}}_{\mathrm{isotropic}} = n\ 4.028\times 10^{-11}\bar{\nu}_0 D^{\mathrm{MD}}_{\mathrm{isotropic}} \quad (D \text{ in } \beta^2). \tag{157}$$

Here D^{MD} is defined as in Eqs. (120) and (123) but expressed in units of β^2 and also expressed in terms of the operators $\vec{L}$ and $\vec{S}$ that do include the factor $\hbar$, contrary to other conventions.

3.8 Degeneracy and population factor

Equations (90), (94), (106), (110) and (138), (144) strictly hold for one single transition in the spectrum, more precisely for a transition between two non-degenerate states and for one polarization orientation ($\rho = x$ or y, $+1$ or -1). In that case all molecules are in the ground state a, leading to the factor N_a in κ which is related to C_a in ε. If several transitions have the same energy, because of degeneracy or because more than one state is populated, N_a remains as such but in Lambert–Beer's law, the concentration becomes C_A, the total concentration of the crystal field manifold states. Therefore, a summation over a and j must be performed leading to the expression:

$$\kappa_\rho(J \leftarrow A) = \chi\frac{2\pi^2}{h}\sum_{a,j} N_a |\langle a|O^{(1)}_\rho|j\rangle|^2 f(\nu), \tag{158}$$

(χ is the correction for the medium effects defined in Section 4.2.1)
where
N_a : fraction of the total population N_A of state A per cm^3 dim: L^{-3}

$$\frac{N_a}{C_A} = \frac{N_a}{N_A}\frac{N_A}{C_A} = \frac{N_a}{N_A}\mathcal{N}\times 10^{-3}. \tag{159}$$

The expression for ε now contains a population factor. Moreover if the ground state is degenerate a factor $1/d_A$ must be introduced:

$$\varepsilon_\rho = \chi\frac{1}{d_A}\frac{8\pi^3\mathcal{N}}{2303hc}\sum_{a,j}\frac{N_a}{N_A}|\langle a|O^{(1)}_\rho|j\rangle|^2 \nu f(\nu). \tag{160}$$

When the ground state is degenerate the factor $1/d_A$ will be included in the dipole strength D and the $\mathcal{A}_1$, $\mathcal{B}_0$ and $\mathcal{C}_0$ parameters as well as the summation over a and j (see below).

$$D = \frac{1}{d_A}\sum_{a,j}|\langle a|O_\pm|j\rangle|^2 = \frac{1}{2d_A}\sum_{a,j}[|\langle a|O_-|j\rangle|^2 + |\langle a|O_+|j\rangle|^2]. \tag{161}$$

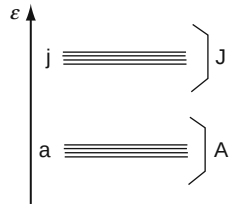

FIGURE 13 Ground and excited degenerate states *A* and *J* of the absorbing centre with the non-degenerate components *a* and *j*. It is assumed that only the ground states *A* are populated.

The reason for introducing these expressions is important for the MCD theory where the Zeeman levels are very close to each other and contribute to the same transition energy. In MCD one considers the Zeeman splitting of the crystal field states as being small with respect to the bandwidth of the peaks, so that the transition from a degenerate A state to a non-degenerate *J* state will occur at the same energy with or without magnetic field. The two components being differently populated according to Boltzmann's law, will show a temperature effect in MCD where now the difference in absorption is measured (see Figure 13 and see *C* term in Figure 4).

4. QUANTITATIVE THEORETICAL TREATMENT OF MCD

4.1 General introduction

MCD is based on the Zeeman effect and measures the difference in absorptivity of left and right circularly polarized light: $\kappa_- \neq \kappa_+$ and $\Delta\kappa = \kappa_- - \kappa_+$ (see Eqs. (40) and (41)) or $\varepsilon_- \neq \varepsilon_+$ and $\Delta\varepsilon = \varepsilon_- - \varepsilon_+$. From another point of view MCD can be regarded as the absorptive counterpart of MORD, the well-known Faraday effect.

Some definitions

Optical rotation is the rotation of linearly polarized light over an angle α, when light with a given energy (mostly expressed in wavelength λ) goes through an optically active substance. *Optical rotation dispersion* (ORD) is the same phenomenon, but reported as a function of a range of energies (or related quantities: λ, ν, $\bar{\nu}$, ω,...). *Natural circular dichroism* (CD) is also this same phenomenon, but in spectral ranges where absorption occurs.

ORD takes place because the refractive index is no longer the same for left and right circularly polarized light ($n_- \neq n_+$). Linear polarized light is the resultant of left and right circularly polarized light. If the refractive index for left is different from that for right polarization, the light will still be linearly polarized but at an angle α with respect to the original orientation of the polarized light.

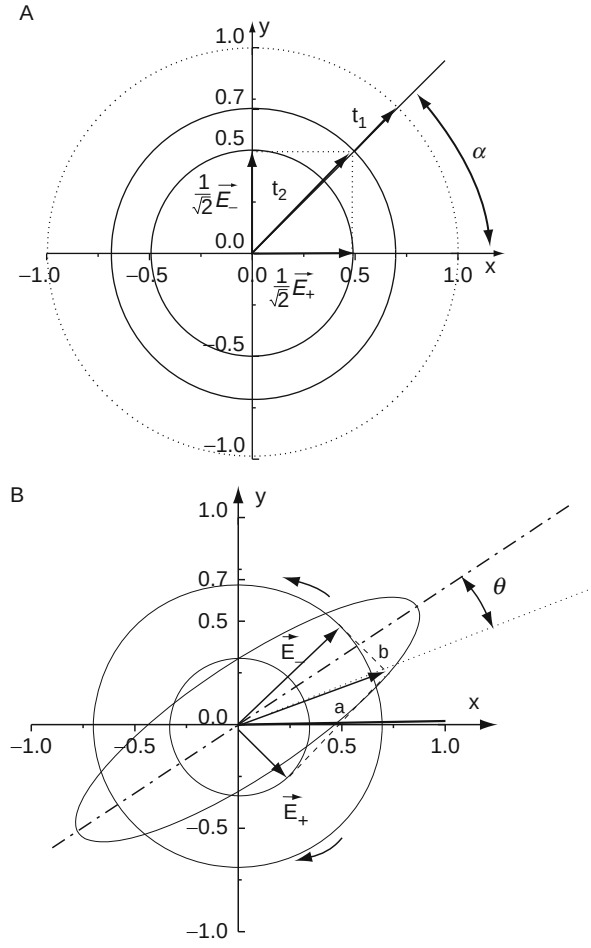

FIGURE 14 (A) Linearly polarized light obtained as the resultant of left and right circularly polarized light for $n_- > n_+$ and (B) elliptically polarized light obtained as the resultant of circularly polarized light with $\kappa_- < \kappa_+$ ($E_- > E_+$).

When there is absorption, the absorption for left polarization will be different from that for right polarization and the original linearly polarized light becomes elliptically polarized. The ellipticity is related to an angle θ that itself is related to the difference in absorption coefficient $\Delta\kappa$ or in molar absorptivity $\Delta\varepsilon$. This is visualized in Figure 14B. If $n_- \neq n_+$, this results in the electric field vector $\vec{E}_-$ being an angle φ in advance with respect to $\vec{E}_+$. In Figure 14A, $\vec{E}_-$ is 90° in advance over $\vec{E}_+$. The resultant is linearly polarized light making an angle $\alpha = \varphi/2$ with the x-axis ($\alpha = 45°$ counter-clockwise in Figure 14A).

Faraday found experimentally that all substances show this effect in presence of a magnetic field (Schatz and Mc Caffery, 1969), leading to *Magnetic optical rotation dispersion* (MORD) and *Magnetic circular dichroism* (MCD) (Caldwell and Eyring, 1976; Dawber, 1964; Foss and Mccarvil, 1965; Schatz et al., 1978; Thorne, 1977). Experimentally however, ORD and MORD were never measured extensively contrary to CD and MCD.

Whereas the experimental setup is the same for natural CD and MCD, the theoretical origin of the difference in refractive index $\Delta n = n_- - n_+$ or absorption coefficient $\Delta\kappa = \kappa_- - \kappa_+$ or molar absorptivity $\Delta\varepsilon = \varepsilon_- - \varepsilon_+$ is totally different. Natural circular dichroism is entirely due to the dissymmetry of the molecules that causes the electrons to move in a helical path of excitation; they may then absorb left circularly polarized light to a greater or lesser extent than right, depending on the ''handedness'' of the helix. Theoretically, natural CD occurs when a transition due to these chiral properties is both electric and magnetic dipole allowed (Schellman, 1975). The measured property is the rotatory strength (R in Debye $\times$ Bohr magneton ($D\beta$) units). The rotatory strength contains the imaginary part of the scalar product $\vec{\boldsymbol{m}} \cdot \vec{\boldsymbol{\mu}}$.

In MCD, left and right circularly polarized lights no longer interact equivalently with the absorbing medium because of the presence of the external magnetic field. This leads to a difference in absorptivity and thus to elliptical polarization of the outcoming light. It explains why in the past the MCD spectra were plotted in these strange units: $^\circ\text{gauss}^{-1}\ \text{mol}^{-1}\ \text{dl}\ \text{dm}^{-1}$, the same as the ones used in natural optical activity.

The problems of units and of the definition of the dipole strength resulted in the introduction of numerical factors to relate theory and experiment. In this respect, we have tried to be consistent with Stephens (1976). However, many spectra we refer to from the literature are not reported in the units: $^\circ\text{gauss}^{-1}\ \text{mol}^{-1}\ \text{dl}\ \text{dm}^{-1}$. For practical reasons we could not redraw them or ask for copyrights; we apologize for this and mention in the captions how to read them.

4.2 MCD as the difference in absorptivity by the Stephens formalism

4.2.1 MCD: Influence of an external longitudinal magnetic field on the circularly polarized absorption process

Making no distinction between the electric and magnetic dipole intensity mechanism, the absorption coefficient for left and right circularly polarized light for a transition $J \leftarrow A$ is written as (see Eq. (158) and Section 3.2.2)

$$\begin{aligned}\kappa_{\pm}(J \leftarrow A) &= \chi \frac{2\pi^2}{h} \sum_{a,j} N_a |\langle a|O_{\pm}^{(1)}|j\rangle|^2 f(\nu) \\ &= \chi \frac{4\pi^3}{h} \sum_{a,j} N_a |\langle a|O_{\pm}^{(1)}|j\rangle|^2 f(\omega) \\ &= \chi \frac{2\pi^2}{hc} \sum_{a,j} N_a |\langle a|O_{\pm}^{(1)}|j\rangle|^2 f(\bar{\nu})\end{aligned} \tag{162}$$

with[2]

$$\begin{aligned}O_{\pm}^{(1)} &= m_{\pm}(\mathrm{ED}) \\ &= \mu_{\pm}(\mathrm{MD}),\end{aligned}$$

$$\chi : \text{correction for medium effects},$$

$$\chi = \frac{(n^2+2)^2}{9n} \quad \text{for} \quad \mathrm{ED},$$

$$\chi = n \quad \text{for} \quad \mathrm{MD}.$$

In MCD the external longitudinal magnetic field will, for a transition $j \leftarrow a$, have an influence on the wave functions $|a\rangle$ and $|j\rangle$, the corresponding eigenvalues v_a and v_j, the population of the ground level N_a, and finally the lineshape $f(v)$.

This magnetic influence will be worked out in the following sections and is designated by a prime in the following equation:

$$\begin{aligned}\Delta\kappa'(J \leftarrow A) &= \kappa'_{-} - \kappa'_{+} \\ &= \chi \frac{2\pi^2}{h} \sum_{a,j} [N'_a \left(|\langle a|O_{-}^{(1)}|j\rangle'|^2 - |\langle a|O_{+}^{(1)}|j\rangle'|^2 \right)] f'(\nu).\end{aligned} \tag{163}$$

This equation can be rewritten in terms of molar absorptivity ε[3]:

$$\begin{aligned}\Delta\varepsilon'(J \leftarrow A) &= \varepsilon'_{-} - \varepsilon'_{+} \\ &= \chi \frac{8\pi^3 \mathcal{N}}{2303hc} \sum_{a,j} \left[\frac{N'_a}{N_A} \left(|\langle a|O_{-}^{(1)}|j\rangle'|^2 - |\langle a|O_{+}^{(1)}|j\rangle'|^2 \right) \right] \nu f'(\nu).\end{aligned} \tag{164}$$

In general, the sublevels $\{a\}$ and $\{j\}$ belong to the states A and J which are degenerate in absence of a magnetic field. Then the resulting

[2] Note that our $m_{\pm}$ operator includes Condon–Shortley convention and is in agreement with the $m_{\pm 1}$ operator reported in Piepho and Schatz 1983, p. 79.

[3] Note that the factor $8\pi^3\mathcal{N}/2303hc$ is in agreement with $\gamma = 2.\mathcal{N}\pi^3 \log_{10}\mathrm{e}/250hc$ defined in Stephens, 1976, p. 201.

absorption coefficient is a summation over all these degenerate sublevels belonging to the states A and J:

$$\kappa_{\pm}(J \leftarrow A) = \sum_{a,j} \kappa_{\pm}(j \leftarrow a). \tag{165}$$

Similarly for circular dichroism:

$$\Delta\kappa'_{\pm}(J \leftarrow A) = \sum_{a,j} \Delta\kappa'_{\pm}(j \leftarrow a). \tag{166}$$

The external magnetic field $\mathcal{H}'_0$ can be treated as a small perturbation by time-independent perturbation theory.

For a magnetic field parallel to the internal molecular z-axis, the Hamiltonian operator becomes

$$\begin{aligned} \mathcal{H}_0 = \mathcal{H}_0^0 + \mathcal{H}'_0 &= \mathcal{H}_0^0 - \vec{\boldsymbol{\mu}}\,\vec{\boldsymbol{H}} = \mathcal{H}_0^0 - \mu_z H_z = \mathcal{H}_0^0 + \beta(L+2S)_0^{(1)} H_z \\ &= \mathcal{H}_0^0 + \beta(L_z+2S_z)H_z \end{aligned} \tag{167}$$

with $H_z = H$.

4.2.2 Influence of the magnetic field on the wave functions and eigenvalues

A and J are considered as the degenerate eigenfunctions of the absorbing molecule in the absence of a magnetic field. The functions that describe the states A and J and their corresponding zeroth-order energies are

$$\{|a^0\rangle\}, \{|j^0\rangle\} \quad \text{and} \quad \{hv_a^0\}, \{hv_j^0\}.$$

A longitudinal magnetic field has its influence on these quantities in the following way:

$$|a\rangle' = |a^0\rangle + \sum_{k^0 \neq a^0} \frac{\langle k^0|\mu_z|a^0\rangle H}{hv_{KA}^0} |k^0\rangle, \tag{168}$$

$$hv_a = hv_A^0 + hv'_a = hv_A^0 - \langle a^0|\mu_Z|a^0\rangle H, \tag{169}$$

$$|j\rangle' = |j^0\rangle + \sum_{k^0 \neq j^0} \frac{\langle k^0|\mu_z|j^0\rangle H}{hv_{KJ}^0} |k^0\rangle, \tag{170}$$

$$hv_j = hv_J^0 + hv'_j = hv_J^0 - \langle j^0|\mu_Z|j^0\rangle H, \tag{171}$$

where a^0, j^0, k^0 are zero-order function chosen to diagonalize μ_z. These new wave functions $\{|a\rangle\}$ and $\{|j\rangle\}$ have to be connected to each other by

the dipole operator $O_\rho^{(1)}$ defined in Eq. (162). To the first-order perturbation in the magnetic field, the matrix element for these operators becomes

$$\begin{aligned}\langle a|O_\pm^{(1)}|j\rangle' &= \langle a^0|O_\pm^{(1)}|j^0\rangle \mp \sum_{k^0\neq a^0}\frac{\langle a^0|\mu_Z|k^0\rangle H}{hv_{KA}^0}\langle k^0|O_\pm^{(1)}|j^0\rangle \\ &\mp \sum_{k^0\neq j^0}\frac{\langle k^0|\mu_Z|j^0\rangle H}{hv_{KJ}^0}\langle a^0|O_\pm^{(1)}|k^0\rangle.\end{aligned} \tag{172}$$

The absolute square of this matrix element then becomes

$$\begin{aligned}|\langle a|O_\pm^{(1)}|j\rangle'|^2 &= |\langle a^0|O_\pm^{(1)}|j^0\rangle|^2 - 2\Re\left\{\sum_{k^0\neq a^0}\frac{\langle k^0|\mu_Z|a^0\rangle H}{hv_{KA}^0}\langle a^0|O_\pm^{(1)}|j^0\rangle\langle j^0|O_\mp^{(1)}|k^0\rangle\right\} \\ &- 2\Re\left\{\sum_{k^0\neq j^0}\frac{\langle j^0|\mu_Z|k^0\rangle H}{hv_{KJ}^0}\langle a^0|O_\pm^{(1)}|j^0\rangle\langle k^0|O_\mp^{(1)}|a^0\rangle\right\}.\end{aligned} \tag{173}$$

4.2.3 Influence of the magnetic field on the population of the ground level

The influence of the magnetic field on the energy of the ground level results in a Boltzmann temperature-dependent redistribution of the population between the sublevels of A. The population of the sublevel a will now be given by

$$\begin{aligned}N_a' &= \frac{N_A\exp(-hv_a'/kT)}{\sum_{a'}\exp(-hv_a'/kT)} \\ &= \frac{N_A}{d_A}\exp(\langle a_0|\mu_Z|a_0\rangle H/kT),\end{aligned} \tag{174}$$

where N_A is the number of absorbing centres in level A per cm^3 and d_A the degeneracy of A.

With $k = 0.695\ \mathrm{cm}^{-1}\ \mathrm{K}^{-1}$, it is clear that, except for very low temperatures (4–10 K), the Zeeman splitting is small compared to kT:

$$\langle a_0|\mu_Z|a_0\rangle H \ll kT. \tag{175}$$

Then, N_a' can be expanded to the first order in the magnetic field:

$$N_a' = \frac{N_A}{d_A}(1+\langle a_0|\mu_Z|a_0\rangle H/kT). \tag{176}$$

4.2.4 Influence of the magnetic field on the shape function

In the absence of an external magnetic field, the transition occurs at the resonance frequency v_{JA}. The magnetic field shifts this transition by the amount that is determined by the Zeeman effects in both a and j:

$$v'_{ja} = v_{JA} + \frac{(\langle j^0|\mu_Z|j^0\rangle - \langle a^0|\mu_Z|a^0\rangle)H}{h}. \tag{177}$$

The shape function $f'(v)$ is identical to $f'(v, v_{ja})$ or $f(v, v_{JA})$ but is shifted along the energy axis (x-axis). When Zeeman shifts are small compared to the bandwidth, a Taylor expansion to the first power in the magnetic field can be used:

$$\begin{aligned} f(v, v_{ja})' &= f(v, v_{JA}) + \frac{\mathrm{d}f(v, v_{JA})}{\mathrm{d}v}(v_{ja} - v_{JA}) \\ &= f(v, v_{JA}) + \frac{\mathrm{d}f(v, v_{JA})}{\mathrm{d}v}\frac{(\langle j^0|\mu_Z|j^0\rangle - \langle a^0|\mu_Z|a^0\rangle)H}{h}. \end{aligned} \tag{178}$$

4.2.5 MCD expression for a $J \leftarrow A$ transition

Taking into account the primed quantities of Eq. (163) we just evaluated, transition moments and ground state population, and discarding quadratic terms, the expressions of κ becomes

$$\kappa_{\pm} = \kappa^0_{\pm} + \chi\frac{2\pi^2}{h}\frac{N_A}{d_A}H\sum_{a^0,j^0}\left\{\begin{array}{l} \left[\begin{array}{l} 2\Re\left\{\displaystyle\sum_{k^0\neq a^0}\frac{\langle k^0|\mu_Z|a^0\rangle}{hv^0_{KA}}\langle a^0|O^{(1)}_{\pm}|j^0\rangle\langle j^0|O^{(1)}_{\mp}|k^0\rangle\right\} \\ +2\Re\left\{\displaystyle\sum_{k^0\neq j^0}\frac{\langle j^0|\mu_Z|k^0\rangle}{hv^0_{KJ}}\langle a^0|O^{(1)}_{\pm}|j^0\rangle\langle k^0|O^{(1)}_{\mp}|a^0\rangle\right\} \end{array}\right] f(v, v_{JA}) \\ \quad + \left[\dfrac{\langle a^0|\mu_Z|a^0\rangle|\langle a^0|O^{(1)}_{\pm}|j^0\rangle|^2}{kT}\right] f(v, v_{JA}) \\ + \left(|\langle a^0|O^{(1)}_{\pm}|j^0\rangle|^2\dfrac{(\langle j^0|\mu_Z|j^0\rangle - \langle a^0|\mu_Z|a^0\rangle)}{h}\right)\dfrac{\mathrm{d}f(v, v_{JA})}{\mathrm{d}v} \end{array}\right\}. \tag{179}$$

Since

$$\mu_z = -\beta(L_z + 2S_z),$$

$$\Delta\kappa = \kappa_- - \kappa_+ = \chi\frac{2\pi^2}{h}N_A\left\{\boldsymbol{\mathcal{A}}_1\left(-\frac{\mathrm{d}f(v, v_{JA})}{h\,\mathrm{d}v}\right) + \left(\boldsymbol{\mathcal{B}}_0 + \frac{\boldsymbol{\mathcal{C}}_0}{kT}\right)f(v, v_{JA})\right\}\beta H. \tag{180}$$

This leads to the difference in molar absorptivities (see Eq. (164)):

$$\Delta\varepsilon = \varepsilon_- - \varepsilon_+ = \chi \frac{8\pi^3 \mathcal{N}}{2303hc} \left\{ \mathcal{A}_1 \left(-\frac{v\,\mathrm{d}f(v, v_{JA})}{h\,\mathrm{d}v} \right) + \left(\mathcal{B}_0 + \frac{\mathcal{C}_0}{kT} \right) v f(v, v_{JA}) \right\} \beta H. \tag{181}$$

Taking into account that

$$v \frac{\mathrm{d}f(v, v_{JA})}{\mathrm{d}v} = \frac{\bar{v}}{c} \frac{\mathrm{d}f(\bar{v}, \bar{v}_{JA})}{\mathrm{d}\bar{v}} \quad \text{and} \quad v f(v, v_{JA}) = \bar{v} f(\bar{v}, \bar{v}_{JA}) \quad \text{dim: L} \tag{182}$$

one obtains

$$\Delta\varepsilon = \varepsilon_- - \varepsilon_+ = \chi \frac{8\pi^3 \mathcal{N}}{2303hc} \left\{ \mathcal{A}_1 \left(-\frac{\bar{v}\,\mathrm{d}f(\bar{v}, \bar{v}_{JA})}{hc\,\mathrm{d}\bar{v}} \right) + \left(\mathcal{B}_0 + \frac{\mathcal{C}_0}{kT} \right) \bar{v} f(\bar{v}, \bar{v}_{JA}) \right\} \beta H. \tag{183}$$

Important remark:

When all energies ($h\,\mathrm{d}v = hc\,\mathrm{d}\bar{v}$, kT, βH, hv^0_{KA}, hv^0_{KJ} (see Eq. (179)) are expressed in cm^{-1}:

$$\Delta\varepsilon = \varepsilon_- - \varepsilon_+ = \chi 326.6 \left\{ \mathcal{A}_1 \left(-\frac{\bar{v}\,\mathrm{d}f(\bar{v}, \bar{v}_{JA})}{\mathrm{d}\bar{v}} \right) + \left(\mathcal{B}_0 + \frac{\mathcal{C}_0}{kT} \right) \bar{v} f(\bar{v}, \bar{v}_{JA}) \right\} \beta H \tag{184}$$

and with $\beta = 0.4669\ \mathrm{cm}^{-1}\ \mathrm{tesla}^{-1}$ and H expressed in tesla:

$$\begin{aligned} \Delta\varepsilon &= \varepsilon_- - \varepsilon_+ \\ &= \chi\ 326.6 \times 0.4669 \left\{ \mathcal{A}_1 \left(-\frac{\bar{v}\,\mathrm{d}f(\bar{v}, \bar{v}_{JA})}{\mathrm{d}\bar{v}} \right) + \left(\mathcal{B}_0 + \frac{\mathcal{C}_0}{kT} \right) \bar{v} f(\bar{v}, \bar{v}_{JA}) \right\} H \\ &= \chi 152.5 \left\{ \mathcal{A}_1 \left(-\frac{\bar{v}\,\mathrm{d}f(\bar{v}, \bar{v}_{JA})}{\mathrm{d}\bar{v}} \right) + \left(\mathcal{B}_0 + \frac{\mathcal{C}_0}{kT} \right) \bar{v} f(\bar{v}, \bar{v}_{JA}) \right\} H, \end{aligned} \tag{185}$$

where:

$\Delta\varepsilon = \varepsilon_- - \varepsilon_+$ is the difference in molar absorptivity between left and right circularly polarized light	in 1 $\mathrm{mole}^{-1}\mathrm{cm}^{-1}$	dim: $\mathrm{L}^2(\mathrm{mole}^{-1})$
$\bar{v}$: the wavenumber	in cm^{-1}	dim: L^{-1}
$f(\bar{v})$: the shape function	in cm	dim: L
$\mathrm{d}\bar{v}$:	in cm^{-1}	dim: L^{-1}
$\dfrac{\mathrm{d}f(\bar{v}, \bar{v}_{JA})}{\mathrm{d}\bar{v}}$	in cm^2	dim: L^2
$\bar{v}\dfrac{\mathrm{d}f(\bar{v}, \bar{v}_{JA})}{\mathrm{d}\bar{v}}$:	in cm	dim: L

n: the refractive index dim: /

$\mathcal{N}$: the Avogadro number = 6.02214×10^{23} dim: /

$|e|$: 4.803×10^{-10} esu dim: $M^{1/2}L^{3/2}T^{-1}$

c:=2.997925×10^{10}cm s^{-1} dim: LT^{-1}

m_e: 9.10904×10^{-28} g dim: M

h:=6.6261×10^{-27}erg s dim: ML^2T^{-1}

$\beta = \frac{|e|\hbar}{2m_e c} = 4.669 \times 10^{-1}\text{cm}^{-1}\text{tesla}^{-1}$: the Bohr magneton[4]

dim: $M^{1/2}L^{5/2}T^{-1}$

H: the magnetic field in tesla dim: $M^{1/2}L^{-1/2}T^{-1}$

(1 tesla = 10, 000 gauss)

$$\frac{8\pi^3\mathcal{N}}{2303hc} = \frac{8 \times (3.14159)^3 \times 6.02214 \times 10^{23}}{2303 \times 6.62554 \times 10^{-27}\text{ergs} \times 2.997925 \times 10^{10}\,\text{cm}\,\text{s}^{-1}}$$

$$= 326.6 \times 10^{36}\,\text{erg}^{-1}\,\text{cm}^{-1}$$

$$= 326.6 \times 10^{36}\,\text{esu}^{-2}.$$

dim: $T^2\,M^{-1}\,L^{-3}$

$$\boldsymbol{a}_1 = \frac{1}{d_A}\sum_{a^0,j^0}\left(\left(|\langle a^0|O_-^{(1)}|j^0\rangle|^2 - |\langle a^0|O_+^{(1)}|j^0\rangle|^2\right)(\langle j^0|L_z+2S_z|j^0\rangle - \langle a^0|L_z+2S_z|a^0\rangle)\right)$$

(in Debye^2) dim: $L^5\,M\,T^{-2}$, (186)

$$\boldsymbol{\mathcal{B}}_0 = \frac{1}{d_A}2\Re\sum_{a^0,j^0}\left[\begin{array}{l}\left\{\sum_{k^0\neq a^0}\frac{\langle k^0|L_z+2S_z|a^0\rangle}{\bar{\nu}^0_{KA}}[\langle a^0|O_-^{(1)}|j^0\rangle\langle j^0|O_+^{(1)}|k^0\rangle - \langle a^0|O_+^{(1)}|j^0\rangle\langle j^0|O_-^{(1)}|k^0\rangle]\right\}\\ +\left\{\sum_{k^0\neq j^0}\frac{\langle j^0|L_z+2S_z|k^0\rangle}{\bar{\nu}^0_{KJ}}[\langle a^0|O_-^{(1)}|j^0\rangle\langle k^0|O_+^{(1)}|a^0\rangle - \langle a^0|O_+^{(1)}|j^0\rangle\langle k^0|O_+^{(1)}|a^0\rangle]\right\}\end{array}\right]$$

(in Debye^2/cm^{-1} or Debye^2 cm) dim: $L^6\,M\,T^{-2}$, (187)

$$\boldsymbol{c}_0 = -\frac{1}{d_A}\sum_{a^0,j^0}\langle a^0|L_z+2S_z|a^0\rangle[|\langle a^0|O_-^{(1)}|j^0\rangle|^2 - |\langle a^0|O_+^{(1)}|j^0\rangle|^2] \quad (188)$$

(in Debye^2) dim: $L^5\,M\,T^{-2}$,

[4] Note that $\beta = 9.273 \times 10^{-21}$ erg gauss^{-1} = 9.273×10^{-21} esu cm = 9.273×10^{-3} Debye = 4.669×10^{-5} cm^{-1} gauss^{-1}.

where
T: is the temperature in Kelvin (K)
k: Boltzmann constant
= 0.695 cm^{-1} K^{-1} dim: energy(here in cm^{-1})/temperature
d_A: the degeneracy of the ground level dim:/
$\mathcal{A}_1\left(-\frac{\bar{\nu}df(\bar{\nu},\bar{\nu}_{JA})}{d\bar{\nu}}\right)$ leads to the $\mathcal{A}$ term
$\mathcal{B}_0\bar{\nu}f(\bar{\nu},\bar{\nu}_{JA})$ leads to the $\mathcal{B}$ term
$\frac{\mathcal{C}_0}{kT}\bar{\nu}f(\bar{\nu},\bar{\nu}_{JA})$ leads to the $\mathcal{C}$ term

Important for further use in Section 4.4 is to remember Eq. (161):

$$D = \frac{1}{d_A}\sum_{a,j}|\langle a|O_{\pm}|j\rangle|^2$$
$$= \frac{1}{2d_A}\sum_{a,j}[|\langle a|O_{-}|j\rangle|^2+|\langle a|O_{+}|j\rangle|^2].$$

The parameters $\mathcal{A}_1$, $\mathcal{B}_0$ and $\mathcal{C}_0$ give the magnitude of the MCD signal while the $\mathcal{A}$, $\mathcal{B}$ and $\mathcal{C}$ terms correspond to the magnitude multiplied by the shape function. The latter is $f(\bar{\nu})$ for $\mathcal{B}$ and $\mathcal{C}$ while a derivative function describes the $\mathcal{A}$ term (see Figures 1–4).

4.2.6 Limits of the MCD theory

As explained above, some approximations have been made. Firstly, a linear limit has been assumed, which implies that both Zeeman splittings of A and J are small compared to kT (see Eq. (175) and the bandwidth (see Eq. (178)). Another approximation, also designated as the ''rigid shift approximation'', assumes that the magnetic field influence on the lineshape can be neglected so that only a ''rigid shift'' is taken into consideration (Piepho and Schatz, 1983).

4.3 MCD as elliptical depolarization

4.3.1 The ellipticity

As explained in Section 3.1.2.7, linearly polarized light can be seen as the resultant of left and right circularly polarized components of equal amplitudes. For media that show different absorption properties for the two polarization components, the corresponding amplitudes after going through the sample become (see Eq. (48)):

$$E_{\pm} = \frac{1}{\sqrt{2}}\Re E_0 \exp\left(i\omega\left(t-\frac{n_{\pm}z}{c}\right)\right)\exp\left(-\frac{\omega\kappa_{\pm}z}{c}\right). \quad (189)$$

According to Lambert–Beer's law, z can be replaced by d (Eq. (52b) in Sections 3.2 and 3.5), so that one obtains

$$\begin{aligned} E_{\pm} &= \frac{1}{\sqrt{2}} E_0 \exp\left(-\frac{\omega\kappa_{\pm} z}{c}\right) \\ &= \frac{1}{\sqrt{2}} E_0 \exp\left(-\frac{2\pi\kappa_{\pm} d}{\lambda}\right), \end{aligned} \tag{190}$$

$$E_{\pm} = \frac{1}{\sqrt{2}} E_0 \exp\left(-\frac{\omega\kappa_{\pm} d}{c}\right).$$

Taking Eq. (134) into account, the transmissions $T_{\pm}$ can be expressed as

$$T_{\pm} = \exp\left(-\frac{2\omega\kappa_{\pm} d}{c}\right) = \exp\left(-\frac{4\pi\kappa_{\pm} d}{\lambda}\right). \tag{191}$$

As shown on Figure 14B, the sum of the two circularly polarized vectors describes an ellipse after interacting with the sample. The ellipticity θ is defined as the arctangent of the ratio of the axes of this ellipse:

$$\mathrm{tg}\,\theta^{\mathrm{rad}} = \frac{b}{a} = \frac{E_+ - E_-}{E_+ + E_-}. \tag{192}$$

Or, in terms of the transmissions $T_{\pm}$

$$\mathrm{tg}\,\theta^{\mathrm{rad}} = \frac{\sqrt{T_+} - \sqrt{T_-}}{\sqrt{T_+} + \sqrt{T_-}} = \frac{(\sqrt{T_+} - \sqrt{T_-})(\sqrt{T_+} + \sqrt{T_-})}{(\sqrt{T_+} + \sqrt{T_-})^2} = \frac{T_+ - T_-}{T_+ + T_- + 2\sqrt{T_+ T_-}}. \tag{193}$$

In practice, the difference in transmission properties for both components is very small, so that one can assume that $T_+ \cong T_- \cong T$:

$$\sqrt{T_+ T_-} = \frac{T_+ + T_-}{2} = T. \tag{194}$$

Moreover when θ^{rad} is small, one obtains

$$\mathrm{tg}\,\theta^{\mathrm{rad}} \cong \theta^{\mathrm{rad}} = -\frac{1}{4}\frac{\Delta T}{T} \quad (\theta \,\mathrm{in\,radians}) \tag{195}$$

with

$$\Delta T = T_- - T_+.$$

To define the ellipticity in terms of the difference in absorbance between the two components, $\Delta A = A_- - A_+$, the relation

$$A = -\log T \tag{196}$$

can first be differentiated to

$$\Delta A = -0.4342 \frac{\Delta T}{T}. \tag{197}$$

Substitution in Eq. (195) results in

$$\theta^{\text{rad}} = -\frac{1}{4}\frac{\Delta T}{T} = \frac{1}{4 \times 0.4342}\Delta A = 0.5756 \Delta A \quad (\theta \text{ in radians}), \tag{198}$$

$$\theta^{\circ} = 0.5756 \times \frac{180}{3.1416}\Delta A = 32.98 \Delta A \quad (\theta \text{ in degrees}). \tag{199}$$

In MCD the angle θ is expressed in the units used for natural optical activity ($^{\circ}\text{mol}^{-1}$ dl dm^{-1}).

Replacing $\Delta\varepsilon$ by Eqs. (185)–(188) gives

$$\begin{aligned}
\frac{\theta}{H} &= 3298 \frac{\Delta A}{cdH} \\
&= 3298 \frac{\Delta \varepsilon}{H} \\
&= \chi\ 3298 \times 152.5 \left\{ \boldsymbol{a}_1 \left(-\frac{\bar{\nu}\, \mathrm{d}f(\bar{\nu}, \bar{\nu}_{JA})}{\mathrm{d}\bar{\nu}} \right) + \left(\boldsymbol{\mathcal{B}}_0 + \frac{\boldsymbol{c}_0}{kT} \right) \bar{\nu} f(\bar{\nu}, \bar{\nu}_{JA}) \right\} \\
&= \chi\ 50.28 \times 10^4 \left\{ \boldsymbol{a}_1 \left(-\frac{\bar{\nu}\, \mathrm{d}f(\bar{\nu}, \bar{\nu}_{JA})}{\mathrm{d}\bar{\nu}} \right) + \left(\boldsymbol{\mathcal{B}}_0 + \frac{\boldsymbol{c}_0}{kT} \right) \bar{\nu} f(\bar{\nu}, \bar{\nu}_{JA}) \right\}
\end{aligned} \tag{200}$$

and vice versa:

$$\frac{\Delta \varepsilon}{H} = 3 \times 10^{-4} \frac{\theta}{H}, \tag{201}$$

where
θ: is the ellipticity (in $^{\circ}\text{mol}^{-1}$dl dm^{-1})
$\Delta\varepsilon$: the difference in molar absorptivity (in l $\text{mol}^{-1}\text{cm}^{-1}$) and
H: the magnetic field (in tesla)

Note that the angle θ is defined counter-clockwise with respect to the x-axis in a right-handed axis system (see Eqs. (8) and (9)). A positive θ value means that left circularly polarized light is more absorbed than right circularly polarized light.

4.3.2 The relationship between θ and $\Delta\kappa$ or $\Delta\varepsilon$

The relationship between θ and $\Delta\kappa$ can be obtained from Eqs. (191) and (192):

$$\text{tg}\, \theta^{\text{rad}} = \frac{1 - \exp(-\Delta\kappa\omega z/c)}{1 + \exp(-\Delta\kappa\omega z/c)}. \tag{202}$$

Taking into consideration that

$$\operatorname{tgh} x = \frac{1 - \mathrm{e}^{-2x}}{1+\mathrm{e}^{-2x}}, \tag{203}$$

one obtains

$$\operatorname{tg}\theta^{\mathrm{rad}} = \operatorname{tgh}\left(\frac{\Delta\kappa z\omega}{2c}\right) = \operatorname{tgh}\left(\frac{\Delta\kappa d\pi}{\lambda}\right). \tag{204}$$

For small values of θ, $\operatorname{tg}\theta \cong \operatorname{tgh}\theta = \theta$ and the relationship between the two quantities leads to

$$\theta^{\mathrm{rad}} = \frac{\pi d}{\lambda}\Delta\kappa = \frac{2\pi\nu d}{2c}\Delta\kappa = \frac{\pi d}{\lambda}\Delta\kappa \quad (\text{with}\,\theta\,\text{in radians}). \tag{205}$$

From this and Eq. (133) one obtains the same relationships as in Eq. (198):

$$\theta^{\mathrm{rad}} = \frac{\pi d}{\lambda}\Delta\kappa = \frac{\pi d}{\lambda} \times \frac{2.303cC\Delta\varepsilon}{2\omega} = \frac{1}{4 \times 0.4342}\Delta A = 0.5756\Delta A. \tag{206}$$

4.3.3 Important remark

Special attention is drawn to earlier work (Fluyt et al., 1994; Görller-Walrand and Beyens, 1980; Görller-Walrand and Godemont, 1977b; Görller-Walrand et al., 1979, 1982a, 1994a; Piepho and Schatz, 1983; Pink, 1975) where θ was expressed per gauss and the dipole strength was defined for an isotropic radiation (see Eqs. (126) and (152)) and Section 3.7.

With the previous definitions of the MCD terms $\boldsymbol{A}_1^{\mathrm{old}}$,$\boldsymbol{B}_0^{\mathrm{old}}$ and $\boldsymbol{C}_0^{\mathrm{old}}$ that include a factor 3/2 as described in Appendix A.4 of the book by Piepho and Schatz (1983), the numerical constant in Eq. (200) becomes

$$\begin{aligned}[\theta_M] &= \chi 33.53\left\{\boldsymbol{A}_1^{\mathrm{old}}\left(-\frac{\bar{\nu}\,\mathrm{d}f(\bar{\nu},\bar{\nu}_{JA})}{\mathrm{d}\bar{\nu}}\right) + \left(\boldsymbol{B}_0^{\mathrm{old}} + \frac{\boldsymbol{C}_0^{\mathrm{old}}}{kT}\right)\bar{\nu}f(\bar{\nu},\bar{\nu}_{JA})\right\} \\ &= \chi\frac{2}{3} \times 10^{-4} \times 50.28 \times 10^4\left\{\boldsymbol{A}_1^{\mathrm{old}}\left(-\frac{\bar{\nu}\,\mathrm{d}f(\bar{\nu},\bar{\nu}_{JA})}{\mathrm{d}\bar{\nu}}\right) + \left(\boldsymbol{B}_0^{\mathrm{old}} + \frac{\boldsymbol{C}_0^{\mathrm{old}}}{kT}\right)\bar{\nu}f(\bar{\nu},\bar{\nu}_{JA})\right\}.\end{aligned} \tag{207}$$

Following the same conventions Eq. (185) becomes

$$\begin{aligned}\frac{\Delta\varepsilon}{H} &= \chi 1.02 \times 10^{-2}\left\{\boldsymbol{A}_1^{\mathrm{old}}\left(-\frac{\bar{\nu}\,\mathrm{d}f(\bar{\nu},\bar{\nu}_{JA})}{\mathrm{d}\bar{\nu}}\right) + \left(\boldsymbol{B}_0^{\mathrm{old}} + \frac{\boldsymbol{C}_0^{\mathrm{old}}}{kT}\right)\bar{\nu}f(\bar{\nu},\bar{\nu}_{JA})\right\} \\ &= \chi\frac{2}{3} \times 10^{-4} \times 152.5\left\{\boldsymbol{A}_1^{\mathrm{old}}\left(-\frac{\bar{\nu}\,\mathrm{d}f(\bar{\nu},\bar{\nu}_{JA})}{\mathrm{d}\bar{\nu}}\right) + \left(\boldsymbol{B}_0^{\mathrm{old}} + \frac{\boldsymbol{C}_0^{\mathrm{old}}}{kT}\right)\bar{\nu}f(\bar{\nu},\bar{\nu}_{JA})\right\}.\end{aligned} \tag{208}$$

With the previous definition of the dipole strength D^{old} that includes a factor 3, the relation with ε in Eq. (138) is

$$\begin{aligned}\varepsilon &= \chi 108.9 D^{\text{old}} \bar{\nu} f(\bar{\nu}) \\ &= \chi \frac{1}{3} \times 326.6 D^{\text{old}} \bar{\nu} f(\bar{\nu}).\end{aligned} \tag{209}$$

4.4 Experimental determination of MCD parameters by the method of moments

In the case of discrete bands, comparison between the experimental data and theoretically calculated values can be made by use of the method of the moments (Stephens, 1968).

The nth order moments for absorption and MCD are defined as

$$\langle \varepsilon \rangle_n = \int \frac{\varepsilon}{\bar{\nu}} (\bar{\nu} - \bar{\nu}_{\text{g}})^n \mathrm{d}\bar{\nu}, \tag{210}$$

$$\langle \Delta\varepsilon / H \rangle_n = \frac{1}{3298} \int \frac{\theta}{H\bar{\nu}} (\bar{\nu} - \bar{\nu}_{\text{g}})^n \mathrm{d}\bar{\nu}. \tag{211}$$

The wave number $\bar{\nu}_{\text{g}}$ is some chosen value about which the moments are taken. In MCD it is usually the wave number value for which the first-order moment in absorption becomes zero:

$$\langle \varepsilon \rangle_1 = \int \frac{\varepsilon}{\bar{\nu}} (\bar{\nu} - \bar{\nu}_{\text{g}}) \mathrm{d}\bar{\nu} = 0 \tag{212}$$

$$\bar{\nu}_{\text{g}} = \frac{\int \varepsilon \, \mathrm{d}\bar{\nu}}{\int \frac{\varepsilon}{\bar{\nu}} \mathrm{d}\bar{\nu}} \cong \bar{\nu}_{JA} = \bar{\nu}_0. \tag{213}$$

For a single electronic band the value $\bar{\nu}_{\text{g}}$ can be set equal to $\bar{\nu}_{JA}$ or $\bar{\nu}_0$. Integration of Eqs. (140) and (185) results in

$$\langle \varepsilon \rangle_0 = \int \frac{\varepsilon}{\bar{\nu}} \mathrm{d}\bar{\nu} = \chi 326.6 D, \tag{214}$$

$$\langle \Delta\varepsilon \rangle_0 = \int \frac{\Delta\varepsilon}{\bar{\nu}} \mathrm{d}\bar{\nu} = \chi 152.5 \left(\mathcal{B}_0 + \frac{\mathcal{C}_0}{kT} \right). \tag{215}$$

The $\mathcal{A}_1$ contribution integrates to zero because of Eq. (58) where ν can simply be replaced by $\bar{\nu}$. In this way it is possible to extract $(\mathcal{B}_0 + \mathcal{C}_0/kT)$ in the presence of large $\mathcal{A}_1$ terms. $\mathcal{B}_0$ and $\mathcal{C}_0$ can be further separated by measuring data at different temperatures.

With the use of Eq. (185) the first-order moment for MCD becomes (with H in tesla):

$$\begin{aligned}\langle \Delta\varepsilon \rangle_1 = &\int \frac{\varepsilon}{\bar{\nu}}(\bar{\nu}-\bar{\nu}_g)\mathrm{d}\bar{\nu} = \chi 152.5 H \int -\boldsymbol{a}_1 \frac{\mathrm{d}f(\bar{\nu}-\bar{\nu}_{JA})}{\mathrm{d}\bar{\nu}}\mathrm{d}\bar{\nu} \\ &+\int \left(\boldsymbol{\mathcal{B}}_0 + \frac{\boldsymbol{c}_0}{kT}\right) f(\bar{\nu}-\bar{\nu}_{JA})\mathrm{d}\bar{\nu}.\end{aligned} \tag{216}$$

The second term vanishes so that

$$\left\langle \frac{\Delta\varepsilon}{H} \right\rangle_1 = \int \frac{\Delta\varepsilon}{\bar{\nu}}(\bar{\nu}-\bar{\nu}_g)\mathrm{d}\bar{\nu} = \chi 152.5 \int -\boldsymbol{a}_1 \frac{\mathrm{d}f(\bar{\nu}-\bar{\nu}_{JA})}{\mathrm{d}\bar{\nu}}\mathrm{d}\bar{\nu}. \tag{217}$$

Knowing that

$$\int \frac{\partial f(\bar{\nu})}{\partial \bar{\nu}}\bar{\nu}\,\mathrm{d}\bar{\nu} = -1, \tag{218}$$

partial integration results in

$$\left\langle \frac{\Delta\varepsilon}{H} \right\rangle_1 = 152.5\,\chi \boldsymbol{a}_1 \tag{219}$$

and vice versa:

$$\begin{aligned}\boldsymbol{a}_1 &= \frac{1}{152.5}\frac{1}{\chi}\left\langle \frac{\Delta\varepsilon}{H} \right\rangle_1 \\ &= 6.6 \times 10^{-3}\frac{1}{\chi}\left\langle \frac{\Delta\varepsilon}{H} \right\rangle_1.\end{aligned} \tag{220}$$

In the same way from Eq. (200):

$$\left\langle \frac{\theta}{H} \right\rangle_1 = \chi 50.28 \times 10^4 \boldsymbol{a}_1 \tag{221}$$

and vice versa:

$$\boldsymbol{a}_1 = \frac{1}{\chi} 2.0 \times 10^{-6} \left\langle \frac{\theta}{H} \right\rangle_1. \tag{222}$$

The ratio between $\langle \frac{\Delta\varepsilon}{H} \rangle_1$ and $\langle \varepsilon \rangle_0$ gives $\boldsymbol{a}_1/D$, the magnetic moment of the involved state through:

$$\begin{aligned}\frac{\boldsymbol{a}_1}{D} &= \frac{326.6}{152.5} \times \frac{\langle \Delta\varepsilon/H \rangle_1}{\langle \varepsilon \rangle_0} = 2.14 \frac{\langle \Delta\varepsilon/H \rangle_1}{\langle \varepsilon \rangle_0} = \frac{326.6}{50.28 \times 10^4}\frac{\langle \theta/H \rangle_1}{\langle \varepsilon \rangle_0} \\ &= \frac{326.6}{50.28 \times 10^4}\frac{\langle \theta/H \rangle_1}{\langle \varepsilon \rangle_0} = 6.5 \times 10^{-4}\frac{\langle \theta/H \rangle_1}{\langle \varepsilon \rangle_0}.\end{aligned} \tag{223a}$$

From the experimental point of view, it is interesting to mention that in terms of absorbance Eq. (223a) becomes

$$\frac{\boldsymbol{a}_1}{D} = 2.14\frac{\langle \Delta\varepsilon Cd/H\rangle_1}{\langle \varepsilon Cd\rangle_0} = 2.14\frac{\langle \Delta A/H\rangle_1}{\langle A\rangle_0}. \tag{223b}$$

Reported detection limits are of the following orders of magnitude: $\Delta A = 10^{-5}$ and $A = 10^{-2}$, respectively (Abushuma and Duffield, 1970; Abushuma et al., 1971; Briat and Djerassi, 1968; Denning, 1975; Görller-Walrand and Beyens, 1980; Osborne et al., 1973).

The setup we used for the MCD measurements was built by the Aviv company and equipped with an Oxford supermagnet (7 tesla).

4.5 Calculation of $\boldsymbol{a}_1/D$ by the method of maxima for a Gaussian lineshape

When the MCD $\boldsymbol{a}$ term corresponds to a Gaussian-like absorption curve, the $\boldsymbol{a}_1/D$ ratio can be deduced from the observation of $\varepsilon_{\max}$ and $\Delta\varepsilon_{\max}/H$, at the maximum and the half-width at half-height Γ_G, respectively. From Eq. (70),

$$f_G(\bar{\nu}, \bar{\nu}_{JA}) = \frac{\sqrt{\ln 2}}{\sqrt{\pi}\Gamma_G}\exp\left[-\frac{(\bar{\nu}-\bar{\nu}_{JA})^2 \ln 2}{\Gamma_G^2}\right] \qquad \text{dim: L} \tag{224}$$

$$\frac{\mathrm{d}f_G(\bar{\nu}, \bar{\nu}_{JA})}{\mathrm{d}\bar{\nu}} = -\frac{2(\bar{\nu}-\bar{\nu}_{JA})(\ln 2)^{3/2}}{\sqrt{\pi}\Gamma_G^3}\exp\left[-\frac{(\bar{\nu}-\bar{\nu}_{JA})^2 \ln 2}{\Gamma_G^2}\right] \qquad \text{dim: L}^2 \tag{225}$$

The absorption curve shows a maximum at $\bar{\nu} = \bar{\nu}_{JA}$ so that $\varepsilon_{\max}$ can then with

$$\varepsilon = 326.6\chi D\bar{\nu}f(\bar{\nu}) \tag{226}$$

be written as

$$\varepsilon_{\max} = \frac{\sqrt{\ln 2}}{\Gamma_G\sqrt{\pi}}326.6\chi\bar{\nu}_{JA}D. \tag{227}$$

Since the MCD $\boldsymbol{a}$ term shows extrema at $\bar{\nu} = \bar{\nu}_{JA} \pm \Gamma_G/\sqrt{2\ln 2} = \bar{\nu}_{JA} \pm 0.85\Gamma_G$, $\Delta\varepsilon_{\max}/H$ from peak to peak is equal to

$$\frac{\Delta\varepsilon_{\max}}{H} = \frac{2\sqrt{2}\ln 2}{\sqrt{\pi}\sqrt{e}}\frac{\chi}{\Gamma_G^2}152.5\left(\bar{\nu}_{JA} + \frac{\Gamma_G}{\sqrt{2\ln 2}}\right)\boldsymbol{a}_1. \tag{228}$$

Neglecting $\Gamma_G/\sqrt{2\ln 2}$ with respect to the value $\bar{\nu}_{JA}$:

$$\frac{\Delta\varepsilon_{max}/H}{\varepsilon_{max}} = \frac{2\sqrt{2\ln 2}}{\sqrt{e}}\frac{1}{\Gamma_G}\frac{152.5}{326.6}\frac{\boldsymbol{a}_1}{D} = 1.428 \times \frac{152.5}{326.6}\frac{1}{\Gamma_G}\frac{\boldsymbol{a}_1}{D} \cong 0.7\frac{1}{\Gamma_G}\frac{\boldsymbol{a}_1}{D} \quad (229)$$

or vice versa:

$$\frac{\boldsymbol{a}_1}{D} = 1.5\Gamma_G\frac{\Delta\varepsilon_{max}/H}{\varepsilon_{max}} \quad (230)$$

or in terms of θ:

$$\begin{aligned}\frac{\theta_{max}/H}{\varepsilon_{max}} &= \frac{2\sqrt{2\ln 2}}{\sqrt{e}}\frac{1}{\Gamma_G}\frac{50.28\times 10^4}{326.6}\frac{\boldsymbol{a}_1}{D} = 1.428 \times \frac{50.28\times 10^4}{326.6}\frac{1}{\Gamma_G}\frac{\boldsymbol{a}_1}{D} \\ &= 2.2\times 10^3\frac{1}{\Gamma_G}\frac{\boldsymbol{a}_1}{D}\end{aligned} \quad (231)$$

or vice versa:

$$\frac{\boldsymbol{a}_1}{D} = 4.5\times 10^{-4}\frac{\theta_{max}/H}{\varepsilon_{max}}\Gamma_G. \quad (232)$$

The $\boldsymbol{a}_1/D$ ratio provides a direct determination of the magnetic moments being equal to the total Zeeman splitting divided by βH, which can also be explicitated from Eqs. (161) and (186):

$$2\sum_{a^0,j^0}(\langle j^0|L_z+2S_z|j^0\rangle - \langle a^0|L_z+2S_z|a^0\rangle). \quad (233)$$

This closes the general theory on MCD based on Piepho and Schatz (1983) and Stephens (1976). The applications discussed by these authors concern mostly transition metal coordination compounds and are not reviewed here. More details can, however, be found in Dobosh (1974), Schatz and Mc Caffery (1969), Schatz et al. (1978), and Stephens (1970, 1974, 1977, 1987, 1991, 1971).

4.6 Theoretical determination of MCD parameters by the Judd–Ofelt theory

To evaluate the matrix elements in the expressions of the $\boldsymbol{a}_1$, $\boldsymbol{\mathcal{B}}_0$ and $\boldsymbol{c}_0$ MCD parameters, a detailed description of the ground and excited state is needed. Here, attention will be focused on the expansions of the $\boldsymbol{a}_1$ term with respect to Judd's notation for the rare-earth spectra (Görller-Walrand and Binnemans, 1998; Judd, 1962).

In the equation of $\boldsymbol{a}_1$,

$$\boldsymbol{a}_1 = \frac{1}{d_A}\sum_{a^0,j^0}\Big(\Big(|\langle a^0|O_-^{(1)}|j^0\rangle|^2 - |\langle a^0|O_+^{(1)}|j^0\rangle|^2\Big) \Big(\langle j^0|L_z{+}2S_z|j^0\rangle - \langle a^0|L_z{+}2S_z|a^0\rangle\Big)\Big), \tag{234}$$

the ground and excited levels a^0 and j^0 can be labelled within the f^N configuration as

$$\langle a^0| \equiv \sum_M \langle 4f^N \psi JM|a_M \tag{235}$$

and

$$|j^0\rangle \equiv \sum_{M'} a'_{M'}|4f^N\psi' J' M'\rangle, \tag{236}$$

where N is the number of electrons; J the total angular momentum; M the quantum number of the projection J_z of the J vector and ψ the additional quantum numbers that may be necessary to define the level uniquely.

Owing to the comparatively small splittings of the levels produced by the crystal field, a good approximation can be made by assuming that the quantum number J remains a useful quantum number. In a simplified notation $\langle JM|$ stands for $\langle 4f^N\psi JM|$ and $|J'M'\rangle$ stands for $|4f^N\psi' J'M'\rangle$. If, moreover, the ground level is non-degenerate ($d_A = 1$) and labelled $M = 0$, and if no cubic or icosahedral symmetries are considered in this treatment, the summation over j^0 reduces to the two components with quantum numbers $|M'|$ and $-|M'|$ and the crystal field ground and excited levels are given by

$$\langle a^0| \equiv \langle J0| \quad \text{and} \quad |j^0\rangle \equiv |J'M'\rangle. \tag{237}$$

Then Eq. (234) can be written as

$$\boldsymbol{a}_1 = \sum_{|M'|,-|M'|}\Big(\Big(|\langle J0|O_{-1}^{(1)}|J'M'\rangle|^2 - |\langle J0|O_{+1}^{(1)}|J'M'\rangle|^2\Big)(\langle J'M'|L_z{+}2S_z|J'M'\rangle)\Big). \tag{238}$$

As

$$\sum_{|M'|,-|M'|}|\langle J0|O_{-1}^{(1)}|J'M'\rangle|^2 = \sum_{|M'|,-|M'|}|\langle J0|O_{+1}^{(1)}|J'M'\rangle|^2. \tag{239}$$

and

$$\langle J', +|M'|L_z{+}2S_z|J', +|M'|\rangle = -\langle J', -|M'||L_z{+}2S_z|J', -|M'|\rangle, \tag{240}$$

one obtains

$$\boldsymbol{\alpha}_1 = 2|\langle J0|O_{-1}^{(1)}|J'M'\rangle|^2\langle J'M'|L_z+2S_z|J'M'\rangle. \tag{241}$$

Considering Russel–Saunders coupling scheme,

$$\langle J', \pm|M'||L_z+2S_z|J', \pm|M'|\rangle = \pm|M'|g, \tag{242}$$

so that

$$\boldsymbol{\alpha}_1 = 2|\langle J0|O_{-1}^{(1)}|J'M'\rangle|^2 gM' \tag{243}$$

with the Landé factor g:

$$g = 1+\frac{J(J+1) - L(L+1)+S(S+1)}{2J(J+1)}. \tag{244}$$

If g is positive, the sign of $\boldsymbol{\alpha}_1$ is determined by the sign of M' used to label the Zeeman component to which left circularly polarized light is absorbed. If g is negative the opposite statement holds true.

Next, we consider the expression of the $\boldsymbol{\alpha}_1$ signal in the light of the two mechanisms that account predominantly for the intensity in the spectra of rare-earth complexes, that is, the magnetic dipole and the induced electric dipole mechanisms.

From Eq. (96),

Magnetic dipole transition

$$O_{-1}^{(1)} = -\frac{|e|\hbar}{2m_e c}(\vec{\boldsymbol{L}}+2\vec{\boldsymbol{S}}), \tag{245}$$

where $(\vec{\boldsymbol{L}}+2\vec{\boldsymbol{S}})$ is dimentionless.

For a magnetic dipole transition the intensity matrix element is expressed as follows, according to Görller-Walrand and Binnemans (1998), p. 122, Eq. 63:

$$|\langle J0|(L+2S)_\rho^{(1)}|J'M'\rangle|^2 = \left|(-1)^J \begin{pmatrix} J & 1 & J' \\ 0 & \rho & M' \end{pmatrix} \langle J\|L+2S\|J'\rangle\right|^2 \tag{246}$$

where $\rho = -1$ and $+1$ for left and right circularly polarized light, respectively. The selection rule for a magnetic dipole transition can be derived from the $3j$ symbol:

$$M' = -\rho = -(-1) = +1 \tag{247}$$

and in general (Görller-Walrand and Fluyt-Adriaens, 1985):

$$\Delta M = M' - M = -\rho = -(-1) = +1. \tag{248}$$

This means that absorption of left circularly polarized light occurs to $M' = +1$ giving always a positive $\boldsymbol{a}_1$ term if g is positive (Görller-Walrand et al., 1993; Lazzeretti et al., 1986).

From Eq. (78):

Induced electric dipole transition

$$O_\rho^{(1)} = -|e|D_\rho^{(1)}. \tag{249}$$

Within the frame of Judd–Ofelt theory, the intensity matrix element of an induced electric dipole transition is given by Görller-Walrand and Binnemans (1998) and Judd (1962):

$$|\langle J0|D_\rho^1|J'M'\rangle|^2 = \left| \sum_{k,q,\text{even }\lambda} (2\lambda+1)(-1)^{q+\rho} A_{kq} \begin{pmatrix} 1 & \lambda & k \\ \rho & -q-\rho & q \end{pmatrix} \Xi(t,\lambda)(-1)^J \begin{pmatrix} J & \lambda & J' \\ 0 & q+\rho & M' \end{pmatrix} \langle J\|U^{(\lambda)}\|J'\rangle \right|^2. \tag{250}$$

The selection rule which is relevant for MCD is

$$M' = -(q+\rho) = -(q+(-1)) = 1 - q \tag{251}$$

or in general:

$$\Delta M = M' - M = -(q+\rho) = -(q+(-1)). \tag{252}$$

The sign of M' is clearly related to the symmetry of the coordination sphere around the rare-earth ion through the q value which appears in the odd crystal field terms:

$$V = \sum_{k,q} A_{kq} D_q^{(k)} = \sum_{k,q} B_q^k C_q^{(k)}. \tag{253}$$

According to Eqs. (243) and (250), the sign of the $\boldsymbol{a}$ term is thus determined by the sign of the M' value that satisfies the $3j$ symbol for $\rho = -1$ (Fluyt et al., 1994).

5. STUDY CASES

5.1 Introduction

To illustrate how MCD can provide structural information about the site symmetry, three study cases featuring different coordination polyhedra have been considered, namely the dodecahedron (Dod), the distorted

square antiprism (SAP) and the tricapped trigonal prism (TCTP). These polyhedra are, respectively, characterized by the site symmetries D_{2d}, C_{4v} and D_{3h}. For the last example, a distortion from D_{3h} to D_3 shows how even small changes in the first coordination sphere are reflected in the MCD signals.

The Eu^{3+} ion was chosen because it acts as an illustrative probe in view of its non-degenerate ground state.

First, we focus on the pure magnetic dipole transition $^5D_1 \leftarrow {}^7F_0$ which acts as an interesting reference transition because of its symmetry independence (Görller-Walrand et al., 1991a). Next the symmetry dependence of the induced electric dipole transition $^5D_2 \leftarrow {}^7F_0$ provides the link to the site symmetry. Experimental data are extracted from the absorption and MCD spectra of single crystals of $LiYF_4/Eu^{3+}(D_{2d})$ (Fluyt et al., 1995; Görller-Walrand et al., 1985a), KY_3F_{10}/Eu^{3+} (C_{4v}) (Fluyt et al., 1999; Görller-Walrand et al., 1985a) and $Na_3[Eu(ODA)_3]\cdot 2NaClO_4\cdot 6H_2O$ (D_{3h} distorted to D_3) (Banerjee et al., 1981; Görller-Walrand et al., 1994a,b).

5.2 The $^5D_1 \leftarrow {}^7F_0$ magnetic dipole transition of Eu^{3+}

The intermediate spin–orbit coupling mixes some $^7F_1$ contribution in the $^5D_1$ state so that all the selection rules for the magnetic dipole transition $^5D_1 \leftarrow {}^7F_0$ are obeyed (Dieke et al., 1968):

$$\begin{aligned} &\Delta l = 0, \quad \Delta S = 0, \quad \Delta L = 0, \\ &\Delta J = 0, \pm 1 \quad (\text{not } 0 \leftrightarrow 0), \\ &\Delta M = 0 \quad (\alpha, \sigma\text{−polarization}), \\ &\Delta M = \pm 1 \quad (\pi\text{−polarization}), \end{aligned} \tag{254}$$

In Figure 15 the crystal field splitting for an axial symmetry with main axis $n > 2$ is given for $J = 1$: the E component is doubly degenerate ($M = \pm 1$) while the A_1 level ($M = 0$) is non-degenerate. A longitudinal magnetic field causes a linear Zeeman splitting into an upper $|M'\rangle = |+1\rangle$ component and a lower $|M'\rangle = |-1\rangle$ one. The ground state corresponds to $\langle M| = \langle 0|$ and shows a field-independent behaviour.

According to the selection rule

$$M' - 0 = -(-1), \tag{255}$$

absorption of left circularly polarized light occurs to the $|M'\rangle = |+1\rangle$ component. The result is a positive $\boldsymbol{a}_1$ term which is independent of the site symmetry.

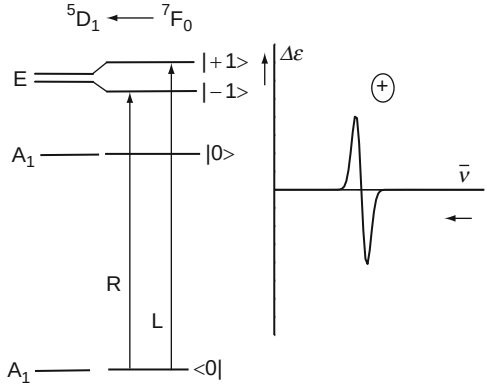

FIGURE 15 MCD signal for the $^5D_1 \leftarrow {}^7F_0$ magnetic dipole transition.

$$\begin{aligned}\mathcal{A}_1 &= \langle +1|L_z+2S_z|+1\rangle|\langle 0|O_{-1}^{(1)}|+1\rangle|^2 - \langle -1|L_z+2S_z|-1\rangle|\langle 0|O_{+1}^{(1)}|-1\rangle|^2 \\ &= +2\langle +1|L_z+2S_z|+1\rangle|\langle 0|O_{-1}^{(1)}|+1\rangle|^2 \\ &= 2g|\langle 0|O_{-1}^{(1)}|+1\rangle|^2,\end{aligned} \tag{256}$$

where $g = 1.5$ for $^5D_1$ (see Eq. (244)).

The experimental spectra for the $^5D_1 \leftarrow {}^7F_0$ transition for the single crystals of $LiYF_4/Eu^{3+}(D_{2d})$, KY_3F_{10}/Eu^{3+} (C_{4v}) and $Na_3[Eu(ODA)_3]\cdot 2NaClO_4\cdot 6H_2O$ (D_{3h} distorted to D_3) are given in Figure 16A–C.

For KY_3F_{10}/Eu^{3+}, only the shaded peaks are considered here. As explained in Section 6 the resulting spectrum is a superposition of three different site orientations encountered in this cubic crystal. Only one site orientation (C_4-axis magnetic field) fulfils in a straightforward way the conditions required for testing the theoretical predictions explained in the previous section. For all three symmetries clearly a positive $\mathcal{A}$ term is observed (Görller-Walrand and Binnemans, 1997; Görller-Walrand et al., 1991a).

5.3 The $^5D_2 \leftarrow {}^7F_0$ induced electric dipole transition of Eu^{3+}

5.3.1 Crystal field potentials

Due to the mixing of for example $^5F_2$ and $^5D_2$ states the transition $^5D_2 \leftarrow {}^7F_0$ is allowed by the induced electric dipole mechanism, the relevant selection rules being:

$$\begin{gathered}\Delta l = \pm 1, \quad \Delta S = 0, \quad |\Delta L| \leq 6, \\ |\Delta J| \leq 6, \quad \text{where if } J \text{ or } J' = 0 \text{ then } |\Delta J| = 2, 4, 6.\end{gathered} \tag{257}$$

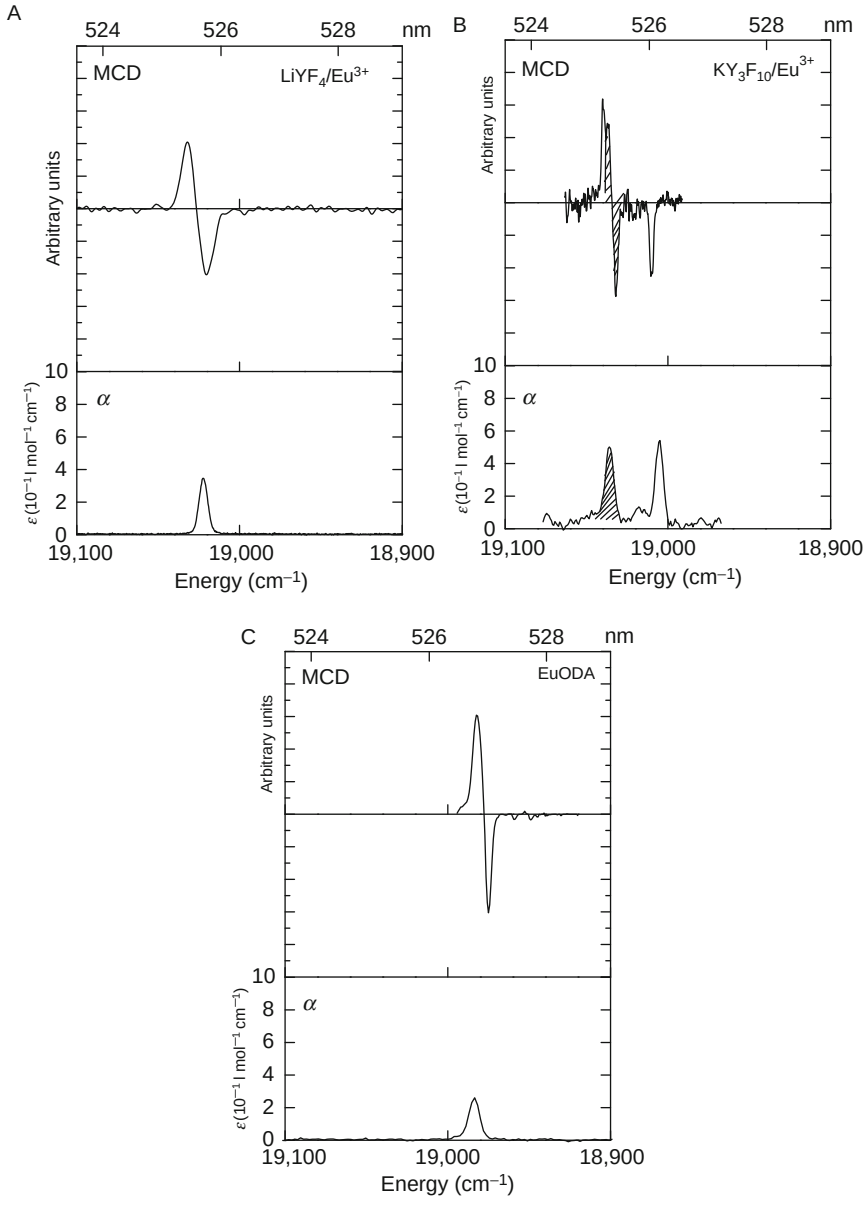

FIGURE 16 Experimental absorption and MCD spectrum for the $^5D_1 \leftarrow {}^7F_0$ transition in (A) $LiYF_4/Eu^{3+}$, (B) KY_3F_{10}/Eu^{3+} and (C) $Na_3[Eu(ODA)_3]\cdot 2NaClO_4\cdot 6H_2O$.

From the fact that $J = 0$ and from the triangular conditions in the $3j$ symbol of Eq. (250): $0 \leq \lambda \leq 2$, so that $\lambda = 2$. The selection rules on k with respect to $\lambda = 2$ are k = 1 or 3. The q values for $k = 1$ and 3 are found in the odd crystal field potential terms (see Görller-Walrand and Binnemans, 1996; Görller-Walrand and Binnemans, 1998; Prather, 1961; Wybourne, 1965). For the four symmetries considered here the even and odd terms are

$$V^{\text{even}}(D_{2\text{d}}) = B_0^2C_0^2+B_0^4C_0^4+B_4^4(C_{-4}^4+C_4^4)+B_0^6C_0^6+B_4^6(C_{-4}^6+C_4^6), \tag{258}$$

$$V^{\text{odd}}(D_{2\text{d}}) = B_2^{'3}\text{i}(C_{-2}^3 - C_2^3)+B_2^{'5}\text{i}(C_{-2}^5 - C_2^5)+B_2^{'7}\text{i}(C_{-2}^7 - C_2^7)+B_6^{'7}\text{i}(C_{-6}^7 - C_6^7), \tag{259}$$

$$V^{\text{even}}(C_{4\text{v}}) = B_0^2C_0^2+B_0^4C_0^4+B_4^4(C_{-4}^4+C_4^4)+B_0^6C_0^6+B_4^6(C_{-4}^6+C_4^6), \tag{260}$$

$$V^{\text{odd}}(C_{4\text{v}}) = B_0^1C_0^1+B_0^3C_0^3+B_0^5C_0^5+B_4^5(C_{-4}^5+C_4^5)+B_0^7C_0^7+B_4^7(C_{-4}^7+C_4^7), \tag{261}$$

$$V^{\text{even}}(D_{3\text{h}}) = B_0^2C_0^2+B_0^4C_0^4+B_0^6C_0^6+B_6^6(C_{-6}^6+C_6^6), \tag{262}$$

$$V^{\text{odd}}(D_{3\text{h}}) = B_3^{'3}\text{i}(C_{-3}^3+C_3^3)+B_3^{'5}\text{i}(C_{-3}^5+C_3^5)+B_3^{'7}\text{i}(C_{-3}^7+C_3^7), \tag{263}$$

$$V^{\text{even}}(D_3) = B_0^2C_0^2+B_0^4C_0^4+B_3^4(C_{-3}^4 - C_3^4)+B_0^6C_0^6+B_3^6(C_{-3}^6 - C_3^6)+B_6^6(C_{-6}^6+C_6^6), \tag{264}$$

$$V^{\text{odd}}(D_3) = B_3^{'3}\text{i}(C_{-3}^3+C_3^3)+B_3^{'5}\text{i}(C_{-3}^5+C_3^5)+B_3^{'7}\text{i}(C_{-3}^7+C_3^7)+B_6^{'7}\text{i}(C_{-6}^7 - C_6^7). \tag{265}$$

Figures 17–20 show the polyhedra formed by the nearest neighbours of the rare-earth ion and the Zeeman splitting of the crystal field levels for the $^5D_2$ and $^7F_0$ states, respectively, for the symmetries $D_{2\text{d}}$, $C_{4\text{v}}$, $D_{3\text{h}}$. and D_3. At the right-hand side of the figure, $\Delta\varepsilon = \varepsilon_- - \varepsilon_+$ is plotted in function of $\bar{\nu}$ and generates a MCD $\boldsymbol{A}_1$ term with the appropriate sign.

5.3.2 $D_{2\text{d}}$ symmetry

The transition E ← A_1 is to be considered for $D_{2\text{d}}$ (De Leebeeck and Görller-Walrand, 1998; De Leebeeck et al., 1998, 1999; Fluyt et al., 1995; Görller-Walrand et al., 1982b, 1985b, 1986, 1994a; Heyde et al., 1998b).

Left circularly polarized light shows absorption to the $M' = -1$ Zeeman component (see Figure 19):

$$M' = -(2 - 1) = -1 \tag{266}$$

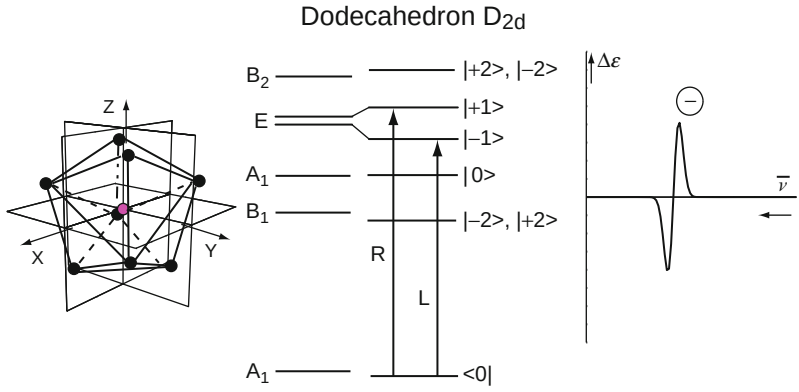

FIGURE 17 Theoretical prediction of the MCD signal for the $^5D_2 \leftarrow {}^7F_0$ transition in D_{2d} symmetry.

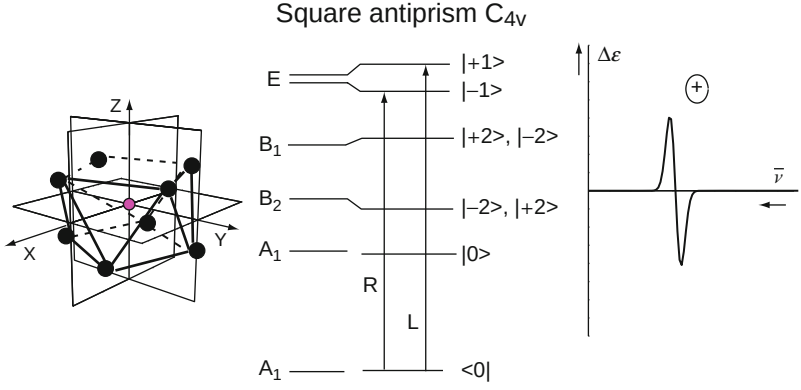

FIGURE 18 Theoretical prediction of the MCD signal for the $^5D_2 \leftarrow {}^7F_0$ transition in C_{4v} symmetry.

leading to a negative $\boldsymbol{a}_1$ term characterized by

$$\boldsymbol{a}_1 = -2g|\langle 0|O^{(1)}_{+1}|+1\rangle|^2 \tag{267}$$

The experimental absorption and MCD spectrum for the $LiYF_4/Eu^{3+}$ are given in Figure 21.

5.3.3 C_{4v} symmetry

The C_{4v} case (Görller-Walrand et al., 1985a; Heyde et al., 1998a) is illustrated in Figure 18. In this symmetry the same transition $E \leftarrow A_1$ is to be considered. Applying the selection rule given in Eq. (251) to left circularly polarized light ($\rho = -1$) results in

$$M' = -(0-1) = +1, \tag{268}$$

leading to a positive $\boldsymbol{a}_1$ term characterized by (see Eq. (243))

$$\boldsymbol{a}_1 = 2g|\langle 0|O_{-1}^{(1)}|+1\rangle|^2. \tag{269}$$

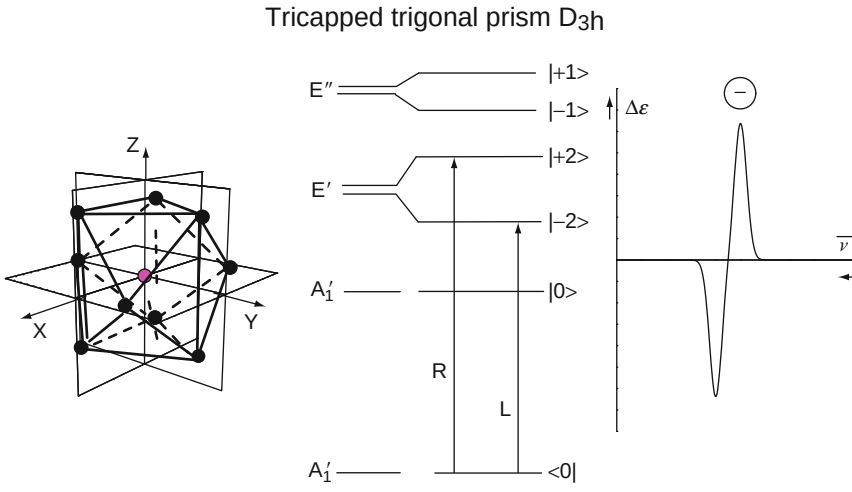

FIGURE 19 Theoretical prediction of the MCD signal for the $^5D_2 \leftarrow {}^7F_0$ transition in D_{3h} symmetry.

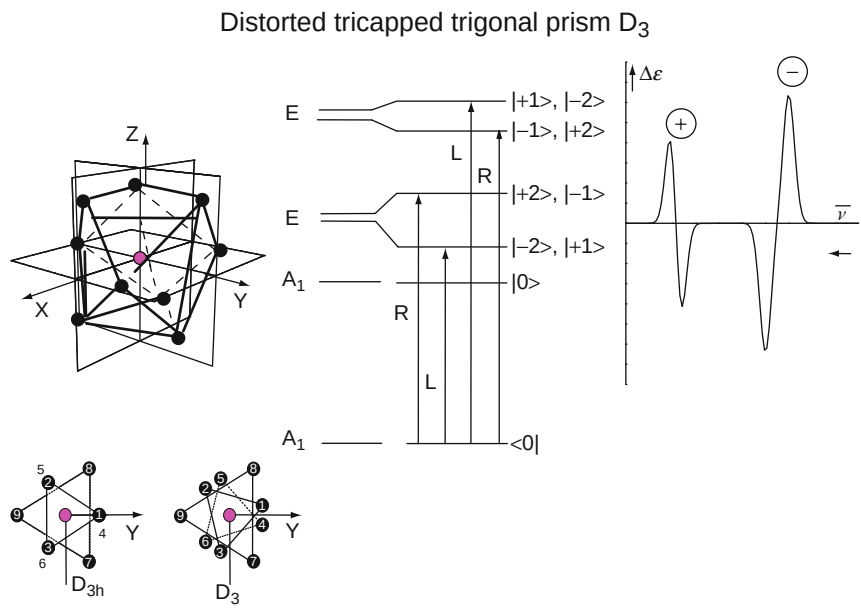

FIGURE 20 Theoretical prediction of the MCD signal for the $^5D_2 \leftarrow {}^7F_0$ transition in D_3 symmetry.

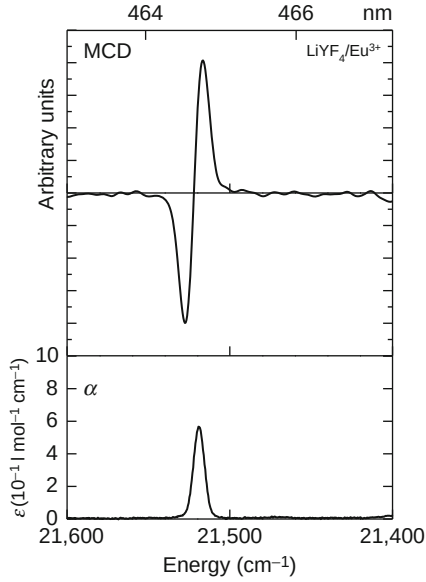

FIGURE 21 Experimental absorption and MCD spectrum for the $^5D_2 \leftarrow {}^7F_0$ transition in $LiYF_4/Eu^{3+}$.

The experimental spectra of KY_3F_{10}/Eu^{3+} single crystal are displayed on Figure 22.

Here also, the shaded peaks form the experimental evidence for the selection rules that apply for the site orientation with the C_4-axis//magnetic field. The other peaks are explained by other site orientations (see Section 6).

5.3.4 D_{3h} symmetry

A third example deals with D_{3h} symmetry (Banerjee and Schwartz, 1981; Banerjee et al., 1981; Fluyt et al., 1996; Görller-Walrand et al., 1994b; Kimpe et al., 2001; Parac-Vogt et al., 2001, 2002).

In this symmetry, the only allowed electric dipole transition is to the E' level ($M' = \pm 2$), as illustrated on Figure 19. Left circularly polarized light is absorbed to the lowest Zeeman level $|M'\rangle = |-2\rangle$ because

$$M' = -(3-1) = -2. \tag{270}$$

The experimental spectra for the $Na_3[Eu(ODA)_3]\cdot 2NaClO_4\cdot 6H_2O$ single crystal are given in Figure 23 and clearly show experimental evidence of a transition to a second E level.

This can be explained by the fact that a distortion from D_{3h} to the lower D_3 symmetry cannot be neglected. This distortion (see Figure 20) results

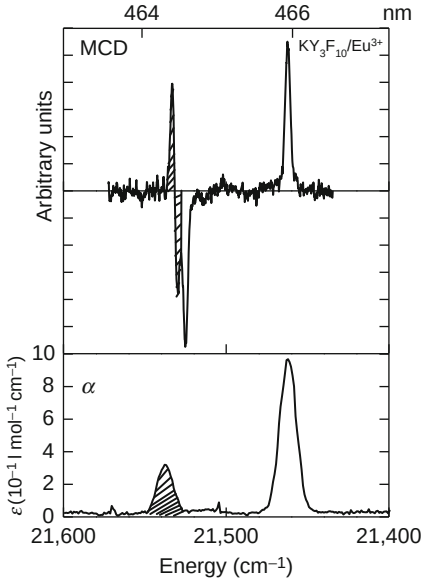

FIGURE 22 Experimental absorption and MCD spectrum for the $^5D_2 \leftarrow {}^7F_0$ transition in KY_3F_{10}/Eu^{3+}.

in a mixing of the two E levels by the even crystal field term B_3^4 (see Eq. (262)). Then absorption of left circularly polarized light is allowed to the $|-2\rangle$ component by the induced electric dipole mechanism and to the $|+1\rangle$ component by the magnetic dipole mechanism. Consequently the sign of the $\boldsymbol{\alpha}$ term is determined by the relative energies of the Zeeman levels to which left and right circularly polarized are absorbed.

Note that for a D_3 symmetry the experimental spectra correspond to both natural CD and MCD contributions. Details how to deal with this complication can be found in the literature (Banerjee et al., 1981; Görller-Walrand et al., 1994b).

Interesting work has been done on organometallic compounds in trigonal symmetries by the group of Amberger (Amberger et al., 1985, 2002).

5.4 Another view on the role of the odd crystal field terms in MCD

The Judd–Ofelt theory explains how the observation of strictly parity forbidden transitions results from non-centro-symmetric interactions that lead to a mixing of states of opposite parity. One of the most obvious mechanisms is simply the coupling of states of opposite parity by the odd terms of the crystal field expansion. The $^5D_2 \leftarrow {}^7F_0$ transition, giving a

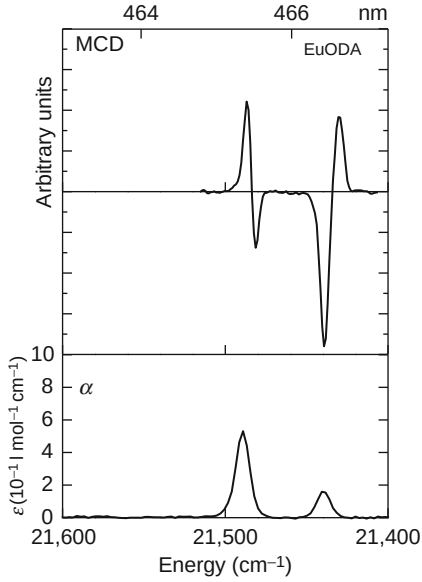

FIGURE 23 Experimental absorption and MCD spectrum for the $^5D_2 \leftarrow {}^7F_0$ transition in $Na_3[Eu(ODA)_3]\cdot 2NaClO_4\cdot 6H_2O$.

positive $\boldsymbol{A}$ term in C_{4v} and a negative $\boldsymbol{A}$ term in D_{3h} and D_{2d} symmetry can best be understood if one bears in mind the significance of the odd terms in the crystal field expansion. The admixing of configurations of opposite parity comes about by the presence of these odd crystal field terms, which means in Judds's notation:

$$\langle l^{N-1}(n'l')\psi'' J'' M'' | C_q^k | l^N \psi J' M' \rangle \neq 0.$$

In other words the C_q^k odd terms (e.g., $k = 3$ for D_{3h} and D_{2d} while q is, respectively, ± 3 and ± 2; $k = 1$ and 3 with $q = 0$ for C_{4v}, see Eqs. (259), (261), (263) and (265)), mixes odd parity configuration $l^{N-1}(n'l')\psi'' J'' M''$, where $l^{N-1}(n'l')$ stands, for example, for $4f^{N-1}5d^1$, into the excited state $l^N \psi J' M'$ (e.g., for Eu^{3+} the $^5D_2$ level will be labelled as $4f^6\psi 2M' = \pm 2, \pm 1$ or 0).

Specifically:

$$\begin{aligned} &\text{for } D_{3h}: \langle M'' | C_q^k | M' \rangle = \langle \pm 1 | C_{\pm 3}^3 | \mp 2 \rangle, \\ &\text{for } C_{4v}: \langle M'' | C_q^k | M' \rangle = \langle \mp 1 | C_0^{1 \text{ and } 3} | \mp 1 \rangle, \\ &\text{for } D_{2d}: \langle M'' | C_q^k | M' \rangle = \langle \pm 1 | C_{\pm q}^k | \mp 1 \rangle. \end{aligned} \tag{271}$$

Thus the odd crystal field terms mix in the $|M'\rangle$ excited states $|\mp 2\rangle$, $|\mp 1\rangle$ and $|\mp 1\rangle$ for D_{3h}, C_{4v} and D_{2d}, respectively, the odd parity states characterized by $\langle M''| = \langle \pm 1|, \langle \mp 1|, \langle \pm 1|$. In fact these small amounts of

mixing in odd parity states are responsible for the intensities induced in the $|M'\rangle$ states. If one bears in mind that left circularly polarized light will be absorbed to $|+1\rangle$, while right circularly polarized light is absorbed to $|-1\rangle$, it is easy to understand that left circularly polarized light will be absorbed to the $|-2\rangle$ Zeeman component in D_{3h} symmetry because of the presence in that wave function of a small amount of $|+1\rangle$ belonging to the $4f^{N-1}5d^1$ configuration. In the same way it becomes clear that right circularly polarized light will be absorbed to the $|+2\rangle$ components that mixes in with $|-1\rangle$. As the g-factor for the $^5D_2$ state is positive, $|+2\rangle$ will be the higher Zeeman component and the absorption of right circularly polarized light to that component results in a negative MCD $\boldsymbol{\alpha}$ signal.

The sign of the $\boldsymbol{\alpha}$ term in the other symmetries can be obtained by the same kind of reasoning (Amberger et al., 1985, 2002; Banerjee and Schwartz, 1981; Binnemans and Görller-Walrand, 1996; Bonardi et al., 1999; Couwenberg and Görller-Walrand, 1998; Fluyt et al., 1997; Görller-Walrand et al., 1989; Kato and Asano, 1979; Kato and Nakano, 1977; Kato and Nishioka, 1974; Kato et al., 1976, 1977; Schwartz et al., 1980; Scrivener et al., 1985).

6. THE CUBIC KY_3F_{10} CRYSTAL: A SPECIAL CASE

6.1 Introduction

The main idea underlying the description of this system is to establish that simulations for MCD transitions in media with randomly oriented molecules can be performed by applying the magnetic field along a trigonal axis, being the resultant of the three equivalent directions in a cube (see Figure 24).

Randomly oriented molecules in solutions can be regarded as one third of the sites having their main axis along x, one third along y and one third along z. This situation shows a very interesting resemblance with the KY_3F_{10}/Eu^{3+} crystal (Fluyt et al., 1999, 2005; Görller-Walrand, 1985; Görller-Walrand and Fluyt-Adriaens, 1985; Görller-Walrand et al., 1985a, 1991b; Heyde et al., 1998b).

Indeed this uniaxial cubic crystal allows MCD measurements with light propagating along the optical axis. In this crystal one third of the sites have their main axis along the crystallographic z-axis; one third have them along the x-axis and another third along the y-axis (see Figure 24). For one third of the sites a parallel Zeeman effect is induced because the crystal z-axis corresponds to the main axis z of the sites while for remaining sites a perpendicular Zeeman effect is induced as the crystallographic main axis corresponds to the x- and y-axes. The final MCD spectrum is a superposition of H_z, H_x and H_y, so that the KY_3F_{10}/Eu^{3+} crystal provides a rather unique tool for experimental verification of the parallel and perpendicular

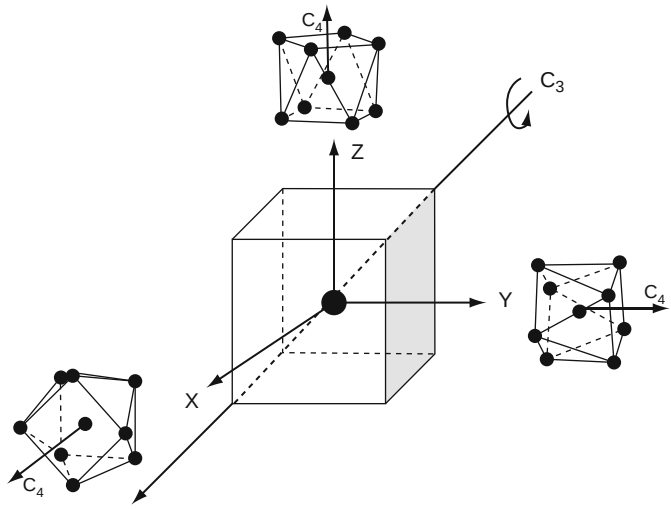

FIGURE 24 Three C_{4v} orientations (representative for KY_3F_{10}/Eu^{3+}) toward the *x*, *y*, *z*-direction and the resultant threefold axis of a cube.

Zeeman effects. Attention will be focused on the pure magnetic dipole $^5D_1 \leftarrow {}^7F_0$ and the induced electric dipole $^5D_2 \leftarrow {}^7F_0$ transitions.

6.2 The magnetic dipole $^5D_1 \leftarrow {}^7F_0$ transition of Eu^{3+}

6.2.1 The parallel Zeeman effect ($H_{\parallel} = H_z$)

As already explained in Section 5.2, $J = 1$ splits into a $M_J = \pm 1$ state and a $M_J = 0$ state in an axial symmetry (e.g., C_{4v}). A longitudinal magnetic field yields a linear Zeeman splitting for $M_J = \pm 1$ and a field-independent behaviour for $M_J = 0$, corresponding to the parallel Zeeman effect described by the Hamiltonian H_z. According to the selection rules for magnetic dipole transitions the $^5D_1 \leftarrow {}^7F_0$ transition generates always a positive A term, which is shown as shaded peaks on Figure 16B.

6.2.2 The perpendicular Zeeman effect ($H_{\perp} = H_x$ or H_y)

We then consider the effect of a perpendicular magnetic field corresponding to the operators H_x and H_y. The operators will mix in $|\pm 1\rangle$ and $|0\rangle$ as a second-order effect and a non-linearity is obtained in the Zeeman pattern. For convenience we will further use H_x the effect of which can also be described by a cyclic rotation of the axis $x \rightarrow y \rightarrow z \rightarrow x$. The same considerations are true for H_y (with a $x \leftarrow y \leftarrow z \leftarrow x$ transformation). The magnetic fields applied in the experiments have a strength of 1 T for the electromagnet and a strength of 7 T for the superconducting magnet. This corresponds, respectively, to a Zeeman splitting of ± 1 and ± 5 cm^{-1}.

For the small magnetic field of 1 T the perpendicular Zeeman effect only slightly affects the energy, but does affect the wave functions largely.

Figure 25 illustrates how one component of the degenerate state mixes with $|0\rangle$ in the original coordinate system. The result is that the upper function achieves $|+1\rangle$ character while the lower function achieves $|-1\rangle$ character so that left circularly polarized light is absorbed at high energy leading to a positive signal. An equivalent negative signal is predicted at the energy corresponding to the z polarized absorption in the original crystal field scheme (see Figure 16).

6.3 The $^5D_2 \leftarrow {}^7F_0$ induced electric dipole transition of Eu^{3+}

6.3.1 The parallel Zeeman effect ($H_{\parallel} = H_z$)

This has been explained in Section 5.3.3 and leads to a positive $\boldsymbol{a}$ term which is shown as shaded peaks in Figure 22.

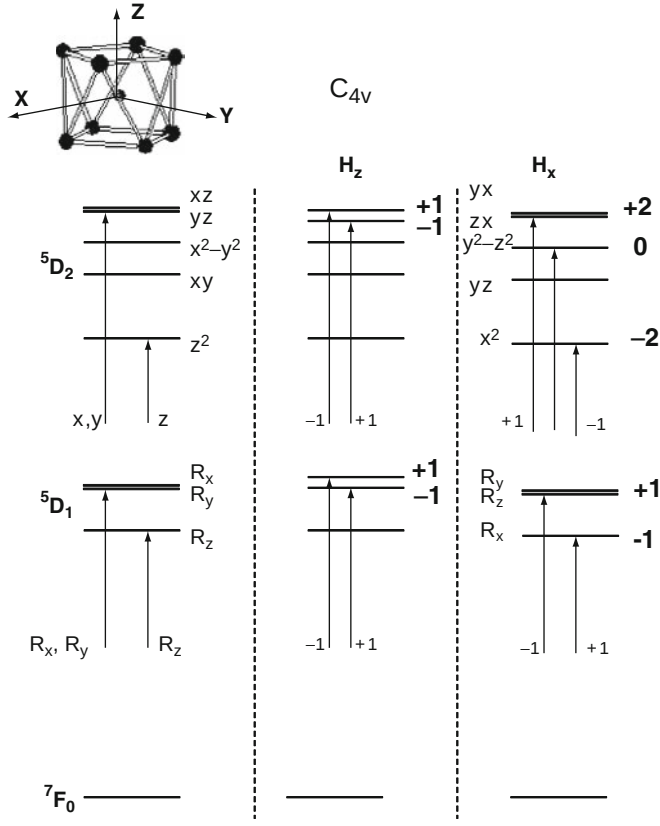

FIGURE 25 Energy levels and MCD transitions (H_z for the parallel and H_x and H_y for the perpendicular Zeeman effect) for the $^5D_{1,2} \leftarrow {}^7F_0$ transitions for Eu^{3+} in C_{4v}.

6.3.2 The perpendicular Zeeman effect ($H_\perp = H_x$ or H_y)

The energy diagram is considered in the rotation schemes $x \to y \to z \to x$ and $x \leftarrow y \leftarrow z \leftarrow x$ (Prather, 1961). Now the absorption of circularly polarized light is governed by the rotated odd crystal field terms. The relevant odd crystal field terms are given in Table 1.

If one considers that C_3^3 or S_3^3 symmetry operation is predominant in mixing the odd parity configuration, one obtains the following matrix elements:

$$\begin{aligned} &\langle +2|C_3^3|-1\rangle, \\ &\langle +2|S_3^3|-1\rangle. \end{aligned} \tag{272}$$

Thus $\langle +2|$ achieves $|-1\rangle$ character and the transition to $\langle +2|$ occurs with positive circularly polarized light. This gives a negative $\boldsymbol{\mathcal{B}}$ term. This level has the label xy in the rotated system and corresponds to xz in the original system; it is at the energy at which the positive $\boldsymbol{\mathcal{A}}$ term is found in the parallel effect. A positive $\boldsymbol{\mathcal{B}}$ term is found for the $\langle -2|$ component that is labelled x^2 and corresponds to the original z^2 level where z absorption occurs (see Figure 22).

6.4 Applying the magnetic field along the trigonal axis

This situation has been completely developed by Fluyt et al. (2005). It is inspired by the special case of this cubic crystal KY_3F_{10}/Eu^{3+} where H_z, H_x and H_y can be measured simultaneously on three sites with main axes following x, y and z. The idea is to simulate what is the effect of applying the magnetic field along the trigonal axis while simultaneously propagating the light along this axis. The three sites become now equivalent with respect to the field and the light. Moreover, a unique energy diagram is obtained corresponding to the application of the Zeeman operator:

$$\frac{1}{\sqrt{3}}H_z + \frac{1}{\sqrt{3}}H_x + \frac{1}{\sqrt{3}}H_y.$$

TABLE 1 Relevant tesseral harmonics for intensity calculations before and after rotations $x \to y \to z \to x$ and $x \leftarrow y \leftarrow z \leftarrow x$ in C_{4v} symmetry (Prather, 1961)

Odd CF[a] H_z	Intensity matrix elements[b]	Odd CF $x \to y \to z \to x$	Odd CF $x \leftarrow y \leftarrow z \leftarrow x$
C_0^1	$\langle \pm 1\|C_0^1 + C_0^3\| \pm 1\rangle$	C_1^1	S_1^1
C_0^3		$-\frac{\sqrt{6}}{4}C_1^3 + \frac{\sqrt{10}}{4}C_3^3$	$-\frac{\sqrt{6}}{4}S_1^3 - \frac{\sqrt{10}}{4}S_3^3$

[a] With S_q^k and C_q^k tesseral and C_q^k spherical harmonics.
[b] Odd crystal field terms acting between the wave function (M quantum number) of the f-configuration in the bra and the wave function of the mixing configuration in the ket.

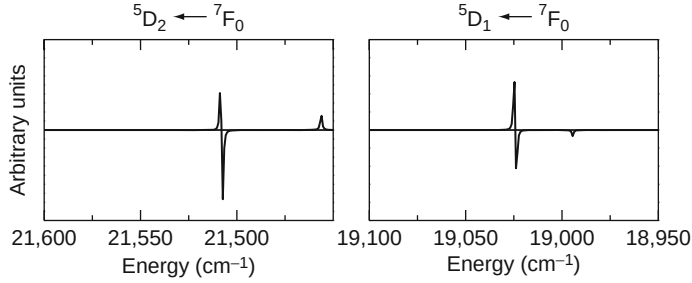

FIGURE 26 Simulated MCD spectra for the $^5D_{1,2} \leftarrow {}^7F_0$ transitions for Eu^{3+} in C_{4v}.

The simulation of the MCD signals is given in Figure 26. The MCD signals reproduce the MCD spectrum of KY_3F_{10}/Eu^{3+} in a cubic symmetry, but now the peaks are not resolved in $\mathcal{A}$ and $\mathcal{B}$ terms.

7. MAGNETIC CIRCULAR DICHROISM OF LANTHANIDE PERCHLORATES IN AQUEOUS SOLUTION

Literature on MCD spectra of aqueous lanthanide perchlorate solutions is extensive (Antipovakarataeva et al., 1982; Görller-Walrand, 1981; Görller-Walrand and Beyens, 1980; Görller-Walrand and Binnemans, 1998; Görller-Walrand and Godemont, 1977a,b; Görller-Walrand et al., 1979, 1980, 1982a, b; Kato and Nishioka, 1974; Kato et al., 1976; Pink, 1975; Sage et al., 1979). On the other hand, a consistent set of absorption spectra for the lanthanides in aqueous $HClO_4$ solution has been given (Carnall, 1979). The MCD spectra shown in Figure 27 provide useful complementary information to these previously reviewed absorption spectra for 10 trivalent Ln^{3+} ions and form to our knowledge the first complete set of MCD data throughout the lanthanide series in aqueous perchlorate solutions.

The solutions were prepared from the commercially available hydrated perchlorates by dissolving a known amount of salt in demineralized water. Concentrations were determined by titration following the Flaschka method (Carnall, 1979; Carnall et al., 1965, 1968). The absorption spectra were measured at room temperature on a Shimadzu spectrophotometer (spectral bandwidth: 0.2 nm). All MCD spectra were recorded at room temperature on a Aviv 62 DS dichrometer (spectral bandwidth 0.1 nm (<7700 nm) and 0.2–0.4 nm (>700 nm), equipped with an electromagnet (Oxford Instruments) to provide a magnetic field of 1 tesla.

Tables 2–11 list all bands according to the classification of Carnall (1979). Peaks with molar absorptivity $\varepsilon < 0.2$ l mol^{-1} cm^{-1} are not listed unless they give rise to a MCD signal.

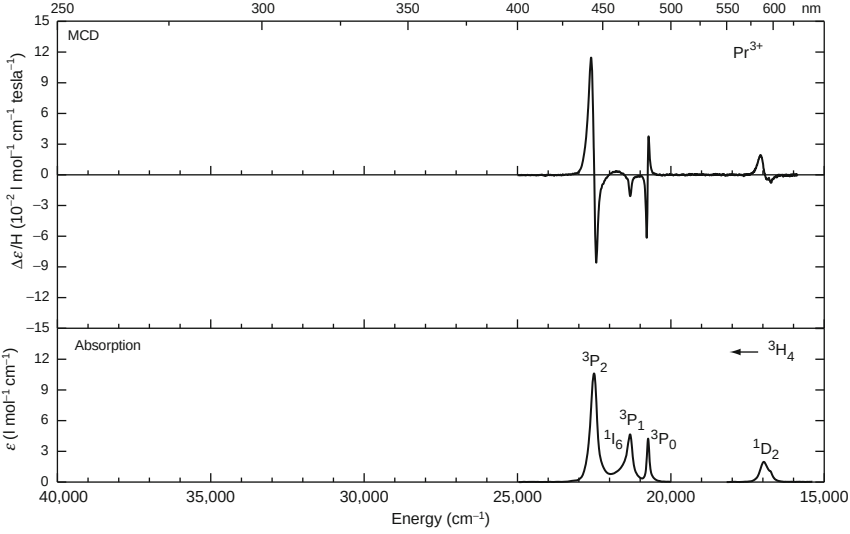
MCD
Pr3+
Δε/H (10−2 l mol−1 cm−1 tesla−1)
Absorption
ε (l mol−1 cm−1)
3H4
3P2
3P1
1I6
3P0
1D2
Energy (cm−1)
nm

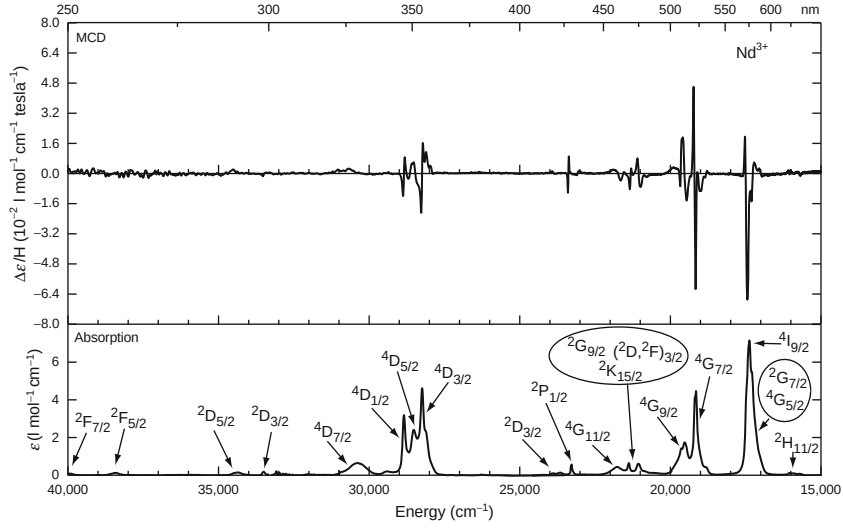
MCD
Nd3+
Δε/H (10−2 l mol−1 cm−1 tesla−1)
Absorption
ε (l mol−1 cm−1)
2F7/2
2F5/2
2D5/2
2D3/2
4D7/2
4D1/2
4D5/2
4D3/2
2D3/2
2P1/2
4G11/2
2G9/2 (2D,2F)3/2
2K15/2
4G9/2
4G7/2
4I9/2
2G7/2
4G5/2
2H11/2
Energy (cm−1)
nm

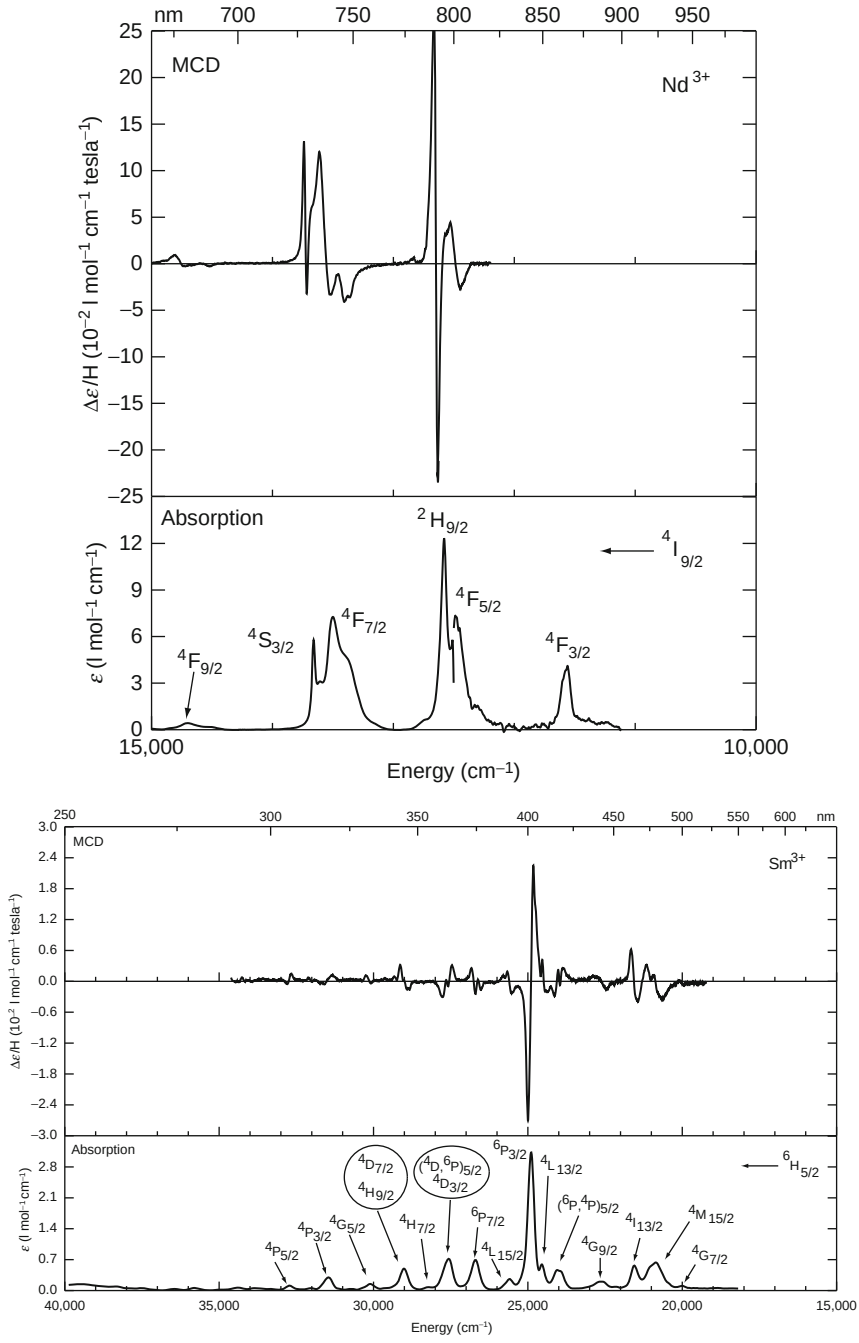

FIGURE 27 Continued

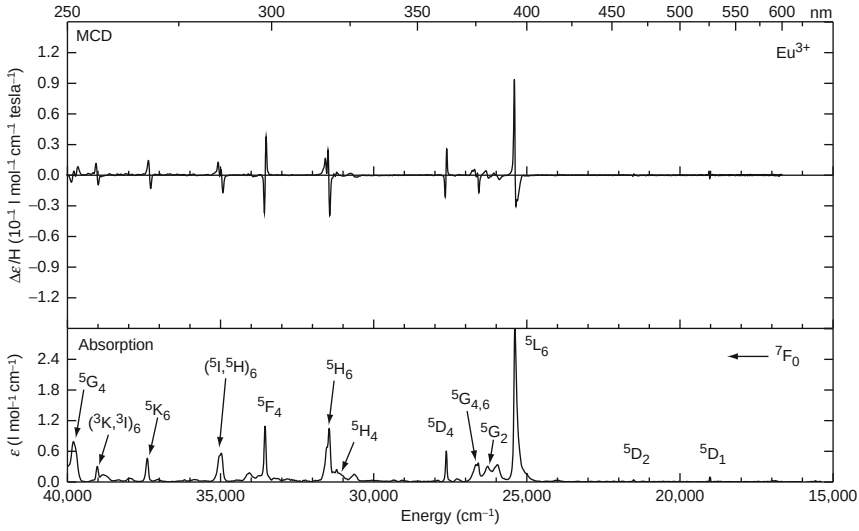
MCD
Eu3+
Δε/H (10−1 l mol−1 cm−1 tesla−1)
Absorption
ε (l mol−1 cm−1)
7F0
5G4
(3K,3I)6
5K6
(5I,5H)6
5F4
5H6
5H4
5D4
5G4,6
5G2
5L6
5D2
5D1
Energy (cm−1)
nm

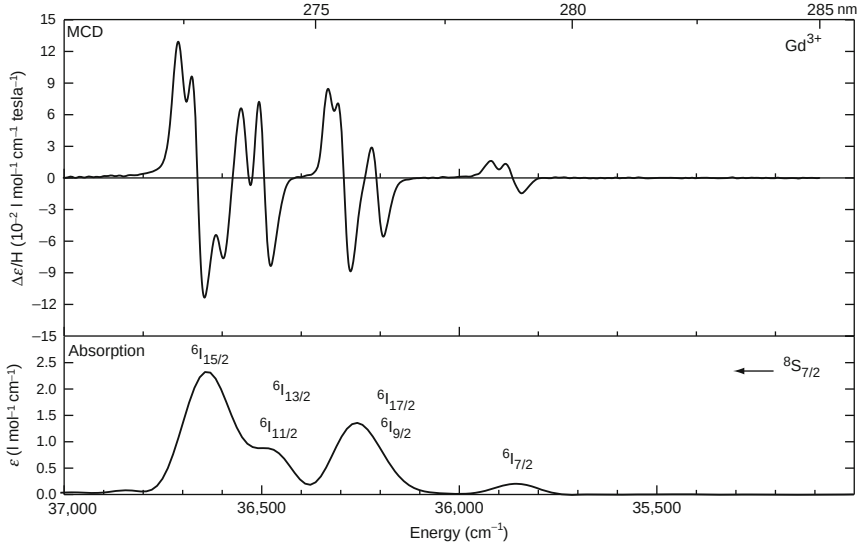
MCD
Gd3+
Δε/H (10−2 l mol−1 cm−1 tesla−1)
Absorption
ε (l mol−1 cm−1)
8S7/2
6I15/2
6I13/2
6I11/2
6I17/2
6I9/2
6I7/2
Energy (cm−1)
nm

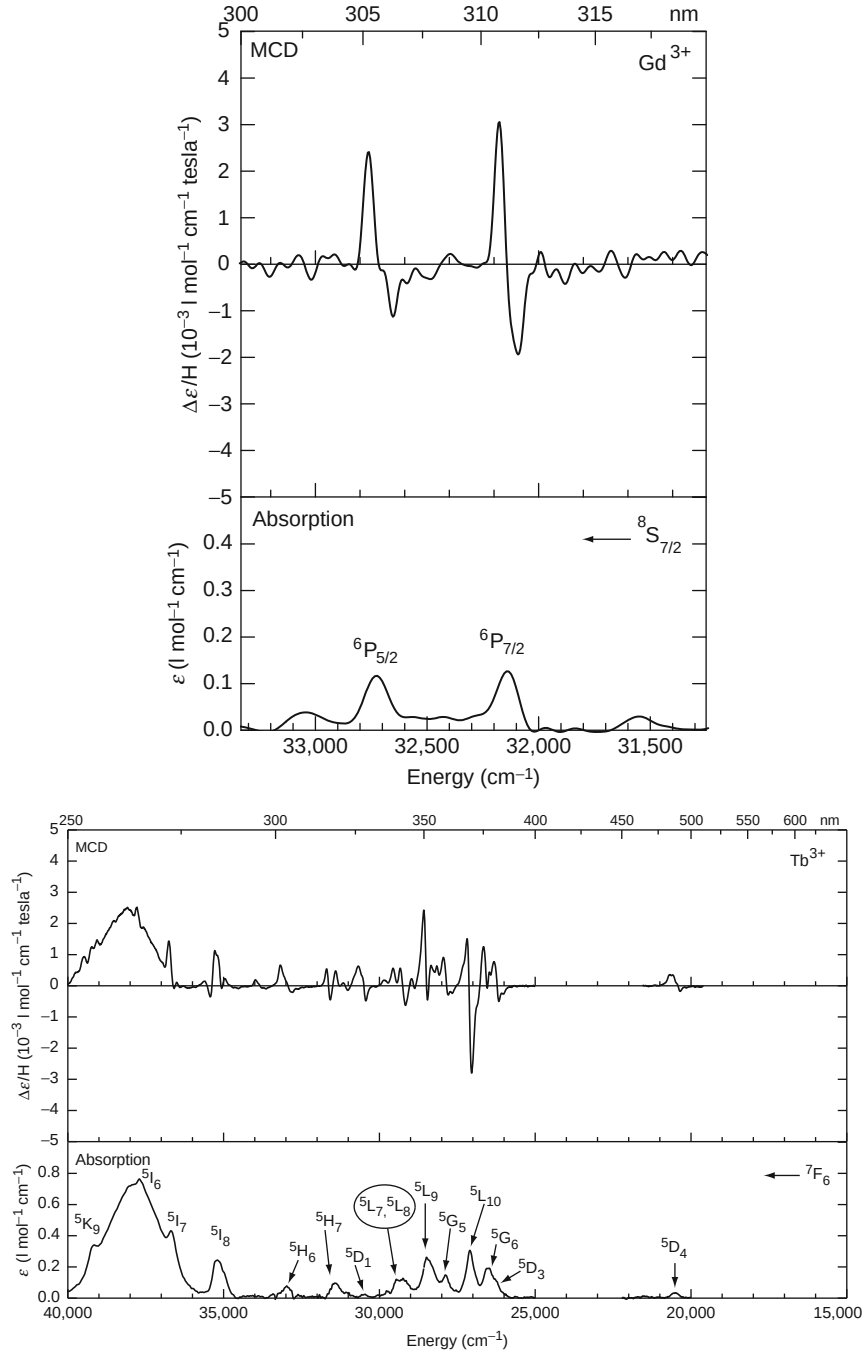

FIGURE 27 Continued

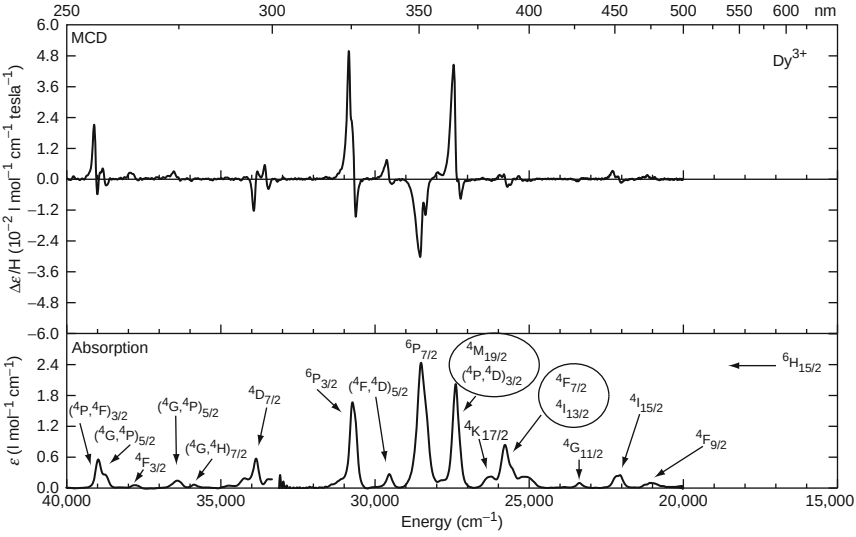
MCD
Dy3+
Absorption
6H15/2
Energy (cm−1)

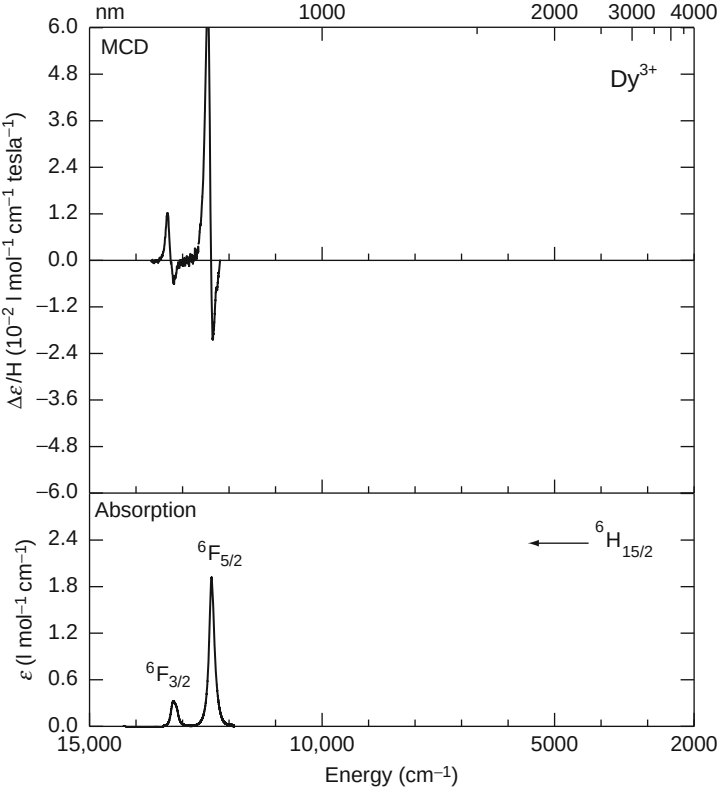
nm
MCD
Dy3+
Absorption
6H15/2
6F5/2
6F3/2
Energy (cm−1)

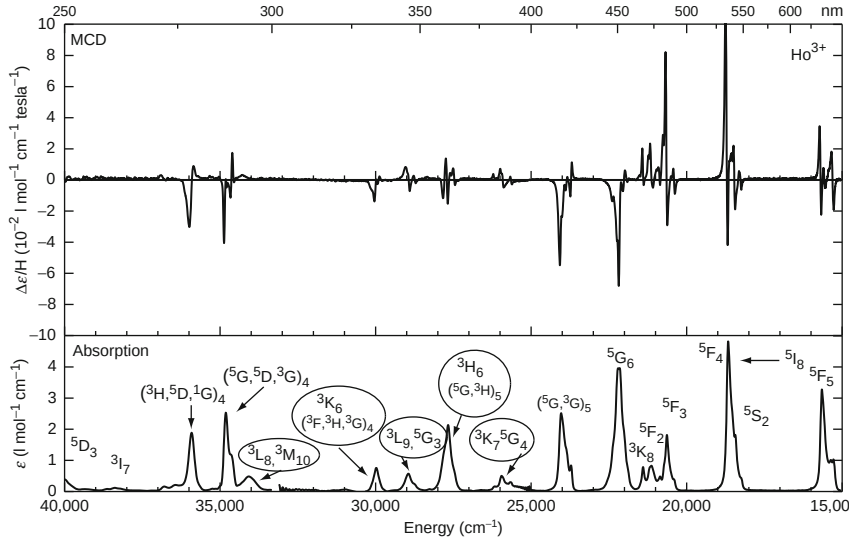

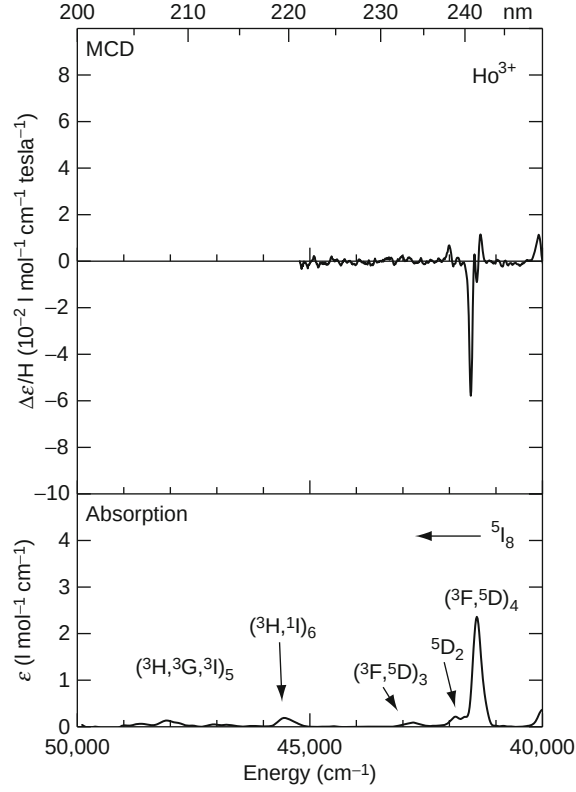

FIGURE 27 Continued

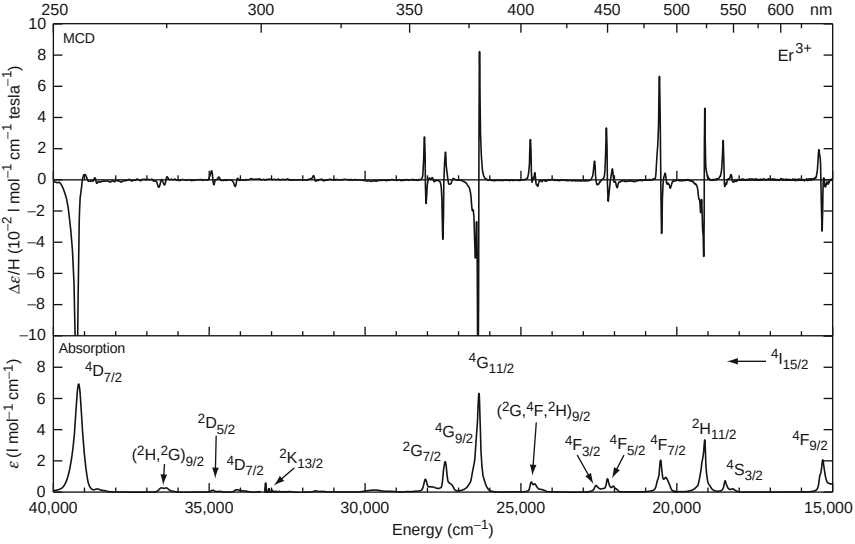
MCD
Er3+
Δε/H (10−2 l mol−1 cm−1 tesla−1)
Absorption
ε (l mol−1 cm−1)
4I15/2
4D7/2
(2H,2G)9/2
2D5/2
4D7/2
2K13/2
2G7/2
4G9/2
4G11/2
(2G,4F,2H)9/2
4F3/2
4F5/2
4F7/2
2H11/2
4S3/2
4F9/2
Energy (cm−1)

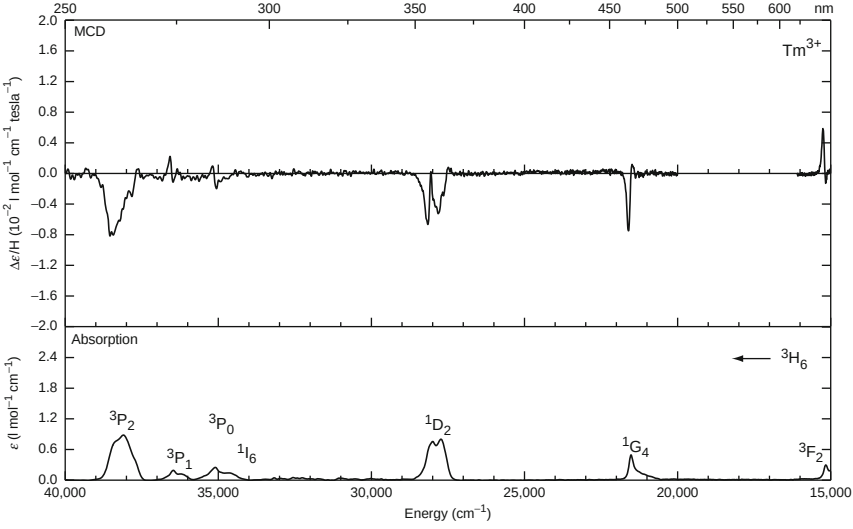
MCD
Tm3+
Δε/H (10−2 l mol−1 cm−1 tesla−1)
Absorption
ε (l mol−1 cm−1)
3H6
3P2
3P1
3P0
1I6
1D2
1G4
3F2
Energy (cm−1)

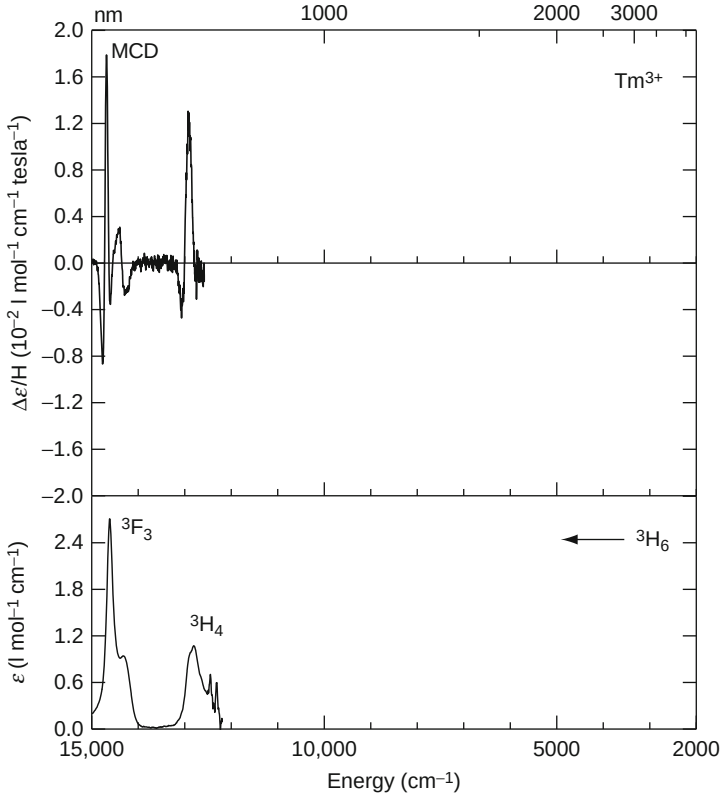

FIGURE 27 MCD and absorption spectra of rare-earth perchlorates in aqueous solution.

In the tables, θ_{max}/H and $\Delta\varepsilon_{max}/H = (1/3298)(\theta_{max}/H)$ correspond to the difference between the extrema. Note that the values in the tables have to be multiplied by the factor that is given in the headings, so that, for example, for the $^1D_2 \leftarrow {}^3H_4$ transition of $Pr(ClO_4)_3$) (Table 2) $P = 3.08 \times 10^{-6}$, $\theta_{max}/H = 1.65 \times 10^2$ °mol^{-1} dl dm^{-1} tesla^{-1} and $\Delta\varepsilon_{max}/H = 5.00 \times 10^{-2}$ l mol^{-1} cm^{-1} tesla^{-1}. Another example is the transition $^5D_1 \leftarrow {}^7F_0$ for Eu^{3+} that will be used in Section 8,[5] for the calculation of a MCD standard:

$P = 1.62 \times 10^{-8}$, $\theta_{max}/H = 40.3°$ mol^{-1} dl dm^{-1} tesla^{-1} and $\Delta\varepsilon_{max}/H = 1.22 \times 10^{-2}$ l mol^{-1} cm^{-1} tesla^{-1}.

The sign of $\boldsymbol{a}$ terms or pseudo-$\boldsymbol{a}$ terms is given with respect to the previous conventions (Section 2.2). When no $\boldsymbol{a}$ shape is found, only the sign of the MCD dispersion is given; (+) and (−) correspond,

[5] Note that a population factor of 65% for $^7F_0$ and 35% for $^7F_1$ is taken into account.

TABLE 2 Absorption and MCD data for $Pr(ClO_4)_3$ in aqueous solution

Transition	$\bar{\nu}$ (cm^{-1})	λ (Å)	$10^{-6} \times P$	Mechanism	Sign *A* term	ε_{max} ($l\ mol^{-1}\ cm^{-1}$)	$10^2 \times (\theta_{max}/H)$ ($°mol^{-1}$ dl dm^{-1} $tesla^{-1}$)	$10^{-1} \times (\Delta\varepsilon_{max}/H)$ ($l\ mol^{-1}$ cm^{-1} $tesla^{-1}$)
$^1D_2 \leftarrow {}^3H_4$	16,840	5938	3.08	ED	+	1.75	1.65	0.500
$^3P_0 \leftarrow {}^3H_4$	20,750	4819	2.54	ED	−	4.26	5.72	1.733
$^3P_1, {}^1I_6 \leftarrow {}^3H_4$	21,300	4695	7.63	ED		4.59	1.15	0.348
$^3P_2 \leftarrow {}^3H_4$	22,520	4440	15.06	ED	+	10.25	12.01	3.639

TABLE 3 Absorption and MCD data for $Nd(ClO_4)_3$ in aqueous solution

Transition	$\bar{\nu}$ (cm^{-1})	λ (Å)	$10^{-6} \times P$	Mechanism	Sign *A* term	ε_{max} (l mol^{-1} cm^{-1})	$10^2 \times (\theta_{max}/H)$ (°mol^{-1} dl dm^{-1} $tesla^{-1}$)	$10^{-1} \times (\Delta\varepsilon_{max}/H)$ (l mol^{-1} cm^{-1} $tesla^{-1}$)
$^4F_{5/2} \leftarrow {}^4I_{9/2}$	12,480	8012	8.84	ED	+	5.78	3.45	1.045
$^2H_{9/2} \leftarrow {}^4I_{9/2}$	12,590	7942		ED + MD	+	11.20	28.87	8.748
$^4F_{7/2} \leftarrow {}^4I_{9/2}$	13,500	7407	8.90	ED + MD	+	6.64	8.61	2.609
$^4S_{3/2} \leftarrow {}^4I_{9/2}$	13,500	7407		ED		5.29	6.40	1.939
$^4F_{9/2} \leftarrow {}^4I_{9/2}$	14,700	6803	0.65	ED + MD	+	0.43	0.66	0.200
$^2H_{11/2} \leftarrow {}^4I_{9/2}$	15,870	6301	0.15	ED				
$^4G_{5/2} \leftarrow {}^4I_{9/2}$	17,300	5780	9.76	ED + hyp		6.34	4.79	1.452
$^2G_{7/2} \leftarrow {}^4I_{9/2}$	17,300	5780						
$^4G_{7/2} \leftarrow {}^4I_{9/2}$	19,160	5219		ED + MD	+	4.12	5.98	1.812
$^2K_{13/2} \leftarrow {}^4I_{9/2}$	19,550	5115	7.01	ED		1.50		
$^4G_{9/2} \leftarrow {}^4I_{9/2}$				ED + MD				
$^2K_{15/2} \leftarrow {}^4I_{9/2}$	21,000	4762	2.33	ED	+	0.60	0.86	0.261
$^2G_{9/2} \leftarrow {}^4I_{9/2}$	21,300	4694		ED + MD	−	0.64	0.59	0.179
$(^2D,^2F)_{3/2} \leftarrow {}^4I_{9/2}$	21,300	4694		ED				
$^4G_{11/2} \leftarrow {}^4I_{9/2}$	21,650	4619		ED + MD	+	0.43		
$^2P_{1/2} \leftarrow {}^4I_{9/2}$	23,250	4301	0.41	ED	−	0.94	1.18	0.358
$^2D_{5/2} \leftarrow {}^4I_{9/2}$	23,900	4184	0.09	ED	+			
$(^2P,^2D)_{3/2} \leftarrow {}^4I_{9/2}$	26,300	3802	0.03	ED	+			
$^4D_{3/2} \leftarrow {}^4I_{9/2}$	28,300	3533	9.42	ED	−	4.74	1.92	0.582
$^4D_{5/2} \leftarrow {}^4I_{9/2}$	28,500	3509		ED	−	2.21		
$^4D_{1/2} \leftarrow {}^4I_{9/2}$	28,850	3466		ED	−	3.44	1.18	0.358
$^4D_{7/2} \leftarrow {}^4I_{9/2}$	30,500	3279		ED + MD		0.56		
$^2D_{3/2} \leftarrow {}^4I_{9/2}$	33,400	2994		ED	−	0.31		
$^2D_{5/2} \leftarrow {}^4I_{9/2}$	34,450	2903		ED	+	0.16		
$^2F_{5/2} \leftarrow {}^4I_{9/2}$	38,506	2597		ED		0.14		

TABLE 4 Absorption and MCD data for $Sm(ClO_4)_3$ in aqueous solution

Transition	$\bar{\nu}$ (cm^{-1})	λ (Å)	$10^{-6} \times P$	Mechanism	Sign *A* term	ε_{max} (l mol^{-1} cm^{-1})	$10^2 \times (\theta_{max}/H)$ (°mol^{-1} dl dm^{-1} $tesla^{-1}$)	$10^{-1} \times (\Delta\varepsilon_{max}/H)$ (l mol^{-1} cm^{-1} $tesla^{-1}$)
$^4G_{7/2} \leftarrow {}^6H_{5/2}$	20,050	4987	0.52	ED + MD				
$^4M_{15/2} \leftarrow {}^6H_{5/2}$	20,800	4808	1.53	ED				
$^4I_{11/2} \leftarrow {}^6H_{5/2}$	21,100	4739	1.53	ED	+	0.55	0.395	0.120
$^4I_{13/2} \leftarrow {}^6H_{5/2}$	21,600	4630	0.68	ED	+	0.50	0.639	0.194
$^4G_{9/2} \leftarrow {}^6H_{5/2}$	22,700	4405	0.39	ED	+			
$(^6P,^4P)_{5/2} \leftarrow {}^6H_{5/2}$	24,050	4158		ED + MD	−	0.41	0.300	0.091
$^4L_{13/2} \leftarrow {}^6H_{5/2}$	24,570	4070	0.43	ED	+	0.54	0.396	0.120
$^6P_{3/2} \leftarrow {}^6H_{5/2}$	24,950	4008	3.84	ED + MD	−	3.02	2.98	0.903
$^4L_{15/2} \leftarrow {}^6H_{5/2}$	25,650	3899	0.42	ED	+	0.22	2.75	0.833
$^6P_{7/2} \leftarrow {}^6H_{5/2}$	26,750	3738	1.06	ED + MD	+	0.59	0.245	0.074
$^4D_{3/2} \leftarrow {}^6H_{5/2}$	27,700	3610	1.23	ED + MD	−	0.68	0.387	0.117
$(^4D,^6P)_{5/2} \leftarrow {}^6H_{5/2}$	27,700	3610	1.23	ED	+			
$^4H_{7/2} \leftarrow {}^6H_{5/2}$	28,250	3540	0.06	ED + MD				
$^4H_{9/2} \leftarrow {}^6H_{5/2}$	29,100	3436	0.80	ED + MD	+	0.44	0.288	0.087
$^4D_{7/2} \leftarrow {}^6H_{5/2}$								
$^4G_{5/2} \leftarrow {}^6H_{5/2}$	30,200	3311		ED + MD	+			
$^4P_{3/2} \leftarrow {}^6H_{5/2}$	31,550	3169		ED + MD	−	0.28	0.095	0.029
$^4P_{5/2} \leftarrow {}^6H_{5/2}$	32,800	3049		ED	−			

TABLE 5 Absorption and MCD data for $Eu(ClO_4)_3$ in aqueous solution

Transition	$\bar{\nu}$ (cm^{-1})	λ (Å)	$10^{-8} \times P$	Mechanism	Sign *A* term	ε_{max} ($l\ mol^{-1}\ cm^{-1}$)	$10^{2} \times (\theta_{max}/H)$ ($^{\circ}mol^{-1}$ dl dm^{-1} $tesla^{-1}$)	$10^{-1} \times (\Delta\varepsilon_{max}/H)$ ($l\ mol^{-1}\ cm^{-1}\ tesla^{-1}$)
$^5D_0 \leftarrow {}^7F_1$	16,920	5910	7.47	MD	+			
$^5D_1 \leftarrow {}^7F_1$	18,691	5350	2.49	ED	−			
$^5D_1 \leftarrow {}^7F_0$	19,028	5255	1.62	MD	+	0.113	0.403	0.122
$^5D_2 \leftarrow {}^7F_1$	21,164	4725	0.90	MD				
$^5D_2 \leftarrow {}^7F_0$	21,519	4647	2.29	ED + hyp	−	0.0500	0.123	0.0370
$^5D_3 \leftarrow {}^7F_1$	24,038	4160	8.94	ED	−			
$^5D_3 \leftarrow {}^7F_0$	24,408	4097		ED				
$^5L_6 \leftarrow {}^7F_0$	25,400	3937	214.98	ED	+	3.41	7.97	2.42
$^5L_7 \leftarrow {}^7F_1$	25,974	3850		ED	+	0.340		
$^5G_2 \leftarrow {}^7F_0$	26,300	3802		ED		0.320		
$^5G_5 \leftarrow {}^7F_1$	26,325	3799		ED	+			
$^5G_4 \leftarrow {}^7F_0$	26,620	3756		ED	+	0.420	1.52	0.461
$^5D_4 \leftarrow {}^7F_1$	27,300	3663	11.82	ED				
$^5D_4 \leftarrow {}^7F_0$	27,641	3614	20.60	ED	−	0.730	3.51	1.06
$^5H_7 \leftarrow {}^7F_1$	30,656	3262	46.51	ED				
$^5H_4 \leftarrow {}^7F_0$	31,250	3200		ED				

(*continued*)

TABLE 5 (*continued*)

Transition	$\bar{\nu}$ (cm^{-1})	λ (Å)	$10^{-8} \times P$	Mechanism	Sign *A* term	ε_{max} ($l\ mol^{-1}\ cm^{-1}$)	$10^2 \times (\theta_{max}/H)$ ($^\circ mol^{-1}$ dl dm^{-1} $tesla^{-1}$)	$10^{-1} \times (\Delta\varepsilon_{max}/H)$ ($l\ mol^{-1}\ cm^{-1}$ $tesla^{-1}$)
$^5H_{5,6} \leftarrow {}^7F_1$	31,200	3205		ED				
$^5H_6 \leftarrow {}^7F_0$	31,520	3172	79.90	ED	+	1.20	3.90	1.18
$^5F_3 \leftarrow {}^7F_1$	32,800	3048	13.15	ED				
$^5F_2 \leftarrow {}^7F_0$	33,190	3013		ED				
$^5F_4 \leftarrow {}^7F_1$	33,280	3005		ED	−			
$^5F_4 \leftarrow {}^7F_0$	33,590	2977		ED		1.30	4.70	1.42
$^5I_4 \leftarrow {}^7F_1$	33,590	2977		ED	−			
$(^5I,{}^5H)_6 \leftarrow {}^7F_1$	34,100	2932		ED				
$(^5I,{}^5H)_6 \leftarrow {}^7F_0$	35,050	2855		ED	+	0.590	1.87	0.567
$^5I_7 \leftarrow {}^7F_1$	35,050	2855		ED	+			
$^5K_5 \leftarrow {}^7F_1$	35,925	2784		ED				
$^5K_5 \leftarrow {}^7F_0$	36,205	2762		ED				
$^5K_6 \leftarrow {}^7F_1$	37,100	2695	7.39	ED	+			
$^5K_6 \leftarrow {}^7F_0$	37,440	2671	23.16	ED	+	0.560	1.73	0.524
$^5F_7 \leftarrow {}^7F_1$	38,060	2627		ED	+			
$^5G2_3 \leftarrow {}^7F_1$	38,640	2588	55.44	ED				
$(^3I,{}^3K)_6 \leftarrow {}^7F_0$	39,062	2560	12.19	ED	+	0.360	1.34	0.406
$^5G_4 \leftarrow {}^7F_0$	39,897	2507		ED	−	0.810	1.03	0.312
$^5G_5 \leftarrow {}^7F_1$	40,100	2494		ED	−			

TABLE 6 Absorption and MCD data for $Gd(ClO_4)_3$ in aqueous solution

Transition	$\bar{\nu}$ (cm^{-1})	λ (Å)	$10^{-6} \times P$	Mechanism	Sign *A* term	ε_{max} (l mol^{-1} cm^{-1})	$10^2 \times (\theta_{max}/H)$) ($^\circ mol^{-1}$ dl dm^{-1} $tesla^{-1}$)	$10^{-1} \times (\Delta\varepsilon_{max}/H)$ (l mol^{-1} cm^{-1} $tesla^{-1}$)
$^6P_{7/2} \leftarrow {}^8S_{7/2}$	32,196	3106	0.073	MD + hyp	+	0.14	0.162	0.049
$^6P_{5/2} \leftarrow {}^8S_{7/2}$	32,722	3056	0.041	ED + MD	+			
$^6I_{7/2} \leftarrow {}^8S_{7/2}$	35,932	2783	0.121	ED	+	0.24	1.42	0.430
$^6I_{9/2} \leftarrow {}^8S_{7/2}$	36,232	2760	0.845	ED + MD	+	0.74	3.13	0.950
$^6I_{17/2} \leftarrow {}^8S_{7/2}$	36,337	2752		ED	+	1.80	8.06	2.442
$^6I_{11/2} \leftarrow {}^8S_{7/2}$	36,536	2737	1.914	ED	+	1.12	6.47	1.961
$^6I_{13/2} \leftarrow {}^8S_{7/2}$	36,576	2734						
$^6I_{15/2} \leftarrow {}^8S_{7/2}$	36,697	2725			+	2.81	11.30	3.424
$^6D_{9/2} \leftarrow {}^8S_{7/2}$	39,620	2524	0.078	ED + MD	−			

TABLE 7 Absorption and MCD data for $Tb(ClO_4)_3$ in aqueous solution

Transition	$\bar{\nu}$ (cm^{-1})	λ (Å)	$10^{-6} \times P$	Mechanism	Sign *A* term	ε_{max} (l mol^{-1} cm^{-1})	$10^2 \times (\theta_{max}/H)$ (°mol^{-1} dl dm^{-1} $tesla^{-1}$)	$10^{-1} \times (\Delta\varepsilon_{max}/H)$ (l mol^{-1} cm^{-1} $tesla^{-1}$)
$^5D_4 \leftarrow {}^7F_6$	20,500	4878	0.52	ED + hyp	+	0.029	0.37	0.112
$^5D_3 \leftarrow {}^7F_6$	26,268	3807	8.46	ED				
$^5G_6 \leftarrow {}^7F_6$	26,500	3773		ED + MD		0.16		
$^5L_{10} \leftarrow {}^7F_6$	27,100	3690		ED	+	0.25	0.282	0.085
$^5G_5 \leftarrow {}^7F_6$	27,800	3597	7.46	ED + MD				
$^5D_2 \leftarrow {}^7F_6$	27,800	3597		ED				
$^5L_9 \leftarrow {}^7F_6$	28,400	3521		ED	+	0.22	0.188	0.057
$^5L_8 \leftarrow {}^7F_6$	29,300	3413	3.04	ED				
$^5L_7 \leftarrow {}^7F_6$	29,450	3395		ED				
$^5D_1 \leftarrow {}^7F_6$	30,650	3262	0.37	ED	+	0.023	0.074	0.022
$^5H_7 \leftarrow {}^7F_6$	31,600	3164	2.02	ED + MD				
$^5H_6 \leftarrow {}^7F_6$	33,000	3030	1.20	ED + MD				
$^5H_5 \leftarrow {}^7F_6$	33,900	2950	0.18	ED + MD				
$^5I_8 \leftarrow {}^7F_6$	35,200	2840	5.05	ED		0.20		

TABLE 8 Absorption and MCD data for $Dy(ClO_4)_3$ in aqueous solution

Transition	$\bar{\nu}$ (cm^{-1})	λ (Å)	$10^{-6} \times P$	Mechanism	Sign *A* term	ε_{max} (l mol^{-1} cm^{-1})	$10^2 \times (\theta_{max}/H)$ (°mol^{-1} dl dm^{-1} $tesla^{-1}$)	$10^{-1} \times (\Delta\varepsilon_{max}/H)$ (l mol^{-1} cm^{-1} $tesla^{-1}$)
$^6F_{5/2} \leftarrow {}^6H_{15/2}$	12,395	8068	1.55	ED	+	1.76	4.72	1.427
$^6F_{3/2} \leftarrow {}^6H_{15/2}$	13,250	7547	0.33	ED	+	0.31	1.07	0.324
$^4F_{9/2} \leftarrow {}^6H_{15/2}$	21,100	4739	0.21	ED				
$^4I_{15/2} \leftarrow {}^6H_{15/2}$	22,100	4525	0.44	ED + MD	+	0.23	0.32	0.097
$^4G_{11/2} \leftarrow {}^6H_{15/2}$	23,400	4273	0.16	ED	−			
$^4F_{7/2} \leftarrow {}^6H_{15/2}$	25,800	3876		ED		0.82	0.22	0.067
$^4I_{13/2} \leftarrow {}^6H_{15/2}$			2.38	MD				
$^4K_{17/2} \leftarrow {}^6H_{15/2}$	26,400	3787		MD		0.22		
$^4M_{19/2} \leftarrow {}^6H_{15/2}$	27,400	3649		ED		1.94	3.12	0.945
$(^4P,^4D)_{3/2} \leftarrow {}^6H_{15/2}$			2.85	ED				
$^6P_{5/2} \leftarrow {}^6H_{15/2}$				ED	+			
$^6P_{7/2} \leftarrow {}^6H_{15/2}$	28,550	3503	4.36	ED	−	2.32	1.92	0.582
$(^4F,^4D)_{5/2} \leftarrow {}^6H_{15/2}$	29,600	3378	0.39	ED	+	0.30	0.52	0.158
$^6P_{3/2} \leftarrow {}^6H_{15/2}$	30,803	3247	2.59	ED	+	1.63	3.72	1.127
$^4H_{13/2} \leftarrow {}^6H_{15/2}$	33,500	2985		MD	+	0.17	0.47	0.142
$^4D_{7/2} \leftarrow {}^6H_{15/2}$	33,900	2950		ED	−	0.58	0.85	0.258
$^4G_{9/2} \leftarrow {}^6H_{15/2}$	(34,311)	(2914)	1.43	ED				
$^4G_{11/2} \leftarrow {}^6H_{15/2}$	34,900	2865		ED	+			
$^4L_{17/2} \leftarrow {}^6H_{15/2}$	34,900	2865		ED	+			
$(^4G,^4H)_{7/2} \leftarrow {}^6H_{15/2}$	35,900	2785	0.05	ED	−			
$(^4G,^4P)_{5/2} \leftarrow {}^6H_{15/2}$	36,550	2736		ED		0.17	0.19	0.058
$^4F_{3/2} \leftarrow {}^6H_{15/2}$	37,900	2639		ED	+			
$(^4G,^4P)_{5/2} \leftarrow {}^6H_{15/2}$	38,900	2570		ED		0.30	0.39	0.118
$(^4P,^4F)_{3/2} \leftarrow {}^6H_{15/2}$	39,100	2557		ED		0.63	1.47	0.445
$(^4F,^2G)_{9/2} \leftarrow {}^6H_{15/2}$	41,050	2436		ED				
$^4I_{15/2} \leftarrow {}^6H_{15/2}$	41,700	2398		ED + MD				

TABLE 9 Absorption and MCD data for $Ho(ClO_4)_3$ in aqueous solution

Transition	$\bar{\nu}$ (cm^{-1})	λ (Å)	$10^{-6} \times P$	Mechanism	Sign *A* term	ε_{max} (l mol^{-1} cm^{-1})	$10^2 \times (\theta_{max}/H)$ (°mol^{-1} dl dm^{-1} $tesla^{-1}$)	$10^{-1} \times (\Delta\varepsilon_{max}/H)$ (l mol^{-1} cm^{-1} $tesla^{-1}$)
$^5F_5 \leftarrow {}^5I_8$	15,500	6452	3.76	ED	+	3.04	3.32	1.006
$^5S_2 \leftarrow {}^5I_8$	18,500	5405	5.23	ED	+	1.65	2.37	0.718
$^5F_4 \leftarrow {}^5I_8$	18,653	5361		ED	+	4.49	9.31	2.821
$^5F_3 \leftarrow {}^5I_8$	20,600	4854	1.78	ED	+	1.75	6.54	1.982
$^5F_2 \leftarrow {}^5I_8$	21,100	4739	1.43	ED	+	0.76	1.57	0.476
$^3K_8 \leftarrow {}^5I_8$	21,370	4679		ED + MD	+	0.76	1.28	0.388
$^5G_6 \leftarrow {}^5I_8$	22,100	4524	6.00	ED + hyp		3.59	4.03	1.221
$(^5G,{}^3G)_5 \leftarrow {}^5I_8$	23,950	4175	3.14	ED		2.35	3.24	0.982
$^5G_4 \leftarrow {}^5I_8$	25,800	3876	1.03	ED	+	0.44	0.57	0.173
$^3K_7 \leftarrow {}^5I_8$	26,200	3817		ED + MD				
$^3H_6 \leftarrow {}^5I_8$	27,700	3610	3.24	ED				
$(^5G,{}^3H)_5 \leftarrow {}^5I_8$	27,700	3610		ED		2.04	1.55	0.470
$^5G_3 \leftarrow {}^5I_8$	28,800	3472	0.83	ED				
$^3L_9 \leftarrow {}^5I_8$	29,000	3448		ED + MD		0.51	0.82	0.248
$(^3F,{}^3H,{}^3G)_4 \leftarrow {}^5I_8$	30,000	3333	0.80	ED	+			
$^3K_6 \leftarrow {}^5I_8$	30,012	3332		ED + hyp		0.78	0.86	0.261
$^5G_2 \leftarrow {}^5I_8$	30,900	3236	0.13	ED				
$^3L_8 \leftarrow {}^5I_8$	34,200	2924	1.01	ED + MD		0.47		
$^3M_{10} \leftarrow {}^5I_8$	34,200	2924		ED				
$(^5G,{}^5D,{}^3G)_4 \leftarrow {}^5I_8$	34,800	2874	2.72	ED		3.06	2.98	0.903
$(^3H,{}^5D,{}^1G)_4 \leftarrow {}^5I_8$	36,000	2777	2.59	ED		1.84	2.16	0.655
$^3I_7 \leftarrow {}^5I_8$	38,500	2597		ED + MD				
$^5D_3 \leftarrow {}^5I_8$	40,000	2500	0.54	ED		0.36		
$(^3F,{}^5D)_4 \leftarrow {}^5I_8$	41,550	2406	2.54	ED		3.12		

TABLE 10 Absorption and MCD data for $Er(ClO_4)_3$ in aqueous solution

Transition	$\bar{\nu}$ (cm^{-1})	λ (Å)	$10^{-6} \times P$	Mechanism	Sign *A* term	ε_{max} (l mol^{-1} cm^{-1})	$10^2 \times (\theta_{max}/H)$ (°mol^{-1} dl dm^{-1} $tesla^{-1}$)	$10^{-1} \times (\Delta\varepsilon_{max}/H)$ (l mol^{-1} cm^{-1} $tesla^{-1}$)
$^4I_{9/2} \leftarrow {}^5I_{15/2}$	12,400	8064	0.29	ED	−	0.24	0.697	0.211
$^4F_{9/2} \leftarrow {}^5I_{15/2}$	15,250	6557	2.25	ED	+	2.09	3.24	0.982
$^4S_{3/2} \leftarrow {}^5I_{15/2}$	18,350	5449	0.66	ED	+	0.70	1.87	0.567
$(^2H,^4G)_{11/2} \leftarrow {}^5I_{15/2}$	19,150	5222	2.89	ED + hyp	−	3.44	5.88	1.782
$^4F_{7/2} \leftarrow {}^5I_{15/2}$	20,450	4889	2.27	ED	+	2.07	6.35	1.924
$^4F_{5/2} \leftarrow {}^5I_{15/2}$	22,100	4525	1.25	ED	+	0.88	2.97	0.900
$^4F_{3/2} \leftarrow {}^5I_{15/2}$	22,500	4444		ED	+	0.41	1.00	0.303
$(^2G,^4F,^2H)_{9/2} \leftarrow {}^5I_{15/2}$	24,500	4037	0.80	ED	+	0.67	1.83	0.555
$^4G_{11/2} \leftarrow {}^5I_{15/2}$	26,400	3788	5.92	ED + hyp	−	7.36	12.92	3.915
$^4G_{9/2} \leftarrow {}^5I_{15/2}$	27,400	3649	1.75	ED	−	2.21	3.46	1.048
$^2K_{15/2} \leftarrow {}^5I_{15/2}$	27,933	3580	0.91	MD		0.37		
$^2G_{7/2} \leftarrow {}^5I_{15/2}$	28,000	3571		ED	+	0.93	2.63	0.797
$(^2P,^2D,^4F)_{3/2} \leftarrow {}^5I_{15/2}$	31,600	3164	0.09	ED	+			
$^2K_{13/2} \leftarrow {}^5I_{15/2}$	33,200	3012	0.12	ED + MD				
$^4G_{5/2} \leftarrow {}^5I_{15/2}$	33,400	2994		ED				
$^4G_{7/2} \leftarrow {}^5I_{15/2}$	34,050	2937	0.21	ED				
$^2D_{5/2} \leftarrow {}^5I_{15/2}$	34,850	2869	0.14	ED	+	0.17	0.498	0.151
$(^2H,^2G)_{9/2} \leftarrow {}^5I_{15/2}$	36,550	2736	0.44	ED		0.32	0.31	0.094
$^4D_{7/2} \leftarrow {}^5I_{15/2}$	39,200	2551	10.2	ED	−	8.08	7.74	2.345
$^2I_{11/2} \leftarrow {}^5I_{15/2}$	41,150	2430		ED	−	0.83		
$^2L_{17/2} \leftarrow {}^5I_{15/2}$	41,650	2400		ED + MD		0.29		
$^4D_{3/2} \leftarrow {}^5I_{15/2}$	42,300	2364		ED				
$^2I_{3/2} \leftarrow {}^5I_{15/2}$	43,550	2296		ED + MD	−	0.56		

TABLE 11 Absorption and MCD data for $Tm(ClO_4)_3$ in aqueous solution

Transition	$\bar{\nu}$ (cm^{-1})	λ (Å)	$10^{-6} \times P$	Mechanism	Sign *A* term	ε_{max} (l mol^{-1} cm^{-1})	$10^2 \times (\theta_{max}/H)$ (°mol^{-1} dl dm^{-1} $tesla^{-1}$)	$10^{-1} \times (\Delta\varepsilon_{max}/H)$ (l mol^{-1} cm^{-1} $tesla^{-1}$)
$^3H_4 \leftarrow {}^3H_6$	12,700	7874	2.12	ED		0.91	0.83	0.252
$^3F_3 \leftarrow {}^3H_6$	14,500	6897	3.91	ED	+	2.38	1.38	0.418
$^3F_2 \leftarrow {}^3H_6$	15,100	6622		ED		0.26	0.40	0.121
$^1G_4 \leftarrow {}^3H_6$	21,350	4684	0.71	ED	−	0.43	0.45	0.136
$^1D_2 \leftarrow {}^3H_6$	28,000	3571	2.38	ED		0.70	0.36	0.109
$^1I_6 \leftarrow {}^3H_6$	34,900	2865	0.84	ED + MD				
$^3P_0 \leftarrow {}^3H_6$	35,500	2817		ED	+	0.33	0.15	0.045
$^3P_1 \leftarrow {}^3H_6$	36,400	2747	0.56	ED		0.36		
$^3P_2 \leftarrow {}^3H_6$	38,250	2614	3.28	ED		0.94	0.43	0.130

respectively, to a signal on the positive and negative side of the MCD scale ($\Delta\varepsilon = \varepsilon_- - \varepsilon_+$). As explained in Section 4.5 the ratio $(\Delta\varepsilon_{\max}/H)/\varepsilon_{\max}$ leads to $\boldsymbol{a}_1/D$ by the use of Eq. (230). This determines the magnetic moment of the involved states.

The importance of the sign of the MCD terms has to a great extent been explained in Section 5. Additionally MCD enables to distinguish two peaks that in absorption are poorly resolved by the presence of two consecutive peaks with opposite sign, see, for example, Dy^{3+} where the $^6P_{5/2} \leftarrow {}^6H_{15/2}$ at 364.5 nm and $^6P_{7/2} \leftarrow {}^6H_{15/2}$ at 350.3 nm show, respectively, a positive and negative MCD signal.

8. CALCULATION OF THE $\mathcal{A}_1/D$ RATIO FOR THE MAGNETIC DIPOLE TRANSITION $^5D_1 \leftarrow {}^7F_0$ IN EU^{3+} AND ITS USE AS A STANDARD

8.1 Absorption

The dipole strengths for $^5D_1 \leftarrow {}^7F_0$ were experimentally measured and theoretically calculated *ab initio* for a series of Eu^{3+} complexes in a solid state or solution (Görller-Walrand et al., 1991a). These values show a high degree of symmetry invariance. A mean value of 17.6×10^{-7} $Debye^2$ was calculated and proposed as a standard for intensity scaling for other transitions. In this chapter, the calculation was made with the old convention for ε (see Section 4.3.3, Eq. (209)). Hereafter we explain how 1/3 of this value is found following the new convention from Eq. (145).

For Eu^{3+} perchlorate in water (see Figure 28) the zeroth-order moment of ε is found by integrating the absorption spectrum and using Eqs. (142) and (214):

$$\langle\varepsilon\rangle_0 = \int \frac{\varepsilon}{\bar{\nu}} \mathrm{d}\bar{\nu} = \chi 326.6D = 1.73 \times 10^{-4} \mathrm{l\,mol^{-1}\,cm^{-1}}. \tag{273}$$

From Eq. (141) the dipole strength is

$$D = \frac{1}{n} 3.062 \times 10^{-3} \times 1.73 \times 10^{-4}\,\mathrm{Debye}^2 = \frac{1}{n} 0.58 \times 10^{-6}\,\mathrm{Debye}^2. \tag{274}$$

From Eq. (155) the oscillator strength is

$$f = 4.32 \times 10^{-9} \bar{\nu}_0 \frac{1}{\chi} \int \frac{\varepsilon(\bar{\nu})}{\bar{\nu}} \mathrm{d}\bar{\nu}$$

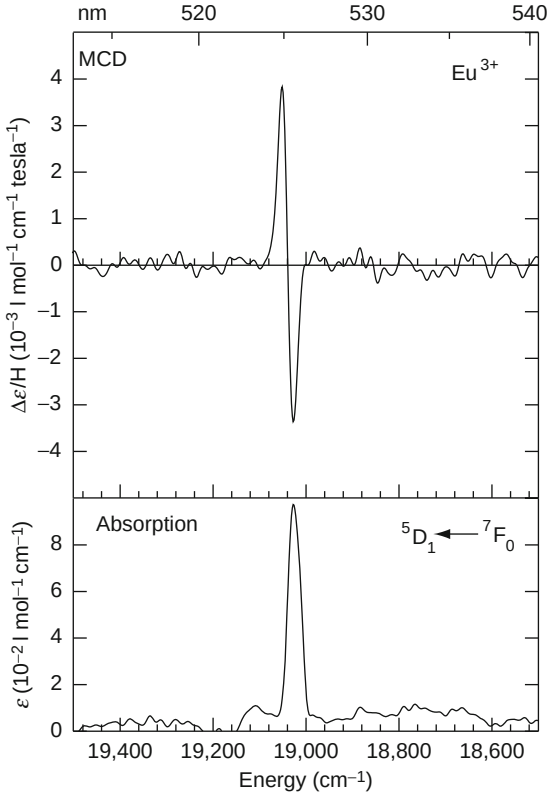

FIGURE 28 MCD and absorption spectra of $^5D_1 \leftarrow {}^7F_0$ in $Eu(ClO_4)_3$.

with

$$\bar{\nu}_0 = \bar{\nu}_{JA} = 19{,}028\,\mathrm{cm}^{-1},$$

one finds

$$f = 4.32 \times 10^{-9} \times 19{,}028 \times 1.73 \times 10^{-4} = 1.62 \times 10^{-8}. \qquad (275)$$

As explained before in Eq. (155) this value is independent from the convention used to define the dipole strength and only dependent on the integration range. This is the calculated value found by W.T. Carnall in his seminal paper on the intensities of the magnetic dipole transitions (Carnall et al., 1968). Note that integration of the absorption signal takes into account the effect of line broadening by the shape function. This is not the case for ε_{max}; it is very hazardous to work with molar absorptivity if the bandwidth of the peaks are not comparable.

8.2 Magnetic circular dichroism

The MCD spectrum of Eu^{3+} perchlorate is also given in Figure 28 (Görller-Walrand, 1981; Görller-Walrand et al., 1980; Pink, 1975).

The first-order moment calculated with $\bar{\nu}_0 = \bar{\nu}_{JA} = 19{,}028\ \mathrm{cm}^{-1}$ from Eqs. (217) and (221) is found from the integration:

$$\left\langle \frac{\Delta\varepsilon}{H} \right\rangle_1 = \int \frac{\Delta\varepsilon}{\bar{\nu}} (\bar{\nu} - \bar{\nu}_{JA}) \mathrm{d}\bar{\nu} = \chi 152.5 \int -\boldsymbol{a}_1 \frac{\mathrm{d}f(\bar{\nu} - \bar{\nu}_{JA})}{\mathrm{d}\bar{\nu}} \mathrm{d}\bar{\nu} \qquad (276)$$
$$= 2.5 \times 10^{-4}\, \mathrm{l\,mol^{-1}\,cm^{-1}\,tesla^{-1}\,cm^{-1}}$$

or

$$\left\langle \frac{\Delta\theta}{H} \right\rangle_1 = \int \frac{\theta}{H} (\bar{\nu} - \bar{\nu}_{JA}) \bar{\nu} \mathrm{d}\bar{\nu} = \chi 50.28 \times 10^4 \int -\boldsymbol{a}_1 \frac{\mathrm{d}f(\bar{\nu} - \bar{\nu}_{JA})}{\mathrm{d}\bar{\nu}} \mathrm{d}\bar{\nu} \qquad (277)$$
$$= 8.4 \times 10^{-1}\, {}^{\circ}\mathrm{mol^{-1}\,dl\,dm^{-1}\,tesla^{-1}\,cm^{-1}},$$

one finds

$$\boldsymbol{a}_1 = 0.0066 \left\langle \frac{\Delta\varepsilon}{H} \right\rangle_1 = 0.0066 \times 2.5 \times 10^{-4} = 1.7 \times 10^{-6}\, \mathrm{Debye}^2 \qquad (278)$$

or

$$\boldsymbol{a}_1 = 0.02 \times 10^{-4} \left\langle \frac{\theta}{H} \right\rangle_1 = 0.02 \times 10^{-4} \times 8.4 \times 10^{-1}\, \mathrm{Debye}^2 \qquad (279)$$
$$= 1.7 \times 10^{-6}\, \mathrm{Debye}^2.$$

The ratio is

$$\frac{\boldsymbol{a}_1}{D} = \frac{1.7 \times 10^{-6}}{0.58 \times 10^{-6}} = 2.9 \cong 3 \qquad (280)$$

or

$$\frac{\boldsymbol{a}_1}{D} = \frac{326.6}{152.5} \frac{\left\langle \frac{\Delta\varepsilon}{H} \right\rangle_1}{\langle \varepsilon \rangle_0} = \frac{2.14 \times 2.5 \times 10^{-4}}{1.73 \times 10^{-4}} \cong 3, \qquad (281)$$

or

$$\frac{\boldsymbol{a}_1}{D} = \frac{326.6}{50.28 \times 10^4} \frac{\left\langle \frac{\theta}{H} \right\rangle_1}{\langle \varepsilon \rangle_0} = 6.5 \times 10^{-4} \times \frac{8.4 \times 10^{-1}}{1.73 \times 10^{-4}} \cong 3. \qquad (282)$$

Theoretically:

$$\boldsymbol{a}_1 = 2gM = 3, \text{ with } g = 1.5.$$

This is obtained from Eqs. (237)–(244) and the definition of the dipole strength in Eq. (161):

$$\frac{\boldsymbol{a}_1}{D} = \frac{2g|\langle J0|O^{(1)}_{-1}|J{+}1\rangle|^2}{|\langle J0|O^{(1)}_{-1}|J{+}1\rangle|^2}, \tag{283}$$

with $g = 1.5$.

The clue for standardization is that the integrated area for absorption and MCD of $^5D_1 \leftarrow {}^7F_0$ for Eu^{3+} are, respectively,

$$\langle\varepsilon\rangle_0 = \int \frac{\varepsilon}{\bar{\nu}} \mathrm{d}\bar{\nu} \cong 1.73 \pm 0.15 \,\mathrm{l\,mol^{-1}\,cm^{-1}},$$

$$\left\langle \frac{\Delta\varepsilon}{H} \right\rangle_1 = \int \frac{\Delta\varepsilon}{\bar{\nu}} (\bar{\nu} - \bar{\nu}_{JA}) \mathrm{d}\bar{\nu} \cong 2.50 \pm 0.55 \times 10^{-4} \,\mathrm{l\,mol^{-1}\,cm^{-1}\,tesla^{-1}\,cm^{-1}},$$

$$\left\langle \frac{\Delta\theta}{H} \right\rangle_1 = \int \frac{\theta}{H} (\bar{\nu} - \bar{\nu}_{JA}) \bar{\nu} \mathrm{d}\bar{\nu} \cong 8.40 \pm 0.65 \times 10^{-1} \,^\circ\mathrm{mol^{-1}\,dl\,dm^{-1}\,tesla^{-1}\,cm^{-1}},$$

with $\bar{\nu}_{JA} = 19{,}030 \pm 5\,\mathrm{cm^{-1}}$.

The Zeeman splitting for a magnetic field H = 1 tesla is

$$2g\beta H = 2 \times 1.5 \times 0.4669 \times 1 \cong 1.5\,\mathrm{cm^{-1}}.$$

8.3 Method of the maxima

From the reported spectra (Görller-Walrand et al., 1980; Pink, 1975) displayed on Figure 28 one finds

$$\varepsilon_{\max} = 1.00 \times 10^{-1} \,\mathrm{l\,mol^{-1}\,cm^{-1}},$$

$$\frac{\Delta\varepsilon_{\max}}{H} = 1.22 \times 10^{-2} \,\mathrm{l\,mol^{-1}\,cm^{-1}\,tesla^{-1}},$$

$$\frac{\theta_{\max}}{H} = 40.3 \,^\circ\mathrm{mol^{-1}\,dl\,dm^{-1}\,tesla^{-1}},$$

$$\Gamma_{\mathrm{G}} = 17\,\mathrm{cm^{-1}},$$

From Eq. (230):

$$\frac{\boldsymbol{a}_1}{D} = 1.5\Gamma_{\mathrm{G}} \frac{\Delta\varepsilon_{\max}}{\varepsilon_{\max}} = 1.5 \times 17 \times \frac{1.22 \times 10^{-2}}{1.00 \times 10^{-1}} \cong 3.2$$

and from Eq. (232):

$$\frac{\boldsymbol{a}_1}{D} = 4.5 \times 10^{-4} \Gamma_G \frac{\theta_{max}/H}{\varepsilon_{max}} = 4.5 \times 10^{-4} \times 17 \times \frac{40.3}{1.00 \times 10^{-1}} \cong 3.1.$$

9. CONCLUSION

In this chapter, we have put the emphasis on going in depth into the theory of both absorption and MCD spectroscopies. We have illustrated how the sign and shape properties of the MCD signals can be derived in a comparative way from group theory. Finally, the complete quantitative treatment of the signal has been derived for the magnetic dipole transition $^5D_1 \leftarrow {}^7F_0$ of Eu^{3+} and shown that it can be used as a standard for scaling the spectral intensity. According to completely *ab initio* calculations, the intensity of absorption of this transition was calculated to be invariant, a fact confirmed experimentally for a series of compounds (Carnall et al., 1968). The same holds true for the MCD signals.

MCD is a very powerful technique in describing the ultimate fine splitting of the energy levels (Zeeman levels). MCD signals can be detected with orders of magnitude more sensitivity than their counterparts in Zeeman spectroscopy. The shape, sign and magnitude of the MCD signals bear specific information about the energy levels. In particular, the information conveyed by the sign of the MCD signals which leads to the precise assignment of the electronic levels cannot be extracted from any other spectroscopic technique. In EPR or classical Zeeman spectroscopy for instance, the energy difference between two states can eventually be measured, but it is impossible to tell which level is higher in energy.

Another very important feature of MCD is that every positive signal has its negative counterpart and vice versa. In the actual terminology one can state that every signal is ''entangled'' with a signal of opposite sign. This opens interesting perspectives for applications in quantum computers. One should realize that this is not the case for natural circular dichroism. In this case, depending on the stereochemical properties of the molecule, ''levogyre'' or ''dextrogyre'', one gets one negative or one positive signal, which stresses that the origin of the MCD and CD signals is completely different.

As for future investigations, the study of vibronic transitions carries interesting perspectives. Although often referred to in the interpretation of spectroscopic data for coordination compounds, these transitions are very difficult to detect experimentally because of the variety and multiple combinations of vibrational modes that overlap. While vibronic transitions have been fairly well interpreted in simple inorganic compounds

such as doped oxides (Meijerink et al., 1996; Weber, 1968) or glasses (Zakharov et al., 1977), osmium (Piepho and Schatz, 1983) and lanthanide halides (Banerjee and Schwartz, 1981; Kuo et al., 1995; Voss et al., 1983; Zhou et al., 2006), as well as salts in aqueous solutions (Lindqvist-Reis et al., 2009; Stavola et al., 1981), less attention has been focused on coordination compounds (Puntus et al., 2007; Strek and Sztucki, 1991; Tsaryuk et al., 2000) despite the fact that detailed theoretical considerations have been made on how to treat vibronic interactions within the frame of the crystal field theory (Malta, 1995). Given the sign properties of the MCD vibronic signals a lot of additional information could be gathered on vibronic transitions, both experimentally and theoretically. For instance, we have recently illustrated how the sign of a MCD vibronic transition can elucidate a photochemical reaction mechanism (Görller-Walrand, 2004). We think that MCD studies on glass ceramics, where the lanthanides are imbedded in a cubic structure, could provide useful supplementary information on the luminescence properties.

As already mentioned applications of MCD spectroscopy are relatively scarce due to the technical constraints of He-cryogenics and the propagation of alternatively left and right circularly polarized light through several optical components. Moreover, if MCD is very powerful for lanthanide spectroscopy because of the sharpness of the peaks, on the other hand this feature imposes special requirements for the instrumentation, such as high resolving power. Last but not least, very few experiments have been performed in luminescence mode (magnetic circular-polarized luminescence or MCPL), with the exception of the seminal initial work done by the group of Richardson (Richardson and Brittain, 1981; Schwartz et al., 1977). This kind of equipment is not commercially available and still provides a challenge for new technical developments in spectroscopy.

ACKNOWLEDGMENTS

We are indebted to the Belgian Fund for Research (FWO-G.0508.07) and to the K.U. Leuven (GOA-03/03) for financial support.

REFERENCES

Abushuma, A., Duffield, J.J., 1970. Appl. Spectrosc. 24, 67.
Abushuma, A., Hooper, G.E., Duffield, J.J., 1971. Appl. Spectrosc. 25, 238.
Amberger, H.D., Jahn, W., Edelstein, N.M., 1985. Spectrochim. Acta Part A 41, 465.
Amberger, H.D., Jank, S., Reddmann, H., Edelstein, N.M., 2002. Spectrochim. Acta Part A 58, 379.
Antipovakarataeva, I.I., Zolotov, Y.A., Kazanova, N.N., 1982. J. Anal. Chem. USSR 37, 1392.

Atkins, P.W., 1970. Molecular Quantum Mechanics: An Introduction to Quantum Chemistry. Clarendon, Oxford.
Atkins, P.W., 1978. Molecular Quantum Mechanics: An Introduction to Quantum Chemistry. Clarendon, Oxford.
Atkins, P.W., 1984. Molecular Quantum Mechanics. Clarendon, Oxford.
Atkins, P.W., 1997. Molecular Quantum Mechanics. Clarendon, Oxford.
Atkins, P.W., 2000. Molecular Quantum Mechanics. Clarendon, Oxford.
Banerjee, A.K., Schwartz, R.W., 1981. J. Phys. Chem. Solids 42, 1057.
Banerjee, A.K., Schwartz, R.W., Chowdhury, M., 1981. J. Chem. Soc., Faraday Trans. 77, 1635.
Binnemans, K., Görller-Walrand, C., 1996. J. Chem. Soc., Faraday Trans. 92, 2487.
Bonardi, C., Carvalho, R.A., Basso, H.C., Terrile, M.C., Cruz, G.K., Bausa, L.E., Sole, J.G., 1999. J. Chem. Phys. 111, 6042.
Briat, B., Djerassi, C., 1968. Nature 217, 918.
Buckingham, A.D., Stephens, P.J., 1966. Annu. Rev. Phys. Chem. 17, 399.
Caldwell, D.J., Eyring, H., 1976. J. Chem. Phys. 64, 915.
Carnall, W.T., 1979. The absorption and fluorescence spectra of rare earth ions in solution. In: Gschneidner Jr., K.A., Eyring, L. (Eds.), Handbook on the Physics and Chemistry of Rare Earths Non-Metallic Compounds I, vol. 3. North-Holland, Amsterdam, pp. 171–208 (Chapter 24).
Carnall, W.T., Fields, P.R., Wybourne, B.G., 1965. J. Chem. Phys. 42, 3797.
Carnall, W.T., Fields, P.R., Rajnak, K., 1968. J. Chem. Phys. 49, 4412.
Couwenberg, I., Görller-Walrand, C., 1998. J. Alloys Compd. 275, 388.
Dawber, J.G., 1964. Analyst 89, 755.
De Leebeeck, H., Görller-Walrand, C., 1998. J. Alloys Compd. 275, 407.
De Leebeeck, H., Görller-Walrand, C., Saez-Puche, R., 1998. J. Alloys Compd. 280, 1.
De Leebeeck, H., Binnemans, K., Görller-Walrand, C., 1999. J. Alloys Compd. 291, 300.
Denning, R.G., 1975. Electron. State Inorg. Compd. p. 157.
Dieke, G.H., Crosswhite, H.M., Crosswhite, H., 1968. Spectra and Energy Levels of Rare Earth Ions in Crystals. Interscience, New York.
Dobosh, P.A., 1974. Mol. Phys. 27, 689.
Eyring, H., Walter, J., Kimball, E., 1944. Quantum Chemistry. John Wiley & Sons, New York.
Eyring, H., Liu, H.C., Caldwell, D., 1968. Chem. Rev. 68, 525.
Fluyt, L., Verhoeven, P., Lambaerts, H., Binnemans, K., Görller-Walrand, C., 1994. J. Alloys Compd. 207, 51.
Fluyt, L., Binnemans, K., Görller-Walrand, C., 1995. J. Alloys Compd. 225, 71.
Fluyt, L., Couwenberg, I., Lambaerts, H., Binnemans, K., Görller-Walrand, C., Reid, M.F., 1996. J. Chem. Phys. 105, 6117.
Fluyt, L., Hens, E., DeLeebeeck, H., Görller-Walrand, C., 1997. J. Alloys Compd. 250, 316.
Fluyt, L., Heyde, K., Görller-Walrand, C., 1999. Rare earths '98 315-3, 424.
Fluyt, L., Driesen, K., Görller-Walrand, C., 2005. J. Solid State Chem. 178, 429.
Foss, J.G., Mccarvil, M.E., 1965. J. Am. Chem. Soc. 87, 228.
Görller-Walrand, C., 1981. Spectroscopische eigenschappen van metaalcomplexen. Koninklijke academie voor wetenschappen, letteren en schone kunsten van België, Brussels.
Görller-Walrand, C., 1985. Chem. Phys. Lett. 115, 333.
Görller-Walrand, C., 2004. Mol. Phys. 102, 1361.
Görller-Walrand, C., Beyens, Y., 1980. Rare Earths in Modern Science and Technology. Proceedings of the 14th Rare Earth Research Conference, vol. 2. p. 87.
Görller-Walrand, C., Binnemans, K., 1996. Chapter 155 Rationalization of crystal-field parametrization. In: Gschneidner Jr., K.A. (Ed.), Handbook on the Physics and Chemistry of Rare Earths. Elsevier, Amsterdam, pp. 121–283.
Görller-Walrand, C., Binnemans, K., 1997. Bull. Soc. Chim. Belg. 106, 685.

Görller-Walrand, C., Binnemans, K., 1998. Chapter 167 Spectral intensities of f–f transitions. In: Gschneidner Jr., K.A. (Ed.), Handbook on the Physics and Chemistry of Rare Earths. Elsevier, Amsterdam, pp. 101–264.
Görller-Walrand, C., Fluyt-Adriaens, L., 1985. J. Less-Common Met. 112, 175.
Görller-Walrand, C., Godemont, J., 1977a. J. Chem. Phys. 67, 3655.
Görller-Walrand, C., Godemont, J., 1977b. J. Chem. Phys. 66, 48.
Görller-Walrand, C., Beyens, Y., Godemont, J., 1979. J. Chim. Phys. Phys.–Chim. Biol. 76, 190.
Görller-Walrand, C., Peeters, H., Beyens, Y., Demoitie-Neyt, N., Behets, M., 1980. Nouv. J. Chim. 4, 715.
Görller-Walrand, C., Colen, W., Dao, N.Q., 1982a. J. Chem. Phys. 76, 13.
Görller-Walrand, C., Demoitieneyt, N., Beyens, Y., Bünzli, J.C., 1982b. J. Chem. Phys. 77, 2261.
Görller-Walrand, C., Behets, M., Porcher, P., Laursen, I., 1985a. J. Chem. Phys. 83, 4329.
Görller-Walrand, C., Behets, M., Porcher, P., Mouneminn, O.K., Laursen, I., 1985b. Inorg. Chim. Acta 109, 83.
Görller-Walrand, C., Behets, M., Porcher, P., Carnall, W.T., 1986. J. Less-Common Met. 126, 271.
Görller-Walrand, C., Hendrickx, I., Fluyt, L., Porcher, P., Mouneminn, O.K., Blasse, G., 1989. J. Lumin. 42, 349.
Görller-Walrand, C., Fluyt, L., Ceulemans, A., Carnall, W.T., 1991a. J. Chem. Phys. 95, 3099.
Görller-Walrand, C., Fluyt, L., Dirckx, V., 1991b. Eur. J. Solid State Inorg. Chem. 28, 201.
Görller-Walrand, C., Fluyt, L., Verhoeven, P., Berghmans, E., Vandenberghe, G.M., 1993. Bull. Soc. Chim. Belg. 102, 99.
Görller-Walrand, C., Huygen, E., Binnemans, K., Fluyt, L., 1994a. J. Phys.: Condens. Mat. 6, 7797.
Görller-Walrand, C., Verhoeven, P., Dolieslager, J., Fluyt, L., Binnemans, K., 1994b. J. Chem. Phys. 100, 815.
Heyde, K., Binnemans, K., Görller-Walrand, C., 1998a. J. Chem. Soc., Faraday Trans. 94, 1671.
Heyde, K., Binnemans, K., Görller-Walrand, C., 1998b. J. Chem. Soc., Faraday Trans. 94, 843.
Judd, B.R., 1962. Phys. Rev. 127, 750.
Kato, Y., Asano, M., 1979. Bull. Chem. Soc. Jpn. 52, 999.
Kato, Y., Nakano, I., 1977. Chem. Phys. Lett. 45, 359.
Kato, Y., Nishioka, K., 1974. Bull. Chem. Soc. Jpn. 47, 1047.
Kato, Y., Nagai, T., Nakaya, T., 1976. Chem. Phys. Lett. 39, 183.
Kato, Y., Nakaya, T., Nagai, T., 1977. Bull. Chem. Soc. Jpn. 50, 589.
Kimpe, K., D'Olieslager, W., Görller-Walrand, C., Figueirinha, A., Kovacs, Z., Geraldes, C.F. G.C., 2001. J. Alloys Compd. 323, 828.
Kuo, S.C., Thompson, L.C., Amberger, H.D., 1995. J. Alloys Compd. 225, 60.
Lazzeretti, P., Zanasi, R., Stephens, P.J., 1986. J. Phys. Chem. 90, 6761.
Lindqvist-Reis, P., Walther, C., Klenze, R., Edelstein, N.M., 2009. J. Phys. Chem. C 113, 449.
Malta, O.L., 1995. J. Phys. Chem. Sol. 56, 1053.
McGlynn, S.P., Vanquickenborne, L.G., Kinoshita, M., Carroll, D.G., 1972. Introduction to Applied Quantum Chemistry. Holt, Rinehart and Winston, New York.
Meijerink, A., Blasse, G., Sytsma, J., Donega, C.D., Ellens, A., 1996. Acta Phys. Pol. A 90, 109.
Osborne, G.A., Cheng, J.C., Stephens, P.J., 1973. Rev. Sci. Instrum. 44, 10.
Parac-Vogt, T.N., Binnemans, K., Görller-Walrand, C., 2001. ChemPhysChem 2, 767.
Parac-Vogt, T.N., Binnemans, K., Görller-Walrand, C., 2002. J. Chem. Soc., Dalton Trans. 1602.
Pauling, L., Wilson, E.B., 1935. Introduction to Quantum Mechanics. McGraw-Hill, New York.
Piepho, S.B., Schatz, P.N., 1983. Group Theory in Spectroscopy: With Applications to Magnetic Circular Dichroism. John Wiley & Sons, New York.

Pink, H.S., 1975. MCD in the Trivalent Lanthanides. Syracuse University, New York.
Prather, J.L., 1961. Atomic Energy Levels in Crystals. National Bureau of Standards Monograph, vol. 19. National Bureau of Standards, Washington, DC.
Puntus, L.N., Chauvin, A.-S., Varbanov, S., Bünzli, J.-C.G., 2007. Eur. J. Inorg. Chem. 2315.
Racah, G., 1960. J. Opt. Soc. Am. B: Opt. Phys. 50, 408.
Racah, G., 1964. J. Quant. Spectrosc. Radiat. Transfer 4, 617.
Reid, M.F., 1988. F-Shell Empirical Programs. University of Canterbury, New Zealand.
Richardson, F.S., Brittain, H.G., 1981. J. Am. Chem. Soc. 103, 18.
Sage, M.L., Buonocore, M.H., Pink, H.S., 1979. Chem. Phys. 36, 171.
Schatz, P.N., Mc Caffery, A.J., 1969. Q. Rev. 23, 552.
Schatz, P.N., Mowery, R.L., Krausz, E.R., 1978. Mol. Phys. 35, 1537.
Schellman, J.A., 1975. Chem. Rev. 75, 323.
Schwartz, R.W., Brittain, H.G., Riehl, J.P., Yeakel, W., Richardson, F.S., 1977. Mol. Phys. 34, 361.
Schwartz, R.W., Banerjee, A.K., Sen, A.C., Chowdhury, M., 1980. J. Chem. Soc., Faraday Trans. 76, 620.
Scrivener, J.G., Shillady, D.S., Vallarino, L.M., 1985. Abst. Pap. Am. Chem. Soc. 189, 262.
Stavola, M., Isganitis, L., Sceats, M.G., 1981. J. Chem. Phys. 74, 4228.
Stephens, P.J., 1968. Chem. Phys. Lett. 2, 241.
Stephens, P.J., 1970. J. Chem. Phys. 52, 3489.
Stephens, P.J., 1974. Ann. Rev. Phys. Chem. 25, 201.
Stephens, P.J., 1976. Adv. Chem. Phys. 35, 197.
Stephens, P.J., 1977. Electron. State Inorg. Compd. 20, 141.
Stephens, P.J., 1987. J. Phys. Chem. 91, 1712.
Stephens, P.J., 1991. Chem. Phys. Lett. 180, 472.
Stephens, P.J., Mowery, R.L., Schatz, P.N., 1971. J. Chem. Phys. 55, 224.
Strek, W., Sztucki, J., 1991. Eur. J. Solid State Inorg. Chem. 28, 195.
Thorne, J., 1977. Proc. Soc. Photo-Optical Instrum. Eng. Optical Polarimetry 112, 120.
Tsaryuk, V., Zolin, V., Puntus, L.N., Savchenko, V., Legendziewicz, J., Sokolnicki, J., Szostak, R., 2000. J. Alloys Compd. 300, 184.
Voss, F.W., Nevald, R., Laursen, I., Amberger, H.D., 1983. J. Less-Common Met. 94, 233.
Weber, M.J., 1968. Phys. Rev. 171, 283.
Wybourne, B.G., 1965. Spectroscopic Properties of the Rare Earths. John Wiley & Sons, New York.
Zakharov, V.K., Kovaleva, I.V., Kolobkov, V.P., Nikolaev, L.F., 1977. Opt. Spectrosc. (Engl. Transl.) 42, 532.
Zhou, X., Reid, M.F., Faucher, M.D., Tanner, P.A., 2006. J. Phys. Chem. B 110, 14939.

This page intentionally left blank

CHAPTER **245**

Cluster Compounds of Rare-Earth Elements

Z. Zheng

Contents

Department of Chemistry, University of Arizona, Tucson, Arizona 85721, USA

Handbook on the Physics and Chemistry of Rare Earths, Volume 40
ISSN 0168-1273, DOI: 10.1016/S0168-1273(10)40005-7

List of Symbols and Acronyms

2D	two-dimensional
3D	three-dimensional
AA	α-amino acid
AAA	allylacetoacetate
Acac	acetylacetonate
AcO	acetate
Ala	alanine
Ap	(2,6-diisopropylphenyl)[6-(2,4,6-triisopropylphenyl) pyridin-2-yl]aminate
Ar	argon
Ar′	$2,6\text{-}C_6H_3Pr^i_2$
BA	benzoylacetonate
BDC	1,2-benzenedicarboxylate
Bu^t	ter-butyl
calix[7]	*p*-Bu^t-calix[7]arene-4H
calix[9]	*p*-Bu^t-calix[9]arene-6H
CB[6]	cucurbit[6]uryl
CBC	cross-bridged cyclam
COT	1,4-bis(trimethylsilyl)cyclooctatetraenyl
Cp	cyclopentadienyl
Cp*	pentamethyl cyclopentadienyl
Cp′	tetramethyltrimethylsilo cyclopebtadienyl
Cp*′	tetramethyl(*n*-propyl) cyclopentadienyl or $C_5Me_4Pr^n$
Cp**	tetra(*iso*propyl) cyclopentadienyl or $C_5H(Pr^i)_4$
Cp^t	ter-butyl cyclopentadienyl or $C_5H_4Bu^t$
DBM	dibenzoylmethanide
DME	1,2-dimethoxyethane
DMSO	dimethyl sulfoxide
EDTA	ethylenediaminetetraacetate
en	1,2-diaminoethane (ethylenediamine)
Et	CH_3CH_2
ETA	4,4,4-trifluoroacetoacetate
FcacacPh	benzoyl(ferrocenoyl)methanide
H_2CBC	cross-bridged cyclam
H_2**L5**	*N*,*N*′-bis(5-bromo-3-methoxysalicylidene)phenylene-1,2-diamine

H_3**L6**	(o-$HOC_6H_4CHNNCH_2)_2CHOH$
H_4**L1**	1,4,7,10-tetrakis(2-hydroxyethyl)-1,4,7,10-tetraazacyclododecane
H_4SO_2calix[4]	p-Bu^t-sulfonylcalix[4]arene
HAsp	Aspartic acid
hfpd	hexafluoropentanedione
HGlu	glutamic acid
H**L2**	2,6-diformyl-4-methylphenol
H**L3**	5-bromo-3-methoxysalicylaldehyde
Hmmp	1-methoxy-2-methylpropan-2-ol
$HOArBu^t_2$	3,5-di(ter-butyl)phenol
$HOArMe_2$	2,6-dimethylphenol
$HOArPr^i_2$	2,6-diisopropylphenol
hpp	1,3,4,6,7,8-hexahydro-2H-pyrimido[1,2-a] pyrimidinate
HTyr	tyrosine
HVan	2-hydroxy-3-methoxybenzaldehyde
IDA	iminodiacetate
IN	isonicotinate
L4	hemiacetal derived from H**L3**
L7	$(+/-)$-5, 6-pinene-2, 2′-bipyridine-13-CO_2^-
Me	CH_3
MeCp	methyl cyclopentadienyl
NDA	1,4-naphthalenedicarboxylate
N-MeIm	N-methylimidazole
OR or RO	generic alkoxo or aryloxo group
OTf	trifluoromethanesulfonate
Ph	C_6H_5
Phgly	phenylglyoxylate
Pr^i	isopropyl
R	rare earth
R′	$C_2H_4OPr^i$
R″	$CH(SiMe_3)_2$
R‴	$N(SiMe_3)_2$
ROP	ring-opening polymerization
SB	bis-5,5′-(2,2-dimethyl-1,3-propanediyldiimino)-2,2-dimethyl-4-hexen-3-one
Ser	serine
SMM	single-molecule magnet
SP–SP	C–C bonded 3, 5-$^{4t}_{Bu}$salophen dimer
thd	2,2,6,6-tetramethylheptane-3,5-dionate
THF	tetrahydrofuran
tpen	N,N,N',N'-tetrakis(2-pyridylmethyl) ethylenediamine

1. INTRODUCTION

According to Cotton's (1966) definition, a metal cluster is ''a finite group of metal atoms that are held together mainly or at least to a significant extent, by bonds directly between metal atoms, even though some nonmetal atoms may also be intimately associated with the cluster.'' Closed polyhedral clusters of varying composition and geometry have fascinated inorganic chemists since the 1950s. Their topologies, chemistries, and physical properties have been an endless source of fundamental research, and such studies have been instrumental in our understanding of the very nature of the chemical bond—advancing the concept of electron delocalization, creating electron counting rules, and establishing the notion of multicenter bonding.

The emphasis of cluster research has traditionally been on that of transition metal elements (Prokopuk and Shriver, 1998). However, a large number of polynuclear lanthanide complexes featuring cluster-like, polyhedral core structures have been quietly emerging in the past two decades, often as unexpected products from reactions that are designed for other synthetic targets. The number of such unintended clusters is still increasing, and a number of prevalent core motifs have been identified. These findings provide the fundamental impetus for the search for and development of reliable synthetic approaches to these structurally novel and potentially useful lanthanide-containing substances. With such efforts, some general synthetic methodologies have been developed, with which many polynuclear lanthanide complexes, even some with core structures never before contemplated, have been obtained. In fact, the cluster chemistry of the lanthanide elements has become a distinct line of research within the general context of lanthanide coordination, organometallic, and solid-state chemistry. The physical properties toward applications such as contrast-enhancing agents (Yu and Watson, 1999) for biomedical imaging have been carried out, while their chemical reactivity pertinent to their applications as catalysts for novel chemical transformations, precursors for advanced materials (Hubert-Pfalzgraf, 2003), and synthetic nucleases (Franklin, 2001) have also been studied carefully and earnestly. Performances distinctly different from or much improved over those with the uses of mononuclear or noncluster polynuclear lanthanide complexes have been observed.

Before continuing, some words of clarification are due. Although there exist a limited number of polynuclear lanthanide complexes whose component metal ions are shown to participate in intramolecular energy transfer (Thompson et al., 2001), for most such complexes, there is no apparent metal–metal bonding, nor are there any significant interactions mediated by the commonly observed bridging ligands, a consequence of

the unique f-electron configuration of these elements. One rare exception is the recently reported dinuclear Tb_2 unit that is confined and stabilized within the interior of a $C_{79}N$ fullerene cage (Zuo et al., 2008). The terbium atoms share a single electron, forming the longest metal–metal bond at a distance of more than 3.9 Å. Therefore, if Cotton's original definition is strictly followed, few of the so-called ''lanthanide clusters,'' despite being structurally and chemically well defined, may be qualified as ''clusters.'' The reference of such species as ''clusters'' is thus primarily from a structural perspective.

Except for a limited number of cluster compounds derived from simple inorganic salts of the lanthanide elements, a majority of lanthanide clusters contain organic ligands of certain type(s). They limit the degree of aggregation of the mononuclear units, and are understandably critical in determining the cluster nuclearity. In some cases, the organic ligands are solely responsible for cluster formation, for example, in cluster compounds of simple lanthanide alkoxides. Frequently, however, small-unit bridging ligands such as oxo, hydroxo, hydrido, halo, and chalcogenido groups are primarily responsible for cluster core building, while the organic ligands provide either mere steric control or additional bridging interactions between the component metal atoms or both.

1.1 Organization of materials

The variety of the cluster core structures is truly amazing. Although a number of interesting and potentially useful applications have been demonstrated or envisioned, it is probably a fair statement that the chemistry of lanthanide-containing clusters is presently dominated by their synthetic and structural aspects. Accordingly, the discussions presented herein will be organized based on the methodologies for the synthesis of the clusters and their distinct compositional and structural features.

Specifically, lanthanide clusters can be categorized as those assembled under conditions typically employed in organometallic synthesis and those obtained by deliberate hydrolysis. Clusters of the first type are assembled, either unexpectedly or purposely, by aggregation of recognizable mononuclear units via multidentate organic bridging/chelating ligands. The formation of such clusters is generally driven by the tendency of the bulky lanthanide ions to fulfill the high-coordination number requirement, particularly when the steric hindrance provided by the organic ligands is inadequate to prevent aggregation of the mononuclear units. In addition to the organic ligands, small-unit O- (oxo, hydroxo, aqua, alkoxo), N- (nitride, amido, imido), H- (hydrido), halogen-, and chalcogen-based bridging ligands are also frequently found in the cluster core structure. These unexpected entities are either due to adventitious

hydrolysis or degradation of solvent molecules under the reaction conditions. Their formation is generally reproducible if the reaction conditions are carefully controlled. In stark contrast, clusters in the second category are obtained by deliberate hydrolysis of the lanthanide ions, generally supported by hydrolysis-limiting organic ligands. Under such conditions, the presence of bridging oxo and hydroxo ligands are expected. This synthetic approach was stimulated by the observations of many oxo and/or hydroxo group-containing species isolated unexpectedly and the number of cluster motifs repeatedly shown in these species; in principle, one should be able to synthesize them by a more rational hydrolytic approach instead of being the helpless ''victim'' of adventitious, unpredictable hydrolysis. Distinct synthetic procedures notwithstanding, one should not be surprised by the fact that a number of cluster motifs are common to many species in these two different categories as adventitious hydrolysis occurs in both organometallic synthesis and lanthanide coordination chemistry conducted in aqueous solutions.

For the clusters obtained under ''nonhydrolytic'' conditions, the discussion will be presented according to the type of cluster core-building ligands. Five different families of clusters prepared under conditions that are typical of organometallic synthesis will be discussed, namely clusters of lanthanide alkoxides/aryloxides/macrocyclic polyaryloxides, clusters of nonalkoxide/nonhydride type, lanthanide hydride clusters, lanthanide chalcogenolate and chalcogenide clusters, and lanthanide clusters featuring dinitrogen-derived ligands. In addition, some miscellaneous lanthanide clusters via nonhydrolytic assembly will also be briefly discussed.

For lanthanide oxide/hydroxide clusters by hydrolytic approach, the discussion will be organized according to the types of hydrolysis-limiting ligands. These include amino acids, polyaminopolycarboxylates, functionalized carboxylates, β-diketonates, and other less commonly used ancillary ligands such as polyoxometalates and cyclic polyaryloxides. In addition, clusters produced by direct hydrolysis of certain lanthanide salts will also be included. Wherever possible and appropriate, discussions of the applications, realized or envisioned, of these unique substances will be presented. This contribution concludes with a brief summary of the current research status of this unique class of lanthanide-containing species and an account of the challenging issues ahead, followed by some personal perspectives as toward what directions this exciting research may be heading.

1.2 Scope of the review

Not all the subclasses of lanthanide clusters have been developed equally. For some systems, reviews with comprehensive coverage of the subject are already available (Arndt and Okuda, 2002; Boyle and Ottley, 2008;

Edelmann et al., 2002; Ephritikhine, 1997; Hou, 2003; Hou et al., 2007; Hubert-Pfalzgraf, 2003; Li et al., 2006a), while for others, systematic discussions of their chemistry have yet to be presented. To keep this chapter within reasonable length, only brief summaries will be provided for materials that have already been collected in previous reviews or monographs; detailed discussions will only be devoted to the work that has not been extensively covered by previous literature.

Due to the large number of polynuclear lanthanide-containing clusters, we have also elected to limit the scope of our presentation according to the following guidelines, to achieve a more focused discussion. However, many of the species not included herein are certainly of inherent interest, both structurally and in terms of their chemistry:

(1) Only crystallographically established lanthanide clusters featuring well-defined core structures will be presented. This limit is set as such because of the following considerations: (1) the solid-state structures of lanthanide compounds are generally different from those observed in solution due to the dynamic behavior that arises from the primarily ionic bonding character of these unique elements and (2) structural elucidations using solution techniques are often complicated by the paramagnetic nature of the lanthanide ions.
(2) Most heterometallic cluster species containing both lanthanide and transition metal elements in the cluster core structure will not be included. Such cluster complexes are of tremendous fundamental and practical interests, and interested readers would be better served with review articles dedicated just to this particular family of lanthanide-containing materials (Benelli and Gatteschi, 2002). However, heterometallic clusters containing recognizable cluster motifs composed solely of lanthanide elements will be discussed.
(3) A large number of dinuclear lanthanide complexes have been reported in the literature. No specific efforts will be made for their general discussion. However, where appropriate, such species are included to provide necessary context for the discussion of the formal assembly of higher-nuclearity clusters from these well-defined, recognizable building blocks.

2. CLUSTERS OBTAINED UNDER NONHYDROLYTIC CONDITIONS

The chemistry of organolanthanides has been dominated by complexes with metallocene and half-sandwich ligand systems because of the rigidity, steric bulk, thermal and chemical stability of the cyclopentadienyl ligands. However, driven by the desire to explore novel structural

patterns and reactivity of organolanthanide compounds, recent years have witnessed the increasing use of nonmetallocene ligand scaffolds.

Regardless of the ligand systems utilized, structurally well-defined mononuclear lanthanide complexes are always desired for unambiguous characterization and study of their reactivity. However, there is a strong tendency for such complexes to form polynuclear species featuring recognizable and well-defined mononuclear ''building blocks.'' This is largely due to the large size of the lanthanide ions and the primarily ionic lanthanide–ligand bonding interactions. The requirement for high-coordination numbers and the facility to accommodate necessary structural reorganization are conducive to cluster formation.

For many lanthanide clusters obtained under conditions typical of organometallic synthesis two general observations can be made. First, saturation of lanthanide coordination is frequently fulfilled by the presence of heteroatom-containing bridging ligands, with oxo, hydroxo, hydrido, chalcogenido, and halo ligands being most frequently observed. Other O/N-containing ligands including those that are not as commonly used, for example, tetramethylaluminato and methylidene groups, have also been utilized for cluster formation. The second observation is the common coordination by solvent molecules. Solvent molecules serve mainly to help achieve coordination saturation in mononuclear complexes. Upon desolvation, some metal coordination sites are freed up, driving the aggregation of the coordinatively unsaturated units to become a cluster. In many cases, the solvent molecules, generally O-containing, are believed to be the source of unexpected cluster core-building oxo group(s).

2.1 Clusters of lanthanide alkoxides, aryloxides, and macrocyclic polyaryloxides

Lanthanide alkoxide complexes are arguably one of the most extensively studied classes of lanthanide-containing compounds. Frequently, polynuclear complexes of the cluster type are obtained from the reactions aiming at the synthesis of mononuclear complexes. It is fair to state that the production of such clusters is more due to serendipity than by design, as is the case of most lanthanide-containing cluster compounds. The formation of polynuclear cluster species is a general reflection of the propensity of the large metal ions to maximize their coordination number and the capacity of the alkoxide ligands to bridge in order to satisfy the ligands' steric and electrical requirement. Not surprisingly, the identity of the cluster compounds depends on both the size of the lanthanide ions and the nature of the alkoxide ligands. In addition to the interesting and diverse molecular structures observed, the research directed at the synthesis of lanthanide alkoxides is driven by the uses of such species

as precursors for advanced materials and their potential of promoting useful chemical transformations. Such efforts have produced numerous alkoxide clusters of various compositions (simple alkoxide or aryloxide ligands vs sterically crowded and/or multidentate alkoxides or aryloxides). These clusters exhibit a great variety of structural patterns and nuclearity. From the extensive research that has been accomplished, a number of general conclusions can be made:

(1) Formation of cluster structures is a general phenomenon in lanthanide alkoxide chemistry unless sterically crowded ligands are utilized. When small and sterically unhindering alkoxides are used, individual **R**–OR (**R** = rare earths; RO or OR = alkoxo or aryloxo) units are prone to aggregation via bridging interactions of the ligands. Such cluster-forming bridging interactions also fulfill the desire of the ligand to achieve steric and electronic ''saturation.''
(2) Presence of small nonalkoxide ligands such as oxo, hydroxo, hydrido, halo, and chalcogenido groups is commonly observed in lanthanide alkoxide clusters. These small anionic species are important in facilitating the formation and maintaining the structural integrity of the cluster structures.
(3) Sterically crowded multidentate, macrocyclic aryloxide ligands tend to engender different chemistry as a result of the constrained and more rigid disposition of their aryloxido moieties in the macrocyclic structure. The linking group between the individual aryloxide units within the macrocycle may also participate in synergetic metal coordination.

Reviews of the coordination chemistry of this particular family of lanthanide-containing compounds are available, but they are generally limited to the chemistry of the simplest forms of alkoxide and aryloxide ligands (Boyle and Ottley, 2008). Interested readers are referred to such reviews for more detailed discussion. With just a brief summary of the key observations and main conclusions regarding these ''simple'' alkoxides, this contribution will be focusing on the discussion of alkoxide clusters that appeared in the literature since the most recent reviews, those featuring small-unit, cluster core-building ligands, and cluster complexes of sterically demanding macrocyclic polyaryloxides.

2.1.1 Clusters of lanthanide alkoxides

Simple lanthanide alkoxide clusters contain only alkoxide ligands and possibly additional organic ancillary ligands. The core structures of these clusters have been thoroughly discussed in a recent review (Boyle and Ottley, 2008). The common core structures are collected in Figure 1. The nuclearity of the various homoleptic ''$\mathbf{R}(OR)_3$'' complexes ranges from mono- to decanuclear. The geometries around these metals have been

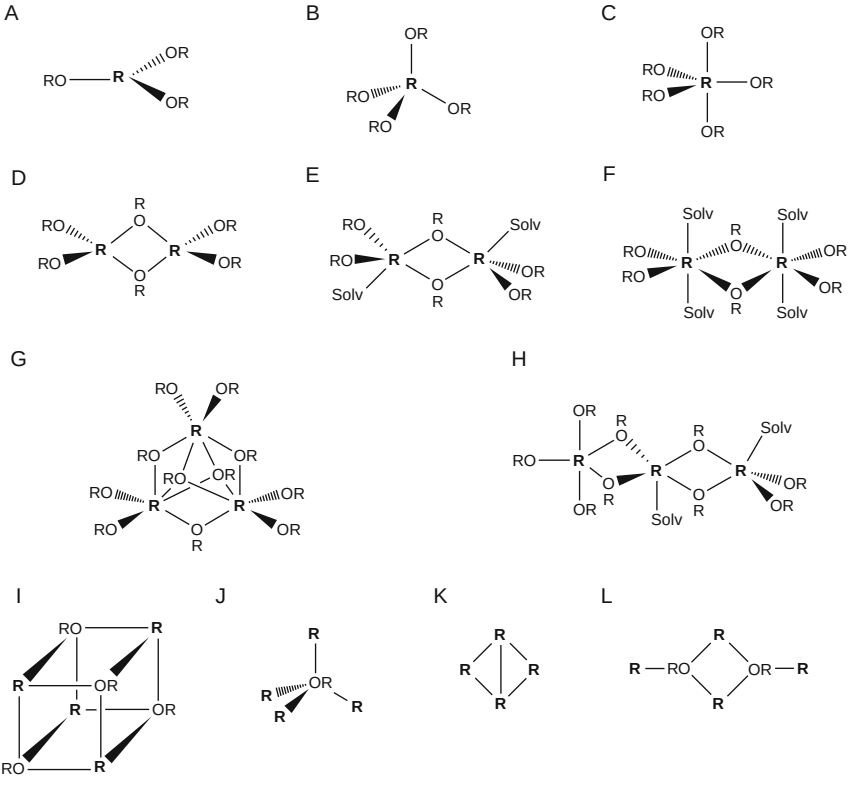

FIGURE 1 Commonly observed central core structures of **R**(OR)$_x$ clusters (redrawn after Boyle and Ottley, 2008).

found to encompass simple trigonal planar, tetrahedral, trigonal bipyramidal, square pyramidal, octahedral, and higher-order coordination geometries. In these motifs, the alkoxide ligands display a variety of coordination modes, from terminal monodentate [**R**(OR)], bridging [**R**(μ-OR)**R**], triply bridging [**R**$_3$(μ_3-OR)], and more rarely quadruply bridging [**R**$_4$(μ_4-OR)] interactions. The different nuclearity of the resulting clusters reflects the degree of steric and electronic saturation required at each metal center.

The second type of cluster compounds of the lanthanide alkoxides features one or several small-unit, inorganic ligands including oxo, hydroxo, halo, and other groups as part of the cluster core structure. Frequently, a combination of such ligands is found in the same cluster species. In a sense, this ''central spherical charge density'' drives the assembly of the polynuclear complexes; without their participation, no clusters are formed or species of completely different structures result.

Cluster-type oligomeric lanthanide oxoalkoxides are common, although their formation is generally unpredictable in terms of product nuclearity and/or the arrangement of the ancillary ligands around the cluster core. The ancillary ligands play important roles, either serving to control the degree of hydrolysis of the metal center, and therefore the degree of condensation and nuclearity of the final cluster species or modulating the sterics around the metal center to control the degree of aggregation, or both. Generally speaking, the physicochemical properties of oxoalkoxides (solubility, the behavior in solutions, volatility, etc.) differ considerably from the properties of the corresponding alkoxides (Caulton and Hubert-Pfalzgraf, 1990; Turova, 2004). They have been used successfully as precursors of oxide materials produced by sol-gel technology.

The hydrolysis of alkoxide ligands is certainly one of the possible routes to the production of oxo and hydroxo ligands. In fact, these steps underlie the all-important sol-gel processes. However, the oxo and hydroxo groups may also be due to solvent degradation under the reaction conditions as O-containing solvents such as tetrahydrofuran (THF), ether, or dimethoxymethane are typically utilized in the preparation of lanthanide alkoxides. In many cases, however, ether byproducts are isolated, suggesting that the alkoxide ligands themselves are the source of the oxo group. Obtained by nonhydrolytic condensation, these oxoalkoxides display reactivity patterns and properties—high solubility, low volatility—different from those of alkoxides (Hubert-Pfalzgraf, 2003).

The reaction of $GdCl_3$ with $KOBu^t$ in THF afforded the tetranuclear cluster $[Na_2(OBu^tGd)_4(\mu_3\text{-}OBu^t)_8(\mu_6\text{-}O)]$ (Schumann et al., 1990). Its structure consists of an oxygen-centered octahedron build-up by two Na and four Gd atoms, connected by eight face-capping and four terminal OBu^t groups (Figure 2, left). Using sterically less hindered methoxide, a cyclopentadienyl coligand was necessary, and the reaction led to the isolation of a pentanuclear cluster $[(Cp)_5\mathbf{R}_5(\mu_5\text{-}O)(\mu_3\text{-}OMe)_4(\mu\text{-}OMe)_4]$

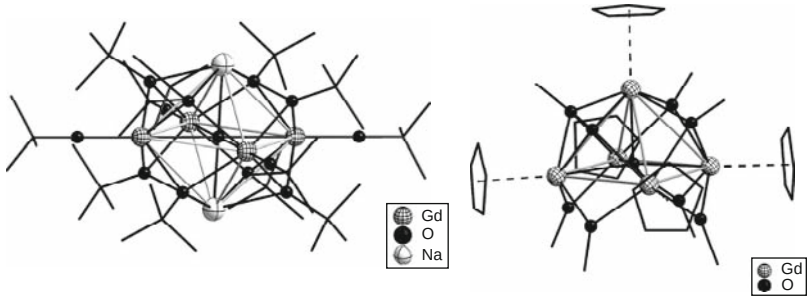

FIGURE 2 Crystal structures of $[Na_2(OBu^tGd)_4(\mu_3\text{-}OBu^t)_8(\mu_6\text{-}O)]$ (left) and $[(Cp)_5Gd_5(\mu_5\text{-}O)(\mu_3\text{-}OMe)_4(\mu\text{-}OMe)_4]$ (right) (redrawn after Schumann et al., 1990).

($\mathbf{R} = $ Yb, Gd). X-ray structure determination shows a square pyramidal assembly of Gd atoms with an oxygen atom in the center of the base and eight bridging methoxide groups, four of which triply bridging and face-capping and the remaining four each bridging two adjacent metal atoms within the basal plane. In addition, each of the metal atoms is coordinated to a Cp ligand (Figure 2, right).

The reaction between Dy chips or $Dy_5O(OPr^i)_{13}$ and $HOPr^i$ afforded an octanuclear cluster $[Dy_4(\mu_3,\eta^2\text{-}OR')_3(\mu,\eta^2\text{-}OR')_2(\eta^1\text{-}OR')_4(\mu,\eta^1\text{-}OR')_3]_2$ with $R' = C_2H_4OPr^i$ (Le Bris et al., 2006). Isostructural with its Y_8 derivative (Hubert-Pfalzgraf et al., 2004), the cluster can be described as the assembly of two tetranuclear units by bridging monodentate η^1-alkoxide ligands (Figure 3).

The cluster complex $[La_3(\mu_3,\eta^2\text{-mmp})_2(\mu_2,\eta^2\text{-mmp})_3(mmp)_4]$ (Figure 4, top) has been prepared by the reaction of $[La\{N(SiMe_3)_2\}_3]$ ($R''' = N(SiMe_3)_2$) with Hmmp (Hmmp = $HOCMe_2CH_2$-OMe, 1-methoxy-2-methylpropan-2-ol) (Aspinall et al., 2007). The crystal structure (Figure 4) shows that three La atoms are linked by face- and edge-bridging mmp ligands, so that each La atom is bonded to the alkoxide groups of two face-bridging and two edge-bridging ligands.

The heterometallic cluster $[NaLa_3(\mu_3\text{-OH})(\mu_3,\eta^2\text{-mmp})_2(\mu_2,\eta^2\text{-mmp})_4(mmp)_3]_4$ (Figure 4, bottom) was isolated from the reaction of $[La(NO_3)_3(tetraglyme)]$ with Na(mmp). The three La atoms of this cluster are linked by face- and edge-bridging and ''dangling'' mmp ligands as well as by a face-bridging μ_3-OH which is unsymmetrically bound to the three La atoms.

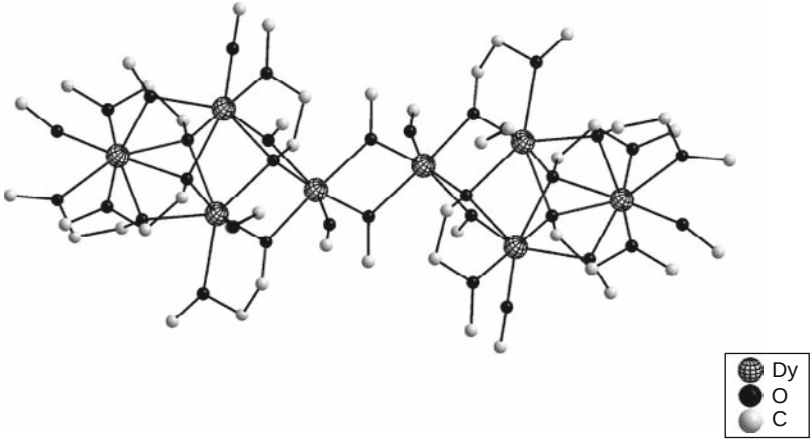

FIGURE 3 Crystal structure of $[Dy_4(\mu_3,\eta^2\text{-}OR')_3(\mu,\eta^2\text{-}OR')_2(\eta^1\text{-}OR')_4(\mu,\eta^1\text{-}OR')_3]_2$. For clarity, the OR′ groups displaying a η^1-coordination mode are limited to the Cα carbon atom (redrawn after Le Bris et al., 2006).

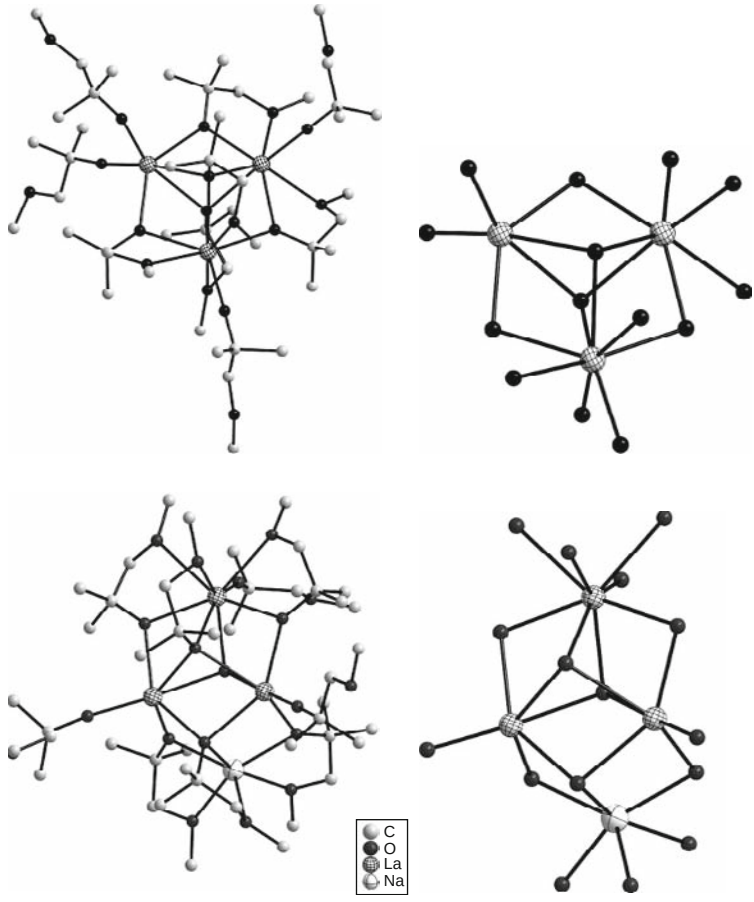

FIGURE 4 Crystal structures of $[La_3(\mu_3,\eta^2\text{-mmp})_2(\mu_2,\eta^2\text{-mmp})_3(mmp)_4]$ (upper left) and its core structure (upper right) and $[NaLa_3(\mu_3\text{-OH})(\mu_3,\eta^2\text{-mmp})_2(\mu_2,\eta^2\text{-mmp})_4(mmp)_3]_4$ (bottom left) and its cluster core structure (bottom right) (redrawn after Aspinall et al., 2007).

Using donor-functionalized alkoxy derivatives, a tetranuclear oxo–hydroxo cluster of net composition $Lu_4(O)(OH)(OR)_9$ was obtained unexpectedly (Anwander et al., 1997). The resulting Lu_4O_{15} ''core'' adopts a ''butterfly'' rather than a tetrahedral geometry (Figure 5). Other previously reported oxo-centered butterfly RE_4 units include $Ce_4(\mu_4\text{-O})(\mu_3\text{-OPr}^i)_2(\mu_2\text{-OPr}^i)_4(OPr^i)_7(HOPr^i)$ (Yunlu et al., 1991) and $[Y_4(\mu_3\text{-OBu}^t)_2(\mu\text{-OBu}^t)_4(\mu\text{-Cl})_2(OBu^t)_4Li_4(\mu\text{-OBu}^t)_2]_2$ (Evans et al., 1988a).

The cluster $[Cp_5Y_5(\mu_5\text{-O})(\mu_3\text{-OMe})_4(\mu\text{-OMe})_4]$ (Evans and Sollberger, 1986) is comprised of a square pyramid of yttrium atoms each of which is coordinated to one Cp group. Upon each triangular face of the square

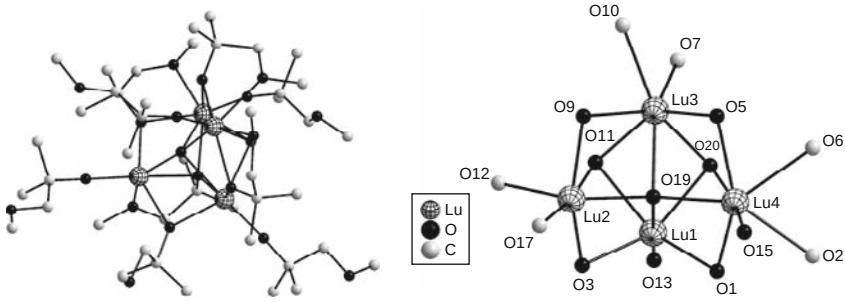

FIGURE 5 Crystal structure of $Lu_4(O)(OH)(OR)_9$ ($OR = OCMe_2CH_2OMe$) (left) with its butterfly-shaped Lu_4O_{15} core (right) (redrawn after Anwander et al., 1997).

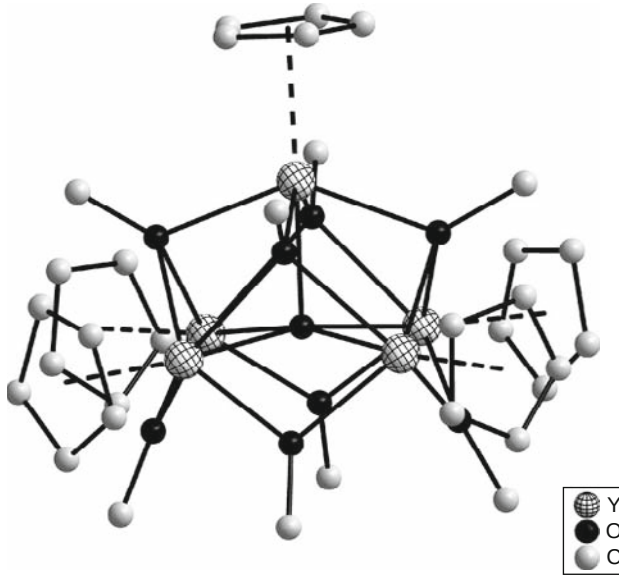

FIGURE 6 Crystal structure of $[Cp_5Y_5(\mu_5\text{-}O)(\mu_3\text{-}OMe)_4(\mu\text{-}OMe)_4]$ (redrawn after Evans and Sollberger, 1986).

pyramid is a triply bridging methoxide ligand and attached to each vertex of the square base is a doubly bridging methoxide group. An oxide ligand lies in the interior of the structure, interacting with five yttrium atoms; each metal atom has a formal coordination number of 10 (Figure 6).

Alkoxide ligands can also come in rather unusual form. A 12-membered cyclen-type macrocycle, 1,4,7,10-tetrakis(2-hydroxyethyl)-1,4,7,10-tetraazacyclododecane (H_4**L1**), has been found to support the

assembly of a tetranuclear cluster $[(La(H_2\mathbf{L1}))\{La(NO_3)_2(\mu_3\text{-}OH)\}_2(La(H\mathbf{L1}))](NO_3)$ and a pentanuclear cluster $[\{La(NO_3)_2\}_3(La(\mathbf{L1}))_2(\mu_5\text{-}OH)]$ (Thompson et al., 2003).

The crystal structure of the tetranuclear complex is assembled from one $[La(H_2\mathbf{L1})]^+$ and two $[La(NO_3)_2]^+$ cations, molecule $[La(H\mathbf{L1})]$, and one NO_3^- and two bridging $[\mu_3\text{-}OH]^-$ anions. The $[La(NO_3)_2]^+$ species are themselves bridged by the two $[\mu_3\text{-}OH]^-$ groups and the alkoxide site (Figure 7, left). The tetranuclear core forms a rare scoop-like motif (Figure 7, right) as opposed to other more frequently observed tetranuclear cluster core structures, such as distorted cubane, tetrahedron, butterfly, or square-shaped assemblies.

The pentanuclear cluster is built from two $[Nd(\mu_4\text{-}\mathbf{L1})]^-$ anions, three $[Nd(NO_3)_2]^+$ cations, and the $\mu_5\text{-}OH^-$ anion which ''glues'' the five cations together to form a square pyramidal C_{4v} arrangement of the Nd(III) ions (Figure 8).

The assembly of clusters is the result of a complex interplay of several factors. It is evident that deprotonation of the alkoxide pendant arms of the chelating ligand promotes the ability of alkoxide sites to form bridges to lanthanide ions. The nature of the product is dependent on the relative Lewis acidity of the lanthanide ions, the harder Lewis acids being more able to displace the hydroxyl protons from the protonated ligand.

In addition to the frequent incorporation of oxo and hydroxo groups into cluster core structures, halo ligands have also been found in many lanthanide alkoxide clusters. An early example is $[Nd_6(\mu_6\text{-}Cl)(\mu_3\text{-}OPr^i)_2(\mu\text{-}OPr^i)_9(OPr^i)_6]$ (Andersen et al., 1978), a hexanuclear cluster obtained from the reaction of $NdCl_3$ with $NaOPr^i$ in $HOPr^i$. The six neodymium

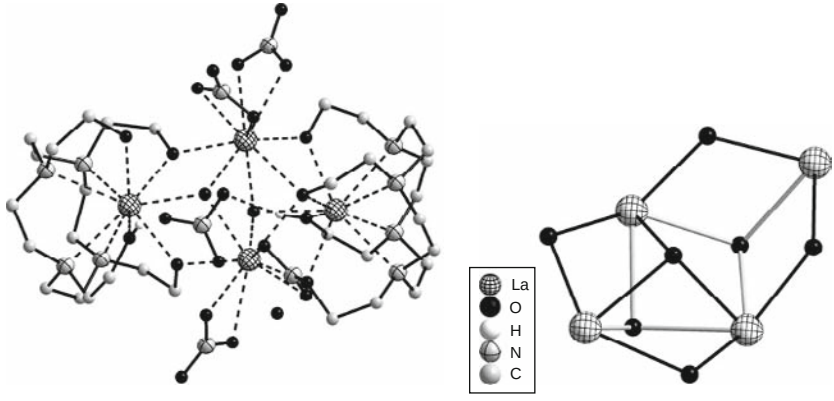

FIGURE 7 Crystal structure of $[(La(H_2\mathbf{L1})\{La(NO_3)_2(\mu_3\text{-}OH)\}_2(La(H\mathbf{L1}))](NO_3)$ (left) and its tetranuclear core containing two triply bridging hydroxo groups (right) (redrawn after Thompson et al., 2003).

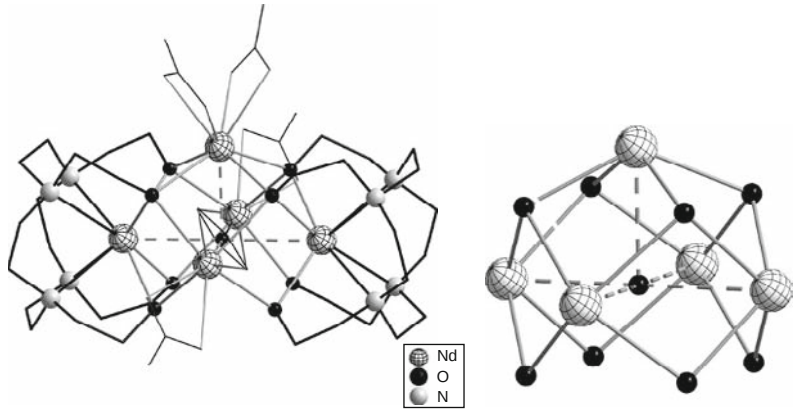

FIGURE 8 Crystal structure of [{Nd(NO_3)$_2$}$_3$(Nd(**L1**))$_2$(μ_5-OH)] (left) and its pentanuclear core containing a μ_5-hydroxo group (right) (redrawn after Thompson et al., 2003).

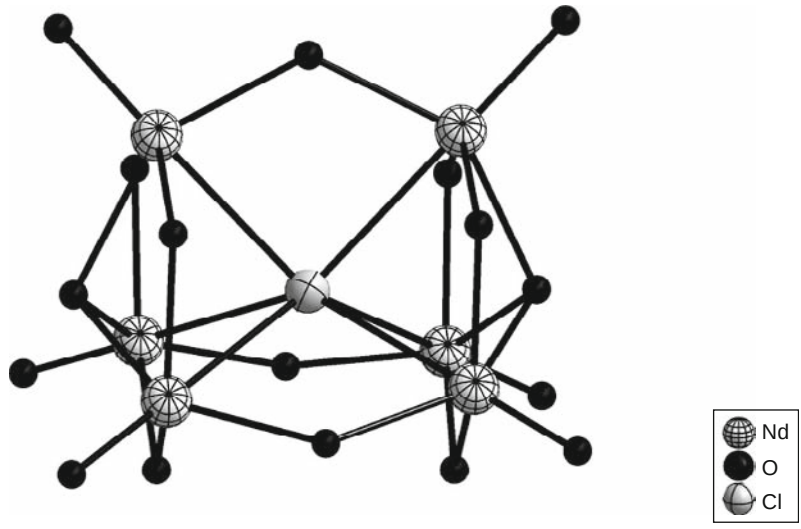

FIGURE 9 Crystal structure of Nd$_6$(μ_6-Cl)(μ_3-OPr^i)$_2$(μ-OPr^i)$_9$(OPr^i)$_6$] featuring an interstitial μ_6-Cl$^-$ ligand (redrawn after Andersen et al., 1978).

atoms form a trigonal prism centered about a μ_6-Cl$^-$ ion (Figure 9). There are a total of 17 OPr^i groups, six being terminally coordinated to the Nd atoms, nine being edge bridging, and two being capping for the trigonal faces of the prism.

A triyttrium cluster Y$_3$(μ_3-OBu^t)(μ_3-Cl)(μ-OBu^t)$_3$Cl(THF)$_2$ was obtained from the reaction of YCl_3 with NaO*t*Bu in THF (Evans and Sollberger,

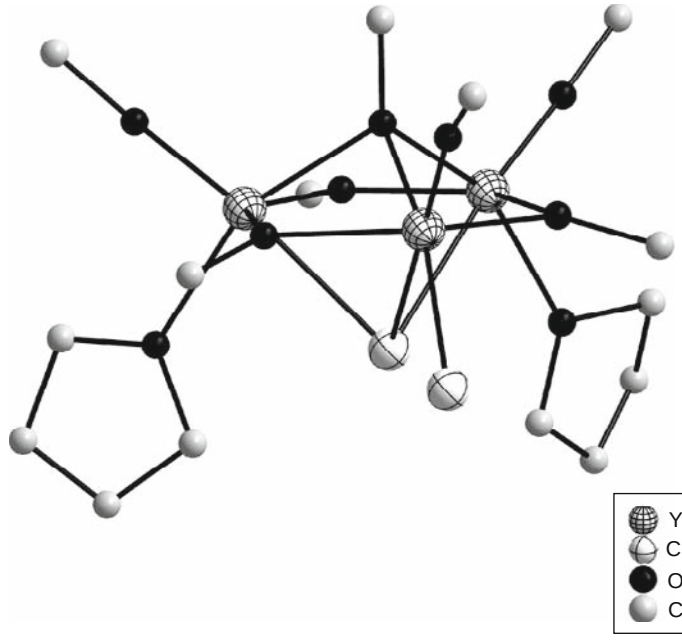

FIGURE 10 Crystal structure of $Y_3(\mu_3\text{-}OBu^t)(\mu_3\text{-}Cl)(\mu\text{-}OBu^t)_3Cl(THF)_2$ featuring a $\mu_3\text{-}Cl^-$ ligand opposite to a $\mu_3\text{-}OBu^t$ (redrawn after Evans and Sollberger, 1988).

1988). The yttrium atoms in this molecule form a triangle that has doubly bridging alkoxide groups along each edge, a μ_3-OBu^t group on one side of the Y_3 plane, and a μ_3-Cl ligand on the other side (Figure 10). One metal is coordinated to a terminal chloride ion and to a terminal alkoxide group. Each of the remaining metal atoms is coordinated to a terminal alkoxide group and a molecule of THF.

Partial desolvation of THF in toluene led to the complete conversion into a tetradecanuclear species formulated as $Y_{14}(OBu^t)_{28}Cl_{10}O_2(THF)_2$ comprised of four trimetallic units of $Y_3(\mu_3\text{-}OBu^t)(\mu_3\text{-}X)(\mu\text{-}Z)_3$ ($X = Cl$, O; $Z = Cl$, OBu^t). The core structure is similar to that of the trinuclear array described above. The four trimetallic subunits are connected by two μ-Cl^- ions, a μ_4-O ion and a $[(\mu\text{-}OBu^t)_2Y(\mu\text{-}Cl)]_2$ group to give the dimer $\{[Y_3(\mu_3\text{-}OBu^t)(\mu_3\text{-}Cl)(\mu\text{-}OBu^t)_3(OBu^t)_3(THF)_2]_2(\mu\text{-}Cl)[Y_3(\mu_3\text{-}OBu^t)(\mu\text{-}OBu^t)_2(\mu\text{-}Cl)(OBu^t)_2](\mu_4\text{-}O)[(\mu\text{-}OBu^t)_2Y(\mu\text{-}Cl)]\}_2$ (Figure 11).

Slightly changing the reaction conditions to a 1:2 molar ratio of YCl_3 and $LiOBu^t$ produced the dimer $[Y_4(\mu_3\text{-}OBu^t)(\mu\text{-}OBu^t)_4(OBu^t)_4(\mu_4\text{-}O)(\mu\text{-}Cl)_2Li_4(\mu\text{-}OBu^t)_2]_2$, in which the Y_4 core has a butterfly arrangement about a μ_4-O group (Figure 12). Interestingly, by replacing YCl_3 for $LaCl_3$ under otherwise identical conditions, a different trinuclear cluster

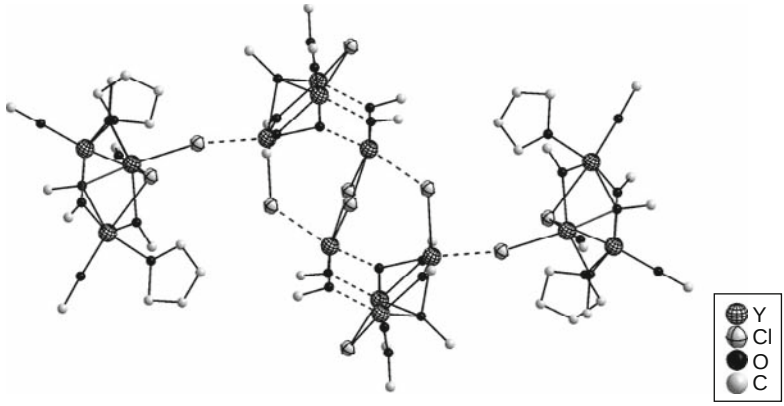

FIGURE 11 Crystal structure of $Y_{14}(OBu^t)_{28}Cl_{10}O_2(THF)_2$ whose four trimetallic subunits are connected by two μ-Cl^- ions, a μ_4-O ion, and a $[(\mu\text{-}OBu^t)_2Y(\mu\text{-}Cl)]_2$ group (redrawn after Evans and Sollberger, 1988).

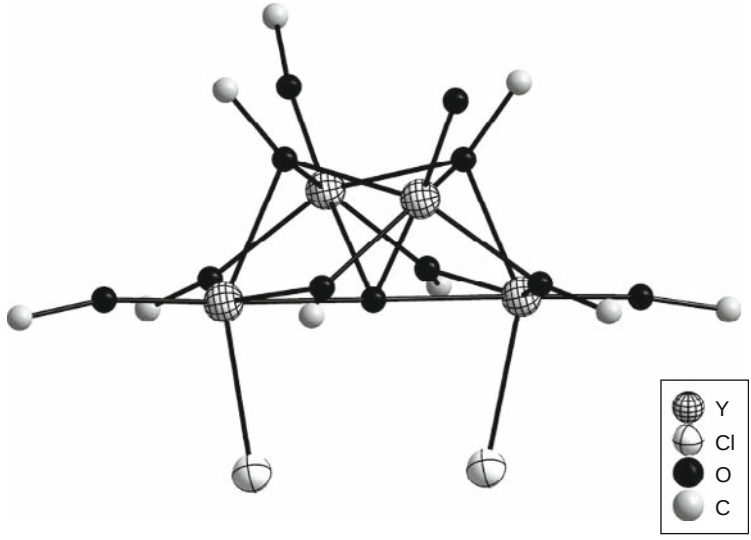

FIGURE 12 Core structure of the tetranuclear cluster $[Y_4(\mu_3\text{-}OBu^t)(\mu\text{-}OBu^t)_4(OBu^t)_4(\mu_4\text{-}O)(\mu\text{-}Cl)_2Li_4(\mu\text{-}OBu^t)_2]_2$. The four Y atoms are in a butterfly arrangement around the μ_4-O group (redrawn after Evans and Sollberger, 1988).

$La_3(\mu_3\text{-}OBu^t)_2(\mu\text{-}OBu^t)(OBu^t)_4(THF)_2$ was obtained wherein a triply bridging OBu^t group replaces the μ_3-Cl ligand in the Y_3 species. These observations clearly indicate the sensitive nature of the reactions.

2.1.2 Clusters of lanthanide aryloxides

Besides the use of alkoxide ligands described above, many aryloxides have also been used to prepare organolanthanide compounds, often affording polynuclear species. Among the attractive features of these ligands is the fact that steric bulk can be manipulated through the substituents on the aromatic ring without significantly altering the electronic structure of the ligand and/or the coordinating ability of the O atom.

Direct reactions of elemental lanthanoids and $HOArBu^t_2$ under high-temperature conditions followed by crystallization from THF or hexane afforded hydrocarbon-soluble, polymetallic, lanthanoid aryloxide clusters $[Nd_3(OArBu^t_2)_9(THF)_4]\cdot 4THF$, $[La_4(OArBu^t_2)_{12}(OH_2)]$, and $[Nd_3(OArBu^t_2)_9(HOArBu^t_2)_2(THF)]\cdot HOArBu^t_2$ ($HOArBu^t_2 = 3,5\text{-}Bu^t_2C_6H_3OH$) (Deacon et al., 2004). The structure of $[La_4(OArBu^t_2)_{12}(OH_2)]$ is remarkable: Four six-coordinate La ions arranged in a square plane with each vertex doubly bridged by two $OArBu^t_2$ ligands and a further terminal $OArBu^t_2$ ligand bound to each lanthanum (Figure 13, right). A single oxygen atom lies on an inversion center in the middle of the square. The square planar La_4O core of the structure is similar to that of $[K_5\{(CH_2{=}CHSiO_2)_8\}_2La_4(\mu_4\text{-}OH)]$ (Igonin et al., 1993), an unusual lanthanum vinylsiloxanolate complex in which the central oxygen was assigned as a hydroxide.

The reactions of Sm, Eu, and Yb metals with the potential bidentate ligand 2-methoxyphenol were studied (Carretas et al., 2004). The Eu and Yb aryloxides were synthesized by dissolution of the metals in liquid NH_3, whereas the Sm aryloxide was obtained by metal vapor synthesis. Recrystallization of $Yb(OC_6H_4OMe)_3$ from THF/pentane produced $[Yb_6(\mu_3\text{-}OH)_4(\mu\text{-}OC_6H_4\text{-}\eta\text{-}OMe)_{10}(OC_6H_4\text{-}\eta\text{-}OMe)_2(OC_6H_4OMe)_2]\cdot 4THF$ (Figure 14). The six ytterbium atoms form a nearly planar arrangement, being joined together by four triply bridging hydroxo ligands and

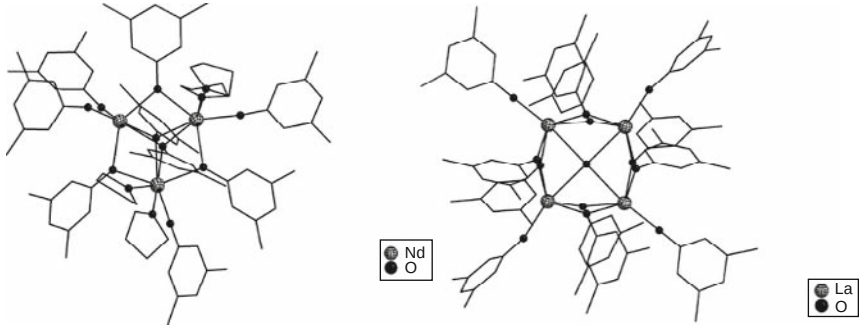

FIGURE 13 Crystal structures of $[Nd_3(OArBu^t_2)_9(THF)_4]\cdot 4THF$ (left) and $[La_4(OArBu^t_2)_{12}(OH_2)]$ (right) (redrawn after Deacon et al., 2004).

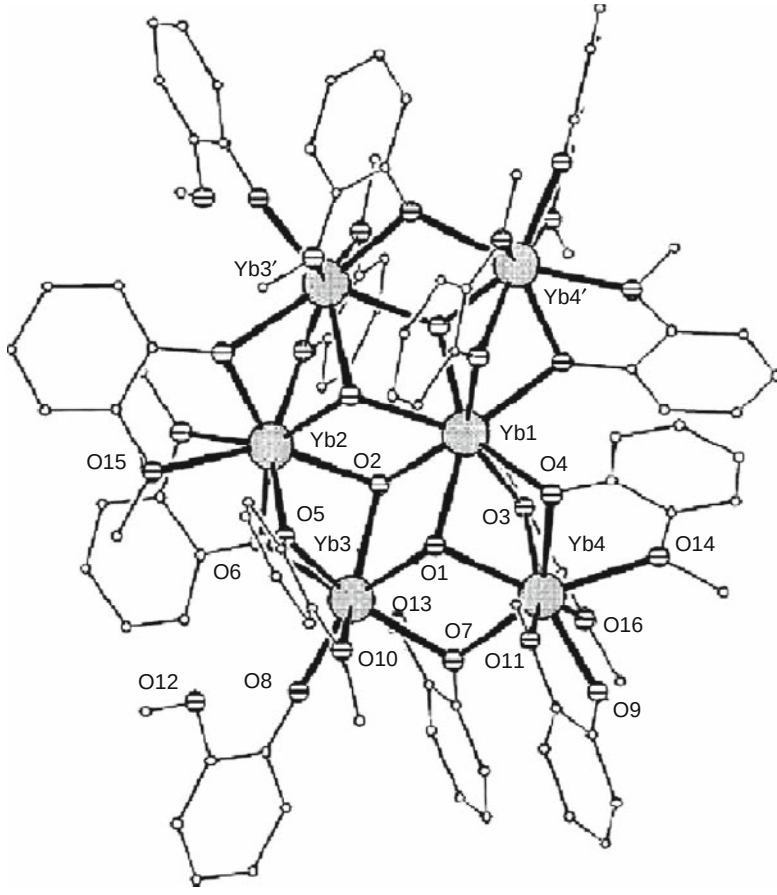

FIGURE 14 Crystal structure of $[Yb_6(\mu_3\text{-}OH)_4(\mu\text{-}OC_6H_4\text{-}\eta\text{-}OMe)_{10}(OC_6H_4\text{-}\eta\text{-}OMe)_2(OC_6H_4OMe)_2]$ (reproduced with permission from Carretas et al., 2004).

by 10 bridging-chelating aryloxides. All metal atoms are octacoordinate with a distorted-square antiprismatic geometry. Alternatively, the cluster core structure may be viewed as two $Yb_4(\mu_3\text{-}OH)_2$ units sharing two Yb atoms (Yb1 and Yb2); the tetranuclear motif is a common one, with the four metal atoms being coplanar and with two triangular faces capped by two triply bridging hydroxo groups, one above and one below the plane.

The reaction of Eu metal with isopropanol produces presumably a reactive species ''$Eu(OPr^i)_2$'' which, in turn, can be reacted with phenols, 2,6-dimethylphenol ($HOArMe_2$) and 2,6-diisopropylphenol ($HOArPr^i_2$), to afford the cluster species $H_x[Eu_8O_6(OArMe_2)_{12}(OPr^i)_8]$ and $H_5[Eu_5O_5(OArPr^i_2)_6(MeCN)_8]$ (MeCN = acetonitrile) (Evans et al., 2000). The octanuclear complex has a cubic arrangement of europium ions with

face-bridging μ_4-O donor atoms, edge-bridging μ-O(phenoxide/phenol) ligands, and terminal O(isopropoxide/2-propanol) ligands (Figure 15, upper left). The pentanuclear cluster is a mixed-valence species and has a square pyramidal europium core with four Eu(II) ions at the basal positions and one Eu(III) ion at the apex (Figure 15, upper right). By tweaking the reaction conditions, including temperature and solvent, a nonanuclear cluster formulated as $H_{18}\{[Eu_9O_8(OArMe_2)_{10}(THF)_7][Eu_9O_9(OArMe_2)_{10}(THF)_6]\}$ can be crystallized which contains two types of capped cubic arrangements of europium ions in the solid state (Figure 15, bottom).

Roesky and coworkers reported unusual tetradecanuclear clusters formulated as $[\mathbf{R}_{14}(o\text{-}O_2NC_6H_4O)_{24}(\mu_4\text{-}OH)_2(\mu_3\text{-}OH)_{16}]$ where $\mathbf{R} = $ Dy, Er, Tm, Yb (Figure 16; Burgstein and Roesky, 2000). The cluster core of

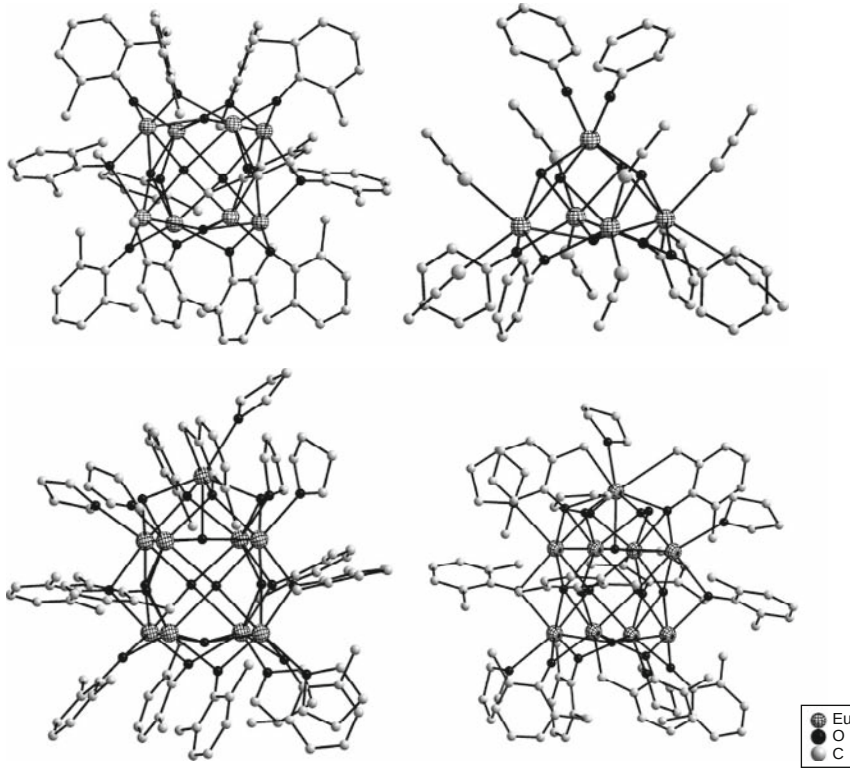

FIGURE 15 Crystal structures of $H_x[Eu_8O_6(OArMe_2)_{12}(O\mathit{i}Pr)_8]$, $H_5[Eu_5O_5(OArPr^i_2)_6(MeCN)_8]$, and the two different types of nonanuclear clusters in $H_{18}\{[Eu_9O_8(OArMe_2)_{10}(THF)_7][Eu_9O_9(OArMe_2)_{10}(THF)_6]\}$ (clockwise from upper left) (redrawn after Evans et al., 2000).

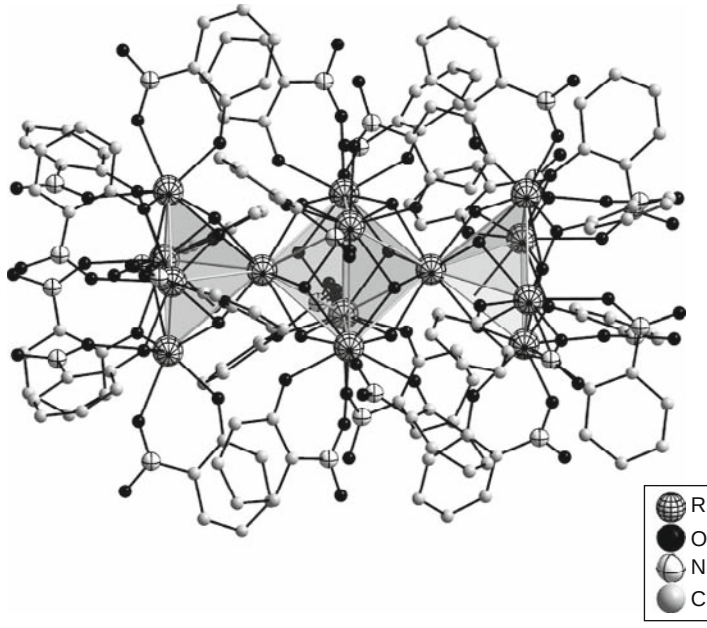

FIGURE 16 Crystal structure of the tetradecanuclear cluster $[\mathbf{R}_{14}(o\text{-}O_2NC_6H_4O)_{24}(\mu_4\text{-}OH)_2(\mu_3\text{-}OH)_{16}]$ formed with nitrophenolate ligands (redrawn after Burgstein and Roesky, 2000).

$[\mathbf{R}_{14}(\mu_4\text{-}OH)_2(\mu_3\text{-}OH)_{16}]$ is the same as those described below when diketonate ligands are used as the ancillary ligands. In fact, this tetradecanuclear cluster core motif is a common one which may be used to construct cluster assemblies of even more sophisticated structures.

Phenolates modified with other functional groups have also been utilized for the controlled hydrolytic assembly of lanthanide clusters (Costes et al., 2001; Tang et al., 2006). For example, using 2-hydroxy-3-methoxybenzaldehyde or *o*-vanillin (HVan)—a multidentate ligand that may be viewed as a modified phenolate upon deprotonation—cationic trinuclear Gd and Dy hydroxo clusters, $[(Van)_3\mathbf{R}_3(OH)_2X_2(OH_2)_4]^{2+}$ ($\mathbf{R} = Gd$, $X = NO_3^-$; $\mathbf{R} = Dy$, $X = Cl^-$) (Figure 17), have been obtained and their magnetic properties studied. The cluster core is a trigonal bipyramid with the two μ_3-OH groups occupying the axial positions. Using its phenoxo group, a Van^- (deprotonated *o*-vanillin) ligand bridges two metal atoms along each side of the triangle. Aldehyde and methoxy groups also coordinate to the metal atoms. Both clusters display complex magnetic behavior. The Gd cluster shows an antiferromagnetic behavior attributable to the three (Gd, Gd) pairs, while features typical of a single-molecule magnet (SMM) are observed for the thermally populated excited state of the Dy cluster.

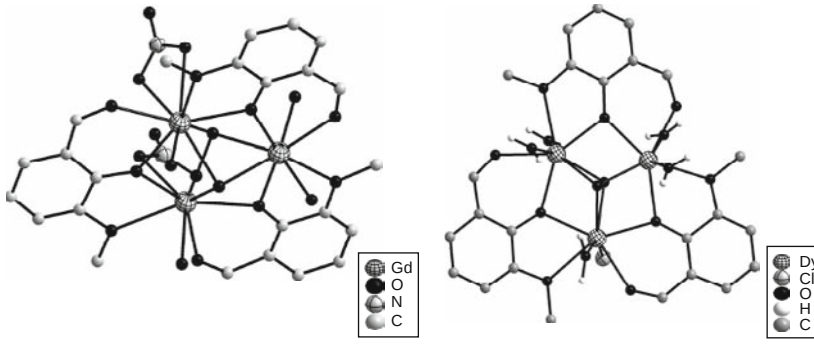

FIGURE 17 Crystal structures of the cationic clusters $[(Van)_3\mathbf{R}_3(OH)_2X_2(OH_2)_4]^{2+}$ (left: $\mathbf{R} = Gd$, $X = NO_3^-$; right: $\mathbf{R} = Dy$, $X = Cl^-$) with *o*-vanillin ligands (redrawn after Costes et al., 2001; Tang et al., 2006).

Condensation of HVan with 1,3-diaminopropan-2-ol affords aminophenol 1,3-bis(2-hydroxy-3-methoxybenzylamino)propan-2-ol. Upon deprotonation, this modified phenolate ligand can be used to support the synthesis of lanthanide hydroxide clusters. Two μ_4-oxo-centered tetranuclear lanthanide (Gd, Tb) clusters have been obtained in this way (Lam et al., 2001). The structure of the Tb(III) complex is shown in Figure 18. The core of the neutral cluster is a rhombohedral arrangement of four lanthanide atoms centered about a μ_4-oxo group which lies on a crystallographic inversion center. By symmetry requirement, this necessitates the cluster core to be exactly planar. Such an arrangement is rare while tetrahedrally organized $\mathbf{R}_4O$ units are more commonly observed; known examples of planar arrangements are limited to the $[(C_6H_5SiO_2)_8N_2\mathbf{R}_4(\mu_4\text{-}O)]$ ($\mathbf{R} = Nd$, Gd), oxo-centered clusters of lanthanide siloxides. The μ_4-oxo ligand is most probably derived from water in the reaction system, as the yields decrease dramatically when carefully predried MeOH was used in the synthesis.

Another modified phenolate ligand that has been successfully utilized for lanthanide cluster synthesis is deprotonated 2,6-diformyl-4-methylphenol (H**L2**). This ligand controls the synthesis of a cationic cluster, $[Nd_4(\mu_2\text{-}\mathbf{L2})_4(\mu_3\text{-}OH)_4(H_2O)_8]^{4+}$, which was obtained from the hydrolysis of $Nd(ClO_4)_3$ (Singh-Wilmot et al., 2006) or $Nd(CF_3SO_3)_3$ (Singh-Wilmot et al., 2005). The cationic cluster features the common distorted-cubane core of $[Nd_4(\mu_3\text{-}OH)_4]^{8+}$ (Figure 19). In addition, the nonacoordinate metal atom is coordinated by the phenolato and terminal aqua ligands. Each organic ligand is shared by two metal centers; its phenolato O is bridging, while each of its two formyl groups coordinates a different metal ion.

The effect of varying alkyl substituents at the two and six positions on the bridging ability of the aryloxide ligands in europium(II) complexes

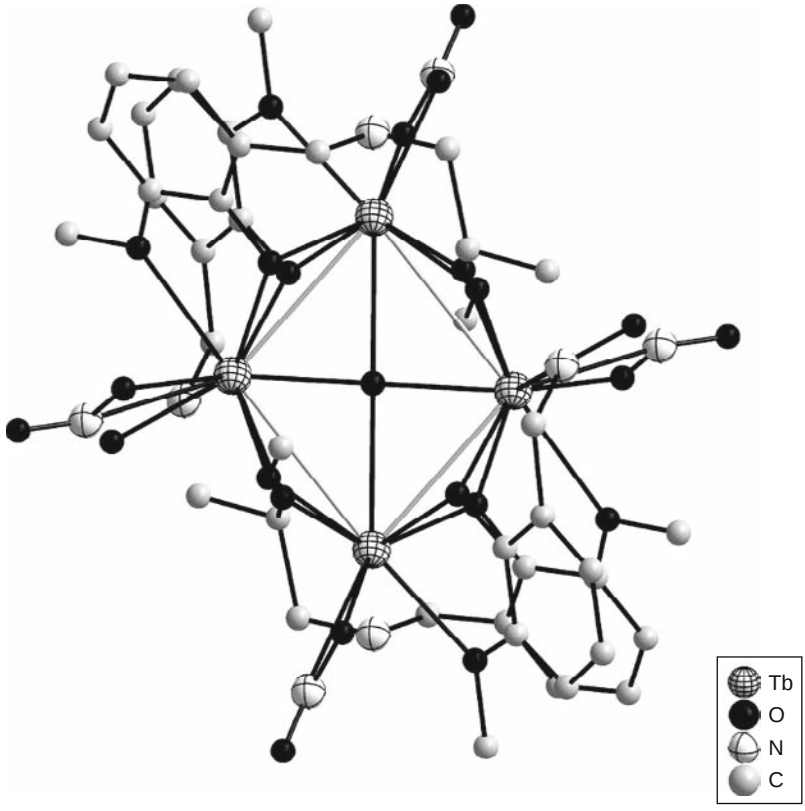

FIGURE 18 Crystal structure of a tetranuclear cluster containing a core of [$Tb_4(\mu_4$-O)] encapsulated by ligand derived from the condensation of *o*-vanillin with 1,3-diamino-propan-2-ol (redrawn after Lam et al., 2001).

has been examined. A tetranuclear cluster containing 2,6-diisopropyl-phenoxide ($OArPr^i_2$), MeCN, and hydroxide ligands $Eu_4(\mu$-$OArPr^i_2$, $-2,6)_4(OArPr^i_2)_2(\mu_3$-$OH)_2(MeCN)_6$ was isolated by Evans et al. (1997) (Figure 20). The cluster core structure features four coplanar lanthanide atoms, divided into two Eu_3 sets in which the three metal ions are connected by triply bridging hydroxo groups, a rather common motif also found in many other clusters prepared using different procedures and supporting ligands.

A slipped sandwich of terbium, $[Tb_{10}(\mathbf{L3})_6(\mathbf{L4})_2(OH)_8(OAc)_6Cl_4(MeOH)_2(H_2O)_2]Cl_2 \cdot 2MeOH$, is formed by reacting 5-bromo-3-methoxy-salicylaldehyde (H**L3**) with $TbCl_3 \cdot 6H_2O$ and $Zn(OAc)_2 \cdot 2H_2O$ (Yang et al., 2004). The cluster complex also features an unusual coordinated hemiacetal **L4** derived from H**L3** (Figure 21).

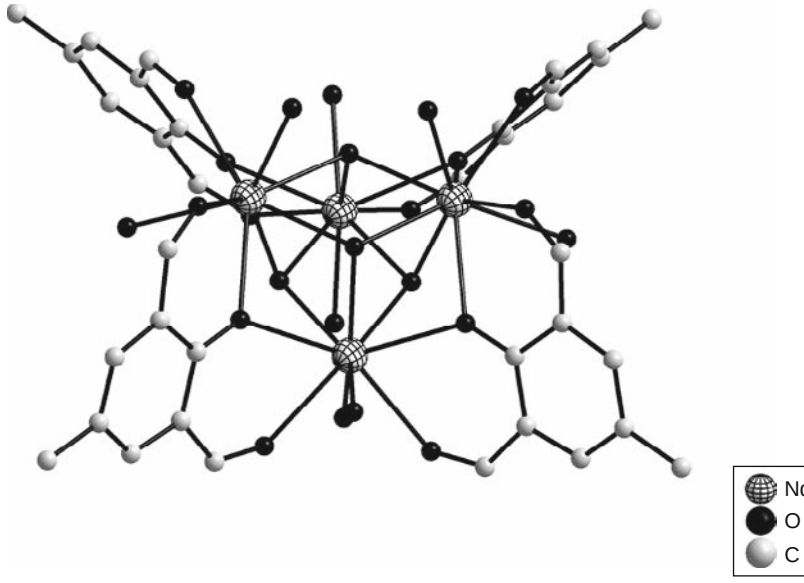

FIGURE 19 Crystal structure of the cationic cluster, $[Nd_4(\mu_2\text{-}\mathbf{L2})_4(\mu_3\text{-}OH)_4(H_2O)_8]^{4+}$ (redrawn after Singh-Wilmot et al., 2005).

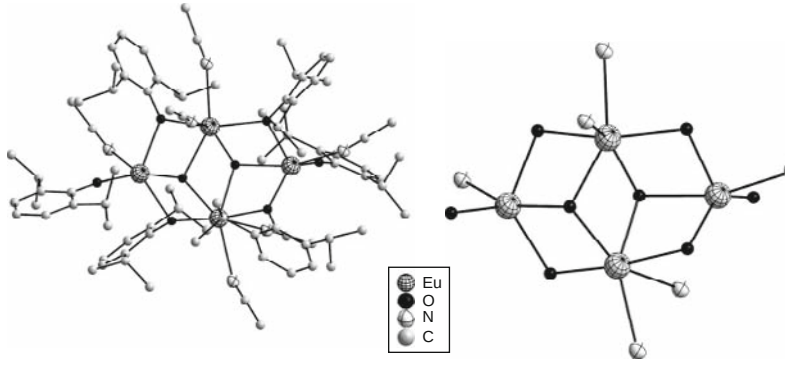

FIGURE 20 Crystal structure of $Eu_4(\mu\text{-}OAr\text{Pr}^i_2\text{-}2,6)_4(OAr\text{Pr}^i_2)_2(\mu_3\text{-}OH)_2(MeCN)_6$ with its core motif shown on the right (redrawn after Evans et al., 1997).

The overall structure of dodecanuclear clusters can be described as a dimer of two Tb_5 units. The Tb_5 unit itself is an assembly of three edge-sharing trinuclear assembly bridged by a μ_3-OH group. The two Tb_5 units are crystallographically equivalent and are connected in an offset manner by two μ_3-OH groups as well as two oxygen atoms of **L4** ligands. Each half sandwich also contains two **L3** ligands and one **L4** ligand, which lie in the

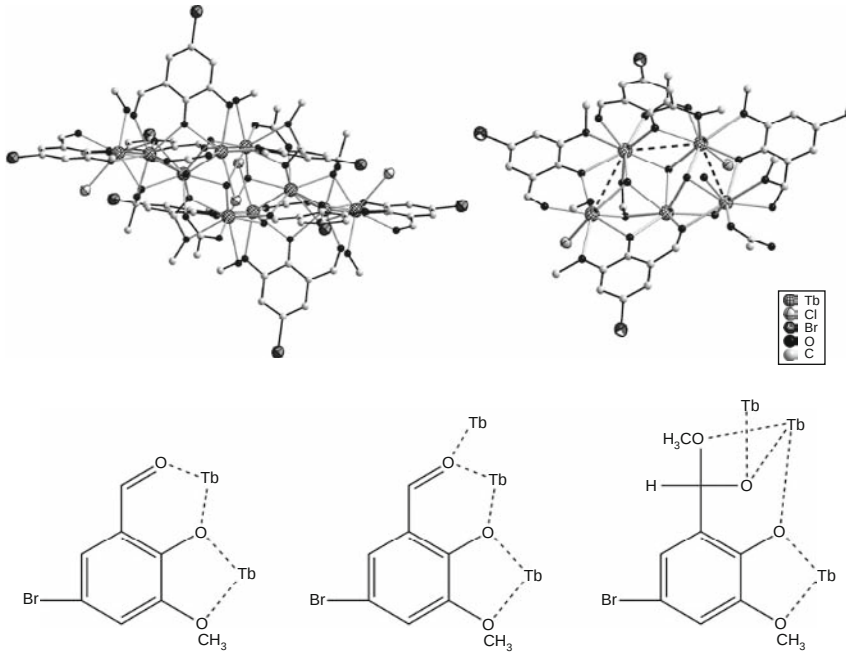

FIGURE 21 Crystal structure of the cationic cluster $[Tb_{10}(\mathbf{L3})_6(\mathbf{L4})_2(OH)_8(OAc)_6Cl_4(MeOH)_2(H_2O)_2]^{2+}$. The coordination modes of the **L3** ligand and that of the hemiacetal **L4** are also shown (bottom) (redrawn after Yang et al., 2004).

Tb_4 plane. The two different coordination modes (μ_2 or μ_3) of **L3** are shown in Figure 21, together with that of **L4**.

Under similar conditions but in the absence of zinc acetate, reactions of $\mathbf{R}Cl_3 \cdot 6H_2O$ ($\mathbf{R} = $ Tb, Er) with H**L3** in methanol gave the isostructural trinuclear complexes $[\mathbf{R}_3(\mathbf{L3})_3(\mu_3\text{-}OH)_2Cl_3(MeOH)_3]Cl \cdot 3MeOH$ ($\mathbf{R} = $ Tb, Er) whose central cores are similar to that of the trinuclear Gd(III) complex shown in Figure 17 (Costes et al., 2001).

A tetranuclear Eu(III) species $[Eu_4(\mathbf{L5})_2Cl_2(OH)_4(H_2O)_4(MeOH)_2] \cdot Cl_2 \cdot 7MeOH \cdot 2H_2O$ was obtained by reacting $EuCl_3 \cdot 6H_2O$ with $H_2\mathbf{L5}$ (*N*,*N*′-bis(5-bromo-3-methoxysalicylidene)phenylene-1,2-diamine) (Yang et al., 2007). The X-ray structure (Figure 22) revealed a centrosymmetric core with two equivalent Eu_2L moieties linked by two μ-Cl^- ions and two μ_3-OH^- ions.

Other phenolato moiety-containing ligands have also been utilized for the assembly of lanthanide–hydroxo clusters. For instance, a $[Sm_4(\mu_3\text{-}OH)_4]^{8+}$ core-containing cluster was obtained by exposing the dimeric Sm(II) complex $[Sm_2(SP\text{–}SP)(THF)_3]$ (SP–SP = C–C bonded 3,5-Bu^t_4salophen dimer) at room temperature to excess dry O_2 (Dubé et al., 1998; Figure 23). The formation of μ_3-OH was unexpected and was

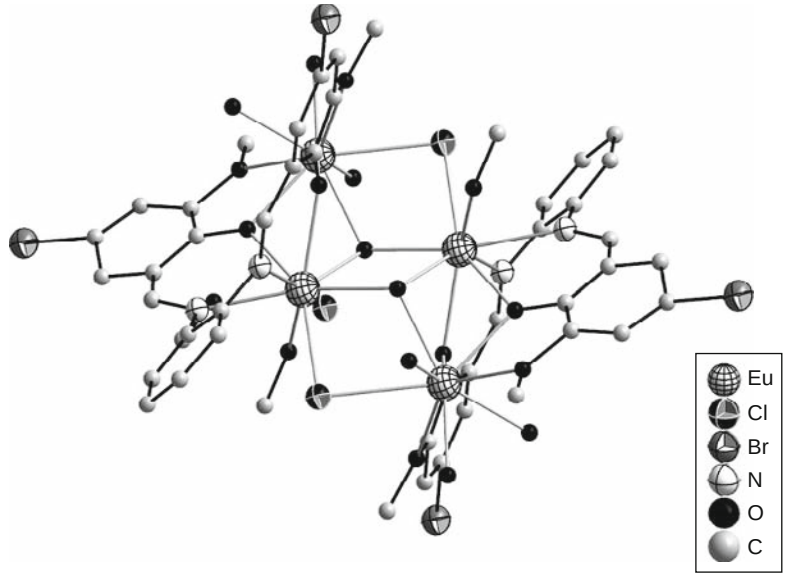

FIGURE 22 Crystal structure of the cationic cluster $[Eu_4(\mathbf{L5})_2Cl_2(OH)_4(H_2O)_4(MeOH)_2]^{2+}$ (redrawn after Yang et al., 2007).

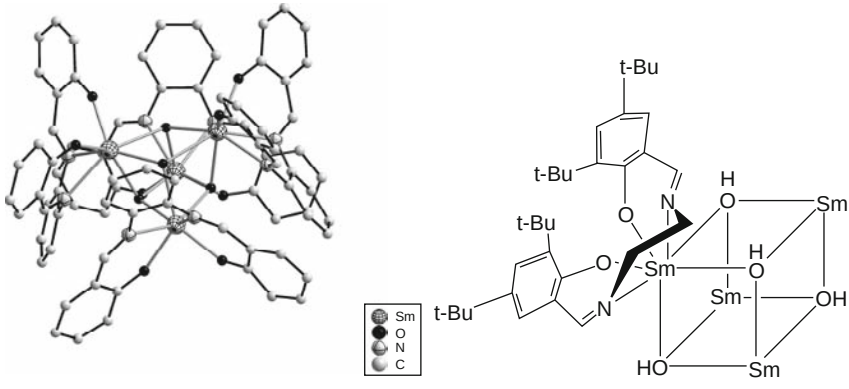

FIGURE 23 Molecular and crystal structures of the $[Sm_4(\mu_3\text{-}OH)_4]^{8+}$ core-containing cluster complex with a functionalized phenoxide ligand (redrawn after Dubé et al., 1998).

rationalized as the result of the abstraction of a hydrogen atom from the solvent during the reduction of O_2 by (salophen)Sm(II) generated *in situ*.

Sometimes, the formation of aryloxide clusters can be quite surprising. The reaction of $K\{PR''(C_6H_4\text{-}2\text{-}OMe)\}$ ($R'' = CH(SiMe_3)_2$) with YbI_2 under similar conditions yields the unexpected alkoxophosphide complex

$[Yb\{PR''(C_6H_4\text{-}2\text{-}O)\}(THF)]_4 \cdot 4Et_2O$ (Et_2O = diethyl ether), via an unusual ligand cleavage reaction involving the transfer of a methyl group from oxygen to phosphorus (Clegg et al., 2000; Figure 24). This unprecedented tetrameric cluster contains an Yb_4O_4 cuboidal core, in sharp contrast to the commonly observed distorted-cubane core featuring triply bridging hydroxo groups. It appears that the cluster formation involves a remarkable shift of a methyl group from oxygen to phosphorus, requiring both C–O cleavage and P–C bond formation, without affecting the oxidation state of the Yb(II) center.

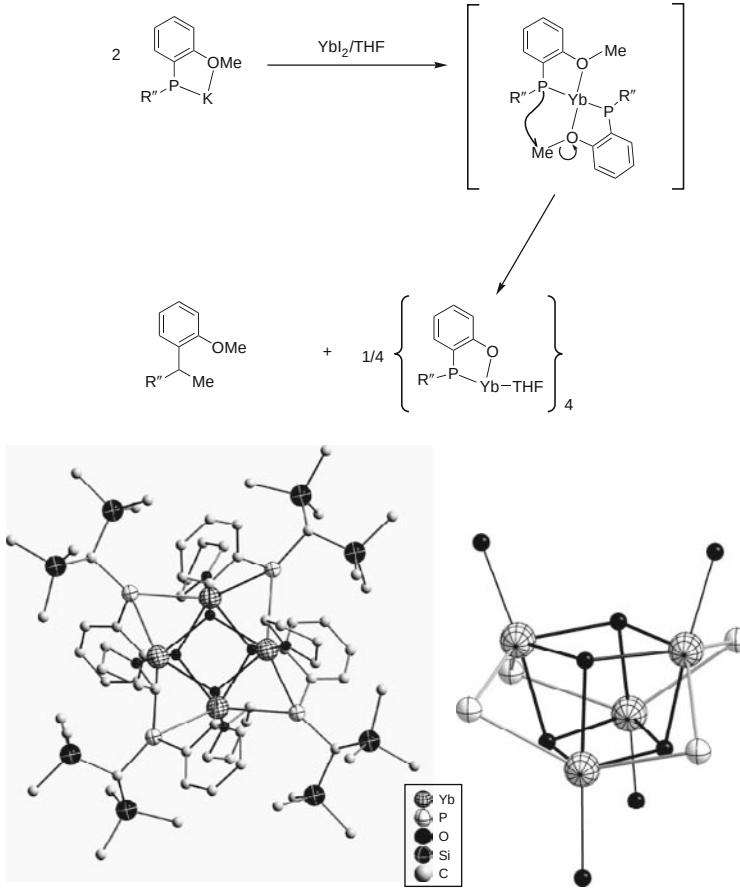

FIGURE 24 Proposed mechanism for the unexpected assembly of the tetranuclear cluster $[Yb\{PR''(C_6H_4\text{-}2\text{-}O)\}(THF)]_4$ whose structure (bottom left) is shown together with the core motif (bottom right) (redrawn after Clegg et al., 2000).

2.1.3 Lanthanide clusters with macrocyclic polyaryloxides

It is clear from the chemistry of lanthanide clusters based on aryloxide ligands that lanthanide coordination chemistry can be further developed by having recourse to other functionalized aryloxide ligands. In this context, the use of constrained, macrocyclic polyaryloxide ligands such as calixarenes or their sulfur-containing analogues appears intriguing.

Calixarenes are macrocyclic ligands featuring n phenol groups connected into a ring structure by n methylene groups. Large calixarenes lead to the assembly of polynuclear clusters such as $[(HO)_2(OCO_2)Eu_4(calix[7])_2(DMSO)_6]$ (calix[7] = p-Bu^t-calix[7]arene-4H; DMSO = dimethyl sulfoxide) which was structurally characterized (Fleming et al., 2003; Figure 25). The solid-state structure may be viewed as a pair of binuclear units bridged by carbonate and adventitious hydroxide, each incompletely surrounded by a calix[7]. With the use of p-Bu^t-calix[9]arene-6H (calix[9]), a larger oligonuclear assembly was isolated, $[(HO)_9(H_2O)_2Eu_7(calix[9])_2(DMSO)_6]$, featuring a core of two corner-sharing cubanes encapsulated by the bulky macrocycle.

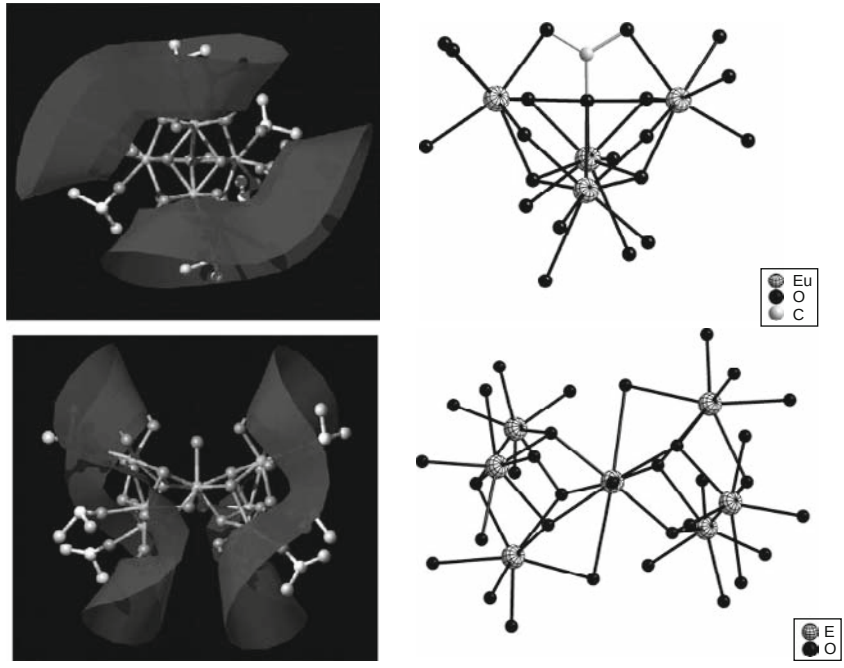

FIGURE 25 The wavy moieties represent the contour of the calixarene ligands in $[(HO)_2(OCO_2)Eu_4(calix[7])_2(DMSO)_6]$ (upper left) and $[(HO)_9(H_2O)_2Eu_7(calix[9])_2(DMSO)_6]$ (bottom left). Their respective core structures are shown on the right (redrawn after Fleming et al., 2003).

The cluster-forming ability of thiacalix[*n*]arenes and its derivatives as multidentate and multinucleating ligands have also been investigated. In addition to the coordinating O atoms on the framework of the macrocycle itself, the sulfur-containing moiety can also participate in metal coordination. For example, sulfonylcalix[4]arene produced a variety of clusters with lanthanide ions depending on the reaction conditions such as reaction ratio, solvents, acidity/basicity of the solution, and presence/absence of coligands. This calixarene showed new functionality as an antenna chromophore for UV and near-UV irradiation based on the pronounced delocalization of its π-conjugated system over the entire molecule, whereas each phenol π-conjugated system in the original calixarene is isolated by methylene groups. Due to the large π-conjugated system of the ligand spanning the entire molecule, this functionality was controllable by conformational changes without the need for any chemical modifications.

The capacity of calixarenes to incorporate small and often unique metal clusters has been revealed in the first crystallographically characterized cluster complex, $[Nd_4(\mu_4\text{-}OH)(S_4calix[4])_2(DMF)_8(DMSO)_2](NO_3)_3 \cdot 3H_2O$ ($H_4S_4calix[4] = p\text{-}Bu^t$-tetrathiacalix[4]arene-4H) (Bilyk et al., 2000). In the cationic unit (Figure 26), four Nd atoms are bound to a common oxygen atom—originating from adventitious hydrolysis. Each Nd has a tricapped trigonal prismatic geometry, with the capping atoms being the bridging hydroxide oxygen and two calixarene sulfur atoms and the trigonal prism made up by four (bridging) calixarene phenoxide and solvent (DMF or DMSO) oxygen atoms. The calixarene entities adopt a symmetrical cone conformation.

Reactions of $p\text{-}Bu^t$-sulfonylcalix[4]arene ($H_4SO_2calix[4]$) and $\mathbf{R}(AcO)_3 \cdot nH_2O$ ($AcO =$ acetate) in presence of $(Bu^n_4N)OH$ afforded cubane-type complexes $(Bu^n_4N)_4[\mathbf{R}_4(SO_2calix[4])_2(OH)_4(AcO)_4]$ ($\mathbf{R} =$ Gd, Eu, and Tb), in which a conical $SO_2calix[4]^{4-}$ behaved as a bis-tridentate ligand bonding via two phenoxo and one sulfonyl oxygen atom to each lanthanide ion (Kajiwara et al., 2006, 2007; Figure 27).

A cage-like trinuclear Er cluster was isolated from the reaction mixture of Er metal, $Hg(C_6F_5)_2$, and HOArOMe. The compound, formulated as $[Er_3(OArOMe)_4(\mu_2\text{-}F)_3(\mu_3\text{-}F)_2(THF)_4]$, has a triangular core capped above and below by two $\mu_3\text{-}F^-$ ligands (Figure 28). Neighboring Er atoms are bridged by $\mu_2\text{-}F^-$ ligands within the triangular plane (Deacon et al., 2006).

Although not as often observed, other small-unit, inorganic ligands can be incorporated into the assembly of lanthanide alkoxide clusters. For example, the tetranuclear Nd cluster $[Na_2Nd_4(\mathbf{L6})_4(CO_3)(DME)_4]$ ($H_3\mathbf{L6} = (o\text{-}HOC_6H_4CHNNCH_2)_2CHOH$; $DME =$ 1,2-dimethoxyethane) has been structurally characterized and contains a tightly bound molecule of sodium carbonate in the bowl-shaped $Nd_4O_{12}N_8$ framework of the $Nd_4(\mathbf{L6})_4$ molecule (Deacon et al., 1997; Figure 29).

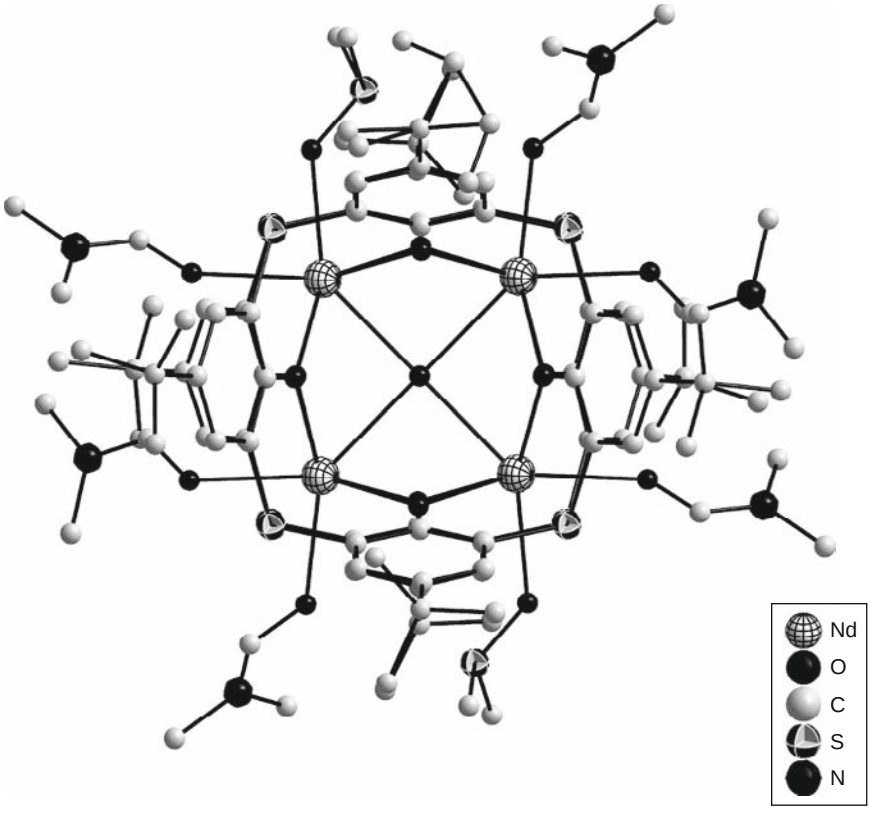

FIGURE 26 Crystal structure of the cationic cluster $[Nd_4(\mu_4\text{-}OH)(S_4calix[4])_2(DMF)_8(DMSO)_2]^{3+}$ (redrawn after Bilyk et al., 2000).

2.2 Nonhydride clusters

Besides alkoxides and aryloxides, other ligands have also been used in the synthesis of organolanthanides, with cyclopentadienyl and its derivatives being most prominent and important (Arndt and Okuda, 2002; Hou, 2003; Hou et al., 2007). Because of their unique bonding interactions and ability to provide steric protection for the metal center, the extensive use of such ligands should not be surprising at all. A great variety of organolanthanide compounds have been prepared, with which many interesting and useful chemical transformations have been identified.

2.2.1 Clusters with cyclopentadienyl (Cp)-type ligands

Although the synthesis of cluster compounds has never been the original goal of Cp-supported organolanthanide chemistry, there nevertheless exist a large number of such species. Despite the steric hindrance

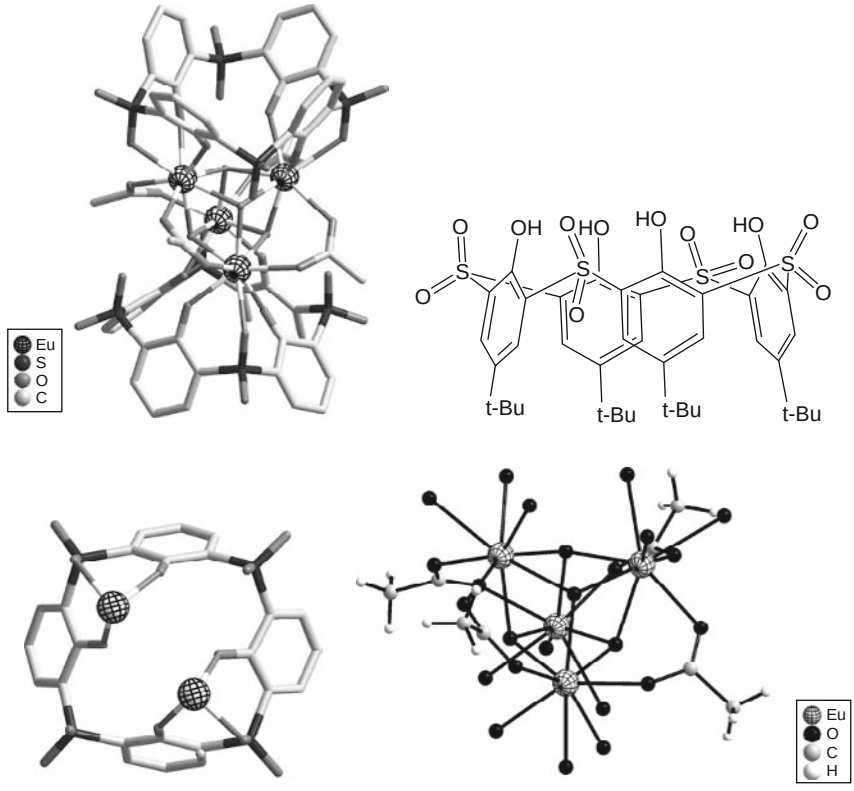

FIGURE 27 Crystal structure of anionic cluster $[Eu_4(SO_2calix[4])_2(OH)_4(AcO)_4]^{4-}$, the molecular structure of the ligand, the structure of one of its dinuclear building units, and the hydroxo-bridged tetranuclear cluster core (clockwise from upper left) (redrawn after Kajiwara et al., 2006, 2007).

generated by Cp ligands, they may not be completely adequate for the large lanthanide ions, in particular when the Cp/**R** ratio is small; a low Cp/**R** ratio inevitably leaves unbound coordination sites at the metal center. It is therefore natural for the mononuclear lanthanide unit to aggregate, by means of bridging ligands, in order to satisfy the high-coordination requirement of the **R** cations, eventually producing polynuclear cluster species.

Another important observation is the presence of central negative charge density in a large number of lanthanide clusters with Cp ligands. It should be noted, however, that this observation is not limited to the Cp ligand system since it has been pinpointed in many of the clusters species presented above. The existence of negative charge density can markedly influence the cluster structure and may even be essential to the cluster formation.

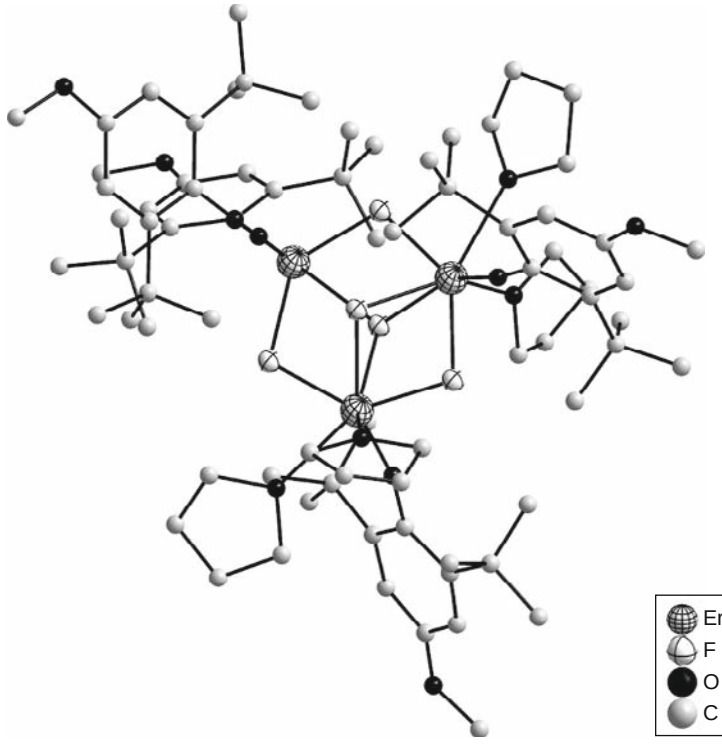

FIGURE 28 Crystal structure of $[Er_3(OArOMe)_4(\mu_2\text{-}F)_3(\mu_3\text{-}F)_2(THF)_4]$ (redrawn after Deacon et al., 2006).

One stunning example in this context is the assembly of 12 $CpSmCl_2$ fragments into a highly symmetrical icosahedral cluster $Cp_{12}Sm_{12}Cl_{24}$ (Kretschmer et al., 1998; Figure 30, left). The electrostatic stabilization of the Sm_{12} icosahedron around a central Cl_4 tetrahedron is truly amazing and structurally pleasing. Each of the Sm atoms is coordinated with one Cp ligand and six chloro groups. All six chloro ligands are triply bridging, five of which being part of the pentagonal–decahedral cage, while the sixth one is located inside the icosahedral cage. The four inside chloro ligands form a negatively charged tetrahedron, presumably providing the support for the assembly of the cluster and its stabilization.

Under similar conditions the use of the smaller and more Lewis acidic Yb(III) ion afforded a hexanuclear anionic $[Cp_6Yb_6Cl_{13}]^-$ cluster whose interstitial position is occupied by a presumably stabilizing μ_6-Cl atom (Figure 30, right). The regular octahedron of Yb_6 contains 12 additional μ-Cl^- groups, each bridging two adjacent metal atoms. The reduced size

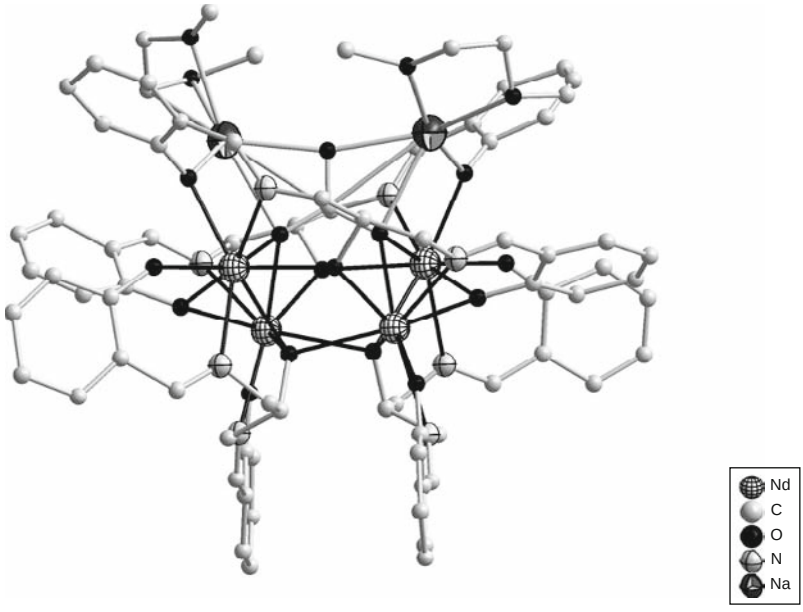

FIGURE 29 Crystal structure of $[Na_2Nd_4(\mathbf{L6})_4(CO_3)(DME)_4]$ (redrawn after Deacon et al., 1997).

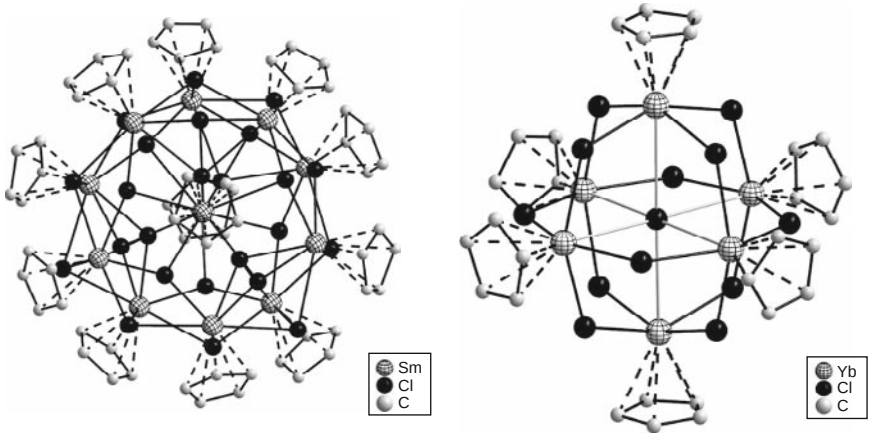

FIGURE 30 Crystal structures of $Cp_{12}Sm_{12}Cl_{24}$ (left) and $[Cp_6Yb_6Cl_{13}]^-$ (right) (redrawn after Kretschmer et al., 1998).

of this cluster when compared to the aforementioned Sm_{12} cluster may be due to incomplete desolvation of the Yb precursor, $[CpYbCl_2(THF)_3]$, due to increased affinity of Yb(III) for THF.

The presence of an interstitial μ_6-Cl group is also observed in the hexameric cluster $(Cp^*NdCl_2)_6(LiCl)_3(THF)_3$, obtained from the reaction of $Cp^*_2NdCl{\cdot}LiCl{\cdot}2THF$ with excess catecholborane (Barnea et al., 2007; Figure 31). The six Nd atoms define a trigonal prism whose two triangular faces are capped by two μ_3-Cl^- ligands. The four Nd atoms of each of the three rectangular faces of the regular trigonal prism and one Li^+ form a square pyramidal arrangement whose four triangular faces are capped by μ_3-Cl^- ligands. As such, there are 15 chloro ligands, with three different bridging modes.

Bridging chloro ligands have also been found in coexistence with other types of small-unit, cluster-building groups. In the rather unusual trinuclear lanthanide methylidene cluster $[Cp^*_3\mathbf{R}_3(\mu\text{-}Cl)_3(\mu_3\text{-}Cl)(\mu_3\text{-}CH_2)(THF)_3]$ ($\mathbf{R} = La, Y$) (Dietrich et al., 2006c), there are four bridging chloro ligands and one methylidene group (Figure 32). The $\mathbf{R}_3$ plane is capped on one side by a μ_3-Cl^- ligand and by the methylidene group on the opposite side. Each of the three μ-Cl^- ligands bridges two adjacent metal atoms along the side of the $\mathbf{R}_3$ plane.

More sophisticated coligands include tetramethylaluminato groups as in the pentanuclear neodymium cluster $[Cp^*_5Nd_5[(\mu\text{-}Me)_3AlMe](\mu_4\text{-}Cl)(\mu_3\text{-}Cl)_2(\mu_2\text{-}Cl)_6]$ (Figure 33, top) and the hexalanthanum cluster $[Cp^*_6La_6\{(\mu\text{-}Me)_3AlMe\}_4(\mu_3\text{-}Cl)_2(\mu_2\text{-}Cl)_6]$ (Figure 33, bottom; Dietrich et al., 2006b).

An interesting fluoro-containing cluster was reported in 1990 (Watson et al., 1990). In this cluster, formulated as $[Yb_5Cp^*_6(\mu_4\text{-}F)(\mu_3\text{-}F)_2(\mu\text{-}F)_6]$, there are three different kinds of bridging fluoro ligands, doubly, triply, and quadruply bridging (Figure 34). The μ_4-F^- and four Yb atoms describe a distorted-square pyramidal array, with the metal atoms

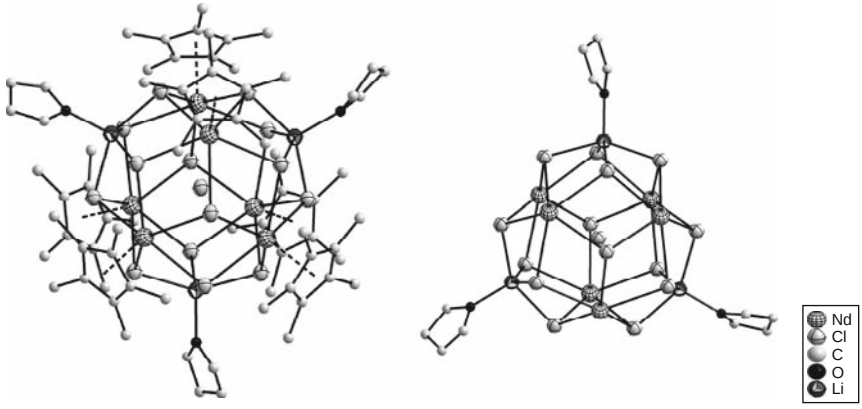

FIGURE 31 Crystal structure of $(Cp^*NdCl_2)_6(LiCl)_3(THF)_3$. In the structure with the Cp ligands removed is shown on the right (redrawn after Barnea et al., 2007).

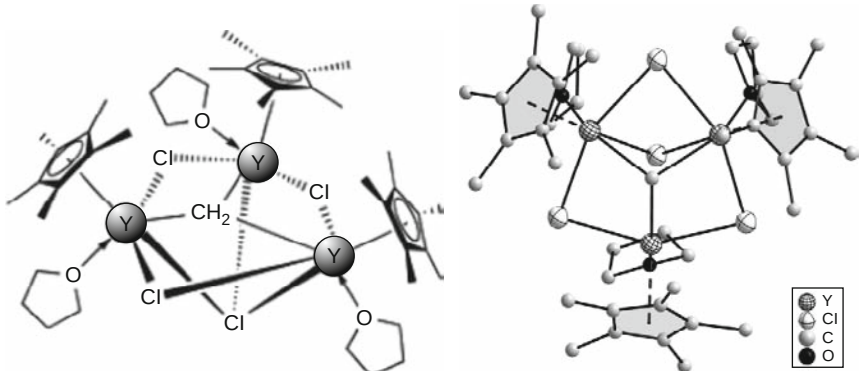

FIGURE 32 Molecular and crystal structure of $[Cp^*_3Y_3(\mu\text{-}Cl)_3(\mu_3\text{-}Cl)(\mu_3\text{-}CH_2)\ (THF)_3]$ (redrawn after Dietrich et al., 2006c).

forming the basal plane and the F^- ligand occupying the vertex position. Bridging two adjacent metal atoms is a μ_2-F^-. There are also two μ_3-F^- ligands bridging two Yb_3 sets, joined together by the μ_4-F^- group.

Less common is the presence of heavier halo ligands such as iodo in organolanthanide clusters. One such example is the hexanuclear Yb(II) octa-iodo dianion $\{Yb_6[C_5Me_4(SiMe_2Bu^t)]_6I_8\}$ (Constantine et al., 1996; Figure 35). The six $[YbC_5Me_4(SiMe_2Bu^t)]$ units occupy the vertices of a regular octahedron whose eight triangular faces are capped by triply bridging iodo ligands.

Not only halo ligands facilitate the assembly of lanthanide clusters supported by Cp ligands, but pseudohalo ligands may also be inserted into the cluster core. In the anionic hexanuclear cluster, $[Cp^{**}_6Yb_6(N_3)_{14}]^{2-}$ (Cp** = tetra(isopropyl)cyclopentadienyl or $C_5H(Pr^i)_4$) (Walter et al., 2006; Figure 36, left), the six {Cp**Yb} units of the anion describe a slightly distorted octahedron. The overall structure may be viewed as two joined vertical 16-membered $\{Yb_4N_{12}\}$ rings fused with an equatorial 12-membered $\{Yb_4N_8\}$ ring in a chair conformation (Figure 36, right).

In addition to the more commonly observed oxo, hydroxo, and halo ligands, there are polymetallic assemblies for which rather exotic ligands are present in the cluster core. For example, a tetranuclear yttrium–aluminum–methine cluster was obtained according to the scheme shown in Figure 37 (left) (Dietrich et al., 2006a).

The trimetallic cluster possesses a high molecular symmetry C_{3h} (Figure 37). The yttrium atoms are coordinated by four μ_2-bridging methyl groups and one Cp* ligand adopting a tetragonal pyramidal geometry. For the tetranuclear cluster, the four yttrium atoms form a rectangle. Each yttrium is surrounded by a Cp* ligand, three methyl, and a methylidine groups, creating a markedly distorted-tetragonal

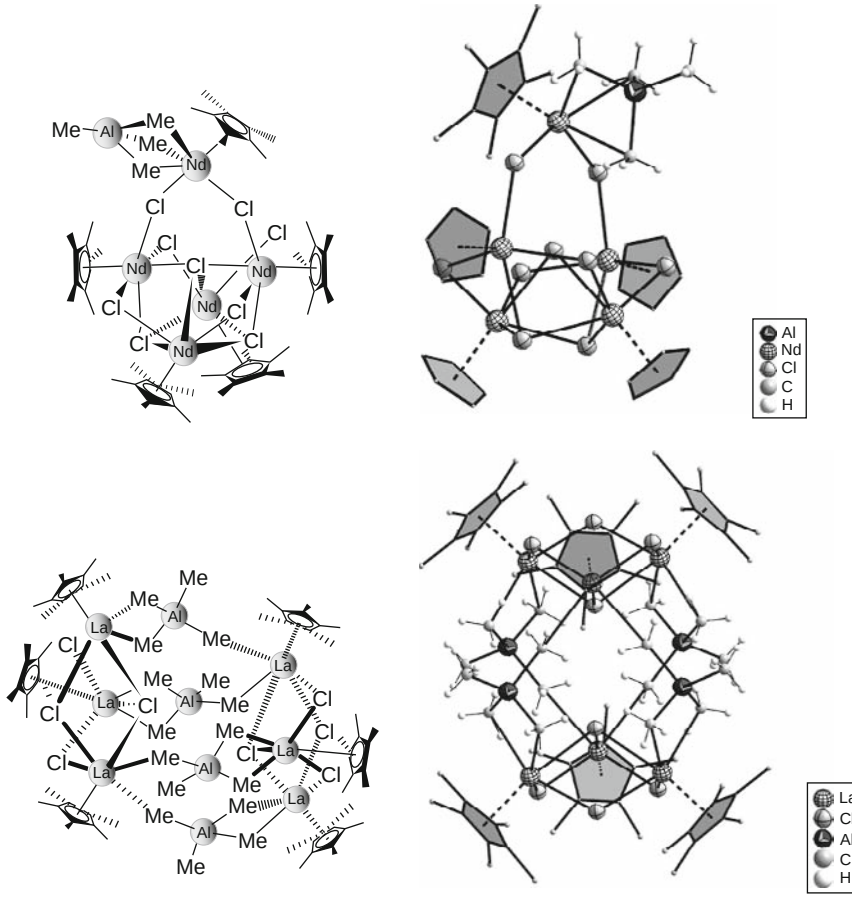

FIGURE 33 Molecular and crystal structures of $[Cp^*_5Nd_5(\mu\text{-}Me)_3AlMe](\mu_4\text{-}Cl)(\mu_3\text{-}Cl)_2(\mu_2\text{-}Cl)_6]$ (top) and $[Cp^*_6La_6\{(\mu\text{-}Me)_3AlMe\}_4(\mu_3\text{-}Cl)_2(\mu_2\text{-}Cl)_6]$ (bottom) (redrawn after Dietrich et al., 2006b).

pyramid. The four carbon atoms of the methylidine and yttrium-bridging methyl groups together with the four yttrium atoms form a planar eight-membered ring. The cage-like structure may alternatively be described as two butterfly arrangements, each composed of two Cp*Y groups linked via $[(AlMe_3)_2(\mu_4\text{-}CH)]$ moieties, themselves connected by the two bridging methyl groups.

Borohydride can also be used to build cluster cores of organolanthanide compounds. The reaction of $\mathbf{R}(BH_4)_3(THF)_3$ or $\mathbf{R}Cl_3(THF)_3$ with KCp*′ (Cp*′ = tetramethyl(*n*-propyl) cyclopentadienyl or $C_5Me_4Pr^n$) afforded hexameric mixed borohydrido/chlorobridged $[Cp^{*\prime}_6\mathbf{R}_6(BH_4)_{(12-x)}Cl_x(THF)_n]$ clusters containing the $[Cp^{*\prime}_3\mathbf{R}_3X_5(THF)]$ building

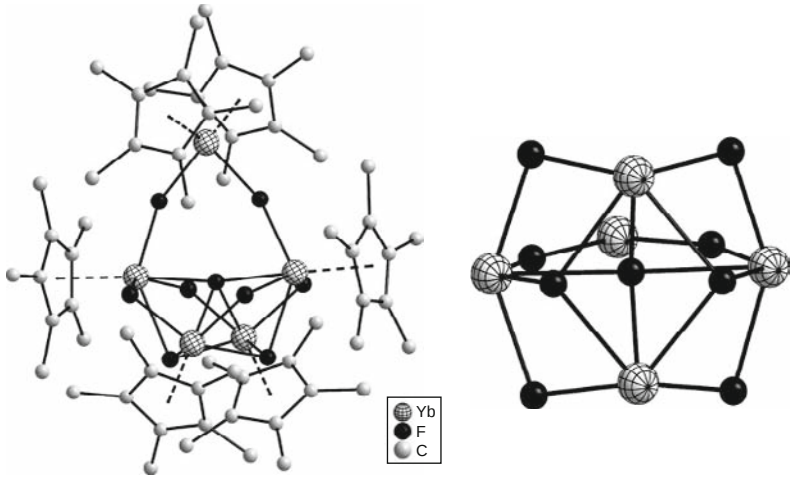

FIGURE 34 Crystal structure of $[Yb_5Cp^*_6(\mu_4\text{-}F)(\mu_3\text{-}F)_2(\mu\text{-}F)_6]$ with its core structure shown on the right (redrawn after Watson et al., 1990).

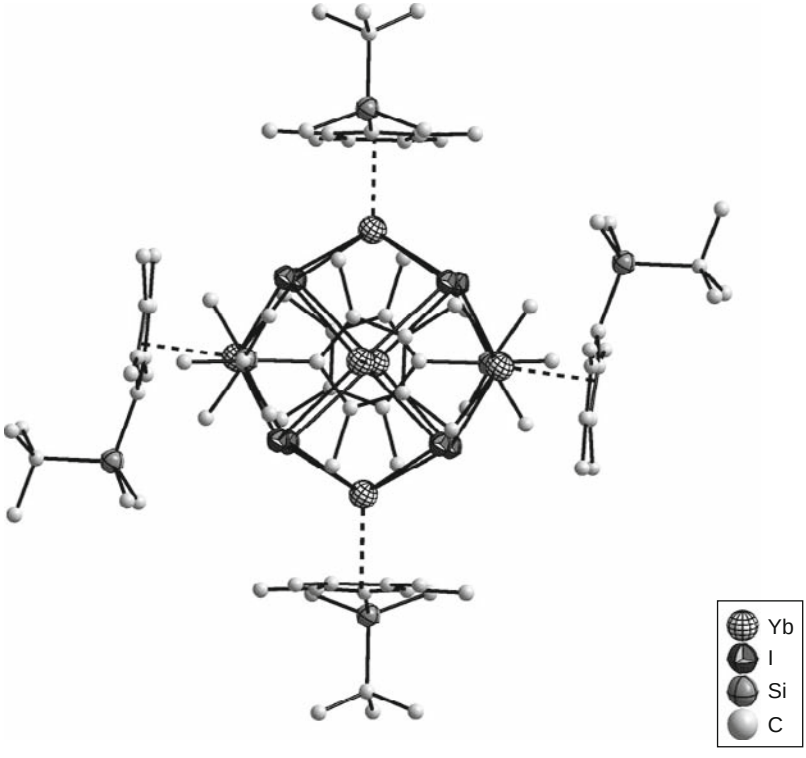

FIGURE 35 Crystal structure of the octa-iodo cluster $\{Yb_6[C_5Me_4(SiMe_2Bu^t)]_6I_8\}$ (redrawn after Constantine et al., 1996).

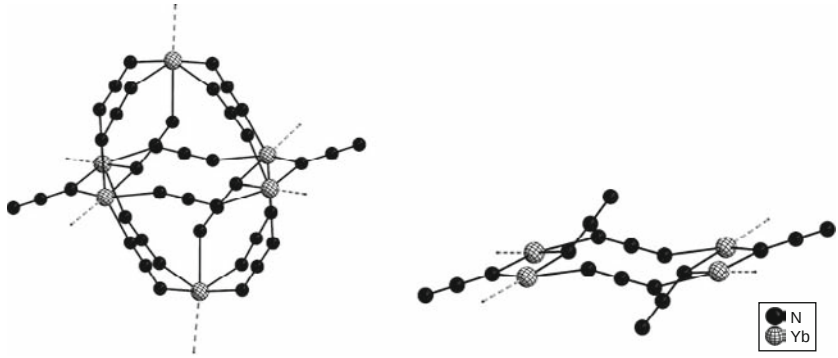

FIGURE 36 Crystal structure of the anionic cluster $[Cp^{**}_6Yb_6(N_3)_{14}]^{2-}$ (left) and the chair-like 12-membered $\{Yb_4N_8\}$ ring shown on the right. The Cp** ligands are removed for clarity (redrawn after Walter et al., 2006).

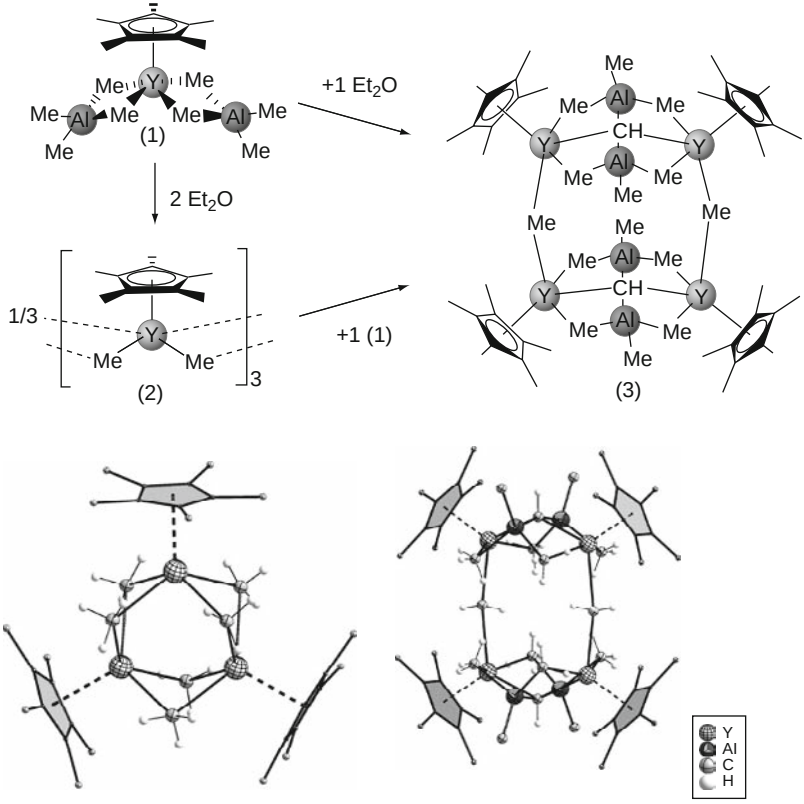

FIGURE 37 Synthetic schemes (top, reproduced with permission from) for and crystal structures of tri- (bottom left) and tetranuclear (bottom right) yttrium–aluminum–methine clusters (redrawn after Dietrich et al., 2006a).

block (Bonnet et al., 2004). The easy clustering is illustrative of the well-known bridging ability of the BH_4 group. In the structure of $[Cp^{*\prime}Sm(BH_4)_2]_6$ (Figure 38, left), the six $Cp^{*\prime}Sm$ units form an approximate octahedral arrangement. The 12 edges of the octahedron are bridged by the same number of BH_4 groups.

The middle structure shown in Figure 38 is that of $(\mu_2\text{-}BH_4)_2[Cp^{*\prime}_3Sm_3Cl_5(THF)]_2$. The overall structure can be viewed as a dimer of $Cp^{*\prime}_3Sm_3Cl_5(THF)$, interlinked by two bridging BH_4 groups. Interestingly, the six component metal atoms are arranged into a chair-like arrangement (Figure 38, right).

An oxo-containing hexanuclear cluster $(Cp^*Sm)_6O_9H_6$ (Evans et al., 2001) has also been reported (Figure 39). Six Sm atoms constitute an approximate octahedron built around a central μ_6-O. Eight face-bridging oxygen atoms are located in a roughly cubic array. The cluster cage is encapsulated in the organic environment formed by six Cp* ligands, with each metal being coordinated by one such ligand.

Reacting a mixture of $YbCl_3$, YbOCl, and Na(MeCp) ($MeCp = CH_3C_5H_4$) produced a tetranuclear cluster $(MeCp)_3Yb_4(\mu\text{-}C1)_6(\mu_3\text{-}C1)(\mu_4\text{-}O)(THF)_3$ (Zhou et al., 1995; Figure 40). The cluster core is a tetrahedron of Yb_4 with an interstitial μ_4-oxo group whose six sides are each bridged by a chloro ligand. In addition, there is a triply bridging chloro group capping the triangular face formed by the three MeCp-coordinated Yb atoms.

An interesting cluster featuring both core-building oxo and chloro ligands has been reported (Zalkin and Berg, 1989). The cluster has the formula $[Yb_5O(Et_2O)_2Cp^*_5Cl_8]$ and its structure consists of a single large cluster in which the five Yb atoms are linked together by Cl and O bridges (Figure 41). The π-bonding Cp* rings and the O atoms of the ether ligands are bonded to the Yb atoms on the periphery of the cluster.

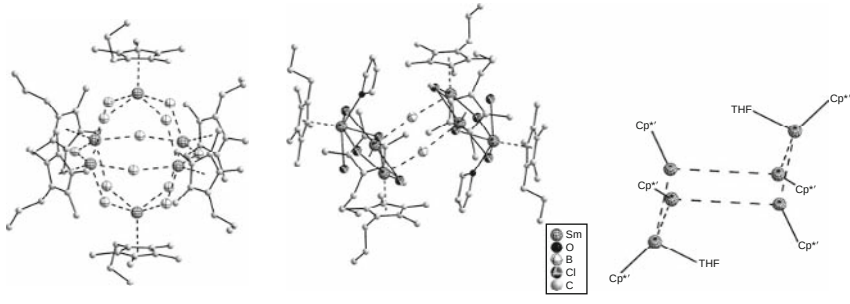

FIGURE 38 Left to right: crystal structures of $[Cp^{*\prime}Sm(BH_4)_2]_6$, $(\mu_2\text{-}BH_4)_2[Cp^{*\prime}_3Sm_3Cl_5(THF)]_2$, and the chair-like arrangement of the six Sm atoms in the latter cluster (redrawn after Bonnet et al., 2004).

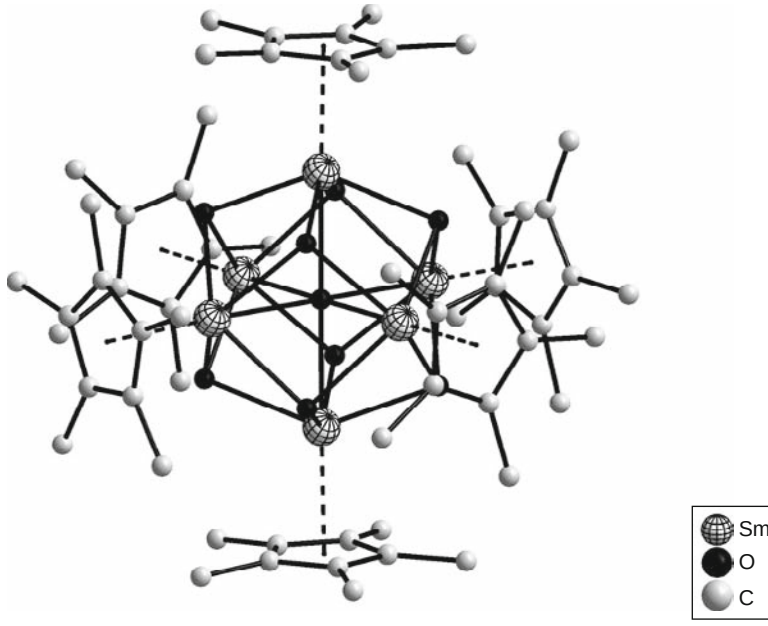

FIGURE 39 Crystal structure of $(Cp^*Sm)_6O_9H_6$ (redrawn after Evans et al., 2001).

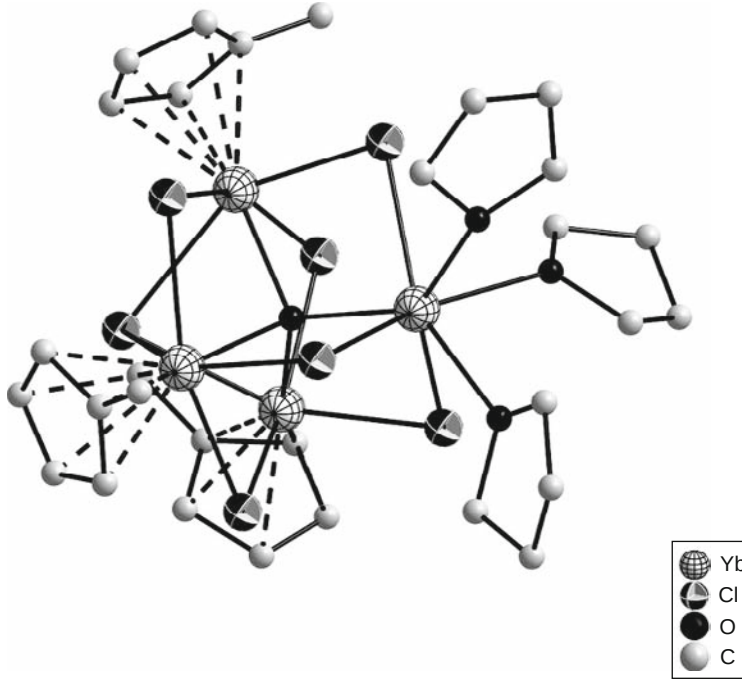

FIGURE 40 Crystal structure of $(MeCp)_3Yb_4(\mu\text{-}Cl)_6(\mu_3\text{-}Cl)(\mu_4\text{-}O)(THF)_3$ (redrawn after Zhou et al., 1995).

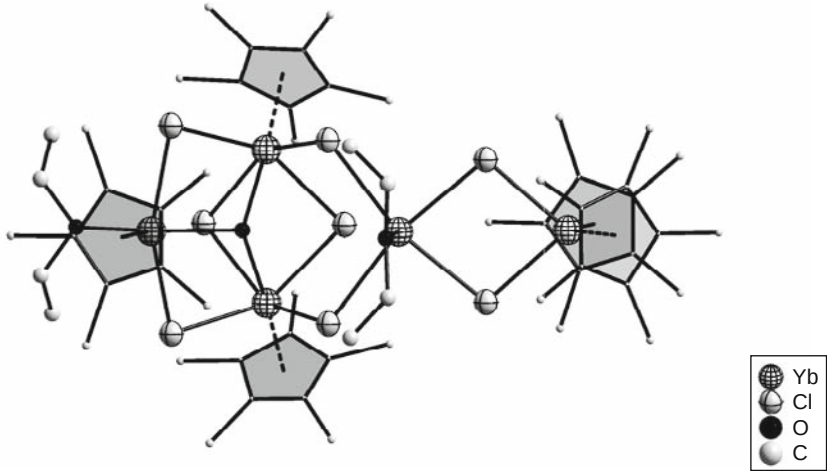

FIGURE 41 Crystal structure of $[Yb_5O(Et_2O)_2Cp^*_5Cl_8]$, a cluster containing both oxo and chloro groups in the core structure (redrawn after Zalkin and Berg, 1989).

2.2.2 Clusters with non-Cp ligands

Non-Cp ligands have also been utilized for the preparation of organolanthanide compounds, often in cluster forms (Edelmann et al., 2002). One such example is the class of ligands based on carboranes. Although they may appear somewhat exotic to the community at large, the chemistry of the metallacarboranes originated actually with the recognition that the *nido*-dicarbollide ion, $C_2B_9H_{11}^{2-}$ is similar to the cyclopentadienide ligand in that both can use delocalized π-type orbitals for metal coordination. Of particular interest for making organolanthanide clusters are smaller members of the family based on the C_2B_4 cage. Two different isomers are available, one termed ''carbons adjacent'' (2,3-C_2B_4), while in the other, ''carbons apart'' (2,4-C_2B_4), the two carbon atoms on the face of the latter isomer are separated by a boron atom. Cluster compounds of the lanthanide elements have been synthesized with both C_2B_4 cage systems, the use of the 2,3-C_2B_4 being, however, more extensive (Hosmane and Maguire, 2005).

Trinuclear lanthanide clusters of carboranes of the general formula $\{[\eta^5$-1-**R**-2,3-$(SiMe_3)_2$-2,3-$C_2B_4H_4]_3[(\mu$-1-Li-2,3-$(SiMe_3)_2$-2,3-$C_2B_4H_4)_3(\mu_3$-OMe)$]$ $[\mu$-Li(THF)$]_3(\mu_3$-O)$\}$ (**R** = Sm, Gd, Tb, Dy, Ho, and Nd) were obtained from the reaction of the THF-solvated dilithium salt of the [2,3-$(SiMe_3)_2$-2,3-$C_2B_4H_4]^{2-}$ dianion with anhydrous **R**Cl_3 in THF (Hosmane et al., 1996). The crystal structure of the Ho_3 cluster is shown as a representative example in Figure 42. The cluster is composed of three half-sandwich lithiacarboranes and three half-sandwich lanthanacarboranes arranged around a

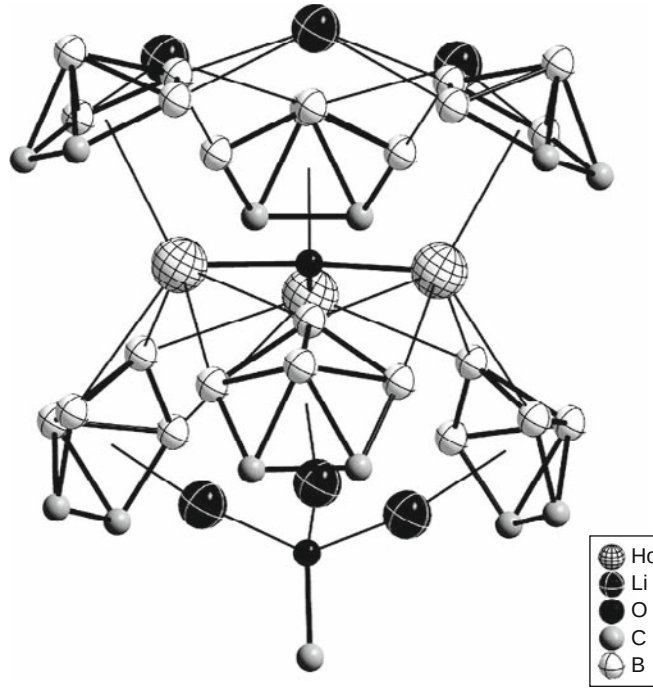

FIGURE 42 Crystal structure of trinuclear carborane cluster {[η^5-1-Ho-2,3-$(SiMe_3)_2$-2,3-$C_2B_4H_4$]$_3$[(μ-1-Li-2,3-$(SiMe_3)_2$-2,3-$C_2B_4H_4$)$_3$(μ_3-OMe)][μ-Li(THF)]$_3$(μ_3-O)} (redrawn after Hosmane et al., 1996).

methoxide ion and an oxide ion, respectively. The Ho_3O geometry is that of a trigonal plane in which the three lanthanides equally surround the central oxide, while the Li_3-OMe unit, located below the Ho_3 plane, can best be described as a distorted-tetrahedral arrangement of the three lithium atoms and the Me unit about a central oxygen. The Ho_3 planes are essentially parallel to one another. The structures of the clusters are such that the nine metal atoms form a tapered tricapped trigonal prism with the lanthanides occupying the capping positions.

Incorporation of the oxo and methoxido groups, albeit unexpected, is not entirely surprising, and they are probably products of solvent degradation by either *t*-BuLi or lanthanide compounds, or both. Presumably due to the stabilizing effects of the triply bridging oxo and methoxido groups, no further reactions were observed for the trinuclear cluster, even with excess $\mathbf{R}Cl_3$.

The required use of THF as solvent and its random decomposition for the production of the oxo-/methoxido trinuclear cluster limits the general synthetic use of this methodology for producing other similar

O-containing organolanthanide clusters. A more general approach is by deliberate introduction of water as the oxo group source (Wang et al., 2003, 2004). Treatment of anhydrous $\mathbf{R}Cl_3$ ($\mathbf{R}$ = La, Nd, Gd, Tb, Ho, and Lu) with stoichiometric amount of freshly distilled H_2O under reflux conditions in THF followed by the reaction of the resulting mixture with *closo-exo*-5,6-Na(THF)$_2$-1-Na(THF)$_2$-2,4-(SiMe$_3$)$_2$-2,4-$C_2B_4H_4$ afforded a series of oxide-encapsulated complexes {[η^5-1-$\mathbf{R}$(THF)$_n$-2,4-(SiMe$_3$)$_2$-2,4-$C_2B_4H_4$]$_4$(μ-Cl)$_2$(μ_4-O)}. Structurally shown in Figure 43 using the Tb(III) complex as a representative, the cluster core contains an oxo group encapsulated by a slightly distorted $\mathbf{R}_4$ tetrahedron. The oxo-centered core is stabilized by coordinating two carborane ligands: one in a η^5-fashion via the C_2B_3-bonding face and the other via two $\mathbf{R}$–H–B bridges to a neighboring cage. In addition, each diagonal pair of $\mathbf{R}$ metals is bridged by a chloride to give the [($C_2B_4\mathbf{R}$)$_4$Cl$_2$O] core. The ionic nature of the bonding is established by DFT calculations using La$_4$OCl$_2$(2,4-$C_2B_4H_6$)$_4$(OH$_2$)$_4$ as a model compound.

Other types of carborane-based ligands have also been explored. The reaction of Me$_2$Si(C_9H_7)($C_2B_{10}H_{11}$), $NaNH_2$, and $\mathbf{R}Cl_3$ aimed at the synthesis of organolanthanide complexes of the ligand sterically encumbered by the carborane substituent, produced unexpected tri- and

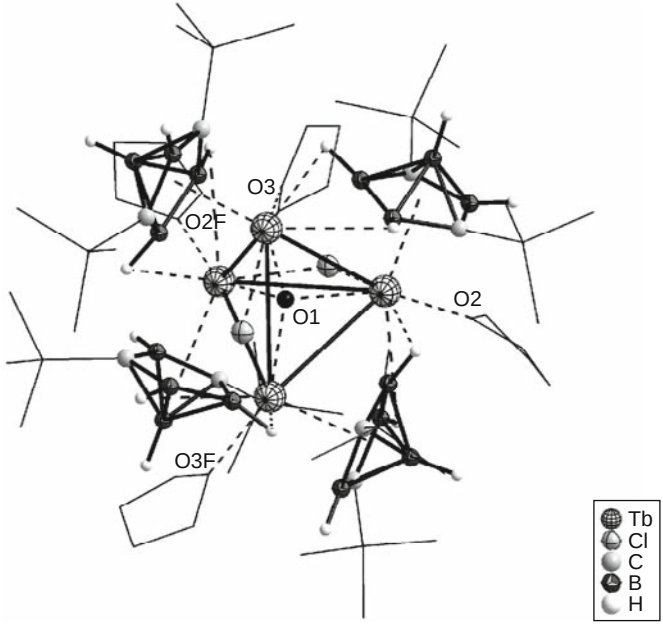

FIGURE 43 Crystal structure of tetranuclear carborane clusters {[η^5-1-Tb(THF)$_n$-2,4-(SiMe$_3$)$_2$-2,4-$C_2B_4H_4$]$_4$(μ-Cl)$_2$(μ_4-O)} (redrawn after Wang et al., 2003, 2004).

tetranuclear clusters featuring coordination by some carborane-less organic ligands. It appeared that the Si–C(cage) bond is broken, and it is reasonable to suggest that excess $NaNH_2$, serving as both base and nucleophile in the reactions, deprotonates the acidic proton of the indenyl group and then attacks the Si atom to afford the intermediate $(C_9H_6)SiMe_2NH_2^-$. The latter reacts further with excess $NaNH_2$ to generate the new ligands $(C_9H_6)SiMe_2NH^{2-}$, $\{(C_9H_6)SiMe_2\}_2N^{3-}$, $Me_2Si(NH)_2^{2-}$, and NH^{2-}. These newly formed ligands then react with $\mathbf{R}Cl_3$ to give three different classes of lanthanide clusters, depending on the reaction conditions.

The first type of clusters have the general formula $[\{(\eta^5\text{-}\mu_2\text{-}C_9H_6SiMe_2NH)\mathbf{R}\}_2(\mu_3\text{-}Cl)(THF)]_2(\mu_4\text{-}NH)$ (Xie et al., 1999). They are the first examples of organometallic clusters containing a central μ_4-imido group. Using the Er cluster as a representative, the structure shown in Figure 44 reveals that the compound contains a butterfly arrangement of four metals which are connected by four doubly bridging μ_2-NHSi-Me_2(indenyl) units over the edges, by two triply bridging μ_3-Cl atoms

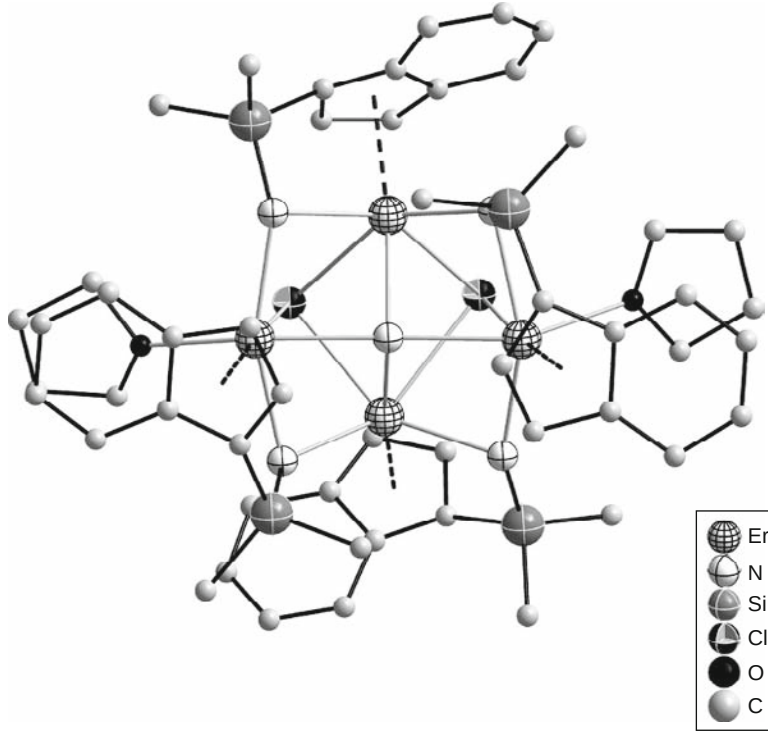

FIGURE 44 Crystal structure of $[\{(\eta^5\text{-}\mu_2\text{-}C_9H_6SiMe_2NH)Er\}_2(\mu_3\text{-}Cl)(THF)]_2(\mu_4\text{-}NH)$ (redrawn after Xie et al., 1999).

spanning two triangular sets of Er_3 of the butterfly-shaped core, and by a quadruply bridging μ_4-NH group located on the crystallographic twofold axis. The coordination sphere around each metal is completed by either bonding to one indenyl in a η^5-fashion or bonding to both η^5-indenyl and one THF molecule. The coordination geometry may be best described as a distorted octahedron.

The second type of clusters, also tetranuclear, with the general formula $[\{(\eta^5\text{-}\mu_2\text{-}C_9H_6SiMe_2)_2N\}(\mu_2\text{-}NH_2)\mathbf{R}_2(THF)_2]_2(\mu_3\text{-}Cl)_2(\mu_2\text{-}Cl)_2$, can be prepared by reacting the aforementioned type I cluster with NaCl. The representative structure ($\mathbf{R} = Gd$) consists of a distorted-tetrahedral arrangement of four Gd from two $[\{(\eta^5\text{-}\mu_2\text{-}C_9H_6SiMe_2)_2N\}(\mu_2\text{-}NH_2)Gd_2(THF)_2]^{2+}$ units that are connected by two doubly bridging μ_2-Cl atoms and two triply bridging μ_3-Cl atoms (Figure 45). Each Gd atom is either η^5-bound to one indenyl group and σ-bound to one oxygen atom, one nitrogen atom, and three chloride atoms or η^5-bound to one indenyl group and σ-bound to one oxygen atom, two nitrogen atoms, and two chloride atoms in a distorted-octahedral geometry.

Trinuclear clusters of general formula $[(\eta^5\text{-}C_9H_6\text{-}SiMe_2)_2N][\mu_2,\mu_2\text{-}Me_2Si(NH)_2](\eta^5\text{-}\mu_2\text{-}C_9H_6SiMe_2NH)(\mu_2\text{-}Cl)_2\mathbf{R}_3(THF)_3$ are the third type of compounds. As shown in Figure 46 ($\mathbf{R} = Er$), three Er and two N atoms are almost coplanar, defining a pentagonal plane with two doubly bridging atoms located above and below this plane. Two kinds of indenyl ligands, $[(C_9H_6)SiMe_2NH]^{2-}$ and $[\{(C_9H_6)SiMe_2\}_2N]^{3-}$, found in the aforementioned two kinds of clusters, respectively, are simultaneously included in this third type of structure. Each metal has a unique coordination

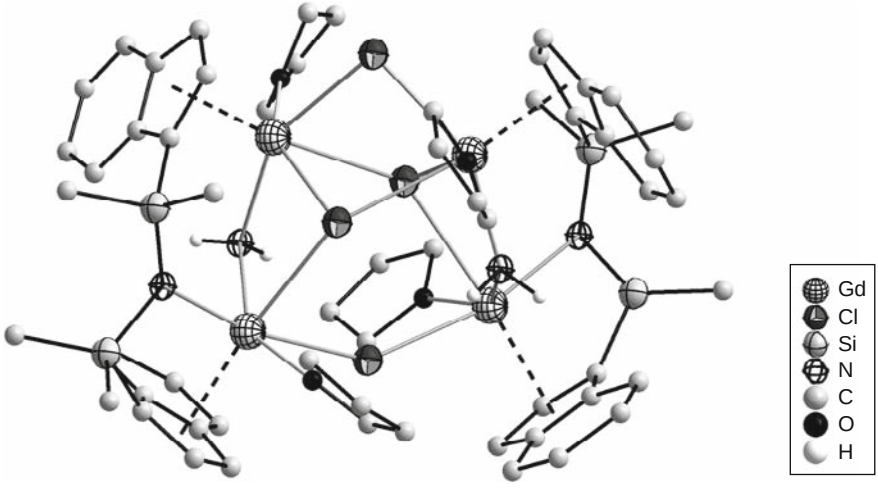

FIGURE 45 Crystal structure of $[\{(\eta^5\text{-}\mu_2\text{-}C_9H_6SiMe_2)_2N\}(\mu_2\text{-}NH_2)Gd_2(THF)_2]_2(\mu_3\text{-}Cl)_2(\mu_2\text{-}Cl)_2$ (redrawn after Xie et al., 1999).

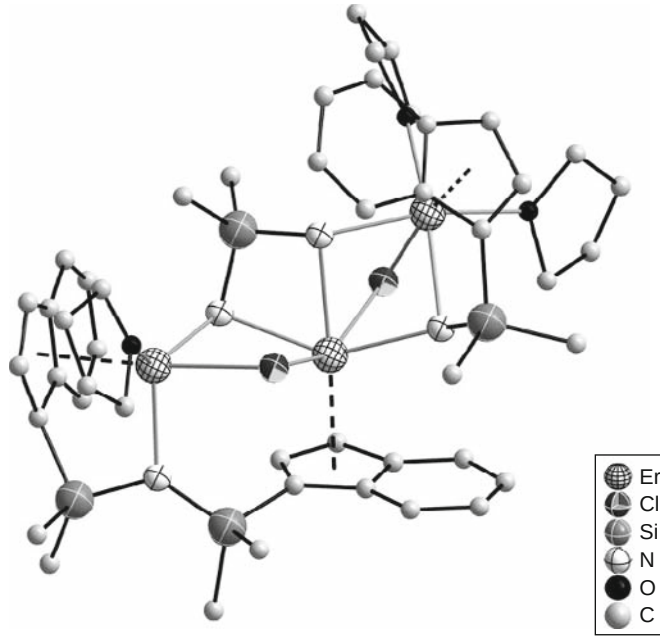

FIGURE 46 Crystal structure of $[(\eta^5\text{-}C_9H_6\text{-}SiMe_2)_2N][\mu_2,\mu_2\text{-}Me_2Si(NH)_2](\eta^5\text{-}\mu_2\text{-}C_9H_6SiMe_2NH)(\mu_2\text{-}Cl)_2Er_3(THF)_3$ (redrawn after Xie et al., 1999).

environment; two of them adopt a distorted-octahedral geometry, while the other adopts a distorted-trigonal bipyramidal geometry.

The reaction between YCl_3 and the lithium salt of 1,3,4,6,7,8-hexahydro-2*H*-pyrimido[1,2-*a*]pyrimidinate (hpp) afforded the tetrametallic cluster $Y_4(hpp)_8Cl_2(\mu_4\text{-O})$ (Coles and Hitchcock, 2004; Figure 47). The oxo group was thought to originate from solvent (THF) degradation or air accidentally admitted into the reaction mixture. The structure consists of a butterfly-like arrangement of yttrium atoms where the Y_4 core is built around the central oxo group. Two symmetrically bridging chlorides are present between opposite pairs of metal atoms, and the coordination sphere of the formally eight-coordinate yttrium is completed by interaction with two bidentate guanidinate anions. The organic ligands display two different types of coordination modes; in the first type, four ligands, each coordinated to a metal atom in a regular and often observed way, η^2-guanidinate. The second type of coordination is previously unknown, with the guanidinate anion involved in an unusual μ,η^2,η^2-bridging mode.

The reaction of the cross-bridged cyclam ligand H_2CBC with divalent ytterbium precursors, $YbR''_2(solvent)_2$ (solvent = THF or Et_2O) produced a trinuclear, cationic μ_3-imido Yb(III) cluster (O'Connor et al., 2006). The edifice is made up of three Yb(III)(CBC) units, arranged into a triangular

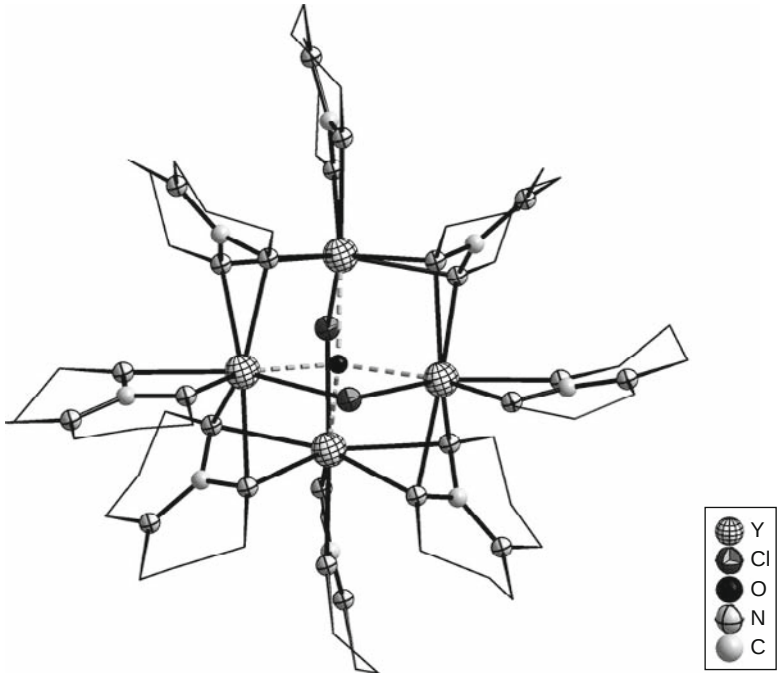

FIGURE 47 Crystal structure of $Y_4(hpp)_8Cl_2(\mu_4\text{-}O)$ (redrawn after Coles and Hitchcock, 2004).

structure via one ligand amido N atom providing the bridge between two neighboring ytterbium centers (Figure 48). The coordination of the trinuclear cluster core is completed by a capping μ_3-NH group. That the cluster can be formed reproducibly in reactions between H_2CBC and $YbR'''_2(\text{solvent})_2$ (solvent = THF or Et_2O) but not when $YbCp^*_2(Et_2O)$ is used suggests that the μ_3-NH cap arises from the cleavage of a R''' group.

The capping μ_3-NH group in the above cluster was the first structurally characterized example of a triply bridging NH in lanthanide chemistry. However, a number of μ_3-NR group-containing lanthanide clusters had been described before (Emel'yanova et al., 1994; Trifonov et al., 1991). The reaction of $\mathbf{R}(C_{10}H_8)(THF)_3$ ($\mathbf{R}$ = Yb, Sm) with PhN=NPh (Ph = C_6H_5) afforded a tetranuclear cluster $\mathbf{R}_4(THF)_4(\mu\text{-}\eta^2\text{:}\eta^2\text{-PhN=NPh})_4(\mu_3\text{-NPh})_2$. Shown in Figure 49 is the structure of the representative Yb cluster. Its four metal atoms are almost coplanar, with two triply bridging NPh group capping two sets of Yb_3 arrays, one above and one below the plane; two of the four metal atoms are shared by the Yb_3 arrays. Each pair of neighboring metal atoms is further bridged by a PhNNPh ligand in a $\mu\text{-}\eta^2\text{:}\eta^2$-bridging/chelating fashion.

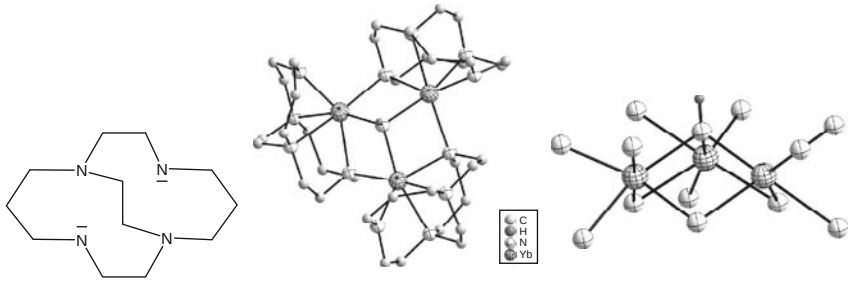

FIGURE 48 Left to right: formula of the ligand CBC, crystal structure of the trinuclear, cationic μ_3-imido Yb(III) cluster $\{[Yb(CBC)]_3(\mu_3\text{-}NH)\}^+$, and atomic connectivity in the cluster core (redrawn after O'Connor et al., 2006).

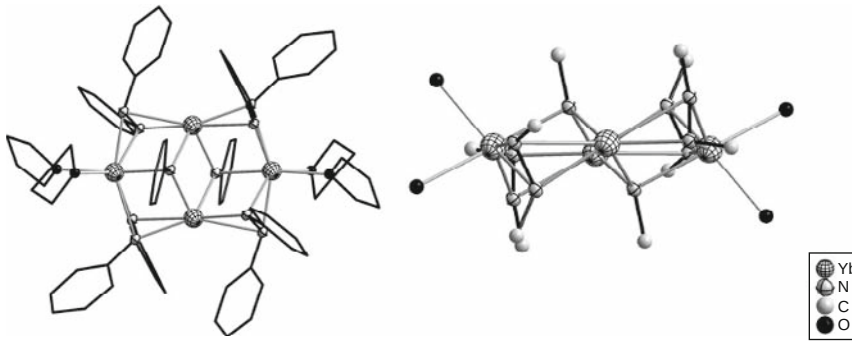

FIGURE 49 Structure of $Yb_4(THF)_4(\mu\text{-}\eta^2\text{:}\eta^2\text{-}PhNNPh)_4(\mu_3\text{-}NPh)_2$ (left) with its tetranuclear core featuring two triply bridging amido ligands (right) (redrawn after Emel'yanova et al., 1994; Trifonov et al., 1991).

Sterically demanding cyclooctatetraenyl ligands have also been utilized to generate cluster aggregates having no precedent in organolanthanide chemistry. The reaction of anhydrous $PrCl_3$ with $Li_2(COT)$ (Figure 50, right; COT = 1,4-bis(trimethylsilyl)cyclooctatetraenyl) in THF solution resulted in a cluster-centered Pr/Li multidecker sandwich complex of composition $[Pr(COT)]_2[Pr_2(COT)_2]_2Li_2(THF)_2Cl_8$, in which a central cube of eight Cl atoms is capped by two $[Pr(COT)]^+$ half-sandwich and two $[Pr_2(COT)_2]^{2+}$ sandwich units as well as two $[Li(THF)]^+$ moieties (Figure 50). The cluster core consists of a Pr_4Li_2 octahedron with the four Pr atoms being in a plane as imposed by symmetry. All eight faces of this octahedron are capped by chlorine atoms (Lorenz et al., 2007).

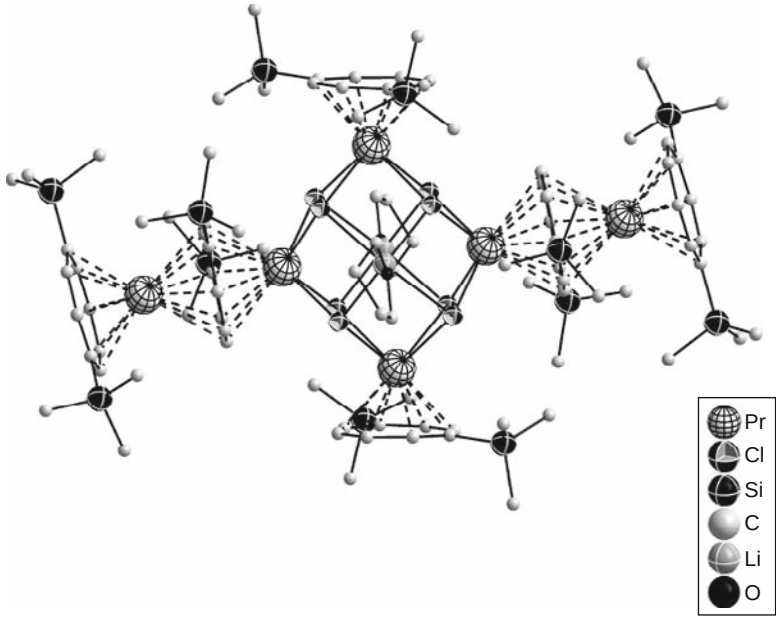

FIGURE 50 Crystal structure of $[Pr(COT)]_2[Pr_2(COT)_2]_2Li_2(THF)_2Cl_8$ (redrawn after Lorenz et al., 2007).

2.3 Lanthanide hydride clusters

One of the most extensively studied classes of organolanthanide clusters is polyhydrido lanthanide clusters. These compounds are of importance, fundamentally for their interesting structural features and practically for their uses in stoichiometric and catalytic reactions. It is necessary to note that a large number of mononuclear lanthanide hydride complexes supported by two generally bulky anionic ancillary ligands have been reported. In stark contrast, the chemistry of di- or polyhydrides have been studied much less, probably due to the synthetic difficulties. However, such compounds are of significant interest because they are expected to possess interesting structures and exhibit chemical reactivity distinctly different from their mononuclear cognates. In such complexes, the hydrido ligands serve to bridge a number of lanthanide atoms constitutive of the cluster core, while the bulky organic ligands provide necessary steric encapsulation of the cluster core. The presence of multiple hydrido ligands in such clusters mandates the use of either a reduced number of organic ancillary ligands or sterically less demanding supporting ligands. Both approaches have been explored with reasonable degree of success in generating polyhydride lanthanide clusters.

2.3.1 Clusters supported by cyclopentadienyl-type ligands

The majority of these lanthanide hydrides rely on the ubiquitous cyclopentadienyl ligand for their stabilization. The chemistry of metallocene-type, biscyclopentadienyl hydrides has long been established. On the other hand, analogous chemistry of systems with the monocyclopentadienyl analogue has not been developed to the same extent. This hiatus is due to the apparent steric unsaturation as well as to synthetic and characterization difficulties when only one Cp-type ligand is present in the molecule. Lanthanide hydrides possessing interesting structural features and displaying unique chemical reactivity may be produced precisely because of this steric unsaturation. It is thus not surprising that the chemistry of lanthanide hydrides containing single Cp-type ligands has received increasing interest in recent years.

2.3.1.1 Clusters supported by simple cyclopentadienyl-type ligands

Assembly of an anionic trinuclear hydride lanthanide species was first reported in the early 1980s (Evans et al., 1982, 1984). One such example is $\{[Cp_2\mathbf{R}H]_3H\}\{Li(THF)_4\}$ ($\mathbf{R} = Y$, Lu). The three metal atoms are bridged by a μ_3-H^- group, and each edge of the Y_3 triangle is bridged by a μ-H ligand. The edge-bridging hydrido groups have been shown to react with methanol, which leads to the corresponding methoxide-bridged triclusters in which three metal atoms are still being connected by a central μ_3-H^- ligand. The structure of the anionic cluster $\{[Cp_2Y(OMe)]_3H\}^-$ is shown in Figure 51 (Evans et al., 1988b).

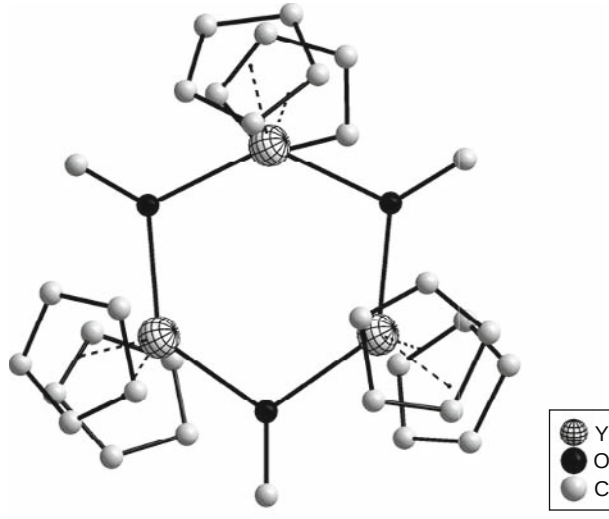

FIGURE 51 Crystal structure of $\{[Cp_2Y(OMe)]_3H\}^-$ (redrawn after Evans et al., 1988b).

The first ''mono(cyclopentadienyl) dihydrido'' complex was reported in 2001 (Hou et al., 2001). This mono-Cp hydride compound, formulated as $[Cp^*Sm(\mu\text{-}H)_2]_6[(\mu\text{-}H)K(THF)_2]_3$ was obtained by reacting the alkyl complex of Sm(II) $[Cp^*SmCH(SiMe_3)_2\{(Cp^*)K(THF)_2\}]_n$ with an excess amount of $PhSiH_3$. The crystal structure (Figure 52) reveals six dihydrido units of $[Cp^*Sm(\mu\text{-}H)_2]$ forming a Sm_6 core with a trigonal prismatic arrangement. This core structure is quite different from the ones found in other hexanuclear lanthanide clusters in which the $\mathbf{R}_6$ core is typically an octahedron. The three square faces of the trigonal prism are each capped by one solvated K^+ ion. There are 15 hydrido ligands in this molecule, one being a body-centered μ_6-hydrido group while the others each cap a metal triangular face in either μ_3-H-Sm_3 or μ_3-H-Sm_2K fashion.

Except for this heterometallic cluster featuring three $[(\mu\text{-}H)K(THF)_2]$ units, reactions using complexes with unsubstituted Cp* ligand have yet to produce any lanthanide-only hydride clusters; in fact, only intractable product mixtures have been obtained. Such observations strongly suggest the critical importance of the ligand in providing sufficient steric protection for the otherwise very reactive lanthanide centers. In fact, almost all reported successful attempts make use of complexes bearing silylene-linked cyclopentadiene-amine or cyclopentadiene-phosphine ligands or cyclopentadienyl ligands sterically hindered by $SiMe_3$, Pr^n, or Bu^t group(s) (Cui et al., 2004; Hou et al., 2007; Li et al., 2006b; Luo and Hou, 2007; Luo et al., 2005; Shima and Hou, 2006; Tardif et al., 2003a).

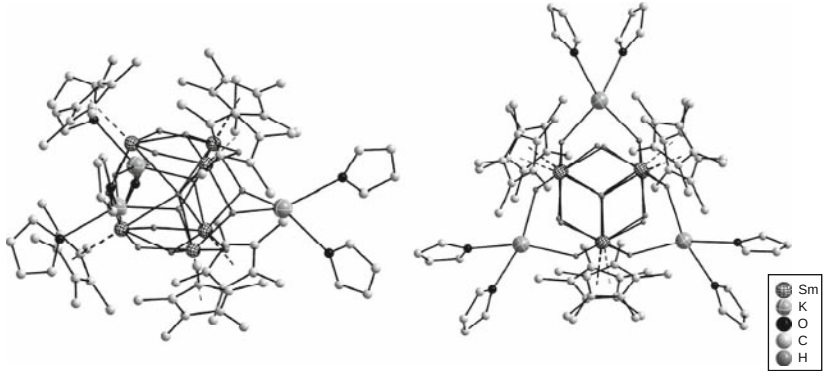

FIGURE 52 Two different views of the crystal structure of $[Cp^*Sm(\mu\text{-}H)_2]_6[(\mu\text{-}H)K(THF)_2]_3$ (redrawn after Hou et al., 2001).

2.3.1.2 Clusters with cyclopentadienyl ligands sterically hindered by noncoordinating group(s)

Hydrido clusters of this type are isolated by reacting bis-alkyl lanthanide complexes bearing a cyclopentadienyl ligand sterically hindered by a $-SiMe_3$ substituent or other bulky and noncoordinating substituents (Hou et al., 2007; Figure 53).

The modified Cp ligand $C_5Me_4SiMe_3$ (Cp′) has been used extensively for the preparation of lanthanide hydride clusters. The crystal structure of one such example, $[Y_4H_8Cp_4'(THF)]$, is shown in Figure 54 (Cui et al., 2004; Luo et al., 2005). The existence and location of the hydrido ligands have been unambiguously established by neutron diffraction studies (Yousufuddin et al., 2008). A four-coordinate hydrogen atom is located in the center of the tetranuclear octahydrido cluster. The core structure

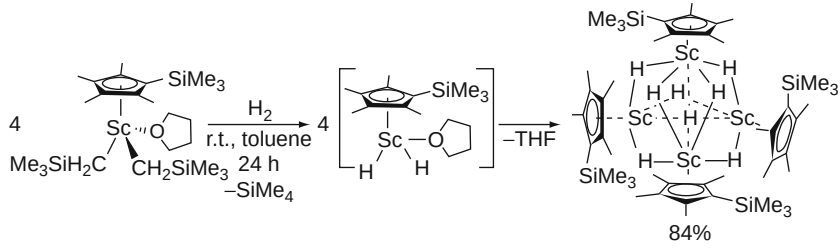

FIGURE 53 Synthesis of a tetranuclear scandium hydride cluster featuring mono-Cp ligands substituted by a $-SiMe_3$ substituent (redrawn after Hou et al., 2007).

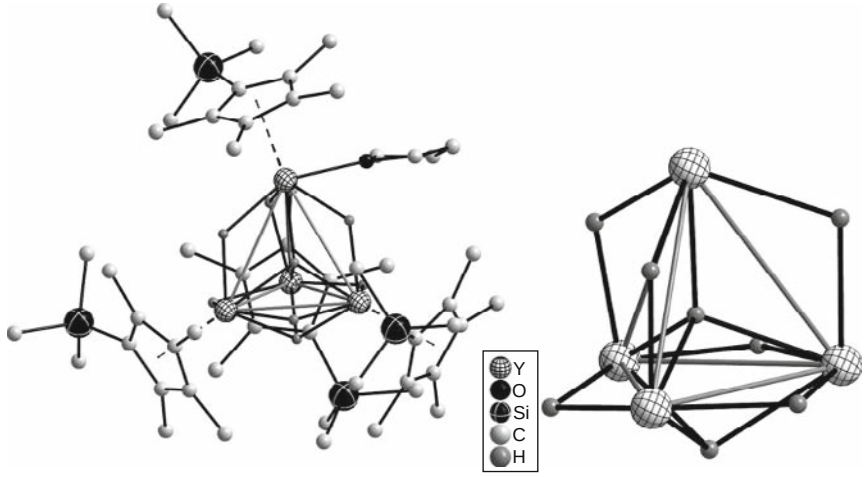

FIGURE 54 Crystal structure of a tetranuclear yttrium hydride cluster (left) as determined by neutron diffraction with its core structure (right) (redrawn after Yousufuddin et al., 2008).

contains one face-capping and six-edging hydrido ligands in addition to the interstitial μ_4-H^- group. At room temperature, only one signal, appearing as a quintet, is observed in the ^1H NMR spectrum, suggesting that all H atoms are equivalent on the NMR time scale and also pointing to the fluxionality of the hydrides.

The unique reactivity of these polyhydrido clusters has been demonstrated. For instance, reactions with substrates containing unsaturated C–C, C–O, and C–N bonds generate corresponding cluster complexes with ligands derived from hydrogenation of the unsaturated bond(s) and the insertion of the newly formed ligand between the involved lanthanide centers (Cui et al., 2004; Li et al., 2006b; Luo et al., 2005). Ring-opening polymerization (ROP) reaction has also been demonstrated wherein the hydrido clusters act as single-component catalysts (Cui et al., 2005a). From these reactions, several new lanthanide clusters distinctly different from the starting polyhydrido species and containing no hydrido ligands have been isolated. These include the tetraoxo and tetraimido cubane-like clusters. The crystal structures of $[Cp'Lu(\mu_3\text{-}O)]_4$ (Shima and Hou, 2006) and $[Cp'Y(\mu_3\text{-}NCH_2Ph)]_4$ (Cui et al., 2004) are shown in Figure 55. Both structures are quite regular, featuring four units of (Cp′**R**) and four triply bridging oxo or imido ligands occupying the alternate vertices of a cube.

Further reactions of the imido cluster complexes with nitriles are possible. Depending on the nature of the organonitriles, either mixed imido clusters are formed or amidinate complexes are produced as a result of nucleophilic addition of the **R**–N (**R** = Lu, Y) imido unit to a C–N triple bond, as shown in Figure 56 (Cui et al., 2005b).

Cationic lanthanide hydrido clusters have also been synthesized by treating the neutral polyhydrido clusters with $Ph_3CB(C_6F_5)_4$ (Li et al., 2006b). The structures of two such complexes are illustrated in Figure 57.

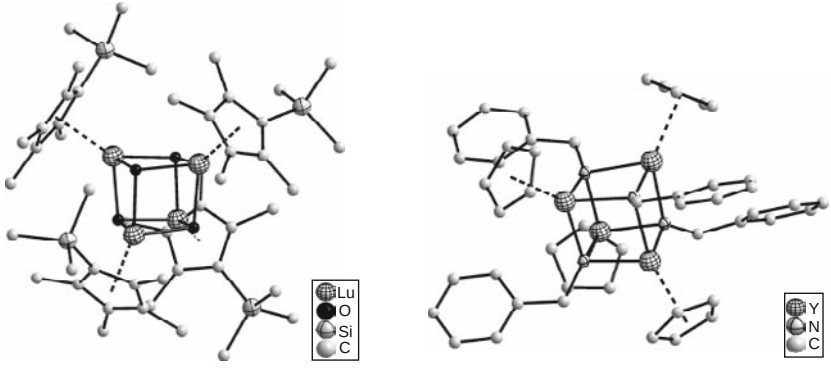

FIGURE 55 Crystal structures of $[Cp'Lu(\mu_3\text{-}O)]_4$ (left) and $[Cp'Y(\mu_3\text{-}NCH_2Ph)]_4$ (right) featuring a triply bridging oxo and imido ligand, respectively (redrawn after Cui et al., 2004; Shima and Hou, 2006).

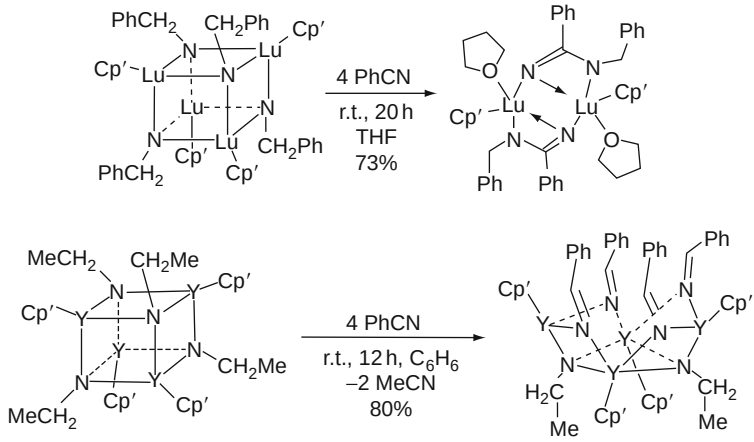

FIGURE 56 Different reactivity of tetranuclear rare-earth imido clusters toward phenylnitrile (redrawn after Cui et al., 2005b).

In stark contrast to the reactivity of the starting neutral cluster toward styrene, which leads to the insertion of the substrate and formation of a single product of **R**-H addition, these cationic clusters are active catalysts for syndiospecific polymerization of styrene and the regio- and stereoselective *cis*-1,4-polymerization of cyclohexyldiene.

Yet another lanthanide hydride cluster with a Cp ligand sterically hindered by noncoordinating substituent(s) is $[Lu_4(1,3\text{-}C_5H_3Bu^t_2)_4H_4][AlH_4(Et_2O)]_2[AlH_4]_2$ (Knjazhanski et al., 1991) the structure of which is shown in Figure 58.

2.3.1.3 Clusters bearing silylene-linked cyclopentadiene-amine or cyclopentadiene-phosphine ligands

Coordination by both the cyclopentadienyl ring and the amine or phosphine moieties are observed for this ligand type of ligands. The reaction between $PhSiH_3$ or H_2 and the lanthanide alkyl complexes with such ligands is used for the general preparation of their hydride complexes. One such reaction affording a tetranuclear hydride cluster, $[(C_5Me_4SiMe_2PC_6H_{11})_4Y_4(\mu_3\text{-}H)_2(\mu_2\text{-}H)_2]$ (Hou, 2003; Tardif et al., 2003b), is shown as a representative example in Figure 59. This particular tetrahydrido lanthanide cluster is essentially insoluble in all common organic solvents, indicating the unusual robustness of the cluster core. In comparison with conventional lanthanide metallocenes or Cp-free analogues, the interesting structures and properties of these cluster compounds attest both to the unique coordination environment such functionalized Cp ligands are able to provide and to the implications associated with such bonding interaction generated by the Cp ring and the ring-bound amido and phosphido functionalities.

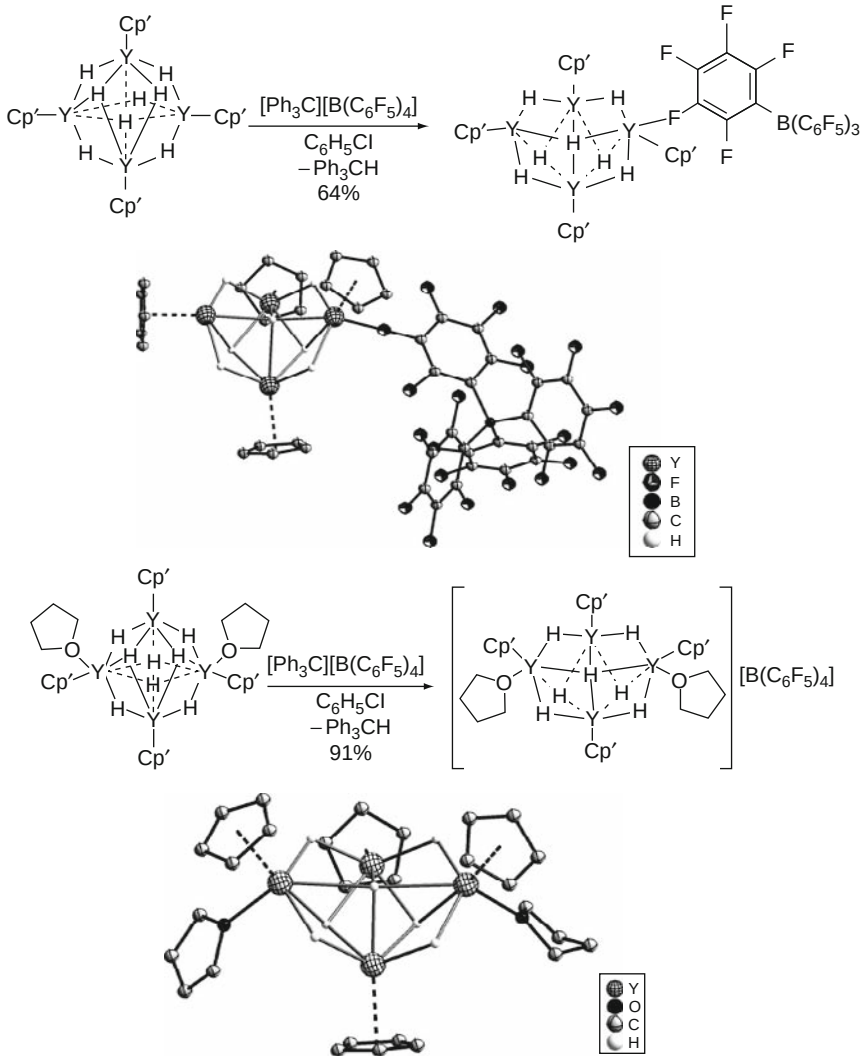

FIGURE 57 Syntheses and crystal structures of two cationic polyhydrido clusters (redrawn after Li et al., 2006b).

2.3.2 Clusters supported by non-Cp ancillary ligands

Organolanthanide chemistry, including hydride clusters, has been dominated by complexes with metallocene and half-sandwich ligand frameworks, as clearly reflected by the discussion above. However, compounds based on nonmetallocene ligand scaffolds have gained recent interest, largely due to the desire to identify new structural patterns and to make

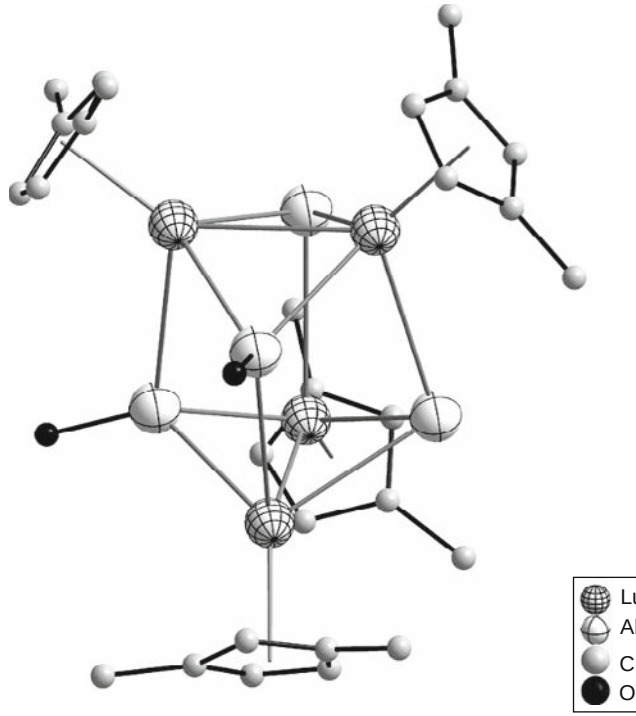

FIGURE 58 Crystal structure of $[Lu_4(1,3\text{-}C_5H_3Bu^t_2)_4H_4][AlH_4(Et_2O)]_2[AlH_4]_2$ featuring a lanthanide atom bridging aluminum hydrido ligands (redrawn after Knjazhanski et al., 1991).

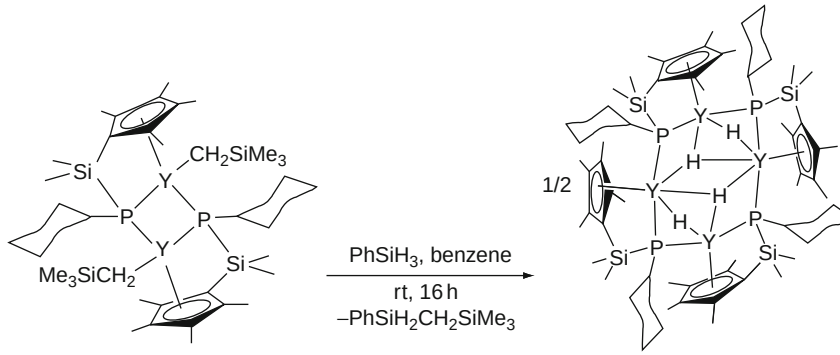

FIGURE 59 Synthesis of a tetranuclear yttrium hydride cluster featuring mono-Cp ligands fitted with a silicon-linked, metal-coordinating phosphine group (redrawn after Hou, 2003; Tardif et al., 2003b).

use of the potential unique reactivity of such new compounds for initiating chemical transformations, in particular as catalysts (O'Connor et al., 2006). Nevertheless, developing hydride complexes with non-Cp ligands is not straightforward. Difficulties lie mainly in the stabilization of the ligand sphere as intramolecular ligand fluxionality and intermolecular scrambling are frequently experienced due to the relatively large size of the lanthanide ions and their highly electropositive electronic character.

Amongst the limited number of successful examples that have been reported in this context are the anionic nitrogen-based amidinate and guanidinate systems. For example, a trinuclear yttrium hydride cluster, $[Y_3\{(ArPr^i_2NH(CH_2)_2N(ArPr^i_2)\}_2\{(ArPr^i_2)N(CH_2)_2N(ArPr^i_2)\}(\mu\text{-}H)_3(\mu_3\text{-}H)_2(THF)]$ was obtained by the hydrogenolysis of the *in situ* generated alkyl complex $[Y\{(ArPr^i_2)NH(CH_2)_2N(ArPr^i_2)\}(R'')(THF)]$ wherein $\{(ArPr^i_2)N(CH_2)_2N(ArPr^i_2)\}^{2-}$ ($ArPr^i_2 = 2,6\text{-}C_6H_3Pr^i_2$) is a chelating diamide ligand (Avent et al., 2004). Crystallographic analysis establishes the cluster core as being a trigonal bipyramid with its two axial positions occupied by two μ_3-H^- ligands and each of the three vertices of the trigonal metallic plane being bridged by a μ-H^- ligand (Figure 60).

Lanthanide hydride clusters have also been obtained with other N-based polydentate ligands. For instance, trinuclear hydride clusters of Y(III), Ho(III), and Lu(III) have been isolated with 1,4,7-trimethyl-1,4,7,10-tetraazacyclododecane, a monoanionic cyclen-type ancillary ligand, and structurally characterized (Ohashi et al., 2008). The crystal structure of the representative Y(III) cluster is shown in Figure 61. Each of the yttrium centers is octacoordinate, bonded to four nitrogen atoms of the macrocyclic ligand and four bridging hydrides to adopt a square-antiprism coordination geometry. Scrambling experiments using two different hydride clusters did not lead to the formation of any mixed-metal hydride clusters, suggesting that the trinuclear framework maintains its structural integrity in solution.

Amidopyridinate ligands also lead to the assembly and stabilization of lanthanide hydride clusters. The reaction of $[Ap\mathbf{R}(CH_2SiMe_3)_2(THF)]$ ($\mathbf{R} = Y$, Lu; Ap = (2,6-diisopropylphenyl)[6-(2,4,6-triisopropylphenyl) pyridin-2-yl]aminate) with either $PhSiH_3$ or H_2 afforded trinuclear alkyl-hydrido clusters $[(Ap\mathbf{R})_3(\mu_2\text{-}H)_3(\mu_3\text{-}H)_2(CH_2SiMe_3)(THF)_2]$ (Lyubov et al., 2008).

The trimeric structure of the yttrium cluster is shown in Figure 62, where three ApY fragments are bound by three μ_2-H^- and two μ_3-H^- ligands, while the alkyl group remains terminal. The metal hydride core structure is identical to that of the cluster formed using a chelating diamide ligand, as described above. Two of the three yttrium atoms have the same coordination sphere, formed by two nitrogen atoms of Ap ligands, four hydrido ligands, and the oxygen atom of the coordinated THF molecule. The third yttrium atom is unique, featuring the

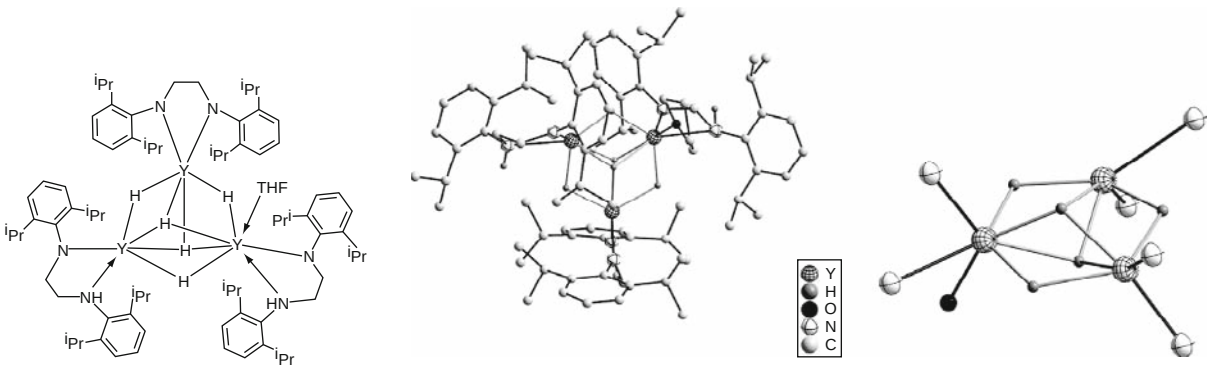

FIGURE 60 Left to right: molecular structure, crystal structure, and core motif of $[Y_3\{Ar'NH(CH_2)_2NAr'\}_2\{Ar'N(CH_2)_2NAr'\}(\mu\text{-}H)_3(\mu_3\text{-}H)_2(THF)]$ (redrawn after Avent et al., 2004).

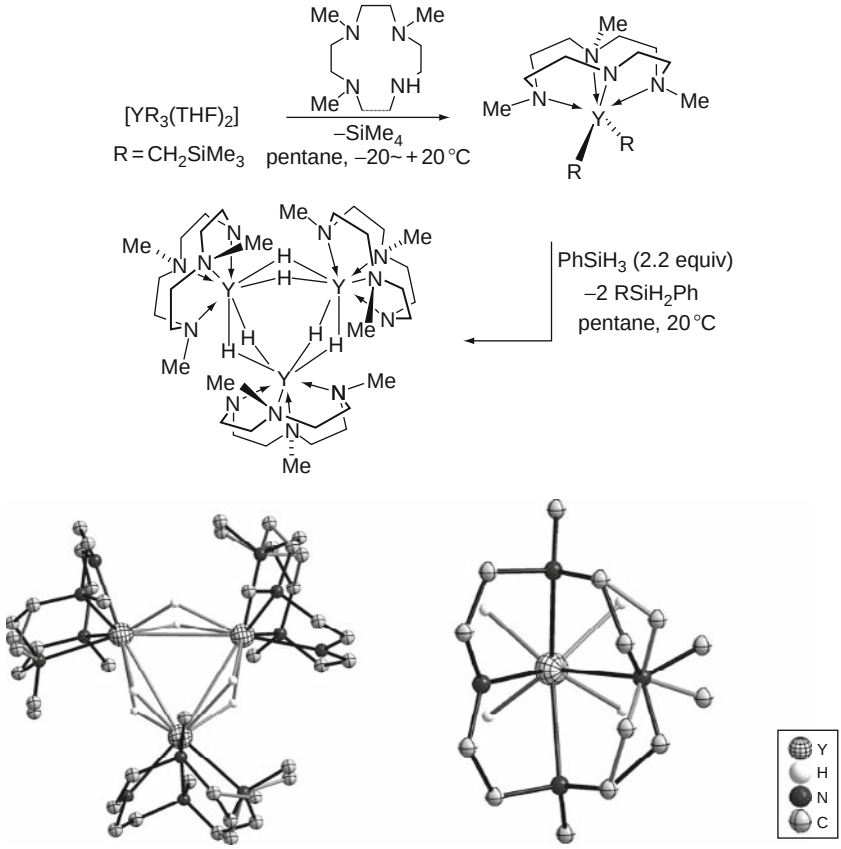

FIGURE 61 Synthesis (top) and crystal structure (bottom left) of trinuclear lanthanide hydride clusters obtained with a monoanionic cyclen-type ancillary ligand. The coordination environment of one particular metal atom is shown on the bottom right (redrawn after Ohashi et al., 2008).

coordination of a CH_2SiMe_3 group instead of one THF molecule, in addition to the common coordination of hydrido and Ap ligands. These species are in fact the first examples of alkyl hydrido lanthanide clusters. Both clusters show moderate activity in catalyzing ethylene polymerization, and ^1H NMR indicates that their trimeric structures are retained in noncoordinating solvents.

An interesting monohydrido tetrasamarium cluster has also been reported in which the dipyrrolide dianion is the organic ancillary ligand (Dubé et al., 2000d). This species was obtained by the reduction of {[$Ph_2C(C_4H_3N)_2$]Sm}Cl ([$Ph_2C(C_4H_3N)_2$]$^{2-}$: diphenylmethyldipyrrolide dianion) with Na in THF under nitrogen atmosphere (Figure 63). The presence of the unexpected hydrido ligand is rationalized as coming from

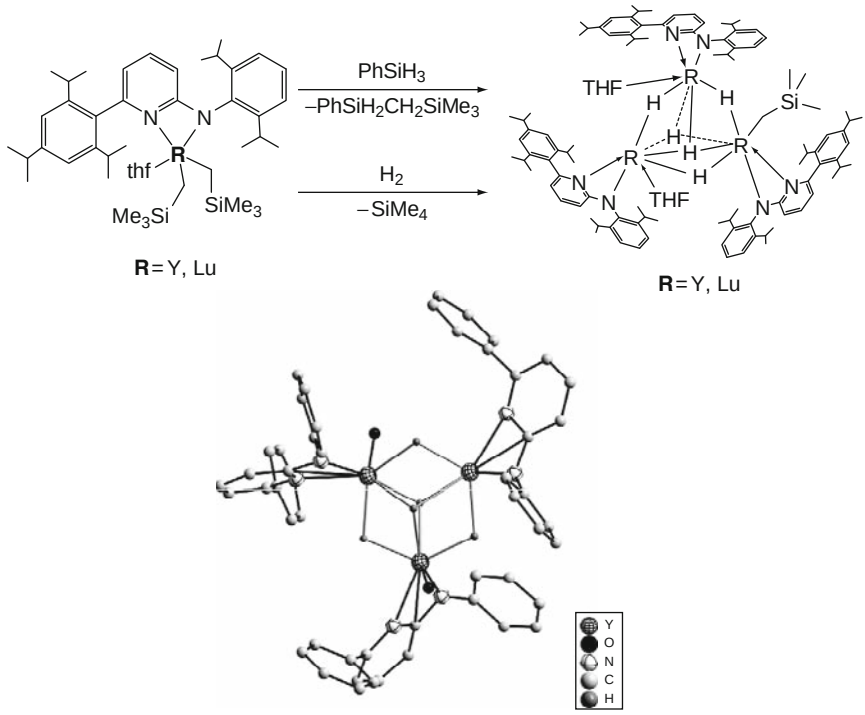

FIGURE 62 Synthesis of trinuclear lanthanide hydride clusters with an amidopyridinate ligand (top). The crystal structure of the Y(III) cluster is shown (bottom) (redrawn after Lyubov et al., 2008).

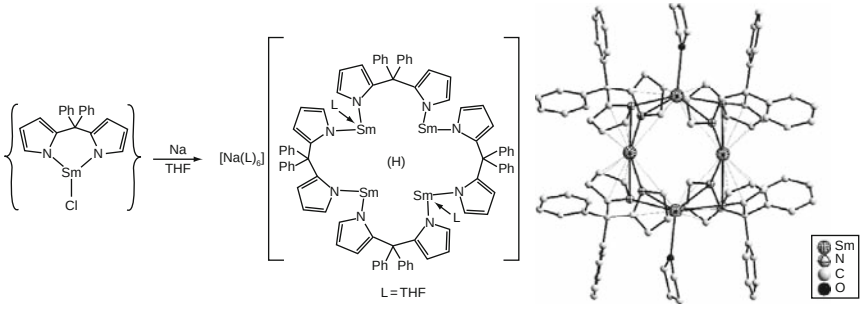

FIGURE 63 Synthesis and crystal structure of a monohydrido tetrasamarium cluster prepared by using dipyrrolide dianions as ligands (redrawn after Dubé et al., 2000d).

NaH, transiently formed during solvent degradation by the Na metal. Surprisingly, neither the anticipated tetranuclear cluster featuring a reduced dinitrogen molecule as ligand, nor species containing a cluster core-building chloro ligand was isolated under such experimental conditions.

2.4 Chalcogenolate and chalcogenide clusters

The chemistry of lanthanide chalcogenides was first stimulated by the synthetic challenge to develop complexes characterized by **R**–E bond (E = S, Se). As in the cases of other lanthanide-containing clusters, almost all the initial discoveries were serendipitous. Some reliable synthetic procedures have since been developed, in which chalcogenido (E^{2-}) or polychalcogenido (E_n^{2-}) ligands are generated *in situ* by the reduction of elemental E with $\mathbf{R}(EPh)_3$. The nature of the cluster compounds are critically dependent on a number of factors, including solvents, the elemental chalcogens, chalcogenolates, oxidation states of the lanthanide salts, the possible use of nonlanthanide reagents. Nevertheless, a number of cluster core motifs have been found to be prevalent in this unique class of lanthanide-containing compounds. Adventitious hydrolysis of lanthanide chalcogenolates/chalcogenides leads to the production of cluster species featuring bridging oxo group(s) in addition to the original chalcogen-based ligands. This chemistry, besides generating many interesting cluster species, has found applications in catalysis and advanced materials research.

Lanthanide clusters featuring chalcogen-containing ligands can be divided into three major types, those containing only chalcogenolates (RE) ligands, those with only (poly)chalcogenido (E^{2-} and E_n^{2-}) ligands, and those containing both or with other nonchalcogen ligands. A recent comprehensive review provides an excellent summary of the preparation, structures, and synthetic applications of lanthanide chalcogenolate and chalcogenide clusters with literature covered up to early 2006 (Li et al., 2006b). Therefore, except for a brief summary of the representative structure types, only clusters that are not collected in this chapter will be discussed. A small number of chalcogen-based ligand-containing cluster compounds are of special note. Although the chalcogenido ligands are not part of the polyhedral cluster core, they are described here because of the distinct feature of these rather diverse and interesting ligands. These include octanuclear clusters of the general formula $[\mathbf{R}_8(DMF)_a(\mu_4\text{-}O)(\mu_3\text{-}OH)_{12}(Se_3)_b(Se_4)_c(Se_5)_d]Cl_e$ (Figure 64, top left: **R** = Eu, Gd, $a = 13$, $b = 1$, $c = d = 2$, $e = 0$; Figure 64, top middle: **R** = Yb, $a = 11$, $b = 0$, $c = d = e = 2$; Figure 64, top right: **R** = Y, $a = 12$, $b = 1$, $c = 0$, $d = 4$, $e = 2$), all possessing a common octanuclear core of $[\mathbf{R}_8(\mu_4\text{-}O)(\mu_3\text{-}OH)_{12}]$

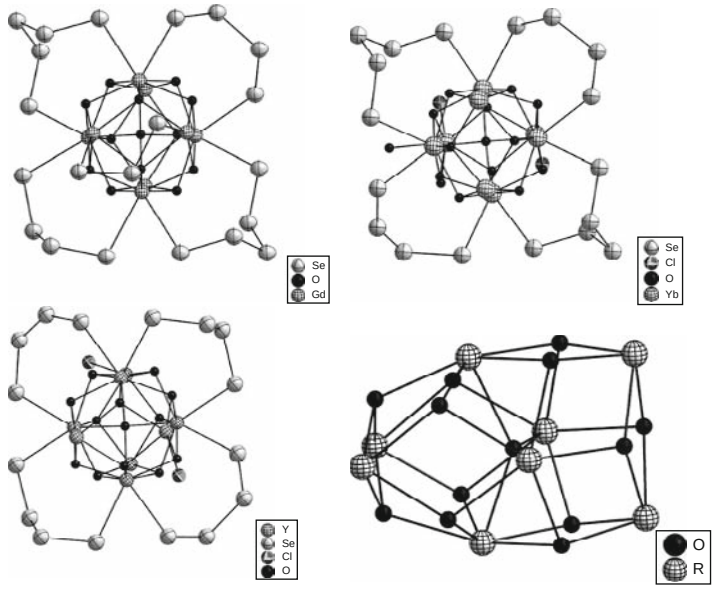

FIGURE 64 Crystal structure of three clusters featuring polyselenido ligands and possessing a common octanuclear core of $[\mathbf{R}_8(\mu_4\text{-O})(\mu_3\text{-OH})_{12}]$ (redrawn after Pernin and Ibers, 1997, 1999).

encapsulated by various (poly)selenido ligands (Pernin and Ibers, 1997, 1999; Figure 64, bottom).

Clusters with nuclearity ranging from 4 to 12 have been reported. The various core motifs are collected in Figure 65. Detailed structural descriptions for clusters with a nuclearity smaller than 10 can be found in a recent review (Li et al., 2006b).

However, a number of cluster species, namely tetranuclear $[\mathrm{Li(THF)_4}][\mathrm{R'''_4}\mathbf{R}_4(\mu_4\text{-SEt})(\mu\text{-SEt})_8]$ (Cheng et al., 2007), hexanuclear $[\mathrm{Cp^*_6Sm_6Se_{11}}]$ (Evans et al., 1994a) and $[\mathrm{Cp^t_6Nd_6Se_{13}}]^-$ ($\mathrm{Cp^t} = \eta^5\text{-}\mathrm{Bu^tC_5H_4}$) (Cheng et al., 2001; Jin et al., 1999), decanuclear $(\mathrm{THF})_{14}\mathbf{R}_{10}\mathrm{S_6(Se_2)_6I_6}$ ($\mathbf{R} = $ Dy, Ho, Er) (Huebner et al., 2005; Kornienko et al., 2005), and dodecanuclear $[(\mathrm{py})_{18}\text{-}\mathrm{Nd_{12}O_6Se_4(Se_2)_4(SePh)_4(Se_2Ph)_2Hg_2(SePh)_4}][(\mathrm{Hg(SePh)_3}]_2$ (py = pyridine) (Banerjee et al., 2007) are either neglected by the recent review or appeared since the review had been published. Their syntheses and salient structural features will therefore be presented here.

A tetranuclear cluster $[\mathrm{Li(THF)_4}][\mathrm{R'''_4}\mathbf{R}_4(\mu_4\text{-SEt})(\mu\text{-SEt})_8]$ was obtained by reacting $\mathrm{R'''_3}\mathbf{R}(\mu\text{-Cl})\mathrm{Li(THF)_3}$ with EtSH (Cheng et al., 2007). The representative anionic cluster of Pr (Figure 66) features a square-like $\mathrm{Pr_4}$ array capped by a μ_4-SEt ligand. Adjacent metal atoms are bridged by a pair of SEt ligands. The existence of a μ_4-SEt ligand is unprecedented in the chemistry of lanthanide chalcogenolate complexes, although

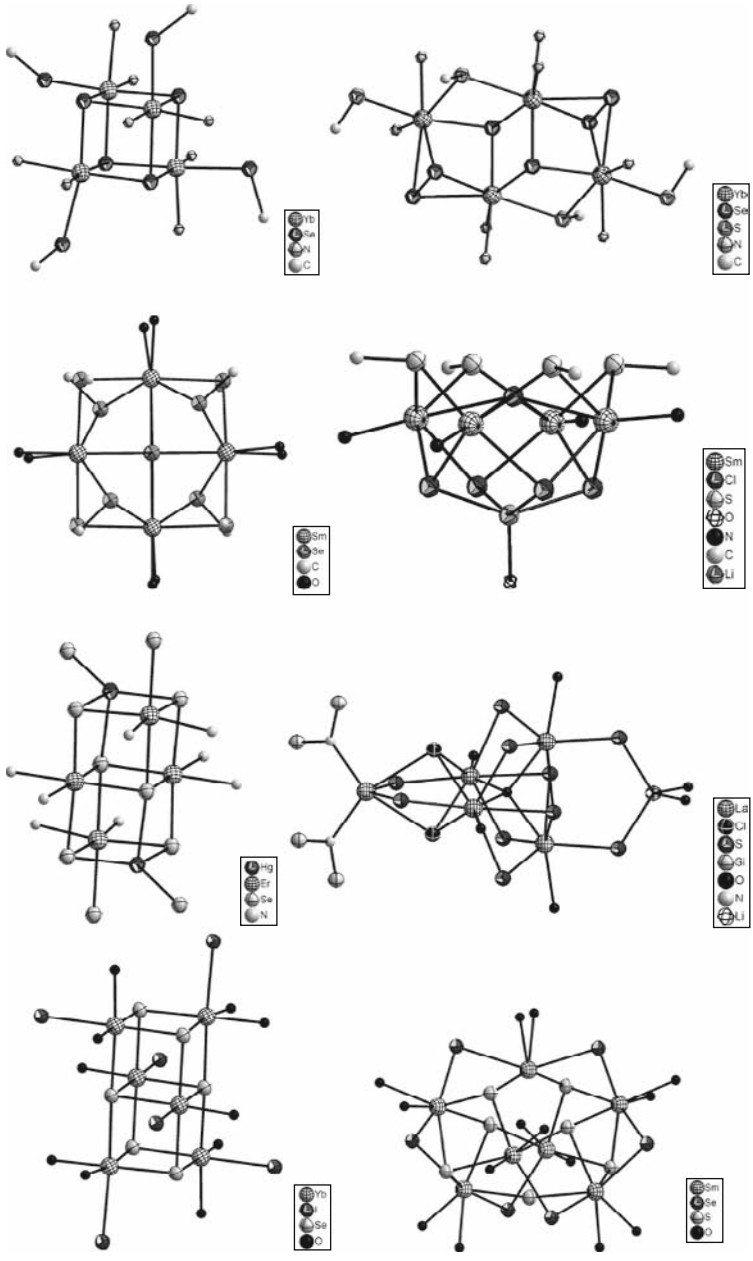

FIGURE 65 (Continued)

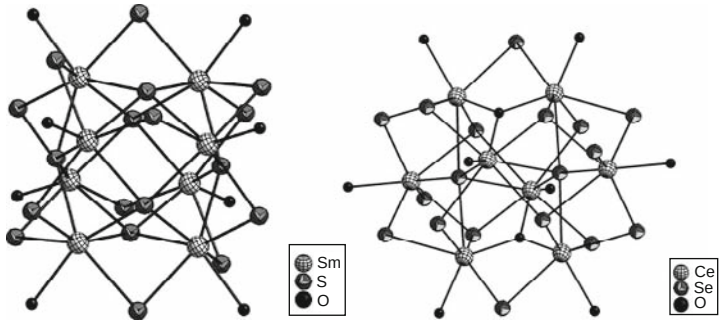

FIGURE 65 Common structural types of lanthanide chalcogenolate and chalcogenide clusters with nuclearity ranging from six to eight (redrawn after Li et al., 2006a).

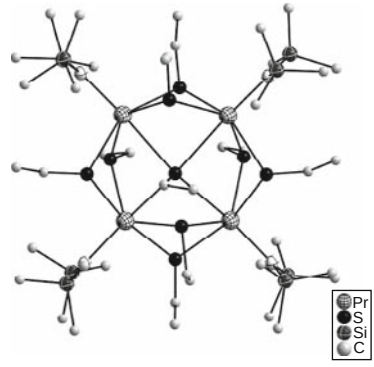

FIGURE 66 Crystal structure of the monoanionic cluster $[R'''_4Pr_4(\mu_4{-}SEt)(\mu{-}SEt)_8]^-$ (redrawn after Cheng et al., 2007).

quadruply bridging chalcogenido ligands in the form of $[\mathbf{R}_4(\mu_4\text{-}E^{2-})]$ (E = S, Se, Te) are commonly found.

The reaction of the same lanthanide starting material with the sterically more hindered benzenethiol afforded an anionic tetranuclear complex $Li[R'''_4(\mu_4\text{-}Cl)Nd_4(\mu\text{-}SPh)_8]$ wherein a μ_4-Cl group rather than a μ_4-SPh as in the example above was found to form a square pyramid with four basal lanthanide atoms (Figure 67). Good catalytic activity of this cluster in the ROP of ε-caprolactone has been demonstrated (Li et al., 2005).

With the even bulkier Bu^{t}SH, the reaction produced dinuclear species containing a diamond-shaped dinuclear core bridged by two μ-SBu^t ligands. The difference in cluster nuclearity can be rationalized in terms of the steric hindrance provided by the thiolate ligands. When a sterically

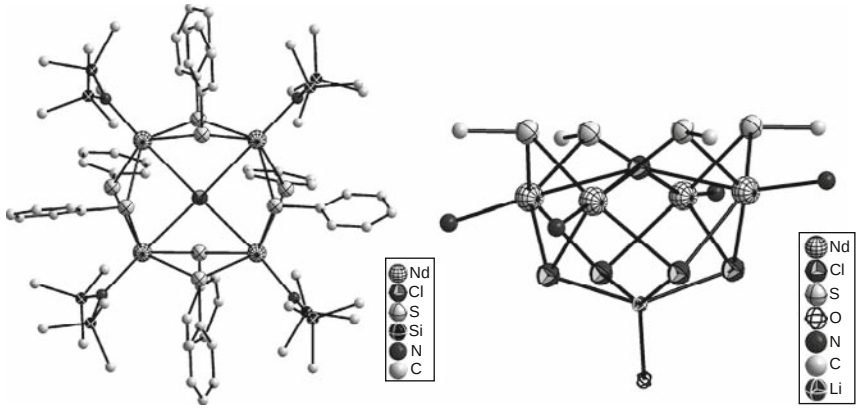

FIGURE 67 Crystal structure of the monoanionic cluster $[R'''_4(\mu_4\text{-Cl})Nd_4(\mu\text{-SPh})_8]^-$ and its core motif (redrawn after Li et al., 2005).

less demanding ligand is used, the not-so well-protected lanthanide center tends to maximize its coordination by aggregation, leading toward the formation of a higher-nuclearity cluster.

The hexanuclear clusters, $[Cp^*_6Sm_6Se_{11}]$ and $[Cp^t_6Nd_6Se_{13}]^-$ ($Cp^t = \eta^5$-$C_5H_4Bu^t$), share a common cluster core of an octahedron of lanthanide atoms centered on one interstitial μ_6-Se atom. The former was obtained unexpectedly from the decomposition of $(Cp^*_2Sm)2(\mu\text{-}\eta^1,\eta^3\text{-}Se_3)(THF)$ in toluene. The mechanism remains unknown (Evans et al., 1994a). Crystal structure determination reveals that two opposite triangular faces of the octahedron are each capped by a μ_3-Se atom, with the central μ_6-Se atom situated at the center of inversion (Figure 68). Charge balancing necessitates the linear Se_3 unit to carry a -4 charge, which is an additional interesting aspect of this unexpected species in addition to its cluster structure. There are four triangular faces that are each capped by a Se_2 bridging unit, with one of its Se atoms coordinating three Sm atoms while the other linking two Sm atoms. Alternatively, the cluster coordination may be summarized as two of the Sm atoms being coordinated with six Se atoms and the other four Sm atoms with five Se atoms, resulting in a distorted-octahedral structure.

The other hexanuclear lanthanide chalcogenido cluster complexes $[Cp^t_6\mathbf{R}_6Se_{13}]^-$ ($\mathbf{R} = Nd$, Jin et al., 1999; $\mathbf{R} = Sm$, Cheng et al., 2001) were obtained from the reaction of a half-sandwich lanthanoid dichloride $[Cp^t\mathbf{R}Cl_2(THF)_2]_2$ with Na_2Se_5. The structure of $[Cp^t_6Nd_6Se_{13}]^-$ is shown in Figure 69. The six Nd atoms form an almost perfect octahedron. The 13 Se atoms are of two different types, one being the central μ_6-Se and the remaining 12 being 6 bridging Se_2 units. In terms of coordination mode, the two Se atoms in each Se_2 unit are of two different kinds, one

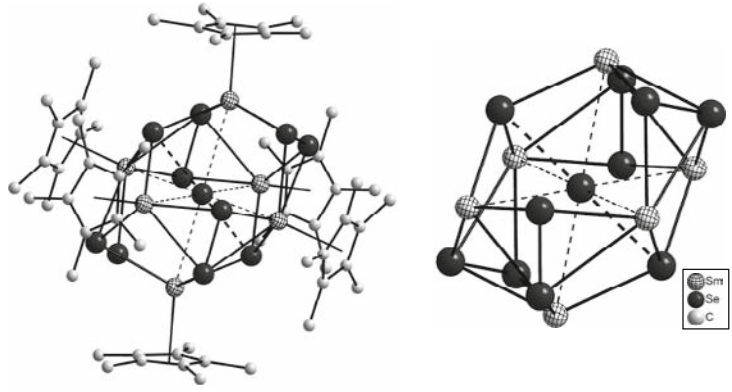

FIGURE 68 Crystal structure of $[Cp^*_6Sm_6Se_{11}]$ (left) and its cluster core motif (right) (redrawn after Evans et al., 1994a).

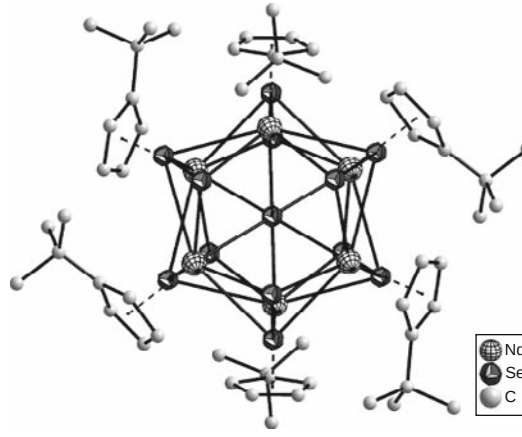

FIGURE 69 Crystal structure of monoanionic cluster $[Cp^t_6Nd_6Se_{13}]^-$ (redrawn after Jin et al., 1999).

coordinating three Nd atoms while the other connecting only two. Each Nd atom is coordinated to six Se atoms: the central μ_6-Se, two units of Se_2, and one Se atom of a third unit Se_2.

Decanuclear clusters $(THF)_{14}\mathbf{R}_{10}S_6(Se_2)_6I_6$ ($\mathbf{R} = $ Dy, Ho, and Er) were obtained from the reaction of $\mathbf{R}I_x(SePh)_{3-x}$ ($\mathbf{R} = $ Dy, Ho) with elemental S/Se (Huebner et al., 2005; Kornienko et al., 2005). The decanuclear cluster core $\mathbf{R}_{10}S_6(Se_2)_6$ may be viewed as being built on the basis of a $\mathbf{R}_6S_6$ double-cubane core, also present in $(py)_{10}Yb_6S_6(SPh)_6$ and $(THF)_{10}Er_6S_6I_6$, with the addition of two $\mathbf{R}_2(Se_2)_3$ units onto opposing rectangular sides of the $\mathbf{R}_6S_6$ fragment (Figure 70). The formation of $\mathbf{R}_2Se_6$ encapsulates

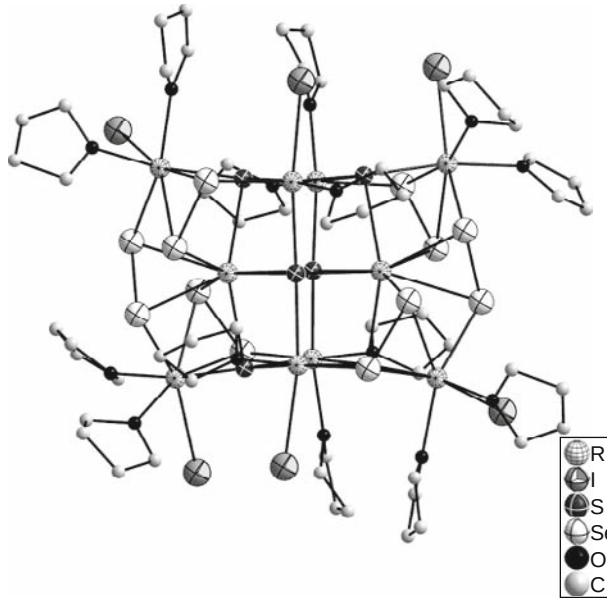

FIGURE 70 Crystal structure of $(THF)_{14}\mathbf{R}_{10}S_6(Se_2)_6I_6$ (**R** = Dy, Ho, and Er) (redrawn after Huebner et al., 2005; Kornienko et al., 2005).

completely the two central **R**s with chalcogen atoms (four S and four Se atoms), making these two lanthanide ions free of coordination by THF or iodido ligands. In fact, these are the only examples of lanthanide clusters with ''internal'' RE ions hitherto known. This feature resembles solid-state RE materials, and because of the protection of the excited metal ion from vibronic quenching by high-energy oscillators such as O–H or C–H, these cluster complexes are highly emissive.

A dodecanuclear neodymium cluster $[(py)_{18}Nd_{12}O_6Se_4(Se_2)_4(SePh)_4(Se_2Ph)_2Hg_2(SePh)_4][(Hg(SePh)_3]_2$ was obtained by reacting $Nd(SePh)_3$ with SeO_2 and Hg in pyridine (Banerjee et al., 2007). The dodecanuclear lanthanide oxide core $Nd_{12}O_6$ can be viewed as six $Nd_4(\mu_4\text{-O})$ tetrahedra arranged into a compact structure that closely resembles the solid-state structure of Nd_2O_3 (Figure 71). Each of the four peripheral tetrahedra has two neighbors, while each of the two central ions has three neighbors of the same kind. Fused adjacent $Nd_4(\mu_4\text{-O})$ tetrahedra result in shared Nd. . .Nd edges. The other ligands, including Se, Se_2, SePh, Se_2Ph, and HgSePh, surround the oxo core. Near IR emission was observed and rationalized in terms of the low-energy phonon environment provided by the soft, heavy Se-based ligands. However, the presence of C–H oscillators in SePh or py ligands and the intimate aggregation of Nd atoms in the solid state may still quench the lanthanide-based luminescence.

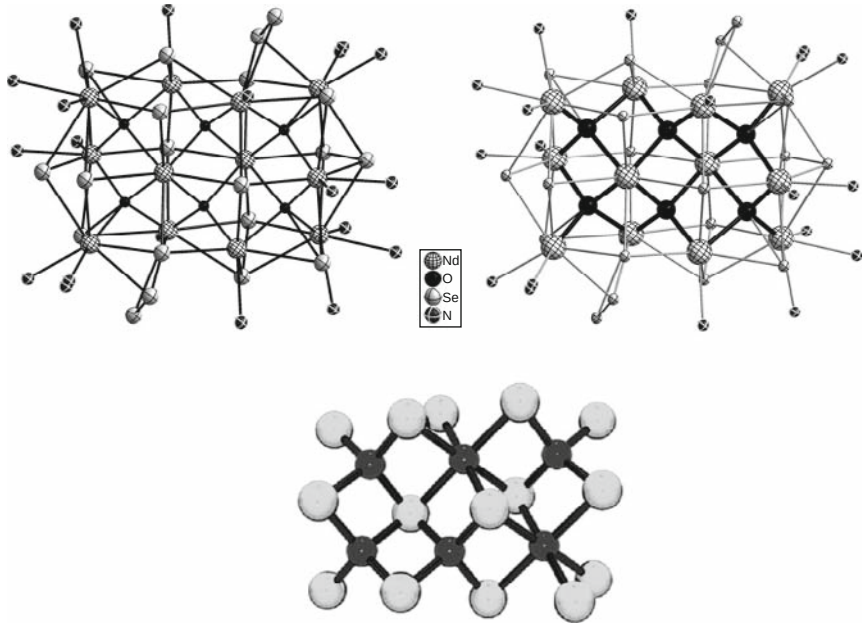

FIGURE 71 Crystal structure of $[(py)_{18}Nd_{12}O_6Se_4(Se_2)_4(SePh)_4(Se_2Ph)_2Hg_2(SePh)_4]^{2+}$ (upper left), its core motif (upper right), and the structure of solid-state Nd_2O_3 (bottom—bigger and lighter sphere: Nd and smaller and darker sphere: O) (redrawn after Banerjee et al., 2007).

The potential uses of lanthanide clusters heavily coordinated with chalcogen-based ligands have been summarized in a recent review (Riman et al., 2005). The term ''molecular minerals'' is coined for materials containing such lanthanide clusters generated by solution processing techniques to emphasize the difference from and advantages over the traditional ceramic materials that typically require high-temperature processing. The key differences include their monodispersity and well-defined molecular structures and compositions. The encapsulation with organic ligands renders them soluble in conventional organic solvents as well as in polymer matrices, thus facilitating the preparation of transparent molecular mineral nanocomposites in forms of bulk polymers, fibers, and films. The luminescent properties of materials prepared as such match or exceed those of ceramics, glasses, and nanomaterials, with parameters such as emission wavelength, emission intensity, and quantum efficiency of these materials covering a wide range previously inaccessible.

2.5 Clusters featuring dinitrogen-derived ligands

Reduction of dinitrogen molecule by divalent lanthanide complexes has been a popular subject in coordination and organometallic chemistry of the lanthanide elements. In the course of these studies, a large number of polynuclear lanthanide clusters featuring a core of lanthanide atoms organized around a dinitrogen unit have been obtained and structurally characterized.

One of the most extensively studied ligands is the dipyrrolide dianion. Depending on the substituents on the C atom that links the two pyrrole moieties, ligands with varying degrees of steric hindrance can be obtained which, in turn, affects the coordination of the lanthanide atoms and the overall structure of the resulting cluster compounds. These ligands are structurally and electronically similar to *ansa*-cyclopentadienyl ligands, and their use in lanthanide coordination chemistry is thus not surprising. However, the presence of deprotonated N atoms in the pyrrolide rings allows additional σ-bonding interactions that proved to be important in assembling polynuclear structures. This ligand system has been exploited extensively by Gambarotta and coworkers for the production of cluster complexes of divalent, trivalent, or mixed-valence samarium, in particular with the aim of promoting dinitrogen reduction.

The synthesis takes two general approaches. In the first method, a dipyrrolide ligand reacts directly with a divalent samarium complex featuring either simple iodo ligands combined with coordinated solvent molecules (typically THF) or sterically hindered bis(trimethylsilo)amido ligands. The second approach is a two-step process, the formation of a trivalent samarium complex with a chosen dipyrrolide ligand, followed by reduction in an inert atmosphere, either dinitrogen or argon, using alkali metals such Li, Na, or K. It has been found that the nature of the product, in most cases cluster complexes, depends on a number of factors, including the aforementioned synthetic methods, the starting metal complexes, the reducing reagents, the ''inert'' atmosphere, and the solvents. The influence of such parameters is reflected by differences in cluster nuclearity, the formal oxidation state of the metal ions, possible incorporation of oxo, hydrido, or halo ligands, coordination of dinitrogen, and reactivity toward cluster degradation. The results collected in Table 1 clearly indicate the rich, yet complex, chemistry of this particular class of ligands.

The cluster nuclearity ranges from three to eight, with four being the most frequently observed. From the reaction of $[SmI_2(THF)_2]$ with $[Ph_2C(C_4H_3N)_2]^{2-}$ under argon atmosphere, a trinuclear, iodide-containing cationic cluster $[\{[\mu\text{-}Ph_2C(\eta^1{:}\eta^5\text{-}C_4H_3N)_2]_2[Sm(THF)]_3\}(\mu_3\text{-}I)]^+$ was obtained as a counterion of the pentanuclear anionic cluster $[\{[\mu\text{-}Ph_2C(\eta^1{:}\eta^5\text{-}C_4H_3N)_2]_2Sm\}_5(\mu_5\text{-}I)]^-$ (Figure 72) that also contains an iodo ligand (Dubé et al., 1999; Table 1, entry 1). An anionic iodo pentanuclear cluster featuring

TABLE 1 Summary of cluster complexes with dipyrrolide ligands under different reaction conditions

Substituents on the backbone of the dipyrrolide ligands (R/R′)	Sm(II)/(III) starting material	Combination of protecting gas and reducing agent (where appropriate)	Cluster product	References	Entry
Ph/Ph	$SmI_2(THF)_2$	Argon	$[Sm_3(\mu_3\text{-}I)]^+$, $[Sm_5(\mu_5\text{-}I)]^-$	Dubé et al. (1999)	1
Ph/Ph	$SmI_2(THF)_2$	Nitrogen	$Sm_4\text{-}N_2$	Dubé et al. (1999)	2
Ph/Me	$SmI_2(THF)_2$	Argon or nitrogen	$[Sm_5(\mu_5\text{-}I)]^-$	Dubé et al. (2000a)	3
Ph/Ph	$SmCl_3(THF)_2$	Argon/Li, Na	$[Sm_8(\mu_4\text{-}Li)]^{2-}$, $[Sm_8(\mu_4\text{-}Na)]^-$	Dubé et al. (2000c)	4
Ph/Ph	$SmCl_3(THF)_2$	Nitrogen/Na	$[Sm_4(\mu_4\text{-}H)]$	Dubé et al. (2000d)	5
Ph/Ph	$SmCl_3(THF)_2$	Nitrogen/K	$[Sm_4(\mu_4\text{-}Cl)]$	Dubé et al. (1999)	6
$1/2(CH_2)_5$ (cyclohexyl)	$SmCl_3(THF)_2$	Nitrogen/Na	$Sm_4\text{-}N_2(Na\cdot THF)_2$	Dubé et al. (2000d)	7
$1/2(CH_2)_5$ (cyclohexyl)	$R_2'''Sm(THF)_2$	Nitrogen	$Sm_4\text{-}N_2$	Dubé et al. (2000d)	8
$1/2(CH_2)_5$ (cyclohexyl)	$SmCl_3(THF)_2$	Argon/Na	$[Sm_4(\mu_2\text{-}O)]$	Dubé et al. (2000a)	9
Ph/Ph	$R_2'''Sm(THF)_2$	Argon	Sm_6	Ganesan et al. (2001)	10
$1/2(CH_2)_5$ (cyclohexyl)	$R_2'''Sm(THF)_2$	Argon	Sm_8	Ganesan et al. (2001)	11
$1/2(CH_2)_5$ (cyclohexyl)	$SmI_2(THF)_2$	Argon	$[Sm_4(\mu_2\text{-}O)]$	Dubé et al. (2000a)	12

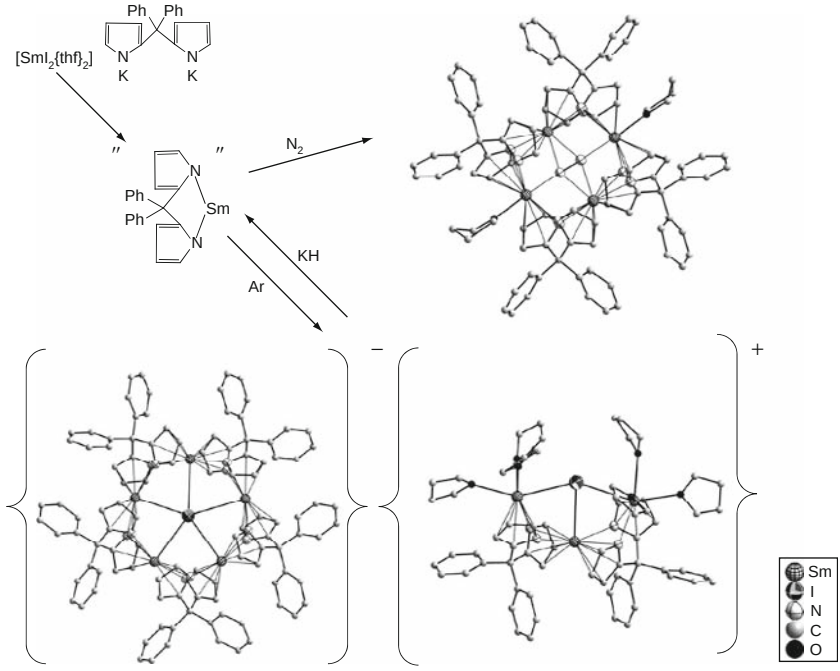

FIGURE 72 Syntheses and crystal structures of double-cluster complex formulated as $[\{[\mu\text{-}Ph_2C(\eta^1{:}\eta^5\text{-}C_4H_3N)_2]_2[Sm(THF)]_3\}(\mu_3\text{-}I)]^+[\{[\mu\text{-}Ph_2C(\eta^1{:}\eta^5\text{-}C_4H_3N)_2]_2Sm\}_5(\mu_5\text{-}I)]^-$ and the tetrasamarium cluster containing a N_2 ligand resulting from 4-e reduction of dinitrogen (redrawn after Dubé et al., 1999).

the same core structure was also obtained from the reaction of $[SmI_2(THF)_2]$ with methylphenyl dipyrromethanyl dianion under either argon or nitrogen (Dubé et al., 2000a; Table 1, entry 3).

The cationic cluster consists of three samarium atoms bridged by one nearly coplanar iodine atom which adopts a distorted ''T-shape'' geometry. The three samarium atoms are also bridged by two diphenylmethyldipyrrolide dianions. The five samarium atoms of the anionic cluster form a nearly perfect pentagon with a central and coplanar iodine atom. Each set of adjacent samarium atoms is bridged by one ligand with the pyrrole rings being in turn σ-bonded to one samarium and π-bonded to a second. The overall effect is the establishment of a samarocene-type environment about each samarium atom which is defined by two σ-bonded and two π-bonded pyrrole rings from two ligand molecules. Although the samarium atoms in this double-cluster salt are divalent, they do not show any reactivity toward nitrogen gas. It has been rationalized in terms of the inhibitory role played by the coordinated iodo ligands.

Treating this double cluster with KH under nitrogen formally removes a SmI_2 unit, leading to a tetranuclear cluster featuring a N_2 molecule

confined in the cavity formed by the four samarium atoms (Figure 72, upper right structure; Table 1, entry 1). The N_2 unit is coordinated side-on to two samarium atoms and end-on to the other two. The N–N bond length of 1.412(17) Å is close to that of an N–N single bond (1.47 Å), suggesting that the coordinated N_2 unit is reduced by four electrons, one from each of the four samarium atoms. The samarium atoms in the tetranuclear cluster are thus formally trivalent. Not surprisingly, no nitrogen gas was released when this cluster was treated with anhydrous HCl. In addition, the cluster remained stable even with prolonged exposure to heat or vacuum, and no sign of reversible nitrogen coordination was observed. This very same tetranuclear cluster was obtained directly by reacting the diphenylmethyldipyrrolide dianion with $[SmI_2(THF)_2]$ under nitrogen (Dubé et al., 1999).

Altering the reaction sequence by first synthesizing trivalent dipyrrolido complexes followed by reduction by alkali metals under argon or nitrogen generated intriguingly diverse results. For example, by reduction of a $[\{[Ph_2C(C_4H_3N)_2]Sm\}Cl]$ precursor, prepared from $SmCl_3$ and the diphenylmethyldipyrrolide dianion, with K in THF under nitrogen, an anionic tetrasamarium cluster was obtained which possesses the same core structure as described above but features a μ_4-Cl ligand centrally coordinated to the four samarium atoms (Figure 73; Table 1, entry 6).

This chloro-containing cluster also failed to react with nitrogen despite the fact that all of the metal ions are formally divalent. These observations provide further support to the conclusion that halide ions, by coordinating the samarium atoms, prevent the reaction of the cluster with nitrogen from occurring.

Surprisingly, using Na instead of K as the reducing agent under otherwise identical conditions afforded a hydrido analogue of the above chloro cluster (Dubé et al., 2000d; Table 1, entry 5). Moreover, the use of

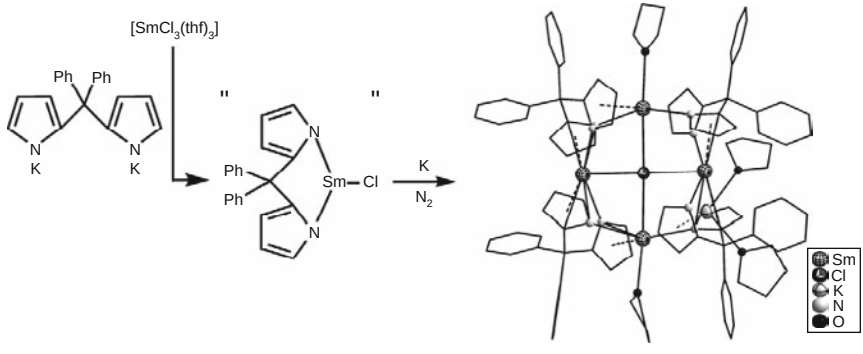

FIGURE 73 Synthesis and crystal structure of a tetrasamarium cluster containing a μ_4-Cl^- ligand (redrawn after Dubé et al., 1999).

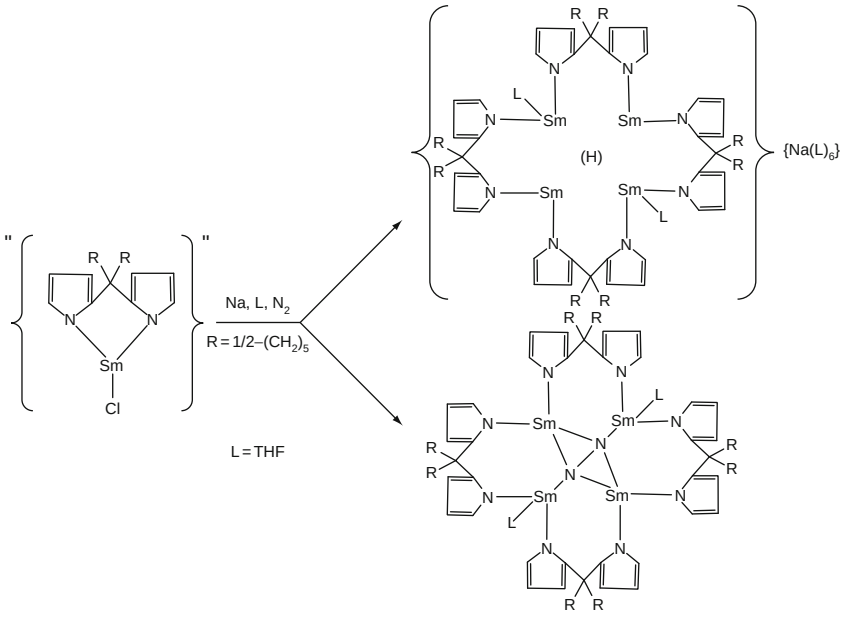

FIGURE 74 Synthesis of tetrasamarium clusters containing a central N_2 or hydrido ligand, depending on the substituents on the backbone of the dipyrrolide ligands (redrawn after Dubé et al., 2000d).

1,1-dipyrrolidecyclohexane under the otherwise identical conditions leads to a tetranuclear cluster containing a dinitrogen unit (Figure 74). That distinctly different cluster species are formed merely due to the different substituents on the dipyrrolide ligands suggests the sensitive dependence of this chemistry on the ligand structure, among many other factors.

The core structure of this dinitrogen-containing cluster is almost the same as the one shown in Figure 72, the only difference being the presence of two additional Na(THF) units, one on each of the two dinitrogen N atoms (Table 1, entry 7). The N–N bond length at 1.371(16) Å is close to that of an N–N single bond, suggesting that the dinitrogen molecule is also reduced by four electrons.

The sodium-free tetranuclear cluster was obtained from the transmetalation reaction between $R'''_2Sm(THF)_2$ and 1,1-dipyrrolylcyclohexane (Table 1, entry 8). The N–N distance of the coordinated dinitrogen unit is essentially the same as in the Na^+-containing cluster (Figure 75). These observations suggest that the Na(THF) units do not affect significantly the bonding within the N_2 unit. In other words, the scenario may be understood as four-electron reduction of dinitrogen by turning each divalent samarium into trivalent state (hence the close-to-single bond N–N

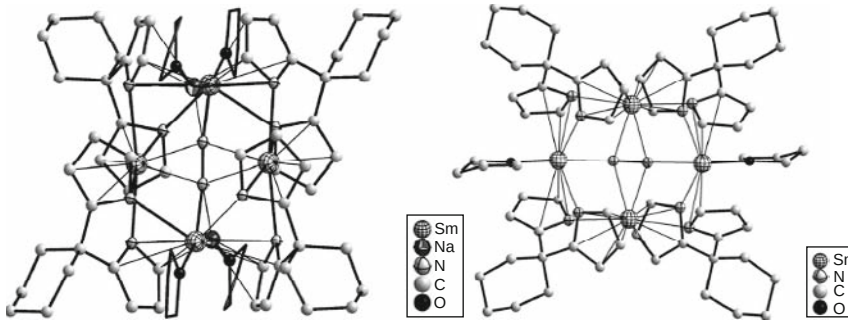

FIGURE 75 Crystal structures of tetrasamarium clusters containing a central N_2 ligand, with (left) and without (right) a Na^+-THF ion attached to the N_2 units, one on each of the N atoms (redrawn after Dubé et al., 2000d).

distance) followed by partial reduction of samarium rather than the cleavage of the N–N bond. These results suggest that the reducing power of divalent samarium may not be adequate for the cleavage of an N–N single bond. However, the confinement of the dinitrogen unit by the rather rigid cyclic structure of the tetranuclear species may be responsible for this ''inaction,'' and reduction of trivalent samarium to chemically accessible divalent samarium is instead achieved. Consistent with the analysis, the partially reduced tetranuclear cluster was successfully synthesized by treating the Na^+-free cluster with finely dispersed Na in THF.

Simply switching the atmosphere from nitrogen to argon also caused significant difference in the resulting cluster species (Table 1, entry 4). As opposed to forming the hydrido cluster complex, the reaction between [{[$Ph_2C(C_4H_3N)_2$]Sm}Cl] precursor and Na in THF under argon produced an anionic octameric cluster whose eight {[$Ph_2C(C_4H_3N)_2$]Sm} units are organized into an overall bowl-shaped arrangement (Dubé et al., 2000c; Figure 76, right). Neighboring samarium atoms are bridged by one ligand with the pyrrole rings being in turn π-bonded to one samarium and σ-bonded to a second. Four chlorine atoms are found within the cavity formed by the eight samarium atoms such that each chloride bridges three adjacent samarium ions. The four chlorides are, in turn, bridged by a single sodium atom which is located in the center of the cluster and is nearly coplanar with the four chlorine atoms. The negative charge of the octameric cluster is balanced by a THF-solvated Na^+ ion.

The overall charge of the cluster requires that the complex is a mixed-valence species with two of the samarium atoms maintaining their original trivalent state and the other ones being divalent. Attempts to further reduce the cluster proved unsuccessful. Not surprisingly, the cluster did not show any reactivity toward dinitrogen as the triply bridging chloro ligands prevent such interactions from occurring.

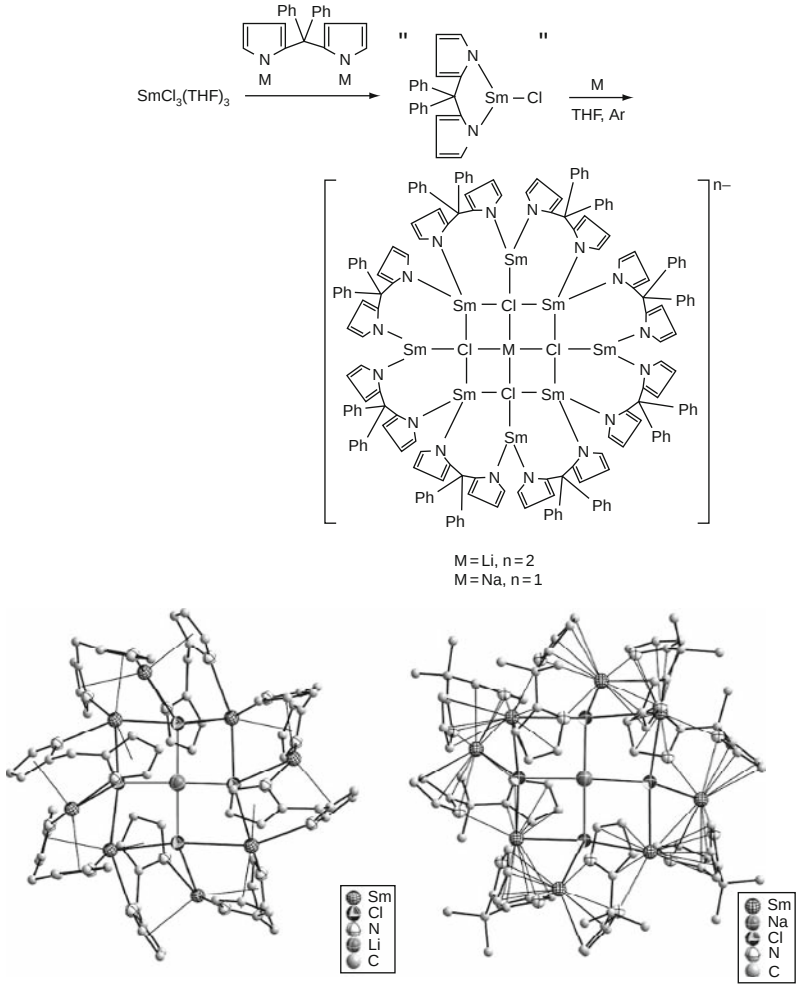

FIGURE 76 (Top) syntheses of unexpected octanuclear samarium clusters containing bridging chloro ligands. Depending on the nature of the reducing metal, the oxidation states of the lanthanide ions are varied. The crystal structures of the Li^+- (bottom left) and Na^+-containing (bottom right) clusters are shown (redrawn after Dubé et al., 2000c).

An analogous reaction using Li as the reducing reagent generated similar yet different results: the resulting octanuclear cluster, although possessing a very similar core structure (Figure 76, left), is dianionic, meaning that one additional samarium center is in the divalent state. Attempts have been made to further reduce it with the use of excess of KH, but without success. As in the case of the monoanionic Na^+-containing cluster, no reactivity toward nitrogen coordination was observed.

The influence of the reaction atmosphere on the nature of the cluster product is also reflected in the case of 1,1-dipyrrolylcyclohexane. While the reaction of the [{[$(CH_2)_5C(C_4H_3N)_2$]Sm}Cl] precursor with Na in THF under nitrogen gas yielded a tetrasamarium cluster with two additional units of Na(THF) coordinated to the N atoms of a confined dinitrogen molecule, an otherwise identical reaction under argon afforded an oxo-centered cluster (Dubé et al., 2000a; Table 1, entry 9). The oxo group, believed to originate from THF degradation by Na metal, is coordinated to two opposite samarium atoms of the tetranuclear cluster core (Figure 77).

Identity of the starting complex also plays an important role in determining the outcome of the cluster formation. Two divalent samarium starting complexes, [$SmI_2(THF)_2$] and $[R'''_2Sm(THF)_2]$, have been used in most of the studies. Under argon, the reaction of the diphenylmethyldipyrrolide dianion with [$SmI_2(THF)_2$] produced the aforementioned double-cluster salt, whereas the use of $[R'''_2Sm(THF)_2]$ in an analogous reaction generated a hexameric paramagnetic cluster (Figure 78, reaction scheme; Ganesan et al., 2001; Table 1, entry 10).

The cluster is composed of six Sm atoms bridged by six ligands arranged to form a neutral macrocyclic Sm(II) complex in which the samarium atoms form a regular, flat hexagon with Sm-Sm distances ranging from 4.359 to 4.225 Å (Figure 78, left). The ligand adopts a characteristic bonding mode, bridging each pair of metals by crossing σ and π interactions. Two sets of samarium atoms are observed: those without coordinated THF, which display the usual bent samarocene-type

FIGURE 77 Crystal structure of a tetrasamarium cluster featuring a central oxo group (redrawn after Dubé et al., 2000a).

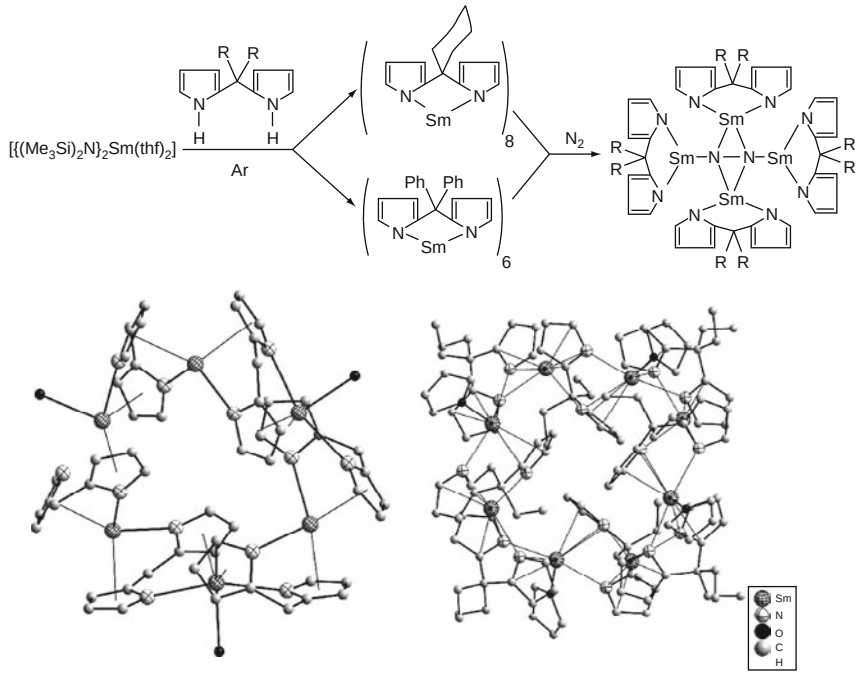

FIGURE 78 Syntheses of hexanuclear and octanuclear samarium cluster complexes and their reaction with dinitrogen to afford tetranuclear cluster species containing a N_2 ligand derived from dinitrogen reduction (top). The crystal structures of the hexanuclear (bottom left) and octanuclear (bottom right) clusters are shown (redrawn after Ganesan et al., 2001).

structures, and those coordinated to THF in which the metal adopts a trigonal bipyramidal geometry. The centroids of two π-bonded pyrrolyl rings and the oxygen atom of the coordinated THF define the equatorial plane, while the nitrogen atoms of two σ-bonded pyrrolyl rings are at the axial positions.

Using 1,1-dipyrrolylcyclohexane, the reaction with $[SmI_2(THF)_2]$ afforded the aforementioned tetranuclear cluster featuring an μ_2-oxo group (Dubé et al., 2000a; Table 1, entry 12), while with $[R'''_2Sm(THF)_2]$, an octameric macrocyclic cluster was obtained (Figure 78, right; Ganesan et al., 2001; Table 1, entry 11). The samarium atoms adopt a flattened boat-like conformation (Figure 1) with the ligand adopting the usual bonding modes as detailed above.

A similar octameric cluster was also isolated from the reaction using diethyldipyrrolylmethane. That different cluster species were obtained for one particular dipyrrolide ligand with the use of different starting

lanthanide complexes manifests the influence of the ''innocent'' starting materials on the product formation. The different cluster compounds obtained with the same lanthanide starting material but different dipyrrolide ligands further support the conclusion reached earlier that ligand substituents profoundly affect the identity of the final products. The neutral hexanuclear and octanuclear clusters are reactive toward dinitrogen. Except for the different substituents on the dipyrrolide ligands, upon exposure to nitrogen gas, tetranuclear samarium clusters featuring a dinitrogen unit have invariably been obtained.

A preponderant share of the research accomplished with the dipyrrolide ligand family concerns samarium complexes. However, this chemistry can be extended to other lanthanide elements whose redox chemistry is also accessible under reasonable conditions. For example, treatment of a solution of the lithium salt of the diphenyl dipyrromethanyl dianion with $YbCl_3(THF)_3$ followed by reduction with Li afforded an octameric cluster $\{[Ph_2C(C_4H_3N)_2Yb]_8(\mu_3\text{-}Cl)_2\}\{Li(THF)_4\}_2 \cdot 10THF$ (Dubé et al., 2000b). The core structure is similar to the octameric samarium clusters presented above except that two Cl^- ions reside within the framework of the eight Yb atoms with each bridging a set of three Yb atoms located at opposite ends of the cavity; two Yb atoms remain uncoordinated to a chloride (Figure 79).

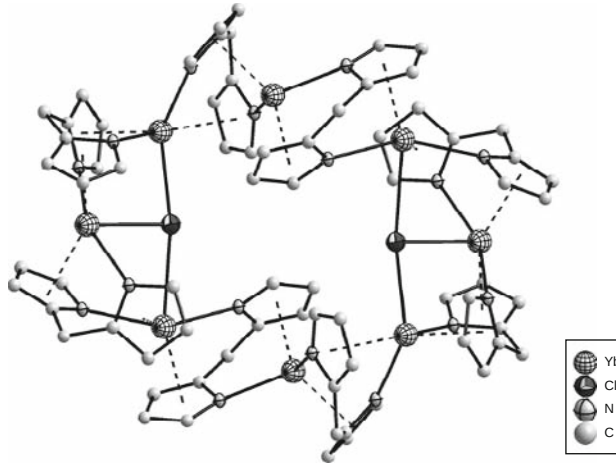

FIGURE 79 Crystal structure of an octanuclear ytterbium cluster $\{[Ph_2C(C_4H_3N)_2Yb]_8(\mu_3\text{-}Cl)_2\}\{Li(THF)_4\}_2 \cdot 10THF$. The solvent molecules and solvated Li^+ ions are removed for clarity (redrawn after Dubé et al., 2000b).

3. LANTHANIDE CLUSTERS OBTAINED UNDER HYDROLYTIC CONDITIONS

In studying the use of *N*-methylimidazole (*N*-MeIm) as solvent for the stabilization and isolation of crystalline samarium iodides, Evans et al. (1994b) came across two unexpected hydroxo complexes, $[(N\text{-MeIm})_5\text{Sm}(\mu\text{-OH})]_2\text{I}_4$ and $\{[(N\text{-MeIm})_4\text{Sm}(\mu\text{-OH})]_3(\mu_3\text{-OH})_2\}\text{I}_4$, the crystal structures of which are shown in Figure 80. The dinuclear complex features two $[(N\text{-MeIm})_5\text{Sm}]$ units bridged by two μ-OH groups, while the trinuclear cluster cation consists of a triangle of $[(N\text{-MeIm})_4\text{Sm}]$ units bridged by three μ-OH ligands in the plane of the metals and two μ_3-OH groups, one above and the other below the plane. The hydroxo ligand is probably the product of adventitious hydrolysis promoted by the hard Lewis acidic metal ions with *N*-MeIm as a base. The unexpected formation of these hydroxide complexes prompted the authors to suggest insightfully that the chemistry of hydroxide-based polynuclear complexes may be as extensive and accessible as the polymetallic lanthanide chemistry that had been dominated by alkoxide ligands.

It is interesting to note that crystallographically characterized lanthanide hydroxides had long before appeared in the literature. Most of these compounds feature a diamond-shaped dinuclear core of $\mathbf{R}_2(\text{OH})_2$. Despite their recurring appearance, their formation has always been attributed to ''adventitious hydrolysis'' without further thought, and the isolation of such hydroxides was frequently characterized as ''unexpected,'' ''surprising,'' or ''serendipitous.''

The formation of these hydroxo complexes manifests the high proneness of lanthanide to hydrolysis, while the lack of activities toward their

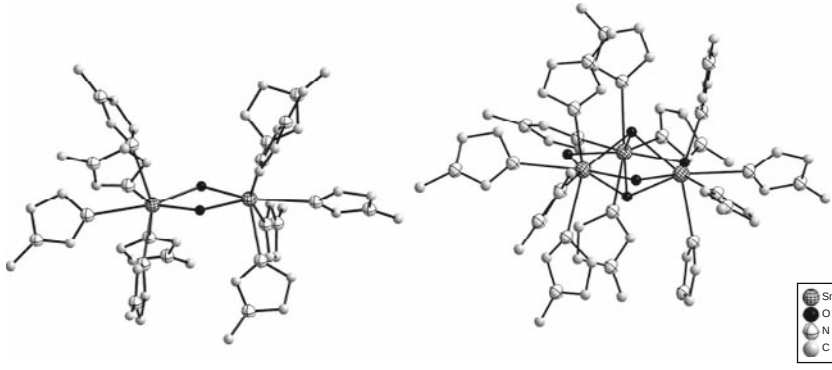

FIGURE 80 Crystal structures of two hydroxide clusters, $[(N\text{-MeIm})_5\text{Sm}(\mu\text{-OH})]_2\text{I}_4$ (left) and $\{[(N\text{-MeIm})_4\text{Sm}(\mu\text{-OH})]_3(\mu_3\text{-OH})_2\}\text{I}_4$ (right) whose formation is supported by imidazole ligands (redrawn after Evans et al., 1994b).

rational synthesis may reflect the general conception (or misconception) of chemists for the complexity of this chemistry. Nevertheless, the repetitive appearance of such ''unexpected'' species and the few seemingly prevalent core motifs clearly suggest that ''higher-pH'' lanthanide coordination chemistry may very well be developed into an independent and rich research. Further stimulation for this chemistry comes from the diamond-shaped hydroxo-bridged dinuclear motif which resembles structurally the active-site structure of many naturally occurring metalloenzymes whose function is to catalyze the hydrolytic cleavage of DNA and RNA (Franklin, 2001; Komiyama, 2005). The hard Lewis acid character, large size for simultaneous accommodation of both the hydroxo nucleophile and the nucleic acid substrates, and flexible coordination for optimal binding of substrates, make the lanthanide–hydroxo species excellent candidates for designing synthetic nucleases (Figure 81). Not surprisingly, there has been extensive research done in the design and synthesis of lanthanide-based synthetic nucleases (Komiyama, 2005). In some cases, unambiguous structural determination of the catalytically active species is established, while in others, the catalytic role of the dinuclear species or its kinetic equivalents have simply been inferred.

Despite all these efforts, the chemistry of molecular lanthanide hydroxides, regardless of the complex nuclearity, has yet to be developed to any significant extent. However, based on the limited number of reports, some general conclusions may already be drawn:

(1) The assembly of polynuclear lanthanide–oxo/hydroxo species, though generally unexpected and structurally unpredictable, is a general phenomenon in lanthanide coordination chemistry.
(2) The presence of hydroxo groups suggests that deliberate hydrolysis should be a rational means of producing such species provided that the experimental conditions are carefully controlled.

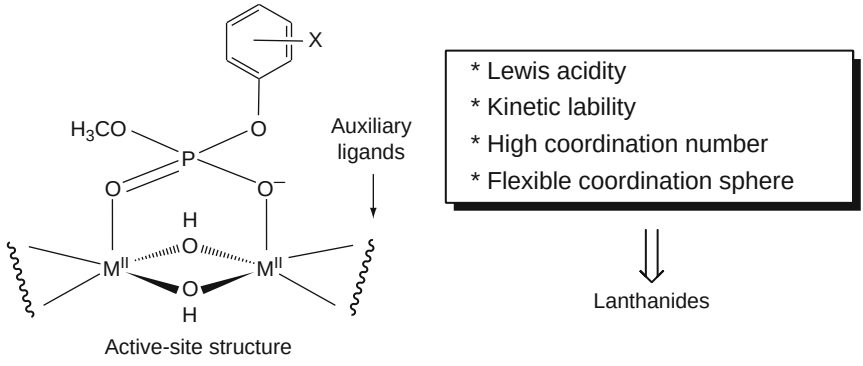

FIGURE 81 A possible activation mechanism of a phosphate diester substrate by the dinuclear active site of a metallophosphodiesterase (redrawn after Zheng, 2001).

(3) It is necessary to introduce multidentate ligands during the synthetic procedure in order to limit the extent of hydrolysis so that only finite-size clusters rather than intractable products are obtained.

3.1 Rationales of ligand-controlled hydrolysis approach to cluster synthesis

The desire to develop better defined hydroxide-based cluster chemistry of the lanthanides and to create novel lanthanide-containing functional materials has facilitated the systematic studies of this particular area of coordination chemistry since the late 1990s. Specifically, the ''ligand-controlled hydrolysis'' approach proved to be highly successful (Zheng, 2001). The general synthetic design is illustrated in Figure 82. It relies on the high propensity of lanthanide ions to undergo hydrolysis, but to a limited degree. The scheme starts with a familiar lanthanide complex whose coordination sphere is occupied by a combination of organic ligands and a number of aqua ligands. Upon increasing pH, the aqua ligands, metal-bound and hence activated, are expected to undergo deprotonation, affording the corresponding hydroxo species. Because of

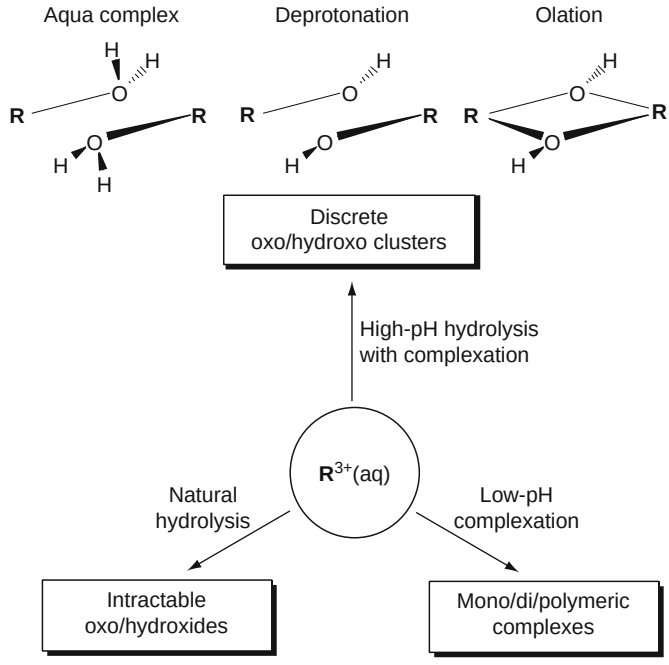

FIGURE 82 Rationales of the ligand-controlled hydrolytic approach to the assembly of lanthanide hydroxide clusters (redrawn after Zheng, 2001).

its coordinative and electrical unsaturation, there is a natural tendency for the hydroxo group to seek other lanthanide ions to form aggregates of the mononuclear hydroxo species. This hydrolysis followed by aggregation is similar to the initial steps in sol-gel chemistry, although generally condensation rather than olation occurs in the latter. Another difference lies in the introduction of generally multidentate ancillary ligands to limit the degree of hydrolysis and aggregation, leading eventually to finite-sized and structurally well-defined clusters as opposed to the less well-defined, gel-like materials obtained in conventional sol-gel syntheses. The degree of olation depends on a number of intertwined factors, including the bulkiness of the organic ligands, the size and possibly Lewis acidity of the metal ion, and the number of aqua ligands. The initial coordination by the ancillary ligands controls the number of sites available for aqua ligands and, in turn, the degree of hydrolysis and the structural type of the cluster eventually assembled. It should be noted that the application of such a ligand-controlled hydrolysis approach has long been successfully exploited for the preparation of transition metal clusters of appealing structures and interesting properties.

In the following, the successful application of the ligand-controlled hydrolytic approach toward lanthanide cluster synthesis will be demonstrated, with the use of a variety of multidentate organic ligands. These ligands are mainly O and/or N-donors, including α-amino acids (Wang et al., 1999, 2000, 2001a,b, 2002; Zheng, 2001), polyaminopolycarboxylates (Wang and Zheng, 2000; Zheng, 2001), functionalized carboxylates (Ouchi et al., 1988), β-diketonates (Barash et al., 1993; Boeyens and De Villiers, 1972; Plakatouras et al., 1994; Poncelet and Hubert-Pfalzgraf, 1989; Toledano et al., 1990), and other less commonly used ligands. The discussion will be organized according to the ligand types. In addition, lanthanide hydroxide clusters can also be prepared by direct hydrolysis of simple lanthanide salts, such as iodide, nitrates, and perchlorates (Wang et al., 2000). In these cases, the strongly coordinating nitrate ligand may be viewed as the inorganic analogue of the hydrolysis-limiting organic ligands, while the role of a less coordinating anion such as perchlorate is not completely clear. Not surprisingly, the latter clusters are not nearly as stable as those with supporting organic ligands; they exist only in a limited range of pH.

3.2 Hydroxide clusters supported by amino acid ligands (Wang et al., 1999, 2000, 2001a,b, 2002; Zheng, 2001)

The coordination of lanthanide elements with amino acids has been studied extensively, and almost all studies prior to the late 1990s have been conducted at low pH. This practice probably originated from the willingness to avoid lanthanide hydrolysis that gives generally intractable

products, particularly at high pH (Baes and Mesmer, 1976; Rizkalla and Choppin, 1991; Suzuki et al., 1986).

α-Amino acids have been used extensively for this purpose, largely due to their biological relevance in mimicking the enzymatic functions of metal-containing nucleases. The extensive low-pH coordination chemistry of lanthanides with amino acids and the diverse structural and functional properties available with the various amino acids add further interest to the use of this unique class of ligands (Kremer et al., 2005).

In a series of systematic studies, highly sophisticated lanthanide–hydroxo complexes have been obtained at near neutral pH (Wang et al., 1999, 2000, 2001a,b, 2002; Zheng, 2001). It has been found that the hydrolytic approach is generally applicable to all the lanthanide ions, but the nature of the final product is profoundly influenced by the supporting amino acids. Depending on the amino acids used, cluster complexes of nuclearity ranging from tetranuclear to pentadecanuclear have been obtained. Tetranuclear hydroxo complexes featuring the cubane-like cluster core and of the general formula $[\mathbf{R}_4(\mu_3\text{-OH})_4(\text{AA})_6]^{8+}$ (AA = α-amino acid) are obtained with alanine (Ala), glycine, proline, serine (Ser), and valine (Hu et al., 2003). The tetranuclear cluster core has a cubane-like structure, but is highly distorted from a regular cubane and may be viewed as the dimer of the dimeric $\mathbf{R}_2(\text{OH})_2$ unit proposed in the rational aggregation of the initially formed lanthanide–hydroxo species resulting from the deprotonation of the aqua complex. Linking the four metal centers produces an almost perfect tetrahedron. The cluster core is generally ''camouflaged'' by six bridging carboxylate groups of the amino acid ligands, one for each of the six edges of the tetrahedron. Any additional coordination sites are filled by aqua ligands. Exceptions exist when not all the six edges are bridged by the amino acid carboxylate group. The structure of one representative of such cluster complexes, featuring Ala as the supporting ligand, is shown in Figure 83.

Treating the $[\mathbf{R}_4(\mu_3\text{-OH})_4]$ core structure as a formal building block, multicubane arrays have been realized by employing α-amino acids bearing a side-chain carboxylate group such as glutamic acid (HGlu) and aspartic acid (HAsp).

The three-dimensional (3D) network structure obtained by treating a mixture of $\text{Er}(\text{ClO}_4)_3$ and *L*-HGlu with aqueous NaOH is shown in Figure 84. The porous network is comprised of discrete $[\text{Er}_4(\mu_3\text{-OH})_4]^{8+}$ units and cluster-linking glutamate ligands, each contributing one carboxylate group for the coordination of one $[\text{Er}_4(\mu_3\text{-OH})_4]^{8+}$ cluster while using the remaining one to coordinate an adjacent cluster cube. A very similar network structure has also been obtained with HAsp (Ma et al., 2000).

Interestingly, different cluster species have been isolated under slightly different reaction conditions even with the same amino acid

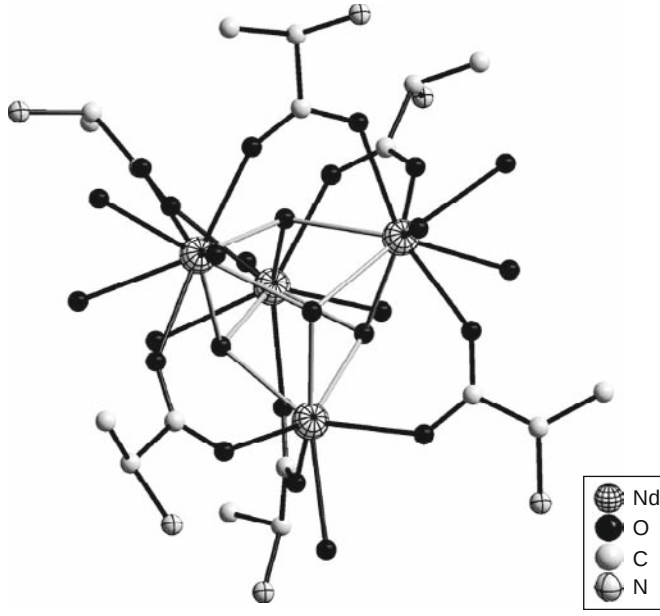

FIGURE 83 Crystal structure of the cationic complex $[Nd_4(\mu_3\text{-}OH)_4(Ala)_6(H_2O)_{10}]^{8+}$ (redrawn after Wang et al., 2001a).

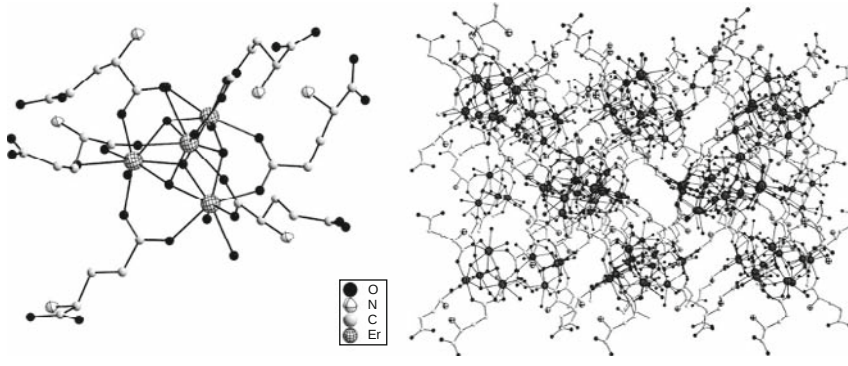

FIGURE 84 An ORTEP drawing of the elementary building unit of $[Er_4(\mu_3\text{-}OH)_4(Glu)_3(H_2O)_8]^{5+}$. Three symmetry-related glutamic acid "arms" are included to complete the coordination of the cuboid $[Er_4(\mu_3\text{-}OH)_4]^{8+}$ core (left). A 3D porous framework with channel dimensions being approximately 4.4 × 9.1 Å (right) (redrawn after Wang et al., 2001a).

ligands. For example, with HAsp, a recent study using a higher ligand: metal ratio at room temperature yielded a discrete tetranuclear cluster $[Eu_4(\mu_3\text{-}OH)_4(L\text{-}Asp)_2(L\text{-}HAsp)_3(H_2O)_7]Cl_{11}\cdot 5H_2O$ (Figure 85), as

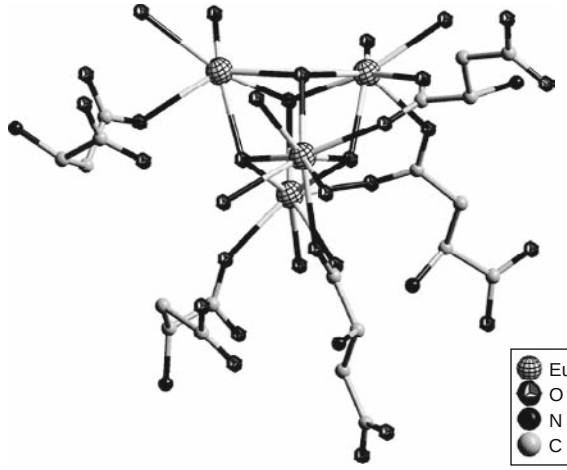

FIGURE 85 Crystal structure of the cationic cluster $[Eu_4(\mu_3\text{-}OH)_4(L\text{-}Asp)_2(L\text{-}HAsp)_3(H_2O)_7]^{11+}$ (redrawn after Zhang et al., 2007).

opposed to the previously reported 3D network structure. The side-chain carboxylic acid groups of two of the five amino acids are deprotonated, while those of the other three are not. In addition, different from bridging carboxylate groups described above, only three of the aspartate ligands are bridging, while the other two are monodentate (Zhang et al., 2007).

Another example showing the diverse coordination behaviors of various amino acids is $[Gd_{14}(\mu_4\text{-}OH)_2(\mu_3\text{-}OH)_{16}(H_2O)_8(L\text{-}Ser)_{20}]^{3+}$, a tetradecanuclear cluster with serine as supporting ligand (Messerle et al., 2005; Figure 86).

Very different clusters with nuclearity up to 15 can also been obtained with different amino acids in which both the carboxylate and the amino groups participate in metal coordination. Using tyrosine (HTyr) as the supporting ligand, tetradeca- and pentadecanuclear lanthanide hydroxide clusters have been obtained. Vertex-sharing $[\mathbf{R}_4(\mu_3\text{-}OH)_4]$ cubanes are shown in the overall wheel-like structures. Surprisingly there exists a μ_5-Cl^- or μ_5-Br^- in the center of the pentadecanuclear cubane wheel (Figure 87), while two μ_4-I^- are found in the tetradecanuclear complexes, one on each side of the square and interacting with the μ_3-OH groups in a μ_4-I^- fashion (Figure 88). The halo ligands are bound to five lanthanide atoms in the former, while the iodo groups lie on both sides of the cubane wheel, in close contact with the triply bridging hydroxo groups.

The distinct clusters with different nuclearity clearly suggest the templating effect exerted by the halo ligands, which is further verified by the outcome of analogous experiments using lanthanide nitrates as starting materials under otherwise identical conditions; hexanuclear clusters were

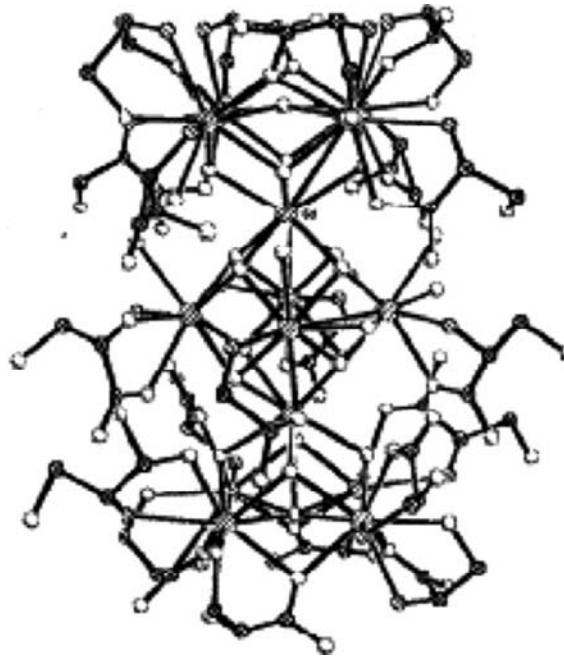

FIGURE 86 Crystal structure of the cationic cluster $[Gd_{14}(\mu_4\text{-}OH)_2(\mu_3\text{-}OH)_{16}(H_2O)_8(L\text{-}Ser)_{20}]^{3+}$ (redrawn after Messerle et al., 2005).

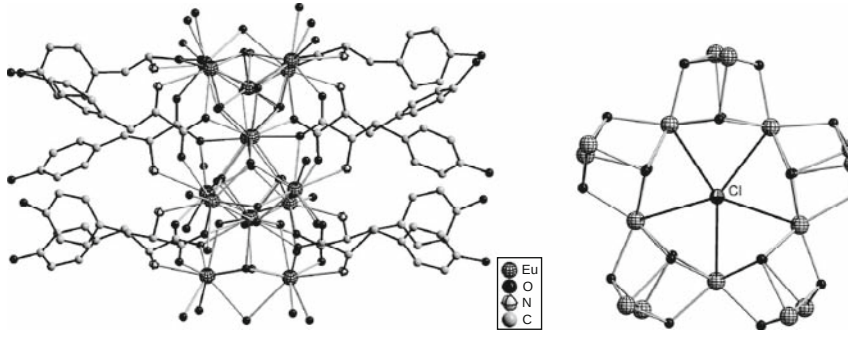

FIGURE 87 Structure of the pentadecanuclear cluster $[Eu_{15}(\mu_3\text{-}OH)_{20}(\mu_5\text{-}Cl)(\mu_3\text{-}Tyr)_{10}(OH)_2(\mu\text{-}H_2O)_5(H_2O)_{18}]^{12+}$ (left). The wheel-like core structure showing five vertex-sharing cuboid $[Eu_4(\mu_3\text{-}OH)_4]^{8+}$ units centered on a $\mu_5\text{-}Cl^-$ ion (right) (redrawn after Wang et al., 2001b).

obtained whose six metal ions form a perfect octahedron centered on an interstitial $\mu_6\text{-}O^{2-}$ group (Figure 89). Each of its triangular faces is capped by a μ_3-OH group. Interestingly, no tyrosinate ion is incorporated in the

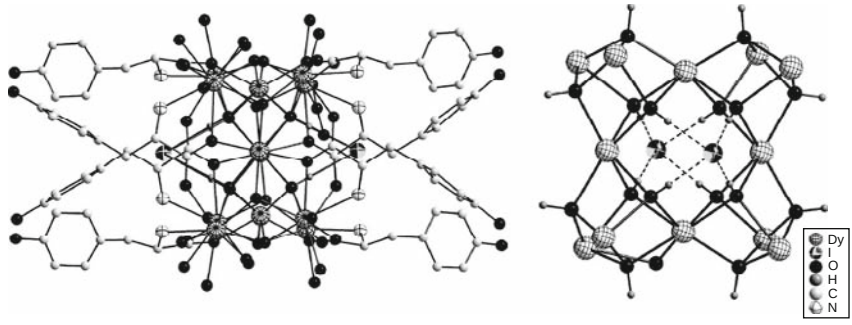

FIGURE 88 A perspective view of the tetradecanuclear Dy(III)-hydroxo complex with Tyr ligands, formulated as $[Dy_{12}(\mu_3\text{-}OH)_{16}(I)_2(\mu_3\text{-}Tyr)_8(H_2O)_{20}]^{10+}$ (left). The wheel-like core structure showing four vertex-sharing cuboid $[Dy_4(\mu_3\text{-}OH)_4]^{8+}$ units in a square-shaped arrangement (right) (redrawn after Wang et al., 2001b).

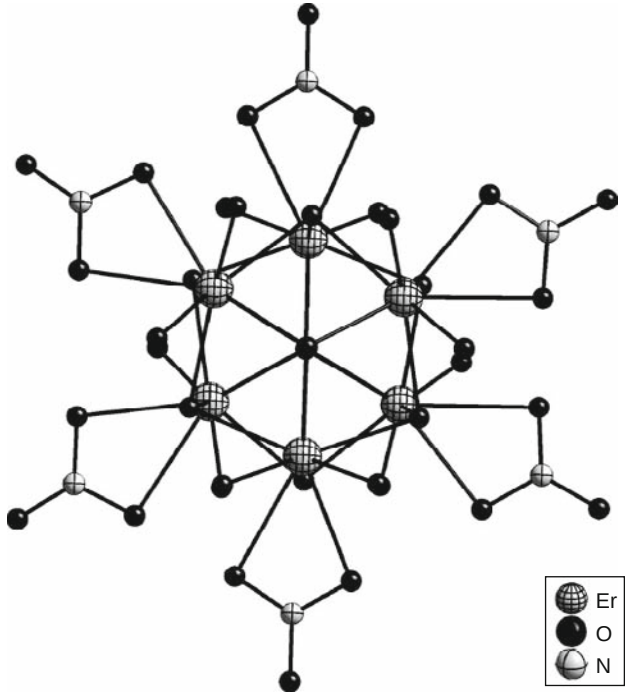

FIGURE 89 Crystal structure of the cationic complex $[Er_6(\mu_6\text{-}O)(\mu_3\text{-}OH)_8(NO_3)_6(H_2O)_{12}]^{2+}$ featuring six terminal nitro ligands and one μ_6-oxo group (redrawn after Giester et al., 1997; Wang et al., 2000; Zák et al., 1994).

structure. Instead, six NO_3^- anions are found, each coordinated to one metal ion in a bidentate fashion. This octahedral core appears to be common in lanthanide cluster compounds and can been produced by other means (Giester et al., 1997; Wang et al., 2000; Zák et al., 1994). Although structurally distinct, the isolation of the μ_6-O-centered cluster once again attests to the important role(s) played by a central anionic entity in assisting the assembly of lanthanide clusters. The templating effect of the spherical halides is further demonstrated in a competitive experiment where both Cl^- and NO_3^- are present; only the pentadecanuclear cluster species with a central Cl^- was obtained.

These results clearly indicate that the lanthanide–amino acid coordination chemistry under higher pH conditions is fairly subtle, and reaction conditions should be carefully monitored and controlled.

3.3 Hydroxide clusters supported by (poly)aminopolycarboxylate ligands

In view of the structural and functional relationship between amino acids and polyaminopolycarboxylic acids, the coordination of some lanthanide ions (La, Pr, Er) with ethylenediaminetetraacetate (EDTA) has also been examined under much higher pH conditions. The formation of lanthanide–hydroxo complexes formulated as $K_2\mathbf{R}(OH)EDTA \cdot 4H_2O$ was reported as early as in 1955 (Djordjevic and Vuletic, 1980), but it is not until recent studies that the first crystal structure of a lanthanide–EDTA hydroxo species was reported. Efforts in this field were also stimulated by the recognition that the $\mathbf{R}(OH_2)_3$ array present in previously known mononuclear EDTA complexes is dimensionally close to the $\mathbf{R}(\mu_3\text{-}OH)_3$ fragment of $[\mathbf{R}_4(\mu_3\text{-}OH)_4]^{8+}$ clusters and by the desire to understand the mechanism of formation of the clusters. A proposal for the latter is outlined in Figure 90.

The crystal structure of a tetranuclear lanthanum hydroxide cluster obtained when the pH of solutions containing $K[La(EDTA)(H_2O)_3]$ was adjusted to about 14 is shown in Figure 91 (left). A distorted $La_4(OH)_4$ cubane core is encapsulated by four EDTA ligands. Each metal vertex is capped by an EDTA ligand whose coordination mode is unusual (Figure 91, right); the EDTA ligand is hexadentate with one of its four coordinating oxygen atoms bridging a second La(III) ion. Each La(III) ion has a coordination number of 10 and the coordination polyhedron maybe best described as a bicapped square antiprism. An isostructural tetranuclear hydroxo complex of Pr(III) with EDTA has also been reported with the same coordination number.

The synthetic methodology can be readily extended to other ligand systems, as evidenced by the isolation of an analogous tetranuclear cluster

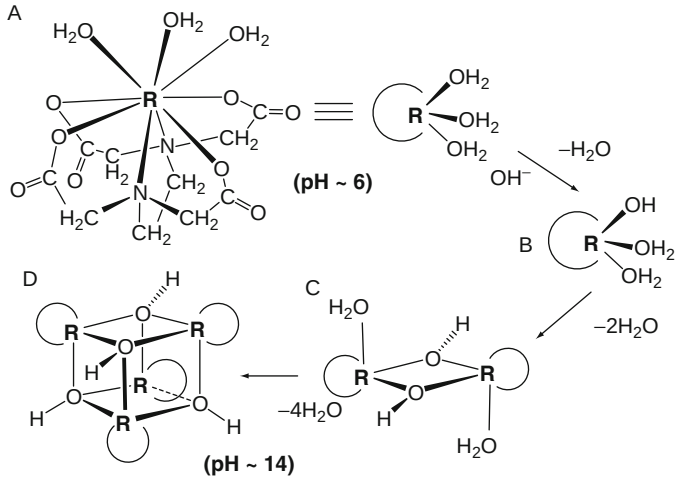

FIGURE 90 Proposed mechanism for the self-assembly of a tetranuclear lanthanide–hydroxo complex with EDTA from its corresponding mononuclear aqua complex (redrawn after Zheng, 2001).

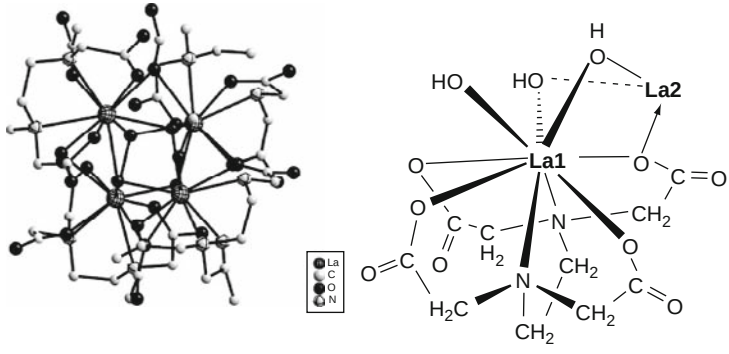

FIGURE 91 Crystal structure of the anionic complex $[La_4(\mu_3\text{-}OH)_4(EDTA)_4]^{8-}$ featuring the familiar cubane-like $[La_4(\mu_3\text{-}OH)_4]^{8+}$ core (left). The well-known hexadentate mode of an EDTA ligand to the metal (La1) with the unprecedented bridging modes to the additional metal atom (La2) is shown to the right (redrawn after Zheng, 2001).

when 1,2-diaminopropane-*N*,*N*′,*N*′,*N*′-tetraacetic acid, a methyl-substituted EDTA, was utilized in place of EDTA.

In the case of the heavier and smaller Er(III) ion, a dinuclear species $[(EDTA)Er(\mu\text{-}OH)_2Er(EDTA)]^{4-}$ was obtained with its dihydroxo-bridged diamond-shaped core structure encapsulated by two EDTA ligands, one coordinated to each of the metal atoms (Figure 92). Each metal atom is octacoordinate, with the six usual coordinating O and N atoms of the

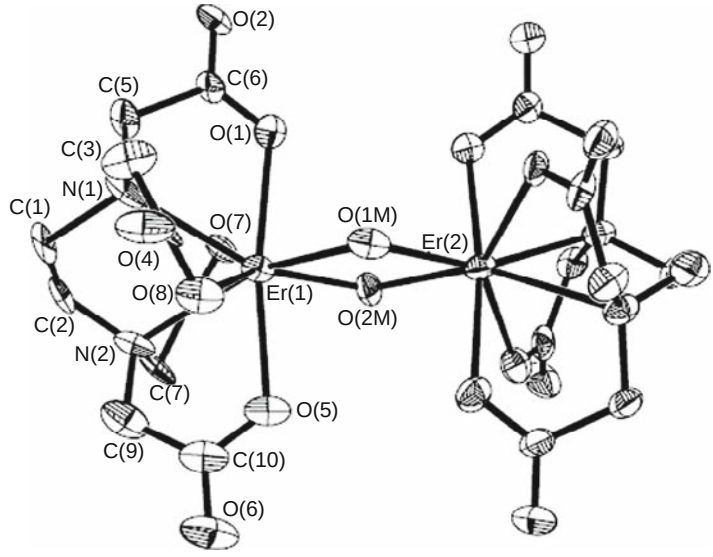

FIGURE 92 Crystal structure of the diamond-shaped dinuclear Er(III)-hydroxo complex with EDTA, $[(EDTA)Er(\mu\text{-}OH)_2Er(EDTA)]^{4-}$ (redrawn after Zheng, 2001).

EDTA ligand and two from the μ-OH ligands. The dinuclear core resembles structurally the active-site structure of many naturally occurring metal-containing nucleases.

Using a lanthanide ion of intermediate size, for example Nd(III), whose preferred coordination number is 9, an interesting and unexpected dodecanuclear complex $[Na(H_2O)_2]_4[Nd_{12}(\mu_3\text{-}OH)_{16}(EDTA)_8]^{8-}$ was obtained (Figure 93). Its core structure is the same as for the dodecanuclear cluster templated by iodo ligands in the aforementioned Tyr–**R** coordination studies (Figure 88), but no iodide was employed in the present case. One salient feature of this cluster is the two types of Nd (III) ions in terms of coordination number: The outer eight metal ions are decacoordinate, while the inner four are octacoordinate. Both these two coordination numbers are less frequently observed for Nd(III) than CN = 9, in particular the decacoordinate one. Such observations may be viewed as a compromise between the dinuclear octacoordinate structure and the tetranuclear 10-coordinate one. The unique EDTA coordination mode in this complex is also shown on Figure 93 (right).

A series of heterometallic 3d–4f cluster compounds have recently been reported, where structurally well-defined polyhedral motifs composed of solely lanthanide atoms are identified (Kong et al., 2007, 2008a,b). Under hydrothermal conditions, reaction mixtures containing $\mathbf{R}(NO_3)_3$, Ni $(NO_3)_2$, and iminodiacetate (IDA) produced a variety of polynuclear

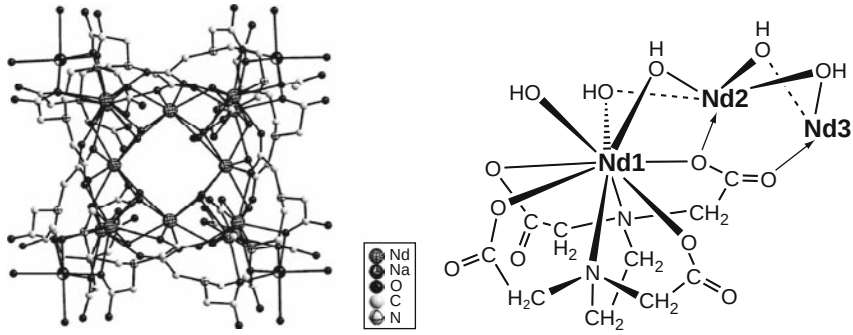

FIGURE 93 Crystal structure of the dodecanuclear Nd(III)-hydroxo complex featuring four vertex-sharing $[Nd_4(\mu_3\text{-}OH)_4]^{8+}$ units in a square-shaped arrangement. The anionic complex is formulated as $\{[Na(H_2O)_2]_4[Nd_{12}(\mu_3\text{-}OH)_{16}(EDTA)_8]\}^{8-}$ (left). The well-known hexadentate mode of an EDTA ligand to the metal (Nd1) with the unprecedented bridging modes to the additional metal atoms (Nd2 and Nd3) is shown to the right (redrawn after Zheng, 2001).

heterometallic clusters, including the double-sphere, sandwich-like $\mathbf{R}_{20}Ni_{21}$ ($\mathbf{R}$ = Nd and Pr) clusters (Kong et al., 2008b), a Keplerate-type $La_{20}Ni_{30}$ cluster (Kong et al., 2007, 2008b), and a four-shell, Russian doll-like $Gd_{54}Ni_{54}$ cluster (Kong et al., 2008a), depending on the relative ratio of the reactants.

In $[\mathbf{R}_{20}Ni_{21}(C_4H_5NO_4)_{21}(OH)_{24}(C_2H_2O_3)_6(C_2O_4)_3(NO_3)_9(H_2O)_{12}](NO_3)_9 \cdot nH_2O$ ($C_2H_2O_3$ is the alkoxide form of glycolate; $\mathbf{R}$ = Pr, $n = 42$; Nd, $n = 50$) (Kong et al., 2008b), the $\mathbf{R}_{20}Ni_{21}$ core is composed of an outer shell of 21 Ni (II) ions encapsulating an inner shell of 20 **R**(III) ions (Figure 94). The dual-shell framework structure may be viewed as constructed from two identical bowl-shaped fragments, each featuring a bowl of Pr_{10} stacked up in the outer bowl of Ni_9. The two Ni_9 bowls are joined together by three Ni(II) ions and bridging NO_3^- and oxalate ligands. As such, a closed-shell structure is formed, holding the Pr_{20} unit inside.

Interestingly, though distinctly different, this core structure can be viewed as being formally transformed from that of the Keplerate-type $\mathbf{R}_{20}Ni_{30}$ cluster (Figure 95). The core of the latter has also a dual-shell structure, with an outer sphere of 30 Ni(II) ions encapsulating the inner sphere of 20 La(III) ions (Figure 95, right). The 30 Ni(II) ions span an icosidodecahedron, one of the Archimedean solids formed by 12 pentagonal and 20 triangular faces, while the 20 La(III) ions occupy the vertices of a perfect dodecahedron, one of the Platonic solids featuring 12 pentagonal faces. The cage-like arrangement of the two distinct sets of metal ions manifests the beauty of symmetry as both ideally possess icosahedral (I_h) symmetry, the highest possible symmetry for molecules.

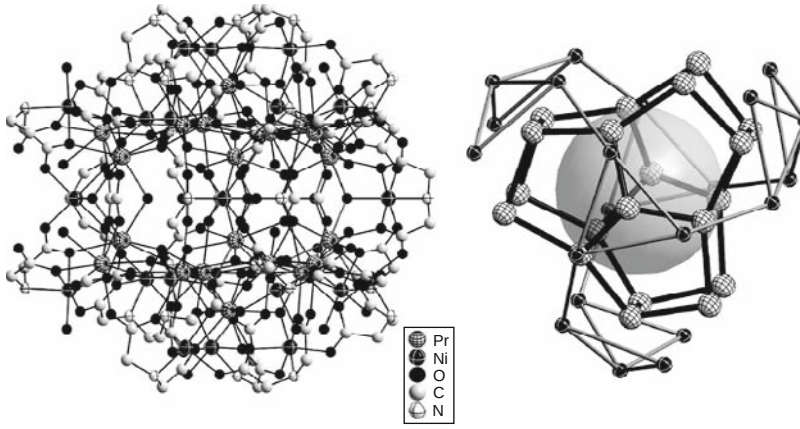

FIGURE 94 Crystal structure of the cationic cluster of $[Pr_{20}Ni_{21}(C_4H_5NO_4)_{21}(OH)_{24}(C_2H_2O_3)_6(C_2O_4)_3(NO_3)_9(H_2O)_{12}]^{9+}$ (left). The cluster core structure showing an outer Ni_{21} framework encapsulating an inner Pr_{20} framework. The inside sphere indicates the empty space housed by the shell-like structure (right) (redrawn after Kong et al., 2008b).

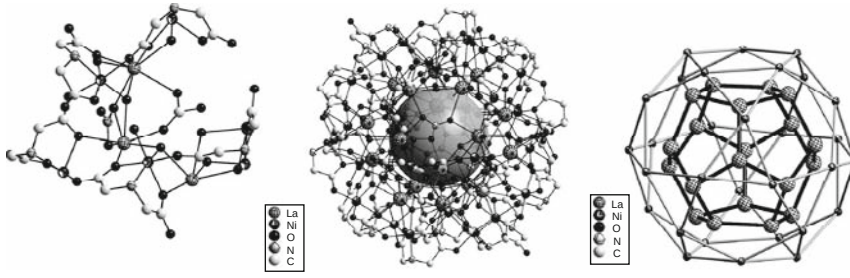

FIGURE 95 Left to right: the asymmetric unit of $[La_{20}Ni_{30}(IDA)_{30}(CO_3)_6(NO_3)_6(OH)_{30}(H_2O)_{12}]^{12+}$, crystal structure with H atoms removed for clarity, and the cluster core structure showing an outer Ni_{30} icosidodecahedron encapsulating an inner La_{20} dodecahedron (redrawn after Kong et al., 2007, 2008b).

The Ni_{21} framework is generated by removing nine uniquely positioned Ni(II) ions from the outer Ni(II) shell of $\mathbf{R}_{20}Ni_{30}$, followed by a rotation of 60° of the red-colored set of Ni(II) ions with respect to the green-colored set (Figure 96). The formal transformation necessary to obtain the inner $\mathbf{R}_{20}$ core from the dodecahedron of $\mathbf{R}_{20}Ni_{30}$ is even more straightforward: a proper C_6 rotation of the red-colored fragment with respect to the light blue set is adequate.

A giant heterometallic cluster with its 108 metal ions organized into a four-shell Russian doll-like structure has been reported recently (Kong

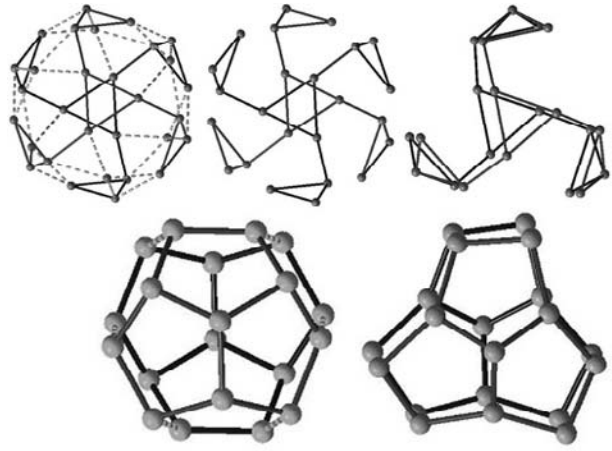

FIGURE 96 Depiction of the formal transformations toward the making of the outer (top) and inner (bottom) frameworks of $[Pr_{20}Ni_{21}(C_4H_5NO_4)_{21}(OH)_{24}(C_2H_2O_3)_6(C_2O_4)_3(NO_3)_9(H_2O)_{12}]^{9+}$ from respective polyhedra of cluster $[La_{20}Ni_{30}(IDA)_{30}(CO_3)_6(NO_3)_6(OH)_{30}(H_2O)_{12}]^{12+}$ (redrawn after Kong et al., 2008b).

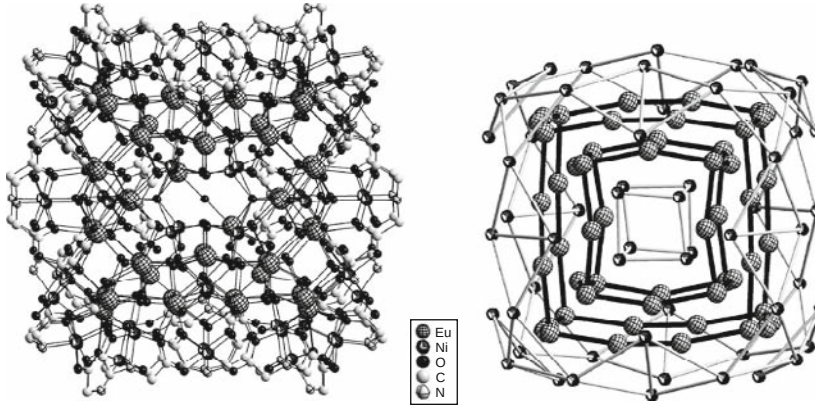

FIGURE 97 A ball-and-stick view of the cationic cluster $[Eu_{54}Ni_{54}(IDA)_{48}(OH)_{144}(CO_3)_6(H_2O)_{25}]$ (left) and a four-shell presentation showing only its metal frameworks (right) (redrawn after Kong et al., 2008a).

et al., 2008a). The cluster compound, formulated as $[Eu_{54}Ni_{54}(IDA)_{48}(OH)_{144}(CO_3)_6(H_2O)_{25}](NO_3)_{18}\cdot 140H_2O$ was obtained under hydrothermal conditions using a mixture of $Ni(NO_3)_2\cdot 6H_2O$, $Eu(NO_3)_3\cdot 6H_2O$, and iminodiacetic acid in deionized water.

The four-shell, nesting doll-like structure of the cationic cluster is shown on Figure 97. Moving outward, the innermost shell (Shell 1)

contains eight Ni(II) ions, followed by Shell 2 with 20 Eu(III) ions, Shell 3 with 32 Eu(III) ions, and the outermost shell (Shell 4) with 48 Ni(II) ions. The geometry of the shells approximates that of a cube. Intershell connections are provided primarily by triply bridging hydroxo groups, affording a highly compact, brucite-like core structure.

These clusters display interesting magnetic properties, from ferromagnetic to antiferromagnetic couplings depending on the nature of the metal elements and the molecular structure.

3.4 Hydroxide clusters supported by carboxylate ligands

Carboxylic acids are important ligands in lanthanide coordination chemistry. This is probably due to the strong oxophilicity of the hard Lewis acid metal ions. Extensive investigations have been accomplished with the use of various carboxylic acids, and a comprehensive review is available (Ouchi et al., 1988). Polymeric lanthanide carboxylates are frequently formed, the solubility of which is somewhat limited in water. This may be responsible for the general lack of hydroxo species of this particular class of lanthanide compounds as hydrolysis is inhibited by the limited water solubility of the resulting aqua complexes. If water solubility of the aqua complexes initially formed at low-pH conditions can be enhanced, the aqua ligands may undergo hydrolysis, limited by the carboxylate groups, to afford finite-size and structurally well-defined clusters as in the case of amino acids. The formation of amino acid-supported lanthanide hydroxide clusters may be viewed as a special case in this respect; the presence of the amino group significantly enhances the water solubility of their corresponding carboxylates, rendering the subsequent hydrolysis of the remaining aqua ligands accessible upon pH increase.

One early example supporting this idea is the unexpected formation of a tetranuclear terbium cluster with pyridinoacetate whose structure is shown in Figure 98 (Chen et al., 1997). The $[Tb_4(\mu_3\text{-}OH)_4]$ core is the same as found in the cubane-like units presented above. Here, pyridinoacetate can be regarded as an amino acid-like ligand.

The combination of a chiral bipyridinecarboxylate ligand ((+/−)-**L7**) with Pr^{3+} in different solvents has led to the assembly of Pr_3- or Pr_4-based clusters (Mamula et al., 2006). The trinuclear cluster is a helical array with formula $[Pr_3\{(+)\text{-}\mathbf{L7}\}_6(\mu_3\text{-}OH)(H_2O)_3](ClO_4)_2$ (Figure 99, bottom). The three metal ions and the μ_3-hydroxy group situated above the pseudo-equilateral trimetallic base form a pyramid whose basis is held together by six chelating and bridging carboxylate groups. Using a different solvent, a tetranuclear cluster of formula $[Pr_4\{(+)\text{-}\mathbf{L7}\}_9(\mu_3\text{-}OH)](ClO_4)_2$ was obtained. Its structure (Figure 99, upper left) can be generated by formally adding the fourth metal atom to the coordination ''pocket'' formed by the

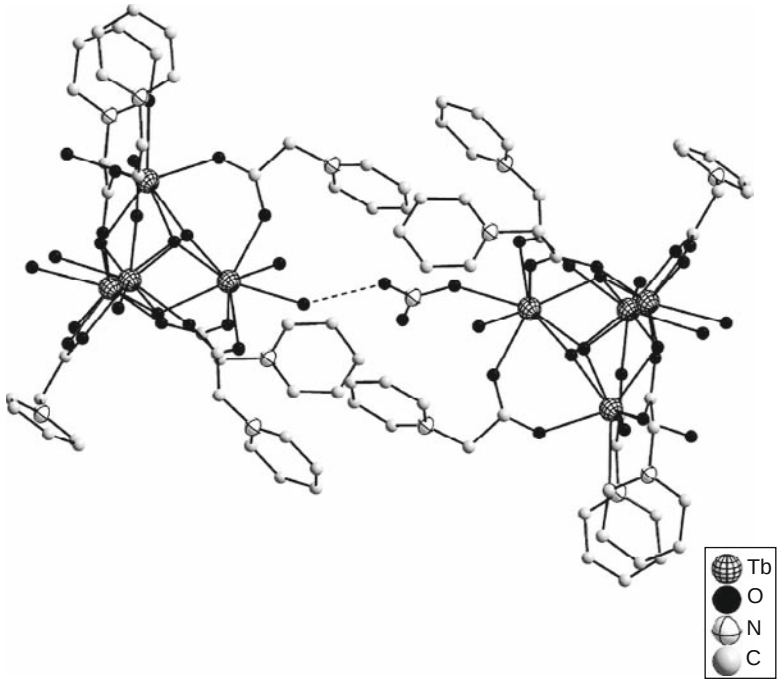

FIGURE 98 Crystal structure of the $[Tb_4(\mu_3\text{-}OH)_4]$ core-containing cluster complex with pyridinoacetato ligand (redrawn after Chen et al., 1997).

three pyridyl groups and above the Pr_3O pyramid (Figure 99, bottom) in the preceding trinuclear structure.

These two clusters display rather interesting solution behaviors. Both clusters maintain their structural integrity in their respective solutions (Pr_3 in CH_2Cl_2 and Pr_4 in MeCN), as evidenced by NMR and mass spectrometric results. However, by dissolving Pr_3 in MeCN, the trinuclear species is gradually converted into Pr_4 and some unidentified minor species. Adding water to this mixture reverses the conversion and regenerates the tetranuclear cluster.

Alternatively, hydrolysis of presumably not so soluble lanthanide carboxylate complexes may be possible by carrying out the hydrolysis under hydrothermal conditions. It appears that such conditions (high temperature and high pressure) are particularly conducive to the formation of polynuclear lanthanide complexes, often with unpredictable but nevertheless interesting structure. Under ambient pressure, analogous synthesis generally produces complexes with carboxylate coordination only and without any involvement of hydroxo groups.

Under hydrothermal reaction conditions, heptanuclear lanthanide clusters $[\mathbf{R}_7(\mu_3\text{-}OH)_8(1,4\text{-}NDA)_6(OH)_{0.5}(Ac)_{0.5}(H_2O)_7]$ ($\mathbf{R} = $ Ho, Yb) were

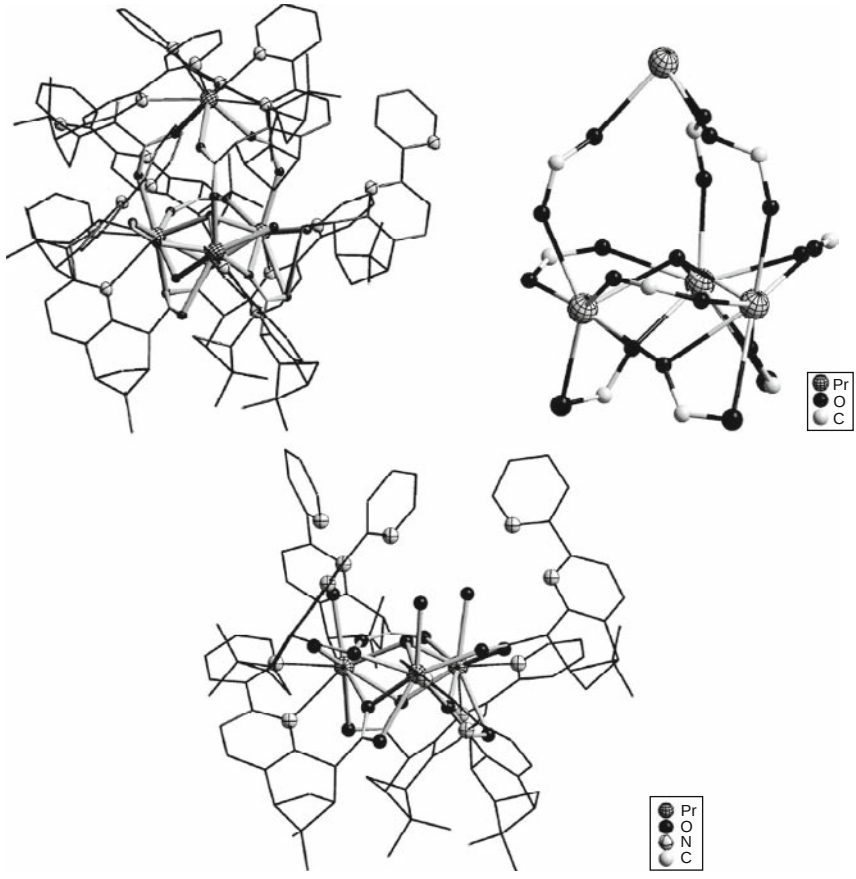

FIGURE 99 Structures of the cationic clusters, $[Pr_4\{(+)\text{-}\mathbf{L7}\}_9(\mu_3\text{-}OH)]^{2+}$ (upper left) with its core motif (upper right), and $[Pr_3\{(+)\text{-}\mathbf{L7}\}_6(\mu_3\text{-}OH)(H_2O)_3]^{2+}$ (bottom), wherein L is a chiral bipyridinecarboxylate ligand (redrawn after Mamula et al., 2006).

obtained with 1,4-naphthalenedicarboxylate (NDA; Zheng et al., 2004). The Yb cluster is shown in Figure 100 as a representative; the heptanuclear $[Yb_7(\mu_3\text{-}OH)_8]^{13+}$ core can be regarded as two tetrahedral tetranuclear units sharing a common vertex. These first examples of heptanuclear lanthanide–hydroxo clusters $[\mathbf{R}_7(\mu_3\text{-}OH)_8]^{13+}$ form a 3D framework structure through the linkage of linear dicarboxylate ligands.

With 2,2′-bipyridine-3,3′-dicarboxylate (bpdc), also under hydrothermal conditions, a lanthanide coordination polymer $[\{Er_4(\mu_3\text{-}OH)_4(bpdc)_4(H_2O)_6\}_2](H_2O)_{16}$ is obtained wherein cubane-like $[Er_4(\mu_3\text{-}OH)_4]^{8+}$ building blocks are assembled into a 2D network structure through the linkage of bpdc (Hu et al., 2007; Figure 101).

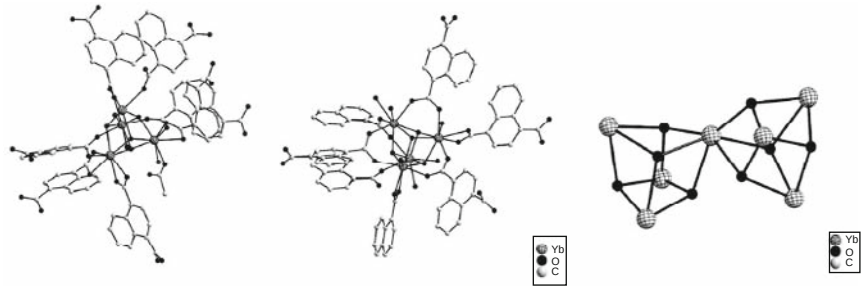

FIGURE 100 Structure of the two types of tetranuclear clusters in $[Yb_7(\mu_3\text{-}OH)_8(1,4\text{-}NDA)_6(OH)_{0.5}(Ac)_{0.5}(H_2O)_7]$ whose heptanuclear $[Yb_7(\mu_3\text{-}OH)_8]^{13+}$ cluster core is shown on the right (redrawn after Zheng et al., 2004).

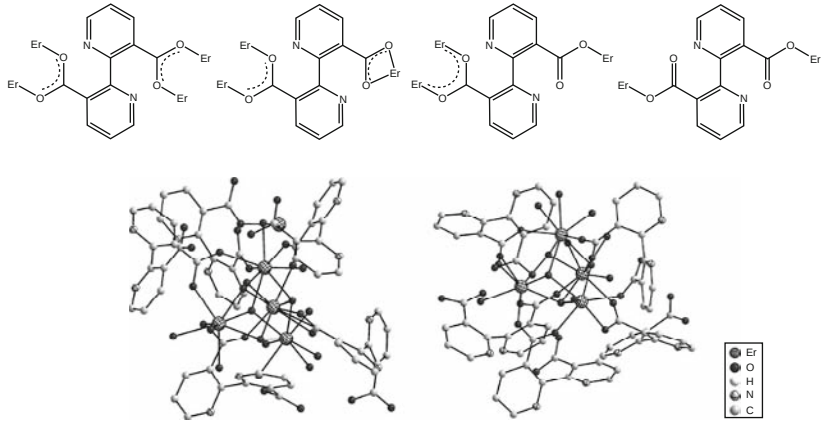

FIGURE 101 Crystal structure of the cubane-like $[Er_4(\mu_3\text{-}OH)_4]^{8+}$ building blocks encapsulated by dimeric nicotinic acid ligands. The various coordination modes of the ligands are shown on the top (redrawn after Hu et al., 2007).

The hydrothermal synthesis of the hexanuclear core-based hydroxidolanthanide coordination polymers, $[\mathbf{R}_3(BDC)_{3.5}(OH)_2(H_2O)_2]\cdot H_2O$ ($\mathbf{R}$ = Y, Yb, and Er; BDC = 1,4-benzenedicarboxylate) further attests the uniqueness of hydrothermal procedures (Weng et al., 2006). The controlled hydrolysis of lanthanide ions led to an open hexanuclear cluster core, drastically different from the commonly observed cubane or octahedral-shaped cluster cores. The hexanuclear core contains six μ_3-OH-bridged **R**(III) ions from two asymmetric units and adopts a chair-like configuration ($\mathbf{R}$ = Y, Figure 102). This hexanuclear building block is linked by the BDC ligands to form a 3D framework.

Two lanthanide hydroxide clusters, $Dy_{30}I(\mu_3\text{-}OH)_{24}(\mu_3\text{-}O)_6(NO_3)_9(IN)_{41}(OH)_3(H_2O)_{38}$ and $Dy_{104}I_4(\mu_3\text{-}OH)_{80}(\mu_3\text{-}O)_{24}(NO_3)_{36}(IN)_{125}(OH)_{19}$

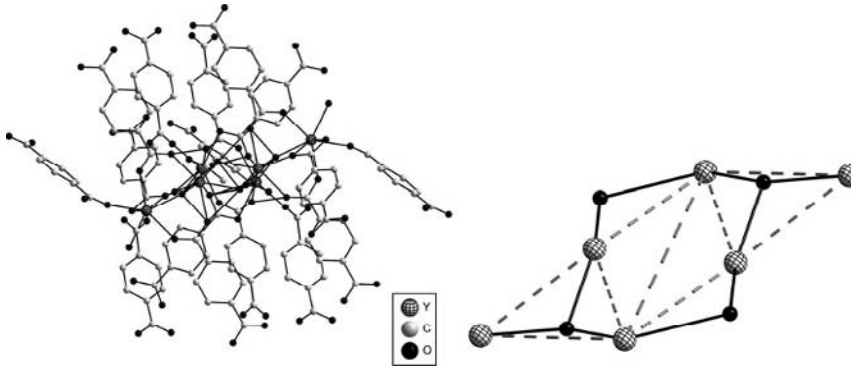

FIGURE 102 Crystal structure of $[Y_3(BDC)_{3.5}(OH)_2(H_2O)_2]\cdot H_2O$. The chair-like core motif is shown on the right (redrawn after Weng et al., 2006).

$(H_2O)_{167}$ (IN = isonicotinate), have been obtained under hydrothermal conditions using isonicotinic acid as the supporting ligand (Gu and Xue, 2007; Figure 103). Both clusters contain a $[Dy_{26}(\mu_3\text{-}OH)_{20}(\mu_3\text{-}O)_6(NO_3)_9I]^{36+}$ core motif which features 26 Dy atoms, 1 I^-, and 9 NO_3^-. It may be viewed as an assembly of five edge-sharing cubane-like $[Dy_4(\mu_3\text{-}OH)_4]^{8+}$ units with six additional Dy atoms connected to this $\{Dy_{20}\}$ framework via bridging NO_3^- ligands. The Dy_{104} species can be viewed as formally constructed from four units of the Dy_{26} building blocks linked by four IN ligands, while the Dy_{30} species is another type of tetramer, composed of two $\{Dy_{26}\}$ and two $\{Dy_4\}$ units, also linked by bridging IN ligands.

Thanks to the synergistic coordination of BDC and IN, lanthanide–transition metal sandwich framework comprising $\{Cu_3\}$ cluster pillars and layered networks of $\{Er_{36}\}$ wheels has been reported. X-ray diffraction studies revealed a stunningly beautiful 3D network structure composed of a 2D network of wheel-shaped cationic clusters $[Er_{36}(\mu_3\text{-}OH)_{30}(\mu_3\text{-}O)_6(BDC)_6]^{54+}$ pillared by anionic clusters of $[Cu_3X_4(IN)_6]^{4-}$ (Cheng et al., 2006; Figure 104).

The Er^{3+} ions are linked by hydroxo and oxo bridges to give two types of small cluster cores: cubic $[Er_4(\mu_3\text{-}O)(\mu_3\text{-}OH)_3]^{7+}$ (Er_4) and dimeric $[Er_2(\mu_3\text{-}OH)_2]^{4+}$ (Er_2) cores (Figure 104, middle). Different from the familiar cubane $[\mathbf{R}_4(\mu_3\text{-}OH)_4]^{8+}$ core which contains four μ_3-OH groups, the present tetranuclear core consists in three μ_3-OH groups and one μ_3-O atom, which is unprecedented. The (Er_4) cores link alternately the (Er_2) units to form a nanosized (Er_{36}) wheel structure.

The aqueous reaction of Gd_2O_3 and CF_3COOH conducted under atmospheric pressure at 50 °C produced the tetrameric gadolinium carboxylate $[Gd_4(OH)_4(CF_3COO)_8(H_2O)_4]_2\cdot 5H_2O$. This is somewhat

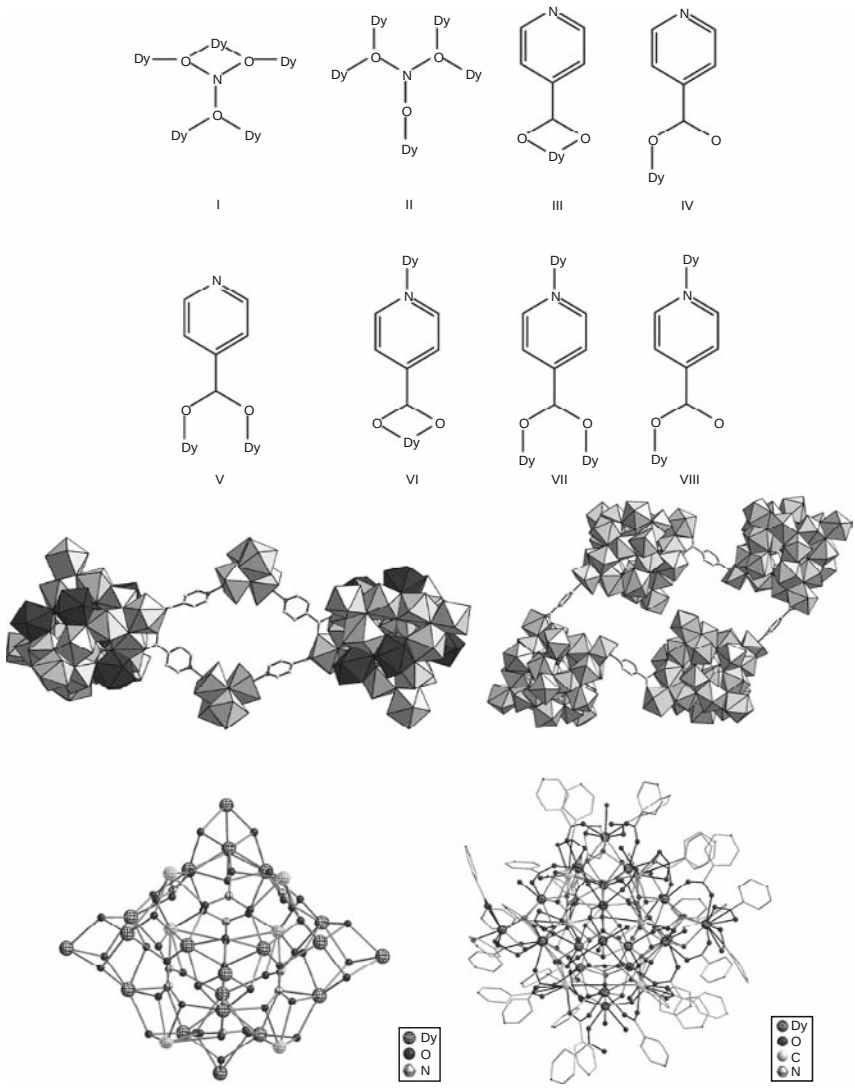

FIGURE 103 Coordination modes of IN toward lanthanide ions (top), structures of $Dy_{30}I(\mu_3\text{-}OH)_{24}(\mu_3\text{-}O)_6(NO_3)_9(IN)_{41}(OH)_3(H_2O)_{38}$ (middle left), $Dy_{104}I_4(\mu_3\text{-}OH)_{80}(\mu_3\text{-}O)_{24}(NO_3)_{36}(IN)_{125}(OH)_{19}(H_2O)_{167}$ (middle right), and the cluster-building blocks of the Dy_{104} cluster (bottom) (redrawn after Gu and Xue, 2007).

surprising as there is no apparent water-soluble enhancing functional group in the ligand nor were hydrothermal conditions used. The hydrolysis is possibly due to the basicity of Gd_2O_3; reaction between a putative hydrated mononuclear lanthanide complex and the basic Gd_2O_3 may be

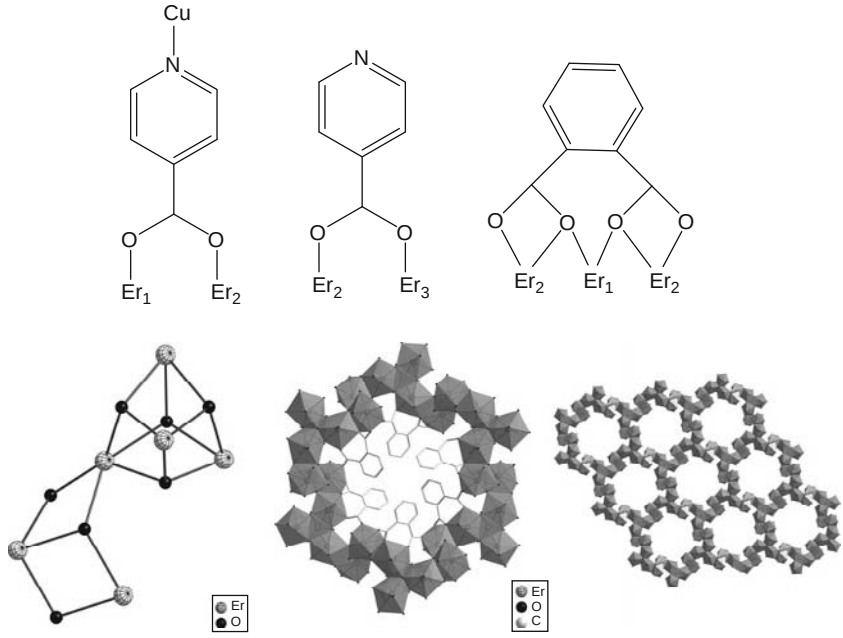

FIGURE 104 Coordination modes of BDC and IN ligands (top) and the structure of a 2D network of wheel-shaped cationic cluster $[Er_{36}(\mu_3\text{-}OH)_{30}(\mu_3\text{-}O)_6(BDC)_6]^{54+}$ (bottom) (redrawn after Cheng et al., 2006).

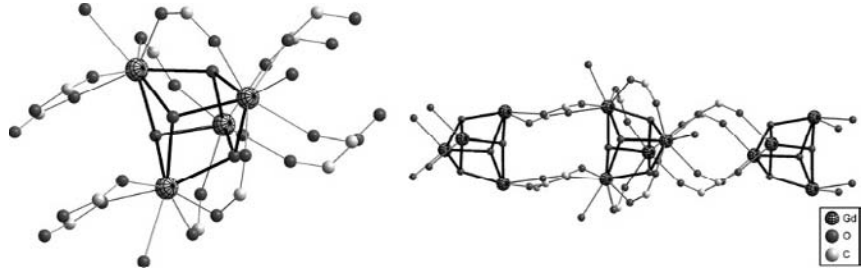

FIGURE 105 Crystal structure of the polymeric gadolinium hydroxide cluster $[Gd_4(OH)_4(CF_3COO)_8(H_2O)_4]_2$ featuring hydrolysis-limiting carboxylate ligands. Individual cubane-like cluster cores are bridged by carboxylate groups to give the polymer (redrawn after John and Urland, 2007).

responsible for aqua ligand deprotonation, eventually leading to the formation of the hydroxide cluster. The distorted $Gd_4(OH)_4$ cubane units are bridged by four carboxylate groups to afford a polymeric assembly with antiferromagnetically coupled lanthanide ions (Figure 105; John and Urland, 2007).

3.5 Hydroxide clusters supported by β-diketonate ligands

Lanthanide β-diketonates are arguably one of the most extensively studied classes of lanthanide-containing compounds. Excellent reviews on the synthesis, structural characterization, and applications of numerous lanthanide diketonates are available (Binnemans, 2005). Although anionic complexes containing four diketonate ligands are not uncommon, most lanthanide diketonates are electrically neutral, featuring three diketonate ligands with the rest of the coordination sphere being completed by O- or N-containing Lewis base ligands. Formation of these neutral Lewis base adducts is achieved either by substituting the coordinated water molecule (s) of an aqua adduct with a chosen nonaqua Lewis base or by one-pot syntheses with a mixture containing the lanthanide starting material, the diketonate ligand, and the desired Lewis base in appropriate relative ratios. Such synthetic procedures have long been established. However, unexpected polynuclear oxide/hydroxide clusters due to adventitious hydrolysis are frequently encountered.

The identity of the resulting lanthanide–oxo/hydroxide clusters featuring diketonate ligands is sensitively dependent on the steric bulk of the ligands and the size of the metal ions. In a number of occasions, unexpected participation of atmospheric CO_2 has led to interesting cluster structures. These lanthanide cluster compounds have been shown to present intriguing molecule-based magnetic phenomena as well as catalytic potentials besides their usually pleasing molecular structures.

As early as in 1972, an octanuclear erbium cluster formulated as $Er_8(\mu_3\text{-}OH)_{12}(\mu_4\text{-}O)(thd)_8$ (thd = 2,2,6,6-tetramethylheptane-3,5-dionate) was obtained in the synthesis of $Er(thd)_3$ (Boeyens and De Villiers, 1972). The cluster core has dodecahedral geometry with a central μ_4-oxide anion and face-capping hydroxides (Figure 106). Each Er atom is chelated by one thd ligand that also uses one of its oxygen atoms to bridge a neighboring metal center. The *t*Bu groups are directed outwards, presumably forming the ''protecting shell'' to limit the degree of hydrolysis. As a consequence, the cluster behaves as a typical nonpolar substance and sublimes without decomposition.

Another early example is the tetranuclear cluster $[Gd_4(\mu_3\text{-}OH)_4(hfpd)_8(H_2O)_6]$ (hfpd = hexafluoropentanedionate) isolated as a minor product from the reaction aimed at the synthesis of gadolinium hexafluoropentanedione (Plakatouras et al., 1994). The cluster features a core of a distorted $[Gd_4(\mu_3\text{-}OH)_4]^{8+}$ cubane with each of its metal atoms chelated by two hexafluoropentanedionato ligands (Figure 107).

Tetranuclear lanthanide clusters of general formula $\mathbf{R}_4(\mu_3\text{-}OH)_2(\mu,\eta^2\text{-}acac)_6(\eta^2\text{-}acac)_4$ ($\mathbf{R}$ = Y, Nd; acac = acetylacetonate) have also been obtained, but by rather different procedures (Barash et al., 1993; Poncelet and Hubert-Pfalzgraf, 1989). The neodymium cluster was

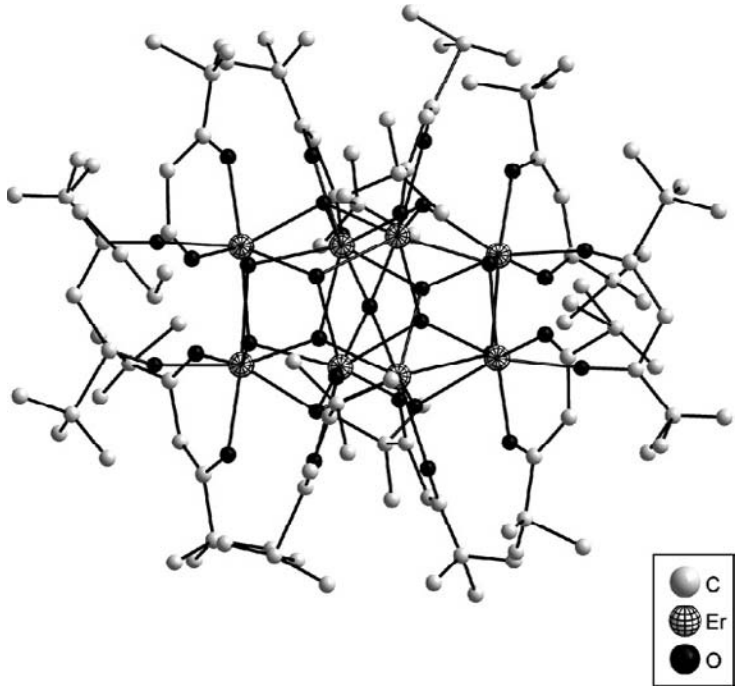

FIGURE 106 Crystal structure of $Er_8(\mu_3\text{-}OH)_{12}(\mu_4\text{-}O)(thd)_8$ (redrawn after Boeyens and De Villiers, 1972).

isolated from a reaction that is synthetically exclusive and much more demanding than straightforward hydrolysis. The Y(III) analogue was reported shortly thereafter as an unexpected outcome of the dehydration of $Y(acac)_3 \cdot 3H_2O$ aimed at the production of the anhydrous complex.

The molecular structure of $Y(\mu_3\text{-}OH)_2(\mu,\eta^2\text{-}acac)_6(\eta^2\text{-}acac)_4$ is shown in Figure 108. The molecule sits on an inversion center, making only half of it unique. The four metal ions defining the parallelogram-shaped core are of two chemically distinct types, one pair being ''hinge'' and the other, ''wing-tip.'' The Y atoms are linked by two triply bridging hydroxo groups on opposite sides of the Y_4 plane. In addition, the ''hinge'' lanthanide atoms are each bound to one η^2-acac (chelating) and one μ,η^2-acac (bridging-chelating) ligand, whereas each ''wing-tip'' lanthanide atom features one η^2-acac and two μ,η^2-acac ligands. As such, the edges of the parallelogram are spanned alternately by one and two bridging oxygen atoms. All metals are octacoordinate, and their coordination polyhedra may be described as distorted-square antiprism. That clusters of the same core structure are obtained by so distinctly different synthetic routes suggests that the tetranuclear hydroxo cluster core may be a common entity in the hydrolytic chemistry of lanthanide diketonates.

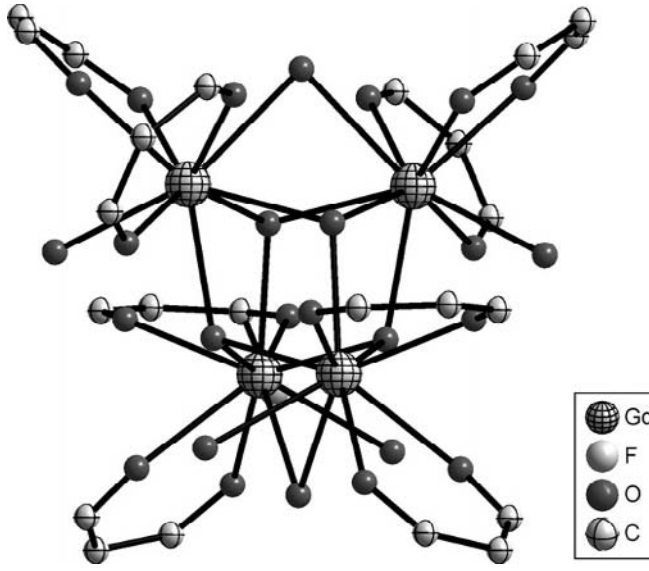

FIGURE 107 Crystal structure of $[Gd_4(\mu_3\text{-}OH)_4(hfpd)_8(H_2O)_6]$. The CF_3 groups are removed for clarity (redrawn after Plakatouras et al., 1994).

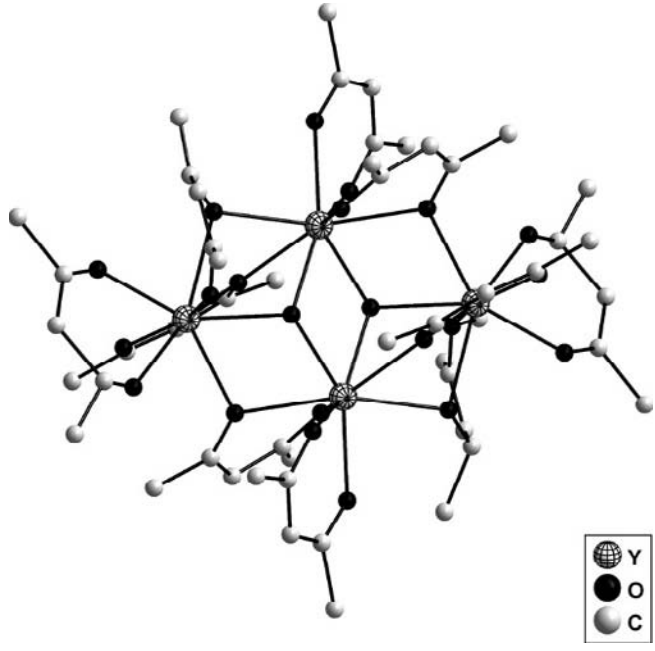

FIGURE 108 Crystal structure of $Y_4(\mu_3\text{-}OH)_2(\mu,\eta^2\text{-}acac)_6(\eta^2\text{-}acac)_4$ (redrawn after Barash et al., 1993).

A hexanuclear cluster, $Ce_6(acac)_{12}(\mu_3\text{-}O)_4(\mu_3\text{-}OH)_4$, was obtained when the chemically modified precursor $Ce(OCHMe_2)_2(acac)_2$ was utilized in making lanthanide-containing sol-gel materials (Toledano et al., 1990). The core structure is similar to the one shown in Figure 89, but without the interstitial μ_6-oxo group. In addition, only four of the eight face-capping ligands are hydroxo groups; the other half are μ_3-oxo ligands. This combination of ligands is mandated by the oxidation number of the Ce(IV) ion.

Tetradecanuclear clusters of general formula $\mathbf{R}_{14}(\mu_4\text{-}OH)_2(\mu_3\text{-}OH)_{16}(\mu,\eta^2\text{-}acac)_8(\eta^2\text{-}acac)_{16}$ ($\mathbf{R}$ = Eu and Tb) were also obtained unexpectedly when the displacement of aqua ligands of $\mathbf{R}(acac)_3 \cdot 2H_2O$ with 2,2′-dipyridylsulfide was attempted (Wang et al., 2002). Apparently, the pyridyl-based ligands, acting as a base, promoted deprotonation of the aqua ligands instead of displacing them, leading to the formation of the clusters.

The structure of the terbium hydroxide cluster is shown in Figure 109 as a representative. Its core features three fused Tb_6 octahedra into a linear arrangement by sharing opposite vertices, but with the outer two vertices missing. This cluster provides another example of a hydroxo–lanthanide complex that has a ''hollow'' octahedral Tb_6 unit without the support of a μ_6-oxo ligand. Every Tb_3 triangular face is capped by a triply bridging hydroxo group, while each of the two terminal Tb_4 faces is capped by a μ_4-OH. Alternatively, the cluster core may be viewed as a ''triple-deckered''

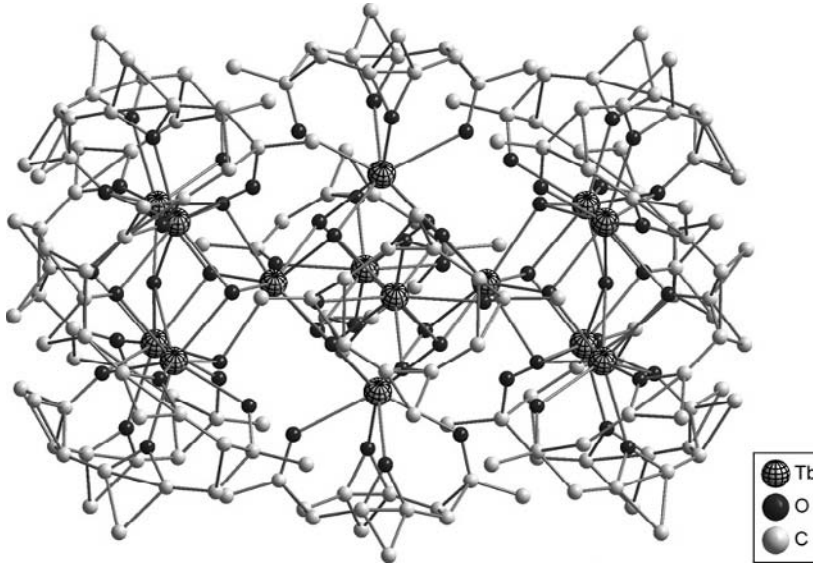

FIGURE 109 Crystal structure of tetradecanuclear $Tb_{14}(\mu_4\text{-}OH)_2(\mu_3\text{-}OH)_{16}(\mu,\eta^2\text{-}acac)_8(\eta^2\text{-}acac)_{16}$ (redrawn after Wang et al., 2002).

structure with two Tb atoms being sandwiched between the three decks of square-shaped Tb_4 units. These three decks are rotated by 45° with respect to their neighbors. The rest of the coordination sphere is occupied by acac ligands, two on each of the Tb atoms. The Tb atoms forming the middle deck are each coordinated by two chelating acac ligands, whereas each of the outer-deck Tb bears one chelating (η^2-acac) and one bridging-chelating (μ,η^2-acac) ligand. The combined effect of this bridging interaction and the face-capping μ_4-OH coordination leads to a significantly shorter Tb–Tb (neighboring atoms) separation in the outer decks than their counterparts within the middle deck. It is noteworthy that the acac ligands essentially form a protective sheath, not only rendering the cluster organically soluble, but also preventing further hydrolysis from occurring. In fact, the cluster remains intact even when the product mixture was extracted with water to remove the excess of organic base used in the synthesis.

Isolation of cluster species of an intermediate nuclearity should offer insights into the seemingly modular assembly. Such intermediates, $[\mathbf{R}_9(acac)_{16}(OH)_{10}]^+[Mo_2(CO)_{10}(\mu\text{-H})]^-$ ($\mathbf{R}$ = Sm, Eu, Gd, Dy, and Yb) and $[Sm_9(acac)_{16}(OH)_{10}]^+[CrW(CO)_{10}(\mu\text{-H})]^-$, were obtained by the hydrolysis of $\mathbf{R}(acac)_3 \cdot 2H_2O$ promoted by homo or heterodinuclear decacarbonyl hydrides, which are rather unusual bases. The resulting cluster salts of the complex counteranion may be interesting candidates for isolating mixed-metal materials ($\mathbf{R}$ = Sm, Eu, Gd, Tb, and Yb) with homo- or heterodinuclear decacarbonyl hydrides $[HMo_2(CO)_{10}]^-$ and $[HCrW(CO)_{10}]^-$ (Volpe et al., 2004, 2006). The nonanuclear cluster anion consists in two apex-shared square pyramids, and the sandwich structure may be viewed as an immediate precursor to the tetradecanuclear double-sandwiched cluster (Addamo et al., 2004) ($\mathbf{R}$ = Sm, Figure 110).

Nonanuclear lanthanide–oxo/hydroxo complexes $[\mathbf{R}_9(\mu_4\text{-O})_2(\mu_3\text{-OH})_8(\mu\text{-BA})_8(BA)_8]^-$ (BA = benzoylacetonate; $\mathbf{R}$ = Sm, Eu, Gd, Dy, and Er) were also prepared by the reaction of hydrous lanthanide trichlorides with benzoylacetone in the presence of triethylamine in methanol (Xu et al., 2002).

Other diketonate ligands have also been tested for the assembly of hydroxide clusters, of which the work with dibenzoylmethanide (DBM) is most notable. Reaction of $\mathbf{R}Cl_3$ and dibenzoylmethane in methanol with an excess of triethylamine resulted in the formation of either tetranuclear $[\mathbf{R}_4(\mu_3\text{-OH})_2(DBM)_{10}]$ ($\mathbf{R}$ = Pr, Nd, and Sm) or pentanuclear species $[Dy_5(\mu_4,OH)(\mu_3\text{-OH})_4(\mu,\eta^2\text{-DBM})_4(\eta^2\text{-DBM})_6]$ as well as $H_5[Y_5(\mu_4\text{-O})(\mu_3\text{-O})_4(\mu,\eta^2\text{-DBM})_4(\eta^2\text{-DBM})_6]$ (Baskar and Roesky, 2005).

The tetranuclear clusters are structurally the same as the aforementioned tetranuclear species (Figure 108), but with DBM rather than acac ligands building up the periphery. The pentanuclear clusters have a square pyramidal core ($\mathbf{R}$ = Dy, Figure 111). Each triangular face of the

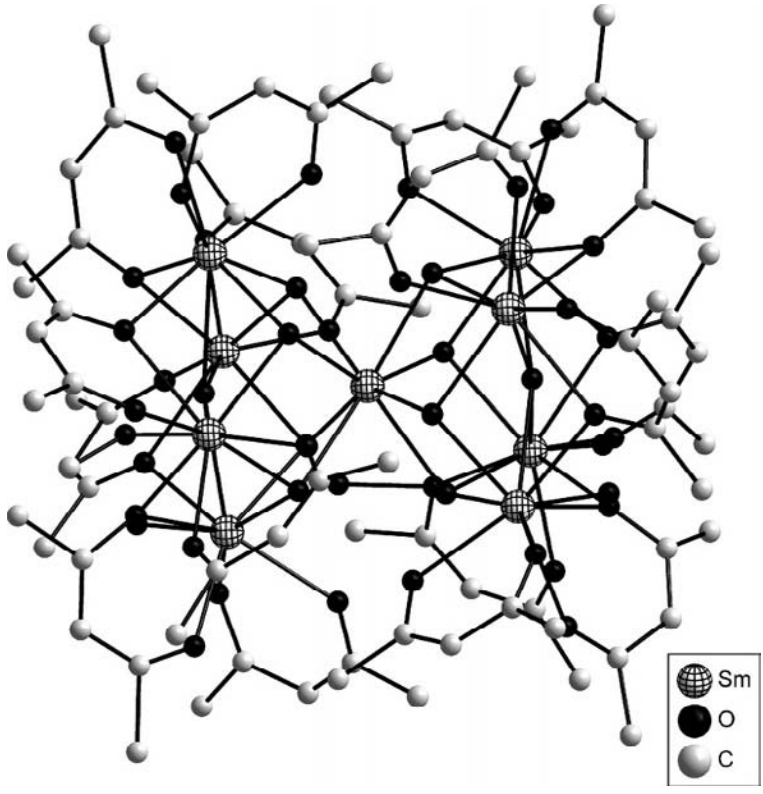

FIGURE 110 Crystal structure of a nonanuclear samarium hydroxide cluster supported by acac ligands (redrawn after Addamo et al., 2004).

square pyramid is capped by one μ_3-O moiety. In the square base, four Dy atoms are linked by one μ_4-O atom.

The formally modular assembly of these clusters of different nuclearity is rather intriguing. The structural relationship between the pentanuclear, nonanuclear, and tetradecanuclear species can be clearly appreciated from Figure 112.

These cluster species possess interesting materials properties and potential for catalysis as well as unique reactivity. For example, the dysprosium hydroxy cluster displays slow relaxation characteristics of the magnetization typical of SMMs at low temperatures (Chibotaru et al., 2008; Gamer et al., 2008). The air- and moisture-stable pentanuclear Y cluster, on the other hand, has been found to catalyze the oxidation of aldehydes to the corresponding carboxylic acids in the presence of air (Roesky et al., 2004).

Addition of *o*-nitrophenol to the reaction mixture causes another twist. Tetranuclear lanthanide clusters $[\mathbf{R}_4(\mu_3\text{-OH})_2(\text{DBM})_8(o\text{-}O_2NC_6H_4O)_2]$

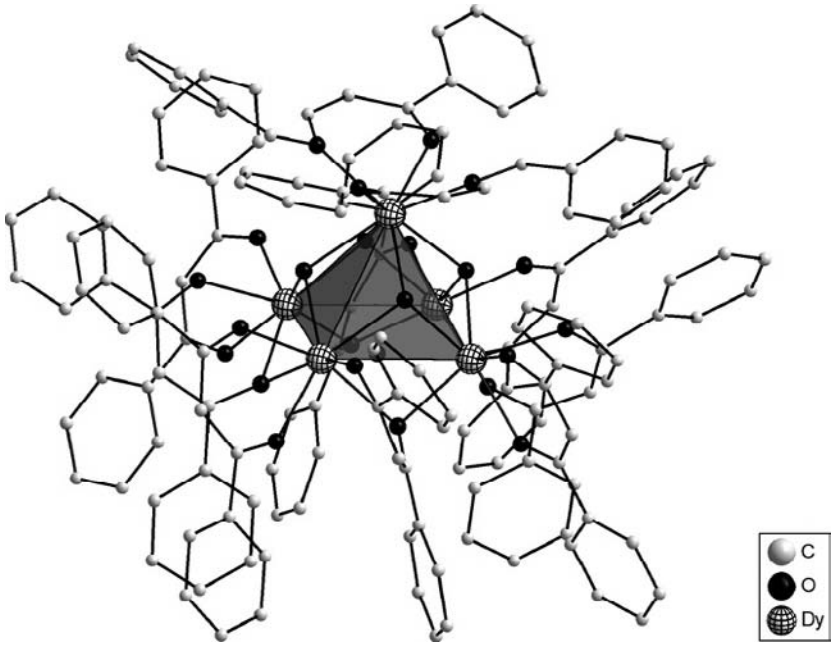

FIGURE 111 Crystal structure of $[Dy_5(\mu_4\text{-OH})(\mu_3\text{-OH})_4(\mu,\eta^2\text{-DBM})_4(\eta^2\text{-DBM})_6]$ (redrawn after Baskar and Roesky, 2005).

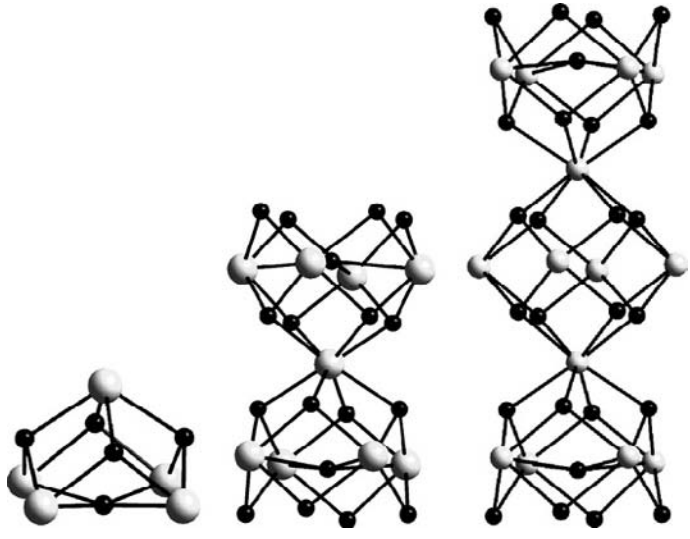

FIGURE 112 Structures of pentanuclear, nonanuclear, and tetradecanuclear cluster cores showing formal modular build-up of their assemblies.

(**R** = Yb, Lu) and pentanuclear lanthanide clusters $HNEt_3[\mathbf{R}_5(\mu_3\text{-}OH)_4(\mu_4\text{-}OH)(DBM)_7(o\text{-}O_2NC_6H_4O)_3Cl]$ (**R** = Er, Tm) were obtained (Datta et al., 2007). Although the fundamental core structures are still maintained, as compared with the above clusters, a number of the DBM ligands are replaced by nitrophenolate.

Using a diketonate ligand modified by redox-active ferrocenyl substituent, tetranuclear lanthanide–hydroxo clusters $[\mathbf{R}_4(\mu_3\text{-}OH)_4(FcacacPh)_8]$ (**R** = Yb, Lu; FcacacPh = benzoyl(ferrocenoyl)methanide) featuring the now familiar distorted-cubane core were obtained (**R** = Lu, Figure 113).

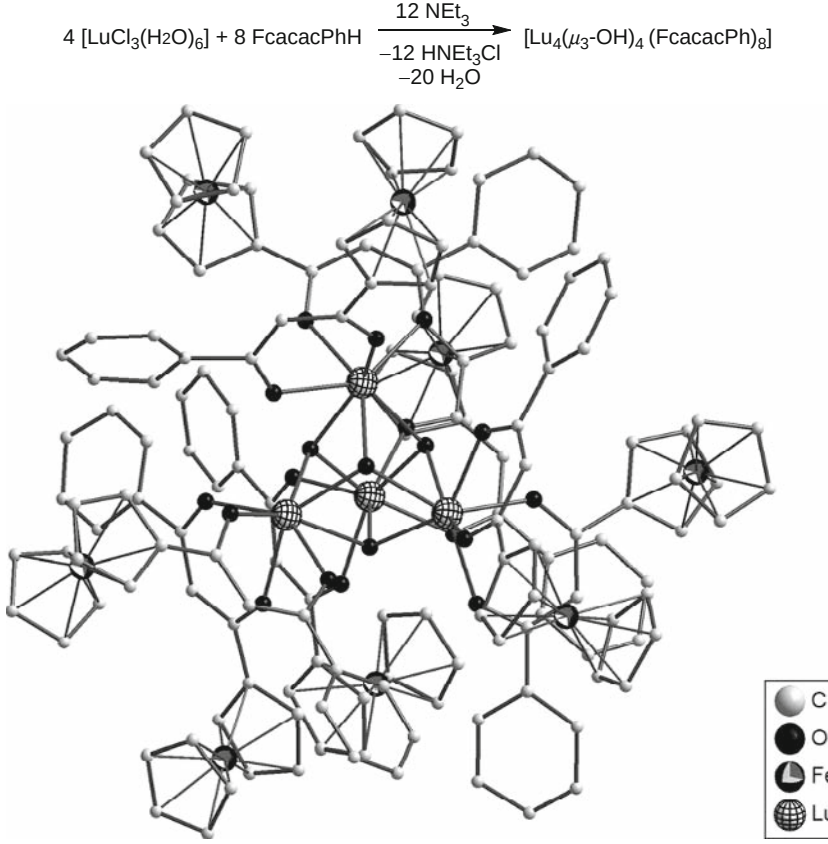

FIGURE 113 Synthesis and crystal structure of $[Lu_4(\mu_3\text{-}OH)_4(FcacacPh)_8]$, featuring eight ferrocenyl groups anchored onto a cubane-like $[Lu_4(\mu_3\text{-}OH)_4]$ via bridging/chelating diketonate ligands (redrawn after Baskar and Roesky, 2006).

These functionalized clusters contain a maximum number of ferrocene units anchored to the molecular framework and may represent model compounds for the fixation of organometallic fragments on a lanthanide oxide surface (Baskar and Roesky, 2006).

When the synthesis of the lanthanum cluster was attempted by reacting $LaCl_3$ and dibenzoylmethane in methanol with an excess of TEA, the unexpected formation of a dodecanuclear hydroxo-bridged La cluster templated by CO_3^{2-} and phenylglyoxylate (Phgly), $[La_{12}(OH)_{12}(H_2O)_4(DBM)_{18}(Phgly)_2(CO_3)_2]$ (Andrews et al., 2007) was achieved. As can be seen from the crystal structure shown in Figure 114, there are surprisingly two apparently templating CO_3^{2-} anions with two Phgly coligands, in addition to the expected DBM, hydroxo and aqua ligands. The formation of the Phgly ligand is rationalized as the oxidation of the original DBM ligand catalyzed by the Lewis acidic lanthanide ion by air. The carbonate is believed to originate from atmospheric CO_2. Other examples of unexpected carbonate incorporation and its role in

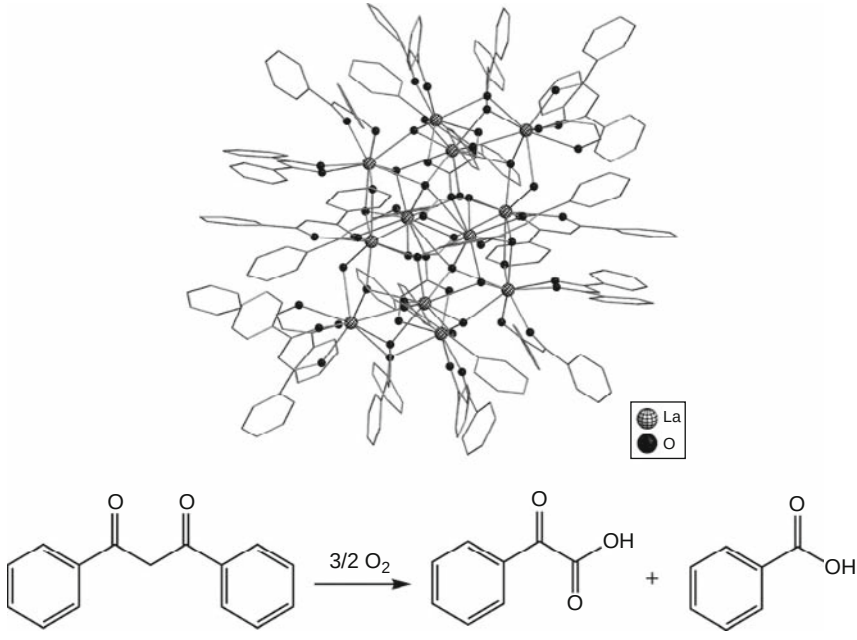

FIGURE 114 Crystal structure of $[La_{12}(OH)_{12}(H_2O)_4(DBM)_{18}(Phgly)_2(CO_3)_2]$ (top), an unexpected carbonate-encapsulating cluster species featuring coordination by both diketonate ligands and glyoxylate ligand resulting from the oxidation of the diketonate (bottom) (redrawn after Andrews et al., 2007).

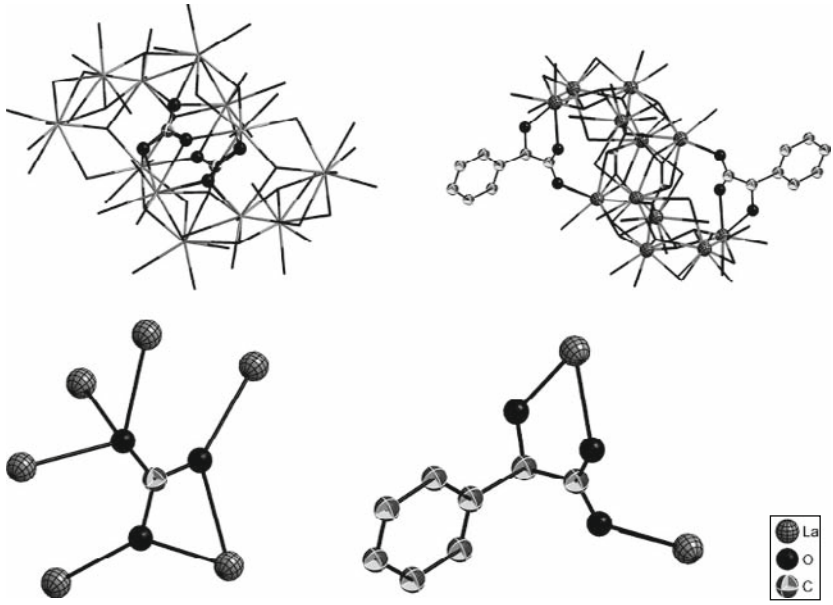

FIGURE 115 Metal coordination sphere of $[La_{12}(OH)_{12}(H_2O)_4(DBM)_{18}(Phgly)_2(CO_3)_2]$ (top) and the coordination modes of the carbonato (bottom left) and glyoxylato ligands (bottom right) (redrawn after Andrews et al., 2007).

templating aggregation and growth of cluster assembly are known. Together, they suggest the important role of these otherwise mundane inorganic entities.

The cluster core, structurally shown in Figure 115, is formed by 12 La^{3+} cations. Each La^{3+} is coordinated by nine oxygen atoms. The oxygen atoms which do not belong to the organic ligands are either μ_3-hydroxo or μ_2-aqua ligands. Each carbonate binds to six different metal centers with a chelating and bridging configuration. Overall the coordination mode is μ_6-η^1:η^1:η^1:η^1:η^1:η^2.

It is noteworthy that ligands with similar functionality to diketonates have promoted the assembly of lanthanide hydroxide clusters. These ligands are mainly β-ketoesterate ligands. The $[Y_9(\mu_4\text{-}O)_2(\mu_3\text{-}OH)_8\{MeC(O)CHC(O)Z\}_{16}]^-$ species was obtained in this way (Hubert-Pfalzgraf et al., 1999; Figure 116), the functional group Z being an allyl group OCH_2CHCH_2 or an ethoxide. The latter is formed from the hydrolysis of the allyl ester followed by esterification with ethanol, the solvent used for the reaction.

The reaction between $Y_5O(OPr^i)_{13}$ and allylacetoacetate (AAA) at room temperature resulted in a compound whose recrystallization from ethanol/toluene gave an octanuclear $[Y_4(\mu_4\text{-}O)(\mu,\eta^2\text{-}AAA)_2(\eta^2\text{-}AAA)_3$

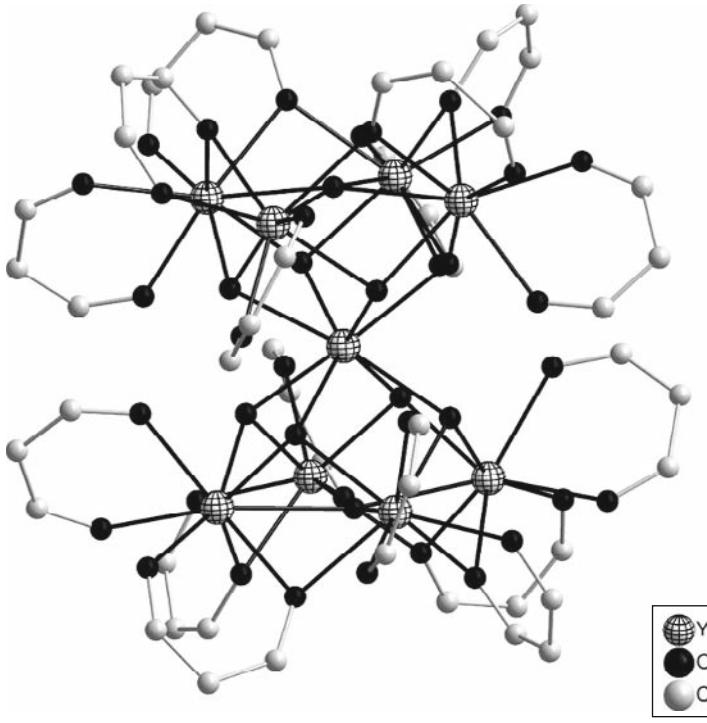

FIGURE 116 Crystal structure of $[Y_9(\mu_4\text{-}O)_2(\mu_3\text{-}OH)_8\{MeC(O)CHC(O)Z\}_{16}]^-$ ($Z = OCH_2CHCH_2$ or EtO^-). Methyl and Z groups are removed for clarity (redrawn after Hubert-Pfalzgraf et al., 1999).

$(\mu\text{-}OEt)_2]_2(\mu_3\text{-}OH)_4(\mu_3\text{-}OEt)_2$ species, based on the assembly of two symmetrically related $[Y_4(\mu_4\text{-}O)(AAA)_5(\mu\text{-}OEt)_2]$ tetrahedral units via μ_3-OH and ethoxide ligands (Hubert-Pfalzgraf et al., 2004). The corresponding crystal structure is shown in Figure 117. The basic building block is a flattened tetrahedron with a μ_4-oxo ligand.

It should be noted that although these high-nuclearity clusters are generally assembled from the corresponding mononuclear starting materials by means of hydrolysis, the Y_8 cluster described above is unique as its building block is derived from $Y_5O(OPr^i)_{13}$. In other words, the oxo ligands result from the oxoisopropoxide starting material, while the condensation proceeds via hydroxo ligands produced by hydrolysis.

Other octanuclear lanthanide oxoalkoxides are known. They are also based on tetranuclear units arranged around square planar oxo ligands such as in $[Er_8(\mu_4\text{-}O)(\mu_3\text{-}OH)_{12}(thd)_{10}]$ (Boeyens and De Villiers, 1972; Figure 106) and $[Pr_8(\mu_4\text{-}O)_4(OC_2H_4OMe)_{16}(OPMe_3)_2]$ (Hubert-Pfalzgraf et al., 1997).

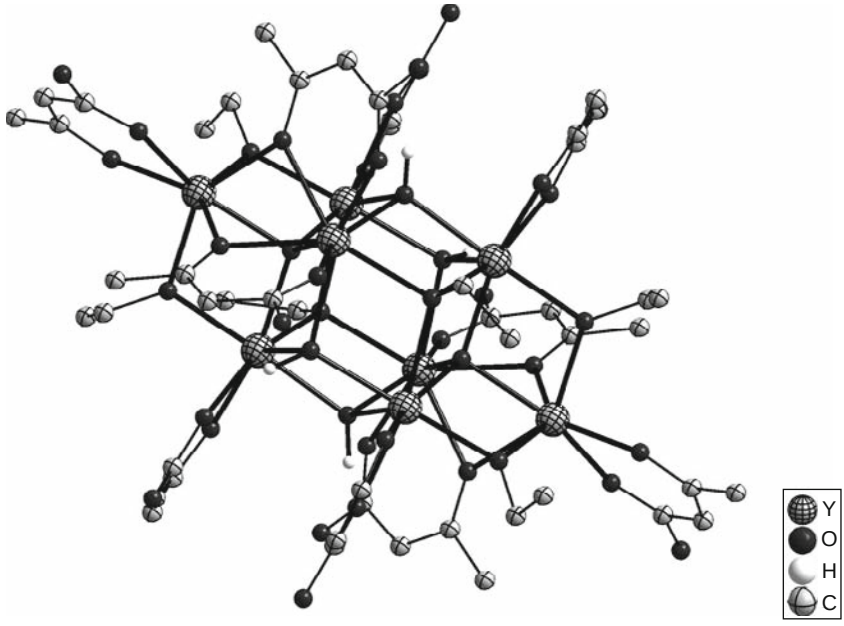

FIGURE 117 Crystal structure of the octanuclear $[Y_4(\mu_4\text{-O})(\mu,\eta^2\text{-AAA})_2(\eta^2\text{-AAA})_3(\mu\text{-OEt})_2]_2(\mu_3\text{-OH})_4(\mu_3\text{-OEt})_2$ species (redrawn after Hubert-Pfalzgraf et al., 2004).

Finally, ethyl 4,4,4-trifluoroacetoacetate (ETA) led to a tetranuclear cluster $[Eu_4(ETA)_9(OH)_3(H_2O)_3]$ and its luminescence properties were investigated (Souza et al., 2007). Modeling studies of the ground-state geometry of the tetramer were carried out, and the results agree well with the structural data with the Eu^{3+} ion occupying four different sites in a low-symmetry environment (Figure 118).

3.6 Hydroxide clusters by direct hydrolysis of lanthanide salts

Most of the lanthanide–hydroxo clusters contain organic ligands, understandably for their role of limiting the degree of hydrolysis. However, there are a number of examples wherein no such ''organics'' are present. Some of these cluster motifs have actually been used as building blocks for the construction of supra/supermolecular structures of even higher order.

Early examples of lanthanide–hydroxo/oxo clusters with general formula $[\mathbf{R}_6O(OH)_8(H_2O)_{12}(NO_3)_6](NO_3)_2 \cdot xH_2O]$ have been synthesized via the thermal decomposition of hydrated $\mathbf{R}(NO_3)_3$ followed by hydrolysis of the decomposition products (Giester et al., 1997; Zák et al., 1994). Crystal structures have been determined for clusters of Y, Gd, Yb, Sm,

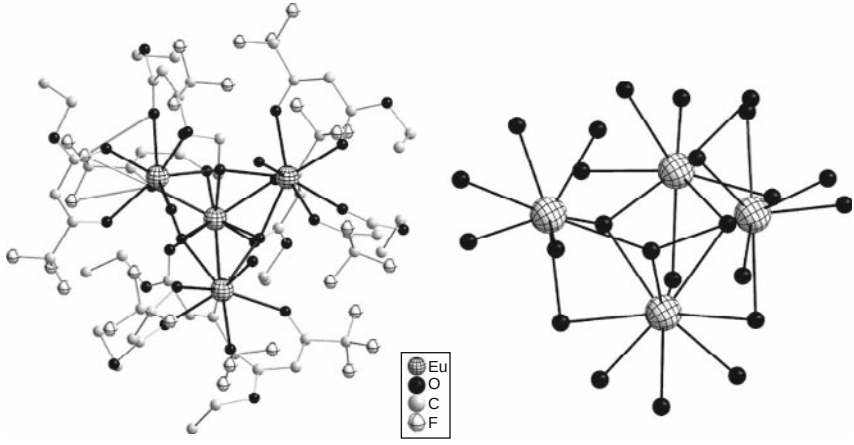

FIGURE 118 Crystal structure of $[Eu_4(ETA)_9(OH)_3(H_2O)_3]$ (left) with the cluster core (right) (redrawn after Souza et al., 2007).

Dy, and Er. Except for the different number of crystallization water molecules, the compounds are isostructural, with a common core structurally shown in Figure 89. The cationic cluster is a perfect octahedron of six lanthanide atoms face capped by eight triply bridging hydroxo groups and with an interstitial μ_6-oxo group. Each metal atom is terminally coordinated by two aqua and one chelating nitrate ligands. The coordination of the nitrate ligands may be viewed as a means of limiting hydrolysis in a capacity similar to that of an organic ancillary ligand.

Recently, analogous clusters of lighter lanthanide elements (Pr and Nd) have been structurally characterized. Two lanthanide atoms occupying the axial positions were found to have three instead of two aqua ligands, possibly a reflection of the larger size of the lighter elements (Calvez et al., 2008). Thermal analysis indicated that the cluster core structure is stable up to 170 °C when all crystallization water and aqua ligands are lost. The clusters are highly soluble in water, but further hydrolysis occurs, affording insoluble mixtures of hydroxides. The cluster is reasonably soluble and stable in a number of organic solvents, including DMF. A reaction between $[Er_6(\mu_6\text{-}O)(\mu_3\text{-}OH)_8(NO_3)_6(H_2O)_{12}](NO_3)_2$ and $ErCl_3$ in DMF led to the formation of a coordination polymer, $[Er_6(\mu_6\text{-}O)(\mu_3\text{-}OH)_8(NO_3)_4(H_2O)_{11}(OH)(ONONO_2)]Cl_3$, featuring hexanuclear cluster units bridged by an original N_2O_4 ligand. This ligand is a result of the condensation of two nitrate ions. It coordinates to one cluster in a chelating fashion, while acting as a monodentate ligand for an adjacent cluster (Figure 119; Mahe et al., 2005).

Direct hydrolysis of lanthanide iodides and perchlorates has also been reported. Cluster-type basic lanthanide iodides $[\mathbf{R}_6(\mu_3\text{-}OH)_8(\mu_6\text{-}O)$

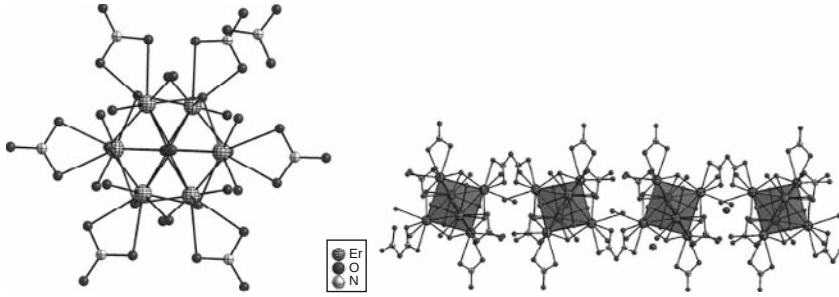

FIGURE 119 Crystal structure of a coordination polymer, $[Er_6(\mu_6\text{-}O)(\mu_3\text{-}OH)_8(NO_3)_4(H_2O)_{11}(OH)(ONONO_2)]$, featuring well-defined hexanuclear cluster units bridged by N_2O_4 ligands (redrawn after Mahe et al., 2005).

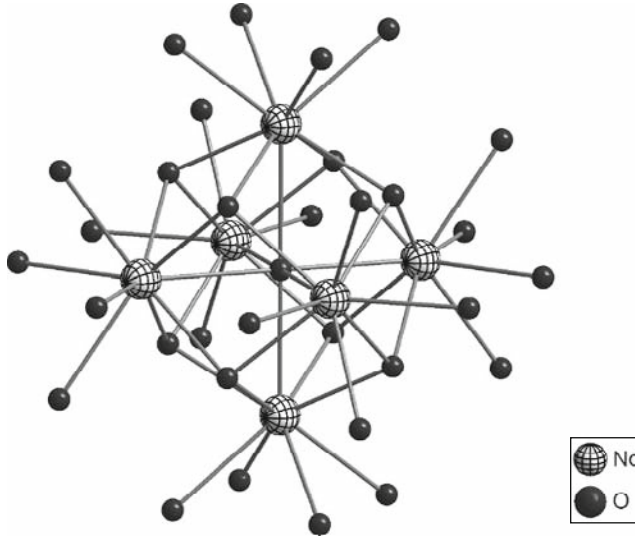

FIGURE 120 Crystal structure of $[Nd_6(\mu_3\text{-}OH)_8(\mu_6\text{-}O)(H_2O)_{24}]^{8+}$ (redrawn after Mudring et al., 2006; Wang et al., 2000).

$(H_2O)_{24}]I_8(H_2O)_8$ (**R** = Nd, Eu, Tb, and Dy) (Mudring et al., 2006; Wang et al., 2000) (**R** = Nd, Figure 120). Different from the clusters obtained from the hydrolysis of lanthanide nitrates, the hexanuclear clusters only contain water-based ligands. Besides the usual μ_6-oxo and face-capping μ_3-OH groups, there are 24 terminal aqua ligands, four on each of the six metal atoms.

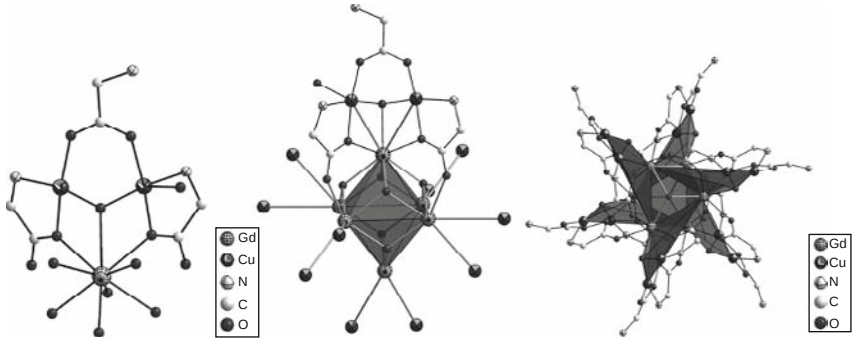

FIGURE 121 Left to right: coordination geometries of Gd^{3+} and Cu^{2+} atoms, six (Cu_2) blades encapsulating the octahedral core of $[Gd_6(\mu_3\text{-}OH)_8]^{10+}$, and overall structure of the heterometallic cluster viewed along one vertex of the octahedral core (redrawn after Xiang et al., 2007).

A similar hexanuclear cluster without the interstitial oxo group has long been established (Toledano et al., 1990). In a recent report, a heterometallic 3d–4f cluster containing such a discrete octahedral core of $[Gd_6(\mu_3\text{-}OH)_8]$ encapsulated by six (Cu_2) has been prepared (Figure 121) and found to be ferromagnetic (Xiang et al., 2007).

An octanuclear europium cluster, formulated as $[Eu_8(\mu_4\text{-}O)(\mu_3\text{-}OH)_{12}(\mu\text{-}OTf)_{14}(OTf)_2]$ (OTf = trifluoromethanesulfonate) was obtained from the thermal decomposition of europium triflate in ionic liquid 1-butyl-1-methylpyrrolidinium trifluoromethanesulfonate (Babai and Mudring, 2006). The cluster core of $[Eu_8(\mu_4\text{-}O)(\mu_3\text{-}OH)_{12}]$ is organized around an oxide anion. The eight metal atoms and the interstitial oxo group form a polyhedron that may be most conveniently described as a triangular dodecahedron, with every single triangular face being capped by a μ_3-OH group (Figure 122). This cluster core has previously been found in $[Eu_8(\mu_4\text{-}O)(\mu_3\text{-}OH)_{12}(DMF)_8(Se_3)(Se_4)_3(Se_5)_2]$ (Pernin and Ibers, 1997, 1999; Figure 64) and $Er_8(\mu_3\text{-}OH)_{12}(\mu_4\text{-}O)(thd)_8$ (Boeyens and De Villiers, 1972; Figure 106), although the accompanying noncore ligands are polyselenido and diketonato ligands instead of triflate anions in the present case. The observation of the same cluster core structure suggests its common existence in lanthanide–oxo/hydroxo cluster chemistry.

3.7 Hydroxide clusters supported by other ancillary ligands

Polyoxometalate anions, due to the large number of oxygen atoms, have also been used to control the hydrolysis of the oxophilic lanthanide ions (Pope, 2008). Hydrolysis of Y(III) or Yb(III) by carbonate in the presence of the trivacant Wells–Dawson polyoxoanion, $\alpha\text{-}[P_2W_{15}O_{56}]^{12-}$ produced

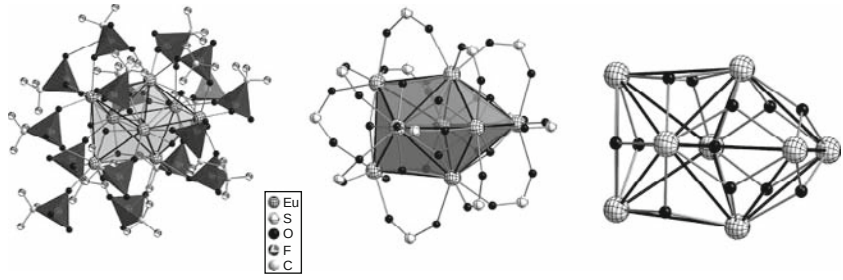

FIGURE 122 Left to right: crystal structure of $[Eu_8(\mu_4\text{-}O)(\mu_3\text{-}OH)_{12}(\mu_2\text{-}OTf)_{14}(OTf)_2]$, its coordination sphere, and cluster core structure (redrawn after Babai and Mudring, 2006).

two polyoxometalate-supported hydroxo/oxo clusters (Fang et al., 2005). The structure of the Y complex consists in a distorted $Y_4(OH)_4$ cubane cluster encapsulated by two lacunary α-$[P_2W_{15}O_{56}]^{12-}$ units (Figure 123, left), while the Yb cluster features a hexametallic core centered around a μ_6-oxo atom with each Yb_3 triangular face capped by an oxo or a hydroxo group (Fang et al., 2003; Figure 123, middle). A templating role is suspected for the carbonate ion even though it is not present in final structure. The isolation of a carbonate-centered Y_3 cluster species sandwiched between two A-α-$PW_9O_{34}^{9-}$ moieties supports this hypothesis (Figure 123, right). In addition, control experiments using NaOH at an adjusted comparable pH as the hydrolysis reagent afforded compounds with completely different structures.

An unusual hexanuclear lanthanum carbonato complex $[La_6(tpen)_4(MeCN)_2(H_2O)_2(\mu_3\text{-}\eta^1\text{:}\eta^2\text{:}\eta^2CO_3)_4(\mu_3\text{-}\eta^1\text{:}\eta^1\text{:}\eta^2CO_3)_2](OTf)_6 \cdot 6MeCN$ (tpen = tetrapodal *N*,*N*,*N*′,*N*′-tetrakis(2-pyridylmethyl)ethylenediamine) has been reported recently as arising from the exposure of a dinuclear hydroxo complex $\{[La(tpen)(\mu\text{-}OH)]_2(\mu\text{-}\eta^1\text{:}\eta^1OTf)\}(OTf)_3$ to air (Natrajan et al., 2006). The dinuclear species contains two La(tpen) moieties connected by two bridging hydroxo groups (Figure 124, up right). One triflate anion coordinates across the dinuclear core in a $\mu\text{-}\eta^1\text{:}\eta^1$ manner. This bridging triflate group may be viewed as a model for the proposed substrate binding in RE^{3+}-(tpen)-accelerated hydrolysis of phosphate diesters.

The cationic, carbonate-containing hexanuclear cluster can be conceptually described as a distorted octahedron with six lanthanum ions located at the vertices spanned by six bridging carbonate ligands (Figure 123, bottom). The six carbonate ligands adopt two different coordination modes: four carbonates bridge three different La ions across four faces of the La_6 octahedron with a $\mu_3\text{-}\eta^1\text{:}\eta^2\text{:}\eta^2$-coordination mode, while the other two, in the equatorial plane, connect three lanthanide ions in an

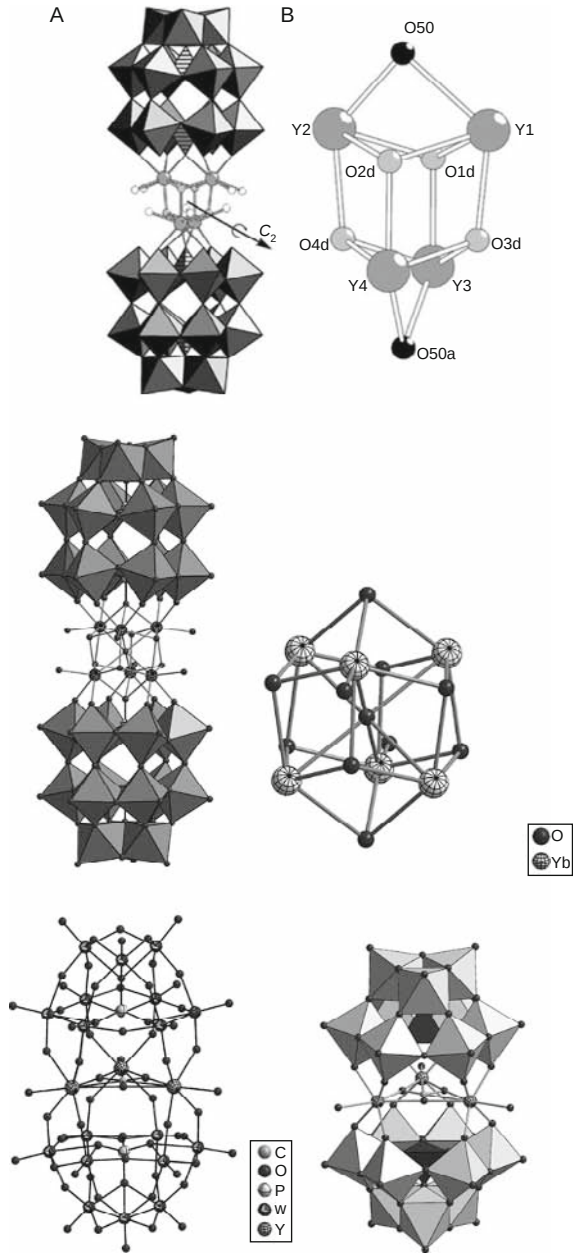

FIGURE 123 Crystal structures of three lanthanide hydroxide clusters: tetranuclear (top), hexanuclear (middle), and trinuclear (bottom) (redrawn after Fang et al., 2003, 2005).

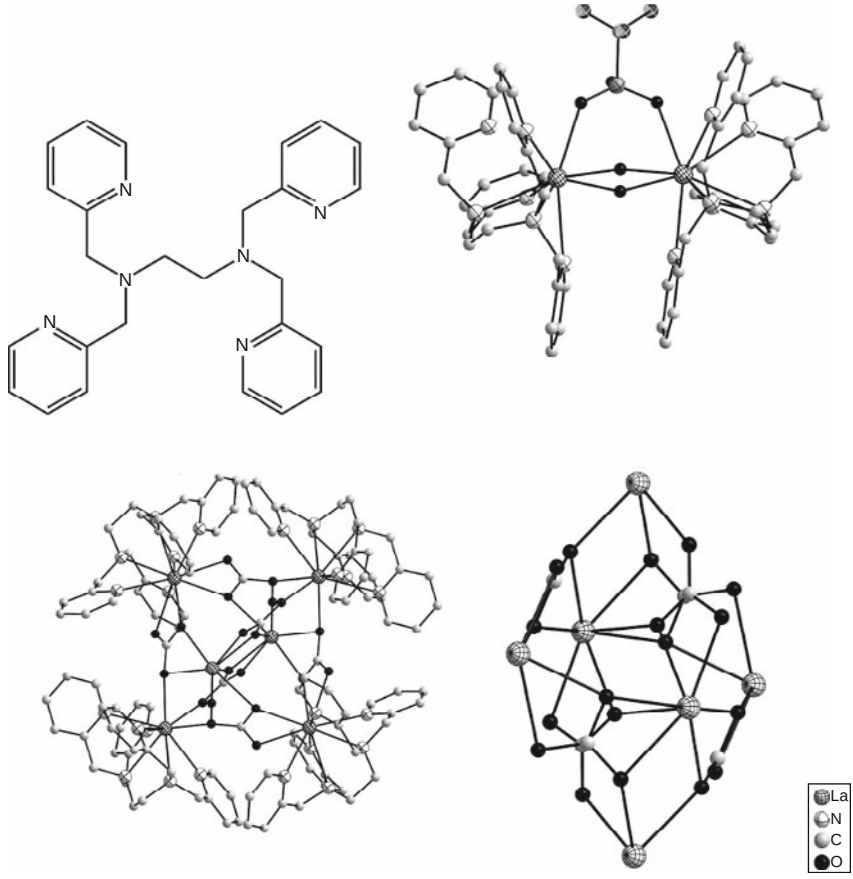

FIGURE 124 Clockwise from top left: molecular structure of tpen, crystal structure of a dinuclear hydroxo complex $\{[La(tpen)(\mu\text{-}OH)]_2(\mu\text{-}\eta^1{:}\eta^1OTf)\}^{3+}$, crystal structure of cationic hexanuclear cluster $[La_6(tpen)_4(MeCN)_2(H_2O)_2(\mu_3\text{-}\eta^1{:}\eta^2{:}\eta^2CO_3)_4(\mu_3\text{-}\eta^1{:}\eta^1{:}\eta^2CO_3)_2]^{6+}$, and its core motif (redrawn after Natrajan et al., 2006).

unusual μ_3-η^1:η^1:η^2 manner, forming a La_2O_2 diamond-shaped core. The incorporation of atmospheric CO_2 by using lanthanide hydroxide clusters has significant ramifications from an environmental point of view. On one hand, it suggests that lanthanide hydroxide complexes may be used for the fixation of CO_2, a green house gas, and on the other hand, such complexes may be used as models for investigating the reactivity of not-readily accessible actinide hydroxides toward CO_2; it may be possible to immobilize the actinides in radioactive waste in the carbonate form.

Under hydrothermal conditions, the hydrolysis of samarium sulfate in presence of ethylenediamine (en) leads to the formation of a diamond-like

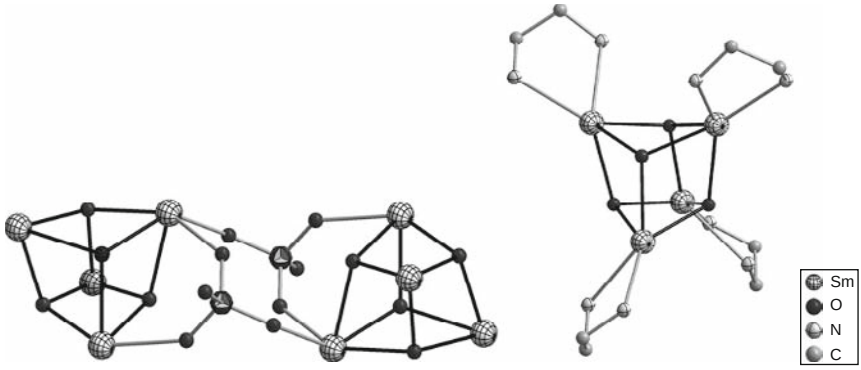

FIGURE 125 Crystal structure showing two units of the $[Sm_4(\mu_3\text{-}OH)_4]$ core, whose component metal atoms are each chelated by an en ligand, bridged by two $\eta^3\text{-}SO_4^{2-}$ ion to form a polymeric network (redrawn after Jia et al., 2005).

polymeric network featuring the familiar cubane-like $[\mathbf{R}_4(\mu_3\text{-}OH)_4]^{8+}$ cluster cores interlinked by $\eta^3\text{-}SO_4^{2-}$ ion bridges (Jia et al., 2005; Figure 125, left). In the cluster, four en-coordinated Sm(III) ions are located at the four corners of the distorted Sm_4 tetrahedron (Figure 125, right). The Sm(III) ion is octacoordinate with contributions from two en N atoms, three μ_3-OH groups, and oxygen atoms from three different sulfate ions.

The macrocyclic ligand cucurbit[6]uril (CB[6]) has been used for the assembly of tetranuclear lanthanide aqua hydroxo–carboxylate complexes from aqueous solutions. Sandwich-type lanthanide complexes featuring a common tetranuclear hydroxo core of $[\mathbf{R}_4(\mu_3\text{-}OH)_4]^{8+}$ being sandwiched between two macrocycles $\{(IN@CB[6])\mathbf{R}_4(\mu_3\text{-}OH)_4(IN@CB[6])\}^{6+}$ were synthesized under hydrothermal conditions from aqueous solutions of lanthanide(III) bromides, CB[6], and 4-cyanopyridine (Gerasko et al., 2008a,b; Mainicheva et al., 2006). Structure determination reveals an interesting organization of the macrocyclic ligand, the IN ligands produced *in situ* from the hydrolysis of starting 4-cyanopyridine, and a tetranuclear lanthanide hydroxide cluster core ($\mathbf{R} = Ho$, Figure 126, left). The distorted cubane is stabilized along the two opposite and mutually perpendicular sides of the Ho_4 tetrahedron by bridging interaction of the IN ligand whose pyridyl moiety is encapsulated into the hydrophobic inner cavity of CB[6], presumably driven by noncovalent interactions. This particular organization facilitates the interaction of the CB[6] carbonyl oxygen with the lanthanide atoms. Although all six carbonyl groups on one particular side of the macrocycle interact with the cluster core, only four of them coordinate directly with two lanthanide ions on one side of the metal tetrahedron; the remaining two carbonyls are hydrogen bonded to the doubly and triply bridging hydroxo groups of the

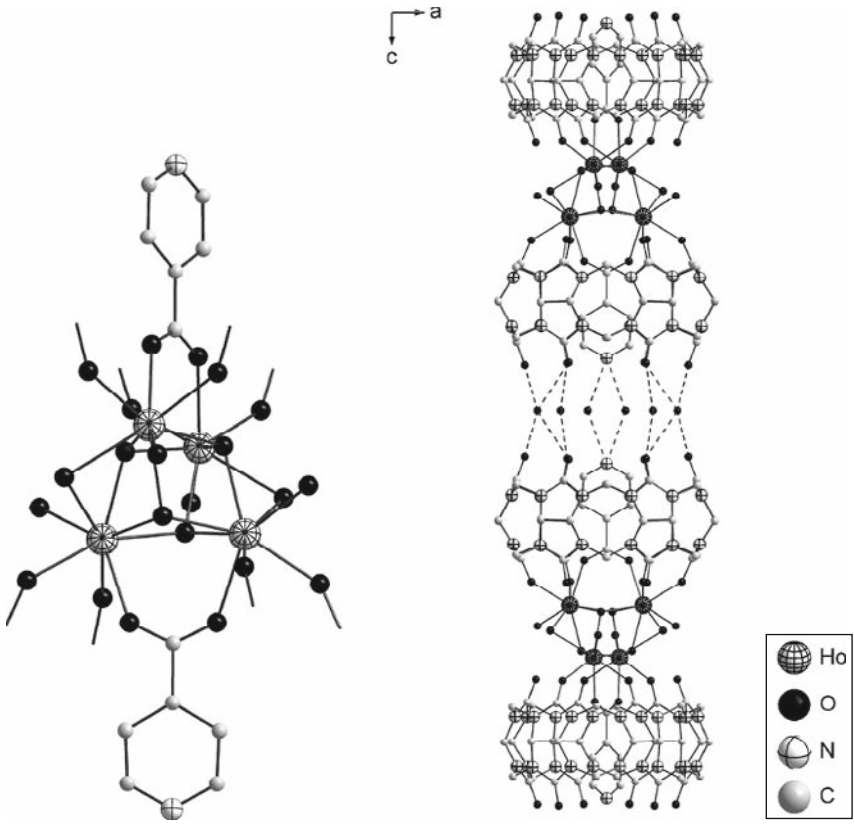

FIGURE 126 Structure of a tetranuclear hydroxo core of $[Ho_4(\mu_3\text{-}OH)_4]^{8+}$ being sandwiched between two CB[6] macrocycles $\{(IN@CB[6])Ho_4(\mu_3\text{-}OH)_4(IN@CB[6])\}^{6+}$ (left) and supramolecular arrays formed by such units via extensive hydrogen bonding between the macrocycles (right) (redrawn after Gerasko et al., 2008a,b; Mainicheva et al., 2006).

distorted-cubane core. The coordination of the two lanthanide ions on the opposite side is identical, again, with one side of a different CB[6] ligand whose hydrophobic cavity houses the aromatic moiety of the cluster stabilizing IN ligand. The overall structure may be viewed as a cluster core sandwiched by two CB[6] ligands. Individual sandwiches of this kind are organized via hydrogen bonding interactions, mediated by H_2O molecules, between the noncluster interacting side of the macrocycle (Figure 126, right).

The sandwiched cluster complexes have been used as complex ligands for the coordination of secondary metal ions, such as Ag(I), generating chain-like coordination polymers via the coordination of silver atoms by the IN nitrogen atoms (Gerasko et al., 2008a).

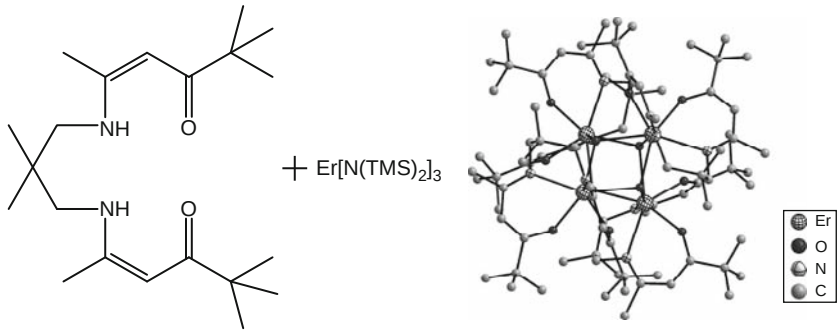

FIGURE 127 Crystal structure of $[Er(\mu_3\text{-}OH)]_4(SB)_4$ with the molecular structure of the Schiff base ligand SB shown on the left (redrawn after Schuetz et al., 2002).

Direct synthesis of a tetranuclear Er(III) hydroxo cluster bearing a saturated Schiff base has also been achieved. The reaction of bis-5,5′-(2,2-dimethyl-1,3-propanediyldiimino)-2,2-dimethyl-4-hexen-3-one (SB) with tris[bis(trimethylsilyl)amido]erbium afforded a pentacoordinate metal amido Schiff base complex. Direct hydrolysis of the latter produced a neutral, tetranuclear hydroxo cluster containing the Schiff base as the hydrolysis-limiting ligand. The tetrameric cluster has a formula of $[Er(\mu_3\text{-}OH)]_4(SB)_4$, featuring the familiar distorted-cubane-like cluster core encapsulated by the organic shell formed by the ligands (Schuetz et al., 2002; Figure 127).

4. SUMMARY AND OUTLOOKS

The chemistry of lanthanide clusters has come up a long way during the 1990s. Similar to the development of many research areas, the initial lanthanide clusters are outcomes of serendipitous discoveries. The repetitive appearance of certain prevalent cluster motifs obtained by using distinctly different procedures has stimulated the efforts to develop methodologies for the reproducible synthesis of such clusters. These efforts are further encouraged by the interesting magnetic and luminescence properties and catalytic potentials of many of these species. After more than two decades of development, the chemistry of lanthanide cluster compounds has now been developed into an exciting area of lanthanide research, and many useful materials have been discovered. Some selected applications of lanthanide clusters are summarized in Table 2.

Significant progresses notwithstanding, there is still a tremendous potential for further development of this research field as the syntheses of such clusters ‘‘(still) cannot yet be planned and are inevitably

TABLE 2 Selected applications of lanthanide clusters

Cluster	Application	References
(Oxo)alkoxide clusters		
Various homogeneous and heterometallic (oxo)alkoxide clusters	Precursors to metal oxide materials	Hubert-Pfalzgraf (2003)
[**R**$(mmp)_3$] (**R** = La, Pr, Nd, and Gd)	Precursors to lanthanide oxides $\mathbf{R}_2O_3$ by MOCVD process	Aspinall et al. (2007) and Gaskell et al. (2007)
[**R**$Al(OPr^i)_6(HOPr^i)]_2$ (**R** = La, Pr, and Nd)	Precursors to stoichiometric, amorphous $\mathbf{R}AlO_3$ by liquid injection MOCVD	Manning et al. (2005) and Veith et al. (2001)
$[GdFe(OPr^i)_6(HOPr^i)]_2$	Precursor to metastable rare-earth iron perovskite $GdFeO_3$ for magneto-optical data storage	Mathur et al. (2002)
Hydride clusters		
$[(Ap\mathbf{R})_3(\mu_2\text{-}H)_3(\mu_3\text{-}H)_2(CH_2SiMe_3)(THF)_2]$ (**R** = Y, Lu)	Catalyzing ethylene polymerization	Lyubov et al. (2008)
Cationic lanthanide hydrido clusters	Catalyzing syndiospecific polymerization of styrene and the regio- and stereoselective *cis*-1,4-polymerization of cyclohexyldiene	Li et al. (2006b)
Various Y(III) and Lu(III) polyhydrido clusters	Single-component catalysts for ROP reaction	Cui et al. (2005a), Hou (2003), and Hou et al. (2007)
Chalcogenolate clusters		
$Li[R'''_4(\mu_4\text{-}Cl)Nd_4(\mu\text{-}SPh)_8]$	Catalyzing ROP of ε-caprolactone	Li et al. (2005)

(*continued*)

TABLE 2 (*continued*)

Cluster	Application	References
Chalcogenide clusters		
Various lanthanide chalcogenide clusters	Molecular minerals or monodisperse precursors to ceramic materials by solution processing techniques	Riman et al. (2005)
Hydroxide clusters		
$[Gd_{14}(\mu_4\text{-}OH)_2(\mu_3\text{-}OH)_{16}(H_2O)_8(L\text{-serine})_{20}]^{3+}$	MRI contrast-enhancing agent	Messerle et al. (2005)
$H_5[Y_5(\mu_4\text{-}O)(\mu_3\text{-}O)_4(\mu\text{-}\eta^2\text{-}DBM)_4(\eta^2\text{-}DBM)_6]$	Catalyzing the oxidation of aldehydes to the corresponding carboxylic acids in the presence of air	Baskar and Roesky (2005) and Roesky et al. (2004)
$[La_{12}(OH)_{12}(H_2O)_4(DBM)_{18}(Phgly)_2(CO_3)_2]$	Adsorption of atmospheric CO_2	Andrews et al. (2007)
$\{[La(tpen)(\mu\text{-}OH)]_2(\mu\text{-}\eta^1\text{:}\eta^1OTf)\}(OTf)_3$	Reaction with atmospheric CO_2	Natrajan et al. (2006)
$[(Van)_3\mathbf{R}_3(OH)_2X_2(OH_2)_4]^{2+}$ ($\mathbf{R}$ = Gd, X = NO_3^-; $\mathbf{R}$ = Dy, X = Cl)	Molecular magnetic materials	Chibotaru et al. (2008), Costes et al. (2001), Gamer et al. (2008), and Tang et al. (2006)

characterized by random self-organization'' (Anwander, 1998). Despite that fact, a number of core motifs have been reproducibly obtained using distinctly different supporting ligands and under diverse reaction conditions; their structure cannot, however, yet be predicted *a priori*. As such, ''the 'rational design' of polynuclear lanthanide (cluster) complexes with specific properties is currently an inexact science, and exploratory syntheses, with the hope of discovering new materials with useful properties, has been a common alternative'' (Thompson et al., 2003). Nevertheless, one shall not fall as victims of this uncertainty. In search for the reproducible synthesis of known cluster structures and any clusters yet to be identified, we are looking for the hints provided by these intriguing lanthanide-containing species. The practice is ''like playing poker; if you play long enough you begin to make decisions based on probability, and if fortunate you may recognize how the cards are marked'' (Winpenny, 1999). It is probably with this kind of enthusiasm and keenness that lanthanide cluster researchers have discovered a great variety of such polynuclear species, as clearly reflected by this far-from-comprehensive review. Besides their aesthetically appealing structures, many of these clusters display interesting properties, and may hold potential, important applications. For example, not only have some of these clusters been used as precursors for oxide materials in advanced technologies (electrical, optical, magnetic, and luminescent materials), they have also been incorporated into polymeric matrices to realize hybrid materials with enhanced mechanical properties. Efficient synthetic nucleases have also been developed that show superior catalytic properties in the hydrolytic cleavage of nucleic acids. Potential applications of certain cluster species as new paradigms of contrast-enhancing agents in biomedical imaging have also been demonstrated in the laboratories. Fixation of atmospheric CO_2 has also been observed in a number of cluster species, which carries significant ramifications from the environmental viewpoint. More fundamentally, many novel chemical transformations have been found to be facilitated by lanthanide-containing clusters. It is thus fair to predict that research activities in this particular direction of lanthanide chemistry will continue to grow with a high possibility of finding many useful applications not yet been realized or even thought of.

ACKNOWLEDGMENTS

This work was supported by the US National Science Foundation (CAREER: CHE-0238790). The author acknowledges coworkers and collaborators whose names appear in the references. Special thanks go to Dr. Xiaoyan Tu and Ms. Yinglan Wu for their assistance with the reproduction of the figures.

REFERENCES

Addamo, M., Bombieri, G., Foresti, E., Grillone, M.D., Volpe, M., 2004. Inorg. Chem. 43, 1603–1605.
Andersen, R.A., Templeton, D.H., Zalkin, A., 1978. Inorg. Chem. 17, 1962–1965.
Andrews, P.C., Beck, T., Forsyth, C.M., Fraser, B.H., Junk, P.C., Massi, M., Roesky, P.W., 2007. Dalton Trans. 5651–5654.
Anwander, R., 1998. Angew. Chem. Int. Ed. 37, 599–602.
Anwander, R., Munck, F.C., Priermeier, T., Scherer, W., Runte, O., Herrmann, W.A., 1997. Inorg. Chem. 36, 3545–3552.
Arndt, S., Okuda, J., 2002. Chem. Rev. 102, 1953–1976.
Aspinall, H.C., Bickley, J.F., Gaskell, J.M., Jones, A.C., Labat, G., 2007. Inorg. Chem. 46, 5852–5860.
Avent, A.G., Geoffrey, F., Cloke, N., Elvidge, B.R., Hitchcock, P.B., 2004. Dalton Trans. 1083–1096.
Babai, A., Mudring, A.-V., 2006. Z. Anorg. Allg. Chem. 632, 1956–1958.
Baes Jr., C.F., Mesmer, R.E., 1976. The Hydrolysis of Cations. Wiley Interscience, New York Chapter 7.
Banerjee, S., Kumar, G.A., Riman, R.E., Emge, T.J., Brennan, J.G., 2007. J. Am. Chem. Soc. 129, 5926–5931.
Barash, E.H., Coan, P.S., Lobkovsky, E.B., Streib, W.E., Caulton, K.G., 1993. Inorg. Chem. 32, 497–501.
Barnea, E., Averbuj, C., Kapon, M., Botoshansky, M., Eisen, M.S., 2007. Eur. J. Inorg. Chem. 4535–4540.
Baskar, V., Roesky, P.W., 2005. Z. Anorg. Allg. Chem. 631, 2782–2785.
Baskar, V., Roesky, P.W., 2006. Dalton Trans. 676–679.
Benelli, C., Gatteschi, D., 2002. Chem. Rev. 102, 2369–2388.
Bilyk, A., Hall, A.K., Harrowfield, J.M., Hosseini, M.W., Skelton, B.W., White, A.H., 2000. Aust. J. Chem. 53, 895–898.
Binnemans, K., 2005. In: Gschneidner Jr., K.A., Bünzli, J.-C.G., Pecharsky, V.K. (Eds.), Handbook on the Physics and Chemistry of Rare Earths, vol. 35. Elsevier, Amsterdam Chapter 225.
Boeyens, J.C.A., De Villiers, J.P.R., 1972. J. Cryst. Mol. Struct. 2, 197–211.
Bonnet, F., Visseaux, M., Barbier-Baudry, D., Hafid, A., Vigier, E., Kubicki, M.M., 2004. Inorg. Chem. 43, 3682–3690.
Boyle, T.J., Ottley, A.M., 2008. Chem. Rev. 108, 1896–1917.
Burgstein, M.R., Roesky, P.W., 2000. Angew. Chem. Int. Ed. 39, 549–551.
Calvez, G., Guillou, O., Daiguebonne, C., Car, P.-E., Guillerm, V., Gerault, Y., Le Dret, F., Mahe, N., 2008. Inorg. Chem. Acta 361, 2349–2356.
Carretas, J., Branco, J., Marçalo, J., Valente, N., Waerenborgh, J.C., Carvalho, A., Marques, N., Domingos, Â., De Matos, A.P., 2004. J. Alloys Compd. 374, 289–292.
Caulton, K.G., Hubert-Pfalzgraf, L.G., 1990. Chem. Rev. 90, 969–995.
Chen, X.-M., Wu, Y.-L., Tong, Y.-X., Sun, Z., Hendrickson, D.N., 1997. Polyhedron 16, 4265–4272.
Cheng, Y., Jin, G.-X., Shen, Q., Lin, Y., 2001. J. Organomet. Chem. 631, 94–98.
Cheng, J., Zhang, J., Zheng, S., Zhang, M., Yang, G., 2006. Angew. Chem. Int. Ed. 45, 73–77.
Cheng, M.-L., Li, H.-X., Zhang, W.-H., Ren, Z.-G., Zhang, Y., Lang, J.-P., 2007. Eur. J. Inorg. Chem. 1889–1896.
Chibotaru, L.F., Ungur, L., Soncini, A., 2008. Angew. Chem. Int. Ed. 47, 4126–4129.
Clegg, W., Izod, K., Liddle, S.T., O'Shaughnessy, P., Sheffield, J.M., 2000. Organometallics 19, 2090–2096.
Coles, M.P., Hitchcock, P.B., 2004. Inorg. Chim. Acta 357, 4330–4334.

Constantine, S.P., De Lima, G.M., Hitchcock, P.B., Keates, J.M., Lawless, G.A., 1996. Chem. Commun. 2421–2422.
Costes, J.-P., Dahan, F., Nicodème, F., 2001. Inorg. Chem. 40, 5285–5287.
Cotton, F.A., 1966. Q. Rev. 20, 389–401.
Cui, D., Tardif, O., Hou, Z., 2004. J. Am. Chem. Soc. 126, 1312–1313.
Cui, D., Nishiura, M., Hou, Z., 2005a. Macromolecules 38, 4089–4095.
Cui, D., Nishiura, M., Hou, Z., 2005b. Angew. Chem. Int. Ed. 44, 959–962.
Datta, S., Baskar, V., Li, H., Roesky, P.W., 2007. Eur. J. Inorg. Chem. 4216–4220.
Deacon, G.B., Feng, T., Hockless, D.C.R., Junk, P.C., Skelton, B.W., White, A.H., 1997. Chem. Commun. 341–342.
Deacon, G.B., Forsyth, C.M., Harika, R., Junk, P.C., Ziller, J.W., Evans, W.J., 2004. J. Mater. Chem. 14, 3144–3149.
Deacon, G.B., Fallon, G.D., Forsyth, C.M., Harris, S.C., Junk, P.C., Skelton, B.W., White, A.H., 2006. Dalton Trans. 802–812.
Dietrich, H.M., Grove, H., Törnroos, K.W., Anwander, R., 2006a. J. Am. Chem. Soc. 128, 1458–1459.
Dietrich, H.M., Schuster, O., Törnroos, K.W., Anwander, R., 2006b. Angew. Chem. Int. Ed. 45, 4858–4863.
Dietrich, H.M., Törnroos, K.W., Anwander, R., 2006c. J. Am. Chem. Soc. 128, 9298–9299.
Djordjevic, C., Vuletic, N., 1980. Inorg. Chem. 19, 3049–3053.
Dubé, T., Gambarotta, S., Yap, G., 1998. Organometallics 17, 3967–3973.
Dubé, T., Conoci, S., Gambarotta, S., Yap, G.P.A., Vasapollo, G., 1999. Angew. Chem. Int. Ed. 38, 3657–3659.
Dubé, T., Conoci, S., Yap, G.P.A., Gambarotta, S., 2000a. Organometallics 19, 1182–1185.
Dubé, T., Freckmann, D., Conoci, S., Gambarotta, S., Yap, G.P.A., 2000b. Organometallics 19, 209–211.
Dubé, T., Gambarotta, S., Yap, G.P.A., Conoci, S., 2000c. Organometallics 19, 115–117.
Dubé, T., Ganesan, M., Conoci, S., Gambarotta, S., Yap, G.P.A., 2000d. Organometallics 19, 3716–3721.
Edelmann, F.T., Freckmann, D.M.M., Schumann, H., 2002. Chem. Rev. 102, 1851–1896.
Emel'yanova, N.S., Bochkarev, M.N., Schumann, H., Loebel, J., Esser, L., 1994. Russ. J. Coord. Chem. 20, 789–793.
Ephritikhine, M., 1997. Chem. Rev. 97, 2193–2242.
Evans, W.J., Sollberger, M.S., 1986. J. Am. Chem. Soc. 108, 6095–6096.
Evans, W.J., Sollberger, M.S., 1988. Inorg. Chem. 27, 4417–4423.
Evans, W.J., Meadows, J.H., Wayda, A.L., Hunter, W.E., Atwood, J.L., 1982. J. Am. Chem. Soc. 104, 2015–2017.
Evans, W.J., Meadows, J.H., Hanusa, T.P., 1984. J. Am. Chem. Soc. 106, 4454–4460.
Evans, W.J., Sollberger, M.S., Hanusa, T.P., 1988a. J. Am. Chem. Soc. 110, 1841–1850.
Evans, W.J., Sollberger, M.S., Khan, S.I., Bau, R., 1988b. J. Am. Chem. Soc. 110, 439–446.
Evans, W.J., Rabe, G.W., Ansari, M.A., Ziller, J.W., 1994a. Angew. Chem. Int. Ed. Engl. 33, 2110–2111.
Evans, W.J., Rabe, G.W., Ziller, J.W., 1994b. Inorg. Chem. 33, 3072–3078.
Evans, W.J., Greci, M.A., Ziller, J.W., 1997. J. Chem. Soc., Dalton Trans. 3035–3039.
Evans, W.J., Greci, M.A., Ziller, J.W., 2000. Inorg. Chem. 39, 3213–3220.
Evans, W.J., Allen, N.T., Greci, M.A., Ziller, J.W., 2001. Organometallics 20, 2936–2937.
Fang, X., Anderson, T.M., Neiwert, W.A., Hill, C.L., 2003. Inorg. Chem. 42, 8600–8602.
Fang, X., Anderson, T.M., Benelli, C., Hill, C.L., 2005. Chem. Eur. J. 11, 712–718.
Fleming, S., Gutsche, C.D., Harrowfield, J.M., Ogden, M.I., Skelton, B.W., Stewart, D.F., White, A.H., 2003. Dalton Trans. 3319–3327.
Franklin, S.J., 2001. Curr. Chem. Biol. 5, 201–208.

Gamer, M.T., Lan, Y., Roesky, P.W., Powell, A.K., Clérac, R., 2008. Inorg. Chem. 47, 6581–6583.
Ganesan, M., Gambarotta, S., Yap, G.P.A., 2001. Angew. Chem. Int. Ed. 40, 766–769.
Gaskell, J.M., Przybylak, S., Jones, A.C., Aspinall, H.C., Chalker, P.R., Black, K., 2007. Chem. Mater. 19, 4796–4803.
Gerasko, O.A., Mainicheva, E.A., Naumova, M.I., Neumaier, M., Kappes, M.M., Lebedkin, S., Fenske, V.P., Fedin, V.P., 2008a. Inorg. Chem. 47, 8869–8880.
Gerasko, O.A., Mainicheva, E.A., Naumova, M.I., Yurjeva, O.P., Alberola, A., Vicent, C., Llusar, V.P., Fedin, V.P., 2008b. Eur. J. Inorg. Chem. 3, 416–424.
Giester, G., Unfried, P., Zák, Z., 1997. J. Alloys Compd. 257, 175–181.
Gu, X., Xue, D., 2007. Inorg. Chem. 46, 3212–3216.
Hosmane, N.S., Maguire, J.A., 2005. Organometallics 24, 1356–1389.
Hosmane, N.S., Wang, Y., Oki, A.R., Zhang, H., Maguire, J.A., 1996. Organometallics 15, 626–638.
Hou, Z., 2003. Bull. Chem. Soc. Jpn. 76, 2253–2266.
Hou, Z., Zhang, Y., Tardif, O., Wakatsuki, Y., 2001. J. Am. Chem. Soc. 123, 9216–9217.
Hou, Z., Nishiura, M., Shima, T., 2007. Eur. J. Inorg. Chem. 2535–2545.
Hu, S.-M., Du, W.-X., Xia, S.-Q., Fu, R.-B., Zhang, J.-J., Wu, X.-T., 2003. Jiegou Huaxue 223, 309–313.
Hu, M., Wang, Q.-L., Xu, G.-F., Zhao, B., Deng, G.-R., Zhang, Y.-H., Yang, G.-M., 2007. Inorg. Chem. Commun. 10, 1177–1180.
Hubert-Pfalzgraf, L.G., 2003. Inorg. Chem. Commun. 6, 102–120.
Hubert-Pfalzgraf, L.G., Daniele, S., Bennaceur, A., Daran, J.C., Vaissermann, J., 1997. Polyhedron 16, 1223–1234.
Hubert-Pfalzgraf, L.G., Miele-Pajot, N., Papiernik, R., Vaissermann, J., 1999. J. Chem. Soc., Dalton Trans. 4127–4130.
Hubert-Pfalzgraf, L.G., Morlens, S., Daniele, S., Thozet, A., 2004. Inorg. Chem. Commun. 7, 751–755.
Huebner, L., Kornienko, A., Emge, T.J., Brennan, J.G., 2005. Inorg. Chem. 44, 5118–5122.
Igonin, V.A., Lindeman, S.V., Struchkov, Y.T., Shchegolikhina, O.I., Molodtsova, Y.A., Pozdnyakova, Y.A., et al., 1993. Izv. Akad. Nauk. SSSR, Ser. Khim. 184–189.
Jia, D., Zhang, Y., Dai, J., Zhu, Q., Lu, W., Guo, W., 2005. Inorg. Chem. Commun. 8, 588–591.
Jin, G.-X., Cheng, Y., Lin, Y., 1999. Organometallics 18, 947–949.
John, D., Urland, W., 2007. Z. Anorg. Allg. Chem. 633, 2587–2590.
Kajiwara, T., Katagiri, K., Hasegawa, M., Ishii, A., Ferbinteanu, M., Takaishi, S., et al., 2006. Inorg. Chem. 45, 4880–4882.
Kajiwara, T., Iki, N., Yamashita, M., 2007. Coord. Chem. Rev. 251, 1734–1746.
Knjazhanski, S.Y., Lobkovsky, E.B., Bulychev, B.M., Belsky, V.K., Soloveichik, G.L., 1991. J. Organomet. Chem. 419, 311–324.
Komiyama, M., 2005. In: Gschneidner Jr., K.A., Bünzli, J.-C.G., Pecharsky, V.K. (Eds.), Handbook on the Physics and Chemistry of Rare Earths, vol. 34. Elsevier B.V., Amsterdam, pp. 405–454.
Kong, X., Ren, Y., Long, L., Zheng, Z., Huang, R., Zheng, L., 2007. J. Am. Chem. Soc. 129, 7016–7017.
Kong, X., Ren, Y., Chen, W., Long, L., Zheng, Z., Huang, R., Zheng, L., 2008a. Angew. Chem. Int. Ed. 47, 2398–2401.
Kong, X., Ren, Y., Long, L., Zheng, Z., Nichol, G.S., Huang, R., Zheng, L., 2008b. Inorg. Chem. 47, 2728–2739.
Kornienko, A., Emge, T., Kumar, G.A., Riman, R.E., Brennan, J.G., 2005. J. Am. Chem. Soc. 127, 3501–3505.
Kremer, C., Torres, J., Dominguez, S., Mederos, A., 2005. Coord. Chem. Rev. 249, 567–590.
Kretschmer, W.P., Teuben, J.H., Troyanov, S.I., 1998. Angew. Chem. Int. Ed. 37, 88–90.

Lam, A.W., Wong, W.-T., Wen, G., Zhang, X.-X., Gao, S., 2001. New J. Chem. 25, 531–533.
Le Bris, J., Hubert-Pfalzgraf, L.G., Rolland, M., Garcia, Y., 2006. Inorg. Chem. Commun. 9, 695–698.
Li, H.-X., Ren, Z.-G., Zhang, Y., Zhang, W.-H., Lang, J.-P., Shen, Q., 2005. J. Am. Chem. Soc. 127, 1122–1123.
Li, H.-X., Zhu, Y.J., Cheng, M.L., Ren, Z.-G., Lang, J.-P., Shen, Q., 2006a. Coord. Chem. Rev. 250, 2059–2062.
Li, X., Baldamus, J., Nishiura, M., Tardif, O., Hou, Z., 2006b. Angew. Chem. Int. Ed. 45, 8184–8188.
Lorenz, V., Edelmann, A., Blaurock, S., Freise, F., Edelmann, F.T., 2007. Organometallics 26, 4708–4710.
Luo, Y., Hou, Z., 2007. Organometallics 26, 2941–2944.
Luo, Y., Baldamus, J., Tardif, O., Hou, Z., 2005. Organometallics 24, 4362–4366.
Lyubov, D.M., Döring, C., Fukin, G.K., Cherkasov, A.V., Shavyrin, A.S., Kempe, R., Trifonov, A.A., 2008. Organometallics 27, 2905–2907.
Ma, B., Zhang, D., Gao, S., Jin, T., Yan, C., Xu, G., 2000. Angew. Chem. Int. Ed. 39, 3644–3646.
Mahe, N., Guillou, O., Daiguebonne, C., Gerault, Y., Caneschi, A., Sangregorio, C., Chane-Ching, J.Y., Car, P.E., Roisnel, T., 2005. Inorg. Chem. 44, 7743–7750.
Mainicheva, E.A., Gerasko, O.A., Sheludyakova, L.A., Naumov, D.Y., Karsanova, I.I., Amirov, R.R., Fedin, V.P., 2006. Russ. Chem. Bull. 55, 1956–1965.
Mamula, O., Lama, M., Stoeckli-Evans, H., Shova, S., 2006. Angew. Chem. Int. Ed. 45, 4940–4944.
Manning, T.D., Loo, Y.F., Jones, A.C., Aspinall, H.C., Chalker, P.R., Bickley, J.F., 2005. J. Mater. Chem. 15, 3384–3387.
Mathur, S., Shen, H., Lecerf, N., Kjekshus, A., Fjellvag, H., Goya, G.F., 2002. Adv. Mater. 14, 1405–1409.
Messerle, L., Nolting, D., Bolinger, L., Stolpen, A.H., Mullan, B.F., Swenson, D., Madsen, M., 2005. Acad. Radiol. 12, S46–S47.
Mudring, A.-V., Timofte, T., Babai, A., 2006. Inorg. Chem. 45, 5162–5166.
Natrajan, L., Pecaut, J., Mazzanti, M., 2006. Dalton Trans. 1002–1005.
O'Connor, P.E., Twamley, B., Berg, D.J., 2006. Inorg. Chim. Acta 359, 2870–2878.
Ohashi, M., Konkol, M., Del Rosal, I., Poteau, R., Maron, L., Okuda, J., 2008. J. Am. Chem. Soc. 130, 6920–6921.
Ouchi, A., Suzuki, Y., Ohki, Y., Koizumi, Y., 1988. Coord. Chem. Rev. 92, 29–43.
Pernin, C.G., Ibers, J.A., 1997. Inorg. Chem. 36, 3802–3803.
Pernin, C.G., Ibers, J.A., 1999. J. Cluster Sci. 10, 71–90.
Plakatouras, J.C., Baxter, I., Hursthouse, M.B., Abdul Malik, K.M., McAleese, J., Drake, S.R., 1994. J. Chem. Soc., Chem. Commun. 2455–2456.
Poncelet, O., Hubert-Pfalzgraf, L.G., 1989. Polyhedron 8, 2183–2188.
Pope, M.T., 2008. In: Gschneidner Jr., K.A., Bünzli, J.-C.G., Pecharsky, V.K. (Eds.), Handbook on the Physics and Chemistry of Rare Earths, vol. 38. Elsevier, Amsterdam, Chapter 240.
Prokopuk, N., Shriver, D.F., 1998. Adv. Inorg. Chem. 46, 1–49.
Riman, R.E., Kumar, G.A., Banerjee, S., Brennan, J.G., 2005. J. Am. Ceram. Soc. 89, 1809–1815.
Rizkalla, E.N., Choppin, G.R., 1991. In: Gschneidner Jr., K.A., Eyring, L. (Eds.), Handbook on the Physics and Chemistry of Rare Earths, vol. 15. Elsevier Science Publishers B.V., Amsterdam, pp. 393–442.
Roesky, P.W., Canseco-Melchor, G., Zulys, A., 2004. Chem. Commun. 20, 738–739.
Schuetz, S.A., Day, V.W., Clark, J.L., Belot, J.A., 2002. Inorg. Chem. Commun. 5, 706–710.
Schumann, H., Kociok-Kohn, G., Loebel, J., 1990. Z. Anorg. Allg. Chem. 581, 69–81.
Shima, T., Hou, Z., 2006. J. Am. Chem. Soc. 128, 8124–8125.
Singh-Wilmot, M.A., Kahwa, I.A., Lough, A.J., 2005. Acta Crystallogr. E61, m970–m972.
Singh-Wilmot, M.A., Kahwa, I.A., Lough, A.J., 2006. Acta Crystallogr. E62, m113–m115.

Souza, A.P., Paz, F.A.A., Freire, R.O., Carlos, L.D., Malta, O.L., Alves Jr., S., de Sa, G.F., 2007. J. Phys. Chem. B 111, 9228–9238.
Suzuki, Y., Nagayama, T., Sekine, M., Mizuno, A., Yamaguchi, K., 1986. J. Less-Common Met. 126, 351–356.
Tang, J., Hewitt, I., Madhu, N.T., Chastanet, G., Wernsdorfer, W., Anson, C.E., et al., 2006. Angew. Chem. Int. Ed. 45, 1729–1733.
Tardif, O., Nishiura, M., Hou, Z., 2003a. Organometallics 22, 1171–1173.
Tardif, O., Nishiura, M., Hou, Z., 2003b. Tetrahedron 59, 10525–10539.
Thompson, M.K., Vuchkov, M., Kahwa, I.A., 2001. Inorg. Chem. 40, 4332–4341.
Thompson, M.K., Lough, A.J., White, A.J.P., Williams, D.J., Kahwa, I.A., 2003. Inorg. Chem. 42, 4828–4841.
Toledano, P., Ribot, F., Sanchez, C., 1990. C. R. Acad. Sci. Paris, Ser. II 311, 1315–1320.
Trifonov, A.A., Bochkarev, M.N., Schumann, H., Loebel, J., 1991. Angew. Chem. Int. Ed. 30, 1149–1151.
Turova, N.Y., 2004. Russ. Chem. Rev. 73, 1041–1064.
Veith, M., Mathur, S., Shen, H., Lecerf, N., Huefner, S., Jilavi, M.H., 2001. Chem. Mater. 13, 4041–4052.
Volpe, M., Bombieri, G., Marchini, N., 2004. J. Alloys Compd. 374, 382–386.
Volpe, M., Bombieri, G., Marchini, N., 2006. J. Alloys Compd. 408–412, 1046–1051.
Walter, M.D., Weber, F., Wolmershäuser, G., Sitzmann, H., 2006. Angew. Chem. Int. Ed. 45, 1903–1905.
Wang, R., Zheng, Z., 2000. Comments Inorg. Chem. 22, 1–30.
Wang, R., Jin, T., Zheng, Z., Staples, R.J., 1999. Angew. Chem. Int. Ed. 38, 1813–1815.
Wang, R., Carducci, M.D., Zheng, Z., 2000. Inorg. Chem. 39, 1836–1837.
Wang, R., Liu, H., Carducci, M.D., Jin, T., Zheng, C., Zheng, Z., 2001a. Inorg. Chem. 40, 2743–2750.
Wang, R., Selby, H.D., Liu, H., Zheng, Z., Carducci, M.D., Jin, T., Anthis, J.W., Staples, R.J., 2001b. Inorg. Chem. 40, 2743–2750.
Wang, R., Song, D., Wang, S., 2002. Chem. Commun. 368–369.
Wang, J., Li, S.-J., Zheng, C., Li, A., Hosmane, N.S., Maguire, J.A., Roesky, H.W., Cummins, C.C., Kaim, W., 2003. Organometallics 22, 4390–4392.
Wang, J., Li, S.-J., Zheng, C., Li, A., Hosmane, N.S., Maguire, J.A., Roesky, H.W., Cummins, C.C., Kaim, W., 2004. Organometallics 23, 4621–4629.
Watson, P.L., Tulip, T.H., Williams, I., 1990. Organometallics 9, 1999–2009.
Weng, D., Zheng, X., Jin, J., 2006. Eur. J. Inorg. Chem. 4184–4190.
Winpenny, R.E.P., 1999. In: Sauvage, J.P. (Ed.), Transition Metals in Supramolecular Chemistry. John Wiley & Son, New York.
Xiang, S., Hu, S., Sheng, T., Fu, R., Wu, X., Zhang, X., 2007. J. Am. Chem. Soc. 129, 15144–15146.
Xie, Z., Wang, S., Yang, Q., Mak, T.C.W., 1999. Organometallics 18, 1578–1579.
Xu, G., Wang, Z.-M., He, Z., Lue, Z., Liao, C.-S., Yan, C.-H., 2002. Inorg. Chem. 41, 6802–6807.
Yang, X., Jones, R.A., Wiester, M.J., 2004. Dalton Trans. 1787–1788.
Yang, X., Hahn, B.P., Jones, R.A., Wong, W.-K., Stevenson, K.J., 2007. Inorg. Chem. 46, 7050–7054.
Yousufuddin, M., Gutmann, M.J., Baldamus, J., Tardif, O., Hou, Z., Mason, S.A., McIntyre, G. J., Bau, R., 2008. J. Am. Chem. Soc. 130, 3888–3891.
Yu, S.-B., Watson, A.D., 1999. Chem. Rev. 99, 2353–2377.
Yunlu, K., Gradeff, P.S., Edelstein, N., Kot, W., Shalimoff, G., Streib, W.E., Vaartstra, B.A., Caulton, K.G., 1991. Inorg. Chem. 30, 2317–2321.
Zák, Z., Unfried, P., Giester, G., 1994. J. Alloys Compd. 205, 235–242.
Zalkin, A., Berg, D.J., 1989. Acta Cryst. C45, 1630–1631.
Zhang, H.-Y., Yu, H.-J., Xu, H.-X., Ren, J.-S., Qu, X.-G., 2007. Polyhedron 26, 5250–5256.

Zheng, Z., 2001. Chem. Commun. 2521–2529.
Zheng, X., Jin, L., Gao, S., 2004. Inorg. Chem. 43, 1600–1602.
Zhou, X., Ma, H., Wu, Z., You, X., Xu, Z., Huang, X., 1995. J. Organomet. Chem. 503, 11–13.
Zuo, T., Xu, L., Beavers, C.M., Olmstead, M.M., Fu, W., Crawford, T.D., Balch, A.L., Dorn, H.C., 2008. J. Am. Chem. Soc. 130, 12992–12997.

This page intentionally left blank

CHAPTER **246**

Molecular Chemistry of the Rare-Earth Elements in Uncommon Low-Valent States

François Nief

Contents

List of Acronyms

Ar	2,6-di-*iso*propylphenyl
Ar*	1,3,5-tri-*tert*butylbenzene
Bipy	2,2′-bipyridyl
BPE	1-bromo-1-phenylethane
Bu	*n*-butyl
CB	4-pentyl-4′-cyanobiphenyl
COT	1,3,5,7-cyclooctatetraene

Laboratoire Hétéroéléments et Coordination, UMR CNRS 7653, DCPH, Ecole Polytechnique, Route de Saclay, 91128 Palaiseau, France

Handbook on the Physics and Chemistry of Rare Earths, Volume 40
ISSN 0168-1273, DOI: 10.1016/S0168-1273(10)40006-9

DAD	1,4-di-*tert*butyl-1,4-diaza-1,3-diene
DME	1,2-dimethoxyethane
HMPA	hexamethylphosphoric triamide
iPr	*iso*propyl
Mes	mesityl
MMA	methyl methacrylate
M_n	mean molecular mass
NAr*	2,4,6-tri-*tert*butylpyridine
PAr*	2,4,6-tri-*tert*butylphosphinine
PDI	polydispersity index
R	any rare earth (Sc, Y, La–Lu)
*t*Bu	*tert*butyl
THF	tetrahydrofuran
TIBA	tri-*iso*butylaluminium

1. INTRODUCTION, SCOPE AND LIMITATIONS OF THE REVIEW

The vast majority of the molecular complexes of rare-earth elements (Sc, Y and La–Lu, hereafter abbreviated as R) are in trivalent state, which is the most stable. The oxidation state of the rare earths in these complexes is $+3$, and the configuration of the Sc^{3+}, Y^{3+} and La^{3+} ions is that of the noble gases ([Ar], [Kr] and [Xe], respectively), and that of the remaining rare-earth tripositive ions (Ce^{3+} to Lu^{3+}) is $[Xe]4f^n5d^06s^0$ ($n = 1-14$); while being formally in the valence shell, the f-electrons in these ions are very contracted and do not normally participate in bonding interactions, which are mostly ionic for all R^{3+}.

However, there are many stable rare-earth compounds that are low-valent. The rare-earth elements are also early transition metals, in which d-electrons are in the valence shell. Since transition metal complexes in general exist in diverse oxidation states in which the electronic configuration is traditionally expressed as $[NG]d^ns^0$ with $n \geq 0$ (NG being Ar, Kr or Xe), by analogy, there are *a priori* no reasons why R^0, R^I and R^{II} complexes should not exist. Considering for instance the adjacent ions Hf^{3+} and La^{2+} which have the same electronic configuration ($[Xe]5d^16s^0$), there are a few compounds of Hf^{III} (Fryzuk et al., 1996) and, as we shall see later, several perfectly characterised La^{II} complexes precisely in this electronic configuration. Until now, monovalent (R^I) molecular compounds have only been found in the case of scandium, and there are several rare earths that can form zero-valent (R^0) complexes.

Furthermore, in the elements Ce to Yb, f-orbitals come into play, to such an extent that most zero-valent metals in this series (except Ce and Gd) have the configuration $[Xe]4f^n5d^06s^2$, which opens the possibility of finding divalent compounds in which the dipositive ions have the $[Xe]4f^n5d^06s^0$ configuration instead of $[Xe]4f^{n-1}5d^16s^0$. This former configuration, as we shall see later, is actually present in many divalent molecular complexes. In the special case of cerium, the +IV oxidation state with configuration $[Xe]4f^05d^06s^0$ is well documented, and we will not consider the Ce^{IV} molecular compounds in this survey.

A comprehensive study of all molecular complexes in an oxidation state different from +3 would require a whole book. In this chapter, we have decided to restrict to a survey of rare-earth molecular complexes in uncommon low-valent states. We feel that this chapter is timely because this subject has benefited from very recent and important advances.

To appropriately outline the purpose of this chapter, let us first define which are the low-valent rare earths that we will consider as ''common''.

Among the many rare earths that can form solid-state compounds existing in the divalent state, such as for instance RX_2, X being a halogen, three of them can be classified as ''common'': europium, ytterbium and samarium. The chemistry of these species has been widely studied, and there are several reasons for this: (a) they are not overly reactive in the sense that their R^{3+}/R^{2+} redox potentials are not too negative so they can be measured in aqueous or polar organic solvents; (b) divalent salts such as the archetypal diiodides RI_2 can be made not only by solid-state techniques involving high temperatures but also by solution chemistry in mild conditions and (c) solutions of molecular compounds of Eu^{II}, Yb^{II} and Sm^{II} in organic solvents are sufficiently stable that they can be studied by common physico-chemical techniques and further transformed into other compounds in reasonable yields and by controlled reactions.

As we shall see, there are now other rare-earth elements that are stable enough in the divalent state in solution, allowing for the successful isolation of molecular complexes that can be fully characterised, including structurally, and their reactivity studied. Recent reviews and highlights have partially addressed this topic (Bochkarev, 2004; Cassani et al., 2002; Evans, 2000, 2002a,b, 2007; Izod, 2002; Meyer, 2008). Furthermore, there are a few reports on low-valent scandium complexes, and also a number of extremely reactive zero-valent rare-earth molecular compounds that could only be made via metal vapour techniques, which have been reviewed some time ago (Cloke, 1993).

Concretely, this chapter will first deal with the molecular chemistry of uncommon divalent rare-earth compounds, excluding those of Eu^{II}, Yb^{II} and Sm^{II} that have now been defined as ''common''. We will describe the molecular chemistry of the salt-like rare-earth diiodides NdI_2, DyI_2 and

TmI_2, and that of other isolated uncommon divalent complexes; there are also two endohedral metallofullerenes: $Sc@C_{84}$ (Takahashi et al., 1995) and $Tm@C_{82}$ (Kirbach and Dunsch, 1996; Pichler et al., 1997) for which spectroscopic evidence points to the divalent nature of Sc and Tm, respectively; they are worth mentioning here but they will not be discussed further. We will also consider the important issue of chemical systems in which uncommon divalent species may be present or have been postulated as intermediates, or displaying divalent-like reactivity. We will also report on the few low-valent scandium species that have been reported and finally on the zero-valent compounds.

All low-valent compounds and low-valent-like reactive systems considered in this report are highly reactive and in particular extremely air and moisture sensitive (some even react with dinitrogen—see Section 2.3.4) and are best handled in an inert-atmosphere dry box or on a vacuum line by the usual Schlenk techniques.

2. THE DIVALENT STATE

2.1 Early studies

The most studied and best-characterised class of divalent rare-earth compounds is represented by the diiodides. By the year 1965, all available RI_2 compounds had been synthesised. They were made by solid-state techniques, such as the high-temperature comproportionation of the triiodides with the metals, with the exception of EuI_2, which can be simply made by heating europium with diiodine. At that time, it was also already known that there were two types of RI_2 compounds according to the electronic configuration of the metals: the salt-like diiodides with $[Xe]d^0f^n$ configuration (NdI_2, SmI_2, EuI_2, DyI_2, TmI_2 and YbI_2), which can also be written as $R^{2+}(I^-)_2$, and the so-called metallic diiodides with $[Xe]d^1f^{n-1}$ configuration (LaI_2, CeI_2, PrI_2 and GdI_2) in which the valence d-electron is in the conduction band so these solid-state compounds have metallic character; they may also be written as $R^{3+}(I^-)_2(e^-)$ (Meyer et al., 2004). As early as 1960, ''about two-tenths of a gram'' of TmI_2 had been sacrificed by dissolving in water, and ''the fleeting violet–red colour'' that resulted was taken (rightly) as an indisputable signature of the transient presence of Tm^{2+} in water (Asprey and Kruse, 1960).

Several years later, Mikheev and his group discovered that the salt-like diiodides were soluble in polar organic solvents (Kamenskaia, 1984; Kamenskaia et al., 1979, 1982, 1983). In particular, it was established that these compounds were soluble in tetrahydrofuran (THF) to ca. 0.1 M at room temperature, the colours of the solutions were correctly described, and it was noticed that while the solutions of DyI_2 and NdI_2 rapidly

decomposed, NdI_2 being the less stable, EuI_2, YbI_2, SmI_2 *and* TmI_2 were reasonably stable in THF at room temperature. The non-classical diiodides were prepared by high-temperature techniques, and the classical ones by reaction of the metals with CuI (Kamenskaia et al., 1979). The behaviour of TmI_2 and SmI_2 in organic solvents in the presence of crown ethers was also studied and it was observed that upon addition of [18]crown-6 to solutions of SmI_2 and TmI_2 in THF, precipitates could be isolated to which the respective compositions $SmI_2 \cdot$([18]crown-6) and $TmI_2 \cdot$([18]crown-6) were assigned; the divalent character was established by spectroscopic techniques. The thulium compound was found to be light sensitive. Although these compounds were not structurally characterised, the isolated compound formulated as ''$TmI_2 \cdot$([18]crown-6)'' might be the first isolated molecular compound of Tm^{II} (Kamenskaia et al., 1984).

Another early study reported a compound formulated as ''$NdCl_2 \cdot 2THF$'' made by reduction of $NdCl_3$ with lithium naphthalenide in THF (Rossmanith, 1979). Bochkarev et al. reinvestigated this reaction and concluded that Nd^{III} was in fact present in ''$NdCl_2 \cdot 2THF$'' and that its real (variable) composition corresponded to $[\{NdCl_2(THF)_2LiCl\}_n C_{10}H_8]$ (Bochkarev et al., 1999a; Kirillov et al., 1999). Edelman et al. reported that by reaction of this compound with KC_5Me_5, a product formulated as an ate complex with the approximate composition $[(C_5Me_5)_2NdCl_2][K_2(THF)_{3-4}]$ could be isolated, which was only characterised by elemental analysis and IR; this compound displayed Nd^{II}-like reactivity, since further reactions, for example, with dimesityl diselenide resulted in the isolation of $[(C_5Me_5)_2Nd(SeMes)]$ (Mes = mesityl) in an apparent monoelectronic reduction (Wedler et al., 1990). However, the divalent oxidation state of Nd in $[(C_5Me_5)_2NdCl_2][K(THF)_{3-4}]_2$ could not be further confirmed by a structural study.

About at the same time, the organometallic and coordination chemistry of the classical divalent rare earths Sm^{II}, Eu^{II} and Yb^{II} had started because the diiodide precursors could now be made by solution chemistry. Especially that of Sm^{II} (the most reactive of the ''common'' divalent rare earths) gained momentum with the milestone discovery by Kagan et al. that SmI_2 could be made in THF solution by the simple Grignard-like reaction of Sm with diiodoethane at room temperature (Namy et al., 1977).

2.2 Molecular chemistry of neodymium, dysprosium and thulium diiodides

The molecular chemistry of NdI_2, DyI_2 and TmI_2 is now well documented. Apart from the characterisation of simple adducts of these diiodides with polar molecules, most of this chemistry is represented by reactions in which irreversible oxidation to the trivalent state occurred. Among these diiodides, until now only TmI_2 has been successfully transformed

into other Tm^{II} compounds by metathesis with anionic ligands. These reactions will be described in a distinct chapter (Section 2.3) devoted to other isolable derivatives of uncommon divalent rare earths, including not only Nd^{II}, Dy^{II} and Tm^{II} but also La^{II} and Ce^{II}.

2.2.1 New syntheses and coordination chemistry

A new breakthrough in the non-classical divalent rare-earth chemistry occurred in 1997, when Bochkarev and Evans in a milestone paper reported that a light-sensitive molecular complex of TmI_2, identified as a solvate of composition $[TmI_2(DME)_3]$ (Figure 1) (DME = 1,2-dimethoxyethane), could be made in relatively mild conditions by the direct reaction of thulium metal with iodine in refluxing DME (Scheme 1).

$$Tm + I_2 \xrightarrow[\text{Reflux}]{\text{DME}} TmI_3 \xrightarrow[\text{Reflux}]{\text{Tm DME}} [TmI_2(DME)_3]$$

SCHEME 1 First solution synthesis of a divalent thulium compound: $[TmI_2(DME)_3]$.

The reaction proceeds through the initial formation of TmI_3, so the actual process is that of a comproportionation reaction of TmI_3 with metallic Tm, like in the high-temperature reaction (Bochkarev et al., 1997a). This complex could be structurally characterised by X-ray diffraction, thus unambiguously establishing that it was the first well-defined molecular compound of divalent thulium. It was further reported that a $[TmI_2(THF)_x]$ solvate could be analogously obtained from Tm and I_2 in THF (Evans et al., 2000). However, the solution method could not be applied to the diiodides of dysprosium and neodymium.

Yet soon after this, Bochkarev and Fagin discovered a new method for the synthesis of NdI_2 and DyI_2 (Bochkarev and Fagin, 1999a,b), which was

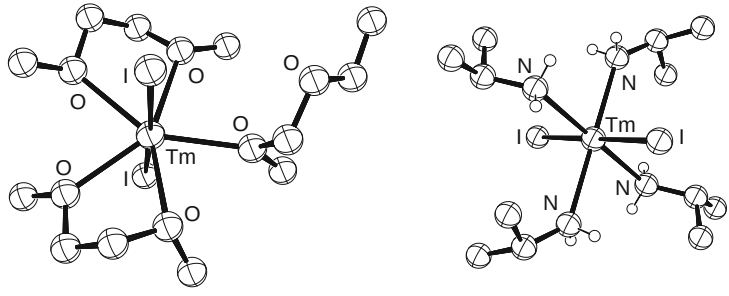

FIGURE 1 The structures of two Tm^{II} diiodide complexes: $[TmI_2(DME)_3]$ (left) and $[TmI_2(NH_2iPr)_4]$ (right). Figure was redrawn after Bochkarev et al. (1997a, 2006b).

also found applicable to TmI_2 (Bochkarev et al., 1999a; Evans et al., 2001). This procedure involved heating a mixture of metal and iodine in a glass or silica crucible under inert atmosphere with a laboratory gas burner. This very exothermic reaction proceeds directly to the diiodide, with little triiodide and unreacted metal as side products that can be easily separated. This method was later refined by Evans et al., who devised a special furnace to prepare NdI_2 and DyI_2 in large quantities (more than 10 g in a single batch) (Evans et al., 2003a).

This technique has the distinct advantage that it does not require special solid-state equipment such as an inert-atmosphere welding apparatus. Also, it does not use anhydrous triiodides that are not so easily available (Scheme 2).

$$R + I_2 \xrightarrow[\text{Glass or silica crucible}]{\text{Heat}} RI_2 \qquad R = \text{Nd, Dy, Tm}$$

SCHEME 2 Direct synthesis of uncommon divalent diiodides from the metal powders and diiodine.

Soon after this new synthesis was established, it was confirmed that the solution stability of these ''rediscovered'' rare-earth diiodides in ethereal solvents such as THF and DME was sufficient, at least at low temperatures, to allow for the successful isolation and X-ray characterisation of solvates like $[DyI_2(DME)_3]$ (Evans et al., 2000) and $[NdI_2(THF)_5]$ (Bochkarev et al., 2001) (Figure 2); their molecular structures unambiguously establish the divalent nature of these complexes. The stability of

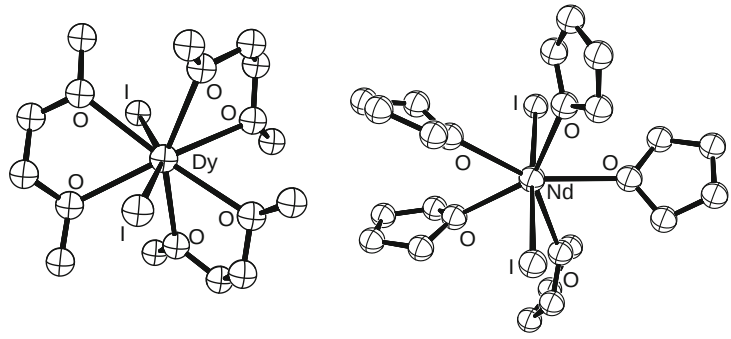

FIGURE 2 The structures of two Dy^{II} and Nd^{II} diiodide complexes: $[DyI_2(DME)_3]$ (left) and $[NdI_2(THF)_5]$ (right). Figure was redrawn after Bochkarev et al. (2001) and Evans et al. (2000).

DyI_2 and NdI_2 in THF was confirmed to be lower than that of TmI_2: khaki-green solutions of DyI_2 decompose above 0 °C, while purple solutions of NdI_2 are unstable above − 20 °C (Bochkarev et al., 2001).

Surprisingly, it has been shown fairly recently that neat TmI_2, DyI_2 and even NdI_2 are soluble in isopropylamine, and that the divalent state of the metals survives for a long enough time to allow the isolation of divalent adducts of composition $[RI_2(iPrNH_2)_n]$ (R = Nd: $n = 5$; R = Tm, Dy: $n = 4$). These complexes have been characterised by their magnetic properties, which are in the correct range for divalent compounds (except for Dy where the distinction between divalent and trivalent is impossible by magnetic measurements), and additionally by elemental analysis and IR data. $[TmI_2(NH_2iPr)_4]$ has been further characterised by X-ray crystallography (Figure 1). Solutions of DyI_2 and NdI_2 in isopropylamine are unstable, however, since they decompose over time, the decomposition being fastest with Nd (see later in Section 2.2.2.1.3). The dissolution of NdI_2 and DyI_2 in isopropylamine is accompanied by initial dihydrogen evolution, which is puzzling, given the fact that apparently no oxidation initially occurs (Bochkarev et al., 2006a,b).

2.2.2 Oxidative chemistry of neodymium, dysprosium and thulium diiodides

The major interest in the chemistry of Nd^{II}, Dy^{II} and Tm^{II} lies in their dual (and seemingly antagonistic) properties as Lewis acids and strong reducing agents. The standard redox potentials $E^0(R^{3+}/R^{2+})$ (R = Nd, Dy or Tm) that have been estimated by reliable spectroscopic techniques are − 2.3 V for Tm^{2+}, − 2.5 V for Dy^{2+} and − 2.6 V for Nd^{2+} (David, 2008), which are thus more reducing than of Sm^{2+}, Eu^{2+} or Yb^{2+}. This is the likely reason for the instability of the THF or DME solutions: The Lewis acidic R^{2+} is strongly bonded to the oxygen atom of the solvent through which it can also subsequently be oxidised by monoelectronic transfer.

2.2.2.1 Reactivity

In this section, we review the reactivity of NdI_2, DyI_2 and TmI_2 towards inorganic, organic and organometallic molecules. This part mainly consists in exploratory chemistry with the diiodides as starting materials. In all cases oxidation of the divalent ions to the more stable + 3 state occurred. The chemistry of other divalent organometallic and coordination complexes is treated in Section 2.3.

2.2.2.1.1 Reaction with hydrocarbons THF solutions of NdI_2 and DyI_2 (but not TmI_2) at low temperature were reported to quickly decompose in the presence of benzene. $[RI_3(THF)_3]$ (R = Nd, Dy) have been identified in the decomposition products together with an elusive pyrophoric

material which composition is compatible with the $RI(THF)_x$ formula ($R = Nd$, $x = 3$; $R = Dy$, $x = 2$) but in fact consisted in a mixture of products in which compounds containing metal-phenyl bonds may be present (Bochkarev et al., 2002).

The diiodides DyI_2 and NdI_2 (but again not TmI_2) cleanly react with naphthalene in DME or THF. In the case of dysprosium, a trivalent complex: $[(C_{10}H_8)DyI(DME)]$ could be structurally characterised, in which the naphthalene ligand which is η^2-bonded to dysprosium is in the dianionic form (Evans et al., 2000) (Figure 3).

TmI_2 did not react with even more condensed aromatic molecules such as anthracene, pyrene or coronene (Fedushkin et al., 2001a). The absence of reactivity in the presence of anthracene is especially interesting since in the same conditions decamethylsamarocene ($[(C_5Me_5)_2Sm]$) did react to give the reduction product $[\{(C_5Me_5)_2Sm\}_2(\mu\text{-anthracene})]$ (Evans et al., 1994). Thus, in this case, Sm^{II} appears as more reducing than Tm^{II}, which suggests that despite the fact that bonding is mostly ionic in divalent rare-earth complexes, the reducing potential is nevertheless strongly dependent on the environment.

However, TmI_2 did react with cyclooctatetraene (COT) (Scheme 3) and acenaphthylene to give well-defined, structurally characterised products, respectively $[(\eta^8\text{-COT})TmI(THF)_2]$, and the interesting $[ansa\text{-}(\eta^8\text{-}C_{12}H_8)_2TmI(THF)]$ (Figure 4) resulting from reductive coupling of the acenaphthylene. Two electrons and thus two equivalents of TmI_2 are needed in this reaction, and therefore one equivalent of TmI_3 was isolated as a side product (Fedushkin et al., 2001a) (Scheme 3).

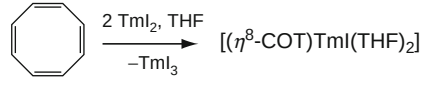

SCHEME 3 Bielectronic reduction of cyclooctatetraene by two equivalents of TmI_2.

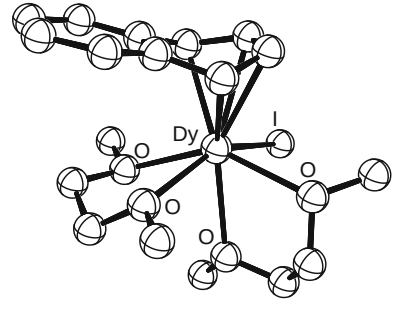

FIGURE 3 The structure of $[(C_{10}H_8)DyI(DME)]$, obtained by reaction of $[DyI_2(DME)_3]$ with naphthalene. Figure was redrawn after Evans et al. (2000).

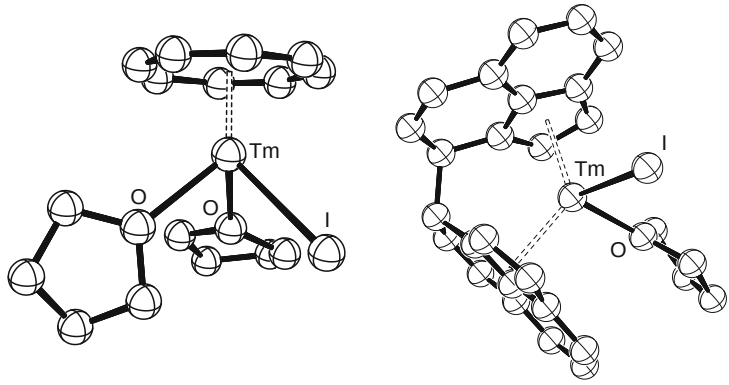

FIGURE 4 The structures of $[(\eta^8\text{-COT})TmI(THF)_2]$ (left) and $[ansa\text{-}(\eta^8\text{-}C_{12}H_8)_2TmI(THF)]$ (right), respectively, obtained by reaction of TmI_2 with cyclooctatetraene and acenaphthylene in THF. Figure was redrawn after Fedushkin et al. (2001a).

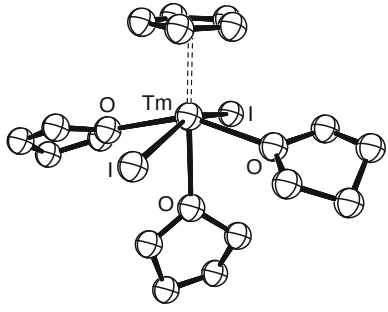

FIGURE 5 The structure of $[(C_5H_5)TmI_2(THF)_3]$, obtained by reaction of TmI_2 with cyclopentadiene in THF. Figure was redrawn after Khoroshenkov et al. (2003).

TmI_2, DyI_2 and NdI_2 reacted with cyclopentadiene to give $[(C_5H_5)RI_2(THF)_3]$ (R = Tm, Dy, Nd). While the reaction of DyI_2 and NdI_2 occurred at room temperature, TmI_2 only reacted at an appreciable rate at 60 °C, and the yield in the structurally characterised $[(C_5H_5)TmI_2(THF)_3]$ (Figure 5) was low because at this temperature it underwent disproportionation into $[TmI_3(THF)_3]$ and $[(C_5H_5)_2TmI(THF)_2]$. Only DyI_2 and NdI_2 reacted with pentamethylcyclopentadiene, yielding $[(C_5Me_5)RI_2(THF)_3]$ (R = Dy, Nd) and $[RI_3(THF)_x]$ as side products: the zwitterionic $[NdI_2(THF)_5][NdI_4(THF)_2]$ thus produced was structurally characterised (Khoroshenkov et al., 2003).

DyI_2 and NdI_2 could also mediate the synthesis of vanadocene or cobaltocene in fair yield from cyclopentadiene and VCl_3 or $CoCl_2$. In the case of vanadium, the diiodides are believed to reduce both V^{III} into V^{II} and the

cyclopentadiene into its anion (Bochkarev and Burin, 2004). Further reaction of vanadocene with DyI_2 in benzene gave dibenzenevanadium (see later in Section 2.2.2.1.5).

The well-known Sm^{III} η^6-arene complexes are generally prepared by the reaction of arenes with rare-earth trihalides in the presence of aluminium halides. This reaction was also effective with samarium diiodide and was extended to thulium diiodide: however, an attempt to react TmI_2 with naphthalene in toluene in the presence of aluminium trichloride was not successful but resulted in the isolation of an η^6-toluene complex of Tm^{III}: $[\eta^6\text{-}(CH_3C_6H_5)Tm(AlCl_4)_3]$ (Figure 6) (Fagin et al., 2005).

2.2.2.1.2 Reaction with water and oxygen-containing organic molecules It is of course not surprising that ions with such negative redox potentials should react with water or alcohols with the formation of trivalent hydroxides or alkoxides and evolution of dihydrogen. The reactions of DyI_2 and NdI_2 with water have been reinvestigated quite recently. Depending on the conditions, mixed iodide/hydroxides such as $RI(OH)_2$ or $RI_2(OH)$ (R = Nd, Dy) were isolated, and were characterised by elemental analysis and infra-red spectroscopy. In these reactions, chemiluminescence has been observed and has been attributed to the radiative decay of an excited state of the oxidised Nd or Dy (Bulgakov et al., 2007).

The reaction of $[TmI_2(DME)_3]$ with *t*-butanol or phenol at room temperature gave good yields of alkoxides of general composition $TmI_2(OR^1)$ (R^1 = *t*-butyl, phenyl); $[TmI_2(OPh)(DME)_2]$ (Figure 7) was structurally characterised. The reaction is much more rapid than with SmI_2. By contrast, TmI_2 was unable to react with sterically hindered phenols such as 2,4,6-$tBu_3C_6H_2OH$, although $[(2,4,6\text{-}tBu_3C_6H_2O)_3Tm]$ could be obtained from the alcohol and a naphthalene Tm^{III} compound (see later in Section 2.3.1) (Bochkarev et al., 1999b) (Scheme 4).

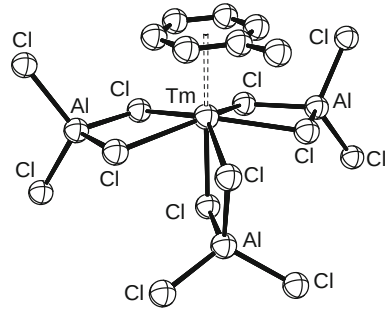

FIGURE 6 The structure of $[\eta^6\text{-}(CH_3C_6H_5)Tm(AlCl_4)_3]$, isolated in the attempted reaction of TmI_2 with naphthalene in toluene. Figure was redrawn after Fagin et al. (2005).

$$ROH + TmI_2 \longrightarrow ROTmI_2 + 0.5\ H_2$$

SCHEME 4 General reaction of TmI_2 with alcohols ($R^1 =$ alkyl, aryl).

The reaction of TmI_2 with a dimethoxycalix[4]arene: {–Ar(OH)CH_2Ar (OMe)–}$_2$ gave a structurally characterised chelate: [{–Ar(O)CH_2Ar (OMe)–}$_2$TmI(Et_2O)] (Figure 7). Two equivalents of TmI_2 are necessary and TmI_3 was isolated as a side product, most likely through a bis alkoxide such as [{–Ar(O)CH_2Ar(OMe)–}$_2$$Tm_2I_4$($Et_2O$)] which further underwent disproportionation (Fedushkin et al., 1999).

The more reactive DyI_2 and NdI_2 also reacted with *t*-butanol or phenol at low temperature to give $RI_2(OR^1)$ (R = Nd, Dy; $R^1 =$ *t*-butyl, phenyl) characterised by IR and microanalytical data. NdI_2 even reacted with phenol at very low temperatures ($-100\,^{\circ}C$) but in this case the reaction is more complicated, since besides the expected NdI_2(OPh), $NdI(OPh)_2$ and NdI_3 were also obtained. An elusive Nd^{I} species has been put forward to account for this observation (Bochkarev et al., 2002).

The reaction of NdI_2 with methanol in acetonitrile had a different outcome. The major product has the composition $NdI_2(OMe)(CH_3CN)_x$ ($x = 3$ or 4, depending on the conditions) but a non-stoichiometric cluster of formula $[Nd_4(\mu_2\text{-}I)_{1.1}(\mu_3\text{-}I)(\mu_2\text{-}OMe)_{4.9}(\mu_4\text{-}O)(CH_3CN)_{12}][(I)_3]$ was obtained as a side product when excess methanol was used. This cluster features a μ_4-oxo group at the centre and an I:OMe 90:10 occupational disorder on one site (Kuzyaev et al., 2007).

It is well known that Sm^{II} or even Yb^{II} complexes will reduce unsaturated ketones such as benzophenone or fluorenone into their respective

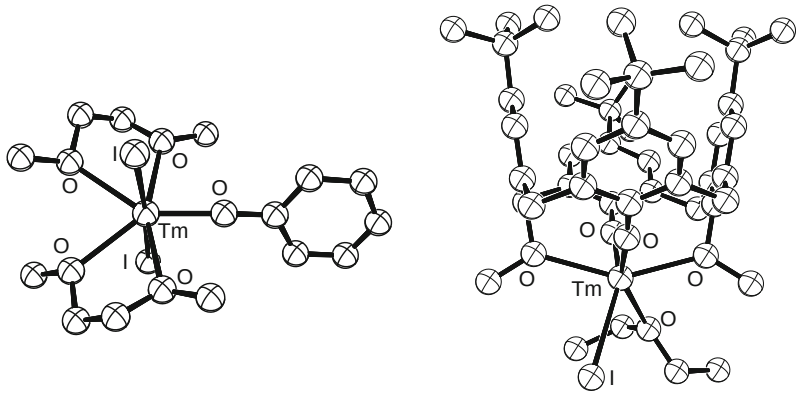

FIGURE 7 The structures of [TmI_2(OPh)$(DME)_2$] (left) and [{–Ar(O)CH_2Ar(OMe)–}$_2$TmI (Et_2O)] (right), obtained by reaction of TmI_2 with the respective phenols. Figure was redrawn after Bochkarev et al. (1999b) and Fedushkin et al. (1999).

ketyls (Hou et al., 1998) and therefore it was very likely that the reaction would also take place with the more reducing TmI_2. In fact, the addition of two equivalents of TmI_2 to one equivalent of unsaturated ketone resulted into its further reduction into the dianion. Thus, when 2,5-di-*tert*butylcyclopentadienone was reacted with two equivalents of TmI_2, an interesting bimetallic Tm^{III} complex: $[(THF)_2I_2Tm(\mu\text{-}\eta^5{:}\eta^1\text{-}tBu_2C_5H_2O)TmI_2(THF)_3]$ was isolated (Scheme 5).

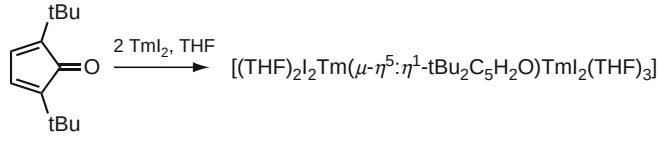

SCHEME 5 Bielectronic reduction of a cyclopentadienone by TmI_2.

It features a bridging oxocyclopentadienyl dianionic ligand, π-complexed with one Tm through the cyclopentadienyl ring and σ-complexed to the second Tm through the oxygen atom (Fedushkin et al., 2003) (Figure 8).

TmI_2 also reacted with 3,5-di-*t*-Butyl-o-quinone (2:1) in DME to give the chelating Tm^{III} diphenoxide $[(3,6\text{-}tBu_2C_6H_2O_2)TmI(DME)]$. Presumably, this compound occurred through elimination of TmI_3 from an initial intermediate such as a dithulium diphenoxide formed by reduction of the quinone by two equivalents of TmI_2. The Tm^{III} diphenoxide was also formed in similar yield from the 2:1 reaction of TmI_2 with 3,5-di-*t*-Butylpyrocatechol (Bochkarev et al., 1999b).

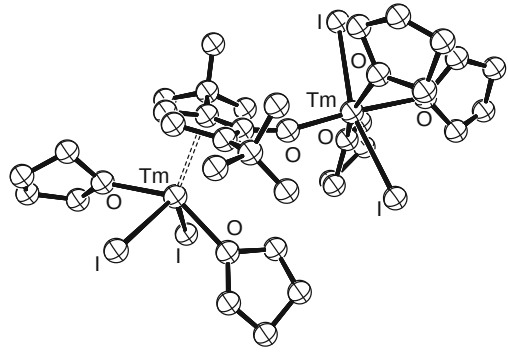

FIGURE 8 The structure of $[(THF)_2I_2Tm(\mu\text{-}\eta^5{:}\eta^1\text{-}tBu_2C_5H_2O)TmI_2(THF)_3]$, obtained by reaction of two equivalents of TmI_2 with 2,5-di-*tert*butylcyclopentadienone. Figure was redrawn after Fedushkin et al. (2003).

2.2.2.1.3 Reaction with nitrogen-containing organic molecules Amines are much less prone to reduction than alcohols and their reactivity with TmI_2, DyI_2 and NdI_2 has been recently investigated. First of all, the diiodides are soluble in liquid ammonia but their solutions decompose immediately. They also react with amines such as methylamine or aniline but we have already seen (in Section 2.2.1) that with isopropylamine, the reaction was slow enough to permit the isolation of divalent compounds. Solutions of DyI_2 and NdI_2 in isopropylamine are still unstable, however, since they decompose over time into $RI_2(NHiPr)(NH_2iPr)_n$ (R = Nd: $n = 4$; R = Dy: $n = 3$), the decomposition being fastest with Nd. An intriguing factor is also that steric protection is not in effect since tBuNH$_2$ rapidly oxidised TmI_2, DyI_2 and NdI_2, which on the other hand are insoluble in Et_3N, Et_2NH or $(Me_3Si)_2NH$ (Bochkarev et al., 2006a,b) (Scheme 6).

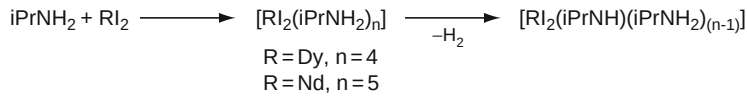

SCHEME 6 Reaction of RI_2 with isopropylamine. The divalent adducts are unstable with R = Nd, Dy but stable with R = Tm.

TmI_2, DyI_2 and NdI_2 have also been used in an acetonitrile/amine coupling reaction, which produced amidines of general formula MeC(=NH)NR^{1}R^2 (R^1, R^2 = H, Me; H, iPr; H, tBu; Et$_2$). The reaction is substoichiometric in rare-earth diiodide but not really catalytic since part of the produced amidine remained tightly held around the rare-earth metal; it could be liberated by heating a trivalent intermediate formulated as $RI_2(amidine)_4(amidinate)$ (R = Nd, Dy, Tm) under vacuum, and the residue could be recycled to produce more amidine. This reaction is not specific of the divalent iodides since many rare-earth triiodides were also effective. In the case of dysprosium and diethylamine, an intermediate trivalent amidine complex has been isolated and structurally characterised in the form of the zwitterionic $[Dy\{MeC(=NH)NEt_2\}_4][(I)_3]$ (Bochkarev et al., 2007) (Figure 9).

TmI_2, DyI_2 and NdI_2 reacted with acetonitrile to give trivalent complexes featuring the 1,1′-bis(iminoethyl)ethylamine neutral tripodal ligand, resulting from an unprecedented trimerisation of acetonitrile. The zwitterionic complexes, which have all been structurally characterised, have the composition $[\{HN{=}CMe)_2C(Me)NH_2\}R(MeCN)_6][(I)_3]$ (R = Nd, Dy, Tm); with neodymium, a variant: $[\{HN{=}CMe)_2C(Me)NH_2\}NdI(MeCN)_5][(I)_2]$ was also isolated (Figure 9); a mechanism has been proposed (Bochkarev et al., 2003; Fagin et al., 2007).

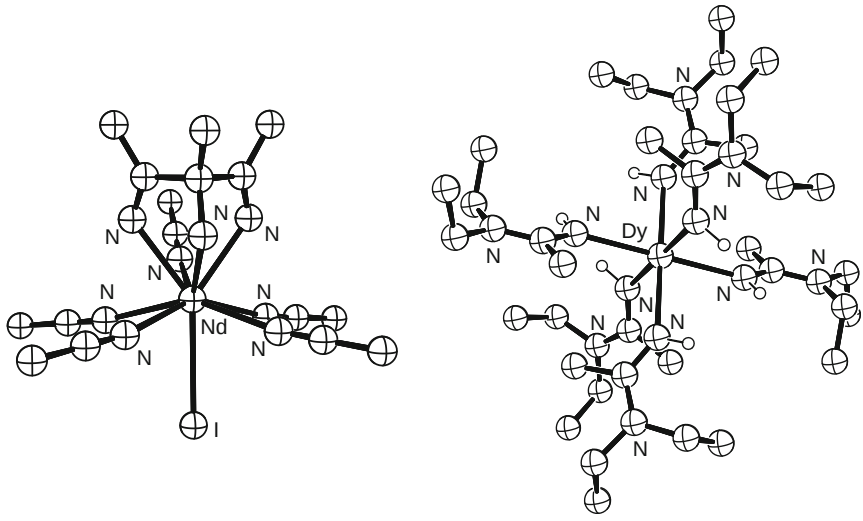

FIGURE 9 The structure of the $[\{HN{=}C(Me)_2C(Me)NH_2\}NdI(MeCN)_5]$ dication (left), obtained by trimerisation of acetonitrile around NdI_2, and of the $[Dy\{MeC(=NH)NEt_2\}_4]$ cation (right), obtained in the reaction of acetonitrile with diethylamine mediated by DyI_2. Figure was redrawn after Bochkarev et al. (2007) and Fagin et al. (2007).

Attempts to liberate the diiminoamine ligand from the dysprosium complex by pyrolysis under vacuum at 195 °C resulted in the isolation of 2,3,5,6-tetramethylpyrazine. A tetraphenylpyrazine was obtained together with 2,4,6-triphenyltriazine and 2,4,5-triphenylimidazole in the reaction of TmI_2, DyI_2 and NdI_2 with benzonitrile followed by hydrolysis (Balashova et al., 2004).

Azobenzene was known to react with organometallic compounds of samarium and ytterbium, therefore its reduction by NdI_2, DyI_2 and TmI_2 was expected. Indeed, when these diiodides were reacted with azobenzene in a 2:1 ratio in THF at room temperature, bridged bimetallic complexes incorporating two azobenzene motifs were obtained. Their assigned composition was $[\{(THF)_2RI\}_2(\mu\text{-}N_2Ph_2)_2]$ (R = Nd, Dy, Tm) on the basis of the X-ray structure of the thulium derivative (Katkova et al., 2003) (Figure 10), which is similar to that of the already described Sm analogue (Nakayama et al., 1997).

The reaction of TmI_2 with pyridine is very sensitive to the reaction conditions. In DME, no definite products could be obtained although magnetic susceptibility measurements point to Tm^{III} species (Evans et al., 1998a). In THF however, the reaction was much cleaner and a binuclear Tm^{III} complex: $[(C_5H_5N)_8Tm_2I_4(\mu\text{-}N_2C_{10}H_{10})]$ was isolated and structurally characterised, featuring a 4,4′-dihydro-4,4′-dipyridinyl dianion as bridging ligand (Figure 11).

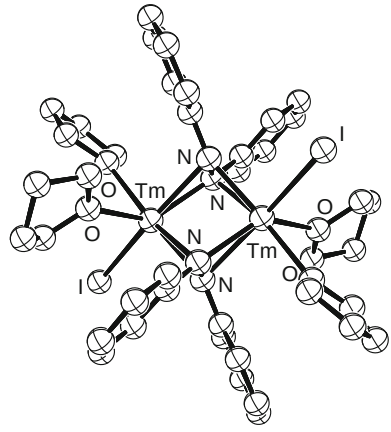

FIGURE 10 The structure of $[\{(THF)_2TmI\}_2(\mu\text{-}N_2Ph_2)_2]$, obtained by reaction of TmI_2 with azobenzene. Figure was redrawn after Katkova et al. (2003).

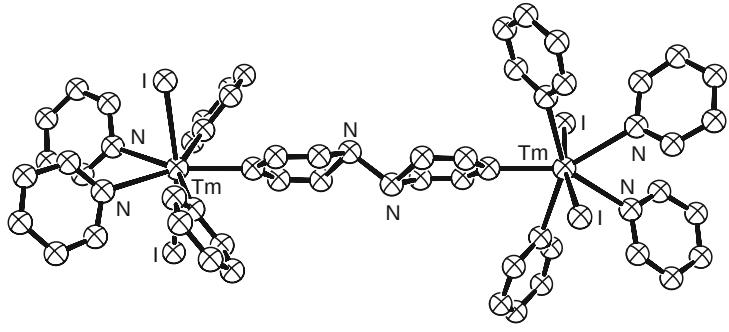

FIGURE 11 The structure of $[(C_5H_5N)_8Tm_2I_4(\mu\text{-}N_2C_{10}H_{10})]$, obtained by reaction of TmI_2 with pyridine in THF. Figure was redrawn after Fedushkin et al. (2003).

The presence of this ligand most likely occurs through monoelectronic reduction of pyridine by Tm^{II} followed by coupling of the resulting radical anion at the 4,4′-position (Fedushkin et al., 2003).

Although Sm^{II} is stable in hexamethylphosphoric triamide (HMPA), $[TmI_2(DME)_3]$ reacted with this solvent with oxidation and $[TmI_3(HMPA)_4]$ precipitated from the solution. This product was also obtained when HMPA was added to TmI_3 in DME. Recrystallisation of this material in pyridine yielded the zwitterionic $[TmI_2(HMPA)_4][I](C_5H_5N)_5]$ (Figure 12) and $[TmI(C_5H_5N)(HMPA)_4][(I)_2]$ (Evans et al., 1998a).

The important issue of the reactivity of divalent compounds or divalent-like systems in the presence of dinitrogen will be addressed later in Section 2.3.4.

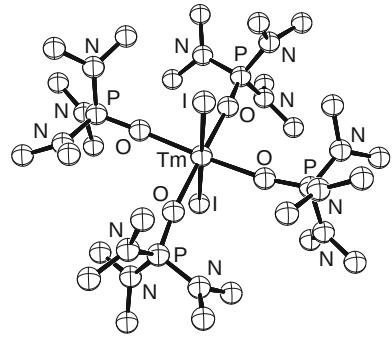

FIGURE 12 The structure of the Tm^{III} cation $[TmI_2(HMPA)_4]$, obtained by reaction of $TmI_2(DME)_3$ with HMPA followed by recrystallisation in pyridine. Figure was redrawn after Evans et al. (1998a).

2.2.2.1.4 Reaction with organic halides Apart from the reactions of organic halides with ketones mediated by rare-earth diiodides (that will be described later in Section 2.2.2.2), a systematic study of the reactivity of NdI_2 with these halides has also been published. This study shows that the reactivity was analogous to that of the alkali metals, in the sense that the organic halides underwent Würtz-type coupling reactions, and were also reduced into alkanes or arenes. The trends in reactivity are complex, but overall the aryl halides were more prone to reduction. Also, interestingly, when an alkyl or benzyl halide was reacted with NdI_2 in benzene, alkylbenzenes or diphenylmethane were obtained: thus, Friedel–Crafts-like reactivity was observed, but with an additional Nd^{II}/Nd^{III} oxidation stage (Fagin et al., 2006).

2.2.2.1.5 Reaction with organometallic compounds Neodymium diiodide reacted with halogenosilanes, germanes and stannanes $(R^1)_3EX$ ($R^1 =$ alkyl; E = Si, Ge, Sn; X = Cl, Br) in polar solvents such as THF or DME. Varying amounts of $(R^1)_3EH$, $(R^1)_3EE(R^1)_3$, or even products of transhalogenidation like $(R^1)_3EI$ were obtained. In THF, $(R^1)_3EOBu$ were also observed. These products are believed to arise through radical-based ring opening of THF either by NdI_2 or by organometallic radicals $(R^1)_3E^{\bullet}$. A ca. 50% yield of digermane was reported when bromotrimethyl- or triethylgermane was treated with NdI_2 in THF (Balashova et al., 2007).

Reactions of pentafluorophenyl germanes or bromogermanes with DyI_2 in THF afforded digermanes or hyperbranched polymers of generic formula $[(C_6F_5)_2Ge(C_6F_4)]_n$. The interaction of the germylmercury compound $[\{(C_6F_5)_3Ge\}_2Hg]$ with DyI_2 resulted in oxidation into the DyI_2^+ cation and the formation of the zwitterionic $[\{(C_6F_5)_3Ge\}_3Hg][DyI_2]$ (Balashova et al., 2005).

NdI_2 and DyI_2 were found to react with vanadocene and chromocene in benzene. Vanadocene is probably reduced into a transient $V^{(0)}$ species that is further stabilised by π-coordination with two molecules of benzene. The yield of bis(benzene)vanadium is 50–70% so this mode of reactivity is viable as a synthetic method. When the reaction was carried out with DyI_2 in isopropylbenzene, however, the yield of bis(isopropylbenzene)vanadium was only 1%. When the same reaction was attempted with naphthalene, no naphthalene-containing products could be obtained but a cyclopentadienyl-based organometallic Dy–V cluster: $[\{(C_5H_5)Dy(\mu\text{-}I)_2\}_7V(\mu\text{-}I)(C_5H_5)_2]$ was isolated instead in low yield. No arene-coordinated compound could be detected in the reaction of NdI_2 and DyI_2 with chromocene or nickelocene in benzene but in one instance, the zwitterionic $[(C_5H_5)_2Cr][(C_5H_5)_2DyI_2]$ was isolated (Bochkarev et al., 2004; Burin et al., 2006) (Figure 13).

2.2.2.2 Applications in organic chemistry

In this section, we consider the organic reactions in which the uncommon rare-earth diiodides have been used as mediators (stoichiometric or catalytic) in organic reactions.

The stability and the solubility of SmI_2 in polar organic solvents have resulted in its application as an extremely successful monoelectronic reducing agent in organic chemistry (Kagan, 2003). However, there are some instances in which its reducing power is insufficient, and the use of cosolvents such as HMPA or inorganic additives like NiI_2 are necessary to significantly improve the reaction kinetics (Dahlén and Hilmersson, 2004). Since the uncommon diiodides are more powerful reducing agents, it is not surprising that they have been used as substitutes to SmI_2 in these reactions, and indeed the results have been generally improved (Scheme 7).

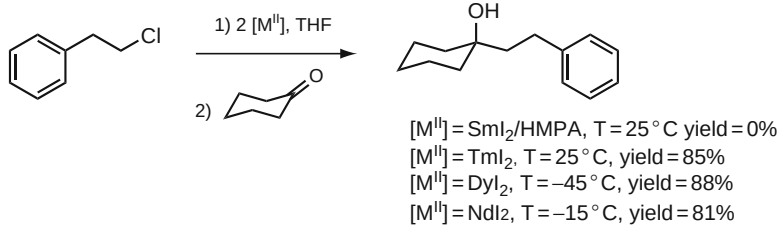

SCHEME 7 A comparative example of the application of rare-earth diiodides in organic chemistry.

The reactivity of TmI_2 has been assessed by comparison with that of samarium diiodide alone and in the presence of HMPA.

The first reaction studied was the coupling of alkyl halides with cyclohexanones mediated by SmI_2/HMPA and TmI_2 in THF or DME in

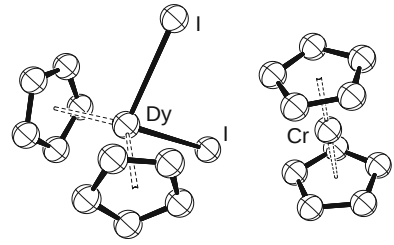

FIGURE 13 The structure of the zwitterionic $[(C_5H_5)_2Cr][(C_5H_5)_2DyI_2]$, obtained in the reaction of DyI_2 with chromocene in benzene. Figure was redrawn after Burin et al. (2006).

the so-called rare-earth-Grignard procedure. Not only bromides were found more active with TmI_2 but also inactivated chlorides were found reactive, while in the same conditions no activity was found with SmI_2/HMPA. Interestingly, a good activity was also found with *in situ* generated TmI_2 from Tm metal and I_2, either in THF or in DME (Evans and Allen, 2000).

The reactivity of the two other non-classical diiodides has also been assessed in similar reactions. Thus, the same ketone coupling reactions have been tried with DyI_2 (Evans et al., 2000) and NdI_2 (Evans et al., 2003b). The reactions work well even at very low temperatures. NdI_2 is particularly interesting because of the advantageous cost of Nd versus that of Dy and Tm. The higher reactivity of NdI_2 has for consequence that the reactions must then be carried out under argon because the solution is unstable under dinitrogen even at $-30\,^{\circ}C$.

In another report, the cross-coupling reactions of 2-acetylthiophene and thiophene 2-carboxylate with carbonyl compounds were studied with SmI_2, SmI_2/HMPA and TmI_2 as coupling agents. Here, the outcome of the reaction was similar with TmI_2 alone and with SmI_2/HMPA in terms of both activity and selectivity: with SmI_2 alone, no coupling reaction occurred and only reduction products were isolated, while with TmI_2 or SmI_2/HMPA coupling products were obtained in similar yields and selectivity. These two studies thus show that the reactivity of TmI_2 is greater or equal to that of SmI_2/HMPA (Shie et al., 2004).

DyI_2 has also been used as a catalyst for the cyclotrimerisation of alkynes. Thus, addition of DyI_2 (10 mol%) to a solution of phenylacetylene in THF gave a modest yield of 1,2,4-triphenylbenzene. Dysprosium acetylides are believed to be intermediates in this reaction, since 1,2,4-triphenylbenzene was also obtained in the reaction of $DyCl_3$ with potassium phenylacetylide followed by addition of phenylacetylene in excess. However, the cyclotrimerisation reaction was greatly improved when an arylacetylene was added to an equimolar amount of DyI_2 and a

chlorosilane (33 mol%) in DME at 70 °C for 3 days. The best results were obtained with phenylacetylene and $DyI_2/SiCl_4$, in which case a 92% yield of 1,2,4-triphenylbenzene was obtained, together with 2% of 1,3,5-triphenylbenzene as a side product. The reported yield was not so good with electron-rich arylacetylenes such as 1-ethynyl-4-methoxybenzene. The actual catalytic species is believed to be a silyl radical, generated by interaction of DyI_2 with the chlorosilane. Thus, with $SiCl_4$ as silane, a trichlorosilyl radical would be produced (Zhu et al., 2006) (Scheme 8). The alkyne cyclotrimerisation reaction has later been simplified by the replacement of $DyI_2/SiCl_4$ as catalyst by $Dy/SiCl_4$ (Zhu et al., 2007).

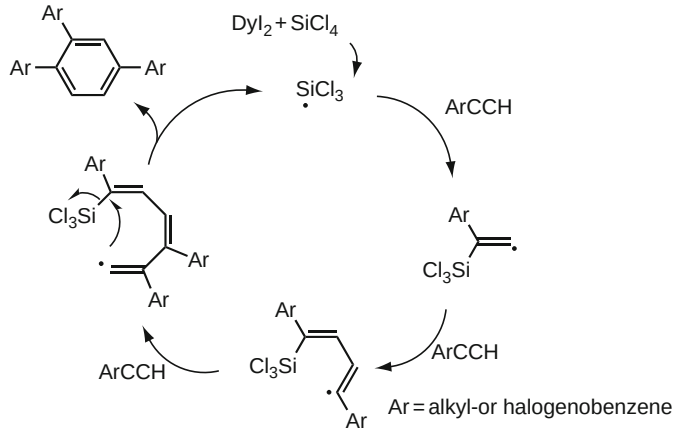

SCHEME 8 Proposed mechanism for the trimerisation of alkynes mediated by $DyI_2/SiCl_4$. Scheme was redrawn after Zhu et al. (2006).

Another use of DyI_2 has been put forward in the cyclopropanation of alkenes. Quite remarkably, this cyclopropanation could be done at room temperature in a Simmons–Smith-type reaction, using dichloromethane instead of the usual diiodoethane and DyI_2 as the reducing agent. When the reaction was run in THF, the optimised yield was good (up to 77% with styrene at 50 °C). DyI_2 could be substituted by a 1:1 mixture of Dy and I_2, but also by Sm/I_2 or even Mg/I_2. The reaction (so far restricted to substituted styrenes) still worked best with the Dy/I_2 system. The proposed mechanism needs two equivalents of DyI_2 (Xiang et al., 2008) (Scheme 9).

Finally, NdI_2 (Evans et al., 2003b) and DyI_2 (Evans et al., 2000) were found sufficiently reducing to react with naphthalene in a Birch-like manner, yielding 1,4-dihydronaphthalene after hydrolysis; an intermediate could be isolated in this reaction (see Section 2.2.2.1.1). Likewise, the reaction of diphenylacetylene with DyI_2 gave *cis*-stilbene after hydrolysis (Evans et al., 2000) (Scheme 10).

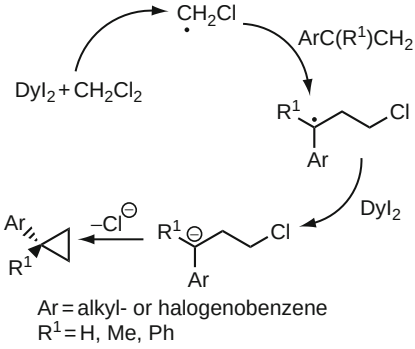

SCHEME 9 Proposed mechanism for the cyclopropanation of styrenes mediated by DyI_2/CH_2Cl_2. Scheme was redrawn after Xiang et al. (2008).

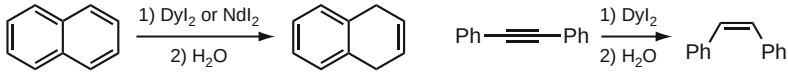

SCHEME 10 Examples of reduction of unsaturated hydrocarbons by NdI_2 and DyI_2.

In conclusion, it appears that, as expected, the overall reactivity of NdI_2, DyI_2 and TmI_2 is superior to that of SmI_2. Especially NdI_2 offers great potential given the reasonable cost of Nd. It is to be noted that NdI_2, DyI_2 and TmI_2 have now been made commercially available by one of the major chemical reagents company.

2.2.2.3 Applications in polymer chemistry

Since rare-earth diiodides are strong Lewis acids and can be seen as persistent radicals, it is not surprising that they have been applied as initiators in polymerisation reactions. For instance, the $DyI_2/SiCl_4$ system mentioned in the previous section has been shown to induce free radical polymerisation of methyl methacrylate (MMA). The Dy^{3+} ions which are produced by this system play a role because of the observed higher syndiotacticity, higher average molecular weight (M_n) and smaller polydispersity index (PDI) than in a typical free radical polymerisation of MMA (Zhu et al., 2006).

MMA could also be polymerised by the NdI_2/1-bromo-1-phenylethane (BPE) or NdI_2/BPE/Bipy systems (Bipy = 2,2′-bipyridyl). Here again, the polymerisation reaction was typically better controlled in terms of M_n and PDI. The NdI_2/BPE/Bipy system has been applied as well to the polymerisation of styrene, also with better control than with a

conventional free radical polymerisation using, for example, azobis (isobutyronitrile) (AIBN) as initiator (Gusev et al., 2008).

Polyacrylonitrile ($M_n = 2700$) could be obtained (after hydrolysis) by interaction of DyI_2 with acrylonitrile (Balashova et al., 2004).

In a short communication, TmI_2, DyI_2 and NdI_2 but also SmI_2 have been shown to initiate the polymerisation of isoprene into high 1,4-*cis*-polyisoprene with or without TIBA (tris-isobutylaluminium) as initiator. Since the reaction may take place in hexane, in which the diiodides are insoluble, the polymerisation reaction is believed to be heterogeneous (Evans et al., 2003c).

2.3 Uncommon divalent complexes

2.3.1 Synthesis by the metathesis pathway

2.3.1.1 Thulium complexes

Several unsuccessful attempts have been made to use TmI_2 as a precursor to the synthesis of divalent organothulium compounds; the results are nonetheless interesting and worth reporting.

Soon after the isolation of $[TmI_2(DME)_3]$, this precursor was reacted with naphthalene–lithium in DME and a triple-decker naphthalene complex: $[\{(DME)Tm\}_2(\eta^4\text{-}C_{10}H_8)_2(\mu^2\text{-}\eta^4\text{:}\eta^4\text{-}C_{10}H_8)]$ was obtained and structurally characterised. The three naphthalene ligands are present in the dianionic form so the thulium is trivalent in this complex. This was confirmed by magnetic susceptibility measurements, which are compatible with Tm^{III}. The formation of the complex might be mediated by a transient naphthalenethulium(II) species which would then be further oxidised by free naphthalene present in solution (Bochkarev et al., 1997b) (Figure 14).

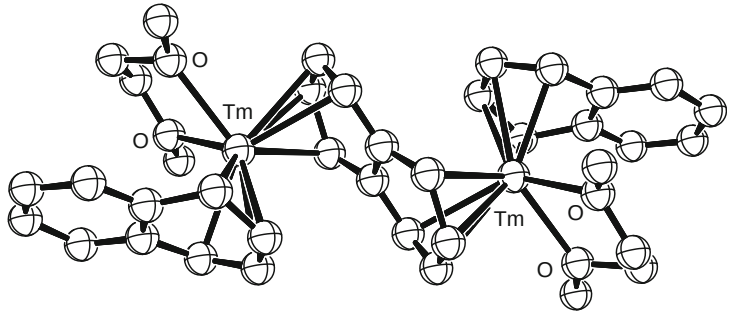

FIGURE 14 The structure of the Tm^{III} complex $[\{(DME)Tm\}_2(\eta^4\text{-}C_{10}H_8)_2(\mu^2\text{-}\eta^4\text{:}\eta^4\text{-}C_{10}H_8)]$, obtained in the reaction of $[TmI_2(DME)_3]$ with naphthalene–lithium in DME.
Figure was redrawn after Bochkarev et al. (1997b).

Similarly, the reaction of TmI_2 with anthracene–lithium results in the formation of $[(\eta^2\text{-}C_4H_{10})TmI(DME)]$ in which the anthracene ligand is in the dianionic form and therefore contains Tm^{III} (Fedushkin et al., 2001a) (Figure 15).

Initial attempts to synthesise thulium(II) metallocenes involved the reaction of TmI_2 with substituted cyclopentadienides of potassium or magnesium. The reaction proved to be dependent on the solvent used and on the presence or absence of dinitrogen. As a general rule, dinitrogen was incorporated in the final product as diazenide (N_2^{2-}) when this gas was used as ''protective'' atmosphere. These reactions together with the important issue of dinitrogen activation by systems displaying divalent-like behaviour will be discussed in Section 2.3.4.

The reaction of TmI_2 and KC_5Me_5 in the absence of dinitrogen resulted in the isolation of $[(C_5Me_5)_2TmI]$ in low yield. The use of the substituted cyclopentadienyl Grignard reagent: 1,3-$(Me_3Si)_2C_5H_3MgCl$ as precursor with $[TmI_2(THF)_2]$ resulted in the formation of the Tm^{III} chloride dimer $[\{1,3\text{-}(Me_3Si)_2C_5H_3\}_4Tm_2(\mu\text{-}Cl)_2]$ (Figure 16) and metallic magnesium, presumably due to reduction of MgICl by a transient Tm^{II} intermediate. In an attempt to stabilise divalent thulium by intramolecular coordination, TmI_2 was reacted with a potassium cyclopentadienide bearing an amine-substituted pendant arm: $K(C_5H_5CH_2CH_2NMe_2)$. Although an initial green colour was observed, no definite product could be isolated after work-up (Fedushkin et al., 2001b).

A mixture of TmI_2 and KC_5Me_5 in diethyl ether under argon initially developed a purple colour that may be indicative of the presence of Tm^{II}. This colour faded to yellow-orange within hours, however, and the isolated product: $[\{(C_5Me_5)_2Tm\}_2(\mu\text{-}OEt)_2\{(C_5Me_5)Tm\}(\mu\text{-}O)\{Tm$

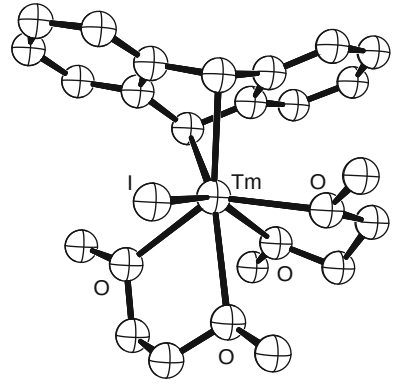

FIGURE 15 The structure of the Tm^{III} complex $[(\eta^2\text{-}C_4H_{10})TmI(DME)]$, obtained in the reaction of TmI_2 with anthracene–lithium in DME. Figure was redrawn after Fedushkin et al. (2001a).

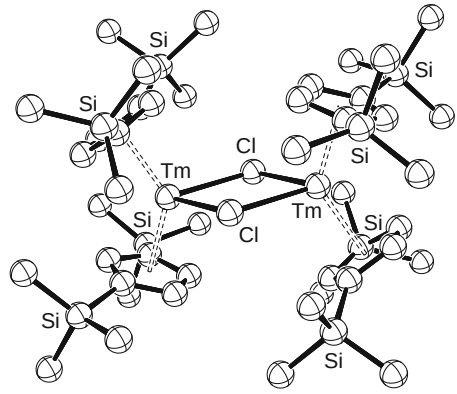

FIGURE 16 The structure of the Tm^{III} complex $[\{1,3\text{-}(Me_3Si)_2C_5H_3\}_4Tm_2(\mu\text{-}Cl)_2]$, obtained in the reaction of TmI_2 with $1,3\text{-}(Me_3Si)_2C_5H_3MgCl$, instead of an expected divalent complex. Figure was redrawn after Evans et al. (2001).

$(C_5Me_5)\}]$ contained both μ-oxo and μ-ethoxy groups originating from cleavage of the diethyl ether solvent.

However, in the same paper, there were some hints for the existence of a stable organothulium(II) compound since it was reported (in a footnote) that the reaction of $K\{1,3\text{-}(Me_3Si)_2C_5H_3\}$ with TmI_2 in diethyl ether under argon gave a purple solution. Such ''divalent-like colours'' have been observed in many instances, but this time this solution could be analysed by proton NMR, and a clean spectrum consisting of paramagnetically shifted peaks with a correct integration was observed (Evans et al., 2001). Although the stability of the solution was not stated in this publication, these observations are consistent with the existence of a Tm^{II} complex.

The tetrapotassium Et_8-calix[4]tetrapyrrolide looked like a good candidate to stabilise Tm^{II} because of its rigid, chelating structure. However, when this precursor was reacted with $[TmI_2(DME)_3]$, two anionic Tm^{III} complexes were obtained: [(Et_8-calix[4]tetrapyrrolide)Tm][K(DME)] in which the ligand remains intact but also a tripotassium–tris(thulium) bipyrrolide: $\{[Et_2C(C_4H_3N)_2]_3Tm[K(toluene)_3]\}$ in which the terrapyrrolide ligand has been cleaved, most likely with assistance from Tm^{II} (Korobkov et al., 2002) (Figure 17).

The reaction of a bulky and bridging dialkylpotassium substituted by silyl- and methoxysilyl-bearing substituents (LK_2: L = [$(MeOSiMe_2)(Me_3Si)C(SiMe_2CH_2)]_2$) with TmI_2 and NdI_2 did not yield the expected Tm^{II} or Nd^{II} dialkyls but methoxide-bearing trivalent complexes: [LTm(OMe)(THF)] and [LNd(OMe)(THF)], respectively. A transient deep green colour might indicate the initial formation of a Tm^{II} intermediate. The methoxide group on the thulium or neodymium likely comes

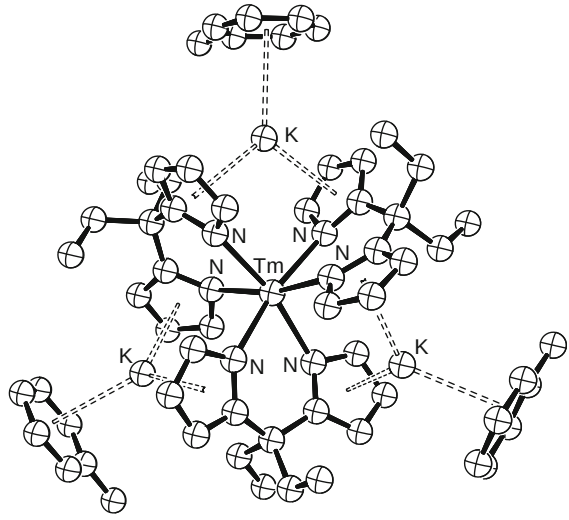

FIGURE 17 The structure of the Tm^{III} complex $\{[Et_2C(C_4H_3N)_2]_3Tm[K(toluene)_3]\}$, obtained in the reaction of TmI_2 with tetrapotassium Et_8-calix[4]tetrapyrrolide, resulting in cleavage of the tetrapyrrolide ligand. Figure was redrawn after Korobkov et al. (2002).

from Si–O bond splitting by the divalent ions (Bowman et al., 2007) (Figure 18).

The reaction of an *N*-heterocyclic gallyl anion $[Ga(ArNCH)_2]^-$ (Ar = 2,6-diisopropyl) with $[TmI_2(THF)_5]$ in a 2:1 ratio in toluene/TMEDA resulted in the isolation of the Tm^{III} complex $[\{Ga(ArNCH)_2\}(ArNCH)_2Tm(TMEDA)]$ (Figure 19) in which gallium has been abstracted from one ligand, thus transformed into a diamide. This gallium abstraction only occurs with Tm since the ''normal'' $[\{Ga(ArNCH)_2\}_2R(TMEDA)_2]$ were obtained with R = Sm, Eu or Yb (Jones et al., 2009) (Scheme 11).

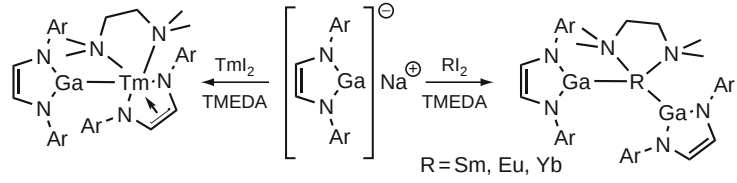

SCHEME 11 The reaction of RI_2 (M = Sm, Eu, Tm and Yb) with an *N*-heterocyclic gallyl anion: while with R = Sm, Eu and Yb a simple metathesis occurs, with R = Tm, gallium was abstracted from the *N*-heterocyclic gallyl anion, thus generating a diamide ligand which ends up bonded to Tm.

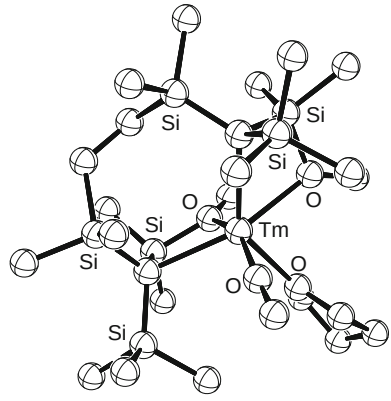

FIGURE 18 The structure of the Tm^{III} complex [{[(MeOSiMe$_2$)(Me$_3$Si)C(SiMe$_2$CH$_2$)]$_2$}Tm(OMe)(THF)], obtained in the reaction of TmI_2 with [(MeOSiMe$_2$)(Me$_3$Si)C(SiMe$_2$CH$_2$)]$_2$K$_2$; the methoxy group on thulium likely occurs from Tm^{II}-assisted cleavage of the ligand. Figure was redrawn after Bowman et al. (2007).

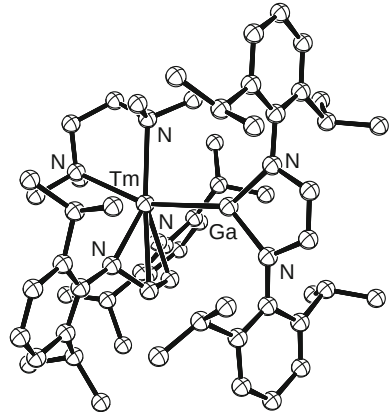

FIGURE 19 The structure of the Tm^{III} complex [{Ga(ArNCH)$_2$}(ArNCH)$_2$Tm(TMEDA)], obtained in the reaction of [TmI$_2$(THF)$_5$] with two equivalents of the *N*-heterocyclic gallyl anion [Ga(ArNCH)$_2$][K(TMEDA)]. Figure was redrawn after Jones et al. (2009).

Soon after the first attempts, it was eventually reported in 2002 that the reaction of K[1,3-(Me$_3$Si)$_2$C$_5$H$_3$] with TmI_2 in THF under argon gave [{1,3-(Me$_3$Si)$_2$C$_5$H$_3$}$_2$Tm(THF)] (Figure 20) that could be crystallised and analysed by X-ray crystallography. This π-complex was the first unambiguously characterised organothulium(II) compound. However, its stability in THF was low at room temperature (Evans et al., 2002). [(1,3-*t*Bu$_2$C$_5$H$_3$)$_2$Tm(THF)] (Figure 18) was later made similarly and

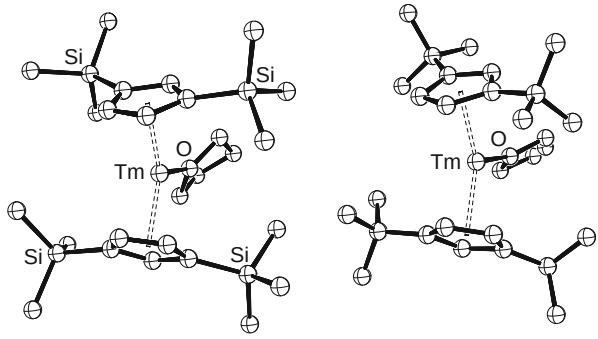

FIGURE 20 The structure of two THF-solvated cyclopentadienylthulium(II) complexes: $[\{1,3\text{-}(Me_3Si)_2C_5H_3\}_2Tm(THF)]$ (left) and $[(1,3\text{-}t\text{Bu}_2C_5H_3)_2Tm(THF)]$ (right), obtained by ionic metathesis of the cyclopentadienyl anions with TmI_2 in THF. These complexes have limited stability at room temperature. Figure was redrawn after Evans et al. (2002c) and Nief et al. (2005).

structurally characterised but the yield was low and a THF solution also quickly decomposed (Nief et al., 2005).

Increasing the stability of Tm^{II} complexes is possible via two ways: (a) electronically, by reducing the π-donating ability of the ligand and (b) sterically, by adding more bulky substituents on the π-ligand.

Substituted phospholyl (phosphacyclopentadienyl) ligands (Quin, 2006) were good candidates for both purposes: electrochemical measurements in the related actinide chemistry have shown that phospholyls were poorer π-bases than cyclopentadienyl ligands (Gradoz et al., 1994), and the addition of bulky substituents on the ring can be easily achieved by straightforward synthetic methods. Furthermore, the phosphorus atom is a useful NMR probe.

Thus, potassium phospholides (and also an arsolide) were reacted with $[TmI_2(THF)_3]$ in diethyl ether and solvated Tm^{II} π-complexes: $[L_2Tm(THF)]$ $(L = (2,5\text{-}t\text{Bu}_2)(3,4\text{-}Me_2)C_4P$, $[2,5\text{-}(Me_3Si)_2](3,4\text{-}Me_2)C_4As$, $[2,5\text{-}(Me_3Si)_2](3,4\text{-}Me_2)C_4P)$, were obtained and two of them were structurally characterised (Figure 21).

Despite their paramagnetism (measured $\mu_{eff} = 4.7\mu_B$), these compounds had clean proton and also phosphorus NMR spectra (for the phospholyl derivatives), and were substantially more stable than Evans' first complex since THF solutions only showed slight decomposition after 24 h at room temperature (Nief et al., 2002).

Lesser-substituted phospholylthulium(II) complexes of the same type: $[L_2Tm(THF)]$ $(L = (2,5\text{-}t\text{Bu}_2)C_4H_2P$, $[2,5\text{-}(Me_3Si)_2]C_4H_2P)$ were also structurally characterised and their solution stability was comparable to that of the previously described phospholylthulium(II) complexes. Examination

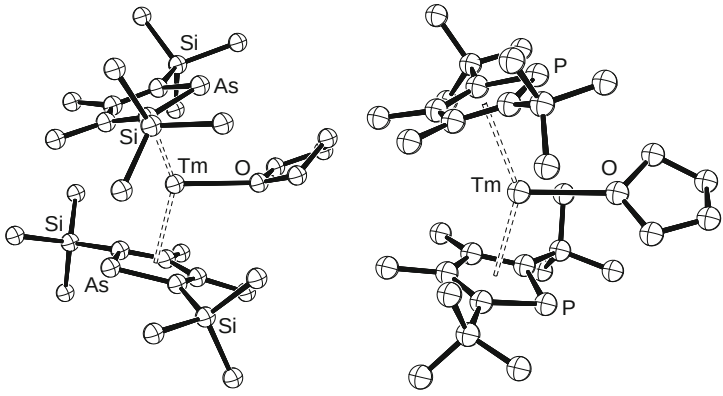

FIGURE 21 The structures of two THF-solvated arsolyl- and phospholylthulium(II) complexes: $[\{[2,5\text{-}(Me_3Si)_2](3,4\text{-}Me_2)C_4As\}_2Tm(THF)]$ (left) and $[\{(2,5\text{-}t Bu_2)(3,4\text{-}Me_2)C_4P\}_2Tm(THF)]$ (right), obtained by ionic metathesis of the arsolyl and phospholyl anions with TmI_2 in THF. These complexes are stable at room temperature. Figure was redrawn after Nief et al. (2002).

of the geometrical data of $[L_2Tm(THF)]$ in which $L = (2,5\text{-}t Bu_2)C_4H_2P$, $[2,5\text{-}(Me_3Si)_2]C_4H_2P$, $[1,3\text{-}(Me_3Si)_2]C_5H_3$, $(1,3\text{-}t Bu_2)C_5H_3$, showed that the steric bulk of the cyclopentadienyl and phospholyl ligands in this series appeared very similar, and, since the cyclopentadienyl complexes are much less stable, it was proposed that the extra stability of the phospholyl complexes is of electronic origin (Nief et al., 2005). It can also be noted that all phospholylthulium(II) complexes prepared so far have been unreactive towards dinitrogen.

However, increasing the steric bulk on the cyclopentadienyl ligand also resulted in increased stability of the Tm^{II} complexes: solutions of $[\{1,2,4\text{-}(Me_3Si)_3C_5H_2\}_2Tm(THF)]$ and $[(1,2,4\text{-}t Bu_3C_5H_2)_2Tm(THF)]$ (Figure 22) are reasonably stable at room temperature (Jaroschik et al., 2006).

One reason for the instability of the $[L_2Tm(THF)]$ complexes is the presence of THF bonded to Tm via the oxygen atom, since it can undergo irreversible electron transfer from Tm. Unsolvated complexes would thus be more stable; however, the synthesis is challenging, since the donor solvents that are used in the metathesis reaction have a very strong affinity for Tm. One workaround is to use a combination of large steric bulk on the ligand and reduced basicity of the solvent. Thus, when $K[(2,5\text{-}t Bu_2)(3,4\text{-}Me_2)C_4P]$ was reacted with unsolvated TmI_2 in the presence of diethyl ether for 24 h at room temperature, the ether-solvated $[\{(2,5\text{-}t Bu_2)(3,4\text{-}Me_2)C_4P\}_2Tm(Et_2O)]$ was observed as an intermediate but the ether could easily be removed by co-evaporation

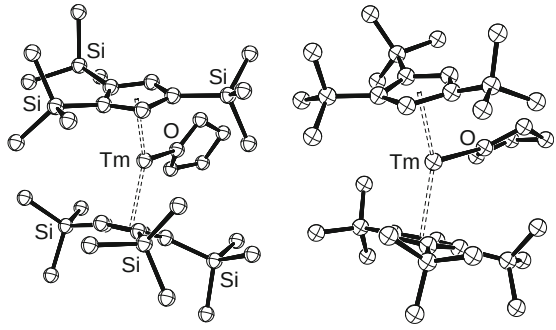

FIGURE 22 The structures of two very crowded THF-solvated cyclopentadienylthulium(II) complexes: [{1,2,4-$(Me_3Si)_3C_5H_2$}$_2$Tm(THF)] (left) and [(1,2,4-tBu$_3C_5H_2$)$_2$Tm(THF)] (right), obtained by ionic metathesis of the cyclopentadienyl anions with TmI_2 in THF. These complexes are stable at room temperature. Figure was redrawn after Jaroschik et al. (2006, 2007b).

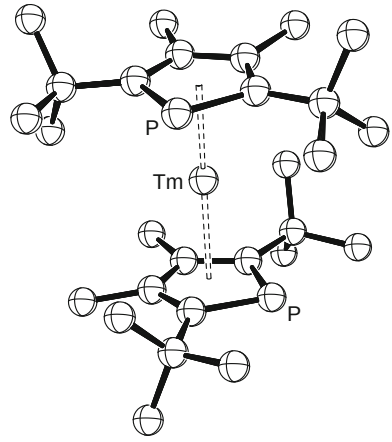

FIGURE 23 The structure of the homoleptic phospholylthulium(II) complex: [{(2,5-tBu$_2$)(3,4-Me_2)C_4P}$_2$Tm], obtained by vacuum evaporation of a pentane solution of [{(2,5-tBu$_2$)(3,4-Me_2)C_4P}$_2$Tm(Et_2O)]. This complex is indefinitely stable in pentane solution at room temperature. Figure was redrawn after Turcitu et al. (2003).

with pentane and a good yield of the structurally characterised [{(2,5-tBu$_2$)(3,4-Me_2)C_4P}$_2$Tm] was obtained (Figure 23). In the crystal structure of this first homoleptic Tm^{II} complex, the six-coordinated thulium(II) has close contacts with methyl groups belonging to the t-butyl substituents on the phospholyl rings and located under the ligand plane. This steric protection and the absence of donor solvent has for consequence that [{(2,5-tBu$_2$)(3,4-Me_2)C_4P}$_2$Tm] is indefinitely stable at room temperature in pentane solution (Turcitu et al., 2003).

The THF molecule is also labile in [(1,2,4-tBu$_3$C$_5$H$_2$)$_2$Tm(THF)] and could be removed by vacuum pumping, but the resulting [(1,2,4-tBu$_3$C$_5$H$_2$)$_2$Tm] could not be structurally characterised (Jaroschik et al., 2006). Another way of synthesising unsolvated Tm^{II} complexes will be addressed in Section 2.3.2.

A completely different ligand system has been used very recently and has permitted the isolation of heteroleptic Tm^{II} complexes. Thus, the reaction of a so-called ''second-generation'' scorpionate in the form of its potassium salt: potassium tris(3-tBu-5-Me-pyrazolyl)borate (KL) with TmI_2 in THF in a 1:1 ratio afforded [LTmI(THF)] which could be further transformed into [LTm(HBEt$_3$)(THF)], the unsolvated [LTmN(SiMe$_3$)$_2$] and the first alkylthulium(II) complex: [LTmCH(SiMe$_3$)$_2$] (Figure 24); the homoleptic [L$_2$Tm] was also isolated (Cheng et al., 2008).

Scheme 12 presents a summary of the characterised Tm^{II} complexes that can be synthesised from TmI_2 by the metathesis reaction.

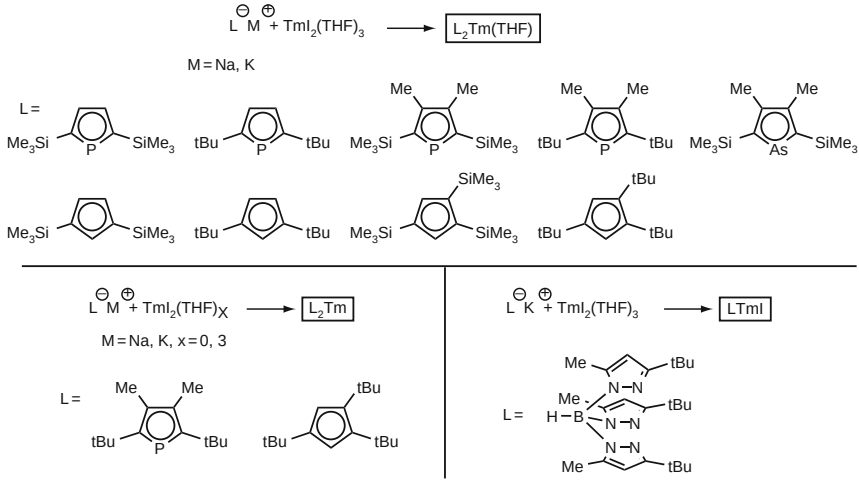

SCHEME 12 TmI_2 as precursor to Tm^{II} complexes.

2.3.2 Synthesis by the reductive pathway

Divalent complexes can also be synthesised by the reductive pathway. This method is less direct, since it involves two steps instead of one for the metathesis reaction: (a) synthesis of a suitable trivalent complex as precursor and (b) chemical reduction of this trivalent complex. This method has a number of advantages, however, since, in addition to organothulium(II) complexes, it has permitted to isolate compounds that could not be synthesised by the metathesis pathway, such as lanthanum(II),

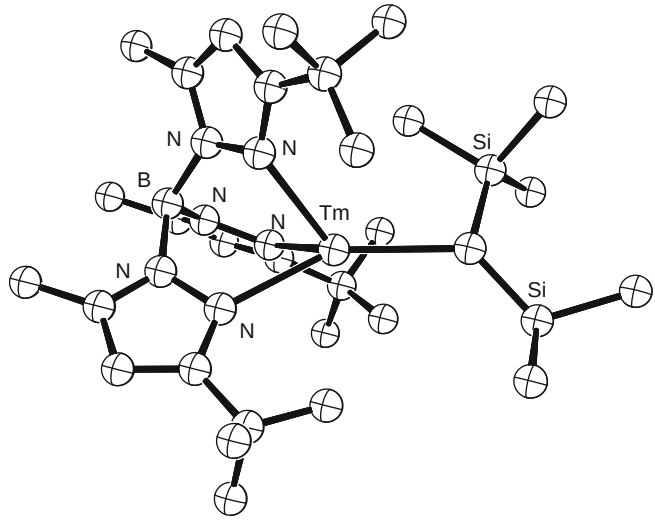

FIGURE 24 The structure of an alkylthulium(II) complex: [LTmCH($SiMe_3$)$_2$], where L is hydrido-tris(3-*t*Bu-5-Me-pyrazolyl)borate, obtained by metathesis of [LTmI] with bis (trimethylsilyl)methylpotassium. Figure was redrawn after Cheng et al. (2008).

cerium(II), neodymium(II) and dysprosium(II) organometallics. Note that the synthesis of lanthanum(II) and cerium(II) complexes by metathesis would appear difficult because LaI_2 and CeI_2 belong to the ''metallic'' type of diiodides and are insoluble in organic solvents.

2.3.2.1 Lanthanum(II) and cerium(II) complexes

The first indications of the possible existence of uncommon divalent rare-earth complexes appeared in a report on the reduction of [{1,3-$(Me_3Si)_2C_5H_3$}$_3$R] (R = Ce, Nd) and [(1,3-*t*$Bu_2C_5H_3)_3$Ce] by potassium in DME. Although ultimately the trivalent [{1,3-$(Me_3Si)_2C_5H_3$}$_4$R$_2$(μ-OMe)$_2$] (R = Ce, Nd), [(1,3-*t*$Bu_2C_5H_3)_4Ce_2(\mu$-OMe)$_2$] (Figure 25) and [{1,3-$(Me_3Si)_2C_5H_3$}Nd(μ-OMe)$_2$Li(DME)] were obtained, the methoxy groups on the metal obviously came from reductive DME cleavage and divalent Ce^{II} and Nd^{II} organometallics appeared as plausible intermediates (Gun'ko et al., 1995). This reduction was repeated with [{1,3-$(Me_3Si)_2$-C_5H_3}$_3$La] and the La^{III} complex [{1,3-$(Me_3Si)_2C_5H_3$}$_4$La$_2$(μ-OMe)$_2$] was also obtained, but additionally the royal blue reaction mixture displayed an ESR spectrum compatible with La^{II} species. Furthermore, a cyclic voltammogram of [{1,3-$(Me_3Si)_2C_5H_3$}$_3$La] in DME showed a reversible wave at the very negative La^{3+}/La^{2+} redox potential of -2.8 V versus ferrocene/ferricinium (Cassani et al., 1997). When the potassium reduction of [{1,3-$(Me_3Si)_2C_5H_3$}$_3$La] was performed in the presence of [18]

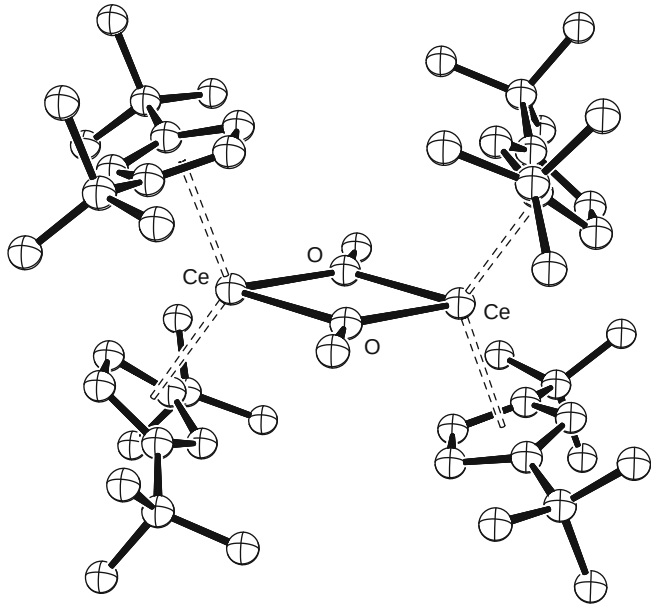

FIGURE 25 The structure of $[(1,3\text{-}t\text{Bu}_2\text{C}_5\text{H}_3)_4\text{Ce}_2(\mu\text{-OMe})_2]$, obtained by potassium reduction of $[(1,3\text{-}t\text{Bu}_2\text{C}_5\text{H}_3)_3\text{Ce}]$ in DME. The bridging methoxy groups are produced by cleavage of DME, possibly by a low-valent cerium species. Figure was redrawn after Gun'ko et al. (1995).

crown-6 in benzene at room temperature, a La^{III} complex: $[\{1,3\text{-}(Me_3Si)_2\text{-}C_5H_3\}_2La(\eta\text{-}C_6H_6)][K([18]crown\text{-}6]$ was isolated, featuring an unprecedented benzene dianionic ligand (Cassani et al., 1996).

However, ESR analysis of the reaction mixture revealed at least four possible La^{II} intermediates (Cassani et al., 1999). Eventually the first strong indication of a stable La^{II} complex came from the reductive chemistry of the related $[(1,3\text{-}t\text{Bu}_2\text{C}_5\text{H}_3)_3\text{La}]$, a system that could be reversibly reduced at -3.1 V (which clearly shows the electronic influence of the more donating *t*Bu groups). Reduction of this complex with potassium in benzene at room temperature in the presence of [18]crown-6 eventually gave the structurally characterised dark green $[(1,3\text{-}t\text{Bu}_2\text{-}C_5H_3)_4La_2(\mu\text{-}C_6H_6)][K([18]crown\text{-}6)(\eta\text{-}C_6H_6)_2]$ (Figure 26). The geometric factors of the μ-benzene ligand point to its radical–anion nature and thus to this complex being the first structurally characterised La^{II} compound. Alternative formulations of a mixed valence La^{III}/La^{II} or a La^{III} compound with the μ-benzene ligand being dianionic or trianionic appear less plausible (Cassani et al., 1998).

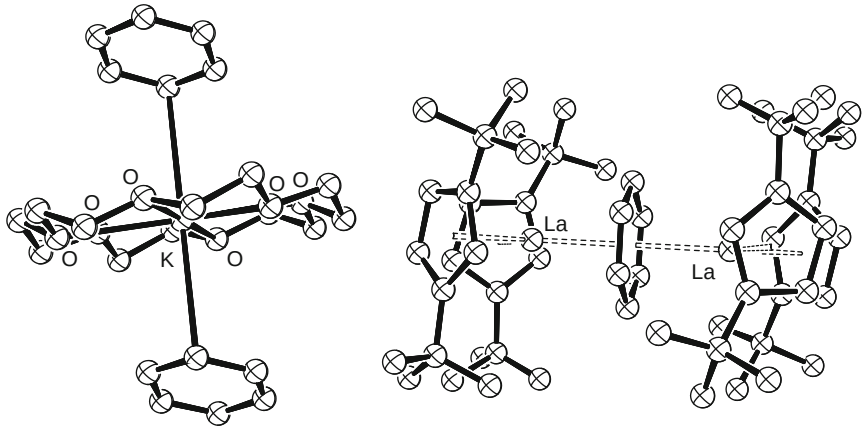

FIGURE 26 The structure of $[(1,3\text{-}t\text{Bu}_2\text{C}_5\text{H}_3)_4\text{La}_2(\mu\text{-}\text{C}_6\text{H}_6)][\text{K}([18]\text{crown-6})(\eta\text{-}\text{C}_6\text{H}_6)_2]$, obtained by potassium reduction of $[(1,3\text{-}t\text{Bu}_2\text{C}_5\text{H}_3)_3\text{La}]$ in benzene in the presence of [18] crown-6. The μ-benzene ligand is best described as a monoanion, and thus the dimeric complex most likely contains La^{II}. Figure was redrawn after Cassani et al. (1998).

When the reduction of $[\{1,3\text{-}(\text{Me}_3\text{Si})_2\text{C}_5\text{H}_3\}_3\text{R}]$ (R = La, Ce) was performed in similar conditions with potassium in toluene, compounds formulated as La^{II} and Ce^{II} compounds, $[\{1,3\text{-}(\text{Me}_3\text{Si})_2\text{C}_5\text{H}_3\}_4\text{R}_2(\mu\text{-}\text{CH}_3\text{C}_6\text{H}_5)][\text{K}([18]\text{crown-6})(\eta\text{-}\text{CH}_3\text{C}_6\text{H}_5)_2]$ were obtained. The Ce^{II} complex was structurally characterised, but its structure was not of good quality. When the reduction was performed on the lesser substituted $[\{(t\text{BuMe}_2\text{Si})\text{C}_5\text{H}_4\}_3\text{R}]$, μ-hydrido La^{III} and Ce^{III} dimers $[\{(t\text{BuMe}_2\text{Si})\text{C}_5\text{H}_4\}_6\text{R}_2(\mu\text{-H})_2][\text{K}([18]\text{crown-6})(\eta\text{-}\text{CH}_3\text{C}_6\text{H}_5)_2]$ were obtained, thus emphasising the necessity of steric protection to stabilise divalent complexes (Gun'ko et al., 2000).

When no aromatic solvent was present and the reduction of $[\{1,3\text{-}(\text{Me}_3\text{Si})_2\text{C}_5\text{H}_3\}_3\text{La}]$ was performed in Et_2O in the presence of [18]crown-6 or in THF in the presence of [2.2.2]cryptand, $[\{1,3\text{-}(\text{Me}_3\text{Si})_2\text{C}_5\text{H}_3\}_3\text{La}][\text{K}([18]\text{crown-6})(\text{Et}_2\text{O})]$ (Figure 27) and $[\{1,3\text{-}(\text{Me}_3\text{Si})_2\text{C}_5\text{H}_3\}_3\text{La}][\text{K}([2.2.2]\text{cryptand})]$ were, respectively, obtained and unambiguously characterised as La^{II} complexes by X-ray diffraction, SQUID magnetic susceptibility measurements and ESR (Hitchcock et al., 2008).

With cerium, in similar conditions, a mixed-valence complex: $[\{1,3\text{-}(\text{Me}_3\text{Si})_2\text{C}_5\text{H}_3\}_6\text{Ce}_2][\text{K}([18]\text{crown-6})(\text{Et}_2\text{O})]$ (Figure 28) was isolated where two distinct $\{1,3\text{-}(\text{Me}_3\text{Si})_2\text{C}_5\text{H}_3\}_3\text{Ce}$ units are present: one is neutral (Ce^{III}) and the other is anionic (Ce^{II}) (Hitchcock et al., 2008). A summary of isolated complexes containing low-valent La^{II} or Nd^{II} is presented on Scheme 13.

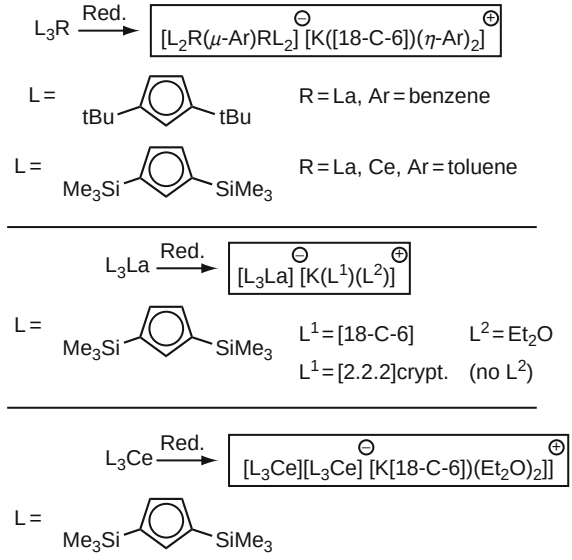

SCHEME 13 The reductive pathway to organometallic complexes containing La^{II} and Ce^{II}.

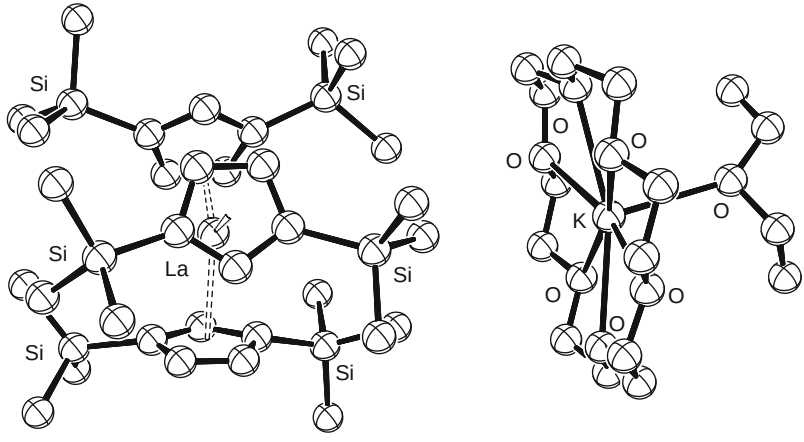

FIGURE 27 The structure of $[\{1,3\text{-}(Me_3Si)_2C_5H_3\}_3La][K([18]crown\text{-}6)(Et_2O)]$, obtained by potassium reduction of $[\{1,3\text{-}(Me_3Si)_2C_5H_3\}_3La]$ in Et_2O in the presence of [18]crown-6. The anionic $[\{1,3\text{-}(Me_3Si)_2C_5H_3\}_3La]$ unit unambiguously contains La^{II}. Figure was redrawn after Hitchcock et al. (2008).

2.3.2.2 Neodymium(II) and dysprosium(II) complexes

Apart from Edelmann's unconfirmed Nd^{II} ate complex (see Section 2.1), the other attempts at the synthesis of Nd^{II} organometallics used the reductive pathway and started from bis(cyclopentadienyl)Nd^{III} compounds: when

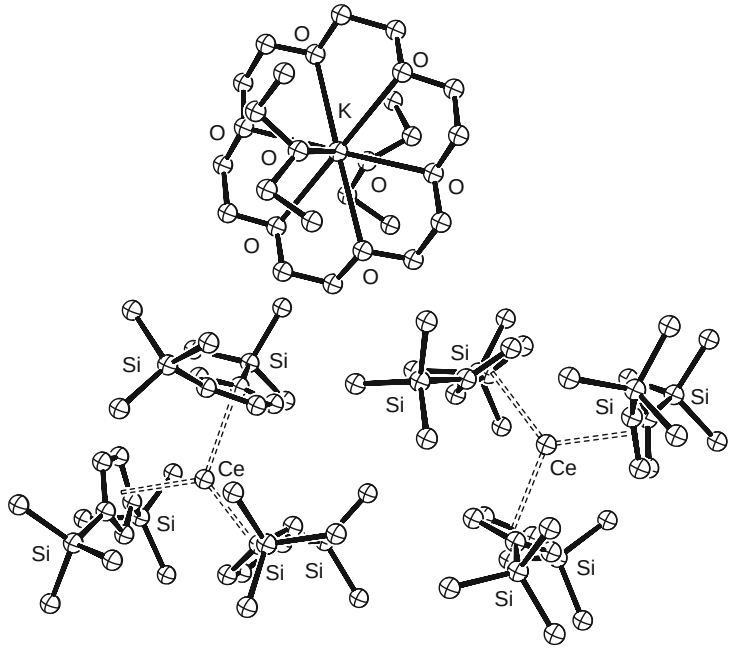

FIGURE 28 The structure of $[\{1,3\text{-}(Me_3Si)_2C_5H_3\}_6Ce_2][K([18]crown\text{-}6)(Et_2O)]$, obtained by potassium reduction of $[\{1,3\text{-}(Me_3Si)_2C_5H_3\}_3Ce]$. One $[\{1,3\text{-}(Me_3Si)_2C_5H_3\}_3Ce]$ unit of this mixed-valent complex is anionic and contains Ce^{II} (on the left of the picture), while the other is neutral and thus contains Ce^{III}. Figure was redrawn after Hitchcock et al. (2008).

sodium or potassium was added to $[(C_5Me_5)_2Nd(BPh_4)]$, no obvious reaction occurred (Evans et al., 1998b) while potassium reduction of $[L_4Nd_2(\mu\text{-}Cl)_2]$ ($L = 1,3\text{-}([Me_3Si]_2CH)_2C_5H_3$ or $1,3\text{-}(SiMe_2CMe_3)_2C_5H_3$) afforded brown products that underwent disproportionation into Nd metal and NdL_3 (Hitchcock et al., 2000). However, the reduction of $[(1,2,4\text{-}t\text{Bu}_3C_5H_2)_2NdI]$ with potassium graphite in the presence of [18] crown-6 successfully afforded the divalent complex $[(1,2,4\text{-}t\text{Bu}_3C_5H_2)_2Nd(\mu\text{-}I)K([18]crown\text{-}6)]$ (Figure 29). This compound is the first structurally described neodymium(II) compound, and it was further characterised by proton NMR and SQUID magnetic susceptibility measurements. The room temperature magnetic moment ($2.8\mu_B$) corresponds to the expected value for an f^4-element ($2.68\mu_B$). This Nd^{II} compound is extremely reactive: a solution of $[(1,2,4\text{-}t\text{Bu}_3C_5H_2)_2Nd(\mu\text{-}I)K([18]crown\text{-}6)]$ in hexane is unstable and deposited crystals of a decomposition product: $[(1,2,4\text{-}t\text{Bu}_3C_5H_2)[2,4\text{-}t\text{Bu}_2C_5H_2C(CH_3)_2CH_2]Nd(\mu\text{-}I)K([18]crown\text{-}6)]$ (Figure 29). This ''tuck-in'' Nd^{III} complex displays an Nd–C bond resulting from CH bond activation of one methyl group in the vicinity of neodymium. The Nd^{II} complex also

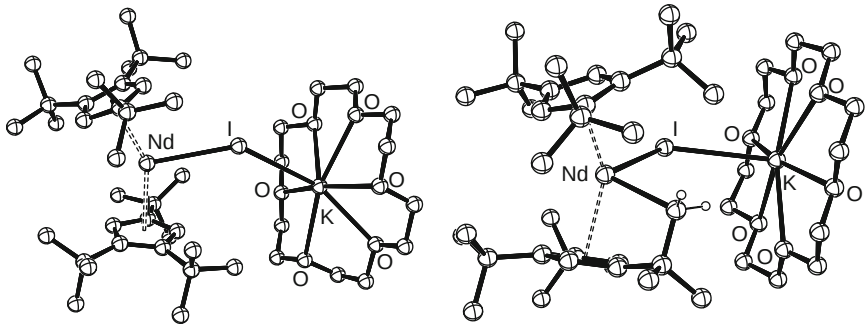

FIGURE 29 The structure of the Nd^{II} complex $[(1,2,4\text{-}t\text{Bu}_3C_5H_2)_2Nd(\mu\text{-}I)K([18]\text{crown-}6)]$, obtained by KC_8 reduction of $[(1,2,4\text{-}t\text{Bu}_3C_5H_2)_2NdI]$ in the presence of [18]crown-6 in cyclohexane (left), and of the "tuck-in" Nd^{III} decomposition product $[(1,2,4\text{-}t\text{Bu}_3C_5H_2)[2,4\text{-}t\text{Bu}_2C_5H_2C(CH_3)_2CH_2]Nd(\mu\text{-}I)K([18]\text{crown-}6)]$ (right). Figure was redrawn after Jaroschik et al. (2009).

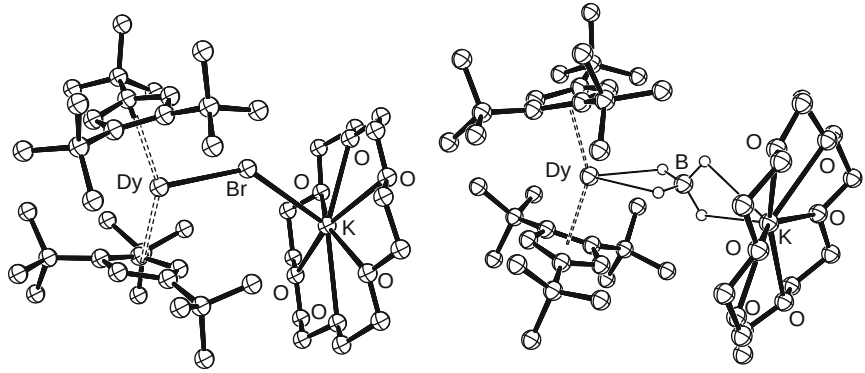

FIGURE 30 The structure of the Dy^{II} complexes $[(1,2,4\text{-}t\text{Bu}_3C_5H_2)_2Dy(\mu\text{-Br})K([18]\text{crown-}6)]$ (left) and $[(1,2,4\text{-}t\text{Bu}_3C_5H_2)_2Dy(\mu\text{-}BH_4)K([18]\text{crown-}6)]$ (right) obtained, respectively, by KC_8 reduction of $[(1,2,4\text{-}t\text{Bu}_3C_5H_2)_2DyBr]$ and $[(1,2,4\text{-}t\text{Bu}_3C_5H_2)_2DyBH_4]$ in the presence of [18]crown-6. Figure was redrawn after Jaroschik et al. (2007a).

reacted with dinitrogen (see later in Section 2.3.4.1) These findings indicate that a high steric crowding on the ligand is paramount for the stability of Nd^{II} (Jaroschik et al., 2009).

The same ligand system was efficient in the case of dysprosium: reduction of $[(1,2,4\text{-}t\text{Bu}_3C_5H_2)_2DyZ]$ (Z = I, BH_4, Br) with potassium graphite in the presence of [18]crown-6 afforded the organodysprosium (II) complexes $[(1,2,4\text{-}t\text{Bu}_3C_5H_2)_2Dy(\mu\text{-Z})K([18]\text{crown-}6)]$ (Z = I, BH_4, Br) (Figure 30) that were characterised by X-ray crystallography. Despite the high paramagnetism of dysprosium, well-resolved proton NMR spectra

could be measured. The spectra show four resonances from $+250$ to -300 ppm corresponding to three inequivalent *t*-butyl groups and the equivalent crown ether protons. In the case of dysprosium, it is impossible to distinguish between the divalent and the trivalent state by magnetic measurements. The Dy^{II} complexes are distinctly more stable than the Nd^{II} analogue (Jaroschik et al., 2007a).

2.3.2.3 Thulium(II) complexes

Several early attempts at the synthesis of organothulium(II) complexes by the reductive pathway are described in the literature. For instance, reduction of the Tm^{III} complex $[(C_5Me_5)_2Tm(I)(THF)]$ by sodium in DME did not afford a divalent species but instead the dimeric Tm^{III} complex: $[\{(DME)_2Na(\mu\text{-}C_5Me_5)Tm(C_5Me_5)(\mu\text{-}OMe)_2\}\{\mu\text{-}[Na(\mu\text{-}C_5Me_5)Na]\}\{C_5Me_5)_2Tm(\mu\text{-}OMe)_2\}]$ (Figure 31) in which the μ-methoxy groups likely arise from fragmentation of DME. An attempt to use a chelating ligand was also unsuccessful since reduction of $[(C_5H_4CH_2CH_2NMe_2)_2Tm(I)(THF)]$ gave a green colour that may be indicative of Tm^{II} but the reaction mixture was intractable (Fedushkin et al., 2001b). Likewise, the reduction product of $[(C_5Me_5)_2Tm(BPh_4)]$ in toluene gave a dark-green/blue colour when dissolved in DME, but no further details were given (Evans et al., 1998b). Finally, reduction of $[\{1,3\text{-}(SiMe_2CMe_3)_2C_5H_3\}_4Tm_2(\mu\text{-}I)_2]$ in THF gave an unstable brown solution from which apparently Tm metal precipitated (Hitchcock et al., 2000).

However, the reduction of highly substituted $L_2Tm^{III}Z$ complexes (L = cyclopentadienyl or phospholyl, Z = I, BH_4) was successful. Thus,

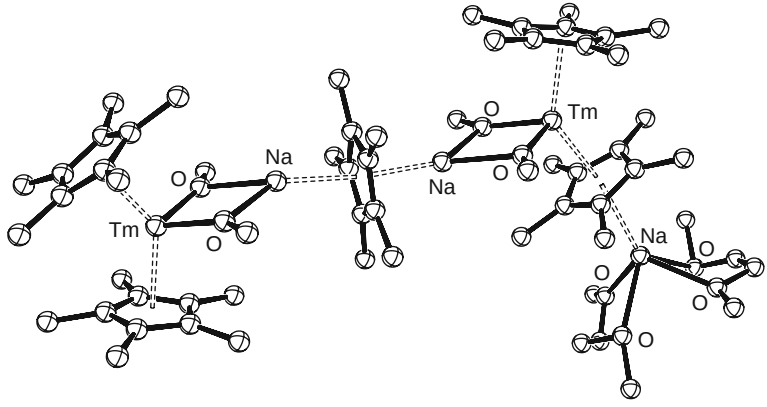

FIGURE 31 The structure of the Tm^{III} complex $[\{(DME)_2Na(\mu\text{-}C_5Me_5)Tm(C_5Me_5)(\mu\text{-}OMe)_2\}\{\mu\text{-}[Na(\mu\text{-}C_5Me_5)Na]\}\{C_5Me_5)_2Tm(\mu\text{-}OMe)_2\}]$ obtained instead of a divalent species by sodium reduction of $[(C_5Me_5)_2Tm(I)(THF)]$ in DME. Figure was redrawn after Fedushkin et al. (2001b).

the already mentioned homoleptic [{(2,5-tBu$_2$)(3,4-Me$_2$)C$_4$P}$_2$Tm] and [(1,2,4-tBu$_3$C$_5$H$_2$)$_2$Tm] could be obtained by KC_8 reduction of the Tm^{III} iodide precursors [{(2,5-tBu$_2$)(3,4-Me$_2$)C$_4$P}$_2$TmI] and [(1,2,4-tBu$_3$C$_5$H$_2$)$_2$TmI], respectively. Divalent [{(1,2,4-tBu$_3$)$_2$C$_5$H$_2$}$_2$Tm] could also be prepared by reduction of [(1,2,4-tBu$_3$C$_5$H$_2$)$_2$Tm(BH$_4$)]. This trivalent complex was obtained from Tm(BH$_4$)$_3$, accessible by reaction of NaBH$_4$ with TmCl$_3$. Thulium chloride being ultimately obtained from Tm$_2$O$_3$, this series of reactions shows that an entry into Tm^{II} chemistry is possible from thulium oxide, which is the least expensive source of thulium. Since the reductive pathway is possible in non-polar solvents, it can be used to synthesise unsolvated Tm^{II} complexes that are impossible to make by metathesis. For instance, reduction of [{1,2,4-(SiMe$_3$)$_3$C$_5$H$_2$}$_2$TmI] and [{(2,5-tBu$_2$)C$_4$H$_2$P}$_4$Tm$_2$(μ-I)$_2$] gave the homoleptic [{1,2,4-(SiMe$_3$)$_3$C$_5$H$_2$}$_2$Tm] and [{(2,5-tBu$_2$)C$_4$H$_2$P}$_2$Tm$_2$[μ-{(2,5-tBu$_2$)C$_4$H$_2$P}$_2$] (Figure 32), respectively; this last compound is also dimeric because the π-phospholyl group is bonded to the second thulium through the phosphorus lone pair. All attempts to obtain these new homoleptic complexes by desolvation of [{1,2,4-(SiMe$_3$)$_3$C$_5$H$_2$}$_2$Tm(THF)] or [{(2,5-tBu$_2$)C$_4$H$_2$P}$_2$Tm(THF)] led to decomposition (Jaroschik et al., 2007b) (Scheme 14).

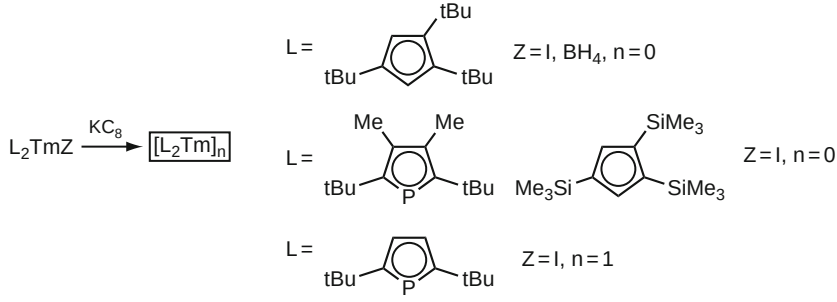

SCHEME 14 The reductive pathway to homoleptic complexes of Tm^{II}. [{1,2,4-(SiMe$_3$)$_3$C$_5$H$_2$}$_2$Tm] and [{(2,5-tBu$_2$)C$_4$H$_2$P}$_2$Tm$_2$[μ-{(2,5-tBu$_2$)C$_4$H$_2$P}$_2$] could not be made by desolvation of [{1,2,4-(SiMe$_3$)$_3$C$_5$H$_2$}$_2$Tm(THF)] and [{(2,5-tBu$_2$)C$_4$H$_2$P}$_2$Tm(THF)], respectively.

2.3.3 Reactivity of divalent complexes

So far, studies on the reactivity of the divalent complexes mentioned above in Section 2.3 have been very limited. Dinitrogen activation has been observed not only for isolated divalent complexes but also for systems containing divalent species or trivalent rare earths in the presence of reducing agents, thus displaying divalent-like behaviour; this important topic will be developed later in Section 2.3.4.

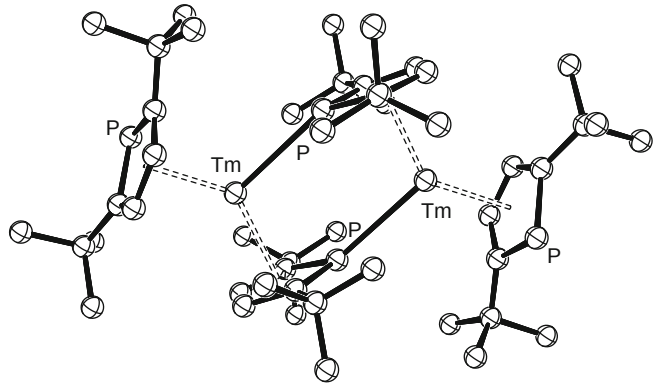

FIGURE 32 The structure of the homoleptic Tm^{II} dimer [{(2,5-*t*Bu_2)C_4H_2P}$_2Tm_2$[μ-{(2,5-*t*Bu_2)C_4H_2P}$_2$] obtained by KC_8 reduction of [{(2,5-*t*Bu_2)C_4H_2P}$_4Tm_2$(μ-I)$_2$] in toluene. Figure was redrawn after Jaroschik et al. (2007b).

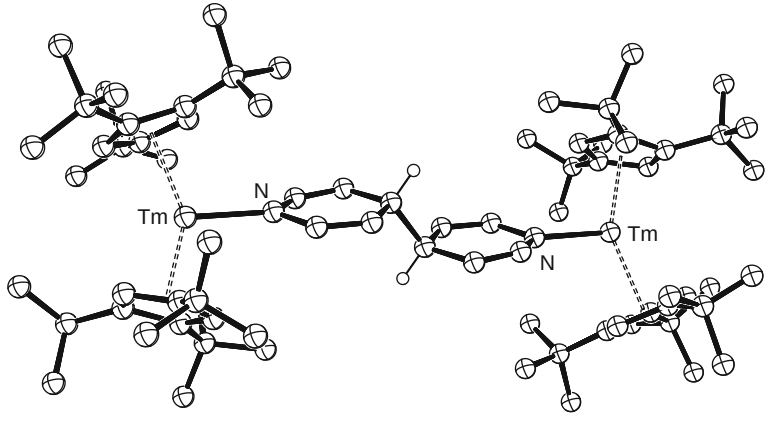

FIGURE 33 The structure of the bimetallic Tm^{III} complex [{(1,2,4-*t*$Bu_3C_5H_2$)$_2$Tm}$_2$(μ-$N_2C_{10}H_{10}$)] obtained by reaction of pyridine with [(1,2,4-*t*$Bu_3C_5H_2$)$_2$Tm]. Figure was redrawn after Jaroschik et al. (2007b).

The reactivity of phospholylthulium(II) complexes appear lower compared to cyclopentadienylthulium(II) compounds of similar steric bulk: reaction of pyridine with [(1,2,4-*t*$Bu_3C_5H_2$)$_2$Tm] led to immediate oxidation of Tm^{II} and dimerisation of pyridine with formation of [{(1,2,4-*t*$Bu_3C_5H_2$)$_2$Tm}$_2$(μ-$N_2C_{10}H_{10}$)] (Figure 33), while NMR experiments showed that the reaction of [{(2,5-*t*Bu_2)(3,4-Me_2)C_4P}$_2$Tm] with pyridine may initially give a simple Tm^{II} adduct, such as [{(2,5-*t*Bu_2)(3,4-Me_2)C_4P}$_2$Tm(NC_5H_5)] (Jaroschik et al., 2007b).

The divalent [{(2,5-tBu$_2$)(3,4-Me$_2$)C$_4$P}$_2$Tm] compound also reacted with azobenzene to give the Tm^{III} complex [{(2,5-tBu$_2$)(3,4-Me$_2$)C$_4$P}$_2$Tm(N$_2$Ph$_2$)] (Figure 34), but this is unexceptional since Sm^{II} and even Yb^{II} complexes display similar reactivity. On the other hand, [{(2,5-tBu$_2$)(3,4-Me$_2$)C$_4$P}$_2$Tm] was able to reduce triphenylphosphine sulphide into triphenylphosphine, with associated formation of a Tm^{III} sulphide dimer: [{[(2,5-tBu$_2$)(3,4-Me$_2$)C$_4$P]$_2$Tm}$_2$(μ-S)] (Figure 34), while the Sm^{II} analogue complex [{(2,5-tBu$_2$)(3,4-Me$_2$)C$_4$P}$_2$Sm] was unreactive in the same conditions (Turcitu et al., 2003).

Clean reactivity with dysprosium(II) complexes was difficult to obtain. For instance, no complex could be crystallised from the reaction of [(1,2,4-tBu$_3$C$_5$H$_2$)$_2$Dy(μ-BH$_4$)K([18]crown-6)] with diphenylacetylene; however, after hydrolysis, (*E*,*E*)-1,2,3,4-tetraphenylbuta-1,3-diene was isolated. This compound most likely results from Dy^{II}-initiated reductive coupling of diphenylacetylene. When [(1,2,4-tBu$_3$C$_5$H$_2$)$_2$Dy(μ-BH$_4$)K([18]crown-6)] was treated with hexachloroethane, an interesting Dy^{III} ate complex was obtained: [(1,2,4-tBu$_3$C$_5$H$_2$)$_2$Dy(μ-Cl)$_2$K([18]crown-6)] (Figure 35); in this complex, there are two bridging chlorides between potassium and dysprosium, instead of one borohydride in the starting Dy^{II} compound (Jaroschik et al., 2007a).

2.3.4 Dinitrogen activation

There are several rare-earth-based systems that have been shown to activate dinitrogen; this topic has been reviewed fairly recently (Evans and Lee, 2005). Some of these systems include Sm^{II} compounds and thus they fall outside the topic of this chapter. Other utilise Tm^{II}, Dy^{II} and Nd^{II} compounds, and dinitrogen is eventually also activated in reactions in which a trivalent rare-earth precursor is present together with a strong

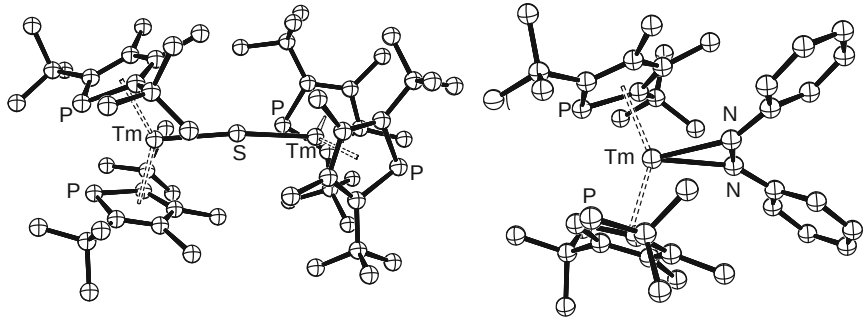

FIGURE 34 The structures of the Tm^{III} complexes [{[(2,5-tBu$_2$)(3,4-Me$_2$)C$_4$P]$_2$Tm}$_2$(μ-S)] (left) and [{(2,5-tBu$_2$)(3,4-Me$_2$)C$_4$P}$_2$Tm(N$_2$Ph$_2$)] (right), respectively, obtained by reaction of [{(2,5-tBu$_2$)(3,4-Me$_2$)C$_4$P}$_2$Tm] with triphenylphosphine sulphide and azobenzene. Figure was redrawn after Turcitu et al. (2003).

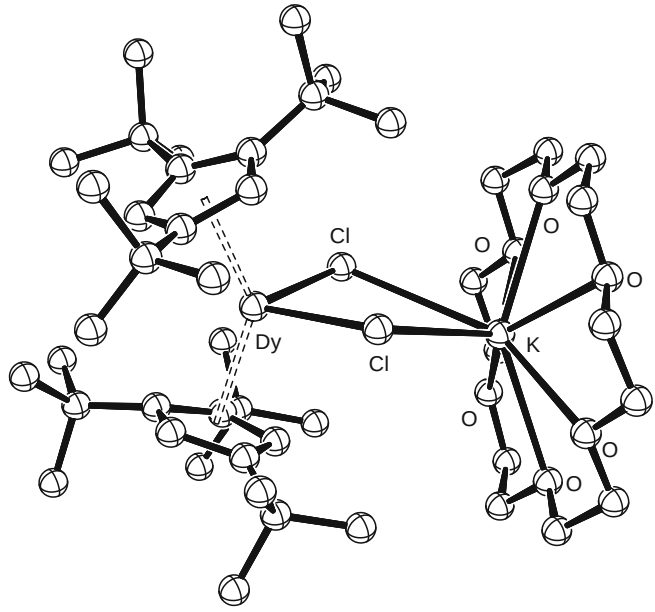

FIGURE 35 The structure of the Dy^{III} complex $[(1,2,4\text{-}t\text{Bu}_3C_5H_2)_2Dy(\mu\text{-}Cl)_2K([18]\text{crown-}6)]$, obtained by reaction of hexachloroethane with the Dy^{II} compound $[(1,2,4\text{-}t\text{Bu}_3C_5H_2)_2Dy(\mu\text{-}Cl)_2K([18]\text{crown-}6)]$. Figure was redrawn after Jaroschik et al. (2007a).

reducing agent (usually an alkali metal). In this respect, these last systems display divalent-like reactivity. Whatever the system considered, trivalent bimetallic complexes are eventually obtained in which dinitrogen is incorporated as a diazenide (N_2^{2-}) side-on bridging ligand. Evidence for this stems from charge balance considerations together with structural data (in particular the *N–N* distance which clearly points to a double bond).

2.3.4.1 By isolated divalent complexes

Although reactivity towards dinitrogen has been observed in systems involving divalent species, clean reactivity with isolated complexes has been observed in few instances. The thulium(II) scorpionate complex $[LTmCH(SiMe_3)_2]$ (L = hydrido-tris(3-*t*Bu-5-Me-pyrazolyl)borate) reacted with 2,5-$t\text{Bu}_2$-aniline and dinitrogen to give $[\{LTm(NHC_6H_3\text{-}2,5\text{-}t\text{Bu}_2)\}_2(\mu\text{-}\eta^2\text{:}\eta^2\text{-}N_2)]$ (Figure 36) for which protonation of the $-CH(SiMe_3)_2$ group and dinitrogen activation occurred concomitantly (Cheng et al., 2008).

The Nd^{II} complex $[(1,2,4\text{-}t\text{Bu}_3C_5H_2)_2Nd(\mu\text{-I})K([18]\text{crown-}6)]$ also activated dinitrogen to give the Nd^{III} complex $[\{(1,2,4\text{-}t\text{Bu}_3C_5H_2)_2Nd\}_2$

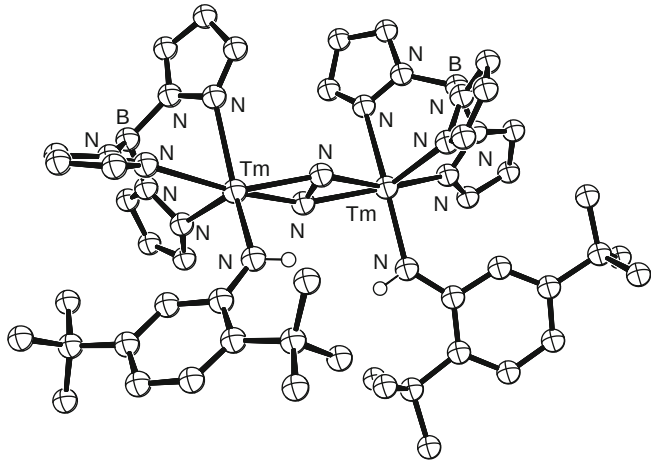

FIGURE 36 The structure of $[\{LTm(NHC_6H_3\text{-}2,5\text{-}t\text{Bu}_2)\}_2(\mu\text{-}\eta^2\text{:}\eta^2\text{-}N_2)]$, where L is hydridotris(3-*t*Bu-5-Me-pyrazolyl)borate, obtained through dinitrogen activation of [LTmCH$(SiMe_3)_2$] in the presence of 2,5-*t*Bu_2-aniline. The substituents on the pyrazolylborate ligand have been omitted for clarity. Figure was redrawn after Cheng et al. (2008).

$(\mu\text{-}\eta^2\text{:}\eta^2\text{-}N_2)]$ (Figure 37), which could also be obtained by reaction of $[(1,2,4\text{-}t\text{Bu}_3C_5H_2)_2\text{NdI}]$ with KC_8 under dinitrogen (Jaroschik et al., 2009).

While phospholylthulium(II) complexes are unreactive towards dinitrogen, the complex $[(1,3\text{-}t\text{Bu}_2C_5H_3)_2\text{Tm(THF)}]$ did react with dinitrogen but the results were intractable (Nief et al., 2005).

2.3.4.2 By divalent systems

The very first complexes resulting from dinitrogen activation by uncommon divalent systems have actually been obtained in attempts to prepare Tm^{II} complexes by ionic metathesis. For instance, reactions of potassium cyclopentadienides with TmI_2 or DyI_2 in THF or diethyl ether under dinitrogen afforded the trivalent complexes $[\{(C_5Me_5)_2\text{Tm}\}_2(\mu\text{-}\eta^2\text{:}\eta^2\text{-}N_2)]$ $[\{(1,3\text{-}(Me_3Si)_2C_5H_3)_2\text{Tm}\}_2(\mu\text{-}\eta^2\text{:}\eta^2\text{-}N_2)]$, $[\{(Me_3SiC_5H_4)_2\text{Tm(THF)}\}_2(\mu\text{-}\eta^2\text{:}\eta^2\text{-}N_2)]$ (Evans et al., 2001) and $[\{[1,3\text{-}(Me_3Si)_2C_5H_3]_2\text{Dy}\}_2(\mu\text{-}\eta^2\text{:}\eta^2\text{-}N_2)]$ (Evans et al., 2002) (Figure 38). The yields are fair to good and the products are structurally characterised.

It appears that dinitrogen activation is also possible with systems involving divalent ions and non-cyclopentadienyl ligands. Thus, the reaction of TmI_2 or DyI_2 with $KN(SiMe_3)_2$ in THF at low temperature afforded deeply coloured solutions, which may be an indication that divalent amides are present in solution; under dinitrogen, the reaction mixtures changed colour and dinitrogen complexes, $[\{[(SiMe_3)_2N]_2R(THF)\}_2$ $(\mu\text{-}\eta^2\text{:}\eta^2\text{-}N_2)]$ (R = Tm (Figure 37), Dy) could be isolated. In the same

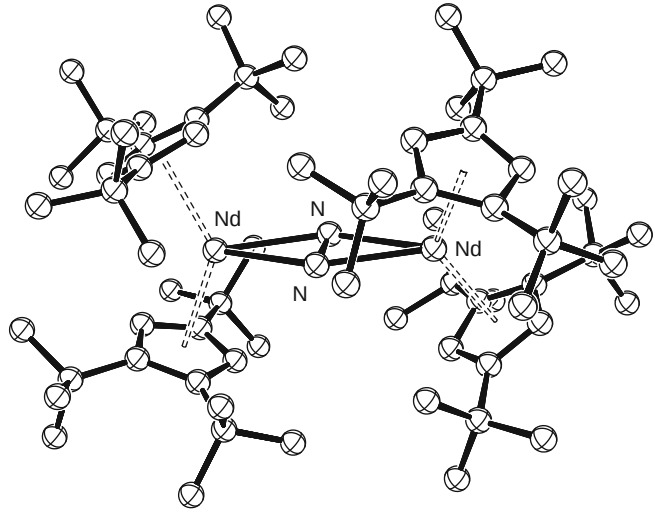

FIGURE 37 The structure of $[\{(1,2,4\text{-}t\text{Bu}_3\text{C}_5\text{H}_2)_2\text{Nd}\}_2(\mu\text{-}\eta^2\text{:}\eta^2\text{-N}_2)]$, obtained by dinitrogen activation of $[(1,2,4\text{-}t\text{Bu}_3\text{C}_5\text{H}_2)_2\text{Nd}(\mu\text{-I})\text{K}([18]\text{crown-6})]$ or by reaction of $[(1,2,4\text{-}t\text{Bu}_3\text{C}_5\text{H}_2)_2\text{NdI}]$ with KC_8 under dinitrogen. Figure was redrawn after Jaroschik et al. (2009).

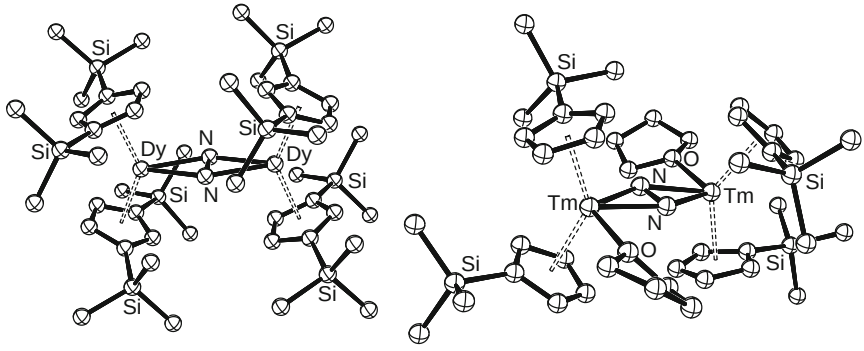

FIGURE 38 The structure of $[\{[1,3\text{-}(\text{Me}_3\text{Si})_2\text{C}_5\text{H}_3]_2\text{Dy}\}_2(\mu\text{-}\eta^2\text{:}\eta^2\text{-N}_2)]$ (left) and $[\{(\text{Me}_3\text{SiC}_5\text{H}_4)_2\text{Tm(THF)}\}_2(\mu\text{-}\eta^2\text{:}\eta^2\text{-N}_2)]$ (right), obtained in the reaction of DyI_2 and TmI_2 with the respective cyclopentadienyl anions under dinitrogen. Figure was redrawn after Evans et al. (2001, 2002).

reaction conditions, NdI_2 and the potassium phenoxide 2,6-$t\text{Bu}_2\text{C}_6\text{H}_3\text{OK}$ under dinitrogen in THF gave $[\{2,6\text{-}t\text{Bu}_2\text{C}_6\text{H}_3\text{O}\}_2\text{Nd(THF)}_2\}_2(\mu\text{-}\eta^2\text{:}\eta^2\text{-N}_2)]$ (Figure 39). The reactions involving thulium or dysprosium are possibly mediated by a transient divalent amide or cyclopentadienide, or with

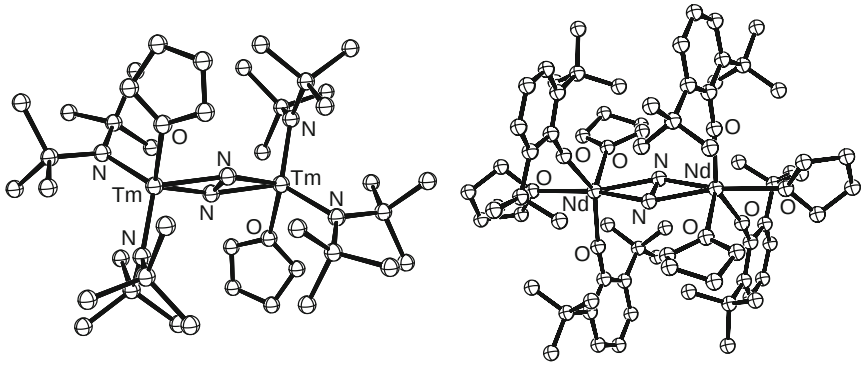

FIGURE 39 The structure of $[\{[(SiMe_3)_2N]_2Tm(THF)\}_2(\mu\text{-}\eta^2\text{:}\eta^2\text{-}N_2)]$ (left) and $[\{2,6\text{-}tBu_2C_6H_3O\}_2Nd(THF)_2\}_2(\mu\text{-}\eta^2\text{:}\eta^2\text{-}N_2)]$ (right), respectively, obtained in the reaction of TmI_2 with $KN(SiMe_3)_2$ and of NdI_2 with $tBu_2C_6H_3OK$ in THF under dinitrogen. Figure was redrawn after Evans et al. (2003d).

neodymium by a divalent alkoxide. However, these transient species have not been isolated or identified as divalent otherwise than by their colour (Evans et al., 2003d).

2.3.4.3 By systems displaying divalent-like reactivity

The first experiments involving dinitrogen activation by praseodymium and neodymium were described by Floriani et al. in 1998 (Campazzi et al., 1998). When the anionic $[Na(THF)_3(Et_8\text{-calix[4]tetrapyrrolyl})R(THF)]$ (R = Pr, Nd) were reacted with sodium naphthalenide in THF under dinitrogen, dimeric products featuring the $\mu - N_2^{2-}$-bridging ligand were isolated. Their general composition is $[\{(Et_8\text{-calix[4]tetrapyrrolyl})RNa_2(solv)_n\}_2(\mu\text{-}N_2)]$ (solv = THF, DME, dioxane), depending on the crystallisation solvent. Interestingly, with dioxane, the structure of the Nd compound (Figure 40) shows the $\mu - N_2^{2-}$-bridging ligand also bonded to sodium. Although a divalent intermediate is conceivable in the case of neodymium, until now no divalent praseodymium compounds have been found.

It was also investigated whether the putative divalent species of type TmL_2 (L = amide) used in dinitrogen activation reactions could be made *in situ* by a reductive pathway starting from TmL_3 and an alkali metal. The one-pot reaction of $[Tm\{N(SiMe_3)_2\}_3]$ with potassium in the presence of dinitrogen indeed afforded the same complex: $[\{[(SiMe_3)_2N]_2Tm(THF)\}_2(\mu\text{-}\eta^2\text{:}\eta^2\text{-}N_2)]$, than the one previously obtained by ionic metathesis with TmI_2 and $KN(SiMe_3)_2$ under dinitrogen, but this time no ''divalent-like colours'' were observed, which questioned the evidence of divalent species in this reaction. This observation prompted the authors to try the same reaction with yttrium, holmium and lutetium, which are not even

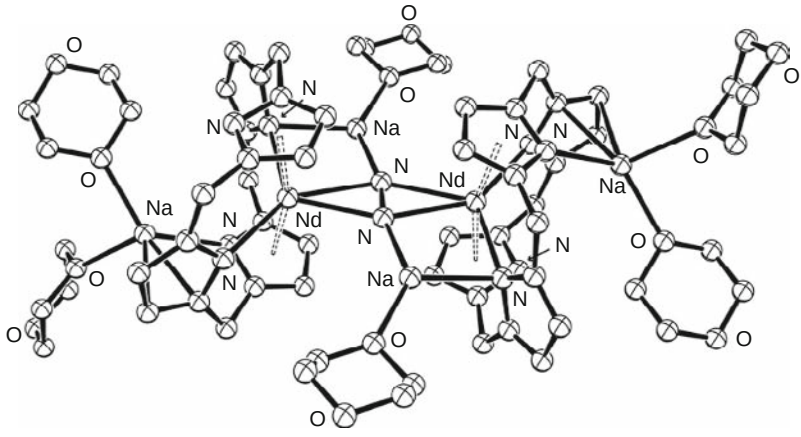

FIGURE 40 The structure of [{[Na(dioxane)$_2$]Et$_8$-calix[4]tetrapyrrolyl)Nd}$_2$(μ-N$_2$[Na(dioxane)]$_2$)], obtained in the reaction of [Na(THF)$_3$(Et$_8$-calix[4]tetrapyrrolyl)Nd(THF)] with sodium naphthalenide under dinitrogen, followed by recrystallisation in dioxane. Ethyl groups have been omitted for clarity. Figure was redrawn after Campazzi et al. (1998).

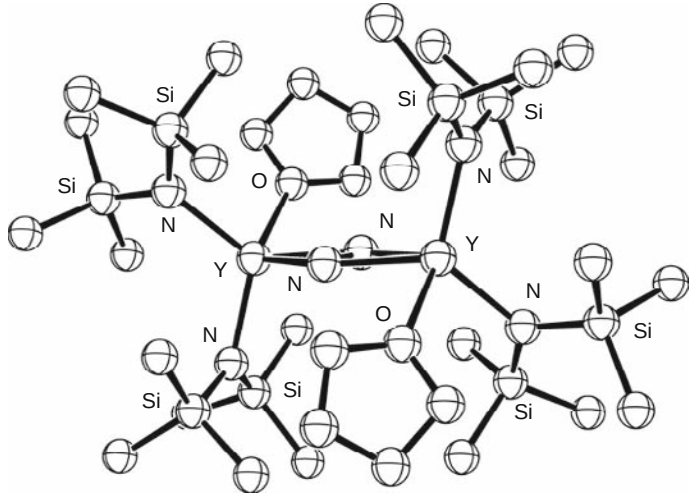

FIGURE 41 The structure of [{[(SiMe$_3$)$_2$N]$_2$Y(THF)}$_2$(μ-η^2:η^2-N$_2$)], obtained in the reaction of [Y{N(SiMe$_3$)$_2$}$_3$] with potassium under dinitrogen in THF: dinitrogen can be activated by systems involving "non-reducible" trivalent rare-earth precursors. Figure was redrawn after Evans et al. (2004a).

known to give divalent compounds in the solid state. Thus [R{N(SiMe$_3$)$_2$}$_3$] (R = Y, Ho, Lu) were subjected to the same reaction conditions and indeed complexes having incorporated dinitrogen were obtained: [{[(SiMe$_3$)$_2$N]$_2$R(THF)}$_2$(μ-η^2:η^2-N$_2$)] (R = Ho, Y (Figure 41), Lu); they

have the same structure as the thulium complex (Evans et al., 2004a). The reducing system ($[RN(SiMe_3)_3]/K/N_2$) has been extended to R = La, Pr, Dy, Nd, Er, Tb and Gd, and the new complexes: $[\{[(SiMe_3)_2N]_2R(THF)\}_2(\mu\text{-}\eta^2\text{:}\eta^2\text{-}N_2)]$ that have been isolated all have the same structure. However, no such complexes were isolated with R = La or Pr, although there is ^{15}N NMR evidence for a transient lanthanum dinitrogen complex. There is no obvious correlation of yield of obtained product versus R^{3+}/R^{2+} redox potential; rather, there is a rough correlation with size since the lowest yield was obtained with neodymium and the highest with the smaller rare earths (Evans et al., 2004b). A summary of the N_2/rare-earth amide systems is presented in Scheme 15.

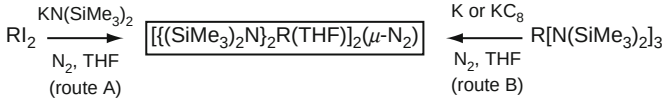

route A: R = Nd (4%), Dy (30%), Tm (49%)

route B: R = Y (18%), Gd (20%), Tb (25%), Dy (45%),
Ho (32%), Er (22%), Tm (49%), Lu (36%);
La (possible traces), Ce(0%), Pr (0%), Nd (low)

SCHEME 15 Different routes to the μ-(diazenido) rare-earth amide dimers. The figures in parentheses are isolated yields.

Trivalent rare-earth organometallic complexes such as the trisubstituted $[(C_5Me_4H)_3R]$ [R = La, Nd (Evans et al., 2004c), Ce (Figure 40), Pr (Evans et al., 2006), Lu (Evans et al., 2005)] reacted similarly with KC_8 under dinitrogen in THF to give $[\{(C_5Me_4H)_2R(THF)\}(\mu\text{-}\eta^2\text{:}\eta^2\text{-}N_2)]$; the lutetium dinitrogen complex could also be obtained by reduction of the cationic $[(C_5Me_4H)_2Lu][BPh_4]$ (Evans et al., 2005). Dinitrogen complexes with the more bulky C_5Me_5 ligand: $[\{(C_5Me_5)_2R(THF)\}(\mu\text{-}\eta^2\text{:}\eta^2\text{-}N_2)]$ were isolated by reduction of cationic $[(C_5Me_5)_2R][BPh_4]$ under dinitrogen [R = La (Evans et al., 2004c), Ce, Pr (Figure 42) (Evans et al., 2006)]. The yields were good in all cases.

Possible mechanisms of dinitrogen activation by these systems have been discussed. Transient divalent species look problematic, at least in the case of terbium and gadolinium, which have calculated reduction potentials seemingly out of reach of any chemical reducing agent. Another option is to consider activation of dinitrogen by a trivalent complex prior to reduction. But since the reactions are conducted in THF, which has a very high affinity for the trivalent metal, this option would involve competition of dinitrogen with THF for coordination to a trivalent complex, which may appear unlikely. Evans et al. have suggested that a

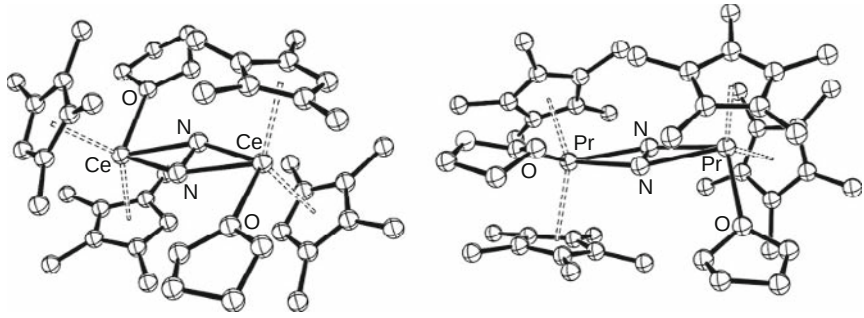

FIGURE 42 The structures of $[\{(C_5Me_4H)_2Ce(THF)_2(\mu\text{-}\eta^2\text{:}\eta^2\text{-}N_2)\}]$ (left) and $[\{(C_5Me_5)_2Pr(THF)_2(\mu\text{-}\eta^2\text{:}\eta^2\text{-}N_2)\}]$ (right), obtained by reduction of $[(C_5Me_4H)_3Ce]$ and of $[(C_5Me_5)_2Pr][BPh_4]$, respectively, in THF under dinitrogen. Figure was redrawn after Evans et al. (2006).

trivalent rare-earth complex would somehow trigger the alkali metal activation of dinitrogen, but this leaves open the question of how this triggering action may proceed. So, the mechanism is still unsettled (Evans et al., 2004b).

2.4 Other divalent-like systems

The coupling reaction between alkyl chlorides and carbonyl compounds that is well documented with divalent diiodides (see Section 2.2.2.2) has also been attempted with a trivalent precursor/reducing agent system similar to those used in dinitrogen activation, namely NdI_3/KC_8. A deep-purple colour appeared prior to the introduction of the alkyl halide, which may be an indication of the presence of Nd^{II} compounds in solution. However, the yields are generally higher than with NdI_2; interestingly, NdI_3/K, NdI_3/Na and even NdI_3/Ca reagents were also efficient for the coupling reaction and the variability in yields seems to indicate that the NdI_3/reducing agent system could be different from NdI_2 (Evans and Workman, 2005).

Finally, the Bochkarev method used for the synthesis of NdI_2 and DyI_2 has also been applied to other rare earths. Thus, heating metal powders with iodine under inert atmosphere gave subvalent iodides RI_x (R = Sc, Y, La, Ce, Pr, Gd, Ho, Er, Lu; $x = 1.86$–2.77) in moderate yields. These subvalent iodides displayed divalent-like behaviour since their reaction with acidic organic substrates such as alcohols or cyclopentadiene (ZH) afforded $ZRI_2(THF)_x$ ($x = 2$–5) that were characterised by IR and elemental analysis. $LaI_{2.37}$ also reacted with 2,2′-bipyridine to give a low yield of $[LaI_2(2,2'\text{-bipyridine})_2(THF)_2]$, characterised by IR and ESR (Khoroshenkov et al., 2002). This compound had been previously prepared by another route (Bochkarev et al., 1996).

3. SCANDIUM COMPLEXES

Solid-state divalent scandium compounds are well documented (Meyer and Jongen, 2006; Poeppelmeier et al., 1980) and there are also some monovalent scandium compounds such as ScCl in which Sc–Sc bonds are present (Poeppelmeier and Corbett, 1977). So scandium opened the possibility to find monovalent molecular compounds, similarly to the well-known Al^{I} coordination chemistry, and since scandium looks like aluminium in some respects. Indeed, low-valent scandium molecular compounds have been found both in the monovalent and in the divalent state.

The first isolated Sc^{I} compound has been prepared by the metal vapour technique, which involves co-condensation of metal vapours with a precursor ligand under high vacuum; this technique has also been used to synthesise zero-valent complexes (see later in Section 4.1; a Sc^{II} complex obtained by admixture of a Sc^{0} compound will also be described in this section). Thus, when Sc vapours were co-condensed with *t*-butylphosphaethyne (*t*BuCP), a remarkable green triple-decker complex $[\{(\eta^5\text{-}P_3C_2t\text{Bu}_2)\text{Sc}\}_2(\mu\text{-}\eta^6\text{:}\eta^6\text{-}P_3C_3t\text{Bu}_3)]$ (Figure 43) was isolated in low yield. The central ring is 2,4,6-tri-*t*-butyl-1,3,5-triphosphabenzene resulting from the trimerisation of *t*BuCP, and the capping ligands (3,5-di-*t*-butyl-1,2,4-triphospholides) are anionic. The central ligand being neutral, charge balance indicates that the complex is monovalent. The measured room temperature magnetic moment ($3.98\mu_B$) is lower than that expected for four unpaired electrons ($4.47\mu_B$) but still compatible with Sc^{I} (Arnold et al., 1996).

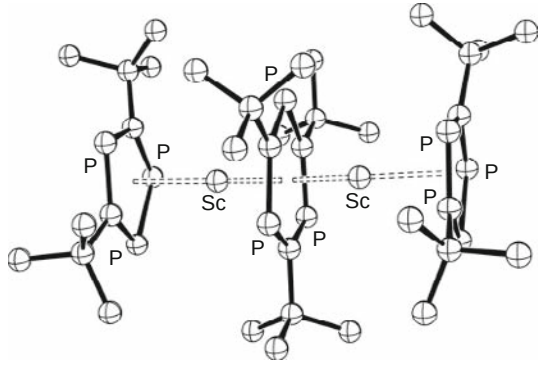

FIGURE 43 The structure of a Sc^{I} complex: $[\{(\eta^5\text{-}P_3C_2t\text{Bu}_2)\text{Sc}\}_2(\mu\text{-}\eta^6\text{:}\eta^6\text{-}P_3C_3t\text{Bu}_3)]$, obtained in low yield by co-condensation of Sc vapours with *t*-butylphosphaethyne under high vacuum. Figure was redrawn after Arnold et al. (1996).

Another low-valent purple compound was obtained from the same reaction mixture after repeated sublimation. Although no X-ray structure could be obtained, it was conclusively identified as a Sc^{II} sandwich complex with the 2,4,5-tri-*t*-butyl-1,3-diphospholide ligand: $[(\eta^5\text{-}P_2C_3t\text{Bu}_3)_2\text{Sc}]$. Evidence came from a well-resolved ESR spectrum and the room temperature magnetic moment ($1.70\mu_B$) which corresponds to the spin-only value for a single electron and thus to Sc^{II} (Arnold et al., 1998).

Sc^{I} has been found in a totally different system. The compound $[LScBr_2]$, where the ligand L is pentane-2,4-di(2-diethylaminoethyl)diketiminate (a diketiminato ligand with two pendent arms each bearing a tertiary amine), was reacted with two equivalents of allylmagnesium bromide. Instead of a metathesis reaction yielding $[LSc(allyl)_2]$, the allyl Grignard reagent was reduced into 1,5-hexadiene and a sandwich-like compound: $[(LMgBr)_2ScBr]$ (Figure 44) was obtained and characterised by X-ray. In this complex, the MgBr unit is chelated by the two tertiary amines and the two imines of the L ligand. If L bears a single negative charge, then the LMgBr unit is neutral and scandium must be monovalent in $[(LMgBr)_2ScBr]$; alternatively, the L ligand might be doubly charged, in which case the complex would be trivalent. Unlike the monovalent triple-decker complex mentioned earlier in this section, $[(LMgBr)_2ScBr]$ is diamagnetic and its ^1H, ^{13}C and ^{45}Sc NMR spectra could be measured (Neculai et al., 2002).

In a later paper, $[(LMgBr)_2ScBr]$ was studied by density functional theory (DFT) calculations and it was concluded that scandium was monovalent and stabilised by δ-bond formation; moreover, the complex

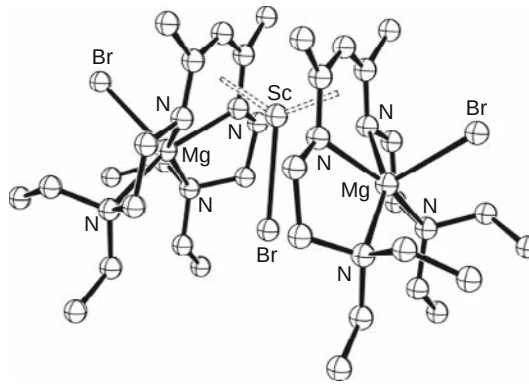

FIGURE 44 The structure of $[(LMgBr)_2ScBr]$ (L = pentane-2,4-di(2-diethylaminoethyl) diketiminate), prepared by the reaction of $[LScBr_2]$ with two equivalents of allylmagnesium bromide. Theoretical studies are consistent with the monovalent nature of scandium in this complex. Figure was redrawn after Neculai et al. (2002).

displays Sc^{I} behaviour, since hydrogen evolved after treatment by water in the form of $H_2O{\cdot}B(C_6F_5)_3$ or by an alcohol (Neculai et al., 2003).

A low-valent scandium complex could also be made by a reductive pathway. $[ScL_3]$ (L = 3,5-di-*t*-butyl-1,2,4-triphospholide) could be reduced by KC_8 in toluene to give $[ScL_2]$ and KL. The crystal structure of this compound is that of a homoleptic dimer: $[(\eta^5\text{-L})_2Sc(\mu\text{-}\eta^2{:}\eta^5\text{-L})Sc(\eta^5\text{-L})]$ (Figure 45). DFT calculations on a model of this dimer indicated that it is best described as a mixed valence Sc^{I}/Sc^{III} compound (rather than a Sc^{II} complex) in which, like in the mixed Sc^{I}/Mg complex described above, Sc^{I} would be stabilised by δ-bonding to the ligand. A solution of the compound in cyclohexane was found to be diamagnetic and cryoscopy measurements are compatible with a dimeric structure in this solvent. However, in toluene or benzene solution at room temperature, the solution became paramagnetic with a magnetic moment ($1.7\mu_B$) corresponding to Sc^{II} in d^1 configuration; yet, no ESR signal corresponding to Sc^{II} could be recorded at low temperature. A plausible explanation is that in an aromatic solvent at room temperature, the Sc^{I}/Sc^{III} dimer would dissociate into the Sc^{II} monomer $[ScL_2]$, which would reassociate at low temperature before an ESR spectrum could be measured (Clentsmith et al., 2003).

Finally, a (butadiene)scandium complex with a chelating cyclopentadienylamine ligand has been described. Thus, the reaction of $[(C_5H_4CH_2CH_2NMe_2)ScCl_2]$ with 2,4-dimethylbutadienemagnesium afforded $[(C_5H_4CH_2CH_2NMe_2)Sc(2,4\text{-dimethylbutadiene})]$ (Figure 46).

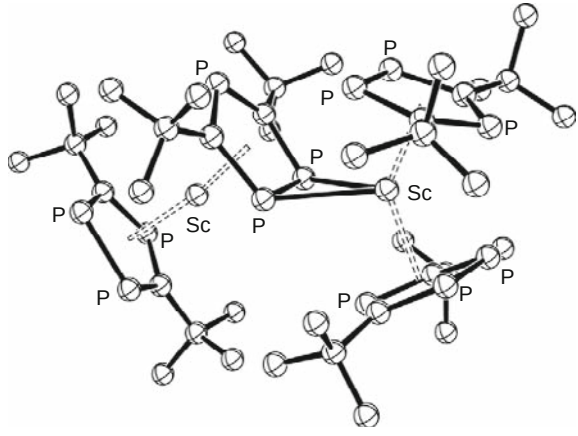

FIGURE 45 The structure of a formal Sc^{II} homoleptic dimer: $[(\eta^5\text{-L})_2Sc(\mu\text{-}\eta^2{:}\eta^5\text{-L})Sc(\eta^5\text{-L})]$ (L = 3,5-di-*t*-butyl-1,2,4-triphospholide), prepared by reduction of $[ScL_3]$ with KC_8. The complex is best described as a Sc^{I}/Sc^{III} mixed-valence compound. Figure was redrawn after Clentsmith et al. (2003).

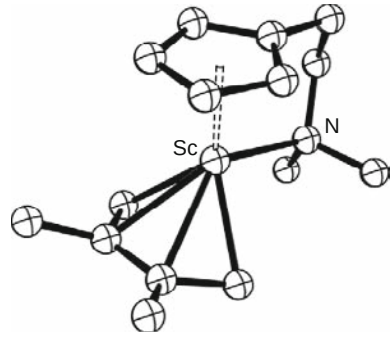

FIGURE 46 The structure of [$(C_5H_4CH_2CH_2NMe_2)$Sc(2,4-dimethylbutadiene)], obtained by reaction of [$(C_5H_4CH_2CH_2NMe_2)ScCl_2$] with 2,4-dimethylbutadienemagnesium. This compound is best described as a Sc^{III} compound, but it behaves as a bielectronic reducing agent and thus as Sc^{I}. Figure was redrawn after Beetstra et al. (2003).

This compound is best structurally described as a Sc^{III} compound, but it reacts with 4,4′-dimethyl-2,2′-bipyridine with elimination of dimethylbutadiene and the formation of the Sc^{III} complex [$(C_5H_4CH_2CH_2NMe_2)Sc(NC_6H_6–C_6H_6N)_2$] in which the two bipyridine ligands have been reduced into radical anions, thus displaying Sc^{I}-like reactivity. It was also briefly mentioned in this paper that the butadienescandium(III) complex also behaved as Sc^{I} in its reactions with diiodine or diphenyldisulphide in which [$(C_5H_4CH_2CH_2NMe_2)ScX_2$] ($X = I$, PhS), were isolated (Beetstra et al., 2003).

4. ZERO-VALENT COMPLEXES

4.1 Synthesis and structure

Metal vapour synthesis in rare-earth chemistry has been used as early as 1977 to prepare rare-earth butadiene and alkyne complexes by interaction of butadienes and alkynes (respectively) with vaporised metals (Evans, 1987; Evans et al., 1977), and we have seen in Section 3 that low-valent scandium complexes can also be made by this technique. Additionally, condensation of rare-earth vapours with a π-acceptor such as 1,4-di-(*t*-Butyl)diazadiene (DAD) has produced compounds of general formula [$R(DAD)_3$], except with scandium where the composition is [$Sc(DAD)_2$]. Extensive metal-ligand electron transfer is effective in these molecules so the real oxidation state of the rare earth (at least at room temperature) is in fact $+3$. Note that the first structurally characterised organosamarium(II)

complex, $[(C_5Me_5)_2Sm(THF)_2]$, was initially made by co-condensation of samarium vapour with pentamethylcyclopentadiene (Evans et al., 1981).

However, interaction of heavily substituted arenes or heteroarenes with vaporised rare-earth metals generally produce sandwich compounds in which the rare-earth element is truly zero valent. This chemistry has been thoroughly reviewed (Cloke, 1993) and only the most important aspects will be summarised hereafter. Few papers have appeared since that date and their results will be also described.

All rare earths (Sc to Lu except Pm) have been investigated and the most significant results have been obtained by co-condensation of the metal vapours with 1,3,5-tris(*t*-butyl)benzene (Ar*), 2,4,6-tris(*t*-butyl)pyridine (NAr*) and 2,4,6-tris(*t*-butyl)phosphinine (PAr*). NAr* and PAr* derive from Ar* by the replacement of one CH group by N or P, respectively (Arnold et al., 2003). Three compounds have been structurally characterised and demonstrate the sandwich structure of the complexes: $[(\eta^6\text{-Ar*})_2Gd]$, $[(\eta^6\text{-Ar*})_2Y]$ (Brennan et al., 1987) and $[(\eta^6\text{-PAr*})_2Ho]$ (Figure 47) (Arnold et al., 1997).

The stability of the compounds varies according to the complexed zero-valent metal and data are summarised in Scheme 16.

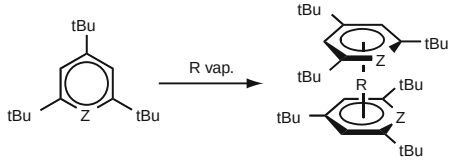

Z=CH	Sc[a]	Y[a]	La[d]	Ce[a]	Pr[a]	Nd[a]	Sm[c]	Eu[c]	Gd[a]	Tb[a]	Dy[a]	Ho[a]	Er[a]	Tm[d]	Yb[d]	Lu[a]
Z=N	Sc[a]						Sm[c]							Tm[d]	Yb[d]	
Z=P			La[b]				Sm[c]					Ho[a]				

SCHEME 16 Stability of bis(arene) rare-earth complexes: (a) compounds stable at room temperature; (b) compounds stable below 273 K; (c) compounds stable below 200 K; and (d) unstable compounds.

In the special case of scandium, another ''tuck-in'' Sc^{II} complex was obtained alongside with the Sc^0 complex; it is proposed that this compound occurs through direct insertion of Sc into a C–H bond of one *t*Bu substituent on the Ar* ring prior to arene complexation (Cloke et al., 1991) (Scheme 17).

The stability of bis(arene)zero-valent metal complexes can be rationalised by molecular orbital arguments (Anderson et al., 1989): the most important bonding interaction lies between d-orbitals on the metal and π-orbitals on the arene ligand (4f-electrons are contracted and their contribution to bonding can usually be neglected). The elements Sc, Y, La,

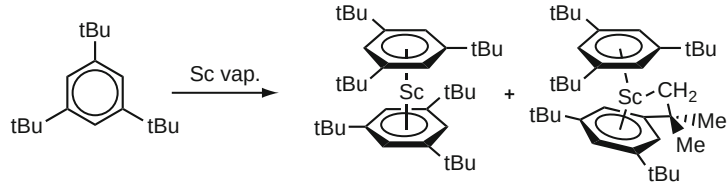

SCHEME 17 Sc^0 and Sc^{II} complexes obtained in the reaction of Sc vapour with 1,3,5-tris (*t*-butyl)benzene. Scheme was redrawn after Cloke (1993).

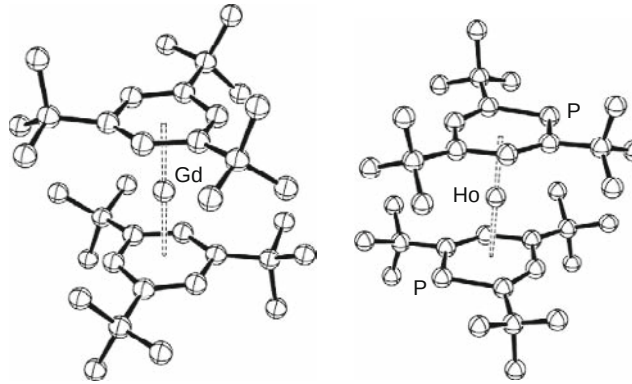

FIGURE 47 The structure of bis(η^6-1,3,5-tris(*t*-butyl)benzene)gadolinium(0) and bis (η^6-2,4,6-tris(*t*-butyl)phosphinine)holmium(0), obtained by co-condensation of metal vapours with the ligands. Figure was redrawn after Arnold et al. (1997) and Brennan et al. (1987).

Ce, Gd and Lu have one d-electron in the valence shell in the ground state and thus a stabilising interaction is possible, contrary to the other rare earths, which have $4f^n5d^06s^2$ configuration and thus no d-electron available, at least in the ground state. Bonding would however be possible with the metal in an excited state configuration such as $4f^{n-1}5d^16s^2$; therefore, the stability of the complexes should be highest with the elements for which the $f \rightarrow d$ promotion energy is the lowest. This is quite well verified except for Ce and La, presumably because their covalent radii are the largest and the steric bulk of the ligand is insufficient to stabilise the complexes.

To gain more insight into the electronic structure of the rare-earth arene sandwich complexes, thermochemical and high-level theoretical calculations have been undertaken. Metal to arene bond energies have been obtained in a number of $[(Ar^*)_2R]$ complexes by calorimetric

methods and have been found to correlate well with the f → d promotion energy (King et al., 1992, 1996). It has actually been found that these bond energies are quite large and, from the experimental data, that the calculated formation of solid $[(Ar^*)_2R]$ from solid Ar* and crystalline metal would be exothermic for rare earths and endothermic for group 4, 5 and 6 metals (Scheme 18).

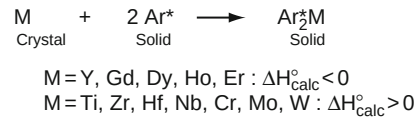

SCHEME 18 Calculated enthalpies for the formation of solid $[(Ar^*)_2M]$ from solid Ar* and crystalline metal (after King et al., 1992, 1996).

From these data, a reaction of, for example, yttrium metal with Ar* appeared feasible; however, this reaction was attempted and was not successful (King et al., 1996).

High-level theoretical calculations included *ab initio* relativistic effective core potentials (RECP) with MP2, MP4 and coupled-cluster methods, which emphasised the importance of electronic correlation in the correct description of the compounds (Di Bella et al., 1996). This initial study was further refined by *ab initio* methods (Hong et al., 1999) and relativistic DFT calculations (Dolg, 2001; Hong et al., 1999, 2000; Lu and Li, 1999) The most recent calculations seem to favour an s → d rather than the f → d promotion scheme in the metal-ligand bonding of the zero-valent complexes.

Finally, 4-pentyl-4′-cyanobiphenyl (CB), a compound with mesogenic properties, has been co-condensed with europium and samarium atoms. On the basis of matrix IR spectra and DFT calculations at the B3LYP level, it has been proposed that at low temperatures (below 30 K) mononuclear sandwich complexes: $[(CB)_2Eu]$ and $[(CB)_2Sm]$ were obtained while with higher concentration of metal and at higher temperatures bimetallic sandwich complexes $[(CB)_2Eu_2]$ and $[(CB)_2Sm_2]$ were present, in which both phenyl rings of CB are coordinated to Eu or Sm (Vlasov et al., 2005).

4.2 Reactivity

To our knowledge, no recent papers have appeared on the reactivity of rare-earth bis arene complexes.

Reactions of $[(Ar^*)_2Y]$ with alcohols and amines afforded the respective yttrium(III) alkoxides and amides (Scheme 19).

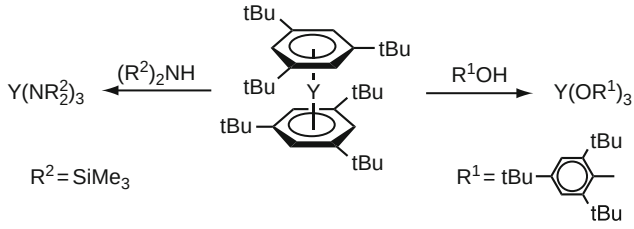

SCHEME 19 Reaction of bis(1,3,5-tris(*t*-butyl)benzene)yttrium with molecules bearing acidic protons.

Finally, rare-earth bis arene complexes have been shown to polymerise ethylene with narrow polydispersity and high turnover numbers (Cloke, 1993).

5. CONCLUSION AND PERSPECTIVES

The molecular chemistry of the rare-earth elements in uncommon low-valent states is now well established.

The divalent state has been the most studied, especially that of neodymium, dysprosium and thulium. The diiodides of these elements have been employed as precursors in many reactions and their use should increase now that they are commercially available. They show good potential as replacements to SmI_2 in organic chemistry: they are powerful reducing agents and should be able to mediate the reactions promoted by SmI_2 more efficiently and without the need of additives such as HMPA. Particularly NdI_2 appears attractive because of the relatively low cost of neodymium and the stronger redox potential of Nd^{2+}.

The other isolable molecular compounds of uncommon divalent rare earths have been until now mostly organometallic complexes featuring cyclopentadienyl ligands or cyclopentadienyl ''equivalents'' such as pyrazolylborates. The vast majority of characterised compounds contain Tm^{II}, the less reactive of the uncommon divalent rare earths (which unfortunately is also the most expensive). Many other stable compounds seem within reach, given that a good steric protection is achieved, such as for instance amides or alkoxides. Also, it may be possible to synthesise more heteroleptic complexes such as $LR^{II}I$ with an open coordination sphere, which could lead to a very rich new chemistry. A pending question finally involves the possibility of finding yet other complexes of rare earths in new divalent states (for instance Y^{2+}).

As far as reactivity is concerned, much is still to be discovered. No reports have yet appeared on the reactivity of uncommon divalent

rare-earth complexes with small molecules such as CO, CO_2 and H_2. This is in sharp contrast to the very rich reactive chemistry of Sm^{II} in decamethylsamarocene. There are also many rare-earth-based reductive systems that have been able to activate dinitrogen in the form of diazenide (N_2^{2-}). The important question about which of these systems really involve the divalent state, and what is the mechanism of dinitrogen activation has not found a definitive answer. From there, a very significant and challenging task would be to further transform these dinitrogen complexes into useful nitrogen-containing molecules; a recent paper by Evans et al. describes the reactivity of μ-N_2 rare-earth complexes with several neutral molecules, but N_2 is not incorporated in any of the resulting complexes (Evans et al., 2009).

The special case of low-valent scandium is worth mentioning, since this element has been found to exist as both Sc^{I} and Sc^{II} in molecular compounds. It is interesting that apparently Sc^{I} compounds can be made in relatively mild conditions, and maybe more complexes can be made according to similar routes.

No significant breakthroughs in zero-valent rare-earth chemistry have been recorded in the last 10 years, and the reactivity studies are rather scarce. However, these molecules appear promising in the sense that they are the source of molecular, soluble zero-valent metals. In particular it would be very interesting to look at the chemistry of $[(Ar^*)_2R]$ to check whether these molecules could be the precursors to new R^{II} complexes through controlled oxidation reactions. $[(Ar^*)_2Dy]$, which is stable, appears as a good candidate for this purpose.

The low-valent molecular chemistry of rare earths was once thought to be restricted to divalent samarium, europium and ytterbium. This chemistry has now been extended to many of the rare earths in the zero-valent state, to mono- and divalent scandium, to divalent lanthanum, cerium, neodymium, dysprosium and thulium, and to systems in which dinitrogen is activated and that may contain yet other highly reactive divalent rare earths. It is the opinion of the author that this research area is likely to find fascinating developments in the near future.

REFERENCES

Anderson, D.M., Cloke, F.G.N., Cox, P.A., Edelstein, N., Green, J.C., Pang, T., et al., 1989. J. Chem. Soc., Chem. Commun. 53–55.

Arnold, P.L., Cloke, F.G.N., Hitchcock, P.B., Nixon, J.F., 1996. J. Am. Chem. Soc. 118, 7630–7631.

Arnold, P.L., Cloke, F.G.N., Hitchcock, P.B., 1997. Chem. Commun. 481–482.

Arnold, P.L., Cloke, F.G.N., Nixon, J.F., 1998. Chem. Commun. 797–798.

Arnold, P.L., Petrukhina, M.A., Bochenkov, V.E., Shabatina, T.I., Zagorskii, V.V., Sergeev, G.B., et al., 2003. J. Organomet. Chem. 688, 49–55.

Asprey, L.B., Kruse, F.H., 1960. J. Inorg. Nucl. Chem. 13, 32–35.
Balashova, T.V., Khoroshenkov, G.V., Kusyaev, D.M., Eremenko, I.L., Aleksandrov, G.G., Fukin, G.K., et al., 2004. Russ. Chem. Bull., Int. Ed. 53, 825–829.
Balashova, T.V., Kuzyaev, D.M., Semchikov, Yu.D., Bochkarev, M.N., 2005. Russ. Chem. Bull., Int. Ed. 54, 2506–2510.
Balashova, T.V., Kusyaev, D.M., Kulikova, T.I., Kuznetsova, O.N., Edelmann, F.T., Gießmann, S., et al., 2007. Z. Anorg. Allg. Chem. 633, 256–260.
Beetstra, D.J., Meetsma, A., Hessen, B., Teuben, J.H., 2003. Organometallics 22, 4372–4374.
Bochkarev, M.N., 2004. Coord. Chem. Rev. 248, 835–851.
Bochkarev, M.N., Burin, M.E., 2004. Russ. Chem. Bull., Int. Ed. 53, 2179–2181.
Bochkarev, M.N., Fagin, A.A., 1999a. Russ. Chem. Bull. 48, 1187–1188.
Bochkarev, M.N., Fagin, A.A., 1999b. Chem. Eur. J. 5, 2990–2992.
Bochkarev, M.N., Fedushkin, I.L., Nevodchikov, V.I., Cherkasov, V.K., Schumann, H., Hemling, H., et al., 1996. J. Organomet. Chem. 524, 125–131.
Bochkarev, M.N., Fedushkin, I.L., Fagin, A.A., Petrovskaya, T.V., Ziller, J.W., Broomhall-Dillard, R.N.R., et al., 1997a. Angew. Chem. Int. Ed. Engl. 36, 133–135.
Bochkarev, M.N., Fedushkin, I.L., Fagin, A.A., Schumann, H., Demtschuk, J., 1997b. Chem. Commun. 1783–1784.
Bochkarev, M.N., Fagin, A.A., Fedushkin, I.L., Trifonov, A.A., Kirillov, E.N., Eremenko, I.L., et al., 1999a. Mater. Sci. For. 315–317, 144–153.
Bochkarev, M.N., Fagin, A.A., Fedushkin, I.L., Petrovskaya, T.V., Evans, W.J., Greci, M.A., et al., 1999b. Russ. Chem. Bull. 48, 1782–1785.
Bochkarev, M.N., Fedushkin, I.L., Dechert, S., Fagin, A.A., Schumann, H., 2001. Angew. Chem. Int. Ed. 40, 3176–3178.
Bochkarev, M.N., Fagin, A.A., Khoroshenkov, G.V., 2002. Russ. Chem. Bull., Int. Ed. 51, 1909–1914.
Bochkarev, M.N., Khoroshenkov, G.V., Schumann, H., Dechert, S., 2003. J. Am. Chem. Soc. 125, 2894–2895.
Bochkarev, M.N., Burin, M.E., Cherkasov, V.K., 2004. Russ. Chem. Bull., Int. Ed. 53, 481–482.
Bochkarev, M.N., Khoroshenkov, G.V., Burin, M.E., Kuzyaev, D.M., Fagin, A.A., Maleev, A.A., et al., 2006a. Russ. Chem. Bull., Int. Ed. 55, 588–590.
Bochkarev, M.N., Khoroshenkov, G.V., Kuzyaev, D.M., Fagin, A.A., Burin, M.E., Fukin, G.K., et al., 2006b. Inorg. Chim. Acta 359, 3315–3320.
Bochkarev, M.N., Balashova, T.V., Maleev, A.A., Fagin, A.A., Fukin, G.K., Baranov, E.V., 2007. Inorg. Chim. Acta 360, 2368–2378.
Bowman, L.J., Izod, K., Clegg, W., Harrington, R.W., 2007. Organometallics 26, 2646–2651.
Brennan, J.G., Cloke, F.G.N., Sameh, A.A., Zalkin, A., 1987. J. Chem. Soc., Chem. Commun. 1668–1669.
Bulgakov, R.G., Kuleshov, S.P., Kinzyabaeva, Z.S., Fagin, A.A., Masalimov, I.R., Bochkarev, M.N., 2007. Russ. Chem. Bull., Int. Ed. 56, 1956–1959.
Burin, M.E., Smirnova, M.V., Fukin, G.K., Baranov, E.V., Bochkarev, M.N., 2006. Eur. J. Inorg. Chem. 351–356.
Campazzi, E., Solari, E., Floriani, C., Scopelliti, R., 1998. Chem. Commun. 2603–2604.
Cassani, M.C., Gun'ko, Yu.K., Hitchcock, P.B., Lappert, M.F., 1996. Chem. Commun. 1987–1988.
Cassani, M.C., Lappert, M.F., Laschi, F., 1997. Chem. Commun. 1563–1564.
Cassani, M.C., Duncalf, D.J., Lappert, M.F., 1998. J. Am. Chem. Soc. 120, 12958–12959.
Cassani, M.C., Gun'ko, Yu.K., Hitchcock, P.B., Lappert, M.F., Laschi, F., 1999. Organometallics 18, 5539–5547.
Cassani, M.C., Gun'ko, Yu.K., Hitchcock, P.B., Hulkes, A.G., Khvostov, A.V., Lappert, M.F., Protchenko, A.V., 2002. J. Organomet. Chem. 647, 71–83.
Cheng, J., Takats, J., Ferguson, M.J., McDonald, R., 2008. J. Am. Chem. Soc. 130, 1544–1545.

Clentsmith, G.K.B., Cloke, F.G.N., Green, J.C., Hanks, J., Hitchcock, P.B., Nixon, J.F., 2003. Angew. Chem. Int. Ed. 42, 1038–1041.
Cloke, F.G.N., 1993. Chem. Soc. Rev. 17–24.
Cloke, F.G.N., Khan, K., Perutz, R.N., 1991. J. Chem. Soc., Chem. Commun. 1372–1373.
Dahlén, A., Hilmersson, G., 2004. Eur. J. Inorg. Chem. 3393–3403.
David, F.H., 2008. Radiochim. Acta 96, 135–144.
Di Bella, S., Lanza, G., Fragalà, I.L., Marks, T.J., 1996. Organometallics 15, 3985–3989.
Dolg, M., 2001. J. Chem. Inf. Comput. Sci. 41, 18–21.
Evans, W.J., 1987. Polyhedron 6, 803–835.
Evans, W.J., 2000. Coord. Chem. Rev. 206–207, 263–283.
Evans, W.J., 2002a. J. Organomet. Chem. 647, 2–11.
Evans, W.J., 2002b. J. Organomet. Chem. 652, 61–68.
Evans, W.J., 2007. Inorg. Chem. 46, 3435–3449.
Evans, W.J., Allen, N.T., 2000. J. Am. Chem. Soc. 122, 2118–2119.
Evans, W.J., Lee, D.S., 2005. Can. J. Chem. 83, 375–384.
Evans, W.J., Workman, P.S., 2005. Organometallics 24, 1989–1991.
Evans, W.J., Engerer, S.C., Neville, A.C., 1977. J. Am. Chem. Soc. 100, 331–333.
Evans, W.J., Bloom, I., Hunter, W.E., Atwood, J.L., 1981. J. Am. Chem. Soc. 103, 6507–6508.
Evans, W.J., Gonzales, S.L., Ziller, J.W., 1994. J. Am. Chem. Soc. 116, 2600–2608.
Evans, W.J., Broomhall-Dillard, R.N.R., Ziller, J.W., 1998a. Polyhedron 17, 3361–3370.
Evans, W.J., Seibel, C.A., Ziller, J.W., 1998b. J. Am. Chem. Soc. 120, 6745–6752.
Evans, W.J., Allen, N.T., Ziller, J.W., 2000. J. Am. Chem. Soc. 122, 11749–11750.
Evans, W.J., Allen, N.T., Ziller, J.W., 2001. J. Am. Chem. Soc. 123, 7927–7928.
Evans, W.J., Allen, N.T., Ziller, J.W., 2002. Angew. Chem. Int. Ed. 41, 359–361.
Evans, W.J., Allen, N.T., Workman, P.S., Meyer, J.C., 2003a. Inorg. Chem. 42, 3097–3099.
Evans, W.J., Workman, P.S., Allen, N.T., 2003b. Org. Lett. 5, 2041–2042.
Evans, W.J., Giarikos, D.G., Allen, N.T., 2003c. Macromolecules 36, 4256–4257.
Evans, W.J., Zucchi, G., Ziller, J.W., 2003d. J. Am. Chem. Soc. 125, 10–11.
Evans, W.J., Lee, D.S., Ziller, J.W., 2004a. J. Am. Chem. Soc. 126, 454–455.
Evans, W.J., Lee, D.S., Rego, D.B., Perotti, J.M., Kozimor, S.A., Moore, E.K., Ziller, J.W., 2004b. J. Am. Chem. Soc. 126, 14574–14582.
Evans, W.J., Lee, D.S., Lie, C., Ziller, J.W., 2004c. Angew. Chem. Int. Ed. 43, 5517–5519.
Evans, W.J., Lee, D.S., Johnston, M.A., Ziller, J.W., 2005. Organometallics 24, 6393–6397.
Evans, W.J., Rego, D.B., Ziller, J.W., 2006. Inorg. Chem. 45, 10790–10798.
Evans, W.J., Lorenz, S.E., Ziller, J.W., 2009. Inorg. Chem. 48, 2001–2009.
Fagin, A.A., Bochkarev, M.N., Kozimor, S.A., Ziller, J.W., Evans, W.J., 2005. Z. Anorg. Allg. Chem. 631, 2848–2853.
Fagin, A.A., Balashova, T.V., Kusyaev, D.M., Kulikova, T.I., Glukhova, T.A., Makarenko, N.P., et al., 2006. Polyhedron 25, 1105–1110.
Fagin, A.A., Salmova, S.V., Fukin, G.K., Baranov, E.V., Bochkarev, M.N., 2007. Inorg. Chim. Acta 360, 2923–2928.
Fedushkin, I.L., Weydert, M., Fagin, A.A., Nefedov, S.E., Eremenko, I.L., Bochkarev, M.N., 1999. Z. Naturforsch. 54b, 466–468.
Fedushkin, I.L., Bochkarev, M.N., Dechert, S., Schumann, H., 2001a. Chem. Eur. J. 7, 3558–3563.
Fedushkin, I.L., Girgsdies, F., Schumann, H., Bochkarev, M.N., 2001b. Eur. J. Inorg. Chem. 2405–2410.
Fedushkin, I.L., Nevodchikov, V.I., Bochkarev, M.N., Dechert, S., Schumann, H., 2003. Russ. Chem. Bull., Int. Ed. 52, 154–159.
Fryzuk, M.D., Mylvaganam, M., Zawarotko, M.J., MacGillivray, L.R., 1996. Polyhedron 15, 689–703.

Gradoz, P., Baudry, D., Ephritikhine, M., Lance, M., Nierlich, M., Vigner, J., 1994. J. Organomet. Chem. 466, 107–118.
Gun'ko, Yu.K., Hitchcock, P.B., Lappert, M.F., 1995. J. Organomet. Chem. 499, 213–219.
Gun'ko, Yu.K., Hitchcock, P.B., Lappert, M.F., 2000. Organometallics 19, 2832–2834.
Gusev, S.I., Zaitsev, S.D., Semchikov, Yu.D., Bochkarev, M.N., 2008. Polym. Sci. Ser. B 50, 185–187.
Hitchcock, P.B., Lappert, M.F., Tian, S., 2000. Organometallics 19, 3420–3428.
Hitchcock, P.B., Lappert, M.F., Maron, L., Protchenko, A.V., 2008. Angew. Chem. Int. Ed. 47, 1488–1491.
Hong, G., Schautz, F., Dolg, M., 1999. J. Am. Chem. Soc. 121, 1502–1512.
Hong, G., Dolg, M., Li, L., 2000. Int. J. Quantum Chem. 80, 201–209.
Hou, Z., Fujita, A., Zhang, Y., Miyano, T., Yamazaki, H., Wakatsuki, Y., 1998. J. Am. Chem. Soc. 120, 754–766.
Izod, K., 2002. Angew. Chem. Int. Ed. 41, 743–744.
Jaroschik, F., Nief, F., Ricard, L., 2006. Chem. Commun. 426–428.
Jaroschik, F., Nief, F., Le Goff, X.-F., Ricard, L., 2007a. Organometallics 26, 1123–1125.
Jaroschik, F., Nief, F., Le Goff, X.-F., Ricard, L., 2007b. Organometallics 26, 3552–3558.
Jaroschik, F., Momin, A., Nief, F., Le Goff, X.-F., Deacon, G.B., Junk, P.C., 2009. Angew. Chem. Int. Ed. 48, 1117–1121.
Jones, C., Stasch, A., Woodul, W.D., 2009. Chem. Commun. 113–115.
Kagan, H.B., 2003. Tetrahedron 59, 10351–10372.
Kamenskaia, A.N., 1984. Zh. Neorg. Khim. 29, 439–449.
Kamenskaia, A.N., Bukietynska, K., Mikheev, N.B., Spytsin, V.I., Jezowska-Trzebiatowska, B., 1979. Zh. Neorg. Khim. 24, 1139–1146.
Kamenskaia, A.N., Mikheev, N.B., Kholmogorova, N.P., Spytsin, V.I., 1982. Dokl. Akad. Nauk SSSR 266, 393–395.
Kamenskaia, A.N., Mikheev, N.B., Kholmogorova, N.P., 1983. Zh. Neorg. Khim. 28, 2499–2503.
Kamenskaia, A.N., Mikheev, N.B., Spytsin, V.I., 1984. Dokl. Akad. Nauk SSSR 275, 913–916.
Katkova, M.A., Fukin, G.K., Fagin, A.A., Bochkarev, M.N., 2003. J. Organomet. Chem. 682, 218–223.
Khoroshenkov, G.V., Petrovskaya, T.V., Fedushkin, I.L., Bochkarev, M.N., 2002. Z. Anorg. Allg. Chem. 628, 699–702.
Khoroshenkov, G.V., Fagin, A.A., Bochkarev, M.N., Dechert, S., Schumann, H., 2003. Russ. Chem. Bull., Int. Ed. 52, 1715–1719.
King, W.A., Marks, T.J., Anderson, D.M., Duncalf, D.J., Cloke, F.G.N., 1992. J. Am. Chem. Soc. 114, 9221–9223.
King, W.A., Di Bella, S., Lanza, G., Khan, K., Duncalf, D.J., Cloke, F.G.N., et al., 1996. J. Am. Chem. Soc. 118, 627–635.
Kirbach, U., Dunsch, L., 1996. Angew. Chem. Int. Ed. Engl. 35, 2380–2383.
Kirillov, E.N., Trifonov, A.A., Nefedov, S.E., Eremenko, I.L., Edelmann, F.T., Bochkarev, M. N., 1999. Z. Naturforsch. 54b, 1379–1384.
Korobkov, I., Aharonian, G., Gambarotta, S., Yap, G.P.A., 2002. Organometallics 21, 4899–4901.
Kuzyaev, D.M., Fukin, G.K., Baranov, E.V., Bochkarev, M.N., 2007. Russ. Chem. Bull., Int. Ed. 56, 1960–1963.
Lu, H.-G., Li, L.-M., 1999. Theor. Chem. Acc. 102, 121–126.
Meyer, G., 2008. Angew. Chem. Int. Ed. 47, 4962–4964.
Meyer, G., Jongen, L., 2006. J. Alloys Compd. 418, 53–57.
Meyer, G., Gerlitzki, N., Hammerich, S., 2004. J. Alloys Compd. 380, 71–78.
Nakayama, Y., Nakamura, A., Mashima, K., 1997. Chem. Lett. 26, 803–804.
Namy, J.-L., Girard, P., Kagan, H.B., 1977. New J. Chem. 1, 5–7.

Neculai, A.-M., Neculai, D., Roesky, H.W., Magull, J., Baldus, M., Andronesi, O., et al., 2002. Organometallics 21, 2590–2592.
Neculai, A.-M., Cummins, C.C., Neculai, D., Roesky, H.W., Bunkòczi, G., Walfort, B., et al., 2003. Inorg. Chem. 42, 8803–8810.
Nief, F., Turcitu, D., Ricard, L., 2002. Chem. Commun. 1646–1647.
Nief, F., Tayart de Borms, B., Ricard, L., Carmichael, D., 2005. Eur. J. Inorg. Chem. 637–643.
Pichler, T., Golden, M.S., Knupfer, M., Fink, J., Kirbach, U., Kuran, P., et al., 1997. Phys. Rev. Lett. 79, 3026–3029.
Poeppelmeier, K.R., Corbett, J.D., 1977. Inorg. Chem. 16, 294–297.
Poeppelmeier, K.R., Corbett, J.D., McMullen, T.P., Torgeson, D.R., Barnes, R.G., 1980. Inorg. Chem. 19, 129–134.
Quin, L.D., 2006. Curr. Org. Chem. 10, 43–78.
Rossmanith, K., 1979. Monatsh. Chem. 110, 1019–1023.
Shie, J.-J., Workman, P.S., Evans, W.J., Fang, J.-M., 2004. Tetrahedron Lett. 45, 2703–2707.
Takahashi, T., Ito, A., Inakuma, M., Shinohara, H., 1995. Phys. Rev. B 52, 13812–13814.
Turcitu, D., Nief, F., Ricard, L., 2003. Chem. Eur. J. 9, 4916–4923.
Vlasov, A.V., Shabatina, T.I., Ivanov, A.Yu., Sheina, G.G., Nemukhin, A.V., Sergeev, G.B., 2005. Mendeleev Commun. 15, 10–11.
Wedler, M., Recknagel, A., Edelmann, F.T., 1990. J. Organomet. Chem. 395, C26–C29.
Xiang, X., Shen, Q., Wang, J., Zhu, Z., Huang, W., Zhou, X., 2008. Organometallics 27, 1959–1962.
Zhu, Z., Wang, C., Xiang, X., Pi, C., Zhou, X., 2006. Chem. Commun. 2066–2068.
Zhu, Z., Wang, J., Zhang, Z., Xiang, X., Zhou, X., 2007. Organometallics 26, 2499–2500.

CHAPTER **247**

Self-Assembled Lanthanide Helicates: From Basic Thermodynamics to Applications

Claude Piguet* and **Jean-Claude G. Bünzli†**

Contents

* Department of Inorganic, Analytical and Applied Chemistry, University of Geneva, 30 quai E. Ansermet, CH-1211 Geneva 4, Switzerland
† Laboratory of Lanthanide Supramolecular Chemistry, École Polytechnique Fédérale de Lausanne, BCH 1402, CH-1015 Lausanne, Switzerland and Department of Advanced Materials Sciences, Korea University, Sejong Campus, Jochiwon, Korea (WCU project R31-10035)

Handbook on the Physics and Chemistry of Rare Earths, Volume 40
ISSN 0168-1273, DOI: 10.1016/S0168-1273(10)40007-0

List of Symbols and Acronyms

1D	one-dimensional
2D	two-dimensional
3D	three-dimensional
5D10	mouse hybridoma cell line
χ	magnetic susceptibility tensor
χ_0	isotropic part of the magnetic susceptibility tensor
δ_i^{dia}	diamagnetic shift in ppm for a nucleus i
$\delta_{ij}^{\mathrm{exp}}$	hyperfine chemical shift for a nucleus i in a complex of a lanthanide j
$\delta_{ij}^{\mathrm{para}}$	paramagnetic hyperfine chemical shift in ppm for a nucleus i in a complex of a lanthanide j
ϕ_i	spherical coordinate of nucleus i
γ	gyromagnetic ratio
η_{et}	efficiency of the ligand-to-metal energy transfer
η_{ISC}	efficiency of intersystem crossing
η_{sens}	efficiency of the sensitization process
μ_{B}	Bohr magneton
μ_{eff}	effective electronic magnetic momentum in μ_{B}
θ_i	spherical coordinate of nucleus i
τ_{c}	characteristic correlation time
τ_{e}	electron spin relaxation characteristic time
τ_{m}	chemical exchange characteristic time
τ_{r}	rotational characteristic time
ω	Larmor precession frequency in Hz
A_i	Fermi hyperfine constant for a nucleus i
B_q^k	crystal-field parameters of rank k
bipy	bipyridine
bp	base pair
BSA	bovine serum albumin
C_j	Bleaney's factor of lanthanide j, scaled to -100 for Dy^{III}
CD	circular dichroism
cDNA	circular DNA
CN	coordination number
COSY	correlated spectroscopy
CPL	circularly polarized luminescence
CY	cyanine dye
Delfia©	dissociation-enhanced fluoroimmunoassay
Dlbt	double-lanthanide-binding tag
DMF	dimethylformamide

DNA	deoxyribonucleic acid
DO2A	1,4,7,10-tetraazacyclododecane-1,7-diacetate
DPA	dipicolinate
dpbt	2-(*N*,*N*-diethylamin-4-yl)-bis(3,5-dimethylpyrazol-1-yl)-1,3,5-triazine
$dppeO_2$	diphenylphosphineethane dioxide
dsDNA	double-stranded DNA
DTPA	diethylenetrinitrilopentaacetate
EB	ethidium bromide
EDC	1-ethyl-3-(3-dimethylaminopropyl) carbodiimide hydrochloride
EDTA	ethylenediaminetetraacetate
ER	endoplasmatic reticulum
ES-MS	electrospray (ion spray) mass spectrometry
eu	electrostatic unit ($1\ \text{eu} = 1.602 \times 10^{-19}\ \text{C}$)
F_i	contact term of the nucleus *i*
fac	facial
fod	6,6,7,7,8,8,8-heptafluoro-2,2-dimethyl-3,5-octanedionate
FRET	Förster resonance energy transfer
g_e	Landé factor
G_i	axial geometrical factor of the nucleus *i*
GM	Göppert-Mayer unit (two-photon absorption cross section)
H_0	applied magnetic field
HeLa	cervix cancer cell line
hfa	hexafluoroacetylacetonate
HHH	head-to-head-to-head
HHT	head-to-head-to-tail
HOPO	1-methyl-2,3-dihydroxypyridone
HS	high spin
HSQC	heteronuclear single quantum coherence
IC	internal conversion
IC_{50}	half-maximal inhibitory concentration
ILCT	intraligand charge-transfer state
Jurkat	human T leukemia cell line
k	Boltzmann's constant
LDH	lactase dehydrogenase
LMCT	ligand-to-metal charge-transfer state
LS	low spin
MCF-7	breast cancer cell line
mer	meridional
Mk	Mischler's ketone

MOF	metal-organic framework
MRI	magnetic resonance imaging
N_A	Avogadro's number
NHE	normal hydrogen electrode
NIR	near-infrared light
NLO	nonlinear optic
NMP	*N*-methyl-2-pyrrolidinone
NOEDIF	nuclear Overhauser effect difference spectroscopy
NOESY	nuclear Overhauser enhancement spectroscopy
OAc	acetate
PCR	polymerase chain reaction
PCS	pseudocontact shift
phen	phenanthroline
PLDS	polylysine dicarboxylate succinate polymer
Q_L^R	overall quantum yield obtained upon ligand excitation
Q_R^R	metal-centered (intrinsic) quantum yield.
r_i	*R*-nucleus *i* distance
rac	racemic
RDC	residual dipolar coupling
RPMI-1640	Rosswell Park Memorial Institute cell culture medium
S	spin quantum number
$\langle S_z \rangle$	expectation value of S_z
SA	streptavidin
SCE	saturated calomel electrode
SMM	single molecule magnet
ssDNA	single-stranded DNA
T_1	longitudinal nuclear relaxation time
T_2	transversal nuclear relaxation time
TAM	2,3-dihydroxyterephthalamide
TL	total luminescence
TPA	two-photon (or biphotonic) absorption
TRD	time-resolved detection
TRLM	time-resolved luminescence microscopy
Tr(χ)	trace of the magnetic susceptibility tensor
tta	thenoyltrifluoroacetylacetonate
UV	ultraviolet light
WST-1	cell proliferation and viability assay [4-(3-(4-iodophenyl)-2-(4-nitrophenyl)-2*H*-5-tetrazolio)-1,3-benzene disulfonate
YAG	yttrium aluminum garnet
ZINDO	Zeners's intermediate neglect of differential overlap

1. INTRODUCTION

1.1 The fascination for molecular helical edifices

The fascination for helical edifices is as old as the human civilization and the Tower of Babel, erected during the first dynasty of the Babylonian (− 1895 to − 1595 BC) represents an archetype of a single-stranded helical pattern (Figure 1A). Interestingly, the Bible (Genesis 11: 1–5) mentions the Tower of Babel for the particular combination of rotation and linear progressions, which is characteristic of a helical structure and which illustrates the creation of several different languages (i.e., the rotation) preventing the ascent (i.e., the linear progression) of the unified mankind toward heaven and God.

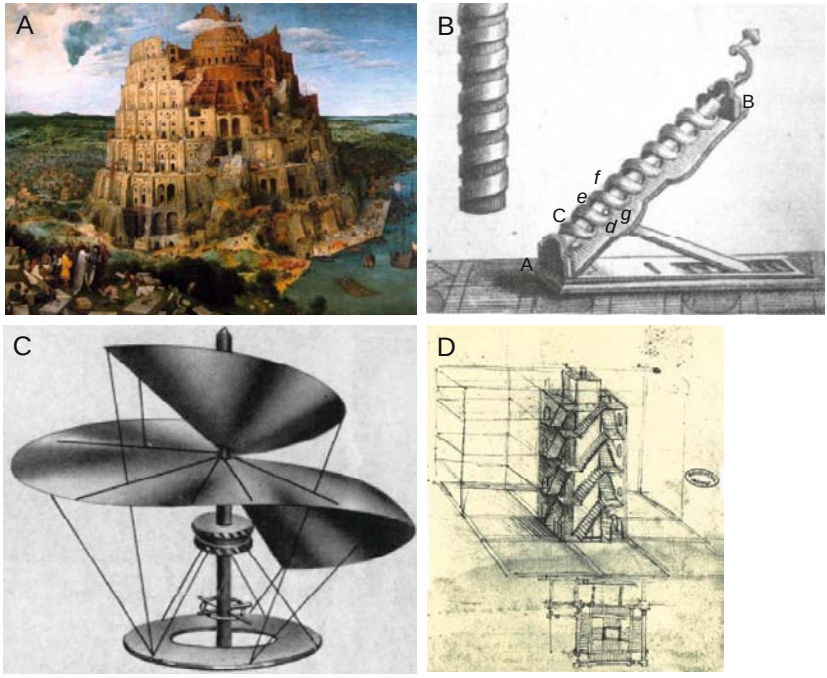

FIGURE 1 (A) Representation of the Tower of Babel by Pieter Bruegel the Elder (1525–1569), from http://artcess.files.wordpress.com. (B) A scheme of Archimedes' screw in *Leçons de Physique Expérimentale*, Jean-Antoine Nollet, Leçon IX, Fig. 12, 1743 (http://chem.ch.huji.ac.il./history/nollet.html). (C) The original scheme of a helicopter by Leonardo Da Vinci (1452–1519), from http://www.century-of-flight.net. (D) Da Vinci's sketch of a quadruple-stranded staircase, which inspired the double-stranded helical staircase built in the center of the castle of Chambord (France, sixteenth century); Léonard Da Vinci, Institut de France, Ms B, fol. 47v, http://www.maat-ingenierie.fr.

Mechanically speaking, these two characteristics were successfully exploited by the ancient Greeks and Egyptians for the pumping of fluids (Archimedes' screw, − 287 to − 212 BC, Figure 1B), then adapted to the first design of a helicopter by Leonardo Da Vinci (1490), when he realized that air can be considered as a fluid (Figure 1C). The obvious extension of the single-stranded helical pattern toward double-, triple-, and even quadruple-stranded helices made of interpenetrated helical strands rapidly followed (Figure 1D), eventually leading to the development of efficient propellers for boats and airplanes during the last century.

It is thus not surprising that a similar fascination and craze for microscopic helical patterns arose at the molecular level as soon as structural characterization techniques were at hand. The seven seminal contributions of Linus *Pauling* published back-to-back in the *Proceedings of the National Academy of Sciences of the United States of America* in 1951 (Pauling and Corey, 1951a,b,c,d,e,f,g), all dealing with the secondary structure of proteins produced by the three-dimensional helical pattern adopted by linked amino acids, would be the key for understanding biology at the molecular level. The helical structure in proteins is induced by noncovalent intramolecular hydrogen bonds connecting every main-chain carbonyl (C=O) and amino (N–H) groups separated by four amino acid residues (Figure 2A). This produces very regular single-stranded right-handed helices, the so-called α-helices, characterized by a pitch of 5.4 Å, that is, a linear progression of 5.4 Å for a complete turn of the molecular strand containing on average 3.6 amino acids. The subsequent recognition, 1 year later, that (i) the helical structure is also crucial for nucleic acids (Watson and Crick, 1953) and (ii) intermolecular hydrogen bonds are also responsible for the formation of deoxyribonucleic acids (DNAs), greatly contributed to make these helical edifices familiar among molecular scientists (Sayre, 1975; Watson, 1968; Wilkins, 2003).

1.2 Nanoscopic metal-containing helices: The helicates

The chemists involved during the last two decades in the manipulation of weak noncovalent interactions as a new tool for the rational building of nanoscopic supramolecular architectures, logically considered the formation of (supra)molecular helical structures as an undeniable demonstration of the validity of their approach for the synthetic preparation of novel micro- and nanoscopic objects (Lehn, 1995). Inspired by previous investigations on the electrochemical behavior of intertwinned dimeric Cu(I) complexes (Lehn et al., 1983), *Lehn* and coworkers selected the noncovalent Cu(I)–N bonds for the programmed connection of two covalent helical strands around a central axis defined by a line of regularly spaced metal ions in the complex $[Cu_3(\mathbf{L1})_2]^{3+}$ (Figure 3; Lehn et al., 1987). This double-stranded helix was the first recognized member of what has

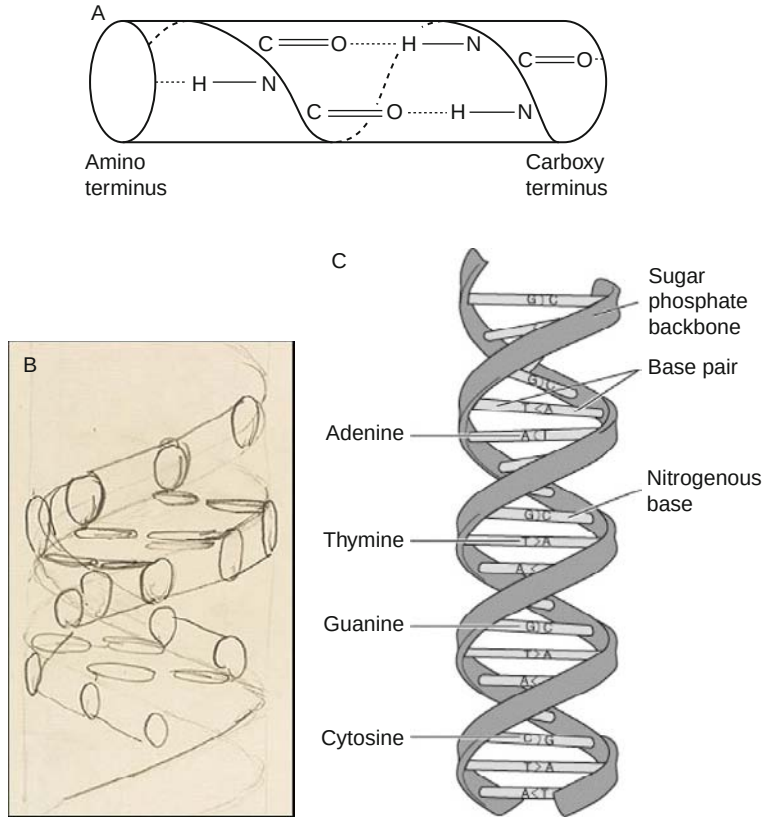

FIGURE 2 (A) Toilet roll representation of the main-chain intramolecular hydrogen bonding in a protein α-helix, from http://cryst.bbk.ac.uk/PPS2/course/section3. (B) An early sketch (1952) representing the double-stranded helical structure of DNA, from http://genome.wellcome.ac.uk. (C) Modern representation of the double-stranded helix in DNA, from http://www.ocean.udel.edu.

become later a novel and large family of polynuclear coordination complexes, termed *helicates*, a contraction of the word helix (Greek: $\varepsilon\lambda\iota\xi$ = winding, convolution, spiral) with the suffix *-ate*, characterizing host–guest complexes between (pre)organized receptors and metal ions (compare for instance coronate, cryptate, etc.; Lehn, 1995; Lehn et al., 1987; Vögtle, 1991). A helicate is thus defined as a discrete helical supramolecular complex constituted by one or more covalent organic strands wrapped about and coordinated to a series of at least two ions defining the helical axis (Lehn et al., 1987; Piguet et al., 1997a).

Though the complexes $[Fe_2(\mathbf{L2}\text{-}2H)_3]$, an analogue of rhodotorulic acid (Figure 4A; Carrano and Raymond, 1978; Carrano et al., 1979; Scarrow

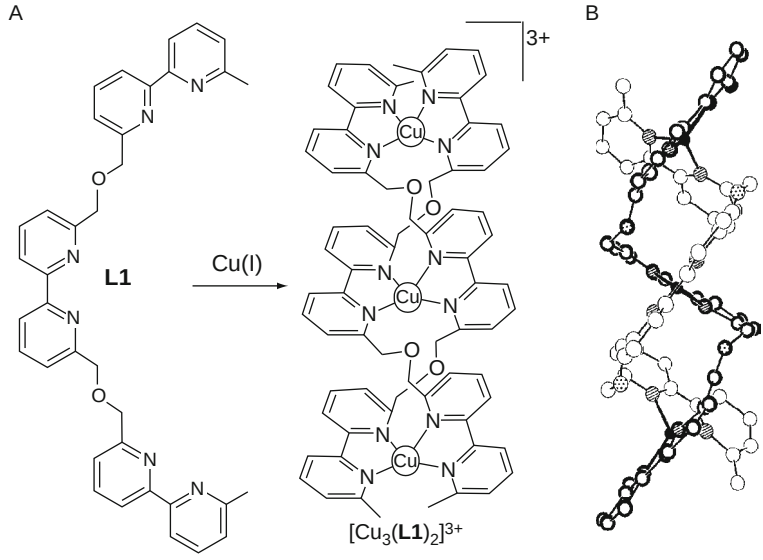

FIGURE 3 (A) Self-assembly and (B) X-ray crystal structure of the trinuclear saturated homotopic double-stranded helicate $[Cu_3(\mathbf{L1})_2]^{3+}$ (reproduced by permission from Hamacek et al., 2006, © 2006 Royal Society of Chemistry; Lehn et al., 1987, © 1987 The National Academy of Sciences USA).

et al., 1985), and $[Cu_2(\mathbf{L3})_3]^{4+}$ (Figure 4B; Harris and McKenzie, 1969) clearly correspond to triple-stranded helicates according to the above definition, they were considered as standard binuclear coordination complexes at the time of their publication. Therefore, the justification for a novel terminology for these complexes entirely relies on some additional rational programming of the final complexes thanks to a judicious match between the stereoelectronic properties of the metal ions and the ligand-binding possibilities (Piguet et al., 1997a,b). In this context, the planned preparation of the complete family of bi- ($[Cu_2(\mathbf{L4})_2]^{2+}$), tri- ($[Cu_3(\mathbf{L1})_2]^{3+}$), tetra- ($[Cu_4(\mathbf{L5})_2]^{4+}$), and pentanuclear ($[Cu_5(\mathbf{L6})_2]^{2+}$) helicates unambiguously confirmed the great potential of the supramolecular approach in coordination chemistry (Figure 5; Lehn and Rigault, 1988). In these complexes, the match between ligand and metal stereochemical requirements is based on the oxopropylene spacers separating the bidentate 2,2′-bipyridine segments, which are short enough to prevent the connection of two bipyridines to the same metal ion, but long enough to allow the wrapping of the organic ligand strands about the helical axis defined by the aligned metals. Moreover, the connection of both oxopropylene spacers and terminal methyl groups at the 6,6′-positions of the bipyridine units in **L1** and **L4–L6** strictly limits their coordination to tetrahedral metal ions.

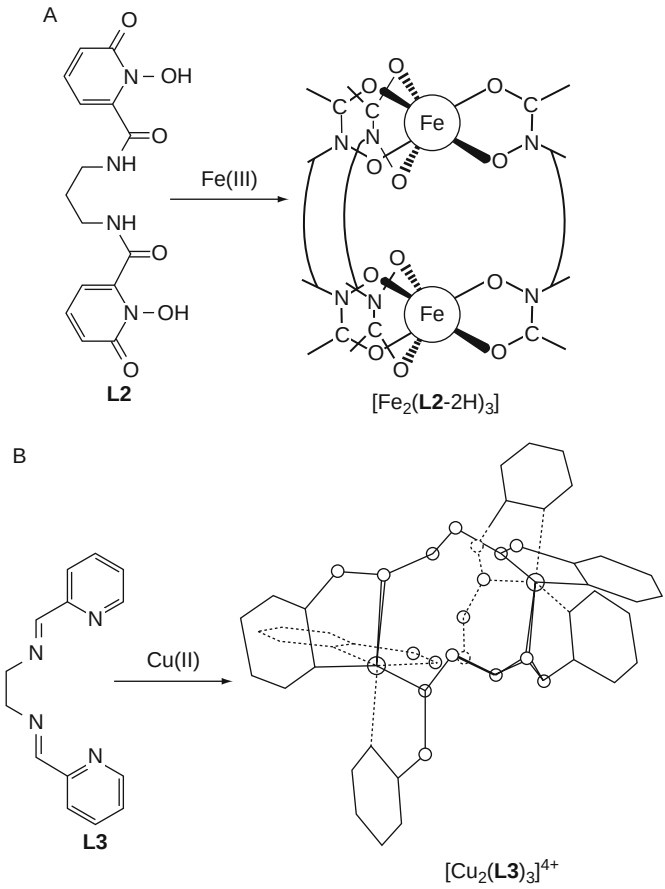

FIGURE 4 The formation of early binuclear triple-stranded helicates with (A) Fe(II) and (B) Cu(II) metal ions (redrawn after (A) Scarrow et al., 1985 and (B) Harris and McKenzie, 1969).

The spherical Cu(I) cation (d^{10} electronic configuration) is thus ideally suited for the formation of double-stranded helicates with **L1** and **L4–L6,** because of its lack of directional coordination bonds and its limited electrostatic factor $z^2/R = 1.30$ eu $Å^{-1}$ (z is the charge of the cation and R is its ionic radius; Shannon, 1976), which is compatible with $CN = 4$ (Figure 5). The demonstration of this novel concept in coordination chemistry, combined with the undeniable aesthetic appeal of helical structures, were at the origin of a considerable enthusiasm leading to the isolation and structural characterization of a plethora of binuclear double-, triple-, and quadruple-stranded helicates during the past two decades (for comprehensive reviews, see Albrecht, 2001; Constable, 1992, 1994, 1996;

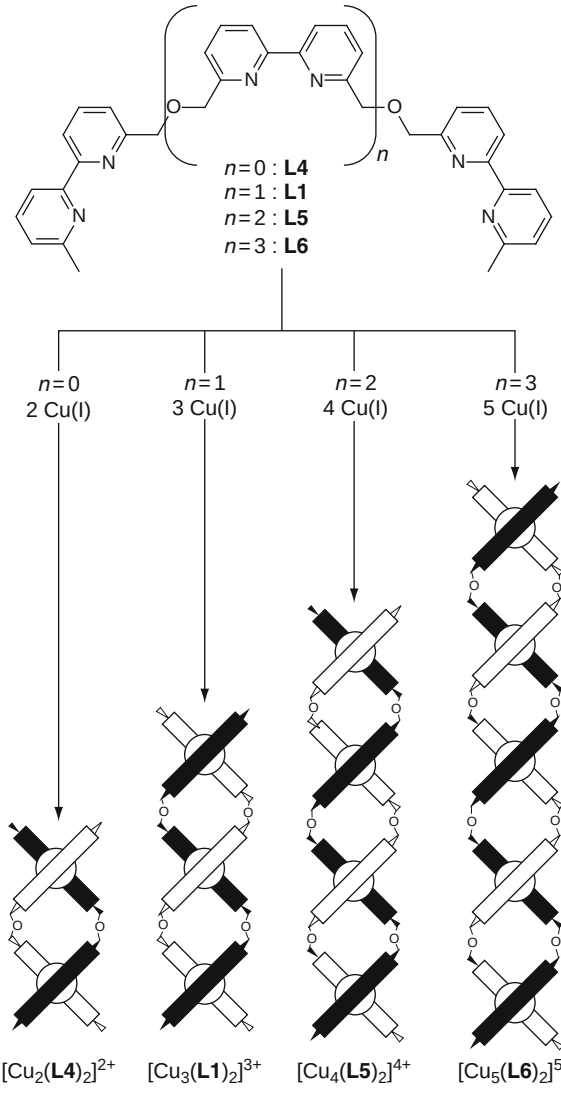

FIGURE 5 Programmed assemblies of bi- to pentanuclear double-stranded helicates (redrawn after Lehn and Rigault, 1988).

Piguet et al., 1997a). However, the preparation of helicates containing three metal ions such as $[Cu_3(\mathbf{L1})_2]^{3+}$ (Lehn et al., 1987) is less common (for selected examples, see Capo et al., 2002; Constable et al., 1991; Garrett et al., 1992; Greenwald et al., 1999; Hutin et al., 2006; Koert et al., 1990; Pfeil and Lehn, 1992; Smith and Lehn, 1996; Zong and Thummel, 2005),

while those with four or more metals are rare (Krämer et al., 2002; Lehn and Rigault, 1988; Marquis-Rigault et al., 1996; Matthews et al., 2003; Maurizot et al., 2004; Potts et al., 1993; Wang et al., 1998).

Probably because it was not clearly identified as standard thermodynamic complexation process for a long time, the formation of supramolecular helicates was accompanied by the emergence of a novel flourishing semantics, often borrowed from biology, whereby noncovalent interactions are crucial. The terms *self-assembly* and *self-organization*, first introduced in 1987 (Lehn et al., 1987), are now among the most used words in chemistry for describing the formation of sophisticated coordination or complexation processes. The competition between different thermodynamic equilibria, often leading to some selectivity depending on the choice of external conditions (stoichiometries, solvent, temperature; see Schneider and Yatsimirsky, 2008), was first termed *self-recognition* (Figure 6; Caulder and Raymond, 1997; Krämer et al., 1993; Lehn, 1995), and slowly evolves to more modern terminologies such as *combinatorial dynamic libraries*, *constitutional dynamic chemistry*, and *adaptative chemistry* (Lehn, 1999, 2007). The thermodynamic origins of these strange coordination behaviors were first tentatively addressed in 1992 with the claim that positive cooperativity drives the assembly processes of the target helicates to completion (Garrett et al., 1992; Pfeil and Lehn, 1992). Although the validity of this proposal was rapidly accepted by the community, the only support for this fundamental explanation relied on two Scatchard plots, which eventually appeared to be inadequate for testing cooperativity in assembly processes mixing intra- and intermolecular processes (Ercolani, 2003; Hamacek and Piguet, 2006; Hamacek et al., 2006; Piguet et al., 2005). The subsequent and remarkable kinetic studies establishing the intimate mechanisms of these assembly processes (Boukhalfa and Crumbliss, 2000; Charbonnière et al., 1997; Fatin-Rouge et al., 2000, 2001; Meyer et al., 1997) indeed remained very elusive on the operation of positive cooperativity, because of the lack, at that time, of clear definition of this concept for multicomponent processes involving intra- and intermolecular connections (Ercolani, 2003; Hamacek et al., 2006). Nevertheless, this belief in a strange and novel driving force favoring the target supramolecular architecture had a deep impact in the community and a large number of discrete 1D (racks, helicates), 2D (grids, circular helicates, metallacrown), and 3D complexes (clusters, boxes, polygons) were obtained thanks to a judicious match between the metal and ligand stereochemical properties (for comprehensive reviews, see Caulder and Raymond, 1999; Fujita et al., 2005; Lawrence et al., 1995; Leininger et al., 2000; Mulder et al., 2004; Piguet, 1999; Stoddart and Philp, 1996).

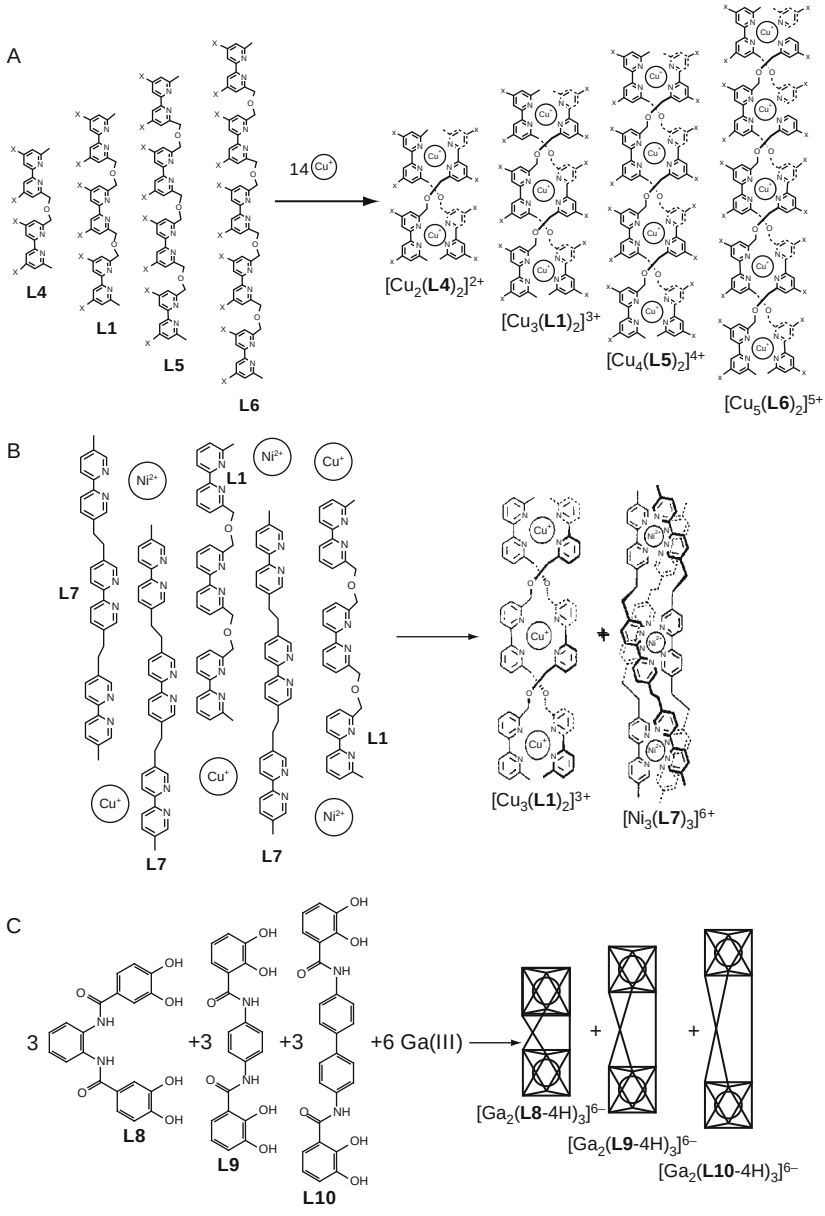

FIGURE 6 Self-recognition of (A) homopolymetallic double-stranded helicates $[Cu_m(\mathbf{L}k)_2]^{m+}$ ($k = 1$, 4–6; Krämer et al., 1993), (B) multiple-stranded helicates $[Cu_3(\mathbf{L1})_2]^{3+}$ and $[Ni_3(\mathbf{L7})_3]^{6+}$ (Krämer et al., 1993), and (C) homoleptic triple-stranded helicates $[Ga_2(\mathbf{L}k\text{-}4H)_3]^{6-}$ ($k = 8$–10; Caulder and Raymond, 1997) (reproduced by permission from Hamacek et al., 2006, © 2006 Royal Society of Chemistry).

1.3 Synthetic strategy, classification, and properties of self-assembled helicates

According to its definition, a helicate can be schematically represented as a series of helical mononuclear coordination complexes multiply linked by spacers and packed along a helical axis passing through the metal ions (Figure 7). Since the dative bonds connecting the peripheral ligand strands to the central metal ions are weak enough to allow reversibility at room temperature, the assembly process may explore the complete potential energy hypersurface, thus systematically providing the thermodynamically most stable complex (a process sometimes termed *self-healing*; Lehn, 1995).

The basic strategy for the generation of one particular helicate therefore relies on three crucial factors: (1) a judicious match between the intrinsic information borne by the metal (size, charge, polarizability, ligand-field stabilization) and the ligand strands (denticity of the binding units, steric constraints, type of donor atoms, nephelauxetic parameters); (2) a suitable set of external constraints, originally termed conditional information (Piguet, 1999), which affects the thermodynamic processes (solvent, stoichiometry, concentration, pressure, temperature); and (3) the free energy driving force brought by the principle of maximum site occupancy (Fyles and Tong, 2007; Hamacek et al., 2005a,b; Krämer et al., 1993; Lehn and Eliseev, 2001). Since 1987, the combinations of hundreds of sophisticated ligand strands with s-block, p-block, and d-block metal ions have been reported (Albrecht, 2001; Piguet et al., 1997a), which can be easily classified according to the simple method illustrated in Figure 8 for a binuclear double-stranded helicate.

Firstly, the total number of helical strands n wrapped about the helical axis defined by the metal ions corresponds to *single-* ($n = 1$), *double-* ($n = 2$), *triple-* ($n = 3$), and *quadruple*-stranded ($n = 4$) helicates. Secondly, ligand strands containing similar successive binding units are termed *homotopic*,

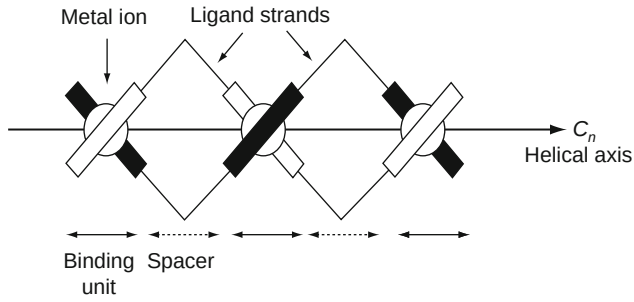

FIGURE 7 Schematic representation of a trinuclear double-stranded helicate.

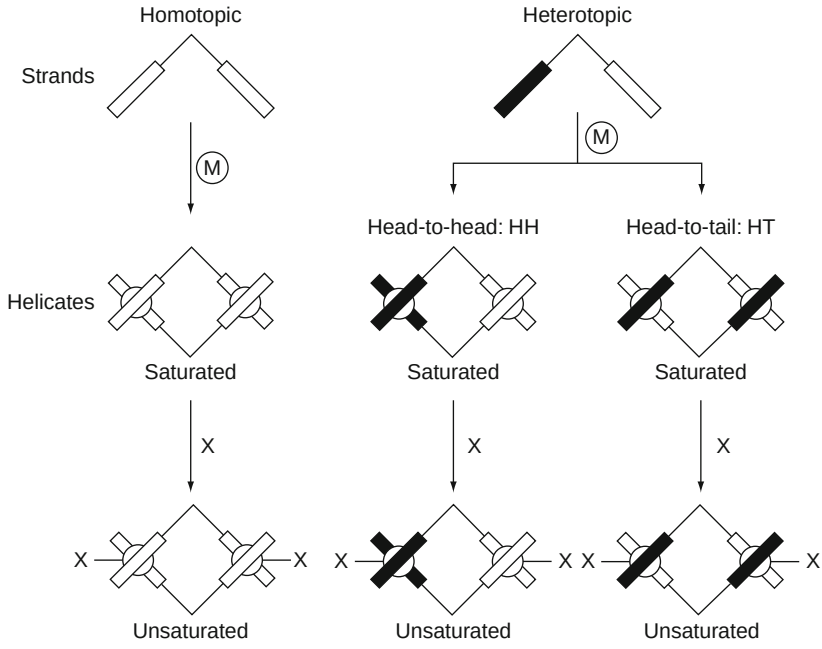

FIGURE 8 Classification of helicates according to their intrinsic information (reproduced by permission from Piguet et al., 1997a, © 1997 American Chemical Society).

while the consideration of different binding units refers to *heterotopic*. In the latter case, the relative orientation of the strands in the helicate is mentioned with the characters *H* (head) and *T* (tail) such as head-to-head and head-to-tail, corresponding to parallel, and, respectively, antiparallel arrangements. Thirdly, the coordination of ancillary ligands to the metal ion transforms a *saturated* helicate into its *unsaturated* counterpart (Figure 8). Finally, the total number of metal ions is indicated by the *multinuclearity* of the helicate, while the presence of different metals along the helical axis is defined by the *multimetallicity* of the helicate. It is, however, worth stressing here the relationship between the wrapping of the strand and the chirality of the final helicate (Cahn et al., 1966). Geometrically speaking, a helix is the figure generated by the motion of a point around and along a line, the helical axis. Ideally, the axis is a straight line and the two kinds of motions are circular at a constant distance *r* and linear, respectively, which eventually produces a cylindrical palindromic helix (i.e., a regular helix with a constant pitch = ratio of axially linear to angular properties; Figure 9; Brewster, 1974).

It may be right-handed (plus, *P*) or left-handed (minus, *M*) according to whether the rotation is clockwise, respectively anticlockwise, when the

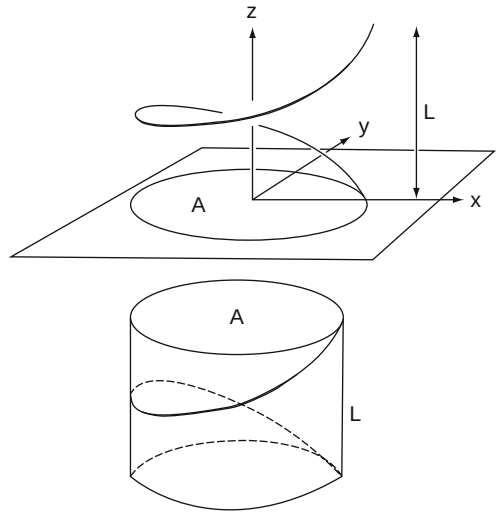

FIGURE 9 A single turn of a right-handed (*P*) circular palindromic single-stranded helix. *L* is the pitch, *z* is the helical axis, and *A* is the area of the subtended circle in the plane *xy* (reproduced by permission from Piguet et al., 1997a,b, © 1997 American Chemical Society).

helix is considered to wind from the viewers' eye toward a point distant from the viewer (Meurer and Vögtle, 1985). Obviously, the application of these theoretical geometrical concepts to a series of atoms connected by covalent bonds forming the strands of the helicate requires some minor adaptations (Piguet et al., 1997a), but the screw direction, measured by *P* or *M* helicities and induced by the wrapping of the strands, is crucial because it prevents the existence of symmetry operation of the second kind, and the helicates are thus potentially chiral objects (Cahn et al., 1966). If we ignore the helical portions produced by the spacers, that is, we neglect the contribution of the spacers to the total helical pitch (Figure 7), the helicity of the final helicate may be simply deduced from the absolute configurations Δ or Λ of the metal ions produced by the chelated strands (Figure 10).

For binuclear homotopic helicates with chelated strands, there are only two possibilities. Either the two metal ions possess the same absolute configurations and a pair of enantiomers is formed (*PP* or *MM*), or the metal ions display opposite absolute configurations, thus leading to an achiral side-by-side complex, sometimes called a mesocate (Albrecht, 2001). However, such unambiguous chiral characteristics are rarely met in practice because (i) the helical fractions defined by the spacers are rarely negligible; (ii) heterotopic strands produce helical portions of

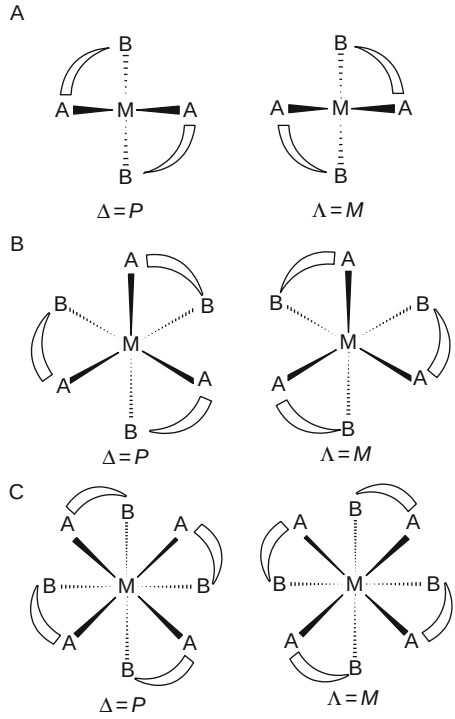

FIGURE 10 Absolute configurations and related helicities of (A) bis-chelate complexes viewed down the C_2-axis, (B) tris-chelate complexes viewed down the C_3-axis, and (C) tetrachelate complexes viewed down the C_4-axis. Bidentate binding units have been selected for the sake of clarity.

different nature, thus leading to chiral pairs of diastereomers for the side-by-side complexes; (iii) monodentate binding units do not induce chiral environments around metal ions; and (iv) for an odd number of metal ions, the side-by-side complexes correspond to amphiverse helices (i.e., helices containing only an excess of one type of helical portion; for a detailed discussion, see Piguet et al., 1997a). However, a more global chiral characteristic of the helices lies in the systematic existence of two opposite helical arrangements, depending on the symmetry axis considered for defining the helical wrapping (Figure 11). This property finds applications in a boat propeller, in which, for technical reasons, it is sometimes more relevant to rotate the helix by 90° while maintaining the same screw direction for the motor.

Please note that the quadruple-stranded helicate shown in Figure 11C is a typical example of a chiral helical object strictly produced by the wrapping of the spacers, while the square-planar Pd–N_4 units are achiral.

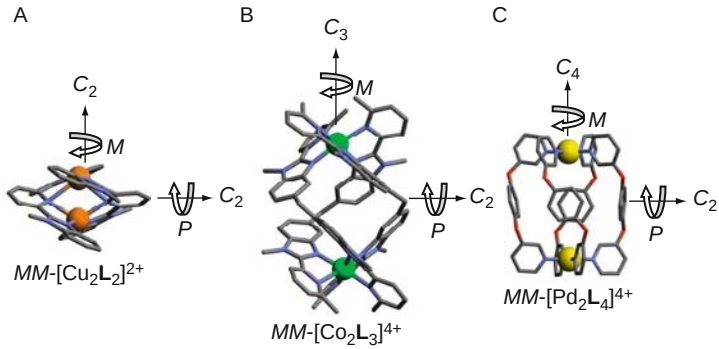

FIGURE 11 Crystal structures of (A) double-stranded (redrawn after Piguet et al., 1989a), (B) triple-stranded (redrawn after Williams et al., 1991), and (C) quadruple-stranded (redrawn after McMorran and Steel, 1998) helicates highlighting the relationship between the helicities about the main axis and the perpendicular twofold axes.

1.4 Introducing lanthanide ions into helicates

Despite their indubitable aesthetic appeal, the helicates severely suffer from the lack of significant applications, except for their confidential use as (i) precursors for topologically nontrivial entangled structures (for a review, see Lukin and Vögtle, 2005) and (ii) structural probes and cleaving agents for DNA (Hannon et al., 2001; Schoentjes and Lehn, 1995). Thanks to their rich metal-centered electronic, magnetic, and optical properties, the trivalent lanthanides, R^{III}, are obvious partners for pushing these supramolecular edifices into the field of nanoscopic functional devices (Bünzli and Piguet, 2002). However, the limited expansion of the valence 4f-orbitals, which are shielded from external perturbations by the filled $5s^2$- and $5p^6$-orbitals, produces R^{III}-ligand coordination bonds displaying faint covalency, and consequently no pronounced stereochemical preferences of electronic origin (Bünzli and Piguet, 2005). The coordination geometry around R^{III} thus results from their large electrostatic factors ($z^2/R = 8.72$–10.45 eu^2 Å^{-1} along the lanthanide series), combined with the minimization of steric interligand repulsions. Coordination numbers $CN = 8 - 10$ are common for complexes in solution (Cotton, 2006), among which $CN = 9$, associated with a D_{3h}-symmetrical tricapped-trigonal prismatic arrangement of the donors atoms, is standard. Consequently, the programming of lanthanide helicates relies almost exclusively on the judicious design of ligand strands possessing either tridentate chelating units to give saturated triple-stranded helicates ($CN = 9$; Figure 12A; Piguet et al., 1992a), or bidentate chelating units to give saturated quadruple-stranded helicates ($CN = 8$; Figure 12B; Basset et al., 2004; Dong et al., 2007; Xu and Raymond, 2006). Though the detailed understanding

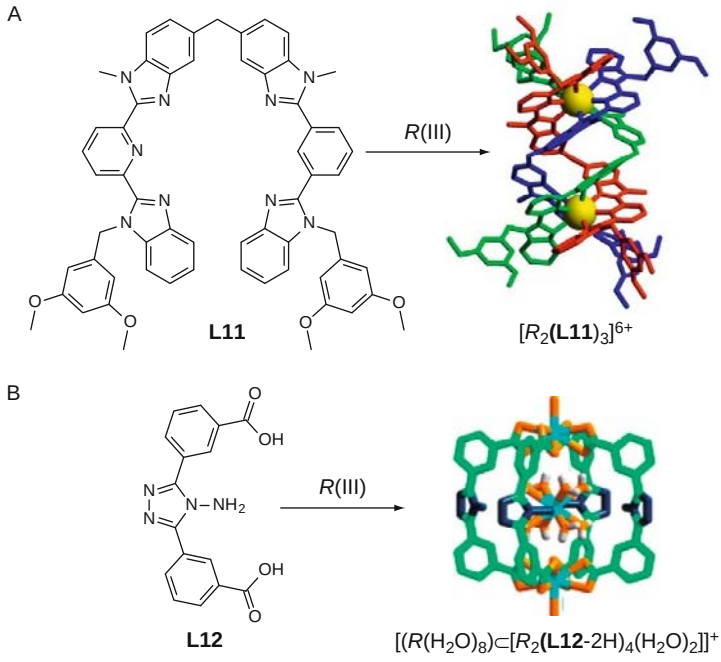

FIGURE 12 Stereochemical match between (A) bis-tridentate (redrawn after Piguet et al., 1992a) and (B) bis-bidentate segmental ligands with trivalent lanthanides to give triple-stranded, respectively, quadruple-stranded helicates (reproduced by permission from Dong et al., 2007, © American Chemical Society).

and control of the self-assembly of lanthanide triple-stranded helicates have been the subject of considerable efforts since their discovery in 1992 (Hamacek et al., 2005a,b), the variable coordination numbers and geometries adopted by R^{III} ions, combined with their entropic affinity for negatively charged oxygen donors, often perturb the assembly process due to the competitive formation of alternative unsaturated complexes. For instance, the bis-bidentate ligand **L13**^{b} reacts with $R(ClO_4)_3$ in acetonitrile to give the expected chiral triple-stranded helicate $[R_2(\mathbf{L13}^{b})_3]^{6+}$ (Figure 13; Martin et al., 1998). However, the use of the slightly more competing triflate anions in $R(CF_3SO_3)_3$ produces the centrosymmetric achiral unsaturated side-by-side complex $[R_2(\mathbf{L13}^{b})_2(H_2O)_4(CF_3SO_3)_4]^{2+}$ with zero net helicity (Figure 13; Martin et al., 1998).

Finally, the choice of the spacer is crucial because minor structural variations may dramatically affect the issue of the thermodynamic assembly process with lanthanides, a situation encountered when the potential free energy hypersurface is rather flat. The bis-tridentate ligand **L14**, which is designed to produce triple-stranded helicates, indeed gives the

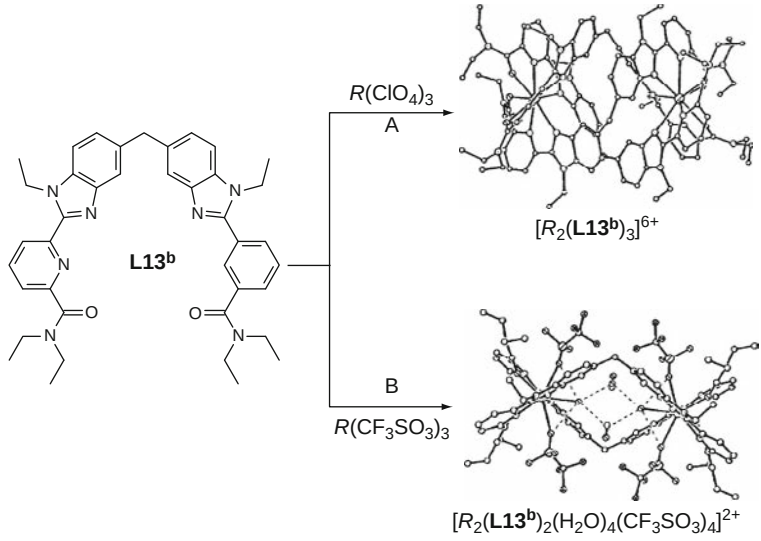

FIGURE 13 Formation of (A) a binuclear saturated triple-stranded lanthanide helicate and (B) a binuclear unsaturated double-stranded side-by-side lanthanide complex (redrawn after Martin et al., 1998).

expected assembly only with diphenylene spacers (Figure 14A), while the use of para-xylyl spacers provides an alternative unsaturated bidimensional circular helicate (Figure 14B; Senegas et al., 2005).

A similar limitation has been recently reported for the synthesis of unsaturated triple-stranded binuclear lanthanide helicates with bis-bidentate acylpyrazolone ligand strands and some analogues of bis-β-diketonate ligands, for which only the ethyl spacer was found to form the targeted helical complex (Semenov et al., 2008).

1.5 Scope of the review

The report on the first lanthanide-containing helicate in 1992 (Figure 12A; Piguet et al., 1992a) established, for more than a decade, the systematic use of 2,6-disubstituted pyridines (N_3, N_2O, and NO_2 donor sites) as the unique building block for the preparation of triple-stranded $[R_m\mathbf{L}_3]^{3m+}$ helicates (Figure 15; Bünzli and Piguet, 2002). The only exception has been the short report by Goodgame et al. (1993) on the triple-helical wrapping of a *p*-xylene-bridged bis(2-pyridone) ligand featuring two monodentate coordination units around two neodymium ions, the inner coordination sphere of the metal ions being completed by three bidentate nitrates. The second deliberate design of a noncontaining pyridine binding unit for the self-assembly of lanthanide helicate has been reported in 2004, whereby

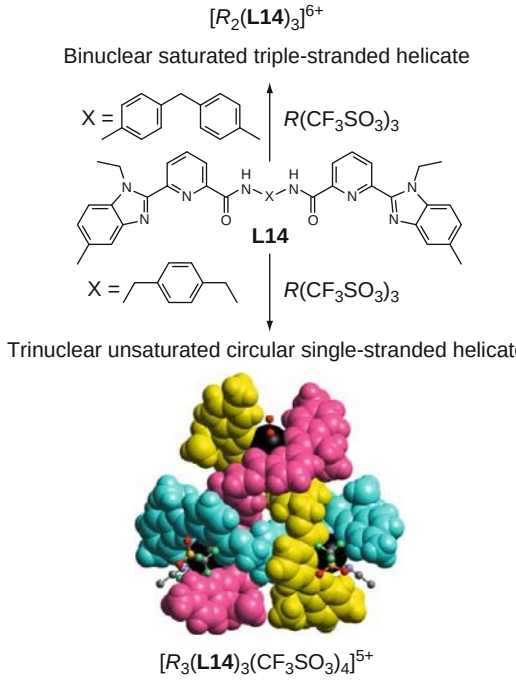

FIGURE 14 Influence of the spacer on the assembly process (bottom structure reproduced by permission from Senegas et al., 2005, © 2005 Royal Society of chemistry).

two bidentate β-diketonates (O_2 donor site) are connected by a spacer to give a bis-bidentate ligand strand, which is able to produce binuclear triple- and quadruple-stranded helicates when reacted with R^{III} (Basset et al., 2004). Later, analogous bidentate O_2 donor sites in bis-acylpyrazolone strands have been reacted with R^{III} to give unsaturated triple-stranded binuclear lanthanide helicates (Semenov et al., 2008), while related bidentate β-diketonates (Xu and Raymond, 2006) or carboxylates (Dong et al., 2007) binding units have been used for the isolation and structural characterization of related actinide and lanthanide quadruple-stranded helicates. More recently, alternative tridentate ligands based on 8-hydroxyquinoline (N_2O donor site) have been described for the design of standard triple-stranded lanthanide helicates (Albrecht et al., 2007a,b; Shavaleev et al., 2008).

After an introductory chapter on mononuclear precursors with benzimidazolepyridine or dipicolinic acid derivatives, this chapter mainly focuses on the rich chemical adventure provided by the systematic exploitation of the 2,6-disubstituted pyridine units for the self-assembly of lanthanide helicates (Sections 2–6). Section 7 aims at opening some

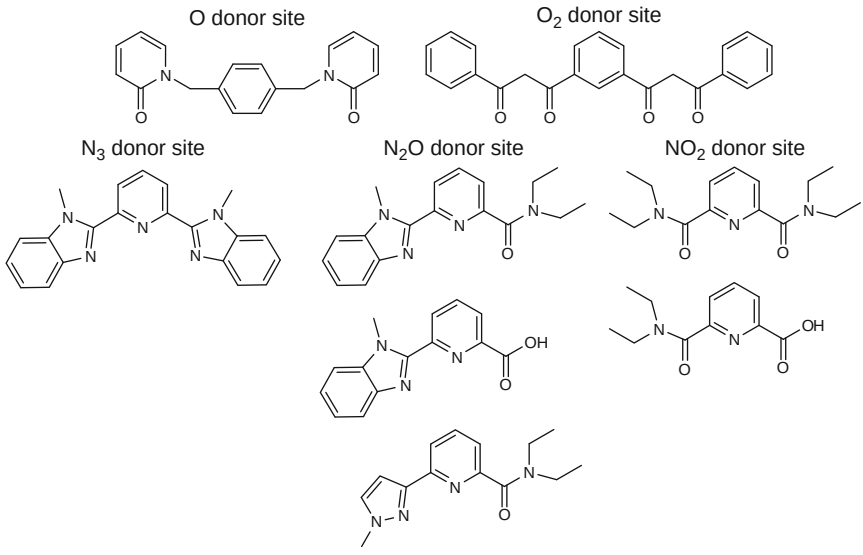

FIGURE 15 Top: oxygen-donor ligands used by Basset et al. (2004) and Goodgame et al. (1993). Bottom: tridentate 2,6-disubstituted pyridines used as binding units for the design of lanthanide helicate since 1992.

perspectives for the design of polymetallic helicates containing at least one trivalent lanthanide, but combined with s-, p-, or d-block metal ions. Finally, Section 8 reports on the few examples of lanthanide or actinide helicates which are built from noncontaining pyridine binding units. In addition to ligand design and structural information, detailed thermodynamic aspects of the self-assembly processes are reviewed, as well as the relationship between the helicate structure and their photophysical properties. Moreover, Section 6 describes practical applications of luminescent binuclear helicates in bioanalyses with emphasis on live cell staining and DNA analysis. Literature is fully covered until the end of October 2008.

Note regarding nomenclature. The term ''nuclear'' (e.g., polynuclear) is used to characterize assemblies into which several metal ions are imbedded while ''metallic'' (e.g., bimetallic, trimetallic) indicates that the molecule contains different metal ions.

2. MONONUCLEAR 4f TRIPLE-HELICAL PRECURSORS

During the last two decades, the supramolecular approach greatly contributed to the rapid evolution of standard coordination chemistry, usually limited to mono- and binuclear complexes, toward more complicated and sophisticated nanometric edifices bearing novel functionalities.

The associated bottom-up process thus relies on the identification of building blocks connected by weak (i.e., noncovalent) interactions and possessing specific physicochemical properties, which can be further tuned by intercomponent communications operating at the (supra)molecular level (Lehn, 1995).

2.1 Choice and synthesis of mononuclear building blocks

Among the different factors controlling the thermodynamic stability of a coordination complex, the free energy change related to the formation of intermolecular metal–ligand bonds, modulated by desolvation, plays a crucial role (see Section 1.3). In view of the apparent preference for nine-coordination in complexes with small unidentate ligands (e.g., water or acetonitrile; see Figure 16, bottom) and given that the resulting tricapped-trigonal prismatic coordination environment both possesses an interesting symmetry (D_{3h}) and usually prevents interaction with additional donor molecules, targeting such a coordinative environment for lanthanide ions results in compounds with intense emissive properties. Because trivalent lanthanides, R^{III}, display no pronounced stereochemical preferences (see Section 1.4), the intrinsic information borne by the ligand entirely controls the structural output of the target mononuclear building blocks. To limit the geometrical and thermodynamic possibilities offered

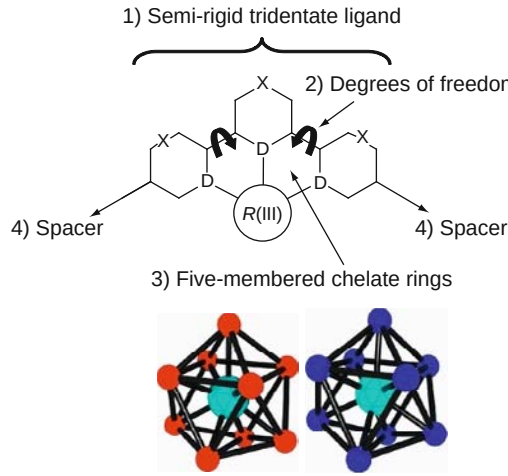

FIGURE 16 Top: stereochemical criteria to be met by a terpyridine-like ligand for the design of regular C_3-symmetrical mononuclear triple-helical building blocks. Bottom: tricapped-trigonal prismatic coordination geometry encountered in (left) R^{III} aquo ions $[Eu(H_2O)_9]^{3+}$ (redrawn after Moret et al., 1991) and (right) $[Eu(MeCN)_9]^{3+}$ (redrawn after Shen et al., 1990).

by the complete exploration of the energy hypersurface, the ligand-binding properties must obey four strict stereochemical requirements (Figure 16):

(1) The use of semirigid tridentate binding units restricts the structural issues to $[R(\mathbf{L}^{k})_{n}]^{3+}$, whereby $n = 1$–3 characterizes the number of strands wrapped about the central metal. The target C_3-symmetrical triple-helical complex $[R(\mathbf{L}^{k})_{3}]^{3+}$ can be further produced as the major species thanks to a strict control of the conditional information expressed in the stoichiometric ratio R:$\mathbf{L}^{k} = 1$:3 (i.e., entropic selection).
(2) An optimum set of degrees of freedom must be implemented in the tridentate binding unit in order to allow helical wrapping while forcing meridional tricoordination leading to the exclusive formation of a tricapped-trigonal prismatic arrangement of the nine donor atoms around the central lanthanide in $[R(\mathbf{L}^{k})_{3}]^{3+}$ (Ruiz-Martinez et al., 2008), much as is found in the aquo ions (Bünzli, 1998) or in the acetonitrile solvates (Shen et al., 1990).
(3) For large cations such as R^{III}, the chelate effect is enthalpically optimized for five-membered chelate rings (Motekaitis et al., 1994).
(4) Since each mononuclear building block has to be connected to its neighbors in the final helicate, spacers must be grafted at the end of tridentate binding units, which are able to transmit the helical twist along the complete strand.

Pyridine rings substituted at the 2- and 6-positions by semirigid coordinating side arms, which are further connected to spacers, indeed fit these criteria (Figure 15). Moreover, the low-energy $\pi \rightarrow \pi^*$ electronic transition centered onto the pyridine ring may be exploited for light-harvesting and indirect sensitization of the central lanthanide cation (Sabbatini et al., 1996). Some aspects of this structural pattern can be found in the commercially available tridentate ligand 2,6-dipicolinic acid (Figure 17A; Grenthe, 1961; Harrowfield et al., 1995) and 2,2′:6′,2″-terpyridine (Figure 17B; Durham et al., 1969; Frost et al., 1969; Semenova et al., 1999).

Both types of triple-helical complexes $[R(\mathbf{L15})_3]^{3-}$ and $[R(\mathbf{L16})_3]^{3+}$ display pseudotricapped-trigonal prismatic arrangements of the nine donor atoms in the solid state (N_3O_6 for $[R(\mathbf{L15})_3]^{3-}$ and N_9 for $[R(\mathbf{L16})_3]^{3+}$). Detailed solution studies of $[R(\mathbf{L15})_3]^{3-}$ in water demonstrate that the dynamically average D_3-symmetrical triple-helical structure is maintained at millimolar concentration, but with a significant increase of the amplitude of the fast flip–flop oscillation of the central pyridine rings with the larger lanthanides (Ouali et al., 2002; Piguet and Geraldes, 2003). The tris-chelates $[R(\mathbf{L15^a})_3]^{3-}$ with R = Eu, Tb display intense luminescence thanks to sensitization through the $(\mathbf{L^{15a}})^{2-}$ triplet

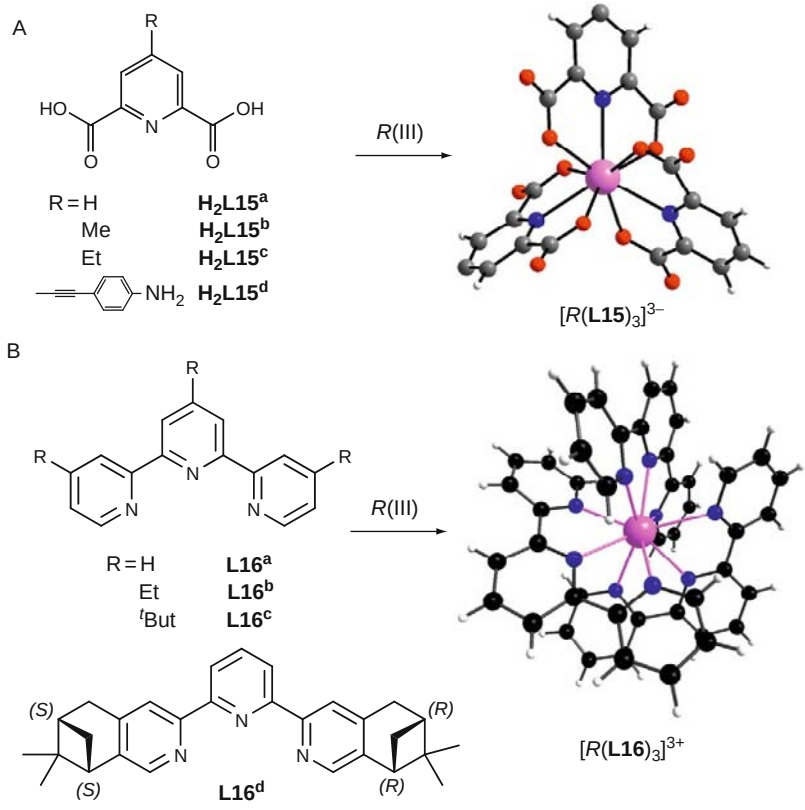

FIGURE 17 Schematic formation of D_3-symmetrical lanthanide triple-helical building blocks with (A) 2,6-dipicolinic acid and (B) 2,2′:6′,2″ terpyridine. Structures of the complexes $[Eu(\mathbf{L15^a})_3]^{3-}$ and $[Eu(\mathbf{L16^a})_3]^{3+}$ are redrawn from Harrowfield et al. (1995) and Semenova et al. (1999), respectively.

state (Aspinall, 2002) or, possibly, as has been suggested for Tb, through the singlet state (Kleinerman, 1969). Because of their strong visible luminescence, the $[R(\mathbf{L15^a})_3]^{3-}$ chelates were thoroughly investigated both in the solid state (Hopkins et al., 1996) and in aqueous solution (An et al., 2000; Chauvin et al., 2004; Huskowska and Riehl, 1995; Meskers and Dekkers, 2001; Werts et al., 2002). Introduction at the 4-position of the pyridine ring of small substituents (e.g., OH, Cl, Br, NH_2, or $NHCOCH_3$) modulates the photophysical properties of Tb complexes (Lamture et al., 1995), while grafting a substituted polyoxyethylene pendant on the same position additionally results in better water solubility and potentiality for conjugation of the helical complexes with biomolecules (see Section 2.5.3; Gassner et al., 2008).

A striking feature of the dipicolinate tris-complexes is the *P*-$[R(\mathbf{L15^a})_3]^{3-} \rightleftharpoons$ *M*-$[R(\mathbf{L15^a})_3]^{3-}$ helical interconversion occurring in the ground state ($k_{rac} = 50$–$200\ s^{-1}$ for $R =$ Eu–Yb; Ouali et al., 2002) and in the excited state ($k_{rac} = 10\ s^{-1}$ for Eu($^5D_0$); Huskowska and Riehl, 1995; Meskers and Dekkers, 2001), which is fast enough to prevent preparative helical separations, but slow enough to evidence Pfeiffer effects or chiral enrichments in the excited state when $[R(\mathbf{L15^a})_3]^{3-}$ interact with chiral substrates (Richardson et al., 1991), respectively, with polarized excitation light beams (Gawryszewska et al., 2006).

Compared with $[R(\mathbf{L15^a})_3]^{3-}$, the stability of the triple-helical cation $[R(\mathbf{L16^a})_3]^{3+}$ is much smaller because of the lack of charge neutralization accompanying the complexation process. Consequently, the triple-helical structure is only observed in the solid state (Semenova et al., 1999). In an aprotic polar solvent such as anhydrous acetonitrile, partial on–off equilibria of the distal pyridine rings gives predominantly eight-coordinated structures at millimolar concentrations (Chapman et al., 1984). Peripheral substitution at the 4-positions of the pyridine rings in $\mathbf{L16^b}$ and $\mathbf{L16^c}$ has only a minor effect on the stability and solution structures of the triple-helical complexes $[R(\mathbf{L16})_3]^{3+}$, but significantly increases metal-centered luminescence upon ligand irradiation (Mürner et al., 2000). Surprisingly, the connection of chiral alkyl six-membered rings at the 4- and 5-positions of the distal pyridine rings in $\mathbf{L16^d}$ improves the stability of the final lanthanide complex to such an extent that a single diastereomer, *P*-$[R(\mathbf{L16^d})_3]^{3+}$ or *M*-$[R(\mathbf{L16^d})_3]^{3+}$, can be detected in 5 mM acetonitrile solution (Muller et al., 2002a). Considering the behavior of the triple-helical lanthanide building blocks with the series of ligands **L15** and **L16**, it is clear that the first series provides final $[R(\mathbf{L15})_3]^{3-}$complexes which are stable enough for the self-assembly process being effective in solution, but which cannot be connected to spacers compatible with the transmission of helical twist in polynuclear helicates. On the other hand, the terpyridine backbone, although more difficult to modify (Cargill Thompson, 1997; Piguet et al., 1993a), is better suited for being incorporated within a segmental helical strand (Hasenknopf et al., 1996; Rapenne et al., 1999). However, the limited thermodynamic stability and the poor kinetic inertness of the triple-helical building blocks $[R(\mathbf{L16})_3]^{3+}$ are severe handicaps for their consideration for the self-assembly of polynuclear helicates. On the other hand, the replacement of the distal pyridine ring in **L16** (Figure 17) with *N*-alkylated benzimidazole rings in **L17** (Figures 18 and 19) leads to semirigid extended aromatic tridentate NNN heterocyclic binding units, which are easy to modify, and well suited for their inclusion into segmental helical ligands (Piguet et al., 1994). Moreover, the basicity of these ligands is comparable to that of terpyridine and the grafting of two five-membered rings at the 2- and 6-positions of the central pyridine ring in **L17** reduces steric crowding

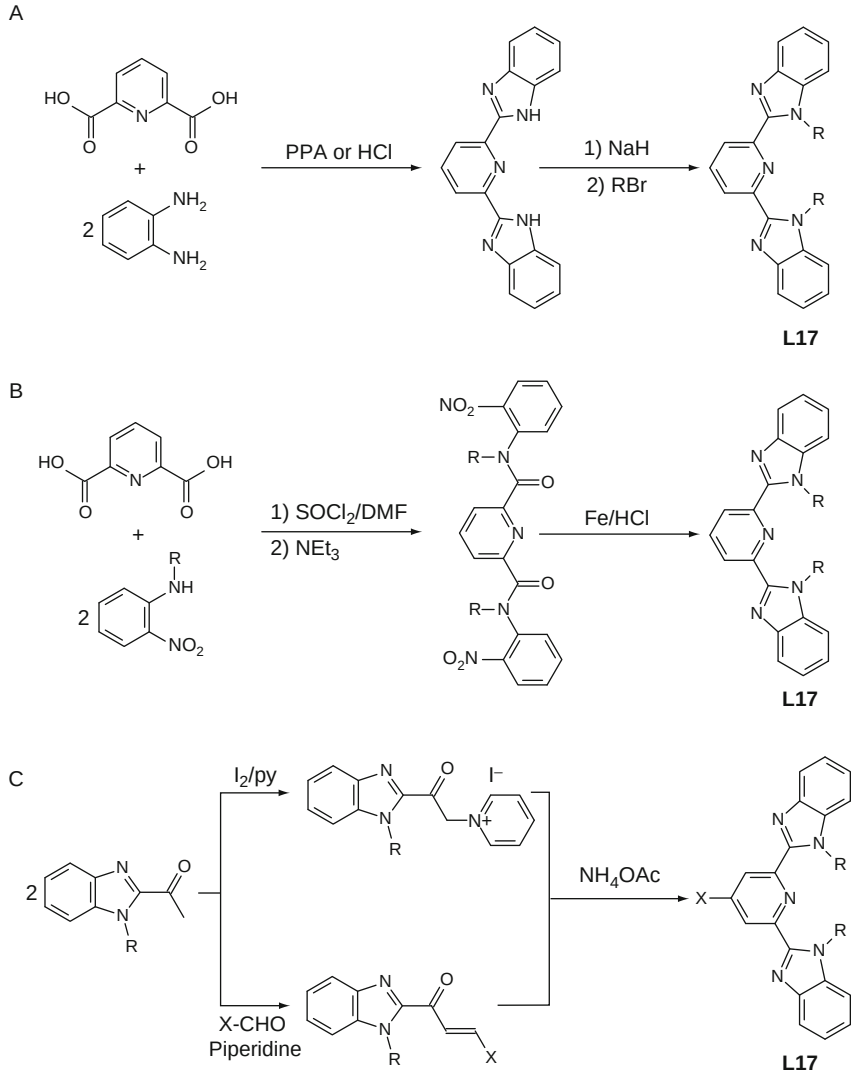

FIGURE 18 Preparation of substituted 2,6-bis(benzimidazol-2-yl)pyridine ligands **L17** following (A) original intermolecular *Phillips* reaction, (B) intramolecular *Piguet* cyclization, and (C) *Kröhnke* methodology.

upon complexation to R^{III} (Piguet et al., 1992b); this eventually produces robust triple-helical building blocks $[R(\mathbf{L17})_3]^{3+}$ for helicate self-assembly in aprotic solvents (Piguet et al., 1993c).

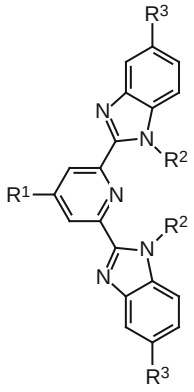

Ligand	R^1	R^2	R^3	References
L17[a]	H	CH_3	H	Piguet et al., 1989b
L17[b]	H	C_2H_5	H	Piguet et al., 1993b
L17[c]	H	C_3H_7	H	Piguet et al., 1993b
L17[d]	H	$(CH_2)_7CH_3$	H	Piguet et al., 1989b
L17[e]	H	$(CH_3O)_2C_6H_3$	H	Piguet et al., 1993b
L17[f]	H	C_2H_5	CH_3	Piguet et al., 1995a
L17[g]	Ph	$(CH_3O)_2C_6H_3$	H	Piguet et al., 1993a
L17[h]	$PhNO_2$	$(CH_3O)_2C_6H_3$	H	Piguet et al., 1993a
L17[i]	$PhNEt_2$	$(CH_3O)_2C_6H_3$	H	Piguet et al., 1993a
L17[j]	$PhNEt_2$	CH_3	H	Petoud et al., 1997a
L17[k]	H		H	Muller et al., 2001a
L17[l]		CH_3	H	Muller et al., 2002b

FIGURE 19 C_2-symmetrical tridentate 2,6-bis(benzimidazol-2-yl)pyridine ligands prepared for the design of lanthanide triple-helical building blocks $[R(\mathbf{L17})_3]^{3+}$.

2.1.1 Synthetic strategy: Benzimidazolepyridine derivatives

A classical intermolecular strategy (Phillips, 1928; Wright, 1951) was first used for preparing 2,6-bis(benzimidazol-2-yl)pyridine (Addison and Burke, 1981; Addison et al., 1983) followed by double *N*-alkylation (Figure 18A; Piguet et al., 1989b). The subsequent development of an intramolecular version of this reaction by Piguet et al. (1994) offers unique perspectives in terms of selectivity and stereochemical control, a crucial point for the preparation of nonsymmetrical tridentate binding units and for the connection of spacers to the terminal benzimidazole rings (Figure 18B). Finally, the central pyridine ring can be modified using either a *Kröhnke* methodology (Kröhnke, 1963) for grafting substituents at the 4-position (Figure 18C; Muller et al., 2002b; Piguet et al., 1993a), or the direct use of adequately 4-substituted dipicolinic acid derivatives **L15** (Chauvin et al., 2001).

Recently, a slightly modified one-pot synthetic approach to 2,6-bis (benzimidazole)pyridine was proposed by reacting aromatic ditopic *o*-nitroamines with aryl diacid chlorides (Figure 20). The noticeable modification from the method proposed by Piguet et al. (Figure 18B) is to run the reaction in *N*-metyl-2-pyrrolidinone (NMP) as solvent while keeping activated iron as the reducing agent in the last step; in this way, a yield of 90% is obtained for the reduction/ring closing reaction. Alternatively, to avoid the disadvantages of activated iron, namely the strong binding of Fe^{II} to the final product, necessitating EDTA treatment to remove it, and its high cost, cheaper sodium dithionite ($Na_2S_2O_4$) can be used as mild

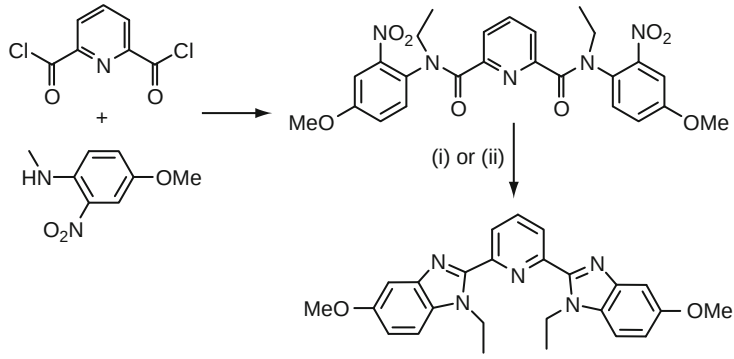

FIGURE 20 One-pot synthetic pathways to 2,6-bis(benzimidazole)pyridines proposed by McKenzie et al. (2008): (i) NMP, 50 °C, 8 h; activated Fe, NMP, HCl, 90 °C; EDTA(aq) and (ii) $Na_2S_2O_4$, DMF, EtOH, H_2O, 85 °C, 18 h.

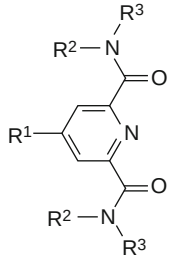

Ligand	R^1	R^2	R^3	References
L18[a]	H	C_2H_5	C_2H_5	Renaud et al., 1997a
L18[b]		C_2H_5	C_2H_5	Muller et al., 2001b
L18[c]	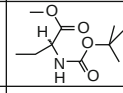	C_2H_5	C_2H_5	Muller et al., 2001b
L18[d]	H	$(CH_3)_2CH$	$(CH_3)_2CH$	LeBorgne et al., 2003
L18[e]	H	C_6H_5-CH_2	C_6H_5-CH_2	LeBorgne et al., 2003
L18[f]	H	C_6H_5-CH_2	H	LeBorgne et al., 2003
L18[g]	H	$C_{10}H_6$-$CH(CH_3)$	H	Leonard et al., 2007

FIGURE 21 C_2-symmetrical tridentate 2,6-bis(carboxamido)pyridine ligands prepared for the design of lanthanide triple-helical building blocks $[R(\mathbf{L18})_3]^{3+}$.

reducing reagent, although to the expense of a reduced yield of about 70% (McKenzie et al., 2008).

Following the endlessly repeated, but questionable assertion that trivalent lanthanide are mainly oxophilic (Jocher et al., 2007; Senegas et al., 2003), the distal benzimidazole groups of **L17** have been replaced with amide groups in **L18** (tridentate ONO donor) to give triple-helical building blocks $[R(\mathbf{L18})_3]^{3+}$ (Figure 21). Whereas the syntheses from dipicolinic acids **L15** are straightforward, the preparation of secondary and tertiary amides ensures the possible connection to spacers and the inclusion of the ONO tridentate binding unit **L18** within helical segmental ligands.

The unsymmetrical tridentate NNO ligands **L19**, in which the central pyridine ring is decorated with one benzimidazole unit and one carboxamide group, have been synthesized by using either 2-carboxamido-6-carboxylatopyridine (Chauvin et al., 2001) or 2-benzimidazole-6-carboxylatopyridine (Le Borgne et al., 2004; Piguet et al., 1994) synthons (Figure 22). Upon reaction with R^{III}, the triple-helical precursors $[R(\mathbf{L19})_3]^{3+}$ exist as mixtures of meridional and facial conformers (see Figure 28 in Section 2.2). Finally, the hydrolysis of the amide group of **L19** produces unsymmetrical 2-benzimidazole-6-carboxylatopyridine ligands, which have been introduced into segmental helical ligands (Chauvin et al., 2007, 2008; Deiters et al., 2008; Edder et al., 1997; Elhabiri et al., 1999, 2004a; Vandevyver et al., 2007) or connected to covalent tripods in order to avoid meridional/facial isomerization (Senegas et al., 2003). It is worth noting that the alternative connection of ester groups at the 2- and 6-position of the pyridine ring gives tridentate ONO ligand whose weak affinity for R^{III} is not compatible with their use in triple-helical complexes (Renaud et al., 1997b).

2.1.2 Synthetic strategy: Dipicolinic acid derivatives

The dipicolinic acid platform has proven to be extremely versatile, leading to numerous applications of its tris-complexes with Eu and Tb, in particular in analytical and bioanalytical chemistry (see Section 2.5 for photophysical properties and Section 6.2 for bioanalytical applications). As a consequence, researchers have invented ways of modulating the photophysical properties, principally by introducing substituents on the para position of the pyridine ring, a relatively easy synthetic procedure. Simple substituents (e.g., Cl, Br, NH_2, $NHCOCH_3$) are introduced by substitution of the hydroxyl function of chelidamic acid under

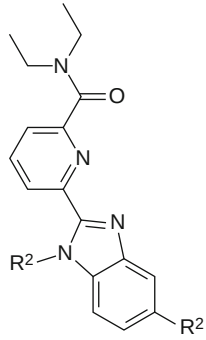

Ligand	R^1	R^2
L19[a]	CH_3	H
L19[b]	C_2H_5	H
L19[c]	$(CH_3O)_2C_6H_3$	H
L19[d]	C_2H_5	CH_3OCH_2

FIGURE 22 C_s-symmetrical tridentate 2-benzimidazole-6-carboxamidopyridine ligands prepared for the design of lanthanide triple-helical building blocks $[R(\mathbf{L19})_3]^{3+}$ (Le Borgne et al., 2004).

appropriate, although harsh, conditions (Figure 23). This substitution is easy in view of the presence of the pyridine electron-withdrawing group in para position with respect to the hydroxyl function. Milder conditions for the synthesis of the 4-bromo derivative **L15^{f}** have been recently proposed which involve reacting chelidamic acid with tetrabutylbromide in toluene and in presence of phosphorus pentoxide (Picot et al., 2008b). One notes, however, that purification of the ligands under their acidic form, either by recrystallization or by ion-exchange chromatography gives poor results. Therefore, a customary procedure is to purify the corresponding ester by silica-gel chromatography and subsequent recrystallization, followed by quantitative hydrolysis under mild conditions (Lamture et al., 1995).

For more elaborate applications, such as bioprobes or nonlinear optical materials, the dipicolinate framework has been considerably expanded and decorated with π-conjugated and/or solubilizing groups (D'Aléo et al., 2008a,b). Introduction of a π-system in the 4-position is meant to induce charge transfer onto the pyridine moiety and is achieved through a

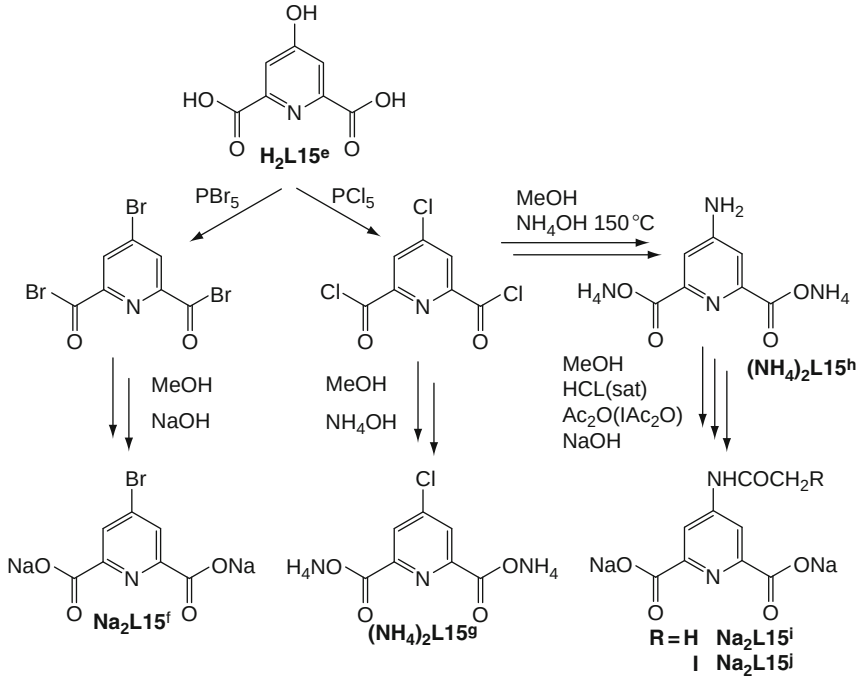

FIGURE 23 Synthetic paths for simple 4-pyridine-substituted dipicolinates (Lamture and Wensel, 1995; Lamture et al., 1995).

Pd-catalyzed Sonogashira cross-coupling reaction (Sonogashira et al., 1975) on 4-bromo or on more reactive iodo-substituted dipicolinic frameworks whereby either the dialkyl (methyl, ethyl) ester or diamide forms can be used (Picot et al., 2008b; Platas-Iglesias et al., 2001). While the bromo derivatives led to deceptively low yields (<45%), the less stable 4-iodo synthons proved to be much more effective with yields for the final ligands larger than 90%. Alternatively, the π-conjugated system can be introduced in the 2- and 6-positions by direct amidation of the carboxylic acid functions (Figure 24; Picot et al., 2008a).

The design of bifunctional chelating agents with a multidentate unit for coordination to R^{III} ions and an additional functionality is essential in bioanalyses, for instance for labeling DNA molecules or targeted proteins with lanthanide luminescent labels. One of the preferred position for the latter functionality is again the 4-position and an early example is $\mathbf{H_2L15^j}$ (Figure 23). Another strategy is to take advantage of the lipophilic properties of polyoxyethylene fragments which, in addition, are amenable to easy derivatization. Ligands $\mathbf{H_2L15^s}$ to $\mathbf{H_2L15^v}$ which bear a $(CH_2–CH_2–O)_3$ short pendant arm functionalized with hydroxyl, methoxy, amine, or phthalimide groups, have been synthesized bearing this idea in mind (Gassner et al., 2008). They were obtained either under the acidic form or as the sodium salt in 45–57% yield, starting from the diethylester of chelidamic acid. The polyoxyethylene pendant was grafted first by using a Mitsunobu reaction (Mitsunobu and Yamada, 1967). Hydrolysis of the resulting ester led to $\mathbf{H_2L15^s}$ whereas treatment with iodotrimethylsilane and subsequent hydrolysis yielded $\mathbf{H_2L15^t}$. For the other two ligands, $\mathbf{H_2L15^u}$ and $\mathbf{H_2L15^v}$, two successive Mitsunobu reactions were used to couple the polyoxyethylene arm onto a phthalimide group and then the resulting product to the dipicolinate framework; hydrolysis under specific conditions yielded either one of the ligands (Figure 25).

2.2 Solid state and solution structures of the mononuclear triple-helical precursors

Upon reaction of hydrated $R(ClO_4)_3$ or $R(CF_3SO_3)_3$ salts with the tridentate ligands **L15** in water and **L17–L19** in organic solvents, the complexes $[R(\mathbf{L15})_n]^{(3-2n)+}$ or $[R(\mathbf{Lk})_n]^{3+}$ ($n = 1$–3) are successively formed. Depending on the specific substituents borne by the ligands, the macroscopic formation constants $\beta_{1,n}^{R,Lk}$ may drastically vary (see Section 2.3), but the large majority of C_2-symmetrical ligands **L15**, **L17**, and **L18** eventually produces D_3-symmetrical triple-helical chelates $[R(\mathbf{L15})_3]^{3-}$ or $[R(\mathbf{Lk})_3]^{3+}$, while the C_1-symmetrical ligands **L19** give mixtures of *mer*-$[R(\mathbf{L19})_3]^{3+}$ (C_1-symmetry) and *fac*-$[R(\mathbf{L19})_3]^{3+}$ (C_3-symmetry) complexes. Numerous crystal and molecular structures have been reported for tris(dipicolinates) $[R(\mathbf{L15})_3]^{3-}$ showing the influence of the counterion on the triple-helical

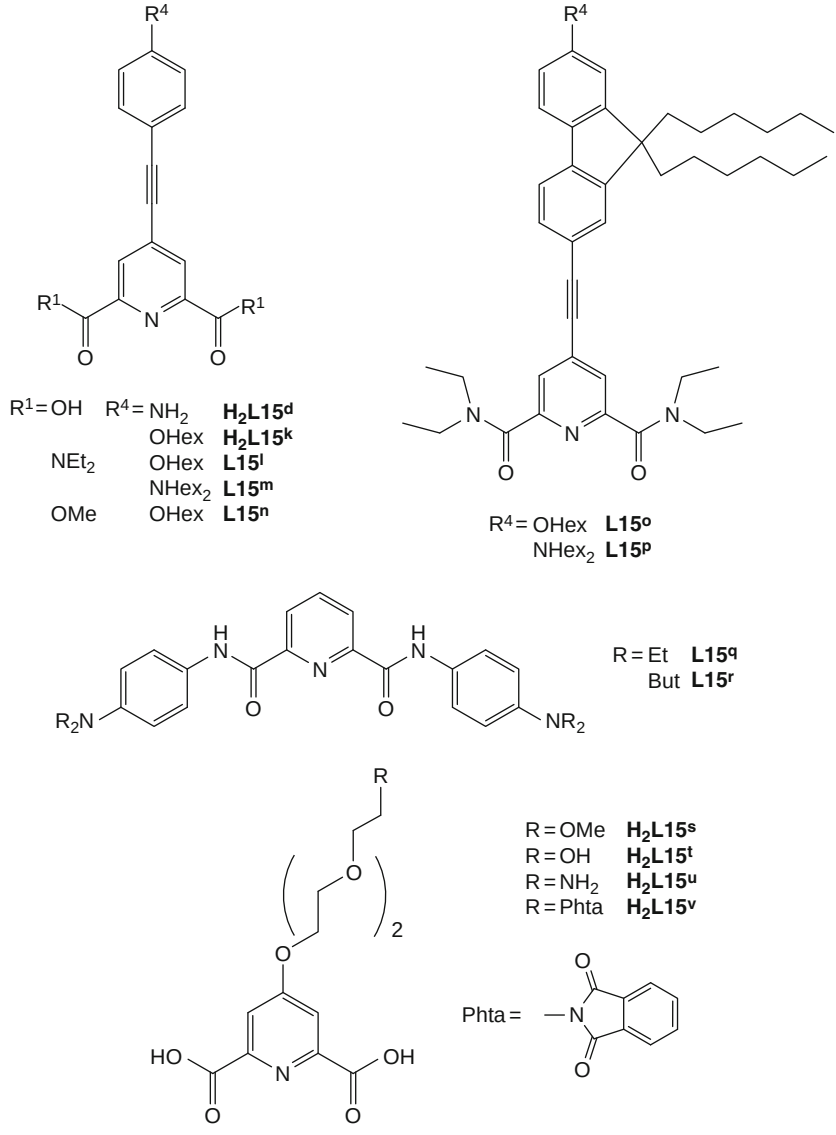

FIGURE 24 π-Conjugated (**L15^{d-r}**; Picot et al., 2008a) and polyoxyethyleneglycol-fitted dipicolinic acid derivatives (**H_2L15^{s-v}**; Gassner et al., 2008).

structure with idealized D_3-symmetry (Brayshaw et al., 1995). The crystal structure of $[Eu(\mathbf{L17^a})_3]^{3+}$ demonstrates the formation of pseudo-D_3-symmetry in the triple-helical complexes with the central lanthanide atom

being nine-coordinated in a pseudotricapped-trigonal prismatic arrangement (Figure 26; Piguet et al., 1993c), a structural pattern previously reported for the analogous complexes $[Eu(\mathbf{L16^a})_3]^{3+}$ (Figure 17B; Durham et al., 1969; Frost et al., 1969; Semenova et al., 1999). The Eu–N bond distances are similar in $[Eu(\mathbf{L17^a})_3]^{3+}$ and $[Eu(\mathbf{L16})_3]^{3+}$, but the extension of the distal aromatic rings in going from $\mathbf{L16^a}$ to $\mathbf{L17^a}$ is responsible for the formation of three intramolecular interstrand π-stacking interactions involving pairs of almost parallel benzimidazole rings in $[Eu(\mathbf{L17^a})_3]^{3+}$ (Figure 26; Piguet et al., 1993c).

At a concentration of 10 mM in acetonitrile, the triple-helical structure found for $[R(\mathbf{L17^a})_3]^{3+}$ in the solid state is maintained for R = Ce–Dy (Petoud et al., 1997a). For smaller lanthanides (R = Ho–Lu), the third

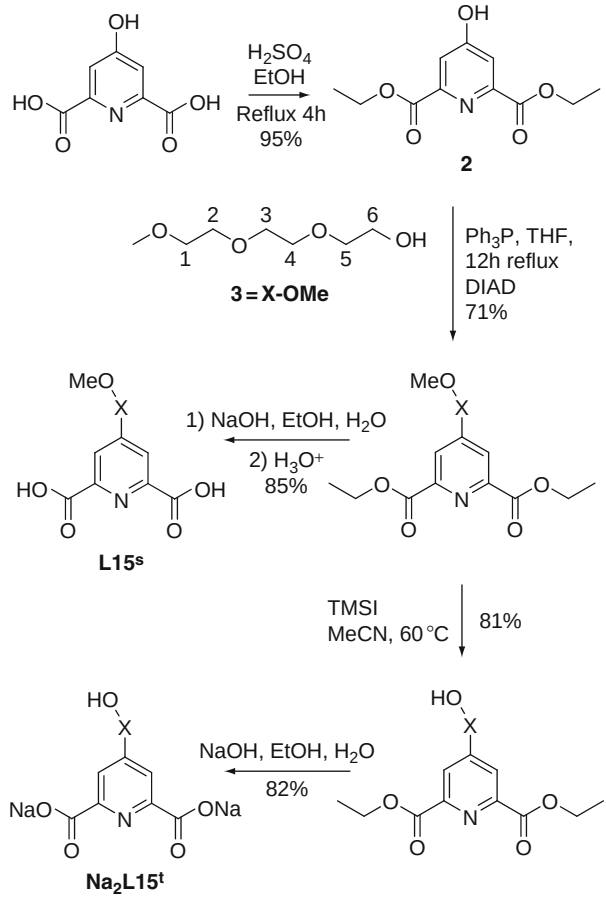

FIGURE 25 Continued

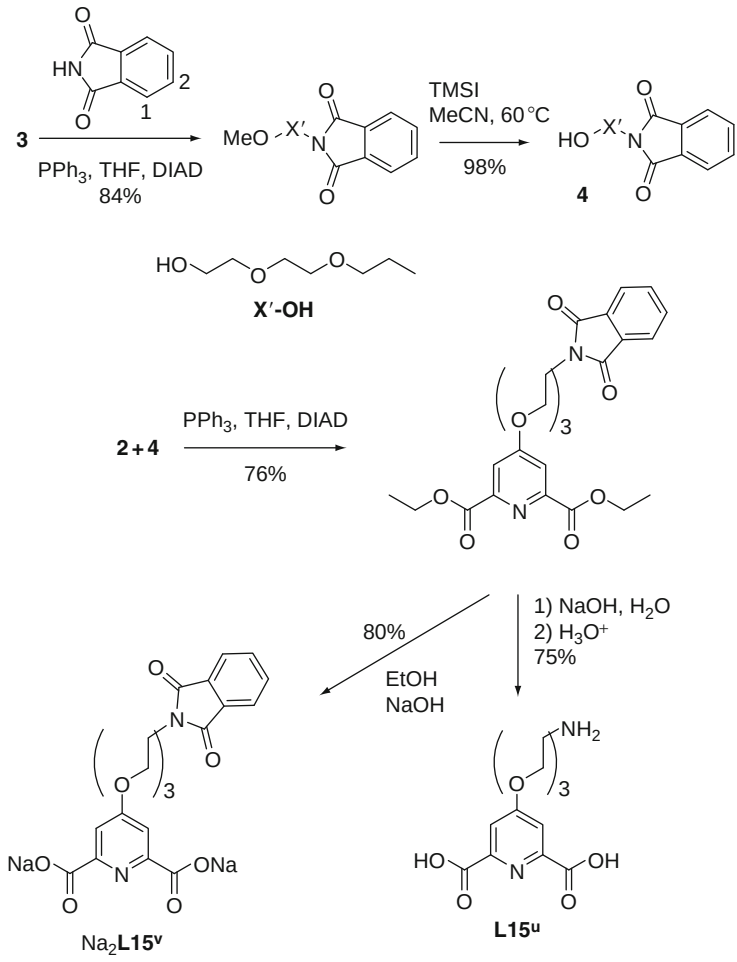

FIGURE 25 Synthesis of the dipicolinic acid derivatives $\mathbf{H_2L15^s}$ to $\mathbf{H_2L15^v}$ fitted with substituted trioxyethyleneglycol pendants (redrawn form Gassner et al., 2008).

successive stability constants measuring the affinity for the coordination of the third tridentate ligand $K_3^{R,\mathrm{L17a}} = \beta_{1,3}^{R,\mathrm{L17a}}/\beta_{1,2}^{R,\mathrm{L17a}}$ is too weak to ensure the quantitative formation of the triple-helical complex under stoichiometric conditions. A mixture of $[R(\mathbf{L17^a})_3]^{3+}$, $[R(\mathbf{L17^a})_2]^{3+}$, and $\mathbf{L17^a}$ in slow exchange on the NMR timescale is thus evidenced in solution (Piguet et al., 1993c). The crystal structure of $[R(\mathbf{L17^f})_3]^{3+}$ confirms the formation of the triple-helical building blocks, but the increased steric congestion produced by the peripheral ethyl groups distorts the regular helical wrapping of the strands and reduces interstrand stacking

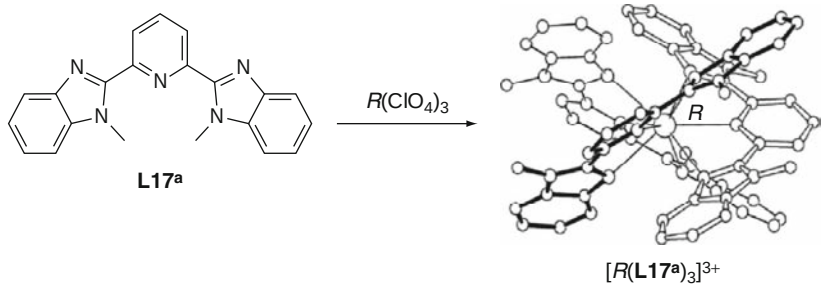

FIGURE 26 Schematic formation of D_3-symmetrical lanthanide triple-helical precursors with 2,6-bis(benzimidazolyl)pyridine **L17**. The representation of the complex corresponds to the crystal structure of $[Eu(\mathbf{L17^a})_3]^{3+}$ (redrawn from Piguet et al., 1993c).

(Piguet et al., 1995b). This trend is stepwise emphasized with $\mathbf{L17^c}$ (R^2 = propyl), $\mathbf{L17^e}$ (R^2 = 3,5-dimethoxybenzyl), and $\mathbf{L17^k}$ (R^2 = neopentyl), which precludes the formation and isolation of triple-helical complexes with these ligands (Muller et al., 2001a; Petoud et al., 1997a). However, the connection of a carboxyl substituent at the 4-position of the pyridine ring in $\mathbf{L17^l}$ has no effect on the complexation process and standard 1:3 triple-helical complexes are formed (Muller et al., 2001b). A very similar structural pattern is found with the amide derivatives **L18**, which lead to the formation of pseudo-D_3-symmetrical triple-helical complexes $[R(\mathbf{L18^a})_3]^{3+}$ (Renaud et al., 1997a), $[R(\mathbf{L18^b})_3]^{3+}$ (Muller et al., 2001b), $[R(\mathbf{L18^f})_3]^{3+}$ (Le Borgne et al., 2003), and $[R(\mathbf{L18^g})_3]^{3+}$ (Leonard et al., 2007) with the poorly constrained tertiary-amide substituents or with secondary-amide groups (Figure 27). However, bulky substituents grafted onto the tertiary-amide functions in $\mathbf{L18^d}$ and $\mathbf{L18^e}$ prevent the formation of triple-helical complexes and only 1:2 complexes $[R(\mathbf{L18^d})_2]^{3+}$ and $[R(\mathbf{L18^e})_2]^{3+}$ can be prepared (Le Borgne et al., 2003).

A thorough paramagnetic NMR study of $[R(\mathbf{L18^a})_3]^{3+}$ in acetonitrile shows the expected dynamically averaged D_3-symmetrical structure corresponding to the existence of a racemic mixture of P-$[R(\mathbf{L18^a})_3]^{3+}$ and M-$[R(\mathbf{L18^a})_3]^{3+}$ blocked on the NMR timescale (Renaud et al., 1997a). When unsymmetrical secondary-amide groups are considered in the ligands $\mathbf{L18^f}$ and $\mathbf{L18^g}$, the three possible blocked arrangements of the terminal alkyl substituents *EE*, *EZ*, and *ZZ* induces the formation of a mixture of 13 different inert isomers for the triple-helical complexes $[R(\mathbf{L18^f})_3]^{3+}$ and $[R(\mathbf{L18^g})_3]^{3+}$, which eventually gives intricate NMR spectra (Le Borgne et al., 2003). Interestingly, the crystal structures of both $[R(\mathbf{L18^f})_3]^{3+}$ (Le Borgne et al., 2003) and $[R(\mathbf{L18^g})_3]^{3+}$ (Leonard et al., 2007) show the selection of a single isomer during the crystallization process with the three ligands adopting *ZZ* conformations. Closely related

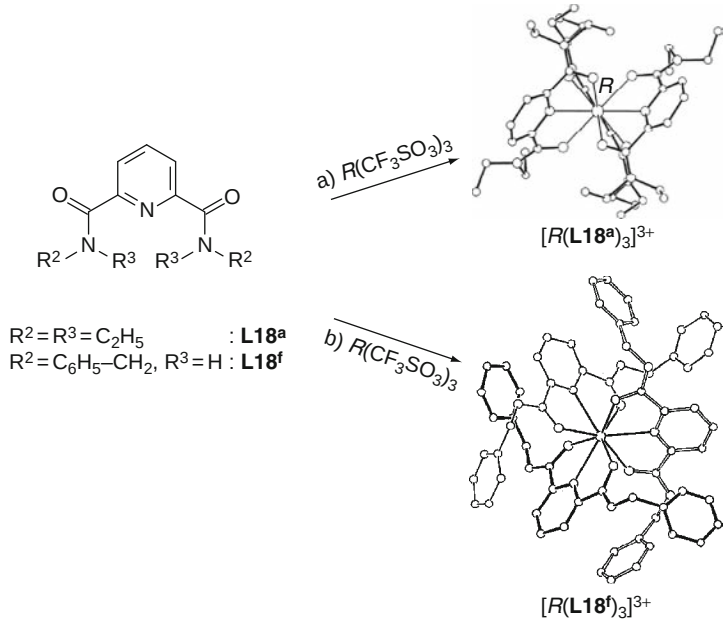

FIGURE 27 Schematic formation of D_3-symmetrical lanthanide triple-helical precursors with (A) 2,6-bis(tertiary-amide)pyridine ligands and (B) 2,6-bis(secondary-amide) pyridine ligands. The representation of the complexes corresponds to the crystal structures of $[Eu(\mathbf{L18^a})_3]^{3+}$ and $[Eu(\mathbf{L18^f})_3]^{3+}$ (redrawn from Le Borgne et al., 2003; Renaud et al., 1997a).

limitations affect the design of triple-helical complexes with the unsymmetrical NNO donor ligands **L19** because of the unavoidable meridional/facial isomerism (Figure 28; Le Borgne et al., 2004). No X-ray quality crystals could be grown from these mixtures, but 1:2 complexes $[Eu(\mathbf{L19^a})_2(CF_3SO_3)_2(H_2O)]^+$ and $[Eu(\mathbf{L19^d})_2(CF_3SO_3)_2(H_2O)]^+$, which possess no conformational isomer, could be fully characterized in the solid state (Le Borgne et al., 2004).

2.3 Thermodynamic stability and size-discriminating effects

Cumulative $\log(\beta_{1,n}^{R,Lk})$ and successive $\log(K_n^{R,Lk})$ stability constants are defined in the following equations:

$$n\mathbf{Lk} + R^{3+} \rightleftharpoons [R(\mathbf{Lk})_n]^{3+} \quad \beta_{1,n}^{R,Lk} \tag{1}$$

$$n\mathbf{Lk} + R^{3+} \rightleftharpoons [R(\mathbf{Lk})_n]^{3+} \quad K_{1,n}^{R,Lk} \tag{2}$$

The initial data of Grenthe (1961) on the mono-, bis-, and tris-complexes with unsubstituted dipicolinate are reported on Figure 29. There is an expected electrostatic trend in the $\log(\beta_{1,3}^{R,\mathrm{L15}})$ values which increase from ≈18 to ≈22 up to Dy, corresponding to a free energy difference $\Delta(\Delta G_{1,3}^{R,\mathrm{L15}^{\circ}}) \approx 23\ \mathrm{kJ\ mol^{-1}}$; the cumulative constants then stay constant up to Tm before slightly decreasing until the end of the series mainly due to the decreasing value of $\log K_1$. With respect to free energy, this eventual decrease corresponds to less than 4 kJ $\mathrm{mol^{-1}}$. With the exception of the first part of the series (up to Nd), the size-discriminating effect is therefore very small. Substitution of the pyridine 4-position by derivatized trioxyethylene fragments does not lead to fundamental changes in thermodynamic stability of the triple-helical chelates, especially if one considers the uncertainties associated with the determination of $\log(\beta_{1,n}^{R,\mathrm{L15}})$ values by spectrophotometry (see Table 1; Gassner et al., 2008).

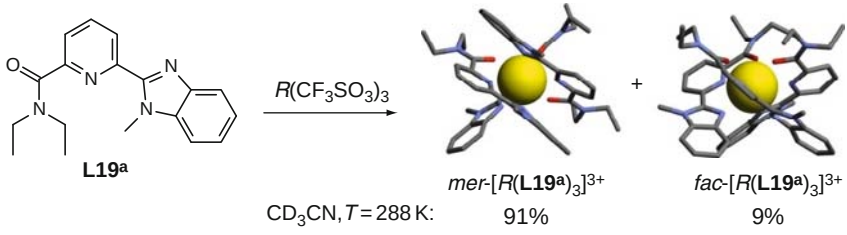

FIGURE 28 Schematic formation of lanthanide triple-helical building precursors with 2-benzimidazole-6-carboxypyridine ligands. The representation of the complexes corresponds to the optimized gas-phase molecular structures obtained for *mer*-[Lu(**L19**$^{\mathbf{a}}$)$_3$]$^{3+}$ and *fac*-[Lu(**L19**$^{\mathbf{a}}$)$_3$]$^{3+}$ (redrawn from Le Borgne et al., 2004).

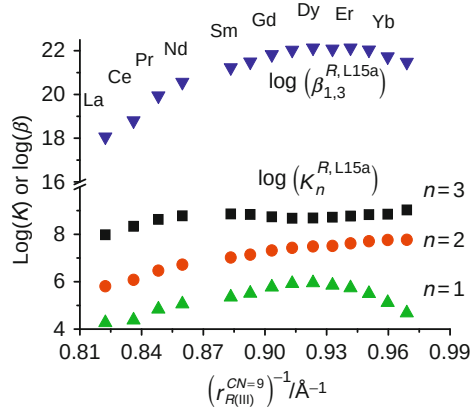

FIGURE 29 Stability constants for [Ln(**L15**$^{\mathbf{a}}$)$_i$]$^{(3-2i)+}$ (data from Grenthe, 1961).

TABLE 1 Cumulative $\log(\beta_{1,n}^{R,Lk})$ and successive $\log(K_n^{R,Lk})$ stability constants reported for the formation of complexes $[R(\mathbf{L15}^j)_n]^{(3-n)+}$ (j = s–v, n = 1–3; see Figure 24) from $R(ClO_4)_3$ in water and of complexes $[R(\mathbf{L}k)_n]^{3+}$ (k = 17–19, n = 1–3; see Figures 19, 21, and 22) from $R(CF_3SO_3)_3$ in acetonitrile; T = 293 K

Ligand	R	$\log(\beta_{1,1}^{R,L})$	$\log(\beta_{1,2}^{R,L})$	$\log(\beta_{1,3}^{R,L})$	$\log(K_2^{R,L})$	$\log(K_3^{R,L})$	References
L15[s]	La	10.2(6)	16.2(8)	20.9(7)	6.5(1.4)	4.2(1.5)	Gassner et al. (2008)
	Eu	8.9	14.3(2)	20.5(2)	4.4(2)	6.2(4)	Gassner et al. (2008)
	Tb	9.1(6)	15.5(6)	21.4(6)	6.4(1.2)	5.9(1.2)	Gassner et al. (2008)
L15[t]	La	7.9(4)	14.2(5)	20.2(6)	6.3(9)	6.0(1.1)	Gassner et al. (2008)
	Eu	8.8(2)	15.1(2)	20.3(3)	6.3(4)	5.2(5)	Gassner et al. (2008)
	Tb	8.7(1)	15.1(2)	20.3(3)	6.4(3)	5.2(5)	Gassner et al. (2008)
	Lu	8.8	16.6(1)	22.8(2)	7.8(1)	6.2(3)	Gassner et al. (2008)
L15[u]	La	7.2(1)	12.9(1)	17.6(1)	5.7(2)	4.7(2)	Gassner et al. (2008)
	Eu	6.8(4)	14.7(4)	20.5(4)	7.9(8)	5.8(8)	Gassner et al. (2008)
	Lu	8.5(3)	15.5(4)	20.4(4)	7.0(7)	4.9(8)	Gassner et al. (2008)
L17[a]	La	8.9(3)	16.8(8)	22.6(9)	7.9(4)	5.8(2)	Petoud et al. (1997a)
	Ce					6.0(1)	Petoud et al. (1997a)
	Pr					6.3(1)	Petoud et al. (1997a)
	Nd	8.7(2)	15.9(8)	22.4(8)	7.2(4)	6.5(2)	Petoud et al. (1997a)
	Sm					6.4(2)	Petoud et al. (1997a)
	Eu	9.0(2)	15.7(7)	22.6(6)	6.7(3)	6.9(4)	Petoud et al. (1997a)
	Gd	8.5(2)	15.2(8)	21.8(8)	6.7(4)	6.6(2)	Petoud et al. (1997a)
	Tb	9.3(3)	16.4(10)	22.5(10)	7.1(5)	6.1(1)	Petoud et al. (1997a)
	Dy					5.8(1)	Petoud et al. (1997a)
	Ho	8.9(3)	16.2(19)	21.5(10)	7.3(5)	5.3(1)	Petoud et al. (1997a)
	Er					4.7(2)	Petoud et al. (1997a)

(*continued*)

TABLE 1 (*continued*)

Ligand	*R*	$\log(\beta_{1,1}^{R,L})$	$\log(\beta_{1,2}^{R,L})$	$\log(\beta_{1,3}^{R,L})$	$\log(K_2^{R,L})$	$\log(K_3^{R,L})$	References
	Tm					3.9(1)	Petoud et al. (1997a)
	Yb	9.4(5)	16.5(14)	19.9(10)	7.1(6)	3.4(1)	Petoud et al. (1997a)
	Lu	9.0(4)	15.4(10)	18.1(10)	6.4(4)	2.7(1)	Petoud et al. (1997a)
L17[b]	Ca	4.4(1)	8.6(1)	11.8(3)			Canard et al. (2008)
	La	6.9(1)	13.0(1)	17.3(1)			Canard et al. (2008)
	Eu	9.2(5)	16.9(8)	21.8(8)			Canard et al. (2008)
	Lu	9.9(3)	17.7(5)	23.4(7)			Canard et al. (2008)
L17[e]	La				5.0(1)	2.2(2)	Petoud et al. (1997a)
	Ce				4.8(1)	2.9(3)	Petoud et al. (1997a)
	Pr				4.9(19	2.8(1)	Petoud et al. (1997a)
	Nd				4.9(1)	3.2(2)	Petoud et al. (1997a)
	Sm				5.5(1)	3.6(1)	Petoud et al. (1997a)
	Gd				4.8(1)	3.2(1)	Petoud et al. (1997a)
	Tb				4.9(1)	3.1(1)	Petoud et al. (1997a)
	Er				5.1(1)	3.0(1)	Petoud et al. (1997a)
	Lu				5.4(1)	2.9(1)	Petoud et al. (1997a)
L17[i]	La					4.8(2)	Petoud et al. (1997a)
	Pr					5.5(2)	Petoud et al. (1997a)
	Sm					6.0(1)	Petoud et al. (1997a)
	Gd					6.1(2)	Petoud et al. (1997a)
	Tb					5.9(1)	Petoud et al. (1997a)
	Dy					5.2(2)	Petoud et al. (1997a)
	Ho					4.8(2)	Petoud et al. (1997a)

	Tm					3.9(1)	Petoud et al. (1997a)
	Yb					3.1(1)	Petoud et al. (1997a)
L17[k]	La	8.1(1)			5.7(5)	1.2(2)	Muller et al. (2001a,b)
	Eu	8.2(2)			5.9(3)	0.9(1)	Muller et al. (2001a,b)
	Lu	6.9(1)			5.7(1)	<0.5	Muller et al. (2001a,b)
L17[l]	La	7.8(4)			6.0(5)	3.8(6)	Muller et al. (2002a,b)
	Eu	8.0(4)			6.4(4)	4.6(5)	Muller et al. (2002a,b)
	Lu	8.0(3)			6.4(4)	2.9(4)	Muller et al. (2002a,b)
L18[a]	La	7.4(3)	14.8(3)	21.0(3)			Renaud et al. (1997a)
	Ce	7.6(3)	14.3(4)	22.0(3)			Renaud et al. (1997a)
	Pr	7.6(3)	14.6(3)	22.2(3)			Renaud et al. (1997a)
	Nd	7.5(3)	13.8(4)	21.5(4)			Renaud et al. (1997a)
	Sm	7.3(3)	14.4(4)	22.0(4)			Renaud et al. (1997a)
	Eu	8.3(3)	15.3(3)	22.3(3)			Renaud et al. (1997a)
	Gd	7.9(3)	14.7(4)	22.6(4)			Renaud et al. (1997a)
	Tb	8.2(3)	14.5(4)	22.9(4)			Renaud et al. (1997a)
	Dy	7.5(3)	14.8(4)	22.5(4)			Renaud et al. (1997a)
	Ho	7.3(4)	14.8(4)	22.3(4)			Renaud et al. (1997a)
	Er	7.7(4)	14.4(4)	22.7(4)			Renaud et al. (1997a)
	Tm	8.5(3)	16.0(3)	22.1(4)			Renaud et al. (1997a)
	Yb	8.5(3)	15.6(3)	22.8(4)			Renaud et al. (1997a)
	Lu	8.1(3)	15.2(3)	22.9(3)			Renaud et al. (1997a)
	Y	7.6(3)	14.6(4)	22.4(4)			Renaud et al. (1997a)
L18[b]	La	7.4(4)	14.0(5)	19.0(5)			Muller et al. (2001a,b)
	Eu	8.2(4)	14.5(5)	19.8(5)			Muller et al. (2001a,b)

(*continued*)

TABLE 1 (*continued*)

Ligand	*R*	$\log(\beta_{1,1}^{R,L})$	$\log(\beta_{1,2}^{R,L})$	$\log(\beta_{1,3}^{R,L})$	$\log(K_2^{R,L})$	$\log(K_3^{R,L})$	References
	Lu	8.7(4)	15.3(5)	20.3(5)			Muller et al. (2001a,b)
L18[c]	La	7.4(4)	13.9(5)	19.0(5)			Muller et al. (2001a,b)
	Eu	8.2(4)	14.6(5)	19.7(5)			Muller et al. (2001a,b)
	Lu	8.7(4)	15.2(5)	20.5(5)			Muller et al. (2001a,b)
L18[d]	La	7.8(5)	14.0(7)	18.0(8)			Le Borgne et al. (2003)
	Ce	7.4(4)	13.0(6)	17.9(7)			Le Borgne et al. (2003)
	Pr	8.0(6)	13.8(8)	17.5(9)			Le Borgne et al. (2003)
	Nd	7.7(5)	13.5(7)	17.5(8)			Le Borgne et al. (2003)
	Sm	8.5(6)	12.9(7)	18.4(8)			Le Borgne et al. (2003)
	Eu	8.3(6)	13.9(6)	17.6(7)			Le Borgne et al. (2003)
	Gd	7.9(7)	13.7(9)	17.5(9)			Le Borgne et al. (2003)
	Tb	7.6(6)	13.8(7)	18.5(7)			Le Borgne et al. (2003)
	Dy	7.7(5)	14.4(6)	17.3(8)			Le Borgne et al. (2003)
	Ho	8.3(6)	14.2(7)	17.9(9)			Le Borgne et al. (2003)
	Er	8.3(5)	13.9(6)	17.5(8)			Le Borgne et al. (2003)
	Tm	7.9(6)	13.8(7)	17.8(9)			Le Borgne et al. (2003)
	Yb	7.7(4)	13.7(5)	16.7(6)			Le Borgne et al. (2003)
	Lu	7.6(4)	13.5(5)	17.3(6)			Le Borgne et al. (2003)
L18[e]	La	5.4(5)	11.1(6)				Le Borgne et al. (2003)
	Eu	4.9(5)	9.8(6)				Le Borgne et al. (2003)
	Lu	5.3(5)	9.7(6)				Le Borgne et al. (2003)

	Y	4.9(5)	9.4(6)		Le Borgne et al. (2004)
L19[a]	La	7.1(3)	11.6(4)	15.9(5)	Le Borgne et al. (2004)
	Pr	7.7(3)	13.7(5)	17.8(6)	Le Borgne et al. (2004)
	Gd	7.3(2)	12.3(3)	17.4(4)	Le Borgne et al. (2004)
	Dy	7.4(3)	12.5(4)	16.5(5)	Le Borgne et al. (2004)
	Er	8.0(4)	13.2(4)	17.9(5)	Le Borgne et al. (2004)
	Lu	7.2(2)	11.5(4)	17.3(4)	Le Borgne et al. (2004)
L19[b]	La	8.6(3)	15.1(4)	19.9(4)	Le Borgne et al. (2004)
	Eu	7.8(2)	13.5(2)	19.2(2)	Le Borgne et al. (2004)
	Lu	9.2(2)	16.8(4)	21.9(4)	Le Borgne et al. (2004)
L19[c]	La	6.7(2)	11.7(3)	17.1(4)	Le Borgne et al. (2004)
	Pr	7.6(4)	13.2(5)	17.6(7)	Le Borgne et al. (2004)
	Gd	7.0(2)	11.8(3)	17.0(5)	Le Borgne et al. (2004)
	Dy	7.7(3)	12.4(4)	16.9(5)	Le Borgne et al. (2004)
	Er	7.8(3)	12.7(3)	17.1(3)	Le Borgne et al. (2004)
	Lu	7.2(2)	12.7(3)	18.5(5)	Le Borgne et al. (2004)
L19[d]	La	7.3(3)	12.7(4)	17.0(5)	Le Borgne et al. (2004)
	Eu	7.6(4)	12.8(5)	18.0(7)	Le Borgne et al. (2004)
	Lu	7.0(8)	11.9(8)	17.5(7)	Le Borgne et al. (2004)

Values without uncertainties have been fixed in the fitting process.

Data characterizing the formation of the complexes $[R(\mathbf{Lk})_n]^{3+}$ ($k = 17$–19, $n = 1$–3) are also collected in Table 1. For unconstrained symmetrical ligands **L17** and **L18**, the free energy changes $\Delta G_{1,n}^{R,Lk}$ accompanying the formation of the complexes $[R(\mathbf{Lk})]^{3+}$ ($\Delta G_{1,1}^{R,Lk} = -42$ to -50 kJ mol^{-1}), $[R(\mathbf{Lk})_2]^{3+}$ ($\Delta G_{1,2}^{R,Lk} = -81$ to -93 kJ mol^{-1}) and $[R(\mathbf{Lk})_3]^{3+}$ ($\Delta G_{1,3}^{R,Lk} = -112$ to -123 kJ mol^{-1}) do not significantly depend on the nature of the donor atoms in the tridentate ligands (N_3 in **L17** and NO_2 in **L18**). This reflects the crucial role played by the entropic contribution in lanthanide complexation processes, which are mainly controlled by charge compensation effects (Choppin, 1989; Comuzzi et al., 2002; Di Bernardo et al., 2008; Piguet and Bünzli, 1999). This translates into a pronounced preference of the trivalent lanthanides for complexing negatively charged donor atoms, often oxygen atoms because of their large electronegativity. The latter trend is usually and erroneously assigned to some specific oxophilicity of R^{III}, but negatively charged nitrogen or carbon atoms are valuable alternatives (Anwander, 1999; Dehnicke and Greiner, 2003; Evans, 2007).

The complexation process involves a *trans–trans* → *cis–cis* conformational interconversion of the tridentate binding unit whose energetic costs is very sensitive to the size and bulkiness of the substituents bound to the N atoms of the benzimidazole rings in **L17**, or to the N atoms of the amide groups in **L18** (Figure 30). Consequently, $K_2^{R,L17}$ decreases by two orders of magnitude when the methyl groups in **L17^{a}** are replaced with bulky 3,5-dimethoxybenzyl groups in **L17^{e}**. Similarly, $\beta_{1,1}^{R,L18}$ (2–3 orders of magnitude) and $\beta_{1,2}^{R,L18}$ (4 orders of magnitude) are reduced when diethylamide groups in **L18^{a}** are replaced with dibenzyl groups in **L18^{e}** (Table 1). Intramolecular interligand interactions resulting from the tight wrapping of the three strands in $[R(\mathbf{Lk})_3]^{3+}$ may also tune the stability of the final triple-helical complexes as revealed by the decrease by two orders of magnitude of $\beta_{1,3}^{R,L18}$ values in going from **L18^{a}** ($R^2 = R^3 = C_2H_5$) to **L18^{d}** ($R^2 = R^3 = CH(CH_3)_2$), while $\beta_{1,2}^{R,L18}$ values are similar for both ligands (Table 1).

The unusual bowl-shaped curve found for $\log(\beta_{1,3}^{R,L17a})$ along the lanthanide series merits special comments since it represents a rare case of size-discriminating effect favoring the complexation of large lanthanides (Figure 31; Petoud et al., 1997a,b). Detailed structural data collected in the solid state (Piguet et al., 1993c) and in solution (Petoud et al., 1997a) for $[R(\mathbf{L17^{a}})_3]^{3+}$ firmly establish that the tight wrapping of the three helical ligand strands produces three efficient intramolecular interstrand interactions involving pairs of benzimidazole rings (Figure 26). Attractive π–π interactions are compatible with *R*-N bond lengths compatible with the coordination of large or midrange trivalent lanthanides, and they further contribute to stabilize the final triple-helical complexes (Table 1). The required contraction of the *R*–N bond

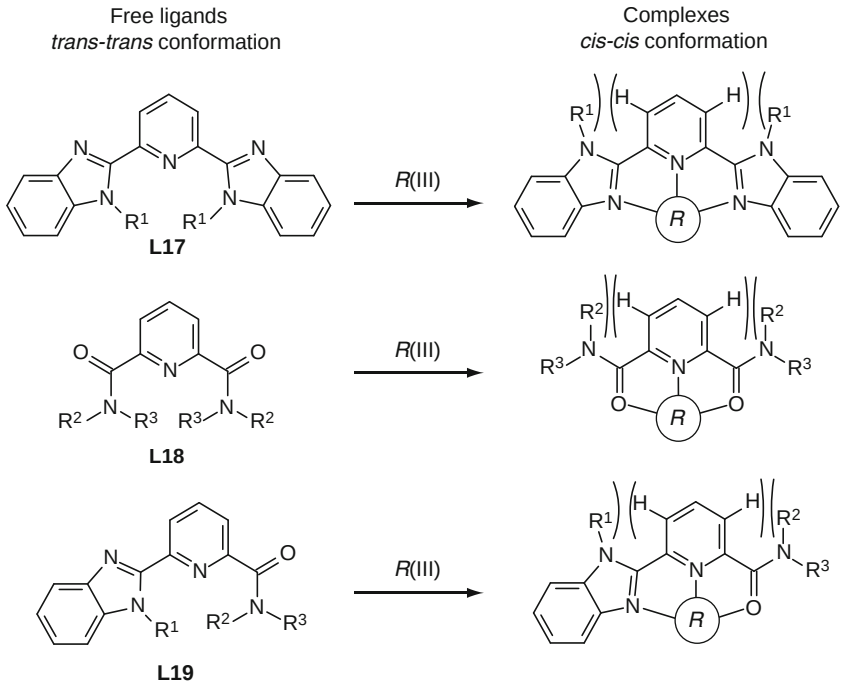

FIGURE 30 *Trans–trans* → *cis–cis* conformational change of the tridentate binding unit occurring upon complexation of **L17**–**L19** to trivalent lanthanides.

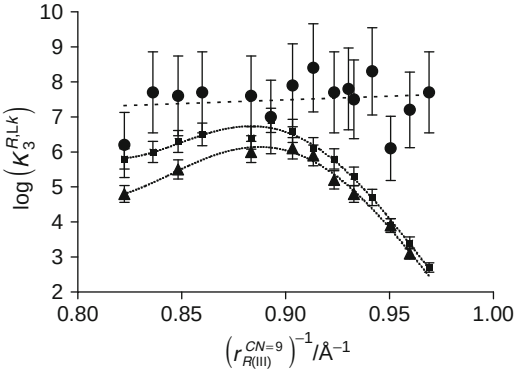

FIGURE 31 Third successive stability constants $\log(K_3^{R,Lk})$ measured in acetonitrile for the triple-helical complexes $[R(\mathbf{L17^a})_3]^{3+}$ (squares), $[R(\mathbf{L17^i})_3]^{3+}$ (triangles), and $[R(\mathbf{L18^a})_3]^{3+}$ (circles) versus the reciprocal of ionic radius for nine-coordinate R^{3+} (redrawn after Petoud et al., 1997a,b).

lengths along the second part of the lanthanide series in $[R(\mathbf{L17^a})_3]^{3+}$ is only possible at the cost of a closer packing of the pairs of benzimidazole rings, which induces repulsive van der Waals interactions and some slipping of the strands (Piguet et al., 1995b). Consequently, the third successive stability constants $\log(K_3^{R,\mathrm{L17a}})$ are significantly reduced for the smaller lanthanides, and a pronounced size-discriminating effect favoring the complexation of midrange R^{III} results (Figure 31; Table 1). Obviously, the latter effect is removed when at least one distal benzimidazole rings is replaced with a carboxamide group in $[R(\mathbf{L18^a})_3]^{3+}$ or $[R(\mathbf{L19^a})_3]^{3+}$, and the standard electrostatic trend is restored (Figure 31; Table 1; Piguet and Bünzli, 1999). Interestingly, the deleterious consequences on the thermodynamic constants produced by the introduction of bulky substituents in $[R(\mathbf{L17^e})_3]^{3+}$ can be overcome by the connection of a strong donor in the back of the central pyridine ring in $[R(\mathbf{L17^i})_3]^{3+}$ (Figure 31; Petoud et al., 1997a,b).

2.4 Isomerization and covalent tripods

When the tridentate binding unit does not possess a C_2-axis as in **L19**, two isomeric triple-helical complexes are formed upon reaction with R^{III} (Figure 28). Therefore, the associated macroscopic formation constant $\beta_{1,3}^{R,\mathrm{L19}}$ is made up of two microconstants, each characterizing the formation of the microspecies *mer*-$[R(\mathbf{L19})_3]^{3+}$ and *fac*-$[R(\mathbf{L19})_3]^{3+}$, Eq. (3), and whose ratio is given in Eq. (4).

$$\beta_{1,3}^{R,\mathrm{L19}} = \beta_{1,3,mer}^{R,\mathrm{L19}} + \beta_{1,3,fac}^{R,\mathrm{L19}} \tag{3}$$

$$fac-[R(\mathbf{L19})_3]^{3+} \rightleftharpoons mer-[R(\mathbf{L19})_3]^{3+} \quad K_{\mathrm{iso}}^{R,\mathrm{L19}} = \beta_{1,3,mer}^{R,\mathrm{L19}}/\beta_{1,3,fac}^{R,\mathrm{L19}} \tag{4}$$

Assuming a pure statistical entropic driving force for equilibrium (4) (i.e., $\Delta H_{\mathrm{iso}}^{R,\mathrm{L19}} = 0$), $K_{\mathrm{iso}}^{R,\mathrm{L19}}$ corresponds to the ratio of the external symmetry numbers of *fac*-$[R(\mathbf{L19})_3]^{3+}$ ($\sigma_{fac} = 3$, C_3-symmetrical) and *mer*-$[R(\mathbf{L19})_3]^{3+}$ ($\sigma_{mer} = 1$, C_1-symmetrical), which gives $K_{\mathrm{iso}}^{R,\mathrm{L19}} = \sigma_{fac}/\sigma_{mer} = 3$ (Ercolani et al., 2007), hence an entropic contribution of $\Delta S_{\mathrm{iso}}^{R,\mathrm{L19}} = R\ln(3) = 9.1\ \mathrm{J\,mol^{-1}\,K^{-1}}$ in favor of the meridional isomer. The detailed investigation of equilibrium (4) in acetonitrile for $\mathbf{L19^a}$, $\mathbf{L19^c}$, and $\mathbf{L19^d}$ shows that both experimental enthalpic, $\Delta H_{\mathrm{iso}}^{\mathrm{Lu,L19}}$, and entropic, $\Delta S_{\mathrm{iso}}^{\mathrm{Lu,L19}}$, contributions deviate from this simple statistical model (Table 2; Le Borgne et al., 2004).

For $[\mathrm{Lu}(\mathbf{L19^a})_3]^{3+}$ and $[\mathrm{Lu}(\mathbf{L19^d})_3]^{3+}$, the negative enthalpic contributions result from residual $\pi-\pi$ stacking interactions, which only operate

TABLE 2 Enthalpic ($\Delta H_{iso}^{Lu,L19}$ in kJ mol^{-1}) and entropic ($\Delta S_{iso}^{Lu,L19}$ in Jmol^{-1}K^{-1}) contributions to the *fac*-[Lu(**L19**)$_3$]$^{3+}$ ⇌ *mer*-[Lu(**L19**)$_3$]$^{3+}$ isomerization in acetonitrile at 293 K (see Eq. (4), Figure 22)

	[Lu(**L19**^{a})$_3$]$^{3+}$	[Lu(**L19**^{c})$_3$]$^{3+}$	[Lu(**L19**^{d})$_3$]$^{3+}$
$\Delta H_{iso}^{Lu,L19}$ (kJ mol^{-}1)	− 4.3(5)	21(2)	− 6.9(2.4)
$\Delta S_{iso}^{Lu,L19}$ (J mol^{-1} K^{-1})	5(5)	82(7)	− 10(10)
$-T\Delta S_{iso}^{Lu,L19}$ (kJ mol^{-}1)	− 1.5(1.5)	− 24(2)	3(3)

in the meridional isomer (Figure 28). The large, but opposite enthalpic contribution found in [Lu(**L19**^{c})$_3$]$^{3+}$ has the same origin because the bulky 3,5-dimethoxybenzyl groups prevent close packing of the strands in the meridional isomer. Although the deviations of the entropy changes from the statistical values of 9.1 J mol^{-1} K^{-1} are more difficult to rationalize, the global free energy changes at 293 K ($-4 < \Delta G_{iso}^{Lu,L19} < -2$ kJ mol^{-1}) systematically favor the meridional isomer, a severe drawback since the introduction of these unsymmetrical building blocks in polynuclear helicates requires the selective preparation of the facial C_3-symmetrical isomer (Le Borgne et al., 2004). To force facial coordination of the three strands about R^{III}, three unsymmetrical tridentate ONO (**L20**: Renaud et al., 1999; **L21**: Senegas et al., 2003; Figure 32), NNO (**L22**: Koeller et al., 2003a; **L23**: Koeller et al., 2003b; Figure 33), and NNN (**L24**: Canard et al., 2008; Figure 34) binding units have been connected to covalent tripods. Upon reaction with $R(ClO_4)_3$ or $R(CF_3SO_3)_3$, the expected C_3-symmetrical podates $[R(\mathbf{L20})]^{3+}$, [R(**L21**-3H)], $[R(\mathbf{L22})]^{3+}$, $[R(\mathbf{L23})]^{3+}$, and $[R(\mathbf{L24})]^{3+}$ are formed in solution and in the solid state (Figures 32–34).

The pair of podands **L20** and [**L21**-3H]$^{3-}$ have been designed for exploring the effect of charge compensation on the energetics and structures of the final triple-helical podates $[R(\mathbf{L20})]^{3+}$ and [R(**L21**-3H)]. The formation constants reported for $[R(\mathbf{L20})]^{3+}$ in acetonitrile (Eq. (5)) and for [R(**L21**-3H)] in water (Eq. (6)) are comparable (Table 3) and correspond to $\log(\beta_{1,1}^{R,Lk}) = 6.5$–$8.0$, which translates into $-45 < \Delta G_{1,1}^{R,Lk^{\circ}} < -36$ kJ mol^{-1}.

$$\mathbf{L}\boldsymbol{k} + R^{3+} \rightleftharpoons [R(\mathbf{L}\boldsymbol{k})]^{3+} \quad \beta_{1,1}^{R,Lk} \tag{5}$$

$$[\mathbf{L21} - 3\mathrm{H}]^{3-} + R^{3+} \rightleftharpoons [R(\mathbf{L21} - 3\mathrm{H})]^{3+} \quad \beta_{1,1}^{R,Lk} \tag{6}$$

Since the solvation of R^{3+} is more energetic in water than in acetonitrile, the formation constants of $[R(\mathbf{L20})]^{3+}$ ($\log(\beta_{1,1}^{R,L20})$) decrease

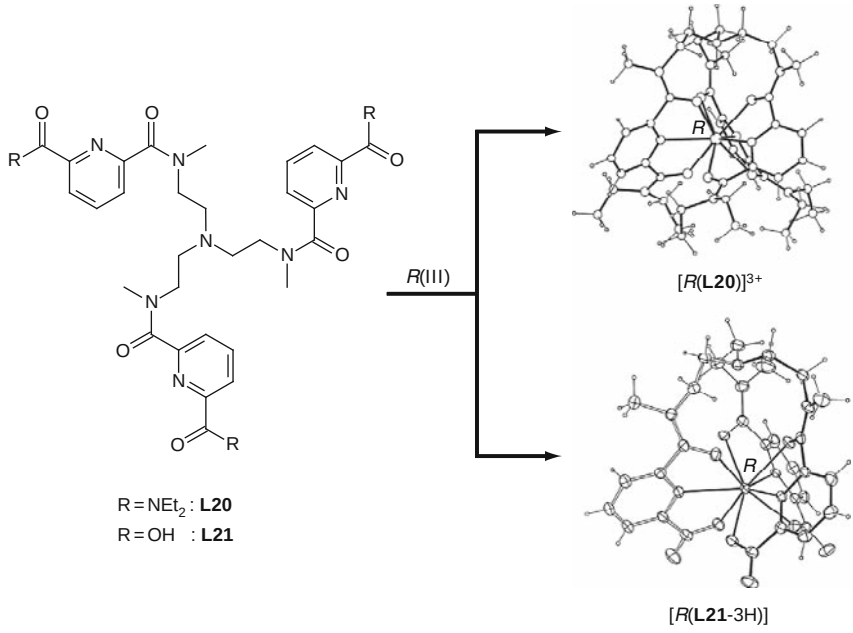

FIGURE 32 Schematic formation of the C_3-symmetrical N_3O_6 nine-coordinate triple-helical lanthanide podates with **L20** and **L21**. The representation of the complexes corresponds to the crystal structures of [Eu(**L20** + H)]$^{4+}$ and [Eu(**L21**-3H)] (redrawn after Renaud et al., 1999; Senegas et al., 2003).

by one order of magnitude in CH_3CN/H_2O (95:5) and $\beta_{1,1}^{R,L20} < 10$ is reached in pure water. However, the formation constants for [*R*(**L21**-3H)] in pure water still amount to $6.7 \leq \log(\beta_{1,1}^{R,L21}) \leq 7.0$, which unambiguously demonstrates the importance of the charge compensation process in the overall stability of the lanthanide complexes (Table 3). In this context, it is worth noting that Eu–O(carboxylate) bond lengths (average 2.45(1) Å) in the crystal structure of [Eu(**L21**-3H)] (Senegas et al., 2003) are similar to Eu–O(carboxamide) bond lengths (average 2.43(1) Å) found in [*R*(**L20** + H)]$^{4+}$ (Renaud et al., 1999). It can be concluded that the favorable charge compensation effect arises almost exclusively from an entropic contribution.

The next pair of podands **L22** and **L23** has been developed for exploring the effect of the conformation of the covalent tripod on the organization and binding efficiency of the tridentate binding units. Table 3 indeed shows that the methylation of the apical carbon atom in **L23** slightly increases the formation constant by approximately one order of magnitude, but the most striking difference concerns the formation of two endo conformers for [*R*(**L22**)]$^{3+}$ (ratio 7:3; Koeller et al., 2003a), while [*R*(**L23**)]$^{3+}$

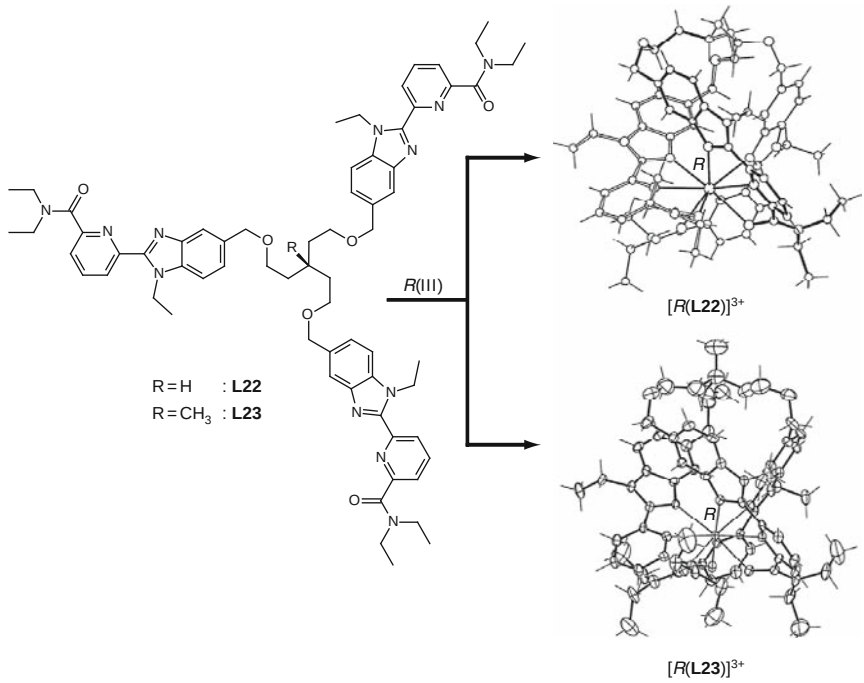

FIGURE 33 Schematic formation of the C_3-symmetrical N_6O_3 nine-coordinate triple-helical lanthanide podates with **L22** and **L23**. The representation of the complexes corresponds to the crystal structures of [La(**L22**)]$^{3+}$ and [Eu(**L23**)]$^{3+}$ (redrawn after Koeller et al., 2003a,b).

exists as a single exo-isomer, whereby the apical methyl group points out of the coordination cavity (Figure 33; Koeller et al., 2003b). Despite the latter structural change, the C_3-symmetrical organization of the three helically wrapped tridentate binding units are almost superimposable in the two podates, which explains the minor variations of the thermodynamic properties (Koeller et al., 2003b).

Taking the methylated exo-tripod of **L23** as a reference, podand **L24** was synthesized for combining the size-discriminating effect associated with 2,6-bis(benzimidazol-2-yl)pyridine ligand (Figure 31) with the preorganization of the covalent tripod (Figure 34; Canard et al., 2008). Surprisingly, the formation constants of [R(**L24**)]$^{3+}$ (three NNN donors) do not evidence measurable size-discriminating effect, and they correspond to a tiny domain of free energy $-48 < \Delta G_{1,1}^{R,\mathrm{L24}} < -36$ kJ mol^{-1}, identical to those observed for [R(**L20**)]$^{3+}$ (three ONO donors), [R(**L22**)]$^{3+}$, and [R(**L23**)]$^{3+}$ (three NNO donors) in the same solvent (Table 3). However, the formation of nine R-ligand bonds in the latter

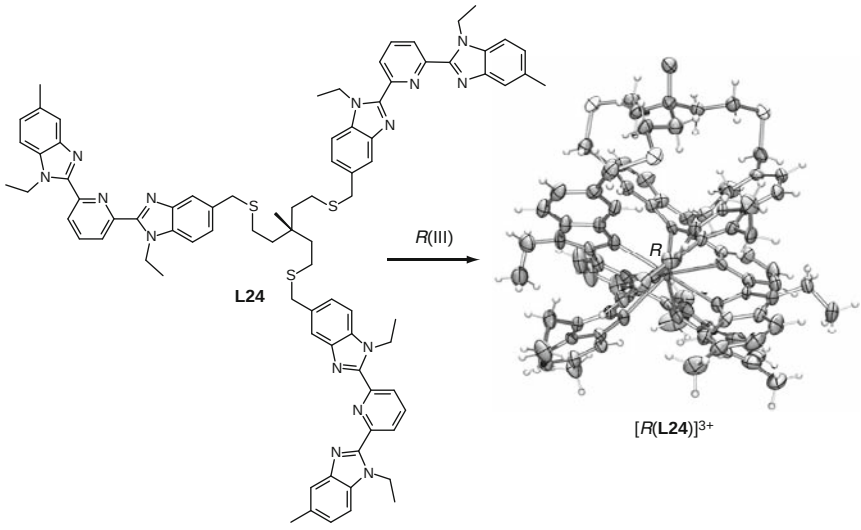

FIGURE 34 Schematic formation of the C_3-symmetrical N_9 nine-coordinate triple-helical lanthanide podates with **L24**. The representation of the complex corresponds to the crystal structure of [Eu(**L24**)]$^{3+}$ (redrawn after Canard et al., 2008).

podates is approximately three times less efficient that the same process observed for the native nonconnected tridentate binding units in [*R*(**L18**^{a})$_3$]$^{3+}$ (three ONO donors: $-128 < \Delta G^{R,L18a^\circ}_{1,3} < -117$ kJ mol^{-1}), [*R*(**L19**^{a})$_3$]$^{3+}$ (three NNO donors: $-100 < \Delta G^{R,L19a^\circ}_{1,1} < -89$ kJ mol^{-1}) and [*R*(**L17**^{a})$_3$]$^{3+}$ (three NNN donors: $-127 < \Delta G^{R,L17a^\circ}_{1,1} < -120$ kJ mol^{-1}; Table 1).

In going from the podates [*R*(**L***k*)]$^{3+}$ to the triple-helical complexes [*R*(**L***k*)$_3$]$^{3+}$ with the same set of donor atoms, the complexation processes only differ by the replacement of three intermolecular *R*-tridentate unit connections in [*R*(**L***k*)$_3$]$^{3+}$ with one intermolecular and two intramolecular connections in [*R*(**L***k*)]$^{3+}$ (Figure 35; Canard et al., 2008). It was thus concluded that the covalent tripod, instead of preorganizing the three tridentate units for their coordination to R^{III}, indeed dramatically disorganizes the binding units and prevents efficient connection processes. It is, however, worth noting that the pseudotricapped-trigonal prismatic coordination spheres in each pair [*R*(**L***k*)$_3$]$^{3+}$/[*R*(**L***k*)]$^{3+}$ are almost superimposable, which implies some drastic torsions and constraints in the covalent tripod. Consequently, minor changes in the structure of the tripod have considerable effects on the complexation process. For instance, insertion of one additional methylene unit in [*R*(**L25**)]$^{3+}$ changes the ratio of the two endo isomers from 7:3 in [*R*(**L22**)]$^{3+}$ to 13:1 in

TABLE 3 Overall stability constants, $\log(\beta_{1,1}^{R,Lk})$, reported at 293 K for the formation of the triple-helical podates $[R(\mathbf{L}k)]^{3+}$ ($k = 20$–24, see Figures 32–34)

Ligand	Salt	Solvent	$\log(\beta_{1,1}^{R,Lk})$	References
L20	$La(ClO_4)_3$	CH_3CN	8.3(2)	Renaud et al. (1999)
L20	$La(ClO_4)_3$	CH_3CN/H_2O (95:5)	5.0(1)	Renaud et al. (1999)
L20	$Ce(ClO_4)_3$	CH_3CN	8.5(7)	Renaud et al. (1999)
L20	$Pr(ClO_4)_3$	CH_3CN	8.0(7)	Renaud et al. (1999)
L20	$Nd(ClO_4)_3$	CH_3CN	8.1(5)	Renaud et al. (1999)
L20	$Sm(ClO_4)_3$	CH_3CN	7.0(4)	Renaud et al. (1999)
L20	$Sm(ClO_4)_3$	CH_3CN/H_2O (95:5)	6.3(3)	Renaud et al. (1999)
L20	$Gd(ClO_4)_3$	CH_3CN	7.6(4)	Renaud et al. (1999)
L20	$Dy(ClO_4)_3$	CH_3CN	7.4(3)	Renaud et al. (1999)
L20	$Tm(ClO_4)_3$	CH_3CN	7.2(6)	Renaud et al. (1999)
L20	$Lu(ClO_4)_3$	CH_3CN	8.0(6)	Renaud et al. (1999)
L20	$Lu(ClO_4)_3$	CH_3CN/H_2O (95:5)	7.5(3)	Renaud et al. (1999)
L20	$Y(ClO_4)_3$	CH_3CN	6.7(4)	Renaud et al. (1999)
L20	$Y(ClO_4)_3$	CH_3CN/H_2O (95:5)	6.8(1)	Renaud et al. (1999)
$[L21\text{-}3H]^{3-}$	$La(ClO_4)_3$	H_2O (pH 8.0)	6.8(1)	Senegas et al. (2003)
$[L21\text{-}3H]^{3-}$	$Nd(ClO_4)_3$	H_2O (pH 8.0)	6.7(2)	Senegas et al. (2003)
$[L21\text{-}3H]^{3-}$	$Sm(ClO_4)_3$	H_2O (pH 8.0)	6.9(2)	Senegas et al. (2003)
$[L21\text{-}3H]^{3-}$	$Gd(ClO_4)_3$	H_2O (pH 8.0)	6.7(2)	Senegas et al. (2003)
$[L21\text{-}3H]^{3-}$	$Dy(ClO_4)_3$	H_2O (pH 8.0)	6.8(2)	Senegas et al. (2003)
$[L21\text{-}3H]^{3-}$	$Ho(ClO_4)_3$	H_2O (pH 8.0)	7.0(2)	Senegas et al. (2003)
$[L21\text{-}3H]^{3-}$	$Er(ClO_4)_3$	H_2O (pH 8.0)	6.8(2)	Senegas et al. (2003)
$[L21\text{-}3H]^{3-}$	$Tm(ClO_4)_3$	H_2O (pH 8.0)	6.9(2)	Senegas et al. (2003)
$[L21\text{-}3H]^{3-}$	$Lu(ClO_4)_3$	H_2O (pH 8.0)	7.0(2)	Senegas et al. (2003)
L22	$La(CF_3SO_3)_3$	CH_3CN	7.0(2)	Koeller et al. (2003a)
L22	$Pr(CF_3SO_3)_3$	CH_3CN	7.3(4)	Koeller et al. (2003a)
L22	$Nd(CF_3SO_3)_3$	CH_3CN	6.5(3)	Koeller et al. (2003a)
L22	$Sm(CF_3SO_3)_3$	CH_3CN	6.8(3)	Koeller et al. (2003a)
L22	$Gd(CF_3SO_3)_3$	CH_3CN	7.6(3)	Koeller et al. (2003a)
L22	$Dy(CF_3SO_3)_3$	CH_3CN	7.2(2)	Koeller et al. (2003a)
L22	$Er(CF_3SO_3)_3$	CH_3CN	7.5(4)	Koeller et al. (2003a)
L22	$Lu(CF_3SO_3)_3$	CH_3CN	6.8(3)	Koeller et al. (2003a)
L23	$La(CF_3SO_3)_3$	CH_3CN	8.2(5)	Koeller et al. (2003b)
L23	$Pr(CF_3SO_3)_3$	CH_3CN	7.6(2)	Koeller et al. (2003b)
L23	$Eu(CF_3SO_3)_3$	CH_3CN	7.7(4)	Koeller et al. (2003b)

(*continued*)

TABLE 3 (*continued*)

Ligand	Salt	Solvent	$\log(\beta_{1,1}^{R,Lk})$	References
L23	$Dy(CF_3SO_3)_3$	CH_3CN	7.6(3)	Koeller et al. (2003b)
L23	$Er(CF_3SO_3)_3$	CH_3CN	7.2(2)	Koeller et al. (2003b)
L23	$Lu(CF_3SO_3)_3$	CH_3CN	7.9(3)	Koeller et al. (2003b)
L24	$Ca(CF_3SO_3)_2$	CH_3CN	8.6(8)	Canard et al. (2008)
L24	$La(CF_3SO_3)_3$	CH_3CN	7.6(2)	Canard et al. (2008)
L24	$Ce(CF_3SO_3)_3$	CH_3CN	7.2(2)	Canard et al. (2008)
L24	$Pr(CF_3SO_3)_3$	CH_3CN	7.3(2)	Canard et al. (2008)
L24	$Nd(CF_3SO_3)_3$	CH_3CN	7.6(2)	Canard et al. (2008)
L24	$Sm(CF_3SO_3)_3$	CH_3CN	7.8(2)	Canard et al. (2008)
L24	$Eu(CF_3SO_3)_3$	CH_3CN	7.2(1)	Canard et al. (2008)
L24	$Gd(CF_3SO_3)_3$	CH_3CN	7.5(2)	Canard et al. (2008)
L24	$Tb(CF_3SO_3)_3$	CH_3CN	7.8(2)	Canard et al. (2008)
L24	$Dy(CF_3SO_3)_3$	CH_3CN	7.4(2)	Canard et al. (2008)
L24	$Ho(CF_3SO_3)_3$	CH_3CN	7.9(1)	Canard et al. (2008)
L24	$Er(CF_3SO_3)_3$	CH_3CN	7.4(1)	Canard et al. (2008)
L24	$Tm(CF_3SO_3)_3$	CH_3CN	7.9(1)	Canard et al. (2008)
L24	$Yb(CF_3SO_3)_3$	CH_3CN	7.4(1)	Canard et al. (2008)
L24	$Lu(CF_3SO_3)_3$	CH_3CN	8.0(1)	Canard et al. (2008)
L24	$Y(CF_3SO_3)_3$	CH_3CN	7.3(2)	Canard et al. (2008)

$[R(\mathbf{L25})]^{3+}$ (Figure 36; Koeller et al., 2006), while the same homologation procedure transforming $[R(\mathbf{L20})]^{3+}$ in $[R(\mathbf{L26})]^{3+}$ eventually gives a podand with strongly reduced affinities for R^{III} in acetonitrile (Figure 36; Renaud et al., 2001).

2.5 Photophysical properties

2.5.1 General considerations: f–f transitions and luminescence sensitization

As a result of the poor expansion of the 4f-orbitals, the *R*-ligand bonds are mainly electrostatic and only some minute mixing of metal and ligand electronic wave functions contributes to covalency. It therefore often appears justified to consider separately ligand-centered and metal-centered excited states in lanthanide complexes, and *Jablonsky* diagrams (Figure 37) are adequate for attempting to rationalize photophysical properties (Bünzli and Piguet, 2002). Since the intrashell electric dipole $4f \rightarrow 4f$ electronic transitions are *Laporte*-forbidden (Bünzli, 1989), efficient light-harvesting is performed by the aromatic ($\pi \rightarrow \pi^*$) and/or

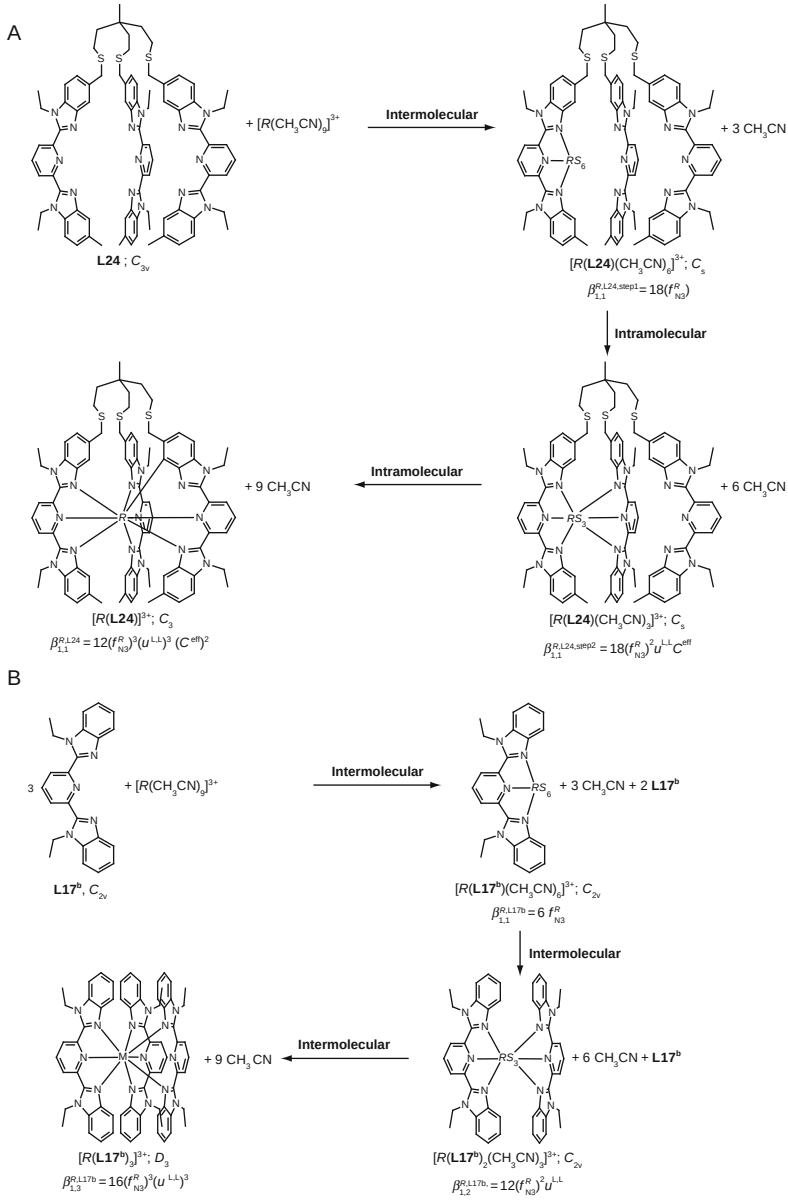

FIGURE 35 Successive complexation processes leading to (A) $[R(\mathbf{L24})]^{3+}$ and (B) $[R(\mathbf{L17^b})_3]^{3+}$. Symmetry point groups and stability constants obtained by the site-binding model are shown (redrawn after Canard et al., 2008).

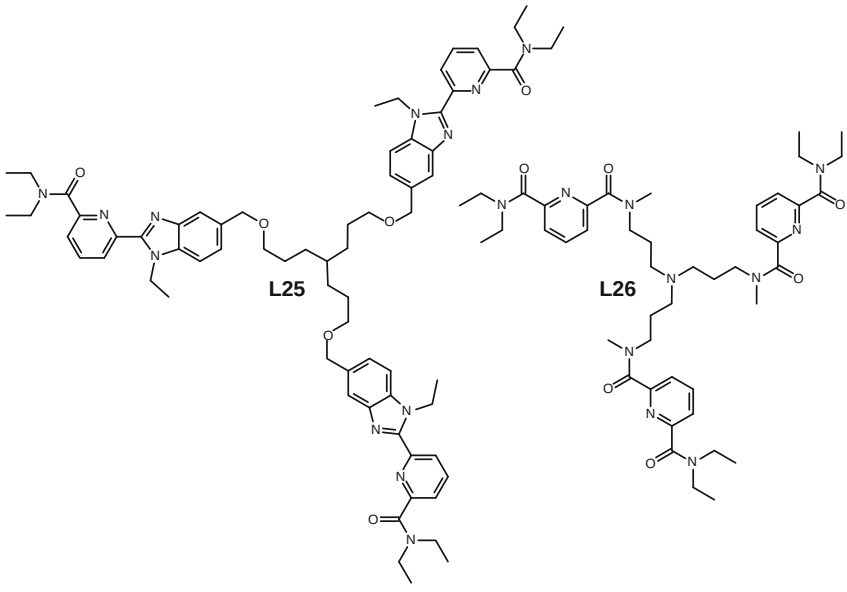

FIGURE 36 Chemical structures of podands **L25** and **L26**.

unsaturated ($n \rightarrow \pi^*$) transitions of ligands displaying large cross sections for one-photon absorption. Alternatively, intraligand charge-transfer states (ILCT, Ali et al., 2008; D'Aléo et al., 2008a,b; Puntus et al., 2007) or ligand-to-metal charge-transfer states (LMCT, Blasse, 1976; Loukova et al., 2007; Puntus et al., 2002) may also collect light. Subsequent intramolecular energy migrations obey *Fermi*'s golden rule modeling resonant energy transfer (Eq. (7)), whereby W_{DA} is the probability of energy transfer, Ω_{DA} is the spectral overlap integral between the absorption spectrum of the acceptor A and the emission spectrum of the donor D, H' is the perturbation operator in the matrix element $\langle DA^*|H'|D^*A\rangle$ (Hendersen and Imbusch, 1989). Depending on the electromagnetic nature of H', a double-electron exchange mechanism (Dexter, 1953) and an electrostatic multipolar (Förster, 1960) mechanism have been proposed and theoretically modeled. Their specific dependences on the distance d separating the donor D from the acceptor A, that is, $e^{-\beta d}$ for double-electron exchange and d^{-6} for dipole–dipolar processes, respectively, often limit *Dexter* mechanism to operate at short distance (typically 30–50 pm) at which orbital overlap is significant, while Förster mechanism may extend over much longer distances (up to 1000 pm). Interestingly, the dipole–quadrupolar mechanism may also be quite effective for short distances

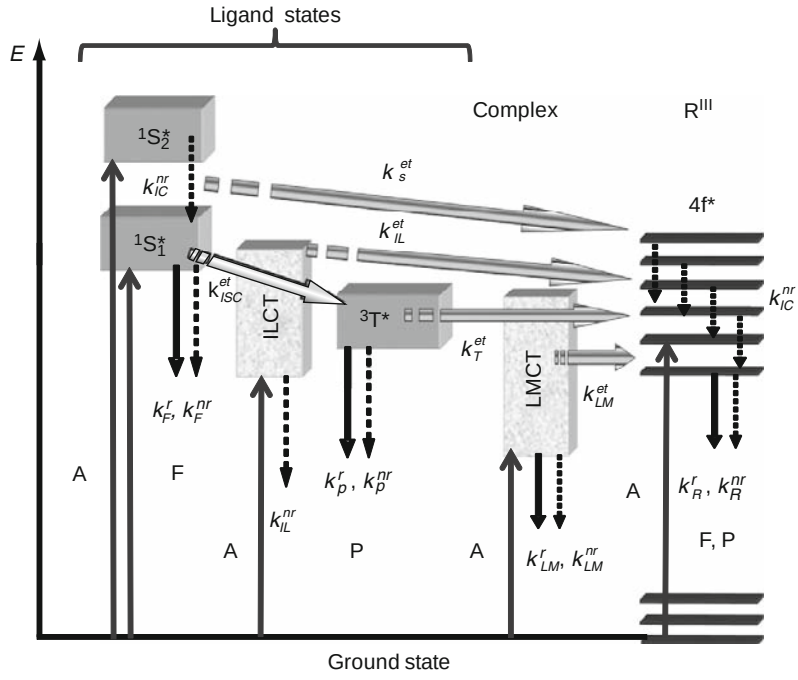

FIGURE 37 Schematic representation of energy absorption, emission, and dissipation (dotted arrows) processes in a lanthanide complex. ^{1}S* or S, singlet state; ^{3}T* or T, triplet state; A, absorption; F, fluorescence; P, phosphorescence; *k*, rate constant; *r*, radiative; *nr*, nonradiative; IC, internal conversion; ISC, intersystem crossing; ILCT (or IL), intraligand charge transfer; LMCT (or LM), ligand-to-metal charge transfer. Back transfer processes are not drawn for the sake of clarity.

(dependence in d^{-8}); in fact depending on Ω_{DA} it may be as efficient as the dipole–dipole mechanism up to distances as long as 300 pm (Malta, 1997).

$$W_{DA} = (2\pi/\hbar)|\langle DA^*|H'|D^*A\rangle|^2\Omega_{DA} \tag{7}$$

One of the main energy migration paths operating in lanthanide complexes implies spin-allowed and *Laporte*-allowed ligand-centered absorptions followed by intersystem crossing ($^1\pi\pi^* \rightarrow {}^3\pi\pi^*$, k_{ISC}) reaching the long-lived ligand-centered triplet state, from which ligand → metal energy transfer ($\pi\pi^* \rightarrow R^*$, k^{et}) eventually excites metal-centered states (Figure 37). Spontaneous metal-centered radiative emission (k_R^r) completes the light-conversion process. It is to be stressed that although important, this energy transfer path is by far not the only operative one. As early as 1969,

Kleinerman who studied over 600 lanthanide chelates pointed out that the excited ligand singlet state can contribute to the transfer and may even be the privileged donor state, depending on the rate constants of the various intervening processes (Kleinerman, 1969). In fact a workable model of the entire energy-converting mechanism has shown that as many as 20–30 rate constants (including those describing back transfers) may be implied (de Sá et al., 2000; Gonçalves e Silva et al., 2002). Efficient transfer from ILCT and LMCT states, as well as from ^{3}MLCT states localized on a transition-metal containing ligand (Chen et al., 2008) is also well documented. All these potential energy funnels render difficult the modeling of the energy transfer and, consequently, the a priori precise design of highly luminescent lanthanide-containing edifices.

Energy transfer from the ligand, evidenced for the first time in 1942 by Weissman (1942), is often referred to as the antenna effect (Sabbatini et al., 1996) or luminescence sensitization (Bünzli and Piguet, 2005). The overall quantum yield Q_{L}^{R} of the metal luminescence upon ligand excitation can be separated into three components characterizing successively: (1) the rate constant $k_{\mathrm{pop}}^{\mathrm{D}}$ ($=k_{\mathrm{ISC}}^{\mathrm{et}}$ for triplet states) for the population of the donor state (^{3}T, ILCT, LMCT, ^{3}MLCT, possibly a 4f5d state; see Burdick and Reid, 2007 for instance), (2) the efficiency of the energy transfer (η_{et}) onto the R^{III} ion, and (3) the metal-centered emission characterized by the intrinsic quantum yield Q_{R}^{R}, that is, the quantum yield of the metal luminescence upon direct f–f excitation (Eq. (8); Beeby et al., 1999; Bünzli and Piguet, 2005; Parker et al., 2002; Werts et al., 2002). For specific lanthanides possessing low-lying charge-transfer excited states (e.g., Eu^{III}, $E^0(Eu^{III}/Eu^{II}) = -0.34$ V vs NHE; Cotton, 2006), or for complexes having low-lying ILCT states, the energy transfer process is further affected by additional nonradiative quenching arising from back energy transfer onto the ligand (not shown on Figure 37). Since in this case the accepting states are quite broad, minute differences in their energy may lead to large differences in the spectral overlap and therefore in the overall quantum yield (see Chauvin et al., 2007, 2008 for a discussion of this phenomenon with respect to Tb^{III} luminescence).

$$Q_{\mathrm{L}}^{R} = \eta_{\mathrm{pop}}^{\mathrm{D}} \eta_{\mathrm{et}} Q_{R}^{R} = \eta_{\mathrm{sens}} Q_{R}^{R} \tag{8}$$

where $\eta_{\mathrm{pop}}^{\mathrm{D}}$ is the efficiency with which the donor state is populated, η_{et} is the yield of the energy transfer to the lanthanide ion, and η_{sens} is the efficacy of the luminescence sensitization by the ligand.

$$\eta_{\mathrm{sens}} = \frac{k_{\mathrm{t}}}{k_{\mathrm{D}}^{\mathrm{r}} + k_{\mathrm{D}}^{\mathrm{nr}} + k_{\mathrm{CT}}^{\mathrm{R}} + k_{\mathrm{t}}} \tag{9}$$

where k_D^r and k_D^{nr} are rate constants for the radiative and nonradiative deactivation of the donor state, k_{CT}^R rate constant for the quenching by the charge-transfer state, and k_t the rate constant of the energy transfer from the donor state D to the lanthanide ion R^{III}.

While the overall quantum yield is relatively easy to measure, Q_R^R, which is needed to evaluate η_{sens}, is quite difficult to determine experimentally in view of the weakness of the f–f transitions. One way to estimate it is by means of Eq. (10) where τ_{obs} is the actual lifetime of the emitting excited state and τ_{rad} is its natural radiative lifetime which obey *Einstein* relation for spontaneous emission probability between two states with quantum numbers J and J', $A(\Psi_J, \Psi_{J'})$ (Görller-Walrand and Binnemans, 1998):

$$Q_R^R = \frac{\tau_{obs}}{\tau_{rad}} \tag{10}$$

$$A(\Psi_J, \Psi'_{J'}) = \frac{1}{\tau_{rad}} = \frac{64\pi^4\tilde{\nu}^3}{3h(2J+1)}\left[\frac{n(n^2+2)^2}{9}D_{ED} + n^3 D_{MD}\right] \tag{11}$$

where $\tilde{\nu}$ is the average energy of the transition in cm^{-1}, h the Planck's constant, and $(2J+1)$ the degeneracy of the initial (emitting) state; the expressions involving the refractive index n are known as the Lorentz local field corrections and D_{ED} and D_{MD} are the electric and magnetic dipole oscillator strengths, respectively (in $esu^2\,cm^2$). The quantity D_{ED} is expressed by Eq. (11) within the frame of the Judd–Ofelt theory (Walsh, 2006):

$$D_{ED} = e^2 \sum_{\lambda=2,4,6} \Omega_\lambda |\langle \Psi || U^\lambda || \Psi' \rangle|^2 \tag{12}$$

in which Ω_λ ($\lambda = 2,4,6$) in cm^2 are phenomenological intensity parameters, e the electron electric charge in coulomb, and $\langle \Psi || U^\lambda || \Psi' \rangle$ are tabulated doubly reduced matrix elements (Nielson and Koster, 1963). The magnetic dipole strength is given by

$$D_{MD} = \left(\frac{eh}{4\pi m_e c}\right)^2 |\langle \Psi || \overrightarrow{L} + 2\overrightarrow{S} || \Psi' \rangle|^2 \tag{13}$$

where m_e is the electron mass and $\overrightarrow{L}$ and $\overrightarrow{S}$ are the orbital and spin angular momentum, respectively. The dipole strengths can be determined experimentally from the absorption spectrum (Walsh, 2006):

$$D(\exp) = \frac{1}{108.9cd\tilde{\nu}_{mean}} \int A(\tilde{\nu}) d\tilde{\nu} \tag{14a}$$

with

$$\tilde{\nu}_{\text{mean}} = \frac{\int \tilde{\nu} \cdot A(\tilde{\nu}) \mathrm{d}\tilde{\nu}}{\int A(\tilde{\nu}) \mathrm{d}\tilde{\nu}} \tag{14b}$$

In the case of Eu^{III} and in view of the special property of the purely magnetic dipole transition $^5D_0 \rightarrow {}^7F_1$, a simplified procedure is at hand whereby

$$A(\Psi_J, \Psi'_{J'}) = \frac{1}{\tau_{\text{rad}}} = A_{\text{MD},0} n^3 \left(\frac{I_{\text{tot}}}{I_{\text{MD}}} \right) \tag{15}$$

with $A_{\text{MD},0}$ being a constant equal to 14.65 s^{-1} and $(I_{\text{tot}}/I_{\text{MD}})$ the ratio of the total integrated emission from the Eu($^5D_0$) level to the integrated intensity of the MD transition $^5D_0 \rightarrow {}^7F_1$. In other cases, authors often rely on published values of τ_{rad} with the wrong hypothesis that the radiative lifetime is a constant for a given emitting level and does not depend on the metal ion surroundings (for a discussion see for instance Comby and Bünzli, 2007).

Since each of the nonradiative rate constants affecting the total quantum yield Q_L^R depend on the localization of the excited states and on the precise transfer mechanism, the correlation between this quantum yield and chemical and structural parameters at the molecular level is complicated and its rational programming is usually not available. On the other hand, Q_R^R depends on less parameters and is easier to rationalize because (i) the main contributions to k_R^{nr} arise from the interactions of the central lanthanide with surrounding high-frequency oscillators (Bünzli, 1989; Bünzli and Piguet, 2005) and (ii) the main contribution to k_R^{r} is usually dominated by forced electric dipole (hypersensitive) transitions, which result from the mixing of levels of opposite parity produced by the crystal field at noncentrosymmetric sites and from additional minute mixing of the ligand-centered and metal-centered wave functions in coordination complexes (Reisfeld and Jørgensen, 1977).

2.5.2 Mononuclear triple-helical precursors

For the triple-helical precursors $[Eu(\mathbf{L17})_3]^{3+}$, detailed photophysical studies show that the sensitization process is particularly inefficient (Table 4; Petoud et al., 1999; Piguet et al., 1993b, 1995b). This can be assigned to the formation of a pseudocentrosymmetric tricapped-trigonal prismatic arrangement of nine heterocyclic nitrogen donor atoms which limits k_R^{r} ($Q[Eu(\mathbf{L17^a})_3]^{3+}) = 0.3 \times Q([Eu(\mathbf{L17^a})(NO_3)_3]^{3+})$ by favoring the

TABLE 4 Photophysical properties of triple-helical complexes $[R(\mathbf{L}k)_3]^{3+}$ (R = Eu, Tb; k = 17–19, see Figures 26–28) in acetonitrile

Ligand	Metal	E($^1\pi\pi^*$) (cm^{-1})[a]	E($^3\pi\pi^*$) (cm^{-1})[b]	Q_L^R (%)	τ_{obs} (ms)[c]	E(Eu($^5D_0$)) (cm^{-1})	References
Terpyridine	Eu	26,670	21,230	32	2.31 (295 K)	–	Comby (2008)
Terpyridine	Tb	26,670	21,230	35	1.20 (295 K)	–	Comby (2008)
L17[a]	Eu	27,700	20,900	2×10^{-3} [d]	1.85 (77 K)	17,236 (77 K)	Piguet et al. (1993c)
L17[a]	Tb	27,700	20,900	–	1.46 (77 K)	–	Piguet et al. (1993c)
L17[b]	Eu	27,800	20,900	2×10^{-2} [d]	1.75 (77 K)	17,235 (77 K)	Piguet et al. (1995a,b,c,d,e)
L17[b]	Tb	27,700	20,900	–	1.95 (77 K)	–	Piguet et al. (1995a,b,c,d,e)
L17[c]	Eu	27,320	–	1.5×10^{-2} [d]		–	Piguet et al. (1995a,b,c,d,e)
L17[e]	Eu	27,700	–	7×10^{-2} [d]		–	Piguet et al. (1995a,b,c,d,e)
L17[f]	Eu	26,970	–	2×10^{-2} [d]		17,219 (77 K)	Piguet et al. (1995a,b,c,d,e)
L17[f]	Tb	26,970	20,900	–	1.14 (77 K)	–	Piguet et al. (1995a,b,c,d,e)
L17[l]	Eu	26,255	19,750	5×10^{-3}	0.85 (13 K)	17,258 (295 K)	Muller et al. (2002b)
L17[l]	Tb	27,175	21,050	–	0.38 (13 K)	–	Muller et al. (2002b)
L18[a]	Eu	35,840	23,600	0.2[d]	1.78 (10 K)	17,216 (10 K)	Renaud et al. (1997a)
L18[a]	Tb	35,830	23,600	26[d]	1.85 (295 K)	–	Renaud et al. (1997a)
L18[c]	Eu	35,850	23,200	0.2	1.45 (13 K)	17,211 (13 K)	Muller et al. (2001b)
L18[a]	Tb	35,630	23,200	1.2	0.92 (13 K)	–	Muller et al. (2001b)
L19[b]	Eu	29,410	20,660	5×10^{-2}	1.86 (77 K)	–	Le Borgne et al. (2004)
L19[b]	Tb	29,410	20,660	–	1.22 (77 K)	–	Le Borgne et al. (2004)

[a] Values obtained from absorption spectra in solution (293 K).
[b] Values obtained from emission spectra (0-phonon transition, 77 K).
[c] Metal-centered lifetime.
[d] Quantum yields have been recalculated by using the most recent values reported for the $[R(\text{terpyridine})_3]^{3+}$ internal references (Comby, 2008).

presence of a low-lying LMCT state (Petoud et al., 1999). Indeed, Eu(II) is stabilized by the heterocyclic nitrogen atoms, which puts the LMCT state close in energy to the **L17**-centered singlet state, thus allowing efficient $^1\pi\pi^* \rightarrow$ LMCT energy transfer (Eq. (7)) and maximizing k_{CT}^R (Eq. (9); Gonçalves e Silva et al., 2000; Petoud et al., 1999). For $[Tb(\mathbf{L17})_3]^{3+}$, the energy gap between the ligand-centered $^3\pi\pi^*$ feeding level (21,050 cm^{-1}) and the accepting metal-centered $Tb(^4D_4)$ level (20,490 cm^{-1}) is too small to ensure efficient and irreversible energy funneling (Steemers et al., 1995). Consequently, thermally activated $Tb(^4D_4) \rightarrow \mathbf{L17}(^3\pi\pi^*)$ back transfer becomes an efficient deexcitation pathway at room temperature, which drastically reduces Q_{Tb}. The replacement of the aromatic benzimidazole side arms in **L17** with carboxamide groups in **L18** significantly increases the energy of both ligand-centered $^1\pi\pi^3$ and $^3\pi\pi^*$ excited states in $[R(\mathbf{L18})_3]^{3+}$ (Table 4). Consequently, Tb^{III}-centered luminescence is detected at room temperature with an encouraging quantum yield of 26% for $[Tb(\mathbf{L18^a})_3]^{3+}$ in acetonitrile (Renaud et al., 1997a). Although the absolute values are less impressive for the related Eu^{III} complexes, the replacement of **L17** with **L18** produces triple-helical red emitters $[Eu(\mathbf{L18})_3]^{3+}$, the global quantum yields of which are larger by two to three orders of magnitude because the low-lying LMCT states have been pushed higher in energy (Table 4). Interestingly, all triple-helical complexes $[R(\mathbf{L17})_3]^{3+}$ and $[R(\mathbf{L18})_3]^{3+}$ ($R =$ Eu, Tb) display metal-centered excited lifetimes characteristics of the absence of high-energy oscillators in the first coordination sphere, which demonstrates that the wrapping of the three ligand strands efficiently protects the metallic sites from external interactions (e.g., solvent molecules). As expected, the connection of three tridentate dicarboxamidopyridine tridentate units analogous to **L18^a**, in podand **L20**, has minor effect on the quantum yields (Table 5; Renaud et al., 1999), but a slight improvement for the Eu-centered emission is evidenced when the terminal carboxamide groups are replaced with carboxylates in [Eu(**L21**-3H)] (Senegas et al., 2003). Finally, the facial organization of three 2-benzimidazole-6-carboxamidopyridine units (NNO donors) in $[R(\mathbf{L22})]^{3+}$ and $[R(\mathbf{L23})]^{3+}$ gives the best light converters of the series ($R =$ Eu, Tb; Table 5).

Some thorough investigations of the energy migration processes according to Eq. (8) for [Eu(**L21**-3H)] in water shows that $Q_L^{Eu} = 4\%$ can be indeed separated into $Q_{Eu}^{Eu} = 31\%$ and $\eta_{sens} = 13\%$ (Senegas et al., 2003), which suggests that the moderate quantum yield originates from both limited intrinsic metal-centered quantum yield and sensitization processes. However, the same investigations performed in acetonitrile for $[Eu(\mathbf{L20} + H)]^{4+}$ ($Q_L^{Eu} = 0.4\%$, $Q_{Eu}^{Eu} = 55\%$, and $\eta_{sens} = 0.7\%$) and for $[Eu(\mathbf{L20})]^{3+}$ ($Q_L^{Eu} = 0.3\%$, $Q_{Eu}^{Eu} = 50\%$, and $\eta_{sens} = 0.6\%$) unambiguously establish that the sensitization process is by far the limiting factor for efficient light conversion in triple-helical complexes with N_3O_6

TABLE 5 Photophysical properties of triple-helical podates $[R(\mathbf{L}k)]^{3+}$ (R = Eu, Tb; k = 20–23, see Figures 32 and 33)

Ligand	Metal	Solvent	E($^1\pi\pi^*$) (cm^{-1})[a]	E($^3\pi\pi^*$) (cm^{-1})[b]	Q_L^R (%)	τ_{obs} (ms)[c]	E(Eu($^5D_0$)) (cm^{-1})	References
L20	Eu	CH_3CN	35,210	[d]	0.3[e]	1.41 (10 K)	17,213 (10 K)	Renaud et al. (1999)
L20	Tb	CH_3CN	35,210	[d]	4[e]	1.11 (295 K)	–	Renaud et al. (1999)
[L20 + H$]^+$	Eu	CH_3CN	35,090	[d]	0.4[e]	1.81 (10 K)	17,215 (10 K)	Renaud et al. (1999)
[L20 + H$]^+$	Tb	CH_3CN	35,090	[d]	25[e]	1.58 (295 K)	–	Renaud et al. (1999)
[L21-3H$]^{3-}$	Eu	H_2O	35,710	23,000	4[e]	1.45 (10 K)	17,209 (10 K)	Senegas et al. (2003)
[L21-3H$]^{3-}$	Tb	H_2O	35,710	23,000	7[e]	1.06 (10 K)	–	Senegas et al. (2003)
L22	Eu	CH_3CN	30,300	20,280	10[e]	2.58 (295 K)	–	Koeller et al. (2003a)
L22	Tb	CH_3CN	30,210	20,370	10[e]	0.02 (295 K)	–	Koeller et al. (2003a)
L23	Eu	CH_3CN	30,120	20,410	14[e]	2.87 (295 K)	–	Koeller et al. (2003b)
L23	Tb	CH_3CN	30,210	20,410	11[e]	0.02 (295 K)	–	Koeller et al. (2003b)

[a] Values obtained from absorption spectra in solution (293 K).
[b] Values obtained from emission spectra (0-phonon transition, 77 K).
[c] Lifetime of the metal excited state.
[d] Too weak to be detected in the emission spectra of the analogous Gd^{III} complexes.
[e] Quantum yields have been recalculated by using the most recent values reported for the $[R(terpyridine)_3]^{3+}$ internal references (Comby, 2008).

coordination spheres (Renaud et al., 1999). Although no intrinsic metal-centered quantum yields are available for the N_6O_3 coordination spheres in $[Eu(\mathbf{L22})]^{3+}$ and $[Eu(\mathbf{L23})]^{3+}$, we can reasonably assume that $Q_{Eu}^{Eu} \approx 50\%$, which translates into $\eta_{sens} \approx 20$–30%, thus making the organization of three helical NNO binding units around Eu^{III} the best candidate for producing luminescent triple-stranded helicates.

2.5.3 Water-soluble complexes derived from dipicolinic acid

Europium and terbium tris(dipicolinates) are known to be highly luminescent, with overall quantum yields of 24% and 22%, respectively, and lifetimes of 1.67 and 1.43 ms, respectively. This property is taken advantage of in simple luminescent methods for the determination of nanomolar concentrations of lanthanides (Barela and Sherry, 1976). In fact, both the quantum yield and lifetime heavily depend on the concentration of the chelates and the pH since the latter governs the speciation in solution (Figure 38). Three or six water molecules are coordinated onto the metal ion in the lower bis and monospecies, respectively. As a consequence, the corresponding quantum yields and lifetimes are drastically reduced with respect to the tris-species. For instance, a quantum yield of only 4.5% has been determined for $[Eu(dpa)_2]^-$ (Aebischer et al., 2009) while $\tau(^5D_0) = 0.35$ ms only for this complex (Chauvin et al., 2004).

The overall shape of the luminescence spectra of the Eu^{III} complex is compatible with a metal ion lying in a coordination site with a pseudo-tricapped-trigonal prismatic geometry. The magnetic dipole transition $^5D_0 \rightarrow {}^7F_1$ is split into two main components ($A_1 \rightarrow A_2$ and $A_1 \rightarrow E$ in trigonal symmetry), the $^5D_0 \rightarrow {}^7F_2$ transition is dominated by two strong components and at least five peaks are detected for the $^5D_0 \rightarrow {}^7F_4$ transition. This pattern is in agreement with a geometry derived from D_3-symmetry around the metal ion. Modulation of the photophysical properties can be achieved by adding a substituent X in the pyridine 4-position. For instance, Lamture et al. (1995) have shown that the relative efficiency for energy transfer (η_{sens}) in $[Tb(\mathbf{L15^{f-j}})_3]^{3-}$ species (see Figure 23) varies in the order $X = NH_2 > OH > NHCOCH_3 > Cl > H \approx Br$. That bromine substitution does not enhance the energy transfer efficiency through the heavy atom effect points to the singlet state playing a decisive role in the sensitization process.

These simple dipicolinates cannot, however, be coupled to biological molecules. Therefore derivatives in which the pyridine ring is decorated with substituted trioxyethylene pendants have been synthesized (Figure 24). In the resulting chelates, the metal-ion environment does not appear to undergo substantial changes, in that both the relative intensities of the $^5D_0 \rightarrow {}^7F_J$ transitions and the energies of the ligand-field sublevels determined for the $[Eu(\mathbf{L15^j})_3]^{3-}$ complexes are similar to those found for $[Eu(dpa)_3]^{3-}$. In addition, the lifetimes of the $Eu(^5D_0)$ level

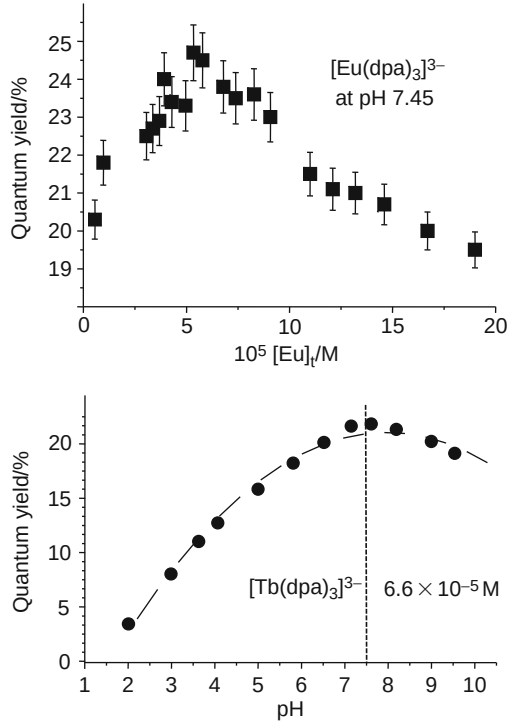

FIGURE 38 Top: variation of Q_{Eu}^{L} of the tris(dipicolinate) complex versus the metal ion concentration. Bottom: variation of Q_{Tb}^{L} versus pH (redrawn from Chauvin et al., 2004).

measured both in water and in deuterated water (Table 6) essentially translate into a hydration number $q = 0$ when known phenomenological equations are used to estimate it (Bünzli and Piguet, 2005). The overall quantum yields of all the solutions (Table 6) surprisingly show a marked dependence on the nature both of the pendant arm and of the metal ion: (i) the quantum yields of the Eu^{III} chelates range between 12% and 29% while those for Tb^{III} complexes are significantly smaller, ranging between 11% and 18%, and (ii) the sequence is different for both ions, Q_{L}^{Eu} decreasing in the series $[Eu(\mathbf{L}^{\mathbf{NH2}})_3]^{3-} > [Eu(\mathbf{L}^{\mathbf{OMe}})_3]^{3-} > [Eu(\mathbf{L}^{\mathbf{Phta}})_3]^{3-} > [Eu(\mathbf{L}^{\mathbf{OH}})_3]^{3-}$ while this series is $[Tb(\mathbf{L}^{\mathbf{OH}})_3]^{3-} > [Tb(\mathbf{L}^{\mathbf{NH2}})_3]^{3-} > [Tb(\mathbf{L}^{\mathbf{OMe}})_3]^{3-} > [Tb(\mathbf{L}^{\mathbf{Phta}})_3]^{3-}$ for Q_{L}^{Tb}. In fact, the intrinsic quantum yield Q_{Eu}^{Eu} is very similar for all chelates with the five dipicolinate ligands, within experimental errors, ranging between 36% and 42%, pointing to the substitution not affecting appreciably the deactivation processes within the triple-helical structures. Differences in the overall quantum yields, therefore, essentially arise from differences in the sensitization efficiency η_{sens} provided by the ligands. With respect

TABLE 6 Photophysical properties of triple-helical podates derived from dipicolinate, $[R(\mathbf{L15^x}\text{-}2H)_3]^{3-}$ (R = Eu, Tb; x = s–v, see Figures 23 and 24) in aqueous solution of Tris–HCl 0.1 M at 295 K (Gassner et al., 2008) compared to those of the parent chelates with **L15**[a]

Ligand	R	$E(^3\pi\pi^*)$ (cm^{-1})[a]	$\tau_{obs}(H_2O)$ (ms)[b]	τobs (D_2O) (ms)[b]	Q_L^R (%)[c]	Q_{Eu}^{Eu} (%)	η_{sens}
L15[a]	Eu	[d]	1.67(3)	3.0(1)	24	39	61
	Tb		1.41(1)	2.35(2)	22		
L15[s]	Eu	26,810	1.36(2)	2.23(1)	26.6	38	70
	Tb		1.25(2)	1.69(1)	12.7		
L15*t*	Eu	27,100	1.36(1)	2.15(1)	11.8	36	33
	Tb		0.99(1)	2.04(1)	17.8		
L15[u]	Eu	26,810	1.47(1)	1.95(2)	18.3	42	44
	Tb		1.08(2)	1.95(2)	10.8		
L15[v]	Eu	25,189	1.43(1)	2.20(1)	28.9	40	72
	Tb		1.58(2)	1.91(1)	15.3		

[a] From phosphorescence spectra of the La^{III} complex at 77 K, 0-phonon transition.
[b] Lifetime of the metal excited state.
[c] ±10%.
[d] Too weak to be detected in the emission spectra of the analogous Gd^{III} complexes.

to the parent dipicolinate (61%), **L15**[s] and **L15**[v] are slightly better sensitizers, with $\eta_{sens} \approx 70\%$, while the two other ligands transfer energy much less efficiently with $\eta_{sens} \approx 33$–45%. This points to a remarkable fine-tuning of the photophysical properties of the europium triple-helical chelates by the terminal functional group of the polyoxyethylene substituent, the most luminescent chelate being 2.4-fold as luminescent as the less emissive one. Para substitution with an ether group in the pyridine 4-position usually leads to a large decrease in Q_L^{Eu}, for example, from 24% for the tris(dipicolinate) to 16.1% for a simple OMe group (Gassner et al., 2008) or to 12% for the triple-helical complex with 4-(naphthalen-2-yloxy)-pyridine-2,6-dicarboxylate (Latva et al., 1997; the quantum yield has been recalculated with $Q([Ln(\mathbf{L15^a})_3]^{3-}) = 24\%$ instead of 13% as in the original paper). Therefore, the detrimental effect of ether substitution in the para position of the pyridine moiety is apparently compensated by the presence of a terminal substituent (X) on the polyoxyethylene arm, at least for X = OMe and NH_2 and, less efficiently, for X = Phta, while the alcohol group has no positive effect. On the other hand, the tuning for Tb^{III} chelates is less remarkable, the improvement factor between $[Tb(\mathbf{L15^u})_3]^{3-}$ and $[Tb(\mathbf{L15^t})_3]^{3-}$ being only 1.6-fold.

3. POLYNUCLEAR HOMOMETALLIC 4f HELICATES

The packing of triple-helical mononuclear precursors along the helical axis produces infinite columns, which are sometimes observed during the crystallization processes. For instance, $[Eu(\mathbf{L17^a})_3](ClO_4)_3$ crystallizes in the $R\bar{3}$ space group and forms polynuclear columns of closely packed triple-helical $[Eu(\mathbf{L17^a})_3]^{3+}$ cations (the Eu...Eu distances amount to 8.364(2) and 8.618(2) Å) possessing alternating helicities along the *c* direction (Figure 39; Piguet et al., 1993c).

However, such lucky and uncontrolled crystallization processes are rare, and the programming of polynuclear homometallic triple-stranded helicates normally relies on the connection of several tridentate segments by using adequate spacers (Figure 40). Homotopicity provides C_2-symmetrical segmental ligands, which eventually form D_3-symmetrical helicates upon reaction with R^{III} (Figure 40, left). The introduction of different binding units along the strand, that is, heterotopicity, results in the design of either axially symmetrical (twofold axis) or nonaxial ligands. Upon reaction with R^{III}, the latter axial ligand also gives D_3-symmetrical helicates, although different lanthanide triple-helical building blocks are packed along the helical axis (Figure 40, center). For nonaxial ligands, the complexation process leads to mixtures of HHH (C_3-symmetrical) and HHT (C_1-symmetrical) isomeric helicates (Figure 40, right).

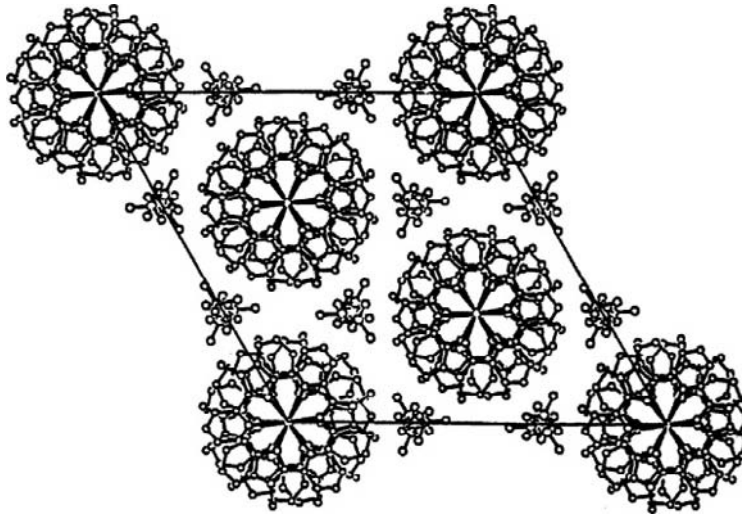

FIGURE 39 View of the unit cell along the *c*-axis in the crystal structure of $[Eu(\mathbf{L17^a})_3](ClO_4)_3$ (reproduced by permission from Piguet et al., 1993c, © American Chemical Society, 1993).

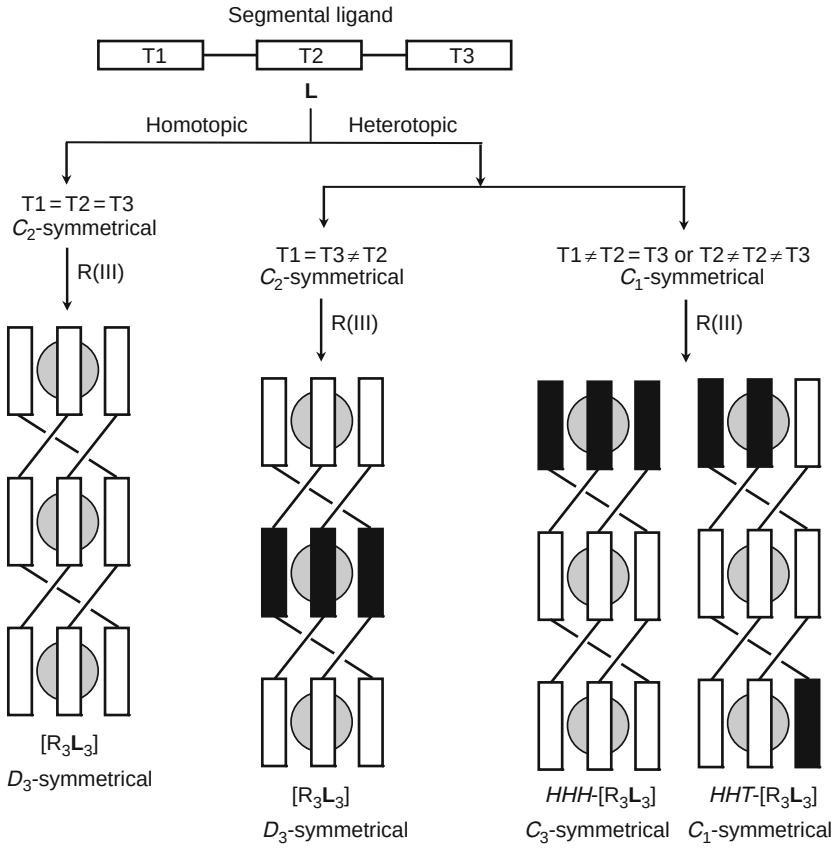

FIGURE 40 Correlations between the symmetry of the segmental multitridentate ligands and the nature of the final lanthanide helicates.

For generalization purpose, we do not consider the existence of symmetry elements of the second kind in the ligand (for instance a mirror plane), because they do not influence the issue of the self-assembly process.

3.1 Designing segmental ligands: Principles and synthetic routes

To minimize synthetic efforts, the design of both axial (i.e., $C_{2(v)}$-symmetrical) and nonaxial (i.e., C_1- or C_s-symmetrical) ligand strands relies on a common strategy, in which the spacer, *S*, plays a crucial role since it must be rigid enough to transmit the helical twist from one binding unit to the other, but flexible enough to allow helication with a minimum of structural constraints. Moreover, *S* must be compatible with its introduction

into homotopic and heterotopic receptors. When using d-block ions, the pronounced stereochemical preferences of these metals may compensate some weaknesses in the spacer design, and a plethora of connectors are then compatible with the formation of helicates (alkyl chains, polyether chains, disubstituted aromatic units; see Albrecht, 2001; Piguet et al., 1997a for extensive reviews), among which we find the diphenylmethane spacer (Hannon et al., 1997; Williams et al., 1991).

For f-block ions, the lack of directional bonding is more restrictive and the diphenylmethane spacer appears to be ideal because of (i) the steric repulsion between the two hydrogen atoms connected at the 2,2′ positions of the phenyl rings, which forces helication, (ii) its easy synthetic access from ortho-nitroamine arene precursors to give 3,3′,4,4′-tetrasubstituted synthon (Figure 41; Piguet et al., 1994), and (iii) its easy connection to tridentate binding units to give symmetrical (i.e., axial, Figures 41–43 and 49), or unsymmetrical (i.e., nonaxial, Figure 48) segmental multitridentate ligands. C_{2v}-symmetrical ligands incorporating NNO and NNN tridentate binding units in **L11** (homotopic: NNN-*S*-NNN), **L13** (homotopic: ONN-*S*-NNO, Figure 41), **L27** (heterotopic: NNN-*S*-NNN-*S*-NNN), **L28** (heterotopic: ONN-*S*-NNN-*S*-NNO, Figure 42), and **L29** (heterotopic: ONN-*S*-NNN-*S*-NNN-*S*-NNO, Figure 43) are obtained according to the standard amidation/reductive cyclization strategy previously developed for mononuclear triple-helical precursors (Figure 18B).

This synthetic path has been slightly modified to develop water-soluble homobimetallic helicates for bioanalyses which bear short polyoxyethylene substituents either on (*N*)1-position of the benzimidazole moiety or on the 4-position of the pyridine rings (Figure 44).

In the former case (Figure 45) the dinitro intermediate is first transformed into a tetra-amino intermediate before condensation with the dipicolinic acid derivative in presence of phosphoric acid at elevated temperature. The polyoxyethylene pendant is then grafted onto the ligand skeleton with the help of a Mitsunobu reaction. The methyl groups are then oxidized via an elaborate three-step route using hydrogen peroxide in acetic acid first, followed by treatment with acetic anhydride and finally conversion of the alcoholic functions by potassium permanganate (Chauvin et al., 2007). The synthesis of ligands derivatized in the 4-position of the pyridine is easier (Figure 46). Here the dinitro derivative is coupled with an asymmetrically derivatized dipicolinic acid bearing one carboxylic acid and one ethyl ester groups. The reaction then follows the same path as the one described in Figure 41, with reduction conducted with iron powder and followed by hydrolysis with sodium hydroxide. When ligands are derivatized both in the pyridine 4-position and in R^4, the synthetic path is accordingly more elaborate. In fact the trioxyethylene substituent is grafted on the dipicolinic acid synthon whereas the other substituent is grafted on the dinitro derivative (Figure 47).

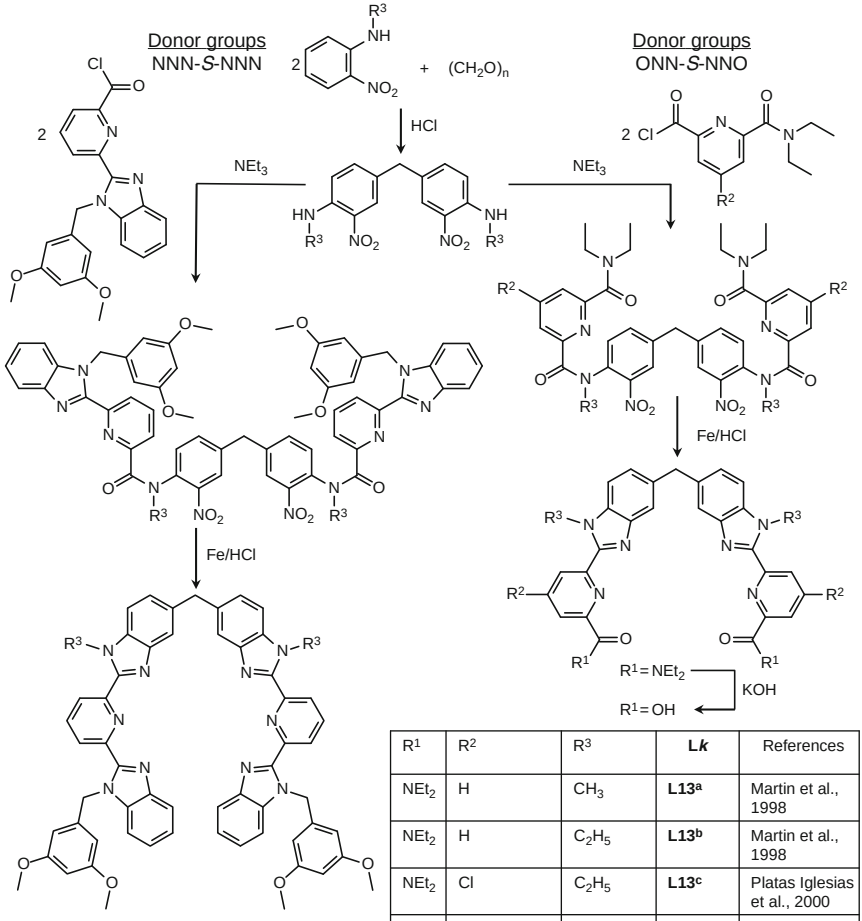

R^1	R^2	R^3	L*k*	References
NEt_2	H	CH_3	**L13**[a]	Martin et al., 1998
NEt_2	H	C_2H_5	**L13**[b]	Martin et al., 1998
NEt_2	Cl	C_2H_5	**L13**[c]	Platas Iglesias et al., 2000
NEt_2	Br	C_2H_5	**L13**[d]	Platas Iglesias et al., 2000
NEt_2	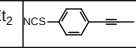	C_2H_5	**L13**[e]	Tripier et al., 2002
HO	H	C_2H_5	**H_2L13**[f]	Elhabiri et al., 1999

FIGURE 41 Synthesis of 3,3′,4,4′-tetrasubstituted diphenylmethane spacers and its incorporation into homotopic C_2-symmetrical bis-tridentate segmental ligands (*S* = spacer).

The preparation of nonaxial C_s-symmetrical bis-tridentate ligands **L30** (heterotopic: NNN-*S*-NNO) and **L31** (heterotopic: ONN-*S*-NNO, Figure 48) relies on the disymmetrization of the diphenylmethane spacer as found in the multistep synthesis of tris-tridentate (Figure 42) and tetratridentate (Figure 43) axial receptors. Finally, two alternative homotopic bis-tridentate ligands possessing a central pyridine ring, but no

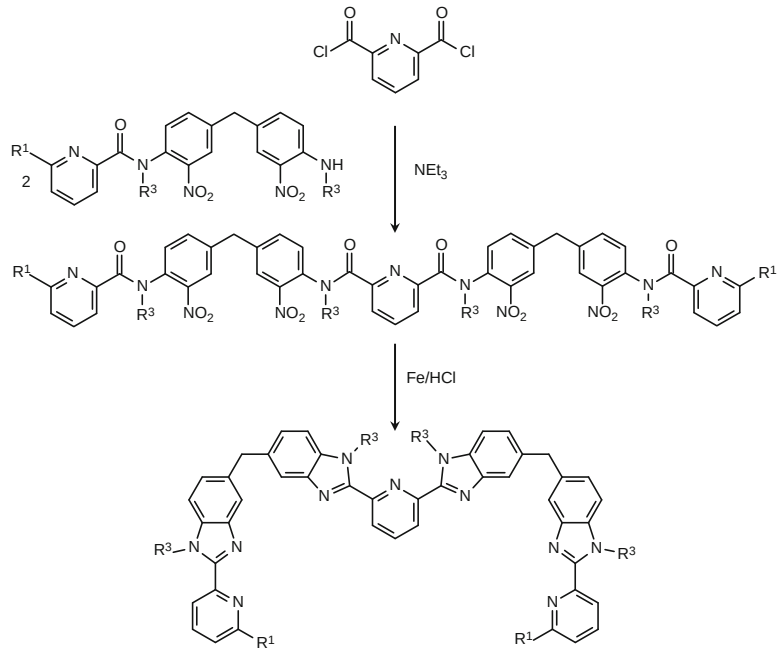

R^1	R^3	**L*k***	References
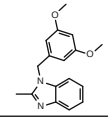	CH_3	**L27**	Piguet et al., 1994
$CONEt_2$	C_2H_5	**L28**	Floquet et al., 2003

FIGURE 42 Synthesis of heterotopic C_2-symmetrical tris-tridentate ligands.

adjacent benzimidazole group have been reported as potential receptors for the formation of binuclear triple-stranded helicates with trivalent lanthanides (ONO-*S*-ONO, **L32**, Lessmann and Horrocks, 2000, Figure 49A and ONN-*S*-NNO, **L33**, Ronson et al., 2007, Figure 49B).

3.2 Solid state and solution structure

Reaction of the homotopic C_{2v}-symmetrical bis-tridentate ligands **L11** or $\mathbf{L13^{a-e}}$ with $R(ClO_4)_3$ or $R(CF_3SO_3)_3$ gives the expected D_3-symmmetrical triple-stranded helicates $[R_2(\mathbf{L11})_3]^{6+}$ (Piguet et al., 1993a,b,c) and $[R_2(\mathbf{L13^{a-e}})_3]^{6+}$ (Martin et al., 1998; Platas-Iglesias et al., 2000; Tripier et al., 2002). The molecular structures of the cations in the solid state are characterized by a tight wrapping of the three strands about a helical axis

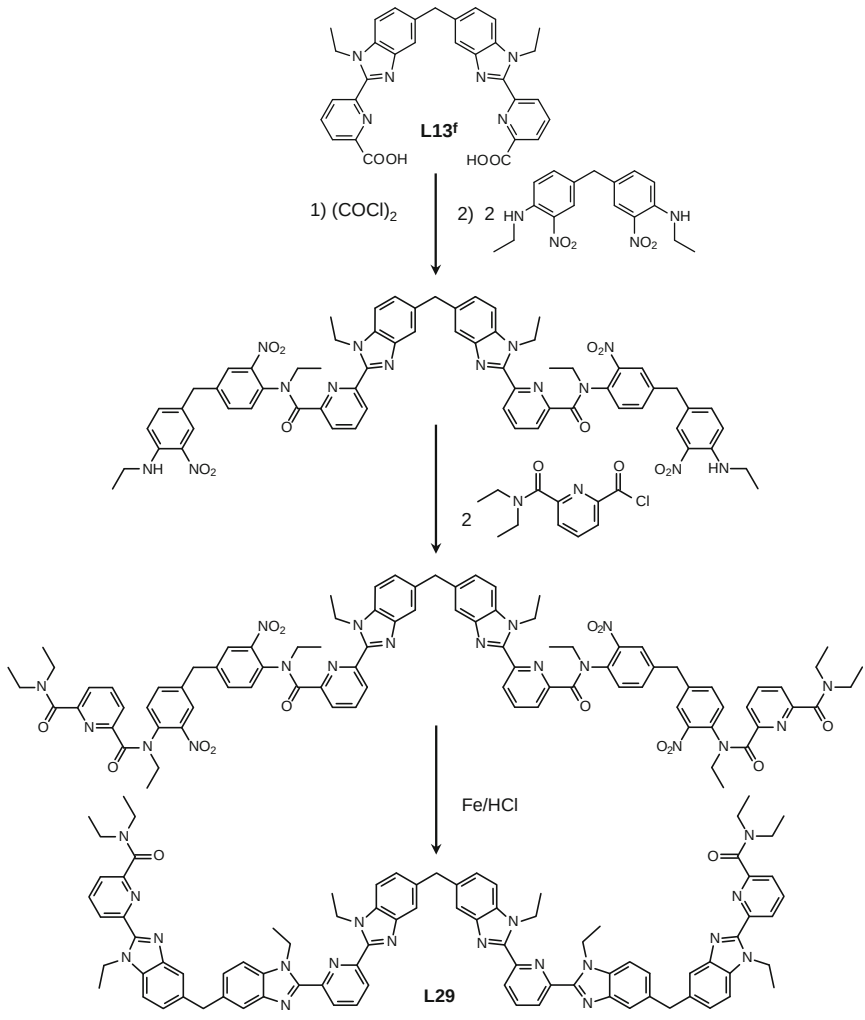

FIGURE 43 Synthesis of a heterotopic C_2-symmetrical tetratridentate ligand (Zeckert et al., 2005).

defined by the two metals, which are separated by ca. 9 Å (Figure 50). Interestingly, the intramolecular $R\ldots R$ separation in $[Eu_2(\mathbf{L11})_2]^{6+}$ (8.8876 Å) is similar to the intermolecular intermetallic distance between two precursors $[Eu(\mathbf{L17^a})_3]^{3+}$ in the packed column found in the crystal structure of the mononuclear complex (8.364(2) and 8.618(2) Å, Figure 39), which suggests, at first sight, that the diphenylmethane spacer ideally transmits helicity, and that the structure of the binuclear helicate can be derived from the packing of two mononuclear building blocks. This naïve view does not resist a more detailed structural analysis, which highlights

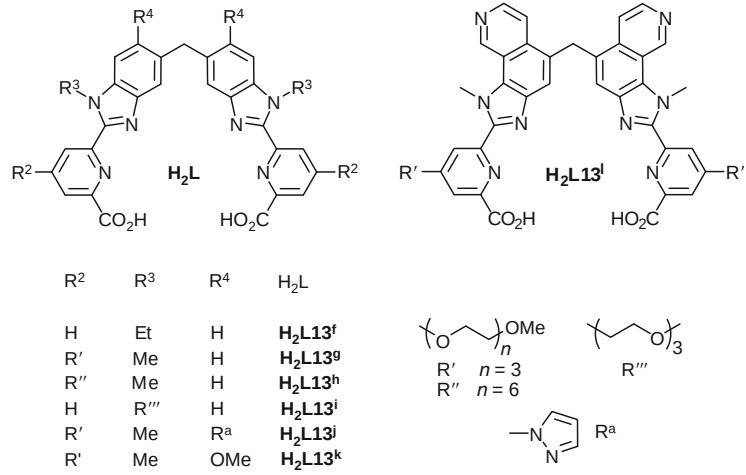

FIGURE 44 Ditopic bis-tridentate C_2-symmetrical ligands used for the self-assembly of bimetallic lanthanide luminescent probes.

two crucial differences. (1) The same screw direction of the helical twist is maintained around both metal ions in the binuclear helicate, thus leading to a discrete palindromic regular helix, while the screw direction systematically inverts along columns of packed mononuclear precursors, thus producing infinite palindromic amphiverse helices. (2) The helical pitch P = linear progression per complete turn of the helix in mononuclear complexes amounts to 9.28 Å for $[Eu(\mathbf{L17^a})_3]^{3+}$ (total rotation = 0.75 turn) and 9.12 Å for $[Eu(\mathbf{L18^a})_3]^{3+}$ (total rotation = 0.4 turn), which show much tighter wrapping of the strands compared to the average pitches in the binuclear helicates $[Eu_2(\mathbf{L11})_3]^{6+}$ (P = 13.9 Å, total rotation = 1.21 turn, Figure 50A) and $[Tb_2(\mathbf{L13^b})_3]^{6+}$ (P = 14.7 Å, total rotation = 0.81 turn, Figure 50B).

Calculation of local pitches for each helical portion along the threefold axis indeed points to P_{local} = 10.5 Å for the EuN_9 coordination spheres in $[Eu_2(\mathbf{L11})_3]^{6+}$ and P_{local} = 9.5 Å for the EuN_6O_3 coordination spheres in $[Tb_2(\mathbf{L13^b})_3]^{6+}$ in agreement with similar helical structures found in the mononuclear precursors. However, P_{local} = 17–18 Å observed within the spacer domain unambiguously demonstrates a severe relaxation of the helical wrapping in the latter intermetallic portion (Floquet et al., 2003). Closely related geometrical parameters are found in the extended D_3-symmetrical trinuclear $[R_3(\mathbf{L28})_3]^{9+}$ (Floquet et al., 2003) and tetranuclear $[R_4(\mathbf{L29})_3]^{12+}$ (Zeckert et al., 2005) triple-stranded helicates of nanometric dimensions (Figure 51).

Because of the very limited degrees of freedom in the rigid diphenylmethane spacers (i.e., rotations about the two single C_{arom}–C_{alkyl} bonds),

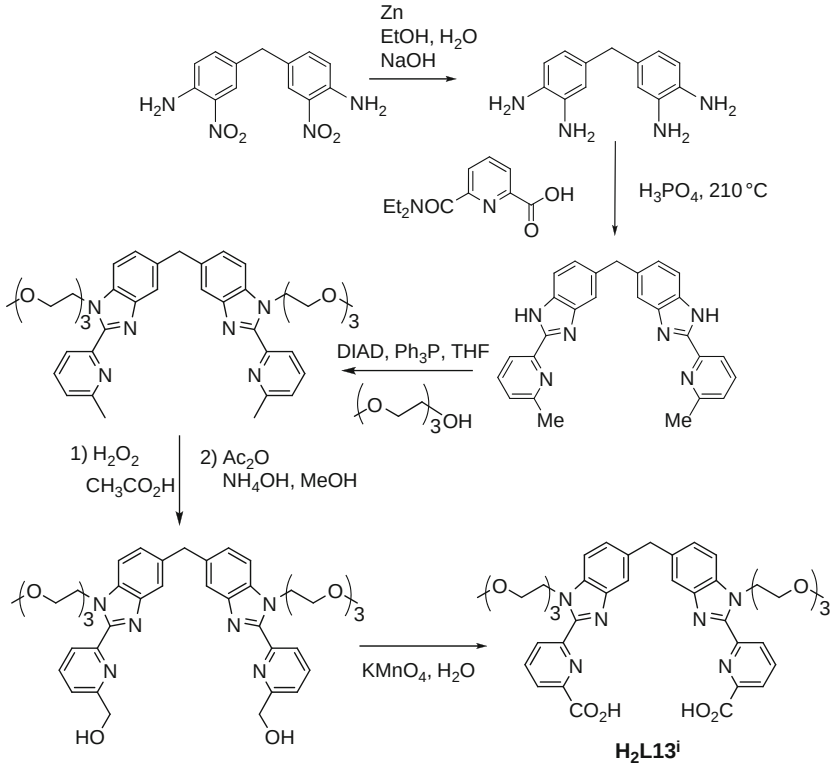

FIGURE 45 Synthesis of a dicarboxylic bis-tridentate receptor substituted in the (*N*)1-position of the benzimidazole moiety for the self-assembly of water-soluble helicates [Ln_2L_3] (redrawn after Chauvin et al., 2007).

the average intermetallic *R*. . .*R* distance of 9 Å combined with a pitch of 14 Å found in the initial series of D_3-symmetrical cationic polynuclear lanthanide helicates are maintained in the neutral analogues [R_2(**L13**$^{\mathbf{f-h}}$-2H)$_3$] (Elhabiri et al., 1999) and in the C_3-symmetrical complexes HHH-[R_2(**L30**$^{\mathbf{a,c,d}}$)$_3$]$^{6+}$ (André et al., 2004; Jensen et al., 2006, 2007, 2008) obtained with heterotopic bis-tridentate C_s-symmetrical ligands (Figure 52).

However, it is inadequate to believe that any mixture of bis-tridentate ligands with R^{III} will produce triple-stranded helicates. We already mentioned in the introduction how some competing counter-ions or solvent molecules may prevent the fixation of the third strand, thus leading to unsaturated complexes (Section 1.3, Figure 13B). A second illustrative example is shown in Figure 53, whereby the use of a 1–4-disubstituted phenyl spacer in **L33**$^{\mathbf{a}}$ makes the output of the assembly process extremely sensitive to the stoichiometric *R*:**L33**$^{\mathbf{a}}$ ratio (Ronson et al., 2007).

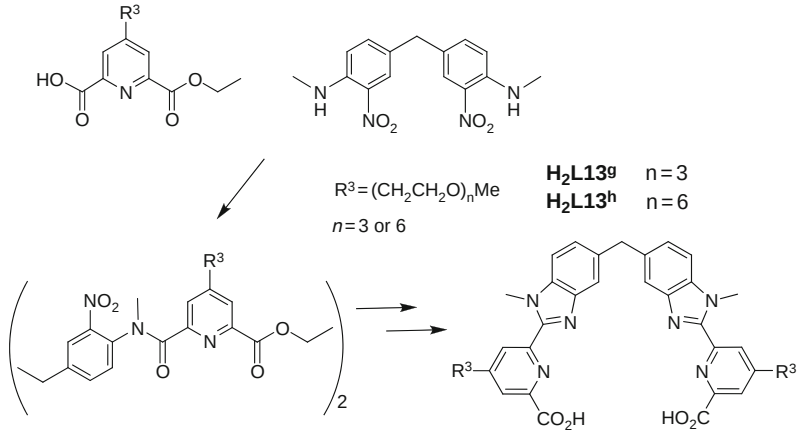

FIGURE 46 Synthesis of dicarboxylic bis-tridentate receptor substituted in R^2 (see Figure 44) for the self-assembly of water-soluble helicates $[Ln_2L_3]$ (Chauvin et al., 2008; Deiters et al., 2008).

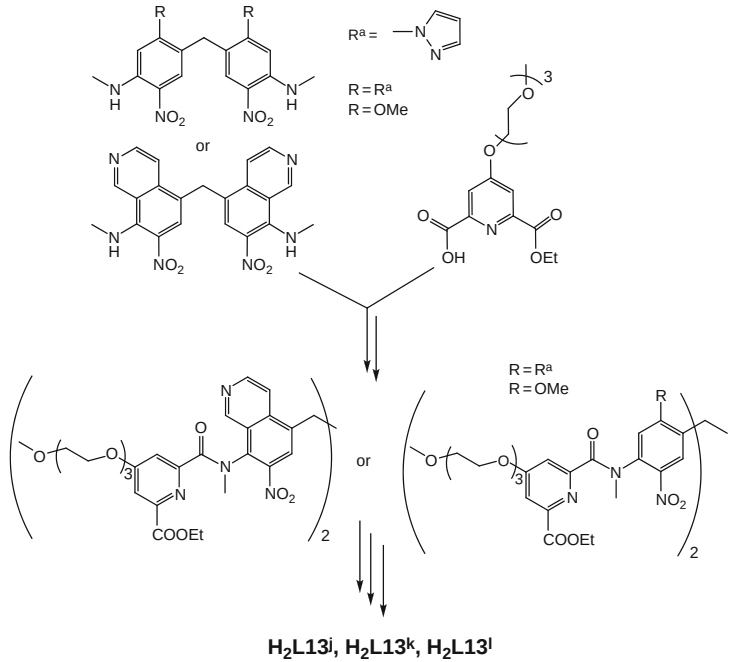

FIGURE 47 Synthesis of dicarboxylic bis-tridentate receptor substituted in R^2 and R^4 (see Figure 44) for the self-assembly of water-soluble helicates $[Ln_2L_3]$ (Deiters et al., 2009).

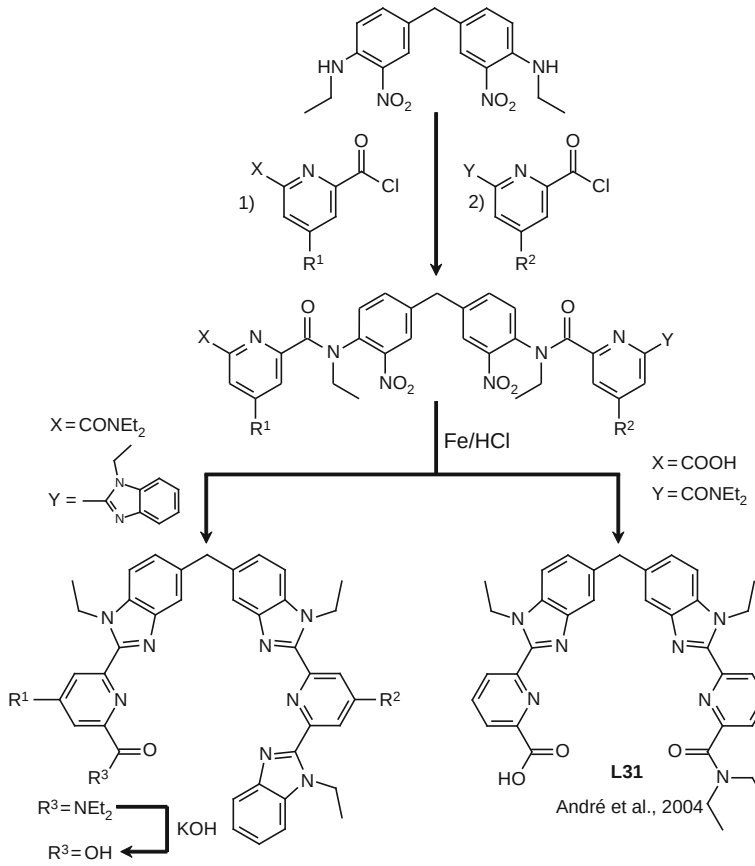

R1	R2	R3	L*k*	References
H	H	NEt_2	**L30**[a]	André et al., 2004
NEt_2	H	NEt_2	**L30**[b]	Jensen et al., 2006
Cl	H	NEt_2	**L30**[c]	Jensen et al., 2006
H	NEt_2	NEt_2	**L30**[d]	Jensen et al., 2008
H	Cl	NEt_2	**L30**[e]	Jensen et al., 2008
H	H	HO	**L30**[f]	André et al., 2004

FIGURE 48 Synthesis of heterotopic C_s-symmetrical bis-tridentate ligands.

Detailed solution structures have been obtained thanks to the analysis of the paramagnetic NMR lanthanide-induced relaxation and chemical shifts (Piguet and Geraldes, 2003, see Section 3.4) combined with high-resolution emission spectra recorded for the Eu^{III} helicates (Bünzli and Piguet, 2005; see Section 3.5). In all cases, the crystal structures represent

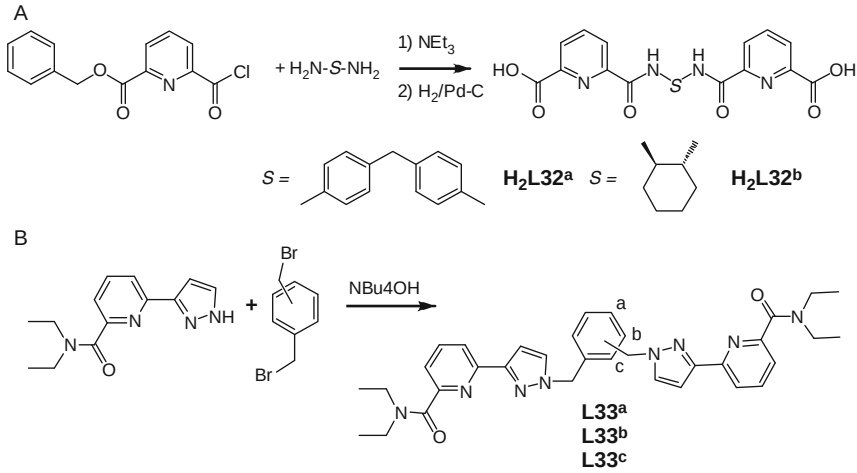

FIGURE 49 Synthesis of C_2-symmetrical bis-tridentate homotopic ligands with various spacers: (A) ONO-*S*-ONO donor groups (Lessmann and Horrocks, 2000) and (B) ONN-*S*-NNO donor groups (Ronson et al., 2007).

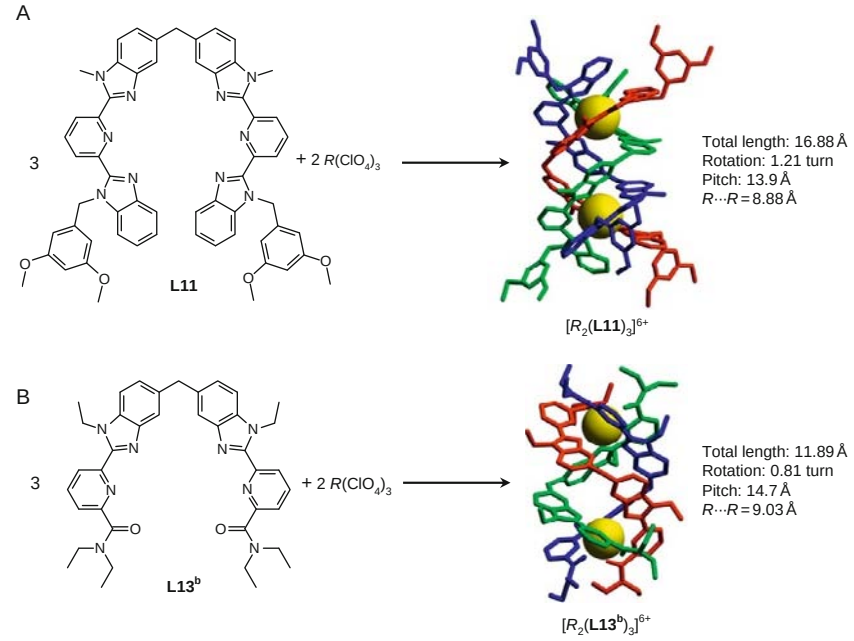

FIGURE 50 Formation of binuclear triple-stranded helicates with neutral bis-tridentate homotopic C_{2v}-symmetrical ligands: (A) NNN-*S*-NNN and (B) ONN-*S*-NNO. The structures of the complexes correspond to the crystal structures of $[Eu_2(\mathbf{L11})_3]^{6+}$ and $[Tb_2(\mathbf{L13^b})_3]^{6+}$ (redrawn after Martin et al., 1998; Piguet et al., 1993a,b,c.

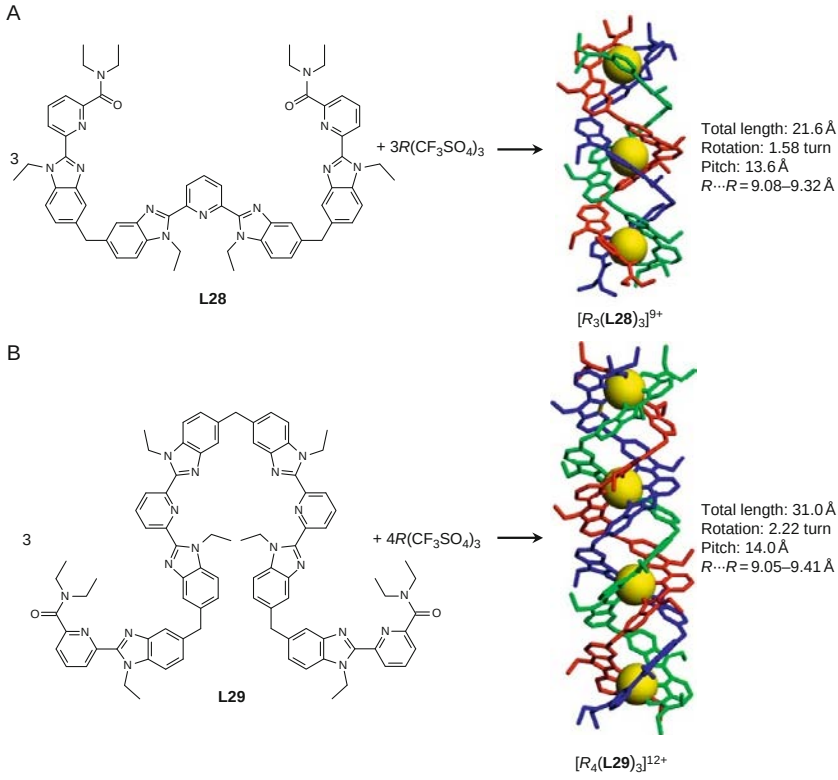

FIGURE 51 Formation of (A) trinuclear and (B) tetranuclear triple-stranded helicates with neutral heterotopic C_{2v}-symmetrical ligands. The structures of the complexes correspond to the crystal structures of $[Eu_3(\mathbf{L28})_3]^{9+}$ and $[Eu_4(\mathbf{L29})_3]^{12+}$ (redrawn after Floquet et al., 2003; Zeckert et al., 2005).

satisfying models for the solution structures. In several cases, such as $[R_2(\mathbf{L13^{c-e}})_3]^{6+}$ (Platas-Iglesias et al., 2000; Tripier et al., 2002), $[R_2(\mathbf{L13^{h}})_3]^{6+}$ (Chauvin et al., 2008), and $[R_2(\mathbf{L32})_3]^{6+}$ (Lessmann and Horrocks, 2000), no crystal structures are available, but the analysis of the UV-vis, NMR, ES-MS, and photophysical data are convincing enough to establish the solid-state and solution structures of these binuclear triple-stranded helicates.

On the contrary, dissolution of the C_3-symmetrical helicates HHH-$[R_2(\mathbf{L30})_3]^{6+}$ in acetonitrile gives mixtures of the HHH (C_3-symmetry) and HHT (C_1-symmetry) isomers (André et al., 2004; Figure 54). Systematic investigation of the enthalpic ($\Delta H_{iso}^{R,L30}$) and entropic ($\Delta S_{iso}^{R,L30}$) contributions to equilibrium (16) yields a scattered diagram, in which one can easily recognize enthalpy/entropy compensations for each studied C_s-symmetrical ligand (Jensen et al., 2007; Table 7; Figure 55).

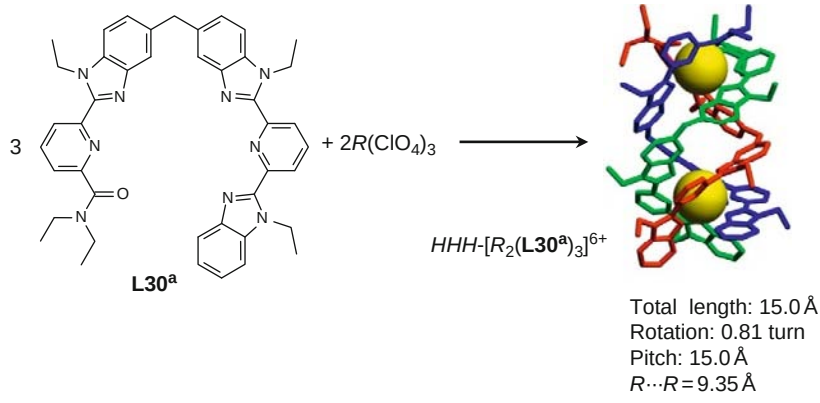

FIGURE 52 Formation of binuclear triple-stranded helicates with a neutral bis-tridentate heterotopic C_s-symmetrical ligand. The structure of the complex corresponds to the crystal structure of $[Eu_2(\mathbf{L30^a})_3]^{6+}$ (redrawn after André et al., 2004).

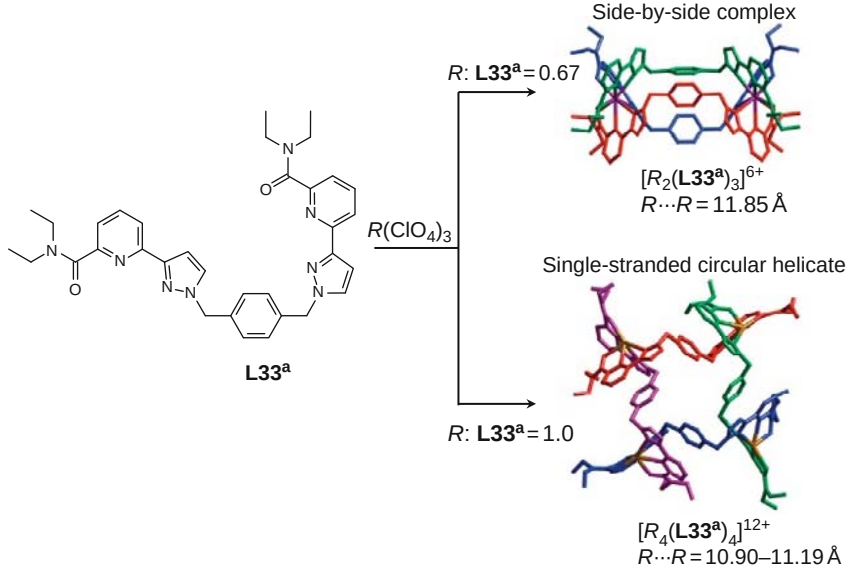

FIGURE 53 Formation of alternative polynuclear complexes with a homotopic C_{2v}-symmetrical bis-tridentate ligand. The structures of the complexes correspond to the crystal structures of $[Nd_2(\mathbf{L33^a})_3]^{6+}$ and $[Nd_4(\mathbf{L33^a})_4]^{12+}$ (redrawn after Ronson et al., 2007).

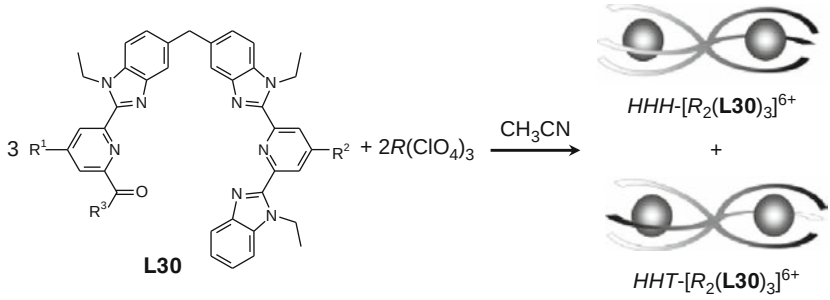

FIGURE 54 Solution structures of $[R_2(\mathbf{L30})_3]^{6+}$.

$$\mathrm{HHT}-[R_2(\mathrm{L}\mathbf{30})_3]^{6+} \rightleftharpoons \mathrm{HHH}-[R_2(\mathrm{L}\mathbf{30})_3]^{6+}\ K_{\mathrm{iso}}^{R,\mathrm{L30}} = \beta_{2,3,\mathrm{HHH}}^{R,\mathrm{L30}}/\beta_{2,3,\mathrm{HHT}}^{R,\mathrm{L30}} \quad (16)$$

Assuming that the metal–ligand, metal–metal and ligand–ligand interactions are identical in HHH-$[R_2(\mathbf{L30})_3]^{6+}$ and HHT-$[R_2(\mathbf{L30})_3]^{6+}$, we can easily deduce that the enthalpic contribution to equilibrium (16) is zero ($\Delta H_{\mathrm{iso,stat}}^{R,\mathrm{L30}} = 0$ kJ mol^{-1}), while the entropic contribution to the free energy change is given by $\Delta G_{\mathrm{iso,stat}}^{R,\mathrm{L30}} = -T\Delta S_{\mathrm{iso,stat}}^{R,\mathrm{L30}} = -RT\ln(K_{\mathrm{iso,stat}}^{R,\mathrm{L30}}) = 2.7$ kJ mol^{-1} because $K_{\mathrm{iso,stat}}^{R,\mathrm{L30}}$ is controlled by the ratio of the statistical factors of the self-assembly processes leading to the two microspecies (Eq. (17), Ercolani et al., 2007).

$$K_{\mathrm{iso,stat}}^{R,\mathrm{L30}} = \omega_{2,3,\mathrm{HHH}}^{R,\mathrm{L30}}/\omega_{2,3,\mathrm{HHT}}^{R,\mathrm{L30}} = 24/72 = 1/3 \quad (17)$$

This translates into a statistical mixture of 25% HHH and 75% HHT isomers in solution, but we observe that none of the experimental data with ligands $\mathbf{L30}^{\mathbf{a-e}}$ follow this model (i.e., no experimental point at, or nearby, the crossing point of the two straight lines $\Delta H_{\mathrm{iso,stat}}^{R,\mathrm{L30}} = 0$ kJ mol^{-1} and $-T\Delta S_{\mathrm{iso,stat}}^{R,\mathrm{L30}} = 2.7$ kJ mol^{-1}, Figure 55). The most striking point concerns the quasi-systematic observation of $\Delta H_{\mathrm{iso}}^{R,\mathrm{L30}} < 0$ kJ mol^{-1} for all ligands, a trend which has been tentatively attributed to the existence of three intramolecular interaromatic π-stacking interactions involving the three wrapped NNN binding sites in the HHH isomer, while only one similar interaction remains in the HHT isomer (Jensen et al., 2007; see Figure 28 for a strict analogy of this phenomenon occurring in the mononuclear triple-helical precursors $[R(\mathbf{L19})_3]^{3+}$). Additional enthalpic contributions have been suggested to arise from some unknown cooperative processes favoring the formation of symmetrical homogeneous nine-coordinated binding sites in the final helicates, in other words the

TABLE 7 Thermodynamic parameters of equilibrium (16) for the triple-stranded binuclear helicates $[R_2(\mathbf{L30})_3]^{6+}$ in CD_3CN (see Figure 48)

	La	Ce	Pr	Sm	Eu	Lu	Y
L30[a]							
$\Delta H_{iso}^{R,L30}$ (kJ mol^{-1})	− 10.18	–	− 4.8(5)	− 1.5(2)	− 2.4(8)	1.9(2)	− 2.4(8)
$\Delta S_{iso}^{R,L30}$ (J mol^{-1} K^{-1})	− 26.1(3)	–	− 10(2)	0.1(7)	− 1(3)	12.6(8)	3.0(3)
% HHH (298 K)	73	–	67	65	69	68	63
L30[b]							
$\Delta H_{iso}^{R,L30}$ (kJ mol^{-1})	− 10.7(4)	− 2.9(5)	− 4(1)	0.60(9)	1(1)	1.1(4)	0.1(2)
$\Delta S_{iso}^{R,L30}$ (J mol^{-1} K^{-1})	− 47(1)	− 25(2)	− 31(5)	− 15.0(3)	− 18(4)	− 19(1)	− 20.4(6)
% HHH (298 K)	20	13	12	11	8	6	8
L30[c]							
$\Delta H_{iso}^{R,L30}$ (kJ mol^{-1})	− 3.3(3)	–	− 6.2(6)	− 6.6(3)	− 9.8(5)	− 12(2)	− 7.2(8)
$\Delta S_{iso}^{R,L30}$ (J mol^{-1} K^{-1})	0(1)	–	− 5(2)	− 8(1)	− 18(2)	25(7)	− 12(3)
% HHH (298 K)	79	–	87	85	85	86	82
L30[e]							
$\Delta H_{iso}^{R,L30}$ (kJ mol^{-1})	− 7.7(5)	− 5.7(3)	− 4.4(2)	− 4.1(2)	− 4.5(2)	− 3.4(3)	− 5.0(5)
$\Delta S_{iso}^{R,L30}$ (J mol^{-1} K^{-1})	− 23(2)	− 18(1)	− 13.8(8)	− 11.8(6)	− 13.9(8)	− 8(1)	− 13(2)
% HHH (298 K)	60	53	53	56	54	60	61

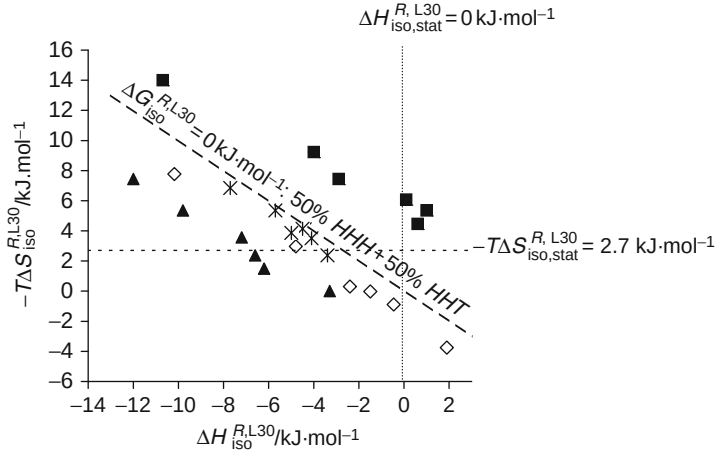

FIGURE 55 Entropic versus enthalpic contributions to the free energy of equilibrium (16); ◇, **L30[a]**; ■, **L30[b]**; ▲, **L30[c]**; *, **L30[e]**. The diagonal line indicates the domain, for which 50% of each isomer is formed in solution. Below this line, the HHH isomer is the major component of the mixture (redrawn from Jensen et al., 2007).

formation of the preorganized N_9-spacer-N_6O_3 binuclear receptor (HHH isomer) is preferred over the alternative N_8O-spacer-N_7O_2 binuclear receptor (HHT isomer, Jensen et al., 2007). In absence of a complete thermodynamic analysis of the self-assembly processes leading to HHH-$[R_2(\mathbf{L30})_3]^{6+}$ and HHT-$[R_2(\mathbf{L30})_3]^{6+}$, these interpretations remain elusive, but the empirical observations firmly establish the unusual formation of a large proportion (> 50%) of HHH isomer with ligands **L30[a]**, **L30[c]**, **L30[d]**, and **L30[e]**, while **L30[b]** is an exception (Figure 55).

3.3 Mechanisms of formation

Elucidation of the intricate mechanisms leading to the self-assembly of lanthanide helicates is indebted to the original kinetic investigations of the formation of binuclear double-stranded $[Cu_3(\mathbf{L1})_2]^{3+}$ (Fatin-Rouge et al., 2001; Figure 56), $[Cu_5(\mathbf{L6})_2]^{5+}$ (Marquis-Rigault et al., 1996), and triple-stranded $[Fe_2(\mathbf{L34})_3]^{4+}$ (Fatin-Rouge et al., 2000; Figure 57) helicates. As far as low charged Cu(I) is concerned, the limited electrostatic intermetallic repulsion can be easily balanced by solvation and polarization effects, and the successive fixation of several cations onto a single strand may offer a valuable route, which contrasts with the commonly invoked preorganization of several ligands prior to metal loading (Figure 56).

For the doubly charged cations Fe(II), the electrostatic metal–metal repulsion becomes strong enough so that the issue of the self-assembly

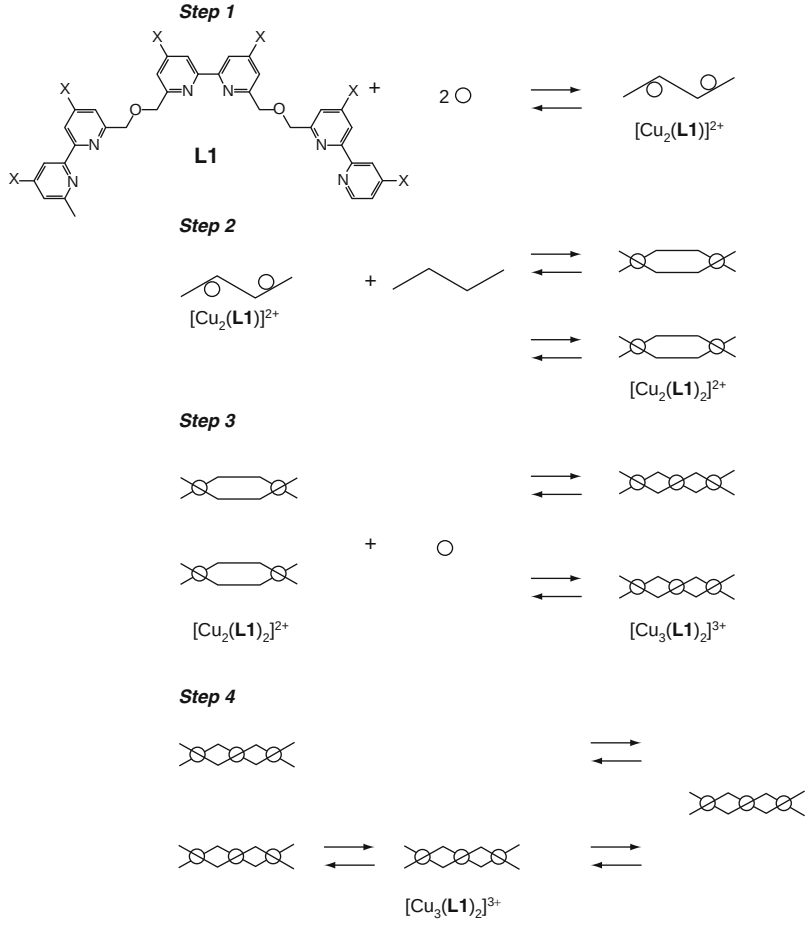

FIGURE 56 Mechanism of the self-assembly of the double-stranded helicate $[Cu_3(\mathbf{L1})_2]^{3+}$ (adapted from Fatin-Rouge et al., 2001).

process depends on the activity of the metal in solution (Figure 57). In excess of ligand, the connection of the third strand in $[Fe(\mathbf{L34})_3]^{2+}$ offers enough charge compensation by polarization for a second Fe(II) to enter into the complex in order to give $[Fe_2(\mathbf{L34})_3]^{4+}$. However, in excess of metal, only the hairpin arrangement of one ligand strand in $[Fe(\mathbf{L34})_2]^{2+}$ is able to reduce the effective charge of the coordinated metal to such an extent that the approach of a second Fe(II) is possible.

In the light of the latter observations, it is thus not so surprising that the mechanism of formation of the triple-stranded lanthanide helicates

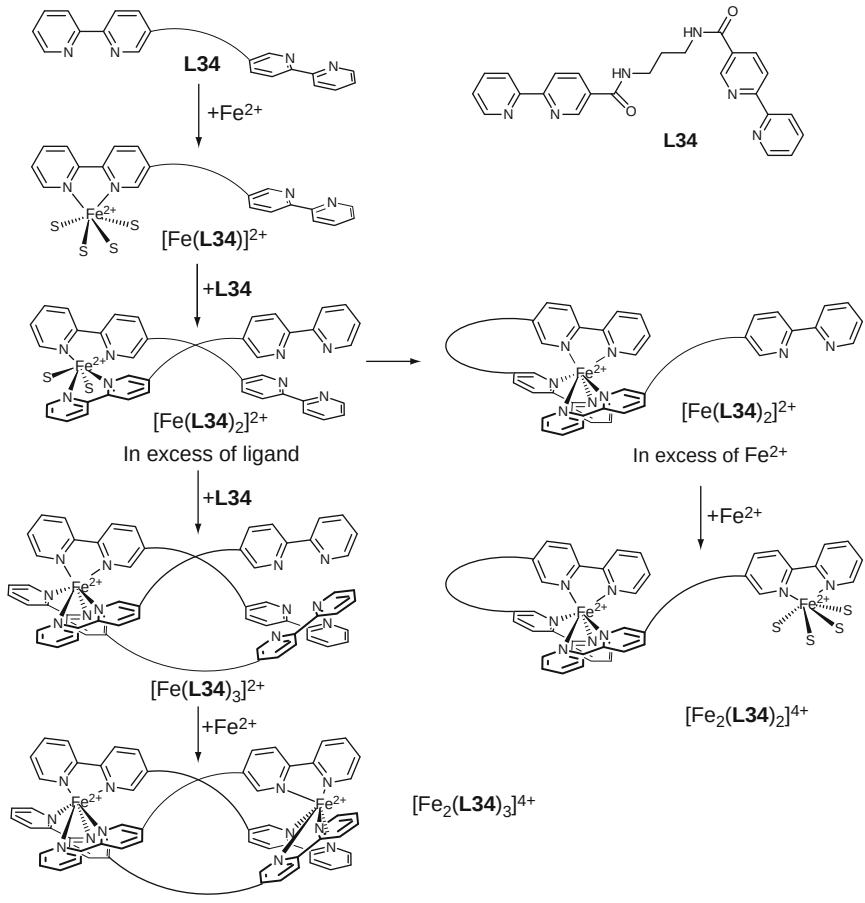

FIGURE 57 Mechanism of the self-assembly of the triple-stranded helicate $[Fe_2(\mathbf{L34})_3]^{4+}$ (adapted from Fatin-Rouge et al., 2000).

$[R_2(\mathbf{L11})_3]^{6+}$ avoids the connection of two triply charged cations in the early steps, but favors the successive fixation of ligand strands to a single metal (Hamacek et al., 2003; Figure 58A). Interestingly, the kinetics data indicate that the rate of the assembly of the different components strongly depends on the stoichiometric R:**L11** ratios. For R:**L11** = 2:3, the self-assembly process leads in a few minutes to the targeted $[R_2(\mathbf{L11})_3]^{6+}$ helicate, while several hours are required to reach thermodynamic equilibrium when R:**L11** = 10:1 (Hamacek et al., 2003).

The use of the hydrolyzed ligand $[\mathbf{L13^f}]^{2-}$ introduces charge neutralization as a novel parameter in helicate self-assembly. In these conditions, the coordination of a second metal to a single strand in $[R_2(\mathbf{L13^f})]^{3+}$ competes with the fixation of a second ligand in $[R(\mathbf{L13^f})_2]^{-}$ (Figure 58B;

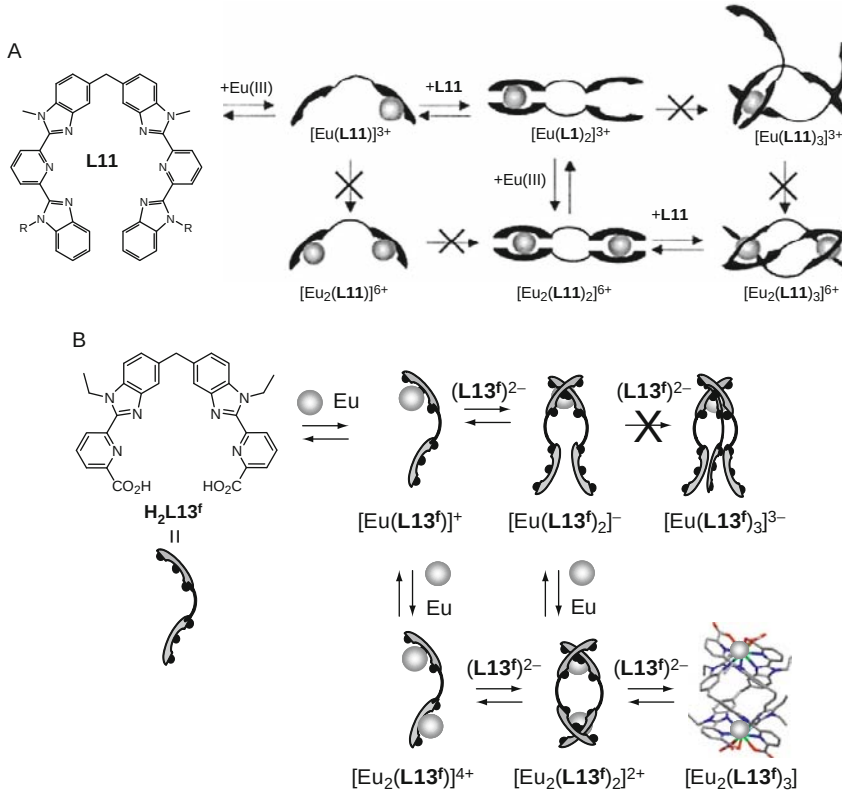

FIGURE 58 Mechanism of the self-assembly of the triple-stranded helicates: (A) $[Eu_2(\mathbf{L11})_3]^{6+}$ (redrawn from Hamacek et al., 2003) and (B) $[Eu_2(\mathbf{L13^f})_3]$ (redrawn from Elhabiri et al., 2004a).

Elhabiri et al., 2004a). The ultimate fixation of the third ligand in the neutral helicate $[R_2(\mathbf{L13^f})_3]$ induces a considerable entropic gain to the overall complexation process, which is responsible for both extreme thermodynamic stability (Elhabiri et al., 1999) and kinetic inertness (Elhabiri et al., 2004b, Figure 59), which make these helicates promising building blocks for the development of luminescent bioprobes (see Section 6).

3.4 Thermodynamics of the recognition processes

The majority of the formation constants $\beta_{m,n}^{R,Lk}$ (equilibrium (18)) characterizing the formation of triple-stranded lanthanide helicates in solution have been determined by direct spectrophotometric titrations in the UV-Vis range (Tables 8 and 9).

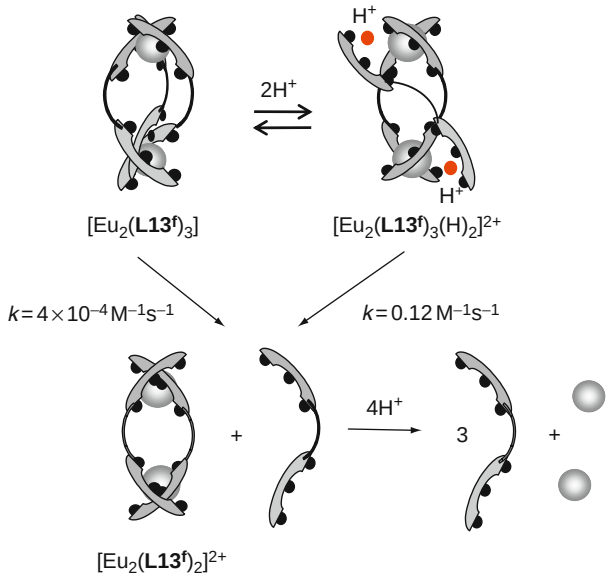

FIGURE 59 Dissociation mechanism of $[Eu_2(\mathbf{L13^f})_3]$ in water (redrawn from Elhabiri et al., 2004b).

$$n\mathbf{L}\boldsymbol{k}+mR^{3+} \rightleftharpoons [R_m(\mathbf{L}\boldsymbol{k})_n]^{3m+} \quad \beta_{m,n}^{R,\mathrm{L}k} \tag{18}$$

Since the allowed ligand-centered $n \rightarrow \pi^*$ and $\pi \rightarrow \pi^*$ transitions only display enough oscillator strength to monitor spectral changes accompanying the formation of the helicates in highly diluted solutions, the investigation of the complexation processes mainly relies on the *trans–trans* → *cis–cis* conformational change occurring upon complexation of the tridentate binding units (Figure 30). In other words, the recorded spectral changes are only sensitive to the on–off complexation of the tridentate binding units, whatever the nature and composition of the investigated complex. It is therefore difficult to detect the formation of poorly stable intermediates by spectrophotometry and only a partial set of stability constants are usually available for each ligand as shown in Tables 8 and 9.

The evolution of the formation constants of the binuclear triple-stranded helicates $[R_2(\mathbf{L11})_3]^{6+}$ (NNN-*S*-NNN donor sets) and $[R_2(\mathbf{L13^{a-d}})_3]^{6+}$ (ONN-*S*-NNO donor sets) along the lanthanide series mimics the size-discriminating effects previously established with the mononuclear precursors (Figure 31). When NNN donor sites are used in **L11**, the stability constants drops for the smaller R^{III}, a trend removed when the terminal benzimidazole rings are replaced with carboxamide units in $\mathbf{L13^{a-d}}$ (Table 8). The connection of electron-withdrawing halogenides (Cl in $\mathbf{L13^c}$, Br in $\mathbf{L13^d}$, Figure 41) at the 4-position of the central

TABLE 8 Cumulative $\log(\beta_{m,n}^{R,Lk})$ stability constants reported for the formation of binuclear helicates: (i) $[R_m(\mathbf{L}k)_n]^{3m+}$, $k = 11$ (Figure 12), 13[a–d] (Figure 41), and 30[a] (Figure 48); (ii) $[R_m(\mathbf{L}k\text{-H})_n]^{(3m-n)+}$, $k = 30$[f] and 31 (Figure 48); and (iii) $[R_m(\mathbf{L}k)_n]^{(3m-2n)+}$, $k = 13$[f–h] (Figures 46 and 47) and 32[a] (Figure 49)

(a) Homotopic binuclear helicates

Ligand	*R*	Solvent	$\log(\beta_{1,1}^{R,Lk})$	$\log(\beta_{1,2}^{R,Lk})$	$\log(\beta_{1,3}^{R,Lk})$	$\log(\beta_{2,1}^{R,Lk})$	$\log(\beta_{2,2}^{R,Lk})$	$\log(\beta_{2,3}^{R,Lk})$	References
L11	Eu	CH_3CN		11.6(3)			18.1(3)	24.3(4)	Hamacek et al. (2003)
	Lu							17.5(4)	Piguet et al. (1993b)
L13[a]	La	CH_3CN					20.4(8)	25.3(9)	Martin et al. (1998)
	Eu						19.9(10)	24.1(10)	Martin et al. (1998)
	La				17.0(4)		19.2(5)	25.1(2)	Zeckert et al. (2004)
	Ce				18.1(5)		18.9(1)	25.0(2)	Zeckert et al. (2004)
	Pr				16.7(4)		19.4(5)	25.3(2)	Zeckert et al. (2004)
	Nd				18.8(5)		19.3(4)	25.4(2)	Zeckert et al. (2004)
	Sm				17.5(4)		20.0(5)	25.9(2)	Zeckert et al. (2004)
	Eu				19.4(5)		19.6(2)	26.0(2)	Zeckert et al. (2004)
	Gd				18.8(5)		19.8(2)	26.0(2)	Zeckert et al. (2004)
	Tb				17.8(3)		20.0(5)	26.0(5)	Zeckert et al. (2004)
	Dy				17.2(4)		20.1(5)	25.0(5)	Zeckert et al. (2004)
	Ho				18.7(5)		19.6(2)	25.8(2)	Zeckert et al. (2004)
	Er				18.4(5)		19.4(3)	25.6(3)	Zeckert et al. (2004)
	Tm				18.7(5)		19.3(3)	25.6(3)	Zeckert et al. (2004)
	Yb				16.1(9)		19.2(5)	25.4(2)	Zeckert et al. (2004)
	Lu				17.1(5)		19.3(4)	25.4(5)	Zeckert et al. (2004)
	Y				17.2(4)		19.6(5)	25.8(2)	Zeckert et al. (2004)

(*continued*)

TABLE 8 (*continued*)

(a) Homotopic binuclear helicates

Ligand	*R*	Solvent	$\log(\beta_{1,1}^{R,Lk})$	$\log(\beta_{1,2}^{R,Lk})$	$\log(\beta_{1,3}^{R,Lk})$	$\log(\beta_{2,1}^{R,Lk})$	$\log(\beta_{2,2}^{R,Lk})$	$\log(\beta_{2,3}^{R,Lk})$	References
L13[c]	Eu	CH_3CN					18.3(15)	21.8(15)	Platas-Iglesias et al. (2000)
L13[d]	Eu	CH_3CN					19.9(15)	23.8(15)	Platas-Iglesias et al. (2000)
(L13[f]**)**$^{2-}$	Eu	H_2O	4.3(1)			6.4(2)		50(2)	Elhabiri et al. (2004a)
H_2L13[f]	La	H_2O						30(1)[a]	Elhabiri et al. (1999)
	Eu							26.1(4)[a]	Elhabiri et al. (1999)
	Lu							27.3(5)[a]	Elhabiri et al. (1999)
H_2L13[g]	La	H_2O				10.9(1)[a]		22.7(2)[a]	Chauvin et al. (2007)
	Eu				16.8(1)[a]	11.4(1)[a]		23.4(1)[a]	Chauvin et al. (2007)
	Lu				17.0[a]	11.0(1)[a]		23.1(1)[a]	Chauvin et al. (2007)
H_2L13[h]	La	H_2O			18.8(2)[a]	11.7(3)[a]		24.9(4)[a]	Chauvin et al. (2008)
	Eu				18.1(2)[a]	11.8(5)[a]		25.5(4)[a]	Chauvin et al. (2008)
	Lu				18.7(3)[a]	12.4(2)[a]		26.3(4)[a]	Chauvin et al. (2008)
H_2L13[i]	La	H_2O		14.8(1)[a]		13.8(2)[a]		28.3(1)[a]	Deiters et al. (2008)
	Eu			14.7(1)[a]				28.0(1)[a]	Deiters et al. (2008)
	Lu			14.4(4)[a]				27.7(5)[a]	Deiters et al. (2008)
H_2L13	La	H_2O		14.2(3)[a]		13.6(3)[a]		28.1(4)[a]	Deiters et al. (2009)
	Eu			14.8(3)[a]		14.3(3)[a]		28.5(5)[a]	Deiters et al. (2009)
	Lu			13.6(1)[a]		14.3(1)[a]		26.3(2)[a]	Deiters et al. (2009)

H_2L13[k]	Eu	H_2O		14.0(1)[a]		15.4(1)[a]		27.9(1)[a]	Deiters et al. (2009)
H_2L13[l]	La	H_2O		14.0(1)[a]		15.9(1)[a]		27.4(3)[a]	Deiters et al. (2009)
	Eu			14.3(3)[a]		14.4(5)[a]		28.6(5)[a]	Deiters et al. (2009)
	Lu					16.0(3)[a]		28.8(3)[a]	Deiters et al. (2009)
H_2L32[a]	Eu	H_2O						31.6(2)[b]	Lessmann and Horrocks (2000)

(b) Heterotopic binuclear helicates

Ligand	Metal	Solvent	$\log(\beta_{1,1}^{R,Lk})$	$\log(\beta_{1,2}^{R,Lk})$	$\log(\beta_{1,3}^{R,Lk})$	$\log(\beta_{2,1}^{R,Lk})$	$\log(\beta_{2,2}^{R,Lk})$	$\log(\beta_{2,3}^{R,Lk})$	References
L30[a]	Eu	CH_3CN						23.9(5)	André et al. (2004)
[L30[f]-H]$^-$	La	CH_3OH	7.8(2)	13(1)	19.0(2)			25(1)	André et al. (2004)
	Eu			12.6(4)	17.9(5)			23.3(7)	André et al. (2004)
	Lu		7.2(2)	12.5(10)	17.3(1)			23.6(10)	André et al. (2004)
[L31-H]$^-$	Eu	CH_3OH		15.1(4)	20.8(4)		22.5(6)	29.7(6)	André et al. (2004)

All data are at 293 K.
[a] Conditional stability constants: pH 7.4, Tris–HCl 0.1 M.
[b] Conditional stability constants: pH 7.0, HEPES 0.05 M.

TABLE 9 Cumulative $\log(\beta_{m,n}^{R,Lk})$ stability constants reported for the formation of heterotopic tri- and tetranuclear helicates $[R_m(\mathbf{L}k)_n]^{3m+}$ ($k = 28$, 29) in acetonitrile at 293 K

Ligand	*R*	$\log(\beta_{2,3}^{R,Lk})$	$\log(\beta_{3,2}^{R,Lk})$	$\log(\beta_{3,3}^{R,Lk})$	$\log(\beta_{4,2}^{R,Lk})$	$\log(\beta_{4,3}^{R,Lk})$
L28[a]	La	25.0(11)	25.8(11)	34.3(12)		
	Nd	26.0(10)	26.4(10)	35.0(11)		
	Eu	25.9(14)	26.0(14)	34.8(16)		
	Tb	25.8(2)	27.2(1)	35.0(12)		
	Ho	26.0(10)	26.5(10)	35.0(12)		
	Tm	26.0(16)	26.9(9)	34.5(18)		
	Lu	25.5(11)	27.4(5)	33.9(3)		
L29[b]	La		25.2(15)	31.9(4)	30.4(15)	39.1(15)
	Nd			29.7(1.8)	29.6(18)	38.4(19)
	Sm			29.7(1.5)		35.7(15)
	Eu		28.9(14)	36.8(1.5)	32.8(14)	43.2(16)
	Ho		26.3(14)	34.5(15)	29.6(15)	40.6(16)
	Er			33.4(15)	28.9(13)	38.1(15)
	Yb		26.5(13)	32.5(15)		41.0(16)
	Lu		27.5(12)	34.5(13)	31.1(12)	40.8(13)

pyridine rings weakens the interactions with R^{III} by, respectively, three and two order of magnitudes in the $[Eu_2(\mathbf{L13})_3]^{6+}$ helicates, in line with decreasing electronegativity of these two substituents. As previously established with mononuclear precursors, the introduction of negatively charged carboxylate donor groups in $[\mathbf{L30^f}\text{-H}]^-$, $[\mathbf{L31}\text{-H}]^-$ or in $[\mathbf{L13^{f-l}}]^{2-}$ and $[\mathbf{L32}\text{-2H}]^{2-}$ drastically increases the stability of the final helicates, which can then easily survive in highly competing solvents such as methanol or water (Table 8). Finally, the combination of several neutral NNN and NNO tridentate binding units in the segmental ligands **L28** and **L29** gives trinuclear, respectively, tetranuclear triple-stranded helicates, whose cumulative formation constants are difficult to measure by direct titration because of the very minute decomplexation occurring at submillimolar concentrations (Table 8). In these conditions, any size-discriminating effect is probably masked by experimental uncertainties (Table 9).

3.5 Photophysical properties

Since the bidentate binding units in the segmental ligands are connected by saturated methylene units, which are poor electronic relays, we can expect that the photophysical properties of the helicates can be easily deduced from those found in the mononuclear triple-helical precursors.

A detailed comparison of Table 10 (dedicated to polynuclear helicates) with Table 4 (dedicated to mononuclear precursors) indeed supports this reasoning.

For the Eu^{III} complexes, the three wrapped tridentate NNN binding units produce poorly luminescent EuN_9 sites due to the quenching by LMCT states located close in energy to the ligand-centered $^1\pi\pi^*$ excited states in $[Eu_2(\mathbf{L11})_3]^{6+}$ (Piguet et al., 1993b) and as firmly established for its precursor $[Eu(\mathbf{L17^a})_3]^{3+}$ (Petoud et al., 1999). It is, however, worth noting that the global quantum yield increases by two orders of magnitude in going from $[Eu(\mathbf{L17^a})_3]^{3+}$ ($Q_L^{Eu} = 2 \times 10^{-3}\%$) to $[Eu_2(\mathbf{L11})_3]^{6+}$ ($Q_L^{Eu} = 0.2\%$), a phenomenon tentatively ascribed to some variation of the energy of the LMCT level in the constrained binuclear triple-stranded helicate. The replacement of the terminal benzimidazole rings with either carboxamide units in $[Eu_2(\mathbf{L13^{a-e}})_3]^{6+}$ or carboxylate groups in $[Eu_2(\mathbf{L13^{f-l}})_3]$ drastically improves quantum yields, as previously noticed in going from $[Eu(\mathbf{L17})_3]^{3+}$ to $[Eu(\mathbf{L18})_3]^{3+}$ or $[Eu(\mathbf{L19})_3]^{3+}$. In this context, $Q_L^{Eu} = 24\%$ measured for $[Eu_2(\mathbf{L13^f})_3]$ in water at pH 7.4 further confirms the high potential of this class of helicates as bioprobes and the detailed photophysical properties of the $[Eu_2(\mathbf{L13^{f-l}})_3]$ helicates will be discussed in Section 6. We also note that Q_L^{Ln} is extremely sensitive to the relative orientation of the tridentate binding units when C_s-symmetrical ligands are considered. Among the EuN_6O_3 coordination sites found in $[Eu(\mathbf{L19^b})_3]^{3+}$ ($Q_L^{Eu} = 0.05\%$ in CH_3CN), in $[Eu(\mathbf{L22})]^{3+}$ ($Q_L^{Eu} = 10\%$ in CH_3CN), in $[Eu(\mathbf{L23})]^{3+}$ ($Q_L^{Eu} = 14\%$ in CH_3CN), and in the binuclear helicate $[Eu_2(\mathbf{L13^b})_3]^{6+}$ ($Q_L^{Eu} = 9\%$ in CH_3CN), only the first one, with the very low quantum yield, exists as the meridional isomer in solution, while the other adopt pure facial organizations. With this empirical observation in mind, it is not so surprising that the heterotopic binuclear helicate $[Eu_2(\mathbf{L30^a})_3]^{6+}$, which mainly exist as the HHH isomer (69% HHH, Table 7), gives a relatively high quantum yield in acetonitrile ($Q_L^{Ln} = 15\%$, Table 10).

Both the ground state ($^7F_0$) and the most luminescent level ($^5D_0$) of Eu^{III} are nondegenerate so that the forbidden and therefore usually very weak $^5D_0 \rightarrow {}^7F_0$ (emission spectra) or $^5D_0 \leftarrow {}^7F_0$ (excitation spectra) transitions are unique whatever the symmetry of the metal-ion environment. As a consequence, Eu^{III} is widely used for monitoring the number of different metallic coordination sites existing in lanthanide complexes both in solution and in crystalline samples (Bünzli, 1989). Except for some broadening of this spectral line due to polycrystallinity, all mononuclear and binuclear triple-helical Eu^{III} complexes reported in Tables 4, 5, and 10 exhibit a single Eu($^7F_0 \rightarrow {}^5D_0$) transition, which is diagnostic for the existence of a single chemical environment around the metal ion. Moreover, the energy of this transition depends on the effective charge borne by Eu^{III} in the complexes (Bünzli, 1989), that is, on the

TABLE 10 Photophysical properties of triple-stranded helicates $[R_m(\mathbf{L}k)_3]^{6+}$ [$k = 11$ ($m = 2$), 13^{a-d} ($m = 2$), 28 ($m = 3$), 29 ($m = 4$), 30($m = 2$)] and $[R_2(\mathbf{L}k\text{-}2H)_3]$ ($k = 13^{f-h}$, 32)

Ligand	Ln	Solvent	E(*π ← π) (cm^{-1})[a]	E($^3\pi\pi^*$) (cm^{-1})[b]	Q_L^{Ln} (%)	τ_{obs} (ms)[c]	E(Eu($^5D_0$)) (cm^{-1})	References
L11	Eu	CH_3CN	25,640	19,880	0.2[d]	2.03[e]	17,227 (77 K)	Piguet et al. (1993b)
	Tb	CH_3CN	25,640	19,880	–	1.35[e]	–	Piguet et al. (1993b)
L13[b]	Eu	CH_3CN	29,760	20,930	9[d]	2.09[e]	17,229 (77 K)	Martin et al. (1998)
	Tb	CH_3CN	29,500	20,930	10[d]	1.96[e]	–	Martin et al. (1998)
L13[c]	Eu	CH_3CN	29,480	20,455	11[d]	2.28[e]	17,218 (10 K)	Platas-Iglesias et al. (2000)
L13[e]	Eu	CH_3CN	28,340	19,800	31[d]	2.02	17,222 (295 K)	Tripier et al. (2002)
$[\mathbf{L13}^f]^{2-}$	Sm	H_2O	30,120	20,660	0.14	0.042	–	Gonçalves e Silva et al. (2002)
	Eu	H_2O	30,120	20,660	24[d]	2.69[f]	17,232 (295 K)	Elhabiri et al. (1999)
	Tb	H_2O	30,120	20,660	1.2[d]	0.05	–	Bünzli et al. (2008) and Elhabiri et al. (1999)
	Yb	D_2O	30,120	20,660	1.8	0.04 (295 K)	–	Gonçalves e Silva et al. (2002)

$[\mathbf{L13^g}]^{2-}$	Nd	H_2O (pH 7.4)	31,250	–	0.031	2.1×10^{-4}	–	Chauvin et al. (2008)
	Sm	H_2O (pH 7.4)	31,150	–	0.38	0.03	–	Chauvin et al. (2008)
	Eu	H_2O (pH 7.4)	31,060	22,050	21	2.34	17,234 (295 K)	Chauvin et al. (2008)
	Tb	H_2O (pH 7.4)	30,960	22,050	11	0.65	–	Chauvin et al. (2008)
	Yb	H_2O (pH 7.4)	30,860	–	0.15	0.0044	–	Chauvin et al. (2008)
$[\mathbf{L13^h}]^{2-}$	Eu	H_2O (pH 7.4)	31,150	21,900	19	2.43	17,233 (295 K)	Deiters et al. (2008)
	Tb	H_2O (pH 7.4)	31,100	21,900	10	0.66		Deiters et al. (2008)
$[\mathbf{L13^i}]^{2-}$	Eu	H_2O (pH 7.4)	30,670	22,150	11	2.2	17,235 (295 K)	Chauvin et al. (2007)
	Tb	H_2O (pH 7.4)	30,670	22,100	0.34	0.39	–	Chauvin et al. (2007)
$[\mathbf{L13^j}]^{2-}$	Eu	H_2O (pH 7.4)	31,450	21,150	15	2.52	17,242 (10 K)	Deiters et al. (2009)
	Tb	H_2O (pH 7.4)	31,450	21,150	2.5	0.12	–	Deiters et al. (2009)

(*continued*)

TABLE 10 (*continued*)

Ligand	Ln	Solvent	E(*π ← π) (cm^{-1})[a]	E(^{3}ππ*) (cm^{-1})[b]	Q_L^{Ln} (%)	τ_{obs} (ms)[c]	E(Eu($^5D_0$)) (cm^{-1})	References
[L13^k]$^{2-}$	Eu	H_2O (pH 7.4)	29,500	19,550	0.35	0.54	17,237 (10 K)	Deiters et al. (2009)
	Tb	H_2O (pH 7.4)	29,500	19,550	–	0.01	–	Deiters et al. (2009)
	Yb	H_2O (pH 7.4)	29,500	19,550	0.15	0.0043	–	Deiters et al. (2009)
[L13l]$^{2-}$	Eu	H_2O (pH 7.4)	28,500	20,800	9	2.3	17,242 (10 K)	Deiters et al. (2009)
	Tb	H_2O (pH 7.4)	28,500	20,800	0.31	0.04	–	Deiters et al. (2009)
	Yb	H_2O (pH 7.4)	28,500	20,800	0.16	0.0043	–	
L32$_a$	Eu	H_2O	–	–	–	1.48	17,226 (295 K)	Lessmann and Horrocks (2000)
L32$_b$	Eu	H_2O	–	–	–	1.56	17,221 (295 K)	Lessmann and Horrocks (2000)
L30^a	Eu	CH_3CN	29,500	20,000	15[d]	2.26[e]	17,232 (295 K)	André et al. (2004)

L28	Eu	CH_3CN	30,390	20,260	0.3[d]	2.3[f] EuN_6O_3 site, 2.1[f] EuN_9 site	17,219 (10 K) EuN6O3 site 17,238 (10 K) EuN9 site	Floquet et al. (2003)
	Tb	CH_3CN	30,080	20,260	–	2.23[f]	–	Floquet et al. (2003)
L29	Eu	CH_3CN	30,580	20,040	–	2.0–2.2 (10 K)	17,221 (10 K) EuN_6O_3 sites, 17,235 (10 K) EuN_9 sites	Dalla Favera et al. (2008)

[a] Values obtained from absorption spectra in solution (293 K).
[b] Values obtained from emission spectra (0-phonon, 77 K).
[c] Metal-centered lifetime at 295 K if not otherwise stated.
[d] Quantum yields have been recalculated by using the most recent values reported for the $[R(\text{terpyridine})_3]^{3+}$ internal references (Comby, 2008).
[e] At 77 K.
[f] At 10 K.

nephelauxetic effect produced by the donor atoms bound to Eu^{III} (Choppin and Wang, 1997; Frey and Horrocks, 1995). Experimentally, the energy of the Eu($^5D_0 \leftarrow {}^7F_0$) transition is obtained from excitation spectra recorded at low temperature (<77 K) whereby vibrational contributions are minimized. Taking into account the accepted 1 cm^{-1}/24 K dependence of the energy of the Eu($^5D_0 \leftarrow {}^7F_0$) transition (Bünzli, 1989), we obtain $\tilde{\nu}^{obs} = 17{,}245$ cm^{-1} for the EuN_9 site in $[Eu_2(\mathbf{L17^a})_3]^{3+}$, $\tilde{\nu}^{obs} = 17{,}238$ cm^{-1} for the facial $Eu(N_{hetero})_6(O_{amide})_3$ site in $[Eu_2(\mathbf{L13^b})_3]^{6+}$, $\tilde{\nu}^{obs} = 17{,}232$ cm^{-1} for the facial $Eu(N_{hetero})_6(O_{acid})_3$ site in $[Eu_2(\mathbf{L13^f})_3]$, $\tilde{\nu}^{obs} = 17{,}227$ cm^{-1} for the $Eu(N_{hetero})_3(O_{amide})_6$ site in $[Eu(\mathbf{L18^a})_3]^{3+}$ and $\tilde{\nu}^{obs} = 17{,}221$ cm^{-1} for the facial $Eu(O_{acid})_3N_3(O_{amide})_3$ site in [Eu(**L21**-3H)] at 295 K (Tables 4, 5, and 10). These systematic, but small variations can be well reproduced by using the empirical linear Eq. (19), whereby $\tilde{\nu}_0 = 17{,}374$ cm^{-1} is the energy of the Eu($^7F_0 \rightarrow {}^5D_0$) transition in the free ion, C_{CN} is an empirical coefficient decreasing with the coordination numbers ($C_{CN=8} = 1.06$, $C_{CN=9} = 1.00$, $C_{CN=10} = 0.95$) and δ_i represents the nephelauxetic effect produced by an atom i bound to Eu^{III} (Frey and Horrocks, 1995).

$$\tilde{\nu}^{calcd} = \tilde{\nu}_0 + C_{CN} \sum_{i=1}^{CN} n_i \delta_i \tag{19}$$

The optimized values of δ_i adapted to $CN = 9$ amount to $\delta_{O\text{-carboxylate}} = -17.2$ $cm^{-1} < \delta_{O\text{-amide}} = -15.7$ $cm^{-1} < \delta_{N\text{-heterocycle}} = -15.3$ cm^{-1}, suggesting an improved delocalization of the electronic density in the order O-carboxylate > O-amide > N-heterocycle. In view of the large amount of data collected for the $Eu(N_{hetero})_9$ and $Eu(N_{hetero})_6(O_{amide})_3$ sites in triple-stranded helicates (ligands **L11**, **L13**, **L28**–**L30**) and in mononuclear precursors (ligands **L17** and **L19**), some further refinements have been proposed leading to the specific assignment $\delta_{N\text{-pyridine}} = -25.3$ cm^{-1} and $\delta_{N\text{-benzimidazole}} = -8.0$ cm^{-1} in 6-substituted-2-(2-benzimidazolyl)pyridine binding segments (Dalla Favera et al., 2008). With these parameters, Eq. (19) predicts $\tilde{\nu}^{calcd} = 17{,}227$ cm^{-1} for $Eu(N_{hetero})_6(O_{amide})_3$ and $\tilde{\nu}^{calcd} = 17{,}250$ cm^{-1} for $Eu(N_{hetero})_9$ at 295 K, in fair agreement with the experimental values found for the Eu ($^5D_0 \leftarrow {}^7F_0$) transition of these sites in $[Eu_3(\mathbf{L28})_3]^{9+}$ and in $[Eu_4(\mathbf{L29})_3]^{12+}$ (1 cm^{-1}/24 K dependence, Figure 60A; Table 10).

The use of powerful laser excitation beam at low temperature indeed allows the detection of two different sources of Eu-centered emission in the latter complexes (Figure 60A). Selective excitation of each site gives different emission spectra, which can be analyzed with crystal-field theory for estimating the strength of the different nonadentate donor sets and the degree of distortion from ideal tricapped-trigonal prismatic geometry (Görller-Walrand and Binnemans, 1996, 1998; Figure 60B). Since

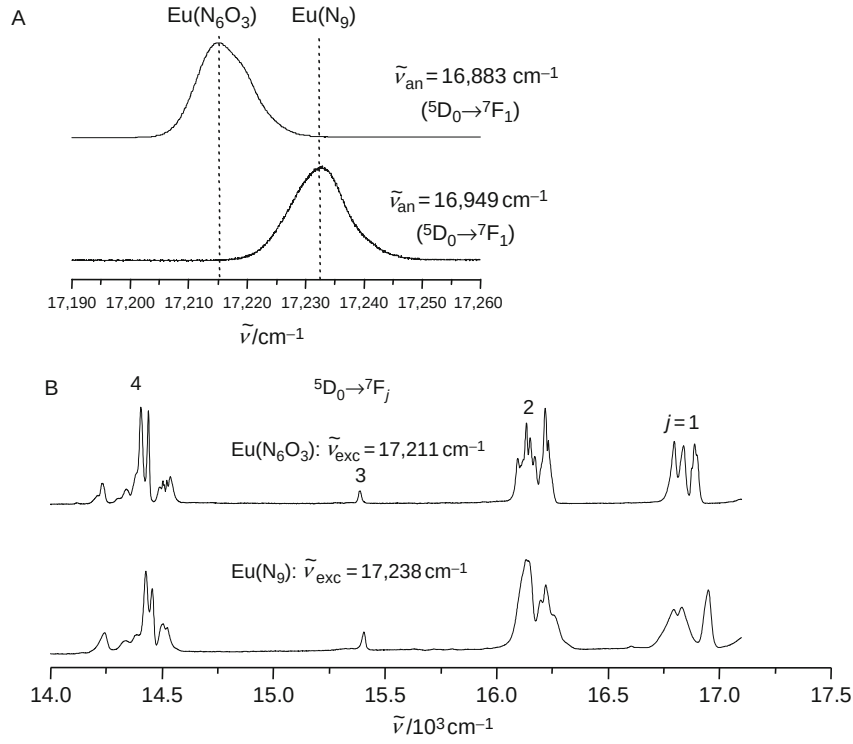

FIGURE 60 (A) Excitation profiles of the Eu($^5D_0 \leftarrow {}^7F_0$) transition for $[Eu_3(\mathbf{L28})_3]^{9+}$ at 10 K upon monitoring different components of the $^5D_0 \rightarrow {}^7F_1$ transition. (B) Emission spectra of $[Eu_3(\mathbf{L28})_3]^{9+}$ at 10 K recorded under selective excitation of the $Eu(N_6O_3)$ and $Eu(N_9)$ sites (adapted from Floquet et al., 2003).

$\tilde{\nu}^{\,obs}_{EuN_9} > \tilde{\nu}^{\,obs}_{EuN_6O_3}$, divergent intramolecular thermally activated energy migration processes from the central EuN_9 sites toward the EuN_6O_3 termini in $[Eu_3(\mathbf{L28})_3]^{9+}$ and $[Eu_4(\mathbf{L29})_3]^{12+}$ eventually produce pure emission of the terminal EuN_6O_3 sites at room temperature.

For Tb^{III} helicates with ligands **L11**, **L13**, and **L28**–**L32**, the ligand-centered $^3\pi\pi^*$ excited state is too close in energy to avoid thermally activated $Tb(^5D_4) \rightarrow {}^3\pi\pi^*$ energy transfers, which drastically reduces the intensity and lifetime of the Tb-centered luminescence upon increasing the temperature. Typically, $Tb(^5D_4)$ lifetimes vary from a few milliseconds at 10–77 K to reach a few tens of microseconds at room temperature in Tb^{III} triple-stranded helicates (Table 10). Interestingly, the stepwise approximate 1000–2000 cm^{-1} energy increase of the ligand-centered $^3\pi\pi^*$ excited state in going from $[Tb_2(\mathbf{L11})_3]^{6+}$ ($E(^3\pi\pi^*) = 19{,}880$ cm^{-1}, $Q_L^{Tb} < 0.01\%$, Table 10) to $[Tb_2(\mathbf{L13^b})_3]^{6+}$ ($E(^3\pi\pi^*) = 20{,}900$ cm^{-1},

$Q_L^{Tb} = 11\%$, Table 10) and $[Tb(\mathbf{L18^a})_3]^{3+}$ ($E(^3\pi\pi^*) = 23{,}600$ cm^{-1}, $Q_L^{Tb} = 26\%$, Table 4) supports this interpretation. Finally, a thorough theoretical modeling of the kinetic issues of the sensitization processes occurring in the triple-stranded helicates $[Sm_2(\mathbf{L13^f})_3]$ and $[Yb_2(\mathbf{L13^f})_3]$ suggests that the pivotal ligand($^3\pi\pi^*$) $\rightarrow R^{III}$ energy transfer is of the exchange type for Sm^{III} ($^3\pi\pi^* \rightarrow {}^5G_{5/2}{}^{(1)}$), but corresponds to an electron transfer mechanism for Yb^{III} (Gonçalves e Silva et al., 2002).

3.6 Paramagnetic properties

Because of the minute mixing of the metal 4f-orbitals with the ligand wave functions, the open-shell trivalent lanthanides can be used not only as luminescent sensors (Bünzli, 1989), but also as paramagnetic probes for elucidating molecular structures in solution. EPR spectroscopy is mainly limited to Gd^{III} complexes because an orbitally nondegenerated ground state ($^8S_{7/2}$ for Gd^{III}) is required for producing electronic relaxation times long enough to allow the detection of EPR signals with reasonable line width (Raitsimiring et al., 2007). Moreover, the structural information is mainly restricted to the first coordination sphere because of the very limited covalency of the Gd-donor bonds, hence producing negligible spin delocalization. On the other hand, the very fast electronic relaxation displayed by the other open-shell trivalent lanthanides possessing orbitally degenerate ground states is compatible with small perturbations of the nuclear relaxation processes and the recording of high-resolution NMR spectra (Bertini and Luchinat, 1996). A thorough review of the use of R^{III} as paramagnetic probes in triple-helical (C_3-symmetry) and quadruple helical (C_4-symmetry) complexes has been recently published (Piguet and Geraldes, 2003). However, the basic principles and concepts used for extracting solution structures of lanthanide complexes are briefly outlined here to discuss the main contribution brought by polynuclear lanthanide helicates in this field. Introduction of a paramagnetic trivalent lanthanide ion in a complex has two major effects on the spectra of the NMR-active atoms of the ligands (usually ^1H, ^{13}C, ^{31}P, and ^{15}N are commonly considered for these studies because of their 1/2 nuclear spin):

(1) The longitudinal ($1/T_{1i}$, Eq. (20)) and transversal ($1/T_{2i}$, Eq. (21)) nuclear relaxation rates of the nucleus i are enhanced by the combination of through-bond (contact *Fermi* interaction, Eqs. (22) and (23)) and through-space (dipolar-transient, Eqs. (24) and (25) and dipolar-Curie, Eqs. (26) and (27)) coupling of the nuclear and electronic magnetic moments.

$$\frac{1}{T_{1i}^{\mathrm{exp}}} = \frac{1}{T_{1i}^{\mathrm{dia}}} + \frac{1}{T_{1i}^{\mathrm{para}}} = \frac{1}{T_{1i}^{\mathrm{dia}}} + \frac{1}{T_{1i}^{\mathrm{para-contact}}} + \frac{1}{T_{1i}^{\mathrm{para-dip-transient}}} + \frac{1}{T_{1i}^{\mathrm{para-dip-Curie}}} \tag{20}$$

$$\frac{1}{T_{2i}^{\mathrm{exp}}} = \frac{1}{T_{2i}^{\mathrm{dia}}} + \frac{1}{T_{2i}^{\mathrm{para}}} = \frac{1}{T_{2i}^{\mathrm{dia}}} + \frac{1}{T_{2i}^{\mathrm{para-contact}}} + \frac{1}{T_{2i}^{\mathrm{para-dip-transient}}} + \frac{1}{T_{2i}^{\mathrm{para-dip-Curie}}} \tag{21}$$

$$\frac{1}{T_{1i}^{\mathrm{para-contact}}} = \frac{S(S+1)}{3}\left(\frac{A_i}{\hbar}\right)^2\left(\frac{2\tau_{\mathrm{e}}}{1+\omega_{\mathrm{S}}^2\tau_{\mathrm{e}}^2}\right) \tag{22}$$

$$\frac{1}{T_{2i}^{\mathrm{para-contact}}} = \frac{S(S+1)}{3}\left(\frac{A_i}{\hbar}\right)^2\left(\tau_e + \frac{\tau_e}{1+\omega_{\mathrm{S}}^2\tau_e^2}\right) \tag{23}$$

$$\frac{1}{T_{1i}^{\mathrm{para-dip-transient}}} = \frac{2}{15}\left(\frac{\mu_0}{4\pi}\right)^2 \frac{\gamma_I \mu_{\mathrm{eff}}^2 \mu_{\mathrm{B}}^2}{r_i^6}\left(\frac{3\tau_c}{1+\omega_{\mathrm{I}}^2\tau_c^2} + \frac{7\tau_c}{1+\omega_{\mathrm{S}}^2\tau_c^2}\right) \tag{24}$$

$$\frac{1}{T_{2i}^{\mathrm{para-dip-transient}}} = \frac{1}{15}\left(\frac{\mu_0}{4\pi}\right)^2 \frac{\gamma_I \mu_{\mathrm{eff}}^2 \mu_{\mathrm{B}}^2}{r_i^6}\left(4\tau_c + \frac{3\tau_c}{1+\omega_{\mathrm{I}}^2\tau_c^2} + \frac{13\tau_c}{1+\omega_{\mathrm{S}}^2\tau_c^2}\right) \tag{25}$$

$$\frac{1}{T_{1i}^{\mathrm{para-dip-Curie}}} = \frac{6}{5}\left(\frac{\mu_0}{4\pi}\right)^2 \frac{\gamma_I^2 \mu_{\mathrm{eff}}^4 \mu_{\mathrm{B}}^4 H_0^2}{r_i^6 (3kT)^2}\left(\frac{\tau_r}{1+\omega_{\mathrm{I}}^2\tau_r^2}\right) \tag{26}$$

$$\frac{1}{T_{2i}^{\mathrm{para-dip-Curie}}} = \frac{1}{5}\left(\frac{\mu_0}{4\pi}\right)^2 \frac{\gamma_I^2 \mu_{\mathrm{eff}}^4 \mu_{\mathrm{B}}^4 H_0^2}{r_i^6 (3kT)^2}\left(4\tau_r + \frac{3\tau_r}{1+\omega_{\mathrm{I}}^2\tau_r^2}\right) \tag{27}$$

The random modulation of the electron-nucleus magnetic coupling via electronic relaxation (characteristic time τ_{e}), molecular tumbling (characteristic time τ_{r}) and chemical exchange (ligand exchange reaction, characteristic time τ_{m} is assumed to be zero for saturated helicates in eqs (22 – 27)) can be combined in a global correlation time

$\tau_c^{-1} = \tau_e^{-1} + \tau_r^{-1} + \tau_m^{-1}$, which controls the extent to which the paramagnetic center affects the nuclear relaxation. When the electronic relaxation time is long as for example in Gd^{III} (typically $\tau_e \geq 1$ ns), the contribution of $1/T_{2i}^{para-contact}$ (Eq. (23)) is so large that NMR signals with reasonable line width cannot be recorded. For all the other paramagnetic lanthanides, τ_e falls in the picosecond range and well-resolved NMR spectra can be obtained. In these conditions, an acceptable approximation only considers the contribution of through-space dipolar interactions to the paramagnetic relaxation because the *Fermi* constants A_i are very small for lanthanide complexes ($1/T_{1i}^{para-contact}$ and $1/T_{2i}^{para-contact}$ are neglected). It is therefore a common practice to combine the transient and Curie contributions to the dipolar coupling in Eqs. (28) and (29), because both depend on r_i^{-6}, whereby r_i is the R^{III}-nucleus distance (Figure 61), E_{1j} and E_{2j} are magnetic constants depending on (i) the lanthanide j present in the complex, (ii) the temperature T, (iii) the external magnetic field of the spectrometer H_0, (iv) the effective electronic magnetic moment μ_{eff}, (v) the type of NMR-active nucleus under investigation, and (vi) the electronic and rotational correlation times. Within a given complex, all these parameters are fixed and once a reference R^{III}-nucleus distance r_{ref} is known for the complex in solution, E_{1j} and E_{2j} can be calibrated and all the others distances can be easily deduced from measurements of nuclear relaxation rates thanks to Eqs. (28) and (29).

$$\frac{1}{T_{1i}^{exp}} - \frac{1}{T_{1i}^{dia}} = \frac{1}{T_{1i}^{para}} = \frac{4}{3}\left(\frac{\mu_0}{4\pi}\right)^2 \frac{\gamma_I \mu_{eff}^2 \mu_B^2}{r_i^6}\tau_e + \frac{6}{5}\left(\frac{\mu_0}{4\pi}\right)^2 \frac{\gamma_I^2 \mu_{eff}^4 \mu_B^4 H_0^2}{r_i^6 (3kT)^2}\left(\frac{\tau_r}{1 + \omega_I^2 \tau_r^2}\right) = \frac{E_{1j}}{r_i^6} \quad (28)$$

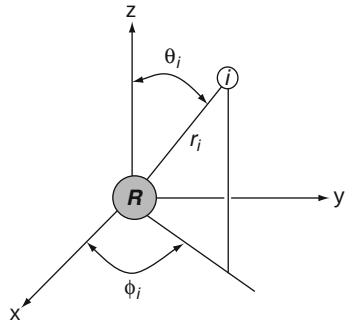

FIGURE 61 Spherical coordinates r_i, θ_i, and ϕ_i for a nucleus i in an arbitrary xyz reference frame with the metal ion R^{III} located at the origin.

$$\frac{1}{T_{2i}^{\text{exp}}} - \frac{1}{T_{2i}^{\text{dia}}} = \frac{1}{T_{2i}^{\text{para}}} = \frac{4}{3}\left(\frac{\mu_0}{4\pi}\right)^2 \frac{\gamma_I \mu_{\text{eff}}^2 \mu_B^2}{r_i^6}\tau_e + \frac{1}{5}\left(\frac{\mu_0}{4\pi}\right)^2 \frac{\gamma_I^2 \mu_{\text{eff}}^4 \mu_B^4 H_0^2}{r_i^6 (3kT)^2} \left(4\tau_r + \frac{3\tau_r}{1+\omega_I^2\tau_r^2}\right) = \frac{E_{2j}}{r_i^6} \tag{29}$$

(2) The NMR chemical shift δ_{ij}^{exp} of a nucleus i in a complex of a lanthanide ion j is also affected by the influence of the electronic magnetic moment on the local magnetic field felt by the nuclear spin under investigation (Eq. (30)). In this equation, the through-bond contribution δ_{ij}^{c} arises from partial delocalization of the electronic spin $\langle S_z \rangle_j$ via the contact *Fermi* mechanism and is expressed by Eq. (31). The through-space contribution δ_{ij}^{pc} is a consequence of residual dipolar effects due to anisotropic electronic magnetic moments in the homogeneous medium and is often referred to as pseudocontact contribution (Eq. (32) in which Tr(χ) represents the trace of the magnetic susceptibility tensor).

$$\delta_{ij}^{\text{exp}} = \delta_i^{\text{dia}} + \delta_{ij}^{\text{para-contact}} + \delta_{ij}^{\text{para-pseudocontact}} = \delta_i^{\text{dia}} + \delta_{ij}^{c} + \delta_{ij}^{\text{pc}} \tag{30}$$

$$\delta_{ij}^{c} = \frac{\Delta H^{\text{c}}}{H_0} = \frac{A_i}{\hbar\gamma_I H_0}\langle S_z \rangle_j = F_i \langle S_z \rangle_j \tag{31}$$

$$\delta_i^{pc} = \frac{\Delta H^{\text{pc}}}{H_0} = \frac{1}{2N_A r_i^3}\left[\left(\chi_{zz}^j - \frac{1}{3}\text{Tr}(\chi)\right)(3\cos^2\theta_i - 1) + (\chi_{xx}^j - \chi_{yy}^j)(\sin^2\theta_i \cos 2\varphi_i)\right] \tag{32}$$

Both through-bond and pseudocontact contributions can be easily factorized into a series of products of two terms, each term depending either on the nucleus i (topologic and geometric location) or from the lanthanide j (electronic structure and crystal-field effects). For axial complexes, that is, possessing at least a three-fold axis as found in triple-stranded helicates, the molecular magnetic susceptibility tensor χ^j written in the principal magnetic axes system is symmetrical ($\chi_{xx}^j = \chi_{yy}^j$, z magnetic axis aligned along C_3). Equation (32) thus reduces to Eq. (33), whereby $G_i = (3\cos^2\theta_i - 1)/r_i^3$ is known as the geometrical factor.

$$\delta_i^{\text{pc}} = \frac{1}{2N_A r_i^3}\left[\left(\chi_{zz}^j - \frac{1}{3}\text{Tr}(\chi)\right)\left(3\cos^2\theta_i - 1\right)\right] = \frac{1}{2N_A}\left(\chi_{zz}^j - \frac{1}{3}\text{Tr}(\chi)\right)G_i \tag{33}$$

In a seminal contribution, *Bleaney* demonstrated that when the crystal-field splitting of the ground multiplet is smaller or comparable to kT, a situation often met with lanthanide complexes, the anisotropic part of the axial paramagnetic susceptibility tensor originates from second-order effects and can be simply estimated by the product of magnetic constants C_j, characteristics of the electronic configuration of each lanthanide (i.e., *Bleaney* factor), multiplied by the second-rank crystal-field parameter B_0^2 (Eq. (34), Bleaney, 1972).

$$\frac{1}{2N_A}\left(\chi_{zz}^{j} - \frac{1}{3}\mathrm{Tr}(\chi)\right) = B_0^2 C_j \tag{34}$$

Finally introducing Eqs. (31), (33), and (34) into Eq. (30) gives the simple linear Eq. (35), which is well adapted for testing isostructurality along the lanthanide series for complexes in solution since numerical values for $\langle S_z\rangle_j$ and C_j calculated at 300 K have been tabulated (Piguet and Geraldes, 2003).

$$\delta_{ij}^{\mathrm{exp}} - \delta_i^{\mathrm{dia}} = \delta_{ij}^{\mathrm{para}} = F_i\langle S_z\rangle_j + B_0^2 G_i C_j \tag{35}$$

However, B_0^2 is often very sensitive to the minor R^{III}-ligand bond contraction accompanying the loading of the 4f-orbitals along the lanthanide series. This often prevents a safe interpretation of deviations of Eq. (35) from linearity as arising from a structural change affecting the geometrical factor G_i (Ouali et al., 2002). The simultaneous consideration of two NMR-active nuclei i (Eq. (35)) and k (Eq. (36)) in the same complex provides two equations, which can be combined to give a novel linear equation (37), in which the influence of the crystal-field parameter has been removed (Platas et al., 1999).

$$\delta_{kj}^{\mathrm{exp}} - \delta_k^{\mathrm{dia}} = \delta_{kj}^{\mathrm{para}} = F_k\langle S_z\rangle_j + C_j B_0^2 G_k \tag{36}$$

$$\frac{\delta_{ij}^{\mathrm{para}}}{\langle S_z\rangle_j} = \left(F_i - F_k\frac{G_i}{G_k}\right) + \frac{G_i}{G_k}\cdot\frac{\delta_{kj}^{\mathrm{para}}}{\langle S_z\rangle_j} \tag{37}$$

Any variation of the slope for linear plots of $\delta_{ij}^{\mathrm{para}}/\langle S_z\rangle_j$ versus $\delta_{kj}^{\mathrm{para}}/\langle S_z\rangle_j$ along a series of lanthanide complexes j implies that the ratio of the geometrical factor G_i/G_k changes, hence the structure of the complex does too. The systematic application of nuclear relaxation measurements (Eqs. (28) and (29)) for obtaining R^{III}-nuclei distances, combined with the detailed analysis of NMR paramagnetic shifts with the help of the two nuclei method (Eq. (37), detection of isostructural series) as well

as the one nucleus analysis (Eq. (35), extraction of geometrical factors) provides an efficient tool for establishing the solution structures of mononuclear axial lanthanide complexes (see Section 2.2 for structural details on these complexes). For the homometallic polynuclear triple-stranded helicates $[R_m\mathbf{L}_3]^{3m+}$, the existence of m identical lanthanide ions packed along the C_3-symmetry axis requires some modifications of the basic equations derived for mononuclear systems (Figure 62).

Since the m identical trivalent lanthanides are not magnetically coupled in triple-stranded helicates (intermetallic separation ≈ 9 Å), the global effect of the electronic magnetic moments onto the nuclear relaxation in solution is given by a simple additive model, which transforms Eqs. (28) and (29) into Eqs. (38) and (39), and in which each specific distance r_i^l between the nucleus i and the lanthanide l is taken into account (Piguet and Geraldes, 2003, Figure 62).

$$\frac{1}{T_{1i}^{\text{exp}}} - \frac{1}{T_{1i}^{\text{dia}}} = \frac{1}{T_{1i}^{\text{para}}} = E_{1j}\sum_{l=1}^{m}\left(\frac{1}{(r_i^l)^6}\right) \tag{38}$$

$$\frac{1}{T_{2i}^{\text{exp}}} - \frac{1}{T_{2i}^{\text{dia}}} = \frac{1}{T_{2i}^{\text{para}}} = E_{2j}\sum_{l=1}^{m}\left(\frac{1}{(r_i^l)^6}\right) \tag{39}$$

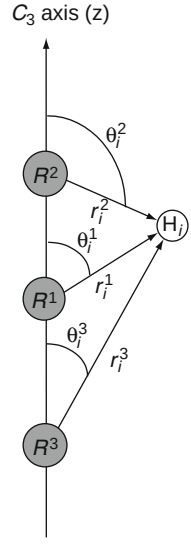

FIGURE 62 Example of axial coordinates in a trinuclear triple-stranded lanthanide helicate (adapted from Floquet et al., 2003).

Due to the dependence of $1/T_i^{\text{para}}$ on a set of different R-nucleus distances, these equations cannot be used for obtaining structural information in polynuclear helicates, but they are useful for confirming the assignment of paramagnetic NMR spectra, once a reasonable structure is at hand (Elhabiri et al., 1999; Ouali et al., 2003). The application of the additive model for the rationalization of the paramagnetic NMR shifts is more promising and Eq. (40) replaces Eq. (35) in a triple-stranded homopolynuclear helicate containing m magnetically noncoupled paramagnetic centers, each lanthanide l being located at the origin of its own reference frame (Figure 62).

$$\delta_{ij}^{\text{exp}} - \delta_i^{\text{dia}} = \delta_{ij}^{\text{para}} = (\sum_{l=1}^{m} F_i^l)\langle S_z\rangle_j + (\sum_{l=1}^{m} (B_0^2)^l G_i^l)C_j \tag{40}$$

The case of the D_3-symmetrical binuclear helicate $[R_2(\mathbf{L13^f})_3]$ (Figure 41) is straightforward because $(B_0^2)^1 = (B_0^2)^2$ for symmetry reasons, and a simple factorization transforms Eq. (38) into the linear Eq. (41) (Elhabiri et al., 1999).

$$\delta_{ij}^{\text{para}} = (F_i^1 + F_i^2)\langle S_z\rangle_j + B_0^2(G_i^1 + G_i^2)C_j \tag{41}$$

Consequently, the removal of the crystal-field parameter requires the same strategy as the one developed for the mononuclear complexes, thus eventually leading to the two nuclei crystal-field independent Eq. (42), which is mathematically analogous to Eq. (37).

$$\frac{\delta_{ij}^{\text{para}}}{\langle S_z\rangle_j} = \left((F_i^1 + F_i^2) - (F_k^1 + F_k^2)\left(\frac{G_i^1 + G_i^2}{G_k^1 + G_k^2}\right)\right) + \left(\frac{G_i^1 + G_i^2}{G_k^1 + G_k^2}\right)\cdot\frac{\delta_{kj}^{\text{para}}}{\langle S_z\rangle_j} \tag{42}$$

Standard two-nuclei $\delta_{ij}^{\text{para}}/\langle S_z\rangle_j$ versus $\delta_{kj}^{\text{para}}/\langle S_z\rangle_j$ plots show straight lines (Eq. (37)) for $[R_2(\mathbf{L13^f})_3]$, except for some deviations for those nuclei, which are strongly affected by both paramagnetic centers (Rigault et al., 2000b). Globally, isostructurality was established along the complete lanthanide series in $[R_2(\mathbf{L13^f})_3]$ (Elhabiri et al., 1999), but with a smooth change in the crystal-field parameter occurring between $R =$ Tb and $R =$ Er ($B_0^2(\text{Ce} - \text{Tb})/B_0^2(\text{Er} - \text{Yb}) = 0.8$, Piguet and Geraldes, 2003). A similar conclusion was reached for the series of helicates with the neutral ditopic ligand $\mathbf{L13^c}$ bearing chloride substituents in the para position of the pyridines, $[R_2(\mathbf{L13^c})_3]^{6+}$. The single nucleus method yields two straight lines (Pr–Dy and Ho–Yb) while the two-nucleus method points to a more intricate behavior: some proton pairs display a single straight line, while others produce two approximately parallel lines. A detailed analysis concluded that if the solution structure is essentially maintained in solution from Pr to Yb, changes in both the crystal-field parameter and

hyperfine coupling constants are responsible for the intricate behavior unraveled by these analyses (Platas-Iglesias et al., 2000). The case of the D_3-symmetrical trinuclear $[R_3(\mathbf{L28})_3]^{9+}$ helicate (Figure 51A) is more challenging because the crystal-field parameter of the central paramagnetic lanthanide $B_0^{2\text{central}} = (B_0^2)^1$ is different from those of the terminal paramagnetic centers $(B_0^2)^2 = (B_0^2)^3 = B_0^{2\text{terminal}}$ for symmetry reasons (Figure 62). In these conditions, factorization of Eq. (40) still gives a linear equation (Eq. (43), but with a second member containing a combination of crystal-field parameters and geometrical factors (Floquet et al., 2003).

$$\delta_{ij}^{\text{para}} = (F_i^1 + F_i^2 + F_i^3)\langle S_z\rangle_j + [B_0^{2\text{central}} G_i^1 + B_0^{2\text{terminal}}(G_i^2 + G_i^3)]C_j \quad (43)$$

The removal of the two different crystal-field parameters requires the simultaneous consideration of three different nuclei i, k, l in the same complex $[R_3(\mathbf{L28})_3]^{9+}$, thus leading to the multicenter Eq. (44), in which the factors B_{ikl}, C_{ikl}, and D_{ikl} are given in Eqs. (45)–(48) (Ouali et al., 2003).

$$\frac{\delta_{ij}^{\text{para}}}{\langle S_z\rangle_j} = B_{ikl} + C_{ikl}\frac{\delta_{kj}^{\text{para}}}{\langle S_z\rangle_j} + D_{ikl}\frac{\delta_{lj}^{\text{para}}}{\langle S_z\rangle_j} \quad (44)$$

$$B_{ikl} = F_i - F_k C_{ikl} - F_l D_{ikl} \quad (45)$$

$$C_{ikl} = R_{ik}\left(\frac{G_i^1 - G_l^1 R_{il}}{G_k^1 R_{ik} - G_l^1 R_{il}}\right) \quad (46)$$

$$D_{ikl} = -R_{il}\left(\frac{G_i^1 - G_k^1 R_{ik}}{G_k^1 R_{ik} - G_l^1 R_{il}}\right) \quad (47)$$

$$R_{xy} = \left(\frac{G_x^2 + G_x^3}{G_y^2 + G_y^3}\right) \quad (48)$$

Equation (44) corresponds to the equation of a plane perpendicular to the vector $(1, -C_{ikl}, -D_{ikl})$ and separated by a distance B_{ikl} from the origin in a homogeneous 3D space in which $\delta_{ij}^{\text{para}}/\langle S_z\rangle_j$, $\delta_{kj}^{\text{para}}/\langle S_z\rangle_j$, and $\delta_{lj}^{\text{para}}/\langle S_z\rangle_j$ define the orthogonal x, y, and z directions. The structural factors C_{ikl} and D_{ikl} are complicated nonlinear combinations of the geometrical factors

G_i^m, G_k^m, and G_l^m ($m = 1-3$), but any deviation of the triplets ($\delta_{ij}^{\text{para}}/\langle S_z\rangle_j$, $\delta_{kj}^{\text{para}}/\langle S_z\rangle_j$, $\delta_{lj}^{\text{para}}/\langle S_z\rangle_j$) from the plane along the lanthanide series affects C_{ikl} and D_{ikl} and implies a structural change occurring in the lanthanide helicates $[R_3(\mathbf{L28})_3]^{9+}$. Application of the three-nuclei Eq. (44) for any i,k,l proton triplets in $[R_3(\mathbf{L28})_3]^{9+}$ gives a single plane along the complete lanthanide series, in agreement with isostructurality (Figure 63). However, the one-nucleus linear Eq. (43) points to a pronounced break near the middle of the series ($R = \text{Dy}$), which implies some variations of the crystal-field parameters (Figure 64). A detailed analysis of these data confirms the expected slight decrease of the crystal-field strength with lanthanide contraction ($B_0^{2\text{central}}(\text{Ce} - \text{Tb})/B_0^{2\text{central}}(\text{Dy} - \text{Yb}) = 1.4$ and $B_0^{2\text{terminal}}(\text{Ce} - \text{Tb})/B_0^{2\text{terminal}}(\text{Dy} - \text{Yb}) = 1.1$), but $B_0^{2\text{terminal}}(\text{Ce} - \text{Yb})/B_0^{2\text{central}}(\text{Ce} - \text{Yb}) = 2.0$ demonstrates that the terminal pseudotricapped-trigonal prismatic N_6O_3 sites produces stronger crystal-field splitting compared with the central N_9 site.

Interestingly, the mathematical treatment leading to Eq. (44) is very general and any paramagnetic system, for which Bleaney's approach requires two independent crystal-field parameters may benefit from its use for testing isostructurality, as demonstrated with the structural analyses of rhombic mononuclear (Terazzi et al., 2006) and polynuclear (Ouali et al., 2004) lanthanide complexes.

4. POLYNUCLEAR BIMETALLIC 4f HELICATES

The reaction of segmental ligand strands with two different trivalent lanthanides R^1(III) and R^2(III) enlarges the possible issues of the self-assembly processes. For axial C_2-symmetrical receptors, the threefold axis is maintained in the final triple-stranded polynuclear helicates $[(R^1)_x(R^2)_{m-x}(\mathbf{Lk})_3]^{3m+}$, but the three perpendicular twofold axes characterizing the homometallic complexes ($R^1 = R^2$) are present in the heterobimetallic systems ($R^1 \neq R^2$) only for some specific successions of metal ions (Dalla Favera et al., 2007). For nonaxial C_s-symmetrical ligands, the HHH $\leftrightarrow$ HHT isomerization of the triple-stranded helicates already limits the final symmetry to C_3 (HHH) and C_1 (HHT) point groups for homometallic complexes, a situation which is further complicated by the consideration of R^1/R^2 pairs (Jensen et al., 2006). Therefore, the detection and the quantitative estimation of deviations from the statistical distribution of the different lanthanides R^1 and R^2 in the final helicates is a crucial theme for the rational design of selective complexation processes along the lanthanide series.

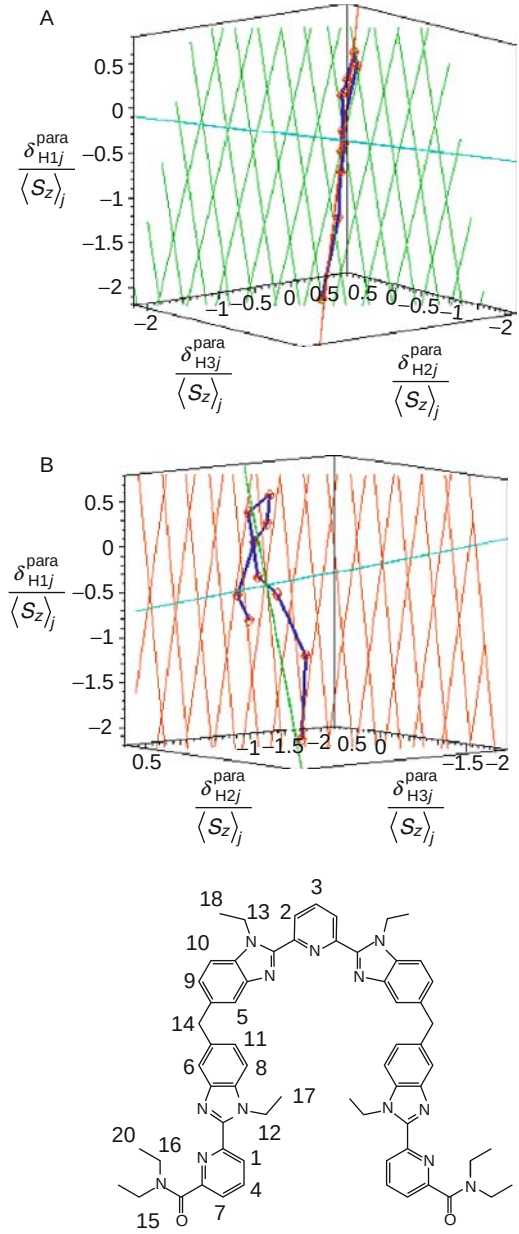

FIGURE 63 3D plots of $\delta^{para}_{ij}/\langle S_z\rangle_j$ versus $\delta^{para}_{kj}/\langle S_z\rangle_j$ and $\delta^{para}_{lj}/\langle S_z\rangle_j$ for H1, H2, H3 in $[R_3(\mathbf{L28})_3]^{9+}$ with numbering scheme of the ligand strand (CD_3CN, 298 K). (A) View of the best plane from profile showing the planar arrangement of the points (rhombs are used to highlight a plane orthogonal to the best plane). (B) View perpendicular to the best plane showing the location of the points within the plane (the lowest point is for $R = Ce$, the highest for $R = Dy$ and the last point is for $R = Yb$, the line is only a guide for the eyes and rhombs are used to highlight the best plane) (adapted from Ouali et al., 2003).

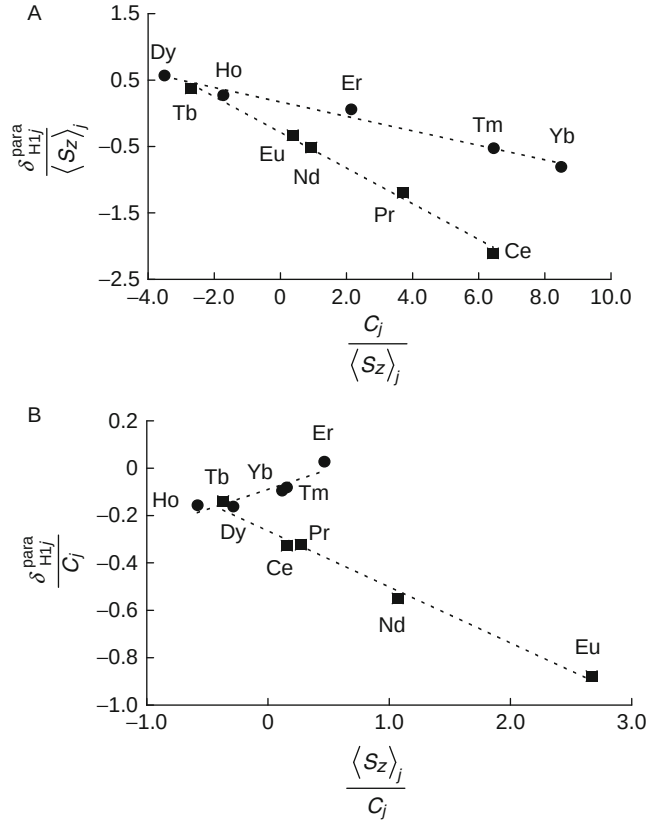

FIGURE 64 Plots of two linear forms of Eq. (43): (A) $\delta_{ij}^{para}/\langle S_z\rangle_j$ versus $C_j/\langle S_z\rangle_j$ and (B) δ_{ij}^{para}/C_j versus $\langle S_z\rangle_j/C_j$, for H1 in $[R_3(\mathbf{L28})_3]^{9+}$ (R = Ce–Yb, except Pm and Gd, CD_3CN, 298 K, numbering scheme in Figure 63) (adapted from Ouali et al., 2003).

4.1 Axial polytopic receptors: Statistical distributions and deviations

4.1.1 Binuclear helicates

Let us first consider the simple C_2-symmetrical bis-tridentate ligands **L11** or **L13**. Assuming that the principle of maximum site occupancy is obeyed (Hamacek et al., 2005b), the reaction of **L11** or **L13** with two different lanthanides gives three complexes $[(R^1)_2(\mathbf{Lk})_3]^{6+}$, $[(R^1)(R^2)(\mathbf{Lk})_3]^{6+}$, and $[(R^2)_2(\mathbf{Lk})_3]^{6+}$ whose intuitive statistical 1:2:1 distribution relies on the binomial distribution (Figure 65). At a lower level of modeling, the three wrapped ligand strands can be considered as a virtual preorganized molecular box of D_3-symmetry to which the zero level of the free energy of the self-assembly process is set (Figure 66, Piguet et al., 2005). The change in free energy accompanying the successive fixations of the

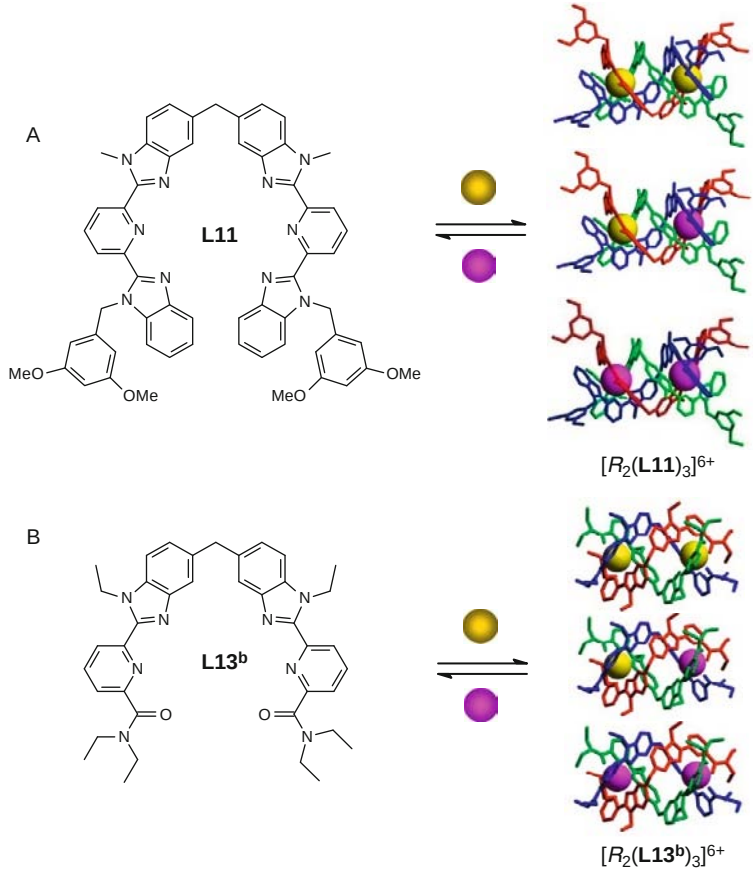

FIGURE 65 Self-assembly of the polynuclear triple-stranded helicates: (A) $[R_2(\mathbf{L11})_3]^{6+}$ (Piguet et al., 1993b) and (B) $[R_2(\mathbf{L13^b})_3]^{6+}$ (Zeckert et al., 2004) in acetonitrile. The final helicates correspond to the X-ray crystal structures of $[Eu_2(\mathbf{L11})_3]^{6+}$ (Piguet et al., 1993c) and $[Tb_2(\mathbf{L13^b})_3]^{6+}$ (Martin et al., 1998).

metal ions can then be easily described with the site-binding model (Koper and Borkovec, 2001), in which $\omega_{m,[L3]}^{R^i,R^j}$ is the statistical factor of the assembly (Ercolani et al., 2007), $f_k^{R^i}$ is the absolute intermolecular affinity (including solvation) of the lanthanide R^i for the k site of the preorganized box and $\Delta E_{1-2}^{R^i,R^j} = -RT \ln(u_{1-2}^{R^i,R^j})$ is the free energy of the intermetallic interaction operating between two nearest metallic neighbors (i.e., geminal) R^i and R^j in the final helicate (Eqs. (49)–(51), Figure 66).

The calculation of the statistical factors relies on the use of symmetry numbers $\sigma = \sigma^{ext}\sigma^{int}$ (Eq. (52), Ercolani et al., 2007), which are easy to obtain once the point groups of all partners contributing to the assembly process are at hand (Figure 66).

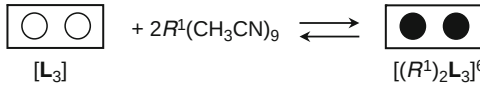

(49)

Point group: D_3	D_{3h}	D_3	C_{3v}
σ_{ext}: 6	6	6	3
σ_{int}: 1	3^9	1	1

$$\omega_{2,[L_3]}^{R^1,R^1} = \frac{6 \cdot 6^2 \cdot (3^9)^2}{6 \cdot 3^{18}} = 36 \Rightarrow \beta_{2,[L_3]}^{R^1,R^1} = 36 \cdot (f_k^{R1})^2 \cdot u_{1-2}^{R^1,R^1}$$

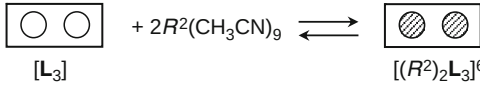

(50)

Point group: D_3	D_{3h}	D_3	C_{3v}
σ_{ext}: 6	6	6	3
σ_{int}: 1	3^9	1	1

$$\omega_{2,[L_3]}^{R^2,R^2} = \frac{6 \cdot 6^2 \cdot (3^9)^2}{6 \cdot 3^{18}} = 36 \Rightarrow \beta_{2,[L_3]}^{R^2,R^2} = 36 \cdot (f_k^{R2})^2 \cdot u_{1-2}^{R^2,R^2}$$

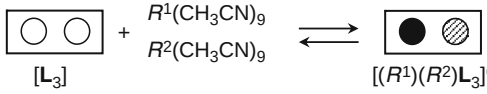

(51)

Point group: D_3	D_{3h}	C_3	C_{3v}
σ_{ext}: 6	6	3	1
σ_{int}: 1	3^9	1	1

$$\omega_{2,[L_3]}^{R^1,R^2} = \frac{6 \cdot 6^2 \cdot (3^9)^2}{3 \cdot 3^{18}} = 72 \Rightarrow \beta_{2,[L_3]}^{R^1,R^2} = 72 \cdot f_k^{R1} \cdot f_k^{R1} \cdot u_{1-2}^{R^1,R^2}$$

FIGURE 66 Thermodynamic modeling of the formation of binuclear triple-stranded helicates with ligands **L11** and **L13** in acetonitrile (Piguet et al., 2005). For the sake of simplicity, the unbound R^{III} cations are systematically considered as tricapped-trigonal prismatic nine-coordinate solvates.

$$\omega_{m,[L_3]}^{R^i,R^j} = \frac{\sigma_{[L_3]} \sigma_{R^i} \sigma_{R^i}}{\sigma_{[R^j R^l L_3]} (\sigma_{CH_3CN})^{18}} \tag{52}$$

From Eqs. (49)–(51), it is trivial to show that the thermodynamic constant characterizing the exchange process in equilibrium (53) only depends on the product of the ratio of statistical factors, which amounts to 4, and on the ratio of the Boltzmann factors referring to the various intermetallic interactions operating in the different complexes (Eq. (54), Piguet et al., 2005).

$$[(R^1)_2\mathbf{L}_3]^{6+} + [(R^2)_2\mathbf{L}_3]^{6+} \rightleftharpoons 2[(R^1)(R^2)\mathbf{L}_3]^{6+} \quad K_{\text{exch,bi}}^{R^1,R^2} \tag{53}$$

$$K_{\text{exch,bi}}^{R^1,R^2} = \frac{(\beta_{2,[\text{L}_3]}^{R^1,R^2})^2}{\beta_{2,[\text{L}_3]}^{R^1,R^1}\beta_{2,[\text{L}_3]}^{R^2,R^2}} = 4\cdot\frac{(u_{1-2}^{R^1,R^2})^2}{u_{1-2}^{R^1,R^1}u_{1-2}^{R^2,R^2}} = 4(u_{1-2}^{\text{mix}})^2 \tag{54}$$

In absence of heterometallic recognition, we have $\Delta E_{1-2}^{R^1,R^2} = 1/2(\Delta E_{1-2}^{R^1,R^1} + \Delta E_{1-2}^{R^2,R^2})$, and the mixing rule gives $\Delta E_{1-2}^{\text{mix}} = \Delta E_{1-2}^{R^1,R^2} - (\Delta E_{1-2}^{R^1,R^1} + \Delta E_{1-2}^{R^2,R^2})/2 = 0$ (Borkovec et al., 2004). Introducing $u_{1-2}^{\text{mix}} = \exp(-\Delta E_{1-2}^{\text{mix}}/RT)=1$ in Eq. (54) eventually confirms that $K_{\text{exch,bi}}^{R^1,R^2} = 4$ under pure statistical conditions, which translates into a 1:2:1 binomial distribution for the complexes $[(R^1)_2(\mathbf{L}k)_3]^{6+}$ (25%), $[(R^1)(R^2)(\mathbf{L}k)_3]^{6+}$ (50%), and $[(R^2)_2(\mathbf{L}k)_3]^{6+}$ (25%) at the stoichiometric ratio $[R^1]_{\text{tot}} : [R^2]_{\text{tot}} : [\text{L}]_{\text{tot}} = 1 : 1 : 3$. A thorough investigation of equilibrium (53) for 11 different R^1/R^2 lanthanide pairs with ligand **L13b** leading to two identical N_6O_3 nonadentate cavities in the virtual $(\mathbf{L13^b})_3$ molecule, indeed demonstrates that the mixing rule with $\Delta E_{1-2}^{\text{mix}} = 0$ is systematically obeyed ($K_{\text{exch,bi}}^{R^1,R^2} = 4.0(3)$, Zeckert et al., 2004), which implies no specific heterometallic recognition. The same trend is observed for ligand **L11** with the La^{III}/Eu^{III} pair, but $K_{\text{exch,L11}}^{\text{La,Lu}} = 1.2$ is found for the La^{III}/Lu^{III} pair, which indicates some deviations from statistical distribution with an approximate 1:1:1 speciation (i.e., $[(La_2(\mathbf{L11})_3]^{6+}$ (32.5%), $[LaLu(\mathbf{L11})_3]^{6+}$ (35%) and $[Lu_2(\mathbf{L11})_3]^{6+}$ (32.5%)) at the stoichiometric ratio $[R^1]_{\text{tot}} : [R^2]_{\text{tot}} : [\text{L}]_{\text{tot}} = 1 : 1 : 3$ (Piguet et al., 1993c). This trend has been tentatively assigned to a change in the affinity of the N_9 site for the smaller lanthanide due to unfavorable intramolecular interstrand packing, which specifically affects $f_{N_9}^{\text{Lu}}$ in $[LaLu(\mathbf{L11})_3]^{6+}$ ($f_{N_9}^{\text{Lu(La)}}$) and $[Lu_2(\mathbf{L11})_3]^{6+}$ ($f_{N_9}^{\text{Lu(Lu)}}$). In these conditions, $K_{\text{exch,bi}}^{\text{La,Lu}}$ depends on the specific affinities $f_{N_9}^{\text{Lu(La)}}$ and $f_{N_9}^{\text{Lu(Lu)}}$ (Eq. (55)), and no unambiguous assignment either to a change in local affinities, or to a change in intermetallic interaction can be proposed (Piguet et al., 1993c; Piguet et al., 2005).

$$K_{\text{exch,L11}}^{\text{La,Lu}} = \frac{(\beta_{2,[\text{L11}_3]}^{\text{La,Lu}})^2}{\beta_{2,[\text{L11}_3]}^{\text{La,La}}\beta_{2,[\text{L11}_3]}^{\text{Lu,Lu}}} = 4\left(\frac{f_{N_9}^{\text{Lu(La)}}}{f_{N_9}^{\text{Lu(Lu)}}}\right)^2\frac{(u_{1-2}^{\text{La,Lu}})^2}{u_{1-2}^{\text{La,La}}u_{1-2}^{\text{Lu,Lu}}} \tag{55}$$

Whatever the origin of this recognition effect is, it can be arbitrarily attributed to the sole effect of changes in intermetallic interactions. Introducing $K_{\text{exch,L11}}^{\text{La,Lu}} = 1.2$ in Eq. (54) gives $u_{1-2}^{\text{mix}} = 0.547$ and $\Delta E_{1-2}^{\text{mix}} = 1.5$ kJ mol^{-1}, a value much smaller than thermal energy $RT = 2.5$ kJ mol^{-1} at room temperature, which slightly disfavors the formation of the heterometallic $[LaLu(\mathbf{L11})_3]^{6+}$ helicate.

4.1.2 Polynuclear helicates

The extension of this approach to the heterobimetallic trinuclear helicates $[(R^1)_x(R^2)_{3-x}(\mathbf{L28})_3]^{9+}$ has to take into account the formation of a total of six microspecies contributing to four macrospecies (Eqs. (56)–(61) in Figure 67, Floquet et al., 2004).

The exchange process between these macrospecies (equilibrium (62)) can be modeled with Eq. (63).

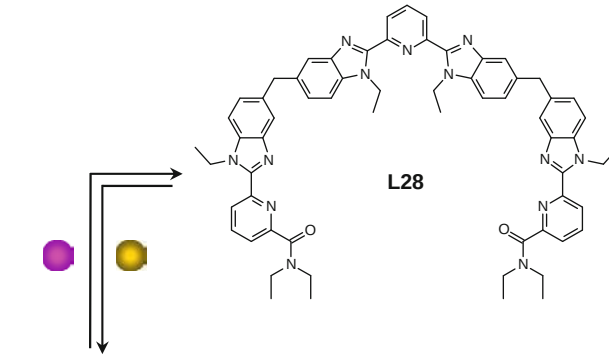

$$\beta^{R^1,R^1,R^1}_{3,[L28_3]} = 396 \cdot \left(f^{R^1}_{N9}\right)\cdot\left(f^{R^1}_{N6O3}\right)^2 \cdot \left(u^{R^1,R^1}_{1-2}\right)^2 \cdot u^{R^1,R^1}_{1-3} \quad (56)$$

$$\beta^{R^2,R^1,R^1}_{3,[L28_3]} = 792 \cdot \left(f^{R^2}_{N6O3}\right)\cdot\left(f^{R^1}_{N9}\right)\cdot\left(f^{R^1}_{N6O3}\right) \cdot u^{R^1,R^1}_{1-2} \cdot u^{R^1,R^2}_{1-2} \cdot u^{R^1,R^2}_{1-3} \quad (57)$$

$$\beta^{R^1,R^2,R^1}_{3,[L28_3]} = 396 \cdot \left(f^{R^2}_{N9}\right)\cdot\left(f^{R^1}_{N6O3}\right)^2 \cdot \left(u^{R^1,R^2}_{1-2}\right)^2 \cdot u^{R^1,R^1}_{1-3} \quad (58)$$

$$\beta^{R^2,R^1,R^2}_{3,[L28_3]} = 396 \cdot \left(f^{R^1}_{N9}\right)\cdot\left(f^{R^2}_{N6O3}\right)^2 \cdot \left(u^{R^1,R^2}_{1-2}\right)^2 \cdot u^{R^2,R^2}_{1-3} \quad (59)$$

$$\beta^{R^2,R^2,R^1}_{3,[L28_3]} = 792 \cdot \left(f^{R^2}_{N6O3}\right)\cdot\left(f^{R^2}_{N9}\right)\cdot\left(f^{R^1}_{N6O3}\right) \cdot u^{R^2,R^2}_{1-2} \cdot u^{R^1,R^2}_{1-2} \cdot u^{R^1,R^2}_{1-3} \quad (60)$$

$$\beta^{R^2,R^2,R^2}_{3,[L28_3]} = 396 \cdot \left(f^{R^2}_{N9}\right)\cdot\left(f^{R^2}_{N6O3}\right)^2 \cdot \left(u^{R^2,R^2}_{1-2}\right)^2 \cdot u^{R^2,R^2}_{1-3} \quad (61)$$

$[R_3(\mathbf{L28})_3]^{9+}$

FIGURE 67 Self-assembly of the polynuclear triple-stranded helicates $[R_3(\mathbf{L28})_3]^{9+}$ in acetonitrile and associated site-binding model for their formation constants (Floquet et al., 2004); $f^R_{N_9}$ and $f^R_{N_6O_3}$ are the microscopic affinities of R^{III} for the N_9 and N_6O_3 sites, respectively, and $\Delta E^{R^i,R^j}_{1-2} = -RT\ln(u^{R^i,R^j}_{1-2})$ represents the intramolecular intermetallic interaction between two nearest neighbors, while $\Delta E^{R^i,R^j}_{1-3} = -RT\ln(u^{R^i,R^j}_{1-3})$ holds for related interaction between the terminal cations. The final helicates correspond to the X-ray crystal structure of $[Eu_3(\mathbf{L28})_3]^{9+}$ (Floquet et al., 2003).

$$[(R^1)_3(\mathbf{L28})_3]^{9+} + [(R^2)_3(\mathbf{L28})_3]^{9+} \rightleftharpoons [(R^1)_2(R^2)(\mathbf{L28})_3]^{9+} + [(R^1)(R^2)_2(\mathbf{L28})_3]^{9+} \quad K^{R^1,R^2}_{\text{exch,tri}} \tag{62}$$

$$K^{R^1,R^2}_{\text{exch,tri}} = \frac{\left(\beta^{R^1,R^1,R^2}_{3,[\text{L28}_3]} + \beta^{R^1,R^2,R^1}_{3,[\text{L28}_3]}\right)\left(\beta^{R^2,R^1,R^2}_{3,[\text{L28}_3]} + \beta^{R^2,R^2,R^1}_{3,[\text{L28}_3]}\right)}{\beta^{R^1,R^1,R^1}_{3,[\text{L28}_3]}\,\beta^{R^2,R^2,R^2}_{3,[\text{L28}_3]}} \tag{63}$$

The subsequent introduction of Eqs. (56)–(61) into Eq. (63) eventually gives an intricate mathematical expression because the additive contributions of the microspecies belonging to the same macrospecies prevent simplification. The equilibrium constant $K^{R^1,R^2}_{\text{exch,tri}}$ thus depends on all microscopic parameters used to model the formation of the microspecies. However, a statistical value of $K^{R^1,R^2}_{\text{exch,tri}} = 9$ can be obtained if (i) the absolute affinities of the N_9 and N_6O_3 sites do not vary along the lanthanide series ($f^{R^1}_{N_9} = f^{R^2}_{N_9}$ and $f^{R^1}_{N_6O_3} = f^{R^2}_{N_6O_3}$) and (ii) the intermetallic interactions also do not depend on the involved lanthanide pair ($\Delta E^{R^1,R^2}_{1-2} = \Delta E^{R^1,R^2}_{1-2} = \Delta E^{R^2,R^2}_{1-2}$ and $\Delta E^{R^1,R^1}_{1-3} = \Delta E^{R^1,R^2}_{1-3} = \Delta E^{R^2,R^2}_{1-3}$). In these conditions, reaction of lanthanide cations with the ligand **L28** in a $[R^1]_{\text{tot}} : [R^2]_{\text{tot}} : [\mathbf{L28}]_{\text{tot}} = 1:1:2$ stoichiometric ratio is expected to give the binomial distribution 1:3:3:1 for the macrospecies $[(R^1)_3(\mathbf{L28})_3]^{9+}$, $[(R^1)_2(R^2)(\mathbf{L28})_3]^{9+}$, $[(R^1)(R^2)_2(\mathbf{L28})_3]^{9+}$, and $[(R^1)_3(\mathbf{L28})_3]^{9+}$ (Floquet et al., 2004). Because of the latter demanding requirements, it is not so surprising that the experimental values $13 \le K^{R^1,R^2}_{\text{exch,L28}} \le 122$ found for nine different R^1/R^2 lanthanide pairs with **L28** in acetonitrile do not match the statistical distribution (Floquet et al., 2004). However, it is sufficient to consider that the absolute affinities vary along the lanthanide series ($f^{R^1}_{N_9} \neq f^{R^2}_{N_9}$ and $f^{R^1}_{N_6O_3} \neq f^{R^2}_{N_6O_3}$) to obtain a good agreement between theoretical (Eq. (63)) and experimental data, which indicates that $\Delta E^{\text{mix}}_{1-2} = 0$ kJ mol^{-1} and $\Delta E^{\text{mix}}_{1-3} = 0$ kJ mol^{-1}. In conclusion, the linear succession of N_6O_3 and N_9 sites in the triple-stranded helicates $[R_3(\mathbf{L28})_3]^{9+}$ does not evidence intermetallic recognition between pairs of lanthanides. The minute selectivity arises from minor difference in the absolute affinities of the N_6O_3 and N_9 sites along the lanthanide series (Floquet et al., 2004).

The tetranuclear homologue $[(R^1)_x(R^2)_{4-x}(\mathbf{L29})_3]^{12+}$ offers a tricky challenge since the reaction of **L29** with a R^1/R^2 pair of lanthanides produces 10 microspecies contributing to 5 macrospecies, and only the La/Lu pair has been investigated (Figure 68, Dalla Favera et al., 2007).

The adequate exchange process (equilibrium (64)), for which the site-binding model (Eq. (65)) predicts a statistical value of

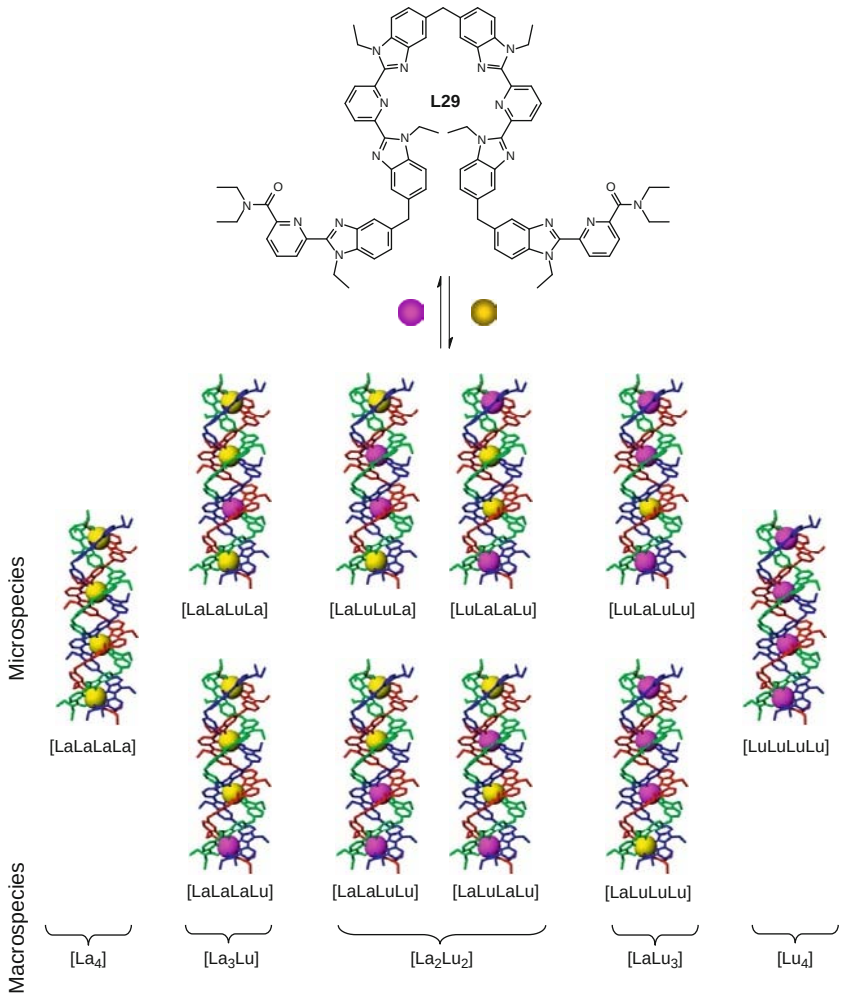

FIGURE 68 Self-assembly of the tetranuclear homo- and heterobimetallic triple-stranded helicates $[La_xLu_{4-x}(\mathbf{L29})_3]^{12+}$ showing the possible micro- and macrospecies (Dalla Favera et al., 2007).

$K_{\text{exch,L29}}^{\text{La,Lu}} = 9216 = \quad 10^{3.96}$ when $f_{N_9}^{La} = f_{N_9}^{Lu}$, $f_{N_6O_3}^{La} = f_{N_6O_3}^{Lu}$, $\Delta E_{1-2}^{La,La} = \Delta E_{1-2}^{La,Lu} = \Delta E_{1-2}^{Lu,Lu}$, $\Delta E_{1-3}^{La,La} = \Delta E_{1-3}^{La,Lu} = \Delta E_{1-3}^{Lu,Lu}$, and $\Delta E_{1-4}^{La,La} = \Delta E_{1-4}^{La,Lu} = \Delta E_{1-4}^{Lu,Lu}$, indeed shows a significant deviation with the experimental value of $K_{\text{exch,L29}}^{\text{La,Lu}} = 10^{8.5}$.

$$\begin{aligned} 3[La_4(\mathbf{L29})_3]^{12+} + 3[Lu_4(\mathbf{L29})_3]^{12+} &\rightleftharpoons 2[La_3Lu(\mathbf{L29})_3]^{12+} \\ + 2[La_2Lu_2(\mathbf{L29})_3]^{12+} + 2[LaLu_3(\mathbf{L29})_3]^{12+} &\; K_{\text{exch,L29}}^{\text{La,Lu}} \end{aligned} \tag{64}$$

$$K_{\text{exch,L29}}^{\text{La,Lu}} = \frac{(\beta_{4,[\text{L29}_3]}^{\text{La,Lu,Lu,Lu}} + \beta_{4,[\text{L29}_3]}^{\text{Lu,La,Lu,Lu}})^2 (\beta_{4,[\text{L29}_3]}^{\text{La,La,Lu,Lu}} + \beta_{4,[\text{L29}_3]}^{\text{La,Lu,La,Lu}} + \beta_{4,[\text{L29}_3]}^{\text{La,Lu,Lu,La}} + \beta_{4,[\text{L29}_3]}^{\text{Lu,La,La,Lu}})^2}{(\beta_{4,[\text{L29}_3]}^{\text{La,La,La,La}})^3 (\beta_{4,[\text{L29}_3]}^{\text{Lu,Lu,Lu,Lu}})^3} \times \frac{(\beta_{4,[\text{L29}_3]}^{\text{La,La,La,Lu}} + \beta_{4,[\text{L29}_3]}^{\text{La,La,Lu,La}})^2}{1} \quad (65)$$

The minor variation of the absolute affinities of the two different sites for $R = \text{La}$ and $R = \text{Lu}$ ($f_{N_9}^{\text{La}} \neq f_{N_9}^{\text{Lu}}$ and $f_{N_6O_3}^{\text{La}} \neq f_{N_6O_3}^{\text{Lu}}$) is responsible for an increase in $K_{\text{exch,L29}}^{\text{La,Lu}}$ by a factor 2.8 from the statistics ($K_{\text{exch,L29}}^{\text{La,Lu}} = 10^{4.4}$), but the experimental values $K_{\text{exch,L29}}^{\text{La,Lu}} = 10^{8.5}$ can be only reproduced with the explicit consideration of intermetallic recognition $\Delta E_{1-2}^{\text{mix}} = \Delta E_{1-2}^{\text{La,Lu}} - (\Delta E_{1-2}^{\text{La,La}} + \Delta E_{1-2}^{\text{Lu,Lu}})/2 = -2.0$ kJ mol^{-1} favoring the formation of adjacent La/Lu pairs in the final helicates. It is difficult to assign an unambiguous origin to such small effects, but we notice that their existence relies on the connection of two adjacent polyaromatic N_9 sites in $[\text{La}_x\text{Lu}_{2-x}(\mathbf{L11})_3]^{6+}$ ($\Delta E_{1-2}^{\text{mix}} = 1.5$ kJ mol^{-1}) and in $[\text{La}_x\text{Lu}_{4-x}(\mathbf{L29})_3]^{12+}$ ($\Delta E_{1-2}^{\text{mix}} = -2$ kJ mol^{-1}) (Dalla Favera et al., 2007).

4.2 Nonaxial polytopic receptors: Statistical distributions and deviations

The heterobitopic C_s-symmetrical ligands **L30** and **L31** (Figure 48) have been designed for emphasizing the changes in absolute metal–ligand affinities *via* the formation of very different coordination sites in the binuclear heterometallic helicates HHH-$[(R^1)_x(R^2)_{2-x}(\mathbf{L30})_3]^{6+}$, HHT-$[(R^1)_x(R^2)_{2-x}(\mathbf{L30})_3]^{6+}$, HHH-$[(R^1)_x(R^2)_{2-x}(\mathbf{L31}\text{-H})_3]^{3+}$, and HHT-$[(R^1)_x(R^2)_{2-x}(\mathbf{L31}\text{-H})_3]^{3+}$ (André et al., 2002, 2004; Jensen et al., 2006, 2008). The existence of the facile HHH ↔ HHT isomerization process (Figure 69A) produces eight microspecies (Eqs. (66)–(73), Figure 69B)

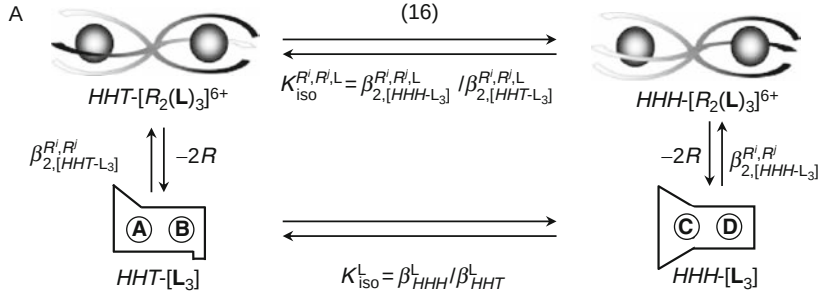

FIGURE 69 Continued

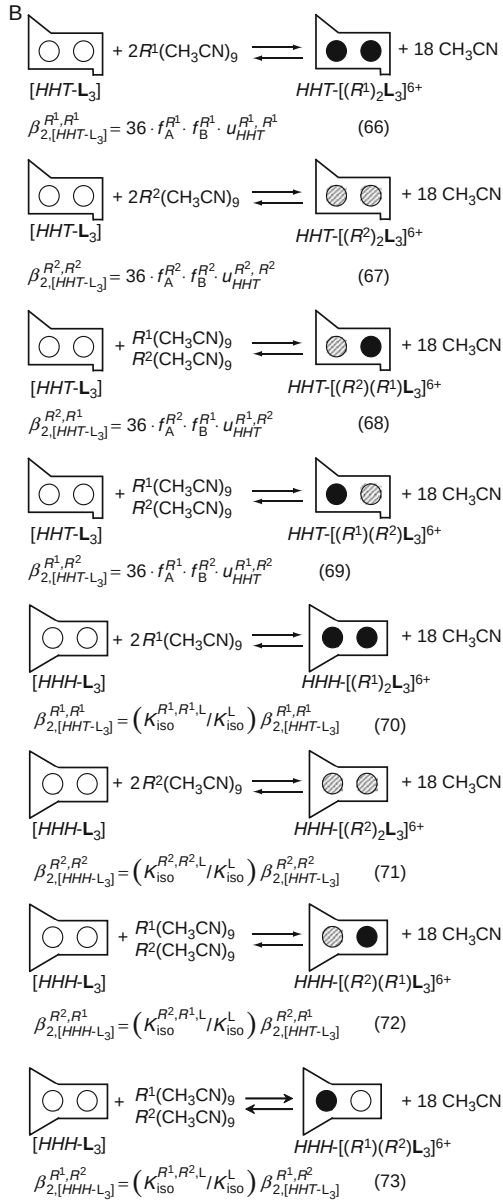

FIGURE 69 Thermodynamic modeling of the formation of the eight microspecies contributing to the binuclear triple-stranded helicates $[(R^1)_x(R^2)_{2-x}\mathbf{L}_3]^{6+}$ in acetonitrile (**L** is a nonaxial ligand). (A) HHT ↔ HHH isomerization process (Eq. (16)) and thermodynamic cycle and (B) complexation reactions. For the sake of simplicity, the unbound R^{III} cations are systematically considered as tricapped-trigonal prismatic nine-coordinate solvates.

contributing to the three macrospecies characterizing the exchange process of bimetallic binuclear helicates (equilibrium (53)).

The introduction of Eqs. (66)–(73) into Eq. (54) gives Eq. (74), which reduces to $K_{\text{exch,bi}}^{R^1,R^2} = 4$ if the absolute affinities ($f_{\text{A}}^{R^1} = f_{\text{A}}^{R^2}, f_{\text{B}}^{R^1} = f_{\text{B}}^{R^2}$), intermetallic interactions ($u_{\text{HHT}}^{R^1,R^1} = u_{\text{HHT}}^{R^1,R^2} = u_{\text{HHT}}^{R^2,R^2}$) and isomerization process ($K_{\text{iso}}^{R^1,R^1,\text{L}} = K_{\text{iso}}^{R^2,R^2,\text{L}} = K_{\text{iso}}^{R^1,R^2,\text{L}} = K_{\text{iso}}^{R^2,R^1,\text{L}}$) do not vary along the lanthanide series.

$$K_{\text{exch,bi}}^{R^1,R^2} = \frac{(\beta_{2,[\text{HHH}-\text{L}_3]}^{R^1,R^2} + \beta_{2,[\text{HHH}-\text{L}_3]}^{R^2,R^1} + \beta_{2,[\text{HHT}-\text{L}_3]}^{R^1,R^2} + \beta_{2,[\text{HHT}-\text{L}_3]}^{R^2,R^1})^2}{(\beta_{2,[\text{HHH}-\text{L}_3]}^{R^1,R^1} + \beta_{2,[\text{HHT}-\text{L}_3]}^{R^1,R^1})(\beta_{2,[\text{HHH}-\text{L}_3]}^{R^2,R^2} + \beta_{2,[\text{HHT}-\text{L}_3]}^{R^2,R^2})} \quad (74)$$

Although this complete derivation has not been previously published, it fully justifies the intuitive proposal of the formation of 50% of the bimetallic macrospecies $[(R^1)(R^2)\mathbf{L}_3]^{6+}$ for a stoichiometric ratio $[R^1]_{\text{tot}} : [R^2]_{\text{tot}} : [\text{L}]_{\text{tot}} = 1 : 1 : 3$ in absence of specific recognition of the metal ions (André et al., 2002). Interestingly, thorough studies of the distribution of the various macrospecies for different R^1/R^2 pairs with the ligands **L30**[a] (André et al., 2004), **L30**[b,c] (Jensen et al., 2006), and **L30**[d,e] (Jensen et al., 2008) show a systematic increase in the quantity of bimetallic complex upon increasing $\Delta r_{1,2}$, whereby $\Delta r_{1,2} = |r^{R^1} - r^{R^2}|$ is the difference in size between the two ionic radii of the lanthanides (Figure 70).

When we combine the latter trend with the observation of statistical distributions for all ligands, except **L30**[b], for $\Delta r_{1,2} \leq 2$ pm (Figure 70), we can tentatively assign a large part of the deviation from statistics to changes in the absolute affinities of the different sites along the lanthanide series. In the most favorable case, the bimetallic $[\text{LaLu}(\mathbf{L30}^{\mathbf{a}})_3]^{6+}$ complex accounts for 90% of the distribution of the microspecies. Moreover, NMR data and X-ray crystal structures unambiguously establish that the macrospecies HHH-$[(R^1)(R^2)(\mathbf{L30})_3]^{6+}$ with the smallest lanthanide occupying the N_6O_3 site largely dominates the distribution of this bimetallic macrospecies. Since $K_{\text{iso}}^{R^i,R^j,\text{L}}$ also affects $K_{\text{exch,bi}}^{R^1,R^2}$ (Eq. (74)), it is not so surprising that an experimental correlation has been evidenced between these two processes, which has been empirically expressed in Jensen et al. (2008) as the favored formation of bimetallic complexes ($K_{\text{exch,bi}}^{R^1,R^2} > 4$) for ligands showing a preference for HHH isomer ($K_{\text{iso}}^{R^i,R^j,\text{L}} > 1$).

4.3 Solid state and solution structures

In view of the minute values of the mixing energies $|\Delta E_{1-2}^{\text{mix}}| \leq 2.0$ kJ mol^{-1} associated with the recognition of the La/Lu pairs in triple-stranded helicates with the C_2-symmetrical ligands **L11**,

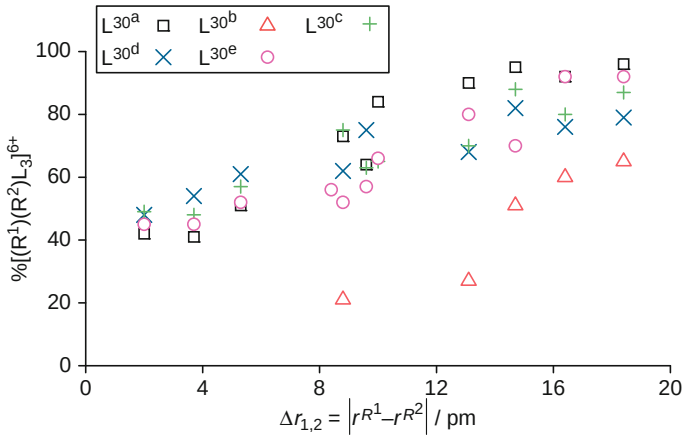

FIGURE 70 Percentage of bimetallic $[(R^1)(R^2)(\mathbf{L30})_3]^{6+}$ complexes in acetonitrile (adapted from Jensen et al., 2008).

L13, **L28**, and **L29**, the preparation of pure bimetallic complexes in solution almost entirely relies on the judicious tuning of the affinities of the various binding sites for given lanthanide ions, combined with entropic driving forces associated with the use of specific stoichiometric R^1:R^2:**L** ratios. The thermodynamic study of the formation of the homometallic trinuclear helicates with ligand **L28** indicates that the La/Eu pair is particularly favorable and 48% of the D_3-symmetrical $[EuLaEu(\mathbf{L28})_3]^{9+}$ microspecies is expected (shortly termed EuLaEu), and indeed observed in acetonitrile upon reaction of **L28** (10 mM) with La^{III} and Eu^{III} in a La:Eu:**L28** = 1:2:3 ratio (Floquet et al., 2004). EuEuEu (23%), LaLaEu (19%), LaEuEu (8%), and LaLaLa + LaEuLa (2%) complete the speciation in solution. Crystallization of this mixture produces X-ray quality crystals of empirical formulae $[La_{0.96}Eu_{2.04}(\mathbf{L28})_3](CF_3SO_3)_9$ and whose molecular structure of the cationic triple-stranded helicate is almost superimposable with that of $[Eu_3(\mathbf{L28})_3]^{9+}$, except for a significant expansion of the *R*–N bonds in the central N_9 coordination site (Figure 71, Floquet et al., 2004).

Refinements of the diffraction data with adjustable population parameters show that the terminal N_6O_3 sites contain 90% of Eu^{III} and 10% of La^{III}, while the central N_9 site accommodates 74% of La^{III} and 26% of Eu^{III}. Further high-resolution emission spectra using Eu^{III} as a probe (see next section) demonstrate that these global population parameters indeed correspond to the cocrystallization of EuLaEu (54%), LaLaEu (20%) and EuEuEu (26%), a distribution in the solid state which closely matches the speciation found in the original solution. Finally, paramagnetic ^1H NMR data collected for EuLaEu, YbLaYb, LuNdLu, and LuEuLu confirm the formation of D_3-symmetrical triple-stranded helicates in solution,

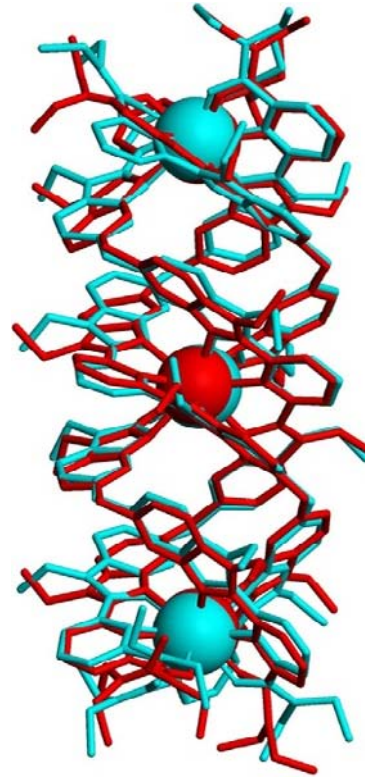

FIGURE 71 Optimized superimposition of the molecular structures of $[EuLaEu(\mathbf{L28})_3]^{9+}$ and $[Eu_3(\mathbf{L28})_3]^{9+}$ viewed perpendicular to the *pseudo*-C_3-axis (adapted from Floquet et al., 2004).

for which the crystal structure of $[Eu_3(\mathbf{L28})_3]^{9+}$ is a satisfying model. The same approach for the tetranuclear bimetallic helicates $[La_xLu_{4-x}(\mathbf{L29})_3]^{12+}$ (shortly termed La_xLu_{4-x}) leads to a more complicated speciation with considerable spectral overlap because of the coexistence of 10 microspecies possessing either C_3- or D_3-symmetry (Figure 68, Dalla Favera et al., 2007). The analysis of the intricate ^{1}H-NMR data requires multilinear least-squares techniques in order to assign clearly identified signals to each microspecies (Figure 72A), which eventually allows a direct access to experimental speciation in solution (Figure 72B).

A nonlinear least-squares fit of the experimental speciation eventually gives the micro- and macroscopic formation constants collected in Figure 73 (Dalla Favera et al., 2007).

The parallel global fit of binuclear (**L11**, **L13**), trinuclear (**L28**), and tetranuclear (**L29**) symmetrical helicates demonstrates that $f^{R^i}_{N_9} \approx f^{R^i}_{N_6O_3}$,

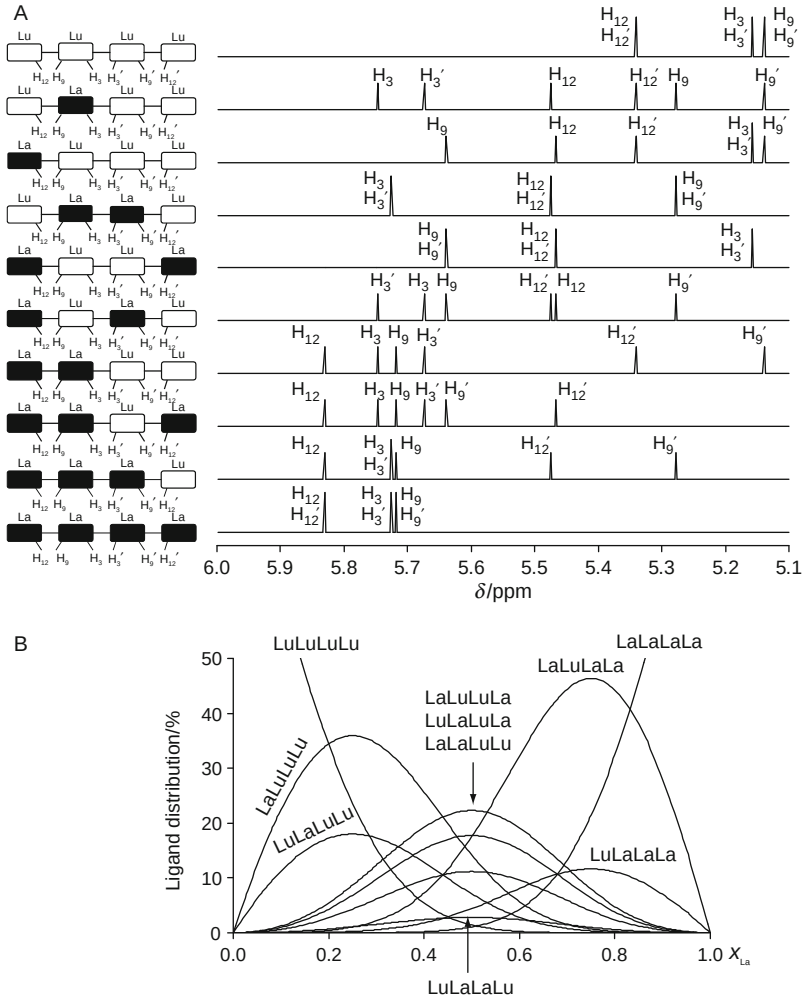

FIGURE 72 (A) Fitted individual ^{1}H NMR spectra of the 10 microspecies $[La_xLu_{4-x}(\mathbf{L29})_3]^{12+}$ in the 5–6 ppm range ($x = 0$–4) and (B) ligand distributions in the microspecies $[La_xLu_{4-x}(\mathbf{L29})_3]^{12+}$ observed during the titration of **L29** with La^{III} and Lu^{III} ($x = 0$–4, total ligand concentration $= 10^{-2}$ M, total metal concentration $= 1.33 \times 10^{-2}$M, lanthanum mole fractions $x_{La} = [La]/([La]+[Lu]) = 0$–1 (adapted from Dalla Favera et al., 2007).

which limits deviation from statistics to $\Delta E_{1-2}^{mix} = -2$ kJ mol^{-1}. In these conditions, no attempt has been made to isolate pure bimetallic tetranuclear helicates because of insufficient selectivity. Surprisingly, basically the same adjacent N_9 and N_6O_3 coordination sites produced by the wrapping of three C_s-symmetrical ligand **L30** in HHH-$[R_2(\mathbf{L30})_3]^{6+}$

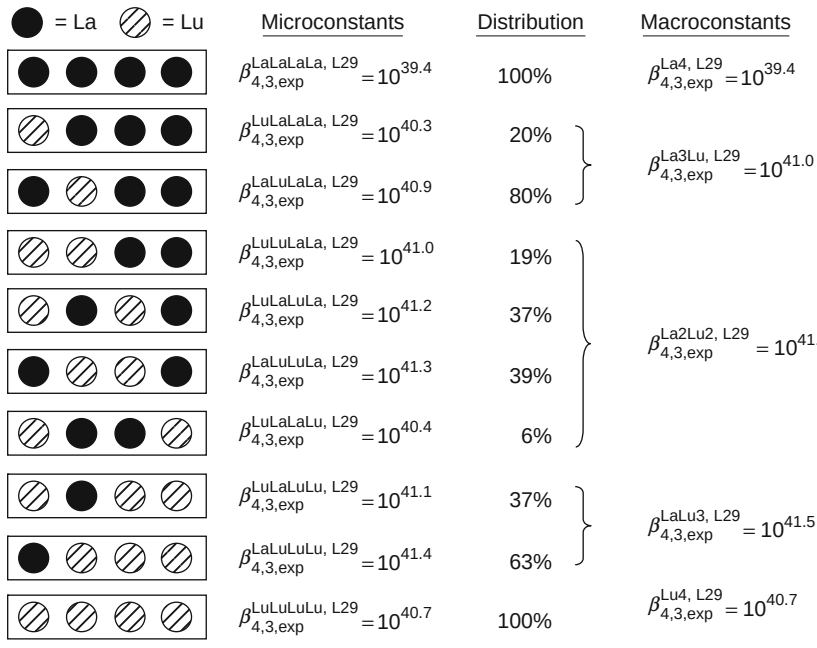

FIGURE 73 Thermodynamic macro- and microconstants characterizing the formation of the bimetallic complexes $[La_xLu_{4-x}(\mathbf{L29})_3]^{12+}$ (adapted from Dalla Favera et al., 2007).

produces more encouraging selectivity. According to ^{1}H-NMR data in acetonitrile solution, the bimetallic $[(R^1)(R^2)(\mathbf{L30^a})_3]^{6+}$ complexes exist mainly as the HHH-isomer with the smaller lanthanide located in the N_6O_3 site (André et al., 2004). X-ray diffraction measurements performed on crystals of $[(R^1)(R^2)(\mathbf{L30^a})_3]^{6+}$ (R^1R^2 = LaTb, LaEu, PrEr, PrLu; André et al., 2004) and $[(R^1)(R^2)(\mathbf{L30^c})_3]^{6+}$ (R^1R^2 = PrLu, NdLu; Jensen et al., 2006) isolated from thermodynamic mixtures indeed confirm the solution structures (Figure 74).

However, the limited quality of the refinement of the X-ray data suggests that some minor scrambling probably occurred, but its quantification within different microspecies is beyond the precision of the method (André et al., 2004). Though no complete thermodynamic analysis is available for helicates with nonaxial ligands, examination of the mathematical form of $K^{R^1,R^2}_{exch,bi}$ (Eq. (74)) implies that a strong selectivity for lanthanide pairs only results when $f^{R^i}_{N_9} \neq f^{R^i}_{N_6O_3}$, which also induces a strong dependency on $K^{R^i,R^j,L30}_{iso}$ (Eq. (16)). We are thus tempted to conclude that the absolute affinities of each adjacent N_9 and N_6O_3 site in C_3-symmetrical HHH-$[R_2(\mathbf{L30})_3]^{6+}$ display a more pronounced dependence on the lanthanide size than their similar counterpart in more symmetrical D_3-symmetrical helicates $[R_2(\mathbf{L11})_3]^{6+}$ or $[R_2(\mathbf{L13})_3]^{6+}$.

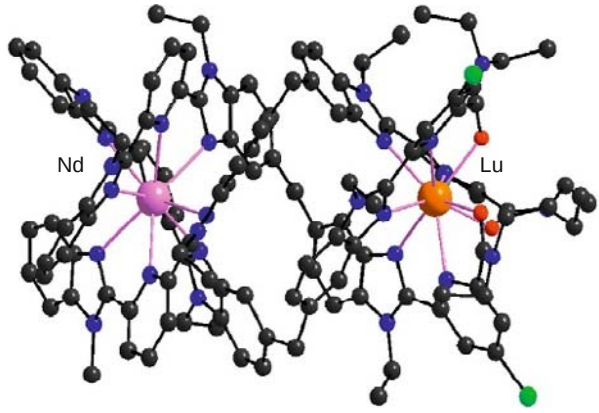

FIGURE 74 Molecular structure of $[NdLu(\mathbf{L30^c})_3]^{6+}$ (reproduced by permission from Jensen et al., 2006, © American Chemical Society, 2006).

4.4 Photophysical properties

The isolation of a heterometallic R^1/R^2 pair in a triple-stranded helicate brings novel photophysical properties, because $R^1 \rightarrow R^2$ energy transfers (or reverse $R^2 \rightarrow R^1$ depending on the relative energies of the donor and acceptor levels) may affect the energy migration processes in the complex and the final emission output (Figure 75).

Let us focus on the photophysical intermetallic communication $k^{et}_{R^1,R^2}$ resulting from intramolecular 4f → 4f energy transfer and whose global efficiency is given in Eq. (75).

$$\eta^{et}_{R^1,R^2} = \frac{k^{et}_{R^1,R^2}}{(k^{nr}_{R^1} + k^{r}_{R^1}) + k^{et}_{R^1,R^2}} \tag{75}$$

Assuming that (i) $k^{obs}_{R^1} = k^{nr}_{R^1} + k^{r}_{R^1} = (\tau^{obs}_{R^1,R^1})^{-1}$ is identical in the homometallic $[(R^1)_2\mathbf{L}_3]^{6+}$ and in the bimetallic $[(R^1)(R^2)\mathbf{L}_3]^{6+}$ complexes and (ii) the $R^1 \rightarrow R^2$ energy transfer is the only source of additional deactivation of the R^1 donor level, the rate transfer constant $k^{et}_{R^1,R^2}$ can be easily deduced from the measurement of the excited state lifetime $(\tau^{obs}_{R^1,R^2})^{-1} = k^{et}_{R^1,R^2} + k^{obs}_{R^1}$ of R^1 in the bimetallic complex $[(R^1)(R^2)\mathbf{L}_3]^{6+}$ (Eq. (76)).

$$k^{et}_{R^1,R^2} = (\tau^{obs}_{R^1,R^2})^{-1} - (\tau^{obs}_{R^1,R^1})^{-1} \tag{76}$$

Obviously, the intermetallic energy transfer rate $k^{et}_{R^1,R^2}$ obeys *Fermi*'s golden rule (Eq. (7)). The large intermetallic distances in bimetallic lanthanide helicates (≥9 Å) combined with the minute expansion of

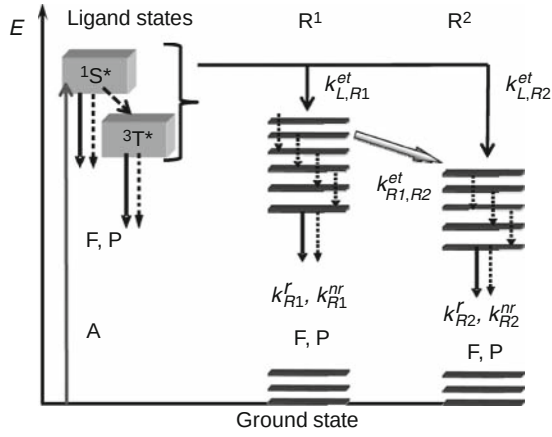

FIGURE 75 Schematic representation of energy absorption, emission, and dissipation processes in a bimetallic (R^1, R^2) lanthanide complex. F, fluorescence; P, phosphorescence; et, energy transfer; r, radiative; nr, nonradiative.

4f-orbitals justify the preponderance of an electrostatic multipolar mechanism limited to the dipole–dipolar interaction, namely *Förster's* mechanism described in Eq. (77), where R^{R^1,R^2} is the separation between the two oscillating dipoles, which is assumed to be the intermetallic distance for $4f \rightarrow 4f$ energy transfer, and $R_0^{R^1,R^2}$ is the contact distance for 50% energy transfer (Bünzli, 1989).

$$\eta^{et}_{R^1,R^2} = \frac{k^{et}_{R^1,R^2}}{(k^{nr}_{R^1} + k^{r}_{R^1}) + k^{et}_{R^1,R^2}} = 1 - \frac{\tau^{obs}_{R^1,R^2}}{\tau^{obs}_{R^1,R^1}} = \frac{1}{1 + (R^{R^1,R^2}/R_0^{R^1,R^2})^6} \qquad (77)$$

This approach has been applied to solid-state mixtures of $[Eu_2(\mathbf{L11})_3]^{6+}$, $[TbEu(\mathbf{L11})_3]^{6+}$, and $[Tb_2(\mathbf{L11})_3]^{6+}$ (Figure 12A), in which Tb^{III} acts as the donor ($R^{Tb,Eu} = 9$ Å, Piguet et al., 1993b). The $Tb(^5D_4)$ luminescence decay is indeed biexponential with one long lifetime corresponding to the emission of $[Tb_2(\mathbf{L11})_3]^{6+}$ ($\tau^{obs}_{Tb,Tb} = 0.66$ ms) and one short lifetime ($\tau^{obs}_{Tb,Eu} = 0.16$ ms) associated with $[TbEu(\mathbf{L11})_3]^{6+}$, in which $Tb \rightarrow Eu$ energy transfer occurs. Concomitantly, the intensity of the Tb emission decreases sharply while the photophysical properties of the Eu emission (spectrum and lifetime) are the same as in the homometallic Eu_2 helicate. Application of Eqs. (76) and (77) gives $k^{et}_{Tb\rightarrow Eu} = 4.7 \times 10^3\ s^{-1}$, $\eta^{et}_{Tb\rightarrow Eu} = 76\%$, and $R_0^{Tb,Eu} = 10.7$ Å at 77 K (Piguet et al., 1993b). Alternatively, the intermetallic distance R^{R^1,R^2} in a structurally noncharacterized helicate can be estimated from lifetime measurements and Eq. (77),

assuming that a theoretical value of $R_0^{R^1,R^2}$ can be obtained with Eq. (78) (Bünzli, 1989), in which κ^2 is an orientation factor having an isotropic limit of 2/3, Q_F is the quantum yield of the donor luminescence in absence of acceptor (i.e., the R^1 quantum yield measured in $[(R^1)_2\mathbf{L}_3]^{6+}$), n is the refractive index of the intermetallic medium and J is the overlap integral between the emission spectrum of the donor (R^1) and the absorption spectrum of the acceptor (R^2) in $cm^6\,mol^{-1}$.

$$(R_0^{R^1,R^2})^6 = 8.75 \times 10^{-25}\kappa^2 Q_F n^{-4} J \quad [cm^6] \tag{78}$$

Following this procedure, Lessmann and Horrocks (2000) computed $R_0^{Eu,Nd} = 9.9$ Å in [EuNd(**L32**)$_3$] which, combined with the determination of the Eu($^5D_0$) lifetimes, gave $R^{Eu,Nd} = 13.2$ Å and 7.4 Å in [EuNd(**L32^a**] and [EuNd(**L32^b**)$_3$], respectively (Figure 49).

When the triple-stranded helicate contains different adjacent sites as in $[R_2(\mathbf{L30})_3]^{6+}$ (Figure 48) or $[R_3(\mathbf{L28})_3]^{9+}$ (Figure 67), intermetallic energy transfers can be already detected in the homometallic complexes because the excited state of the same metal in different environments is slightly different. This is demonstrated in HHH-$[Eu_2(\mathbf{L30^a})_3]^{6+}$ (André et al., 2004) and $[Eu_3(\mathbf{L28})_3]^{9+}$ (Floquet et al., 2003), for which the only Eu^{III}-centered emission detected at room temperature arises from the EuN_6O_3 sites. At 10 K, a dual emission from both EuN_9 and EuN_6O_3 is observed because both the intramolecular intermetallic $EuN_9 \rightarrow EuN_6O_3$ energy migration and the temperature-assisted back transfer to the low-lying MLCT state become less efficient. Finally, the combination of Eu^{III} as a luminescent probe with closed-shell La^{III} and Lu^{III} has been exploited for structurally and electronically characterizing the different emission sites in [EuLa(**L30^a**)$_3$]$^{6+}$ (André et al., 2004) and in [EuLaEu(**L28**)$_3$]$^{9+}$ (Floquet et al., 2004). The latter is a nice example of the analytical power of the unsplit $^5D_0 \rightarrow {}^7F_0$ transition. The spectrum of the homotrimetallic EuEuEu helicate displays two components arising from the terminal and central sites (Figure 76); the central site has a smaller quantum yield due to the N_9 coordination environment. The proportion of the integrated emission intensity of the central site (obtained after decomposition of the band with Gaussian functions) is $F_c/(F_c + F_t) = 0.27$, from which the ratio of the quantum yields can be extracted, $Q_c/Q_t = 0.74$. Taking this value into consideration, as well as the experimental $F_c/(F_c + F_t)$ ratio of 0.094 for the heterotrimetallic species EuLaEu, and a suitable model inspired from NMR data which show that the LaLaEu species accounts for about 20% in solution, the following composition of the microcrystals can be extracted: EuLaEu (54%), LaLaEu (20%), and EuEuEu (26%), in excellent agreement with elemental analysis and X-ray data. That is the microcrystal composition reflects fairly closely the speciation obtained in solution.

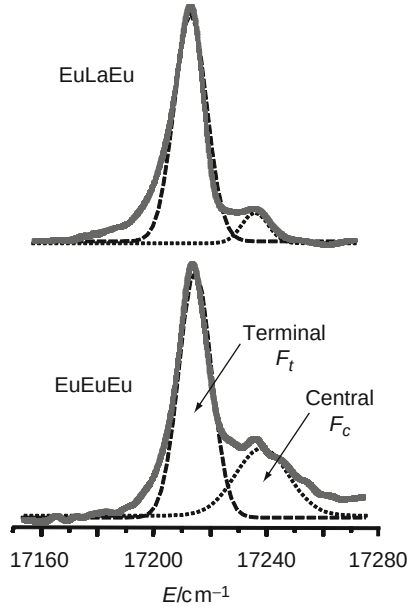

FIGURE 76 $^5D_0 \rightarrow {}^7F_0$ transitions of the hetero- (top) and homometallic (bottom) helicates with **L28** and their decomposition into Gaussian functions (redrawn after Floquet et al., 2004).

5. MODELING THE THERMODYNAMIC STABILITY OF HELICATES

In both living (Mammen et al., 1998) and inert (Huck et al., 2000; Thalladi et al., 2002) macroscopic systems, the multicomponent assembly of basic subunits plays a crucial role for the design of sophisticated organizations and functions. Replication of this approach at the molecular level is at the origin of supramolecular chemistry (Lehn, 1988), an aspect of chemistry which focuses on the combination of molecular building blocks (i.e., ligands and metal ions in coordination chemistry) to give complex nanoscopic architectures (Balzani et al., 2002, 2008; Lehn, 1995, 2007; Stoddart and Philp, 1996). The mechanical processes operating at the macroscopic level are controlled by enthalpic changes, which are much more intuitive than the cohesion of molecular units implying both enthalpic and entropic contributions. This statement can be illustrated if we consider a single macroscopic object that can be thrown from a distance and so be randomly distributed between two boxes, one twice the size of the other. The entropic contribution is simply given by Boltzmann relationship $\Delta S = k \ln (2/1) = 10^{-23}\,\mathrm{J\,K^{-1}}$, which translates into a negligible contribution to the total energy at room temperature ($\Delta E = -T\Delta S = -2.9 \times 10^{-21}\,\mathrm{J}$), which is

not necessary to take into account for further energetic calculations with this system. At the molecular level, the huge amount of particles contained in an acceptable macroscopic quantity such as one mole ($N_A = 6.02 \times 10^{23}$ molecules mol^{-1}) produces an entropic contribution of $\Delta S = k\ln(2^{N_{Av}}) = R\ln(2) = 5.8\ \ J\,K^{-1}$, which gives $\Delta E = -T\Delta S = -1.73$ kJ mol^{-1} at room temperature; a substantial and far from negligible contribution (Smith, 2004). Consequently, the rationalization of multicomponent helicate self-assembly requires an adequate modeling of the total free energy changes $\Delta G = \Delta H - T\Delta S$ occurring in solution. Since the number of independent components is only two for homometallic helicates (the metal M and the ligand L) or three for bimetallic helicates (two metals M^1, M^2, and a ligand L), these molecular edifices can serve as simple basic systems for the development of new thermodynamic tools in coordination and metallosupramolecular chemistry (Elhabiri and Albrecht-Gary, 2008; Elhabiri et al., 2004a; Fatin-Rouge et al., 2001; Hamacek et al., 2003, 2006; Pfeil and Lehn, 1992; Piguet et al., 2005).

5.1 Theoretical model for intermolecular connections: The site-binding model

The successive intermolecular connections of metal ions to a single multisite receptor represents the prototype of basic complexation processes. Its thermodynamic modeling is firmly established since the beginning of the twentieth century (Hill, 1910) and is often referred to as the protein–ligand model because of its widespread use in biology and biochemistry (Ben-Naim, 1998; Perlmutter-Hayman, 1986; van Holde, 1985). This additive free energy model has been recently formulated by introducing statistical mechanics in the site-binding model for the successive fixations of protons onto polyelectrolytes (Koper and Borkovec, 2001), and further extended for unraveling the fixation of metal ions onto a single ligand strand (Borkovec et al., 2004). Let us focus on the most simple case of the successive intermolecular connection of m trivalent lanthanide ions R to a preorganized receptor **L** possessing m binding sites (equilibrium (79), Figure 77).

$$\mathbf{L} + mR^{3+} \rightleftharpoons [R_m\mathbf{L}]^{3m+} \quad \beta_{m,1}^{R,L} \tag{79}$$

The total free energy change associated with equilibrium (79) is given by the sum of the individual free energies of connection of R to the different binding sites $\Delta G^0_{conn.,tot} = -RT\sum_{i=1}^{m}\ln(f_i^R)$ modulated by the sum of the intramolecular intermetallic interactions given by

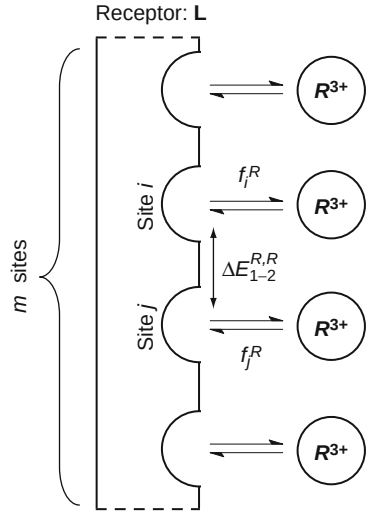

FIGURE 77 Thermodynamic protein–ligand model adapted for the successive intermolecular connections of metal ions to a one-dimensional multisite receptor (adapted from Piguet et al., 2005). f_i^R is the absolute affinity of site *i* for the entering lanthanide *R*, and $\Delta E_{1-2}^{R,R}$ is the intramolecular intermetallic interaction between two nearest neighbors.

$\Delta G_{\text{tot}}^{R,R} = \sum_{i<j} \Delta E_{1-2}^{R,R}$, if we restrict these interactions to the nearest neighbors (Eq. (80), Koper and Borkovec, 2001). Note that the notation of the last sum has been simplified; it should really be written as $\Delta G_{\text{tot}}^{R,R} = \sum_{i<j=2}^{i<j=m} \Delta E_{i-j}^{R_i,R_j}$; such simplified notation is used throughout in the following developments. However, depending on the symmetry of the reactants and products of the assembly process, several microspecies of the same energy contribute to the macrospecies, and this non-negligible entropic contribution is introduced as an additional statistical factor $\Delta G_{\text{stat}}^{R,\text{L}} = -RT\ln(\omega_{m,1}^{R,\text{L}})$ (Eq. (81), Benson, 1958, 1976).

$$\Delta G_{m,1}^{R,\text{L}} = -RT\ln(\beta_{m,1}^{R,\text{L}}) = -RT\ln(\omega_{m,1}^{R,\text{L}}) - RT\sum_{i=1}^{m}\ln(f_i^R) + \sum_{i<j}\Delta E_{1-2}^{R,R} \quad (80)$$

Since the formation constants are easily accessible in chemistry, the standard vant'Hoff isotherm transforms Eq. (80) into Eq. (81), whereby $u_{1-2}^{R,R} = \text{e}^{-\Delta E_{1-2}^{R,R}/RT}$ is often referred to as the Boltzmann factor of intermetallic interaction (Koper and Borkovec, 2001).

$$\beta_{m,1}^{R,\mathrm{L}} = \omega_{m,1}^{R,\mathrm{L}} \prod_{i=1}^{m} f_i^R \prod_{i<j} \mathrm{e}^{-\Delta E_{1-2}^{R,R}/RT} = \omega_{m,1}^{R,\mathrm{L}} \prod_{i=1}^{m} f_i^R \prod_{i<j} u_{1-2}^{R,R} \tag{81}$$

Surprisingly, one of the major difficulties encountered when applying this model in coordination chemistry is connected with the calculation of reliable statistical factors. Two parallel methods have been developed by using either the symmetry numbers of the molecules or the direct count of the microspecies formed in the reactants and products (Ercolani et al., 2007). Both techniques converge to the same result, but the symmetry number method, though less intuitive, is easier to handle and we will limit our discussion to this technique. According to Benson (1976), the symmetry number σ of a molecule affects its rotational entropy by a factor $-R\ln(\sigma)$. Consequently, the statistical contribution to the stability constant $\beta_{m,1}^{R,\mathrm{L}}$ of equilibrium (79) is given by the ratio of the symmetry numbers of the reactants and products (Eq. (82)).

$$\omega_{m,1}^{R,\mathrm{L}} = \frac{(\sigma^R)^m \cdot \sigma^{\mathrm{L}}}{\sigma^{R_m\mathrm{L}}} \tag{82}$$

Each factor σ is itself the product of the external (σ_{ext}) and internal (σ_{int}) symmetry numbers. The external symmetry number corresponds to the number of different but indistinguishable atomic arrangements that can be obtained by rotating a given molecule as a whole. It thus only considers symmetry operations of the first kind (that is not involving an inversion center or a symmetry plane) and it is found in practice by multiplying the order of the *independent* simple rotation axes of the point group to which the molecule belongs (axes of infinite orders are not considered because they do not generate different atomic arrangements). For instance, the tricapped-trigonal prismatic solvate $[R(CH_3CN)_9]^{3+}$ of D_{3h}-symmetry contains two types of *independent* rotational axes of the first kind: one twofold axis and one threefold axis, thus leading to $\sigma_{\mathrm{ext}} = 2 \times 3 = 6$ (Table 11).

The internal symmetry number σ_{int} is similarly defined as the number of different but indistinguishable atomic arrangements that can be obtained by internal rotation about single bonds. The contribution of σ_{int} in a self-assembly process is nonzero only when internal rotations of the components are either blocked or released during the chemical transformation. The most straightforward application of the site-binding model (Eq. (81)) to lanthanide assembly concerns the successive fixation of Eu^{III} to $[\mathbf{L13^f}]^{2-}$ in water (equilibria (83) and (84), Piguet et al., 2005), the experimental stability constants of which have been obtained by a combination of thermodynamic and kinetic studies (Elhabiri et al., 2004a).

TABLE 11 External symmetry numbers for various point groups (Ercolani et al., 2007)

Point group	σ_{ext}
C_1, C_i, C_s, $C_{\infty v}$, R_3	1
$D_{\infty h}$	2
C_n, C_{nv}, C_{nh}	n
D_n, D_{nd}, D_{nh}	$2n$
S_n (n even)	$n/2$
T_d	12
O_h	24
I_h	60

$$[\mathbf{L13^f}]^{2-} + Eu^{3+} \rightleftharpoons [Eu(\mathbf{L13^f})]^{+} \quad \beta_{1,1}^{Eu,L13f} = 10^{4.28} \tag{83}$$

$$[\mathbf{L13^f}]^{2-} + 2Eu^{3+} \rightleftharpoons [Eu_2(\mathbf{L13^f})]^{4+} \quad \beta_{2,1}^{Eu,L13f} = 10^{6.36} \tag{84}$$

The modeling with Eq. (81) is trivial (Eqs. (85) and (86)) except for the calculation of the statistical factors. Originally, the trivalent europium atoms were considered as free cations with R_3 symmetry and $\omega_{1,1}^{Eu,L13f} = 2$ and $\omega_{2,1}^{Eu,L13f} = 1$ (Figure 78A). A fit of the model (Eqs. (85) and (86)) to the experimental data (Eqs. (83) and (84)) gave $\log(f_{N_2O}^{Eu}) = 3.98$ and $\Delta E_{1-2}^{Eu,Eu} = 9.1$ kJ mol^{-1} (Piguet et al., 2005).

$$\beta_{1,1}^{Eu,L13f} = \omega_{1,1}^{Eu,L13f} f_{N_2O}^{Eu} \tag{85}$$

$$\beta_{2,1}^{Eu,L13f} = \omega_{2,1}^{Eu,L13f} (f_{N_2O}^{Eu})^2 u_{1-2}^{Eu,Eu} \tag{86}$$

The first microscopic parameter $\Delta G_{connection}^{0} = -RT\ln(f_{N_2O}^{Eu}) = -22.7$ kJ mol^{-1} refers to the favorable free energy balance between the desolvation of the components and their binding in the complex to give one Eu-(**L13^f**) connection. $\Delta E_{1-2}^{Eu,Eu} > 0$ indicates a repulsive Eu. . .Eu interaction in $[Eu_2(\mathbf{L13^f})]^{4+}$ and thus the operation of an anticooperative process for the successive fixation of two Eu^{III} to $(\mathbf{L13^f})^{2-}$. Obviously, the explicit consideration of solvated cations $[Eu(H_2O)_9]^{3+}$ changes the statistical factors ($\omega_{1,1}^{Eu,L13f} = 12$ and $\omega_{2,1}^{Eu,L13f} = 36$, Figure 78B), which

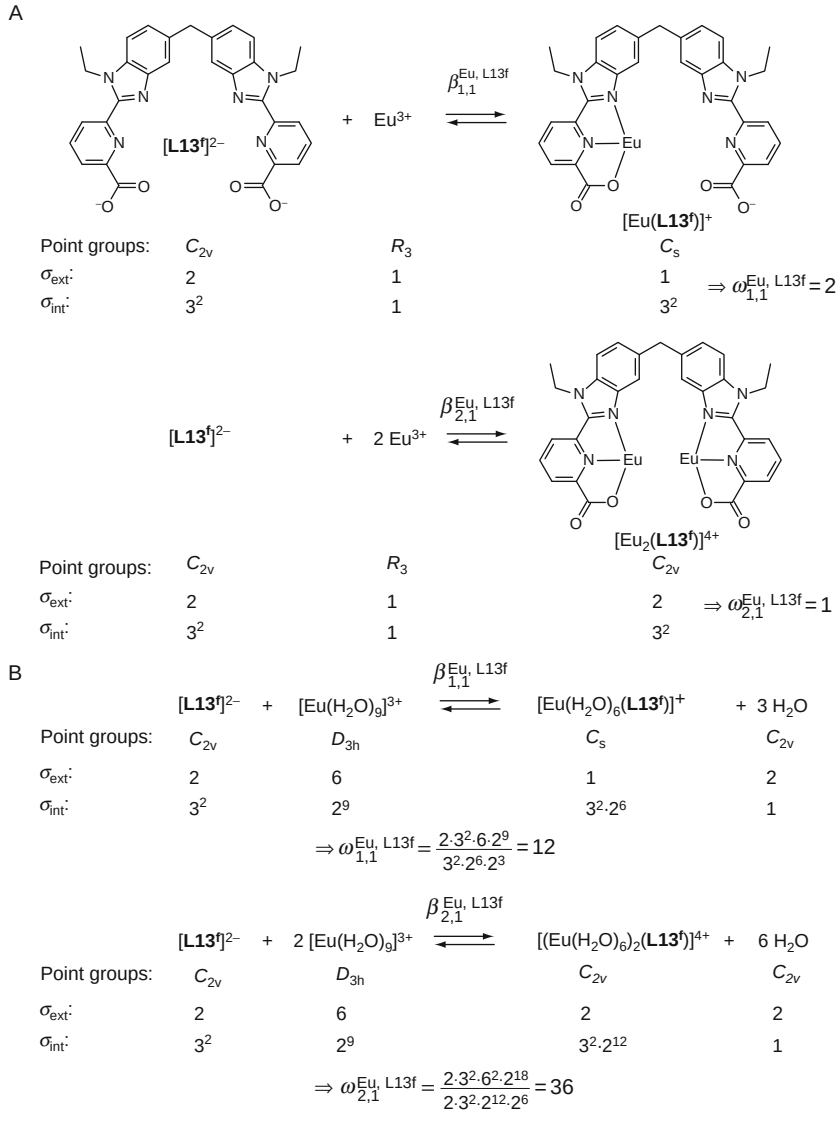

FIGURE 78 Calculation of statistical factors by using the method of the symmetry numbers for equilibrium (83) and (84). (A) The metal ions are considered as nonsolvated species and (B) the metal ions are considered as nine-coordinate tricapped-trigonal prismatic solvates.

consequently slightly affects the fitted R-ligand affinity $\log(f_{N_2O}^{Eu}) = 3.20$, but does not alter $\Delta E_{1-2}^{Eu,Eu} = 9.1$ kJ mol^{-1}.

To extend the use of the site-binding model for the assembly of lanthanide triple-stranded helicates, it is necessary to consider the three

wrapped strands as a virtual preorganized D_3-symmetrical molecular box, as exemplified for $[(\mathbf{L13^b})_3]$ in Figure 79. In these conditions, the global complexation process described by equilibrium (87) (path *i* in Figure 79A) can be partitioned into a first assembly process providing the virtual preorganized receptor $[(\mathbf{L13^b})_3]$ (equilibrium (88)) followed by purely intermolecular complexation of R^{III} (equilibrium (89), path *ii* in

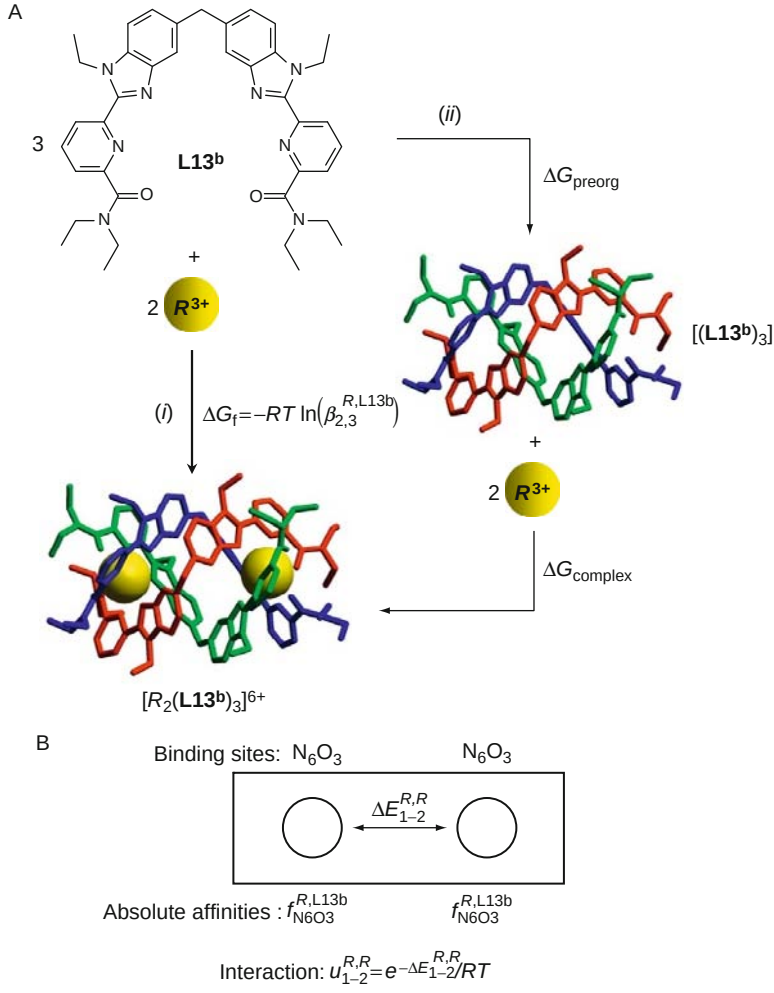

FIGURE 79 (A) Formation and solution structures of $[R_2(\mathbf{L13^b})_3]^{6+}$ showing the complete assembly process (ΔG_f, path *i*), and its partition into one virtual preorganization step (ΔG_{preorg}) followed by intermolecular complexation ($\Delta G_{complex}$, path *ii*). (B) Associated thermodynamic site-binding model.

Figure 79A), which can be easily modeled with the site-binding model (Eq. (81), Hamacek et al., 2006).

$$3\mathbf{L13^b} + 2R^{3+} \rightleftharpoons [R_2(\mathbf{L13^b})_3]^{6+} \quad \beta_{2,3}^{R,\mathrm{L13b}} \tag{87}$$

$$3\mathbf{L13^b} \rightleftharpoons (\mathbf{L13^b})_3 \quad e^{-\Delta G_{\mathrm{preog}}/RT} \tag{88}$$

.

$$[(\mathbf{L13^b})_3] + 2R^{3+} \rightleftharpoons [R_2(\mathbf{L13^b})_3]^{6+} \quad e^{-\Delta G_{\mathrm{complex}}/RT} \tag{89}$$

$\Delta G_{\mathrm{preorg}}$ is difficult to assess, but it similarly affects any complex of a given family derived from the same $[(\mathbf{L13^b})_3]$ box. In these conditions, $\Delta G_{\mathrm{preorg}}$ corresponds to a translation of the zero-level of the free energy of formation, and it can be arbitrarily set to $\Delta G_{\mathrm{preorg}} = 0$. Application of the site-binding model is then straightforward by using $[(\mathbf{L13^b})_3]$ as a preorganized D_3-symmetrical receptor containing two N_6O_3 binding sites characterized by absolute affinities $f_{N_6O_3}^R$, $\Delta E_{1-2}^{R,R}$ being the usual intramolecular intermetallic interaction (Figure 79B). The two experimental stability constants respecting these conditions (equilibria (90) and (91)) have thus been fitted to the model (Eqs. (92) and (93)) along the lanthanide series (Table 8) to give $\log(f_{N_6O_3}^R)$ and $\Delta E_{1-2}^{R,R}$ collected in Figure 80 (R^{3+} were considered as nonsolvated cations of R_3 symmetry, Zeckert et al., 2004).

$$[(\mathbf{L13^b})_3] + R^{3+} \rightleftharpoons [R(\mathbf{L13^b})_3]^{3+} \quad \beta_{1,3}^{R,\mathrm{L13b}} \tag{90}$$

$$[(\mathbf{L13^b})_3] + 2R^{3+} \rightleftharpoons [R_2(\mathbf{L13^b})_3]^{6+} \quad \beta_{2,3}^{R,\mathrm{L13b}} \tag{91}$$

$$\beta_{1,3}^{R,\mathrm{L13b}} = 2f_{N_6O_3}^R \tag{92}$$

$$\beta_{2,3}^{R,\mathrm{L13b}} = (f_{N_6O_3}^R)^2 u_{1-2}^{R,R} \tag{93}$$

The scattered data and highly correlated parameters are mathematically reliable, but physically meaningless because two microscopic parameters $f_{N_6O_3}^R$ and $\Delta E_{1-2}^{R,R}$ are fitted to experimental data (i.e., including uncertainties) *via* exactly two equations (Eqs. (92) and (93)). To overcome this limitation, equilibria (90) and (91) have been simultaneously considered for a pair of lanthanide R^1/R^2, thus leading to four equations for four parameters ($f_{N_6O_3}^{R^1}$, $f_{N_6O_3}^{R^2}$, $\Delta E_{1-2}^{R^1,R^1}$, and $\Delta E_{1-2}^{R^2,R^2}$), together with one additional equilibrium (94) corresponding to the formation of the bimetallic helicate modeled with Eq. (95).

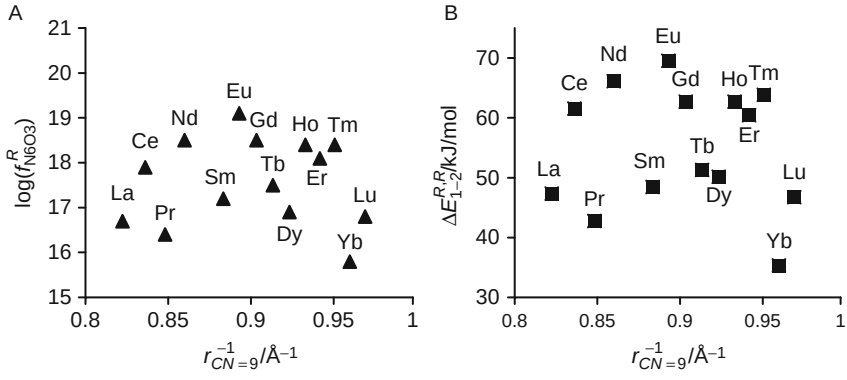

FIGURE 80 (A) Computed absolute affinities for the terminal sites ($\log(f^R_{N_6O_3})$) and (B) intermetallic interaction parameters ($\Delta E^{R,R}_{1-2}$) in the triple-stranded bimetallic helicates $[R_2(\mathbf{L13^b})_3]^{6+}$ as a function of the inverse of nine-coordinate ionic radii (fit of Eqs. (92) and (93)) (adapted from Zeckert et al., 2004).

$$[(\mathbf{L13^b})_3] + (R^1)^{3+} + (R^2)^{3+} \rightleftharpoons [(R^1)(R^2)(\mathbf{L13^b})_3]^{6+} \quad \beta^{R^1,R^2,\mathrm{L13b}}_{2,3} \tag{94}$$

$$\beta^{R^1,R^2,\mathrm{L13b}}_{2,3} = 2f^{R^1}_{N_6O_3} f^{R^2}_{N_6O_3} u^{R^1,R^2}_{1-2} \tag{95}$$

The demonstration that no intermetallic recognition occurs and that the mixing rule $\Delta E^{R^1,R^2}_{1-2} = 1/2(\Delta E^{R^1,R^1}_{1-2} + \Delta E^{R^2,R^2}_{1-2})$ is obeyed ($K^{R^1,R^2,\mathrm{L13b}}_{\mathrm{exch,bi}} = 4.0(3)$, Eq. (54), Section 4) for 11 R^1/R^2 pairs obtained from $R =$ La, Nd, Sm, Eu, Yb, Lu, and Y limits the number of microscopic parameters to four for a total of five experimentally accessible stability constants. Absolute affinities and intermetallic interactions can be then obtained with large, but physically meaningful uncertainties (Figure 81, Zeckert et al., 2004). The arbitrary value of $\Delta G_{\mathrm{preorg}} = 0$, which fixes the zero-point energy, prevents a physical interpretation of the absolute values of $\Delta G^0_{\mathrm{connection}} = -RT\ln(f^R_{N_6O_3})$ and $\Delta E^{R,R}_{1-2}$, but the relative trends along the series can be analyzed. According to Figure 81, we deduce that the N_6O_3 binding site is optimum for midrange R^{III} and that the intermetallic interaction is systematically repulsive (i.e., anticooperative) and roughly constant along the complete series (Zeckert et al., 2004). The same approach has been applied for the virtual preorganized receptor $[(\mathbf{L28})_3]$ in the self-assembly of the trinuclear helicates $[R_3(\mathbf{L28})_3]^{9+}$, which possess two different nine-coordinate N_9 and N_6O_3 binding sites (Figure 82, Floquet et al., 2003, 2004; Zeckert et al., 2004). Since two stability constants $\beta^{R,\mathrm{L28}}_{2,3}$ and $\beta^{R,\mathrm{L28}}_{3,3}$ for homometallic complexes, together with two macroscopic constants for the bimetallic macrospecies

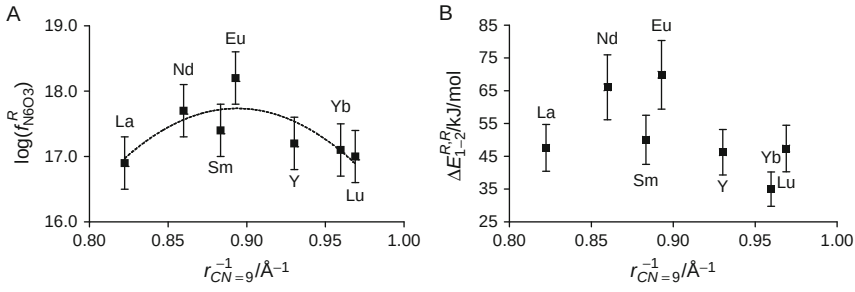

FIGURE 81 (A) Computed absolute affinities for the terminal sites ($\log(f^R_{N_6O_3})$) and (B) intermetallic interaction parameters ($\Delta E^{R,R}_{1-2}$) in the triple-stranded bimetallic helicates $[R_2(\mathbf{L13^b})_3]^{6+}$ as a function of the inverse of nine-coordinate ionic radii (fit of Eqs. (92), (93), and (95) for 11 R^1/R^2 pairs) (adapted from Zeckert et al., 2004).

$[(R^1)_2(R^2)(\mathbf{L28})_3]^{9+}$ and $[(R^1)(R^2)_2(\mathbf{L28})_3]^{9+}$ meet the conditions of their formation from the preorganized $[(\mathbf{L28})_3]$ box (Table 9), any R^1/R^2 pair provides six stability constants. This is, however, not sufficient for fitting a minimal set of six parameters ($f^{R^1}_{N_6O_3}$, $f^{R^2}_{N_6O_3}$, $f^{R^1}_{N_9}$, $f^{R^2}_{N_9}$, $\Delta E^{R^1,R^1}_{1-2}$, and $\Delta E^{R^2,R^2}_{1-2}$) even if we assume that (i) long-range intermetallic interactions are neglected ($\Delta E^{R,R}_{1-3} = 0$) and (ii) the mixing rule is obeyed ($\Delta E^{mix}_{1-2} = 0$, Eq. (63), Section 4). An attempt to overcome this limitation considers that (i) $\Delta G^{L13b}_{preorg} = \Delta G^{L28}_{preorg} = 0$ and (ii) the six adjustable microscopic parameters are identical for the two $[(\mathbf{L13^b})_3]$ and $[(\mathbf{L28})_3]$ preorganized boxes. Under these debatable hypotheses (particularly point i, Hamacek et al., 2006), a total of 11 experimental stability constants (5 for the binuclear and 6 for the trinuclear helicates) are then available for fitting the six parameters shown in Figure 82 (Zeckert et al., 2004).

Interestingly, the absolute affinities of the N_6O_3 and N_9 sites are comparable in magnitude, but with a slightly different trend along the lanthanide series (Figure 83). The short-range intermetallic interactions remain repulsive and roughly constant along the series. Whatever the quality of the hypotheses leading to this result, it is clear that the site-binding model has reached its limits for describing the assembly of polynuclear helicates and more fundamental thermodynamic concepts are required for avoiding the need of a virtual preorganized receptor, to which metal ions are attached through ''intermolecular'' bonds. It is, however, worth noting that the simple site-binding model is well-adapted for the rationalization of metal exchange processes occurring in heterometallic triple-stranded helicates (equilibria (53), (62), and (64)), because only saturated complexes participate to the equilibria, which automatically agrees with the consideration of pure intermolecular binding processes (see Section 4).

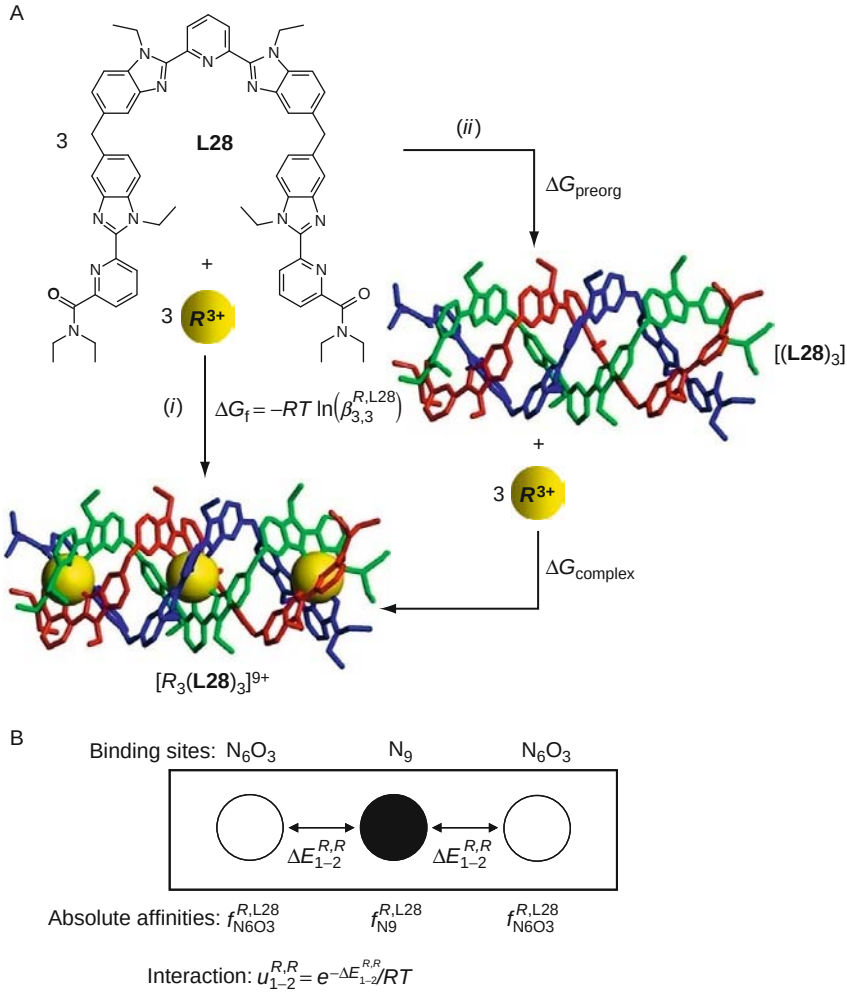

FIGURE 82 (A) Formation and solution structures of $[R_3(\mathbf{L28})_3]^{9+}$ showing the complete assembly process (ΔG_f, path *i*), and its partition into one virtual preorganization step (ΔG_{preorg}) followed by intermolecular complexation ($\Delta G_{complex}$, path *ii*). (B) Associated thermodynamic site-binding model.

5.2 Mixing intra- and intermolecular connections: The extended site-binding model

Let us consider the fixation of a bidentate ligand to a single metal as depicted in Figure 84. The first step simply corresponds to a standard intermolecular binding process modeled by a statistical factor and an absolute intermolecular affinity f_{site}^{M} according to the site-binding model

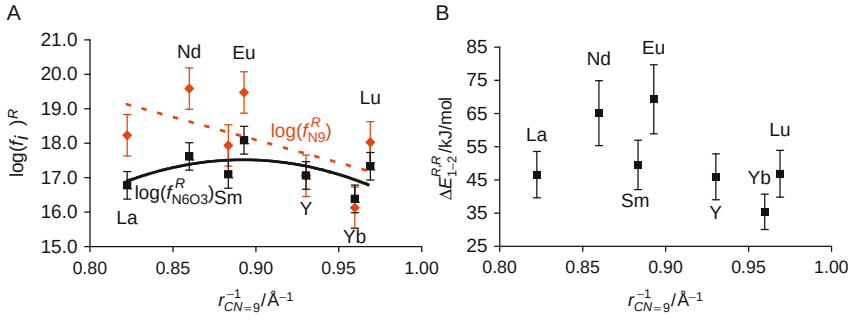

FIGURE 83 (A) Computed absolute affinities for the binding sites ($\log(f^R_{N_6O_3})$ in black and $\log(f^R_{N_9})$ in red) and (B) intermetallic interaction parameters ($\Delta E^{R,R}_{1-2}$) in the triple-stranded helicates $[R_2(\mathbf{L13^b})_3]^{6+}$ and $[R_3(\mathbf{L28})_3]^{9+}$ as a function of the inverse of nine-coordinate ionic radii (adapted from Zeckert et al., 2004).

(Eq. (81)). However, the second step is slightly different because the entering donor atom on the ligand is mechanically coupled to the first binding site, already bound to the metal ion. Both enthalpic and entropic contributions to the free energy of connection of the second site are modified and a global correction term, often referred to as the effective concentration c^{eff}, is used for correlating inter- and intramolecular processes (Eq. (96), Ercolani, 2006; Flory et al., 1976; Fyles and Tong, 2007; Gargano et al., 2001; Jacobson and Stockmayer, 1950; Jencks, 1981; Kuhn, 1934; Winnik, 1981; Figure 84).

$$-RT\ln(c^{\text{eff}}) = \Delta G^{\text{M,intra}}_{\text{connection}} - \Delta G^{\text{M,inter}}_{\text{connection}} = -RT\,\ln(f^{\text{M,intra}}_{\text{site}}) + RT\ln(f^{\text{M,inter}}_{\text{site}}) \tag{96}$$

Even if we consider that the chain of atoms connecting the two binding site of the ligand is long and flexible enough to produce no additional strain during the intramolecular connection ($\Delta H^{\text{M,intra}}_{\text{connection}} = \Delta H^{\text{M,inter}}_{\text{connection}}$), the entropic contribution of the two processes will be different because the degrees of freedoms of the second binding site of the ligand to reach an available coordination site on the metal is different from that of an independent ligand molecule. A theoretical approach based on the systematic Gaussian exploration of the available space by the free end of a flexible polymeric chain is available (Ercolani, 2006; Gargano et al., 2001; Kuhn, 1934). It indeed predicts that $c^{\text{eff}} \propto d^{-3/2}$, whereby d is the average length of the chain of atoms connecting the two binding sites of the ligand. We are now in a position to extend the site-binding model, which is limited to the assembly of $[R_m\mathbf{L}]^{3m+}$ edifices (Eq. (79)) possessing m

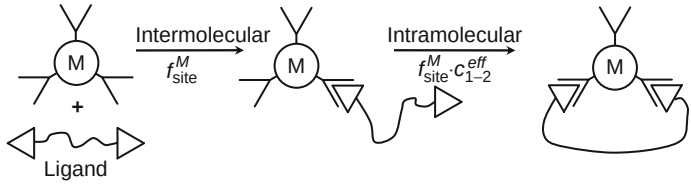

FIGURE 84 Intermolecular and intramolecular connection processes operating during complexation.

intermolecular bonds, toward the rationalization of the formation of $[R_m\mathbf{L}_n]^{3m+}$ complexes (Eq. (97)), in which the mn R-ligand bonds are partitioned between $m+n-1$ intermolecular and mn-$(m+n-1)$ intramolecular connections (Ercolani, 2003).

$$n\mathbf{L} + mR^{3+} \rightleftharpoons [R_m\mathbf{L}_n]^{3m+} \quad \beta^{R,\mathrm{L}}_{m,n} \tag{97}$$

The total free energy is given in Eq. (98) if we assume that metal–metal and ligand–ligand interactions do not contribute to the stability of the final helicate.

$$\begin{aligned}\Delta G^{R,\mathrm{L}}_{m,n} &= -RT\ln(\beta^{R,\mathrm{L}}_{m,n}) \\ &= -RT\ln(\omega^{R,\mathrm{L}}_{m,n}) - RT\sum_{i=1}^{m+n-1}\ln(f_i^R) - RT\sum_{i=1}^{mn-m-n+1}\ln(f_i^R c_i^{\mathrm{eff}})\end{aligned} \tag{98}$$

Regrouping the absolute intermolecular affinities followed by application of the standard vant'Hoff isotherm eventually leads to Eq. (99), which is known as Ercolani's model (Ercolani, 2003; Hamacek et al., 2006).

$$\beta^{R,\mathrm{L}}_{m,n} = \omega^{R,\mathrm{L}}_{m,n}\prod_{i=1}^{mn}(f_i^R)\prod_{i=1}^{mn-m-n+1}(c_i^{\mathrm{eff}}) \tag{99}$$

When both f_i^R and c_i^{eff} are constant for all inter- and intramolecular connections in $[R_m\mathbf{L}_n]^{3m+}$, the self-assembly is said to be statistical or noncooperative (Ercolani, 2003). The initial application of Eq. (99) for rationalizing the formation of Lehn's famous helicate $[Cu_3(\mathbf{L1})_2]^{3+}$ (Figure 3), indeed evidenced the occurrence of a noncooperative process (Ercolani, 2003), despite previous claims for positive cooperativity based on the erroneous neglect of the separation of intra- and intermolecular

binding processes (Fatin-Rouge et al., 2001; Garrett et al., 1992; Pfeil and Lehn, 1992). Any variation of c^{eff} is assigned to changes in preorganization occurring during the self-assembly process, while change of f_i^R refers to cooperativity, which can be either positive (f_i^R increases during the assembly process) or negative (f_i^R decreases during the assembly process). The ''sign'' (i.e., positive or negative) of cooperativity for pure intermolecular assemblies can be easily deduced from the construction of Langmuir isotherms (Hamacek et al., 2006) or from the more popular Scatchard or Hill plots (Perlmutter-Hayman, 1986), while a quantitative assessment of cooperativity requires the estimation of the homocomponent interactions $\Delta E^{R,R}$ ($n = 1$ in $[R_m\mathbf{L}]^{3m+}$) or $\Delta E^{\mathrm{L,L}}$ ($m = 1$ in $[R\mathbf{L}_n]^{3+}$) by using the site-binding model (Eq. (81)). When both inter- and intramolecular connections occur in $[R_m\mathbf{L}_n]^{3m+}$, partial Langmuir isotherms are required to graphically detect cooperativity in Hamacek plots (Hamacek and Piguet, 2006). A quantitative assessment now requires the simultaneous estimation of intermetallic and interligand interactions expressed as Boltzmann factors in Eq. (100), an equation referred to as the extended site-binding model (Hamacek et al., 2005a,b, 2006).

$$\begin{aligned}\beta_{m,n}^{R,\mathrm{L}} &= \omega_{m,n}^{R,\mathrm{L}} \prod_{i=1}^{mn} f_i^R \prod_{i=1}^{mn-m-n+1} c_i^{\text{eff}} \prod_{i<j} \mathrm{e}^{-\Delta E_{1-2}^{R,R}/RT} \prod_{k<l} \mathrm{e}^{-\Delta E_{1-2}^{L,L}/RT} \\ &= \omega_{m,n}^{R,\mathrm{L}} \prod_{i=1}^{mn} f_i^R \prod_{i=1}^{mn-m-n+1} c_i^{\text{eff}} \prod_{i<j} u_{1-2}^{R,R} \prod_{k<l} u_{1-2}^{L,L}\end{aligned} \tag{100}$$

Application of Eq. (100) to Lehn's helicate $[Cu_3(\mathbf{L1})_2]^{3+}$ and some of its analogues indeed demonstrates a modest negative cooperativity, which disfavors the successive fixation of ligands ($\Delta E_{1-2}^{\mathrm{L1,L1}} = 4(2)$ kJ mol^{-1}) and of metals ($\Delta E_{1-2}^{\mathrm{Cu,Cu}} = 5(3)$ kJ mol^{-1}) in solution (Hamacek et al., 2005b). However, these minute values fully agree with the prior conclusion of noncooperativity deduced from the use of Eq. (99) for a partial set of experimental data.

5.3 Modeling lanthanide helicate self-assembly in solution

Since the application of Eq. (100) may become complicated and tedious for assembly processes involving a considerable amount of microspecies (Dalla Favera et al., 2008), we first focus on the self-assembly of the well-studied binuclear helicate $[Eu_2(\mathbf{L13^f})_3]$, in which each macrospecies contains a single microspecies (Figure 58B, Elhabiri et al., 1999, 2004a). Figure 85 shows the complete set of five thermodynamic equilibria with

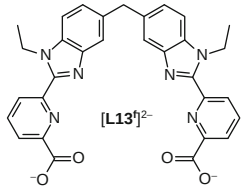

$$[\mathbf{L13^f}]^{2-} + [Eu(H_2O)_9]^{3+} \overset{\beta_{1,1}^{Eu,L13f} = 10^{4.3}}{\rightleftharpoons} [Eu(H_2O)_6(\mathbf{L13^f})]^{+} + 3\,H_2O \quad (83)$$

Point groups:	C_{2v}	D_{3h}	C_s	C_{2v}
σ_{ext} :	2	6	1	2
σ_{int} :	3^2	2^9	$3^2 \cdot 2^6$	1

$$\omega_{1,1}^{Eu,L13f} = 12 \Rightarrow \beta_{1,1}^{Eu,L13f} = 12 \cdot f_{N2O}^{Eu}$$

$$2\,[\mathbf{L13^f}]^{2-} + [Eu(H_2O)_9]^{3+} \overset{\beta_{2,1}^{Eu,L13f} = 10^{6.4}}{\rightleftharpoons} [Eu(H_2O)_6)_2(\mathbf{L13^f})]^{4+} + 6\,H_2O \quad (84)$$

Point groups:	C_{2v}	D_{3h}	C_{2v}	C_{2v}
σ_{ext} :	2	6	2	2
σ_{int} :	3^2	2^9	$3^2 \cdot 2^{12}$	1

$$\omega_{2,1}^{Eu,L13f} = 36 \Rightarrow \beta_{2,1}^{Eu,L13f} = 36 \cdot (f_{N2O}^{Eu})^2 \cdot u_{1-2}^{Eu,Eu}$$

$$2\,[\mathbf{L13^f}]^{2-} + [Eu(H_2O)_9]^{3+} \overset{\beta_{1,2}^{Eu,L13f} = 10^{9.3}}{\rightleftharpoons} [Eu(H_2O)_3(\mathbf{L13^f})_2]^{-} + 6\,H_2O \quad (101)$$

Point groups:	C_{2v}	D_{3h}	C_{2v}	C_{2v}
σ_{ext} :	2	6	2	2
σ_{int} :	3^2	2^9	$3^4 \cdot 2^3$	1

$$\omega_{1,2}^{Eu,L13f} = 12 \Rightarrow \beta_{1,2}^{Eu,L13f} = 12 \cdot (f_{N2O}^{Eu})^2 \cdot u_{1-2}^{L,L}$$

$$2\,[\mathbf{L13^f}]^{2-} + 2\,[Eu(H_2O)_9]^{3+} \overset{\beta_{2,2}^{Eu,L13f} = 10^{16.0}}{\rightleftharpoons} [Eu(H_2O)_3)_2(\mathbf{L13^f})_2]^{2+} + 12\,H_2O \quad (102)$$

Point groups:	C_{2v}	D_{3h}	C_{2h}	C_{2v}
σ_{ext} :	2	6	2	2
σ_{int} :	3^2	2^9	$3^4 \cdot 2^6$	1

$$\omega_{2,2}^{Eu,L13f} = 72 \Rightarrow \beta_{2,2}^{Eu,L13f} = 72 \cdot \left(f_{N2O}^{Eu}\right)^4 \cdot c_{1-2}^{eff} \cdot \left(u_{1-2}^{L,L}\right)^2 \cdot u_{1-2}^{Eu,Eu}$$

$$3\,[\mathbf{L13^f}]^{2-} + 2\,[Eu(H_2O)_9]^{3+} \overset{\beta_{2,3}^{Eu,L13f} = 10^{26.1}}{\rightleftharpoons} [Eu_2(\mathbf{L13^f})_3] + 18\,H_2O \quad (103)$$

Point groups:	C_{2v}	D_{3h}	D_3	C_{2v}
σ_{ext} :	2	6	6/2	2
σ_{int} :	3^2	2^9	3^6	1

$$\omega_{2,3}^{Eu,L13f} = 96 \Rightarrow \beta_{2,3}^{Eu,L13f} = 96 \cdot \left(f_{N2O}^{Eu}\right)^6 \cdot \left(c_{1-2}^{eff}\right)^2 \cdot \left(u_{1-2}^{L,L}\right)^6 \cdot u_{1-2}^{Eu,Eu}$$

FIGURE 85 Available thermodynamic data characterizing the self-assembly of $[Eu_2(\mathbf{L13^f})_3]$ in water (Elhabiri et al., 1999, 2004a). Each tridentate N_2O binding site is considered as a single point connector.

associated stability constants, statistical factors and extended site-binding equations, required for satisfying the multilinear least-squares fit of the four pertinent microscopic parameters collected in Table 12. The two initial complexation steps leading to $[Eu(\mathbf{L13^f})]^{+}$ (Eq. (83)) and $[Eu_2(\mathbf{L13^f})]^{4+}$ (Eq. (84)) strictly involve intermolecular connection processes and the extended site-binding model reduces here to the original site-binding model. The formation of $[Eu(\mathbf{L13^f})_2]^{-}$ (Eq. (101)) still corresponds to a pure intermolecular mechanism, but it introduces the interligand parameter $\Delta E^{L,L}_{1-2}$, which is assumed to operate when two binding units are coordinated to the same metal. The next complex $[Eu_2(\mathbf{L13^f})_2]^{2+}$ (Eq. (102)) involves the formation of the first metallomacrocycle resulting from an intramolecular binding event.

Finally the fixation of the third ligand to give $[Eu_2(\mathbf{L13^f})_3]$ further involves an intramolecular connection leading to a macrobicyclic complex (Eq. (103)). It is worth noting that $[Eu_2(\mathbf{L13^f})_3]$ is a chiral molecule (D_3 point group), which exists at equilibrium as a racemic mixture. Its symmetry number must be divided by two to account for the entropy of mixing of the two enantiomers (Figure 85, Ercolani et al., 2007).

Despite the large uncertainties induced by (i) the very limited number of available stability constants (five constants for fitting four microscopic parameters) and (ii) the use of kinetic data for estimating some thermodynamic constants, we conclude that the assembly of $[Eu_m(\mathbf{L13^f})_n]^{(3m-2n)+}$ complexes is characterized by a favorable connection of Eu^{III} to the N_2O site (including desolvation), a negligible preorganization, which does not significantly favor intramolecular connection processes, and two opposite contributions to the global cooperativity. The successive binding of ligands to the same metal ion is favorable ($\Delta E^{L,L}_{1-2} < 0$), while the successive filling of two adjacent N_2O sites with Eu^{III} is unfavorable ($\Delta E^{Eu,Eu}_{1-2} > 0$). To improve the quality and reliability of the fitting process, a larger number of experimental thermodynamic constants is required, while limiting the number of microscopic thermodynamic descriptors. This can be obtained with the combination of the thermodynamic data collected for the assemblies of a series of closely related helicates such as

TABLE 12 Fitted thermodynamic parameters for the formation of $[Eu_m(\mathbf{L13^f})_n]^{(3m-2n)+}$ complexes in water at 298 K and pH 6.15 (Hamacek et al., 2005b)

Parameters		Free energies		kJ mol^{-1}
$\log(f^{Eu}_{N_2O})$	3.7(4)	$\Rightarrow$	$\Delta G^{Eu,L13f}_{connection}$	−21(2)
$\log(c^{eff}_{1-2})$	0.3(1.5)	$\Rightarrow$	$\Delta G^{intra}_{correction}$	−2(8)
$\log(u^{L,L}_{1-2})$	0.7(7)	$\Rightarrow$	$\Delta E^{L,L}_{1-2}$	−4(3)
$\log(u^{Eu,Eu}_{1-2})$	−2.4(1.0)	$\Rightarrow$	$\Delta E^{Eu,Eu}_{1-2}$	14(6)

$[Eu_m(\mathbf{L11})_n]^{3m+}$, $[Eu_m(\mathbf{L13^b})_n]^{3m+}$, $[Eu_m(\mathbf{L28})_n]^{3m+}$, and $[Eu_m(\mathbf{L29})_n]^{3m+}$ (Tables 8 and 9). Assuming the following reasonable simplifications:

(1) $f^R_{N_2O}$, $f^R_{N_3}$, $u^{L,L}_{1-2}$, and $u^{R,R}_{1-2}$ are identical in all microspecies.
(2) $\Delta E^{R,R}_{1-n} \propto d^{-1}$ in agreement with Coulomb's law, which allows the estimation of long-range intermetallic interactions $\Delta E^{R,R}_{1-3} = \Delta E^{R,R}_{1-2}/2$ and $\Delta E^{R,R}_{1-4} = \Delta E^{R,R}_{1-2}/3$ in linear helicates (d is the intermetallic distance).
(3) $c^{eff}_{1-n} \propto d^{-3/2}$ in agreement with Kuhn's theory for nonconstrained polymers (Kuhn, 1934), which allows the estimation of long-range macrocyclization processes $c^{eff}_{1-3} = c^{eff}_{1-2}/2^{3/2}$ and $c^{eff}_{1-4} = c^{eff}_{1-2}/3^{3/2}$.

we obtain 13 available macroconstants by using the extended site-binding model (Eqs. (104)–(116)) corresponding to 13 macrospecies. The 17 contributing microspecies (with adapted statistical factors) are shown in Figure 86 (binuclear helicates), Figure 87 (trinuclear helicates), and Figure 88 (tetranuclear helicates).

$$\beta^{R,L11}_{1,2} = 48(f^R_{N_3})^2(u^{L,L}_{1-2}) \tag{104}$$

$$\beta^{R,L11}_{2,2} = 144(f^R_{N_3})^4(u^{L,L}_{1-2})^2(u^{R,R}_{1-2})(c^{eff}_{1-2}) \tag{105}$$

$$\beta^{R,L11}_{2,3} = 96(f^R_{N_3})^6(u^{L,L}_{1-2})^6(u^{R,R}_{1-2})(c^{eff}_{1-2})^2 \tag{106}$$

$$\beta^{R,L13b}_{2,2} = 144(f^R_{N_2O})^4(u^{L,L}_{1-2})^2(u^{R,R}_{1-2})(c^{eff}_{1-2}) \tag{107}$$

$$\beta^{R,L13b}_{1,3} = 32(f^R_{N_2O})^3(u^{L,L}_{1-2})^3 \tag{108}$$

$$\beta^{R,L13b}_{2,3} = 96(f^R_{N_2O})^6(u^{L,L}_{1-2})^6(u^{R,R}_{1-2})(c^{eff}_{1-2})^2 \tag{109}$$

$$\begin{aligned}\beta^{R,L28}_{2,3} &= \beta^{R,L28}_{2,3}(tt) + \beta^{R,L28}_{2,3}(ct) + \beta^{R,L28}_{2,3}(cctctt)\\ &= 96(f^R_{N_2O})^6(u^{L,L}_{1-2})^6(u^{R,R}_{1-2})^{0.5}(c^{eff}_{1-2}/2^{3/2})^2\\ &\quad + 768(f^R_{N_2O})^3(f^R_{N_3})^3(u^{L,L}_{1-2})^6(u^{R,R}_{1-2})(c^{eff}_{1-2})^2\end{aligned} \tag{110}$$

$$\beta^{R,L28}_{3,2} = 864(f^R_{N_2O})^4(f^R_{N_3})^2(u^{L,L}_{1-2})^3(u^{EuEu}_{1-2})^{2.5}(c^{eff}_{1-2})^2 \tag{111}$$

$$\beta^{R,L28}_{3,3} = 576(f^R_{N_2O})^6(f^R_{N_3})^3(u^{L,L}_{1-2})^9(u^{EuEu}_{1-2})^{2.5}(c^{eff}_{1-2})^4 \tag{112}$$

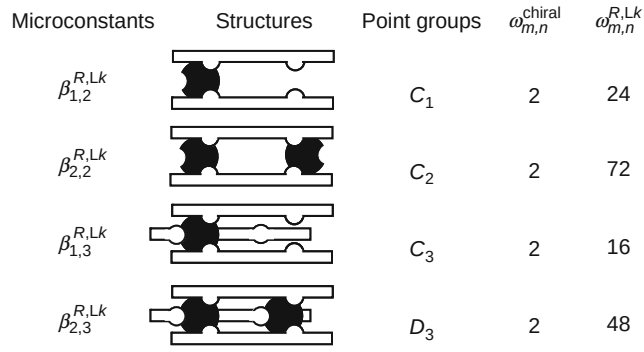

FIGURE 86 Schematic structures, symmetries, and statistical factors for $[R_m(\mathbf{L}k)_n]^{3m+}$ ($k = 11$, 13b) microspecies.

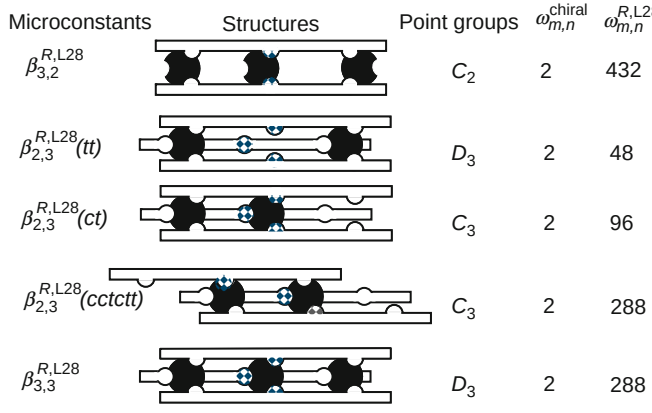

FIGURE 87 Schematic structures, symmetries, and statistical factors for $[R_m(\mathbf{L28})_n]^{3m+}$ microspecies.

$$\begin{aligned}\beta_{3,2}^{R,L29} &= \beta_{3,2}^{R,L29}(tcc) + \beta_{3,2}^{R,L29}(ttc) + \beta_{3,2}^{R,L29}(tcc-s)\\ &= 1728(f_{N_2O}^{R})^2(f_{N_3}^{R})^4(c_{1-2}^{\text{eff}})^2(u_{1-2}^{R,R})^{2.5}(u_{1-2}^{L,L})^3\\ &\quad + 864(f_{N_2O}^{R})^4(f_{N_3}^{R})^2(c_{1-2}^{\text{eff}})^2/2^{3/2}(u_{1-2}^{R,R})^{1.83}(u_{1-2}^{L,L})^3\end{aligned} \tag{113}$$

$$\begin{aligned}\beta_{3,3}^{R,L29} &= \beta_{3,3}^{R,L29}(tcc) + \beta_{3,3}^{R,L29}(ttc) + \beta_{3,3}^{R,L29}(tcc-s)\\ &= 4608(f_{N_2O}^{R})^3(f_{N_3}^{R})^6(c_{1-2}^{\text{eff}})^4(u_{1-2}^{R,R})^{2.5}(u_{1-2}^{L,L})^9\\ &\quad + 1152(f_{N_2O}^{R})^6(f_{N_3}^{R})^3(c_{1-2}^{\text{eff}})^4/2^3(u_{1-2}^{R,R})^{1.83}(u_{1-2}^{L,L})^9\end{aligned} \tag{114}$$

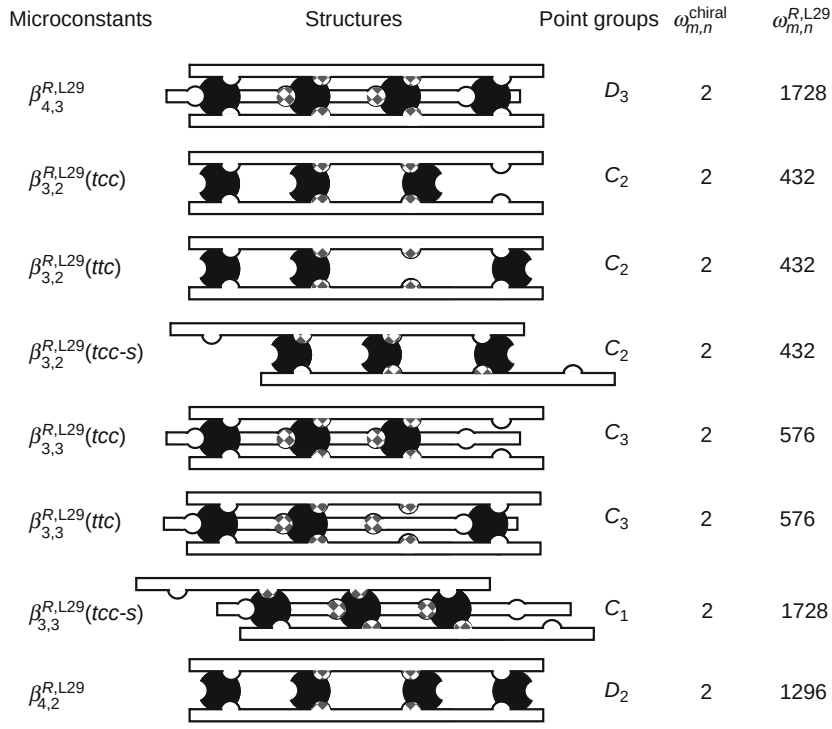

FIGURE 88 Schematic structures, symmetries, and statistical factors for $[R_m(\mathbf{L29})_n]^{3m+}$ microspecies.

$$\beta_{4,2}^{R,L29} = 2592(f_{N_2O}^{R})^4(f_{N_3}^{R})^4(c_{1-2}^{eff})^3(u_{1-2}^{R,R})^{4.33}(u_{1-2}^{L,L})^4 \quad (115)$$

$$\beta_{4,3}^{R,L29} = 3456(f_{N_2O}^{R})^6(f_{N_3}^{R})^6(c_{1-2}^{eff})^6(u_{1-2}^{R,R})^{4.33}(u_{1-2}^{L,L})^{12} \quad (116)$$

A nonlinear least-squares fit of these 13 equations with five microscopic parameters $f_{N_2O}^{R}$, $f_{N_3}^{R}$, $u_{1-2}^{L,L}$, $u_{1-2}^{R,R}$, and c_{1-2}^{eff} ($R = Eu$, Table 13) provides a satisfying model for the reproduction of the experimental stability constants, as shown on Figure 89, Dalla Favera et al., 2008).

The absolute affinities of Eu^{III} for the neutral N_2O and N_3 sites are very similar ($f_{N_2O}^{Eu} \approx f_{N_3}^{Eu}$, Table 13), which confirms that the so-called oxophilicity of trivalent lanthanides is limited to negatively charged donor atoms as found in carboxylates or in phosphonates (Senegas et al., 2003). Obviously, comparison of the absolute affinity of the neutral N_2O site for Eu^{III} in $\mathbf{L13^b}$ (-33 kJ mol^{-1}, Table 13) with that of the negatively charged N_2O site in $(\mathbf{L13^f})^{2-}$ (-21 kJ mol^{-1}, Table 12) is precluded by the use of water as solvent in the second case. The small magnitude of

TABLE 13 Fitted thermodynamic parameters for the formation of $[Eu_m(\mathbf{L}k)_n]^{3m+}$ complexes ($k = 11$, 13[b], 28, 29) in acetonitrile at 298 K (from Dalla Favera et al., 2008)

Parameters		Free energies		kJ mol^{-1}
$\log(f_{N_3}^{Eu})$	5.4(2)	$\Rightarrow$	$\Delta G_{connection}^{Eu,N_3}$	$-31(1)$
$\log(f_{N_2O}^{Eu})$	5.6(2)	$\Rightarrow$	$\Delta G_{connection}^{Eu,N_2O}$	$-33(1)$
$\log(c_{1-2}^{eff})$	$-1.0(9)$	$\Rightarrow$	$\Delta G_{correction}^{intra}$	6(5)
$\log(u_{1-2}^{L,L})$	$-1.0(3)$	$\Rightarrow$	$\Delta E_{1-2}^{L,L}$	6(2)
$\log(u_{1-2}^{Eu,Eu})$	$-1.8(7)$	$\Rightarrow$	$\Delta E_{1-2}^{Eu,Eu}$	10(4)

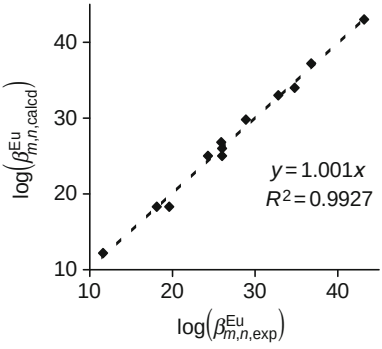

FIGURE 89 Comparison between experimental ($\log(\beta_{m,n,exp}^{Eu})$) and calculated ($\log(\beta_{m,n,calcd}^{Eu})$) stability constants for the 13 macroscopic equilibria described in Eqs. (104)–(116) (Dalla Favera et al., 2008).

$c_{1-2}^{eff} = 0.1$ M indicates a moderate preorganization of the ligand strands for macrocyclization. It is in line with the theoretically predicted value of $c^{eff} = 0.25$ M for two binding sites separated by 10 Å and connected by a bidentate ligand with optimum flexibility (Gargano et al., 2001). Finally, both homocomponent interactions are repulsive ($\Delta E_{1-2}^{L,L} > 0$, $\Delta E_{1-2}^{R,R} > 0$), which implies that any intermediate or triple-stranded helicate in this family of complexes is driven to complexion with negative cooperativity.

5.4 The origin of the unusual stability of highly charged lanthanide helicates in solution

The considerable stability of trinuclear $[R_3(\mathbf{L28})_3]^{9+}$ and tetranuclear $[R_4(\mathbf{L29})_3]^{12+}$ helicates, which indeed correspond to more than 90% of the ligand speciation at millimolar concentration, can be assigned to the nontrivial apparent minute repulsive intramolecular intermetallic interaction $\Delta E_{1-2}^{R,R} \approx 10$ kJ mol^{-1} operating between two R^{3+} held at a distance of ≈9Å in these complexes. The straightforward application of Coulomb's

Eq. (117) ($N_A = 6.023 \times 10^{23}\,\text{mol}^{-1}$ is Avogadro's number, z_i are the atomic charges of the interacting particles in electrostatic units, $e = 1.602 \times 10^{-19}\,\text{C}$ is the elemental charge, $\varepsilon_0 = 8.859 \times 10^{-12}\,\text{CN}^{-1}\,\text{m}^{-2}$ is the permittivity constant of the vacuum, ε_r is the relative permittivity constant of the medium, $d = 9.0$ Å is the intermetallic separation in the complex) predicts $39\ \text{kJ mol}^{-1}$ ($\varepsilon_r = 36.1$) $\leq \Delta E^{R,R}_{1-2,\text{calcd}} \leq 1389\ \text{kJ mol}^{-1}$ ($\varepsilon_r = 1.0$) for two R^{3+} in these helicates considered as dielectric continuums with limiting relative permittivities of $\varepsilon_r = 36.1$ (pure acetonitrile) or $\varepsilon_r = 1.0$ (vacuum). Assuming that the major contribution to the electrostatic work arises for distances close to equilibrium whereby $\varepsilon_r \to 1.0$, we can safely conclude that $\Delta E^{R,R}_{1-2,\text{calcd}}$ is approximately two orders of magnitude larger than its apparent value in acetonitrile (Canard and Piguet, 2007).

$$\Delta E^{R,R}_{1-2,\text{calcd}} = W_{\text{elec}} = -\frac{N_{\text{Av}} z_1 z_2 e^2}{4\pi\varepsilon_0} \int_{\infty}^{d=9\,\text{Å}} \frac{\mathrm{d}r}{\varepsilon_r r^2} \tag{117}$$

The use of thermodynamic Born–Haber cycles modeling the successive coordination of the second and third Eu^{III} in $[Eu(\mathbf{L28})_3]^{3+}$ to give $[Eu_2(\mathbf{L28})_3]^{6+}$ (Figure 90A) and $[Eu_3(\mathbf{L28})_3]^{9+}$ (Figure 90B) provides some rationalizations for this surprising dichotomy (Canard and Piguet, 2007).

Let us first apply the extended site-binding model (Eq. (100)) to the four complexation processes shown in Figure 90 (Eqs. (118)–(121)).

$$\beta_{K2,\text{gas}} = \mathrm{e}^{-\Delta G^0_{K2,\text{gas}}/RT} = 1(f^{\text{Eu}}_{\text{N}_3,\text{g}})^3 (u^{\text{L,L}}_{1-2,\text{g}})^3 u^{\text{Eu,Eu}}_{1-2,\text{g}} (c^{\text{eff}}_{1-2,\text{g}})^2 \tag{118}$$

$$\beta_{K3,\text{gas}} = \mathrm{e}^{-\Delta G^0_{K3,\text{gas}}/RT} = \frac{1}{2}(f^{\text{Eu}}_{\text{N}_3,\text{g}})^3 (u^{\text{L,L}}_{1-2,\text{g}})^3 u^{\text{Eu,Eu}}_{1-2,\text{g}} u^{\text{Eu,Eu}}_{1-3,\text{g}} (c^{\text{eff}}_{1-2,\text{g}})^2 \tag{119}$$

$$\beta_{K2,\text{sol}} = \mathrm{e}^{-\Delta G^0_{K2,\text{sol}}/RT} = 6(f^{\text{Eu}}_{\text{N}_3,\text{s}})^3 (u^{\text{L,L}}_{1-2,\text{s}})^3 u^{\text{Eu,Eu}}_{1-2,\text{s}} (c^{\text{eff}}_{1-2,\text{s}})^2 \tag{120}$$

$$\beta_{K3,\text{sol}} = \mathrm{e}^{-\Delta G^0_{K3,\text{sol}}/RT} = 3(f^{\text{Eu}}_{\text{N}_3,\text{s}})^3 (u^{\text{L,L}}_{1-2,\text{s}})^3 u^{\text{Eu,Eu}}_{1-2,\text{s}} u^{\text{Eu,Eu}}_{1-3,\text{s}} (c^{\text{eff}}_{1-2,\text{s}})^2 \tag{121}$$

From the Born–Haber cycles, we can write

$$\Delta G^0_{K2,\text{gas}} = \Delta G^0_{K2,\text{sol}} + \Delta_{\text{solv}} G^0\left(\text{Eu}(\mathbf{L28})_3\right) + \Delta_{\text{solv}} G^0(\text{Eu}) - \Delta_{\text{solv}} G^0\left(\text{Eu}_2(\mathbf{L28})_3\right) \tag{122}$$

$$\Delta G^0_{K3,\text{gas}} = \Delta G^0_{K3,\text{sol}} + \Delta_{\text{solv}} G^0\left(\text{Eu}_2(\mathbf{L28})_3\right) + \Delta_{\text{solv}} G^0(\text{Eu}) - \Delta_{\text{solv}} G^0\left(\text{Eu}_3(\mathbf{L28})_3\right) \tag{123}$$

which can be combined in Eq. (124).

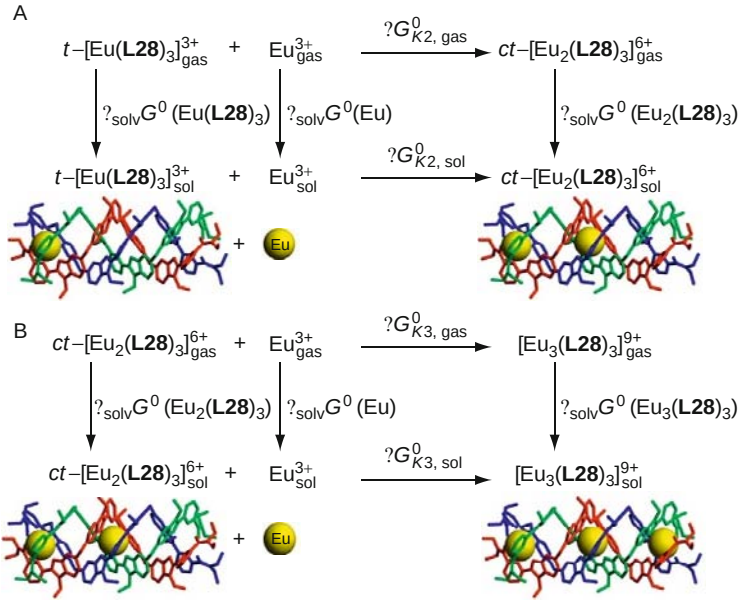

FIGURE 90 Thermodynamic Born–Haber cycles for the successive complexation of Eu^{III} to (A) *t*-$[Eu(\mathbf{L28})_3]^{3+}$ to give *ct*-$[Eu_2(\mathbf{L28})_3]^{6+}$ and (B) *ct*-$[Eu_2(\mathbf{L28})_3]^{6+}$ to give $[Eu_3(\mathbf{L28})_3]^{9+}$. Letters *c* and *t* denote the central and terminal sites, respectively.

$$\Delta G^0_{K3,\mathrm{sol}} - \Delta G^0_{K2,\mathrm{sol}} = \Delta G^0_{K3,\mathrm{gas}} - \Delta G^0_{K2,\mathrm{gas}} + \Delta_{\mathrm{solv}}G^0\left(\mathrm{Eu}(\mathbf{L28})_3\right) + \Delta_{\mathrm{solv}}G^0\left(\mathrm{Eu_3}(\mathbf{L28})_3\right) - 2\Delta_{\mathrm{solv}}G^0\left(\mathrm{Eu_2}(\mathbf{L28})_3\right) \tag{124}$$

The introduction of Eqs. (118)–(121) into Eq. (124) eventually gives

$$\Delta E^{\mathrm{Eu,Eu}}_{1-3,\mathrm{sol}} - 3RT\ln\left(\frac{f^{\mathrm{Eu}}_{\mathrm{N_3,s}}}{f^{\mathrm{Eu}}_{\mathrm{N_2O,s}}}\right) = \Delta E^{\mathrm{Eu,Eu}}_{1-3,\mathrm{gas}} - 3RT\ln\left(\frac{f^{\mathrm{Eu}}_{\mathrm{N_3,g}}}{f^{\mathrm{Eu}}_{\mathrm{N_2O,g}}}\right) + \Delta_{\mathrm{solv}}G^0\left(\mathrm{Eu}(\mathbf{L28})_3\right) + \Delta_{\mathrm{solv}}G^0\left(\mathrm{Eu_3}(\mathbf{L28})_3\right) - 2\Delta_{\mathrm{solv}}G^0\left(\mathrm{Eu_2}(\mathbf{L28})_3\right) \tag{125}$$

Assuming that (i) the ratio of the absolute affinities of the N_3 and N_2O sites for Eu^{III} are similar in the gas phase and in solution ($f^{\mathrm{Eu}}_{\mathrm{N_3,g}}/f^{\mathrm{Eu}}_{\mathrm{N_2O,g}} = f^{\mathrm{Eu}}_{\mathrm{N_3,s}}/f^{\mathrm{Eu}}_{\mathrm{N_2O,s}}$) and (ii) $\Delta E^{\mathrm{Eu,Eu}}_{1-3,\mathrm{gas}}$ is reasonably approximated by Coulomb's Eq. (117) with $\varepsilon_r = 1.0$, we can deduce that the deviation of the intermetallic interaction in solution from classical electrostatic trends

can be ascribed to the contribution of the solvation energies of the different complexes (Eq. (126), Canard and Piguet, 2007).

$$\Delta E^{\mathrm{Eu,Eu}}_{1-3,\mathrm{sol}} = \frac{9N_{\mathrm{Av}}e^2}{4\pi\varepsilon_0 2d} + \Delta_{\mathrm{solv}}G^0\left(\mathrm{Eu}(\mathbf{L28})_3\right) + \Delta_{\mathrm{solv}}G^0\left(\mathrm{Eu}_3(\mathbf{L28})_3\right) - 2\Delta_{\mathrm{solv}}G^0\left(\mathrm{Eu}_2(\mathbf{L28})_3\right) \tag{126}$$

Estimating $\Delta_{\mathrm{solv}}G^0\left(\mathrm{Eu}_m(\mathbf{L28})_3\right)$ with Born Eq. (127) for these large molecular ions in acetonitrile with $\varepsilon_r = 36.1$ and gas-phase radii $r(\mathrm{Eu}(\mathbf{L28})_3) = 10$ Å, $r(\mathrm{Eu}_2(\mathbf{L28})_3) = 11$ Å and $r(\mathrm{Eu}_3(\mathbf{L28})_3) = 12$ Å gives $\Delta_{\mathrm{solv}}G^0\left(\mathrm{Eu}(\mathrm{L28})_3\right) = -607$ kJ mol^{-1}, $\Delta_{\mathrm{solv}}G^0\left(\mathrm{Eu}_2(\mathrm{L28})_3\right) = -2208$ kJ mol^{-1} and $\Delta_{\mathrm{solv}}G^0\left(\mathrm{Eu}_3(\mathrm{L28})_3\right) = -4554$ kJ mol^{-1} (Canard and Piguet, 2007).

$$\Delta_{\mathrm{solv}}G^0\left(\mathrm{Eu}_m(\mathbf{L28})_3\right) = -\frac{N_{\mathrm{Av}}(3m)^2e^2}{8\pi\varepsilon_0 r}\left(1-\frac{1}{\varepsilon_r}\right) \tag{127}$$

The introduction of these values into Eq. (126) shows that the solvation correction and the Coulombic repulsion are of the same magnitude, but of opposite trend, which explains the minute apparent intermetallic interaction detected in solution when using the extended site-binding model (Eq. (128)).

$$\Delta E^{\mathrm{Eu,Eu}}_{1-3,\mathrm{sol,\ exp}} = +694 - 745 = -51\,\mathrm{kJ/mol} \tag{128}$$

Interestingly, a refined treatment of the experimental data which does not impose a Coulombic correlation between $\Delta E^{\mathrm{Eu,Eu}}_{1-2,\mathrm{sol}}$ and $\Delta E^{\mathrm{Eu,Eu}}_{1-3,\mathrm{sol}}$, eventually concludes that $\Delta E^{\mathrm{Eu,Eu}}_{1-3,\mathrm{sol,\ exp}} = -7(3)$ kJ mol^{-1}, in good agreement with the rough attractive interaction predicted in Eq. (128) (Riis-Johannessen et al., 2009). The same thermodynamic approach applies for unraveling $\Delta E^{\mathrm{Eu,Eu}}_{1-4,\mathrm{sol}}$ in $[\mathrm{Eu}_m(\mathbf{L29})_3]^{3m+}$, while some modifications are required for $\Delta E^{\mathrm{Eu,Eu}}_{1-2,\mathrm{sol}}$ (Riis-Johannessen et al., 2009). Altogether, the conclusions are similar with the observation of unusually small intermetallic interactions resulting from the competition between electrostatic repulsion, which prevents the formation of small and highly charged polynuclear helicates, and opposite favorable solvation effects, which are maximum for small ions with high charge density. For linear (i.e., one-dimensional) complexes such as helicates, the coordination of an additional trivalent lanthanide involves a single short-range intermetallic repulsion $\Delta E^{\mathrm{Eu,Eu}}_{1-2}$, while the total charge of the supramolecular edifice is increased by three unit and its size by a concomitant increase of ca. 10% (Canard and

Piguet, 2007). The balance of these effects for the intermetallic interaction operating in solution is close to zero (see Eq. (128) for $\Delta E^{Eu,Eu}_{1-3,sol}$), which explains the considerable stability of lanthanide helicates in solution.

5.5 Predictive approaches

Although not explicitly considered to date in the literature, the balance between intermetallic repulsion and solvation energies as a major contribution to the stability (or instability) of the final polynuclear lanthanide complexes is not limited to one-dimensional lanthanide helicates, but obviously extends to two-dimensional (2D, Chapon et al., 2001, 2002; Chen et al., 2007; Lama et al., 2007; Mamula et al., 2005; Ronson et al., 2007; Senegas et al., 2005; Xu and Raymond, 2000) and three-dimensional (3D) lanthanide complexes (Hamacek et al., 2008; He et al., 2008; Mamula et al., 2006) in solution. One can thus easily realize that 2D and 3D organizations involve a large amount of short-range intermetallic interactions affected by strong electrostatic repulsion, which requires very compact structures avoiding large increase in size for maintaining large and favorable solvation effects. In this context, it is worth noting that the vast majority of stable 2D and 3D polynuclear lanthanide complexes in solution incorporate negatively charged binding units, for which the absolute affinities f^R are maximum and can overcome unfavorable intermetallic interactions. This understanding of the parameters controlling the stability of lanthanide complexes paves the way for evolving from the usual deductive approach toward some inductive counterpart. The prediction of the formation constants and ligand distributions in the heterobimetallic trinuclear complexes $[La_xEu_{3-x}(\mathbf{L28})_3]^{9+}$ represents a first attempt in this direction (Floquet et al., 2004). Taking into account the absolute affinities $f^{Eu}_{N_2O}$, $f^{Eu}_{N_3}$, $f^{La}_{N_2O}$, $f^{La}_{N_3}$, and the intermetallic interactions $u^{La,La}_{1-2}$, $u^{Eu,Eu}_{1-2}$, and $u^{La,Eu}_{1-2}$ obeying the mixing rule, it was possible to predict that the target microspecies $[EuLaEu(\mathbf{L28})_3]^{9+}$ accounts for 48% of the thermodynamic mixture (La:Eu:**L28** = 1:2:3, total ligand concentration = 10 mM). Detailed ^{1}H-NMR investigations confirmed these predictions, which allowed to unravel the effect of the crystallization process on the distribution of La^{III} and Eu^{III} in solid-state materials (Floquet et al., 2004). A second success arose with the prediction that $[Eu_4(\mathbf{L29})_3]^{12+}$ would be the major component (>90%) for a Eu:**L29** ratio = 4:3 in acetonitrile with a global stability constant $\log(\beta^{Eu,L29}_{4,3,calcd}) = 42.5$ (Zeckert et al., 2005). After 11 synthetic steps leading to **L29** (Figure 43), subsequent spectrophotometric titration in acetonitrile with $Eu(CF_3SO_3)_3$ indeed confirmed these predictions with $\log(\beta^{Eu,L29}_{4,3,exp}) = 43.2(1.9)$, in very good agreement with the calculated value (Dalla Favera et al., 2008).

6. HELICATES AS LUMINESCENT BIOPROBES

6.1 Lanthanide luminescent bioprobes

Luminescence and time-resolved luminescence have grown during the past 20 years into major methodologies in biochemistry, biophysics, biotechnology, and medicine. They are indispensable research tools in noninvasive medical diagnostics, flow cytometry, analysis of polymerase chain reaction (PCR) products, gene analysis, DNA sequencing, luminescence microscopy, and cellular imaging, only to name a few. The reason is very simple. Light travels almost instantaneously through a sample (about 30 cm ns^{-1}) and can reach regions of complex molecular edifices not accessible to other molecular probes, such as magnetic resonance probes. Furthermore, light is easily detected by highly sensitive devices (e.g., charge-coupled device cameras) and techniques, including single-photon detection, so that analyses based on luminescence are the most sensitive available, while being environmentally clean, as opposed to methods using radiolabels.

Luminescence is defined as emission of light from an electronically excited state. Depending on the spin of the initial (emitting) and final (often ground) states, two categories of emission are distinguished: *fluorescence* for transitions without spin change ($\Delta S = 0$) and *phosphorescence* for transitions with spin change ($\Delta S > 0$). In the case of organic luminophores, which usually bear aromatic residues, absorption of light leads to a singlet excited state and the return to the ground state is allowed, so that the emission rate is fast, in the range $k_F = 10^7$–$10^9\ s^{-1}$, corresponding to a lifetime of the excited state $\tau_F = 100$–1 ns. Due to this short timescale, time-resolved detection (TRD) of fluorescence necessitates sophisticated optics and detection systems. On the other hand, spectral discrimination is often impossible to achieve because the Stokes' shifts of the organic chromophores are small. Quinine sulfate (blue), fluorescein (green), acridine orange (AO, yellow), rhodamine (orange), and pyridine-1 (red) are common fluorescent analytical probes covering the entire visible range while cyanine (CY), Alexa Fluor®, and BODIPY® dyes are examples of more recently proposed luminescent tags (Lakowicz, 2006). In some cases, the excited organic luminophore relaxes to a triplet state and since transitions from this state to the singlet ground state are forbidden by the spin selection rule, the emission of light is slow with rates in the range $k_P = 1$–$10^3\ s^{-1}$, corresponding to lifetimes τ_P of 1 s to 1 ms. Time-resolved experiments are consequently easy to conduct, but the fraction of molecules reaching the triplet state is usually small, at least at room temperature, and due to their long lifetime, triplet states often give rise to photochemical reactions which destroy the luminophore, a phenomenon known as photobleaching. The need for time or spectral discrimination, or

both, is considerable in bioanalyses because the samples contain a large variety of aromatic substances and when illuminated with UV or blue light, they generate a highly undesirable and intense luminescence background (autofluorescence).

Given these limitations, lanthanide ions emerge more and more as alternatives to organic bioprobes for time-resolved bioanalyses. Indeed, the $4f^n$ electronic configurations of R^{III} ions are protected from outside interactions by the more external $5s^25p^6$ subshells of the xenon core. Since the 4f wave functions are fairly pure, the plentiful electronic transitions (the $4f^6$ configuration of Eu^{III} generates 3003 electronic levels for instance) are narrow and easily recognizable, their energy being fairly insensitive to the chemical environment. Additionally, most of the ions are luminescent and their emissions extend over a broad spectral range (Figure 91), from UV (Gd^{III}) to visible (e.g., Sm^{III}, Eu^{III}, Tb^{III}, Dy^{III}, Tm^{III}) and near infrared (NIR, e.g., Nd^{III}, Ho^{III}, Er^{III}, Yb^{III}). Some ions are fluorescent, others are phosphorescent, and some are both. Electric-dipole intraconfigurational 4f–4f transitions are forbidden by Laporte's rule so that the lifetimes of the excited states are long (μs ms) allowing easy TRD experiments with rugged and cheap instrumentation. The inherent drawback of these ions, namely the very weak oscillator strengths of the f–f transitions, can be circumvented by exciting the *R*-containing chromophores into their surroundings through a process termed ''luminescence sensitization'' and discussed in Section 2.5.1 (Figure 37). A lanthanide luminescent bioprobe (LLB) usually consists in a lanthanide chelate the luminescence of which is modulated by interaction with the biological material.

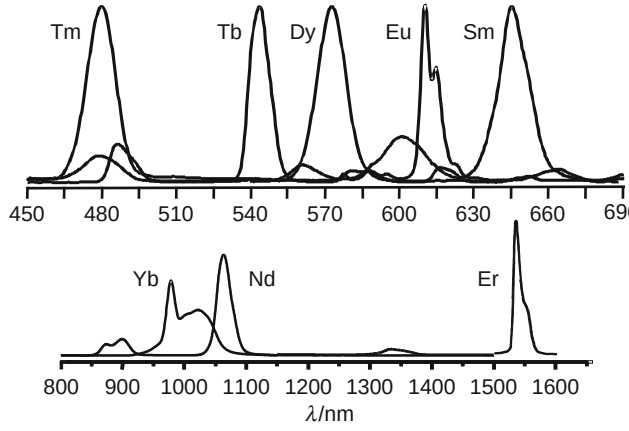

FIGURE 91 Luminescence of lanthanide β-diketonates (redrawn from Eliseeva et al., 2006).

An LLB may be used in a variety of different techniques. Initial applications include (i) simple substitution of Ca^{II} or Zn^{II} by luminescent R^{III} ions in proteins to obtain information on the composition of metal-binding sites, for instance the number of coordinated water molecules, or metal-to-metal and metal-to-chromophore distances by energy transfer experiments, or (ii) titration of a biocompound with salts of luminescent R^{III} ions to determine the number of metal-binding sites (Bünzli, 1989). Starting in the early 1980s, more subtle applications have been proposed, primarily for the design of luminescent time-resolved immunoassays (Siitari et al., 1983). The luminescent lanthanide ion is embedded into a suitable coordinating cavity and the resulting chelate is either used directly as an analytical responsive probe without specific targeting, or conjugated to a protein or to an antibody which specifically couples with a targeted biomolecule (Bünzli, 2009).

Requirements for an efficient LLB are numerous and challenging: (i) water solubility, (ii) large thermodynamic stability, (iii) kinetic inertness, (iv) intense absorption at least above 330 nm and if possible in the visible or NIR ranges, (v) efficient sensitization of the lanthanide ion luminescence, (vi) protection of the emitting ion by inserting it into a rigid and protective cavity minimizing nonradiative deactivation processes, (vii) long excited state lifetime, and (viii) when relevant, ability to couple to bioactive molecules while simultaneously retaining the sought for photophysical properties and leaving the bioaffinity of the host unchanged. Hundreds of chelates have been synthesized and tested during the past 30 years so that the design of LLBs is becoming well understood at least from the chemical and biochemical points of view, since *in silico* predictions are still far from being feasible. An LLB can be used directly, its luminescence being detected (usually in TRD mode) after a suitable and specific reaction with the analyte, or indirectly by transferring the excitation energy onto an organic acceptor by a process called Förster resonance energy transfer (FRET). An example of direct measurement is depicted in Figure 92 for an assay in which the luminescent lanthanide

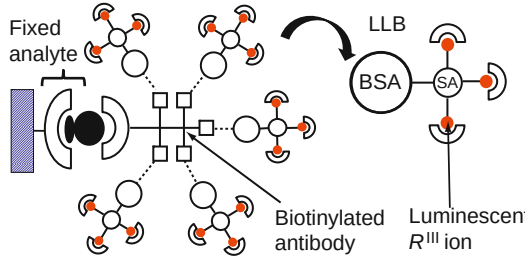

FIGURE 92 Direct use of an LLB conjugated to a biotinylated antibody (redrawn after Bünzli, 2009).

chelate is coupled firstly to streptavidin (SA) itself linked to bovine serum albumin (BSA); BSA can be easily conjugated to almost any biotinylated antibody. The latter reacts specifically with the (antigen) analyte and luminescence is detected after removal of the reactants in excess.

On the other hand, FRET occurs when the donor (D) and the acceptor (A) lie at distances $R_{DA} > 40$ pm, the corresponding mechanism being dipole–dipolar (through space), as opposed to through-bond (Dexter) mechanism which operates at shorter distances (Selvin, 2000). The yield of the FRET transfer is given by an equation similar to Eq. (77), Section 4.4, with R_0 defined by Eq. (78):

$$\eta_{FRET} = 1 - \frac{\tau_{obs}}{\tau_0} = \frac{1}{1 + \left(\frac{R_{DA}}{R_0}\right)^6} = \frac{R_0^6}{R_0^6 + R_{DA}^6} \tag{129}$$

This efficiency can therefore be easily estimated from lifetime measurements. Alternatively, it can be extracted from the absorption and emission spectra (Charbonnière and Hildebrandt, 2008):

$$\eta_{FRET} = \frac{A_A(\lambda_D)}{A_D(\lambda_D)}\left[\frac{E_{AD}(\lambda_D)}{E_A(\lambda_D)} - 1\right] \tag{130}$$

where λ_D is the excitation wavelength of the (donor) LLB, A_D and A_A are the absorbances of the donor and acceptor at this wavelength while E_A and E_{AD} are the integrated emission intensities of the acceptor in absence and in presence of the donor, respectively. The corresponding bioanalysis is sketched on Figure 93. The LLB is bioconjugated to a biotinylated antibody while a cyanine dye is linked to another such antibody. Both antibodies are specific for the (antigen) analyte. The advantage of this technique is that no washing is required since the transfer only occurs when the two antibodies are connected to the analyte simultaneously. In addition the excited state of the organic acceptor dye is populated with a lifetime equal to the one of the excited R^{III} ion so that TRD discriminates between this emission and the emission of the dye upon direct excitation. Finally, emission from the LLB upon direct excitation is discriminated spectrally; that is, the dye is chosen so that its emission range is distinct from the R^{III} emission bands.

Covalent coupling of a lanthanide luminescent chelate to bioactive molecules such as peptides, proteins, or nucleic acids makes use of the chemically reactive groups of these molecules. The most common ones are aliphatic α- or ε-amines. A typical example of ε-amine is lysine, the pK_a of which is 9.2 so that it reacts cleanly above pH 8 to yield stable

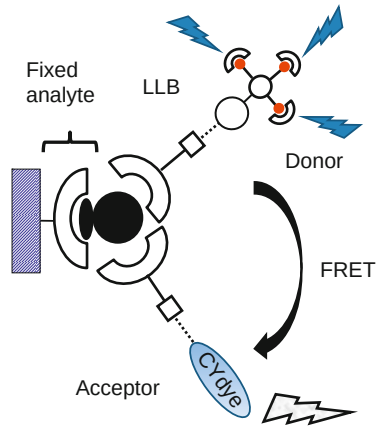

FIGURE 93 Förster resonant energy transfer between an LLB bioconjugated to a biotinylated antibody and a cyanine dye coupled to another biotinylated antibody.

covalent binding. There are usually several lysine groups per protein, compare streptavidin which bears 36 of them, so that several luminescent lanthanide chelates may be conjugated simultaneously. The α-amino group is more acidic with pK_a around 7 and every protein bears at least one such group per subunit or peptide chain. Thiol residues are other common reactive groups. The free thiol group (e.g., in cysteine) is more nucleophilic than amines and generally is the more reactive group in proteins, even at neutral pH. Phenol (e.g., in tyrosine) or carboxylic acids (e.g., in aspartic and glutamic acids) are other potential candidates. The lanthanide chelate must be activated before coupling with these functional groups. In immunoassays and many other bioanalyses, coupling between proteinic amines and LLBs fitted with isothiocyanato, chlorosulfonyl (particularly arenesulfonyl), or 2,4-dichloro-1,3,5-triazinyl groups have proved to be the most successful (Nishioka et al., 2007). Another very convenient coupling group is *N*-hydroxysuccinimide (NHS, or its sulfo derivative, sulfo-NHS) which can be easily generated by direct reaction of a carboxylic acid with *N*-hydroxysuccinimide in presence of the dehydrating agent (1-ethyl-3-(3-dimethylaminopropyl) carbodiimide hydrochloride (EDC or EDAC). Since proteins bear many coupling functions, the number of attached LLBs may be large, up to 46 as reported to date, especially if the bioconjugate is further attached to a protein such as BSA which smoothly reacts with biotinylated biomolecules, as shown in Figures 92 and 93, and this results in more sensitive analyses.

6.2 Dipicolinic acid derivatives as LLBs

The intense luminescence displayed by lanthanide dipicolinates (Table 6) as well as their easy synthesis have prompted their use in various analytical and imaging applications and some of them are briefly reviewed in this section.

6.2.1 Simple analyses

Bacterial spores are the most resistant microbial structures toward extreme conditions. As a consequence, they find applications in the evaluation of the efficiency of sterilization processes. They are also present in the ominous *Bacillus anthracis* spores which have been the biological vectors in anthrax attacks. Dipicolinic acid is a remarkable constituent of these spores so that they may be detected through complexation with Tb^{III}. In the proposed procedure, Cable et al. (2007) start from a macrocyclic complex, $[Tb(DO2A)]^+$ where DO2A is 1,4,7,10-tetraazacyclododecane-1,7-diacetate, to saturate the lanthanide inner coordination sphere in $[Tb(DO2A)(\mathbf{L15^a})]^-$ for maintaining excellent photophysical properties. Detection limits are as low as 2.1×10^4 spores per ml.

The lanthanide tris(dipicolinates) usually exist as racemic mixtures of Δ and Λ isomers. However, the luminescent complexes may be used for chirality recognition by perturbing the racemic equilibrium with enantiomerically resolved nonluminescent acceptor molecules or complexes (see Aspinall, 2002 for a review). Along these lines, Metcalf et al. (1992) have proposed a method based on time-resolved chiroptical luminescence spectroscopy for investigating enantioselective excited-state quenching processes in solutions containing the racemic LLB and a small concentration of dissymmetric quencher molecules. The latter are six-coordinate $[Co^{III}(NH_3)_4(L)]$ complexes with diphosphate or triphosphate nucleotides (adenosine, guanosine, inosine, cytidine, uridine, and deoxythymidine). The quenching rate constants display significant variations among the different systems. More interestingly, all of the Co^{III} complexes exhibit differential quenching of Λ-*R** compared to Δ-*R** enantiomers of the europium and terbium tris(dipicolinates) which can be related to structural differences between the nucleoside base moieties.

6.2.2 Immunoreactive conjugates of proteins

The 4-iodo(acetoamido) derivative of dipicolinic acid ($\mathbf{Na_2L15^i}$, Figure 23) readily alkylates proteins. However, the stability of its R^{III} chelates is not very large and since three ligands are needed to saturate the lanthanide inner coordination sphere, some crosslinking by the R^{III} ions occurs. To circumvent these problems, Lamture and Wensel (1995) have proposed to couple $(\mathbf{L15^i})^{2-}$ onto a polylysine framework, simultaneously to succinate, to produce a

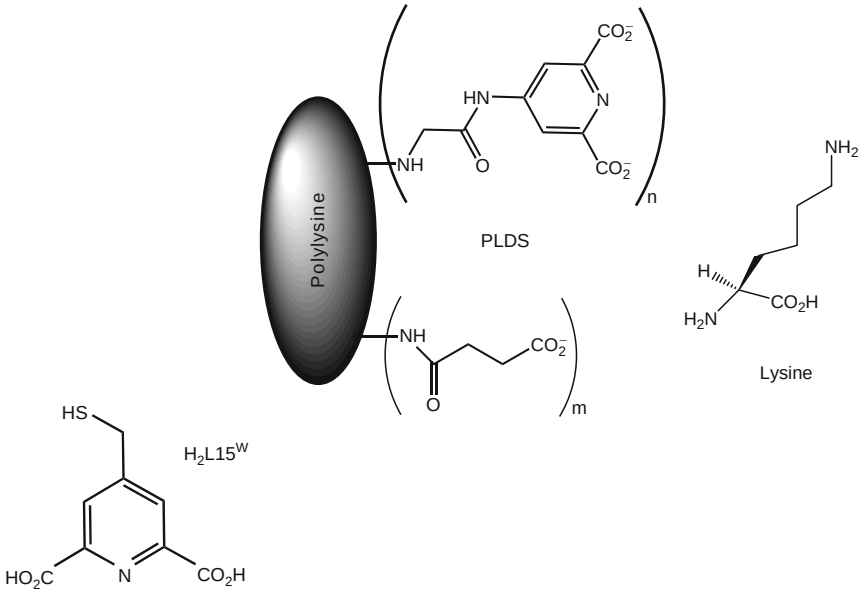

FIGURE 94 Top: polylysine derivatized with dipicolinate and succinate (PLDS) (redrawn from Lamture and Wensel, 1995). Bottom: chelating unit for paramagnetic tags used for exploring the magnetic susceptibility anisotropy sensors of proteins (Su et al., 2008a).

polylysine dicarboxylate succinate polymer (PLDS) bearing 50–100 4-substituted dipicolinate moieties per molecule while the remaining lysyl chains are succinylated (Figure 94). The binding affinity of PLDS for Tb^{III} is larger than the affinity of EDTA (ethylenediamine tetraacetate) and carbodiimide-mediated coupling reactions to proteins result in highly luminescent protein-PLDS-Tb conjugates. These conjugates retain sufficient immunoreactivity to design luminescent assays of proteins immobilized on nitrocellulose, such as BSA, protein A and ovalbumin. When simultaneously probed with a rabbit antiovalbumin and the protein-PLDS-Tb conjugate, a quantity as small as 10 ng of ovalbumin can be detected by the naked eye.

Lanthanide ions with anisotropic molecular magnetic susceptibility tensor $\Delta\chi$, for example, Er^{III}, Tm^{III}, or Yb^{III}, allow valuable structural information to be extracted from pseudocontact shifts (PCS, see also Section 3.6) and residual dipolar couplings (RDCs) arising from the partial alignment of the R^{III}-labeled biomolecules in the induced magnetic field (Su et al., 2008b):

$$\Delta\delta^{\mathrm{PCS}} = \frac{1}{12\pi r^3}\left[\Delta\chi_{\mathrm{ax}}(3\cos^2\theta - 1) + 1.5\Delta\chi_{\mathrm{rh}}\sin^2\theta\cos 2\varphi\right] \qquad (131)$$

where r, θ, and φ are the polar coordinates of the nucleus spin with respect to the principal axes of the $\Delta\chi$ tensor; $\Delta\chi_{\mathrm{ax}}$ and $\Delta\chi_{\mathrm{rh}}$ are the axial and rhombic components of the susceptibility anisotropy tensor, respectively. The RDC between spins i and j, D_{ij}, is given by a similar equation:

$$D_{ij} = -\frac{S\gamma_i\gamma_j\mu_0\hbar}{8\pi^2 r_{ij}^3}[A_{ax}(3\cos^2\partial - 1) + 1.5A_{rh}\sin^2\partial\cos 2\varphi] \quad (132)$$

in which ∂ and φ characterize the orientation of the internuclear vector with respect to the principal axes of the alignment tensor, A_{ax} and A_{rh} are the axial and rhombic components of this tensor, S is the order parameter, γ_i and γ_j are the magnetogyric ratios for nuclei i and j separated by a distance r_{ij}, and $\hbar$ is Planck's constant divided by 2π. When a rigid molecule is partially aligned in the magnetic field as a result of its paramagnetism, the alignment tensor A is directly proportional to the susceptibility tensor (B_0 is the magnetic induction field strength, k is Boltzmann's constant, and T the temperature):

$$A_{ax,rh} = \frac{B_0^2}{15\mu_0 kT}\Delta\chi_{ax,rh} \quad (133)$$

Therefore, PCS and D_{ij} data bear orientation information useful for structure analysis and study of protein mobility, particularly when data are collected for several orientations. Alternatively, PCS induced by several different R^{III} ions provide similar information. For the latter investigations, the lanthanide paramagnetic tag is attached at different positions of the protein or lanthanide tags with different $\Delta\chi$ tensors are used.

In a recent study, Su et al. (2008b) have designed a protein-specific lanthanide tag based on the derivatized dipicolinic acid $\mathbf{H_2L15^w}$ (Figure 94, bottom). The 4-mercaptomethyl-dipicolinate unit coordinates to lanthanide ions with nanomolar affinity and builds a disulfide bond with proteins. In this way, the lanthanide dipicolinate is close to the protein domain to be investigated, resulting in an accurate determination of the $\Delta\chi$ tensor and in a rigid attachment of the tag to the protein, limiting variation in PCS and D_{ij} when the lanthanide tag reorientates with respect to the protein. The *N*-terminal DNA-binding domain of an *E. coli* Arginine repressor was derivatized with $\mathbf{H_2L15^w}$ and heteronuclear single quantum coherence (HSQC) ^{15}N-NMR spectra were recorded. In presence of R^{III} ions, a single crosspeak was observed for each backbone amide; Yb^{III} induced shifts up to 2 ppm. The geometric parameters of the $\Delta\chi$ tensor were determined in the simultaneous presence of Tb^{III}, Tm^{III}, and Yb^{III}. Although the $\Delta\chi$ tensor is only half as large as the ones reported for proteins and peptides, the new tags present decisive advantages, such as their straightforward synthesis, their nonchirality (reduction of the number of NMR signals by a factor 2), and a reduced probability of unwanted interferences.

6.2.3 Two-photon luminescence microscopy

One difficulty encountered when working with LLBs is the relatively short excitation wavelength they require, typically 270–360 nm, very few of them, particularly those containing Eu^{III} or Tb^{III}, being amenable to excitation wavelength above 400 nm. In addition to having a comparatively short penetration depth, UV and blue lights are detrimental to living systems, so that alternate ligands are being developed for which either longer wavelength excitation or higher-order excitation is feasible. In the case of dipicolinic acid derivatives, longer excitation wavelengths have been achieved by tuning the energy of the charge-transfer states in push–pull type ligands (Figure 95).

For instance, $[Eu(\mathbf{L15^{Wi}})_3]^{3-}$ ($i = 2$, 3, and 4) have absorption maxima around 320 nm instead of 280 for the parent dipicolinate and their quantum yield in CH_2Cl_2 are sizeable, between 0.15 and 0.43. However, extending one-photon excitation of the ligand into the visible range often proves to be problematic because the lowering of the ligand excited levels facilitates back transfer processes. When the excitation wavelength is shifted to 427 nm in $[Eu(\mathbf{L13^{W5}})_3]^{3-}$, no emission from Eu^{III} is detected at room temperature (D'Aléo et al., 2008b). As a consequence scientists are now turning to multiphoton excitation, especially that presently two-photon excitation is commercially available in confocal microscopy, following the pioneering work of Denk et al. (1990) and the commercialization of femtosecond laser sources. This allows noninvasive 3D imaging of biological tissue without creating collateral damage. Two-photon (or biphotonic, TPA) absorption is related to nonlinear optical (NLO) properties of the chromophore under consideration. It turns out that lanthanide tris(dipicolinates) possess NLO properties as demonstrated by their second-order hyperpolarizability coefficient $\langle\beta\rangle$ which was measured by the harmonic light scattering method (Tancrez et al., 2005). In this experiment, the intensity of the scattered light $I^{2\lambda}$ is plotted versus the square of the intensity of the incident light, I^{λ}, according to

$$I^{2\lambda} = G(N_S\langle\beta_S\rangle + N\langle\beta\rangle)(I^{\lambda})^2 \tag{134}$$

where indices S denote the solvent and N is the number of molecules per cm^3. Data plotted on Figure 96 clearly point to a contribution of the 4f-orbitals to this parameter in that the second-order hyperpolarizability increases with the number of 4f electrons and, moreover, it is the same for Y^{III} and La^{III}, within experimental errors. When excited with a laser line at 532 nm, an aqueous solution of $Na_3[Eu(\mathbf{L15^a})_3]$, which possesses two absorption bands at 270 and 278 nm, exhibits the characteristic Eu ($^5D_0$) emission. However, the plot of the emitted intensity versus the excitation power is linear, indicating that excitation is a single-photon absorption by the weak $^5D_1 \leftarrow {}^7F_1$ transition centered at

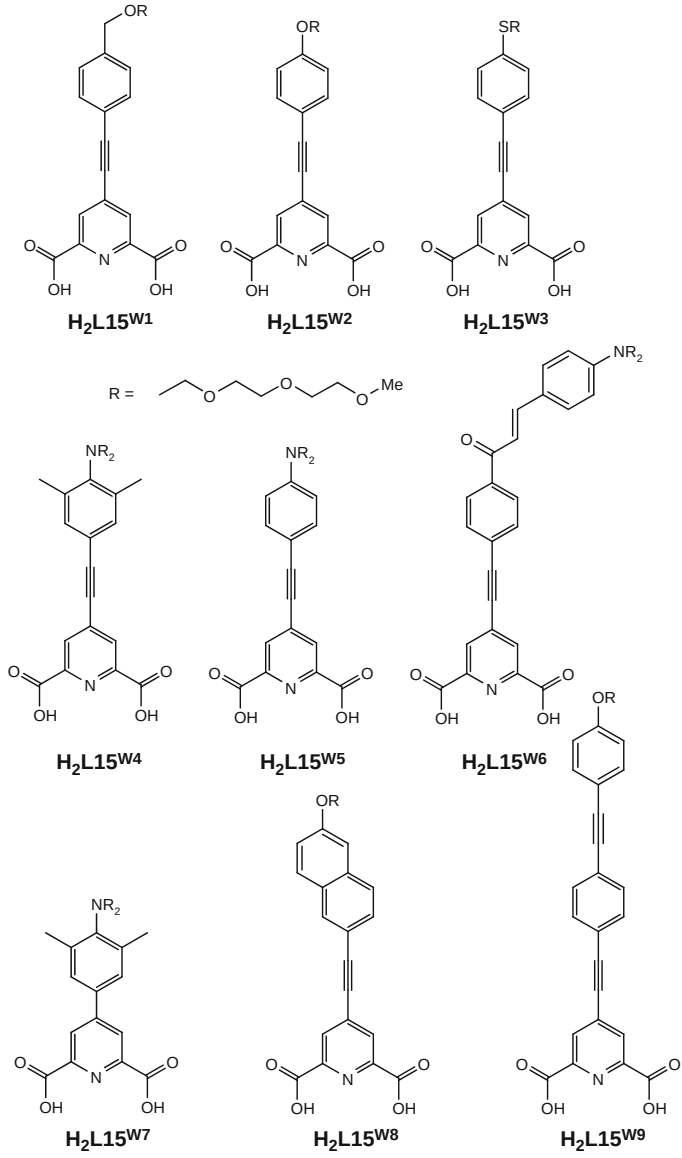

FIGURE 95 Push–pull derivatives of dipicolinic acid leading to longer excitation wavelengths for the $[Ln(\mathbf{L15})_3]^{3-}$ complexes (top two rows: D'Aléo et al., 2008b; bottom row: D'Aléo et al., 2008a).

536 nm. This transition has an estimated molar absorption coefficient of only 0.015 $M^{-1}cm^{-1}$ at 532 nm (also partly due to the fact that the fractional population of the $^7F_1$ sublevel at room temperature is only

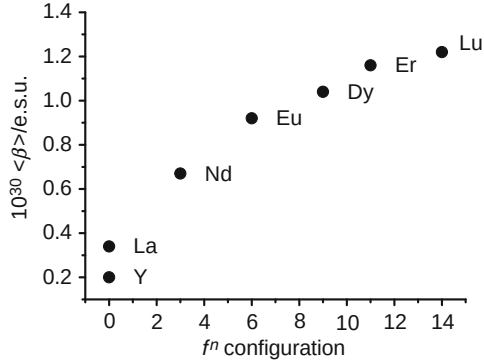

FIGURE 96 Second-order hyperpolarizability constant of lanthanide tris(dipicolinates) [*R*(**L15**$^{\mathbf{a}}$)$_3$] 0.1 M in water (redrawn after Tancrez et al., 2005).

0.33) but the large laser power (0.1–1.7 mW) compensates for this weak oscillator strength. On the other hand, the same plot for $Na_3[Tb(\mathbf{L15}^{\mathbf{a}})_3]$ reveals a quadratic variation of the Tb($^5D_4$) emission intensity with excitation power (between 0.5 and 3 mW, experimental exponent: 1.95), indicating that the luminescence originates from TPA absorption in the organic ligand. Similarly, crystals of the guanidinium salt of $[Tb(\mathbf{L15}^{\mathbf{a}})_3]^{3-}$ could be observed under biphotonic excitation at 532 nm (D'Aléo et al., 2007).

In addition to the octupolar D_3-symmetry found in lanthanide tris (dipicolinates), favorable to NLO effects, the bulk of the NLO properties of a complex depend on the electronic properties of the ligands. With this in mind, Picot et al. (2007) have developed new push–pull chromophores based on the pyridine-carboxamide framework (**L15**$^{\mathbf{k-p}}$, see Figure 24). The best chromophore is ligand **L15**$^{\mathbf{l}}$ in which the hexyloxy donor on the phenylacetylene para position pushes the charge-transfer state to a sufficiently high energy to avoid quenching of the Eu^{III} luminescence. The corresponding tris(complex), $[Eu(\mathbf{L15}^{\mathbf{l}})_3]^{3+}$, has a relatively modest quantum yield (5.6% in acetonitrile), but it displays two-photon excitation luminescence, contrary to the parent compound discussed above. This is demonstrated in Figure 97 in which the TPA excitation spectrum is superimposed to the absorption spectrum of the complex. The calculated two-photon absorption cross section amounts to 96 GM at 720 nm (1 Göppert-Mayer unit (GM) $= 10^{-50}$ cm^4 s photon^{-1}), a value somewhat lower compared to the best dipolar lanthanide β-diketonate complexes, for example, [Eu(tta)$_3$(dpbt)], where tta stands for thenoyltrifluoroacetylacetonate and dpbt for 2-(*N*,*N*-diethylanilin-4-yl)-4,6-bis(3,5-dimethylpyrazol-1-yl)-1,3,5-triazine (157 GM at 810 nm), or [Eu(fod)$_3$(Mk)] where fod is 6,6,7,7,8,8,8-heptafluoro-2,2-dimethyl-3,5-octanedionate and Mk Mischler's ketone (253 GM at 810 nm).

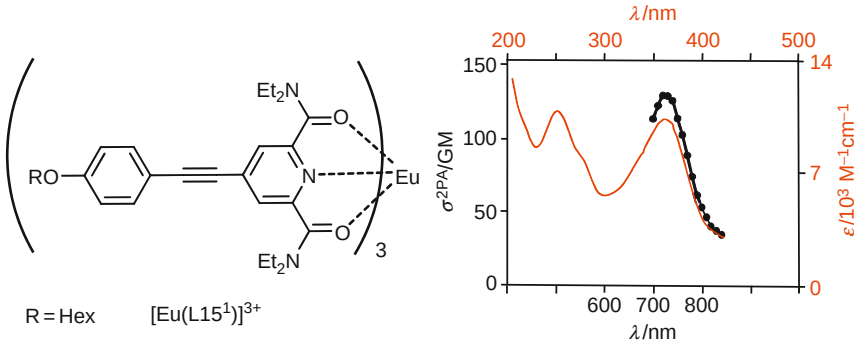

FIGURE 97 Left: formula of the Eu^{III} complex displaying a large TPA cross section. Right: absorption spectrum (top and right scales) and biphotonic excitation spectrum (bottom and left scales) of $[Eu(\mathbf{L15^{I}})_3]^{3+}$ in acetonitrile solution (redrawn from Picot et al., 2007).

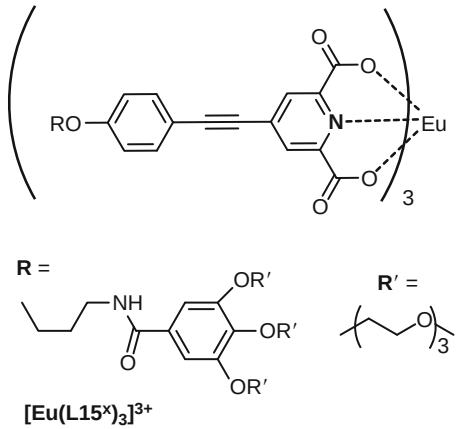

FIGURE 98 Structure of the $[Eu(\mathbf{L15^{x}})_3]^{3-}$ complex used for two-photon luminescence microscopy (Picot et al., 2008a).

Ligand $\mathbf{L15^{I}}$ was further modified to ensure water solubility through triethyleneglycol moieties, better stability by substitution of the amide groups with carboxylate units, as well as improved photophysical properties of the resulting Eu^{III} chelate (Figure 98, Picot et al., 2008a). The quantum yield of the tris-complex $Na_3[Eu(\mathbf{L15^{x}})_3]$ amounts to 15.6% in water and can be excited by a TPA process at 720 nm, the corresponding excitation spectrum again matching the absorption spectrum. The biphotonic absorption cross section remains modest, but is comparable to the one of the previous complex, 92 GM. T24 cancer cells were incubated in a solution of this complex 20 μM in phosphate buffer solution and fixed

with ethanol. Images taken with a biphotonic femtosecond laser scanning microscope with excitation wavelength at 760 nm ($\sigma^{TPA} = 19$ GM at this wavelength) indicates that the complex localizes in the perinuclear region of the cells, possibly in the endoplasmatic reticulum. This demonstrates the feasibility of two-photon LLBs for this type of analysis.

After publication of this work, the same authors have shown that $[Eu(\mathbf{L15^{Wi}})_3]^{3-}$ complexes with $i = 5$–9 (Figure 95) have much larger TPA cross sections, ranging from 110 ($i = 8$) to 173 ($i = 6$), 193 ($i = 7$), 218 ($i = 9$), and to the record 775 ($i = 5$) GM (D'Aléo et al., 2008a).

6.3 Homobinuclear helicates as LLBs for cell imaging and sensing

Despite the known advantages of lanthanide luminescent probes for bioanalyses (see Section 6.1), there has been few attempts to use them for cell imaging and sensing and some are summarized below. To our knowledge, the first experiments were carried out by Scaff et al. (1969) who treated bacterial smears from *E. coli* cell walls with a millimolar solution of europium thenoyl-trifluoroacetonate, $[Eu(tta)_3(H_2O)_2]$ in 50% ethanol before examining them under a luminescence microscope illuminated by a continuous mercury lamp: the intense emission from the $Eu(^5D_0)$ level brightly stained the cells especially when the pH was around 7. Later, Canada (1983) investigated the calcium-binding site of GH3/B6 pituitary tumor cells by binding Tb^{III} to these cells; in this way two sites were evidenced, one of which being specific for calcium. Furthermore, the luminescent properties of the Tb–GH3/B6 complex are sensitive to the presence of various analytes, such a adriamycin, or drugs, such as cisplatin, which allows their quantification (Canada, 1988). The same authors have also examined the binding sites of cisplatin to cisplatin-resistant human breast and ovarian cancer cells thanks to the Tb^{III} luminescence detected in TRD mode (Canada and Paltoo, 1998). The Eu^{III} ion has also been often used as luminescent bioprobe, for instance for characterizing the binding sites on the cell walls of *Datura Innoxia* (Ke et al., 1992). A thermal imaging method based on a Eu^{III} β-diketonate succeeded in mapping receptor-activated heat waves in Chinese hamster ovaries (Zohar et al., 1998) while the usefulness of LLBs for eliminating the autofluorescence background of biological samples by TRD was further demonstrated by Phimphivong and Saavedra (1998): a lipid-conjugated Tb^{III} diethylenetrinitrilotetraacetate complex proved to be an efficient membrane-staining agent for morphological studies of Swiss albino mouse 3T3 cultured cells. The first long-lasting efforts toward developing LLBs for imaging stemmed from the group of D. J. Bornhop who advocated a highly luminescent terbium macrocyclic complex for the *in vitro* and *in vivo* imaging of anomalous tissues as well as

for specific targeting of cancerous tissues (Bornhop et al., 1999, 2003; Manning et al., 2006). More recently, Parker and coworkers have designed macrocyclic Eu^{III} complexes staining either the nucleoli or the cytoplasm of several live cell lines such as NIH 3T3, HeLa, and HDF (Frias et al., 2003; Poole et al., 2007; Yu et al., 2006).

Taking into account the luminescent chelates developed for bioanalyses (mainly immunoassays), most of the presently available LLBs fall into the following classes: (i) polyaminocarboxylates (Latva et al., 1997; Takalo et al., 1997), (ii) bipyridine-based cryptates (Guillaumont et al., 2007), (iii) cyclen derivatives (Pandya et al., 2006), (iv) aza macrocycles incorporating a pyridine, bipyridine, or terpyridine unit (Bornhop et al., 1999; Nasso et al., 2005), (v) β-diketonates (Nishioka et al., 2007), or (vi) chelates bearing 2-hydroxyisophthalamide chromophores (Samuel et al., 2008a). With few exceptions, all of the above-mentioned LLBs are mononuclear species. However, associating two luminescent stains emitting different colors or one luminescent and one magnetic stains into a single-probe system is an attractive way of integrating the advantages of multiplex analyses. This has been achieved by attaching an organic chromophore to a Gd^{III} contrast agent for instance (Manning et al., 2004) or by developing receptors able to bind Gd^{III} and luminescent R^{III} ions while preserving the specific physicochemical properties of each metal ion (Picard et al., 2006). Finally, Imperiali has recently advocated ''double-lanthanide-binding tags'' (Dlbt) consisting in homobinuclear Tb^{III} species in which the metal ion is bound by encoded amino acids (Martin et al., 2007); in this case the presence of the two metal ions simply reinforce the luminescent and/or X-ray diffracting properties of the conjugates.

For testing the utility of binuclear LLBs, Bünzli and coworker have developed a library of water-soluble hexadentate ditopic ligands with benzimidazole-pyridine cores, $\mathbf{H_2L13^{f-1}}$ (see Figure 44), which self-assemble in water, at room temperature, and physiological pH 7.4 to give the corresponding homobinuclear helicates in large yield (usually $>95\%$ at millimolar total ligand concentration). This molecular framework possesses two additional properties: (i) rendering the two tridentate binding units slightly different allows the formation of heterobinuclear helicates, for the time being only in organic solvents though (see Section 4.2) and (ii) the helical edifices are potentially chiral which opens interesting perspectives for chiral recognition.

6.3.1 Thermodynamic, photophysical, and kinetic properties of the neutral, water-soluble $[R_2(\mathbf{L13})_3]$ helicates

The cumulative stability constants for the formation of the homobinuclear helicates with the seven ligands $\mathbf{H_2L13^{f-1}}$ are reported in Table 8 and a typical distribution diagram is represented on Figure 99 for ligand

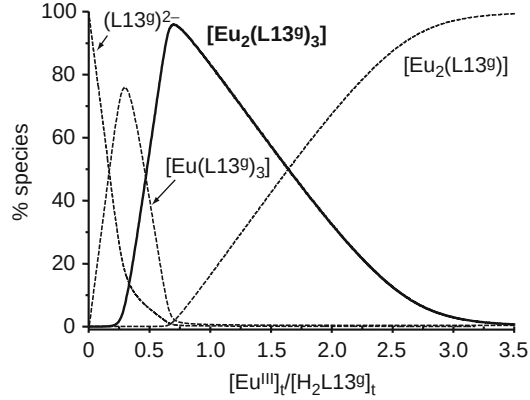

FIGURE 99 Distribution diagram for the system Eu^{III}/**H_2L13^g** at pH 7.4 (Tris–HCl buffer) and for $[\mathbf{H_2L13^g}]_t = 10^{-4}$ M (redrawn from Chauvin et al., 2008).

H_2L13^g. With respect to the parent ''unsubstituted'' helicates $[Ln_2(\mathbf{L13^f})_3]$ the grafting of the polyoxyethylene pendant has relatively little effect on the stability constant of the main 2:3 species, given the fact that the spectrophotometrically determined constants have been calculated from heavily correlated spectra. Indeed, if the log $\beta_{23}(Eu^{III})$ values span a range from 23.4 (**H_2L13^g**) to 28.6 (**H_2L13^k**) the speciation of the homobinuclear helicate at stoichiometric ratio 2:3 and total ligand concentration of 4.5×10^{-4} M (Table 14) varies between relatively narrow limits: from 88.7% (**H_2L13^l**) to 99.5% (**H_2L13^f**).

Moreover, the next more abundant species (1:2 or 1:3, R^{III}:L) accounts for most of the remaining speciation; that is, the stoichiometric 2:3 solutions contain only minute concentrations of uncomplexed R^{III}, an important feature when it comes to put them into contact with living materials. Another finding is that the stability does not vary much along the lanthanide series, so that one lanthanide ion may be replaced by another one with different photophysical properties without affecting much the speciation, another useful feature for multiplex experiments.

Biological media contain a wealth of substances potentially able to interfere with the LLB, either chemically by ligand exchange or transmetallation, or photophysically by quenching of the metal-centered luminescence by endogenous antioxidants. To both ascertain the stability data gathered by spectrophotometric titration and to test the action of potential interfering substances, several experiments were conducted on $[Eu_2(\mathbf{L13^g})_3]$ to which were added 10–100 equivalents of EDTA, DTPA, citrate, L-ascorbate or zinc. The luminescence of the resulting solutions did not decrease substantially (0–10%) 24 h after the addition (Table 15) meaning that the binuclear LLB is well suited for bioanalyses which are

TABLE 14 Percentage of the main complexed species in stoichiometric 2:3 solutions of Eu^{III} and $\mathbf{H_2L13^{f-l}}$ in aqueous solutions at pH 7.4 (Tris–HCl 0.1 M), as recalculated from published conditional stability constants for a total ligand concentration of 4.5×10^{-4} M

Ligand	2:3 species (%)	1:2 species (%)	References
$\mathbf{H_2L13^f}$	99.5	NA	Elhabiri et al. (1999)
$\mathbf{H_2L13^g}$	97.1	2.1[a]	Chauvin et al. (2008)
$\mathbf{H_2L13^h}$	92.9	7.1	Deiters et al. (2008)
$\mathbf{H_2L13^i}$	89.2	7.9[a]	Chauvin et al. (2007)
$\mathbf{H_2L13^j}$	92.5	5.9	Deiters et al. (2009)
$\mathbf{H_2L13^k}$	94.6	4.5	Deiters et al. (2009)
$\mathbf{H_2L13^l}$	88.7	9.1	Deiters et al. (2009)

[a] 1:3 species.

TABLE 15 Stability of the $[Eu_2(\mathbf{L13^g})_3]$ helicate versus pH, several complexing agents, and Zn^{II}, as monitored by luminescence, at room temperature and pH 7.4 (Tris–HCl) (from Bünzli et al., 2008)

Parameter/chemical species	Eqs added	Time (h)	Loss in luminescence intensity (%)
pH	(pH 3)	24	No
	(pH 10)	24	No
EDTA	100	48	No
DTPA	100	24	10
Citrate	100	96	No
L-Ascorbate	100	96	10
Zn^{II}	10	24	10
	100		15

usually carried out in far less than 24 h. The ditopic ligand $\mathbf{H_2L13^g}$ has also been added to solutions of [Eu(EDTA)] and [Eu(DTPA)] and formation of the helicate was almost complete (92.5%) after 21 days in the first case, but partial in the second case. This shows that the helicate is more stable than the EDTA chelate and has stability comparable to that of the DTPA complex. Moreover, no ligand exchange occurs and transmetallation with zinc starts only to be problematic when 100 equivalents are added, a concentration far more important than the largest one found in biosystems.

Since no single crystal suitable for X-ray diffraction analysis could be obtained for the helicates with $\mathbf{H_2L13^{g-l}}$, Eu^{III} was chosen as a structural

luminescent tag to probe the chemical environment of the metal ions in the homobinuclear helicates. As shown in Table 10, the $^5D_0 \rightarrow {}^7F_0$ transition of all of the $[Eu_2(\mathbf{L13^{g-1}})_3]$ helicates is unique, as for $[Eu_2(\mathbf{L13^f})_3]$, pointing to the equivalence of the two metal ion sites. Moreover, its energy is predicted to be 17,231 cm^{-1}, taking into account the nephelauxetic effect described by Eq. (19) (see Section 3.5) for a N_6O_3 environment. The experimental values for the seven investigated helicates deviate by at most 4 cm^{-1} from this expected energy. The emission spectra recorded at low temperature (10 K) to remove the broadening due to vibronic contributions can be interpreted as arising from a species with idealized D_3-symmetry (Figure 100). In addition to the unique and very weak $^5D_0 \rightarrow {}^7F_0$ transition (forbidden in this symmetry), the $^5D_0 \rightarrow {}^7F_1$ transition displays a sharp component corresponding to the transition to the A_1 ligand-field sublevel and a second band corresponding to a transition terminating onto the split E sublevel. The A_1-E separation reflects the strength of the B_0^2 crystal-field parameter, which can be estimated to be around -600 cm^{-1} for $\Delta E(A_1\text{-E}) \approx 160$ cm^{-1} (Binnemans and Görller-Walrand, 1995), while the splitting of the E component, ΔE(E-E), is indicative of the distortion from the idealized D_3-symmetry. Data reported in Table 16 point to these two parameters being very similar for the seven studied helicates, meaning that the inner coordination sphere of the Eu^{III} ions is little affected by the various substituents grafted on the bis(benzimidazole)pyridine core. The luminescence decays confirm this finding in that they are usually single

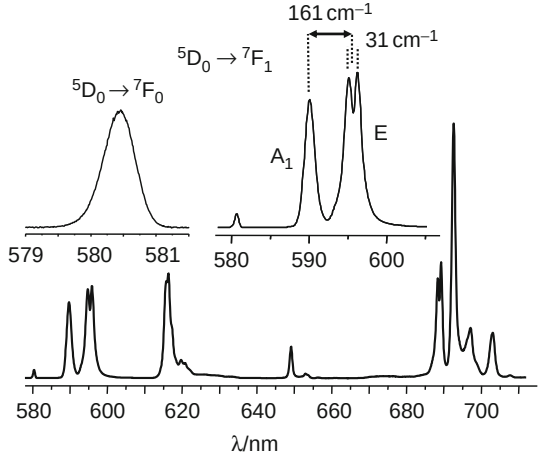

FIGURE 100 High-resolution emission spectrum of $[Eu_2(\mathbf{L13^g})_3]$ 10^{-4} M in water/glycerol 9/1, v/v at 10 K, under ligand excitation. Top: details of the $^5D_0 \rightarrow {}^7F_J$ ($J = 0, 1$) transitions (redrawn from Bünzli et al., 2008).

TABLE 16 Photophysical properties of solutions of the helicates $[Eu_2(\mathbf{L13})_3]$ in aqueous solution (Tris–HCl 0.1 M) at pH 7.4 and 295 K (references: see Table 14)

		$^5D_0 \rightarrow {}^7F_1$[a]			Q_{Eu}^{L}	τ_{rad} (ms)	Q_{Eu}^{Eu}	η_{sens}
Ligand	$^5D_0 \rightarrow {}^7F_0$ E_{exp} (cm^{-1})	ΔE(A–E) (cm^{-1})	ΔE(E–E) (cm^{-1})	q[b]	±15%	±0.3[c]	±15%[d]	±15%[e]
$\mathbf{H_2L13}$[f]	17,232	156	28	0.2	0.24	6.9	0.37	0.67
$\mathbf{H_2L13}$[g]	17,234	161	31	−0.1	0.21	6.9	0.36	0.58
$\mathbf{H_2L13}$[h]	17,233	146	31	−0.1	0.19	6.3	0.37	0.52
$\mathbf{H_2L13}$[i]	17,235	162	38	0.0	0.11	6.2	0.36	0.30
$\mathbf{H_2L13}$[j]	17,235	168	26	−0.1	0.15	6.4	0.40	0.38
$\mathbf{H_2L13}$[k]	17,235	160	34	−0.1	0.9	6.7	0.34	0.26
$\mathbf{H_2L13}$[l]	17,227	145	31	0.1	0.035	6.8	0.08	0.044

[a] At 10 K in water/glycerol 9/1, v/v; see text.
[b] Hydration number calculated from the phenomenological equation of Supkowski and de Horrocks (2002); estimated error: ±0.3.
[c] $Eu(^5D_0)$ radiative lifetime calculated from Eq. (15).
[d] Intrinsic quantum yield estimated from Eq. (10).
[e] Ligand sensitization efficiency obtained from Eq. (8).

exponential functions associated with a long Eu($^5D_0$) lifetime (2.3–2.4 ms), except in the case of $\mathbf{H_2L13^l}$. The latter ligand has too low a triplet state, so that back transfer occurs in the helicate, reducing both the lifetime and the quantum yield. In the case of $\mathbf{H_2L13^i}$ the decay measured under high-resolution conditions is biexponential, from which two lifetimes can be extracted, a longer one (2.2 ms) and a shorter one (0.53 ms) assigned to a hydrated species with a population of about 10%, reflecting the speciation reported in Table 14. A similar situation is met for $\mathbf{H_2L13^h}$, the shorter lifetime (0.89 ms) corresponding to a population of about 6%, again in line with the speciation for this system. Finally, an estimate of the hydration number by means of the phenomenological equation of Supkowski and de Horrocks (2002) taking into account lifetimes determined in water (τ_{H_2O}) and deuterated water (τ_{D_2O}) and correcting for second sphere effects, leads to a value which is essentially equal to zero.

$$q = 1.11 \times \left(\frac{1}{\tau_{H_2O}} - \frac{1}{\tau_{D_2O}} - 0.31 \right) \tag{135}$$

Insight into the energy transfer processes operating in the Eu^{III} helicates can be gained by analyzing the emission spectra and lifetimes in terms of Eqs. (8), (10), and (15) (Section 2.5). The relevant data are also listed in Table 16. Surprisingly, the radiative lifetime (6.2–6.9 ms) and intrinsic quantum yields (0.34–0.37, except for $\mathbf{H_2L13^l}$, 0.08) are the same for all the chelates, within experimental errors. This is again in line with an almost identical and fairly rigid nine-coordinate environment for the metal ions featuring very similar deactivation processes. Therefore, the differences observed in the overall quantum yields Q^L_{Eu}, which are among the largest reported for this ion in water, almost exclusively arise from differences in the ligand-to-metal energy transfers, as indicated by the sensitization efficiency η_{sens} which decreases about two-fold from 0.67 in [$Eu_2(\mathbf{L13^f})_3$] to 0.26–0.38 in [$Eu_2(\mathbf{L13^{i-k}})_3$], and to only 0.08 in [$Eu_2(\mathbf{L13^l})_3$], while it is much less affected in the remaining two helicates [$Eu_2(\mathbf{L13^{g,h}})_3$]. Comparing [$Eu_2(\mathbf{L13^g})_3$] and [$Eu_2(\mathbf{L13^h})_3$] shows that the lengthening of the polyoxyethylene pendant does not affect the photophysical properties. On the other hand, its grafting on the benzimidazole core in $\mathbf{H_2L13^i}$ is detrimental to both the thermodynamic stability (Table 14) and the photophysical properties of the helicates (Table 16). Finally, when the energy of the triplet state is lowered in $\mathbf{H_2L13^k}$ and $\mathbf{H_2L13^l}$, back transfer starts to be operative, henceforth the decrease in the quantum yield and sensitization efficiency, a phenomenon particularly acute for the latter ligand. It is common to discuss sensitization efficiency with respect to the energy gap between the emitting level and the 0-phonon energy of the triplet state and some phenomenological correlations have been found. For

instance, the quantum yield of Eu^{III} appears to be maximum when ΔE ($^3\pi\pi^*$–$^5D_0$) is around 2700 cm^{-1} in β-diketonates (Sato and Wada, 1970), between 2500 and 5000 cm^{-1} in polyaminocarboxylates (Latva et al., 1997), and only a few hundred cm^{-1} in Schiff base derivatives (Archer et al., 1998). For Tb^{III}, substantial quantum yields are obtained when ΔE ($^3\pi\pi^*$–$^5D_4$) > 1500 cm^{-1} for polyaminocarboxylates (Latva et al., 1997) or for complexes of *p*-substituted 2-hydroxyisophthalamides (Samuel et al., 2008b). On the other hand, the correlation between η_{sens} and $\Delta E(^3\pi\pi^*$–$^5D_0)$ for binuclear helicates is not obvious, especially when considering $\mathbf{H_2L13^f}$ and $\mathbf{H_2L13^i}$ (Figure 101, top).

In the case of Tb^{III}, the quantum yield is indeed very low when the ΔE ($^3\pi\pi^*$–$^5D_4$) gap is <1500 cm^{-1}. Vibration-assisted back energy transfer is operating, which results in very short lifetimes at room temperature (Table 10). The corresponding activation energy is around 1600–1800 cm^{-1} for $[Tb_2(\mathbf{L13^g})_3]$, roughly corresponding to the energy of CO and CC vibrations (Chauvin et al., 2008). As a consequence, hydration

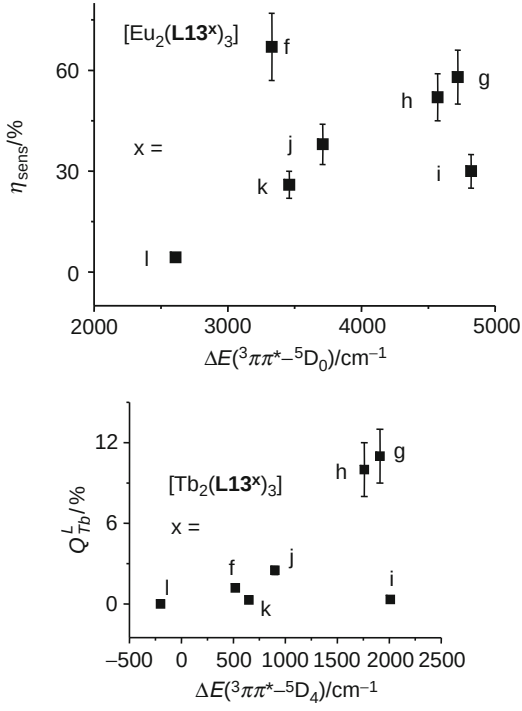

FIGURE 101 Top: sensitization efficiency of the $(\mathbf{L13^x})^{2-}$ ($x = j - l$) ligands for Eu^{III} luminescence versus the energy gap. Bottom: overall quantum yield of the $[Tb_2(\mathbf{L13^x})_3]$ helicates versus the energy gap (redrawn after Deiters et al., 2009).

numbers cannot be estimated with Eq. (135) because nonradiative deactivation by O–H vibrators is not the main quenching process in the helicates. Only two of the seven ligands $\mathbf{H_2L13^{f-l}}$ sensitize the Tb^{III} luminescence reasonably well, $\mathbf{H_2L13^{g}}$ and $\mathbf{H_2L13^{h}}$ (Figure 101, bottom) although quantum yields (11% and 9%, respectively) are not up to those reported in the literature for other chelates, ≈60% for water-soluble podates featuring 2-hydroxyisophthalamide antennae for instance (Petoud et al., 2003; Samuel et al., 2008a,b). The best ditopic ligand for both Eu^{III} and Tb^{III} is therefore $\mathbf{H_2L13^{g}}$ and it also sensitizes the luminescence of other ions such as Nd^{III}, Sm^{III} ($Q^{L}_{Sm} = 0.38\%$), and Yb^{III} ($Q^{L}_{Yb} = 0.15\%$).

6.3.2 Biocompatibility of the neutral water-soluble $[Ln_2(\mathbf{L13})_3]$ helicates

Absence of or small cytotoxicity is an important prerequisite for LLBs intended for the sensing and imaging of live biomaterials. Bünzli et al. (2008) have conducted WST-1 cell viability and proliferation tests on various cancerous cell lines, 5D10 (mouse hybridoma), Jurkat (human T leukemia), MCF-7 (human breast carcinoma), HeLa (human cervical adenocarcinoma), as well as on a noncancerous line, HaCat (human keratinocyte). Typically, cells are grown in RPMI-1640 supplemented cell culture medium containing various concentrations of the helicate, at 37 °C in an atmosphere containing 5% CO_2. The viability test is performed at several time intervals between 0.5 and 24 h and selected results are reported in Table 17 while a typical example of the influence of $[Eu_2(\mathbf{L13^{i}})_3]$ on cell proliferation is shown on Figure 102. These data clearly demonstrate that the cytotoxicity of all the tested helicates is very small, with half-maximal inhibitory concentration $IC_{50} > 500\ \mu M$. Some of these results were also confirmed by the lactase dehydrogenase (LDH) test which allows an assessment of damages caused to the cell membrane by determining the LDH leakage out of the cell; in the case of $[Eu_2(\mathbf{L13^{i}})_3]$, this leakage was found to be less than 4% for the three tested cell lines, Jurkat, 5D10, and MCF-7 (Chauvin et al., 2007). Not only cell viability and proliferation are not affected by the presence of the binuclear LLBs in the cell culture medium but, also, their morphology remains unchanged. No swollen nuclei or visible granules developed upon incubation of HeLa cells during 7 h with $[Eu_2(\mathbf{L13^{g}})_3]$ 100 μM for instance. As a comparison, a popular nucleic acid intercalating dye, acridine orange (AO), induces swollen nuclei after the same incubation time, and necrotic cells are seen after 24 h (Figure 103). These results point to the lanthanide helicates being indeed biocompatible luminescent tags (Song et al., 2008c).

TABLE 17 Selected cell viability values (%) as determined from the WST-1 test after incubation for 24 h at 37 °C in RPMI-1640 containing various concentrations of $[Eu_2(\mathbf{L13})_3]$ helicates

Ligand	c (μM)	Jurkat	$^5D_{10}$	MCF-7	HeLa	References
None	0	100	100	100	100	
$\mathbf{H_2L13}^{f}$	125	NA	NA	NA	111 ± 3	Bünzli et al. (2008)
$\mathbf{H_2L13}^{g}$	125	92 ± 16	93 ± 1.1	92 ± 13	88 ± 3	Chauvin et al. (2008) and Vandevyver et al. (2007)
	250	101 ± 4	99 ± 1	102 ± 7	101 ± 1	Chauvin et al. (2008) and Vandevyver et al. (2007)
	500	107 ± 4	89 ± 4	101 ± 1	108 ± 2	Chauvin et al. (2008) and Vandevyver et al. (2007)
$\mathbf{H_2L13}^{h}$	500	NA	NA	NA	101 ± 1	Deiters et al. (2008)
$\mathbf{H_2L13}^{i}$	125	90 ± 1	88 ± 1	89 ± 1	119 ± 2	Chauvin et al. (2007)
	250	89 ± 1	87 ± 2	87 ± 1	105 ± 6	Chauvin et al. (2007)
	500	89 ± 1	90 ± 6	89 ± 1	110 ± 3	Chauvin et al. (2007)
$\mathbf{H_2L13}^{k}$	500	NA	NA	NA	101 ± 1	Deiters et al. (2009)

Data are averages of 3–4 independent determinations.

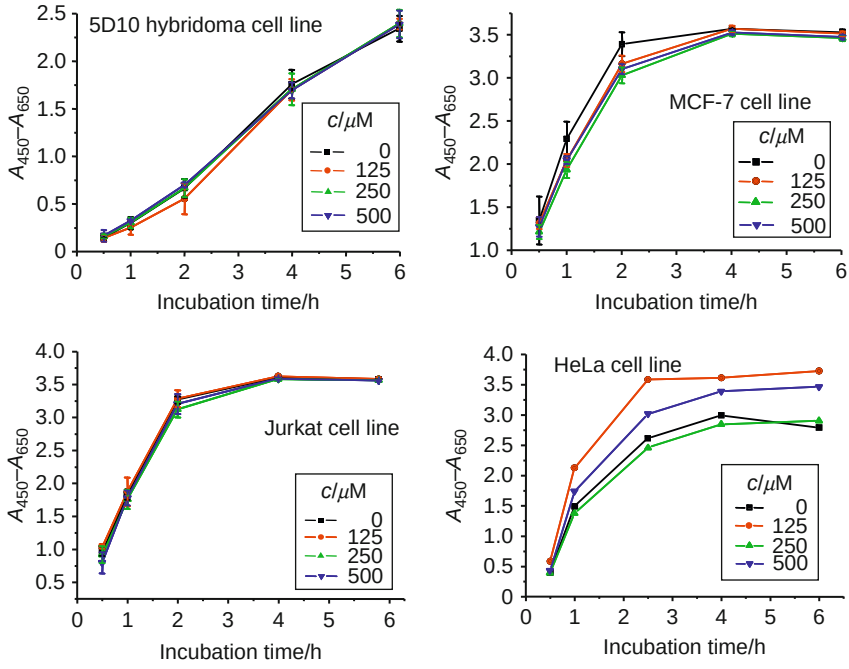

FIGURE 102 Cell proliferation of various cancerous cell lines when incubated with $[Eu_2(\mathbf{L13^i})_3]$ (redrawn from Chauvin et al., 2007).

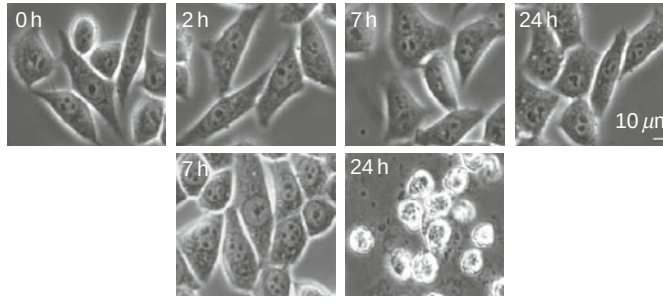

FIGURE 103 Phase contrast microscopy of HeLa cells exposed to 100 μM $[Eu_2(\mathbf{L13^g})_3]$ (top row) or 3.2 μM acridine orange (bottom row) at 37 °C for the indicated time interval (reproduced by permission from Song et al., 2008a, © The Royal Society of Chemistry, 2008).

6.3.3 Uptake of the neutral water-soluble $[Ln_2(\mathbf{L13})_3]$ helicates in living cells

Most of the work published to date with lanthanide helicates as LLBs has been performed on the easy-to-grow HeLa cell line (Bünzli et al., 2008). When incubated with the $[Ln_2(\mathbf{L13})_3]$ helicates, live HeLa cells uptake the LLBs in a concentration-dependent way (Chauvin et al., 2007, 2008; Deiters et al., 2008, 2009; Song et al., 2008c; Vandevyver et al., 2007). There are essentially two mechanisms by which an exogenous substance can penetrate membrane cells. The first one is ''tunneling'' through the hydrophobic cell membrane through channels having usually some specificity; this occurs when the molecular weight of the penetrating molecule is not too large (typically < 800 Da). Otherwise, a process known as endocytosis is operating. In this process the cell membrane engulfs the incoming molecule to form a pocket which escapes into the cell to produce a vesicle filled with extracellular fluid, including the exogenous substance. The vesicle moves into the cytosol and then merges with endosomes and liposomes. As the $[Ln_2(\mathbf{L13})_3]$ helicates have molecular weight around 2600–3100 Da, this mechanism is likely to occur. An easy way to prove it is to conduct the uptake experiments at 4 °C because endocytosis is not occurring at low temperature. As depicted on Figure 104, the total emitted light by HeLa cells grown under the usual conditions in absence or in presence of an helicate is the same at low temperature. On the other hand, if the background noise remains the same at 37 °C in absence of helicate in the culture medium, the intensity increases considerably when the cells are loaded with the helicate. Additional proofs for this receptor-mediated uptake mechanism come from the use of endocytosis inhibitors. When the same HeLa cells are incubated with the Eu^{III} helicate in a hypertonic medium containing 0.45 M of sucrose, a 92% decrease in the uptake of the LLB is observed because hypertonicity prevents the association

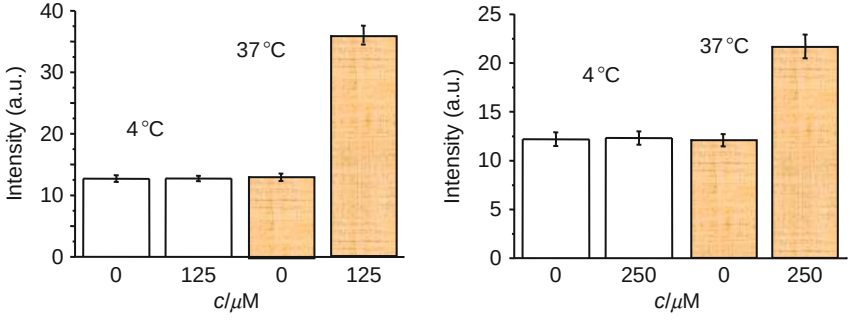

FIGURE 104 Integrated emitted light by HeLa cells grown in absence and presence of $[Eu_2(\mathbf{L13^g})_3]$ 125 μM (left) or $[Eu_2(\mathbf{L13^i})_3]$ 250 μM (right) at 4 and 37 °C (redrawn from Chauvin et al., 2007, 2008).

between the receptor-LLB complex and the clathrin lattice to form the coated pit; it also blocks the receptor clustering necessary to the formation of the endosomes. Similarly, potassium depletion blocks the receptor clustering and indeed, low concentration of this ion in the culture medium results in a decrease of 83% of the LLB uptake in the cells (Song et al., 2008c).

Initial experiments with a conventional luminescence microscope equipped with the relevant filters point to the $[Ln_2(\mathbf{L13})_3]$ helicates penetrating into HeLa cells in a concentration- and time-depending manner. In Figure 105 (top), the Eu^{III} luminescence is plotted versus the concentration of the $[Eu_2(\mathbf{L13})_3]$ helicates in the culture medium after an incubation time of 7 h at 37 °C. The luminescence emitted by the $[Eu_2(\mathbf{L13^i})_3]$ chelate at all concentrations is understandably smaller than the light emitted by the two other helicates, in view of it smaller quantum

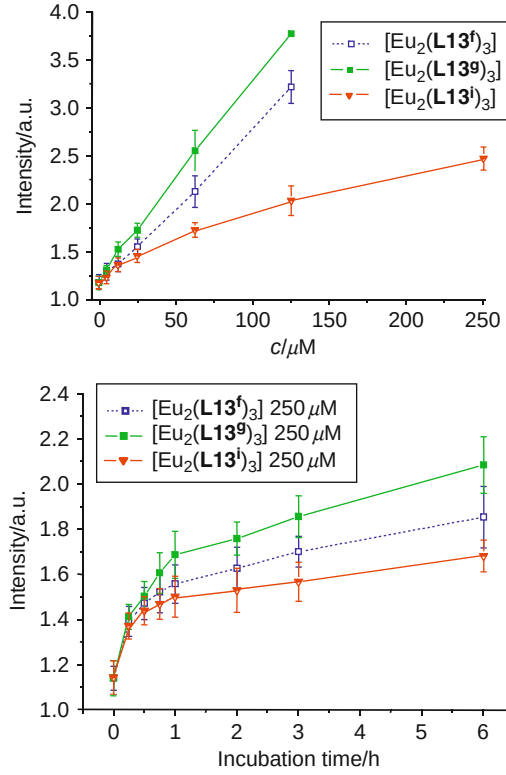

FIGURE 105 Integrated luminescence intensity from $[Eu_2(\mathbf{L13})_3]$ helicates internalized in HeLa cells versus (top) the concentration of the LLB in the culture medium and (bottom) the incubation time (redrawn from Bünzli et al., 2008).

yield, 11% versus 21% and 24%, for $[Eu_2(\mathbf{L13^g})_3]$ and $[Eu_2(\mathbf{L13^f})_3]$, respectively (Table 10). On the other hand, $[Eu_2(\mathbf{L13^g})_3]$ appears to be the best cell-staining agent despite its somewhat reduced quantum yield compared to $[Eu_2(\mathbf{L13^f})_3]$. It is noteworthy that readable images can be obtained for a helicate concentration in the culture medium as low as 10 μM (Deiters et al., 2008). With a time-resolved luminescence microscope (TRLM, Connally and Piper, 2008), this limit is still lower, elimination of the background auto-fluorescence of the cells improving the signal-to-noise ratio considerably (Figure 106). The time-course experiments depicted on the bottom of Figure 105 confirm that $[Eu_2(\mathbf{L13^g})_3]$ is the best cell-staining helicate since for a given time, its intracellular luminescence is always brighter compared to the two other stains (Bünzli et al., 2008).

An important information is to find out where the luminescent helicates are located within the cytosol of the live cells. Several experiments have been conducted, including colocalization experiments in which the cells were incubated successively with the helicate and with organic stains known to localize in specific compartments of the HeLa cells, such as acridine orange (AO) which stains the cell nuclei. Part of these experiments are shown on Figure 107. In the top part, the helicate is shown, after a short incubation time, to be entrapped into isolated vesicles which diffuse into the cytoplasm and the size of which is usually around 0.5–1.5 μm, with shapes ranging from flecks, spheres to ellipsoids.

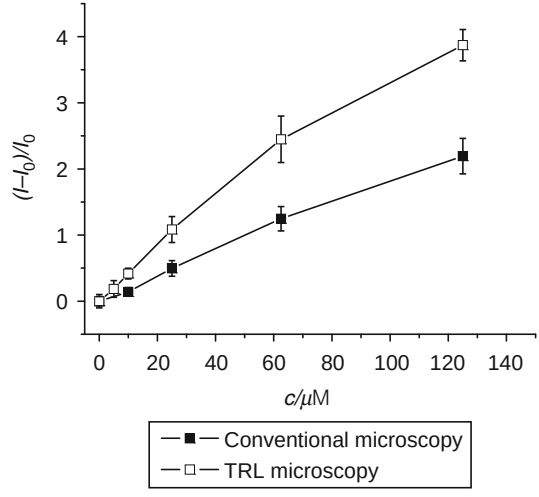

FIGURE 106 Plot of the luminescence intensity ratio $(I - I_0)/I_0$, where I_0 is the intensity of the background noise for HeLa cells incubated during 6 h at 37 °C with various concentrations of $[Eu_2(\mathbf{L13^g})_3]$ (redrawn from Song et al., 2008a).

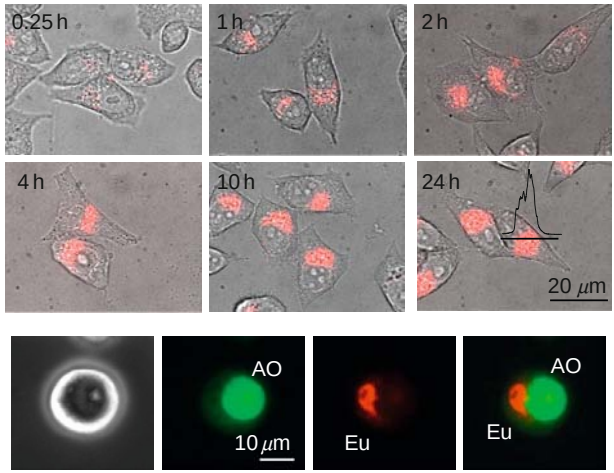

FIGURE 107 Top: successive TRLM images showing the penetration of the LLB into HeLa cells incubated at 37 °C in presence of $[Eu_2(\mathbf{L13^g})_3]$ 100 μM (redrawn from Song et al., 2008a). Bottom: colocalization experiment with AO, pointing to the helicate remaining out of the cell nucleus (redrawn from Chauvin et al., 2008).

After 1 h of incubation, vesicles have concentrated around the nucleus, as ascertained by the counter-staining experiment with AO (Figure 107, bottom). In fact, other counter-staining experiments with the Lyso-Tracker blue (localizing in the lysosomes), Golgi-Tracker (Golgi apparatus), and ER-Tracker (endoplasmatic reticulum) demonstrate a localization in the endoplasmatic reticulum (Song et al., 2008a).

All the helicates with ligands $\mathbf{H_2L13}$ behave similarly: lengthening of the polyoxyethylene chain (Deiters et al., 2008) or adding various substituents in an effort to shift the excitation wavelength toward the visible (Deiters et al., 2009) does not affect their cell-staining properties. The best luminescent tag with respect to lengthening the excitation wavelength is $[Eu_2(\mathbf{L13^l})_3]$ with absorption maxima at 350 and 365 nm and an ability to be excited at 405 nm by a confocal microscope (Deiters et al., 2009).

Egress of the LLBs from the cells is slow and both the emission spectra recorded in cellulo and the excited state lifetimes for Eu^{III} or Tb^{III} helicates, as well analysis of the Eu($^5D_0 \leftarrow {}^7F_0$) transition, prove that the LLBs are essentially undissociated in the intracellular medium. The intracellular concentration of the helicates was determined after incubation of HeLa cells 12 h with 25 μM of LLB by measuring the lanthanide concentration with the time-resolved Delfia© method. It was found to be surprisingly high: under the loading conditions used, there is, on average, 8.8×10^{-16} mol $[Eu_2(\mathbf{L13^h})_3]$ per cell, which, taking into account an estimated cell volume between 2600 and 4200 μm^3, translates into 0.21–0.34 mM

(Deiters et al., 2008). Similar concentrations were found for the helicates with $\mathbf{H_2L13^f}$, $\mathbf{H_2L13^g}$, $\mathbf{H_2L13^i}$ (Bünzli et al., 2008), and $\mathbf{H_2L13^l}$ (Deiters et al., 2009), as well as for complexes with cyclen derivatives (Yu et al., 2006).[1]

Other cell lines can be stained (MCF-7, HaCat, for instance) and multistaining with Sm^{III}, Eu^{III}, Tb^{III}, and even Yb^{III} is possible. In the latter case, no image was obtained, but an emission spectrum could be measured *in cellulo* (Chauvin et al., 2008; Deiters et al., 2009). The next step will be to bioconjugate the helicates with specific peptides and proteins in order to perform targeting experiments. The polyoxyethylene pendants of ligand $\mathbf{H_2L13^g}$ have been derivatized with carboxylic acid, amine, and pthalimide groups for this purpose.

6.3.4 The $[Eu_2(L13^g)_3]$ helicate as luminescent sensor for DNA and PCR products

Many biological and diagnostic applications require accurate quantification of nucleic acids extracted from various sources (e.g., blood, cells, bones). In addition to spectrophotometry, several fluorometric DNA assays have been proposed based on intercalating fluorescent reagents which display enhanced fluorescence upon interaction with DNA. Many of these dyes have high autofluorescence, which limits the accuracy of the assay or its sensitivity, and some are quite specific with respect to the nature of the sample. Given the photophysical properties of $[Eu_2(\mathbf{L13^g})_3]$, Song et al. (2008b) have proposed a rugged and versatile assay applicable to several different types of DNA (single-stranded, ssDNA; double-stranded, dsDNA; circular, cDNA) and to small PCR products, that is, having less than 500 base pairs (bp). The principle of the method takes advantage of the quenching of the Eu^{III} luminescence induced by acridine orange (AO). This quenching is purely dynamic, with a bimolecular rate constant of $k_q = 2.7 \times 10^8\,M^{-1}s^{-1}$ and a quenching constant $K_D = 6.7 \times 10^5\,M^{-1}$ (see Eq. (136), where I and I_0 are the luminescence intensities in absence and in presence of the quencher and τ_0 is the observed lifetime in absence of quencher). This is the reason why AO has been preferred to ethidium bromide (EB) which induces simultaneous dynamic and static quenching processes.

$$\frac{I_0}{I} = 1 + K_D[AO] = 1 + k_q\tau_0[AO] \tag{136}$$

When DNA is added to a solution containing $[Eu_2(\mathbf{L13^g})_3]$ and AO, the latter intercalates into the nucleic acid and Eu^{III} luminescence is restored (Figure 108). In TRD mode, detection limits are in the range

[1] This high concentration is so surprising that both the Durham and Lausanne groups have mentioned concentrations in the micromolar range in their respective papers; however, careful recalculation from the number of complex molecules found per cell indeed yields figures in the mM range.

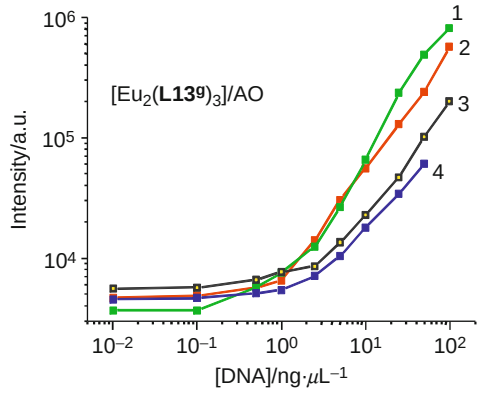

FIGURE 108 Luminescence intensity in TRD mode upon addition of DNA to [Eu$_2$(**L13^g**)$_3$] 0.1 μM + AO 33.1 μM in 0.1 M Tris–HCl buffer; 1: plasmid DNA; 2: actin sens-2 DNA; 3: salmon sperm DNA; 4: λDNA/*Hind*III (redrawn after Song et al., 2008b).

TABLE 18 Influence of potentially interfering analytes on the luminescence intensity of the DNA analytical system based on the [Eu$_2$(**L13^g**)$_3$]–AO mix[a] (from Song et al., 2008b)

Compound	c (mM)	ΔI (%)	Compound	c (mM)	ΔI (%)
BSA	10[b]	+ 6.2	Cu^{II}	0.1	− 32.9
Glucose	0.1	+ 3.2	Fe^{II}	0.1	+ 0.021
SDS	0.2[c]	+ 9.2	Fe^{III}	0.1	− 3.2
Na_2HPO_4	0.1	− 0.03	Co^{II}	0.1	− 14.9
EDTA	1	+ 1.1	Mn^{II}	0.1	− 9.4
Ca^{II}	0.1	+ 0.34	Citrate	0.1	+ 3.6
Mg^{II}	0.1	+ 0.89	Ascorbate	0.1	− 6.5
Zn^{II}	0.1	− 1.5	Urate	0.1	+ 4.6

[a] [Eu$_2$(**L13^g**)$_3$] 0.1 μM, 10 μg ml^{-1} AO, and 100 ng μl^{-1} sheared salmon sperm DNA in 0.1 M Tris–HCl buffer, pH 7.4.
[b] In ng μl^{-1}.
[c] In mass %.

0.2 – 0.7 ng μl^{-1} for the four investigated DNAs. Reinstatement of luminescence can also be monitored by measuring the Eu($^5D_0$) lifetime which increases when DNA is added, but the sensitivity is about ten-fold less. The method is quite rugged, being insensitive to pH in the range 3–10 and to the presence of many potentially interfering species added in 100- to 1000-fold excess (see Table 18). Only Cu^{II} and Co^{II} have a detrimental influence, probably because they induce transmetallation of the helicate.

Finally, smaller dsDNA fragments, such as PCR products are also detected by this method, which compares very well with existing

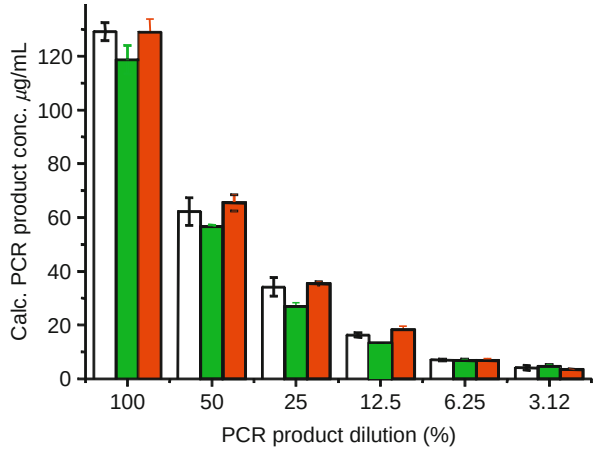

FIGURE 109 Comparison between three DNA quantification methods used in the assay of a PCR product (347 bp fragment of the actin gene); from left to right: UV absorption, PicoGreen® -dye method, and [Eu(**L13^{8}**)$_3$]/AO method (redrawn after Song et al., 2008b).

procedures (Figure 109). An additional advantage of the proposed protocol is the measurement of Eu^{III} luminescence with a cheap, easy-to-use, and commercially available time-resolved spectrometer.

7. BIMETALLIC POLYNUCLEAR nd–4f HELICATES

7.1 Choosing the d-transition partner

Metal ions from the d-transition series display rich spectroscopic and magnetic properties which are extremely sensitive to the metal-ion environment, contrary to f-transition ions, in view of the outer nature of d-orbitals allowing easy mixing with ligand orbitals. In addition, these ions have usually strong stereochemical requirements which may prove useful in preorganizing ligand strands and subsequently facilitating complexation of 4f ions. Combining the unique properties of both series of ions into a single molecular edifice is therefore appealing. For instance, despite its programmed weakness resulting from the lack of expansion of the 4f-orbitals, the magnetic coupling between d and 4f ions has been and is still the focus of much attention (Barta et al., 2008; Benelli, 2002), especially when it comes to searching for single molecule magnets (Costes et al., 2006; Novitchi et al., 2008). On the other hand, a wealth of efforts have been devoted by the authors of the present chapter for designing adequate ligands able to simultaneously recognize an isolated d–f ion pair while leading to triple-helical molecular assemblies with programmed magnetic and/or photophysical functionalities (Bünzli

and Piguet, 2002, 2005; Bünzli et al., 1997; Piguet, 1996; Piguet and Bünzli, 1996, 1998, 1999; Piguet et al., 2000). Most of this work relies on the exciting possibility to tune the properties of one ion by intramolecular communication with the other metal along the C_3-axis of the binuclear helicate.

There are three main mechanisms through which two metal ions may interact and exchange information. (i) Through-bond interaction requiring large orbital overlap, which compels the two protagonists to be located close enough from each other for their valence orbitals to interact; this distance should be smaller than 40 pm for instance for noticeable magnetic interactions to operate between nd and 4f ions or between two 4f ions; as an example, the coupling parameter J for antiferromagnetic coupling of two R^{III} ions is usually on the order of -0.1 cm^{-1} when the intermetallic distance is in the range 35–40 pm and drops sharply with increasing distance. (ii) Through-space interaction arising via multipolar energy transfers; one common mechanism for this is Förster's dipole–dipolar model with a $1/r^6$ dependence (see Section 4.4, Eqs. (77) and (78)); such transfers have been detected over very large distances, up to 10 nm when the donor is a lanthanide ion. (iii) Mechanical coupling of the two metal ions, that is, modification of the inner coordination sphere of one ion, the coordination of the other metal ion inducing some deformation of the ditopic ligand linking the two centers; this is well documented in solid state networks, particularly with respect to thermal magnetic hysteresis.

In the case of the 4f–4f polynuclear helicates, the polytopic ligands described in Sections 3–6 position the two lanthanide ions at a distance of about 90 pm in the final supramolecular assemblies. In addition, the various tridentate coordination moieties are separated by methylene bridges which prevent electronic density from flowing between these units. As a result, the lanthanide ions are isolated and can only communicate by a through-space mechanism, as seen in Section 4.4. If the bis (tridentate) ligands are modified into tridentate-bidentate guests to match the often observed octahedral coordination of nd transition metal ions, it is foreseen that the intermetallic distance will not be much affected. Therefore in this case again, only the last two types of intermetallic communications can be programmed in the self-assembled molecular edifices. The extensive work performed on nd–4f helicates since 1995 by the authors has pursued the following main objectives:

(1) Inducing a preorganization of the ligand strands to provide a less energetic pathway facilitating lanthanide coordination during the self-assembly process. Initially, a spectroscopically silent, nonmagnetic ion, Zn^{II}, was chosen for this purpose (Piguet et al., 1995c) since, in addition, R^{III} ions are often used as replacement probes for this cation when studying the properties of Zn^{II} sites in proteins and

other biological molecules. In this way, it was expected that the facial ZnL_3 tripod will serve as a dedicated receptor for the selective complexation of R^{III} ions. This strategy was then expanded to include more transition metal ions in the *fac*-ML_3 noncovalent tripods which self-assemble with R^{III} ions to yield the HHH-[$RM^{II/III}L_3$] supramolecular triple-helical edifices (M = Cr, Fe, Co, Ru, and Os).

(2) Isolation of enantiomerically pure helicates. One disadvantage of Zn^{II} is its relatively large lability with respect to transmetallation, so that successful attempts have been made to replace it with Cr^{III} which, in addition to be optically active (see point 4 below), is kinetically inert, opening the way to designing chiral helical luminescent probes (Cantuel et al., 2004). Another possibility to produce inert 3d–4f helicates is to insert Co^{II} ions into the self-assembled edifices, followed by a mild and selective oxidation into the low-spin diamagnetic, and kinetically inert Co^{III} ion (Rigault et al., 1998).

(3) Modification of Fe^{II} spin-crossover parameters through mechanical coupling with $R^{III}L_3$ moieties containing different lanthanide ions. Indeed, minute distortions of the octahedral, or pseudo-octahedral, coordination environment of the d^6 transition metal ion leads to sizeable changes in these parameters and/or in the thermal hysteresis loop (Kahn and Kodjovi, 1999). This study is coupled with the investigation of the electrochemical behavior of the MLn helicates (Fe^{II}/Fe^{III}, Co^{II}/Co^{III}, Ru^{II}/Ru^{III}, and Os^{II}/Os^{III}).

(4) Tuning the photophysical properties of one ion by means of energy transfer from the other ion. The energy transfer may take place in either direction, depending on the effect sought for. A first candidate is Cr^{III} the $3d^3$ electronic structure of which is such that its first electronic excited state (^2E_g in octahedral symmetry) is fairly insensitive to ligand-field effects and has a spin multiplicity different from the ground state ($^4A_{2g}$) leading to a bright red, and long-lived phosphorescence. Excitation can be achieved through the spin-allowed $^4T_{2g} \leftarrow {}^4A_{2g}$ transition which is very sensitive to the ligand-field strength and can therefore easily be tuned. Partial overlap of the Cr^{III} levels with those of several lanthanide ions has prompted the introduction of Cr^{III} as sensitizer for near-infrared emissive R^{III} ions such as Nd^{III} (e.g., in neodymium YAG lasers), Er^{III}, and Tm^{III}. Feeding the excited state of a NIR-emissive R^{III} ion through the long-lived ^2E_g level of Cr^{III} will artificially increase its lifetime, providing an original handle to control this parameter. Other luminescent d-transition metal ions such as Ru^{II} and Os^{II} possess long-lived metal-to-ligand charge-transfer states (^{3}MLCT) which also overlap with R^{III} electronic levels facilitating energy transfer from these states via either conjugated bridging ligands (Herrera et al., 2006b; Lazarides et al., 2008) or through-space (Förster-like) energy transfer.

7.2 Tailoring adequate pentadentate ligands

The design of adequate ligands for the self-assembly of nd–4f isolated pairs into triple-stranded helical molecular edifices is straightforward in that it only requires modification of one of the tridentate coordination units of the bis(tridentate) receptors presented earlier, all the other modulation possibilities described for the assembly of 4f–4f helicates remaining open. One tridentate unit is simply trimmed to a bidentate chelating one featuring an α,α'-diimine group and allowing pseudo-octahedral coordination of a d-transition metal ion (Figure 110). Such pentadentate ligands are programmed for the simultaneous recognition of a nd–4f pair of ions by strict self-assembly under stoichiometric conditions, the three ligand strands being designed so that they will adopt a ''natural'' HHH orientation in the final binuclear edifices, with the three bidentate chelating units bound to the nd transition metal ion. They appear to be optimally designed for this purpose since a maximum of ion–dipole bonds will be produced upon self-assembly of three ligand strands with a

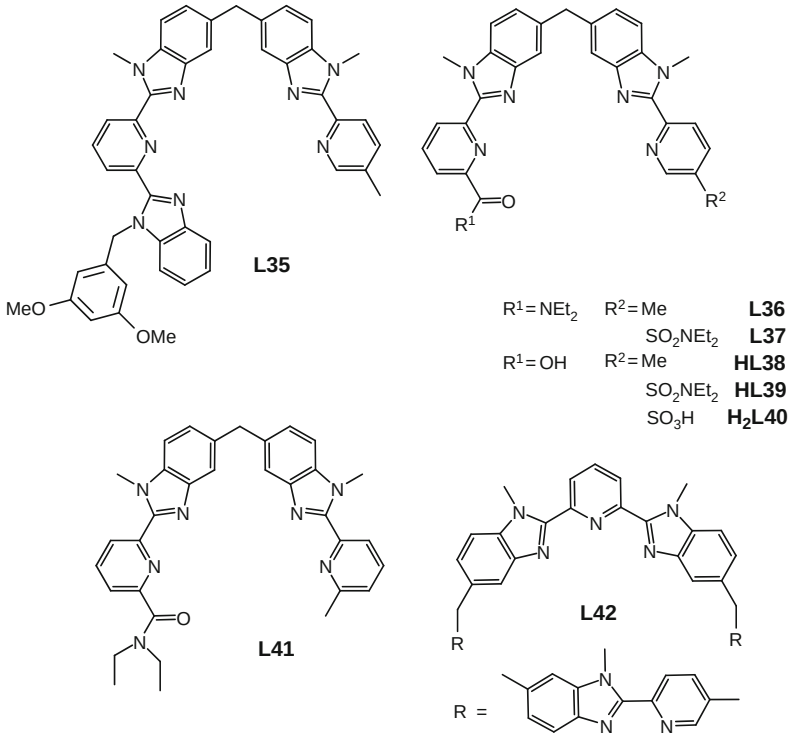

FIGURE 110 Segmental ligands for nd–4f triple-stranded heterometallic helicates.

stoichiometric mix of nd and 4f ions. Indeed, the receptor ligands obey the maximum occupancy rule (Lehn and Eliseev, 2001), henceforth maximizing the favorable part of the enthalpic contribution to the overall free energy change during the recognition process, especially if this process is conducted in a weakly coordinating solvent such as acetonitrile. The entropic contribution is also maximized through a large chelate effect. Finally, the stereochemical preferences of both nd and 4f metal ions are met by the ligand design with the methylene bridge inducing the right helical twist when the ligand strands wrap around the metal ions. Programming higher nuclearity for the self-assembled edifices translates into increasing the number of coordinating units, either bidentate or tridentate, along the ligand strand so that incoming metal ions can ''read'' the information specific to their coordination requirements.

The polydentate ligands investigated so far are schematized on Figure 110. Ligand **L35** with N_3 and N_2 chelating units is the pendent of the bis(tridentate) receptor **L11** (Section 3.1, Figure 41). The 3,5-dimethoxy-benzyl group has been introduced both for increasing solubility and for its easy recognition in mass spectra when it is cleaved from the ligand backbone. Ligands **L36–L41** with N_2O and N_2 chelating units correspond to the hexadentate ligand **L13^b**, while the N_2-N_3-N_2 heptadentate host **L42**, tailored for trinuclear M*R*M recognition, is derived from ligands **L27–L28** (Section 3.1, Figure 42).

As for the hexadentate ligands, the synthesis of the bidentate-tridentate receptors relies on the modified Phillips coupling reaction. The starting point in the synthesis of **L35** is the production of the nonsymmetrical **Int-1** intermediate by monoacylation of symmetrical 4,4′-methylene-2,2′-dinitrobis(benzamide) with 6-methylpyridine-2-carbonyl chloride obtained from the parent carboxylic acid (Figure 111). A second acylation with the adequately derivatized picolinic acid leads to the key intermediate *N*-(2-nitroaryl)arenecarboxamide. *In situ* reduction of the latter with metallic iron followed by cyclization under mild acidic conditions represents the key step of the synthetic path for the formation of aromatic 1H-benzimidazole rings (Piguet et al., 1994). Similar reactions are used for **L36** (Piguet et al., 1996) and **L42** (Piguet et al., 1994), see Figure 112. Ligand **HL38** is obtained by hydrolysis of **L36** with potassium hydroxide (Edder et al., 1997).

A slightly different starting dinitro compound (**Int-2**) is used for the synthesis of ligands **L37**, **HL39**, and **H2L40** but the overall procedure is the same, with **HL39** obtained by hydrolysis of **L37** with KOH and **H_2L40** by hydrolysis of **HL39** with concentrated sulfuric acid. Introduction of sulfonate groups is generally achieved by regioselective sulfonation occurring during the final step of the synthetic scheme because the purification of sulfonated compounds is time-consuming. However in the case of ligands **L37-H_2L40**, the lack of strong electronic effects favoring

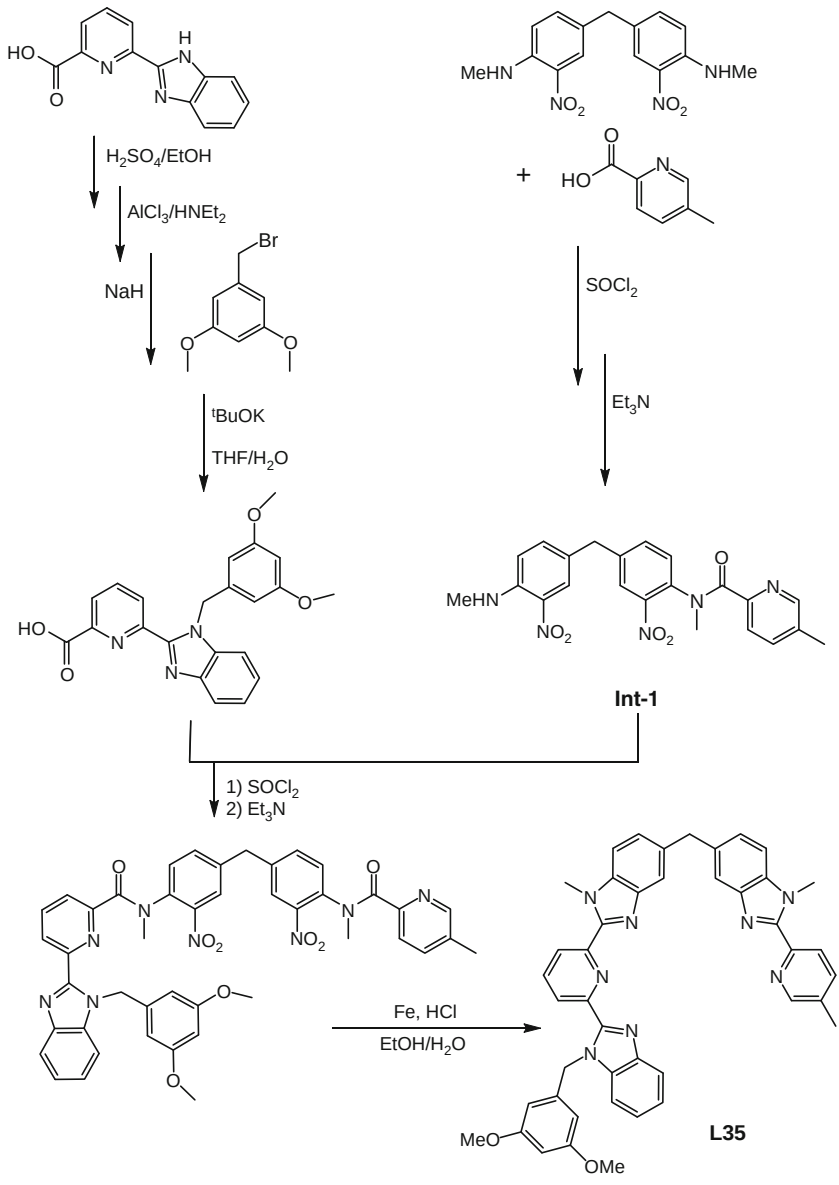

FIGURE 111 Synthetic scheme for ligand **L35** (redrawn after Piguet et al., 1994).

one particular carbon for the electrophilic attack in the targeted pentadentate ditopic ligands and the considerable number of aromatic carbon atoms suitable for sulfonation required a different approach in which 2-methyl-5-pyridinesulfonic acid (obtained by reacting 2-picoline with

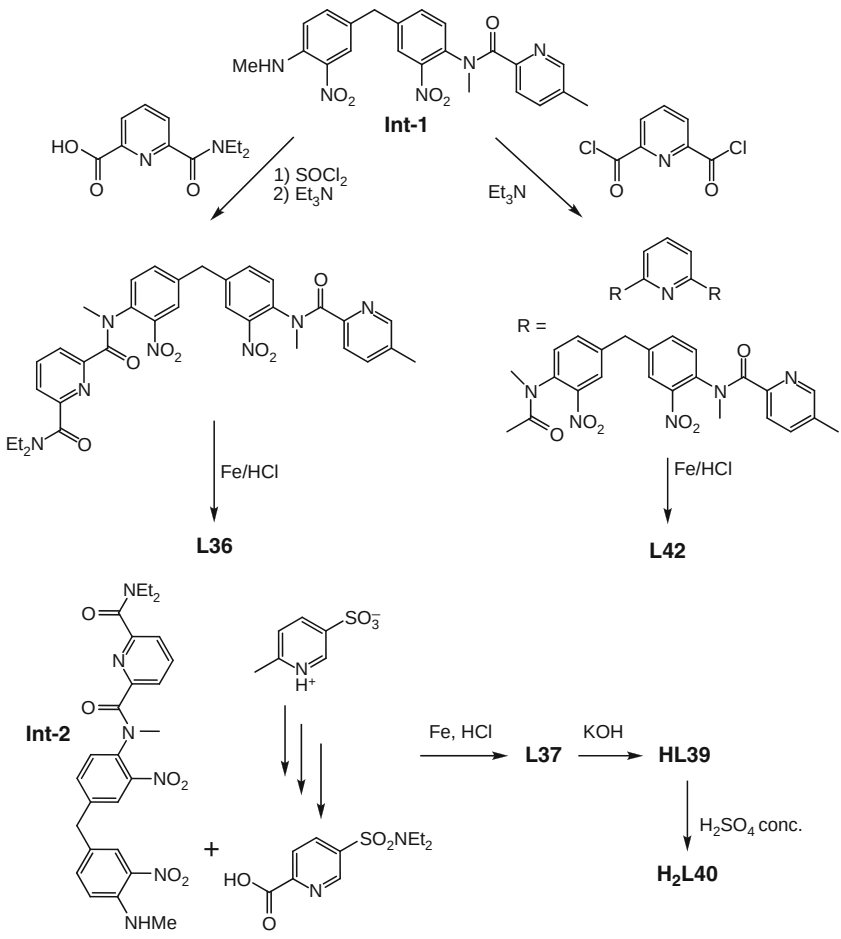

FIGURE 112 Top: synthetic scheme for ligands **L36** (Piguet et al., 1996) and **L42** (Piguet et al., 1994); for the synthesis of the starting dinitro compound **Int-1**, see Figure 111. Bottom: synthetic route to ligands **L37**, **HL39**, and **H_2L40** (Edder et al., 2000).

oleum followed by extensive separation/purification) was coupled to **Int-2** (Edder et al., 2000).

7.3 Preparation of the nd–4f helicates in acetonitrile and corresponding speciation

The self-assembly of helicates is a relatively complex process (see Section 3.3), even for homometallic binuclear 4f–4f species. Introducing dissymmetry both in the receptor ligand and in the nature of the metal

ions renders the process yet more intricate. Experimental techniques such as NMR and ES-MS are ideally suited for characterizing the species formed in solution, an essential step before quantifying the stability of the binuclear helicates and other species with UV-vis titrations. NMR spectra will be discussed in the following section, together with solution structures so that we concentrate here on ES-MS data. The binuclear helicates are easy to recognize in the ES-MS spectra because the molecular peak is often accompanied by adduct ions with perchlorates (Hopfgartner et al., 1994) or triflates, and can be further characterized by their isotopic distributions. The species evidenced during the titration of ligands **L35**–**L37**, **HL38**, and **L41** 10^{-4} M in acetonitrile by metal perchlorates or triflates are reported in Table 19. When $R^{III}/M^{II/III}$ mixtures are used, the preponderant species is always by far the RML_3 helicate, at stoichiometric ratio, whatever the lanthanide and the d-transition metal ions are; this is particularly well illustrated for **L36** for which lanthanide helicates with Zn^{II}, Cr^{III}, Fe^{II}, Co^{II}, Ru^{II}, and Os^{II} have been investigated. Similarly to the 4f–4f helicates, stability constants have been determined by electronic absorption spectroscopy, with the same limitations, for example, the difficulty of detecting poorly stable intermediates or complexes due to correlated spectra.

Titration of the ditopic pentadentate ligands with either a kinetically labile d-transition metal ($M = Fe^{II}$, Co^{II}, Zn^{II}) or a lanthanide ion often leads to the observation of several different species in equilibrium. On the other hand, the RML_3 helicate is always the most abundant species when the titrant is a stoichiometric R^{III}/M^{II} mixture, when the total ligand concentrations is $>10^{-3}$ M, and in presence of poorly coordinating anions; the other complexes are often not detected in NMR spectra under these conditions. The spectrophotometric data have been fitted to the following set of equations (A stands for nd (M) or for 4f (R) ion, charges are omitted for clarity):

$$\mathrm{A} + n\mathbf{L}\boldsymbol{k} \rightleftarrows [\mathsf{A}(\mathbf{L}\boldsymbol{k})_n] \quad \beta_{1,n}^{\mathrm{A,L}k} \tag{137}$$

$$2\mathrm{A} + n\mathbf{L}\boldsymbol{k} \rightleftarrows [\mathsf{A}_2(\mathbf{L}\boldsymbol{k})_n] \quad \beta_{2,n}^{\mathrm{A,L}k} \tag{138}$$

$$3A + 2\mathbf{L}\boldsymbol{k} \rightleftarrows [\mathsf{A}_3(\mathbf{L}\boldsymbol{k})_2] \quad \beta_{2,3}^{\mathrm{A,L}k} \tag{139}$$

$$R + \mathrm{M} + 3\mathbf{L}\boldsymbol{k} \rightleftarrows [R\mathrm{M}(\mathbf{L}\boldsymbol{k})_3] \quad \beta_{1,1,3}^{R,\mathrm{M,L}k} \tag{140}$$

Alternatively, thermodynamic data for inert d-transition metal ions Cr^{III}, Co^{III}, Ru^{II}, and Os^{II} cannot be obtained easily because the formation

TABLE 19 Metal-containing species observed by ES-MS from solutions in acetonitrile during the titration of the pentadentate ligands **L35–L41** (Figure 110) with transition metal (3d, 4f) perchlorates

Ligand	Metal ions	Species	References
L35	M^{II} (M = Zn, Fe)	$[M(\mathbf{L35})_n]^{2+}$, $n = 2, 3$	Piguet et al. (1995d)
		$[M_2(\mathbf{L35})_2]^{4+}$	Piguet et al. (1995e)
	R^{III} (R = La, Eu)	$[R_2(\mathbf{L35})_2(ClO_4)_x]^{(6-x)+}$, $x = 1$–3	
	R^{III}/Zn^{II} (R = Y, La, Nd, Tb, Lu)	$[RZn(\mathbf{L35})_3(ClO_4)_x]^{(5-x)+}$, $x = 0$–3	
		$[Zn(\mathbf{L35})_2]^{2+}$	
	R^{III}/Fe^{II} (R = La, Nd, Eu)	$[RFe(\mathbf{L35})_3(ClO_4)_x]^{(5-x)+}$, $x = 0$–3	
		$[Fe(\mathbf{L35})_2]^{2+}$	
	Eu^{III}/Fe^{II}	$[EuFe(\mathbf{L35})_3(ClO_4)_x]^{(5-x)+}$, $x = 0$–4	Hopfgartner et al. (1994)
L36	Zn^{II}	$[Zn(\mathbf{L36})_n(ClO_4)_x]^{(2-x)+}$, $n = 2, 3$; $x = 0, 1$	Piguet et al. (1996)
		$[Zn_2(\mathbf{L36})_n(ClO_4)_x]^{(4-x)+}$, $n = 2, 3$; $x = 0, 2$	
	R^{III}/Zn^{II} (R = La, Eu, Gd, Tb)	$[RZn(\mathbf{L36})_3(ClO_4)_x]^{(5-x)+}$, $x = 0$–3	
	Fe^{II}	$[Fe(\mathbf{L36})_n(ClO_4)_x]^{(2-x)+}$, $n = 1$–3; $x = 0, 1$	Piguet et al. (1997b)
		$[Fe_2(\mathbf{L36})_n(ClO_4)_x]^{(4-x)+}$, $n = 2, 3$; $x = 0, 2$	
	R^{III}/Fe^{II} (R = La, Eu, Gd, Tb, Lu)	$[RFe(\mathbf{L36})_3(ClO_4)_x]^{(5-x)+}$, $x = 0$–3	
		$[Fe(\mathbf{L36})_2]^{2+}$	
	R^{III}/Co^{II} (R = La, Eu, Lu)	$[RCo(\mathbf{L36})_3]^{5+}$	Rigault et al. (1998)
		$[Co(\mathbf{L36})_2]^{2+}$ (traces)	
	R^{III}/Cr^{III} (R = La, Eu, Gd, Tb, Tm, Lu)	$[RCr(\mathbf{L36})_3(CF_3SO_3)_x]^{(6-x)+}$, $x = 0$–4	Cantuel et al. (2002)
		$[Cr(\mathbf{L36})_3(CF_3SO_3)_x]^{(3-x)+}$, $x = 0$–1 (R = La, Gd)	
	Lu^{III}/Ru^{II}	$[LuRu(\mathbf{L36})_3(CF_3SO_3)]^{4+}$	Torelli et al. (2004)
	Lu^{III}/Os^{II}	$[LuRu(\mathbf{L36})_3(CF_3SO_3)_x]^{(5-x)+}$, $x = 1$–3	Riis-Johannessen et al. (2008)

L37	M^{II} (M = Zn, Fe)	$[M(\mathbf{L37})_n]^{2+}$, $n = 2, 3$ $[M_2(\mathbf{L37})_2(ClO_4)_x]^{(4-x)+}$, x = 0–2 (Zn), 0–1 (Fe)	Edder et al. (2000)
	La^{III}	$[La(\mathbf{L37})_n(ClO_4)_x]^{(3-x)+}$, $n = 2, 3$; $x = 0, 1$ $[La(\mathbf{L37})_n]^{3+}$, $n = 4, 5$	
	La^{III}/M^{II} (M = Zn, Fe)	$[LaM(\mathbf{L37})_3(ClO_4)_x]^{(5-x)+}$, x = 0–2 $[M(\mathbf{L37})_n]^{2+}$, $n = 2, 3$ $[Zn_2(\mathbf{L37})_2(ClO_4)_x]^{(4-x)+}$, x = 0–3 $[Zn_2(\mathbf{L37})_3]^{4+}$	
HL38	R^{III}/Zn^{II} (R = La, Eu)	$[RZn(\mathbf{L38})_3]^{2+}$	Edder et al. (1997)
L41	La^{III}/M^{II} (M = Zn, Fe)	$[LaM(\mathbf{L41})_3(ClO_4)_x]^{(5-x)+}$, x = 0–3 $[M(\mathbf{L41})_n]^{2+}$, $n = 2, 3$ $[M_2(\mathbf{L41})_2(ClO_4)_x]^{(4-x)+}$, x = 0–2 (Zn); $x = 0$ (Fe)	Edder et al. (2001)

of $[R\mathrm{M}(\mathbf{L}\boldsymbol{k})_3]^{m+}$ by reacting stoichiometric mixtures of R, M and $\mathbf{L}\boldsymbol{k}$ proved to be not feasible in that this invariably led to intricate mixtures of species with varying stoichiometry and symmetry (HHH, HHT, HH, HT isomers). Therefore, thermodynamic data for heterometallic binuclear species including inert d-block ions are limited to the formation of the final helicate from its preorganized tripodal receptor (Eq. (141)):

$$[\mathrm{M}(\mathbf{L}\boldsymbol{k})_3]^{z+} + R^{3+} \rightleftarrows [R\mathrm{M}(\mathbf{L}\boldsymbol{k})_3]^{(z+3)+} \quad \beta_{1,1}^{R,\mathrm{M}(\mathrm{L}k)3} \tag{141}$$

Due to these difficulties, only a limited number of stability constants could be determined and are listed in Table 20. For a given d-transition metal ion, the evolution of the data along the lanthanide series seems to parallel the tendency observed with the mononuclear precursors: the N_3 chelating unit in **L35** induces less stable complexes with heavier lanthanides, contrary to the N_2O donor site in **L36**. The difference, however, remains small and close to the experimental uncertainties. On the other hand, the 3d-transition metal ion has a much larger influence, compare for instance $\beta_{1,1,3}^{\mathrm{La,M,L36}}$ values for the LaM complexes with **L36**: the $\mathrm{M} = \mathrm{Zn^{II}}$ complex is 6 orders of magnitude more stable than the $\mathrm{M} = \mathrm{Fe^{II}}$ edifice, itself one order of magnitude more stable than the $\mathrm{M} = \mathrm{Co^{II}}$ helicate. Finally the expected stabilization of the pseudotricapped-trigonal prismatic coordination to lanthanides in going from a N_9 (**L35**) to a N_6O_3 (**L36**) environment is only seen with the $\mathrm{Zn^{II}}$ helicates, $\beta_{1,1,3}^{R,\mathrm{Zn,L}k}$ increasing by three orders of magnitude, while the $\mathrm{Fe^{II}}$ helicates have a tendency to be somewhat less stable with **L36** compared to **L35**.

The most striking feature of these thermodynamic data is the selectivity of the recognition process for a $R^{\mathrm{III}}/\mathrm{M^{II}}$ pair, which is schematized for **L37** on Figure 113. When this ligand is reacted with either $\mathrm{M^{II}}$ (M = Zn, Fe) or R^{III}, it generates a mixture of several species with different stoichiometries and conformations; this is referred to as a dynamical combinatorial library of species (Lehn and Eliseev, 2001). On the other hand, when an equimolar mixture of R^{III} and $\mathrm{M^{II}}$ is mixed with **L37**, only one major species forms with stability far larger than the stability of any of the other mono- and binuclear species. To substantiate this further, the dissociation constant of the RML_3 helicate can be recalculated from available stability data for the other species (Eq. (142)). In the case of **L35** for instance:

$$4[R\mathrm{Fe}(\mathbf{L35})_3]^{5+} \rightleftarrows 2[R_2(\mathbf{L35}_3)]^{6+} + [\mathrm{Fe}_2(\mathbf{L35}_2)]^{4+} + 2[\mathrm{Fe}(\mathbf{L35}_2)]^{2+} \quad log(K) \tag{142}$$

$\log(K) = -8$ and -2 for $R = \mathrm{La}$ and Eu, respectively.

TABLE 20 Cumulative stability constants reported for the formation of mononuclear and homometallic binuclear complexes in acetonitrile solution (spectrophotometric titration of **L***k* or $[M(\mathbf{L}k)_3]^{m+}$ 10^{-4} M)

Ligand	M	*y*:*n*	$\log(\beta_{y,n}^{M,Lk})$	*R*	*y*:*n*	$\log(\beta_{y,n}^{R,Lk})$	M/*R*	$\log(\beta_{1,1,3}^{R,M,Lk})$ or $\log(\beta_{1,1}^{R,ML3})$	Reference
L35	Zn^{II}	1:2	15.4(8)	La	2:3	22.3(3)	La/Zn	26.2(3)	Piguet et al. (1995d)
		2:2	22(1)	Eu	2:3	23.5(8)	Eu/Zn	25.3(4)	
	Fe^{II}	1:2	14.1(4)				La/Fe	25.2(5)	Piguet et al. (1995e)
		2:2	20.0(8)				Eu/Fe	24.3(8)	
L36	Zn^{II}	1:3	22(1)	La	1:3	19.6(5)	La/Zn	29.0(4)	Piguet et al. (1996)
		2:2	28.4(8)		2:3	27.5(9)	Eu/Zn	28.6(6)	
		2:3	21.5(9)		2:2	22.3(9)			
	Fe^{II}	1:2	13.0(8)		3:2	29.0(9)	La/Fe	23.0(8)	Piguet et al. (1997b)
		2:2	18.0(9)				Eu/Fe	24.6(9)	
							Lu/Fe	23.6(7)	
	Co^{II}	1:2	14.4(6)				La/Co	21.7(6)	Rigault et al. (1998)
							Eu/Co	23.2(9)	
							Lu/Co	23.9(6)	
	Cr^{III}						La/Cr	5.9(3)[a]	Cantuel et al. (2004)
							Lu/Cr	5.3(3)[a]	
	Ru^{II}						La/Ru	5.4(2)[a]	Canard and Piguet (2007)
							Lu/Ru	5.2(2)[a]	
L37	Zn^{II}	1:2	14.4(2)	La	1:3	15.1(4)	La/Zn	30(2)	Edder et al. (2000)
		1:3	18.8(3)		2:3	20.1(4)			
		2:2	21.9(3)						
		2:3	28.5(3)						

(*continued*)

TABLE 20 (*continued*)

Ligand	M	*y*:*n*	$\log(\beta_{y,n}^{\mathrm{M,L}k})$	*R*	*y*:*n*	$\log(\beta_{y,n}^{R,\mathrm{L}k})$	M/*R*	$\log(\beta_{1,1,3}^{R,\mathrm{M,L}k})$ or $\log(\beta_{1,1}^{R,\mathrm{ML3}})$	Reference
	Fe^{II}	1:2	14.8(6)				La/Fe	26(2)	
		1:3	20.4(8)						
		2:2	21.2(7)						
		2:3	27.6(8)						
L41	Zn^{II}	1:2	12.2(5)	La	1:3	17.7(3)	La/Zn	[b]	Edder et al. (2001)
		2:2	17.3(5)		2:3	22.9(3)	Eu/Zn	[b]	

[a] $\log(\beta_{1,1}^{R,\mathrm{ML3}})$, Eq. (141).
[b] Spectra are too correlated for allowing the extraction of the stability constants; however, ^{1}H-NMR data point to the ''quantitative'' formation of the 1:1:3 species.

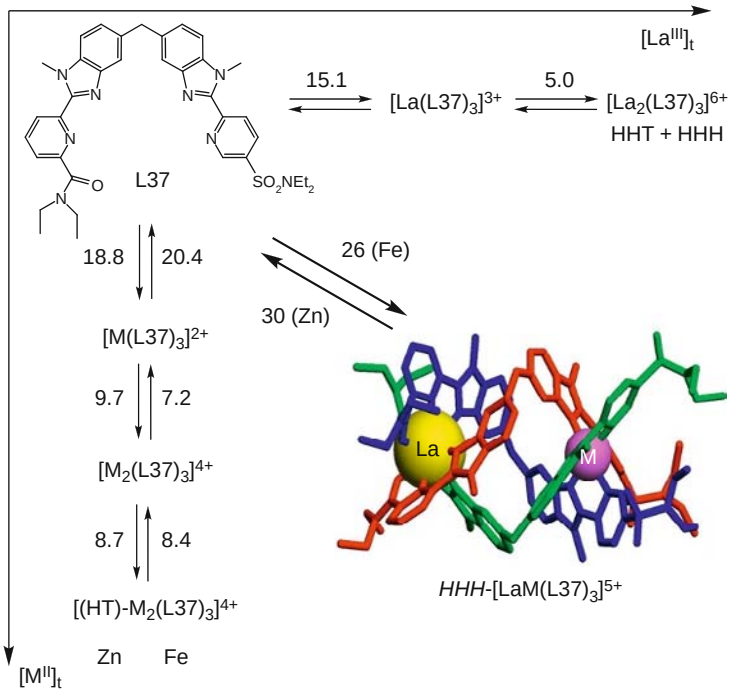

FIGURE 113 Selective formation of the heterometallic binuclear helicate $[LaM(\mathbf{L37})_3]^{5+}$ (M = Fe, Zn) in acetonitrile from a dynamic library of species. The numbers correspond to logarithmic values of the thermodynamic constants (redrawn after Edder et al., 2000).

Origin of the thermodynamic stability of the $[RM(\mathbf{L36})_3]^{m+}$ helicates ($M = Cr^{III}$, Ru^{II})

As discussed for polynuclear f–f helicates (Section 5.4), the surprising stability of highly charged d–f helicates in solution results from a balance between the unfavorable intramolecular electrostatic intermetallic repulsion and the favorable increase in solvation energy accompanying the successive fixation of charged cations within the complex. Interestingly, an intermetallic separation of 90 pm, as found in the triple-stranded helicates with ligands **L11**, **L13**, **L28**–**L31** (f–f helicates), or **L35**–**L42** (d–f helicates), leads to an almost exact compensation of these two opposite contributions produced by the fixation of a trivalent lanthanide. This is illustrated by the negligible variation of the formation constants $\log(\beta_{1,1}^{R,M(Lk)3})$ (Eq. (141)) in going from HHH-$[Ru(\mathbf{L36})_3]^{2+}$ ($5.4 \geq \log(\beta_{1,1}^{R,Ru(Lk)3}) \geq 5.2$ which translates into $-31 \geq \Delta G_{c,sol}^{\circ}(RRu) \geq -30$ kJ mol^{-1}) to HHH-$[Cr(\mathbf{L36})_3]^{3+}$ ($5.9 \geq \log(\beta_{1,1}^{R,Cr(Lk)3}) \geq 5.3$ which

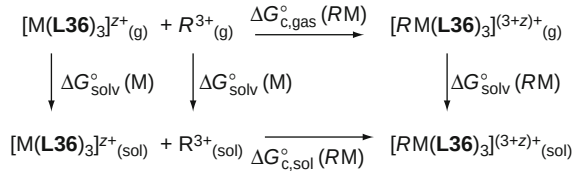

FIGURE 114 Born–Haber cycle for the formation of $[R\mathrm{M}(\mathbf{L36})_3]^{(3+z)+}$ helicates.

translates into $-34 \geq \Delta G^{\circ}_{c,sol}(R\mathrm{Cr}) \geq -30\ \mathrm{kJ\ mol^{-1}}$); this can be summarized with $\Delta G^{\circ}_{c,sol}(R\mathrm{Ru}) - \Delta G^{\circ}_{c,sol}(R\mathrm{Cr}) \approx 0$ despite the obvious increase of the d–f electrostatic repulsion in going from the $\mathrm{Ru^{II}}$-R^{III} to the $\mathrm{Cr^{III}}$- R^{III} helicates (Canard and Piguet, 2007; Figure 114).

The introduction of the solvation free energies estimated by using Born's Eq. (127) for $[\mathrm{Ru}(\mathbf{L36})_3]^{2+}$ ($-342\ \mathrm{kJ\ mol^{-1}}$), $[\mathrm{Cr}(\mathbf{L36})_3]^{3+}$ ($-771\ \mathrm{kJ\ mol^{-1}}$), $[\mathrm{LuRu}(\mathbf{L36})_3]^{5+}$ ($-2091\ \mathrm{kJ\ mol^{-1}}$), and $[\mathrm{LuCr}(\mathbf{L36})_3]^{6+}$ ($-3012\ \mathrm{kJ\ mol^{-1}}$) into the adequate thermodynamic Born–Haber cycles (Figure 114) allows the calculation of the difference in free energies for these two complexation processes in the gas phase $\Delta G^{\circ}_{c,gas}(\mathrm{LuCr}) - \Delta G^{\circ}_{c,gas}(\mathrm{LuRu}) = 492\ \mathrm{kJ\ mol^{-1}}$ (Eq. (143), Canard and Piguet, 2007).

$$\begin{aligned}\Delta G^{\circ}_{c,gas}(\mathrm{LuCr}) - \Delta G^{\circ}_{c,gas}(\mathrm{LuRu}) = {} & \Delta G^{\circ}_{c,sol}(\mathrm{LuCr}) - \Delta G^{\circ}_{c,sol}(\mathrm{LuRu}) \\ & + \Delta G^{\circ}_{solv}(\mathrm{Cr}) - \Delta G^{\circ}_{solv}(\mathrm{Ru}) \\ & + \Delta G^{\circ}_{solv}(\mathrm{LuRu}) - \Delta G^{\circ}_{solv}(\mathrm{LuCr})\end{aligned} \tag{143}$$

Assuming that the *R*-ligand-binding energies (including the reorganization of the $[\mathrm{M}(\mathbf{L36})_3]^{z+}$ tripod) are identical for M = Ru or M = Cr, the calculated difference of the free energies of complexation in the gas-phase strictly corresponds to the difference in the electrostatic works accompanying the fixation of $\mathrm{Lu^{3+}}$ at $d_{\mathrm{LuRu}} = 90.8$ pm from $\mathrm{Ru^{II}}$ in $[\mathrm{LuRu}(\mathbf{L36})_3]^{5+}$, respectively, at $d_{\mathrm{LuCr}} = 93.5$ pm from $\mathrm{Cr^{III}}$ in $[\mathrm{LuCr}(\mathbf{L36})_3]^{6+}$ (Eq. (144)).

$$\begin{aligned}\Delta G^{\circ}_{c,gas}(\mathrm{LuCr}) - \Delta G^{\circ}_{c,gas}(\mathrm{LuRu}) &= W_{\mathrm{Lu,gas}}(\mathrm{Cr}) - W_{\mathrm{Lu,gas}}(\mathrm{Ru}) \\ &= 492\ \mathrm{kJ\,mol^{-1}}\end{aligned} \tag{144}$$

This value can be thus compared with that computed from Coulomb's law (Eq. (145)), and the reasonable agreement, given the approximation made, confirms that solvation processes indeed overcome standard electrostatic repulsions for these d–f helicates in solution (Canard and Piguet, 2007).

$$W_{\mathrm{Lu,gas}}(\mathrm{Cr}) - W_{\mathrm{Lu,gas}}(\mathrm{Ru}) = \frac{3e^2 N_A}{4\pi\varepsilon_0}\left[\frac{2}{d_{\mathrm{LuRu}}} - \frac{3}{d_{\mathrm{LuCr}}}\right] = 419\ \mathrm{kJ\,mol^{-1}} \tag{145}$$

Formation of RML_3 helicates with kinetically inert trivalent 3d-transition metal ions: Cr^{III} and Co^{III}

The syntheses of inert HHH-$[R\mathrm{Cr}^{III}\mathbf{L}_3]^{6+}$ and HHH-$[R\mathrm{Co}^{III}\mathbf{L}_3]^{6+}$ take advantage of the lability of the chemically accessible parent Cr^{II} and Co^{II} precursors, for which standard self-assembly processes, similar to that described in Figure 113, lead to HHH-$[R\mathrm{Cr}\mathbf{L}_3]^{5+}$ and HHH-$[R\mathrm{Co}\mathbf{L}_3]^{5+}$. Postmodification reactions under oxidative conditions eventually transform the M^{II} cations into inert M^{III} centers (Cantuel et al., 2002; Rigault et al., 1998). In the case of Cr^{III}, the initial thermodynamic self-assembly process starts from Cr^{II} triflate and the resulting blue-green solutions in degassed acetonitrile are diagnostic for the presence of the $3d^4$ metal ion in the helicates. Post-assembly oxidation by diffusion of air is fast and quantitative; the solutions turn yellow after a few minutes, owing to the low reduction potential of divalent chromium, for example, $E_{1/2}^{Cr^{III}/Cr^{II}} = -0.40$ V versus SCE for the tris (bipyridine) complex. The presence of Cr^{III} is ascertained by several analytical techniques including electronic absorption spectroscopy, ^{1}H-NMR, ES-MS, and X-ray crystallography (Cantuel et al., 2002). The known kinetic inertness of the $3d^3$ chromium cation allows the separation of enantiomerically pure helicates (see Section 7.6 below). For HHH-$[\mathrm{LnCo}^{II}(\mathbf{L36})_3]^{5+}$ helicates, cyclic voltammograms in acetonitrile show a quasi-reversible Co^{II}/Co^{III} oxidation wave (+0.41 to 0.43 V vs SCE) compatible with the use of bromine as the outer sphere oxidative agent, which indeed yields the diamagnetic HHH-$[\mathrm{LnCo}^{III}(\mathbf{L36})_3]^{6+}$ complexes (Ln = La, Lu; Rigault et al., 1998, 2000a).

Formation of RML_3 helicates with kinetically inert bivalent 4d- and 5d-transition metal ions: Ru^{II} and Os^{II}

For Ru^{II} and Os^{II}, there is no available parent labile oxidation states, and the self-assembly processes must include some poorly reversible elementary steps (Torelli et al., 2004). For the synthesis of HHH-$[R\mathrm{Ru}(\mathbf{L36})_3]^{5+}$, the procedure implies an intricate strategy, in which undesired coproducts are stepwise separated from the target helicate (Canard and Piguet, 2007; Figure 115).

For the more kinetically inert Os^{II} cation, the problem is even more challenging and the self-assembly reaction has to be performed in ethylene glycol at elevated temperature (160 °C) and under pressure (8–10 bar) to yield only a limited amount of a 3:1 mixture of HHH-$[\mathrm{Os}(\mathbf{L36})_3]^{2+}$ and HHT-$[\mathrm{Os}(\mathbf{L36})_3]^{2+}$. The targeted HHH-$[\mathrm{LuOs}(\mathbf{L36})_3]^{5+}$ helicate is eventually obtained after several purification cycles by column chromatography on alumina (yield < 10%) followed by recombination with Lu^{III} (Riis-Johannessen et al., 2008).

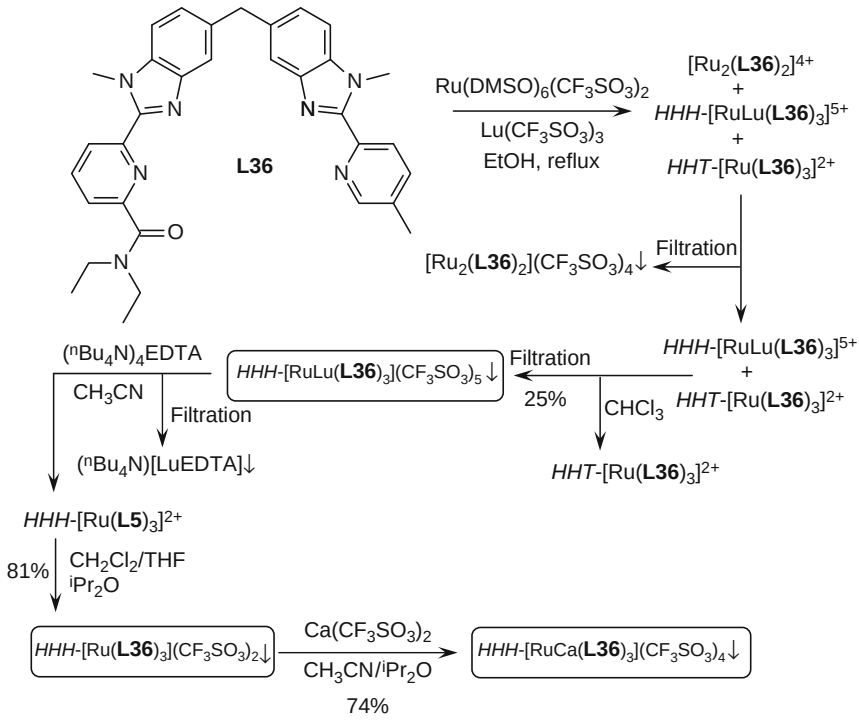

FIGURE 115 Synthesis of the inert HHH-[Ru(**L36**)$_3$]$^{2+}$ tripodal receptor and of its triple-stranded d–f HHH-[RuLu(**L36**)$_3$]$^{5+}$ and HHH-[RuCa(**L36**)$_3$]$^{4+}$ helicates (adapted from Canard and Piguet, 2007).

7.4 Solid state and solution structures

All of the reported molecular structures of crystals of *R*ML$_3$ helicates correspond to the HHH disposition of the ligands around the metal ions and have a pseudo-C_3-symmetry with the main axis going through the metal centers. With one exception, the available structures feature ligand **L36**. Generally speaking, the nine-coordinate lanthanide ion lies in a site with pseudotricapped-trigonal prismatic geometry while six-coordinate M^{II}/M^{III} ions display a more or less distorted pseudo-octahedral geometry, except for **EuZn**.[2] Selected structural parameters are listed in Table 21 and typical structures are shown in Figure 116.

In the **EuZn** structure (Piguet et al., 1996), five of the Zn–N bonds (2.01–2.19 Å) are close to the standard 2.11 Å value (Orpen et al., 1989) while the fifth one is much longer, 2.52 Å. The transition metal ion may thus be considered as being five-coordinate, with distorted trigonal prismatic geometry. Its ionic radius is then 0.62 Å, as compared to the

[2] For all the structures with L36, a simplified notation will be used, namely *RM* for [*RM*(L36)$_3$]$^{m+}$.

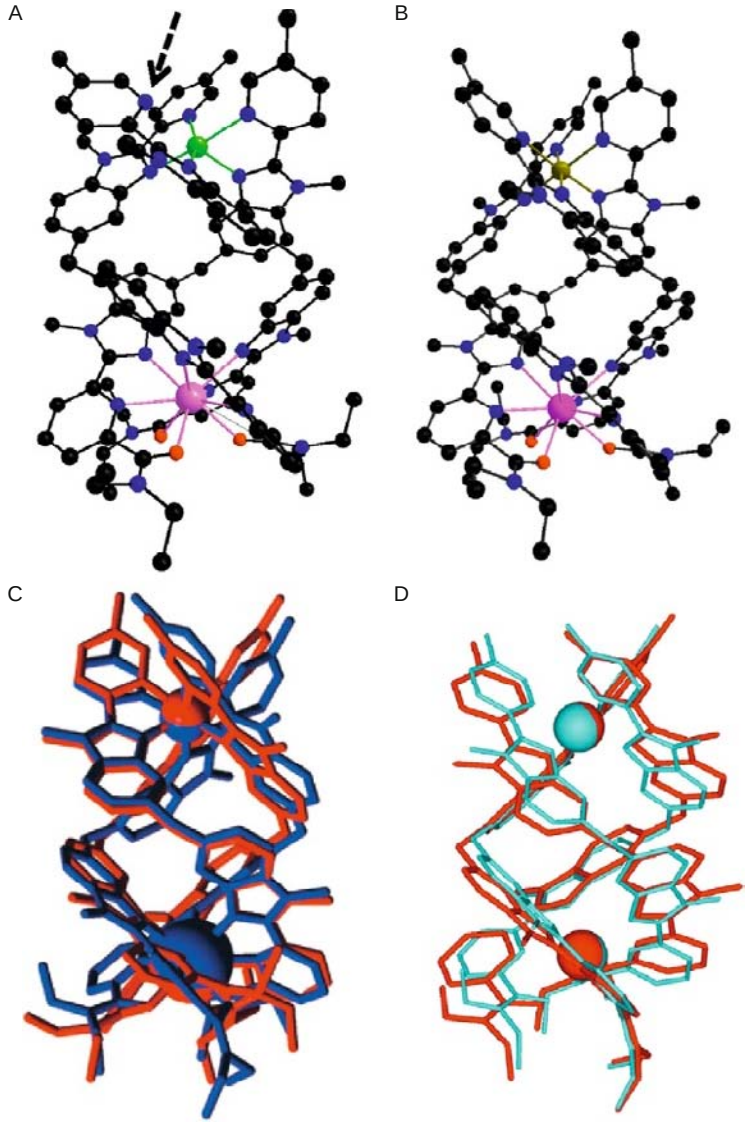

FIGURE 116 Typical structures of *R*M helicates with ligand **L36**: (A) **EuZn** (redrawn from Piguet et al., 1996); (B) **LaFe** (redrawn from Piguet et al., 1997b); (C) superposition of the structures of **EuCr** and **EuRu** (reproduced by permission from Torelli et al., 2005, © Wiley-VCH Verlag, 2005); and (D) superposition of the structures of **LuOs** and **LuRu** (redrawn from Riis-Johannessen et al., 2008).

expected 0.68 Å for a standard five-coordinate Zn^{II} ion (Shannon, 1976). Out of the three ligand strands, only one achieves a relatively symmetrical bidentate binding to the 3d ion. The distortion sustains by the two other ligand strands results from a close packing of the **EuZn** cations by pairs having opposite helicities in the unit cell, with intermolecular Zn...Zn contacts as short as 8.31 Å. Despite a significant deformation of the screw thread for the tridentate unit coordinated to Eu^{III}, the coordination polyhedron is close to the ideal tricapped-trigonal prism (TTP), with standard Eu–O and Eu–N distances. Interestingly, the Zn^{II} coordination sphere in $[EuZn(\mathbf{L37})_3]^{5+}$ is far less distorted and can be described as a octahedron flattened along the intermetallic axis while the 3d metal ion is now six-coordinate, as shown by its larger ionic radius (0.72 Å, reported standard value: 0.74 Å). This may be related to the effect of the SO_2NEt_2 substituent since the triple helices are now packed with their axis along the same direction, forming infinite columns compared to dimers for **EuZn**. The intramolecular intermetallic Eu...Zn contact distance is shorter by about 0.4 Å, but the Eu^{III} environment is unchanged (Edder et al., 2000). The crystal structure of **LaFe** has been determined at 170 K to ensure a maximum fraction of low-spin (LS) iron. The La^{III} environment is very similar to the pseudo-TTP structure evidenced for Eu^{III} in **EuZn** except for a larger twist between the two opposite facial tripods of the trigonal prism (17° versus 10°) and for the lengthening of the Ln-N and Ln-O bonds due to its larger ionic radius. On the other hand, the 3d metal ion is six-coordinate with an octahedral coordination polyhedron somewhat flattened along the C_3-axis. This is typical of a stereochemical demanding low-spin Fe^{II} ion which limits the deformation of the octahedral coordination despite the packing in pairs of opposite helicities, much as in **EuZn**. The Fe–N distances are standard and the calculated ionic radius (0.52 Å) is also in line with a LS divalent iron.

When iron is replaced by the low-spin, trivalent Co^{III} in ***R*Co**, the influence of the lanthanide ion is seen in the Co–N distances which are, on average, 0.05 Å shorter in **LuCo** compared to **LaCo.** This suggests that the Co–N bonds are stretched to accommodate the larger La^{III} ion in the nona-coordinate cavity, exemplifying the mechanical coupling between the two metal ions. As a result, The intramolecular *R*...Co contact distance increases by about 0.4 Å in going from **LaCo** to **LuCo** (Rigault et al., 2000b; Table 21). Examination of the series of structures ***R*Cr** (R = Nd, Eu, Yb, Lu) in which the Co^{III} ion is replaced slightly larger Cr^{III} ion points to the remarkable adaptability of the triple-stranded helical core to small variations in the ionic radii of either the 3d or the 4f transition metals. The overall structures with Co^{III} or Cr^{III} are very similar, the only noticeable difference being a somewhat longer intermetallic distance, ca. 9.3 Å versus ca. 9 Å, and a concomitant longer helical pitch (ca. 15.5 Å compared to ca. 13.5 Å) for ***R*Cr** helicates. On the other hand, variation of the R^{III} from

Nd to Lu induces only a 0.8% lengthening of the *R*-Cr contact distance and a 2% shortening of the helical pitch. These effects are smaller than the changes induced by the replacement of the 3d transition metal ion, despite that the variation in ionic radius between Nd^{III} and Lu^{III} (ca. 0.14 Å) is larger than the difference between Co^{III} and Cr^{III} (0.11 Å). The structural parameters are little affected when divalent Ru^{II} replaces Cr^{III} in **EuRu** and **LuRu**; the two ions have similar ionic radii but different charges and the intermetallic distance decreases to reach values similar to the one found in **LaFe** (Torelli et al., 2004, 2005). The structure of the helicate with the isoelectronic Os^{II} ion, **LuOs**, revealed an unusual distribution of the Os–N bonds, as well as bizarre anisotropic thermal parameters; careful examination of the data led to the conclusion that a preferential alignment of subdomains within the crystal may be responsible for this. In any case, averaged values do not deviate from those reported for **LuRu** (Riis-Johannessen et al., 2008).

The TTP coordination polyhedra of the R^{III} ions in the 12 reported structures are alike, as demonstrated by the geometrical analysis shown in Figure 117 and for which the relevant angles are reported in Table 21: all mean angles vary in short ranges, θ between 48° and 55°, ϕ between 178° and 179°, and ω between 50° and 56°.

Solution structure determination essentially relies on NMR data, via either a classical analysis of the number of signals and of their chemical shifts with the help of two-dimensional COSY, NOESY, and NOEDIF measurements, or the more sophisticated investigation of both lanthanide-induced shifts (LIS) and relaxation times (LIR). When the major species in solution is the heterobimetallic helicate, analysis of the ^{1}H-

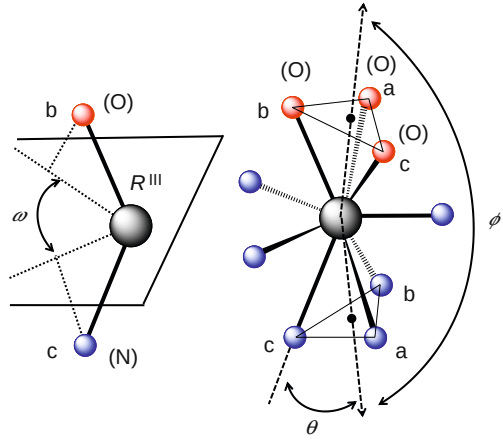

FIGURE 117 Definition of the angles for the analysis of the R^{III} coordination polyhedra in *R*M helicates (redrawn after Piguet et al., 1996).

NMR spectra is relatively simple. For instance, 26 and 23 signals are observed for the ***R*M** (M = Zn, Fe) helicates with ligands **L35** (Piguet et al., 1995d,e) and **L36** (Piguet et al., 1996, 1997b), respectively, pointing to the equivalence of the three ligand strands and therefore to C_3- or C_{3v}-symmetry for the molecular assembly, on the NMR timescale. The methylene protons of the bridge between the two chelating units of the ligands and of the dimethoxybenzyl or diethylamine substituents exhibit AB spin systems, precluding the presence of a mirror plane and therefore pointing to a HHH arrangement of the ligands with C_3-symmetry. The NOE effects observed, both intrastrand (Figure 118) and interstrand for a range of complexes (R = La, Ce, Nd, Sm, Eu, Yb, Lu, and Y) further confirm the helical twist of the ligands. Finally, analysis of the lanthanide-induced shift with separation of the contact and dipolar (pseudocontact) contributions according to Eq. (35) (see Section 3.6) substantiates the coordination of the lanthanide ion to the tridentate unit and of the 3d cation to the bidentate unit. For instance, small F_i values (<0.06) are observed for the protons of the bidentate unit in $[R\text{Zn}(\mathbf{L35})_3]^{5+}$ because of their large topological separation from the paramagnetic R^{III} ion. On the other hand, the F_i values are significantly larger for the protons of the tridentate binding unit and they increase to reach values as high as 0.25–0.33 when the protons are separated from the paramagnetic center by only three bonds, reflecting a large spin delocalization onto the bound tridentate unit. Similar conclusions hold for the Fe^{II} helicates with ligand **L35** (Piguet et al., 1997b), for Co^{II}, Co^{III} (Rigault et al., 1998), Ru^{II} (Torelli et al., 2004), and Os^{II} (Riis-Johannessen et al., 2008) helicates with ligand **L36**, as well as for Zn^{II} helicates with ligands **L36** (Piguet et al., 1996) and **HL38** (Edder

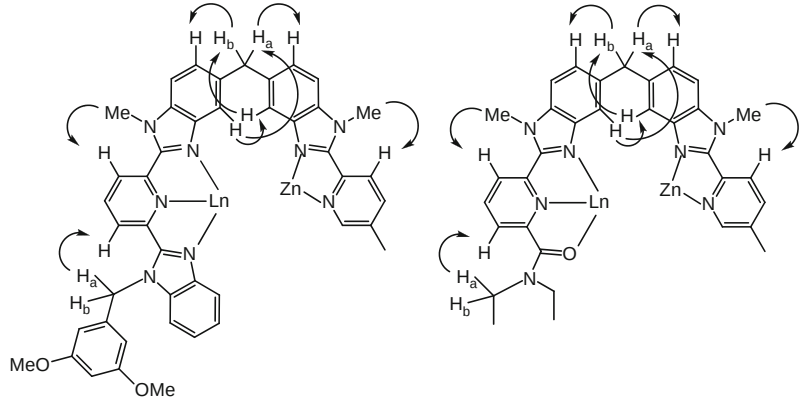

FIGURE 118 Intrastrand NOE effects observed for $[R\text{Zn}(\mathbf{L35})_3]^{5+}$ (left) and $[R\text{Zn}(\mathbf{L36})_3]^{5+}$ (right) in acetonitrile solution (R = La, Ce, Pr, Nd, Sm, Eu, Yb, Lu, Y) (redrawn after Piguet et al., 1995d, 1996).

TABLE 21 Selected structural parameter for the heterometallic *R*M helicates with ligands **L36** and **L37**

				R			M	
Ligand	*R*M	*R*. . .M (Å)	Pitch (Å)[a]	θ (°)[b]	ϕ (°)[b]	ω (°)[b]	r_i (Å)	References
L36	$EuZn^{II}$	8.96	15.4	55	178	50	0.62	Piguet et al. (1996)
L37	$EuZn^{II}$	8.58	14.6	48	179	55	0.72	Edder et al. (2000)
L36	$LaFe^{II}$	9.03	NA	52	179	52	0.52	Piguet et al. (1997b)
	$LaCo^{III}$	8.86	13.7	52	178	52	0.53	Rigault et al. (2000b)
	$LuCo^{III}$	9.23	13.5	49	179	55	0.48	Rigault et al. (2000b)
	$NdCr^{III}$	9.28	15.8	51	178	53	0.59	Torelli et al. (2005)
	$EuCr^{III}$	9.32	15.7	50	178	56	0.59	Cantuel et al. (2002)
	$YbCr^{III}$	9.33	15.4	49	179	52	0.59	Torelli et al. (2005)
	$LuCr^{III}$	9.35	15.4	49	179	56	0.59	Cantuel et al. (2002)
	$EuRu^{II}$	9.06	14.8	49	178	54	0.60	Torelli et al. (2005)
	$LuRu^{II}$	9.08	14.9	49	178	55	0.60	Torelli et al. (2004)
	$LuOs^{II}$	9.09	13.3	50	178	55[c]	0.63	Riis-Johannessen et al. (2008)

[a] Helical pitch corresponding to a 360° turn of the ligand strands.
[b] See Figure 117 for the definition of the angles.
[c] Individual values are highly dispersed, in the range 41–61°.

et al., 1997). When a fast-relaxing and highly paramagnetic 3d metal ion such as high-spin Co^{II} ($3d^7$, $\mu_{eff} \approx 4.9–5\mu_B$) is inserted into the triple-helical complexes, the NMR spectra span a 100 ppm range but are nevertheless fully interpretable (Rigault et al., 1998). In the case of **L36**, C_3-averaged values of the polar coordinates extracted from the crystal structure of **EuZn** have been used to recalculate the structural factors $(1–3\cos^2\theta)/r_i^3$, which significantly improved the fit of the experimental data. Values of the axial component χ_j^{zz} of the magnetic susceptibility tensor relative to Pr^{III} (Table 22) are in qualitatively good agreement with theoretical calculations for the larger ions (Ce, Nd, Eu) while they deviate more for Tm and Yb, although the general trend is maintained. These results not only point to the presence of C_3 triple-stranded helicates in solution but, also, to the **EuZn** crystal structure being a satisfying model for the averaged solution structures on the NMR timescale.

For the $[R\text{Fe}(\mathbf{L36})_3]^{5+}$ series of helicates, the signals of the protons belonging to the bidentate binding unit are very different from those of $[R\text{Zn}(\mathbf{L36})_3]^{5+}$ at room temperature, even for diamagnetic R^{III} ions, some of these protons being strongly shifted toward lower field as a result of the $^1A \rightleftarrows {}^5T_2$ spin-state equilibrium. The two NMR spectra become only similar when the temperature is lowered to 233 K, where iron is essentially in its diamagnetic low-spin state. The localization of Fe^{II} in the pseudo-octahedral site is further confirmed by cyclic voltammetry which shows the $[R\text{Fe}(\mathbf{L36})_3]^{5+}$ helicates being oxidized in a reversible one-electron process at $E_{1/2} \approx 0.82$ V (vs SCE), independent of the nature of the R^{III} ion (Piguet et al., 1997b).

Applying Reilley's method for the separation of contact and dipolar paramagnetic shifts to $[R\text{Co}^{III}(\mathbf{L36})_3]^{6+}$ helicates, that is, the linear forms of Eq. (35) (see Section 3.6):

$$\frac{\delta_{ij}^{\text{para}}}{\langle S_z \rangle_j} = F_i + G_i B_0^2 \frac{C_j}{\langle S_z \rangle_j} \tag{146}$$

TABLE 22 Comparison of theoretical and experimental values of the axial term of the magnetic susceptibility tensor relative to Pr^{III} for $[R\text{Zn}^{II}(\mathbf{L36})_3]^{5+}$ complexes (Piguet et al., 1996)

*R*Zn	Theoretical	Experimental	*R*Zn	Theoretical	Experimental
CeZn	0.57	0.63	EuZn	− 0.36	− 0.54
PrZn	1.00	1.00	TmZn	− 4.82	− 2.86
NdZn	0.38	0.47	YbZn	− 2.00	− 1.07

$$\frac{\delta_{ij}^{\text{para}}}{C_j} = F_i \frac{\langle S_z \rangle_j}{C_j} + G_i B_0^2 \tag{147}$$

leads to the plots reproduced on Figure 119A and B, in which a straight line is observed for R = Ce-Eu, but Tm and Yb are not included, pointing to a possible structural change between lighter and heavier lanthanide ions. When Tb, Dy, Ho, and Er are included in the plots, after succeeding in assigning the proton resonances for the paramagnetic heavier lanthanide ions, the Tb-Yb series fits a second straight line (Rigault and Piguet, 2000). This counterintuitive result, in view of the similarities in the crystal structures of $[R\text{Co}^{\text{III}}(\mathbf{L36})_3]^{6+}$ with R = La, Lu (Rigault et al., 2000a), can be corrected by applying the crystal-field independent method (Eq. (37), Section 3.6), as shown on Figure 119C so that the break resulting from the classical separation method is in fact due to a change in the ligand-field parameters along the lanthanide series, the ligand field being 1.6-fold smaller for the series Tb–Yb compared to Ce–Eu (Rigault et al., 2000a). A further comparison of the LIS and LIR data for the entire series of Co^{III} helicates with calculated data using the geometrical parameters of

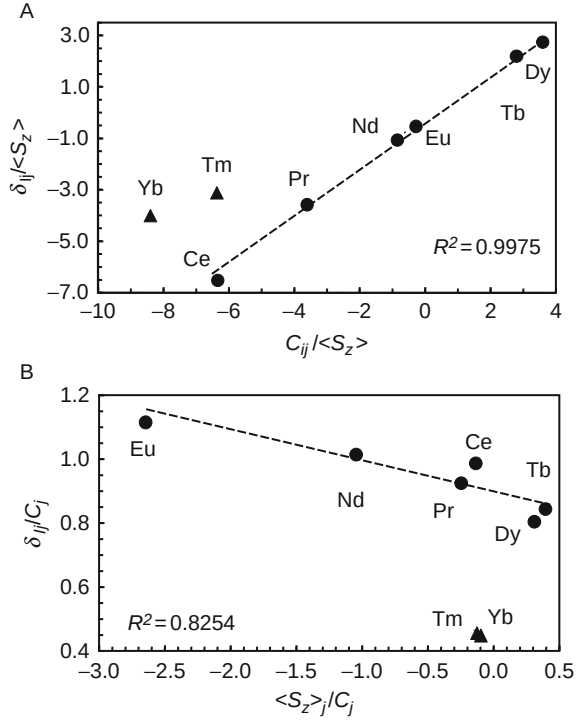

FIGURE 119 Continued

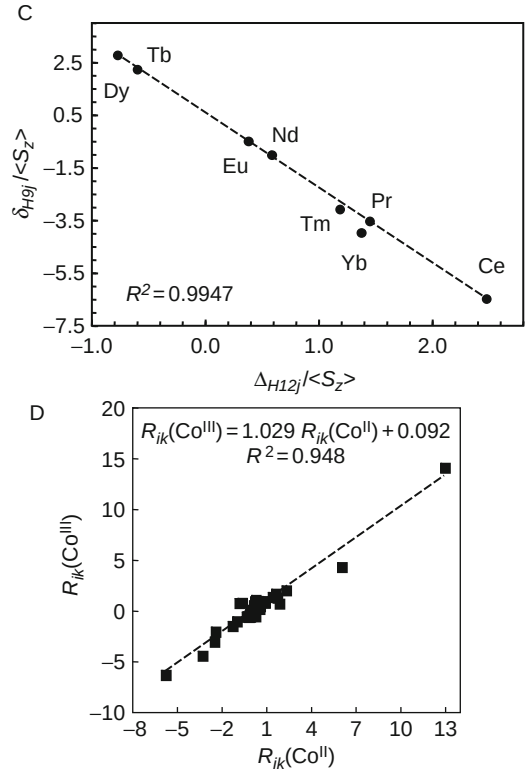

FIGURE 119 Plots of the paramagnetic-induced shifts for $[RCo^{III}(\mathbf{L36})_3]^{6+}$ in acetonitrile according to (A) Eq. (146), (B) Eq. (147), and (C) Eq. (37) (redrawn after Rigault et al., 2000a). (D) Plots of the structural factors $R_{ik} = G_i/G_k$ of the Co^{III} helicates versus those of the Co^{II} complex (redrawn after Rigault et al., 2000b).

the crystal structures for La and Lu confirms the isostructurality of the series, as well as a close match between the less-distorted crystal structure of the Lu helicate and the solution structure in acetonitrile, but for minor deviations due to a larger fluxionality in solution. A similar analysis on the Co^{II} helicates had to take into account the presence of two paramagnetic centers. However, the latter are magnetically independent, since the magnetic moments of the $\boldsymbol{RCo^{II}}$ helicate obey Eq. (148) with $\mu_{eff}^{Co^{II}} = 4.8$ MB, so that the LIS are identical in $\boldsymbol{RCo^{II}}$ and in $\boldsymbol{RCo^{III}}$. The complete NMR analysis yields similar results as for the trivalent cobalt compounds. This is illustrated in Figure 119D in which the structural factors $R_{ik} = G_i/G_k$ (see Eq. (37), Section 3.6) of RCo^{III} versus RCo^{II} plotted for 22 pairs of protons are indeed in linear relationship with a unit slope (Rigault et al., 2000a), consistent with the axial magnetic anisotropic susceptibilities reported in

TABLE 23 Comparison of theoretical and experimental values of the axial magnetic anisotropic susceptibility relative to the value for Dy^{III} ($C_j = -100$) for $[RCo^{II}(\mathbf{L36})_3]^{5+}$ and $[RCo^{III}(\mathbf{L36})_3]^{6+}$ helicates; data are corrected for ligand-field effects (Rigault et al., 2000b)

R	$C_j(RCo^{III})$	$C_j(RCo^{II})$	Theoretical	R	$C_j(RCo^{II})$	$C_j(RCo^{III})$	Theoretical
Ce	−5.2	−6	−6.3	Dy	−100	−100	−100
Pr	−8.0	−10	−11	Ho	−53	−57	−39
Nd	−3.8	−5.5	−4.2	Er	11	12	33
Eu	4.3	6	4.0	Tm	33	37	53
Tb	−91	−94	−86	Yb	13	13	22

Table 23 for the two series of complexes. That is both the Co^{II} and Co^{III} helicates have very similar rigid C_3 solution structure, exemplifying the ability of the $(\mathbf{L36})_3$ supramolecular receptor to adapt to 3d metal ions with various charges and ionic radii without disrupting the overall architecture of the final RML_3 helicates.

$$\mu_{\text{eff}}^{RCo^{II}} = \sqrt{(\mu_{\text{eff}}^{R})^2 + (\mu_{\text{eff}}^{Co^{II}})^2} \tag{148}$$

The structural studies by X-ray diffraction and NMR have been complemented by a high-resolution luminescence analysis of the Eu^{III}-containing complexes similar to the one conducted for the homometallic bioprobes (Section 6.3.1). Data are collected in Table 24. Firstly, the energy of the $^5D_0 \rightarrow {}^7F_0$ transition calculated with Eq. (19) (see Section 3.5) and the usual nephelauxetic parameters $\delta_{N(heter)} = -15.3$, $\delta_{O(amide)} = -15.7$, and $\delta_{O(carbox)} = -17.2\ cm^{-1}$ amounts to 17,236, 17,235, and 17,231 cm^{-1} for N_9, N_6O_3(amide), and N_6O_3(carbox) environments, respectively. The experimental data are in good agreement for **L35** but somewhat lower than predicted for **L36** and **L37** (17,224–17,229 cm^{-1}), possibly due to the large spin delocalization evidenced by NMR and causing a larger nephelauxetic effect. On the other hand, the experimental nephelauxetic effect for **HL38** is somewhat smaller (5 cm^{-1}) than calculated. All the emission spectra match an analysis based on a distorted ternary (C_3) symmetry as seen from the splitting of the $^7F_1$ level into two sublevels labeled A and E according to group-theoretical considerations. There are, however, large differences between the various helicates and, also, between solid state and solution samples, particularly in the case of **L37**. Looking at the ΔE (A–E) energy difference for the Zn^{II} helicates, which is directly proportional to the B_0^2 ligand-field parameter (Binnemans and Görller-Walrand, 1995), the strength of the ligand field induced by the various ligands at 10 or 13 K increases in the series **L35** (93 cm^{-1}) < **L37** (118) < **L36** (127) < **HL38**

TABLE 24 High-resolution analysis of the Eu($^5D_0$) emission to the $^7F_0$ and $^7F_1$ levels for $[EuM(\mathbf{L})_3]^{n+}$ and $[MEuM(\mathbf{L})_3]^{n+}$ helicates in solid state (s) or acetonitrile (as) solutions

					$^5D_0 \rightarrow {}^7F_1$		
Ligand	M	State	T (K)	$^5D_0 \rightarrow {}^7F_0$ E_{exp} (cm^{-1})	ΔE(A–E) (cm^{-1})	ΔE(E–E) (cm^{-1})	References
L35	Zn^{II}	as	10	17,224	94	43	Piguet et al. (1995d)
	Zn^{II}	as	295	12,236	NA	NA	
L36	Zn^{II}	s	10	17,220	127	21	Piguet et al. (1996)
	Zn^{II}	s	295	17,229	140	55	
	Zn^{II} [a]	s	295	17,226	134	63	
	Cr^{III}	s	10	17,216	100	48	Cantuel et al. (2002)
HL38	Zn^{II}	s	10	17,224	138	42	Edder et al. (1997)
	Zn^{II}	s	295	17,235	145	35	
	Zn^{II}	as	295	17,237	149	NA	
L37	Zn^{II}	s	10	17,221	118	37	Edder et al. (2000)
	Zn^{II}	s	295	17,225	117	NA	
	Zn^{II}	as	295	17,224	82	49	
L41	Zn^{II}	s	13	17,221	146	35	Edder et al. (2001)
	Zn^{II}	as	295	17,232	147	NA	
	Fe^{II}	s	13	17,221	144	37	
L42	$Zn^{II}Zn^{II}$	s	10	17,221	98	32	Cantuel et al. (2006)
	$Cr^{III}Cr^{III}$	s	10	17,218	80	34	

[a] Eu-doped (2%) $[GdZn(\mathbf{L36})_3]^{5+}$.

(138) < **L41** (146). This can be understood with respect to the inner sphere composition, a N_9 environment generating a weaker field than a N_6O_3 one. The weaker field induced by **L37** with respect to **L36** most probably arises from the less distorted coordination polyhedron in $[EuZn(\mathbf{L37})_3]^{5+}$ compared with $[EuZn(\mathbf{L36})_3]^{5+}$ (Edder et al., 2000) while the largest field observed for the helicate with **L41,** with respect to the carboxylic acid **HL38,** may be traced back to the weaker coordination of the 3d transition metal, allowing a tighter wrapping of the ligand strands around the lanthanide ion.

7.5 Intermetallic communication as a tool for tuning magnetic and photophysical properties

7.5.1 Tuning the spin-crossover parameters of Fe^{II}

Spin equilibria between the $^1A_1$ and $^5T_2$ states occur for all the Fe^{II}-containing helicates, that is, with ligands **L35-L37**. The effective magnetic moment of the iron partner is deduced from susceptibility measurements of $[R\mathrm{Fe}(\mathbf{L})_3]^{5+}$ and the corresponding $[R\mathrm{Zn}(\mathbf{L})_3]^{5+}$ helicates for assessing the diamagnetic contribution and the contribution from the lanthanide ions. The observed magnetic behavior of Fe^{II} allows the evaluation of the spin-crossover constant K_{sc} according to

$$\mu^2_{\mathrm{eff}}(\mathrm{Fe}) = \mu^2_{\mathrm{eff}}(R\mathrm{Fe}) - \mu^2_{\mathrm{eff}}(R\mathrm{Zn}) \tag{149}$$

$$^1\mathrm{A}_1(\mathrm{S}=0,\mathrm{LS}) \rightleftarrows {}^5\mathrm{T}_2(\mathrm{S}=2,\mathrm{HS})\ K_{\mathrm{SC}} \tag{150}$$

$$K_{\mathrm{SC}} = \frac{\mu^2_{\mathrm{eff}} - \mu^2_{\mathrm{LS}}}{\mu^2_{\mathrm{HS}} - \mu^2_{\mathrm{eff}}} = \frac{x_{\mathrm{HS}}}{1 - x_{\mathrm{HS}}} = \exp\left(-\frac{\Delta H_{\mathrm{SC}}}{RT} + \frac{\Delta S_{\mathrm{SC}}}{R}\right) \tag{151}$$

$$T_{\mathrm{SC}} = \frac{\Delta H_{\mathrm{SC}}}{\Delta S_{\mathrm{SC}}} \tag{152}$$

where μ_{LS} and μ_{HS} are the magnetic moments of the low and high-spin forms, taken as 5.0 and $0.3\mu_{\mathrm{B}}$, respectively (Sugiyarto et al., 1994), ΔH_{SC} and ΔS_{SC} are the corresponding thermodynamic parameters, while T_{SC} is the critical temperature for which $x_{\mathrm{HS}} = 0.5$. Relevant data obtained by either NMR or spectrophotometric determinations are collected in Table 25 while the high-spin mole fractions versus temperature are displayed on Figure 120 for helicates with **L37**. The temperature range investigated, 243–333 K, is limited by the physical properties of the solvent, acetonitrile, so that the spin transition cannot be directly evidenced, but its temperature can be calculated from Eq. (152). For **L35,**

TABLE 25 Parameters for the magnetic low-spin/high-spin equilibria of $[RFeL_3]^{5+}$ helicates in acetonitrile

L	*R*Fe	ΔH_{sc} (kJ mol^{-1})	ΔS_{sc} (J mol^{-1}K^{-1})	τ_{sc} (K)	x_{HS} (293 K)	References
L35	LaFe	20.6(6)	57(3)	361	0.16	Piguet et al. (1995e)
	CeFe	23.1(8)	66(4)	350	0.17	
	PrFe	22.2(8)	62(3)	358	0.16	
	NdFe	21.8(8)	60(3)	363	0.16	
	SmFe	20.0(9)	55(4)	364	0.15	
	EuFe	23.0(9)	64(3)	359	0.15	
L36	CaFe	30.3(3)	90(1)	336	0.17	Piguet et al. (1997b)
	LaFe	30.5(3)	92(1)	331	0.19	
	NdFe	30.2(3)	90(1)	334	0.18	
	EuFe	29.6(5)	89(1)	336	0.18	
	YFe	29.6(3)	88(1)	338	0.17	
	YbFe	28.3(4)	83(1)	342	0.16	
	LuFe	28.4(4)	82(2)	346	0.14	
	ScFe	25.8(7)	74(2)	349	0.16	
L37	LaFe	30.1(2)	94(1)	320	0.31	Edder et al. (2000)
	YFe	29.2(2)	89(1)	327	0.26	
	LuFe	29.8(2)	87(1)	331	0.24	

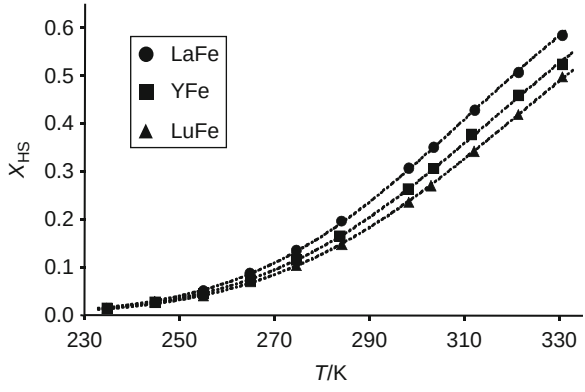

FIGURE 120 Mole fraction of high-spin Fe^{II} in $[RFe(\mathbf{L37})_3]^{5+}$ solutions in acetonitrile versus temperature (redrawn after Piguet et al., 1997b).

this temperature is relatively insensitive to the nature of the lanthanide ion (359–363 K), with the exception of Ce^{III}. On the other hand, there is smooth dependence of T_{SC} on the size of the metal ion for the **L36**

helicates, with an increase from 336 K (La) to 349 K (Sc), allowing a remarkable tuning of this parameter by the R^{III} ion (Piguet et al., 1997b). Replacement of the methyl substituent on the pyridine moiety (**L37**) has little consequence on the thermodynamic parameters, but lowers T_{SC} by a welcome 10 K, although the tuning range is somewhat reduced (320–331 K). The inner-sphere reorganization energy associated with the elongation of the Fe-N bond upon conversion from low-spin to high-spin Fe^{II} is in the range 8–25 kJ mol^{-1} and is expected to be the dominant contribution to ΔH_{SC}. The entropic factor encompasses a small electronic contribution associated with the difference in the degeneracy of the low- and high-spin states and larger ones arising from vibrational partition functions, the disorder of the high-spin state being more pronounced owing to longer Fe-N bonds.

Associating a luminescent R^{III} ion with paramagnetic Fe^{II} in the same supramolecular structure leads to materials with a fascinating combination of properties and tuning abilities thanks to a judicious ligand choice (Edder et al., 2001). For instance, the steric constraint linked to the introduction of a methyl group in the 6-position of the pyridine in **L41** results in the sole presence of high-spin HHH-$[EuFe(\mathbf{L41})_3]^{5+}$ helicate, both in solution and in the solid state (2–300 K) instead of the usual spin-state equilibrium, as observed for $[EuFe(\mathbf{L36})_3]^{5+}$; this is ascertained by the weak LMCT absorption band ($\varepsilon \approx 500\ M^{-1}cm^{-1}$) around 450 nm, responsible for the yellow color of the complex, and the faint d-d transitions at 910 ($14\ M^{-1}cm^{-1}$) and 1130 nm ($11\ M^{-1}cm^{-1}$). For comparison, the LMCT of the pure low-spin complexes $[LnFe(\mathbf{L36})_3]^{5+}$, accounting for their violet color, extends from 430 to 630 nm and is much more intense, with ε reaching 5800 $M^{-1}cm^{-1}$ at the maximum at 530 nm. As a result, the $^5D_0$ luminescence in $[EuFe(\mathbf{L36})_3]^{5+}$ is totally quenched in the range 10–400 K in view of the overlap between the Eu emission spectrum and this broad LMCT state (Piguet et al., 1997b). A similar quenching happens for $[EuFe(\mathbf{L35})_3]^{5+}$ as well (Piguet et al., 1995e). On the other hand, $[EuFe(\mathbf{L41})_3]^{5+}$ is luminescent, even at room temperature, yet less than the corresponding Zn^{II} complex, as indicated by the $Eu(^5D_0)$ lifetime which drops from 2.63 ms (ligand excitation, solid state, 13 K) in the zinc helicate to 0.28 ms in the iron complex due to partial directional $Eu^{III} \rightarrow Fe^{II}_{HS}$ energy transfer, the latter ion acting as a semitransparent partner (Figure 121).

7.5.2 Tuning visible lanthanide emission

The ligand-centered photophysical properties of the helicates with a spectroscopically silent nd-transition partner are not essentially different from those of the previously discussed homobimetallic helicates and will not be detailed here. When a nd-transition ion amenable to form MLCT states with the ligand strands is introduced into the helical edifices,

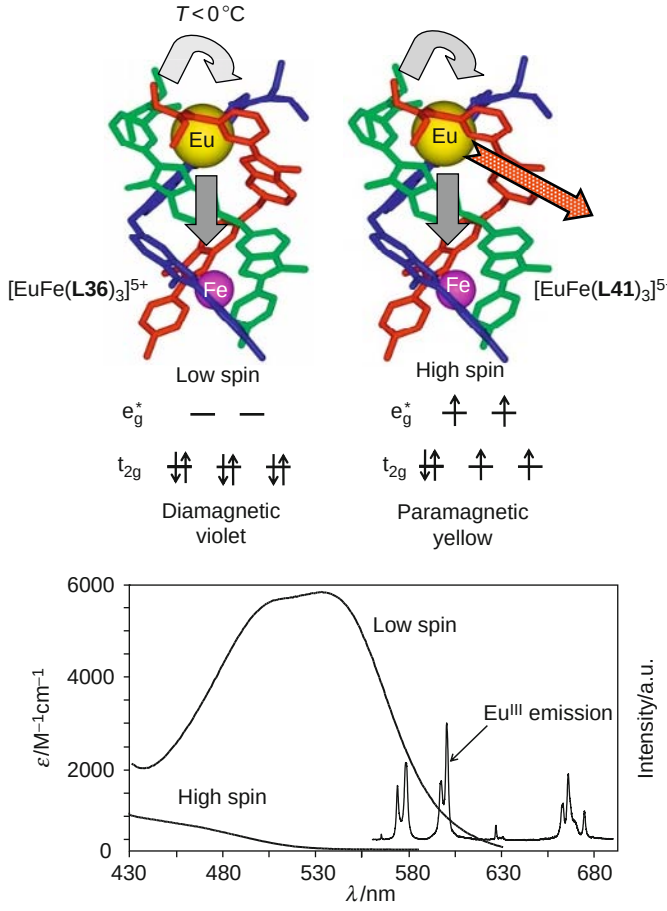

FIGURE 121 Top: schematic representation of energy transfer processes in low-spin $[EuFe(\mathbf{L36})_3]^{5+}$ (left) and high-spin $[EuFe(\mathbf{L41})_3]^{5+}$ (right). Bottom: absorption spectra at 295 K (left scale) of high-spin $[EuFe(\mathbf{L41})_3]^{5+}$ and of spin-crossover $[EuFe(\mathbf{L36})_3]^{5+}$ complexes in acetonitrile, as well as the overlapping Eu^{III} emission spectrum (right scale) of high-spin $[EuFe(\mathbf{L41})_3]^{5+}$ (solid state, 13 K) (redrawn after Edder et al., 2001).

specific absorption and, possibly, emission bands from these state are also observed, as well as d-d transitions. Relevant data are collected in Table 26 and show a relatively small influence of the lanthanide complexation on the ligand levels when M = Zn but a more pronounced one for the other ions. Lifetimes and quantum yields for lanthanide-centered luminescence are listed in Table 27. Except for $[EuCr(\mathbf{L36})_3]^{6+}$, in which Eu-to-Cr energy transfer is operating, and for $[EuFe(\mathbf{L41})_3]^{6+}$ for reasons discussed above, the Eu($^5D_0$) lifetimes are long, ca. 2.3–3.0 ms. This is

TABLE 26 Selected ligand-centered photophysical properties of the ligands and some of the $[RML_3]^{m+}$ and $[Cr^{II/III}RCr^{II/III}L_3]^{m+}$ helicates

L	*R*	M	State[a]	*T* (K)[b]	*E*(*π ← π) (cm^{-1})	*E*(MLCT) + *E*(d–d) (cm^{-1})	*E*($^1ππ^*$) (cm^{-1})	*E*($^3ππ^*$) (cm^{-1})	τ($^3ππ^*$) (ms)	References
L35			s	77	29,600, 28,600		25,000	19,200, 18,650	350, 88	Piguet et al. (1995d)
	La	Zn^{II}	s	77	29,600, 26,200		22,600	19,700, 18,900	124, 37	
	Lu	Zn^{II}	s	77	30,300, 25,650		22,200	19,700, 18,900	243, 79	
L35			$CHCl_3$	293	35,490, 31,450		NA	NA	NA	Piguet et al. (1995e)
	La	Fe^{II}	$CHCl_3$	293	30,550, 26,880	18,800	23,000[c]	19,000[c]	NA	
	Eu	Fe^{II}	$CHCl_3$	293	30,270, 27,020	18,870	23,000[c]	19,000[c]	NA	
L36			s	77	30,770		24,940	20,040, 18,870	560, 41[d]	Piguet et al. (1996)
	La	Zn^{II}	s	77	31,000		22,600	19,960, 19,050	250, 36[d]	
	Gd	Zn^{II}	s	77	31,250		22,600	19,960, 19,050	12, 5[d]	
L36			MeCN	293	33,320, 31,750		NA	NA	NA	Piguet et al. (1997b)
	La	Fe^{II}	MeCN	293	29,940, 28,570	19,050	22,220[c]	18,520[c]	NA	
	Lu	Fe^{II}	MeCN	293	29,940, 28,570	19,080	22,220[c]	18,520[c]	NA	
L36	La	Cr^{II}	MeCN	293	40,486, 30,121	23,640, 16,475, 14,368, 11,710, 9090, 8368				Cantuel et al. (2002)
	La	Cr^{III}	MeCN	293	40,486, 30,030	25,700, 22,800, 21,600, 20,000				
	Lu	Cr^{III}	MeCN	293	40,486, 29,940	25,700, 22,800, 21,600, 20,000				
L36	Lu	Ru^{II}	MeCN	296	39,525, 29,940	21,100	[e]	14,730[f]	0.38×10^{-3}[f]	Torelli et al. (2004)

(*continued*)

TABLE 26 (*continued*)

L	*R*	M	State[a]	*T* (K)[b]	*E*(*π ← π) (cm^{-1})	*E*(MLCT) + *E*(d–d) (cm^{-1})	*E*($^1ππ^*$) (cm^{-1})	*E*($^3ππ^*$) (cm^{-1})	τ($^3ππ^*$) (ms)	References
	Gd	Ru^{II}	MeCN	293	40,160, 30,120	21,185	25,800[g]	24,300, 20,700[g]	94[g]	Torelli et al. (2005)
L36	Lu	Os^{II}	MeCN	293	29,850	19,920, 14,500	[e]	12,400[f]	31×10^{-6}[f]	Riis-Johannessen et al. (2008)
L37			CH_2Cl_2	293	30,490					Edder et al. (2000)
	La	Zn^{II}	CH_2Cl_2	293	29,670					
	La	Fe^{II}	CH_2Cl_2	293	29,940	18,180, 17,270				
	Lu	Fe^{II}	CH_2Cl_2	293	29,670	18,180, 17,250				
L37			s	77	28,170		22,936	23,900, 22,650	68[d]	Edder et al. (2000)
	La	Zn^{II}	s	77	27,174		21,740	19,230, 18,250, 17,390	480[d]	
	Eu	Zn^{II}	s	77	26,675		21,645	[e]	[e]	
HL38	Eu	Zn^{II}	MeCN	293	41,000, 30,580		[e]	[e]	[e]	Edder et al. (1997)
L41			s	77	30,670		25,250	21,260, 19,690, 19,120, 16,550	605, 45[d]	Edder et al. (2001)
	La	Zn^{II}	s	77	30,210		23,700	20,920, 19,530, 18,140, 16,750	221	
	La	Fe^{II}	s	77	30,210	19,010	[e]	18,870[d]	261, 30	Cantuel et al. (2006)
L42	Lu	$Cr^{II}Cr^{II}$	MeCN	293	31,150, 27,300	16,690, 14,200, 11,765, 10,225, 8300		18,900[d]	2.45, 0.49[d]	
	Lu	$Cr^{III}Cr^{III}$	MeCN	295	31,350, 27,100	27,100, 20,000		24,450[d]	2.45, 0.49[d]	

[a] s, solid state.
[b] Except for *π ← π transitions of solid state samples, recorded by reflectance spectroscopy at room temperature.
[c] Very weak signal.
[d] At low temperature (77, 13, or 10 K).
[e] Luminescence quenched.
[f] From the ^{3}MLCT state.
[g] At 77 K.

TABLE 27 Quantum yields and lifetimes of the $[RML_3]^{n+}$ helicates, $R = Eu$, Tb upon ligand excitation

L	R	M	$\tau(^5D_J)$ (ms)[a]	c (M)	Q_L^{Ln} (%)[b]	References
L35	Eu	Zn	2.30(5)	10^{-4}	≈0.01	Piguet et al. (1995d, 1996)
	Tb	Zn	1.17(4)		NA	Piguet et al. (1995d)
L36	Eu	Zn	2.56	10^{-3}	4.2	Piguet et al. (1996)
			(10)	10^{-4}	9.3	
	Tb	Zn	1.89(6)		NA	
	Eu	Cr^{III}	0.55(4)[c]	10^{-4}	3.2	Cantuel et al. (2002)
L37	Eu	Zn	2.35(2)	10^{-3}	8.2	Edder et al. (2000)
HL38	Eu	Zn	2.99(9)	10^{-4}	32	Edder et al. (1997)
			2.43(2)[d]	10^{-4} [d]	15	
L41	Eu	Zn	2.63(1)	10^{-3}	7.4	Edder et al. (2001)
	Eu	Fe^{II}	0.28(1)	10^{-3}	0.03	

[a] Solid state sample, at 10 or 13 K, ligand excitation.
[b] In acetonitrile at room temperature; recalculated by using the most recent values reported for the $[R(terpyridine)_3]^{3+}$ internal references, 32 ± 1 ($R = Eu$) and $35 \pm 1\%$ ($R = Tb$) in acetonitrile (Comby, 2008); uncertainty: ±10–15%.
[c] For $[EuCr(\mathbf{L36})_3](CF_3SO_3)_6 \cdot 4H_2O$; 0.75(1) ms for $[EuCr(\mathbf{L36})_3](CF_3SO_3)_6 \cdot 4MeCN$, and 0.87(4) ms for a solution 10^{-4} M in acetonitrile.
[d] 10^{-4} M in H_2O.

clearly in line with an inner coordination sphere devoid of water molecules. On the other hand, $Tb(^5D_4)$ lifetimes are shorter, probably due to some back transfer operating, the $^3\pi\pi^*$ states of the coordinated **L35** and **L36** ligands having an energy (≈19,000–20,000 cm^{-1}) close to the one of the $^5D_4$ level, 20,500 cm^{-1}. Quantum yields have only been determined for Eu^{III} helicates. They span a wide range, from 0.01% in $[EuZn(\mathbf{L35})_3]^{5+}$ because the N_9 environment made up of benzimidazolepyridine units is known to generate a rather low-lying and quenching LMCT state (Gonçalves e Silva et al., 2000; Petoud et al., 1999), to a high 32% for the sparingly soluble carboxylate $[EuZn(\mathbf{L38})_3]^{2+}$. The robustness of the triple-helical edifice is exemplified by the fact that adding up to 0.93 M water to $[EuZn(\mathbf{L36})_3]^{5+}$ does not alter either the $^5D_0$ lifetime or the quantum yield (Piguet et al., 1996). Similarly, the quantum yield of $[EuCr(\mathbf{L36})_3]^{5+}$ in acetonitrile ($Q = 3.2\%$) remains unchanged up to 3 M added water (Cantuel et al., 2002). If the same experiment is conducted on the even more robust $[EuZn(\mathbf{L38})_3]^{2+}$ helicate in acetonitrile, the quantum yield slightly drops to reach 87% of its initial value up to 2 M of added water, probably in view of the second sphere effect of fast diffusing O–H

vibrators, and then further decreases slowly to reach about 80% of its initial value for a water concentration of 10 M. The quantum yield in pure water is about half that in acetonitrile and the lifetime is still long, 2.43 ms; with $\tau(D_2O) = 4.48$ ms, one calculate $q \approx 0$, using Supkowski and de Horrocks (2002) equation, a remarkable result in that even in pure water, there is no inner sphere interaction with the solvent (Edder et al., 1997).

When one metal ion plays the role of a donor for sensitizing the emission of a second accepting metal ion, the characteristic lifetimes τ of their excited states, which are related to their deactivation rates by $\tau_{em} = (k_{em})^{-1}$, are affected by the intermetallic communication process (Figure 122). If the energy transfer rate is much faster than the deactivation rate of the donor ion, the situation is very simple and assuming a Förster's dipole–dipolar mechanism, the yield of the transfer is given similarly to Eq. (77) by

$$\eta_{DA} = 1 - \frac{\tau^{D}_{obs}}{\tau^{D}_{0}} = 1 - \frac{Q^{D}_{obs}}{Q^{D}_{0}} = \frac{1}{\left(1 + \frac{R^{DA}}{R^{DA}_{0}}\right)^{6}} \tag{153}$$

where D stands for the donor and A for the acceptor, while subscript 0 for τ and Q denotes the situation without energy transfer; R^{DA} is the distance between the donor and the acceptor and R^{DA}_0 is the critical distance for 50% transfer. The experimental parameters corresponding to the situation without transfer are usually measured on $[RZnL_3]^{m+}$ or $[GdML_3]^{m+}$ complexes.

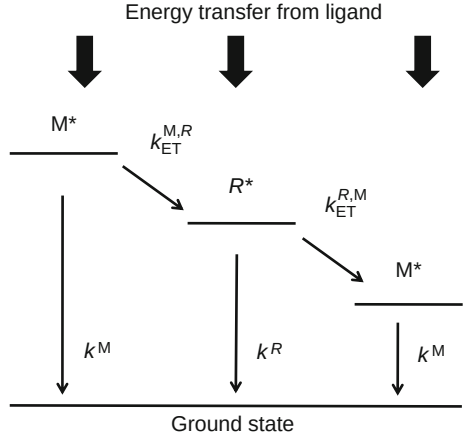

FIGURE 122 Schematic representation of a nd-to-4f energy transfer (left) and of a 4f-to-nd transfer (right) along with the definition of the rate constants.

The chromium helicate $[EuCr^{III}(\mathbf{L36})_3]^{6+}$ displays both $Cr(^2E \rightarrow {}^4A_2)$ and $Eu(^5D_0 \rightarrow {}^7F_j)$ emission. The lifetime of the latter is considerably shorter than in $[EuZn(\mathbf{L36})_3]^{5+}$, which is assigned to unidirectional $Eu \rightarrow Cr$ transfer along the C_3-axis (Cantuel et al., 2002). Determination of η_{CrEu} for two types of crystalline samples (hydrated and anhydrous, see Table 28) provides the same temperature-independent (10–295 K) efficiencies for this transfer, within experimental errors, $\approx 70 \pm 5\%$. The energy transfer yield is also insensitive to the nature of the sample, as shown by the same calculation carried out for 10^{-4} M solutions in acetonitrile using either quantum yields (see Table 27, $\eta_{CrEu} = 66\%$) or lifetimes (70%), a proof of the dipole–dipolar mechanism operating in these fairly rigid triple-helical structures (the calculated R_0 distance is ≈ 10.3 Å). In the case of Tb, the transfer is quantitative, no $^5D_4$ luminescence being observed even upon direct Tb excitation, because of the near resonance between the $Tb(^5D_4)$ and $Cr(^4T_2)$ electronic levels.

7.5.3 Tuning near-infrared lanthanide emission

Because of its transparency to biological tissue, NIR light is praised for bioprobes and many R^{III} ions seem to be ideally suited for this purpose. There are, however, two problems with these probes (Comby and Bünzli, 2007): (i) due to the small energy gap, the excited states are readily deactivated by all kind of vibrational oscillators, even by those residing in the outer coordination sphere, and (ii) the excited state lifetime is usually short, limiting the ease of application of TRD. The latter inconvenience may be remedied by populating the excited state of the NIR-emitting R^{III} ion by a slow emitting donor. Some transition metal ions such as Cr^{III} meet the necessary criteria and the triple-helical receptors dealt with in this chapter appear to be ideal hosts for facilitating such an energy transfer. The $[RCr^{III}(\mathbf{L36})_3]^{6+}$ and $[RRu^{II}(\mathbf{L36})_3]^{5+}$ complexes (R = Nd, Gd, Er, Yb), have been thoroughly tested for this purpose (Imbert et al., 2003; Torelli et al., 2005). The situation can be modeled as follows (Figure 122). In absence of energy transfer, the excited states of the isolated chromophores have deactivation rates k^R and k^M which are the sum of the radiative and nonradiative rate constants:

$$d[M^*]/dt = -\left(k_{ET}^{M,R} + k^M\right)[M^*] \tag{154}$$

$$d[R^*]/dt = k_{ET}^{M,R}[M^*] - k^R[R^*] \tag{155}$$

TABLE 28 Lifetimes, quantum yields, and energy transfer yields in microcrystalline samples of $[RZn(\mathbf{L36})_3]^{5+}$ and $[RCr^{III}(\mathbf{L36})_3]^{6+}$ helicates (data from Cantuel et al., 2002)

*R*M	*T* (K)	$\tau(^5D_J)$ (ms)[a]	$\tau(^2E)$ (ms)[a]	η_{RCr} (%)[b]	*R*M	*T* (K)	$\tau(^5D_J)$ (ms)[a]	$\tau(^2E)$ (ms)[a]	η_{RCr} (%)
GdCr	10	–	3.66(3)		GdCr	295		0.29(1)	
EuZn[b]	10	2.53(1)			EuZn[b]	295	1.67(2)		
EuCr[c]	10	0.55(4)	3.46(1)	78 (73)	EuCr[c]	295	0.59(1)	0.09(1)	65
EuZn[d]	10	2.19(1)			EuZn[d]	295	1.98(1)		
EuCr[e]	10	0.75(1)	3.12(1)	66 (70)	EuCr[e]	295	0.66(1)	0.05(1)	67
TbCr	10	[f]	3.39(1)	100	TbCr	295	[f]	0.17(1)[g]	100

[a] Upon ligand excitation.
[b] Values between parentheses are averages of data recorded at different excitation wavelengths.
[c] $[EuZn(\mathbf{L36})_3](ClO_4)_5 \cdot 2H_2O$.
[d] $[EuCr(\mathbf{L36})_3](CF_3SO_3)_6 \cdot 4H_2O$.
[e] $[EuCr(\mathbf{L36})_3](CF_3SO_3)_6 \cdot 4MeCN$.
[f] No $^5D_4$ luminescence.
[g] Direct excitation in the $Tb(^5D_4)$ level.

Integration gives:

$$[\mathrm{M}^*] = [\mathrm{M}_0^*]\cdot\exp\left\{-\left(k_{\mathrm{ET}}^{\mathrm{M},R} + k^{\mathrm{M}}\right)t\right\} \tag{156}$$

$$[R^*] = [\mathrm{M}_0^*]\frac{k_{\mathrm{ET}}^{\mathrm{M},R}}{k^R - \left(k_{\mathrm{ET}}^{\mathrm{M},R} + k^{\mathrm{M}}\right)}\left(\exp\left\{-\left(k_{\mathrm{ET}}^{\mathrm{M},R} + k^{\mathrm{M}}\right)t\right\} - \mathrm{e}^{-k^R t}\right) \tag{157}$$

Equation (156) reveals that the decay rate of the excited state of the donor (in this case M*) increases, when energy is transferred onto the acceptor. The experimental decay of the donor metal ion thus corresponds to the sum of the two deactivation rate constants $k_{\mathrm{obs}}^{\mathrm{M}} = k^{\mathrm{M}} + k_{\mathrm{ET}}^{\mathrm{M},R}$, which translates into a reduced lifetime $\tau^{\mathrm{M}} = (k_{\mathrm{obs}}^{\mathrm{M}})^{-1} = (k^{\mathrm{M}} + k_{\mathrm{ET}}^{\mathrm{M},R})^{-1}$. Interpretation of Eq. (157) is complicated, because the magnitude of $k_{\mathrm{ET}}^{\mathrm{M},R}$ controls the population rate of the R^* excited state. Therefore, the decay profile of R^* after initial excitation of the donor depends much on the relative magnitudes of the rate constants $k_{\mathrm{obs}}^{\mathrm{M}} = k^{\mathrm{M}} + k_{\mathrm{ET}}^{\mathrm{M},R}$ and k^R. Two limiting cases can be considered.

The first one refers to a situation for which $k_{\mathrm{obs}}^{\mathrm{M}} \gg k^R$, that is, the R^* level is almost completely populated before any significant lanthanide-centered deactivation occurs. As a consequence, the experimental deactivation rate k_{obs}^R mirrors the one found in absence of intermetallic communication, k^R. Introducing $k_{\mathrm{obs}}^{\mathrm{M}} \gg k^R$ into Eq. (157) produces Eq. (158), whereby the time dependence of the luminescence decay corresponds to an apparent rate constant $k_{\mathrm{app}}^R = k^R$:

$$[R^*] = [\mathrm{M}_0^*]\frac{k_{\mathrm{ET}}^{\mathrm{M},R}}{k_{\mathrm{ET}}^{\mathrm{M},R} + k^{\mathrm{M}}}\mathrm{e}^{-k^R t} \tag{158}$$

This situation is met for several d–f pairs, because the intrinsic deactivation rates of the d-block donors k^{M} are often considerably larger than the deactivation of the NIR-emitting R-centered excited states. This is for instance true for the Ru → Yb transfer in $[\mathrm{YbRu}(\mathbf{L36})_3]^{5+}$ (Figure 123, top). As expected, the experimental decay rate of the donor $k_{\mathrm{obs}}^{\mathrm{Ru}} = 1.2{\cdot}10^5\,\mathrm{s}^{-1}$ is larger than $k^{\mathrm{Ru}} = 1.0{\cdot}10^5\,\mathrm{s}^{-1}$ (measured for $[\mathrm{RuGd}(\mathbf{L36})_3]^{5+}$), which is diagnostic for the existence of the Ru → Yb energy transfer. Since $k_{\mathrm{obs}}^{\mathrm{Ru}} = 1.2{\cdot}10^5\,\mathrm{s}^{-1} > k^{\mathrm{Yb}} = 5{\cdot}10^4\,\mathrm{s}^{-1}$ (measured for $[\mathrm{ZnYb}(\mathbf{L36})_3]^{5+}$), Eq. (158) predicts that the apparent (experimental) Yb-centered decay rate recorded for $[\mathrm{RuYb}(\mathbf{L36})_3]^{5+}$ should roughly mirror k^{Yb}, which is the case, within experimental errors: $k_{\mathrm{app}}^{\mathrm{Yb}} = 4.4{\cdot}10^4\,\mathrm{s}^{-1}$.

The second limiting case arises when $k_{\mathrm{obs}}^{\mathrm{M}} \ll k^{\mathrm{Ln}}$, that is, when the R-centered excited state relaxes almost instantaneously upon being

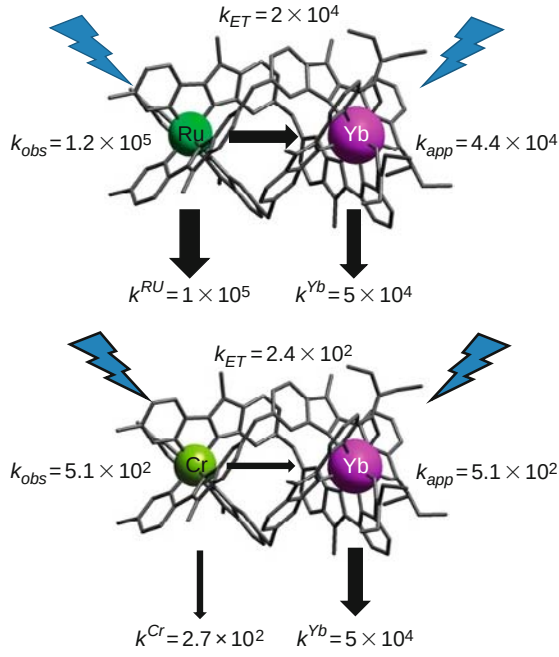

FIGURE 123 Schematic representation of the energy migration processes taking place in $[YbM(\mathbf{L36})_3]^{m+}$ helicates ($M = Ru^{II}$, Cr^{III}). Rate constants are given in s^{-1} (redrawn from Bünzli and Piguet, 2005).

populated by the slow-decaying d-block chromophore. Therefore, the deexcitation of the d-block ion ($k^{M}_{obs} = k^{M} + k^{M,R}_{ET}$) controls the overall deactivation process, and the apparent *R*-centered deactivation rate k^{R}_{app} should be equal to k^{M}_{obs}. Introduction of the condition $k^{M}_{obs} \ll k^{R}$ into Eq. (157), provides a simplified equation (159), showing that the time dependence of the *R** luminescence decay indeed corresponds to $k^{R}_{app} = k^{M}_{obs}$:

$$[R^*] = [M^*_0]\frac{k^{M,R}_{ET}}{k^R}\exp\left\{-\left(k^{M,R}_{ET} + k^{M}\right)t\right\} = [M^*_0]\frac{k^{M,R}_{ET}}{k^R}e^{-k^{M}_{obs}t} \qquad (159)$$

This situation is illustrated when Ru^{II} is replaced with Cr^{III} as the donor in $[CrYb(\mathbf{L36})_3]^{6+}$. Indeed, the combination of the intrinsic deactivation rate of the Cr-centered donor levels $k^{Cr} = 2.7 \cdot 10^2\,s^{-1}$ (measured for $[CrGd(\mathbf{L36})_3]^{6+}$), with the rate of energy transfer $k^{Cr,Yb}_{ET} = 2.4 \cdot 10^2\,s^{-1}$ gives $k^{Cr}_{obs} = k^{Cr} + k^{Cr,Yb}_{ET} = 5.1 \cdot 10^2\,s^{-1}$. The latter value is small compared to the inherent rate of deactivation of $Yb(^2F_{5/2})$, $k^{Yb} = 5 \cdot 10^4\,s^{-1}$ (measured for

$[ZnYb(\mathbf{L36})_3]^{5+}$), so that $k^{Yb} \gg k^{M}_{obs}$ (Figure 123, bottom). As predicted by Eq. (159), the experimental decay of the Yb-centered emission amounts to $k^{Yb}_{app} = 5.1 \cdot 10^2\ s^{-1}$, which exactly matches the slow deactivation rate of the Cr^{III} chromophore k^{Cr}_{obs}. These rate constants can be transformed into characteristic excited lifetimes, thus leading to $\tau^{Yb}_{app} = (k^{Yb}_{app})^{-1} = 23\ \mu s$, when Yb^{III} is sensitized by Ru^{II} in $[RuYb(\mathbf{L36})_3]^{5+}$, and $\tau^{Yb}_{app} = (k^{Yb}_{app})^{-1} = 1960\ \mu s = 1.96$ ms, when Yb^{III} is sensitized by Cr^{III} in the isostructural complex $[CrYb(\mathbf{L36})_3]^{6+}$. Such apparent lengthening of the lanthanide-centered NIR luminescence by two orders of magnitude demonstrates the tuning capacity of the binuclear supramolecular edifices and may be valuable for improving the sensitivity of time-gated bioanalyses, provided that a judicious choice of the donor chromophore is made. The relevant parameters for $R = Nd$, Er, Yb and $M = Ru$, Cr are listed in Table 29 for two temperatures, 10 and 295 K. At low temperature, at which phonon-assisted transfer would be minimized, Cr^{III} is a better donor than Ru^{II} and the efficiency of the process decreases in the order $Nd > Er > Yb$. The latter order is understandable in that the overlap integral between the emission spectrum of the donor and the absorption spectrum of the acceptor is largest for Nd owing to more lanthanide-centered excited states in the 13–15,000 cm^{-1} range as compared to Er and Yb. As a consequence, the largest critical distance for 50% transfer occurs for **NdCr**. It is also noteworthy that the apparent rate constants for the *R* ions are smaller by one to two orders of magnitude compared to the situation in which the lanthanide ion is not populated by the energy transfer (Torelli et al., 2005).

7.6 Enantiomerically pure lanthanide-containing helicates

The rationale for producing enantiomerically pure lanthanide-containing complexes lies in their potentiality for probing biological molecules or for sensing chiral substances (Shinoda et al., 2005). For instance, optically active lanthanide chelates with tetrapodal ligands intercalate selectively into DNA strands (Bobba et al., 2002) and their utility for live cell imaging has been proved (Poole et al., 2005). But the bioprobes need not to be optically pure in that the interaction of racemic mixtures with chiral substrates may stabilize one diastereomer, thus producing a diastereomeric excess which can be detected by circular dichroism (CD) or circularly polarized luminescence (CPL); this is for instance true for triple-helical $[Pr(2,2'\text{-dioxydiacetate})_3]^{3-}$ which interacts with L-proline in its ground state to generate a significant residual CD spectrum (Parac-Vogt et al., 2002).

When chirality is detected by CD, which probes the ground state chirality, either the coordinated chromophore absorption or the intraconfigurational f–f transitions are measured. The extent of the effect is

TABLE 29 Experimental deactivation rates (see text for definitions), calculated energy transfer efficiencies, Eq. (153), and critical distances for 50% transfer ($R_0^{M,R}$) in microcrystalline samples of $[RM(\mathbf{L36})_3]^{m+}$ helicates ($M = Cr^{III}$, Ru^{II}) (data from Torelli et al., 2005)

RM	*T* (K)	k_{obs}^{M} (s^{-1})	k^{M} (s^{-1})[a]	k_{app}^{R} (s^{-1})	k^{R} (s^{-1})[b]	$k_{ET}^{M,R}$ (s^{-1})	$\eta_{ET}^{M,R}$ (%)	$R_0^{M,R}$ (Å)
NdCr	10	2.13×10^3	2.73×10^2	2.13×10^3	6.84×10^5	1.86×10^3	87	12.8
YbCr	10	5.10×10^2	2.73×10^2	5.10×10^2	5.00×10^4	2.37×10^2	46	9.1
NdRu	10	1.55×10^5	1.04×10^5	1.65×10^5	6.84×10^5	5.10×10^4	33	8.1
ErRu	10	1.44×10^5	1.04×10^5	1.44×10^5	NA	4.00×10^4	28	7.7
YbRu	10	1.27×10^5	1.04×10^5	4.4×10^4	5.00×10^4	2.30×10^4	18	7.1
NdCr	295	8.33×10^3	3.45×10^3	8.33×10^3	6.25×10^5	4.88×10^3	59	12.8
YbCr	295	4.17×10^3	3.45×10^3	4.17×10^2	4.35×10^4	7.20×10^2	17	9.1
NdRu	295	3.45×10^6	1.16×10^6	6.94×10^5	NA	2.99×10^6	66	8.1
ErRu	295	1.85×10^6	1.16×10^6	1.85×10^6	NA	6.90×10^5	37	7.7
YbRu	295	1.68×10^6	1.16×10^6	5.71×10^4	NA	5.20×10^5	31	7.1

[a] Measured on GdM samples.
[b] Measured on *R*Zn samples.

characterized by the absorption dissymmetry factor defined from the difference in absorption between left (L) and right (R) circularly polarized light (Riehl and Muller, 2005):

$$g_{\text{abs}} = \frac{2\Delta\varepsilon}{\varepsilon} = \frac{2(\varepsilon_{\text{L}} - \varepsilon_{\text{R}})}{\varepsilon_{\text{L}} + \varepsilon_{\text{R}}} \tag{160}$$

CPL is the emissive pendent of CD and therefore probes the excited state chirality; it also reflects the molecular motions taking place between absorption and emission. In this case, the parameter of interest is the luminescence dissymmetry factor:

$$g_{\text{lum}} = \frac{2\Delta I}{I} = \frac{2(I_{\text{L}} - I_{\text{R}})}{I_{\text{L}} + I_{\text{R}}} \tag{161}$$

Theoretically, g_{lum} can be related to the electric and magnetic dipole transition moments μ^{gn} and m^{gn} (g denotes the ground state and n the excited state):

$$g_{\text{lum}}(\lambda) = 4\frac{f_{\text{CPL}}(\lambda)}{f_{\text{TL}}(\lambda)}\frac{\mu^{\text{gn}} m^{\text{gn}}}{(\mu^{\text{gn}})^2} \tag{162}$$

where $f_{\text{CPL}}(\lambda)$ and $f_{\text{TL}}(\lambda)$ are the line shapes for CPL and total luminescence (TL) signals. Since μ^{gn} is much larger than m^{gn}, CPL usually focuses on Laporte's allowed magnetic dipole transitions. For lanthanides, the best suited transitions are Sm($^4G_{5/2} \rightarrow {}^6H_J$, $J = 7/2$, $5/2$), Eu ($^5D_0 \rightarrow {}^7F_1$), Tb($^5D_4 \rightarrow {}^7F_J$, $J = 3$–5), Gd($^8S_{7/2} \rightarrow {}^6P_{7/2}$), Dy($^4F_{9/2} \rightarrow {}^6H_{11/2}$), and Yb($^2F_{5/2} \rightarrow {}^2F_{7/2}$). One advantage of lanthanide complexes over organic chiral probes is their often large luminescence dissymmetry factors, which can reach ± 0.5 (up to -0.78 for one of the common standards, tris(3-trifluoroacetyl-d-camphorato)europium) compared to $\pm 10^{-3}$ to $\pm 10^{-2}$ for organic molecules, including helicenes. CPL is not yet a very popular instrumental technique because of the weakness of the signals measured but substantial improvements are being made, particularly with respect to the excitation wavelength used for Eu^{III}, and instrumentation can be expanded to use TRD so that CPL may develop as a essential tool for the enantiomeric recognition of biological substrates (Do et al., 2008).

7.6.1 Mononuclear precursors

There are numerous examples of lanthanide chiral complexes, including many pseudo-C_3 compounds with tridentate receptors such as terpyridines (Muller et al., 2002a) or pseudo-C_4 chelates with tetrapodal hosts (Parker, 2004) but here we only briefly discuss the precursors of the binuclear helicates described in this chapter, namely derivatives of bis(benzimidazole)pyridine and of dipicolinic acid. A contribution to the understanding of the helical wrapping of the ligands around the

lanthanide ion on the chiroptical properties was gained by studying the 1:*n* complexes of Eu^{III} with ligand **L17**[k] (Section 2.1, Figure 19): the measured weak CPL effect (attesting of the presence of a small diastereomeric excess in acetonitrile solution) of the 1:1 complex essentially arises from the influence of the remote asymmetric centers while for the 1:2 and 1:3 complexes, the structural contribution of the ligand wrapping intervenes as well, as confirmed by specific rotary dispersion measurements (Muller et al., 2003). Similar conclusions were reached for $[Eu(L)_3]^{3+}$, L = **L18**[b] and **L18**[c] (Section 2.1, Figure 21; Muller et al., 2001b, 2002b). In fact, isolation of pure enantiomers is difficult because of the usually large lability of the lanthanide ions.

7.6.2 Resolution of the PP and MM isomer of $[EuCr(\mathbf{L36})_3]^{6+}$

The synthesis of pure chiral nd–4f helicates requires the availability of facial noncovalent tripodal receptors $[M\mathbf{L}_3]^{n+}$ which feature an inert transition metal ion to avoid scrambling in solution. Within the range of investigated nd–4f compounds, both Co^{III} and Cr^{III} qualify, but the difficult oxidation of the former leaves traces of Co^{II} in solution which catalyzes the *fac*-$[Co(\mathbf{L36})_3]^{3+} \rightleftarrows$ *mer*-$[Co(\mathbf{L36})_3]^{3+}$ isomerization, so that Cr^{III} has been preferred (Figure 124). The inert receptors are obtained from the racemic 3d–4f helicate $[LaCr(\mathbf{L36})_3]^{6+}$ by removing the *R* ion with EDTA, followed by sorption onto a Sephadex® ion-exchange resin and elution with $Na_2Sb_2[(+)\text{-}C_4O_6H_2)]_2$. A careful examination of the Cotton effect experienced by the two separated isomers and comparison with M-(+)-$[CrL_3]^{3+}$ (L = phen, bipy) confirms the assignment of *P*-(+)-$[Cr(\mathbf{L36})_3]^{3+}$ and *M*-(-)-$[Cr(\mathbf{L36})_3]^{3+}$. Subsequent complexation with Eu^{III} affords the final chiral helicates *P*,*P*-(+)-$[EuCr(\mathbf{L36})_3]^{6+}$ and *M*,*M*-(-)-$[EuCr(\mathbf{L36})_3]^{6+}$.[3] The chiral isomers display mirror CD and CPL spectra, the latter for both the Eu ($^5D_0 \rightarrow {}^7F_J$, $J = 1$–4) and Cr($^2E \rightarrow {}^4A_2$) transitions and the crystal structure of the *M*,*M* isomer could be solved (Cantuel et al., 2004). Relevant chiroptical data are reported in Table 30.

Addition of R^{III} to the inert and chiral chromium podate *M*-$[Cr(\mathbf{L36})_3]^{3+}$ to self-assemble the *M*,*M*-$[RCr(\mathbf{L36})_3]^{6+}$ helicates (*R* = Eu, Gd, Tb) results in an inversion in the CD signal (Figure 125). The modeling of this effect by ZINDO calculations takes into account the exciton coupling model with three types of interaction, intranuclear between the ligand strands around each metal ions, and internuclear between ligand strands bound to different metal ions (Telfer et al., 2004). C_3-symmetry was assumed for the rigid CrN_6 chromophore in *M*,*M*-$[RCr(\mathbf{L36})_3]^{6+}$ and the results of the calculations show that a pair of oppositely signed rotational strengths appear in the range of the $^*\pi \leftarrow \pi$ transitions centered around 330–340 nm, with the positive rotational strength being of lower energy.

3 An alternate labeling for *M*,*M* is Λ,Λ while Δ,Δ is also used for *P*,*P*.

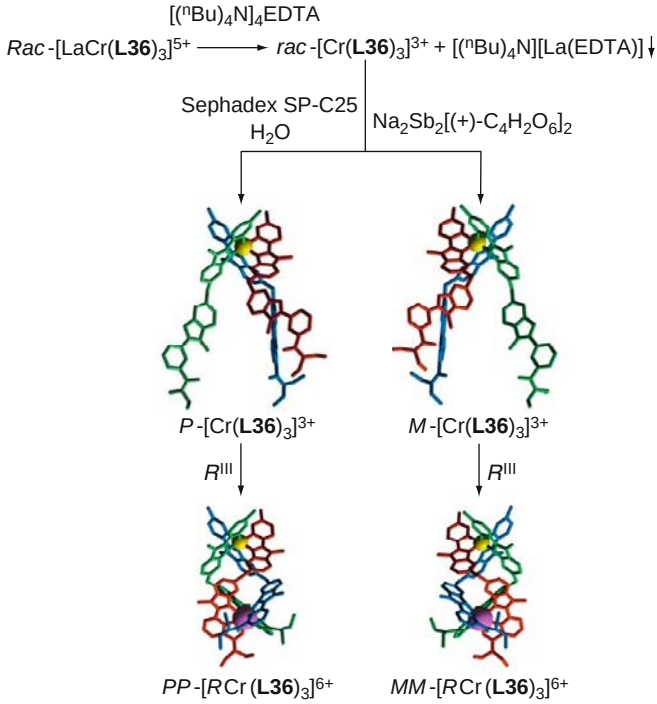

FIGURE 124 Chiral resolution of the tripodal receptor *rac*-$[Cr(\mathbf{L36})_3]^{3+}$ and formation of the pure chiral helicates *PP*-$[R Cr(\mathbf{L36})_3]^{6+}$ and *MM*-$[R Cr(\mathbf{L36})_3]^{6+}$ (redrawn after Telfer et al., 2004).

The RN_6O_3 center being more fluxional than CrN_6, prediction of the Cotton effect depends on the relative orientation of the chromophores; in particular, the CD signal inverses when the angle between two chromophores increases. This change in sign occurs without formal change in helicity! Taking a reasonable geometry into consideration though, the calculations predict that the ligands strands around the R^{III} ion give rise to CD signals of opposite phase compared to Cr^{III} despite the same absolute conformation they adopt.

The relative intensities of the CD spectra of the $[R Cr(\mathbf{L36})_3]^{6+}$ helicates are inversely proportional to the size of the R^{III} ion (Tb > Gd > Eu), supporting the assertion that chromophoric cavity around R^{III} produces a large negative exciton couplet, the coupling being strengthened when the ligand strands are tighter bound to the smaller R^{III} ions. A third contribution to the CD signal is the internuclear coupling giving rise to three excitons of moderate strength contributing to a negative signal at lower energy (i.e., in phase with the intranuclear *R* contribution). The relative contributions of these signals are depicted on Figure 125 (bottom). The computational model used excludes the metal ions, so that the

TABLE 30 Relevant chiroptical data for $[EuCr^{III}(\mathbf{L36})_3]^{6+}$ 1 mM in acetonitrile at 295 K (data from Cantuel et al., 2004)

Isomer	α^{20}(589) (deg mol^{-1} dm^2)	$\lvert\Delta\varepsilon^{340}_{max}\rvert$ (M^{-1}cm^{-1})	g_{lum}(Cr) $^2E \rightarrow {}^4A_2$	g_{lum}(Eu) $^5D_0 \rightarrow {}^7F_1$	g_{lum}(Eu) $^5D_0 \rightarrow {}^7F_2$	g_{lum}(Eu) $^5D_0 \rightarrow {}^7F_3$[a]	g_{lum}(Eu) $^5D_0 \rightarrow {}^7F_4$[a]
M,M	-1239	74	$+0.01$	-0.154	$+0.07$	-9.2×10^{-4}	$+0.033$
P,P	$+1146$		-0.01	$+0.163$	-0.07	$+8.9 \times 10^{-4}$	-0.034

[a] From Gawryszewska et al. (2006).

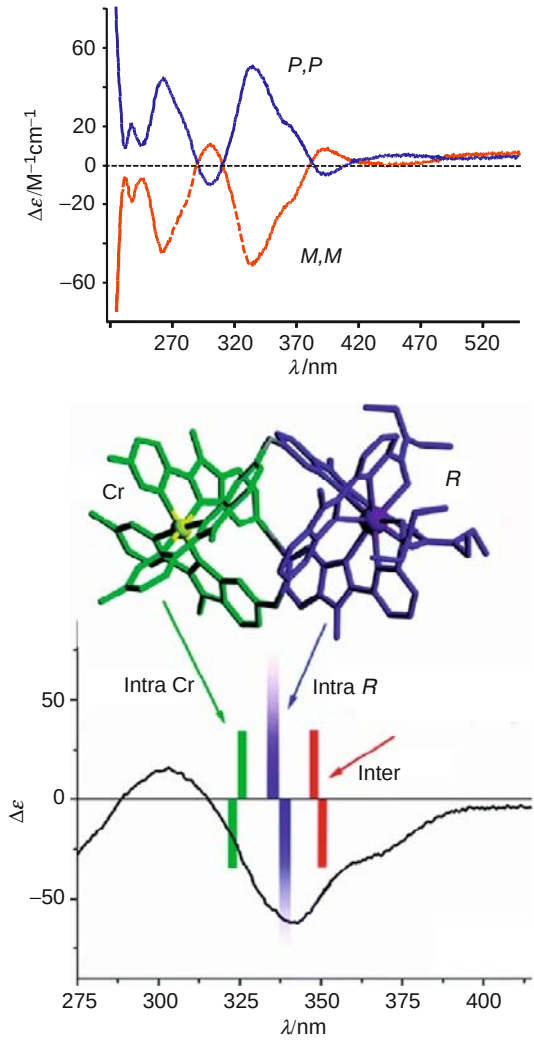

FIGURE 125 Top: CD spectra of *P,P*-[EuCr(**L36**)$_3$]$^{6+}$ and *M,M*-[EuCr(**L36**)$_3$]$^{6+}$ 1 mM in acetonitrile at 295 K (redrawn from Cantuel et al., 2004). Bottom: simulation of the 340-nm band with the exciton theory (redrawn from Telfer et al., 2004).

contribution of the MLCT state around 385 nm cannot be evaluated). The CPL spectra of *M,M*-[EuCr(**L36**)$_3$]$^{6+}$ and *P,P*-[EuCr(**L36**)$_3$]$^{6+}$ (Figure 126) have opposite values of g_{lum} for all four investigated transitions ($^5D_0 \rightarrow {}^7F_J$, $J = 1$–4); however, the signs are alternating, for example, for the *M,M* isomer, negative for $J = 1$ and 3 and positive for the other two

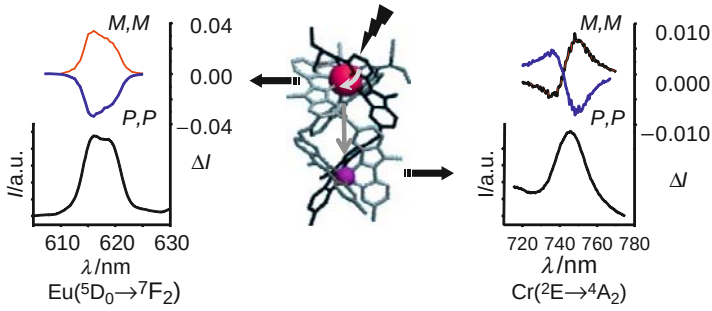

FIGURE 126 Parts of the CPL spectra of *P,P*-[EuCr(**L36**)$_3$]$^{6+}$ and *M,M*-[EuCr(**L36**)$_3$]$^{6+}$ 1 mM in acetonitrile at 295 K (redrawn from Cantuel et al., 2004).

transitions. A correlation between these signs and the structure of the helicate could not be established yet, probably because of a too large deviation from the idealized D_3-symmetry used for theoretical predictions (Gawryszewska et al., 2006).

7.7 Extension to polynuclear helicates: Pseudolanthanide cryptates

Associating Cr^{III} with R^{III} ions in binuclear triple-helical complexes leads to intramolecular energy transfers along the C_3-axis of the edifice, the directionality and yield of which depend on the nature of the R^{III} ion, $R \rightarrow Cr$ for Eu and Tb and $Cr \rightarrow R$ for the NIR-emitting Nd, Er, and Yb ions. In the latter case, the combination of the long-lived Cr(^{2}E) level ($k_{em} \approx 300$–$3000\ s^{-1}$ depending on the temperature) with a comparable energy transfer rate ($k_{ET}^{Cr,R} \approx 200$–$5000\ s^{-1}$, depending on the temperature) results in the R^{III} ion being preferentially populated by the 3d-metal ion and having an apparent lifetime mirroring that of the Cr(^{2}E) level. This apparent lengthening of the lifetime of the NIR emitting state is helpful for TRD analyses but does not improve the intrinsic quantum yield of the lanthanide ion. To boost the sensitivity of the overall sensitization process, without affecting the energy migration regime, several Cr^{III} chromophores would have to be connected to the lanthanide moiety. Expanding the binuclear helicate into a trinuclear molecule is an obvious first step in this direction and the tris(tridentate) ligand **L27** (Section 3.1, Figure 42) has been modified to the bidentate-tridentate-bidentate host **L42** (Section 7.2, Figure 110) thanks to a well established synthetic route (Section 7.2, Figure 112). An initial study has dealt with the resulting Eu and Tb trinuclear helicates [M*R*M(**L42**)$_3$]$^{m+}$ with both Zn^{II} and Cr^{III} (Cantuel et al., 2006). Although no stability constants could be determined, a fruitful combination of NMR, ES-MS and UV-vis spectroscopies

demonstrates that under strict stoichiometric conditions (2:1:3, M:*R*:L) and for a millimolar total ligand concentration, the target trinuclear helicate $[ZnRZn(\mathbf{L42})_3]^{7+}$ (R = La, Eu, Lu) is the major species in acetonitrile solution. Similarly to their binuclear counterparts, the helicates with Cr^{II} undergo an easy and rapid oxidation to $[Cr^{III}RCr^{III}(\mathbf{L42})_3]^{9+}$. Suitable crystals for X-ray structural determination could not be obtained, but high-resolution luminescence spectroscopy of $[ZnEuZn(\mathbf{L42})_3]^{7+}$ and $[CrEuCr(\mathbf{L42})_3]^{9+}$ is compatible with Eu^{III} located in a site with pseudo-D_3-symmetry (Figure 127, top). In particular both the energy of the $^5D_0 \rightarrow {}^7F_0$ transition and the splitting of the $^7F_1$ level matches very well those reported for $[EuZn(\mathbf{L35})_3]^{5+}$ (Table 24). In addition, analysis of the LIR for Zn*R*Zn complexes in acetonitrile (R = La, Eu, Tb, Lu, Y) shows that

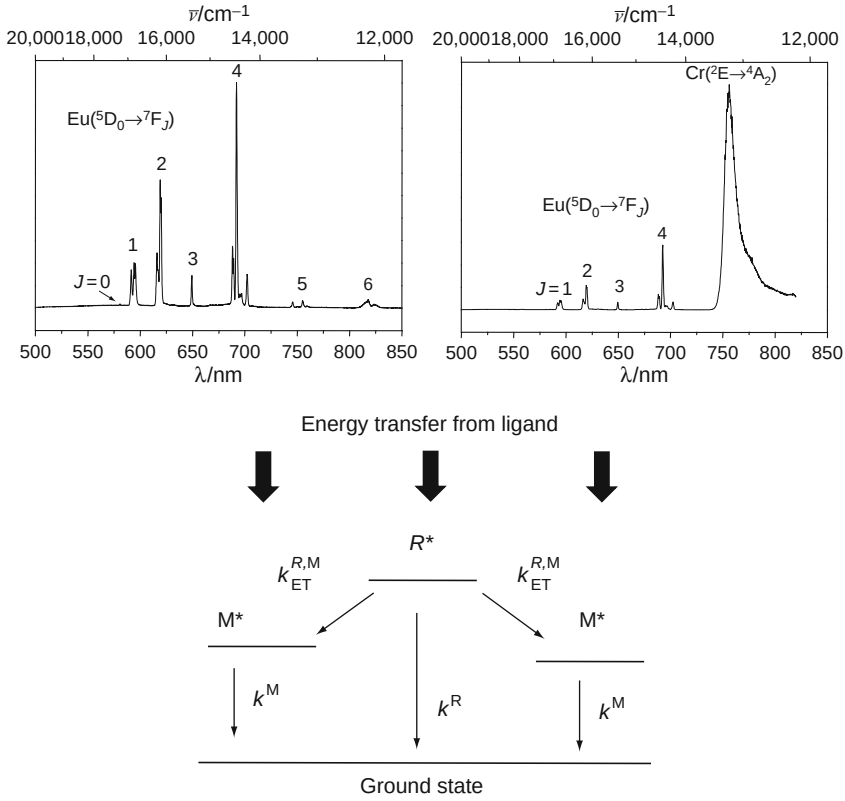

FIGURE 127 Top: luminescence spectra of $[MEuM(\mathbf{L42})_3]^{n+}$ (M = Zn^{II}, left; Cr^{III}, right). Bottom: rate constants used to model the divergent energy transfer in the CrEuCr edifice (redrawn from Cantuel et al., 2006).

the $[EuCr(\mathbf{L36})_3]^{5+}$ helicate is a reliable structural model for the solution structure of the trinuclear edifices.

The intramolecular communication along the C_3-axis generates two ''divergent'' $R \rightarrow Cr$ energy transfer processes, as exemplified by the dramatic decrease in the $Eu(^5D_0)$ lifetime (Table 31) which can be analyzed as follows, given the symmetry of the molecule and within the frame of the dipole–dipolar mechanism (Figure 127, bottom):

$$\eta_{tot}^{R,Cr} = \frac{2k_{ET}^{R,Cr}}{k^R + 2k_{ET}^{R,Cr}} \tag{163}$$

Assuming further that k^R is identical in the Zn^{II} and Cr^{III} helicates:

$$k_{obs}^{CrRCr} = \frac{1}{\tau_{obs}^{CrRCr}} = k^R + 2k_{ET}^{R,Cr} \tag{164}$$

and therefore:

$$k_{ET}^{R,Cr} = \frac{k_{obs}^{CrRCr} - k_{obs}^{ZnRZn}}{2} = \frac{(\tau_{obs}^{CrRCr})^{-1} - (\tau_{obs}^{ZnRZn})^{-1}}{2} \tag{165}$$

$$\eta_{tot}^{R,Cr} = 1 - \frac{\tau_{obs}^{CrRCr}}{\tau_{obs}^{ZnRZn}} \tag{166}$$

As expected, the efficiency of the $Eu \rightarrow Cr$ transfer increases from its value in the binuclear edifice $[EuZn(\mathbf{L36})_3]^{5+}$ (65% and 78% at 10 and 295 K, respectively) to reach values close to 90%, both in the solid state and in acetonitrile solution, at 10 or 295 K (Table 31), while the $Tb \rightarrow Cr$ transfer remains almost quantitative. The ratio of the rate constants for the total directional transfer, $k_{ET}^{Eu,Cr}(CrEuCr)/k_{ET}^{Eu,Cr}(EuCr)$ is 1.6(2) at 10 K and (surprisingly) 3.9(6) at 295 K. The critical distances for 50% transfer calculated assuming $R_{EuCr} = 9.32$ Å, as in $[EuZn(\mathbf{L36})_3]^{5+}$, are only marginally larger than those found in the binuclear analogue, reflecting a $\approx$2.5-fold increase in the overlap integral J (see Section 4.4, Eq. (78)).

For the time being, the trinuclear $[MRM(\mathbf{L42})_3]^{m+}$ helicates represent the first examples of supramolecular structures combining inert pseudo-octahedral Cr^{III} building blocks with the wrapping of three such ligand strands forming a cryptand-like, chiral cavity ideally suited for the complexation of lanthanide ions. In addition, these edifices have more flexibility than cryptands in that the cavity may be finely tuned to accommodate lanthanides ions with minute differences in size, a case study example of the induced fit principle at work! To our knowledge, the only other examples of binuclear 3d-transition metalloreceptors for R ions are {2}-metallacryptands based on 2,6-pyridyl-bis(β-diketones) which form

TABLE 31 Lifetimes, and energy transfer parameters in microcrystalline samples of $[MEuM(\mathbf{L42})_3]^{m+}$ ($M = Zn^{II}$, Cr^{III}), or their solution 1 mM in acetonitrile, under ligand excitation

Sample		T (K)	$\tau(^2E)$ (ms)	$\tau(^5D_J)$ (ms)	$k_{ET}^{Eu,Cr}$ (ms^{-1})	$\eta^{R,Cr}$ (%)	$R_0^{Eu,Cr}$ (Å)
CrGdCr	s	10	2.27(1)				
	s	295	0.031(1)				
ZnEuZn	s	10		1.96(1)			
	s	295		0.69(1)			
CrEuCr	s	10	2.08(2)	0.20(1)	2.2(1)	90(4)	11.9(2)
	s	295	0.033(1)	0.10(1)	4.3(4)	86(8)	11.2(4)
ZnTbZn	s	10		1.67(6)			
CrTbCr	s	10	1.8(2)	$1.75(4) \times 10^{-3}$	2.9×10^5	99.9	
ZnEuZn	MeCN	10		2.21(5)			
	MeCN	295		1.48(1)			
CrEuCr	MeCN	10	3.1(1)	0.24(1)	1.9(1)	89(6)	11.8(2)
	MeCN	295	0.012(1)	0.076(1)	6.2(5)	95(8)	13.5(3)

helical Fe_2L_3 host molecules able to incorporate K^I, Sr^{II}, or La^{III} (Saalfrank et al., 1998). Additionally, the group of K. Raymond has self-assembled GdFeGd macromolecular MRI contrast agents from the bis(bidentate) ligands 2,3-dihydroxyterephthalamide (TAM) and 1-methyl-2,3-dihydroxypyridone (HOPO), in which the Fe^{III} partner lies in the center of the cryptand-like cavity (Pierre et al., 2006). In these molecules, the ligand strands are arranged in a side-by-side fashion and therefore the assemblies cannot be termed helicates since they are achiral.

8. 4f- AND 5f-HELICATES WITH OTHER LIGANDS

8.1 Homo- and heterometallic polynuclear helicates

A combination of two venerable classes of ligands, β-diketonates (Binnemans, 2005) and bis(acylpyrazolonates) (Jensen, 1959), have produced some of the first characterized rare-earth $R_2\mathbf{L}_3$ triple-stranded helicates with the bis(bidentate) ligand $\mathbf{H_2L43^a}$ (Figure 128). The same year Piguet et al. (1992a,b) announced the isolation and structural characterization of $[Eu_2(\mathbf{L11})_3]^{6+}$, an initial report by a Chinese group (Xing et al., 1992) presented the isolation and full characterization of $[R_2(\mathbf{L43^a})_3] \bullet nH_2O$ (R = Y, La–Yb, except Ce, Pm; n = 3–8), including luminescence spectra for R = Pr, Sm, Eu, Tb, Dy, Tm, and Eu-doped Y and Gd. The crystal structure of the samarium helicate $[Sm_2(\mathbf{L43^a})_3(DMF)_4] \bullet DMF$, published 3 years later, reveals eight-coordinate Sm^{III} ions bound each to three bidentate units of each ligand strand and to two DMF molecules (Yang and Yang, 1995; Figure 129A). The coordination polyhedron is a distorted square antiprism, the oxygen atoms of two ligand strands forming one plane while the second plane consists of the two donor atoms of the third ligand strand and of the oxygen atoms of the two solvent molecules; the dihedral angle between these planes is small, ca. 1.5° for Sm1 and 3.3° for Sm2. The two coordination environment are not completely equivalent, distances between the Sm^{III} ions and the square planes being -1.27 and $+1.27$ Å for Sm1 and -1.22 and $+1.32$ Å for Sm2; the internuclear distance is 7.98 Å, considerably shorter than in $[Sm_2(\mathbf{L30^e})_3]^{6+}$ (9.18 Å; Jensen et al., 2008; see Section 3.2, Figure 48).

Increasing the bridge by one CH_2 unit ($\mathbf{H_2L43^b}$) does not change much the final products except for the coordination number of the R^{III} ion (Semenov et al., 2008). In $[Tb_2(\mathbf{L43^b})_3(H_2O)_2]$ (Figure 129B) and $[Tb_2(\mathbf{L43^b})_3(DMF)_2]$ for instance, Tb^{III} ions are only seven-coordinate being bound to only one ancillary ligand, with the oxygen atoms from these ligands lying on the pseudo-C_3 internuclear Tb-Tb axes. Both structures are very similar, with a helical pitch of approximately 21 Å that is considerably longer than those reported in Table 21.

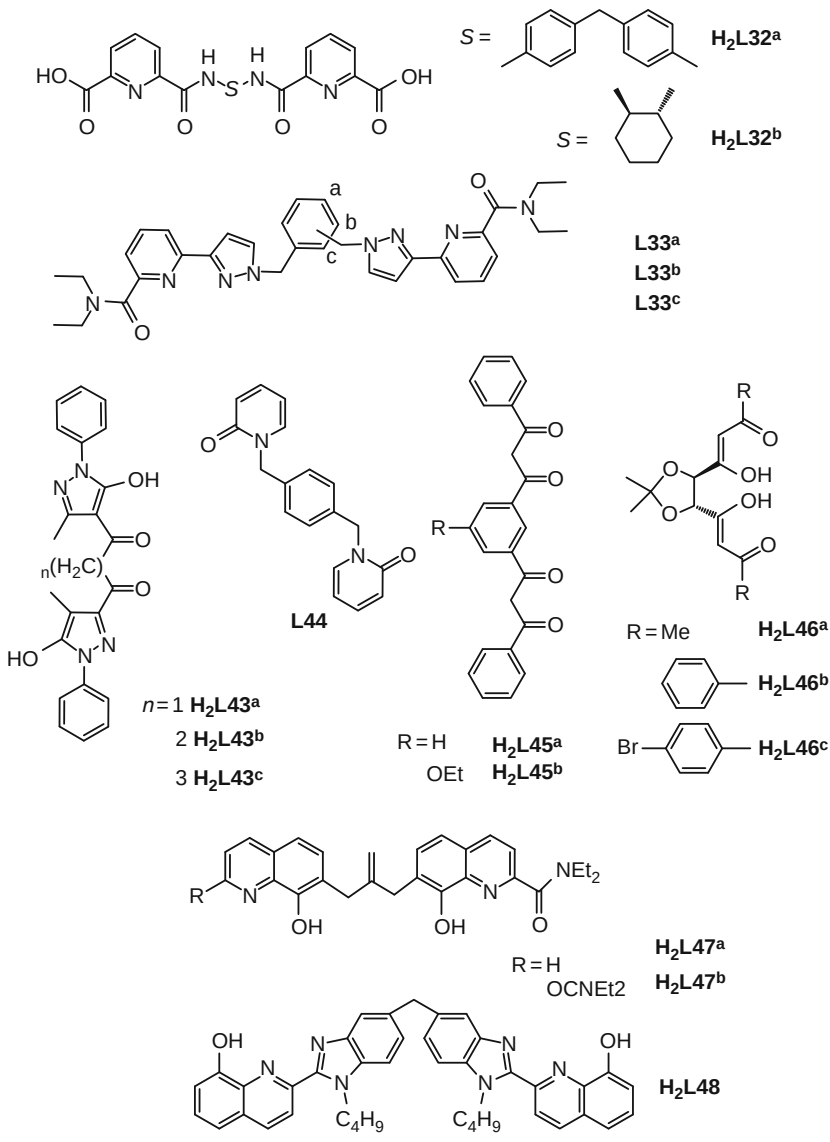

FIGURE 128 Ligands not based on bis(benzimidazole)pyridine for the self-assembly of homometallic binuclear helicates.

Obviously, the bis(monodentate) ligand **L44** cannot fulfill the coordination requirements of the R^{III} ions and the neodymium ion in the triple-stranded $[Nd_2(\mathbf{L44})_3(NO_3)_6]$ helicate (Figure 129C) is held outside the L_3 cavity, which is capped by ''stoppers'' made up of three bidentate nitrate

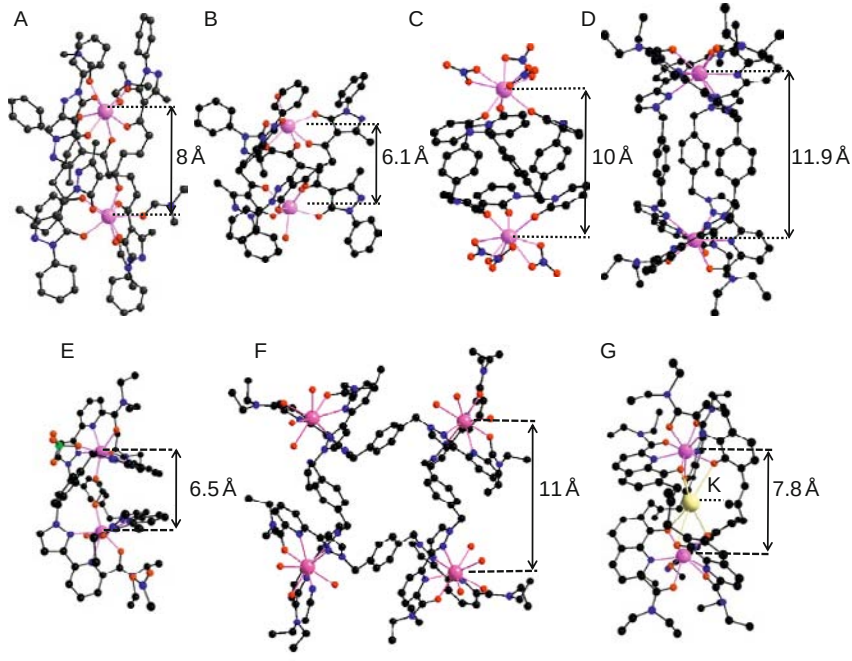

FIGURE 129 Molecular structures of (A) $[Sm_2(\mathbf{L43^a})_3(DMF)_4] \cdot DMF$ (redrawn from Yang and Yang, 1995), (B) $[Tb_2(\mathbf{L43^b})_3(H_2O)_2]$ (redrawn from Semenov et al., 2008), (C) $[Nd_2(\mathbf{L44})_3(NO_3)_6] \cdot 1.5MeCN$ (redrawn from Goodgame et al., 1993), (D) $[Nd_2(\mathbf{L33^a})_3]^{6+}$, (E) $[Yb_2(ClO_4)(\mu\text{-}HCO_2)(\mathbf{L33^b})_2]^{4+}$, (F) $[Nd_4(\mathbf{L33^a})_4(H_2O)_{11}(MeCN)]^{12+}$ (redrawn from Ronson et al., 2007), and (G) $[KYb_2(\mathbf{L47^a})_3]^{+}$ (redrawn from Albrecht et al., 2007a).

ions each. The resulting electrostatic attraction pulls the Nd^{III} ions far apart, the internuclear distance being 9.95 Å. The helix is substantially elongated in that it makes only one third of a turn between the two metal ions (Goodgame et al., 1993), that is, its pitch is on the order of 30 Å. Similarly to the parent diketones, the bis(bidentate) ligands $\mathbf{H_2L45^a}$ and $\mathbf{H_2L45^b}$ produce hexacoordinate environments upon wrapping in a helical fashion around two rare-earth ions ($R = Y$, Nd, Sm, Eu, Gd) which are easily completed with two water or methanol molecules (Basset et al., 2004). In organic solvents, ^1H NMR confirms the presence of three equivalent ligand strands with local C_2 symmetry and addition of Pirkle's reagent, {(*S*)-(+)-2,2,2-trifluoro-1-(9-anthryl)ethanol}, leads to the splitting of several resonances, indicating the presence of a racemic mixture of triple-stranded helices in solution. The bis(diketonate) ditopic ligand $(\mathbf{L45^a})^{2-}$ has singlet and triplet states with 0-phonon transitions at about 25,000 and 20,400 cm^{-1}, well suited for the sensitization of the Sm^{III}, Eu^{III}, and Nd^{III} ions. The quantum yield for $[Eu_2(\mathbf{L45^a})_3]$ in DMF amounts to 5%

and the $^5D_0$ lifetime is temperature dependent, increasing from 0.22 ms at room temperature to 0.46 ms at 77 K, pinpointing the probable presence of a thermally activated quenching by a relatively low-lying LMCT state, since the $\Delta E(^3\pi\pi^*-^5D_0)$ gap is too large ($\approx$3000 cm^{-1}) for substantial back transfer to occur. In methanol, use of the phenomenological equation (Beeby et al., 1999):

$$q_{MeOH} = 2.2[(k_{MeOH} - k_{MeOD}) - 0.125] \quad (167)$$

yields $q_{MeOH} = 3.7$, close to the expected value of 4 if the two Eu^{III} ions are octacoordinate. The quantum yields for the Sm^{III} helicate in DMF is smaller, 0.16%, with $\tau(^4G_{5/2}) = 13$ μs; the $Nd(^4F_{3/2})$ lifetime of $[Nd_2(\mathbf{L45^a})_3]$ in DMF is 1.5 μs, leading to a reasonable intrinsic quantum yield of 0.6%. A tetra-stranded helicate, $[Eu_2(\mathbf{L45^a})_4]^{2-}$ forms in presence of an excess ligand, as ascertained by ES-MS and NMR data, and it is more luminescent than the corresponding triple-stranded edifice. Introducing a chiral (*R*,*R*)-tartaric acid in the framework of bis(diketones) leads to ligands $\mathbf{H_2L46^{a-c}}$ which self-assemble under stoichiometric conditions with lanthanide chlorides in methanol and in presence of potassium carbonate into binuclear triple-stranded and neutral helicates: $[R_2(\mathbf{L46^a})_3] \cdot nH_2O$, $[R_2(\mathbf{L46^b})_3] \cdot nH_2O$ (R = La–Yb, except Pm), and $[R_2(\mathbf{L46^c})_3] \cdot nH_2O$ (R = La–Yb, except Pm and Gd), n = 2–5 (Albrecht et al., 2007b). The complexes are characterized by ES-MS in solution, as well as by their CD spectra. The ligands sensitize the luminescence of Eu^{III} and Tb^{III}, but no quantitative data are reported (lifetimes, quantum yields), except for $[Eu_2(\mathbf{L46^c})_3]$ for which $\tau(^5D_0)$ is equal to 0.1 and 0.5 ms in the solid state and in DMF solution, respectively, with an estimated quantum yield of 10% in solution. In addition, a tetra-stranded helicate can be obtained by reacting $\mathbf{H_2L46^c}$, $EuCl_3 \cdot 6H_2O$, and piperidine in a 4:2:2 ratio in chloroform-methanol, $(H\text{-}pip)_2[Eu_2(\mathbf{L46^c})_4]$. The latter has a longer $^5D_0$ lifetime (0.25 ms) than the corresponding triple-stranded complex but it dissociates into the triple-stranded helicate in DMF solution.

No crystal structure of the triple-stranded helicates with ligands $\mathbf{H_2L32^a}$ and $\mathbf{H_2L32^b}$ featuring two dipicolinic acid tridentate coordinating units is available either, but molecular mechanics calculations slightly favor $R_2\mathbf{L}_3$ helicate formation with Δ,Δ or Λ,Λ configurations at the metal centers over ''side-by-side'' (meso)helicates in which the metal ions lie in sites with Δ,Λ configuration. The calculated stabilization energy of the ''true'' helicates over the meso species is –25 and –209 kJ mol^{-1} for $\mathbf{H_2L32^a}$ (Δ,Δ configuration) and $\mathbf{H_2L32^b}$, respectively (Lessmann and Horrocks, 2000). Internuclear Eu–Eu distances of 13.9 ($\mathbf{H_2L32^a}$) and 8.0 Å ($\mathbf{H_2L32^b}$) are estimated from these calculations. Titrations of

europium triflate with $\mathbf{H_2L32^a}$ and *R*,*R*-$\mathbf{H_2L32^b}$ in water and followed by high-resolution luminescence excitation spectroscopy of the $^5D_0 \leftarrow {}^7F_0$ transition clearly point to the formation of a preponderant 2:3 species under 2:3 *R*:**L** stoichiometric conditions: the hydration number *q* is strictly zero and the lifetimes of the main species amount to 1.48 and 1.56 ms for the complexes with $\mathbf{H_2L32^a}$ and *R*,*R*-$\mathbf{H_2L32^b}$, respectively, a value typical of a tris(dipicolinate) environment for the metal ion. The internuclear distances determined from Eu → Nd energy transfer experiments with the help of Eqs. (77) and (78) (Section 4.4) reproduce satisfyingly the theoretical calculations: 13.7(8), and 7.4(8) Å, for the helicates with $\mathbf{H_2L32^a}$ and *R*,*R*-$\mathbf{H_2L32^b}$, respectively. Finally, the conditional stability constant estimated for $[Eu_2(\mathbf{L32^a})_3]$ is large and comparable to those of the dicarboxylic helicates $[R_2(\mathbf{L13})_3]$ (Table 8).

The bis(tridentate) ligands $\mathbf{L33^{a-c}}$ are tailored for nonacoordination of R^{III} ions if three strands wrap around two metallic centers (Ronson et al., 2007). In reality, the branching of the second pyrazole–pyridine amide unit on the anchor benzene in *para*, *ortho*, or *meta* position plays a crucial role in the final structures of the polynuclear complexes obtained, few of them being helicates. For instance, $\mathbf{L33^a}$ with its para-substituted anchors lacks the required stereochemistry for inducing helical turns. As a consequence, it reacts with $R(ClO_4)_3$ (R = La, Nd) to produce, in acetonitrile and under 2:3 *R*:**L** stoichiometric ratio, achiral binuclear complexes in which the three ligand strands are arranged in a side-by-side configuration building a cylindrical molecule (Figure 129D). Both cylinder ends are topped by a nonadentate coordination pocket encapsulating a R^{III} ion in a chiral environment. However, there is a mirror plane between the two R^{III} ions which have therefore opposite configuration and which lie at a large distance of about 11.9 Å. When the stoichiometric ratio is reduced to 1:1, a rare example of circular helicate[4] self-assembles, with overall chemical formula $[Nd_4(\mathbf{L33^a})_4(H_2O)_{11}(MeCN)]^{12+}$ (Figure 129F). The structure is very close to D_4 symmetry with the four Nd^{III} ions lying approximately in a square with internuclear distances of ≈11 Å and defined by the four helically wrapped ligand strands. This tetranuclear species should in principle be entropically disfavored with respect to the formation of smaller oligomers and a possible explanation for its preferential formation is the occurrence of π–π stacking interactions between almost parallel pyridine-pyrazole units. Under the same synthetic conditions, but in nitromethane, La^{III} gives a nonhelicate binuclear complex with the two ligands in a side-by-side configuration while increasing the *R*:**L** ratio to 5:1 in acetonitrile leads to a one-dimensional coordination polymer with nonhelical chains. Nonhelical mono- and binuclear complexes are mainly

[4] Another recent example of circular helicate is the C_3-symmetrical pyramidal architecture with general formula $[Ln_4(L)_9(\mu_3\text{-}OH)](ClO_4)_2$ obtained from an enantiomerically pure monotopic pinene-bipyridine receptor (Lama et al., 2008).

obtained with the *meta* and *ortho* ligand **L33^{b}** and **L33^{c}** with the exception of the double-stranded binuclear helix $[Yb_2(\mathbf{L33^b})_2(\mu\text{-}HCO_2)(ClO_4)(H_2O)]^{4+}$ in which a bridging formate anion holds the two Yb^{III} metal ions at a short 6.5 Å distance (Figure 129E).

Another popular strongly chelating unit for rare-earth ions which, in addition, sensitizes the luminescence of NIR-emitting lanthanides is 8-hydroxyquinoline (Comby and Bünzli, 2007). The latter has been inserted in the bis(tridentate) and tridentate-bidentate host molecules **H_2L47^{a-b}**. Crystalline bimetallic and trimetallic trinuclear helicates are obtained, $[KYb_2(\mathbf{L47^a})_3]^+$, and $[KAlYb(\mathbf{L47^b})_3]$ which display sizeable luminescence with overall quantum yields of 1.0(1) and 1.2(1)% and lifetimes of the $^2F_{5/2}$ level of 18.9(1) and 22.6(2) μs, respectively (Albrecht et al., 2007a). It is noticeable that the green luminescence from the Al(quinoline)$_3$ moiety is totally quenched in the latter compound to the benefit of energy transfer onto the Yb chromophore. The templating potassium ion plays an unusual role in the structure of $[KYb_2(\mathbf{L47^a})_3]^+$ being connected to four oxygen atoms by standard distances (2.7–2.8 Å) and to others by longer bond lengths (3.4–3.6 Å); one vinylic group of a ligand strand is directed toward the potassium ion is such a way that a weak K. . .C = C η_2-interaction occurs. The K^I ion is encapsulated approximately at the center of the helicate, with K–Yb distances in the range 3.9–4.0 Å while the Yb^{III} ions are separated by 7.8 Å and bound to the three tridentate and syn-arranged amidoquinolate units (Figure 129G). Another interesting feature of these systems is that despite the prominent templating role played by potassium in the solid state structure, its presence does not seem to be required to form the $[R_2(\mathbf{L47^a})_3]$ helicate in solution: $\log(\beta_{2,3}^{R,\mathrm{L47a}}) = 26.1(3)$ and 25.7(3) for R = Eu and Yb, respectively, while the 2:2 ($\log(\beta_{2,2}^{R,\mathrm{L47a}}) \approx 19$), 1:3 ($\log(\beta_{1,3}^{R,\mathrm{L47a}}) \approx 18$), and 1:2 ($\log(\beta_{1,2}^{R,\mathrm{L47a}}) \approx 13$–14) species have much lower stability.

Using a similar coordination strategy, ligand **H_2L48** produces the triple-stranded helicates $[R_2(\mathbf{L48})_3] \bullet nH_2O$ (R = La, $n = 3$; R = Nd, $n = 2$); their structure in solution is proved by ^{1}H-NMR spectroscopy. The Nd^{III} complex is luminescent, with an overall quantum yield of 0.15% and a single exponential luminescence decay corresponding to a lifetime of 1 μs (Shavaleev et al., 2008). The connectivity in the solid state has also been established by X-ray diffraction (Terazzi et al., 2009).

In addition to the *R*K and *R*Al helicates described above, there are, to our knowledge, only two other examples of helical molecular structures encompassing both a 4f ion and a transition metal ion which could be included into the concept ''helicate.'' The first one features a trinuclear Zn^{II} metallohelicene $[Zn_3(\mathbf{L49})]$ (Figures 130A and 131A) as chiral receptor and was synthesized with the aim of investigating its inversion rate (Akine et al., 2006). The helical host contains a cavity that can easily incorporate a large spherical ion such as R^{III} or Ba^{II} which, in fact, acts

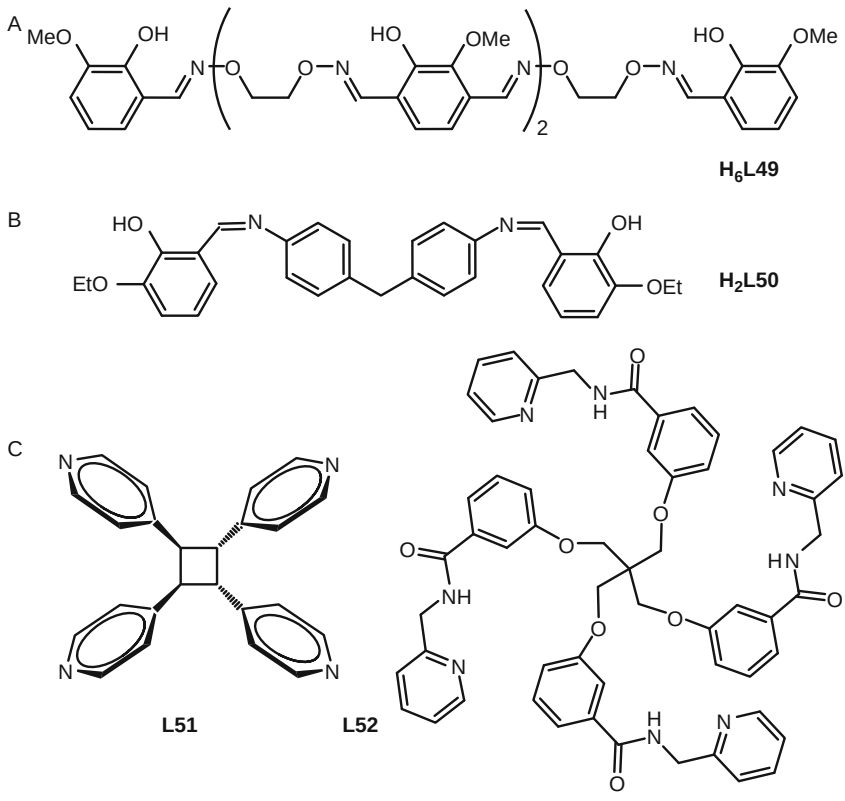

FIGURE 130 (A) Linear hexaoxime ligand **H_6L49** for building metallohelicenes, (B) segmental heterotopic ligand **H_2L50**, (C) polytopic ligands for assembling lanthanide-containing helical metal–organic frameworks.

as templating ions, the reaction of **H_6L49** with zinc acetate alone giving rise to a mixture of complexes. The helical wrapping of the receptor around the R^{III} ion is clearly visible in the crystal structure of $[LaZn_3(\mathbf{L49})(OAc)_3(EtOH)]$ (Figure 132A), the metallohelicene accomplishing a 421° turn. The interconversion between the right-handed and left-handed configuration of the tetranuclear complex is slow (Figure 131B), the ^{1}H-NMR resonances of the three pairs of diastereotopic methylene protons remaining distinct even at 353 K, while if La^{III} is replaced by Ba^{II}, coalescence occurs at this temperature. The reason lies in a tighter helix with shorter La–O bonds compared to Ba–O and, possibly in the stronger electrostatic interaction created by the +3-charged lanthanum ion.

The second example is a tetranuclear double-stranded helicate $[Cu_2Gd_2(\mathbf{L50})_2(NO_3)_6(H_2O)_2]$ (Figures 130B and 132B) featuring quite

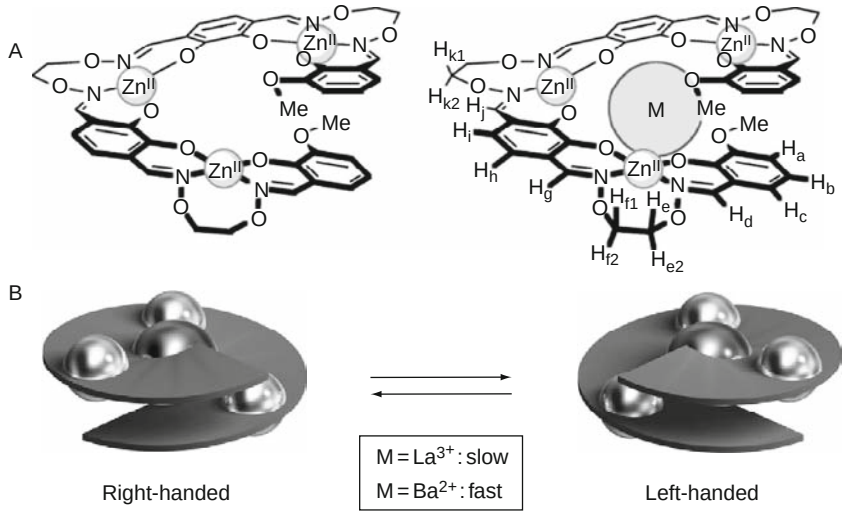

FIGURE 131 (A) Schematized structures of the trinuclear Zn^{II} metallohelicene and of the corresponding La^{III} metallohelicates. (B) Inversion process of the metallohelicates (reproduced by permission from Akine et al., 2006, © The Royal Society of Chemistry, 2006).

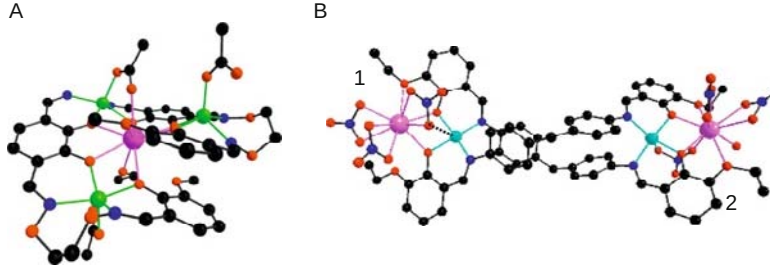

FIGURE 132 Molecular structures of (A) $[Zn_3La(\mathbf{L49})(Oac)_3(EtOH)]$ (redrawn from Akine et al., 2006) and (B) $[Cu_2Gd_2(\mathbf{L50})_2(NO_3)_6(H_2O)_2]$ (redrawn from Novitchi et al., 2008).

short Gd–Cu distances, 3.3–3.4 Å (Novitchi et al., 2008). Due to the helical arrangement of the two ligand strands, the Cu^{II} coordination polyhedron is different in the two compartments; Cu^{II} ions are primarily square planar with tetrahedral distortion of the N_2O_2 set of donor atoms but additionally, one nitrate ion is bridging the Cu and Gd atoms in a η^1,η^2, μ-mode for Cu1 with a long Cu–O bond (2.75 Å) and in a η^1,η^1,μ-mode for Cu^{II} with a shorter 2.5 Å Cu–O contact. The corresponding Gd^{III} ions are (somewhat unusually) ten-coordinate, Gd1 being bound to three

bidentate nitrates, one water molecule, two phenoxo, and one ethoxy oxygen atoms while for Gd2, one oxygen from a nitrate ion is replaced by an oxygen atom from a second ethoxy group.

The two Cu–Gd pairs are located at a distance long enough to be considered as isolated. When the susceptibility versus temperature data are modeled with the assumption that the magnetic interaction is the same within the two Cu-Gd pairs of the helicate, an interaction parameter $J = 4.5\ cm^{-1}$ is found. This model is substantiated by the weak intramolecular Cu...Cu interaction occurring when Gd^{III} is replaced with diamagnetic Y^{III}: $J = -0.44\ cm^{-1}$, using the isotropic Hamiltonian $H = -JS_{Cu1}S_{Cu2}$. Magnetization versus direct current (dc) field measurements for the corresponding Tb^{III} helicate $[Cu_2Tb_2(\mathbf{L50})_2(NO_3)_6)(H_2O)_2]$, in which ferromagnetic interactions also occur, reveals a single molecule magnet (SMM) behavior with a small hysteresis loop nearly sweep rate-independent. Substitution of the nitrate ions by hexafluoroacetylacetonate (hfa) ions in $[Cu_2Tb_2(\mathbf{L50})_2(hfa)_6)]$ ensures a better isolation of the tetranuclear helicates with respect to each other and amplifies the SMM behavior, the hysteresis loop being sweep-rate and temperature dependent.

8.2 Helical structures in coordination polymers and macrocyclic complexes

The assembly of a molecular helicate into a 1D coordination polymer has been reported recently (Semenov et al., 2008). The building block only differs from those mentioned earlier, $[Tb_2(\mathbf{L43^b})_3(L_2)]$ with $L = H_2O$, DMF, or $PPhe_3O$, by the nature of the ancillary ligand, diphenylphosphineethane dioxide ($dppeO_2$) replacing the monodentate donor. The bulkier ancillary ligand causes a slightly larger distortion from the idealized D_3-symmetry than the monodentate ligands. The helical units $[Tb_2(\mathbf{L43^b})_3(dppeO_2)_{1.5}]_n$ are connected through Tb^{III} ions by $dppeO_2$ bridges into infinite parallel chains, as shown on top of Figure 133.

There are two types of chains corresponding to the two different optical isomers. The length of the repetitive unit along the 1D chain is 16.3 Å with neighboring interchain Tb–Tb distances of 10.1 Å, somewhat longer than in the reference polymeric compound $[Ln(NO_3)_3(dppeO_2)_{1.5}]_n$ (9.2 Å). This distance can also be compared to the intramolecular Tb–Tb contacts of 6.5 Å. It is noteworthy that both the Tb^{III} molecular helicate $[Tb_2(\mathbf{L43^b})_3(H_2O)_2]$ and coordination polymer are highly luminescent, with quantum yields of $21 \pm 2\%$ ($\tau(^5D_4) = 0.45 \pm 0.05$ ms), despite the coordinated water molecule, for the former and $28 \pm 2\%$ (0.60 ± 0.05 ms) for the latter (S. Semenov and J.-C.G. Bünzli, 2008, unpublished results).

Numerous examples of supramolecular helical structures are documented for extended 1D, 2D, or 3D metal–organic frameworks, essentially built up from H-bond networks. An amazing variety of structures have

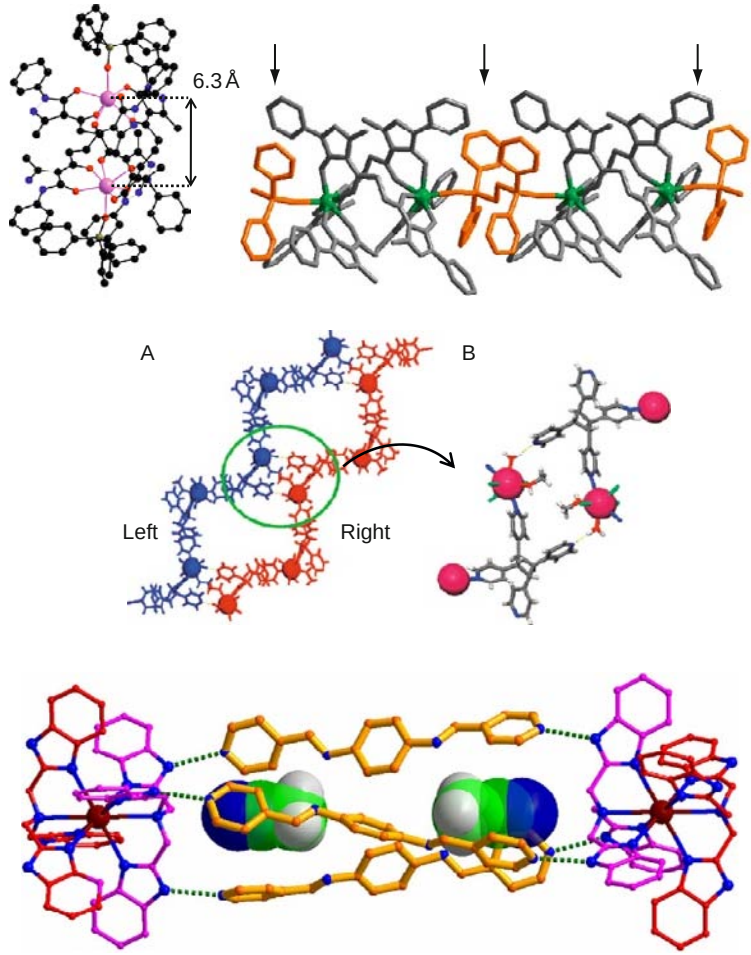

FIGURE 133 Top: structure of the first coordination polymer assembled from a helicate: (left) binuclear building block $[Tb_2(\mathbf{L43^b})_3(PPhe_3O)_2]$ (redrawn from Semenov et al., 2008), (right) fragment of the polymeric 1D chain with the bridging ligands indicated by arrows and colored (reproduced by permission from Semenov et al., 2008, © The Royal Society of Chemistry, 2008). Middle: perspective view of $\{[PrCl_3(\mathbf{L51})(MeOH)(H_2O)]\}_n$ (A) left- and right-handed helical chains and (B) the hydrogen-bonded polygon (reproduced by permission from Bucar et al., 2008, © The Royal Society of Chemistry (RSC) for the Centre National de la Recherche Scientifique and the RSC, 2008). Bottom: hydrogen-bonded triple-helical cylindrical motif of $\{[Pr(\mathbf{L53})_2(ClO_4)_3] \bullet (\mathbf{L54})_3 \bullet 2MeCN\}_n$ encapsulating acetonitrile guest molecules (reproduced in part by permission from Jiang et al., 2008, © American Chemical Society, 2008).

been reported including single-, double-, triple-, and even quadruple-stranded helices; in some instances, tubular channels walled with helical features are present in these materials and can host small molecules. We first present one recent example in which the authors have used the tetratopic molecule *crtt*-4,4′-tetrapyridyl-butane, **L51**, as the rigid bridging spacer acting as a bis(monodentate) ligand to assemble a single-stranded helical coordination polymer, $\{[PrCl_3(\mathbf{L51})(MeOH)(H_2O)] \cdot 2MeOH \cdot H_2O)\}_n$ (Bucar et al., 2008). The Pr^{III} cation is seven-coordinate in a pentagonal bipyramidal geometry (Figure 133, middle) being bound to three chlorides, two oxygen atoms from water and methanol, and two nitrogen atoms from pyridyl groups belonging to two different ligand molecules. This produces a single-stranded helical polymer along a 2_1 screw axis with a helical pitch of 20.1 Å. As in the previous example, helices of both hands are present and related by an inversion center. The self-assembly process is very sensitive to the nature of the anion: replacing chloride with nitrate ions gives rise to a 3D network consisting in a two-fold interpenetrated bimodal net with $(4.6^2)_2(4^2.6^{10}.8^3)$ topology for instance.

Developing luminescent materials for telecommunication or bioprobes, radiopharmaceuticals, MRI contrast agents, materials with special magnetic properties, or porous frameworks for the adsorption of small molecules are among the motivations often invoked for tailoring lanthanide-containing coordination polymers. Hydrothermal synthesis is the most common method for obtaining these materials also referred to as metal–organic frameworks (MOFs), or inorganic-organic hybrids. However, very few published works describe detailed physicochemical properties of the isolated materials, but for structural characterization. For instance, when R^{III}-centered luminescence is reported, only assignments are usually given, with no quantitative data such as lifetime or quantum yield, not to speak about the sensitization efficiency of the ligands. As a consequence, we have simply gathered in Table 32 the main characteristics of selected lanthanide-containing coordination polymers with helical structures published recently. When different types of structures, helical and nonhelical, were found in the investigated systems, only the helical structures are referred to in this table.

In the case of the porous $\{[R(phos)_3] \cdot 2H_2O\}_n$ networks, the adsorption isotherms have been recorded to test the intake capacity for N_2, H_2O, MeOH, and EtOH, of which 1.1, 1.76, 0.8, and 0 molecule(s) per formula unit can enter into the pores of the material, respectively. The network is stable to several dehydration/hydration cycles, maintaining its homochiral structure (Yue et al., 2006). Another clever approach to porous materials able to host small molecules starts by producing a mixture of monometallic helical complexes with different chirality from lanthanide perchlorate and tris(2-benzimidazoylmethyl)amine **L53** (Jiang et al., 2008):

TABLE 32 Structural and other characteristics of selected rare-earth containing coordination polymers with helical structures published in 2006–2008

Ligand[a]	*R*	Formula	Dim[b]	Helicity[c]	Other properties[d]	References
Homometallic coordination polymers						
L43[b]	Tb, Gd	$[R_2(\mathbf{L43^b})_3(dppeO_2)]_n$	1D	s, 16.3	Lum (Tb, τ, *Q*)	Semenov et al. (2008)
L51	Pr	$\{[PrCl_3(\mathbf{L51})_3(MeOH)(H_2O)]\}_n$	1D	s, 20.1	–	Bucar et al. (2008)
NTA	Eu	$\{[Eu(NTA)(H_2O)_2]H_2O\}_n$	1D	s, 8.1	Magn	Chen et al. (2008)
	Ho, Tm	$\{[R(NTA)(H_2O)_2]H_2O\}_n$	3D	t, 22.8	Magn	
pic	Nd, Sm	$[R(pic)_3]_n$	1D	s, 7.7	Magn (Nd, Sm); Lum (Sm)	Li et al. (2008)
ip	La, Pr, Nd, Dy	$\{Him[R(ip)_2(H_2O)]\}_n$	3D	s, 19.1; d, 9.5	Lum (NIR, Nd; vis, Dy)	Zhou et al. (2008)
	Y	$[Y(ip)_3(H_2O)_2]_n$	2D	s, 14.2; t, 42.7		
pydc	Y, Sm, Eu, Dy, Er, Yb	$[R_3(\mu\text{-}OH)_4(pydc)(Hpydc)_3(H_2O)_4]_n$	3D	d, NA	Lum (Sm, Eu, Dy; τ); Magn (all)	Huang et al. (2007)
imc	Eu, Dy	$[R(Himc)(SO_4)(H_2O)]_n$	2D	s, 6.5	Lum (Eu, Dy)	Sun et al. (2006a)
phos	Eu, Gd, Tb, Dy	$\{[R(phos)_3]\cdot 2H_2O\}_n$	3D	s, 18.8	Lum (Eu, Tb); Ads (all)	Yue et al. (2006)
L52	Er		1D	s, 14.8	–	

(*continued*)

TABLE 32 (*continued*)

Ligand[a]	*R*	Formula	Dim[b]	Helicity[c]	Other properties[d]	References
		{[Er(**L52**)$(NO_3)_3(H_2O)] \cdot H_2O\}_n$				Song et al. (2008c)
L53, **L54**	Pr	$\{[Pr(\mathbf{L53})_3(ClO_4)_3] \cdot (\mathbf{L54}) \cdot 2MeCN\}_n$	1D	t, NA	Thermal analysis, solution studies	Jiang et al. (2008)
Heterometallic coordination polymers						
H_2L15[a]	Er	$\{[ErAg_3(\mathbf{L15}^a)_3(H_2O)]\}_n$	1D	t, 26.4	Lum (NIR, Er)	Zhou et al. (2008)
in	Nd, Eu	$[R Ag(OAc)(in)_3]_n$	3D	t, 27.4	Lum (Eu)	Gu and Xue (2006)
bpym	Nd, Sm, Gd	$\{[Ru(CN)_4(bpym)][R(NO_3)(H_2O)_5]_2\}_n$	1D	2, 12.5	Lum (NIR, Nd; τ)	Herrera et al. (2006a)
imdc	Y, Nd, Pr, Eu, Gd, Tb, Dy, Er, Yb	$\{[RCd(imcd)(SO_4)(H_2O)_3] \cdot 0.5H_2O\}_n$	1D	3, 10.5	Lum (Eu, Tb, Dy; τ, Eu, Tb)	Sun et al. (2006b)

[a] NTA, nitrilotriacetate; pic, picolinate; im, imidazole; ip, isophthalate; pydc, pyridine-2,5-dicarboxylate; imc, imidazolecarboxylate; phos, (*S*)-HO_3PCH_2–NHC_4H_7–CO_2H; **H_2L15[a]**, dipicolinic acid (Figure 17); in, isonicotinate; bpym, bipyrimidine; imdc, 4,5-imidazoledicarboxylate.
[b] Dimensionality of the network.
[c] Number of strands (s, single-stranded; d, double-stranded; t, triple-stranded; q, quadruple-stranded) and pitch in Å.
[d] Lum, luminescence (τ = lifetime, Q = quantum yield); Magn, magnetic susceptibility; Ads, adsorption isotherm.

$$R(ClO_4)_3 + \mathbf{L53} \rightarrow \Delta\Delta - [R(\mathbf{L53})_3](ClO_4)_3 \rightleftarrows \Delta\Lambda$$
$$-[R(\mathbf{L53})_3](ClO_4)_3 \rightleftarrows \Lambda\Lambda - [R(\mathbf{L53})_3](ClO_4)_3$$

Subsequent self-assembly with **L54** through hydrogen bonding leads to three types of chiral arrays, the two chiral species D_3-symmetry ($\Delta\Delta$,*P*, $\Delta\Delta$,*P*) and ($\Lambda\Lambda$,*M*, $\Lambda\Lambda$,*M*) as well as the *meso* form with inversion center ($\Lambda\Delta$,*M*, $\Delta\Lambda$,*P*) or ($\Delta\Lambda$,*P*, $\Lambda\Delta$,*M*). The one-dimensional channels of the former appear to be more permeable than those of the *meso* form and the two guest acetonitrile molecules (see bottom of Figure 133) can be removed but the framework then collapses.

Finally, some large macrocycles can wrap helically around two metal ions. Documented examples are the large Schiff base $\mathbf{H_2L55}$ (Kahwa et al., 1989, Figure 134) or R^{III}Zn iminophenolate cryptates (Rodriguez-Cortias et al., 2002). This aspect is not further discussed here.

8.3 Actinide helicates

To our knowledge, there is a single report describing the synthesis and structural characterization of actinide helicates. By analogy with the first triple-stranded lanthanide helicates isolated (Piguet et al., 1992a; Xing

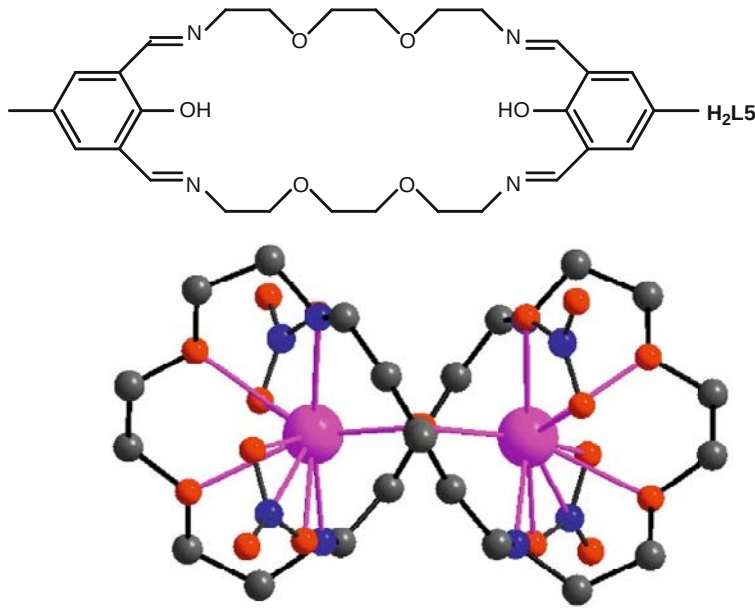

FIGURE 134 Structure of the ditopic Schiff base $\mathbf{H_2L55}$ and of its binuclear homometallic Gd^{III} complex (redrawn from Kahwa et al., 1989).

et al., 1992), Raymond and coworkers in Berkeley reasoned that the nine-coordinate tetravalent Th^{IV} ion would lead to quadruple-stranded helicates with ligands **H_2L43** (Figure 128) because the high charge of the actinide cation would favor four monoanionic bidentate pyrazolone ligand strands to bind at each metal ion (Xu and Raymond, 2006). MS and NMR data indeed point to the formation of such helicates upon reacting Th^{IV} acetylacetonate with **H_2L43^b** or **H_2L43^c** in MeOH/$CHCl_3$ 1/1. In both homochiral helicates, the Th^{IV} ions are nine-coordinate, the coordination sphere being completed by a bound DMF molecule; the coordination polyhedra are close to monocapped square antiprisms (C_{4v}). The helical pitch is 42.3 Å with a Th–Th internuclear distance of 8.30 Å in [Th_2(**L43^b**)$_4$(DMF)$_2$]; in the helicate with the ligand having a longer spacer, the Th–Th distance is about the same (8.15 Å) in [Th_2(**L43^c**)$_4$(DMF)$_2$], but the pitch is much shorter (29.6 Å). The explanation comes from the fact that the helicates are not palindromic; that is, the pitch is not constant all along the structure. The two subpitches of the capped square antiprisms are very similar in the two structures (ca. 19–22 Å) but the alkyl-bridge pitch is far longer in [Th_2(**L43^c**)$_4$(DMF)$_2$] (442 versus 50 Å!), which explains the larger overall pitch. As a comparison, the pitch of the terbium helicate with the short-bridged **H_2L43^a** ligand, [Tb_2(**L43^b**)$_3$(dppeO_2)] is much shorter, 16.3 Å (Figure 135).

9. CONCLUSIONS

The term ''helicate'' was introduced by Lehn et al. (1987) for metal complexes embedding two or more metal centers connected by one or more bridging ligand strands and since then the field has burgeoned and produced astonishing supramolecular structures (Albrecht, 2001; Piguet,

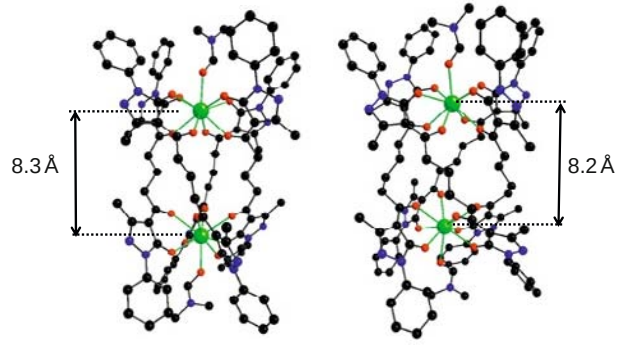

FIGURE 135 Molecular structures of the two characterized Th^{IV} helicates: [Th_2(**L43^b**)(DMF)$_2$] (left) and [Th_2(**L43^c**)(DMF)$_2$] (right) (redrawn from Xu and Raymond, 2006).

1999; Piguet et al., 1997a). Extension to the f-elements followed rapidly, with the first lanthanide binuclear helicates being reported in 1992 (Piguet et al., 1992a,b; Xing et al., 1992). The present chapter is a state of the art of this research domain 17 years after its debut and highlights how chemists have succeeded in taming the difficult programming of ligand strands for a selective recognition of the spherical rare-earth ions. Not only a suitable topological design of coordination sites has been achieved, for instance in C_2-symmetrical ditopic receptors derived from bis(benzimidazole)pyridine (Piguet et al., 1993b) but, also, introduction of subtle differences in the two tridentate chelating units allowed the preferential (if not unique) formation of heterobimetallic 4f–4f′ edifices (André et al., 2004). Increasing the number of coordinating unit according to a rationally thought design led to linear, triple-stranded tri- (Bocquet et al., 1992) and even tetranuclear 4f helicates (Zeckert et al., 2005). An innovative site-binding model mixing intra- and intermolecular connections, and taking advantage of the numerous stability constants published to date allows a close understanding of the thermodynamic stability of these helicates, despite the a priori large repulsion Coulomb's energy between the metal centers and, also the fact that some of these architectures are highly charged (+6 to +12). The mastering of these parameters makes the design of any 4f-metal containing helical edifice easily predictable.

Another crucial step has been the modification of the C_2-symmetrical bis(benzimidazole)pyridine ligands toward tridentate-bidentate host able to build nd–4f helicates (Piguet et al., 1995a). Indeed, easy modulation of the spectroscopic and magnetic properties of d-transition metal ions is achieved thanks to the large overlap of the d-orbitals with surrounding wave-functions. The unique combination of two nd and 4f ions into a cylindrical supramolecular architecture results in intermetallic communication which, in turn, materializes under the form of a tuning of one ion properties by the other. Demonstration of this effect in two particular cases, Fe^{II} spin-crossover parameters (Piguet et al., 1995e), and energy transfer modulating luminescent properties (Cantuel et al., 2002; Imbert et al., 2003) proved the feasibility of this approach and given that several different d-transition metal ions may be introduced into the helicates (to date: $Cr^{II/III}$, Fe^{II}, $Co^{II/III}$, Ni^{II}, Zn^{II}, Ru^{II}, Os^{II}) a whole range of molecular architectures having predetermined unique properties can be envisaged.

Modification of the C_2-symmetrical ligands to allow water solubility for the assembled helicate is another landmark (Elhabiri et al., 1999; Vandevyver et al., 2007) since it opens the way for the binuclear complexes to be used as lanthanide luminescence probes with a variety of applications ranging from cell imaging (Bünzli et al., 2008) to nucleic acid detection (Song et al., 2008b). The chemical robustness of the helicates, both thermodynamically and kinetically speaking, their inherent

chirality, as well as the ease with which they are taken into live cells and remain into them without affecting their biological functions are real advantages. Bioconjugation of the helicates should improve their specificity toward given cell lines and prove useful both in diagnostic and in the follow-up of cancer therapy, among others.

Future prospects for f-containing helicates seem to be incommensurable. Several subjects are not yet fully explored, for instance, 5f helicates are in their infancy (Xu and Raymond, 2006), 3d–4f constructions can be modulated almost at will, particularly when it comes to intermetallic communication, and the advent of extended networks constructed from helicate building blocks (Semenov et al., 2008) and/or incorporating helical features (Jiang et al., 2008) are promising. With respect to the latter, a mixture of nd and 4f ions could lead to interesting optical and/or magnetic materials (e.g., networks with large spin cross hysteresis) which are more and more needed for telecommunications, analytical and bioanalytical sensing, and storage of small molecules. In fact the present level of knowledge, particularly with respect to the modeling of the thermodynamic stability of these entities and to the various structural entities susceptible to be assembled, combined with the emergence of new types of ligands besides the archetypical, very efficient, and easily adjustable, bis(benzimidazole)pyridine framework, are an insurance for the unfolding of exciting science in the future.

REFERENCES

Addison, A.W., Burke, P.J., 1981. J. Heterocycl. Chem. 18, 803.
Addison, A.W., Rao, T.N., Wahlgren, C.G., 1983. J. Heterocycl. Chem. 20, 1481.
Aebischer, A., Gumy, F., Bünzli, J.-C.G., 2009. Phys. Chem. Chem. Phys. 11, 1346.
Akine, S., Taniguchi, T., Matsumoto, T., Nabeshima, T., 2006. Chem. Commun. 4961.
Albrecht, M., 2001. Chem. Rev. 101, 3457.
Albrecht, M., Osetska, O., Fröhlich, R., Bünzli, J.-C.G., Aebischer, A., Gumy, F., Hamacek, J., 2007a. J. Am. Chem. Soc. 129, 14178.
Albrecht, M., Schmid, S., Dehn, S., Wickleder, C., Shuang, Z., Basset, A.P., Pikramenou, Z., Fröhlich, R., 2007b. New J. Chem. 31, 1755.
Ali, H.D.P., Kruger, P.E., Gunnlaugsson, T., 2008. New J. Chem. 32, 1153.
An, Y., Berry, M.T., van Veggel, F.C.J.M., 2000. J. Phys. Chem. A 104, 11243.
André, N., Jensen, T.B., Scopelliti, R., Imbert, D., Elhabiri, M., Hopfgartner, G., Piguet, C., Bünzli, J.-C.G., 2004. Inorg. Chem. 43, 515.
André, N., Scopelliti, R., Hopfgartner, G., Piguet, C., Bünzli, J.-C. G., 2002. Chem. Commun. 214.
Anwander, R., 1999. Principles in organolanthanide chemistry. In: Kobayashi, S. (Ed.), Topics in Organometallic Chemistry, vol. 2. Springer-Verlag, Berlin, pp. 1–62.
Archer, R.D., Chen, H., Thomson, L.C., 1998. Inorg. Chem. 37, 2089.
Aspinall, H.C., 2002. Chem. Rev. 102, 1807.
Balzani, V., Credi, A., Venturi, M., 2002. Chem. Eur. J. 8, 5525.
Balzani, V., Credi, A., Venturi, M., 2008. Chem. Eur. J. 14, 26.
Barela, T.D., Sherry, A.D., 1976. Anal. Biochem. 71, 351.

Barta, C.A., Bayly, S.R., Read, P.W., Patrick, B.O., Thompson, R.C., Orvig, C., 2008. Inorg. Chem. 47, 2294.
Basset, A.P., Megennis, S.W., Glover, P.B., Lewis, D.J., Spencer, N., Parsons, S., Williams, R. M., De Cola, L., Pikramenou, Z., 2004. J. Am. Chem. Soc. 126, 9413.
Beeby, A., Clarkson, I.M., Dickins, R.S., Faulkner, S., Parker, D., Royle, L., de Sousa, A.S., Williams, J.A.G., Woods, M., 1999. J. Chem. Soc., Perkin Trans. 2 3, 493.
Benelli, C., 2002. Chem. Rev. 102, 2369.
Ben-Naim, A.J., 1998. J. Chem. Phys. 108, 6937.
Benson, S.W., 1958. J. Am. Chem. Soc. 80, 5151.
Benson, S.W., 1976. Thermochemical Kinetics, 2nd ed Wiley-Interscience, New York p. 37.
Bertini, I., Luchinat, C., 1996. Coord. Chem. Rev. 150, 1.
Binnemans, K., Görller-Walrand, C., 1995. Chem. Phys. Lett. 245, 75.
Binnemans, K., 2005. Rare earth β-diketonate complexes: functionalities and applications. In: Gschneidner, K.A. Jr., Pecharsky, V., Bünzli, J.-C.G. (Eds.), Handbook on the Physics and Chemistry of Rare Earths Vol. 35. Amsterdam: Elsevier Science. Chapter 225, pp. 107–272.
Blasse, G., 1976. Struct. Bond. 26, 45.
Bleaney, B.J., 1972. Magn. Reson. 8, 91.
Bobba, G., Frias, J.C., Parker, D., 2002. Chem. Commun. 8, 890.
Bocquet, B., Bernardinelli, G., Ouali, N., Floquet, S., Renaud, F., Hopfgartner, G., Piguet, C., 1992. Chem. Commun. 930.
Borkovec, M., Hamacek, J., Piguet, C., 2004. Dalton Trans. 4096.
Bornhop, D.J., Hubbard, D.S., Houlne, M.P., Adair, C., Kiefer, G.E., Pence, B.C., Morgan, D. L., 1999. Anal. Chem. 71, 2607.
Bornhop, D.J., Griffin, J.M.M., Goebel, T.S., Sudduth, M.R., Motamedi, M., 2003. Appl. Spectrosc. 57, 1216.
Boukhalfa, H., Crumbliss, A.L., 2000. Inorg. Chem. 39, 4318.
Brayshaw, P.A., Bünzli, J.-C.G., Froidevaux, P., Harrowfield, J.M., Kim, Y., Sobolev, A.N., 1995. Inorg. Chem. 34, 2068.
Brewster, J.H., 1974. Top. Curr. Chem. 47, 29.
Bucar, D.K., Papaefstathiou, G.S., Hamilton, T.D., MacGillivray, L.R., 2008. New J. Chem. 32, 797.
Bünzli, J.-C.G., 1989. Luminescent probes. In: Bünzli, J.-C.G., Choppin, G.R. (Eds.), Lanthanide Probes in Life, Chemical and Earth Sciences. Elsevier, Amsterdam, pp. 219–293 (Chapter 7).
Bünzli, J.-C.G., 1998. Coordination chemistry of the trivalent lanthanide ions: An introductory overview. In: Saez-Puche, R., Caro, P. (Eds.), Rare Earths. Editorial Complutense, Madrid, pp. 223–259.
Bünzli, J.-C.G., 2009. Chem. Lett. 38 (2), 104.
Bünzli, J.-C.G., Piguet, C., 2002. Chem. Rev. 102, 1897.
Bünzli, J.-C. G., Chauvin, A.-S., Vandevyver, C. D. B., Song, B., Comby, S., Ann. N.Y. Acad. Sci. 2008, 1130, 97.
Bünzli, J.-C.G., Piguet, C., 2005. Chem. Soc. Rev. 34, 1048.
Bünzli, J.-C.G., Petoud, S., Piguet, C., Renaud, F., 1997. J. Alloys Compd. 249, 14.
Burdick, G.W., Reid, M.F., 2007. $4f^n$–$4f^{n-1}5d$ transitions. In: Gschneidner Jr., K.A., Pecharsky, V., Bünzli, J.-C.G. (Eds.), Handbook on the Physics and Chemistry of Rare Earths, vol. 37. Elsevier Science, Amsterdam, pp. 61–98 (Chapter 232).
Cable, M.L., Kirby, J.P., Sorasaenee, K., Gray H.B., Ponce, A., 2007. J. Am. Chem. Soc., 129, 1474.
Cahn, R.S., Ingold, C., Prelog, V., 1966. Angew. Chem. Int. Ed. Engl. 5, 385.
Canada, R.G., 1983. Biochem. Biophys. Res. Commun. 111, 135.
Canada, R.G., 1988. Anal. Chim. Acta 205, 77.
Canada, R.G., Paltoo, D.N., 1998. Biochem. Biophys. Acta Mol. Cell Res. 1448, 85.

Canard, G., Piguet, C., 2007. Inorg. Chem. 46, 3511.
Canard, G., Koeller, S., Bernardinelli, G., Piguet, C., 2008. J. Am. Chem. Soc. 130, 1025.
Cantuel, M., Bernardinelli, G., Imbert, D., Bünzli, J.-C.G., Hopfgartner, G., Piguet, C., 2002. J. Chem. Soc., Dalton Trans. 1929.
Cantuel, M., Bernardinelli, G., Muller, G., Riehl, J.P., Piguet, C., 2004. Inorg. Chem. 43, 1840.
Cantuel, M., Gumy, F., Bünzli, J.-C.G., Piguet, C., 2006. Dalton Trans. 2647.
Capo, M., Saa, J.M., Alvarez, A., 2002. Chem. Commun. 1982.
Cargill Thompson, A.M.W., 1997. Coord. Chem. Rev. 160, 1.
Carrano, C.J., Raymond, K.N., 1978. J. Am. Chem. Soc. 100, 5371.
Carrano, C.J., Cooper, S.J., Raymond, K.N., 1979. J. Am. Chem. Soc. 101, 599.
Caulder, D.L., Raymond, K.N., 1997. Angew. Chem. Int. Ed. Engl. 36, 1440.
Caulder, D.L., Raymond, K.N., 1999. Acc. Chem. Res. 32, 975.
Chapman, R.D., Loda, R.T., Riehl, J.P., Schwartz, R.W., 1984. Inorg. Chem. 23, 1652.
Chapon, D., Husson, C., Delangle, P., Lebrun, C., Vottéro, P.J.A., 2001. J. Alloys Compd. 323–324, 128.
Chapon, D., Delangle, P., Lebrun, C., 2002. J. Chem. Soc., Dalton Trans. 68.
Charbonnière, L.J., Hildebrandt, N., 2008. Eur. J. Inorg. Chem. 3241.
Charbonnière, L.J., Williams, A.F., Frey, U., Merbach, A.E., Kamalaprija, P., Schaad, O., 1997. J. Am. Chem. Soc. 119, 2488.
Chauvin, A.-S., Tripier, R., Bünzli, J.-C.G., 2001. Tetrahedron Lett. 42, 3089.
Chauvin, A.-S., Gumy, F., Imbert, D., Bünzli, J.-C.G., 2004. Spectrosc. Lett. 37, 517 erratum 2007, 40, 193.
Chauvin, A.-S., Comby, S., Song, B., Vandevyver, C.D.B., Thomas, F., Bünzli, J.-C.G., 2007. Chem. Eur. J. 13, 9515.
Chauvin, A.-S., Comby, S., Song, B., Vandevyver, C.D.B., Bünzli, J.-C.G., 2008. Chem. Eur. J. 14, 1726.
Chen, X.-Y., Bretonnière, Y., Pécaut, J., Imbert, D., Bünzli, J.-C.G., Mazzanti, M., 2007. Inorg. Chem. 46, 625.
Chen, Z., Zhao, B., Zhang, Y., Shi, W., Cheng, P., 2008. Cryst. Growth Des. 8, 2291.
Choppin, G.R., 1989. Chemical properties of the rare earth elements. In: Bünzli, J.-C.G., Choppin, G.R. (Eds.), Lanthanide Probes in Life, Chemical and Earth Sciences. Elsevier, Amsterdam, pp. 1–41 (Chapter 1).
Choppin, G.R., Wang, Z.M., 1997. Inorg. Chem. 36, 249.
Comby, S., 2008. Ph.D.Dissertation No. 4052, École Polytechnique Fédérale de Lausanne. p. II-39.
Comby, S., Bünzli, J.-C.G., 2007. Lanthanide near-infrared luminescence in molecular probes and devices. In: Gschneidner Jr., K.A., Pecharsky, V., Bünzli, J.-C.G. (Eds.), Handbook on the Physics and Chemistry of Rare Earths, vol. 37. Elsevier Science, Amsterdam, pp. 217–470 (Chapter 235).
Comuzzi, C., Di Bernardo, P., Portanova, R., Tolazzi, M., Zanonato, P.L., 2002. Polyhedron 21, 1385.
Connally, R.E., Piper, J.A., 2008. Ann. NY Acad. Sci. 1130, 106.
Constable, E.C., 1992. Tetrahedron 48, 10013.
Constable, E.C., 1994. Prog. Inorg. Chem. 42, 67.
Constable, E.C., 1996. Atwood, J.L., Davies, J.E.D., MacNicol, D.D., Vögtle, F. (Eds.), Comprehensive Supramolecular Chemistry. Pergamon, Oxford (Chapter 6).
Constable, E.C., Ward, M.D., Tocher, D.A., 1991. J. Chem. Soc., Dalton Trans. 1675.
Costes, J.-P., Dahan, F., Wernsdorfer, W., 2006. Inorg. Chem. 45, 5.
Cotton, S., 2006. Lanthanide and Actinide Chemistry. John Wiley & Sons, Chichester.
D'Aléo, A., Pompidor, G., Elena, B., Vicat, J., Baldeck, P.L., Toupet, L., Kahn, R., Andraud, C., Maury, O., 2007. ChemPhysChem. 8, 2125.
D'Aléo, A., Picot, A., Baldeck, P., Andraud, C., Maury, O., 2008a. Inorg. Chem. 47, 10269.

D'Aléo, A., Picot, A., Beeby, A., Williams, J.A.G., Le Guennic, B., Andraud, C., Maury, O., 2008b. Inorg. Chem. 47, 10258.
Dalla Favera, N., Hamacek, J., Borkovec, M., Jeannerat, D., Ercolani, G., Piguet, C., 2007. Inorg. Chem. 46, 9312.
Dalla Favera, N., Hamacek, J., Borkovec, M., Jeannerat, D., Gumy, F., Bünzli, J.-C.G., Ercolani, C., Piguet, C., 2008. Chem. Eur. J. 14, 2994.
Dehnicke, K., Greiner, A., 2003. Angew. Chem. Int. Ed. Engl. 42, 1340.
Deiters, E., Song, B., Chauvin, A.-S., Vandevyver, C.D.B., Bünzli, J.-C.G., 2008. New J. Chem. 32, 1140.
Deiters, E., Song, B., Chauvin, A.-S., Vandevyver, C.D.B., Gumy, F., Bünzli, J.-C.G., 2009. Chem. Eur. J. 15, 895.
Denk, W., Strickler, J.H., Webb, W.W., 1990. Science 248, 73.
de Sá, G.F., Malta, O.L., Donega, C.D., Simas, A.M., Longo, R.L., Santa-Cruz, P.A., da Silva, E. F., 2000. Coord. Chem. Rev. 196, 165.
Dexter, D.L., 1953. J. Chem. Phys. 21, 836.
Di Bernardo, P., Zanonato, P.L., Melchior, M., Portanova, R., Tolazzi, M., Choppin, G., Wang, Z., 2008. Inorg. Chem. 47, 1155.
Do, K., Muller, F., Muller, G., 2008. J. Phys. Chem. A 112, 6789.
Dong, Y.-B., Wang, P., Ma, J.-P., Zhao, X.-X., Wang, H.-Y., Tang, B., Huang, R.-Q., 2007. J. Am. Chem. Soc. 129, 4872.
Durham, D.A., Frost, G.H., Hart, F.A., 1969. J. Inorg. Nucl. Chem. 31, 833.
Edder, C., Piguet, C., Bünzli, J.-C.G., Hopfgartner, G., 1997. J. Chem. Soc., Dalton Trans. 4657.
Edder, C., Piguet, C., Bernardinelli, G., Mareda, J., Bochet, C., Bünzli, J.-C.G., Hopfgartner, G., 2000. Inorg. Chem. 39, 5059.
Edder, C., Piguet, C., Bünzli, J.-C.G., Hopfgartner, G., 2001. Chem. Eur. J. 7, 3014.
Elhabiri, M., Albrecht-Gary, A.-M., 2008. Coord. Chem. Rev. 252, 1079.
Elhabiri, M., Scopelliti, R., Bünzli, J.-C.G., Piguet, C., 1999. J. Am. Chem. Soc. 121, 10747.
Elhabiri, M., Hamacek, J., Bünzli, J.-C.G., Albrecht-Gary, A.-M., 2004a. Eur. J. Inorg. Chem. 51.
Elhabiri, M., Hamacek, J., Humbert, N., Bünzli, J.-C.G., Albrecht-Gary, A.-M., 2004b. New J. Chem. 28, 1096.
Eliseeva, S.V., Ryazanov, M., Gumy, F., Troyanov, S.I., Lepnev, L.S., Bünzli, J.-C.G., Kuzmina, N.P., 2006. Eur. J. Inorg. Chem. 4809.
Ercolani, G., 2003. J. Am. Chem. Soc. 125, 16097.
Ercolani, G., 2006. Struct. Bond. 121, 167.
Ercolani, G., Piguet, C., Borkovec, M., Hamacek, J.J., 2007. Phys. Chem. B 111, 12195.
Evans, W.J., 2007. Inorg. Chem. 46, 3435.
Fatin-Rouge, N., Blanc, S., Leize, E., van Dorsselaer, A., Baret, P., Pierre, J.-L., Albrecht-Gary, A.-M., 2000. Inorg. Chem. 39, 5771.
Fatin-Rouge, N., Blanc, S., Pfeil, A., Rigault, A., Albrecht-Gary, A.-M., Lehn, J.-M., 2001. Helv. Chim. Acta 84, 1694.
Floquet, S., Ouali, N., Bocquet, B., Bernardinelli, G., Imbert, D., Bünzli, J.-C.G., Hopfgartner, C., Piguet, C., 2003. Chem. Eur. J. 9, 1860.
Floquet, S., Borkovec, M., Bernardinelli, G., Pinto, A., Leuthold, L.-A., Hopfgartner, G., Imbert, D., Bünzli, J.-C.G., Piguet, C., 2004. Chem. Eur. J. 10, 1091.
Flory, P.J., Suter, U.W., Mutter, M., 1976. J. Am. Chem. Soc. 98, 5733.
Förster, T., 1960. Burton, M., Kirby-Smith, J.S., Magee, L.L. (Eds.), Comparative Effects of Radiation. John Wiley & Sons, New York, p. 300.
Frey, S.T., Horrocks Jr., W.deW., 1995. Inorg. Chim. Acta 229, 383.
Frias, J.C., Bobba, G., Cann, M.J., Hutchison, C.J., Parker, D., 2003. Org. Biomol. Chem. 1, 905.
Frost, G.H., Hart, F.A., Hursthouse, M.B., 1969. J. Chem. Soc., Chem. Commun. 1421.
Fujita, M., Tominaga, M., Hori, A., Therrien, B., 2005. Acc. Chem. Res. 38, 371.
Fyles, T.M., Tong, C.C., 2007. New J. Chem. 31, 296.

Gargano, J.M., Ngo, T., Kim, J.Y., Acheson, D.W.K., Lees, W.J., 2001. J. Am. Chem. Soc. 123, 12909.
Garrett, T.M., Koert, U., Lehn, J.-M., 1992. Phys. Org. Chem. 5, 529.
Gassner, A.-L., Duhot, C., Bünzli, J.-C.G., Chauvin, A.-S., 2008. Inorg. Chem. 47, 7802.
Gawryszewska, P., Legendziewicz, J., Ciunik, Z., Esfandiari, N., Muller, G., Piguet, C., Cantuel, J.P., Riehl, J.P., 2006. Chirality 18, 406 and references therein.
Gonçalves e Silva, F.R., Longo, R.L., Malta, O.L., Piguet, C., Bünzli, J.-C.G., 2000. Phys. Chem. Chem. Phys. 2, 5400.
Gonçalves e Silva, F.R., Malta, O.L., Reinhard, C., Güdel, H.U., Piguet, C., Moser, J.E., Bünzli, J.-C.G., 2002. J. Phys. Chem. A 106, 1670.
Goodgame, D.M.L., Hill, S.P.W., Williams, D.J., 1993. J. Chem. Soc., Chem. Commun. 1019.
Görller-Walrand, C., Binnemans, K., 1996. Rationalization of crystal field parameters. In: Gschneidner, K.A., Eyring, L. (Eds.), Handbook on the Physics and Chemistry of Rare Earths, vol. 23. Elsevier Science, Amsterdam, pp. 121–283.
Görller-Walrand, C., Binnemans, K., 1998. Spectral intensities of f–f transitions. In: Gschneidner, K.A., Eyring, L. (Eds.), Handbook on the Physics and Chemistry of Rare Earths, vol. 25. Elsevier Science, Amsterdam, pp. 101–264.
Greenwald, M., Wessely, D., Goldberg, I., Cohen, Y., 1999. New J. Chem. 337.
Grenthe, I., 1961. J. Am. Chem. Soc. 83, 360.
Gu, X., Xue, D., 2006. Inorg. Chem. 45, 9257.
Guillaumont, D., Bazin, H., Benech, J.M., Boyer, M., Mathis, G., 2007. ChemPhysChem. 8, 480.
Hamacek, J., Piguet, C.J., 2006. Phys. Chem. B 110, 7783.
Hamacek, J., Blanc, S., Elhabiri, M., Leize, E., van Dorsselaer, A., Piguet, C., Albrecht-Gary, A.-M., 2003. J. Am. Chem. Soc. 125, 1541.
Hamacek, J., Borkovec, M., Piguet, C., 2005a. Chem. Eur. J. 11, 5217.
Hamacek, J., Borkovec, M., Piguet, C., 2005b. Chem. Eur. J. 11, 5227.
Hamacek, J., Borkovec, M., Piguet, C., 2006. Dalton Trans. 1473.
Hamacek, J., Bernardinelli, G., Filinchik, Y., 2008. Eur. J. Inorg. Chem. 14, 2994.
Hannon, M.J., Painting, C.L., Jackson, A., Hamblin, J., Errington, W., 1997. Chem. Commun. 1807.
Hannon, M.J., Moreno, V., Prieto, M.J., Moldrheim, E., Sletten, E., Meistermann, I., Isaac, C.J., Sanders, K.J., Rodger, A., 2001. Angew. Chem. Int. Ed. Engl. 40, 880.
Harris, C.M., McKenzie, E.D., 1969. J. Chem. Soc. A 746.
Harrowfield, J.M., Kim, Y., Skelton, B.W., White, A.H., 1995. Aust. J. Chem. 48, 807 and references therein.
Hasenknopf, B., Hall, J., Lehn, J.-M., Balzani, V., Credi, A., Campagna, S., 1996. New J. Chem. 20, 725.
He, C., Lin, Z., He, Z., Duan, C., Xu, C., Wang, Z., Yan, C., 2008. Angew. Chem. Int. Ed. Engl. 47, 877.
Hendersen, B., Imbusch, G.F., 1989. Optical Spectroscopy of Inorganic Solids. Clarendon Press, Oxford.
Herrera, J.-M., Pope, S.J.A., Adams, H., Faulkner, S., Ward, M.D., 2006a. Inorg. Chem. 45, 3895.
Herrera, J.-M., Ward, M.D., Adams, H., Pope, S.J.A., Faulkner, S., 2006b. Chem. Commun. 1851.
Hill, A.V., 1910. J. Physiol. (London) 4, 40.
Hopfgartner, G., Piguet, C., Henion, J.D., 1994. J. Am. Soc. Mass Spectrom. 5, 748.
Hopkins, T.A., Bolender, J.P., Metcalf, D.H., Richardson, F.S., 1996. Inorg. Chem. 35, 5356.
Huang, Y., Wu, B., Yuan, D., Xu, Y., Jiang, F., Hong, M., 2007. Inorg. Chem. 46, 1171.
Huck, W.T.S., Bowden, N., Onck, P., Pardoen, T., Hutchinson, J.W., Whitesides, G.M., 2000. Langmuir 16, 3497.
Huskowska, E., Riehl, J.P., 1995. Inorg. Chem. 34, 5615 and references therein.

Hutin, M., Schalley, C.A., Bernardinelli, G., Nitschke, J.R., 2006. Chem. Eur. J. 12, 4069.
Imbert, D., Cantuel, M., Bünzli, J.-C.G., Bernardinelli, G., Piguet, C., 2003. J. Am. Chem. Soc. 125, 15698.
Jacobson, H., Stockmayer, W.H., 1950. J. Chem. Phys. 18, 1600.
Jencks, W.P., 1981. Proc. Natl. Acad. Sci. USA 78, 4046.
Jensen, B.S., 1959. Acta Chem. Scand. 13, 1668.
Jensen, T.B., Scopelliti, R., Bünzli, J.-C.G., 2006. Inorg. Chem. 45, 7806.
Jensen, T.B., Scopelliti, R., Bünzli, J.-C.G., 2007. Chem. Eur. J. 13, 8404.
Jensen, T.B., Scopelliti, R., Bünzli, J.-C.G., 2008. Dalton Trans. 1027.
Jiang, J.-J., Zheng, S.-R., Liu, Y., Pan, M., Wang, W., Su, C.-Y., 2008. Inorg. Chem. 47, 10692.
Jocher, C.J., Moore, E.G., Xu, J., Avedano, S., Botta, M., Aime, S., Raymond, K.N., 2007. Inorg. Chem. 46, 9182.
Kahn, O., Kodjovi, E., 1999. Philos. Trans. R. Soc. Lond. A 354, 359.
Kahwa, I.A.K., Folkes, S., Williams, D.J., Ley, S.V., O'Mahoney, C.A., McPherson, G.L., 1989. J. Chem. Soc., Chem. Commun. 1531.
Ke, H.Y.D., Birnbaum, E.R., Darnall, D.W., Jackson, P.J., Rayson, G.D., 1992. Appl. Spectrosc. 46, 479.
Kleinerman, M., 1969. J. Chem. Phys. 51, 2370.
Koeller, S., Bernardinelli, G., Bocquet, B., Piguet, C., 2003a. Chem. Eur. J. 9, 1062.
Koeller, S., Bernardinelli, G., Piguet, C., 2003b. Dalton Trans. 2395.
Koeller, S., Bernardinelli, G., Piguet, C., 2006. C. R. Chimie 9, 1158.
Koert, U., Harding, M.M., Lehn, J.-M., 1990. Nature 346, 339.
Koper, G., Borkovec, M., 2001. J. Phys. Chem. B 105, 6666.
Krämer, R., Lehn, J.-M., Marquis-Rigault, A., 1993. Proc. Natl. Acad. Sci. USA 90, 5394.
Krämer, R., Fritsky, I.O., Pritzkow, H., Kovbasyuk, L.A., 2002. J. Chem. Soc., Dalton Trans. 1307.
Kröhnke, F., 1963. Angew. Chem. Int. Ed. 2, 225.
Kuhn, W., 1934. Kolloid Z. 68, 2.
Lakowicz, J.R., 2006. Principles of Fluorescence Spectroscopy, 3rd ed Springer-Verlag, New York.
Lama, M., Mamula, O., Kottas, G.S., Rizzo, F., De Cola, L., Nakamura, A., Kuroda, R., Stoeckli-Evans, H., 2007. Chem. Eur. J. 13, 7358.
Lama, M., Mamula, O., Kottas, G.S., de Cola, L., Stoeckli-Evans, H., Shoa, S., 2008. Inorg. Chem. doi:10.1021/ic7021006 (published on the web, December 12, 2008).
Lamture, J.B., Wensel, T.G., 1995. Bioconj. Chem. 6, 88.
Lamture, J.B., Zhou, Z.H., Kumar, A.S., Wensel, T.G., 1995. Inorg. Chem. 34, 864.
Latva, M., Takalo, H., Mukkala, V.M., Matachescu, C., Rodriguez-Ubis, J.-C., Kankare, J., 1997. J. Lumin. 75, 149.
Lawrence, D.S., Jiang, T., Levett, M., 1995. Chem. Rev. 95, 2229.
Lazarides, T., Sykes, D., Faulkner, S., Barbieri, A., Ward, M.D., 2008. Chem. Eur. J. 14, 9389.
Le Borgne, T., Bénech, J.-M., Floquet, S., Bernardinelli, G., Aliprandini, C., Bettens, P., Piguet, C., 2003. Dalton Trans. 3856.
Le Borgne, T., Altmann, P., André, N., Bünzli, J.-C.G., Bernardinelli, G., Morgantini, P.-Y., Weber, C., Piguet, C., 2004. Dalton Trans. 723.
Lehn, J.-M., 1988. Angew. Chem. Int. Ed. Engl. 27, 89.
Lehn, J.-M., 1995. Supramolecular Chemistry, Concepts and Perspectives. VCH, Weinheim.
Lehn, J.-M., 1999. Supramolecular Chemistry/Science: Some Conjectures and Perspectives. Kluwer Academic Publishers, Dordrecht.
Lehn, J.-M., 2007. Chem. Soc. Rev. 36, 151.
Lehn, J.-M., Eliseev, A.V., 2001. Science 291, 2331.
Lehn, J.-M., Rigault, A., 1988. Angew. Chem. Int. Ed. Engl. 27, 1095.

Lehn, J.-M., Sauvage, J.-P., Simon, J., Ziessel, R., Piccinni-Leopardi, C., Germain, G., Declerq, J.-P., van Meersche, M., 1983. Nouv. J. Chimie 17, 413.
Lehn, J.-M., Rigault, A., Siegel, J., Harrowfield, J., Chevrier, B., Moras, D., 1987. Proc. Natl. Acad. Sci. USA 84, 2565.
Leininger, S., Olenyuk, B., Stang, P.J., 2000. Chem. Rev. 100, 853.
Leonard, J.P., Jensen, P., McCabe, T., O'Brien, J.E., Peacock, R.D., Kruger, P.E., Gunnlaugsson, T., 2007. J. Am. Chem. Soc. 129, 10986.
Lessmann, J.L., Horrocks Jr., W.W., 2000. Inorg. Chem. 39, 3114.
Li, W., Wang, X.L., Song, X.Y., Li, L.C., Liao, D.Z., Jiang, Z.H., 2008. J. Mol. Struct. 885, 1.
Loukova, G.V., Huhn, W., Vasiliev, V.P., Smirnov, V.A., 2007. J. Phys. Chem. A 111, 4117.
Lukin, O., Vögtle, F., 2005. Angew. Chem. Int. Ed. Engl. 44, 1456.
Malta, O.L., 1997. J. Lumin. 71, 229.
Mammen, M., Choi, S.-K., Whitesides, G.M., 1998. Angew. Chem. Int. Ed. Engl. 37, 2754.
Mamula, O., Lama, M., Telfer, S.G., Nakamura, A., Kuroda, R., Stoeckli-Evans, H., Scopelliti, R., 2005. Angew. Chem. Int. Ed. Engl. 44, 2527.
Mamula, O., Lama, M., Stoeckli-Evans, H., Shova, S., 2006. Angew. Chem. Int. Ed. 45, 4940.
Manning, H.C., Goebbel, T., Thompson, R.C., Price, R.R., Lee, H., Bornhop, D.J., 2004. Bioconj. Chem. 15, 1488.
Manning, H.C., Smith, S.M., Sexton, M., Haviland, S., Bai, M.F., Cederquist, K., Stella, N., Bornhop, D., 2006. J. Bioconjugate Chem. 17, 735.
Marquis-Rigault, A., Dupont-Gervais, A., Van Dorsselaer, A., Lehn, J.-M., 1996. Chem. Eur. J. 3, 1395.
Martin, N., Bünzli, J.-C.G., McKee, V., Piguet, C., Hopfgartner, G., 1998. Inorg. Chem. 37, 577.
Martin, L.J., Hahnke, M.J., Nitz, M., Wohnert, J., Silvaggi, N.R., Allen, K.N., Schwalbe, H., Imperiali, B., 2007. J. Am. Chem. Soc. 129, 7106.
Matthews, C.J., Onions, S.T., Morata, G., Davis, L.J., Heath, S.L., Price, D.J., 2003. Angew. Chem. 115, 3274.
Maurizot, V., Linti, G., Huc, I., 2004. Chem. Commun. 924.
McKenzie, B.M., Miller, A.K., Wotjecki, R.J., Johnson, J.C., Burke, K.A., Tzeng, K.A., Mather, P.T., Rowan, S.J., 2008. Tetrahedron 64, 8488.
McMorran, D.A., Steel, P.J., 1998. Angew. Chem. Int. Ed. Engl. 37, 3295.
Meskers, S.C.J., Dekkers, H.P.J.M., 2001. J. Phys. Chem. A 105, 4589 and references therein.
Metcalf, D.H., Stewart, J.M.M., Snyder, S.W., Grisham, C.M., Richardson, F.S., 1992. Inorg. Chem. 31, 2445.
Meurer, K.P., Vögtle, F., 1985. Top. Curr. Chem. 127, 1.
Meyer, M., Kersting, B., Powers, R.E., Raymond, K.N., 1997. Inorg. Chem. 36, 5179.
Mitsunobu, O., Yamada, Y., 1967. Bull. Chem. Soc. Jpn. 40, 2380.
Moret, E., Nicolo, F., Bünzli, J.-C.G., Chapuis, G., 1991. J. Less-Common Met. 171, 273.
Motekaitis, R.J., Martell, A.E., Hancock, R.A., 1994. Coord. Chem. Rev. 133, 39.
Mulder, A., Huskens, J., Reinhoudt, D.N., 2004. Org. Biomol. Chem. 2, 3409.
Muller, G., Bünzli, J.-C.G., Schenk, K.J., Piguet, C., Hopfgartner, G., 2001a. Inorg. Chem. 40, 2642.
Muller, G., Schmidt, B., Jiricek, J., Hopfgartner, G., Riehl, J.P., Bünzli, J.-C.G., Piguet, C., 2001b. J. Chem. Soc., Dalton Trans. 2655.
Muller, G., Bünzli, J.-C.G., Riehl, J.P., Suhr, D., von Zelewsky, A., Mürner, H.-R., 2002a. Chem. Commun. 1522.
Muller, G., Riehl, J.P., Schenk, K.J., Hopfgartner, G., Piguet, C., Bünzli, J.-C.G., 2002b. Eur. J. Inorg. Chem. 3101.
Muller, G., Maupin, C.L., Riehl, J.P., Birkedal, H., Piguet, C., Bünzli, J.-C.G., 2003. Eur. J. Inorg. Chem. 4065.
Mürner, H.-R., Chassat, E., Thummel, R.P., Bünzli, J.-C.G., 2000. J. Chem. Soc., Dalton Trans. 2809.

Nasso, I., Galaup, C., Havas, F., Tisnes, P., Picard, C., Laurent, S., VanderElst, L., Muller, R.N., 2005. Inorg. Chem. 44, 8293.
Nielson, C.W., Koster, G.F., 1963. Spectroscopic Coefficients for p^n, d^n, and f^n Configurations. MIT Press, Cambridge.
Nishioka, T., Fukui, K., Matsumoto, K., 2007. Lanthanide chelates as luminescent labels in biomedical analyses. In: Gschneidner Jr., K.A., Pecharsky, V., Bünzli, J.-C.G. (Eds.), Handbook on the Physics and Chemistry of Rare Earths. Elsevier Science B.V., Amsterdam, p. 171ff (Chapter 234).
Novitchi, G., Costes, J.-P., Tuchagues, J.-P., Vendier, L., Wernsdorfer, W., 2008. New J. Chem. 32, 197.
Orpen, A.G., Brammer, L., Allen, F.H., Kennard, O., Watson, D.G., Taylor, R., 1989. J. Chem. Soc., Dalton Trans. S1.
Ouali, N., Bocquet, B., Rigault, S., Morgantini, P.-Y., Weber, J., Piguet, C., 2002. Inorg. Chem. 41, 1436.
Ouali, N., Rivera, J.-P., Morgantini, P.-Y., Weber, J., Piguet, C., 2003. J. Chem. Soc., Dalton Trans. 1251.
Ouali, N., Rivera, J.-P., Chapon, D., Delangle, P., Piguet, C., 2004. Inorg. Chem. 43, 1517.
Pandya, S., Yu, J.H., Parker, D., 2006. Dalton Trans. 2757.
Parac-Vogt, T.N., Binnemans, K., Görller-Walrand, C., 2002. J. Chem. Soc., Dalton Trans. 1602.
Parker, D., 2004. Chem. Soc. Rev. 33, 156.
Parker, D., Dickins, R.S., Puschmann, H., Crossland, C., Howard, J.A.K., 2002. Chem. Rev. 102, 1977.
Pauling, L., Corey, R.B., 1951a. Proc. Natl. Acad. Sci. USA 37, 235.
Pauling, L., Corey, R.B., 1951b. Proc. Natl. Acad. Sci. USA 37, 241.
Pauling, L., Corey, R.B., 1951c. Proc. Natl. Acad. Sci. USA 37, 251.
Pauling, L., Corey, R.B., 1951d. Proc. Natl. Acad. Sci. USA 37, 256.
Pauling, L., Corey, R.B., 1951e. Proc. Natl. Acad. Sci. USA 37, 261.
Pauling, L., Corey, R.B., 1951f. Proc. Natl. Acad. Sci. USA 37, 272.
Pauling, L., Corey, R.B., 1951g. Proc. Natl. Acad. Sci. USA 37, 282.
Perlmutter-Hayman, B., 1986. Acc. Chem. Res. 19, 90.
Petoud, S., Bünzli, J.-C.G., Renaud, F., Piguet, C., Schenk, K.J., Hopfgartner, G., 1997a. Inorg. Chem. 36, 5750.
Petoud, S., Bünzli, J.-C.G., Schenk, K.J., Piguet, C., 1997b. Inorg. Chem. 36, 1345.
Petoud, S., Bünzli, J.-C.G., Piguet, C., Xiang, Q., Thummel, R., 1999. J. Lumin. 82, 69.
Petoud, S., Cohen, S.M., Bünzli, J.-C.G., Raymond, K.N., 2003. J. Am. Chem. Soc. 125, 13324.
Pfeil, A., Lehn, J.-M., 1992. J. Chem. Soc., Chem. Commun. 838.
Phillips, M.A., 1928. J. Chem. Soc. 2393.
Phimphivong, S., Saavedra, S.S., 1998. Bioconj. Chem. 9, 350.
Picard, C., Geum, N., Nasso, I., Mestres, B., Tisnes, P., Laurent, S., Muller, R.N., Vander Elst, L., 2006. Bioorg. Med. Chem. Lett. 16, 5309.
Picot, A., Malvolti, F., Le Guennic, B., Baldeck, P.L., Williams, J.A.G., Andraud, C., Maury, O., 2007. Inorg. Chem. 46, 2659.
Picot, A., D'Aléo, A., Baldeck, P.L., Grichine, A., Duperray, A., Andraud, C., Maury, O., 2008a. J. Am. Chem. Soc. 130, 1532.
Picot, A., Feuvrie, C., Barsu, C., Malvolti, F., Le Guennic, B., Le Bozec, H., Andraud, C., Toupet, O., Maury, O., 2008b. Tetrahedron 64, 399.
Pierre, V.C., Botta, M., Aime, S., Raymond, K.N., 2006. J. Am. Chem. Soc. 128, 9272.
Piguet, C., 1996. Chimia 50, 144.
Piguet, C.J., 1999. Incl. Phen. Macrocycl. Chem. 34, 361.
Piguet, C., Bünzli, J.-C.G., 1996. Eur. J. Inorg. Chem. 33, 165.
Piguet, C., Bünzli, J.-C.G., 1998. Chimia 52, 579.

Piguet, C., Bünzli, J.-C.G., 1999. Chem. Soc. Rev. 28, 347.
Piguet, C., Geraldes, C.F.G.C., 2003. Paramagnetic NMR lanthanide induced shifts for extracting solution structures. In: Gschneidner Jr., K.A., Bünzli, J.-C.G., Pecharsky, V.K. (Eds.), Handbook on the Physics and Chemistry of Rare Earths, vol. 33. Elsevier Science, Amsterdam, pp. 353–463.
Piguet, C., Bernardinelli, G., Williams, A.F., 1989a. Inorg. Chem. 28, 2920.
Piguet, C., Bocquet, B., Müller, E., Williams, A.F., 1989b. Helv. Chim. Acta 72, 323.
Piguet, C., Bernardinelli, G., Williams, A.F., 1992a. Angew. Chem. Int. Ed. Engl. 31, 1624.
Piguet, C., Williams, A.F., Bernardinelli, G., Moret, E., Bünzli, J.-C.G., 1992b. Helv. Chim. Acta 75, 1697.
Piguet, C., Bochet, C.G., Williams, A.F., 1993a. Helv. Chim. Acta 76, 372.
Piguet, C., Bünzli, J.-C.G., Bernardinelli, G., Hopfgartner, G., Williams, A.F., 1993b. J. Am. Chem. Soc. 115, 8197.
Piguet, C., Bünzli, J.-C.G., Bernardinelli, G., Williams, A.F., 1993c. Inorg. Chem. 32, 4139.
Piguet, C., Bocquet, B., Hopfgartner, G., 1994. Helv. Chim. Acta 77, 931.
Piguet, C., Bernardinelli, G., Bünzli, J.-C.G., Petoud, S., Hopfgartner, G., 1995a. J. Chem. Soc., Chem. Commun. 2575.
Piguet, C., Bünzli, J.-C.G., Bernardinelli, G., Bochet, C.G., Froidevaux, P., 1995b. J. Chem. Soc., Dalton Trans. 83.
Piguet, C., Hopfgartner, G., Williams, A.F., Bünzli, J.-C.G., 1995c. J. Chem. Soc., Chem. Commun. 491.
Piguet, C., Rivara-Minten, E., Hopfgartner, G., Bünzli, J.-C.G., 1995d. Helv. Chim. Acta 1541.
Piguet, C., Rivara-Minten, E., Hopfgartner, G., Bünzli, J.-C.G., 1995e. Helv. Chim. Acta 1651.
Piguet, C., Bünzli, J.-C.G., Bernardinelli, G., Hopfgartner, G., Petoud, S., Schaad, O., 1996. J. Am. Chem. Soc. 118, 6681.
Piguet, C., Bernardinelli, G., Hopfgartner, G., 1997a. Chem. Rev. 97, 2005.
Piguet, C., Rivara-Minten, E., Bernardinelli, G., Bünzli, J.-C.G., Hopfgartner, G., 1997b. J. Chem. Soc., Dalton Trans. 421.
Piguet, C., Edder, C., Rigault, S., Bernardinelli, G., Bünzli, J.-C.G., Hopfgartner, G., 2000. J. Chem. Soc., Dalton Trans. 3999.
Piguet, C., Borkovec, M., Hamacek, J., Zeckert, K., 2005. Coord. Chem. Rev. 249, 705.
Platas, C., Avecilla, F., de Bas, A., Geraldes, C.F.G.C., Rodriguez-Blas, T., Adams, H., Mahia, J., 1999. Inorg. Chem. 38, 3190.
Platas-Iglesias, C., Elhabiri, M., Hollenstein, M., Bünzli, J.-C.G., Piguet, C., 2000. J. Chem. Soc., Dalton Trans. 2031.
Platas-Iglesias, C., Piguet, C., André, N., Bünzli, J.-C.G., 2001. J. Chem. Soc., Dalton Trans. 3084.
Poole, R.A., Bobba, G., Cann, M.J., Frias, J.C., Parker, D., Peacock, R.D., 2005. Org. Biomol. Chem. 3, 1013.
Poole, R.A., Montgomery, C.P., New, E.J., Congreve, A., Parker, D., Botta, M., 2007. Org. Biomol. Chem. 5, 2055.
Potts, K.T., Keshavarz-K, M., Tham, F.S., Gheysen Raiford, K.A., Arana, C., Abruña, H.D., 1993. Inorg. Chem. 32, 5477.
Puntus, L.N., Zolin, V.F., Puntus, L.N., Zolin, V.F., Kudryashova, V.A., Tsaryuk, V.I., Legendziewicz, P., Gawryszewska, P., Szostak, R., 2002. Phys. Sol. State (Engl. Transl.) 44, 1440.
Puntus, L.N., Chauvin, A.-S., Varbanov, S., Bünzli, J.-C.G., 2007. Eur. J. Inorg. Chem. 2315.
Raitsimiring, A.M., Gunanathan, C., Potapov, A., Efremenko, I., Martin, J.M.L., Milstein, D., Goldfarb, D., 2007. J. Am. Chem. Soc. 129, 14138.
Rapenne, G., Patterson, B.T., Sauvage, J.-P., Keene, F.R., 1999. Chem. Commun. 1853.
Reisfeld, R., Jørgensen, C.K., 1977. Lasers and Excited States of Rare Earths. Springer-Verlag, Berlin.

Renaud, F., Piguet, C., Bernardinelli, G., Bünzli, J.-C.G., Hopfgartner, G., 1997a. Chem. Eur. J. 3, 1646.
Renaud, F., Piguet, C., Bernardinelli, G., Bünzli, J.-C.G., Hopfgartner, G., 1997b. Chem. Eur. J. 3, 1660.
Renaud, F., Piguet, C., Bernardinelli, G., Bünzli, J.-C.G., Hopfgartner, G., 1999. J. Am. Chem. Soc. 121, 9326.
Renaud, F., Decurnex, C., Piguet, C., Hopfgartner, G., 2001. J. Chem. Soc., Dalton Trans. 1863.
Richardson, F.S., Metcalf, D.H., Glover, D.P., 1991. J. Phys. Chem. 95, 6249.
Riehl, J.P., Muller, G., 2005. Circularly polarized luminescence spectroscopy from lanthanide systems. In: Gschneidner Jr., K.A., Pecharsky, V., Bünzli, J.-C.G. (Eds.), Handbook on the Physics and Chemistry of Rare Earths, vol. 34. Elsevier Science, Amsterdam, pp. 289–357 (Chapter 220).
Rigault, S., Piguet, C., 2000. J. Am. Chem. Soc. 122, 9304.
Rigault, S., Piguet, C., Bernardinelli, G., Hopfgartner, G., 1998. Angew. Chem. Int. Ed. Engl. 37, 169.
Rigault, S., Piguet, C., Bünzli, J.-C.G., 2000a. J. Chem. Soc., Dalton Trans. 2045.
Rigault, S., Piguet, C., Bernardinelli, G., Hopfgartner, G., 2000b. J. Chem. Soc., Dalton Trans. 4587.
Riis-Johannessen, T., Dupont, N., Canard, G., Bernardinelli, G., Hauser, A., Piguet, C., 2008. Dalton Trans. 3661.
Riis-Johannessen, T., Dalla Favera, N., Todorova, T.K., Huber, S.M., Gagliardi, L., Piguet, C., 2009. Chem. Eur. J. (in press, DOI 10.1002/chem.200900904).
Rodriguez-Cortias, R., Avecilla, F., Platas-Iglesias, C., Imbert, D., Bünzli, J.-C.G., de Blas, A., Rodiguez-Blas, T., 2002. Inorg. Chem. 41, 5336.
Ronson, T.K., Adams, H., Harding, L.P., Pope, S.J.A., Sykes, D., Faulkner, S., Ward, M.D., 2007. Dalton Trans. 1006.
Ruiz-Martinez, A., Casanova, D., Alvarez, S., 2008. Chem. Eur. J. 14, 1291.
Saalfrank, R.W., Seitz, V., Caulder, D.L., Raymond, K.N., Teicher, M., Stalke, D., 1998. Eur. J. Inorg. Chem. 1313.
Sabbatini, N., Guardigli, M., Manet, I., 1996. Antenna effect in encapsulation complexes of lanthanide ions. In: Gschneidner, K.A., Eyring, L. (Eds.), Handbook on the Physics and Chemistry of Rare Earths, vol. 23. Elsevier Science, Amsterdam, pp. 69–120 (Chapter 154).
Samuel, A.P.S., Moore, E.G., Melchior, M., Xu, J.D., Raymond, K.N., 2008a. Inorg. Chem. 47, 7535.
Samuel, A.P.S., Xu, J., Raymond, K.N., 2008b. Inorg. Chem. 47, 7535.
Sato, S., Wada, M., 1970. Bull. Chem. Soc. Jpn. 43, 1955.
Sayre, A., 1975. Rosalind Franklin and DNA. W.W. Norton and Company, New York.
Scaff, W.L., Dyer, D.L., Mori, K., 1969. J. Bacteriol. 98, 246.
Scarrow, R.C., White, D.L., Raymond, K.N., 1985. J. Am. Chem. Soc. 107, 6540.
Schneider, H.-J., Yatsimirsky, A.K., 2008. Chem. Soc. Rev. 37, 263.
Schoentjes, B., Lehn, J.-M., 1995. Helv. Chim. Acta 78, 1.
Selvin, P.R., 2000. Nat. Struct. Biol. 7, 730.
Semenov, S.N., Rogachev, A.Y., Eliseeva, S.V., Pettinari, C., Marchetti, F., Drozdov, A.A., Troyanov, S.I., 2008. Chem. Commun. 1992.
Semenova, L.I., Sobolev, A.N., Skelton, B.W., White, A.H., 1999. Aust. J. Chem. 52, 519.
Senegas, J.-M., Bernardinelli, G., Imbert, D., Bünzli, J.-C.G., Morgantini, P.-Y., Weber, J., Piguet, C., 2003. Inorg. Chem. 42, 4680.
Senegas, J.-M., Koeller, S., Piguet, C., 2005. Chem. Commun. 2235.
Shannon, R.D., 1976. Acta Crystallogr. Sect. A 32, 751.
Shavaleev, N.M., Scopelliti, R., Gumy, F., Bünzli, J.-C.G., 2008. Inorg. Chem. 47 (19), 9055.
Shen, Q., Hu, J.-Y., Jin, Z.-S., 1990. Zhongguo Xitu Xuebao (J. Chin. Rare Earth Soc.) 8, 359.

Shinoda, S., Miyake, H., Tsukube, H., 2005. Molecular recognition and sensing via rare earth complexes. In: Gschneidner Jr., K.A., Pecharsky, V., Bünzli, J.-C.G. (Eds.), Handbook on the Physics and Chemistry of Rare Earths, vol. 35. Elsevier Science, Amsterdam, pp. 276–331 (Chapter 226).
Siitari, H., Hemmilä, I., Pettersson, K., Lövgren, T., 1983. Nature 301 (5897), 258.
Smith, E.B., 2004. Basic Chemical Thermodynamics, 5th ed Imperial College Press, London p. 31.
Smith, V.C., Lehn, J.-M., 1996. Chem. Commun. 2733.
Song, B., Vandevyver, C.D.B., Chauvin, A.-S., Bünzli, J.-C.G., 2008a. Org. Biomol. Chem. 6, 4125.
Song, B., Vandevyver, C.D.B., Deiters, E., Chauvin, A.-S., Hemmilä, I., Bünzli, J.-C.G., 2008b. Analyst 133, 1749.
Song, X., Zhou, X., Liu, W., Dou, W., Ma, J., Tang, X., Zheng, J., 2008c. Inorg. Chem. doi:10.1021/ic8008267 (published on the web, November 8, 2008).
Sonogashira, K., Tohda, Y., Hagihara, N., 1975. Tetrahedron Lett. 50, 4467.
Steemers, F.J., Verboom, W., Reinhoudt, D.N., Vandertol, E.B., Verhoeven, J.W., 1995. J. Am. Chem. Soc. 117, 9408.
Stoddart, J.F., Philp, D., 1996. Angew. Chem. Int. Ed. Engl. 35, 1154.
Su, X.C., Man, B., Beeren, S., Liang, J., Simonsen, S., Schmitz, C., Huber, T., Messerle, B.A., Otting, G., 2008a. J. Am. Chem. Soc. 130, 10486.
Su, X.C., McAndrew, K., Huber, T., Ottong, G., 2008b. J. Am. Chem. Soc. 130, 1681.
Sugiyarto, K.H., Craig, D.C., Rae, D.A., Goodwin, H.A., 1994. Aust. J. Chem. 47, 869.
Sun, Y.Q., Zhang, J., Yang, G.Y., 2006a. Chem. Commun. 1947.
Sun, Y.Q., Zhang, J., Yang, G.Y., 2006b. Chem. Commun. 4700.
Supkowski, R.M., de Horrocks Jr., W., 2002. Inorg. Chim. Acta 340, 44.
Takalo, H., Mukkala, V.M., Merio, L., Rodriguez-Ubis, J.C., Sedano, R., Jusnes, O., Brunet, E., 1997. Helv. Chim. Acta 80, 372.
Tancrez, N., Feuvrie, C., Ledoux, I., Zyss, J., Toupet, L., Le Bozec, H., Maury, O., 2005. J. Am. Chem. Soc. 127, 13474.
Telfer, S.G., Tajima, N., Kuroda, R., Cantuel, M., Piguet, C., 2004. Inorg. Chem. 43, 5302.
Terazzi, E., Rivera, J.-P., Ouali, N., Piguet, C., 2006. Magn. Reson. Chem. 44, 539.
Terazzi, E., Guénée, L., Bocquet, B., Lemonnier, J.-F., Dalla Favera, N., Piguet, C., 2009. Chem. Eur J. (in press) ; DOI 10.1002/chem.20090226.
Thalladi, V.-R., Schwartz, A., Phend, J.N., Hutchinson, J.W., Whitesides, G.M., 2002. J. Am. Chem. Soc. 124, 9912.
Torelli, S., Delahaye, S., Hauser, A., Bernardinelli, G., Piguet, C., 2004. Chem. Eur. J. 10, 3503.
Torelli, S., Imbert, D., Cantuel, M., Bernardinelli, G., Delahaye, S., Hauser, A., Bünzli, J.-C.G., Piguet, C., 2005. Chem. Eur. J. 11, 3228.
Tripier, R., Hollenstein, M., Elhabiri, M., Chauvin, A.-S., Zucchi, G., Piguet, C., Bünzli, J.-C. G., 2002. Helv. Chim. Acta 85, 1915.
Vandevyver, C.D.B., Chauvin, A.-S., Comby, S., Bünzli, J.-C.G., 2007. Chem. Commun. 1716.
Van Holde, K.E., 1985. Physical Biochemistry, 2nd ed Prentice Hall, Englewood Cliffs, NJ.
Vögtle, F., 1991. Supramolecular Chemistry. John Wiley & Sons, Chichester (Chapter 2).
Walsh, B.M., 2006. Judd–Ofelt theory: Principles and practices. In: Di Bartolo, B. (Ed.), Advances in Spectroscopy for Lasers and Sensing: Part 1. Springer-Verlag, Berlin, pp. 403–433.
Wang, C.-C., Lo, W.-C., Chou, C.-C., Lee, G.-H., Chen, J.-M., Peng, S.-M., 1998. Inorg. Chem. 37, 4059.
Watson, J.D., 1968. The Double Helix. Atheneum, New York.
Watson, J.D., Crick, F.H.C., 1953. Nature 171, 737.
Weissman, S.I., 1942. J. Chem. Phys. 10, 214.
Werts, M.H.V., Jukes, R.T.F., Verhoeven, J.W., 2002. Phys. Chem. Chem. Phys. 4, 1542.

Wilkins, M., 2003. The Third Man of Double Helix: An Autobiography. Oxford University Press, New York.
Williams, A.F., Piguet, C., Bernardinelli, G., 1991. Angew. Chem. Int. Ed. Engl. 30, 1490.
Winnik, M.A., 1981. Chem. Rev. 81, 491.
Wright, J.B., 1951. Chem. Rev. 48, 397.
Xing, Y., Li, Y., Yan, L., Yang, R., 1992. Gaodeng Xuexiao Huaxue Xuebao 13, 14.
Xu, J., Raymond, K.N., 2000. Angew. Chem. Int. Ed. Engl. 39, 2745.
Xu, J., Raymond, K.N., 2006. Angew. Chem. Int. Ed. Engl. 45, 6480.
Yang, L., Yang, R., 1995. Polyhedron 14, 507.
Yu, J.H., Parker, D., Pal, R., Poole, R.A., Cann, M.J., 2006. J. Am. Chem. Soc. 128, 2294.
Yue, Q., Yang, J., Li, G.H., Li, G.D., Chen, J.S., 2006. Inorg. Chem. 45, 4431.
Zeckert, K., Hamacek, J., Rivera, J.-P., Floquet, S., Pinto, A., Borkovec, M., Piguet, C., 2004. J. Am. Chem. Soc. 126, 11589.
Zeckert, K., Hamacek, J., Senegas, J.-M., Dalla-Favera, N., Floquet, S., Bernardinelli, G., Piguet, C., 2005. Angew. Chem. Int. Ed. Engl. 44, 7954.
Zhou, R.S., Cui, X.B., Song, J.F., Xu, X.Y., Xu, J.Q., Wang, T.G., 2008. J. Solid State Chem. 181, 1565.
Zohar, O., Ikeda, M., Shinagawa, H., Inoue, H., Nakamura, H., Elbaum, D., Alkon, D.L., Yoshioka, T., 1998. Biophys. J. 74, 82.
Zong, R., Thummel, R.P., 2005. Inorg. Chem. 44, 5984.

This page intentionally left blank

AUTHOR INDEX

This page intentionally left blank

SUBJECT INDEX